

2

AGARD-CP-390

AGARD-CP-390

AGARD

ADVISORY GROUP FOR AEROSPACE RESEARCH & DEVELOPMENT

7 RUE ANCELLE 92200 NEUILLY SUR SEINE FRANCE

AD-A162 080

AGARD CONFERENCE PROCEEDINGS No.390

Heat Transfer and Cooling in Gas Turbines

DTIC
SELECTED
NOV 27 1985
S D

DTIC FILE COPY

NORTH ATLANTIC TREATY ORGANIZATION



DISTRIBUTION STATEMENT A
Approved for public release
Distribution Unlimited

**DISTRIBUTION AND AVAILABILITY
ON BACK COVER**

85 11 27 002

**Best
Available
Copy**

AGARD-CP-390

NORTH ATLANTIC TREATY ORGANIZATION
ADVISORY GROUP FOR AEROSPACE RESEARCH AND DEVELOPMENT
(ORGANISATION DU TRAITE DE L'ATLANTIQUE NORD)

AGARD Conference Proceedings No.390
HEAT TRANSFER AND COOLING IN GAS TURBINES

Papers presented at the Propulsion and Energetics Panel 65th Symposium, held in Bergen, Norway,
6--10 May 1985.

THE MISSION OF AGARD

The mission of AGARD is to bring together the leading personalities of the NATO nations in the fields of science and technology relating to aerospace for the following purposes:

- Exchanging of scientific and technical information;
- Continuously stimulating advances in the aerospace sciences relevant to strengthening the common defence posture;
- Improving the co-operation among member nations in aerospace research and development;
- Providing scientific and technical advice and assistance to the North Atlantic Military Committee in the field of aerospace research and development;
- Rendering scientific and technical assistance, as requested, to other NATO bodies and to member nations in connection with research and development problems in the aerospace field;
- Providing assistance to member nations for the purpose of increasing their scientific and technical potential;
- Recommending effective ways for the member nations to use their research and development capabilities for the common benefit of the NATO community.

The highest authority within AGARD is the National Delegates Board consisting of officially appointed senior representatives from each member nation. The mission of AGARD is carried out through the Panels which are composed of experts appointed by the National Delegates, the Consultant and Exchange Programme and the Aerospace Applications Studies Programme. The results of AGARD work are reported to the member nations and the NATO Authorities through the AGARD series of publications of which this is one.

Participation in AGARD activities is by invitation only and is normally limited to citizens of the NATO nations.

The content of this publication has been reproduced directly from material supplied by AGARD or the authors.

Published September 1985
Copyright © AGARD 1985
All Rights Reserved

ISBN 92-835-0378-3



Printed by Specialised Printing Services Limited
40 Chigwell Lane, Loughton, Essex IG10 3TZ

RECENT PUBLICATIONS OF THE PROPULSION AND ENERGETICS PANEL

Conference Proceedings

Testing and Measurement Techniques in Heat Transfer and Combustion
AGARD Conference Proceedings No.281, 55th A Meeting, May 1980

Centrifugal Compressors, Flow Phenomena and Performance
AGARD Conference Proceedings No.282, 56th B Meeting, May 1980

Turbine Engine Testing
AGARD Conference Proceedings No.293, 56th Meeting, Sep/October 1980

Helicopter Propulsion Systems
AGARD Conference Proceedings No.302, 57th Meeting, May 1981

Ramjets and Ramrockets for Military Applications
AGARD Conference Proceedings No.307, 58th Meeting, October 1981

Problems in Bearings and Lubrication
AGARD Conference Proceedings No.323, 59th Meeting, May/June 1982

Engine Handling
AGARD Conference Proceedings No.324, 60th Meeting, October 1982

Viscous Effects in Turbomachines
AGARD Conference Proceedings No.351, 61st A Meeting, June 1983

Auxiliary Power Systems
AGARD Conference Proceedings 352, 61st B Meeting, May 1983

Combustion Problems in Turbine Engines
AGARD Conference Proceedings 353, 62nd Meeting, October 1983

Hazard Studies for Solid Propellant Rocket Motors
AGARD Conference Proceedings 367, 63rd A Meeting, May/June 1984

Engine Cyclic Durability by Analysis and Testing
AGARD Conference Proceedings No.368, 63rd B Meeting, May/June 1984

Gears and Power Transmission Systems for Helicopters and Turboprops
AGARD Conference Proceedings No. 369, 64th Meeting October 1984

Heat Transfer and Cooling in Gas Turbines
AGARD Conference Proceedings No.390, 65th Meeting, May 1985

Working Group Reports

Aircraft Fire Safety
AGARD Advisory Report 132, Vol.1 and Vol.2. Results of WG11 (September and November 1979)

Turbulent Transport Phenomena (in English and French)
AGARD Advisory Report 150. Results of WG 09 (February 1980)

Through Flow Calculations in Axial Turbomachines
AGARD Advisory Report 175. Results of WG 12 (October 1981)

Alternative Jet Engine Fuels
AGARD Advisory Report 181, Vol.1 and Vol.2. Results of WG 13 (July 1982)

Suitable Averaging Techniques in Non-Uniform Internal Flows
AGARD Advisory Report 187 (in English and French). Results of WG 14 (June/August 1983)

Producibility and Cost Studies of Aviation Kerosines
AGARD Advisory Report 227. Results of WG 16 (June 1985)

Accession For		
NTIS	CRA&I	<input checked="" type="checkbox"/>
DTIC	TAB	<input type="checkbox"/>
Unannounced		<input type="checkbox"/>
Justification		
By		
Distribution		
Availability Codes		
Dist	Avail and/or Special	
A-1		



Lecture Series

Non-Destructive Inspection Methods for Propulsion Systems and Components
AGARD LS 103 (April 1979)

The Application of Design to Cost and Life Cycle Cost to Aircraft Engines
AGARD LS 107 (May 1980)

Microcomputer Applications in Power and Propulsion Systems
AGARD LS 113 (April 1981)

Aircraft Fire Safety
AGARD LS 123 (June 1982)

Operation and Performance Measurement of Engines in Sea Level Test Facilities
AGARD LS 132 (April 1984)

Ramjet and Ramrocket Propulsion Systems for Missiles
AGARD LS 136 (September 1984)

3-D Computation Techniques Applied to Internal Flows in Propulsion Systems
AGARD LS 140 (June 1985)

Other Publications

Airbreathing Engine Test Facility Register
AGARD AG 269 (July 1981)

THEME

Heat transfer and cooling in gas turbines is one of the crucial fields in the quest for higher performance as well as improved life and reliability. The purpose of this Symposium was to bring together experts from industry, research establishments and universities to discuss fundamental and applied heat transfer problems relevant to gas turbines and to exchange practical experience gained in component and engine development and testing.

The Symposium focussed on turbine blade cooling including the interaction of cooling and aerodynamics. Furthermore, heat transfer in compressors, combustion systems, as well as heat exchangers was covered. Emphasis was also placed on heat transfer modelling, experimental techniques and test facilities.

Le transfert thermique et le refroidissement dans les turbines à gaz constituent l'un des domaines critiques qui caractérisent la recherche de performances supérieures ainsi que d'une longévité et d'une fiabilité accrues. L'objectif du Symposium qui vient de se tenir fut de réunir des experts appartenant à des milieux industriels, à des établissements de recherche et à des universités pour étudier les problèmes de transfert thermique liés aux turbines à gaz tant dans le domaine fondamental que dans celui des applications, et pour procéder à des échanges de vues basés sur l'expérience acquise en matière de développement et d'essais de composants et de moteurs.

Le Symposium a porté tout spécialement sur le refroidissement des aubes de turbine, en tenant compte de l'interaction entre refroidissement et aérodynamique. Il a couvert en outre les problèmes de transfert thermique dans les compresseurs, les systèmes de combustion ainsi que les échangeurs de chaleur. L'accent a été également mis sur la modélisation du transfert thermique, les techniques expérimentales et les installations d'essais.

PROPULSION AND ENERGETICS PANEL

Chairman: Prof. C.Hirsch
Vrije Universiteit Brussel
Dienst Stromingsmechanica
Pleinlaan 2
1050 Brussel
Belgium

Deputy Chairman: Prof. Ir H.Wittenberg
Delft University of Technology
Department of Aerospace Engineering
Kluyverweg 1
2629 HS Delft
Netherlands

PROGRAMME COMMITTEE

Prof. D.K.Hennecke (Chairman)
Technische Hochschule
Petersenstrasse 30
D-6100 Darmstadt
Germany

Prof. F.Breugelmans
Von Kármán Institute for Fluid Dynamics
72 Chaussée de Waterloo
B-1640 Rhode-Saint-Genèse
Belgium

Mr H.I.Bush
Director, Turbine Engine Division
AF Wright Aeronautical Labs/POT
Wright Patterson AFB
OH 45433
USA

Prof. D.Dini
Università degli Studi
Istituto di Macchine
Via Diotisalvi 3
51600 Pisa
Italy

Dr M.Førde
Institute for Aero- and Gas Dynamics
N-7034 Trondheim NTH
Norway

Mr D.L.Martlew
Ministry of Defence (PE)
Royal Aircraft Establishment
Pyestock
Farnborough, Hants GU13 0LS
UK

Prof. M.N.R.Nina
CTAMFUTL
Instituto Superior Tecnico
Avenida Rovisco Pais
1096 Lisboa
Portugal

Mr M.Pianko
Institut de Mécanique des Fluides
5 Boulevard Paul Painlevé
59000 Lille
France

Prof. H.I.H.Saravanamuttoo
Chairman, Mechanical and Aeronautical Engineering
Carleton University
Ottawa, Ontario K1S 5B6
Canada

HOST NATION COORDINATOR

Mr G.Kristofersen
Norwegian Defence Research Est.
P.O. Box 225
N-2007 Kjeller
Norway

PANEL EXECUTIVE

Dr E.Riester
AGARD-NATO
7 rue Ancelle
92200 Neuilly sur Seine
France

ACKNOWLEDGEMENT

The Propulsion and Energetics Panel wishes to express its thanks to the Norwegian National Delegate for the invitation to hold this meeting in Bergen, Norway, and for the facilities and personnel which made the meeting possible.

CONTENTS

	Page
RECENT PUBLICATIONS OF PEP	iii
THEME	v
PROPULSION AND ENERGETICS PANEL	vi
TECHNICAL EVALUATION REPORT by S.Wittig	xi
	Reference
COOLING TECHNIQUES FOR GAS TURBINE AIRFOILS - A SURVEY by D.E.Metzger	1
<u>SESSION I - TURBINE BLADE INTERNAL HEAT TRANSFER</u>	
ROTATING HEAT TRANSFER INVESTIGATIONS ON A MULTIPASS COOLING GEOMETRY by R.J.Clifford	2
LOCAL AND MEAN HEAT TRANSFER ON THE LEADING AND TRAILING SURFACES OF A SQUARE-SECTIONED DUCT ROTATING IN THE ORTHOGONAL-MODE by W.D.Morris and S.P.Haragama	3
PRESSURE DROP AND HEAT TRANSFER CHARACTERISTICS OF CIRCULAR AND OBLONG LOW ASPECT RATIO PIN FINS by S.C.Arora and W.Abdel Messch	4
<u>SESSION II - TURBINE BLADE EXTERNAL HEAT TRANSFER</u>	
EXTERNAL HEAT TRANSFER STUDY ON A HP TURBINE ROTOR BLADE by T.Arts and C.G.Graham	5*
EFFECTS OF WAKES ON THE HEAT TRANSFER IN GAS TURBINE CASCADES by S.Wittig, A.Schulz, H.J.Bauer and K.H.Sill	6
WAKE-PASSING IN A TURBINE ROTOR CASCADE by D.J.Doorly, M.L.Oldfield and C.T.J.Scrivener	7
EFFECT OF HOLE GEOMETRY, WALL CURVATURE AND PRESSURE GRADIENT ON FILM COOLING DOWNSTREAM OF A SINGLE ROW by H.Kruse	8
EFFECTS OF SURFACE ROUGHNESS ON HEAT TRANSFER TO GAS TURBINE BLADES by A.B.Turner, F.H.A.Tarada and F.J.Bayley	9
THE EFFECT OF DENSITY RATIO ON THE FILM-COOLING OF A FLAT PLATE by C.J.P.Forth, P.J.Loftus and T.V.Jones	10
<u>SESSION III - TURBINE COOLING</u>	
Paper 11 withdrawn	
ETUDES DES TRANSFERTS THERMIQUES SUR LES PLATES-FORMES DE DISTRIBUTEUR DE TURBINE AVEC ET SANS FILM DE REFOIDISSEMENT par A.E.Bourguignon	12
SHROUD SEGMENTS FOR UNSHROUDED BLADE TURBINES by R.S.Attwood	13

*Presented in Session VIII

	Reference
ENGINE TESTS ON A COOLED GAS TURBINE STAGE by H.J.Graf	14
HEAT TRANSFER TEST EVALUATION OF THE SHELL-SPAR BLADE COOLING CONCEPT APPLIED TO INDUSTRIAL GAS TURBINES by G.P.Butt and W.Edward North	15
HEAT-FLUX MEASUREMENTS AND ANALYSIS FOR A ROTATING TURBINE STAGE by M.G.Dunn	16

SESSION IV – MODELLING

Paper 17 withdrawn

CALCULATION OF LAMINAR-TURBULENT BOUNDARY LAYER TRANSITION ON TURBINE BLADES by W.Rodi and G.Scheuerer	18
A MODEL FOR CORRELATING FLAT PLATE FILM COOLING EFFECTIVENESS FOR ROWS OF ROUND HOLES by M.R.L'Ecuyer and F.O.Soechting	19
COMPUTATION OF THERMAL RADIATION FOR GAS TURBINE CONDITIONS by M.G.Carvalho, D.F.G.Durão and F.C.Lockwood	20
PREDICTION OF TRANSIENT TEMPERATURES FOR AN AIR-COOLED ROTATING DISC by C.A.Long and J.M.Owen	21

SESSION V – COMBUSTION SYSTEMS

Paper 22 withdrawn

HEAT TRANSFER IN GAS TURBINE COMBUSTORS by B.F.Magnussen	23
EFFECTIVENESS MEASUREMENTS FOR A COOLING FILM DISRUPTED BY A SINGLE JET WITH WALL PLUNGING by B.L.Button	24
ALTERNATE COOLING CONFIGURATIONS FOR GAS TURBINE COMBUSTION SYSTEMS by D.A.Nealy, S.B.Reider and H.C.Mongia	25
FULL COVERAGE IMPINGEMENT HEAT TRANSFER: THE VARIATION IN PITCH TO DIAMETER RATIO AT A CONSTANT GAP by G.E.Andrews, A.A.Asere, C.I.Hussain and M.C.Mkpadi	26
TECHNIQUES DE REFROIDISSEMENT DES CANAUX DE RECHAUFFE DES TURBOREACTEURS par M.Desautly, P.Trouillot et S.Coutor	27

SESSION VI – EXPERIMENTAL TECHNIQUES

THE MEASUREMENT OF LOCAL HEAT TRANSFER COEFFICIENTS IN BLADE COOLING GEOMETRIES by P.T.Ireland and T.V.Jones	28
PYROMETRIE OPTIQUE INFRAROUGE POUR LA MESURE DES TEMPERATURES D'AUBES DE TURBINE par M.Charpenel et J.Wilhem	29
HIGH FREQUENCY RESPONSE HEAT FLUX GAUGE FOR METAL BLADING by A.H.Epstein, G.R.Guenette, R.J.G.Norton and J.Cao Yuzhang	30

	Reference
THE ISENTROPIC LIGHT PISTON ANNULAR CASCADE FACILITY AT RAE PYESTOCK by A.J.Brooks, D.E.Colbourne, E.T.Wedlake, T.V.Jones, M.L.G.Oldfield, D.L.Schultz and P.J.Loftus	31
MEASUREMENTS OF FLUCTUATING GAS TEMPERATURES USING COMPENSATED FINE WIRE THERMOCOUPLES by M.N.R.Nina and G.P.Pita	32
TWO SPOT LASER VELOCIMETER MEASUREMENTS OF VELOCITY AND TURBULENCE INTENSITY IN SHOCK TUBE DRIVEN TURBINE FLOWS by R.B.Rivir, W.C.Elrod and M.G.Dunn	33
INFLUENCE ET MESURE DU JEU EN BOUT D'AUBES DANS LES TURBOMACHINES par J.Paulon	34
<u>SESSION VII – COMPRESSORS/HEAT EXCHANGERS</u>	
SIMULATION NUMERIQUE D'ECOULEMENTS TURBULENTS DANS DES CAVITES ANNULAIRES ENTRE DISQUES FIXES ET MOBILES par D.Dutoya	35
TRANSIENT THERMAL BEHAVIOUR OF A COMPRESSOR ROTOR WITH VENTILATION – TEST RESULTS UNDER SIMULATED ENGINE CONDITIONS by E.Reile, U.Radons and D.K.Hennecke	36
HEAT EXCHANGERS IN REGENERATIVE GAS TURBINE CYCLES by M.N.R.Nina and M.P.N.Aguas	37
INTERET DES ECHANGEURS EN CERAMIQUE POUR TURBINE A GAZ OU TURBOREACTEURS par S.Boudigues et J.Fabri	38
<u>SESSION VIII – INTERACTION</u>	
EFFECT OF FILM COOLING ON THE AERODYNAMIC PERFORMANCE OF A TURBINE CASCADE by O.Köllen and W.Koschel	39
ETUDE EXPERIMENTALE ET THEORIQUE D'UN JET TRIDIMENSIONNEL INTRODUIT DANS L'ECOULEMENT SECONDAIRE D'UNE GAILLE DISTRIBUTRICE DE TURBINE par A.Oavani, C.Ollivier, F.Bario et F.Lebouef	40
AERODYNAMIC EFFECT OF COOLANT EJECTION IN THE REAR PART OF TRANSONIC ROTOR BLADES by F.H.Kost and A.T.Holmes	41
THE BOUNDARY LAYER BEHAVIOUR OF AN ADVANCED GAS TURBINE ROTOR BLADE UNDER THE INFLUENCE OF SIMULATED FILM COOLING by R.Kiock, H.Hoheisel, H.J.Dietrichs and A.T.Holmes	42

TECHNICAL EVALUATION REPORT

by

S. Wittig
Lehrstuhl und Institut für
Thermische Strömungsmaschinen
Universität Karlsruhe
D-7500 Karlsruhe
Federal Republic of Germany

In considering recent developments in engine design it is obvious that the understanding of the heat transfer processes in gas turbines and the advancement of cooling techniques are crucial elements in the quest for higher performance and reduced fuel consumption as well as for improved life and reliability. This Symposium, therefore, was aimed at the discussion and analysis of problems concerning fundamental and applied heat transfer problems. In order to limit the scope of the meeting, heat transfer problems as related to icing, bearings and lubrication etc. were not subjects of the meeting as those topics have been covered individually by similar AGARD meetings.

Induced by the well balanced program, the papers as well as the discussions were directed towards current problems. It was shown that:

- despite recent progress, turbine blade cooling remains a major focus of interest. In particular, questions concerning the internal heat transfer need to be addressed in depth, including the effects of rotation. Furthermore, the influence and aerodynamic performance of coolant ejection require continuing attention,
- with increasing performance requirements, modified and even new technologies will have to be applied for other components also, especially the combustor, the compressor and heat exchangers,
- progress has been made in modelling with successful application of numerical codes for the prediction of at least external boundary layer flows. Problems arise in considering pressure side flow and wake cutting effects,
- sophisticated experimental techniques are of crucial importance for continuing success. The benefits of the utilization of steady flow hot gas experiments and of short duration tunnels were compared. Non-intrusive, optical instrumentation as well as miniaturised fast response gauges were shown to hold the key to further developments.

An increasing acceptance and use of theoretical models by industry was recognized. By including results derived from stationary gas turbines it was shown that -- despite different design philosophies -- measurements on generally larger components of gas turbines yield test results which can be utilized in jet engine development.

There was general agreement between the participants that intensive research efforts on heat transfer processes and cooling beyond the scope of turbine stages are necessary for engine improvement and cost reduction.

1. INTRODUCTION

The development of high performance gas turbines and especially of jet engines has always been -- and continues to be -- dependent on a rise in thermal efficiency and specific thrust primarily due to increasing turbine inlet temperatures and simultaneously raising pressure ratios. Thus, high thermal loads in the engine components of the hot gas passages -- i.e. combustor and turbine -- are observed as well as in the high pressure section of the compressor, a problem of fast growing importance especially when considering transient engine operation. Furthermore, the efficient integration of heat exchangers into smaller regenerative engines is a well recognized problem with far-reaching consequences. Although numerous papers have been published on various aspects of these problems central to gas turbine design, the 65th Symposium on Heat Transfer and Cooling in Gas Turbines, organized by the AGARD Propulsion & Energetics Panel and held May 6-10, 1985 in Bergen, Norway, was seen by the participants as an extremely useful meeting. In attracting specialists from research groups working in the field -- in industry, as well as research establishments and universities, -- a stimulating exchange of current research results was achieved.

The meeting was divided into eight sessions with 42 papers originally submitted, three of which were not presented. Special subjects such as icing and bearings, and lubrication were not included as they have been covered by other meetings. This Symposium, therefore, focussed on the areas of turbine blade heat transfer, internal (3 papers) and external (6 papers), turbine cooling (5 papers), modelling (4 papers), combustion systems (5 papers), experimental techniques (7 papers), compressors (2 papers) and heat exchangers (2 papers) and the interaction of coolant with main flow (4 papers).

2. CONTENT OF THE SYMPOSIUM

In his introductory survey paper, D.F. Metzger (Arizona State University, U.S.) emphasized the difficult nature of turbine heat transfer analysis as, in general, convection problems with extremely complex flow fields are to be described. He stressed the fact that experimental results still remain the foundation for design whereas computational fluid dynamics have not been used extensively in cooled turbine development. During the course of the meeting, however, it was shown that computational methods are rapidly gaining importance and provide a fairly high degree of accuracy, at least for preliminary predictions. This is particularly true for external flows with heat transfer. In keeping with his own experience, Professor Metzger wanted his contribution to be seen as a sampling rather than a survey. In using examples from his own as well as other's current work, he was able to introduce the major topics of the meeting's sessions. It was stressed, that

- considerable work remains to be done in understanding the internal blade flows. Professor Metzger emphasized the problems associated with
 - i - serpentine cooling passages with centrifugal forces in a turning flow, roughness effects etc. enhancing the heat transfer. The understanding of the influence of rotation deserves attention.
 - ii - jet array impingement, which actually is of longstanding interest with its three-temperature problem.
 - iii - pin fin arrays, which should be tailored to augmenting the internal heat transfer to match the local character of the external heat loads. Heat transfer characteristics as well as pressure loss coefficients are of importance.
- a variety of specific problems concerning the external flows should be addressed. For example
 - i - blade tip heat transfer. Professor Metzger concluded that the leakage flow is basically an inviscid pressure driven flow with Nusselt and Reynolds numbers based on the clearance gap.
 - ii - disk heat transfer on the faces of turbine and compressor disks remains an important problem in gas turbine heat transfer.
 - iii - film cooling will remain one of the most important subjects. Professor Metzger stressed the fact that more consistency in acquiring, presenting and comparing the data is needed.
- experimental methods focus on the acquisition of localized heat transfer data. Improved and relatively new techniques were discussed and shown to be vital for the future success and development of theoretical models. Mass transfer and melting point techniques were highlighted. The importance of appropriate experimental techniques is mirrored in the high number of papers directly or indirectly presented on this subject during the course of the meeting.

From the contributions made during the Symposium, most of Professor Metzger's conclusions can be supported and additional current information was presented. Several tendencies for current and future development can be distinguished and will be discussed along with the major aspects of the papers,* not necessarily in order of the program but following their actual content.

Blade Internal Heat Transfer

The understanding of internal heat transfer including the effects of rotation is extremely important to modern engine design. Progress is being made in developing appropriate experimental facilities by engine manufacturers and research establishments as shown by R.J.Clifford (Rolls-Royce, UK) and W.D.Morris and S.F.Haragama (University of Hull and Royal Aircraft Establishment, UK). Due to the complicated nature of the rotating flow with Coriolis-induced fluid motion, enhancement as well as reduction in the heat transfer is observed depending on the radial direction of the coolant flow.

In the ongoing search for optimal enhancement of internal heat transfer by pin fins, benefits can be derived from careful selection of the geometries with considerable reductions in the pressure loss as shown by S.C.Arora and W.A.Messeh (Pratt and Whitney, Canada). In comparing results of various groups, difficulties can arise from the large number of parameter variations and the non-uniformity of data reductions.

The advantages and the potential of shell-spar cooling arrangements were illustrated by G.P.Butt (Westinghouse Canada) and W.E.North (Westinghouse Electric Corp, US) for nozzle cooling of stationary gas turbines indicating the benefits for stationary as well as jet engine designers from mutual exchange.

External Heat Transfer on Blades, Platforms and Casings

Although considerable progress has been made in describing the external blade heat transfer, improved methods of prediction are a necessity. Theoretical and experimental efforts seem to complement each other quite well, indicating growing confidence in the modelling and in recently developed codes. Three major areas of interest were identified

- i - effects of turbulence, pressure gradients, roughness etc. on the heat transfer coefficient
- ii - wakes and their influence on the heat transfer

*See References and an Author-Subject-Matrix in Appendix

iii — film cooling and aerodynamic interactions

Using the VKI short duration isentropic compressor tube facility for the study of Mach number, Reynolds number and turbulence effects on the heat transfer coefficient, P.Arts (VKI Belgium) finds good agreement in comparing measurements with predictions (STAN 5). A problem, though, in this approach remains the modelling of the boundary layer transition which was triggered by a momentum thickness Reynolds number value provided by the user. W.Rodi (Universität Karlsruhe, Ge.) and G.Scheufler (Universität Erlangen, Ge.) present calculations of transitional boundary layer using the low-Reynolds-number version of the k- ϵ model of Lam and Bremhorst in simulating the physical transport and transition mechanisms. In general, though, more rapid transition is predicted than is found in the experiments. This is supported by the results presented by S.Wittig, A.Schulz, H.J.Bauer and K.H.Sill (Universität Karlsruhe, Ge.) from their study of turbulence and wake effects on the heat transfer coefficients in a continuous hot gas tunnel. It is illustrated that the wake plays an important role in triggering the transition as long as the main flow turbulence intensity, is relatively low. The unsteady process of wake-cutting is monitored by D.J.Dooley and M.L.G.Oldfield (University of Oxford, UK) and C.P.J.Scrivener (Rolls-Royce, UK) in the transient cascade of the Isentropic Light Piston Tunnel (ILPT) at Oxford. As in Wittig's et al. experiments under steady conditions it was concluded that the primary effect of wake-passing is to promote an early, unsteady transition. The effects on the pressure surface seem to be somewhat less.

The Symposium provided an excellent opportunity for comparing the flow tunnels used by the various research groups, i.e. continuous hot gas flow tunnels vs. short duration compression and piston tunnels. As indicated before, Arts and Dooley et al. used short duration facilities. C.J.P.Forth, P.J.Loftus and P.V.Jones (University of Oxford, UK) in their study of density ratio effects on the film-cooling also used the Oxford ILPT. The new Isentropic Light Piston Annular Cascade facility at RAE Pyestock, described by A.J.Books, D.E.Colbourne, E.T.Wedlake (RAE Pyestock, UK), P.V.Jones, M.L.G.Oldfield, D.L.Schultz (University of Oxford, UK) and P.J.Loftus (University of Maryland, US) utilizes experiences gained with the Oxford facility and conditions close to engine operations are simulated. A vast amount of experience has been gained by M.G.Dunn (Calspan, Buffalo, US) in using a shock tunnel for turbine stage tests. Wide variations in test conditions, flexibility and availability of appropriate instrumentation seem to be the major advantages.

If, however, detailed information on physical phenomena such as turbulence intensities and length scales, boundary layer structures, mixing processes etc. is required, continuous flow and suction-type tunnels appear to be used more frequently and appear to hold some advantages. In addition to Wittig's et al. work, A.B.Turner, F.H.A.Taradah and F.J.Bayley (University of Sussex, UK) used a continuous flow cascade effectively in studying the influence of surface roughness on the heat transfer, stressing the combined effects of the influence parameters such as roughness, turbulence levels etc.

The various investigations on film cooling discussed in the course of this Symposium, exclusively utilized continuous flow facilities. H.Kruse (DFVLR, Köln-Wahn, Ge.) analyzed the influence parameters such as geometry and main flow characteristics on the heat transfer downstream of a single row of injection holes, concluding that the effect of pressure gradients seems to be weak, which supports previous findings. O.Köllen and W.Koschel (Technical University of Aachen, Ge.) determine the effects of film cooling on the aerodynamic performance in an annular cascade, whereas F.Leboeuf, A.Onvani and C.Ollivier (Ecole Centrale de Lyon, Fr) report on the aerodynamic interaction of a 3-D flow with a jet. Trailing edge ejection is the subject of a study by F.H.Kost (DFVLR; Göttingen, Ge) and A.T.Holmes (Rolls-Royce, UK) performed in the DFVLR-tunnel. The loss mechanisms were separated and practical conclusions for the blade design are derived. The boundary layer interaction with shock waves and simulated cooling flows was examined in a cascade wind tunnel by R.Kiock and H.Hoheisel (DFVLR, Braunschweig, Ge), H.J.Dietrichs (MTU — München, Ge) and A.T.Holmes (Rolls-Royce, UK). A major problem has been and continues to be the generalization and transfer of the large amounts of specific experimental data obtained by various groups. M.R.L'Ecuyer (Purdue University, US) and F.O.Soechting (Pratt and Whitney, US), in a very useful contribution, take data available from the literature and develop a generalized correlation for film cooling effectiveness. A similar approach would be quite helpful in a variety of other areas.

Continuing efforts are required in understanding the flow with and without coolant injection along platforms, shrouds and casings and across blade tip clearances as stressed by Prof. Metzger. A.E.Bourguignon (SNECMA, Fr) reports on her studies of platforms of practical interest with various film cooling configurations. The data seem to correlate quite well with predictions. Unfortunately, though, the comparison with results from other research groups is largely impossible as only qualitative and relative data without reference values were presented. R.S.Attwood (Rolls-Royce, UK), using simplified heat conduction analysis, explored the design of static shroud casing segments using ceramic coatings. It appears that more work in this area should and will be done, as in various AGARD member Countries activities are under way.

Professor Metzger's comment on the importance of tip clearance flow was not reflected in the program. More work is clearly needed in this area.

A very thorough and detailed account of the transfer of available experimental data and theoretical models to prototype engine designs and the subsequent test of the cooled components in the engine was given by H.J.Graf (Brown Boveri and Company, Switzerland). It can be concluded that available codes yields good results for turbulent boundary layers. Larger deviations still occur for transitional flows. Graf confirms the conclusions of the previously cited papers that improvements in the model especially under consideration of film cooling parameters are in order. It seems that due to the larger scale of the stationary gas turbine, relatively high data accuracy was achieved which is also quite helpful to future jet engine research. More work of similar accuracy is needed for a final evaluation of the theoretical tools developed and compared with data derived from cascades.

Rotating Disk Cooling

The development of advanced aero-engines requires detailed knowledge of the transient thermal behaviour of the compressor and turbine rotor disks. Three papers -- a number which does not reflect the importance of the problem -- were directed towards this subject during the course of the meeting.

C.A.Long and J.M.Owen (University of Sussex, UK) reported on their ongoing work utilizing a heated free disk and a heated disk in a rotating cavity. The numerical solution of Fourier's equation seem to correlate with the experiments although care should be taken in the application to gas turbine design with modified boundary conditions. F.Reile, U.Radons and D.K.Henneke (MTU -- München, Ge) studied the transient thermal behaviour of a compressor rotor under simulated engine conditions with final tests done in an engine. Heat transfer coefficients derived from Owen's et al. model lead to good agreement between calculated and measured component temperatures and time constants.

The development of a numerical code for the description of turbulent flow and heat transfer within cavities of stationary and rotating disks was described by D.Dutoya (ONERA, Fr). The prediction of pressure losses under steady flow conditions indicates the applicability of turbulence modelling to comparable configurations.

Combustion Systems

With rising performance requirements, the question of combustor liner cooling and heat transfer processes within the combustor needs increasing attention. D.A.Nealy, S.B.Reider and H.C.Mongia (Allison Gas Turbine Division, US) presented a characterization of the problems by analysing a variety of alternate cooling configurations. Simultaneous efforts to provide the appropriate background in the manufacturing processes, the understanding of advanced materials and the heat transfer processes are essential. Heat release and transfer as well as cooling of the linear wall were the subject of several papers.

B.F.Magnussen (Norwegian Institute of Thermodynamics, No) presented a modified method for calculation of combustion characteristics and M.G.Carvalho, D.F.G.Durao and F.C.Lockwood (Instituto Superior Técnico, Po) were primarily concerned with determining the thermal radiation from the gaseous species. Various aspects such as the emittance characteristics under gas turbine operational conditions need further attention. B.L.Button (Trent Polytechnic, UK) addressed the problem of the disruption of the cooling film by a jet with wall plunging whereas G.E.Andrews, A.A.Ascere, C.I.Hussain and M.C.Mkpadi (University of Leeds, UK) outlined the geometrical requirements for full coverage impingement cooling emphasizing various new aspects for the transfer to practical combustor systems. M.Lecassault, P.Trouillot and S.Couton (SNECMA, Fr) illustrated the cooling requirements of afterburners. Thermography was used in analyzing various practical cooling configurations. Good qualitative comparisons were achieved for several cooling arrangements.

Experimental Techniques

The importance of proper instrumentation and experimental analysis was illustrated by a relatively large number of contributions in this area. Improvements and new aspects of known techniques were presented.

Liquid Crystal thermochromic indicators (P.T.Ireland and P.V.Jones, University of Oxford, UK) and high frequency response heat flux gauges (A.H.Epstein, G.R.Guenette, MIT, U.S. and R.J.G.Norton, Rolls-Royce, UK and Cao Yuzhang, Beijing Institute of Aeronautics and Astronautics, PRC) demonstrate remarkable improvements and broader use of this technique will probably be found in coming years. Optical, non-intrusive measurements of surface temperature and flow characteristics will not only be applied in laboratory tests but also in prototype engines. Optical pyrometry again was shown by M.Charpenel and J.Wilhelm (ONERA, Fr) to be a promising tool and R.B.Rivir, W.C.Elrod (Wright Patterson AFB, US) and M.G.Dunn (Calspan, US) demonstrated the feasibility and limitations of the Laser Two Spot Velocimetry for application in short duration flows.

The importance of the blade tip clearance has been emphasized earlier. Efficient systems for active clearance control require appropriate sensors. J.Paulon (ONERA, Fr) described the successful development of a new capacitive transducer.

Finally, M.N.R.Nina and G.P.Pita (Instituto Superior Técnico, Po) discussed the possible improvements of compensated fine wire thermocouples for measuring fluctuating gas temperatures, a problem of longstanding importance. Especially in reacting flows extreme care is in order.

Heat Exchanger

Advanced helicopter engines as well as a variety of other applications increasingly demand the incorporation of efficient heat exchangers. During the course of the meeting, insufficient time was available to address this important problem in depth. Only two papers were presented. M.N.R.Nina and M.P.N.Agus (Instituto Superior Técnico, Po) presented a theoretical study on the optimization of cycle parameters and heat exchanger design. In considering modified cycles also S.Boudigues and J.Fabri (ONERA, Fr) emphasized the advantages and design requirements in utilizing ceramics such as Silicon carbide as heat exchanger material. Obviously, much work remains to be done in this area and should be the subject

of a separate future meeting.

3 CONCLUSIONS AND EVALUATION

In considering recent developments in engine design it is obvious that the understanding of the heat transfer processes in gas turbines and the advancement of cooling techniques are crucial elements in the quest for higher performance and reduced fuel consumption as well as for improved life and reliability. This Symposium, therefore, was aimed at the discussion and analysis of subjects concerning fundamental and applied heat transfer problems. In order to limit the scope of the meeting, heat transfer problems as related to icing, bearings and gears etc. were not subject of the meeting as these topics have been covered individually by similar AGARD meetings. Furthermore, several topics such as heat exchangers were not covered in depth.

Induced by the well balanced structure of the program, the papers as well as the discussions were directed towards current problems. Better than average participation by researchers from industry was observed, leading to a relatively high level of currency of the information exchanged. In particular, the need and opportunities for immediate solutions were illustrated along with more advanced approaches. It was shown that:

- despite recent progress, turbine blade cooling remains a major focus of interest. In particular, questions concerning the internal heat transfer need to be addressed in depth including the effects of rotation. Furthermore, the influence on the aerodynamic performance of coolant ejection requires continuing attention,
- with increasing performance requirements, modified and even new technologies will also have to be applied for other components, especially the combustor, the compressor and heat exchangers. Close cooperation in the areas of heat transfer analysis, material sciences and manufacturing was shown to be crucial for further development. However, it remains to be seen to what extent and how soon newer materials — ceramics, for example — can be introduced,
- progress in modelling has been made with the successful application of numerical codes for the prediction of at least external boundary layer flow. Problems arise in considering pressure side flow and wake cutting effects,
- sophisticated experimental techniques are of crucial importance for continuing success. The benefits of the utilization of steady flow hot gas experiments and of short duration tunnels were compared. Non-intrusive, optical instrumentation as well as miniaturised fast response gauges were shown to hold the key to further developments. More comparisons of actual engine tests with laboratory results and predictions would have been desirable.

AUTHOR - SUBJECT - MATRIX

	Theoretical	Experimental	Engine	Combustor	Turbine	Disk	Cascade	Blade	Heat Transfer	Cooling	Internal	External	Optimization
1. Metzger	x	x			x			x	x	x	x	x	
2. Clifford		x			x			x	x		x		
3. Morris		x			x				x		x		
4. Arora		x			x			x	x		x		
5. Arts*	x	x			x		x		x			x	
6. Wittig	x	x			x		x		x			x	
7. Doorly	x	x			x		x		x			x	
8. Kruse		x			x					x		x	
9. Turner		x			x		x		x			x	
10. Forth		x			x				x			x	
11. withdrawn													
12. Bourguignon		x			x		x		x				
13. Atwood	x	x			x					x		x	
14. Graf	x	x	x		x				x			x	
15. Butt	x	x			x			x		x	x		
16. Dunn	x	x			x		x		x			x	
17. withdrawn													
18. Rodi	x				x			x	x			x	
19. L'Ecuyer	x				x					x		x	
20. Carrallo	x			x									
21. Long	x	x			x	x			x				
22. withdrawn													
23. Magnussen				x						x			
24. Button		x		x						x			
25. Nealy		x		x						x			
26. Andrews		x		x	x				x		x		
27. Bayle-L.		x		x						x			
28. Ireland		x			x			x		x	x		
29. Charpenel		x			x			x					
30. Epstein		x			x			x	x		x		
31. Brooks		x			x		x		x		x		
32. Nina		x		x									
33. Rivir		x			x		x						
34. Paulon		x			x			x					
35. Dutoya	x				x	x							
36. Reile	x	x				x			x				

AUTHOR - SUBJECT - MATRIX

	Theoretical	Experimental	Engine	Combustor	Turbine	Disk	Cascade	Blade	Heat Transfer	Cooling	Internal	External	Optimization
37. Nina	x		x										x
38. Boudigues	x		x										x
39. Köllen	x				x		x			x		x	
40. Onvani	x				x		x			x			
41. Kost					x		x			x			
42. Kiock	x				x		x			x		x	

COOLING TECHNIQUES FOR GAS TURBINE AIRFOILS A SURVEY

Darryl E. Metzger

Mechanical and Aerospace Engineering Department
Arizona State University
Tempe, Arizona 85287, USA
and
Lehrstuhl und Institut für Thermische Strömungsmaschinen
Universität Karlsruhe
7500 Karlsruhe, Germany

SUMMARY

A brief general background discussion of turbine heat transfer and cooling with compressor discharge air is given to provide an introduction for the papers scheduled for delivery at this meeting. Specific reference is made to a selection of current research areas for gas turbine engine cooling, including blade tip heat transfer, heat transfer in serpentine passages, multiple jet array impingement, heat transfer in pin fin arrays, disk heat transfer, and film cooling. An overview of various experimental methods used to acquire heat transfer data is also given, with an emphasis on newer methods used to acquire detailed local convection heat transfer information.

INTRODUCTION

It is interesting to look over some of the earliest literature about gas turbine engine research and development to see how remarkably clearly the authors anticipated, and even worked on, the problems faced still today. One of the best examples is the 1949 review paper on aircraft gas turbine engine research by Silverstein [1]. In a section entitled "Turbine Cooling," the following outline of the basic aerodynamic and heat transfer problems involved was given: (a) determination of the three-dimensional compressible flow of the gas through the turbine-blade passages, (b) evaluation of the heat transfer from the gas stream to the blade surface, and (c) evaluation of the heat transfer from the inner surfaces to the cooling medium. In addition, the article states that "many internal arrangements of the cooling passages have been suggested for air-cooled turbines," and "film-cooling methods, in which the cooling fluid is discharged around the blade periphery by means of slots or allowed to seep through porous blade walls, have also been suggested."

Fig. 1 is a cross-section sketch showing a typical cooling arrangement for a modern turbine blade which employs a combination of impingement and film cooling in the leading edge region, serpentine passages in the mid-chord region, and a pin fin array in the trailing edge region. Although the blade shapes have changed markedly and the capability to manufacture current complex internal cooling arrangements was probably not foreseen by Silverstein, current cooled airfoils nonetheless fit his description.

Over the years since the address published in [1] was given, the problems of turbine heat transfer and turbine cooling have been pursued vigorously, and turbine inlet temperatures have increased steadily. Turbine cooling technology developments account for a significant portion of the resulting powerplant improvement history summarized in Fig. 2. At any given time, engine performance (and durability) depends critically on the then current state of turbine cooling technology. For a given level of this technology, turbine inlet temperature and resulting cycle performance can be increased only to a certain point (Fig. 3). Beyond that point, penalties associated with the use of cooling air (power required for compression and pumping, aerodynamic losses produced when the coolant reenters the hot gas stream) overpower the benefits.

The present problems of heat transfer and cooling for gas turbine engine components are very similar to the statements given in [1]. They are (a) to know the external or hot gas side heat transfer in detail, (b) to know the detailed component internal heat transfer for a variety of families of cooling schemes, and (c) to choose from among and within those families to optimize for combinations of (i) minimum use of cooling air, (ii) minimum interference with the hot gas side aerodynamics, and (iii) minimum component temperature and temperature gradient levels.

In this context the present paper deals mainly with the cooling side of turbine heat transfer, in keeping with the author's own experience. Even with respect to cooling, the treatment is far from comprehensive. It covers briefly only some of the areas that are presently of interest in turbine cooling. The coverage is limited to experimental studies and most of the results presented are those of the author and his students and colleagues at Arizona State University. Thus the paper is not really a survey, as the title implies, but is more a sampling from among the many areas that will be covered at the present meeting.

BLADE TIP HEAT TRANSFER

The clearance gap between the tip of an axial turbine blade and the adjacent stationary shroud provides a narrow flow passage between the pressure and suction sides of the blade. The clearance in general cannot be eliminated altogether because it must accommodate centrifugal growth of the blade as well as differential thermal expansion between the blade and shroud through a variety of operating conditions [2].

The primary detrimental effect of the tip leakage flow is on the blade aerodynamic performance, but a second important effect is the convection heat transfer associated with the flow. The surface area at the blade tip in contact with the hot gas represents an additional thermal loading on the blade which must be removed by the blade internal cooling flows. Also, heat transfer rates at the tip have recently been shown to be very high, of the same order as those present at or near the airfoil leading edge [3,4]. As a result, blade tips have been one of the turbine areas most susceptible to structural damage. Damage in this region, even if minor, can have a severe effect on turbine performance. Loss of material from the tip increases clearance gap, which in turn increases both the flow and heat transfer across the tip and exacerbates the problems.

Recent work [5] confirms previous findings [6] that the leakage flow through the gap is basically an inviscid, pressure-driven flow whose magnitude and direction can be calculated from knowledge of the suction and pressure side pressure distribution alone. Normal clearance gap heights are, in effect, small enough that the flows through the gap are uncoupled from the details of the flowfields on either side, and are largely two-dimensional. In [5] also it is demonstrated that the sink-like flow entering the clearance gap (Fig. 4) is composed almost entirely of mainstream gas drawn directly from the hot blade passage flow, and that the convection heat transfer coefficients on the tip are little influenced by the relative blade-to-shroud motion. It seems reasonable to assume that this latter characteristic will also be the case for various blade tip treatments, and in [7], stationary modeling has been used to examine the heat transfer and flow characteristics of grooved tip treatments in detail.

Fig. 5 shows a typical set of local Nusselt numbers from [7] for a shallow ($D/W = 0.1$) grooved tip model (solid lines) in comparison with values for the same flow over a plain, ungrooved tip (dashed lines). Nusselt and Reynolds numbers here are based on the clearance gap height. In general, the results show that the overall heat transfer to the blade tip is reduced by the presence of a groove. However, reduced heat transfer levels on the groove floor are substantially offset by the added heat transfer area created by the groove side walls. Additional study of blade tip heat transfer is being initiated at Arizona State University under a grant from NASA-Lewis Research Center.

SERPENTINE COOLING PASSAGES

Radially aligned coolant channels of basically rectangular cross section are used extensively to cool the midchord regions of turbine blades; these channels are connected by 90 and 180 degree turns to form serpentine cooling passages as shown in Fig. 1. Current trends are towards increasing numbers of channels so that the flow and heat transfer characteristics around bends and turns with and without roughened walls is of high current interest [8-12]. It is well known that both the nature of the flow and the associated convection heat transfer are usually significantly altered in and around the turn. In general, the centrifugal forces present in a turning flow induce secondary flows which have the effect of augmenting heat transfer in the streamwise direction and creating azimuthal variations in heat transfer.

Fig. 6 shows the very sharp 180 degree test geometry used in [8] and [12], and Fig. 7 shows typical regional (Nu_w) heat transfer results on upper, lower, and side walls. Here $W^* = W_1/W_2$, $H^* = H/(W_1+W_2)$, and $D^* = D/(W_1+W_2)$. Reynolds and Nusselt numbers are based on channel hydraulic diameter. Azimuthal average heat transfer rates (Nu_w) increase markedly through the turn, with the highest values for this particular geometry occurring downstream of the turn. The sidewall heat transfer rates change, in a relatively short distance, from significantly lower to significantly higher than the top/bottom wall rates.

Fig. 8 shows some very recent results for a 90 degree turn in a rectangular cross-sectioned channel with an outside/inside radius ratio of 2:0 and a 3:1 section aspect ratio. The channel is rib-roughened on both long sides as shown in the sketch of the test section. The general increase in heat transfer level as the flow proceeds through the turn would be expected to be the result of either or both the secondary flows associated with the turn and the developing flow disruption caused by the ribs. Rib roughness enhancement of heat transfer usually develops fully after only a few rib spacings, so the turn itself is evidently responsible for the continuing enhancement in this geometry. However, the Nusselt number enhancement here, from the beginning to the end of the turn, is considerably greater than the 20-25% observed in the same turn with smooth walls [12]. Thus it appears that the turn and the ribs are mutually complimentary in producing a relatively large enhancement of heat transfer. The same conclusion is reached whether or not ribs are present in the straight upstream and downstream channels (not shown) on either side of the the test section.

It should be noted that rotation can significantly influence the heat transfer in serpentine passages used to cool the rotating turbine blades, and that this is a topic of considerable current attention which will be addressed by several authors at the present meeting.

JET ARRAY IMPINGEMENT

Fig. 9 depicts a turbine airfoil which utilizes jet array impingement for midchord region cooling. The jet flow, after impingement, is constrained to exit in a single direction along the channel formed by the perforated insert and the airfoil shell. This cooling scheme has received attention for a number of years [13-15]. However, in addition to the crossflow which originates from the jets following impingement, an initial crossflow may be present from impingement air used to cool the leading edge region [16]. The temperature of

the initial crossflow in general will be different than the jet array temperature, leading to a complex three-temperature situation with many similarities to the three-temperature problems encountered in film cooling.

This three-temperature problem has been studied extensively at Arizona State University over the past several years. The appropriate fluid driving potential, t_{aw} , can be expressed in terms of a non-dimensional effectiveness for use with corresponding Nusselt numbers. Figs. 10 and 11 show typical results from [16]. Here effectiveness, although resolved in the streamwise direction, is defined in terms of the initial crossflow temperature at the upstream end of the array. Nusselt numbers are based on the jet hole diameter, which is uniform over the entire array.

The geometries covered by Figs. 10 and 11 represent entirely different effects of the initial crossflow on array heat transfer. The Fig. 10 configuration is one that results in a highly non-uniform jet flow distribution in the array, with much larger jet velocities at the downstream end of the array than at the upstream end. For this case the effect of initial crossflow can dominate ($\eta \approx 1$) more than halfway through the array. This dominance can also be seen in the Nusselt profiles which remain essentially at their upstream initial crossflow channel levels well into the array. In contrast, the Fig. 11 configuration is one which has a nearly uniform jet flow distribution. Here η has dropped significantly at the first or second row. Similarly, the strong immediate influence of the jets is reflected in a very large increase in Nusselt values at the first or second row of jets.

This information on η and Nu, if converted to heat fluxes for prototype conditions, imply that local cooling rate predictions within the array could, in many cases, easily be in error by 100% or more depending on the designer's guess in the absence of such information. There is evidence that unacceptable levels of design uncertainty for jet arrays with initial crossflow have existed in practice, and that premature failures of impingement cooled airfoils have been the result. This is unfortunate, since the jet array cooling scheme is very high performing from a heat transfer point of view, and offers great potential for tailoring internal heat transfer coefficients to match local variations in external heat transfer to the cooled component. Work is ongoing [17,18] to provide information that will support the design of tailored non-uniform arrays.

PIN FIN ARRAYS

Pin fin arrays find frequent application as augmentation devices in the airfoil trailing edge region, as in the blade of Fig. 1. The pin height in these applications is typically the order of the pin diameter. They represent an intermediate case between the long cylinder tube bank case where essentially all of the heat transfer area is on the cylindrical surfaces of the tubes, and the plate-fin heat exchanger surface case where most of the area is on the plates or end walls. Considerable information exists for both of these extremes, but neither case correctly predicts heat transfer for the gas turbine cooling application.

Recently, a number of papers have appeared directed specifically at providing the needed information [19-23]. Continuing emphasis is on the acquisition of streamwise resolved heat transfer and pressure loss coefficients for a variety of candidate geometries, including pins with cross sectional shapes other than circular. Similar to the situation with jet array impingement, pin fin arrays with non-uniform pin spacing and size offer potential for tailoring the internal augmentation to match the local character of the external heat load.

Figs. 12-14 show some recent results from [24] for three different pin fin arrangements. In all three cases the pins are located in a staggered pattern, with spacing in the streamwise direction equal to one and one-half pin diameters, and in the transverse direction equal to two and one-half diameters. Nusselt numbers and Reynolds numbers are based on pin diameter, and the Reynolds number in all cases is 20,000. Nusselt numbers are spanwise average values, resolved to one row spacing. Fig. 12 is an arrangement with pins attached only to one side of the channel, extending two-thirds of the way across. In an actual application some of the pins would have to be extended all of the way across for structural reasons, but these results give a feel for the differential between top and bottom heat transfer that could be established.

Fig. 13 is the standard staggered pin arrangement, with smooth channel walls between the pins. The results display the characteristic observed in [19] with heat transfer rates peaking at about the third to fifth row, followed by a gradual decline. Fig. 14 is the same arrangement as in Fig. 13, with the addition of staggered transverse roughness ribs as shown. Heat transfer rates are significantly higher than those of the smooth wall case; and, in fact, the arrangement shown in Fig. 14 is one of the highest heat transfer performing pin fin arrays yet observed.

DISK HEAT TRANSFER

Convection heat transfer on the faces of turbine and compressor disks remains an important problem in turbine heat transfer despite several decades of work in an effort to gain an understanding of the phenomena and to provide the designer with useful information [25-30]. The designer is forced to vent cooling air through the cavities adjacent to the disks in an attempt to control the disk growth and thus the clearance gaps at the blade tips. In the turbine stages, the vented flow also helps to prevent the ingestion of hot blade passage gases into the cavities where it can directly heat the disks.

Heat transfer coefficients between normally vented cooling air and the rotating disk surfaces are usually relatively low compared with those achieved in other cooled components. Jet impingement of air directly onto the disk can enhance heat transfer, and thus has the potential for reduction in required coolant flow. However, jet impingement of turbine disks has been applied infrequently in practice, and only very few studies have been published. One early study [31] of an actual jet cooled turbine reported anomalies where heat transfer under some conditions unexpectedly decreased with increasing disk speed. Such behavior is possibly related to the flow regime transition reported in [32]. This transition phenomena was observed with flow visualization over a large range of combinations of jet flow rates, disk speeds, and impingement radii, and it appears to separate a zone of impingement dominated behavior from a rotationally dominated zone. Fig. 15 shows the correlation of observed transition conditions in terms of the ratio of jet flowrate to rotationally induced disk pumping flow. Higher rotational speeds, larger impingement radii, and smaller jet flowrates favor a flow pattern which appears rotationally dominated whereas the opposite trends favor an impingement dominated interaction.

Corresponding heat transfer rates are essentially independent of jet flowrate in the rotationally dominated regime, but increase strongly with increasing flowrate in the impingement dominated regime. Fig. 15 also shows that, in terms of this correlation, the location of the anomalous results of [31] are within the transition zone. Other results presented in [31] were strongly in the impingement dominated zone and did not exhibit the anomalous behavior.

Fig. 16 presents results from [33] showing how heat transfer coefficients increase as jet flowrate is increased through the rotationally dominated regime into the impingement dominated regime. The heat transfer sensing area was a narrow annulus at the rim of the disk, and tests were run with four different disk face contours as shown. The most noticeable characteristic of the results is the lack of almost any effect of face contour. The Nusselt numbers are relatively independent of jet flow at values of the flowrate ratio below about 0.1. At jet flow rates larger than this, Nusselt numbers increase strongly. For the designer, these results indicate that rotating disk heat transfer rates can be increased significantly if enough cooling air is available for impingement through individual jets. Conversely, some disk cooling schemes tried in the past may have been ineffective because many jets with small individual flowrates were used.

FILM COOLING

Film cooling is, with little doubt, the most complex subject in the entire turbine cooling field. It is also one of the most important subjects since it appears unavoidable that more and more film cooling is required as turbine inlet temperatures continue to rise. To all the phenomena present in the main gas flow and its boundary layers, film cooling adds the fluid dynamical influences of injection and the imposition of another temperature, creating a three-temperature problem. Actually, the three-temperature representation is only an approximation, the complete problem is a multi-temperature one.

Current interest and activity in film cooling is high, and current topics of investigation include the shape of injection sites, effects of surface roughness and curvature, effects of density differences between main and injected flows, persistence of the film in highly three-dimensional flows and over and around obstacles, and more [34-39]. Many methods have been developed to acquire information about film cooling performance; and sometimes quite heated arguments are heard about the choice of the "correct" method. Consistency is sometimes shown between separate sets of results, but more often than not, and especially recently, each investigator's results are presented on their own, with little comparison to the results of others. This situation is understandable, given the number of variables that influence the results; seldom is there close correspondence between conditions of two different experiments. It is therefore relatively easy to rationalize differences between only somewhat similar sets of results; and this situation is compounded by the proprietary nature of much of the current work.

Nevertheless, it is this author's opinion that there remain fundamental and not widely appreciated differences between film cooling results acquired with differing experimental methods (even without the complications of large temperature difference and density gradient effects), and that these can lead to appreciably different performance predictions when the results are interpreted in design terms. Such differences are probably not very important far from the injection sites, but as more and more film cooling is used, the nearinjection region grows in importance.

Consider the heat flux on an isothermal film cooled wall written as a three-temperature problem [40]:

$$q_w/A = f_c(t_c - t_w) + f_w(t_w - t_m) \quad (1)$$

Here f_c and f_w are influence functions, and f_w can be thought of as the heat transfer coefficient, h_D , (based on the wall-mainstream temperature difference) when the coolant-mainstream temperature difference is zero. A corresponding two-temperature description can be written for the same surface and mainstream conditions, but without injection.

$$q_w/A = h_w(t_w - t_m) \quad (2)$$

This without-injection condition might represent the surface with injection sites present, but with no injection flow; or, it might represent the solid surface without injection

sites. The interpretation of h_w , usually used is the first, but the second interpretation is the more logical one for design.

Rationing (1) and (2) for the same wall temperature yields:

$$\phi = (f_c/h_{w1})\theta^* + (h_0/h_{w1}) \quad (3)$$

where:

$$\phi = Q_w/Q_{w1}, \text{ the ratio of film cooled flux} \quad (4)$$

to unblown wall flux at the same
mainstream and wall conditions

$$\theta^* = (t_c - t_m)/(t_w - t_m) \quad (5)$$

There will be a value of the isothermal wall temperature (the reference temperature t_{ref}) at which the net surface heat flux will be zero. Using this temperature, (3) becomes:

$$\phi = \phi_0 - (\phi_0/\theta_{ref}^*) \theta^* \quad (6)$$

where:

$$\theta_{ref}^* = (t_c - t_m)/(t_{ref} - t_m) \quad (7)$$

$$\phi_0 = h_0/h_{w1} \quad (8)$$

Fig. 17 shows the graphical interpretation of (6) for a particular situation. The abscissa intercept represents the non-dimensional reference temperature with film cooling present. This value can range from zero to infinity. The ordinate intercept represents the ratio of film cooled to unblown wall flux when the coolant temperature equals the mainstream temperature. This can also be viewed as the purely aerodynamic effect that coolant injection has on convection. The horizontal dashed line represents the corresponding unblown wall case. Thus, plots like Fig. 17 give a visual comparison of film cooling performance with unblown wall performance. For the particular case shown, film cooling enhances the thermal transport properties and the two curves must cross somewhere within the likely design region. Design points to the right of the crossover point will obtain the reduction in heat flux that is normally assumed to occur with film cooling. Design points to the left of the crossover will experience an increase in wall flux due to the presence of film cooling. Such increases are definitely possible, especially in multiple hole film cooling where the aerodynamic transfer capability is enhanced by injection and the film coverage in some locations is relatively poor.

The similarities between traditional film cooling effectiveness, η , and the inverse of θ_{ref}^* have been noted [41] and the two terms have at times been used interchangeably. In multiple hole film cooling such interpretations can lead to errors in design predictions. As a closure to this section, Fig. 18 presents a comparison from [40] of one situation where suitable adiabatically obtained and isothermally obtained film cooling results are available under otherwise quite similar circumstances [42,43]. Both studies use the same hole spacing and the same compound injection angle. In [42] local effectiveness data was obtained on an adiabatic surface, as well as regionally averaged heat transfer data on an isothermal surface. In [43] regionally averaged heat transfer data was obtained on an isothermal surface.

Fig. 18 compares results at the fifth injection row. Both sets show similar aerodynamic increases in heat transfer capability, but the inverse of θ_{ref}^* and the averaged value of η are not in good agreement. In any present design application of film cooling information, averaging is necessary. It is this averaging of local information, what to average, how to average, and how to acquire test information that can be used easily and properly in design, that is of concern.

EXPERIMENTAL METHODS

The pressure for more detailed design information, for better understanding of the phenomena, and for detailed results to compare with computational efforts all drive experimentalists to seek more localized heat transfer information. It therefore seems appropriate here to review some of the more common techniques used to acquire such data. Only the most widely used methods will be discussed; a more complete review is available in [44].

The most common method used to determine heat transfer coefficients on localized regions of a convectively cooled surface is to thermally isolate segments of the surface and apply a known amount of electrical power to each segment through attached electric resistance heaters. Usually control is provided for each segment heater so that a desired overall surface thermal boundary condition (commonly isothermal) can be established. By measuring segment surface temperatures and associated fluid temperatures, heat transfer coefficients are determined [16]. The necessary finite size of the segments and heaters dictates that the measured coefficients are always regional averages, rather than true local values, although quite fine resolution can be achieved with this method [45] if the expense can be justified.

Electric heating of the surface can also be effected by passing current directly through the surface material, without the use of separate heater elements. If electrical resistivity varies only slightly with temperature, a nearly uniform heat flux thermal boundary condition can be established. Thermocouple or radiometer measurements are used to determine local strip temperatures and fine resolution of local heat transfer coefficients

is possible [46,47]. A variation on this same method, currently used frequently, is to overlay the heating surface with a thin layer of encapsulated liquid crystals. The liquid crystals allow visual determination of the surface temperatures and contours of constant heat transfer coefficients. Quite accurate and localized determinations of the heat transfer coefficients are possible [48].

In recent years, mass transfer methods, principally the sublimation of naphthalene, have been used to determine both average and local convective heat transfer coefficients [49]. Average coefficients are determined by weighing the naphthalene surface or surface segment before and after exposure to the air stream. Local coefficients are determined by measuring the local depth of sublimed surface with a profilometer. By using microprocessor control to automate data acquisition, highly detailed and accurate heat transfer coefficient maps over a surface can be obtained [50].

Finally, various types of heat flux gages, for example thin foil and Gardon types, have been used for convection heat transfer studies. Although good resolution of local heat transfer coefficients can be achieved, the expense and complexities of multiple gages usually precludes highly detailed mapping of coefficient distributions. This same issue of expense and complexity exists in many instances with other methods discussed here as well. In particular, as the surface geometry of interest becomes more complicated, the difficulty an expense of determining local surface heat transfer coefficients through application of electric heaters or profile measurements of a subliming surface increases markedly. In many cases, a particular technique becomes essentially impossible to apply. Even if possible, it may be prohibitively expensive to instrument more than a single fixed test geometry, so that the systematic effects of geometry changes cannot be studied.

A relatively new method which is relatively inexpensive and convenient, and which appears to be applicable to even the most irregular surfaces, is a technique employing melting point surface coatings. In this method the surface of interest is sprayed with a thin layer of material having a precise melting point temperature that can be visually observed [51,52]. A transient test is conducted where the surface is exposed to a heated air flow and melting times at each point on the surface are recorded and related to the heat transfer coefficients at those points. The capability of the method for obtaining highly detailed accurate heat transfer coefficient maps has recently been demonstrated [12]. Figs. 19 and 20 show examples of this method applied to a sharp 180 degree turning flow.

CLOSURE

The preceding discussion, although far from complete, should serve to introduce what many of the papers of the present meeting will elaborate on; namely, that what must be dealt with in turbine heat transfer in general are convection problems with extremely complex flowfields. The highly three-dimensional and highly turbulent nature of most turbine cooling situations, in many instances including separation and recirculating flow zones, has so far kept the methods of computational fluid dynamics from being used extensively in direct cooled turbine component design. In this climate, experimental results remain the foundation for design; and this paper has attempted to describe some of the many efforts underway to provide designers with information needed for continued improvement in turbine performance and durability.

REFERENCES

1. Silverstein, Abe, "Research on Aircraft Propulsion Systems-The Twelfth Wright Brothers Lecture," *J. Aeronautical Sciences*, 16, 1949, pp. 197-226.
2. Henneke, D.K., "Heat Transfer Problems in Aero-Engines," *Heat and Mass Transfer in Rotating Machinery*, Hemisphere, Washington, D.C., 1984, pp. 353-379.
3. Dunn, M.G., Rae, W. J., and Holt, J.L., "Measurement and Analysis of Heat Flux Data in a Turbine Stage: Part I - Description of Experimental Apparatus and Data Analysis," ASME Paper No. 83-GT-121, 1983.
4. Dunn, M.G., Rae, W. J., and Holt, J.L., "Measurement and Analysis of Heat Flux Data in a Turbine Stage: Part II - Discussion of Results and Comparison with Predictions," ASME Paper No. 83-GT-122, 1983.
5. Mayle, R.E. and Metzger, D.E., "Heat Transfer at the tip of an Unshrouded Turbine Blade," *Heat Transfer 1982 - Proceedings, Seventh International Heat Transfer Conference*, 3, 1982, pp. 87-92.
6. Booth, T.C., Dodge, P.R., and Hepworth, H.K., "Rotor-Tip Leakage: Part I Basic Methodology," *J. Engr. for Power, Trans. ASME*, 104, 1982, pp. 154-161.
7. Metzger, D.E. and Bunker, R.S., "Cavity Heat Transfer on a Transverse Grooved Wall in a Narrow Flow Channel," to be presented, 1985 ASME/ATChE National Heat Transfer Conference, Denver, USA, August 1985.
8. Metzger, D.E., Plevich, C.W., and Fan, C.S., "Pressure Loss Through Sharp 180 Degree Turns in Smooth Rectangular Channels," *J. Engr. for Gas Turbines and Power, Trans. ASME*, 106, 1984, pp. 677-681.
9. Boyle, R.J., "Heat Transfer in Serpentine Passages with Turbulence Promoters," ASME Paper No. 84-HT-24, 1984.

10. Johnson, R.W., and Launder, D.E., "Local Heat Transfer Behaviour in Turbulent Flow Around 180 Degree Bend of Square Cross Section," ASME Paper No. 85-GT-68, 1985.
11. Sahn, M.K. and Metzger, D.E., "Heat Transfer Around Sharp 180 Degree Turns in Rectangular Ducts," ASME Paper No. 85-GT-122, 1985.
12. Metzger, D.E., and Larson, D.E., "Use of Melting Point Surface Coatings for Local Heat Transfer Measurements in Rectangular Channel Flows With 90 Degree Turns," to appear, J. Heat Transfer, 1985.
13. Kercher, D.M., and Tabakoff, W., "Heat Transfer by a Square Array of Round Jets Impinging Perpendicular to a Flat Surface Including the Effect of Spent Air," J. Engr. for Power, Trans. ASME, 92, pp. 73-82, 1970.
14. Metzger, D.E., Florschuetz, L.W., Takeuchi, D.I., Behee, R.D., and Berry, R.A., "Heat Transfer Characteristics for Inline and Staggered Arrays of Circular Jets With Crossflow of Spent Air," J. Heat Transfer, Trans. ASME, 101, pp. 526-531, 1979.
15. Saud, N.R., Mujumdar, A.S., Abdel Messch, W., and Douglas, W.J.M., "Local Heat Transfer Characteristics for Staggered Arrays of Circular Impinging Jets with Crossflow of Spent Air," ASME Paper No. 80-HT-23, 1980.
16. Florschuetz, L.W., Metzger, D.E., and Su, C.C., "Heat Transfer Characteristics for Jet Array Impingement with Initial Crossflow," J. Heat Transfer, Trans. ASME, 106, pp. 34-41, 1984.
17. Florschuetz, L.W., and Tseng, H.H., "Effect of Nonuniform Geometries on Flow Distributions and Heat Transfer Characteristics for Arrays of Impinging Jets," J. Engr. for Gas Turbines and Power, Trans. ASME, 107, pp. 68-75, 1985.
18. Florschuetz, L.W. and Su, C.C., "Recovery Effects on Heat Transfer Characteristics Within an Array of Impinging Jets," Symposium on Transport Phenomena in Rotating Machinery, Honolulu, 1985.
19. Metzger, D.E., Berry, R.A., and Bronson, J.P., "Developing Heat Transfer in Rectangular Ducts with Arrays of Short Pin Fins," J. Heat Transfer, Trans. ASME, 104, pp. 700-706, 1982.
20. VanFossen, G.J., "Heat Transfer Coefficients for Staggered Arrays of Short Pin Fins," J. Engr. for Power, Trans. ASME, 104, pp. 268-274, 1982.
21. Brigham, B.A., and VanFossen, G.J., "Length to Diameter and Row Number Effects in Short Pin Fin Heat Transfer," J. Engr. for Gas Turbines and Power, Trans. ASME, 105, pp. 241-245, 1984.
22. Metzger, D.E., Fan, C.S., and Halay, S.W., "Effects of Pin Shape and Array Orientation on Heat Transfer and Pressure Loss in Pin Fin Arrays," J. Engr. for Gas Turbines and Power, Trans. ASME, 106, pp. 252-257, 1984.
23. Arora, S.C., and Abdel Messch, W., "Heat Transfer Experiments in High Aspect Ratio Rectangular Channel With Epoxied Short Pin Fins," ASME Paper No. 83-GT-57, 1983.
24. Steuber, G.D. "Heat Transfer and Flow Friction Characteristics of Full and Partial Height Short Pin Fin Arrays in Smooth and Roughened Channels," M.S. Thesis, Arizona State University, 1985.
25. Kapinos, V.M. "Heat Transfer From a Disk Rotating in a Housing With Radial Flow of Coolant," J. Engr. Physics, 8, pp. 35-48, 1965.
26. Owen, J.M. "The Reynolds Analogy Applied to Flow Between a Rotating and a Stationary Disk," Int. J. Heat and Mass Transfer, 14, pp. 451-466, 1971.
27. Hennecke, D.K., Sparrow, E.M., and Eckert, E.R.G., "Flow and Heat Transfer in a Rotating Enclosure With Axial Throughflow," Wärme-und Stoffübertragung, 4, pp. 222-228, 1971.
28. Metzger, D.E., "Heat Transfer and Pumping on a Rotating Disk with Freely Induced and Forced Cooling," J. Engr. for Power, Trans. ASME, 92, pp. 342-247, 1970.
29. Haynes, C.M., and Owen, J.M., "Heat Transfer From a A Shrouded Disk System With a Radial Outflow of Coolant," J. Engr. for Power, Trans. ASME, 97, pp. 28-38, 1975.
30. Owen, J.M., "Fluid Flow and Heat Transfer in Rotating Disk Systems," Heat and Mass Transfer in Rotating Machinery, Hemisphere, pp. 81-103, 1984.
31. Devyatov, V.I., "Investigation of Heat Transfer for Two Versions of Turbine Disk Cooling," Aviatzionnaya Teknika, 8, pp. 56-64, 1965.
32. Metzger, D.E., and Grochowsky, L.D., "Heat Transfer Between an Impinging Jet and a Rotating Disk," J. Heat Transfer, Trans. ASME, 99, pp. 663-667, 1977.

33. Metzger, D.E., Mathis, W.J., and Grochowsky, I.D., "Jet Cooling at the Rim of a Rotating Disk," *J. Engr. for Power, Trans. ASME*, 101, pp. 68-72, 1979.
34. Loftus, P.J. and Jones, T.V., "The Effect of Temperature Ratios on the Film Cooling Process," ASME Paper No. 82-GT-305, 1982.
35. Goldstein, R.J., Eckert, E.R.G., Chiang, H.D. and Elovic, E., "Effect of Surface Roughness on Film Cooling Performance," ASME Paper No. 84-GT-41, 1984.
36. Hay, N., Lampard, D., and Saluja, C.L., "Effects of the Condition of the Approach Boundary Layer and of Mainstream Pressure Gradients on the Heat Transfer Coefficients on Film-Cooled Surfaces," ASME Paper No. 84-GT-47, 1984.
37. Miller, K.L. and Crawford, M.E., "Numerical Simulation of Single, Double, and Multiple Row Film Cooling Effectiveness and Heat Transfer," ASME Paper No. 84-GT-112, 1984.
38. Goldstein, R.J., and Chen, H.P., "Film Cooling on a Gas Turbine Blade Near the End Wall," ASME Paper No. 84-GT-42.
39. Kruse, H., "Measurements of Film Cooling Effectiveness and Heat Transfer on a Flat Plate," *Heat and Mass Transfer in Rotating Machinery, Hemisphere*, pp. 451-461, 1984.
40. Kuenatler, P.A. "Linear Modeling in Forced Convection and an Experimental Study of Film Cooling With Multiple Rows of Discrete Injection Holes," Ph.D. Dissertation, Arizona State University, 1982.
41. Eckert, E.R.G., "Discussion of Metzger, D.E., Carper, H.J., and Swank, L.R., 'Heat Transfer with Film Cooling Near Nontangential Injection Slots'," *J. Engr. for Power, Trans. ASME*, 90, pp. 157-163, 1968.
42. Mayle, R.E. and Camarata, F.J., "Heat Transfer Investigation for Multihole Aircraft Turbine Blade Cooling," USAF Aero Propulsion Laboratory, AFAPL-TR-73-30, 1973.
43. Kim, H.K., Moffat, R.J., and Kays, W.M., "Heat Transfer to a Full-Coverage, Film-Cooled Surface With Compound-Angle Hole Injection," Stanford University, ME Dept., Report No. HMT-28, 1978.
44. Bulton, B.L., and Mohamad, T.T., "Experimental Techniques to Determine the Convective Heat Transfer Coefficients for Flat and Curved Surfaces," *High Temperature Tech.*, pp. 163-170, 1983.
45. Graziani, R., Blair, M.F., Kopper, F.C., and Mayle, R.E., "An Experimental Study of Endwall and Airfoil Surface Heat Transfer in a Large Scale Turbine Blade Cascade," *J. Engr. for Power, Trans. ASME*, 102, pp. 257-267, 1980.
46. Mayle, R.E., "A Composite Constant Heat Flux Test Surface," *Heat and Mass Transfer in Rotating Machinery, Hemisphere*, pp. 259-268, 1984.
47. Baughn, J.W., Takahashi, R.K., Hoffman, M.A., and McKillop, A.A., "Local Heat Transfer Measurements Using an Electrically Heated Thin Gold-Coated Plastic Sheet," *New Experimental Techniques in Heat Transfer - 1984*, ASME, pp. 9-17, 1984.
48. Hippensteele, S.A., Russell, L.M., and Stepka, F.S., "Evaluation of a Method for Heat Transfer Measurements and Thermal Visualization Using a Composite of a Heat Element and Liquid Crystals," *J. Heat Transfer, Trans. ASME*, 105, pp. 184-189, 1983.
49. Sparrow, E.M. and Tao, W.Q., "Enhanced Heat Transfer in a Flat Rectangular Duct With Streamwise-Periodic Disturbances at One Principal Wall," *J. Heat Transfer, Trans. ASME*, 105, pp. 851-861, 1983.
50. Chyu, M.K., "Local Heat/Mass Transfer Distribution for Turbulent Flow Over Roughened Surfaces," Ph.D. Dissertation, University of Minnesota, 1985.
51. Throckmorton, D.A. and Stone, D.R., "Model Wall and Recovery Temperature Effects on Experimental Heat-Transfer Data Analysis," *AIAA J.*, 12, pp. 169-170, 1974.
52. Clifford, R.J., Jones, T.V., and Dunne, S.T., "Techniques for Obtaining Detailed Heat Transfer Coefficient Measurements Within Gas Turbine Blade and Vane Cooling Passages," ASME Paper No. 83-GT-58, 1983.

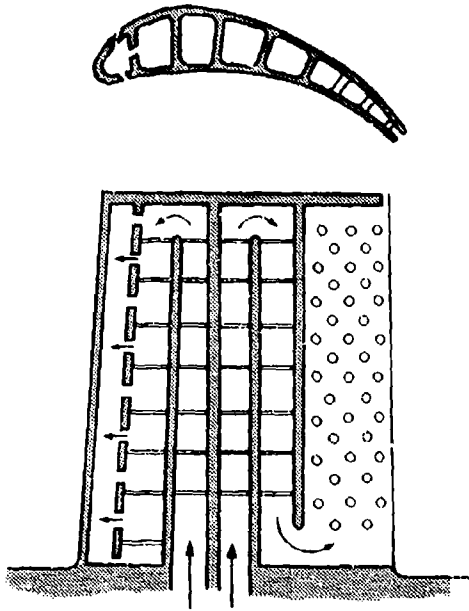


Figure 1 Schematic of a Cooled Airfoil

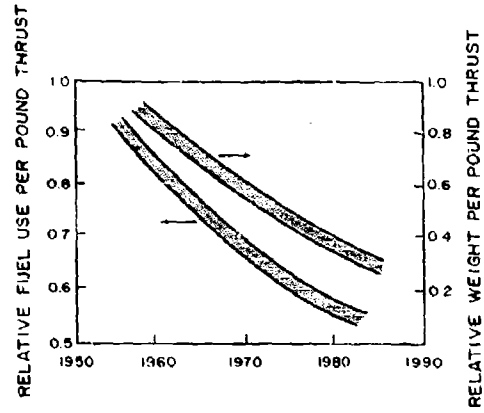


Figure 2 Performance Increases

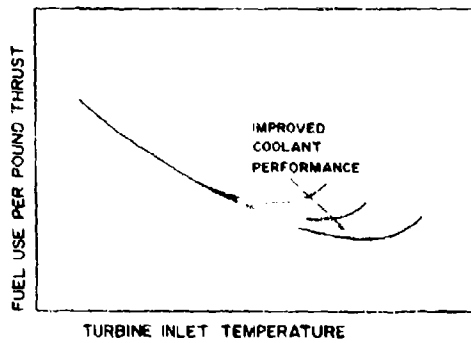


Figure 3 Coolant Performance Influence on Engine Performance

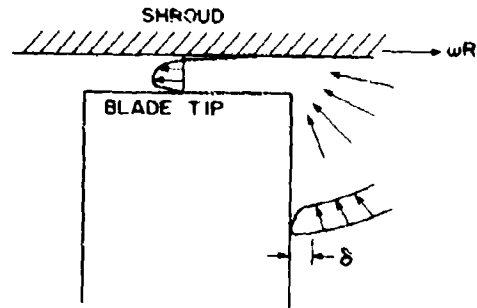


Figure 4 Tip Clearance Gap Flow

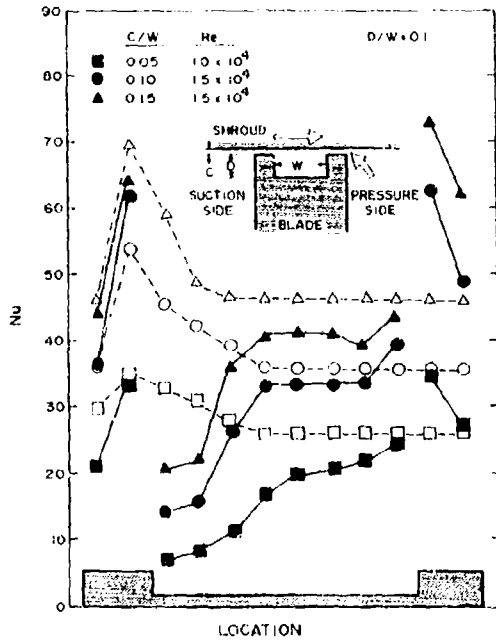


Figure 5 Heat Transfer on a Grooved Tip Model

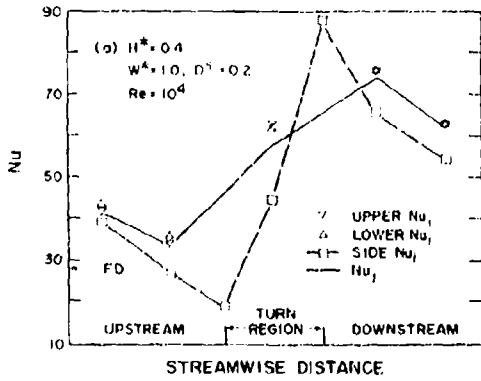


Figure 7 Typical Sharp 180 Degree Turn Heat Transfer

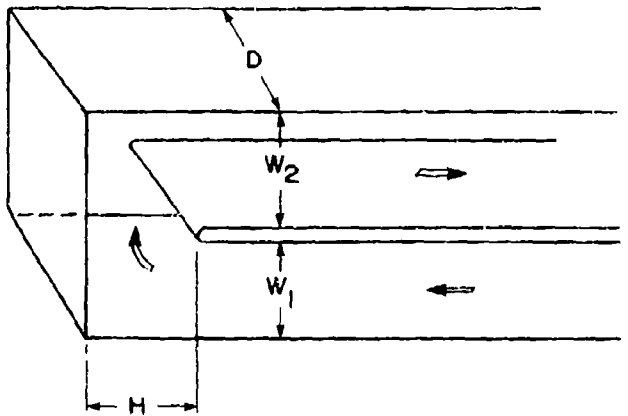


Figure 6 Sharp 180 Degree Turn Geometry

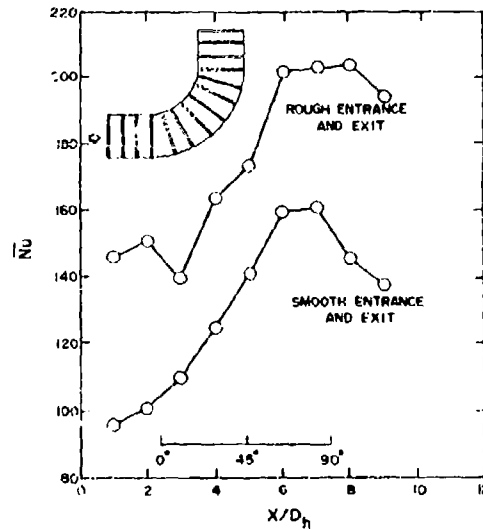


Figure 8 Typical Curved 90 Degree Turn Heat Transfer



Figure 9 Schematic of a Jet Array Cooled Airfoil

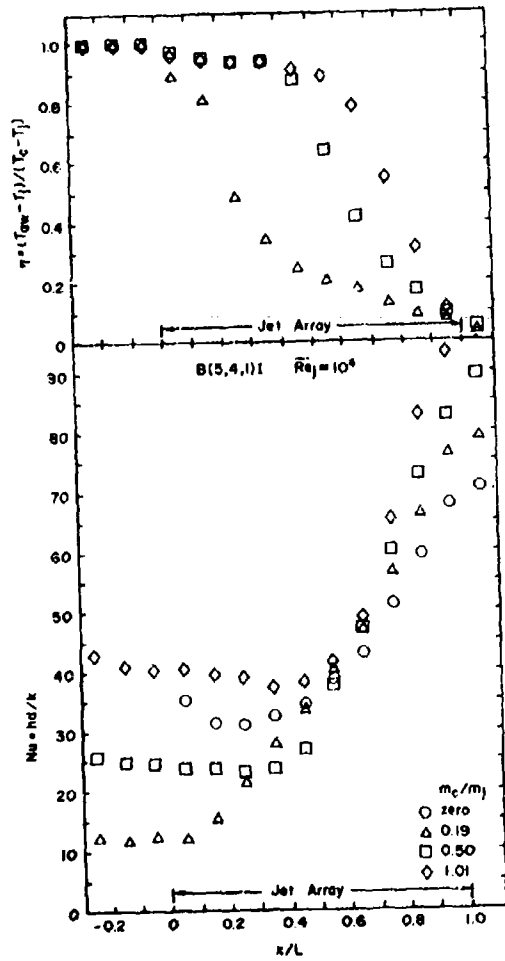


Figure 10 Jet Array Heat Transfer for Highly Non-Uniform Flow Distribution

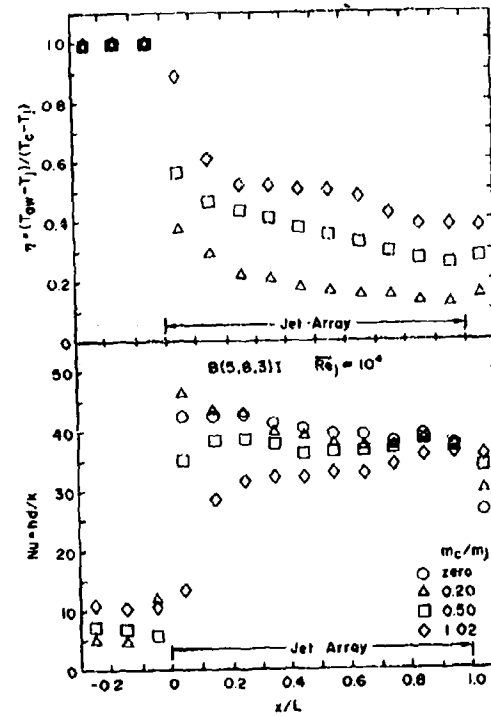


Figure 11 Jet Array Heat Transfer for Uniform Flow Distribution

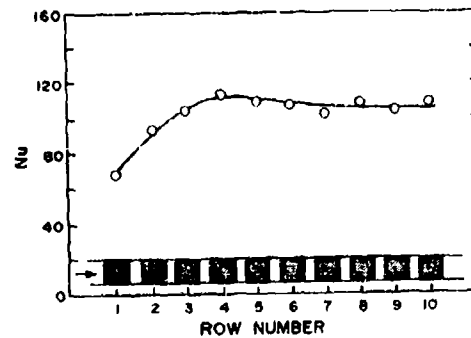


Figure 13 Full Length Pin Fin Heat Transfer

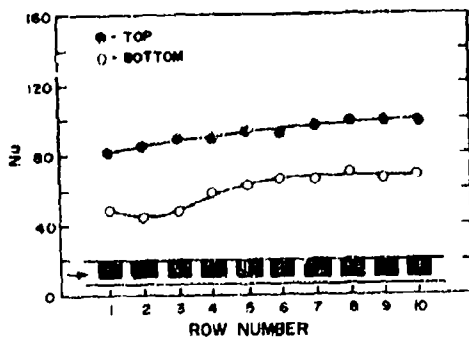


Figure 12 Partial Length Pin Fin Heat Transfer

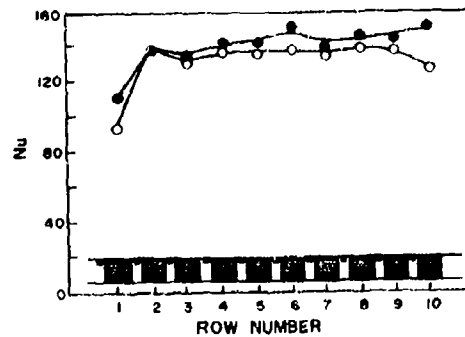


Figure 14 Pin Fin Heat Transfer with Rib-Roughened Walls

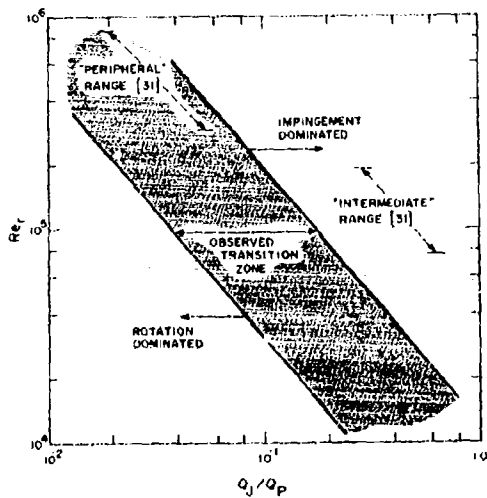


Figure 15 Flow Regimes for Impingement on Rotating Disks

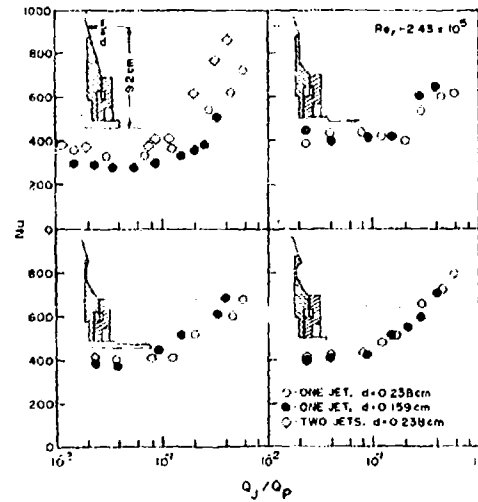


Figure 16 Rotating Disk Heat Transfer With Jet Cooling

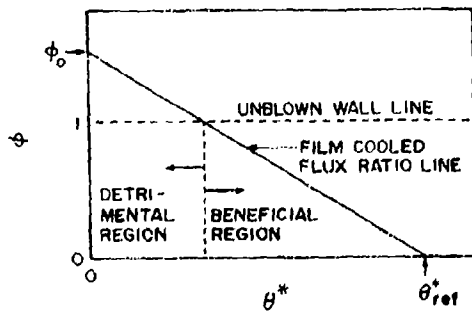


Figure 17 Film Cooling Performance Characteristics

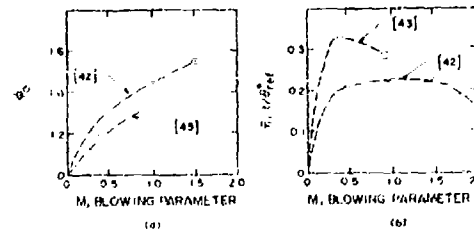


Figure 18 Comparison of Results, Refs. [42] and [43]

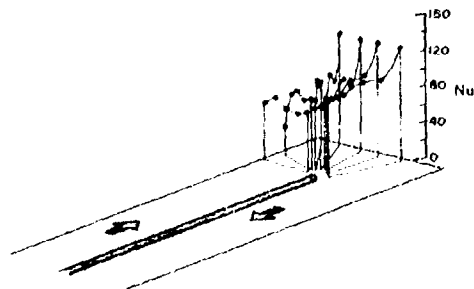


Figure 19 Local Heat Transfer Within a 180 Degree Turn

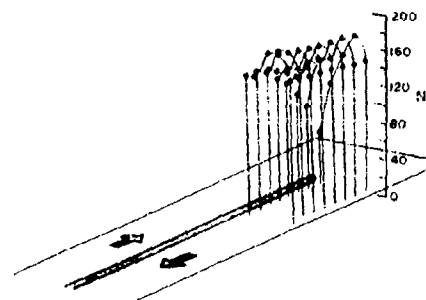


Figure 20 Local Heat Transfer Downstream of a 180 Degree Turn

DISCUSSION

G.M.Dibelius, Ge

You have raised the question of whether cooling of rotating discs by single jets has been applied. One reason why this has not been the case is the cyclic changes from cooling to heating and to cooling again. At least at the surface this might cause fatigue by thermal stresses.

Author's Reply

Your point is well taken and this may indeed be a problem with such applications. However, my impression is that some early failures with jet cooling on rotating parts were associated with failure to achieve the time-averaged heat transfer levels expected.

D.K.Hennecke, Ge

Your 180° turn channel has square corners. In many actual turbine blades one uses round corners to reduce the pressure loss. Do you think that the large increase in heat transfer you measured would be smaller with a round corner?

Author's Reply

We have measured the effect of rounded corners on the pressure loss in these 180° turns (Ref.8). Such rounding has only a very small effect on pressure loss and on the overall flow patterns which we have investigated through surface streamline visualization. Therefore I expect that the large overall rise in heat transfer that we measure would also be the case with rounded corners. Of course, severe rounding of the entire channel by use of a relatively thicker centre dividing rib would be expected to have an effect. In the present case we do expect that rounding of the upstream corner would eliminate or reduce the stalled flow zone in that corner which contributes to low heat transfer on the side wall in that region.

F.E.C.Culick, US

It seems that in general, unsteadiness in the flow field, whether it be associated with separation, turbulence, or acoustical motions, has striking effects on surface heat transfer rates. In your experimental work do you make measurements of unsteady motions? I have in mind particularly the possibility of forming a more coherent picture and understanding of diverse phenomena by using some measure(s) of unsteadiness in the flow.

Author's Reply

The measurement of unsteady motion is the exception, rather than the rule, in internal cooling channel heat transfer investigations. There is no question, however, that such motions are important to the convection heat transfer. In our laboratory we occasionally use hot wire and LDA in limited attempts to help us understand the observed heat transfer behaviour. For example, we have found in pin fin arrays that the peaking of row-averaged heat transfer at about the third to fifth row is associated with a peaking and subsequent decay of the turbulence intensity. Much more detailed mapping of the turbulence characteristics in internal cooling flows will be required for efforts to predict such flows numerically. There is a start on this work in various places. For example, turbulent motions have been measured in detail for 180° turns of rectangular cross section (turns with moderate radius ratio and no separation) at UMIST, UK and UCB, USA.

ROTATING HEAT TRANSFER INVESTIGATIONS ON A MULTI-PASS COOLING GEOMETRY

MR. R.J. CLIFFORD
 HEAD OF TURBINE RESEARCH & METHODS
 ROLLS-ROYCE LIMITED
 PO BOX 3
 FILTON
 BRISTOL BS12 7QE
 ENGLAND

SUMMARY

This paper reviews the effect of rotation on the heat transfer in a complex 3D multi-pass turbine blade cooling geometry. The test rig, the experimental technique and the initial results are discussed in detail.

Basic checks at zero rotational speed showed good agreement with data obtained earlier on this model using an alternative transient technique. Rotation was shown to have a significant effect on the heat transfer distribution ($\pm 30\%$) which when averaged over the gas washed surfaces showed a reduction to 90% of the static value. The effect of these changes on the blade predicted metal temperatures and lives are also reviewed.

Investigations are continuing to fully evaluate the implications of both Coriolis and buoyancy effects on the heat transfer distributions in these complex 3D geometries.

NOMENCLATURE

A, B & C	constants
A	area (m^2)
C_p	specific heat ($J/Kg \text{ } ^\circ K$)
D	characteristic dimension of passage (m)
d	wall thickness (m)
g	acceleration due to gravity (m/sec^2)
h	heat transfer coefficient ($w/m^2 K$)
$J = \frac{\Omega d^2}{\nu}$	Rotational Reynolds number
k	Thermal conductivity ($W/m K$)
m	mass flow (Kg/sec)
q	heat flux (w/m^2)
$Nu = \frac{h D}{k}$	Nusselt Number
Nu_m	mean Nusselt Number
Nu_0	Nusselt Number at zero rpm
$Pr = \frac{\mu C_p}{k}$	Prandtl Number
Ra	rotational Rayleigh Number $\frac{\mu \Omega^2 \beta d^3 (\Delta T)}{\nu^2} Pr$
$Re = \frac{m}{A} \cdot \frac{D}{\mu}$	Reynolds Number
$Ro = \frac{\Omega D}{u}$	Rosby Number
$St = \frac{h}{(m/A) C_p}$	Stanton Number
T	Temperature (K)
T_g	gas temperature (K)
T_w	wall temperature (K)
$\Delta T = T_w - T_g$	temperature difference (K)
t	time (seconds)
u	mean velocity (m/sec)
x	distance to wall (m)

GREEK SYMBOLS

$\alpha = \frac{k}{\rho c_p}$	diffusivity (m^2/sec)
β	volume expansion coefficient
$\nu = \frac{\mu}{\rho}$	kinematic viscosity
μ	dynamic viscosity
Ω	angular velocity (RAD/sec)
ρ	density (Kg/m^3)

INTRODUCTION

The major gas turbine aero engine manufacturers provide a range of engines to meet the differing requirements for the civil airline and military markets. The airline requirement demands engines with good specific fuel consumption and long turbine blade lives, whilst military engines generally operate with high thrust to weight ratios and therefore at higher turbine entry temperatures (TET). In order to satisfy these objectives the cooling air to the turbines needs to be used in the most efficient manner, and to do this the heat transfer on both the cooling side and hot gas side need to be fully understood.

Cooling techniques have changed markedly over the past three decades. This is reflected in the variation of TET over this period shown in Fig. 1. Early cooling methods were rudimentary whereby air was passed through hollow blades, this was subsequently refined to groups of small radial passages with cooling air flowing from root to tip. The nozzle guide vanes from these engines generally incorporated fabricated metal inserts which cooled the component with a combination of impingement and convective cooling flows. Over the past decade significant improvements accrued from the introduction of film cooling together with complex internal cooling passages on both blades and vanes.

In the past much effort was directed at measuring and understanding the hot side heat transfer, but only rudimentary studies were carried out on typical internal cooling geometries. This was because on simply cooled blades a large error in internal heat transfer coefficient had only a small effect on blade metal temperature. However, since more heat is removed by the modern cooling systems than their predecessors it becomes necessary to determine more accurately the internal as well as external heat transfer coefficients. This may be appreciated when it is realised that a given percentage error in the internal heat transfer coefficient corresponds to 3 times the error in blade metal temperature on the more sophisticated system, and any such error has a significant effect on turbine life.

An experimental technique was developed jointly by R-R and Oxford University (Ref. 1) to enable the heat transfer distributions on complex geometries to be accurately and comprehensively measured under scaled static conditions. At the same time work by Morris and Ayhan on circular ducts (Refs 2 and 3) and more recently by Clifford, Morris and Haragama on triangular ducts (Ref. 4) indicated that rotation can significantly change the heat transfer distribution obtained statically in simple ducts. These studies suggested that the Coriolis and centripetal components of acceleration would influence the heat transfer in the complex multi-pass cooling geometries employed in turbine blades of today.

This paper reviews a series of investigations which used the multi-pass cooling geometry evaluated statically in Ref. 1 (see Fig. 2) to study the effect of rotation up to and beyond the non-dimensionally correct engine operating point.

THE EXPERIMENTAL TECHNIQUE

This is a transient technique in which a steady flow of coolant is suddenly established through the model passage. By monitoring the temperature time history of the surface of the model wall it is possible to deduce the surface heat flux.

The model was not viewable during the experiment and so air and wall thermocouples were employed to provide data within the model passages since the full surface mapping technique described in Ref. 1 could not easily be used. It was considered that these localised data would provide an adequate guide as to the effects of rotation. Also, in order to model the buoyancy forces correctly it was necessary to employ a 'hot' model with 'cold' coolant flow. After considerable feasibility studies it was decided to operate with the model at ambient temperature and use cold gaseous nitrogen as the cooling medium. Despite some initial doubts this system worked exceedingly well.

To obtain local heat transfer coefficients it was necessary that the following conditions be satisfied:

1. The model be of a low conductivity material.

2. The model wall be sufficiently thick as to be regarded mathematically as semi infinite.
3. The experimental time be sufficiently short so that
 - (i) the heat flux will penetrate only a short way into the wall (diffusion depth)
 - (ii) the heat flow can be regarded as 1 dimensional.

THEORY

1. To obtain heat transfer coefficients from the experiment.

The equation governing heat conduction is

$$\nabla^2 T = \frac{1}{\alpha} \frac{\partial T}{\partial t} \quad (1)$$

The time at which the measurements are taken are such that one-dimensional conditions prevail in the model. Since the diffusion depth of the temperature pulse is small the lateral conduction can be ignored and the surface temperature regarded as effectively constant. The surface temperature history may therefore be related to the convective heat transfer using the one-dimensional equation

$$\frac{\partial^2 T}{\partial x^2} = \frac{1}{\alpha} \frac{\partial T}{\partial t} \quad (2)$$

The heat transfer rate to be measured occurs at $x = 0$. In this case the temperature is always ambient at the rear surface so the boundary conditions became

$$x = 0: \quad q = -k \frac{\partial T}{\partial x}$$

$$x = \infty: \quad T = 0$$

$$q = h(T_g - T_w)$$

The above equations were therefore solved numerically and an iterative procedure developed whereby the heat transfer coefficient could be determined from the measured surface and local air temperature historys (5). The heat transfer coefficient is itself a function of the upstream wall temperature distribution and this was not taken into account. This was justified because, in test cases using well established expressions for the variation of h with upstream wall temperature it was found that the value of h determined was relatively insensitive to the upstream wall temperature effect. This was also confirmed in earlier experiments on circular tubes. (Ref. 1).

2. Effects of Rotation

A comprehensive mathematical explanation as to the effects of rotation are presented by Morris and Aynan in Ref. 2. They suggest that the change in heat transfer due to rotation in a circular duct can be correlated using the expression

$$\frac{Nu_m}{Nu_0} = \left(\frac{Ra}{Re^2} \right)^{-0.186} \cdot Ro^{0.33} \quad (3)$$

On completion of the present investigations attempts were made to correlate the data in terms of Coriolis and centripetal effects, using the expression

$$\frac{Nu_m}{Nu_0} = A \left(\frac{Ra}{Re^2} \right)^B Ro^C \quad (4)$$

THE MODEL

The model used in these investigations was a typical multi-pass blade cooling system cast 3x full size in a thick walled epoxy resin - see Fig. 2. Prior to commencing considerable studies were undertaken to ensure that the model material could operate with cold gases at the high 'g' loadings necessary to arrive at the correct non-dimensional operating conditions.

The model was instrumented with 30 wall and 11 air thermocouples positioned at the stations shown in Fig. 3. The wall thermocouples were fast response 0.0002 in. thin foils supplied by Rotadata Ltd. The air thermocouples were 0.005 in. diameter chromel/alumel wire simply supported on the duct centre line. Again, before the model was instrumented tests were conducted to ensure that both types of thermocouple would operate at 12,000 g and -120°C.

The complete model assembly with its thermocouple leads and peripherals is shown in Fig. 4.

THE TEST RIG

The test rig is shown diagrammatically in Fig. 5 and fully installed in its reinforced test cell with nitrogen supply and other services in Fig. 6.

Fig. 5 shows the model located at the top of its 1m long 0.2 m dia. rotor arm. The cooling air was supplied to the model through the centre of the front bearing and via a radial tube. To enable this feed pipe to be pre-cooled to the required operating temperature, the cooling air supply system was encased in a secondary duct. The cold gaseous nitrogen was pumped around this secondary (bypass) circuit prior to the test commencing.

The model instrumentation leads were taken out through the rig drive shaft to a 60 channel slip ring unit. The test unit health monitoring instrumentation was coupled to the rotor arm only when the model was static, this link being disconnected immediately prior to the test.

The test cell was evacuated to 1 psia prior to the test to reduce the power needed and avoid cell heating problems. The rig was coupled to and driven by a 500 HP motor.

TEST PROCEDURE

Prior to commencing a test the model and bypass line control valves were set to provide the required coolant flow to the model. The test cell was evacuated and coolant flowed through the bypass line until the air supply duct was at the required operating temperature. (The model was monitored throughout this period to ensure that it remained at ambient temperature). The static instrumentation was then disconnected by a mechanical arm, the model spun to the required test speed and the coolant feed switched to the model.

The thermocouples were monitored throughout the test by on line data logging equipment and the results finally processed on a PDP11-34 computer.

DISCUSSION

The heat transfer data obtained for this model from the static full surface coverage studies (Ref. 1) are shown in Fig. 7. These datum conditions were repeated using the current experimental technique at zero rpm in order to check the validity of the data obtained and test results found to be reproducible to within 5%. Having established a viable datum, tests were then conducted at a range of speeds up to 4000 rpm. (The original blade design point (engine) conditions were equivalent to 3200 rpm, 72,000 Reynolds Number and $\left(\frac{\Delta T}{T_0}\right)_{\text{INLET}} = 0.32$).

The general effects of rotation were similar at all speeds with Coriolis and centripetal effects resulting in considerable circumferential changes in heat transfer. These are summarised in Fig. 8 where it can be seen that in general:

- (i) With outward flowing coolant the pressure surface heat transfer is enhanced and that on the suction surface reduced.
- (ii) With inward flowing coolant the suction surface heat transfer is enhanced and the pressure surface reduced.

The magnitude of these changes at the design point conditions can be seen in Fig. 9. Reductions in heat transfer of up to 30% were noted at some stations, whilst others exhibited enhancements up to 35%, with the most significant changes being noted close to the bends. Averaging these data suggests that the overall effect of rotation is to reduce the heat removal from this system to around 90% of that measured statically.

These changes in heat transfer were fed into the TACITUS design suite to evaluate the effect of rotation on blade metal temperature (TACITUS is a linked suite of interactive computer programs developed by Rolls-Royce to cover the aerodynamic, heat transfer and stress routines needed to design cooled turbine blades - Ref. 6). The metal temperature distributions with and without rotation for the tip section only are shown in Fig. 10. At first glance it appears that the isotherm patterns are similar. However, closer examination reveals that local changes of up to 40°C have resulted due to including the effects of rotation. Local errors of this magnitude could change the predicted blade lives by a factor of 3. This shows the vital importance of accurately investigating both the internal and external heat transfer distributions during a blade design.

It was not possible to evolve a general correlation for the effects of rotation on this complex geometry based on the relationship suggested by Morris. At each station in the duct a different set of constants were found to apply (equation 4) see Table I. Analysis of the data (100,000 test points) are continuing to try to evolve a more representative relationship for these complex 3D geometries. Meanwhile, experimental data obtained from investigations using the technique described in this document are being used to improve the predictions from TACITUS so that future turbines will be designed right

first time.

CONCLUSIONS

An experimental techniques has been successfully developed to enable the effects of rotation on heat transfer to be accurately quantified on a complex 3D cooling geometry.

The basic checks at zero speed showed good agreement with data obtained using earlier transient techniques.

Rotation was found to have a significant effect on the heat transfer distribution in the cooling passages with reductions and enhancements in excess of 30% being recorded. The overall effect at design point conditions was to reduce the heat removed to around 90% of the static value.

Investigations are continuing to enable the effects of rotation on complex 3D cooling systems to be better understood, and the methodology used in the blade design suites updated.

Table 1

Correlations of all data at each location in the first and second pass of the model.

$$Nu_{ROT}/Nu_{STAT} = A \left(\frac{Ra}{Re^2} \right)^B (Ro)^C$$

POSITION		CONSTANT		
PASS	LOCATION	A	B	C
1st	HUB S.S.	.56	-.11	.08
"	MID P.S.	1.61	.03	.03
"	MID S.S.	.45	-.01	-.14
"	TIP P.S.	6.49	-.03	.52
"	TIP S.S.	.39	-.10	-.01
2nd	TIP P.S.	1.22	-.03	.09
"	TIP S.S.	9.89	.26	-.02
"	MID P.S.	.59	-.12	.13
"	MID S.S.	.99	-.09	.15
"	HUB P.S.	.85	-.05	.07
"	HUB S.S.	1.00	-.05	-.10

ACKNOWLEDGEMENTS

The author gratefully acknowledges permission from Rolls-Royce to publish the studies described.

In addition the author would like to thank his colleagues at Rolls-Royce for their support in the work described, in particular, Mr. F. Richardson and Mr. I. Charters.

REFERENCES

1. Clifford, R.J., Jones, T.V. and Dunne, S.T.
"Techniques for Obtaining Detailed Heat Transfer Coefficient Measurements within Gas Turbine Blade and Vane Cooling Passages."
ASME Paper 83-GT-58, 1983.
2. Morris, W.D. and Ayhan, T.
"Observation on the Influence of Rotation on Heat Transfer in the Coolant Channels of Gas Turbine Rotor Blades".
Proc. Inst. Mech. Eng. Vol. 193, No. 21, 1979, p.303.
3. Morris, W.D. and Ayhan, T.
"An Experimental Study of Turbulent Heat Transfer in a Tube which Rotates about an Orthogonal Axis" presented at the XIVth ICHMT Symposium, Dubrovnik, Yugoslavia Sept. 1982.

4. Clifford, R.J., Morris, W.D., Haragama, S.P.
"An Experimental Study of Local and Mean Heat Transfer in a Triangular-Sectioned Duct Rotating in the Orthogonal Mode".
ASME Paper 84-GT-142, 1984.
5. R-R Unpublished Research 1978-1982.
6. Holland, M.J. and Thake, T.F.
"Rotor Blade Cooling in High Pressure Turbines".
Journal of Aircraft AIAA 80-4061, June 1980.

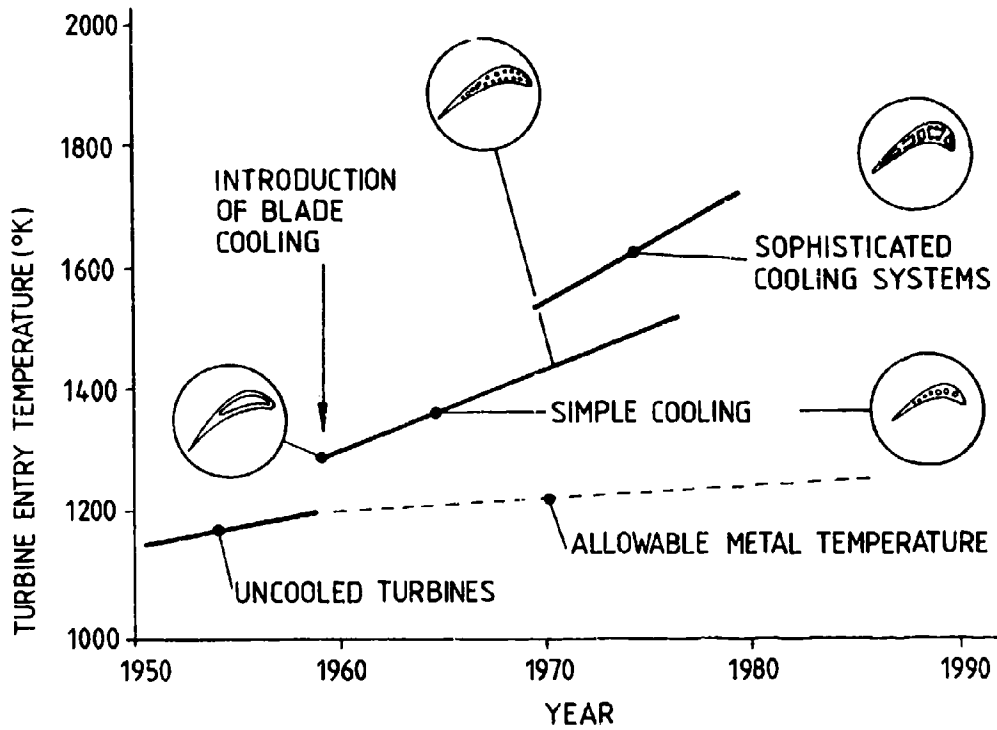


Fig.1 Variation of engine TET over recent years

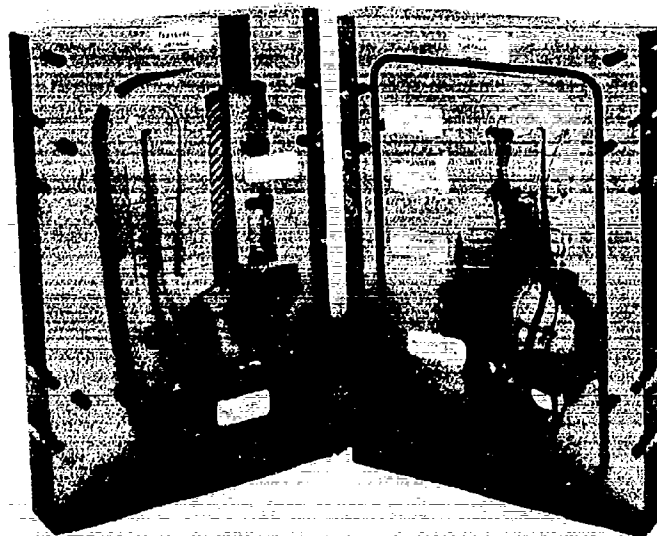


Fig.2 Typical multipass cooling geometry

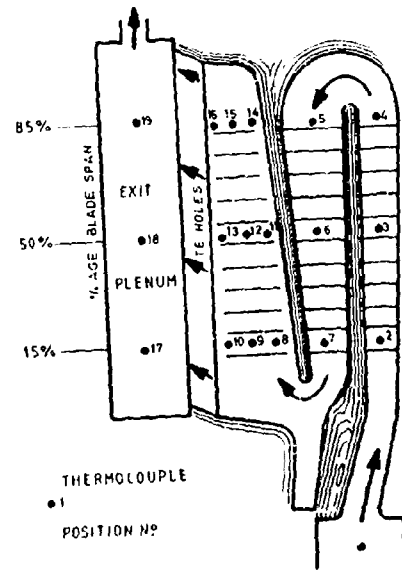


Fig.3 Position of air and wall thermocouples in multipass blade

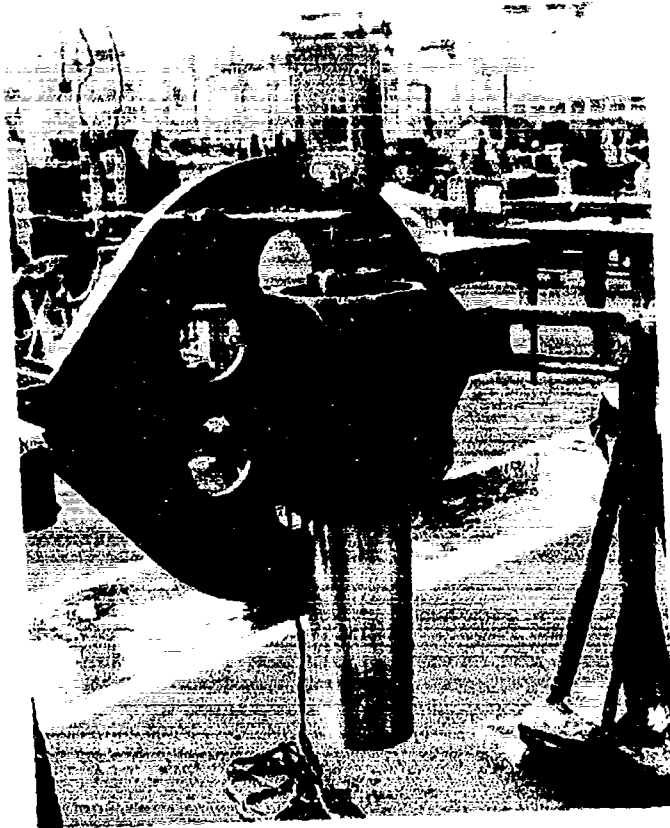


Fig.4 Model assembly with thermocouple leads

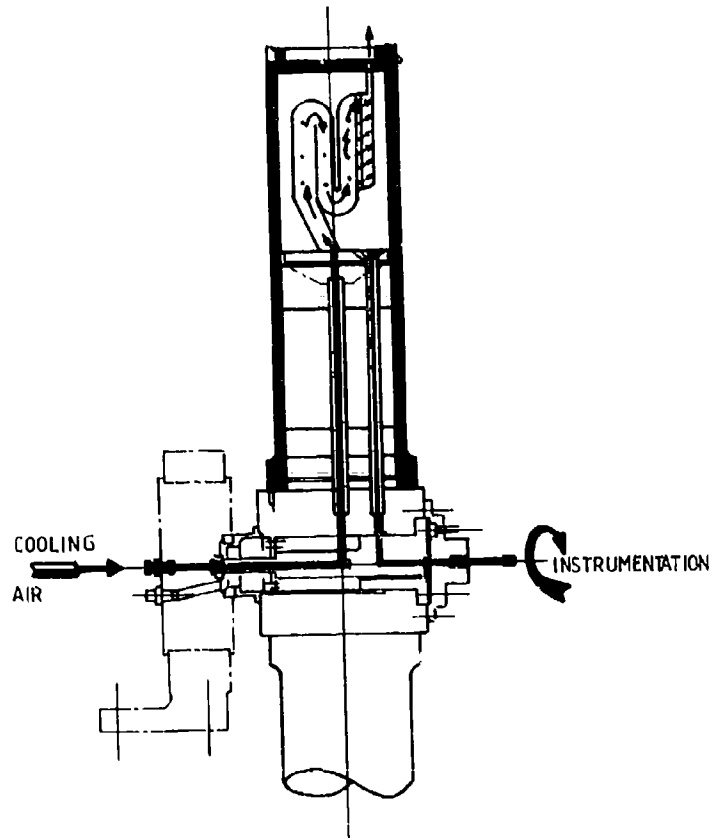


Fig.5 Diagram of rotating heat transfer rig

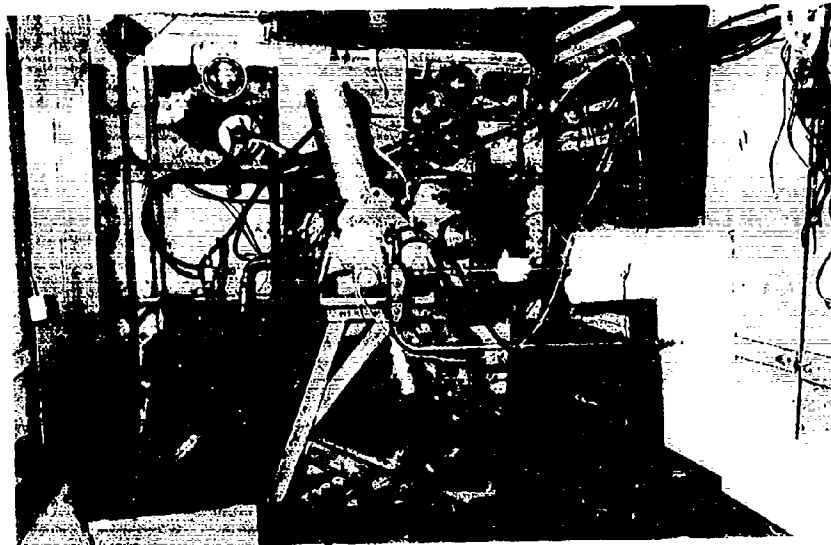


Fig.6 Rotating rig installed in spinning cell

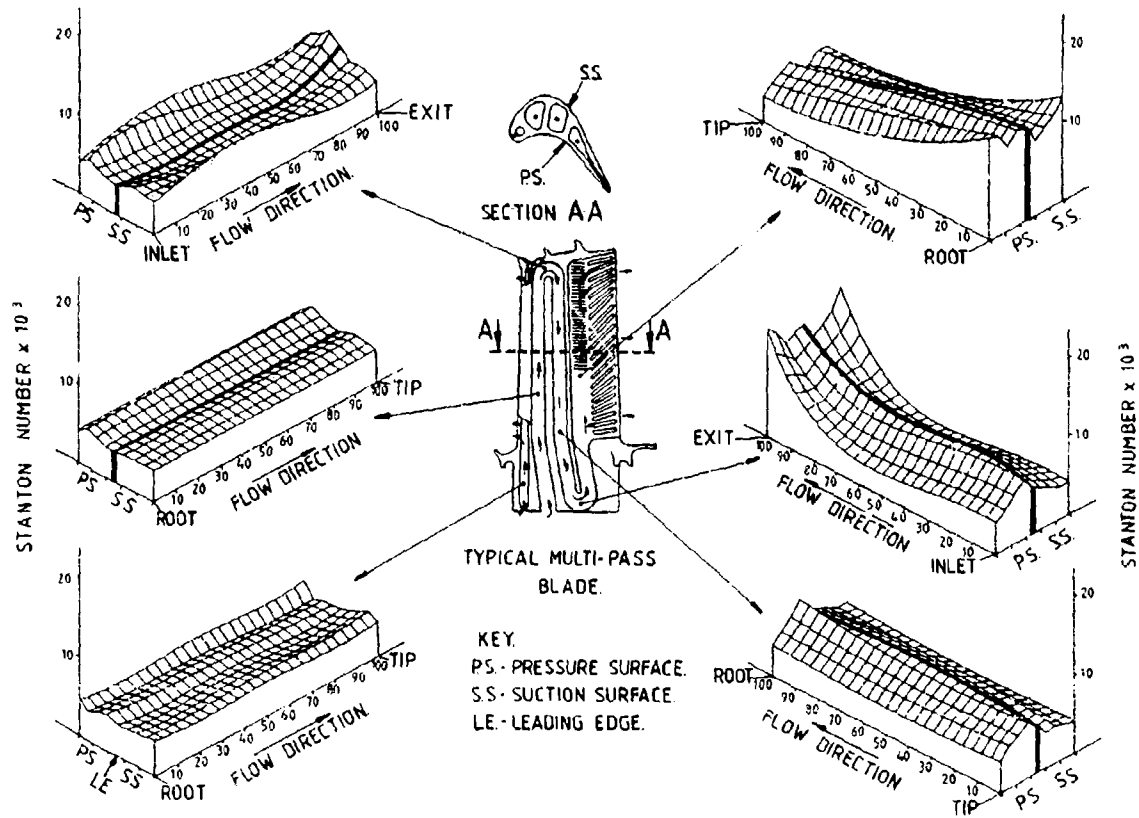


Fig.7 Composite showing the variation of heat transfer inside a typical engine multipass cooling geometry

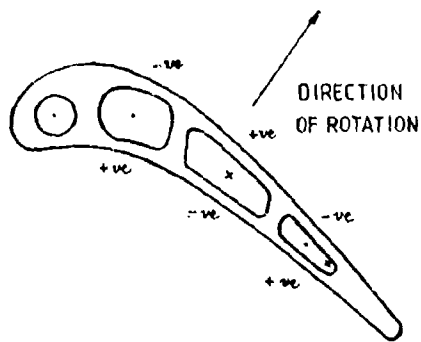


Fig.8 Summary of effects of rotation on experimentally obtained heat transfer coefficients

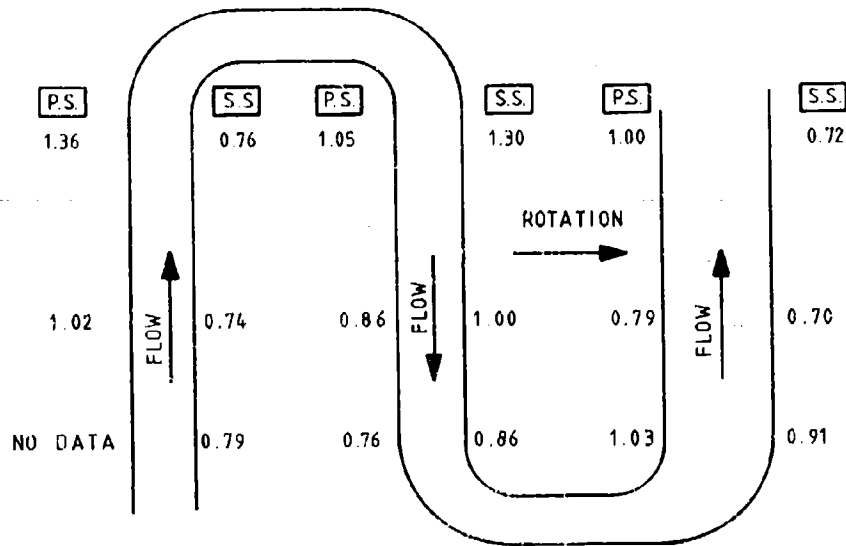


Fig. 9 $\left(\frac{\text{St. Rotating}}{\text{St. Static}}\right)$ results at design conditions ($Re = 72000$ Speed 3200 r.p.m.
 $\frac{DT}{T} = 0.32$)

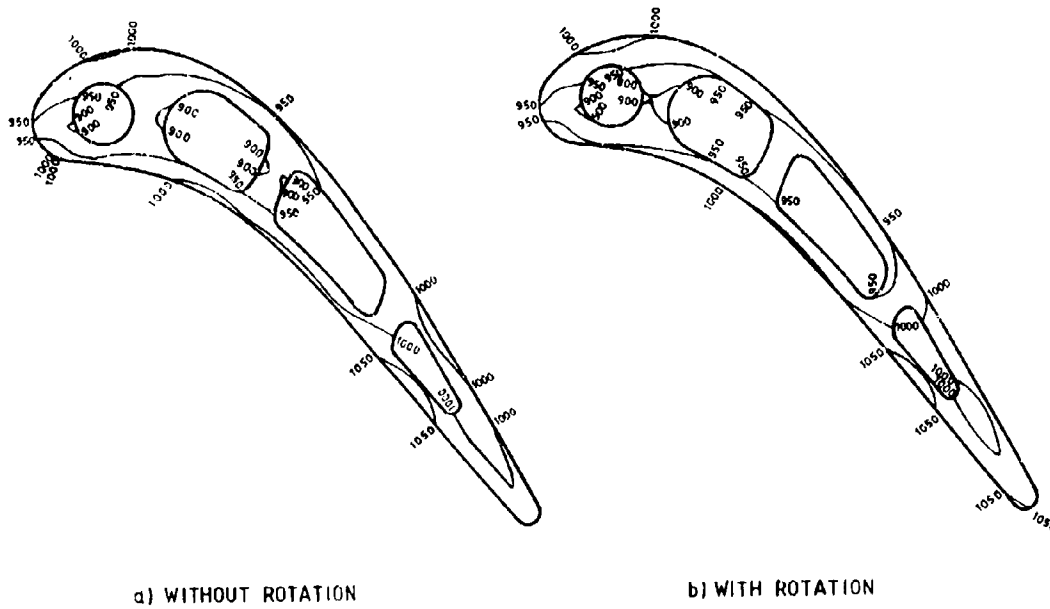


Fig. 10 Comparison of predicted blade metal temperatures with and without rotation

DISCUSSION

J.M.Hannis, UK

Were the rotational Rayleigh number and Rossby number in the rig representative of real engine conditions? Was it necessary to extrapolate the rig data to obtain the effects of rotation on engine blade temperatures?

Author's Reply

The rig conditions were non-dimensionally correct for:

- Rayleigh No.
- Rossby No.
- Reynolds No.
- Mach No.

No extrapolation of data was required to arrive at engine conditions.

LOCAL AND MEAN HEAT TRANSFER ON THE LEADING AND TRAILING SURFACES OF A
SQUARE-SECTIONED DUCT ROTATING IN THE ORTHOGONAL-MODE.

W D Morris
Fenner Professor of Mechanical Engineering
Head of Department of Engineering Design and Manufacture
University of Hull
Hull, HU6 7RX
United Kingdom

S P Horagame
Senior Scientific Officer
Propulsion Department, TID
Royal Aircraft Establishment
Pyestock, Farnborough, GU14 0LS
United Kingdom

SUMMARY

This paper describes the results of an experimental study of local and mean heat transfer over the leading and trailing surfaces of a square-sectioned duct which is constrained to rotate about an axis perpendicular to the main direction of through flow. Both radially outward and inward coolant flow conditions are considered.

Physical arguments are discussed which explain the data trends found in terms of Coriolis-induced secondary flows and rotational buoyancy and these trends are compared with the corresponding problem in circular-sectioned tubes.

NOMENCLATURE

English Symbols

C_p Constant pressure specific heat of coolant
 d Hydraulic diameter of duct
 h Heat transfer coefficient
 H Eccentricity of mid cross-sectional plane of duct
 J Rotational Reynolds number
 k Thermal conductivity of coolant
 l Length of duct
 Nu Nusselt number
 Pr Prandtl number
 Re Rotational Rayleigh number
 Re Duct flow Reynolds number
 Ro Version of the Rossby number
 V Mean coolant velocity along duct
 X Parameter defined in equation (6)
 z Axial location along the duct measured from duct inlet.

Greek Symbols

β Coefficient of volume expansion of coolant
 Γ Parameter defined in equation (7)
 ΔT_w Representative difference in temperature difference
 ν Absolute viscosity of coolant
 ρ Density of coolant
 ϕ Functional relationship
 Ω Angular velocity

Subscripts

∞ Evaluated with developed flow
 m Mean value for the duct
 z Evaluated locally at axial position z .

1. INTRODUCTION

The sustained improvement in the performance and fuel economy of aero gas turbines over the last two decades may be attributed to a wide variety of research and development programmes in virtually all the engineering sciences, materials and manufacturing technology. In particular the mutually conflicting desire to operate with progressively higher turbine entry temperatures with the attendant temperature-induced degradation of material strength has necessitated the use of very sophisticated air cooling passages in the turbine rotor blades. Not only are these coolant passages complex in the sense that the coolant flows through interconnected multi-pass channels which are often non-circular, but additionally the cooling surfaces themselves incorporate a variety of extended surface devices to improve local heat transfer. These typically take the form of transverse ribs or cylindrical pillar-like protrusions.

The accurate determination of heat transfer coefficient distributions in these blade passages is vital at the design stage in order to assess blade life via the corresponding operational temperatures expected in the blade material. In this respect the above-mentioned complexities of channel geometry are problematic in their own right for precise heat transfer predictions. Additionally the problem is further complicated by the fact that, since the coolant is constrained to rotate with the passage, the influence of rotation on the flow field and its resultant effect on heat transfer must also be taken into account.

The present authors have been involved with other University-based specialist heat transfer groups in a coordinated programme to study fundamental aspects of blade cooling. In general terms our own University role has been concerned with assessing the importance of rotation on local and mean heat transfer in ducts of relatively simple, but not necessarily circular, cross section. The ducts rotate about an axis perpendicular to the main direction of flow as depicted in Figure 1. This configuration is often referred to as orthogonal-mode rotation in the technical literature. In each case flow may be radially outward or inward in practice depending on the design concept adopted. Specifically this paper describes the results of an experimental investigation of heat transfer over the leading and trailing surfaces of a square-sectioned tube rotating in this orthogonal mode.

2. FORMULATION OF PROBLEM

Rotation of a duct will generally influence internal flow in three ways. For steady rotational speed Coriolis and centripetal acceleration components must be included in the fundamental momentum conservation equations to account for the non-inertial nature of the flow reference system. If the rotor is either accelerating or decelerating then the angular rate of velocity change must also be taken into account. For the case of steady rotational speed Morris (1), using laminar flow as an illustrative case, has shown that the Coriolis terms are capable of sustaining vorticity generation in the fluid relative to the duct. This vorticity generation can severely alter the nature of the stationary duct flow field and hence the fluid temperature distribution when the duct walls are heated. This in turn changes the local heat transfer at the fluid/duct wall interface. For constant density flow the centripetal terms are mainly conservative in nature and do not tend to act as source terms for relative vorticity generation. Thus only if temperature-induced density variations are present in a heated flow will the centripetal terms tend to create velocity field changes and this will be via a buoyancy-type mechanism. When rotational buoyancy is present the direction of flow along the duct will be an important interactive consideration since buoyancy could in principle either enhance or impair the usual forced convection mechanism operating in the stationary tube mode.

A number of theoretical and experimental studies of flow in circular tubes with orthogonal-mode rotation have been undertaken by Harus (2), Trefethen (3), Benton and Boyer (4), Mori and Nakayama (5), Ito and Nambu (6), Mori et al (7), Skiadreas and Spalding (8), Metzger and Stan (9), Lokui and Limanski (10), Zysina-Molozken et al (11). In the main the theoretical treatments have involved both laminar and turbulent flow with either heated or non-heated duct walls. The theoretical studies have included Coriolis terms but the centripetal buoyancy possibility has not been included in those theoretical models. Theoretical data for flow resistance and heat transfer has been compared with experimental data for developed flow conditions. In the main the relative vorticity generated in the tube because of the Coriolis terms tends to improve heat transfer; a result mainly confirmed by experiment.

Morris and Ayhan (12), (13) have argued that some of the experimental scatter evident in reported heat transfer studies with orthogonal-mode rotation could possibly be explained as a buoyancy effect. Using circular-sectioned tubes these authors presented experimental data for radially outward and inward flow to substantiate this proposal. It was shown that rotational buoyancy tended to impair heat transfer when the flow was radially outward whilst the converse was true for radially inward flow. Clifford et al (14) have presented experimental data for triangular-sectioned ducts with radially outward flow. This work highlighted the problem associated with conduction in the wall material but nevertheless was able to show that buoyancy tended to have an adverse effect on mean heat transfer. It was not possible to draw definitive conclusions from this particular study but the overall complexity of the flow and heat transfer present was clearly brought out.

The nature of the cross stream secondary flows generated by the Coriolis terms resulting from the theoretical studies mentioned above are shown schematically in Figure 1. Note that the core region fluid tends to move towards the trailing surface when the flow is radially outwards. The resulting distortion of the fluid temperature distribution will tend to give rise to a non-uniform distribution of surface heat flux in the circumferential direction with a region of relatively higher heat transfer coefficient over the trailing edge region when the flow is radially outwards. This effect can be seen in the theoretical study of Skiadreas and Spalding (8) and in the experimental work of Mori and Nakayama (5). In practice this non-uniformity in circumferential heat transfer could result in corresponding differences in the wall temperature being established in actual rotor blades.

As mentioned above the present authors have been conducting an ongoing programme to study the overall influence of rotation on heat transfer in ducts rotating in the orthogonal-mode. In the work reported here a square-sectioned duct with either radially outward or radially inward flow has been investigated. Because of the circumferential variation in heat transfer coefficient outlined above simultaneous measurements of heat transfer have been conducted on the leading and trailing surfaces of the duct. Details of this investigation now follow.

3. APPARATUS, EXPERIMENTAL PROGRAMME AND METHOD OF DATA PRESENTATION

The heated test section was designed as an easily removable sub-assembly which could be attached to a rotating arm which formed part of a general rotary test facility. The constructional details of the test section are shown in figure 2. The heated section was cast from Nimonic steel and subsequently machined externally to permit the attachment of insulated inlet and exit sections, the embedding of

thermocouples on the leading and trailing surfaces and Nichrome electrical wire for heating. The active length of this test section was 150 mm and the section was 7.5 mm square. When fitted the mid section of the heater had an eccentricity of 250 mm.

Air could be blown radially outwards through the test section via a circular sectioned rotating plenum as shown in figure 2 so that a reasonably good approximation to a "sharp edged" entry was formed at the inlet plane of the heated test section. The air entered the plenum via a rotating seal. Another similarly constructed test section was used for radially inward flow tests.

In both cases the inlet air temperature to the section and the emerging air temperature was measured by means of thermocouples. In the case of the exit air temperature a number of mixing gauzes were fitted in an insulated exit extension in order to mix the flow prior to making a bulk temperature measurement. This was done with two thermocouples.

The rotating facility available incorporated a controlled motor drive system, power slipping, instrumentation slipping, test arm and air delivery system. This facility has been previously described in detail by Morris and Ayhan (12) and the general layout is as shown in figure 3. Rotational speed was limited to a maximum level of 1850 rev/min with this facility.

All the thermocouple signals were fed to an automatic data acquisition system. Rotational speed was measured with a digital interval meter and magnetic shaft encoder, air flow rate with a series of rotameters and/or anubar system, and the electric dissipation in the heater with a Wattmeter.

The standard test procedure adopted was that described by Morris and Ayhan (12) in their work with circular sectioned tubes. In principle this involves a careful energy balance involving the generation rate in the electrical heater, external loss to atmosphere and conduction along the walls of the test section in order to determine the local variation of heat flux to the fluid. External losses from the test assembly were determined from a series of calibration tests undertaken prior to the main convective tests. These loss characteristics were periodically re-checked during the programme. By this means it was possible to determine both mean and local heat transfer coefficients for the test section over a variety of operating conditions within the performance envelope of the facility.

The conservation equations of momentum and energy may be used to identify suitable non-dimensional groups to characterise the effect of rotation on heat transfer or indeed conventional dimensional analysis. For this class of rotating system the outcome of such analyses suggest that in general

$$Nu = \phi(Re, Pr, Ra, J, L/d, H/d) \quad (1)$$

where

$$Nu = \frac{hd}{k} \quad (\text{Nusselt Number})$$

$$Re = \frac{Vd\rho}{\mu} \quad (\text{Through Flow Reynolds Number})$$

$$Pr = \frac{\mu C_p}{k} \quad (\text{Prandtl Number}) \quad (2)$$

$$Ra = \frac{H\Omega^2 \beta \rho^2 k C_p d^3 \Delta T_w}{\mu k} \quad (\text{Rotational Rayleigh Number})$$

$$J = \frac{\Omega d^2 \rho}{\mu} \quad (\text{Rotational Reynolds Number})$$

and other individual symbols have the significance given in the Nomenclature. Note that the inclusion of rotation in the most general case proposed above results in the appearance of the rotational Rayleigh number to characterise buoyancy via the centripetal acceleration component and the rotational Reynolds number via the Coriolis acceleration component. The eccentricity ratio H/d has been included for the sake of generality.

The experiments described below were conducted with air as the convective fluid and the temperature range covered did not cause noticeable changes in the Prandtl number. Also the tests were conducted with a single geometric configuration. Equation (1) can thus be simplified in this case to

$$Nu = \phi(Re, Ra, J) \quad (3)$$

Note that some workers have characterised the Coriolis effect in non-dimensional terms using a form of the Rossby number, Ru , defined as

$$Ru = \frac{\Omega d}{V} \quad (4)$$

The choice is mainly one of preference and the rotational Reynolds number has been selected in this instance.

The groups shown defined in equation (2) may be evaluated at specific locations in the duct or on a mean basis as required. In the present case all raw experimental data was stored on disc by the data acquisition system and automatically processed along the lines suggested by equation (3) as required.

A synopsis of the geometric features of the test assembly and the range of non-dimensional variables covered with the present investigation is given in Table 1.

Test Section Geometry

Internal dimensions of test section	7.5 x 7.5 mm sq
Length of test section	150 mm
Wall thickness of duct	1.0 mm
Eccentricity at mid section of test section	250 mm
Hydraulic diameter	7.5 mm
Length/hydraulic diameter ratio	20
Eccentricity/hydraulic diameter ratio	33.3
Entry plenum diameter	29.3 mm
Plenum/test section area ratio	12

Radially Outward Flow

Rotational speed range	0 - 1850 rev/min
Reynolds number range	7000 - 45000
Rayleigh number range	5×10^6 maximum
Rotational Reynolds number range	0 - 920
Rossby number range	0 - 0.085

Radially Inward Flow

Rotational speed	1000 rev/min
Reynolds number	7000 - 15000
Rayleigh number range	1.5×10^6 maximum
Rotational Reynolds number	0 - 360
Rossby number range	0 - 0.042

TABLE 1 : SYNOPSIS OF TEST SECTION GEOMETRY AND RANGE OF EXPERIMENTAL VARIABLES COVERED.

4. RESULTS AND DISCUSSION

Experiments were originally conducted with a stationary test section in order to establish a forced convection reference datum for heat transfer. Although minor variations of wall temperature along the wall of the test section were detected at corresponding axial locations on the leading and trailing surfaces they were not systematic and evaluation of local and mean Nusselt numbers with either surface temperature history was virtually identical. It is important to emphasise this point here since a totally different behaviour was found with rotation.

The mean Nusselt number, Nu_m , was evaluated using the difference between the mean wall temperature and the mean fluid temperature as the motivating potential for heat transfer with fluid properties evaluated at the mean fluid temperature. A similar reference temperature for properties was used for the through flow Reynolds number, Re , and the hydraulic diameter was taken as the length characteristic. For the range of test variables covered Figure 4 shows the zero speed variation of mean Nusselt number with Reynolds number. Also shown in this graph is the theoretical prediction for square tubes taken from the recommendation of Launder and Ying (15) and the well-known Dittus-Boelter (16) correlation for circular tubes with developed flow. The present data agreed very well with the Dittus-Boelter line. The variation of local Nusselt number, evaluated with the local wall to bulk fluid temperature differences and properties at local bulk temperature along the duct, is shown in Figure 5. This curve is included for later comparison with rotating conditions. The distributions clearly show the high regions of local heat transfer coefficient in the immediate entry region and their decay towards a fully developed-like value.

When tests were undertaken with rotation (1000 rev/min and 1850 rev/min) and radially outward flow noticeably different wall temperature distributions were detected over the leading and trailing surfaces. This may be seen on reference to Figure 6 which shows the typical differences in measured wall temperature. The leading edge surface was found consistently to run at a higher temperature than its trailing counterpart. This would be in keeping with the presence of a strong cross-stream secondary flow as indicated in Figure 1. The movement of relatively cool fluid from the central region of the duct is improving the cooling effect over the trailing surface.

Mean Nusselt numbers were evaluated in accordance with the definitions used for the stationary duct but individually over the leading and trailing surfaces. For each of the nominal values of through flow

Reynolds number studied, Figure 7 shows the variation of mean Nusselt number with the Rotational Reynolds number. The following features are highlighted.

On the leading surface it was found that although causing changes in heat transfer, rotation produced a somewhat confusing picture at first sight. At the lowest value of through flow Reynolds number (7200) heat transfer was increased with rotation as shown by comparison with the Dittus-Boelter (16) line. The relative increase in heat transfer at this value of Reynolds number indicated a slight reduction as the speed was increased. At Reynolds number values of 14600 and 24750 the heat transfer did show a progressive increase as the rotational Reynolds number was increased but in these two instances it was possible to produce an overall reduction in heat transfer relative to the stationary tube condition. This effect had been detected previously for circular-sectioned tubes by Morris and Ayhan (12) and attributed to rotational buoyancy. At the highest value of through flow Reynolds number (44250) no significant change in Nusselt number with rotation was detected.

For circular-sectioned tubes the proposals of Mori et al (7) and Lokai and Limanoki (10) for orthogonal-mode rotation are relatively easy to evaluate. Thus Mori et al (7) suggest that the rotating developed Nusselt number, Nu_{ω} , may be estimated using the equation

$$Nu_{\omega} = \frac{0.0349 Pr^{2/3} X^{1/20}}{[Pr^{2/3} - 0.074]} \left(1 + \frac{0.093}{X^{1/5}} \right) \quad (5)$$

where

$$X = \frac{J^2}{4 Re \Gamma^2} \quad (6)$$

and

$$\Gamma = \left[1 + 1.285 \frac{J^2}{Re^2} \right]^{1/2} - 1.135 \frac{J}{Re} \quad (7)$$

Lokai and Limanski (1975) propose that the mean Nusselt number, Nu_m , for the tube may be estimated using

$$Nu_m = 0.023 Pr^{0.33} Re^{0.6} \left[1 + 136.97 \frac{J^{0.7}}{Re^{1.08}} \right] \quad (8)$$

For comparative purposes both these proposals have been plotted on Figure 7 using the hydraulic diameter concept. Although equations (5) and (8) do not exhibit total mutual agreement they both suggest far more significant values of Nusselt number in relation to those measured on the leading surface of the square-sectioned duct.

On the trailing surface the influence of rotation on mean heat transfer is seemingly more consistent than its leading counterpart. In this case, at all values of through flow Reynolds numbers, there was a tendency for rotation to produce an overall increase in mean heat transfer. Although the proposals of Mori et al (7) and Lokai and Limanski (10) are still suggesting a greater increase in heat transfer than that measured the trailing surface data is nearer to these lines than the case of the leading edge.

Within the limits of their experimental envelope for circular tubes and orthogonal-mode rotation Morris and Ayhan (12) attempted to uncouple the effects of Coriolis acceleration and centripetal buoyancy. These authors proposed the tentative correlation given below for the case of radially outward flow.

$$Nu_m = 0.022 \left[\frac{Ru}{Re^2} \right]^{-0.186} Ro^{0.33} Re^{0.6} \quad (9)$$

The present data for a square tube has been compared to this equation using the hydraulic diameter concept and the results are shown in Figure 8. For the leading surface it is interesting to note that, despite data scatter, equation (9) does pass through the majority of data point clusters. Indeed on careful examination of the location of the stationary tube mean Nusselt number this equation is still capable of suggesting the two sets of impaired heat transfer at through flow Reynolds numbers of nominally 7200 and 14600.

Figure 8 also compares the trailing surface data with equation (9). The relatively higher heat transfer detected on the trailing surface is still clearly evident and the majority of data is underpredicted by equation (9). Even so the slope of the line is in tolerable agreement. The trailing edge mean Nusselt numbers are approximately 15% higher than those resulting from the use of equation (9). It is interesting to note that Morris and Ayhan (12) actually constructed equation (9) using measured wall data on the leading surface of their circular-sectioned tube.

To conclude the description of results obtained with radially outward flow Figure 9 shows typically representative variations of local Nusselt number over the leading and trailing surfaces. The general features are similar with the zones of relatively high local heat transfer in the developing regions but the noticeably better heat transfer on the trailing surface may be clearly seen.

A limited amount of experimentation has also been undertaken with radially inward flow and the same basic flow configuration. Due to time pressures prior to the need to prepare the present paper only data for a rotational speed of 1000 rev/min and nominal through flow Reynolds numbers of 7200 and 14200 respectively have been undertaken at the time of writing. Nevertheless some interesting trends are emerging.

There are two effects which might be expected on changing the direction of flow from radially outward to radially inward. Firstly the Coriolis acceleration components reverse in direction and this would tend to reverse the direction of the secondary flow patterns shown simplistically in Figure 1. In turn this would suggest that relatively better heat transfer coefficients should occur on the leading surface of the duct. This in turn would tend to reduce the wall temperature on the leading surface. This tendency was detected with the present experiments and Figure 10 shows a typical variation of wall temperature for the leading and trailing surfaces which was measured. After about 40% of the tube length, measured from inlet, there is a clear tendency for the leading surface to operate at relatively lower temperature in relation to the trailing surface.

Figure 11 shows the mean values of Nusselt number obtained as a function of the rotational Reynolds number. Very significant improvements in heat transfer are evident with once more a clear reversal in the relative mean Nusselt number values between the leading and trailing surfaces. The leading surface is now operating with higher heat transfer coefficients compared with its trailing counterpart. Note also that no overall tendency for impaired heat transfer relative to the stationary case has occurred as a possible result of buoyancy interaction. This is exactly the same result in principle as described by Morris and Ayhan (13) for circular-sectioned tubes.

These authors proposed the following correlation for the circular-sectioned tube rotating in the orthogonal-mode with radially inward flow

$$Nu_m = 0.036 \left[\frac{Ra}{Re^2} \right]^{0.112} Ro^{-0.083} Re^{0.8} \quad (10)$$

The present data, although limited at the time of writing, is compared with equation (10) in Figure 12. For the leading edge the data obtained at both values of Reynolds number is evenly scattered about the values suggested by the Morris-Ayhan correlation. Also shown is the zero speed mean Nusselt number for the two values of through flow Reynolds number. Equation (10) is clearly a reasonably good correlation for the leading surface and was actually developed from circular tube data measured on the leading surface.

Although data exhibits a typical scatter band for this type of experiment, the results obtained for the trailing edge tends in the main to be underpredicted by equation (10), particularly at the lower values of Reynolds number, although the trends are again similar. Reducing the Nusselt number obtained from using equation (10) on the trailing surface of a square-sectioned tube by approximately 11.5% would appear to give a reasonably conservative estimate for design purposes.

Figure 13 gives some indication of the variation of local Nusselt number over the leading and trailing edges. For the example shown the relative differences are more pronounced over the mid/exit region of the duct. This trend will be examined in greater depth when the completed programme of experiments for radially inward flow has been evaluated.

5. CONCLUDING REMARKS

Although the experimental conditions covered by the investigation reported in this paper do not span completely those likely to be encountered in operational gas turbines the fundamental trends and observations are nevertheless important. The most important general results may be highlighted as follows.

Radially Outward Flow

The Coriolis-induced secondary fluid motion produced with radially outward coolant flow results in significantly enhanced cooling on the trailing surface of the duct in relation to the leading surface. In practice this will cause corresponding girthwise variations in material temperature over the surface of the coolant channel with regions of higher temperature being located on the leading surfaces.

The overall effect of rotation can result in regions of reduced heat transfer relative to the stationary duct reference condition particularly over the leading surface. It appears that this region of reduced heat transfer is more likely to occur on the leading edges where the surface temperatures of the coolant channel are greatest. This reinforces the suggestion that rotational buoyancy is an important contributing factor since it tends to suppress heat transfer with radially outward flow. Theoretical-based predictions which do not include buoyancy will not apparently be capable of detecting this phenomenon. Although derived from experimental data obtained with circular-sectioned tubes the proposal of Morris and Ayhan (12) which includes buoyancy, appears to detect the possibility of impaired heat transfer on the leading surface when the hydraulic analogy is invoked.

Radially Inward Flow

The experimental data obtained with the limited tests currently available with radially inward flow tended to support the general idea that Coriolis-induced secondary flow will now improve the cooling on the leading surface in relation to the trailing surface. Further, in this case, no regions of impaired heat transfer relative to the stationary case were detected. This is consistent with similar data obtained with circular-sectioned tubes and also with the suggestions that rotational buoyancy with this relative flow configuration will also tend to augment the stationary tube forced convection. Again the

proposals of Morris and Ayhan (13) based on the hydraulic diameter analogy are in good agreement with the present data over the leading edge.

REFERENCES

1. Morris W D. (1981). Heat Transfer and Fluid Flow in Rotating Coolant Channels. Research Studies Press (John Wiley & Sons Ltd). ISBN 0 471 10121 4.
2. Barua S N. (1955). Secondary flow in a rotating straight pipe. *Proc Roy Soc A*, 227, 133.
3. Trefethen L. (1957). Fluid flow in radial rotating tubes. *Actes, IX. Congres International de Mecanique Appliquee, Universite de Bruxelles*, 2, 341.
4. Benton G S and Bower D. (1966). Flow through a rapidly rotating conduit of arbitrary cross-section. *J Fluid Mech.* 26, Part 1, 69.
5. Mori Y and Nakayama W. (1968). Convective heat transfer in rotating radial circular pipes (1st report - laminar region). *Int J Heat Mass Trans.* 11, 1027.
6. Ito H and Nanbu K. (1971). Flow in rotating straight pipes of circular cross section. *Trans ASME J Basic Eng.* 93, (3), 383.
7. Mori Y., Fukada T and Nakayama W. (1971). Convective heat transfer in a rotating radial circular pipe (2nd report). *Int J Heat Mass Trans.* 14, 1807.
8. Skiaderessis D and Spalding D B. (1977). Heat transfer in a pipe rotating around a perpendicular axis. *ASME Paper No 77-WA/HT-39*.
9. Metzger D E and Stan R L. (1977). Entry region heat transfer in rotating radial tubes. *AIAA 15th Aerospace Sciences Meeting, Los Angeles*. Paper No 77-189.
10. Lokai V I and Limanski A S. (1975). Influence of rotation on heat and mass transfer in radial cooling channels of turbine blades. *Izvestiya VUZ, Aviatsionnaya Tekhnika*, 18, 3, 69.
11. Zysina-Molozhen L M., Dergach A A and Kogan G A. (1977). Experimental investigation of heat transfer in a radially rotating pipe. *NGEEE High Temp.* 14, 988.
12. Morris W D and Ayhan T. (1979). Observations on the influence of rotation on heat transfer in the coolant channels of gas turbine rotor blades. *Proc Inst Mech Eng.* 193, 21, 303.
13. Morris W D and Ayhan T. (1982). An experimental study of turbulent heat transfer in a tube which rotates about an orthogonal axis. *Proc XIV ICHMT Symposium on Heat and Mass Transfer in Rotating Machinery*, Dubrovnik, August 30 - September 3, 1982.
14. Clifford R J., Morris W D and Haraagama S P. (1984). An experimental study of local and mean heat transfer in a triangular sectioned duct rotating in the orthogonal-mode. *Proc ASME 29th int Gas Turbine Conference, Amsterdam*.
15. Launder B E and Ying W M. (1973). Prediction of flow and heat transfer in ducts of square cross section. *Proc IMechE., Thermo and Fluid Mechanics Group.* 187, 37/73, 455.
16. Dittus F W and Boelter L M K. (1930). *Univ Calif Publs., Engng.* 2, 443.

ACKNOWLEDGEMENTS

The authors would like to record their gratitude to Mr R J Clifford (Rolls Royce Ltd, Bristol) and Dr D Colbourne (Royal Aircraft Establishment, Farnborough) for their constant support, interest and encouragement. Also the financial support of the Ministry of Defence and the Science and Engineering Research Council is acknowledged with thanks. Finally the skill and dedication of Mr A Hird for the construction and maintenance of the equipment is gratefully appreciated.

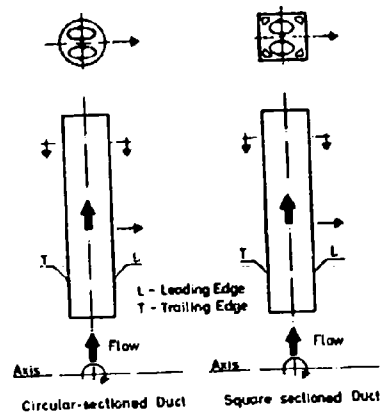
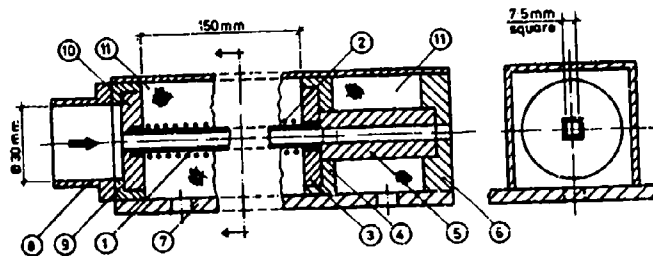


FIGURE 1 ORTHOGONAL-MODE ROTATION

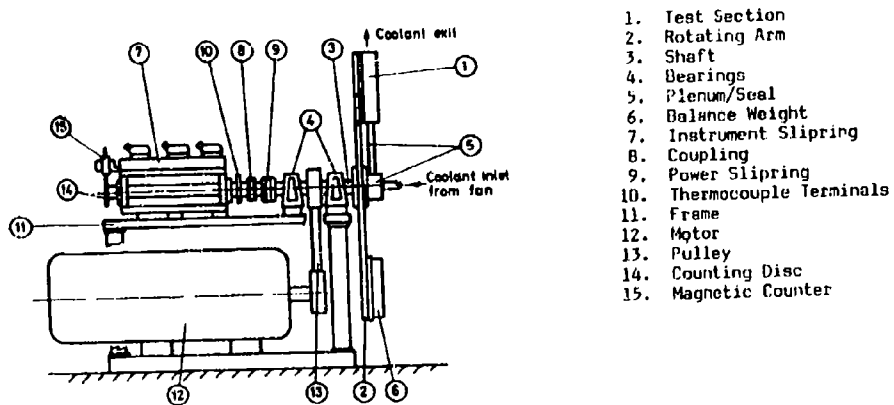


1. Test Section
2. Heater
3. Insulation
4. Support

5. Insulation
6. Support
7. Base
8. Plenum

9. Support
10. Insulation
11. Foamed Backfill

FIGURE 2 DETAILS OF TEST SECTION



1. Test Section
2. Rotating Arm
3. Shaft
4. Bearings
5. Plenum/Seal
6. Balance Weight
7. Instrument Slipring
8. Coupling
9. Power Slipring
10. Thermocouple Terminals
11. Frame
12. Motor
13. Pulley
14. Counting Disc
15. Magnetic Counter

FIGURE 3 SCHEMATICS OF ROTATION TEST FACILITY

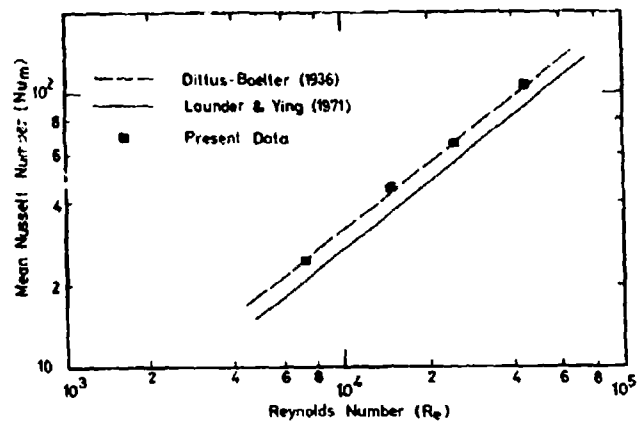


FIGURE 4 MEAN NUSSLET NUMBERS AT ZERO SPEED

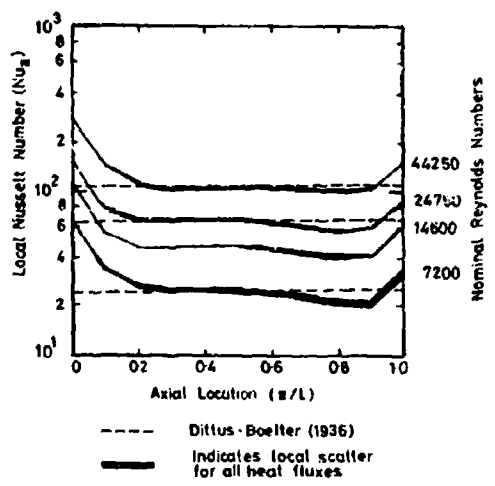


FIGURE 5 LOCAL NUSSLET NUMBERS AT ZERO SPEED

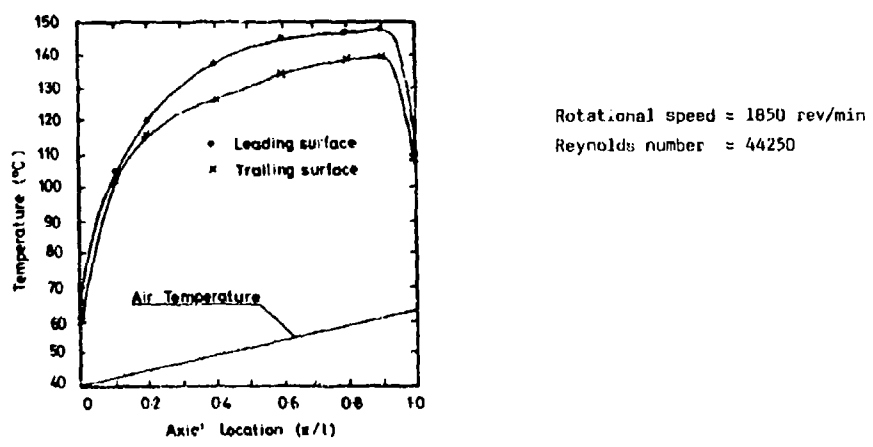


FIGURE 6 TYPICAL VARIATION OF TEMPERATURE OVER LEADING AND TRAILING SURFACES (OUTWARD FLOW)

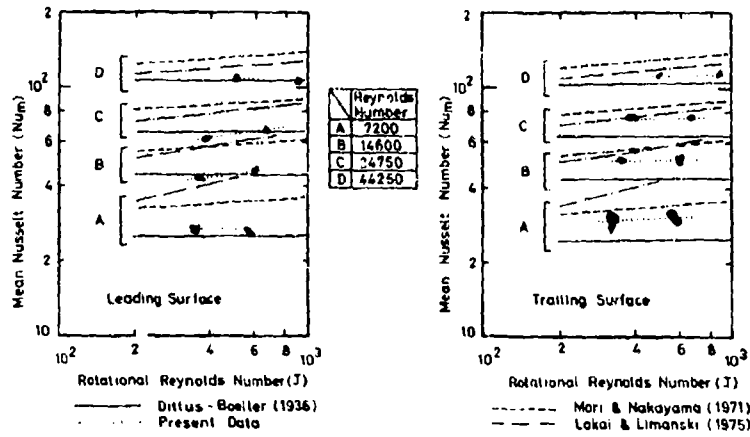


FIGURE 7 MEAN NUSSLETT NUMBERS OVER LEADING AND TRAILING SURFACES (OUTWARD FLOW)

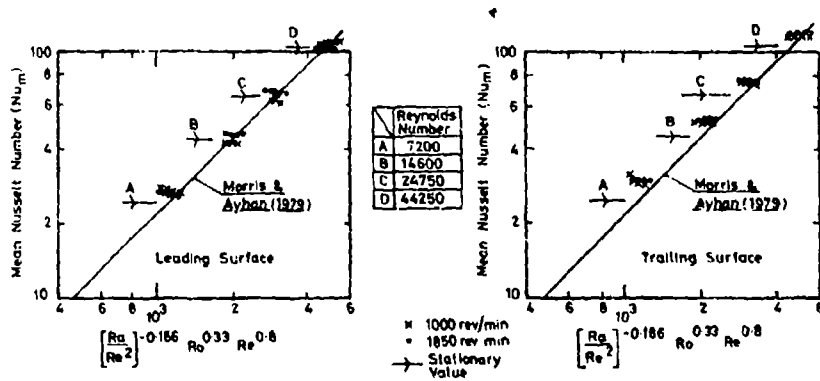


FIGURE 8 COMPARISON OF MEAN NUSSLETT NUMBERS WITH CIRCULAR TUBE RECOMMENDATIONS OF MORRIS AND AYHAN (1979) (OUTWARD FLOW).

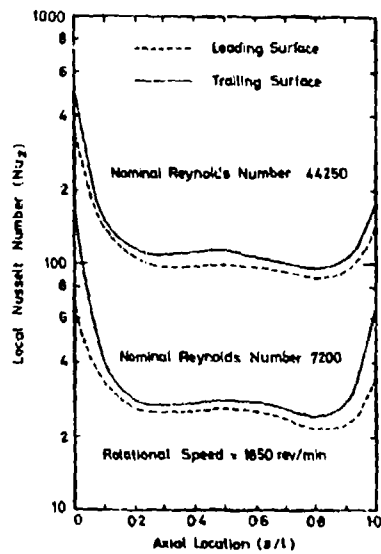
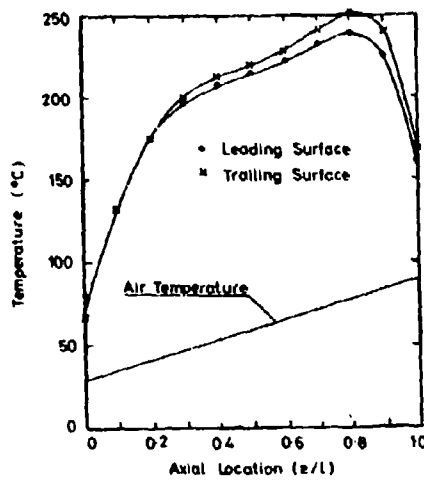


FIGURE 9 TYPICAL VARIATION OF LOCAL NUSSLETT NUMBERS OVER LEADING AND TRAILING SURFACES (OUTWARD FLOW)



Rotational Speed = 1000 rev/min
Reynolds number = 14200

FIGURE 10 TYPICAL VARIATION OF TEMPERATURE OVER LEADING AND TRAILING SURFACES (INWARD FLOW)

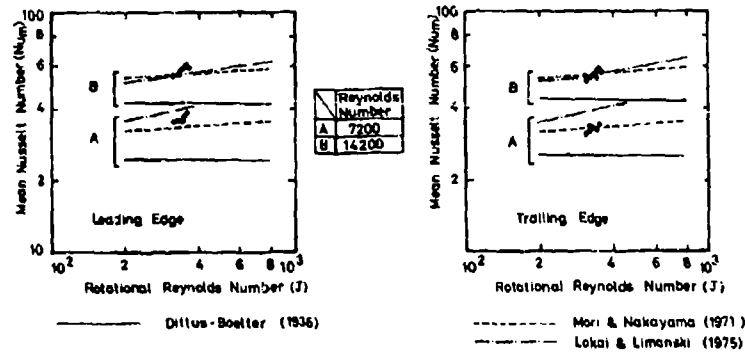


FIGURE 11 MEAN NUSSULT NUMBERS OVER LEADING AND TRAILING SURFACES (INWARD FLOW)

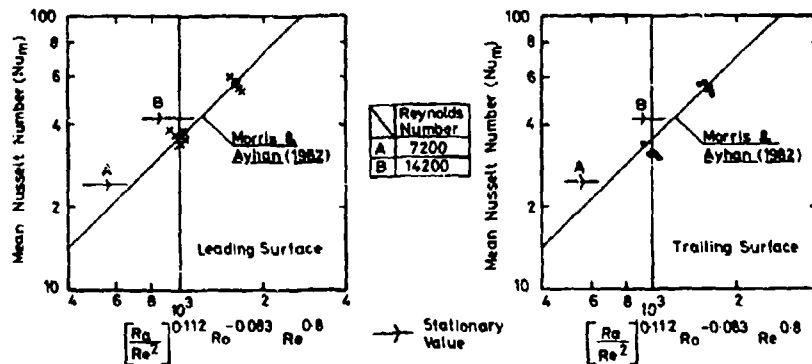


FIGURE 12 COMPARISON OF MEAN NUSSULT NUMBERS WITH CIRCULAR TUBE RECOMMENDATIONS OF MORRIS AND AYHAN (1982) (INWARD FLOW)

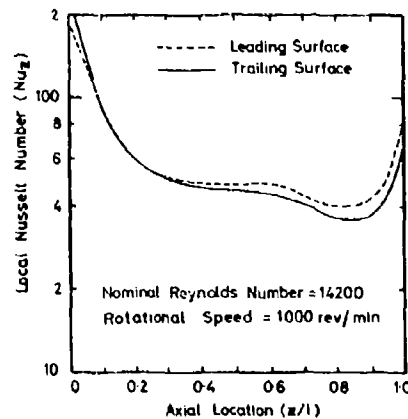


FIGURE 13 TYPICAL VARIATION OF LOCAL NUSSULT NUMBERS OVER LEADING AND TRAILING SURFACES (INWARD FLOW)

DISCUSSION

M.Owen, UK

The inlet and exit effects create larger than average local Nusselt numbers in both the stationary and the rotating tubes (see, for example, Fig. 5). Were these effects removed from the average? If not, why is the agreement between the measured average Nusselt numbers and the Dittus-Boelter equation, shown in Fig. 4, so good?

Author's Reply

On Fig. 5 a nominal Dittus-Boelter line has been included only. This was an oversight and the means did in reality conform well to the Dittus-Boelter equation as indicated in Fig. 4.

S.C.Arora, Ca

Most internal cooling channels employ some roughening elements such as ribs and pin fins. Depending on the type and the geometry of these elements, the secondary flows generated in the channel could be as important, if not more, than the secondary flows due to forces associated with rotation. Is it not possible that under such circumstances the effect of rotation could be very small or negligible and of no concern to the designer?

Author's Reply

It is as yet unclear as to how the Coriolis and centripetal buoyancy interact to generate secondary flows within a rotating passage. The influence of rotation as a whole has an extremely strong effect on both the local and hence the mean levels of heat transfer. Although the other effects (roughness/ribs/pins) also have a strong influence on heat transfer, we believe that rotation may be equally important.

Additional Comment of R.J.Clifford

It was in an attempt to quantify the relative importance of these parameters in a 'real engine' geometry that the work described in his paper was undertaken by RR. These studies had clearly indicated that in ducts with roughening devices, bends and non uniform cross section, rotation had a significant effect on the heat transfer.

D.K.Hennecke, Gc

You presented results on the leading and trailing sides of the duct. Have you also measured it on the other sides? Are you planning to change the angle orientation of the square channel to the direction of rotation?

Author's Reply

We have measured levels of heat transfer on all four sides of the square duct. Within the experimental uncertainty (10%) we could find no difference between the sidewall and the leading side with radially outward flow. The same holds for the sidewalls and the trailing side with radially inward flow.

A new program of work is currently under way to investigate the influence of orientation on the heat transfer.

PRESSURE DROP AND HEAT TRANSFER CHARACTERISTICS OF CIRCULAR AND OBLONG
LOW ASPECT RATIO PIN FINS

S.C. Arora, Staff Analyst and W. Abdel Messeh, Supervisor
Pratt & Whitney Canada Inc., Longueuil, Quebec, J4K 4X9, Canada.

SUMMARY: The pressure drop and heat transfer characteristics of circular and oblong pin fins of height-to-diameter ratio of unity used to augment internal cooling of gas turbine airfoils are presented. Data were obtained for an array of 10 rows of staggered pin fins in a 25:1 aspect ratio channel, with both pins and channel endwalls forming the heat transfer surface.

Results show that the array average friction factor increases with increasing blockage caused by different arrangement of pin fin geometries in the channel. The local heat transfer coefficient increases up to the 3rd row of pin fins and decreases thereafter. Oblong pin fins with $\gamma=90^\circ$ (major axis parallel to the direction of flow) result in higher heat transfer rates and lower friction factor than the circular pin fins. For other orientations ($\gamma \neq 90^\circ$), oblong pin fins do not offer any advantage over circular pin fins for $Re \leq 20,000$ (typical of small gas turbine engines).

Nomenclature

A	Streamwise clearance of Pin fins; Heat transfer area	
B	Spanwise clearance of Pin Fins	
C _p	Specific heat of air	
D	Diameter of circular pins; Minor axis of oblong pins	
f _r	Friction factor; $f_r = \frac{dP}{dx} \frac{D}{\rho V_{max}^2}$	
H	Pin height; Channel height	
h	Convective heat transfer coefficient	
K	Thermal conductivity of air	
k	Thermal conductivity of pin material	
m	Mass flow rate	
N	Number of pin rows in streamwise direction	
Nu	Nusselt number; $Nu = \frac{hD}{K}$	
P	Pressure	
q	Heat flux	
Re	Reynolds number; $Re = \rho V_{max} D/\mu$	
S	Pin spacing in spanwise direction	
T	Temperature	
V _{max}	Average streamwise velocity at the minimum flow area	<u>Subscripts</u>
X	Pin spacing in streamwise direction	b Bulk average
x	Axial co-ordinate	c Circular pins
Y	Angle of orientation of oblong pin fins	f Film
Δ	Denotes differential	m Mixing Chamber
μ	Fluid dynamic viscosity	o Oblong pins
ρ	Fluid density	s Surface
—	indicates average quantity	

INTRODUCTION: It is common knowledge in the gas turbine field that in order to increase the thermodynamic efficiency and power output, and lower the weight to thrust ratio and specific fuel consumption, it is necessary to operate the turbine at higher inlet temperatures. This increase in temperature leads to high thermal stresses, accelerated creep, and chemical deterioration and because of limited capabilities of the available materials, the life of the component is generally lowered. Therefore, to withstand these high temperatures, turbine components must be maintained at acceptable temperature levels with the aid of a suitable cooling method. Cooling is accomplished by feeding compressor bleed air through passages inside the engine to the turbine area where the air is led to different stages of hot turbine components.

One of the most common airfoil cooling schemes is the application of channel flow heat transfer, augmented with pin fins of circular or oblong cross-section (Figure 1 & 2). For gas turbine applications, the height-to-diameter (H/D) ratio of pin fins is generally of the order of unity whereas the majority of published work deals mainly with the flow and heat transfer characteristics of rod bundles of large H/d ratios (Ref. 1 & 2). Some recent literature (Ref. 3 - 6) for circular pin fins has shown that the average heat transfer rates from shorter pin fins are significantly lower than those from rod bundles. It has also been reported that the pin height to diameter ratio is the dominant factor in determining the level of array averaged heat transfer coefficients (Ref. 7 & 8). This implies that the large data bank obtained for rod bundles could not be directly used for the design of internal cooling schemes for turbine airfoils. Furthermore, heat transfer from an array of pin fins is controlled by a complex flow structure dominated by channel endwalls and pin fins. Hence, rod bundle data (where endwall effects are negligible) can not be easily corrected to apply to gas turbines with pin fins of height-to-diameter ratio of about unity. Therefore, to understand the flow mechanisms associated with short pin fins and to characterize the heat transfer process for airfoil cooling scheme design, it is necessary to test large number of pin fin geometries. This implies a large number of test sections and a prohibitively high overall cost. Alternatively, the test section could be designed to have removable pins, whilst not sacrificing the accuracy of heat transfer measurements.

Metzger and Haley (Ref. 6) used non-conducting circular pins made of balsa wood epoxied to heated endwalls (as opposed to heat conducting pins as an integral part of the test section) to obtain the heat transfer rates from the endwalls only. The data thus gathered were used to evaluate the effects of array geometry. Since these wood pins have a finite thermal conductivity and because of small height of pins, their thermal conductance is not negligible. Therefore, the heat transfer data included some finite contribution, though not quantified, from the surface of pin fins. The same technique was also used by Metzger et al (Ref. 9) to evaluate the performance of pin fins of oblong cross-section. The experimentally obtained data were analytically corrected on the basis of fin analysis, to account for the non-uniform temperature in wood pins. A ratio of $h_{pin}/h_{endwall}$ was obtained for circular pin fins using the data of Ref. 5 and 6. The same ratio was assumed for oblong pin fins, though, without any verification. The fin analysis had indirectly assumed absence of any contact resistance between the copper endwall and the wood pins, which could be significant. The heat transfer data obtained with wood pins may provide relative array effects but can not be used with confidence for the design of oil cooling schemes. Since there are no other available data in the published literature on the heat transfer characteristics of oblong pin fins, the validity of Metzger's et al's data (Ref. 9) obtained with wood pin fins can not be verified.

Arora and Abdel-Messeh (Ref. 10) presented another flexible test technique to obtain good quality heat transfer data for different arrays of conducting pin fins in the same test section, thereby significantly reducing the cost of experimental set up. The technique involves the use of high conductivity micro-electronics grade silver based epoxy ($K=22.5W/m^{\circ}C$) to bond the pins (made of conductive material) to the endwalls of the test section. The study had shown that it introduces a temperature drop across a thin layer of epoxy ($\sim .005-.006$ cm) between the copper pin and the endwalls of less than 1% of the heat transfer surface temperature. The resulting local (row-by-row) and array averaged heat transfer data showed excellent agreement with the previously published data. Thus no correction was required to the measured data. This technique was used in the present study to obtain the heat transfer and the pressure drop data.

The geometrical parameters of circular and oblong pin fin arrays (Figure 2) tested in this study are listed in Table 1. These geometries were selected such that the respective axial (A/D) and transverse (B/D) clearances between circular and oblong pin fins were similar. This permitted direct comparison of the pressure drop and the heat transfer characteristics of the pin fins of both cross sections. The oblong pins have semi-circular ends and a cross-sectional length along the major axis of twice the end diameter (Figure 2). Ten rows of pins in the direction of flow were employed in all tests as shown in Figure 3. Because of the staggered arrangement of pin fins, the even numbered rows had one less pin than the odd numbered rows. In addition, the axial spacing (X/D) of the pin fin geometries tested in this study was such that there was always a blank (smooth) slab in between two successive rows of pins.

EXPERIMENTAL DETAILS A schematic layout of the heat transfer test rig used in pin fin experiments is shown in Figure 4. Compressed air is fed to the rig through a 3.8 cm diameter supply line which also houses an orifice meter to measure the mass flow rate. Air then passes through a plenum chamber (10.16 cm x 30.48 cm) equipped with a honeycomb and screens to settle the flow before the contraction nozzle.

The entrance duct upstream of the test section has the same cross section (.51 cm x 12.7 cm) as the test section, and is over 50 hydraulic diameters long to provide a fully developed velocity profile at the entrance to the test section. Static pressure holes are drilled at 8 locations (4 each on top and bottom walls) to measure the pressure distribution. The entrance duct is heated to the same temperature as the test section for simultaneous development of the thermal boundary layer. Air after the test section passes through a smooth channel (of same cross-section) to avoid any "exit effects". Thereafter, it enters the mixing chamber where its bulk average temperature is measured. The air then passes through another orifice plate before being discharged to the atmosphere. The second orifice plate is used to verify the mass flow rate and to ensure that there is no leakage from the rig. The complete test assembly from the plenum chamber to the mixing chamber is insulated with about 6 cm thick layer of Kao wool to minimize any conduction losses during the heat transfer testing.

The top and bottom walls of the test section (Figure 5) consisted of 30 copper slabs (Figure 3) of which only 29 were fully instrumented. Each slab measured .635 cm long in the direction of flow, 12.7 cm wide and 1.27 cm thick. The copper slabs were separated from each other by .035 cm thick etched teflon sheet cemented to the copper slabs to thermally isolate each endwall segment. Each copper slab had 2 copper constantan thermocouples to monitor its temperature during testing. A .318 cm square cartridge heater located at the back of each slab (Figure 6) was used as a heat source. The top and bottom heaters were connected in parallel and controlled by automatic/manual a.c. power controllers. Therefore, only the total power supplied to the two copper slabs as a unit was measured. The top and bottom walls were maintained at a constant channel height of .51 cm by two units of spacers (one for each side), which also formed the side walls of the test section. These sidewall units (spacers) were machined from phenolic laminated plastic with special care. The channel height of the assembled smooth wall (without pins) test section was measured to be $.51 \pm .012$ cm, thus suggesting a step (roughness) of $\pm .006$ cm on each wall. This was within the sublayer thickness and therefore the top and the bottom walls were considered to be hydraulically smooth. Thirty static pressure holes of .12 cm diameter (one per endwall unit of top and bottom copper slabs) were drilled through both spacer side wall units. The heater and thermocouple leads also passed through the spacer and were then connected to multi-pin connectors for quick assembly and disassembly of the test section.

Special jigs were designed to locate copper pins at desired locations on endwall slabs. A thin layer ($\sim .005 - .006$ cm thick) of the UNISEI's C-805-1 silver filled micro-electronics grade conductive epoxy (Ref. 10) was applied at both ends of the pins prior to positioning them between the copper slabs in the jig. The whole assembly was then placed in an oven at $150^{\circ}C$ for 1 hour to cure the epoxy bond. Ten units of copper slabs were mounted with pins to provide 10 rows of pin fins. However, no pins were mounted on the first 3 slabs to avoid 'end effect'.

The heat transfer tests were carried out at steady state by maintaining endwalls at a constant surface temperature ($\sim 71^{\circ}C$) by varying the power input to heaters. The isothermal condition of endwall segments 1 to 29 was generally maintained to within $\pm .3^{\circ}C$, however, the temperature of two adjoining slabs was

maintained to within $\pm .14^\circ\text{C}$.

The heat transfer coefficient, h , for each segment (top & bottom copper slabs with or without pins) was obtained from the total power supplied (q) to the top and the bottom slab heaters corrected for conduction losses from the back ends of the segments and for inter segment conduction across the teflon insulation. The inter-segment losses were calculated for each test run and were generally small. The back losses were measured experimentally and varied from about 2 to 10 percent depending on test Reynolds number. Then using the temperature difference between the segment surface, T_s , and the air flowing over as the driving potential, the heat transfer coefficients were calculated as:

$$h = \frac{q}{A (T_s - T_b)} \quad (1)$$

The heat transfer area, A , for all experiments was the actual copper surface area (pin + endwall) exposed to the flow. The local bulk average temperature, T_b , as a function of streamwise endwall segment position, was determined in the present experiment from an energy balance. The air temperature measured in the mixing chamber (T_{bm}) was taken as the bulk average temperature at the end of slab no. 29. Working towards the upstream end of the test section, the bulk temperature for use with the j th segment is calculated as:

$$T_{bj} = T_{bm} - \frac{\dot{q}_j}{2 \dot{m} c_p} - \begin{cases} \sum_{k=i+1}^{29} \frac{\dot{q}_k}{\dot{m} c_p} & \text{for } j \leq 29 \\ = 0 & \end{cases} \quad (2)$$

where c_p was evaluated at the film temperature. Since the specific heat, c_p , to be input in equation 2 should be at true T_b which is initially unknown, the first approximation of c_p may not be correct. Therefore, 2 iterations were carried out to properly calculate the segment bulk average temperature. The calculated air temperature at the inlet to the rig using this procedure differed from the measured temperature by less than 1.5%.

The measured heat transfer coefficients are reported in terms of Nusselt number, Nu , defined as:

$$Nu = \frac{hD}{K} \quad (3)$$

The heat transferred from the blank endwall segment between two successive pin rows was integrated with the segments having pins. One half of the endwall was integrated with the upstream row of the pins and the other half with the downstream row.

Reynolds numbers in the channel were calculated on the basis of pin diameter and the flow velocities using the minimum flow area:

$$Re = v_{\max} D \rho / \mu \quad (4)$$

where μ was evaluated at the first row of pin fins. The friction factor for the pin arrays was estimated as:

$$fr = \frac{dP}{dx} \frac{D}{2\rho v_{\max}^2} \quad (5)$$

where dP/dx is the pressure gradient through the pin fin array.

Metzger et al (Ref. 5 & 9) used the following definition to compute the array friction factors:

$$fr = \frac{\Delta P}{2\rho v_{\max}^2 N} \quad (6)$$

where N is the number of pin fin rows in the array. This definition, however, does not take into consideration the length of the test section over which the given number of pin rows are located (i.e. axial pitch of the pin rows). Therefore, this definition was not used in this study and the pressure drop data were reduced using the definition of equation 5.

All relevant properties (k , ρ , μ) were evaluated at the film temperature (T_f), defined as:

$$T_f = \frac{T_s + T_b}{2} \quad (7)$$

The experimental uncertainty was estimated, using the method of Kline and McClintok (Ref. 11), to be $\pm 2.5\%$ on Re , $\pm 4.5\%$ on fr and $\pm 5\%$ on Nu .

RESULTS AND DISCUSSION: Heat Transfer: The average Nusselt number (\bar{Nu}) distribution for circular pin arrays is shown in Figure 7 as a function of Reynolds number. The experimental test data were integrated (area weighted average) over an area extending $\lambda/2$ (half of axial pitch) distance before the first and after the last row of pin fins (Fig. 3).

Figure 7 also shows a line representing the 10 row array average heat transfer data of Metzger et al (Ref. 5) for somewhat similar pin fin geometry. In order to compare the two data sets, possible contribution due to variation in geometric parameters (S/D, X/D and H/D) must be kept in mind. Though H/D is an important variable, it can be assumed that the small differences present in these two studies will not have significant effect on array average \bar{Nu} . To estimate the effect of axial (X) and lateral (S) pitches on average Nusselt numbers, Zukauskas (Ref. 1) proposed the following correlation for arrays of large cylinders:

$$\bar{Nu}_c = 0.35 (S/X)^{-2} Re^{.6} Pr^{.36} \quad (8)$$

for $10^3 \leq Re \leq 2 \times 10^5$ and $S/X < 2$. Assuming the same dependency on S/X, the Nusselt numbers for arrays tested in the present study should be about 3-6% lower than that of Metzger et al. Generally, the data (Figure 7) are in agreement with this observation, however, some data points indicate larger deviations but are within the experimental uncertainty of the tests.

It is interesting to note that the present data were obtained by epoxing the copper pins to copper endwalls, whereas the data of Ref. 5 were obtained by fixing the copper pins through interference fit in holes drilled in copper endwalls. Thus in both these studies, the endwalls and the pin surfaces both formed the heat transfer surface and the resulting data show good agreement with each other.

The row-to-row distribution of the local Nusselt numbers for circular pin fins is shown in Figure 8. The plotted local Nusselt number has been normalized with the array average data of Figure 7. The results show that the normalized Nu_c/\bar{Nu}_c is the same (within the range of normal data scatter) for all 3 pin fin array geometries. The local Nusselt number increases up to the 3rd row and decreases gradually thereafter. This behavior is similar to that reported by Metzger et al (Ref. 5). Although the local to array average Nusselt number ratios plotted in Figure 8 are for one value of Reynolds number for each array, a similar behavior was observed at other Reynolds numbers as well.

The array averaged and the normalized row-by-row Nusselt number distribution for oblong pin fins is shown in Figures 9 & 10 respectively. The ratio of local to array average Nusselt number (Fig. 10) shows higher scatter than the corresponding circular pin fin data. However, the scatter appears to be random in nature and does not exhibit any definite pattern. Thus, it can be concluded that the normalized row-by-row heat transfer behavior of oblong pin fins is also independent of the array geometry as the data tend to collapse onto a single curve. Similar to circular pin fins, the heat transfer coefficient increases to about the 3rd row and decreases thereafter. Though data shown in Figure 10 is only for one value of Reynolds number for each array, a similar behavior was observed at other values of Reynolds numbers as well.

The array average Nusselt numbers for different geometries of oblong pin fins (Figure 10) do not show any significantly large differences. However, this does not imply that the angle of orientation (γ) is not an important parameter, as the plotted data represent wide differences in geometrical parameters (A/D and B/D) as well. The effect of angle of orientation (γ) will be discussed later while evaluating the relative performance of oblong and circular pin fins.

Friction Factor: A typical streamwise pressure distribution for one of the circular pin fin arrays is shown in Figure 11. The ordinate in the figure is the differential pressure ($\Delta P = P_{ref} - P$) between pressure (P) at any location in the test section and the reference pressure (P_{ref}) in the entrance duct. The abscissa is the streamwise distance in the test section normalized with the hydraulic diameter of the smooth channel ($D_h = .977$ cm). There are 20 pressure readings corresponding to 10 rows of pin fins, i.e. two readings for each row. One set of readings is taken at the location corresponding to the row of pin fins and the 2nd in between two rows of pin fins. Similar pressure data profiles were prepared for every test run and linear regression analysis was carried out to obtain the best fit line and slope of the data (dP/dx) required in equation 5 to compute the array friction factors. The friction factors thus computed are shown in Figures 12 & 13 for circular and oblong pin fins respectively. One set of pressure data for oblong pin fins (for $\gamma = 0^\circ$) was lost during data transfer from the G.A. computer (used to collect the data from the rig) to the main frame computer (used for analysis of the data) and is therefore not shown in Figure 13.

The results show that the friction factors for both arrays of pin fins decrease with increasing Reynolds numbers. For circular pin fins the friction factor for two arrays with X/D = 2.83 with slightly different S/D (Fig. 12) are equal, and higher than for the array with X/D = 3.39. The difference between the two curves increases with increasing Re. However the data for the array at X/D = 3.39 decreases at a faster rate than the data for the array at X/D = 2.83.

In case of oblong pin fins, the friction factor is minimum for the array with $\gamma = 90^\circ$ and increases with decreasing angle of orientation. However, the friction factor for arrays with $\gamma = 45^\circ$ & 30° are similar. Though the friction factors for the array with $\gamma = 0^\circ$ are not presented but are expected to be highest as this pin fin geometry would offer the maximum blockage to the flow.

Relative Performance of Oblong Pin fins: To evaluate the relative performance of the oblong pin fins, the average Nusselt numbers (\bar{Nu}) and friction factors for oblong pin fins were normalized by those for circular pin fins of comparable axial (A/D) and lateral (B/D) spacings. The normalized data are shown in Figures 14 and 15. The comparison of two arrays is based on the fact that the arrangement of circular and oblong pins resulted in about the same open area for coolant flow in the channel. However, the small differences that do exist between some of the corresponding circular and oblong pin fins (Table 1) are not expected to significantly alter the resulting findings on the relative heat transfer and pressure drop performance of the arrays.

The normalized heat transfer coefficients (\bar{Nu}_o/\bar{Nu}_c), oblong over circular pin Nusselt numbers, increases with increasing Reynolds number (Figure 14) and is generally greater than unity for $Re > 20,000$. This ratio of the two heat transfer coefficients for $Re > 20,000$ is maximum for the array with $\gamma = 45^\circ$ and minimum for the array with $\gamma = 30^\circ$ and the other two configurations fall in between. This suggests that for design applications with high Reynolds numbers, the oblong pin fins can be used to provide high heat transfer augmentation for the coolant side than the corresponding circular pin fins. However, for Reynolds numbers less than 20,000, the performance of oblong pins with $\gamma = 0^\circ$ (resulting in maximum blockage) is significantly lower whereas that of pins with $\gamma = 90^\circ$ (resulting in minimum blockage) is slightly better than or equal to that of circular pins. It is also observed that for $Re \leq 20,000$, the ratio \bar{Nu}_o/\bar{Nu}_c for

arrays with $\gamma = 30^\circ$ & 45° is nearly equal and only slightly lower than for the array with $\gamma = 90^\circ$.

The average heat transfer coefficient for the channel with pin fins is a function of the heat transfer rates from the pin and the endwalls, which are in turn governed by the associated structure of the flow. The upper and lower sides of the pins experience boundary layer flow whereas the rear portion is washed by the separated flow. The formation of boundary layer will be symmetrical on the upper and lower surfaces of the oblong pins for arrays with $\gamma = 0^\circ$ and 90° and will be asymmetrical for $\gamma = 30^\circ$ & 45° . A so called 'separation bubble' may also be present on the pin surface, and the separated shear layer may re-attach as laminar or turbulent or may not re-attach at all depending on the angle γ and the Reynolds number. The size of the separated region at the rear and the wake behind the pin would also depend on the angle of orientation (γ) of oblong pins. The wake is expected to be largest for the array with $\gamma = 0^\circ$ (maximum blockage) and minimum for $\gamma = 90^\circ$ (minimum blockage). The channel flow region that exists in between the pin will decrease with increasing wake size. Since, the overall heat transfer rate is a result of complex interaction of different flow phenomena in the channel dominated by the angle γ and the Re , it is not surprising that the Nu_o/Nu_c ratio (Figure 14) shows a dependency on γ and Re as well.

The ratio of the friction factors (f_{ro}/f_{rc}) is shown in Figure 15. The oblong pin array geometry with $\gamma = 90^\circ$ has friction factors which are lower than the corresponding circular pin fins, though the difference decreases with increasing Re . This is because of the streamlining of the pins with the direction of flow thereby minimizing the blockage and the size of the wake. The friction factor for oblong pins at $\gamma = 30^\circ$ & 45° is significantly higher than the circular pins, and again the difference decreases with increasing Re . At $\gamma = 0^\circ$, the friction factor though not shown would be highest because of maximum flow blockage offered by the pins. It is interesting to note that the oblong pin fin array with $\gamma = 90^\circ$ also resulted in better heat transfer performance compared to arrays with $\gamma = 30^\circ$ & 45° for $Re \leq 20,000$. This characteristic is also apparent in Figure 16 where the Nusselt number ratio (Nu_o/Nu_c) is plotted against the friction factor ratio (f_{ro}/f_{rc}) for one value of $Re = 20,000$. These results (Figures 14 - 16) show that the oblong pin fins with $\gamma = 90^\circ$ result in higher heat transfer rate with lower friction factors than circular pin fins with the same open area. Arrays with other values of orientation angle (γ) result in higher heat transfer rate only at $Re > 20,000$ but at substantially higher friction factors. For $Re > 20,000$, the oblong pin fins with $\gamma = 90^\circ$ are beneficial because of lower friction factors with same or slightly higher heat transfer rates than the circular pin fins.

Metzger et al (Ref. 9) also showed that the oblong pin fins with $\gamma = 90^\circ$ result in lower friction factor than the arrays with other values of γ as well as the circular pin fins of comparable geometry. However, their data also show that the Nusselt number ratio Nu_o/Nu_c is lowest (less than unity) for the array with $\gamma = 90^\circ$ (Figure 17). The friction factor results of the present study are in agreement with Ref. 9, but the heat transfer data for oblong pin fins are not. This is thought to be related to the experimental test technique used to obtain the two heat transfer data sets. In the present study, endwall and the pins were both made of conducting material and thus forming the heat transfer surface. In the test set up of Ref. 9, the pins were made of wood and the transfer of heat to air flowing in the channel was mainly from the conducting endwalls. Since the test set up used in the present study realistically simulates the heat transfer phenomenon in channel with pins, it can be concluded that the results of the present study for oblong pins are more accurate and thus reliable for design applications.

CONCLUSIONS: The heat transfer and pressure drop characteristics of circular and oblong pin fins were measured experimentally in a test set up with both the endwalls and the pins forming the heat transfer surface. For small gas turbine applications ($Re \leq 20,000$) the oblong pin fins with angle of orientation (γ) equal to 90° (major axis aligned with the direction of flow) result in higher heat transfer coefficient and lower friction factors than the circular pin fins. For other values of γ , the oblong pin fins do not provide any significant advantage over circular pin fins. However, for applications where large pressure drops are needed, use of oblong pin fins may be desirable.

REFERENCES:

1. Zukauskas, A., "Heat Transfer from Tubes in Lossflow," Advances in Heat Transfer, 8, 1972, pp 93-160.
2. Morgan, V.T., "The Overall Convective Heat Transfer from Smooth Circular Cylinders," Advances in Heat Transfer, 11, 1975, pp 199-264.
3. Theoclitus, G., "Heat Transfer and Flow Friction Characteristics of Nine Pin Fin Surfaces," Journal of Heat Transfer, 1966, pp 383-390.
4. VanFossen, G.J., "Heat Transfer Coefficients for Staggered Arrays of Short Pin Fins," ASME Paper No. 81-GT-75, March 1981.
5. Metzger, D.E., Berry, R.A., and Bronson, J.P., "Developing Heat Transfer in Rectangular Ducts with Arrays of Short Pin Fins," ASME Paper No. 81-WA/HT-6, November 1981.
6. Metzger, D.E., and Haley, S.W., "Heat Transfer Experiments and Flow Visualization for Arrays of Short Pin Fins," ASME No. 82-GT-138, April 1982.
7. Dringham, B.A., and VanFossen, G.J., "Length to Diameter Ratio and Row Number Effects in Short Pin Fin Heat Transfer," ASME paper No. 83-GT-54, March 1983.
8. Peng, Y., "Heat Transfer and Friction Loss Characteristics of Pin Fin Cooling Configuration," ASME Paper No. 83-GT-123, March 1983.
9. Metzger, D.E., Fan, C.S. and Haley, S.W., "Effects of Pin Shape and Array Orientation on Heat Transfer and Pressure Loss in Pin Fin Arrays," ASME Paper No. 83-GTJ-1, 1983.
10. Arora, S.C. and Abdel Messeh, W., "Heat Transfer Experiments in High Aspect Ratio Rectangular Channel with Epoxied Short Pin Fins," ASME Paper No. 83-GT-57, March 1983.
11. Kline, S.J. and McClintock, F.A., "Describing Uncertainties in Single Sample Experiments," Mechanical Engineering, 75, January 1953, pp 3-8.

TABLE 1
PIN FIN ARRAY TEST CONFIGURATIONS

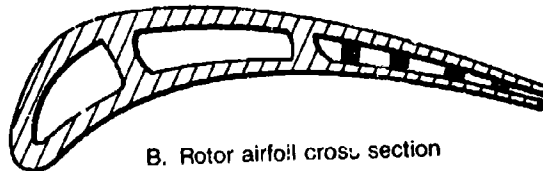
1. <u>Circular Pin Fins*</u>							
<u>Test #</u>	<u>S/D</u>	<u>X/D</u>	<u>H/D</u>	<u>S/X</u>	<u>A/D</u>	<u>B/D</u>	<u>D, inches</u>
1	2.22	2.83	1.07	.78	1.83	1.22	.1875
2	2.42	2.83	1.07	.86	1.83	1.42	.1875
3	2.46	3.39	1.28	.73	2.39	1.46	.1562

2. <u>Oblong Pin Fins*</u>							
<u>Test #</u>	<u>γ°</u>	<u>S/D</u>	<u>X/D</u>	<u>H/D</u>	<u>A/D</u>	<u>B/D</u>	<u>D, inches</u>
1	0	3.33	2.83	1.07	1.83	1.33	.1875
2	30	2.96	2.83	1.07	1.83	1.23	.1875
3	45	2.91	3.08	1.16	1.67	1.50	.1719
4	90	2.50	4.24	1.6	2.24	1.50	.125

* For nomenclature, see Figure 2



A. Stator airfoil cross section



B. Rotor airfoil cross section

FIGURE 1: PIN FIN AUGMENTED CHANNEL FLOW COOLING SCHEMES FOR TYPICAL HIGH PRESSURE TURBINE AIRFOILS

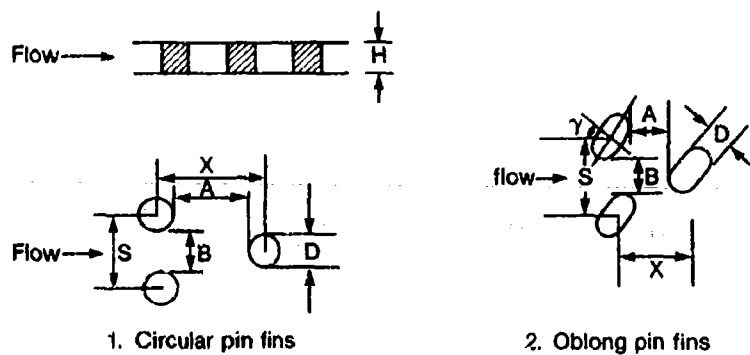


FIGURE 2: PIN FIN ARRAY NOMENCLATURE

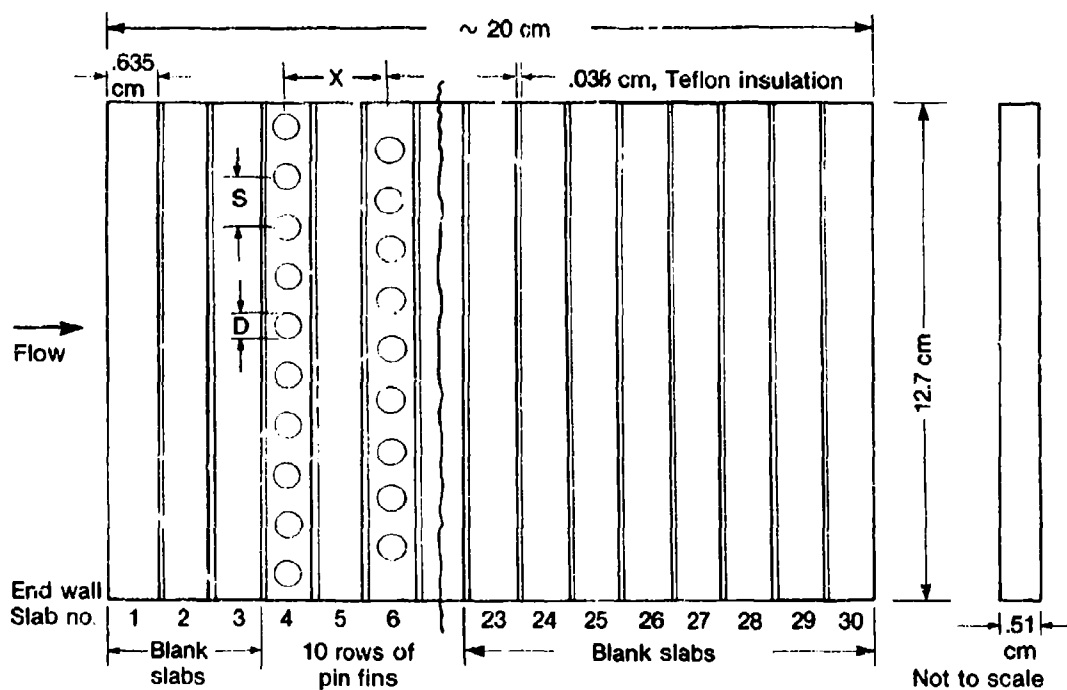


FIGURE 3: TEST SECTION GEOMETRIC SET UP

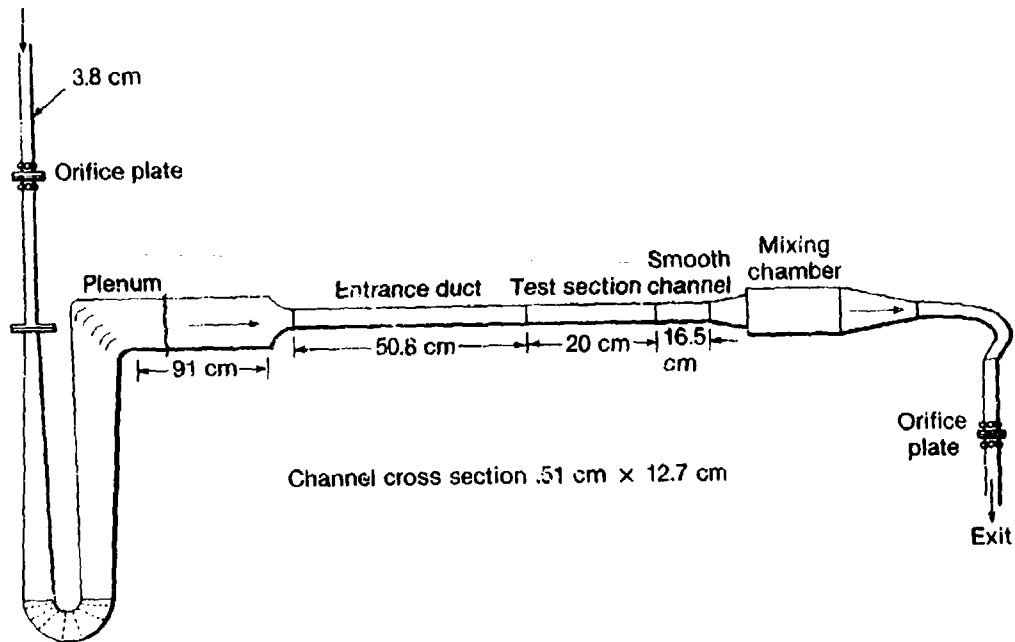


FIGURE 4: SCHEMATIC LAYOUT OF THE TEST RIG

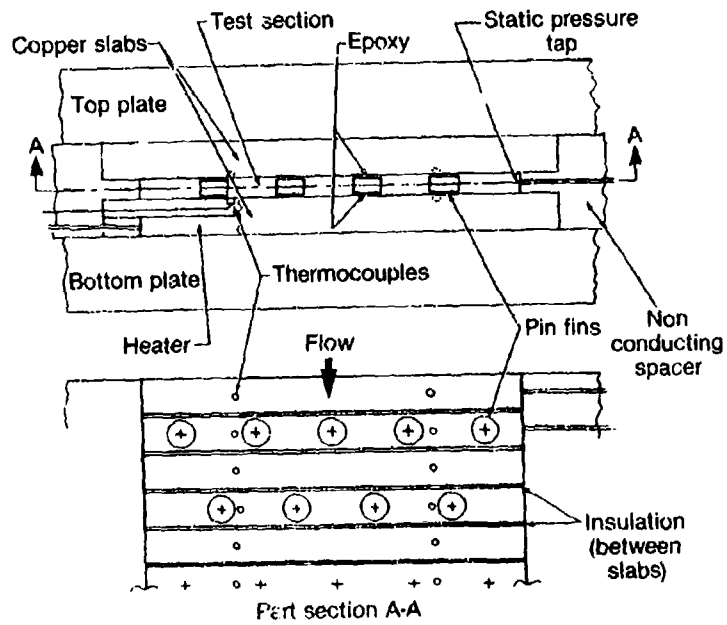


FIGURE 5: TEST SECTION DETAILS

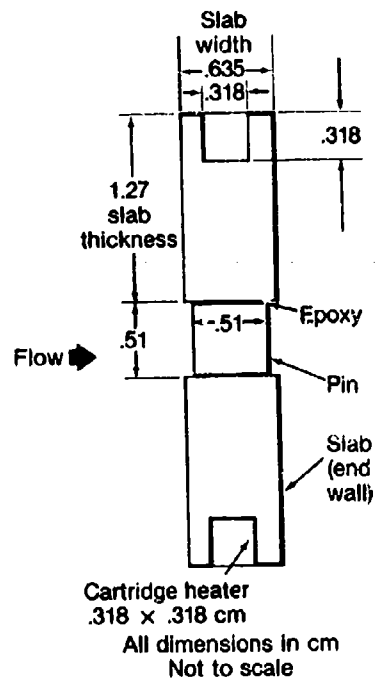


FIGURE 6: ENDWALL AND PIN FIN ARRANGEMENT

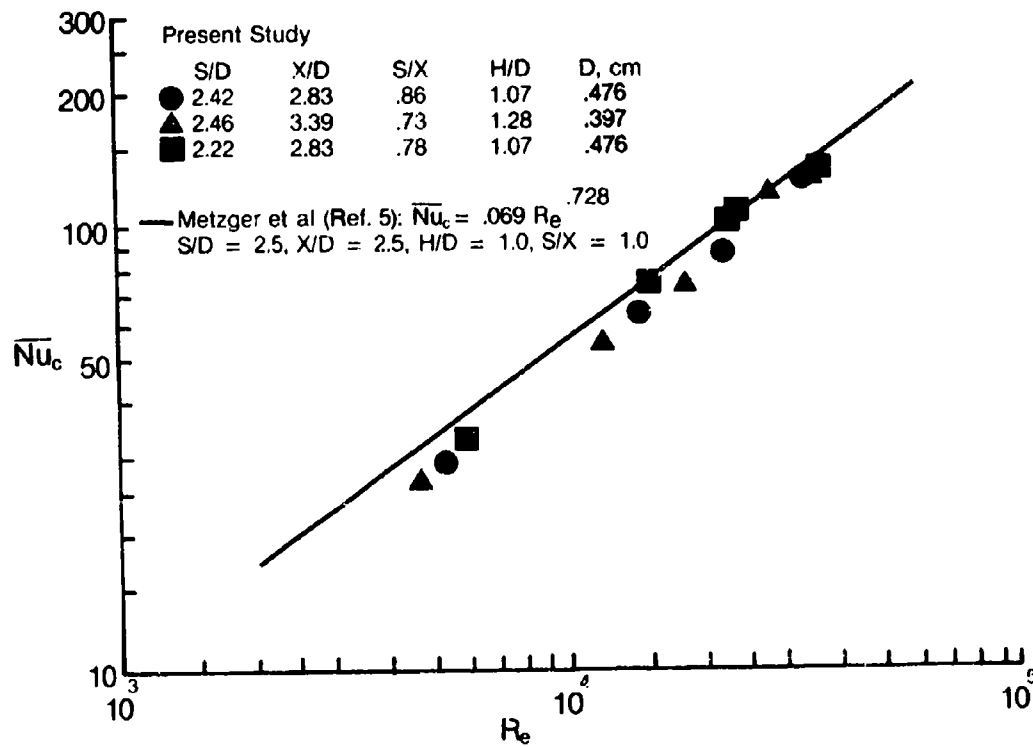
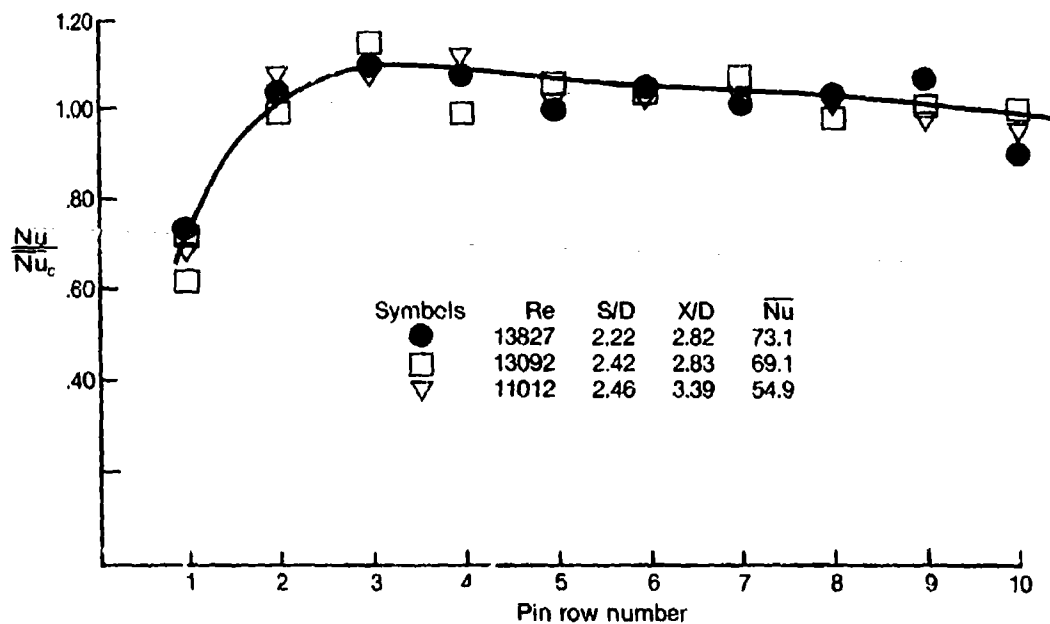
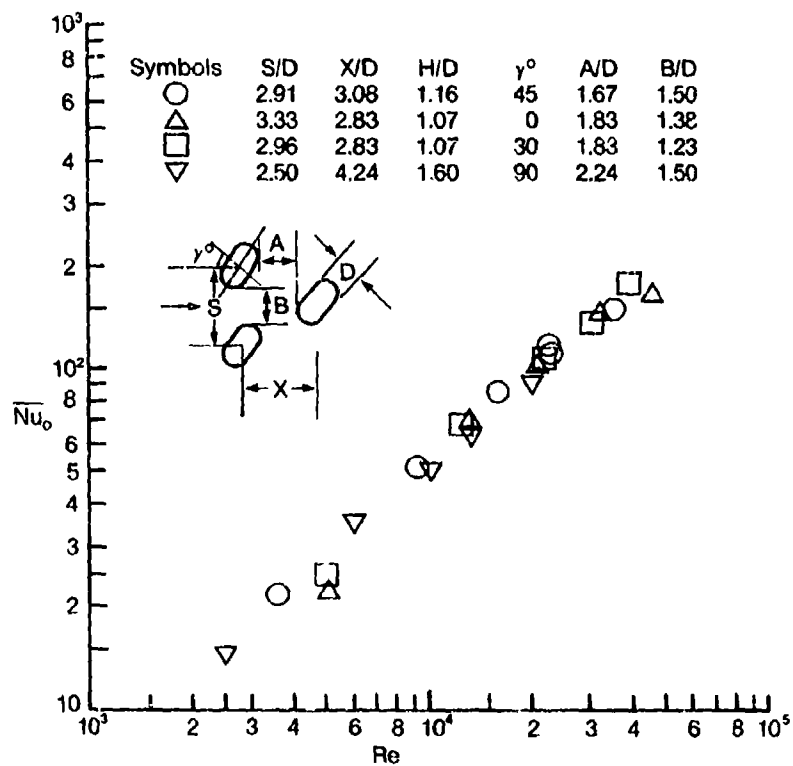


FIGURE 7: AVERAGE NUSSULT NUMBERS FOR CIRCULAR PIN FIN ARRAY

FIGURE 8: Nu/\bar{Nu}_c OF CIRCULAR PIN FINSFIGURE 9: \bar{Nu} vs Re FOR OBLONG PEDESTALS

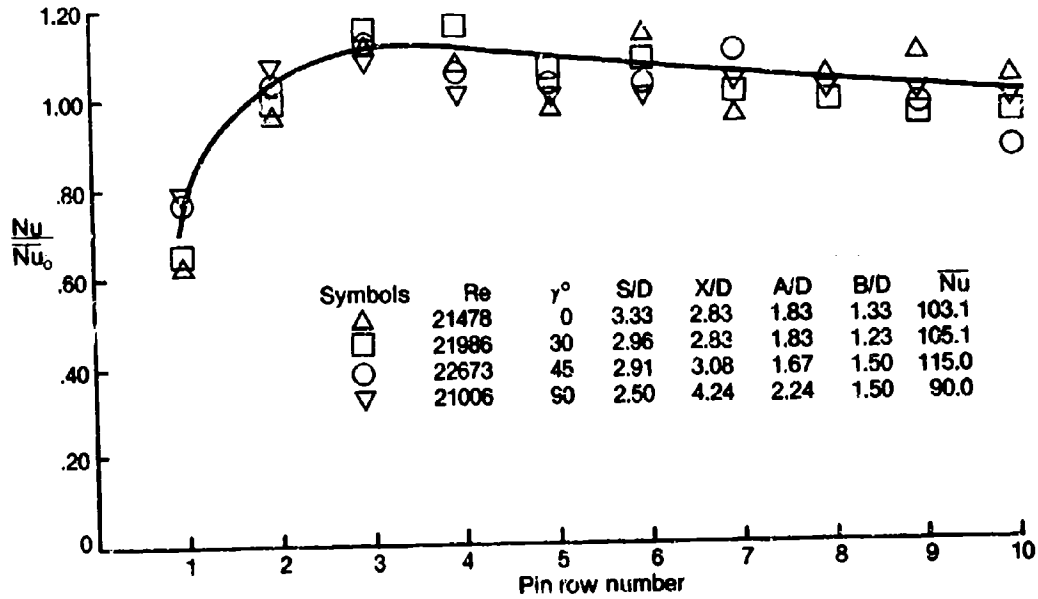
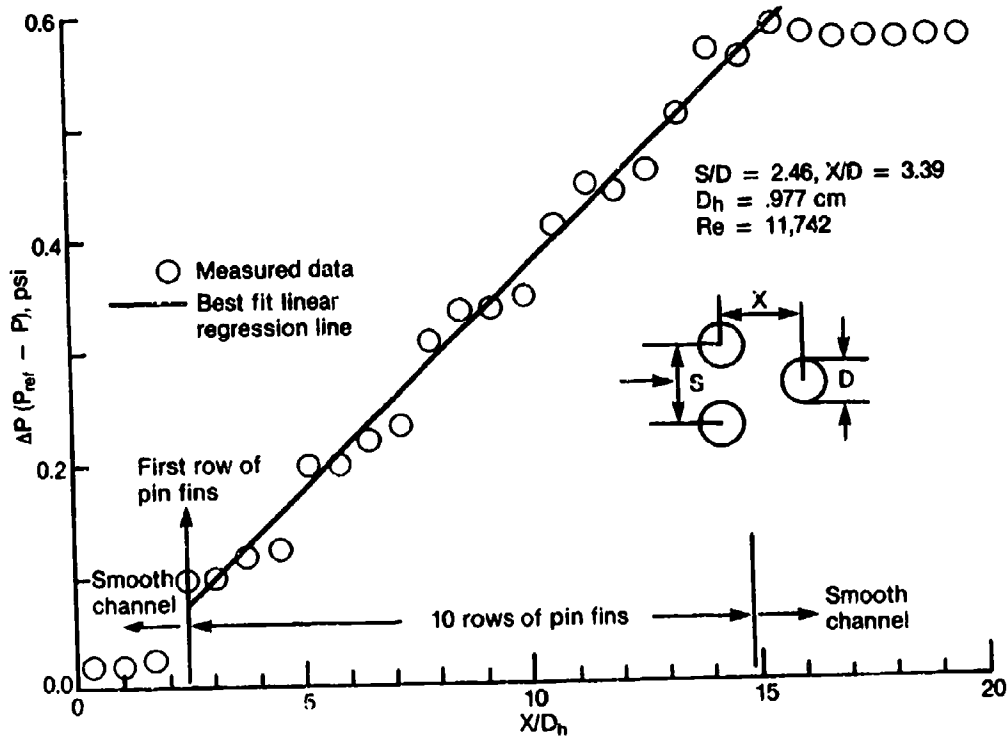
FIGURE 10: Nu/\bar{Nu} FOR OBLONG PIN FINS

FIGURE 11: STREAM WISE PRESSURE DISTRIBUTION FOR CIRCULAR PIN FINS

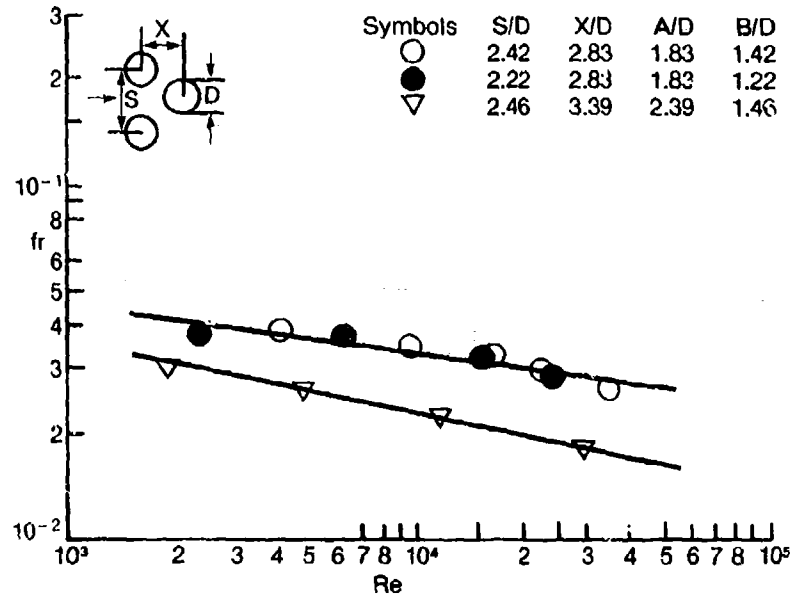
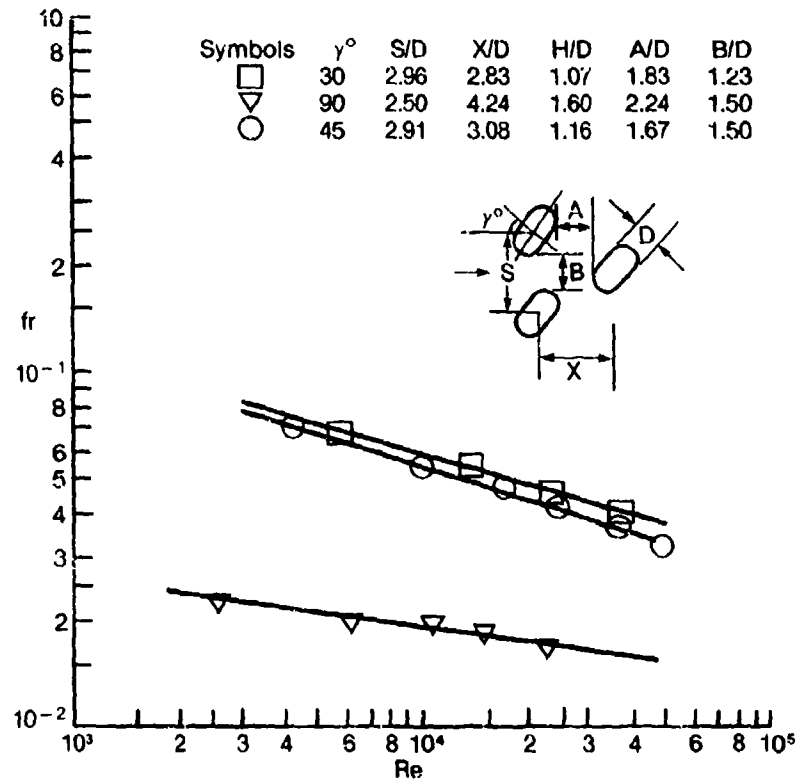


FIGURE 12: DISTRIBUTION OF FRICTION FACTORS FOR CIRCULAR PIN FINS

FIGURE 13: fr VS Re FOR OBLONG PIN FINS

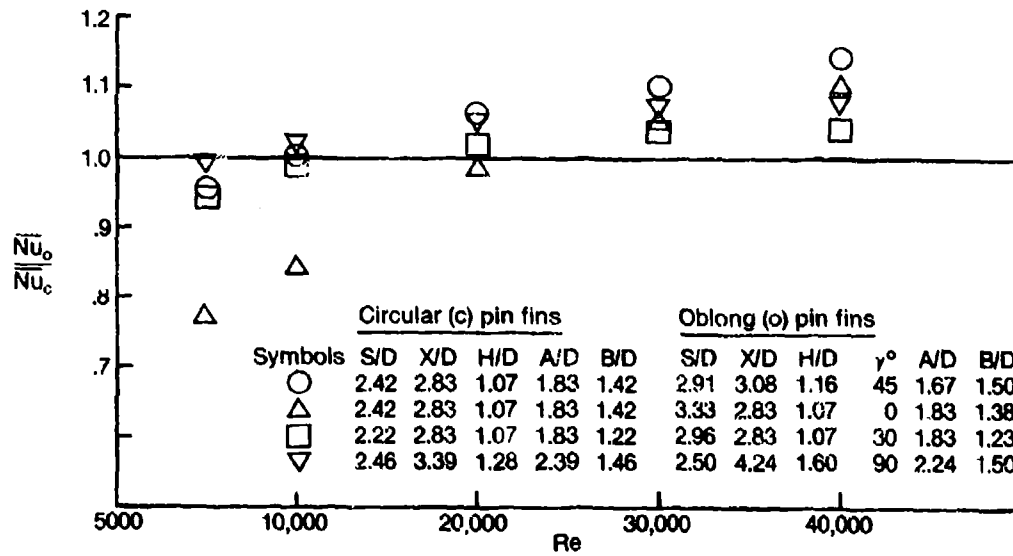


FIGURE 14: HEAT TRANSFER CHARACTERISTICS OF OBLONG PIN FINS
RELATIVE TO CIRCULAR PIN FINS

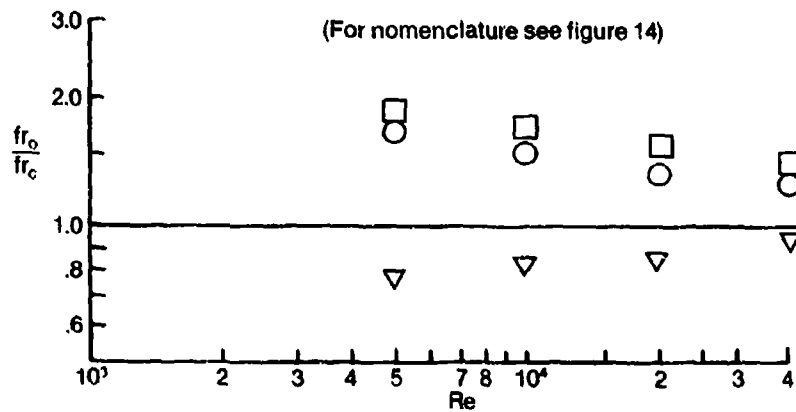


FIGURE 15: FRICTION FACTOR CHARACTERISTICS OF OBLONG PIN FINS
RELATIVE TO CIRCULAR PIN FINS

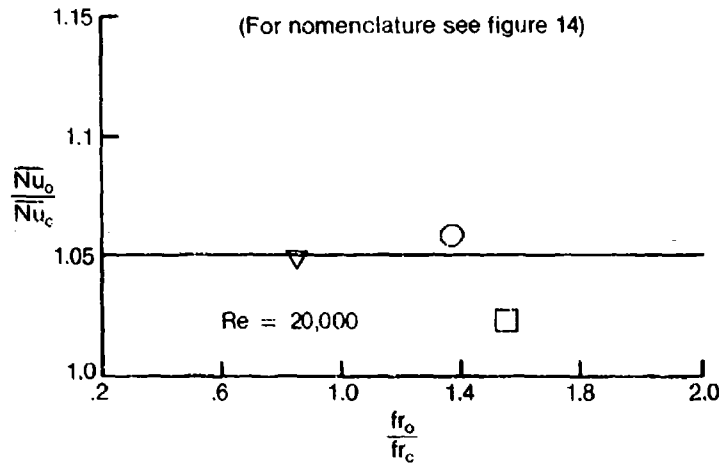


FIGURE 16: RELATIVE HEAT TRANSFER vs. FRICTION FACTOR PERFORMANCE OF PIN FIN ARRAYS

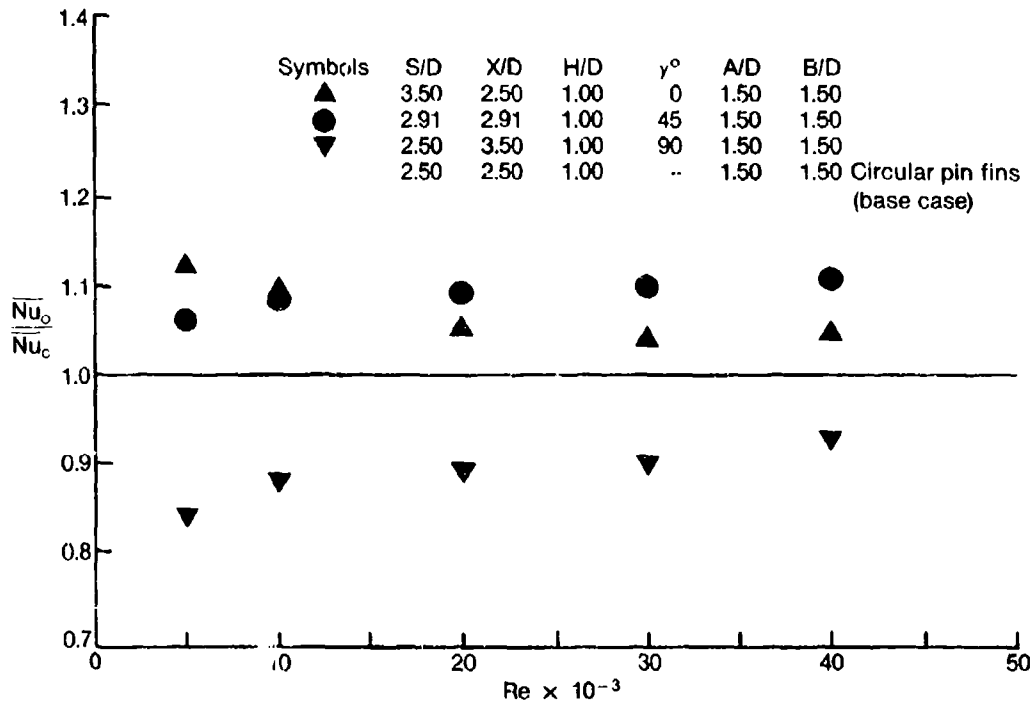


FIGURE 17: NON-CONDUCTING PIN FIN DATA TAKEN FROM REFERENCE 9

DISCUSSION**D.K.Hennecke, Ge**

You presented data for one geometry of the oblong pin fins. On which basis did you select this geometry and are you planning to investigate different geometries in order to find the optimum geometry for heat transfer and pressure drop?

Author's Reply

Some of the existing hardware uses this geometry of oblong pin fins, which was used to provide increased structural strength to the airfoil trailing edge. The present study was undertaken to obtain the necessary design data. At present, we have no plans to test any other geometry of oblong pin fins.

EXTERNAL HEAT TRANSFER STUDY ON A HP TURBINE ROTOR BLADE

T. ARTS
 von Karman Institute for Fluid Dynamics
 Chaussée de Waterloo, 72
 B - 1640 Rhode Saint Genèse, Belgium

C.G. GRAHAM
 Rolls Royce Ltd.,
 Bristol
 United Kingdom

SUMMARY

The paper deals with an experimental investigation of the effects of Mach number, Reynolds number and free stream turbulence intensity on the heat transfer performance of a high pressure gas turbine rotor blade in a stationary linear cascade arrangement. This study was undertaken in the VKI short duration isentropic compression tube facility. The tests were performed for outlet Mach numbers ranging between 0.7 and 1, whereas the outlet Reynolds number was varied between 500,000 and 1,500,000; free stream turbulence levels between 1% and nearly 8% were considered. The experimental results were compared with boundary layer predictions provided by a finite difference program (STANS), which solves the simplified, two dimensional, steady Navier-Stokes equations.

LIST OF SYMBOLS

A^*/B	calibration coefficient of the analog circuits
E_0	thin film gauge reference voltage
h	heat transfer coefficient
λ	mixing length
M	Mach number
p	pressure
\dot{q}_w''	wall heat flux
R	radius of curvature
Re	Reynolds number
Ri	Richardson number
R_0	thin film gauge resistance
s	curvilinear coordinate measured along the blade
T	temperature
t	time
Iu	turbulence intensity
ΔN	digitized raw heat transfer signal
$\Delta R/\Delta T$	thin film gauge resistance/temperature ratio
α_R	thin film temperature coefficient = $\frac{1}{R_0} \frac{\Delta R}{\Delta T}$
δ	boundary layer thickness
θ	boundary layer momentum thickness
γ	ratio of specific heats (1.4)
$\sqrt{\rho c k}$	substrate thermal product

Subscripts

0	total condition
2	downstream condition
w	condition at the wall
cal	calibration condition
∞	free stream condition

1. INTRODUCTION

In the quest for better performance, gas turbine aero-engines are being designed to operate at ever-increasing levels of pressure ratio and turbine gas temperature [1]. This frequently results in the requirement for a highly cooled two stage high pressure (HP) turbine. The optimization of such a turbine involves the study of many parameters such as rim speed, hub/tip radius, flow coefficient, work split between stages. This last parameter provides interesting possibilities from the blade cooling point of view. It influences both the gas temperatures and the insulating effect of the blade external boundary layers (due to the change in blade velocity distribution required for a variation in stage work). An accurate knowledge of the variation of convective external heat transfer with changing stage work split is therefore necessary to optimize cooled two stage HP turbines.

An experimental program at VKI was formulated to measure the external heat transfer performance of two HP1 turbine rotor blade profiles, representative of high and low first stage work. This work is in support of the Rolls-Royce HITECH Advanced Engineering Programme.

This paper deals only with the first 'high work' rotor blade and has two objectives. Firstly, to present detailed velocity and heat transfer data, measured in the VKI isentropic compression tube facility, around the blade profile, mounted in a 6 blade, stationary, linear cascade arrangement. The measurements were taken at a wall to free stream temperature ratio and range of Mach and Reynolds numbers representative of hot engine conditions. The second objective is to present a comparison of measured and predicted heat transfer coefficient distributions around the blade profile. The predictions were obtained from a two dimensional, compressible boundary layer code (STAN5), with developments at VKI to take into account the stream-wise curvature effects.

2. EXPERIMENTAL APPARATUS

2.1 Test facility

A short duration measurement technique was applied and use was made of the VKI isentropic compression tube facility (Fig. 1). The operating principles of this kind of tunnel were developed by Schultz and Jones [2,3] about ten years ago. The VKI CT-2 facility, constructed in 1978, consists of a 5 m long, 1 m diameter cylinder containing a light weight piston, driven by the air of a high pressure reservoir. This cylinder is isolated from the test section by a fast-opening slide valve. As the piston moves, the gas in front of it is nearly isentropically compressed until it reaches the pressure, and hence temperature, levels defined by the operator. The fast opening valve is then actuated by means of a detonator, allowing the pressurized air to flow through the test section. Constant free stream conditions are maintained in the test section until the piston completes its stroke. The maximum test section dimensions are $250 \times 100 \text{ mm}^2$. The free stream gas conditions can be varied between 300 and 600 K and 0.5 and 7 bar. A 5 m^3 dump tank allows downstream pressure adjustments between 0.1 and 4 bar. A typical test duration is about 400...500 ms. Further details about this facility are described in [4,5,6].

2.2 Data acquisition system

All the pressure, temperature and heat flux measurements were directly acquired by a DIGITAL PDP 11/34 computer by means of a high speed data acquisition system. This unit, designed and built at the VKI, is characterised by three separate sections. The first one consists of 24 analog circuits, which provide the transformation of the heat flux gauge signals, proportional to the surface temperature, into signals proportional to the surface heat flux. The second section is composed of a series of 48 amplifiers and "low pass" filters. The last section consists of three analog to digital converters, a multiplexer and a buffer. The signals are digitized using 12 bit words. This data acquisition system can operate on 48 channels, with a maximum sampling frequency as high as 500 kHz. For the present measurements, the sampling rate was selected to be 1 kHz.

2.3 Description of the model

The measurements and calculations presented in this paper were carried out on the "high work" HP1 rotor blade profile designed at Rolls Royce. The blade coordinates are listed in table 1 whereas the main blade and cascade dimensions are summarized as follows (Fig. 2) :

- blade height	: 100.0 mm
- chord	: 69.84 mm
- pitch	: 59.84 mm
- pitch to chord ratio	: 0.8568
- inlet angle	: 40° (from the axial direction)
- gauging angle	: $68^\circ 4'$ (from the axial direction)
- trailing edge thickness	: 2.8 mm
- number of blades	: 6

The blades, milled from aluminium, and the aluminium/perspex sidewalls were manufactured at the VKI. One of the profiles was instrumented with 27 static pressure tappings along the suction and pressure surfaces in order to determine the velocity distribution (Fig. 3). Wall static pressure tappings were also located downstream of the cascade, covering almost 2 pitches, in order to check the periodicity of the flow. A supplementary profile was milled from low conductivity "Macor" glass ceramic and 40 platinum thin films were painted on its surface in order to obtain a heat transfer distribution (Fig. 4). These films act as variable resistance thermometers and provide a local temperature history; the use of an electrical analogy allows a direct determination of the wall heat flux [7,8]. This approach provides negligible conduction phenomena and, because of the smoothness of the blade surface, no artificial boundary layer transition is induced. The technique applied to deposit the thin film gauges has been fully described in earlier publications [7,8].

2.4 Free stream turbulence generation

The free stream turbulence was generated by a grid of bars oriented in the spanwise direction. The turbulence level was varied by displacing the grid upstream of the model; a maximum of 8% could be obtained. The natural turbulence of the facility (i.e., without the grid), is about 1%. The turbulence level, defined in the present paper as $\sqrt{u'^2}/U$, was measured using a VKI constant temperature hot wire probe. The total pressure loss caused by the grid was taken into account.

3. WALL HEAT FLUX EVALUATION

The evaluation of the local wall heat flux was performed using the following equation, applied for each thin film [7] :

$$\dot{q}_w'' = \frac{A^* \Delta N}{\beta E_0 (\Delta R/\Delta T)} R_0 \left(1 + \alpha_R (T_w - T_{ca}) \right) \quad (1)$$

The present measurement technique first requires a calibration of all 24 circuits providing the temperature/heat flux conversion, in order to obtain their gain, i.e., the $\frac{A^*}{\beta}$ coefficient. The value of each reference voltage E_0 , applied to the thin films, is measured before each test and, additionally, provides a correct evaluation of the initial wall temperature T_w . The substrate thermal product $\sqrt{\rho c k}$ is determined by a comparative measurement from gauges mounted on both ceramic and quartz substrates in an impingement flow situation; a value of $0.175 \text{ J cm}^{-2} \text{ K}^{-1} \text{ s}^{-1/2}$ is used. The ratio $(\Delta R/\Delta T)$ is determined for each film from a preliminary resistance versus temperature calibration, performed in a temperature-controlled oil bath. The resistance R_0 of each gauge is measured at a given temperature T_{ca} and corrected for the current initial wall temperature T_w using the factor $\left\{ 1 + \alpha_R (T_w - T_{ca}) \right\}$, α_R being equal to $\left\{ \frac{1}{R_0} \frac{\Delta R}{\Delta T} \right\}$. The raw signal ΔN , acquired by the computer, consists of a series of integer values.

The application of equation (1) provides the wall heat flux time history of each of the platinum thin films during a test. The temperature time history is then numerically obtained from the following equation [9] :

$$T(t) = \frac{4}{3\sqrt{\rho c k \pi}} \sum_n \left[\frac{\dot{q}_{n+1} - 2\dot{q}_n + \dot{q}_{n-1}}{\Delta \tau} \right] (t - t_n)^{3/2} H(t - t_n) \quad (2)$$

where \dot{q}_n is the measured heat flux at time $t_n = n\Delta\tau$ and $H(t - t_n)$ is equal to 1 for $t > t_n$ and to 0 for $t < t_n$. A combination of both wall heat flux and temperature evolutions provides a heat flux versus temperature relation for each thin film and each test. This curve is then extrapolated to isothermal wall conditions, i.e., zero surface temperature rise. In the present paper, the heat transfer coefficient is defined as the ratio of the measured wall heat flux to the mainstream total-wall temperature difference :

$$h = \frac{\dot{q}_w''}{T_{0w} - T_w} \quad (3)$$

4. VELOCITY DISTRIBUTIONS

In order to verify the periodicity of the flow downstream of the cascade, schlieren pictures were taken and wall static pressure measurements were performed. A typical visualization is shown in figure 5a ($M_2 = 0.919$) whereas the corresponding downstream wall static pressure distribution is plotted in figure 5b. The apparent thickness of the shock (Fig. 5a) might be explained either by a possible oscillation of this discontinuity inside the blade passage or by the existence of a curved shock in the spanwise direction. The downstream periodicity (Fig. 5b) is not absolutely perfect but quite sufficient; we are indeed concerned with heat transfer measurements on the blade rather than aerodynamic ones downstream of the passage.

The velocity distributions around the blade were obtained from local static pressure measurements. They were referred to the measured inlet total pressure in order to define an isentropic Mach number as follows:

$$M_{is} = \left\{ \frac{2}{\gamma - 1} \left[\left(\frac{p}{p_0} \right)^{\frac{1-\gamma}{\gamma}} - 1 \right] \right\}^{1/2} \quad (4)$$

The measurement results, presented in figure 6 for several outlet Mach number values, have been plotted as a function of a non-dimensional curvilinear coordinate measured along the profile surface, starting from the theoretical stagnation point. A 2% uncertainty was attributed to the pressure measurements; as a result, the maximum uncertainty on the Mach number was calculated to be 1.5%. Repeatability was found to be very good.

It is clearly seen from the velocity distributions that the experimentally determined stagnation point is located very close to the theoretical one. Along the rear part of the suction side some diffusion exists and might be responsible for boundary layer transition. Along the pressure side, a slight deceleration is observed downstream of the leading edge and will probably trigger an early boundary layer transition.

5. HEAT TRANSFER DISTRIBUTIONS - MEASUREMENTS

The heat transfer measurement results, presented in figures 7-10, have been plotted under the form of a heat transfer coefficient ($\text{W/m}^2\text{K}$) evolution as a function of a curvilinear coordinate measured along the profile surface, starting from the theoretical stagnation point. The overall hydrodynamic conditions were chosen to vary independently the free stream Reynolds and Mach number values and the turbulence intensity; they are summarized, for each configuration, in table 2. The low turbulence (1%) tests were performed without turbulence grid. Due to the limited number of analog circuits (only 24 were available), two runs were needed for each configuration to obtain the complete heat transfer distribution around the blade. Moreover,

each test was duplicated to check the repeatability of the measurement technique; the latter was found to be within 3%. The experimental uncertainty on the heat transfer coefficient has been evaluated to be of the order of 7% to 9%.

Before looking at the effect of various free stream parameters upon heat transfer, the main flow field characteristics will briefly be described (Fig. 7). The highest heat flux level is measured in the stagnation region. Along the suction side, it decreases quite rapidly as a laminar boundary layer develops; this behaviour corresponds to laminar heating. Further downstream, depending upon the free stream flow characteristics, a laminar to turbulent transition takes place, resulting in a significant increase in heat flux. A turbulent boundary layer then develops up to the trailing edge. Along the pressure side, the boundary layer state, and hence the heat flux level, are principally determined by the counteracting effects of surface curvature, free stream turbulence and streamwise pressure gradient.

As suggested in [10], an attempt was made to determine the onset of transition by looking at the time history of the wall heat flux signals. Along the suction side, a typical example is presented in figure 11 ($Re_2 = 10^6$; $M_2 = 0.9$; $Tu = 4\%$). A typical laminar trace is first shown at $s = 33$ mm. The transition onset seems to take place at $s = 43 \dots 49$ mm; some agitation, corresponding to turbulent spikes, is observed on these traces. This agitation becomes larger and larger for $s = 55 \dots 60 \dots 67$ mm and it looks like a turbulent boundary layer is established around $s = 85 \dots 90$ mm. As a matter of fact, the heat transfer signals acquisition frequency was 1 kHz and they were filtered at 800 Hz; higher frequency phenomena present in the turbulent boundary layer could therefore obviously not be detected. Looking at figure 7 (nominal conditions), the boundary layer transition seems to take place only at $s = 65$ mm. It should, however, be recalled that the heat transfer coefficient is a global quantity and that, on a boundary layer level, fluctuations can already be present before any heat flux increase. The onset of transition, determined from the observation of heat flux signals, has been indicated on the suction side for all the distributions (Figs. 7 to 10). Along the pressure side, no definite conclusions could be drawn. As a matter of fact, the boundary layer was expected to be transitional rather than laminar or turbulent; therefore, no typical differences were observed on the heat flux traces.

5.1 Effect of turbulence intensity

The effect of free stream turbulence intensity at nominal Mach (≈ 0.9) and Reynolds ($\approx 10^6$) numbers is presented in figure 7. In the stagnation area, the heat flux level increases with free stream turbulence, as demonstrated by several authors [11,12]. Along the suction side, the laminar heating also increases, but less significantly, with the turbulence intensity, in accordance with other observations on the flow submitted to a pressure gradient along a curved surface. When the free stream turbulence is increased from 1% to 8%, the transition onset (defined from the heat flux traces) moves upstream, towards the leading edge. However, the net heat flux increase occurs almost at the same position ($s = 65 \dots 75$ mm) for Tu_{∞} equal to 1% and 4%, this variation is very steep and most probably forced by the shock-boundary layer interaction (Fig. 5a). Nevertheless, looking at the 4% turbulence data, the heat transfer coefficient evolution downstream of the onset of transition is nearly horizontal. This denotes a transitional flow behaviour, influenced by a strong favourable pressure gradient. For the 1% turbulence data, the heat transfer coefficient decreases over a longer distance, which is typical of a laminar boundary layer. For a higher turbulence level (8%), a more gradual transitional behaviour takes place. If the Reynolds number is increased up to about $1.5 \cdot 10^6$ (Fig. 8), a gradual boundary layer transition is observed for Tu_{∞} equal to 4% and 8% whereas the steep shock induced transition still occurs for the low intensity (1%). Along the pressure side, the exact boundary layer state is difficult to define: destabilization of the boundary layer is expected because of concave curvature whereas the important favourable pressure gradient measured along the rear part of this surface (Fig. 6) would rather have a stabilizing effect. The flow is most probably transitional over the entire length of the pressure side. This idea is supported by looking at the effect that free stream turbulence has on the heat transfer distribution: a fully established turbulent boundary layer would not be affected at all [5]. These conclusions are supported by the higher Reynolds number data (Fig. 8).

5.2 Effect of free stream Reynolds number

The effect of free stream Reynolds number at nominal Mach number (≈ 0.9) and turbulence intensity (4%) is presented in figure 9. In the stagnation region, the heat flux level increases with the Reynolds number, as demonstrated by several authors [11,12]. Along the suction side, an increase of the downstream Reynolds number, as expected, results in an enhancement of the overall heat flux level as well as in an earlier transition onset (defined from the heat flux traces). The jump in heat transfer, delayed by the favourable pressure gradient, is still steep, induced by the shock, at low and nominal Reynolds number whereas a more gradual transitional behaviour is observed at high Reynolds number. Along the pressure side, the boundary layer remains most probably transitional, dominated by a three dimensional flow of the streamwise vortex type [13,14]. The heat transfer, however, still increases with the Reynolds number.

5.3 Effect of free stream Mach number

The effect of free stream Mach number at nominal Reynolds number ($\approx 10^6$) and turbulence intensity (4%) is presented in figure 10 and will be interpreted with the aid of the velocity distributions (Fig. 6). In the stagnation region, the heat transfer coefficient slightly increases when the downstream Mach number decreases. This might be explained by the fact that, in order to keep a constant downstream Reynolds number, the inlet total pressure had to be continuously modified (table 2). As the inlet Mach number value is almost constant, this resulted in an increasing inlet Reynolds number and consequently in an augmentation of heat transfer. Along the pressure side, the velocity distributions are almost similar, except in the trailing edge vicinity. As a result, no significant differences appear in the heat transfer coefficient distributions; only the rear region is slightly affected. The small gradual heat flux increase can be explained by the inlet Reynolds number variation. Along the suction side, the onset of transition (defined from the heat flux traces) moves upstream, towards the leading edge, as the downstream Mach number decreases. The boundary layer transition process seems to be governed by variations in the acceleration rate rather than by the flow deceleration. For M_2 equal to almost 0.9 and 1.0, the steep heat flux increase is still a shock-induced phenomenon (Fig. 5a) whereas a more gradual transition is observed for M_2 equal to almost 0.7 and 0.8.

6. HEAT TRANSFER DISTRIBUTIONS - PREDICTIONS

6.1 Calculation method

In order to numerically predict the heat transfer rate evolution along the blade surface, the well known "STANS" computer program, developed by Crawford et al. [15] at Stanford University, was selected. This program is based on the classical Spalding-Patankar approach [16] to compute boundary layer flows. It uses a finite difference technique to solve, through a streamwise space marching procedure, the simplified two dimensional boundary layer equations as applied to flows developing along, e.g., a flat wall or in an axisymmetric tube. In the present paper, the modelling of the turbulent quantities was provided through a Prandtl mixing length approach.

The original version of the code was modified at VKI in order to take, along the suction side and in the case of a turbulent boundary layer, the streamwise curvature effects into account. The mixing length model developed by Adams and Johnston [17] was incorporated; valuable results were already obtained using this approach [18]. The outer layer mixing length model-equation taking streamwise convex curvature effects into account is written as follows :

$$\frac{\lambda}{R} = 0.0025 \tanh \left(34.5 \frac{\delta}{R} \right) \quad (5)$$

In the log region, the mixing length is related to a Richardson number through the following relations :

$$Ri = Sc (1 + Sc) \quad (6)$$

$$Sc = \frac{2 \frac{U}{R}}{\frac{\partial U}{\partial y} - \frac{U}{R}} \quad (7)$$

$$\frac{\lambda}{\lambda_0} = \frac{1}{1+5Ri} \quad (\lambda_0 = \text{flat wall mixing length}) \quad (8)$$

The initial velocity and enthalpy boundary layer profiles, necessary to start the calculation, were obtained from the analytical solution for a cylinder in cross flow [19]. The external streamwise velocity gradient was directly derived from the velocity measurements. The boundary layer transition was triggered by a momentum thickness Reynolds number value provided by the user.

6.2 Comparison with the measurements

The transitional momentum thickness Reynolds number was determined from an integral boundary layer analysis [20,21]. At nominal Reynolds and Mach numbers, the following results were obtained :

Tu(%)	1	4	8
Re _{0,transition}	550	490	360

and the predictions of figure 12 were plotted for different values of Re₀. For the low turbulence intensities, the agreement is quite satisfactory along the suction side. However, for Tu_∞ equal to 8%, it appears clearly that the mathematical model is not adapted to deal with complex intermittency phenomena. Moreover, the computed heat transfer across a laminar boundary layer is not affected by a variation in free stream turbulence intensity. Along the pressure side, the trends are almost correctly predicted. However, the situation is obviously more complicated considering the interaction between the free stream turbulence and the three dimensional effects which occur along concave surfaces. Only one prediction (Re₀ = 50) was plotted. In fact, the boundary layer transition was assumed to start at the pressure side slight velocity peak (s = 4 mm). An internal correlation takes care, during the computation, of the existence of a strong favourable streamwise pressure gradient, allowing a better simulation of the transitional regime.

The heat transfer distributions computed at low and high free stream Reynolds numbers are presented in figures 13 and 14 for several turbulence intensities. Along the suction side, the laminar and fully established turbulent boundary layers are quite well predicted. Except for Tu_∞ equal to 1%, the transitional regions, submitted to intermittency phenomena, are far from being satisfactorily reproduced by the calculation. Along the pressure side, the trends are quite correctly predicted.

7. CONCLUSIONS

Detailed heat transfer data have been obtained for a high pressure rotor blade, looking at the influence of free stream Mach and Reynolds numbers as well as turbulence intensity. The measurements were taken using the VKI short duration facility, under correctly simulated aero-engine conditions and have been used to assess a heat transfer prediction method based on STANS. The main conclusions are :

- an increase in turbulence intensity results in an earlier boundary layer transition and an increase in laminar and transitional heating, whereas the turbulent heating is not affected;

- an increase in free stream Reynolds number provides an overall augmentation in heat flux as well as an earlier boundary layer transition;
- at low turbulence intensity and Reynolds number, the suction surface boundary layer transition is induced by diffusion, whereas an earlier, more gradual, transition is observed for higher values of either of these parameters;
- along the suction side, the transition process is governed by the local free stream acceleration rate rather than by the existence of a velocity peak.

An attempt was also made to determine the transition onset by looking at the time history of the heat flux signals.

The results obtained from a two dimensional boundary layer code (STANS) are compared with some typical measurements. These comparisons are found to be encouraging, especially along the suction side, where a correction for curvature was added to the code. Nevertheless, a considerable work needs still to be done, particularly concerning intermittency phenomena as well as concave curvature effects.

REFERENCES

1. Olsson, U.: Advanced engine technology and its influence on aircraft performance. AIAA J. of Aircraft, Vol. 19, No. 5, May 1982, pp 380-384.
2. Schultz, D.L.; Jones, T.V.; Oldfield, M.L.G; Daniels, L.C.: A new transient facility for the measurement of heat transfer rates. In: "High Temperature Problems in Gas Turbine Engines", AGARD CP 229, 1977, p 31.
3. Jones, T.V.; Schultz, D.L.; Hendley, A.D.: On the flow in an isentropic free piston tunnel. ARC R&M 3731, 1973.
4. Richards, B.F.: Heat transfer measurements related to hot turbine components in the von Karman Institute hot cascade tunnel. In "Testing and Measurement Techniques in Heat Transfer and Combustion". AGARD CP 281, 1980, paper 6. Also VKI Preprint 1980-15.
5. Consigny, H. & Richards, B.E.: Short duration measurements of heat transfer rate to a gas turbine rotor blade. ASME Trans., Series A - J. Engineering for Power, Vol. 104, No. 3, July 1983, pp 542-551.
6. Arts, J. & Cau, G.: Short duration heat transfer measurements on simplified gas turbine components. Paper presented at the 39th A.T.I. Congress, L'Aquila, Italy, September 1984. Also VKI Preprint 1984-19.
7. Schultz, D.L. & Jones, T.V.: Heat transfer measurements in short duration hypersonic facilities. AGARDograph 165, 1973.
8. Ligrani, P.M.; Camci, C.; Grady, M.S.: Thin film heat transfer gauge construction and measurement details. VKI TM 33, 1982.
9. Oldfield, M.L.G.; Jones, T.V.; Schultz, D.L.: On-line computer for transient turbine cascade instrumentation. Transact. IEEE, Vol. AES-14, No. 5, September 1978.
10. Oldfield, M.L.G.; Kiock, R.; Holmes, A.T.; Graham, C.G.: Boundary layer studies on highly loaded cascades using heated thin films and a traversing probe. ASME Trans., Series A - J. Engineering for Power, Vol. 103, No. 1, January 1981, pp 237-246.
11. Smith, M.C. & Kuethe, A.M.: Effects of turbulence on laminar skin friction and heat transfer. Physics of Fluids, Vol. 9, No. 12, December 1966, p 2337.
12. Kestin, J. & Wood, R.T.: The influence of turbulence on mass transfer from cylinders. ASME Trans., Series C - J. Heat Transfer, Vol. 93, No. 4, November 1971, pp 321-327.
13. Kestin, J. & Wood, R.T.: The mechanism which causes freestream turbulence to enhance stagnation line heat and mass transfer. Heat Transfer, Vol. 2, Amsterdam, Elsevier, 1970.
14. Sadeh, W.Z.; Brauer, H.J.; Garrison, J.A.: Visualization study of vorticity amplification in stagnation flow. Colorado State University, SQUID-CSU-1-PU, 1977.
15. Crawford, M.E. & Kays, W.M.: STANS - A program for numerical computation of two dimensional internal and external boundary layer flows. NASA CR 2742, 1976.
16. Patankar, S.V. & Spalding, D.B.: Heat and mass transfer in boundary layers. London, Morgan-Grampian, 1st edition, 1967.
17. Adams, E.W. & Johnston, J.P.: A mixing length model for the prediction of convex curvature effects on turbulent boundary layers. ASME Trans., Series A - J. Engineering for Gas Turbines and Power, Vol. 106, No. 1, January 1984, pp 142-148.
18. Camci, C. & Arts, T.: Short duration measurements and numerical simulation of heat transfer along the suction side of a film cooled gas turbine blade. Paper to be presented at the 30th ASME Gas Turbine Conf., Houston, March 1985. Also VKI Preprint 1984-33.
19. Schlichting, H.: Boundary layer theory. New York, McGraw-Hill Book Co., 1979.
20. Huo, S.: Optimization based on boundary layer concept for compressible flow. ASME Trans., Series A - J. Engineering for Power, Vol. 97, No. 2, April 1975, pp 195-206.

- 2). Roberts, W.B.: The effects of Reynolds number and laminar separation on axial cascades performance. ASME Trans., Series A - J. Engineering for Power, Vol. 97, No. 2, April 1975, pp 261-274.

ACKNOWLEDGEMENTS

The authors wish to thank Rolls-Royce Limited for permission to publish this paper. They are also grateful to the personnel of the VKI Turbomachinery Department for their technical assistance.

X	y_{SS}	y_{PS}
0.	0.	0.
1.4	4.10	- 3.14
2.9	6.61	- 4.00
4.7	9.10	- 4.10
6.8	11.20	- 3.78
9.1	12.92	- 3.51
11.7	14.30	- 3.42
14.4	15.13	- 3.61
16.8	15.41	- 4.00
19.4	15.32	- 4.59
22.3	14.67	- 5.59
25.4	13.37	- 7.32
28.9	10.98	-10.09
32.2	7.76	-13.29
35.6	3.55	-16.99
38.8	- 1.49	-20.90
41.8	- 7.30	-25.08
44.6	-13.81	-29.50
47.3	-20.89	-33.80
49.4	-26.50	-37.15
51.2	-31.49	-40.00
52.5	-34.90	-41.79
53.7	-38.40	-41.82
54.45	-40.60	-40.60

TABLE 1 - BLADE COORDINATES

Tu(%)	1.	1.	4.	4.	4.	4.	4.	4.	8.	8.
$Re_2(10^6)$	0.980	1.411	0.469	0.989	1.006	1.028	1.018	1.495	1.085	1.614
M_2	0.888	0.873	0.863	0.658	0.768	0.870	0.961	0.813	0.880	0.874
P_{01} (bar)	1.577	2.271	0.816	1.798	1.668	1.608	1.538	2.399	1.688	2.504
T_{01} (K)	423.5	421.4	412.1	411.9	411.7	412.5	411.4	409.7	411.1	409.0

↓
nominal conditions

TABLE 2 - HEAT TRANSFER MEASUREMENTS: FREE STREAM CONDITIONS



FIG. 1 V.K.I. ISENTROPIC COMPRESSION TUBE FACILITY

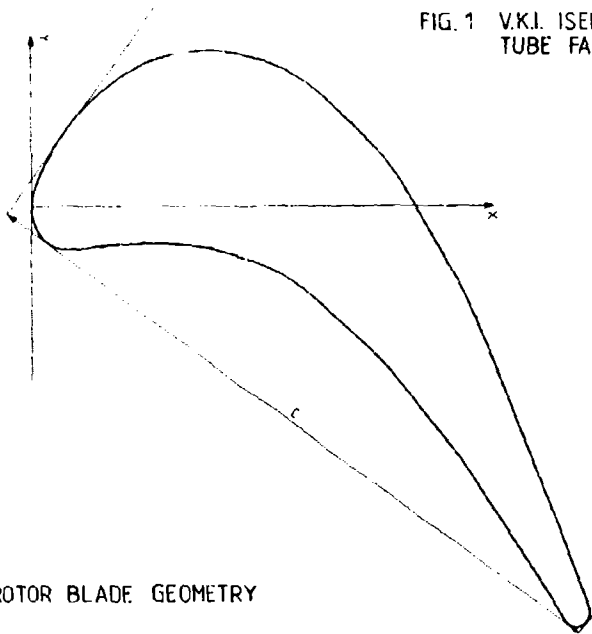


FIG. 2 ROTOR BLADE GEOMETRY

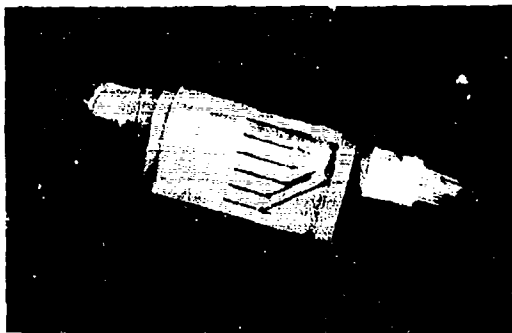


FIG. 3 STATIC PRESSURE INSTRUMENTED BLADE

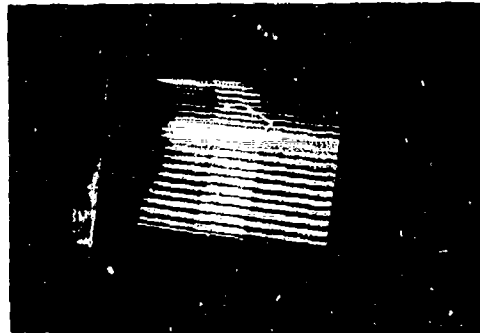


FIG. 4 HEAT TRANSFER INSTRUMENTED BLADE

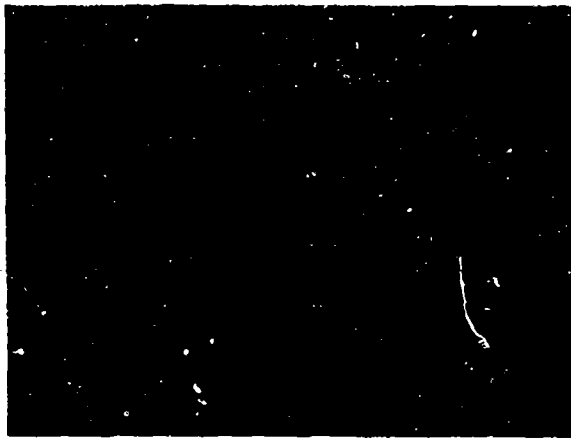


FIG. 5a SCHLIEREN VISUALIZATION ($M_2 = 0.919$)

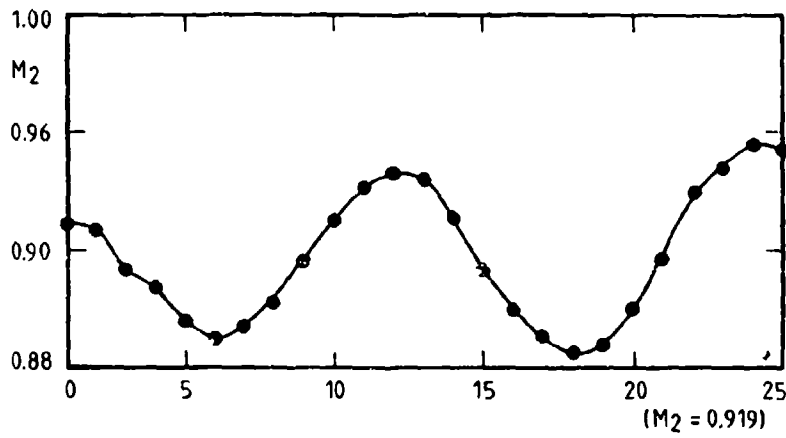


FIG. 5b DOWNSTREAM PERIODICITY

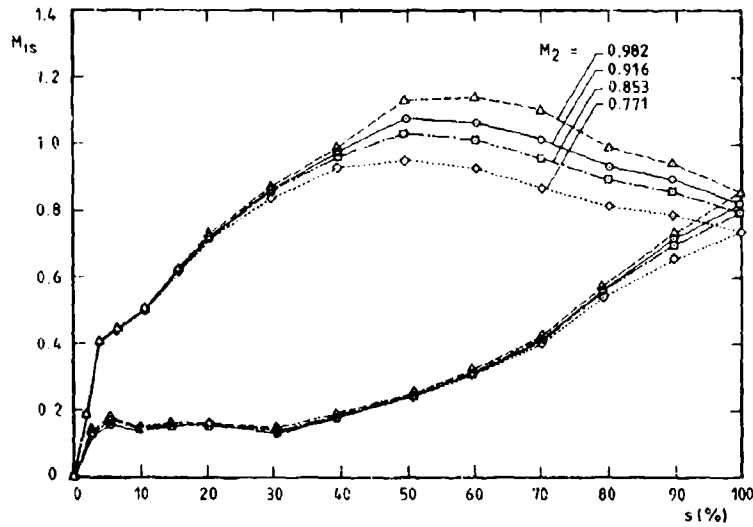


FIG. 6 MEASURED VELOCITY DISTRIBUTIONS

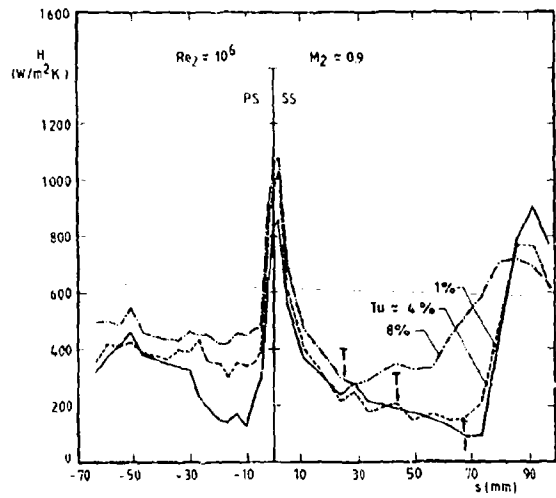


FIG. 7

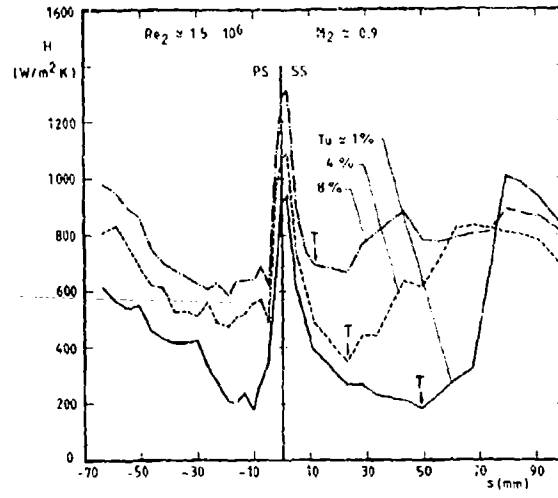


FIG. 8

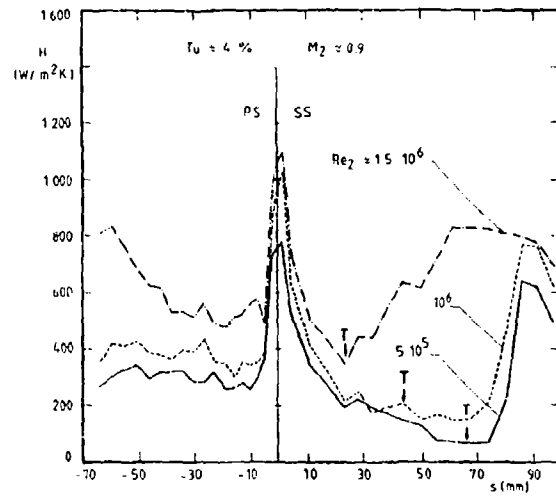


FIG. 9

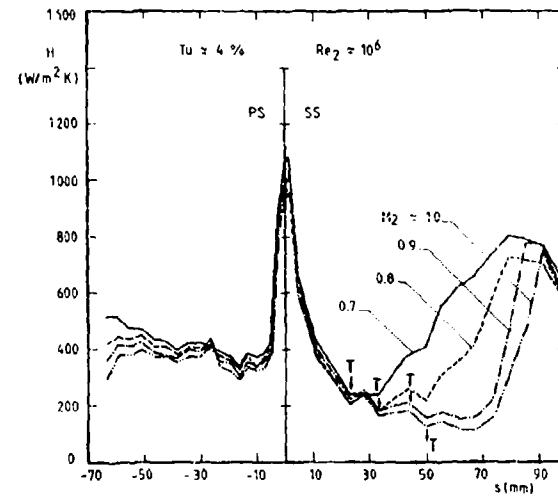


FIG. 10

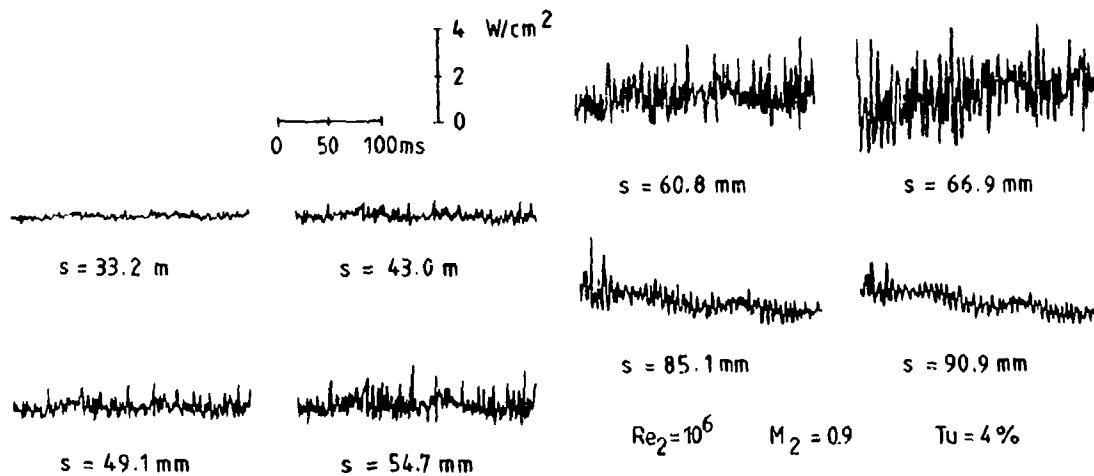


FIG. 11 ONSET OF TRANSITION DETERMINATION

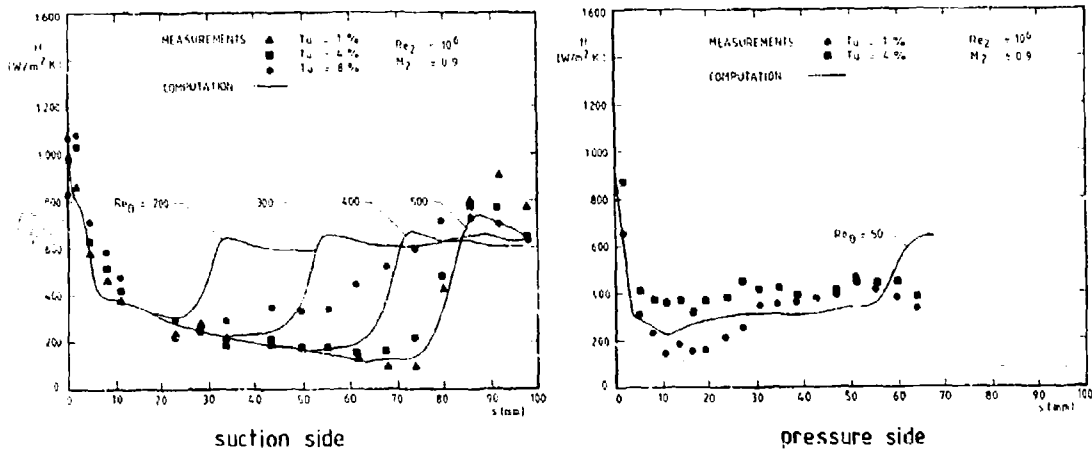


FIG. 12 COMPUTED HEAT TRANSFER

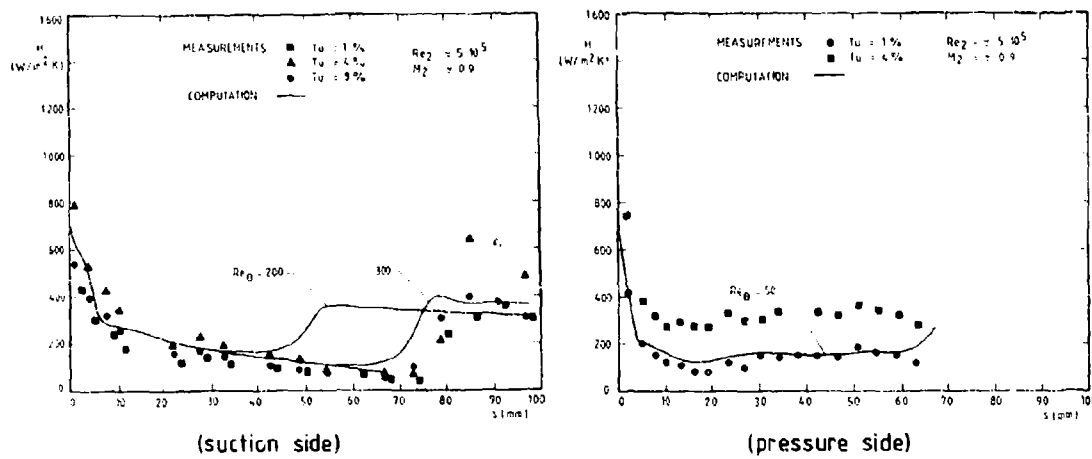


FIG. 13 COMPUTED HEAT TRANSFER

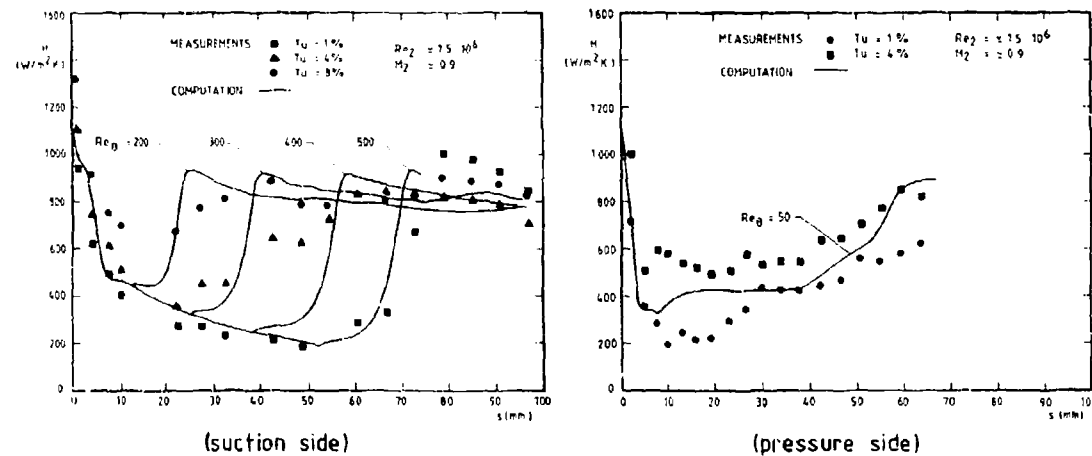


FIG. 14 COMPUTED HEAT TRANSFER

DISCUSSION

G.Scheuerer, Ge

It is not quite clear, why you used an integral procedure in addition to the finite-difference code. Was it because a transition criteria was implemented in the former?

Author's Reply

The integral procedure provides the relationship between freestream turbulence level and momentum thickness Reynolds number. This procedure allows us to fix the transition onset position (expressed as a Re_θ).

G.Scheuerer, Ge

How sensitive were your calculations towards the curvature correction?

Author's Reply

Along the suction side, a decrease of about 7-10% was observed. It should be noted that the correction is only done along the turbulent part of the boundary layer.

EFFECTS OF WAKES ON THE HEAT TRANSFER IN GAS TURBINE CASCADES

by
S.Wittig, A.Schulz, H.J.Bauer and K.H.Sill
Lehrstuhl und Institut für Thermische Strömungsmaschinen
Universität Karlsruhe (T.H.)
Kaiserstr.12, D-7500 Karlsruhe 1 (West-Germany)

SUMMARY

The interaction between consecutive blade rows can be expected to have important effects on the heat transfer in cooled gas turbine cascades. In the present study, the influence of the wake from a blade profile - traversed in front of a cooled gas turbine cascade in planes with varying distances from the leading edge - on the local heat transfer coefficient along the suction and pressure side has been analyzed. The investigation is part of a research program to develop experimentally verified numerical codes for heat transfer calculations.

With the aid of a finite element program, the local heat transfer coefficients along the cooled blades are derived from surface and coolant temperature measurements. It is shown that in addition to the axial distances the orientation of the wake with respect to the leading edge is of dominant influence. In particular, the measurements demonstrate with increasing free stream turbulence levels a rapid rise of the heat transfer rate along the pressure surface as well as in the stagnation region. The laminar-turbulent transition is relocated towards the leading edge along the suction surface. The measurements are compared with those derived from flows with grid-produced turbulence. In general slower transition behaviour is observed than found with numerical codes.

NOMENCLATURE

A	surface area
a	axial distance between airfoil and cascade inlet plane
d	cooling bore diameter
L	cooling bore length
l	chord
n	normal to surface
p	static pressure
Pr	Prandtl number
Q	heat flux
Re	Reynolds number
Re _{δ²}	Momentum thickness Reynolds number
s	distance along surface
S.P.	design stagnation point
t	blade spacing
T	temperature
Tu _u	turbulence intensity in mean flow direction
u	velocity
x	airfoil position with respect to the test blade's stagnation plane
x,y	coordinates
α	heat transfer coefficient
λ	heat conductivity
f	friction coefficient of turbulent pipe flow

SUBSCRIPTS

l	inlet to cascade
e	outer boundary conditions
k	coolant
w	wall conditions
∞	ambient conditions

INTRODUCTION

The development of high performance gas turbines has always been connected with a rise of the thermal efficiency primarily due to increasing turbine inlet temperatures and simultaneously increasing pressure ratios. Obviously, the high thermal loads of the turbine components exceedingly surpass the allowed data of modern alloys. Cooling, therefore, is a necessity which also has to be viewed under safety and reliability aspects. The durability analysis of turbine blades in a jet engine requires detailed knowledge of the heat transfer from the fluid to the blade surface which has been of longstanding interest.

The heat transfer along turbine blades is determined by a variety of different parameters such as turbulence intensity, pressure gradient, curvature, temperature ratio between gas and blade surface and periodic flow variations due to interaction of rotor and stator. In our opinion a separation of the various effects is necessary for a full understanding of the heat exchange phenomena. In addition it should be possible to support

generalisations and similarity considerations. In the larger context of the present experimental and analytical study we (see Küd et al. [7,8]) made an attempt to describe the effects of turbulence parameters, pressure gradients and temperature ratios on the heat transfer along a convectively cooled flat plate. The results of the study presented in this paper are directed towards an indepth understanding and application of the heat transfer along actual turbine blades. In continuing the basic studies, an attempt is made to determine the local heat transfer coefficient along the blade.

Utilizing a cascade with five blades, various inlet flow conditions were applied. The central three blades were instrumented and watercooled. In the first phase of the study, the free-stream turbulence levels were altered by inserting grids into the entrance flow. Three different gas temperatures and Reynolds numbers between 1×10^5 and 4×10^5 were chosen.

The second aspect of the study is concerned with the influence of the wake flow on the local heat transfer. Here, the turbulence grids were replaced by a straight blade profile placed within the cascade entrance flow. It is possible to position the blade profile at various distances from the entrance plane of the cascade. In addition, the wake generating airfoil could be placed across adjoining blade channels. The dynamic process in the real turbine which actually is unsteady can be modelled by changing sequentially the position of the blade relative to the cascade. But it should be noticed that the changes of the flow vector as found in the real case are not exactly realized in the quasi steady model.

EXPERIMENTAL SETUP

The hot gas tunnel used for the experiments is shown in Fig. 1. Air from the compressor is heated in the primary zone of an oilfired combustor. Primary air and fuel injection are predetermined and secondary air is added by means of 40 circumferential injection holes for the adjustment of the temperature level. A maximum thermal power of two MW can be verified in the combustor with maximum temperatures up to 1500°C . However, for reasons of accurate data acquisition lower temperatures are generally chosen.

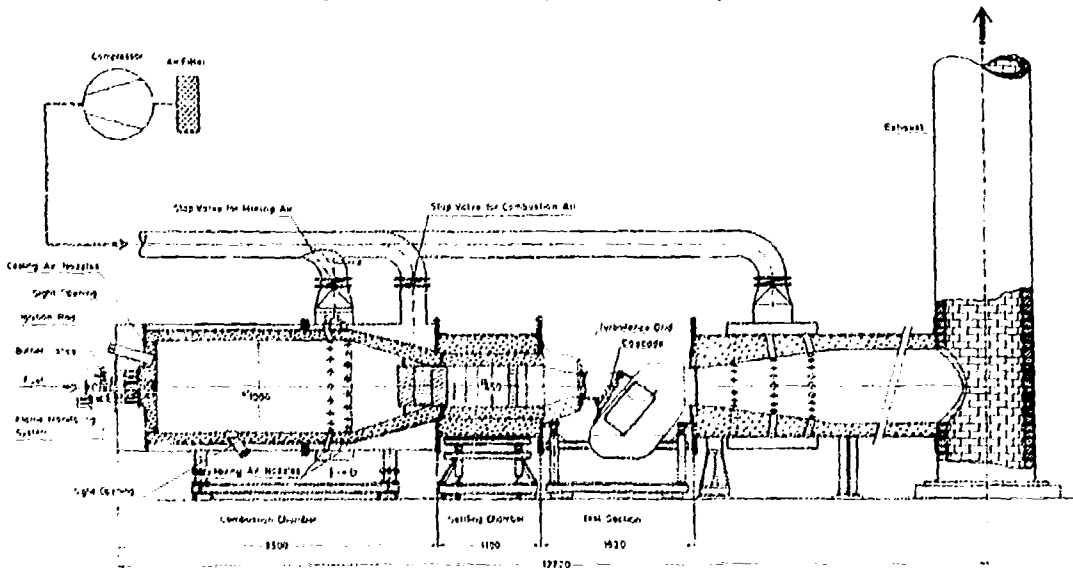


Fig. 1: Hot gas testing plant

The temperature and velocity profiles at the exit of the combustor which are not uniform originally are equalized in a settling chamber equipped with specially designed mixers and honey comb. Relatively high accelerations are subsequently induced by a nozzle with rectangular cross-section equipped with a transition from the circular settling tank.

The test section entrance itself has a cross section of 250×100 mm (see Fig. 2). In leaving the test section the hot gas flow is mixed with additional air for cooling purposes and exhausted. Special inserts behind the cascade serve to avoid circulation and to center the test section and to influence the measurements. Within limited ranges independent variation of pressure and temperature can be accomplished.

In generating different free stream turbulence levels three turbulence grids are available. They can be positioned at two inlet planes of the cascade. Fig. 3 illustrates geometry as well as the characteristic data of the grids. In addition the experimental conditions are summarized.

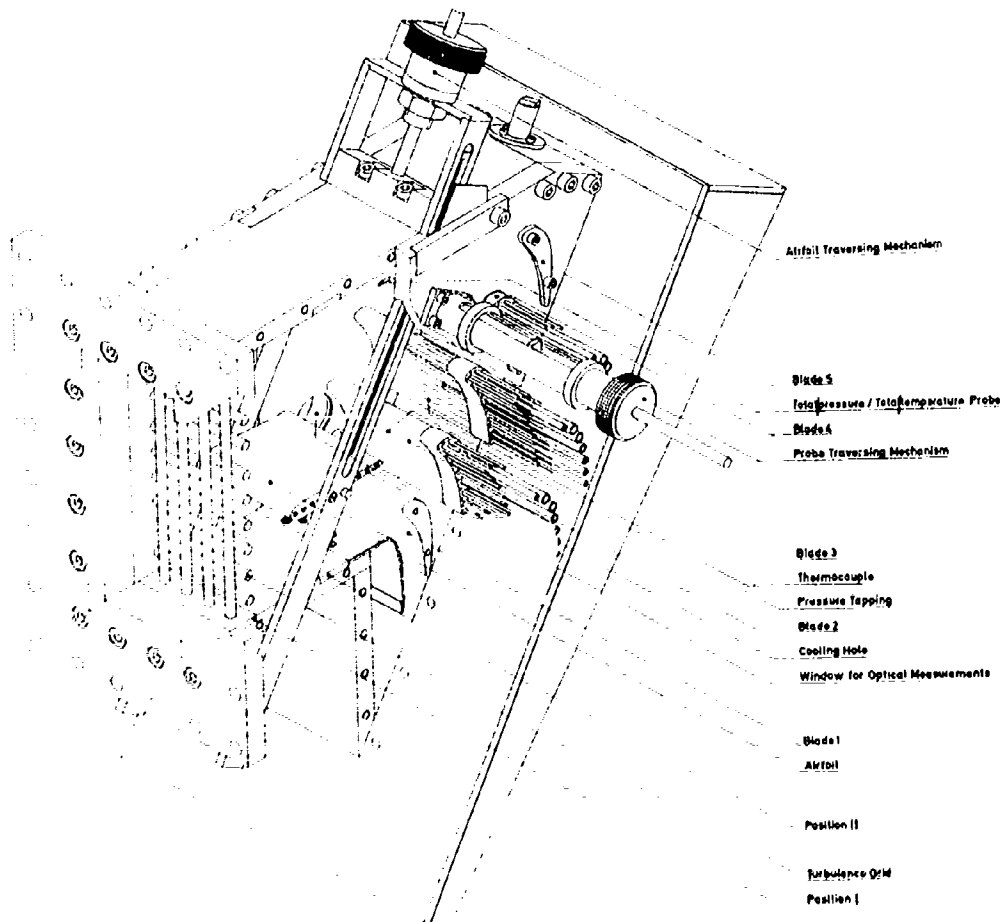


Fig. 2: Test section

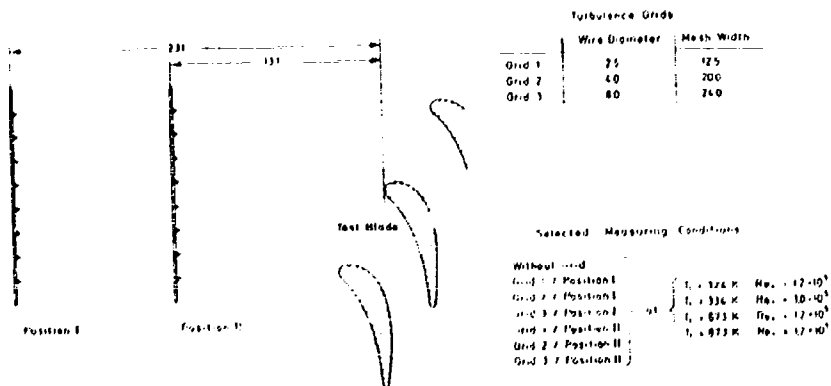


Fig. 3: Turbulence grid positions

In simulating the effects of wake flow, a straight blade profile is used in replacing the turbulence grids. To achieve relatively realistic flow conditions, the relative location of the wake flow can be changed. The traverse of the blade is illustrated in Fig. 2. The mechanism allows a parallel displacement in front of the cascade. The profile of the wake producing airfoil is derived from the coordinates of the blades in the cascade. Fig. 4 demonstrates the geometrical arrangement of the cascade and the leading airfoil.

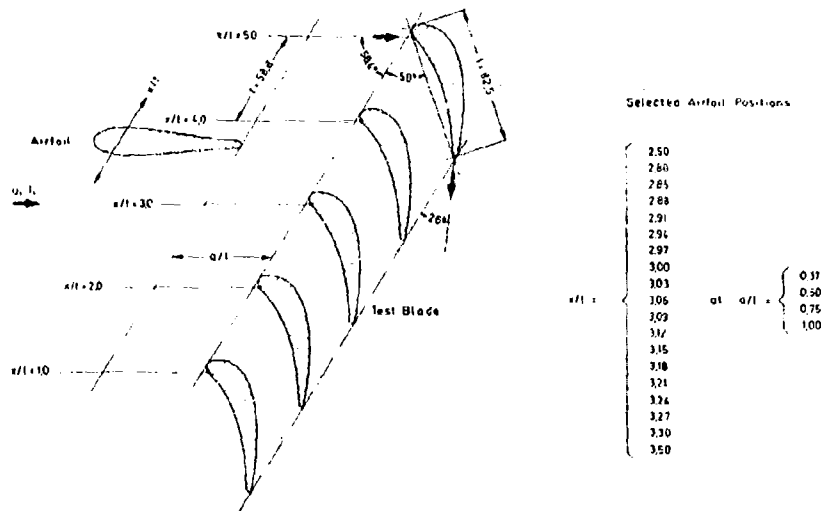
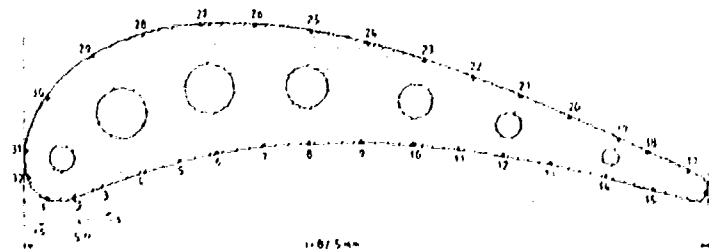


Fig. 4: Arrangement of the Cascade and the Airfoil

The cascade consists of five untwisted blades as shown. Basically it is a high performance profile. The three inner blades are used for the actual measurements. They are convectively cooled by seven cylindrical cooling channels with blade No. 3 being the test blade. Blades No. 2 and No. 4 are used for reference purposes. Thus, deviations in the temperature and pressure fields are easily observed. The outer blades (No. 1 and No. 5) are used to provide uniform two-dimensional flow without major disturbances from the side walls.

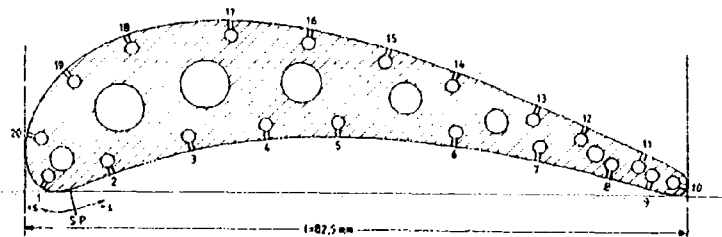
As indicated in Fig. 5, blade No. 3 is equipped with 32 NiCr-Ni-thermocouples of 0.25 mm diameter. They are embedded in grooves machined spanwise. The pressure taps of 0.5 mm diameter along blades No. 2 and No. 4 are positioned in mid span height (see Fig. 6). The relatively large number of thermocouples and pressure taps leads to an excellent resolution of the flow field. Total pressure and total temperature measurements are achieved by three probes at different locations in front of the cascade. The probes also can be traversed within the test section. It is, therefore, possible to obtain velocity and temperature profiles at three different planes.



Thermocouple Positions

No.	x/l	No.	x/l	No.	x/l	No.	x/l
1	0.0417	7	0.5	1	0.9679	4	0.9792
2	0.5616	8	0.7016	2	0.9845	5	0.9819
3	0.6288	9	0.7653	3	0.9728	6	0.9376
4	0.7983	10	0.7950	4	0.8471	7	0.9670
5	1.2227	11	0.6666	5	1.1189	8	1.0611
6	0.5670	12	0.8615	6	0.8197	9	0.7251
7	0.6196	13	0.5558	7	0.6745	10	0.9108
8	0.9084	14	0.2166	8	0.4115	11	0.8090

Fig. 5: Position of Thermocouples



Static Pressure Tapping Positions			
Nr	s/l	Nr	s/l
1	0.043	11	1.194
2	-0.067	12	1.085
3	-0.189	13	1.009
4	0.307	14	0.871
5	-0.417	15	0.761
6	-0.593	16	0.638
7	-0.719	17	0.516
8	-0.831	18	0.356
9	-0.990	19	0.251
10	1.274	20	0.138

Fig. 6: Position of pressure taps

DATA ACQUISITION AND ANALYSIS

Due to the relatively small dimensions it was not practical to determine the heat flux directly as used in our previous studies. (Rüd [8]). In the present case a finite element analysis developed by Marsal [5] is employed similar to that described in the work of Turner [11]. Starting with the known heat transfer at the cooling channel, the steady two dimensional equation for conduction is solved. Triangular finite elements are used in generating the net. A quadratic approximate solution of the temperature is determined through the six nodes of each element. The program provides for three different boundary conditions:

- I. The temperature at specific positions is known
- II. There is no heat flux across the boundary
- III. The heat flux is known across the boundary

In the present case, due to the experimental information the temperature distribution along the blade's surface - i. e. the outer boundary - as well as the heat loss through the inner boundary - i. e. the channel parameter - are used for the solution. As indicated earlier, the heat transfer coefficients and the water temperatures in the cooling channels are a necessary requirement. The temperatures of the coolant flow are obtained by simple averaging of the inlet and exit temperatures. It should be noted, however, that the difference of these temperatures is relatively small. An additional effect of the small temperature rise of the coolant is the development of a two dimensional temperature field within the blade which is of high importance in the context of the study. The heat transfer in the coolant channel is calculated following Schlönder's equation [10]

$$\alpha_K = \frac{1/8(Re_K - 1000)Pr_K}{1 + 12.7 \sqrt{f/8} (Pr_K^{2/3} - 1)} \left[1 + \left(\frac{d}{L} \right)^{2/3} \right] \frac{\lambda_K}{d^2} \quad (1)$$

for turbulent pipe flow with f , the friction coefficient for hydraulically smooth pipes.

$$f = (1.82 \lg Re_K + 1.64)^{-2} \quad (2)$$

The properties used in the determination of the dimensionless parameters Re_K and Pr_K are temperature corrected.

Despite an excessive number of thermocouples employed, the temperatures for the 172 outer nodes of the calculation net are obtained by interpolation of the measured data. With these boundary conditions, the two-dimensional calculation of the temperature field within the blade cross-section is possible. Fig. 7 illustrates a typical temperature field. The local heat transfer coefficient can be defined by using the freestream temperature obtained from a total temperature probe and the calculated temperature gradient normal to the wall:

$$\alpha = \frac{\lambda \frac{\partial T}{\partial n}}{T_\infty - T_w} \quad (3)$$

As a brief comparison with numerical codes lateron will be presented, it should be mentioned that the finite difference scheme employed requires - in addition to the surface temperature distribution and the free-stream temperature - the distribution of the velocity along the surface as well as the velocity and the turbulence intensity of the enter-

ing flow. The velocity distribution of the blade flow is derived from the static pressure distribution. Fig. 8 shows a typical pressure distribution and the resulting velocity distribution.

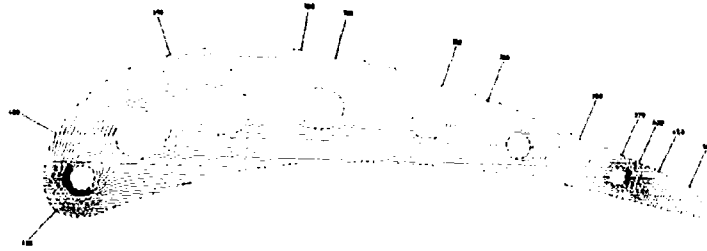


Fig. 7: Temperature field in the mid-span plane of the test blade

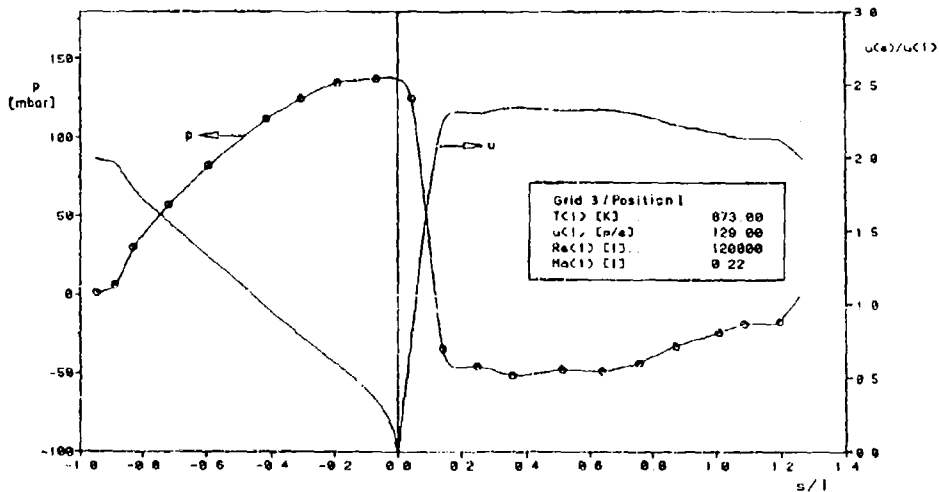


Fig. 8: Static pressure and velocity distribution

The turbulence intensity of the entering flow is determined by means of Laser-Doppler-Anemometry. Table 1 summarizes the results from measurements at $T_1 = 873$ K and a Reynolds number of 1.2×10^5 . The location where the turbulence levels are measured lies predominantly 15 mm in front of the cascade entrance plane half space between the blades.

	Grid Position I (see Fig.3)	Grid Position II (see Fig.3)
Without Grid		1.4 %
Grid 1	4.8 %	9.2 %
Grid 2	5.5 %	10.7 %
Grid 3	7.6 %	13.9 %

Table 1: Turbulence intensities

RESULTS

MEASUREMENTS WITH TURBULENCE GRIDS

In employing the turbulence grids as described in the previous chapter the distributions of the heat transfer coefficient as shown in Figs. 9 - 12 are obtained. For reasons of clarity, only four turbulence levels from 1.4 % to 14 % are shown. It is interesting

to note that at constant Reynolds numbers slightly increasing heat transfer coefficients are observed with decreasing temperature ratio, it is T_w/T_∞ . However, in calculating the Stanton numbers it can be seen that the data are in excellent agreement with smaller temperature ratios extending the laminar domain of the suction surface. Furthermore, increased heat transfer is found with rising turbulence levels in the stagnation region and on the pressure side as expected. Similar dependences are observed by Turner [11], Bayley and Priddy [1], Nicholson et al. [6], Krishnamoorthy [3] and Consigny and Richards [2]. Relatively high heat transfer coefficients along the pressure side of the blade are due to high acceleration (see Fig. 8). An additional explanation could be found in the formation of Goertler vortices which lead to a rise of the laminar heat transfer on the pressure side. The heat transfer on the suction side of the blade is characterized by the laminar - turbulent transition of the boundary flow and its dependence on free-stream turbulence. Considering the experimental results with high turbulence levels the flows show a tendency towards relaminarisation due to very high accelerations within the range $0.1 \leq s/l \leq 0.15$. It should be mentioned that there is a slight discrepancy between the stagnation point determined from pressure measurements and the position of highest heat transfer coefficients. This has been verified by numerous measurements. In the latter part of the suction side a relatively slow transition laminar - turbulent which is considerably slower than predicted by numerical codes [12] is observed. It is largely dependent on the free-stream turbulence level. (see Fig. 11)

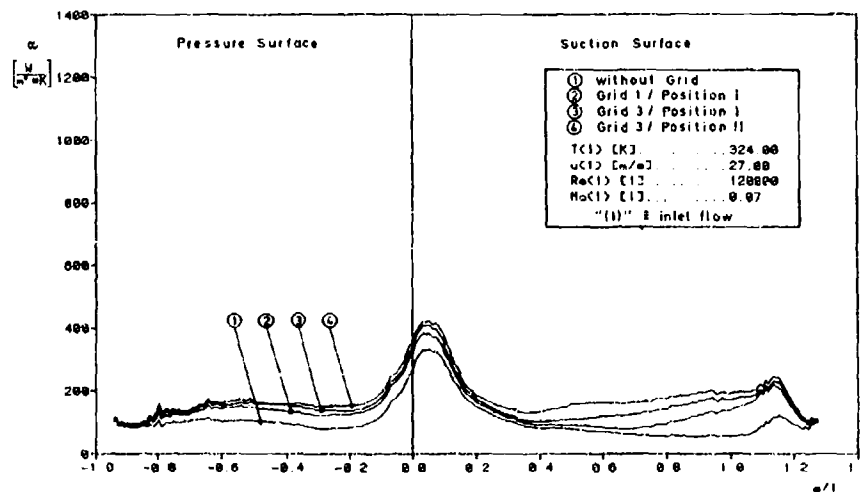


Fig. 9: Heat transfer coefficients $Tu_u = 1.4\%$; 4.8% ; 7.6% and 14.0% $T_w/T_\infty = 0.91$

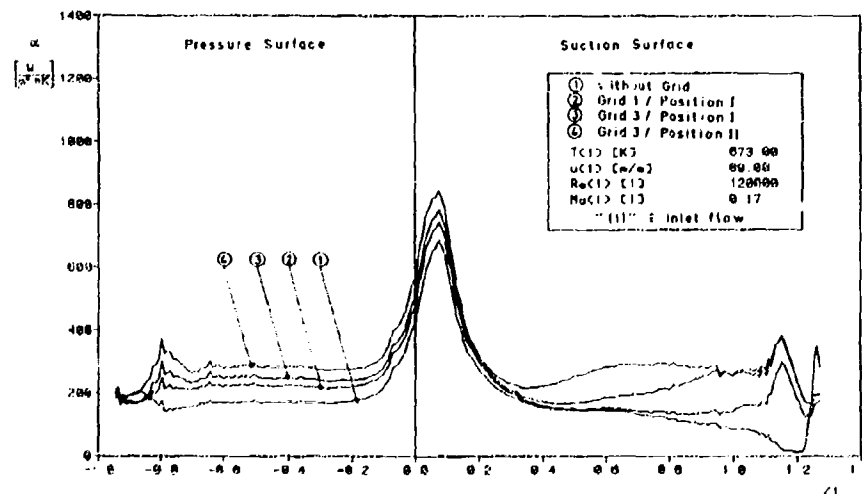


Fig. 10: Heat transfer coefficients $Tu_u = 1.4\%$; 4.8% ; 7.6% and 14.0% $T_w/T_\infty = 0.53$

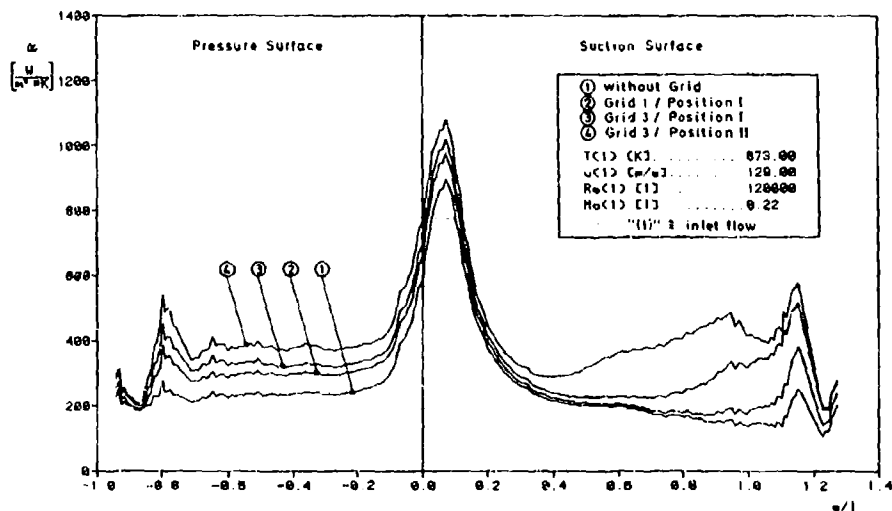


Fig. 11: Heat transfer coefficients $Tu_{in} = 1.4\%$; 4.8% ; 7.6% and 14.0% $T_w/T_{in} = 0.48$

Qualitatively similar characteristics are observed for higher Reynolds numbers as shown in Fig. 12. To us, the determining factors along the pressure side where slightly increasing heat transfer coefficients are observed are not entirely clear. It seems that a stronger tendency towards transition is indicated. The suction side is characterized by a well defined laminar turbulent transition and here no influence of the turbulence level after transition was found. The fluctuations in the trailing edge region are probably due to the cooling configuration. Basically, only one cooling channel is located in this area thus inducing nonuniform surface temperature distributions.

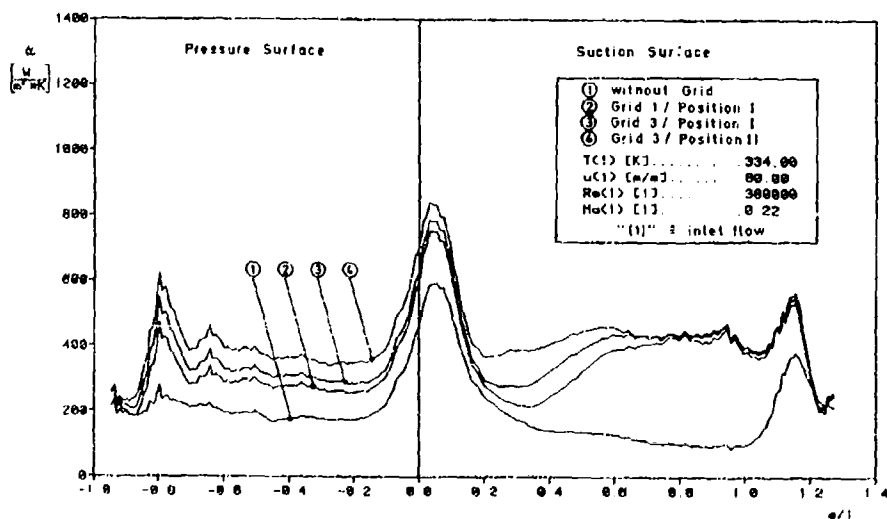


Fig. 12: Heat transfer coefficients $Tu_{in} = 1.4\%$; 4.8% ; 7.6% and 14.0% $T_w/T_{in} = 0.89$

WAKE FLOW MEASUREMENTS

The effects of wakes on the heat transfer along a blade is illustrated in Figs. 13 and 14. As indicated, the wake generating airfoil was traversed in discrete steps over the spacing of the test blade. ($3.5 = x/t = 2.5$, compare Fig. 4). Here, the distance of the trailing edge to the entrance plane of the cascade is $a/l = 1.0$. The Reynolds number in each case was 3.8×10^5 . The location of the wake is imaged in the heat transfer coefficients. Starting from the center of the flow channel ($x/t = 3.5$), where the influence of the wake on the subsequent blade is relatively low (see curve No. 1 in Fig. 13) with laminar flow throughout, a gradual onset of transition is found in moving the airfoil's wake towards the stagnation point of the cooled blade. The transition is very pronounced for near centerline positions. Also, the effects of the pressure

are pronounced. This is in agreement with the results described earlier for grid experiments. In considering the stagnation point area the highest heat transfer was expected to be at $x/t = 3.0$ whereas the actual maximum was found at $x/t = 3.06$. Optical diagnostics revealed that the flow is slightly deflected in the cascade inlet plane. The strongest influence of the wake, therefore, is found for a position of the airfoil slightly on the suction side of the measurement blade. In continuing the traverse of the airfoil across the leading edge ($x/t = 3.00$) towards the pressure side of the test blade, the results of Fig. 14 are obtained. The heat transfer rate stays relatively high over the whole blade surface down to the position $x/t = 2.07$ of the wake generating blade. Subsequently the transition along the suction side is relocated towards the trailing edge with decreasing x/t . In comparing Figs. 13 and 14 it is interesting to note that the transition characteristics are not identical. This is due to the particular geometric effects of the wake and its relative effects. Considering the pressure side, a reduction of the heat transfer coefficient is observed starting from the airfoil's position of approximately $x/t = 2.88$. As can be seen, the heat transfer coefficient decreases by about 40 % with respect to the maximum curve. Further traverse to lower x/t values beyond 2.80 will be of negligible influence.

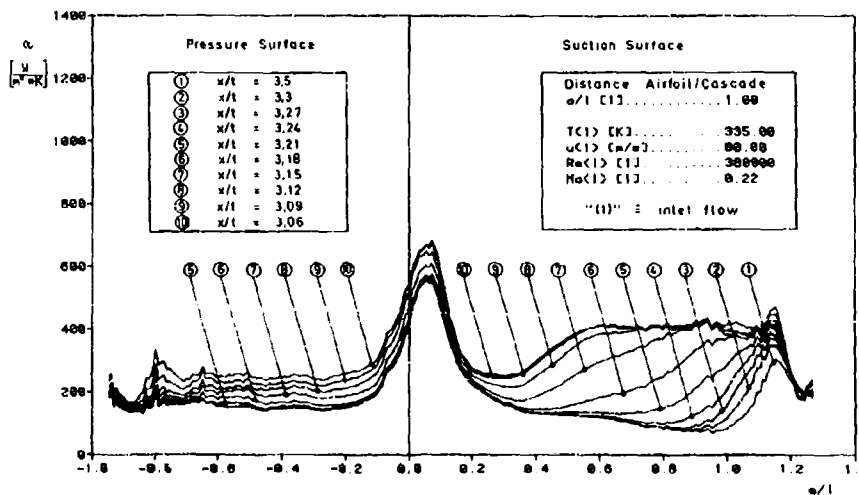


Fig. 13: Heat transfer coefficients (wake influence)

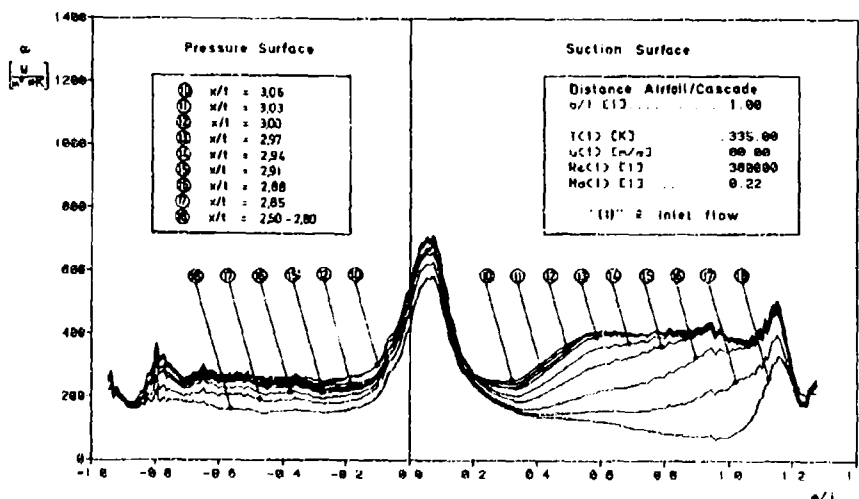


Fig. 14: Heat transfer coefficients (wake influence)

In summarizing the results, the three dimensional plot of Fig. 15 relays a qualitative impression of the phenomena discussed. The heat transfer coefficient along the blade's surface ($-0.94 \leq s/l \leq 1.27$) is plotted as a function of the position of the wake-producing airfoil. ($2.5 \leq x/t \leq 3.5$)

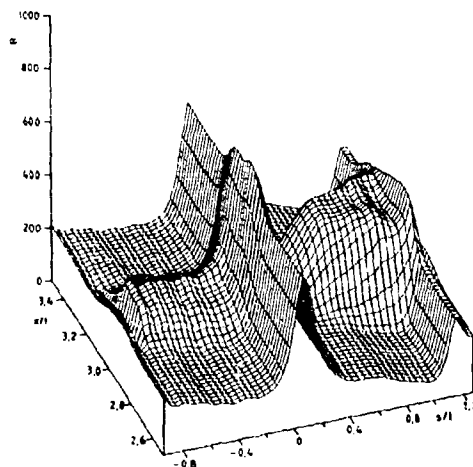


Fig. 15: Heat transfer distribution

In order to analyse the influence of the axial distance of the wake from the entrance plane into to the cascade, detailed measurements were performed with varying axial distances of the airfoil from the cascade. A typical result is shown in Fig. 16 with the wake generating profile fixed at $x/t = 3.09$ and with the axial distance reduced from $a/l = 1.0$ to $a/l = 0.37$. It can be seen that the heat transfer on the pressure side is reduced by about 35 % in approaching the cascade entrance plane. This can be explained by the different location of the test blade within the divergent wake flow. At present we are performing detailed numerical studies in combination with associated measurements to model the dynamic characteristics of the wake and its influence on the time dependent heat transfer of the cascade effected by the wake.

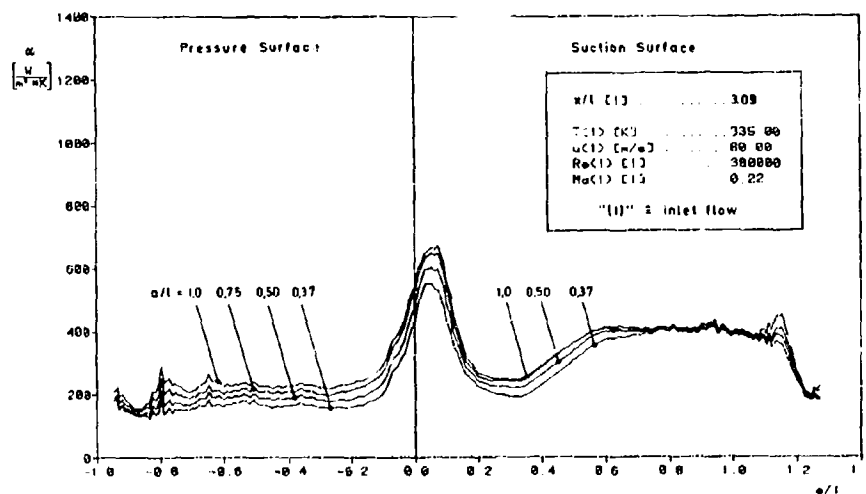


Fig. 16: Heat transfer coefficients (different axial distances)

COMPARISON WITH THEORETICAL RESULTS

As described elsewhere [9, 12, 13] a modified code for the description of the boundary layer flow with heat transfer has been applied in comparing the experimental results with a theoretical analysis. As usual, the $k - \epsilon$ model - here in a form suggested by Lam and Bremhurst [4] - has been utilized and the turbulence effects on the temperature field - i. e. the turbulent heat transport - are included by means of the turbulent Prandtl number.

The comparisons are based on heat transfer measurements at higher Reynolds numbers ($Re_1 = 3.8 \cdot 10^5$) and relatively low wall cooling ($T_w/T_\infty = 0.89$) with turbulence intensities of the main flow of 1.4%, 4.8% and 7.6%. In starting the calculation procedure, a Reynolds number based on the momentum thickness of $Re_{\delta_2} = 30$ on the suction side and $Re_{\delta_2} = 10$ on the pressure side has been assumed. Using Thwaites' suggestion (see Ref. [16]) the appropriate distance from the leading edge could be calculated. In starting the program the turbulence intensities were derived as follows

$$Tu = Tu_1 \cdot \frac{u_1}{u_w} \quad (4)$$

with the assumption that the turbulent kinetic energy is constant up to the location of the start of the calculation.

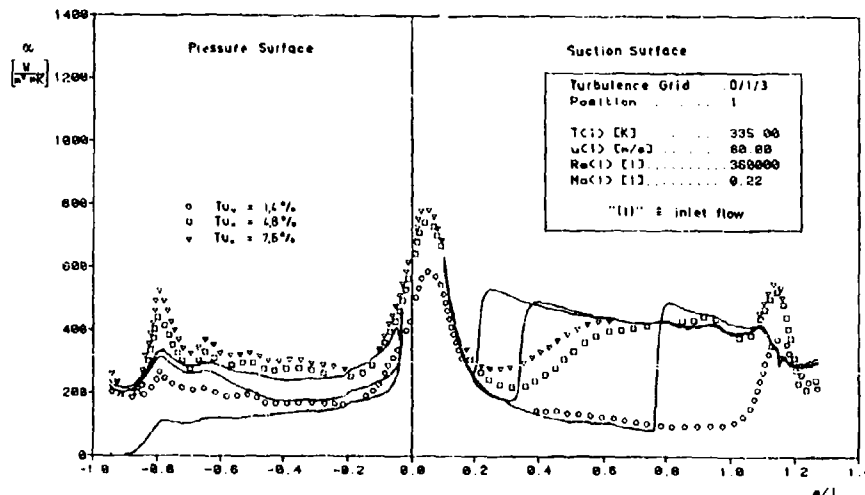


Fig. 17: Comparison of predicted and measured heat transfer coefficients

As shown in Fig. 17, the determining effects along the suction side is the rapid laminar-turbulent transition. Apparently, for low free-stream turbulence the onset of transition appears to be too soon. For high turbulence intensities it is found that the location of transition is reasonably well predicted. However, the levels of turbulent flow are approached too soon. For purely laminar as well as for fully turbulent flow good agreement is found between experiments and predictions.

Along the pressure side good agreement is found for low free stream turbulence levels in the frontal region of the blade. Towards the trailing edge, however, the heat transfer is considerably underpredicted. Relatively strong differences between measurements and numerical results are found for turbulence levels of $Tu_1 = 4.8\%$, at least over the first two thirds of the pressure side with improvements towards the trailing edge. Following the calculations, the highest turbulence intensity of the main entrance flow induces a laminar-turbulent transition soon after the start. Good agreement between the measured and calculated heat transfer coefficients is found up to $x/l = 0.2$ with an almost constant underprediction of the heat transfer down to the trailing edge.

CONCLUSION

The present study is directed toward a detailed understanding of the heat transfer along convectively cooled gas turbine blades under consideration of various flow conditions. In a first series of experiments the influence of free stream turbulence intensities, Reynolds numbers and temperature ratios was analysed. Here, turbulence grids were utilized. At all temperature ratios the dependence of the heat transfer over the whole blade surface on the free-stream turbulence is illustrated. The dependence on the Reynolds number is characterized by the level of the heat transfer and especially in the laminar-turbulent transition along the suction side. The comparison with theoretically derived heat transfer coefficients reveals good agreement along the suction side for laminar and turbulent boundary layer flow. The calculated transition, however, seems to be too spontaneous. For the complex pressure side flow, the theoretical model leads to results which are not quite satisfactory: The heat transfer coefficients obtained are too low for all flow conditions analyzed.

In extending the experiments, measurements were performed under wake conditions. As expected, a strong influence of the distribution of the heat transfer coefficient on the relative position of the wake generating profile with respect to the test blade was found. Special significance of the position of the wake with respect to the leading

edge can be seen. On-line axial positioning of the leading airfoil induces turbulent boundary layer flow along a major region of the suction side and induces heat transfer coefficients which exceed the laminar heat transfer by approximately a factor of three. An increase of about 100 % is found on the pressure side. The differences of the heat transfer distribution due to varying distances a/l between the blades - i.e. the wake generating blade and the cascade - are related to the appropriate width of the wake. Principally, it can be stated that a strong rise of the heat transfer is found for large axial distances for relatively long traverse ($3.21 \pm x/t \pm 2.8$). Lower heat transfer is found for shorter axial distances except the region of strong influence ($3.06 \pm x/t \pm 2.97$). This is of importance to actual turbine application where a larger axial distance between the blade rows will yield higher heat transfer rates. At present, the results are used in studying unsteady engine conditions.

ACKNOWLEDGEMENTS

Thanks are due to Dipl.-Ing. K. Dullenkopf and Dipl.-Ing. R. Hestermann for their support in obtaining the turbulence data. Financial support for the earlier study and the equipment used was obtained from the Forschungsvereinigung Verbrennungskraftmaschinen (FVV). Dr.-Ing. Mukherjee was the chairman of the working group.

REFERENCES

- [1] Bayley, P.J. and Priddy, W.J.:
Effects of Free-Stream Turbulence Intensity and Frequency on Heat Transfer to Turbine Blading. J. of Engineering for Power, Vol. 103, January 1981, pp. 60-64
- [2] Consigny, H. and Richards, B.E.:
Short Duration Measurements of Heat Transfer Rate to a Gas Turbine Rotor Blade Transactions of the ASME, Paper No. 81-GT-146, 1981
- [3] Krishnamoorthy, V.:
Effect of Turbulence on the Heat Transfer in a Laminar and Turbulent Boundary Layer over a Gas Turbine Blade. ASME-Paper No. 82-GT-140, 1982
- [4] Lam, C.K.G. and Bremhurst, U.A.:
Modified Form of the k, ϵ -Model for Predicting Wall Turbulence. J. of Fluids Eng., Vol. 103, pp. 456-460, 1981
- [5] Marsal, D.:
Die numerische Lösung partieller Differentialgleichungen. B.I. Wissenschaftsverlag, Mannheim/Wien/Zürich, 1976
- [6] Nicholson, J.H., Forcst, A.E., Oldfield, M.D.G. and Schultz, D.L.:
Heat Transfer Optimized Turbine Rotor Blades - An Experimental Study Using Transient Techniques. ASME-Paper No. 82-GT-304, 1982
- [7] Rüd, K., Sill, K.H. and Wittig, S.:
Einfluß der Freistromturbulenz auf den Wärmeübergang an stark gekühlten Oberflächen. VDI-Paper No. 487, presented at VDI-Tagung "Thermische Strömungsmaschinen", Köln, June 1983
- [8] Rüd, K. and Wittig, S.:
Free-Stream Turbulence and Pressure Gradient Effects on Heat Transfer and Boundary Layer Development on Highly Cooled Surfaces. Transactions of the ASME, Paper No. 84-GT-180
- [9] Scheuerer, G.:
Entwicklung eines Verfahrens zur Berechnung zweidimensionaler Grenzschichten an Gasturbinenschaufeln. Dissertation, Universität Karlsruhe 1983
- [10] Schlünder, E.U.:
Einführung in die Wärme- und Stoffübertragung. Vieweg-Verlag, Braunschweig, 1981
- [11] Turner, A.B.:
Local Heat Transfer Measurements on a Gas Turbine Blade. J. Mech. Eng. Science, Vol. 13, No. 1, 1971
- [12] Wittig, S., Rodi, W., Sill, H., Rüd, K., Eriksen, S., Scheuerer, G. and Schulz, A.:
Experimentelle und theoretische Untersuchung zur Bestimmung von Wärmeübertragungszahlen an gekühlten Gasturbinenschaufeln. FVV-Vorhaben No. 241, Abschlußbericht 1982
- [13] Wittig, S., Rodi, W., Sill, H., Rüd, K., Eriksen, S., Scheuerer, G. and Schulz, A.:
Experimentelle und theoretische Untersuchung zur Bestimmung von Wärmeübergangszahlen an gekühlten Gasturbinenschaufeln. FVV-Vorhaben No. 241, Anhang zum Abschlußbericht, Programmbeschreibung 1982

DISCUSSION**D.L.Schultz, UK**

Did you measure the integral scale of the turbulence behind the turbulence grid?

Author's Reply

In the set-up as shown in Fig.1 we only determined the turbulence intensity. However, as the turbulence grids are identical to those used in a parallel study (S.Eriksen et. al.*) we have a fairly decent knowledge of the turbulence scale. It should be noted that the cross-sectional areas are of equivalent dimensions. In our opinion the turbulence scale is not of dominant influence except in the stagnation region of the blade. The advantage of a continuous tunnel operation in comparison to short-duration facilities, though is the accessibility for detailed turbulence analysis.

*Eriksen, S.; Wittig, S.; Rüd, K.P.

Optical Measurements of the Transport Properties in a Highly Cooled Turbulent Boundary Layer at Low Reynolds Number. Paper presented at 'Turbulent Shear Flow Conference 4', Karlsruhe 1983.

Eriksen, S.; Wittig, S.; Dullenkopf, K.

The Application of LDA and LDF Anemometry to the Study of Boundary Layer Transport Properties under Gas Turbine Conditions. Paper presented at 'Second International Symposium on Applications of Laser Anemometry to Fluid Mechanics', Lisbon, July 1984.

D.L.Schultz, UK

The wake generated by the stationary upstream vane does not correctly simulate the inlet velocity triangle so the wake cutting by the moving rotor is not reproduced.

Author's Reply

You are certainly correct that with the present set-up we are not simulating the wake-cutting. However, we are planning to utilize moving bars of different diameters and spacing to approximate that process. We deliberately designed our experiment as described to separate the various effects, i.e. we were first interested in a relatively isotropic turbulence which was then changed to turbulent flow generated by an airfoil wake which is nonisotropic and the final check will be after superpositioning these two effects on the wake cutting process.

WAKE-PASSING IN A TURBINE ROTOR CASCADE

† D. J. Doorly, M. L. G. Oldfield and * C. T. J. Scrivener

† University of Oxford
Department of Engineering Science
Parks Road
Oxford
OX1 3PJ
U.K.

* Rolls-Royce Ltd.
P.O. Box 31
Derby
DE2 8BJ
U.K.

SUMMARY

This paper describes a technique for generating realistic wakes upstream of a stationary turbine blade cascade at full scale Mach Numbers and Reynolds Numbers. High speed Schlieren photographs showing the development of the wake flow through the cascade are presented, together with unique high speed measurements of the fluctuations of the surface heat transfer rate as the NGV wakes pass over the rotor blade surface. Combining the flow visualisation results with the unsteady heat transfer measurements reveals radically different nature of the boundary layer transition caused by wake passing; an understanding of which will be essential for the development of improved prediction techniques.

INTRODUCTION

The flow around the compressor and turbine blades of an axial flow gas turbine engine is highly unsteady, largely as a consequence of the relative motion of the blades, which are arranged in alternately stationary and rotating rows. The relative motion of the blade rows results in a periodically generated unsteadiness both through purely inviscid means, and through the action of viscosity. Firstly, the inviscid flow around each blade alters cyclically, to take account of the influence of the instantaneous positions of the blades belonging to the upstream and downstream rows on the inlet and exit flowfields. This form of unsteadiness has been studied by [1], [2] and [3], who have shown both that it decays rapidly with increasing axial spacing, and that for a given stage, the magnitude of the unsteadiness due to the interaction is likely to be greater on the upstream blade, than on the downstream blade. Secondly, the boundary layers on the surfaces of the blades in each row separate at the trailing edge, forming wakes, which pass through, and are "chopped" by the blades in the succeeding stage, which is in relative motion. This unsteady flow is referred to here as "wake-passing flow".

Further effects, such as those due to the shock waves generated in transonic blade rows, and the secondary flow near the blade root and tip, produce distortions in the flow at the exit of a given blade row. Unsteadiness is thus produced (in a manner analogous to wake-passing) as the blades of the downstream row pass cyclically through these distortions. Non-periodically generated flow unsteadiness, which may significantly contribute to the total flow unsteadiness, occurs in the flow around the nozzle guide vanes (NGV's) and turbine blades of the first (high pressure) turbine stage, as a result of turbulence and flame instability in the combustion chamber.

In the high pressure turbine rotor blade passages of an aircraft gas turbine, which are the present concern, it is expected that wake-passing and turbulence effects will predominate over the inviscid flow unsteadiness, given the magnitude of the wakes shed by a cooled nozzle guide vane row, the comparatively large axial spacing (of the order of 40% axial chord), and the high flow Mach numbers. The effect due to shock-wave passing, may be totally absent or negligible for shockless exit flows, but will assume progressively increased significance as the NGV exit Mach number is raised. (Conversely, within the vane passages of the NGV row, the unsteadiness is produced solely by combustion chamber turbulence, and the inviscid interaction of the flowfield around the downstream rotor with the NGV flow. In experimental studies with a small turbine stage, the effect of the downstream rotor on the vane heat transfer has been found [4] to be significant.)

Measurements of the effect of high levels of freestream turbulence on the mean heat transfer to turbine blades have been obtained by [5], who used a rotating "squirrel cage" turbulence generator mounted upstream of a turbine rotor cascade. Although this arrangement was too small, and the interference effects thereby too big, to allow the nature of wake-passing with discrete wakes to be simulated, the results indicated that high levels of freestream turbulence could significantly augment the blade heat transfer.

The first detailed studies of the wake-passing flow were performed on compressor blades, by [6], [7] and [8] among others. Turbine blade studies using low speed axial flow turbines have since been performed by [9], and [10]. Unlike compressor blades, where the effects of unsteady flow on the aeromechanical performance is of sole concern, the effects on the heat transfer rate to the blade surface is of equal importance in the case of turbine blades.

In both cases, however, the nature of the unsteady boundary layer which develops in response to the freestream unsteadiness is of fundamental importance in determining the scale of the heat transfer and aerodynamic effects. The work of [6] and [7] indicated that an unsteady transition process resulted from the wakes, although the nature of the transition was not satisfactorily resolved. Likewise [9] and [10] indicated

that again, on a turbine rotor blade, an unsteady transition occurred. Although these tests were very successful, and have greatly contributed to the understanding of the unsteady flow in an engine, comparatively little information on the detailed process of the boundary layer transition caused by the wakes was obtained. This was unavoidable, in view of the limitations on measurement techniques which could successfully be applied to the rotating rig, and the flow complexity.

The extensive work of Pfeil et al. [11] has provided the most detailed measurements on the effects of wake-passing on the transition behaviour of the incompressible flat plate boundary layer. There is, however, a lack of similarly detailed measurements of the action of wake-passing on blades operating at the high Reynolds and Mach number conditions representative of large aircraft engines. Apart from the mechanical complexities involved in obtaining measurements from a high speed, high temperature rotating turbine stage, which has precluded their use for detailed studies of the unsteady rotor blade boundary layer, the fully rotating experiment is not convenient for detailed investigations. As a result, an alternative experimental procedure has been developed at Oxford for the high Reynolds and Mach number study of wake-passing, as described briefly by [12].

DESIGN OF EXPERIMENT

The unsteady wake-passing flow onto the rotor blades of a first stage turbine may be reproduced at the inlet of a stationary cascade of rotor blades mounted in a wind tunnel, Fig. 1. As shown, the correct relative velocity vector diagram of the rotor unsteady flow may be simulated by moving a row of circular cylindrical bars at the correct velocity in front of the cascade. (Cylindrical bars of an appropriate small size may be used to reproduce the NGV wakes, as prior experiments [13] showed that the NGV wake-velocity distribution was practically symmetrical by a distance downstream corresponding to the blade row spacing.)

In this experimental scheme, the ideal rectilinear motion of a ladder of bars past the cascade is approximated over one instrumented blade passage by mounting the bars on the rim of a large diameter rotating disc, (Fig. 2). The mechanical arrangement of the wake-generator, powered by a small air turbine, and mounted in a sealed housing attached to the tunnel sidewall is shown in Fig. 3. This arrangement does not suffer from the disadvantage of upstream interference effects which occur with a squirrel cage type of wake-generator, as employed by [5] and [11]. (A squirrel cage of sufficiently large diameter to minimise upstream interference effects, such as that used by [11] for incompressible studies, is not mechanically practical for high speed cascade work.)

The transient cascade tunnel used for the tests was the Isentropic Light Piston Tunnel (ILPT) at Oxford ([14], [15]). Prior to the run, the tunnel working section was evacuated, and the wake-generator accelerated by a small air turbine to a steady speed. The tunnel was then fired to give a typically 0.4 second steady flow, with a downstream variable area choked throat serving to maintain the cascade exit conditions. During the run, the speed of the wake-generator decayed by up to 20%, however, for the 15 ms interval in which the high frequency (200 kHz sampling rate) heat transfer measurements were made, the inertia of the disc limited the speed decay to less than 1%.

The flow Reynolds number (based on a model blade chord of 67.8 mm, and exit Mach number of 0.96) was 2.0×10^6 ; the freestream total temperature was 430 K for the heat transfer measurements, corresponding to a gas-to-wall temperature ratio for the blade surface (at initially ambient conditions) of 1.5. The surface Mach number distribution for the rotor blade profile used is shown in Fig. 4, from the data of Nicholson [16]. Two sizes of bars (actually stranded steel wires) were fitted to the wake generator, measuring either 0.9 mm or 1.7 mm, with the larger size representing a high loss NGV, and the smaller size modelling a more highly efficient NGV.

For the particular NGV - turbine rotor combination chosen for the experiment, the simulation of wake-passing flow at the design operating conditions of the engine required the bars to be moved at Mach 0.94 relative to the inlet flow; and with 8 bars attached to the wake-generator disc, the mid span radial spacing of the bars was 116 mm, or nearly 2.05 times the pitch of the rotor cascade. To reproduce most nearly the unsteady flow around the turbine blades in the engine, where turbulence from the combustion chamber may be superposed on the basic wake-passing flow, a stationary turbulence grid was, (for some tests), fitted in the flow upstream of the wake-generator.

The primary objective of the experiment was not confined to measuring the unsteady heat transfer rate under flow conditions most nearly approaching those occurring in an engine, on a particular rotor profile. Clearly the fully rotating instrumented stage could (at least in principle), perform this function more exactly. It was instead intended to use the facility to determine both the nature of the unsteady boundary layer on the turbine blade in response to a range of wake-passing regimes, and the consequent implications for the mean and fluctuating heat transfer rate. In order to achieve this, the experimentation was carried out as a progressive series of tests, whereby the effect of the various types of disturbance were first studied in isolation, before multiple disturbances and combinations of different types of unsteadiness were studied.

First in this series, the most basic type of wake-passing flow studied was that produced by running the wake-generator with only two bars fitted (instead of the normal 8) at a slightly reduced speed, and without a turbulence grid fitted. This allowed the action of isolated (widely spaced) wakes of various strength, without associated shock-waves or additional freestream turbulence, to be studied in detail.

In the succeeding experiments, measurements were made in which the complexity of the freestream unsteadiness was increased both by reducing the wake-spacing (fitting the remaining bars to the wake generator), and by raising the freestream turbulence level (by fitting various turbulence grids). Furthermore, the effects of shock waves in isolation, and in combination with the wakes, were studied by running the wake generator at a higher rotational speed, and with first 2, then 8 bars fitted. This paper is concerned only with the studies of shock-less wake-passing flow; the results of the studies of shock-wave passing in isolation, and in addition to wake-passing flow are reported in Dooly and Oldfield[17].

FLOW VISUALISATION STUDIES

The optical arrangement of the spark Schlieren system is shown in Fig. 5. The exposure time is approximately 0.25 μ s for the spark source used. The electronic system designed to fire the Schlieren spark at a desired time in the wake-passing cycle, and the arrangement of the transient recorder data logging system used to record the bar speed and position information are shown in Fig. 5(ii). Both the Schlieren photographs and the heat transfer measurements were referenced in time to the wake-passing cycle by means of a light beam and photo-detector in the wake-generator disc housing. This produced a sharp (5 μ s rise-time) voltage pulse each time the beam was interrupted by a bar, at which instant the corresponding bar at 180° was mid-way on its trajectory through the tunnel working section. This allowed the position of the bar in relation to the blades shown in the Schlieren photographs to be established accurately. Furthermore, by recording this signal simultaneously with the signals from the heat transfer gauges, the motion of the chopped wake (travelling in the external flow around the blade and recorded in the photographs), could be related to the time history of the resulting unsteady heat transfer disturbances.

To allow the leading and trailing boundaries of the chopped wake segments (passing through the rotor cascade) to be clearly distinguished on the photographs, only two bars were fitted to the wake-generator for the Schlieren work. In addition, to remove the undesirable Schlieren effects of the turbulent thermal boundary layers on the windows, the wind tunnel was operated "cold" ($T = 200$ K), but at the design bar speed, and blade Reynolds and Mach numbers.

Extracts from a sequence of Schlieren photographs showing a wake from a 1.7 mm diameter bar passing through the cascade are reproduced in Figs. 6 - 12. The bar relative Mach number (at mid span in the cascade) was 0.94 for these photographs, and the recompression shock wave behind the bar which impinges on the suction surface of the rotor blade (and the reflected wave) are clearly visible in the first photograph. The wake from the bar, visible as a band of highly turbulent flow, is swept into the rotor passage at a later time, and undergoes massive distortion as a result of the high acceleration in the passage (Figs. 6 - 12).

STRIPED AIR FLOW CALCULATION

To relate the imposed freestream unsteadiness (wake-passing), to the resultant unsteady boundary layer, an accurate knowledge of the wake position on the surfaces of the blade at any given instant, together with the boundary layer state at all points along the surfaces is required. The position of the wake is particularly important, as the flat plate studies of [11] suggest that the turbulence content of the wake has a very significant effect on the transition behaviour of the boundary layer.

A simple technique to estimate the position of the wake was used for the rotor cascade under investigation. The primary objective was to allow the wake-position between the instants when the Schlieren photographs were taken to be estimated, and secondly to test the accuracy of such a naive approach, by comparison with the Schlieren which provided a record of the actual wake behaviour.

The approach consists of representing the wake as a "stripe" of finite width (equal to the mean physical wake width), but of infinitesimal strength, in the freestream. The convection of this model wake was calculated by using the results of a numerical steady flow passage velocity solution to compute the position of the lines corresponding to the leading and trailing edges of the wake stripe at successive times. The steady flow passage velocities were calculated for this rotor cascade by [16], who used a time-marching algorithm due to [18].

The position of a line leaving a wake-generating bar at the relative flow angle thus computed for increasing time intervals is shown in Fig. 13 and a comparison of the predicted wake at a given instant using this method, and the corresponding Schlieren photograph is shown in Fig. 14. This simple technique gave quite good agreement for the rotor cascade, demonstrating that the wake distortion is governed mostly by the high freestream acceleration. More sophisticated techniques (requiring substantial computer time) have been developed, such as that developed by [19].

HEAT TRANSFER INSTRUMENTATION AND TECHNIQUE

The technique for the measurement of the surface heat transfer rate using thin film surface thermometers and electronic analog circuitry is outlined by [20], and the references noted therein, whilst the 100 kHz bandwidth heat transfer instrumentation developed for this work is described by [21]. Details of the minicomputer based data acquisition system for low speed (2 kHz) measurements may be found in [22]. For the high speed measurements, a Datalab 2800 transient recorder was used to acquire 4096

simultaneously sampled data points from each of up to 8 channels. By using the pre-triggering mode of operation, 1096 samples were recorded on each channel at a slow sampling rate (2 kHz), from a time just before the run, and extending about 0.2 seconds after the run start, by which time the flow was well established. A burst of 3000 samples was then recorded on each channel at a fast sampling rate of 200 kHz. Details of the data reduction and processing procedures applied to the unsteady heat transfer data are contained in [13].

Gauge Locations

The locations of the thin film gauges on the suction and pressure surfaces of the model blades are shown in Fig. 4. Only the gauges on the first 50% surface length along the suction surface are marked, as the remainder were damaged prior to testing. As the results presented later will indicate, however, the most significant effects produced by wake-passing occur on the early portion of the blade. Furthermore, beyond 50% surface length, unsteady movements of the passage shock might be expected to exert a complicating influence.

MEAN HEAT TRANSFER RATE MEASUREMENTS AND PREDICTIONS

The measurements of the mean heat transfer rate to the rotor profile suction and pressure surfaces for conditions of "low" ($< 0.4\% Tu$) and "high" ($4.5\% Tu$) are shown in Fig. 15, along with the predicted distributions. Considering first the heat transfer rate to the suction surface:

(i) In an undisturbed, low ($< 0.4\%$ intensity) turbulence freestream, the steadily decreasing heat transfer rate from the leading edge strongly suggests that the boundary layer remains laminar to beyond 50% surface length ($X/S = 0.5$). Furthermore, the results of [16], who also measured the mean heat transfer rate to this profile (though at a smaller scale) in the course of his work, show near identical mean heat transfer rate levels with a low turbulence freestream. Beyond 50% X/S , Nicholson's measurements indicate that the passage shock, or shock waves (Figs. 6 - 12) cause a full transition of the boundary layer to turbulence. The predicted values are in good agreement along the first 50% length, though they do not allow for the effects of the passage shock on the late transition.

(ii) With a turbulence grid fitted, (for approx. $4.5\% Tu$ intensity), both the measurements and the predictions show that the very early and complete (by $X/S = 0.2$) transition leads to a dramatic increase in the mean heat transfer rate.

Considering next the effects on the pressure surface:

(i) With an undisturbed low turbulence freestream, the sudden dip to a very low heat transfer level immediately around from the leading edge at an X/S of 0.04 is due to a separation bubble, as had been found by [17], and was confirmed by the character of the fluctuating signals from the film gauges. From the reattachment point, up to an X/S of 0.6, the heat transfer rate is observed to remain substantially constant, although the nature of the boundary layer on this portion of the blade has not been definitively established. Beyond an X/S of 0.6, however, the results indicate that the boundary layer is turbulent, and remains so to the trailing edge.

(ii) The effect of freestream turbulence (with the grid fitted), is principally to augment the heat transfer rate between an X/S of 0.05 and 0.6, where the boundary layer is probably transitional in the undisturbed state. After this point, however, where the undisturbed boundary layer is turbulent, the effects on the heat transfer are slight.

UNSTEADY HEAT TRANSFER RESULTS

1. Effects of Freestream Turbulence Alone

The high frequency heat transfer instrumentation was first used to measure the fluctuating heat transfer signals under "steady" freestream conditions, comprising varying levels of grid-produced turbulence. The results were of considerable interest, both for indicating the magnitude and frequency of the fluctuating surface heat transfer produced by a turbulent, and by a transitional boundary layer, and for fundamental reasons. Of fundamental interest, comparison of the signals obtained under "steady" (i.e. a homogeneously turbulent freestream), and an unsteady freestream (dominated by wake-passing), revealed considerable information on the nature of the transition of the blade boundary layer, caused by wake-passing. As the effects produced by wake-passing on the suction surface of the blade were the most dramatic, the discussion of the unsteady results is confined to this surface.

The first tests considered compared the fluctuating heat transfer records from the suction surface gauges with

A: no turbulence grid fitted ($Tu < 0.4\%$)

B: a grid designed to produce 2% turbulence intensity placed in the flow upstream of the cascade.

The low degree of fluctuation evident in the heat transfer signals for case "A", coupled with the decrease in the mean heat transfer level, are characteristic of a laminar

boundary layer. This develops from the leading edge, and has evidently still not begun transition at the location of the last gauge recorded (gauge 11, $X/S = .48$).

On trace "B", (i.e. with 2% freestream Tu), small disturbances are first discernible as increases of the heat transfer level at gauge 4, and are rapidly amplified by gauge 6. At all gauges, from 4 to 9, the heat transfer rate between upward disturbances corresponds to that associated with an undisturbed laminar boundary layer. By gauge 11, the signal is considerably calmer, and displays only occasional dips to an intermediate value.

The character of traces "B" is strongly indicative of a gradual transition of the laminar boundary layer, beginning at an X/S value of approximately 0.1 (gauge 4), and finishing near an X/S value of 0.5 (gauge 11). The upward pulses in heat transfer, first appearing on gauges 4 to 6, indicate the stochastic formation of turbulent spots. Furthermore, FFT-based cross correlation techniques applied to the fluctuating signals reveals a mean convection rate of about 0.65 times the local freestream speed for the heat transfer disturbances. This value is roughly equivalent to the mean propagation velocity of a turbulent spot in the flat plate boundary layer [23].

In considering the fluctuating heat transfer traces, it is worth noting that the film gauges are effectively span-wise averaging; although they are only 0.5 to at most 1 mm wide in the streamwise direction, they extend over approximately the centre 10 mm of blade span. As the process of natural transition involves the formation and spreading of three dimensional spots, it is clear that the instantaneous level of heat transfer rate measured at any gauge location in the transition zone depends on the percentage of the gauge which is covered by turbulent spots.

Comparing next the effects of high (4.5%) and low (<0.4%) turbulence intensity, Fig. 17, it is immediately evident that the high level of turbulence results in a much more rapid completion of transition (by $X/S 0.2$), than was observed with only 2% turbulence.

2. The Effects of Isolated Wakes on an (Otherwise) Laminar Boundary Layer

With only 2 bars fitted to the wake-generator, the spacing between successive disturbance cycles may be increased to four times the approximate engine scaled spacing. (Thus the boundary layer is allowed to relax fully between each cycle.) In Fig. 18, a comparison is made between the effects of isolated wakes (without superposed grid turbulence), and the effect of a high, and very low level respectively of freestream turbulence acting alone (from Fig. 17). (For these tests the wake generator was run at a reduced speed, so that there is no complicating effect due to a noticeable shock wave from the bar.)

The traces clearly indicate that the effect of each passing wake is to induce a rapid and complete transition of an otherwise laminar boundary layer to a temporarily fully turbulent state. It may be observed that the temporary high heat transfer level is very close to that which could have been generated by inducing transition at a similarly early location, by some other means, such as high level of freestream turbulence. (This has been further confirmed by comparing the heat transfer signals on a laminar and an artificially tripped boundary layer, [17].)

The almost "square wave" shape of the transient heat transfer disturbance caused by each wake, which indicates that a full transition occurs, is in marked contrast to the traces obtained where "natural" transition is occurring. In the latter case, the instantaneous level depends on the fraction of the gauge covered by turbulent spots; whereas with wake-passing, the form of the signals suggests that fully turbulent patches are generated across the entire blade span by each succeeding wake.

3. The Effects of Isolated Wakes on a Transitional Boundary Layer

The effects of wake-passing on a transitional (suction surface) boundary layer are illustrated by the sample traces in Fig. 19. By placing a turbulence grid in the flow well upstream of the cascade, to generate 2% intensity at the cascade inlet, it was found (referring to Fig. 16) that a gradual transition may be induced on the suction surface. The transition process which results from the combination of isolated wake-passing and moderate freestream turbulence is not significantly different than would have been anticipated from a consideration of Figs. 16 and 18. In particular, there is no evidence that the so-called "becalmed regions" (temporary regions of enforced laminarity which occur after the passage of a turbulent spot in the flat plate boundary layer), and which were observed in Pfeil's [11] study of wake-passing on a flat plate, exist. Examination of the unsteady heat transfer records did not show each temporary turbulent patch produced by a wake to be followed by a short interval of laminar flow. A consideration of the proposed spot calming behaviour, however, indicates that in cases where the blade transition begins so close to the leading edge, as in this test profile, the effect (even if it may, in fact, occur on a blade) is precluded from playing a significant role.

4. The Effects of Closely Spaced Wakes on Transitional and Turbulent Boundary Layers

The effects of closely spaced wakes on an otherwise laminar suction surface blade boundary layer are shown in Fig. 20A. The basic process, whereby each passing wake causes a turbulent patch to form, which is then convected downstream, is similar to that which occurred with isolated wakes. With closely spaced wakes, however, the successive turbulent patches eventually merge to form a continuously turbulent boundary layer. The patches are just beginning to merge by gauge 11 in Fig. 20A. In tests with a large (1.7 mm) diameter bar fitted, [13],[17], the broader patches, produced by the wider wake

shed by the larger bar, were in fact observed to have fully merged by this point ($X/S = 0.5$).

A reasonably high level of homogeneous freestream turbulence has been shown (Fig. 17) by itself to be sufficient to cause an early transition of the boundary layer on the suction surface of the test blade. The most dramatic heat transfer effects of the wakes, which are due to the characteristic forced transition, are absent in the case of combined wake-passing and high freestream turbulence (Fig. 20B). The heat transfer effects of wakes on a turbulent boundary layer were thus found to be much less than on a laminar boundary layer. This was further supported by artificially tripping the boundary layer [17]. The only effect of adding wakes to the basic turbulent flow is to increase the level of fluctuation of the heat transfer signal somewhat, as the mean level is almost everywhere close to that caused by high turbulence alone. It is tempting to conclude that in each of these cases the type of (turbulent) boundary layer is virtually identical, and is not significantly modified by the unsteady wake passing flow. Further detailed studies are clearly needed to examine this aspect of the effects of wake-passing.

BOUNDARY LAYER TIME HISTORY

Typical variation in the boundary layer response to the passing of individual isolated wakes at an $X/S = 0.5$ is shown in Fig. 21. It is interesting to note that the forward transition from the laminar to the turbulent level may vary by up to 100 μ s, whereas relaxation back to the laminar state occurs with a variation of not more than 20 μ s. As the boundary of the wake is not a smooth curve, but consists of an irregular, wavy interface there will effectively be a small uncertainty in time between the arrival of the leading edge, and departure of the trailing edge of each individual wake past a given location of the blade. This may be expressed as a time uncertainty, which a very crude estimate suggests to be of the order of 10 μ s for the case considered. This is nearly sufficient to account for the variation in the relaxation back to the laminar level of the individual wakes, but does not account for the variation in the forward transition.

A simple comparison between the rate of progression of the wake (travelling in the freestream), and the boundary layer disturbance which it produces, reveals much about the transition process responsible for the fluctuating heat transfer rate. By defining the time at which the leading edge of a wake-induced turbulent patch reaches a given gauge location on the blade, as the instant when the heat transfer rate rises to 50% of the maximum level attained, and conversely for the patch trailing edge, it is possible to chart the progress of the turbulent patches along the blade surface. The Schlieren photographs, supplemented by the simple prediction scheme record the progress of the wake, and the comparison is made in Fig. 22.

The trajectories of points travelling along the blade surface at the freestream velocity, and at half the freestream velocity respectively, calculated from the predicted surface velocity distribution are also shown. It is strikingly clear that the trailing edge of the wake-induced disturbance propagates at very nearly half the freestream velocity, which corresponds to the trailing edge velocity of a turbulent spot in the flat plate boundary layer [23]. There is a noticeable delay between the arrival of the wake at a given point on the blade surface, and the instant when transition begins at that point. Also remarkable is the fact that, unlike relaminarisation, the forward transition to turbulence does not appear to propagate at a uniform rate along the blade. Instead it would appear that the transition is accomplished slightly earlier at an X/S of 0.5, than at an X/S of 0.35. The process of forward transition at a given point is a more formidable problem than relaminarisation, since in the former case the stability problem involves a potential contest between simultaneously evolving freestream and boundary layer disturbances interacting with the entire boundary layer, whereas in the latter case, only the decay of boundary layer disturbances remaining after the passing wake are of concern.

MEAN HEAT TRANSFER RESULTS

The mean heat transfer rate to the rotor profile suction surface is shown in Fig. 23, and to the pressure surface in Fig. 24. Considering the suction surface first:

The steadily decreasing heat transfer associated with a laminar boundary layer, and the nearly constant, high level associated with a turbulent boundary layer caused by the grid turbulence have been already discussed.

With the wake-generator run (and the small bars fitted), but without combined high freestream turbulence, the mean heat transfer rate level is observed to lie between that associated with a laminar (low Tu freestream) boundary layer, and that associated with a boundary layer which undergoes an early, full transition (high Tu freestream). The unsteady heat transfer traces (Fig. 20A) revealed that wake-passing causes an unsteady transition on this portion of the blade surface, with the boundary layer periodically alternating between the fully turbulent and laminar states. The mean heat transfer at each point in this region thus depends on the proportions of each cycle which are spent in the laminar and fully turbulent states respectively.

With a background level of 4 - 5% turbulence (produced by a grid) superposed on the unsteady flow, the mean heat transfer rate to the majority of the instrumented portion of this surface is practically identical to that resulting with grid turbulence alone.

Considering next the effects on the pressure surface:

Between an X/S of 0.2 and 0.6, where it is thought that the boundary layer may still be transitional, the superposition of wake-passing with high freestream turbulence noticeably increases the mean heat transfer level above that associated with an undisturbed freestream. After this point, where even the undisturbed boundary layer is fully turbulent, there does not appear to be any increase in mean heat transfer level with increased freestream unsteadiness.

These results reinforce the conclusion that the most dramatic effects of wake-passing on the mean heat transfer rate occur where wake-passing causes an otherwise laminar boundary layer to undergo an unsteady transition. Where the boundary layer is already turbulent the effects on the mean level are much less significant, although there may still remain increased heat transfer fluctuations.

CONCLUSIONS

A facility has been developed which enables studies to be made of the effects of wake-passing on a model turbine blade mounted in a stationary cascade. The simulation technique allows detailed measurements of heat transfer (or pressure), and high quality Schlieren flow visualisation to be obtained at conditions representing full scale engine Reynolds and Mach numbers. In addition, the flexibility of the technique has enabled the effects of wakes of varying strength and spacing, shock-waves (not reported here), and freestream turbulence to be studied both in isolation, and in multiple combinations.

The spark Schlieren photographs which were obtained showed in considerable detail the distortion of the wakes in the rotor blade passages. The relative success of the simple wake prediction technique used indicated that much of the behaviour of the wake segments is dominated by the very high accelerations which occur in first stage modern turbines.

The results of the high frequency heat transfer measurements, indicated that the primary effect of wake-passing on an otherwise laminar blade boundary layer is to promote an early, unsteady, transition. This unsteady transition may significantly affect the blade performance, both by greatly increasing the mean level, and by causing severe periodic fluctuations in the heat transfer rate. Analysis of the convection and spreading of the turbulent boundary layer patches produced by each passing wake has shown that there is a marked delay between the time at which the wake segment, travelling in the freestream, has cleared a given point on the surface, and the instant when the boundary layer reverts to the laminar state. This delay, which is caused by the slow rate at which events propagate in the boundary layer, further increases the mean heat transfer level, and leads to an earlier completion of transition.

For the purpose of estimating the mean heat transfer rate in the transition region, the regular "square wave" form of the fluctuating heat transfer caused by the switching of the boundary layer state suggests the use of an intermittency function. Suitable intermittency functions can only, however, be satisfactorily calculated with reference to the evolution of the turbulent patches, as shown in the X-T diagram of Fig. 22.

The effects of wake-passing on the heat transfer rate to an already transitional boundary layer (as occurs naturally on much of the pressure surface of the test profile, or as could be induced on the suction surface), were found to be somewhat less. The mean heat transfer rate is nevertheless raised, as each passing wake generates a fully turbulent patch, thus increasing the mean level.

Where a fully turbulent boundary layer occurs either naturally, or is forced by the addition of freestream turbulence, the effects of wake-passing on the heat transfer rate were found to be very much reduced for the test profile considered. Although the mean level was not noticeably affected by the addition of wake-passing to the basic flow, there was, however, a noticeable increase in the fluctuation level.

REFERENCES

1. Kemp, N. H. and Sears, W. R., "Aerodynamic Interference between Moving Blade Rows", *J. Aero. Sci.*, Vol. 20, No. 9, Sept. 1953, pp. 585 - 597.
2. Lefcourt, M. D., "An Investigation into Unsteady Blade Forces in Turbomachines", *A.S.M.E., Journal Eng. Power*, Oct. 1965, pp. 345 - 354.
3. Parker, R. and Watson, T. F., "Interaction Effects between Blade Rows in Turbomachines", *Proc. I. Mech. Eng.*, Vol. 186, No. 21, 1972.
4. Dunn, M. G., "Turbine Heat Flux Measurements: Influence of Slot Injection on Vane Trailing Edge Heat Transfer, and Influence of Rotor on Vane Heat Transfer" *ASME 84GT175*
5. Bayley, F. J. and Priddy, W. J., "Effects of Free-Stream Turbulence Intensity and Frequency on Heat Transfer to Turbine Blading", *A.S.M.E., Paper No. 80-GT-79* (New Orleans 1980)
6. Evans, R. L., "Boundary Layer Transition and Separation on a Compressor Rotor Airfoil", *A.S.M.E., Jnl. of Eng. Power*, Vol. 104, Jan. 1982, pp. 251 - 253.
7. Walker, G. J., "The Unsteady Nature of Boundary Layer Transition on an Axial-Flow Compressor Blade", *A.S.M.E. Paper No. 74-GT-135*, Zurich, 1974.

3. Kerrebrock, J. L. and Mikolajczak, A. A., "Influence of Unsteadiness of the Flow on Efficiency of Turbine Stages", *Teploenergetika*, Vol. 17, No. 10, 1970, pp. 21 - 23.
9. Dring, R. P., Joslyn, H. D., Hardin, L. W. and Wagner, J. H., "Turbine Rotor-Stator Interaction", A.S.M.E., Paper No. 82-GT-3.
10. Hodson, H. P., "Boundary Layer and Loss Measurements on the Rotor of an Axial Flow Turbine", A.S.M.E. Paper No. 83-GT-4, Phoenix, Arizona, March, 1983.
11. Pfeil, H., Herbst, R. and Schroeder, T., "Investigation of the Laminar-Turbulent Transition of Boundary Layers Disturbed by Wakes", A.S.M.E. Paper No. 82-GT-124.
12. Doorly, D. J. and Oldfield, M. L. G., "Simulation of Wake-Passing in a Stationary Turbine Rotor Cascade", paper submitted to the A.I.A.A. J.P.P.
13. Doorly, D. J., D.Phil. Thesis, Oxford University, 1983.
14. Jones, T. V., Schultz, D. L. and Hendley, A., "On the Flow in an Isentropic Light Piston Tunnel", ARC, R and M, 3731; 1973.
15. Jones, T. V., Schultz, D. L., Oldfield, M. L. G. and Daniels, L. C., "A New Transient Facility for the Measurement of Heat Transfer Rates", A.G.A.R.D., CP-229, "High Temperature Problems in Gas Turbine Engines", Ankara, 1979.
16. Nicholson, J. H., D.Phil. Thesis, 1981, Oxford University.
17. Doorly, D. J. and Oldfield, M. L. G., "Simulation of the Effects of Shock Wave Passing on a Turbine Rotor Blade", to be presented at ASME Gas Turbine Conference, Houston, March, 1985.
18. Denton, J. D., (1975), A Timemarching Method for Two and Three Dimensional Blade to Blade Flows, ARC R and M 3775.
19. Hodson, H. P., D.Phil. Thesis, Cambridge University, 1983.
20. Schultz, D. L. and Jones, T. V., "Heat Transfer Measurements in Short Duration Hypersonic Facilities", A.G.A.R.D., AG-165, 1973.
21. Oldfield, M. L. G., Burd, H. J. and Noe, N. G., "Design of Wide-Bandwidth Analogue Circuits for Heat Transfer Instrumentation in Transient Tunnels", Proc. 14th ICHMT Symposium on Heat and Mass Transfer in Rotating Machinery, Dubrovnik, August, 1982.
22. Oldfield, M. L. G., Jones, T. V. and Schultz, D. L., "On-Line Computer for Transient Turbine Cascade Instrumentation", I.E.E.E. Transactions on Aerospace and Electronic Systems, Vol. AES-14, No. 5, pp. 738-749, Sept. 1978.
23. Wygnanski, I., Sokolov, M. and Friedman, D., "On a Turbulent Spot in a Laminar Boundary Layer", J.F.M., Vol. 78, Part 4, 1976, pp. 785 - 819.

ACKNOWLEDGEMENT

The authors are grateful to the SERC and to Rolls-Royce Ltd. for their support of this work.

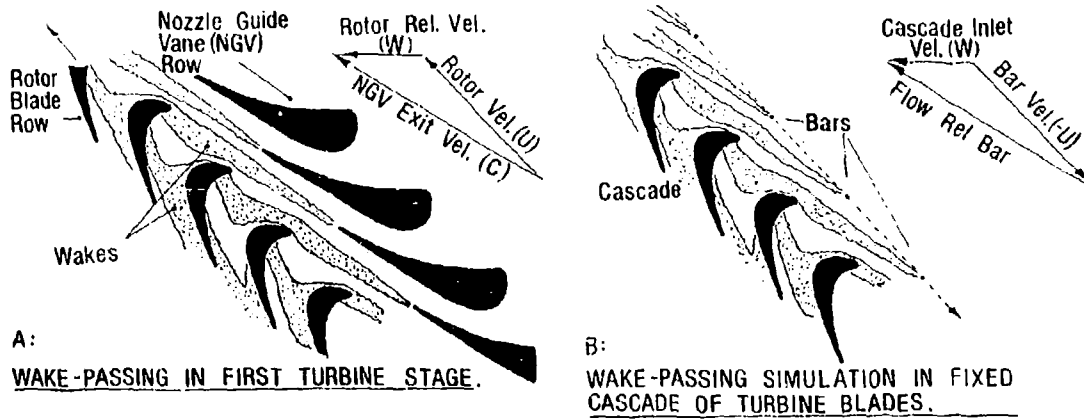


Fig. 1

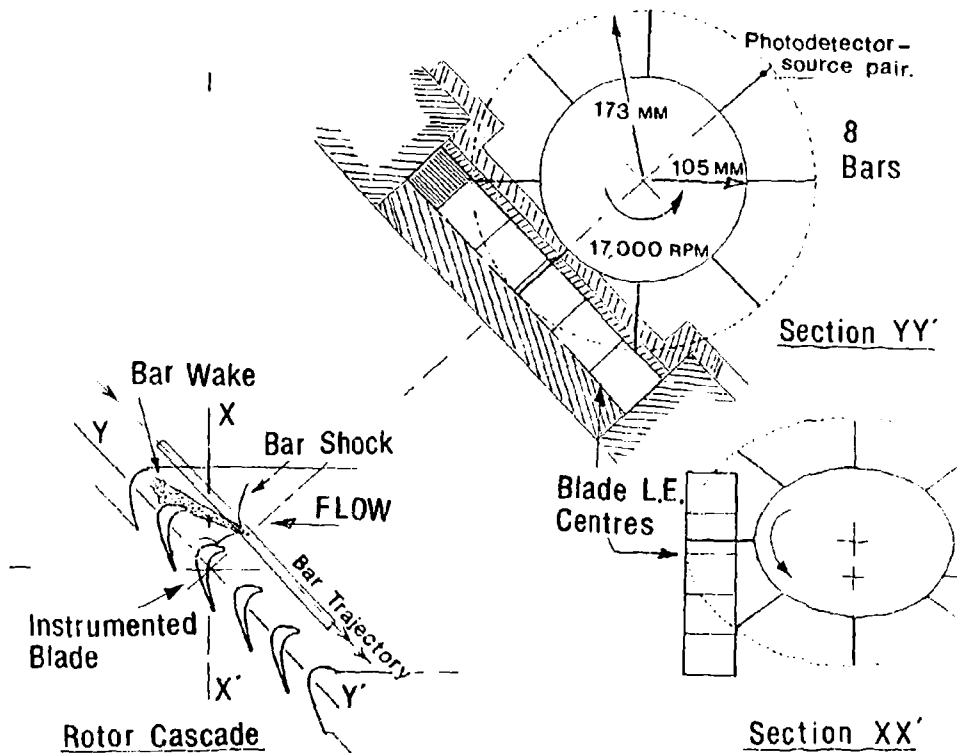


Fig. 2

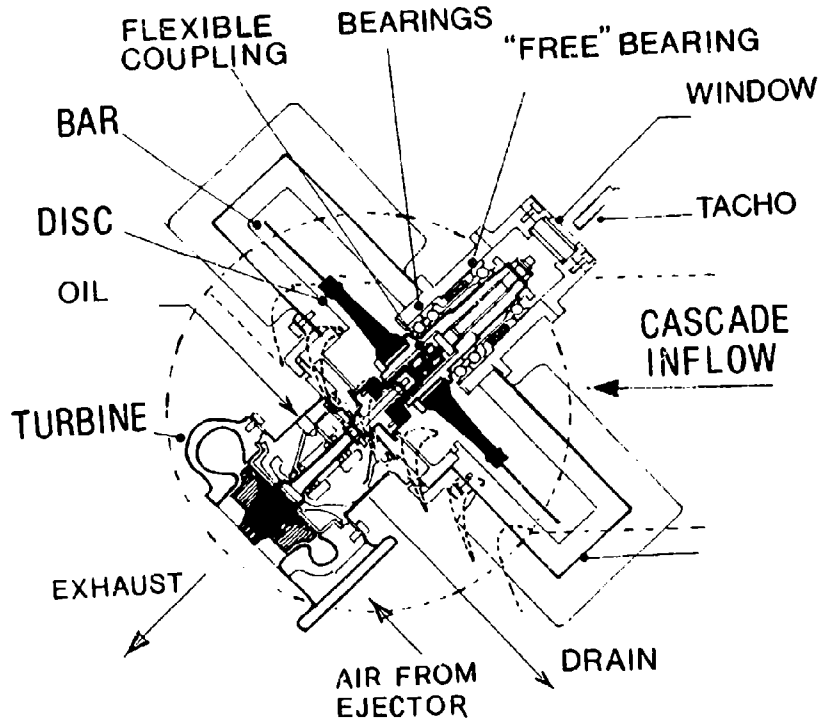


Fig. 3

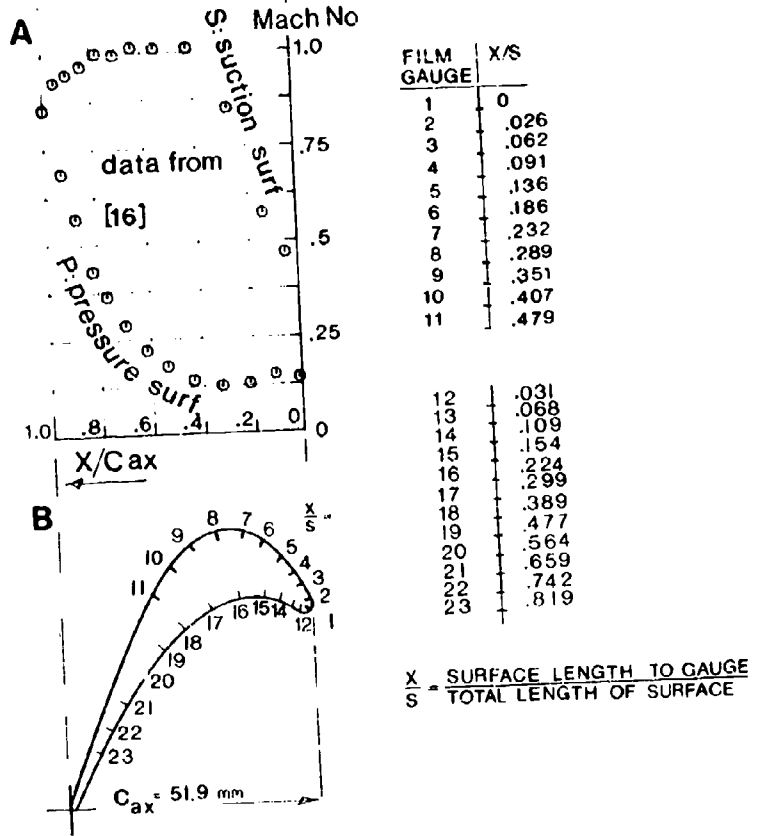


Fig. 4

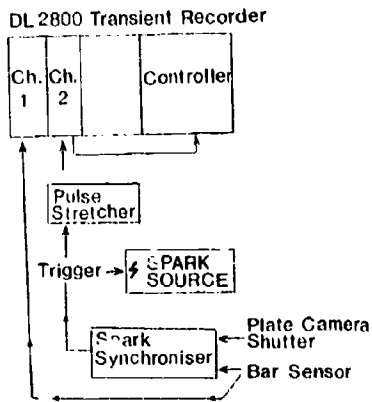


Fig 5-ii

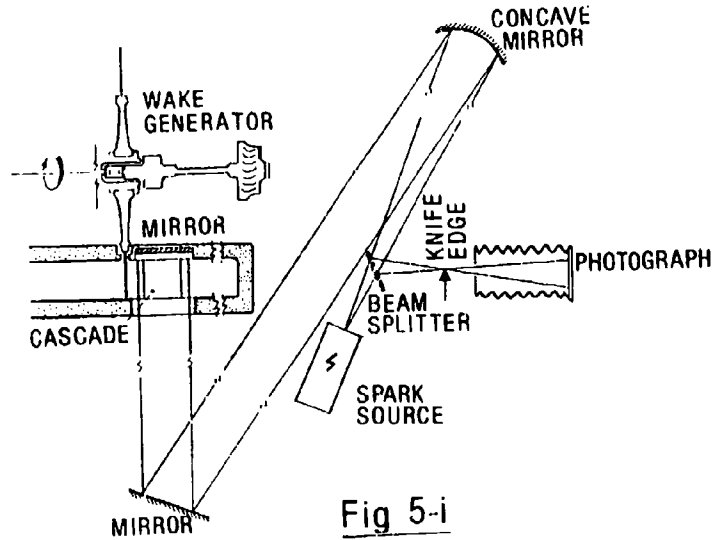


Fig 5-i

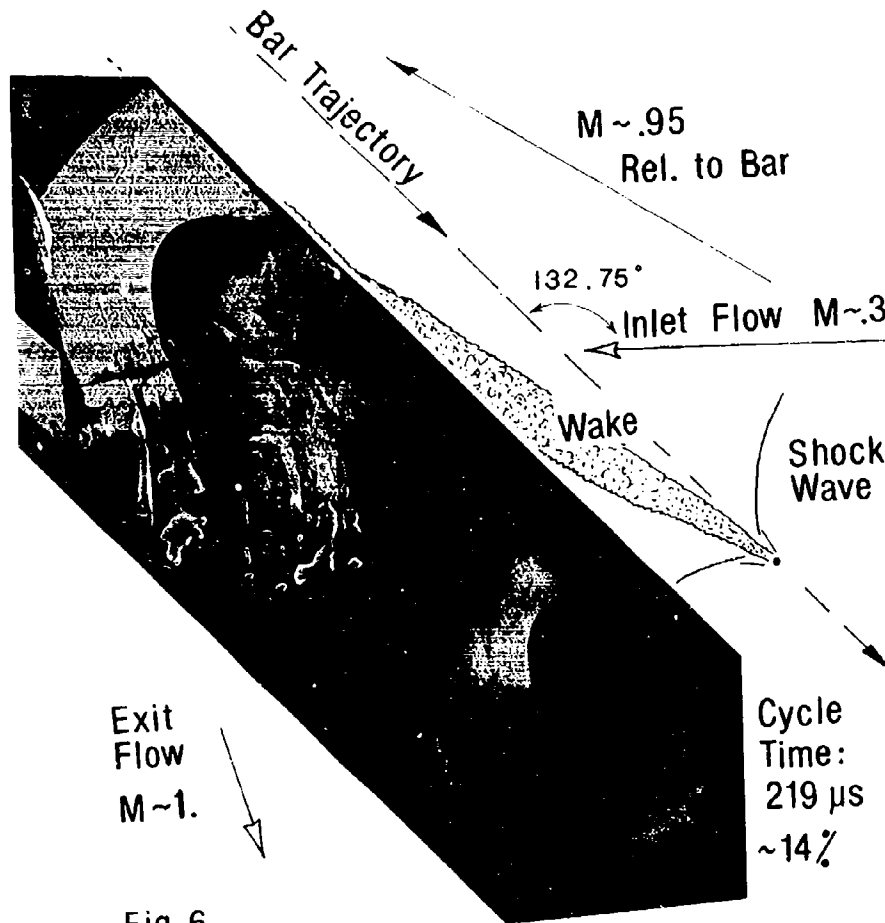
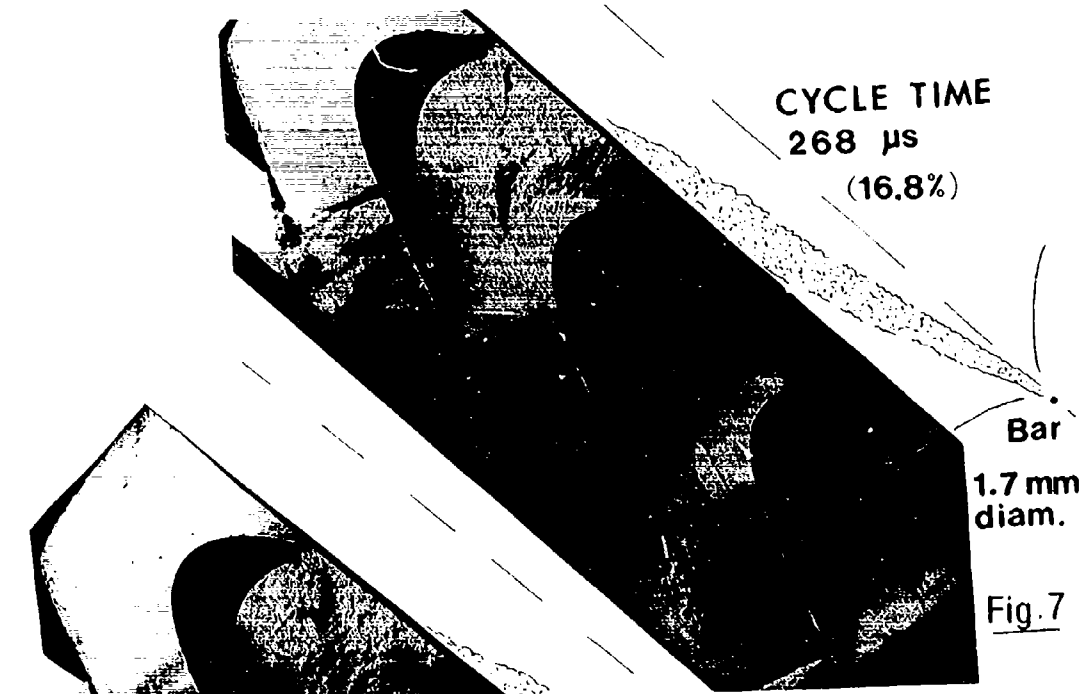


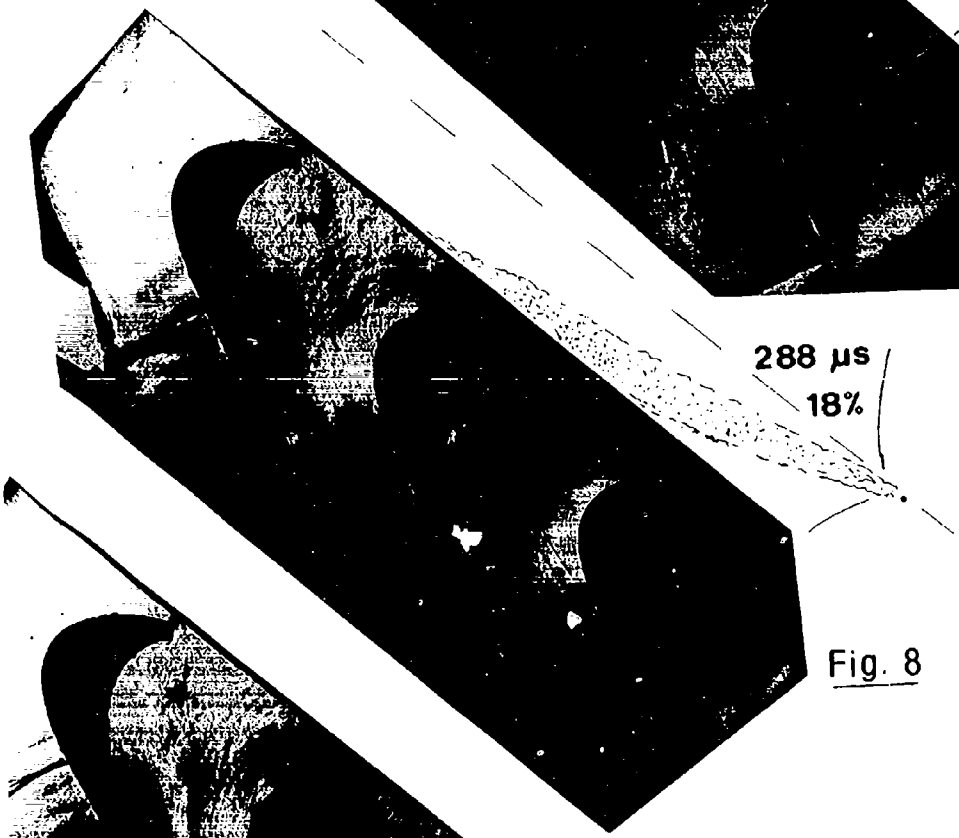
Fig. 6



CYCLE TIME
268 μ s
(16.8%)

Bar
1.7 mm
diam.

Fig. 7



288 μ s
18%

Fig. 8



355 μ s
22.2%

Fig. 9

812 μ s
51%

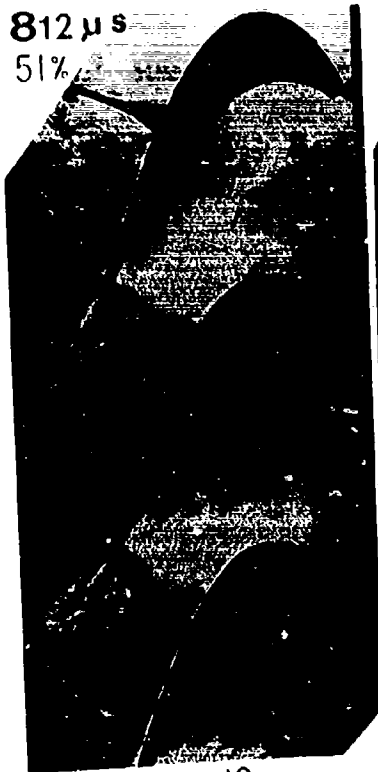


Fig. 12

511 μ s
32%



Fig. 11

392 μ s
24%



Fig. 10

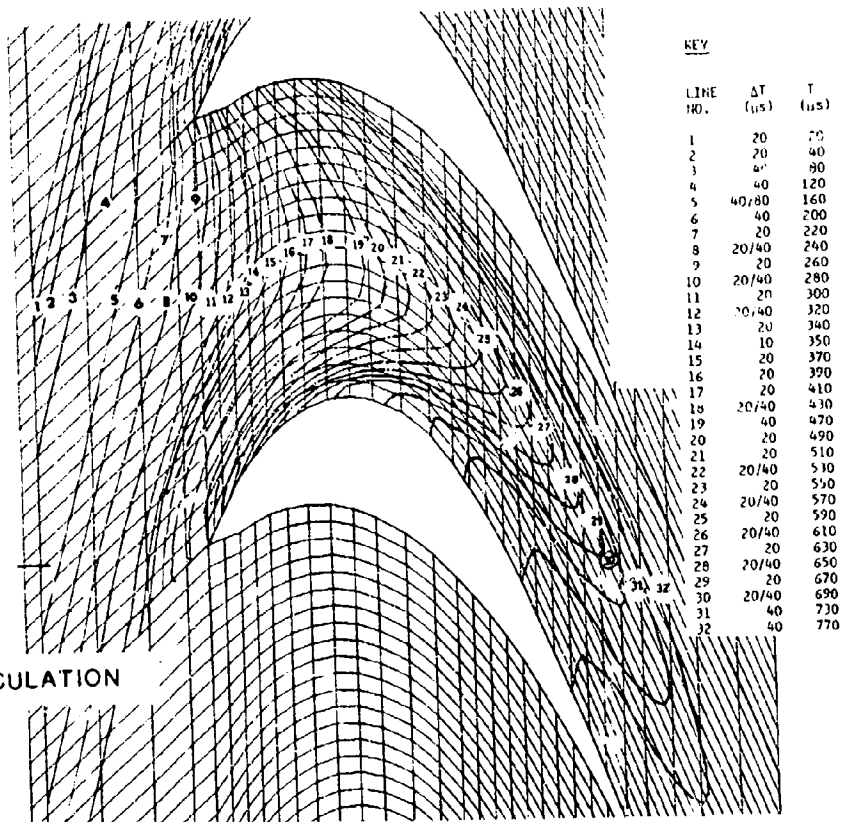
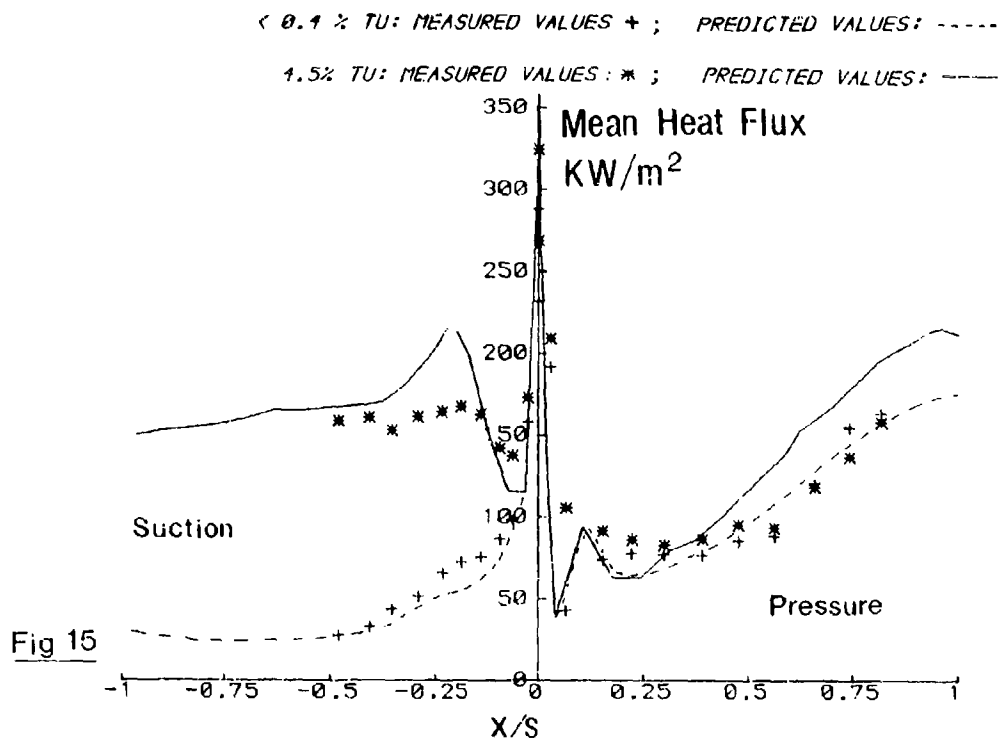
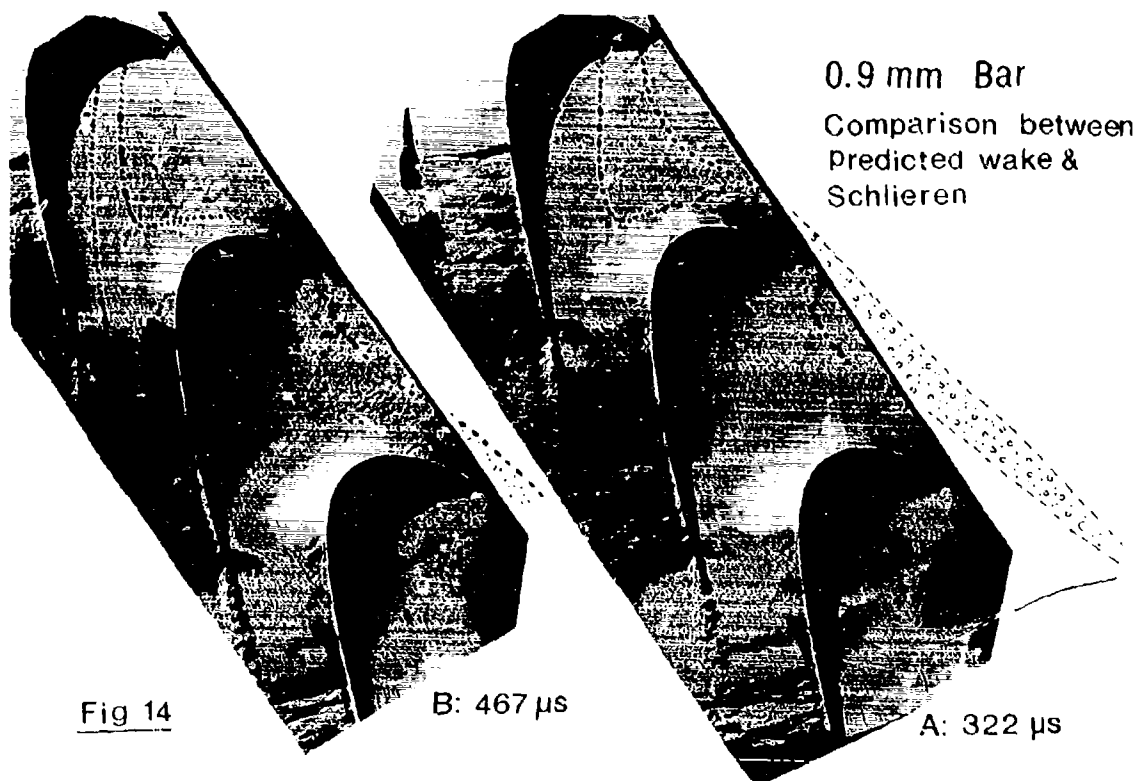


Fig. 13
STRIPED AIR CALCULATION



FLUCTUATING HEAT TRANSFER SIGNALS

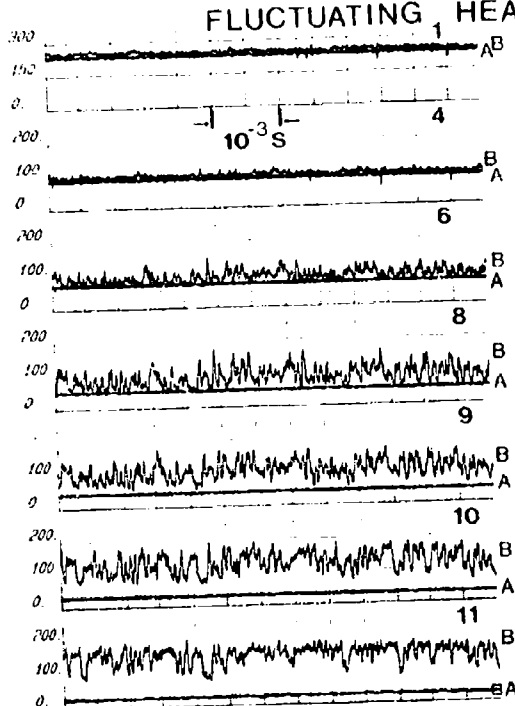


Fig. 16

A: $Tu < 0.4\%$, Laminar at all gauges
 B: $Tu = 2.0\%$, Gradual transition

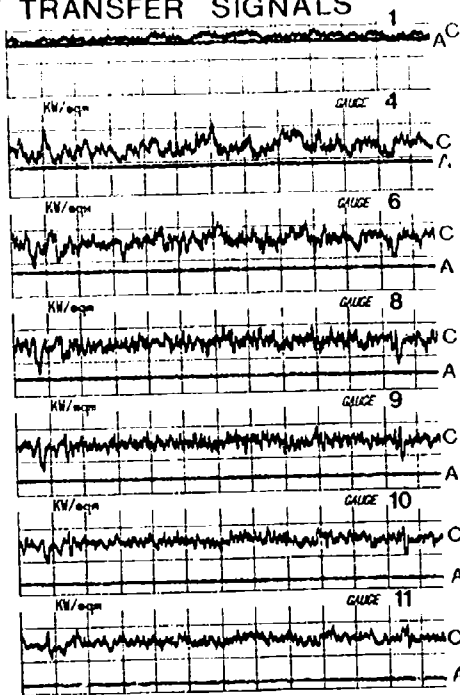


Fig. 17

A: $Tu < 0.4\%$, Laminar at all gauges
 C: $Tu = 4.5\%$, Rapid transition.

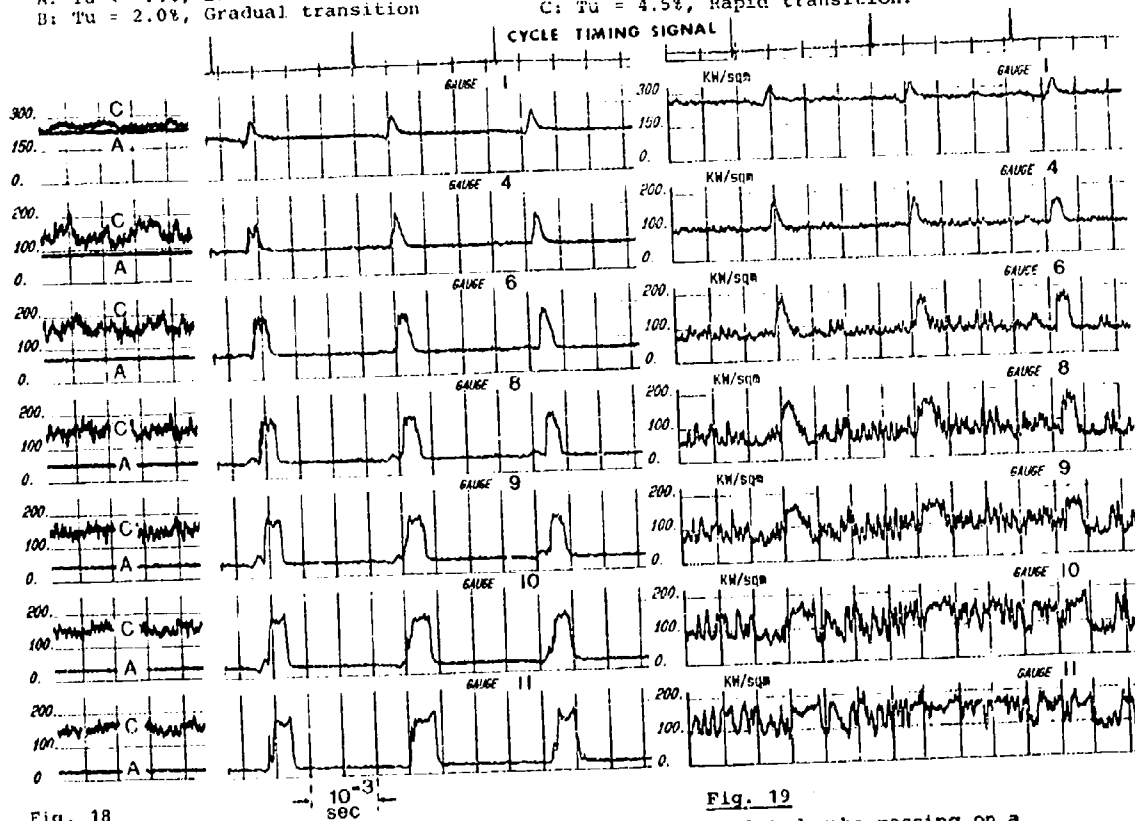


Fig. 18

Comparison between effects of freestream turbulence, (A: $Tu < 0.4\%$, C: $Tu = 4.5\%$), and isolated wake-passing alone. (2 bars, 0.9mm diam., Bar relative Mach no. = 0.75).

Fig. 19

Isolated wake-passing on a transitional boundary layer. (0.9mm bars, no shock-effects)

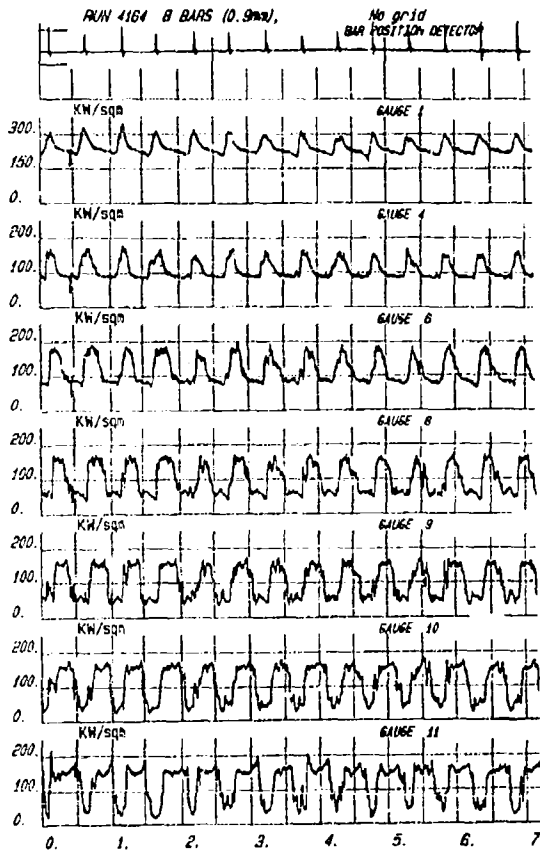


Fig. 20A

Closely spaced wake-passing alone.
 (Bar Mach no. 0.75, 0.9mm bars)
 Unsteady transition to beyond gauge 11.

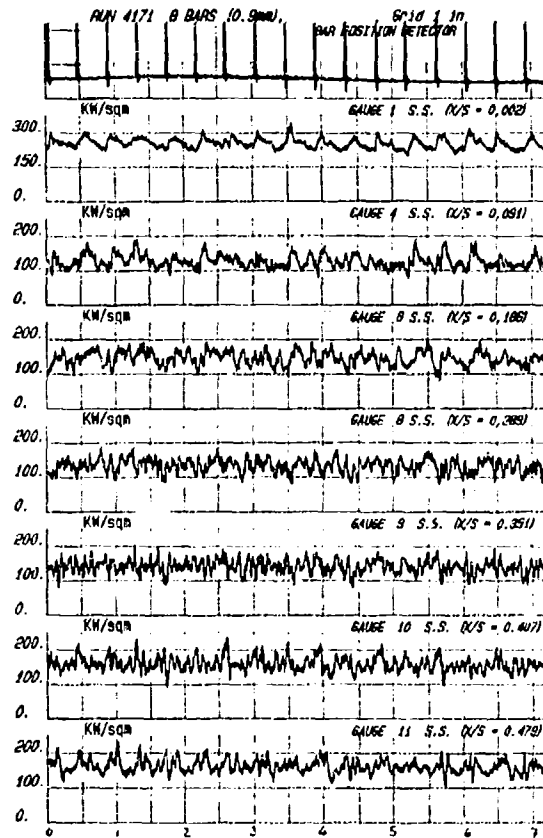


Fig. 20B

Combined freestream turbulence
 ($Tu = 4.5\%$) and closely spaced
 wake-passing.
 Transition complete by $X/S = 0.1$

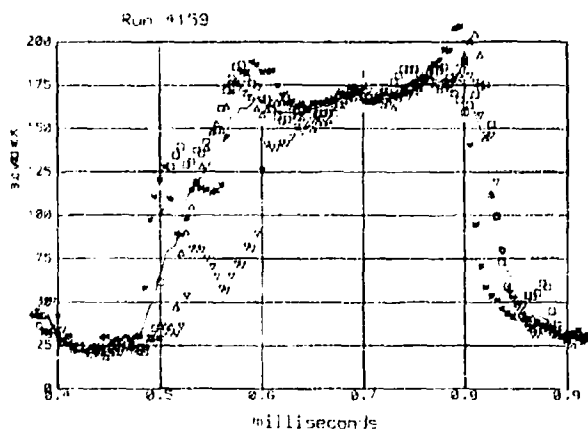
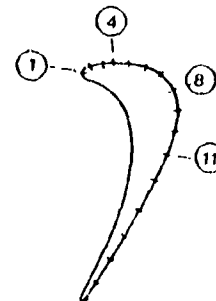


Fig. 21

Unsteady heat transfer rate traces from gauge 11
 on the suction surface, illustrating the variation
 in the boundary layer response to isolated wakes.

There is up to 100 μs variation in the time at which
 the forward transition is accomplished, but only 20 μs
 variation in the time for relaminarisation.

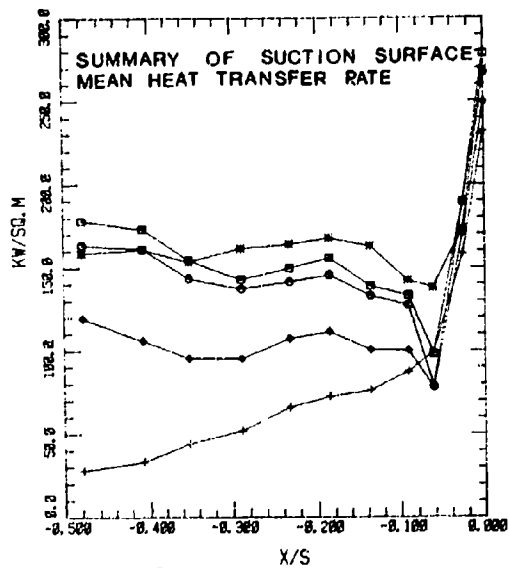
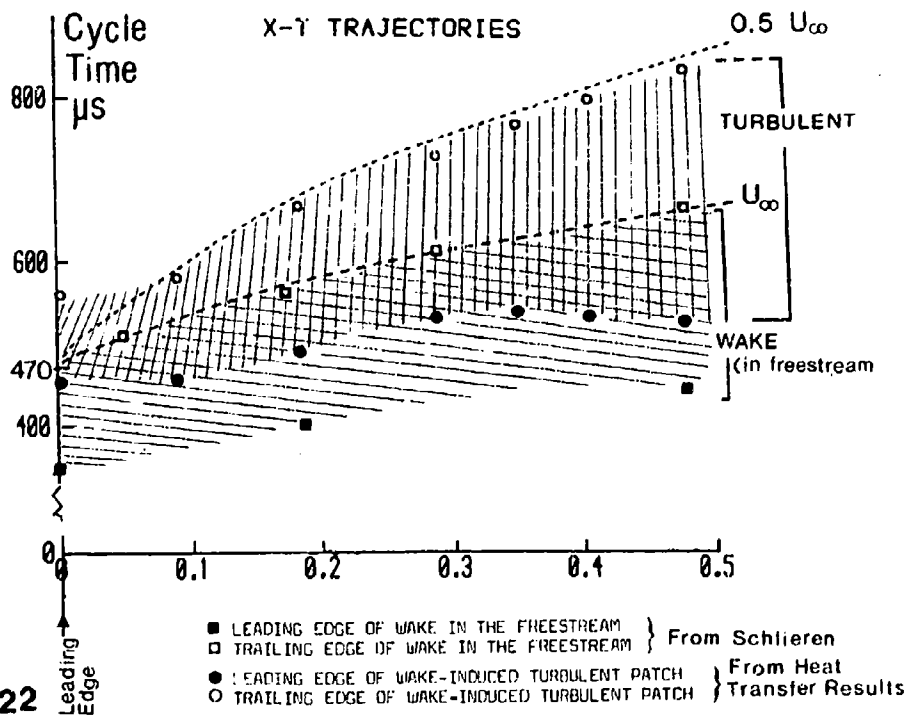


KEY:

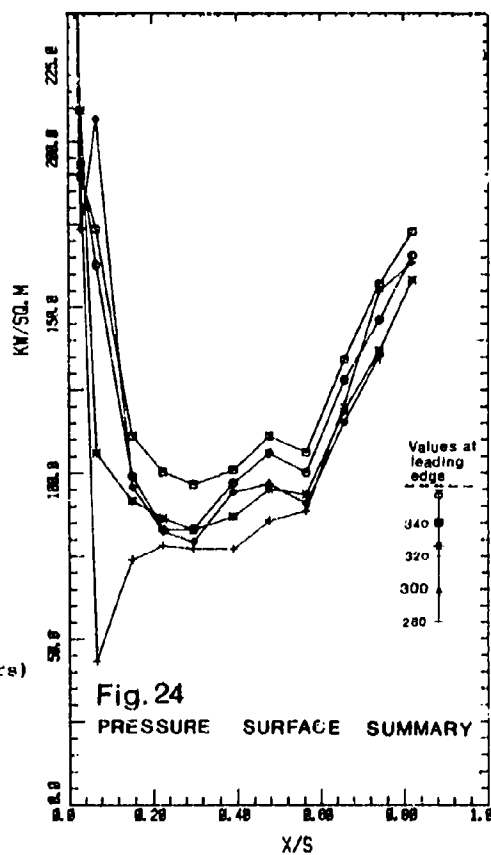
Unaveraged Traces:

- * Cycle 2
- Cycle 3
- ∇ Cycle 4
- △ Cycle 5

— ENSEMBLE AVERAGED OVER 7 CYCLES.

**KEY:**

- +- Undisturbed flow ($Tu < 0.4\%$)
- * Freestream $Tu (\approx 4.5\%)$ only
- ◇ Closely spaced wake-passing only (0.9 mm bars)
- ◇ Closely spaced wake-passing (0.9 mm bars) & combined 4.5% freestream turbulence.
- Closely spaced wake-passing (1.7 mm bars) & combined 4.5% freestream turbulence.



DISCUSSION

G.H. Dibelius, Ge

The results of your experiment with rotating bars in front of a turbine cascade are really extremely interesting. However, I still keep wondering, if it resembles completely the situation of a moving cascade behind a stationary cascade. Isn't there a difference in the three dimensional, non-isotropic structure of the turbulence in both cases? Did you make any comparison?

Author's Reply

I agree that there may be differences in the wave-number spectra of fluctuating velocities in the wakes produced by rotating bars and by actual nozzle guide vanes respectively. Such differences will be very pronounced in the near-wake, but probably much reduced at inlet to the rotor. These differences are not considered to be significant for the engine situation considered here, for the following reasons:

Firstly, for the representative, high-efficiency nozzle-guide vane, turbine stage considered, the comparatively large mid-height axial spacing between vane and rotor (approx. 40% rotor axial chord), and the high vane deflection angle (greater than 70°), result in the wake travelling a large streamwise distance from vane trailing edge, to point of first impingement on the rotor blade surface. Wake traverse measurements, reported in [13], of the wakes shed by a vane cascade, and circular cylinder, indicated that at the rotor inlet, the wake (of the vane used), could be closely simulated in terms of mean width and velocity defect by the wake from a circular cylinder of a diameter close to the vane trailing edge circle diameter. Thus, for a high efficiency vane (small diameter trailing edge), the wake may travel 200 effective cylinder diameters before impinging on the rotor blade. After such large distances, it is thus not anticipated that the difference between the respective turbulence spectra will be severe.

Furthermore, the experiments have indicated that the most dramatic feature of unsteady rotor heat transfer is caused by the formation and convection of turbulent patches, produced by the impinging wakes, in an otherwise laminar boundary layer. The very early generation of these turbulent patches results from the high turbulence content of the wakes, which contain abundant energy at the high wavenumber part of the spectrum. The transient level of heat transfer pertaining to each turbulent patch appears virtually independent of how the patch was generated, however, as demonstrated by the results reported here, (comparing the heat transfer produced momentarily by wakes, and continuously by high freestream turbulence) and by those of [12, 13] where the effect of varying wake size, and of tripping the boundary layer were considered.

As the wakes appear guaranteed to initiate an early transition therefore, it is concluded that it is the convection, and transport of the wakes within the passage, which define the regions of laminar, and highly turbulent freestream respectively, which is of greater significance than the precise spectral content of the wakes. Lastly I should say that a more serious difference between this simulation and the actual engine is that the simulation does not reproduce the vane secondary flow.

S. Wittig, Ge

In commenting on Prof. Dibelius and Prof. Schultz's questions (see previous paper), it is our feeling that the details of the turbulence structure of the wakes are of second order importance. This seems to be supported by our measurements where the effects of main flow turbulence and wakes were deliberately separated.

In addition, excluding shock interactions, our modeling seems to indicate that wake cutting at frequencies beyond 1 kHz with its effects on the blade -- i.e. temperature and stresses -- can be described by quasi-steady analysis. What is your opinion on that observation?

Author's Reply

In so far as the turbulence content of the wake produces turbulent patches in the boundary layer, which may merge forming a continuously turbulent boundary layer, then I fully agree with you that the heat transfer rate is determined by the boundary layer state, and once turbulent, is largely independent of freestream disturbance spectra. The measurements which you reported in paper No.6 showed that towards the rear position of the blade suction surface, where the boundary layer is fully turbulent, the effect of varying the level of freestream turbulence has negligible influence.

These results agree with our measurements which indicated that the transient level of heat transfer produced instantaneously by a wake, and the mean level of heat transfer which occurs when the turbulent patches produced by the wakes have merged, are identical to the heat transfer which could be produced by tripping the boundary layer by high levels of grid turbulence. So the answer appears to be that provided the wake (engine or simulated) contain sufficient energy (which is not doubted) to provoke early transition, then the fine details of spectral content appears significant. I should add that this conclusion may not equivalently hold on the pressure surface, where it does not appear that the boundary layer state is simple.

I think that in transition region, if it is accepted that the boundary layer may be laminar between wakes (I accept that there may be some doubt if there remains sufficient turbulence between the wakes to initiate an early transition, or other factors are present) then the unsteady problem must be studied, and a quasi-static analysis will not suffice. Certainly the quasi-static approach does not appear to work in analytical studies of flat plate transition and as contained in the answer to Prof. Dibelius, the motion of the wakes within the blade passages must be considered. Lastly we must also consider the effects of shock waves which unfortunately cannot be excluded.

EFFECTS OF HOLE GEOMETRY, WALL CURVATURE AND PRESSURE GRADIENT
ON FILM COOLING DOWNSTREAM OF A SINGLE ROW

by
H. Kruse
Institut fuer Antriebstechnik
DFVLR, 5000 Koeln 90
Germany

SUMMARY

Film cooling with injection through a single row of discrete circular holes is a 3-dimensional process which becomes more and more 2-dimensional with downstream distance from the injection site. In order to develop and verify prediction methods experimental investigations within the mixing region downstream of the coolant injection were undertaken.

The measurements discussed in this paper were carried out using simple film cooled models at a mainstream temperature of about 100 °C and a coolant temperature of about 30 °C. Coolant distributions on the adiabatic wall, adiabatic wall effectiveness and heat transfer coefficients affected by blowing are presented.

The blowing parameter was varied from 0.5 to 2 and the pitch to diameter ratio was varied from 1.5 to 5 with a constant hole diameter of 2 mm. Injection angles of 10 deg., 45 deg. and 90 deg. are covered. A flexible wall was used to produce zero, favourable and adverse pressure gradients along the flat plate.

Additional measurements were conducted on concave and convex curved walls with zero pressure gradient.

LIST OF SYMBOLS

A	Cross section
b	equivalent slot width
d	hole diameter
h_0	heat transfer coefficient without blowing
h_F	heat transfer coefficient with blowing
p	stat. pressure
\dot{q}_F	film cooling heat flux
R	radius of streamwise curvature
s	hole spacing
T	local gas temperature
T_c	coolant temperature
T_0	free stream temperature
T_{wad}	adiabatic wall temperature
Tu	free stream turbulence
u_0	free stream velocity
v_c	blowing velocity
x	streamwise distance
X	dimensionless parameter
α	inclination of the hole (in streamwise direction)
δ_0	boundary layer thickness
η_F	film cooling effectiveness
θ	dimensionless temperature
ρ_0	freestream density
ρ_c	coolant density
φ	blowing rate

INTRODUCTION

The development of gas turbines is characterized by increasing the compressor pressure ratio and the turbine inlet temperature in order to increase specific power and efficiency.

But near the physical limits, e.g. capacity of the coolant or stoichiometric combustion

temperature, great care is necessary to protect highly loaded parts of the high pressure turbine, because a small increase in metal temperature can lower the engine lifetime drastically. The use of film cooling is a means to intensify the convection cooling at critical locations on the blade. With film cooling, air is blown out from the surface to be cooled and mixes with the hot gas flow near the wall so that a film of cooler gas is formed which is effective over a certain region downstream from the point of blowing. It is known that ejecting the coolant through inclined or tangential slots is most effective, but high stress levels and aerodynamic penalties dictate the use of discrete holes in one or more rows.

Blowing through slots as well as full coverage film cooling geometries offer the advantage of nearly two dimensional conditions within the mixing layer and in these cases successful calculation schemes have been developed. But downstream of discrete holes the processes in the boundary layer and beyond it are of more or less three dimensional character and the design of such configurations requires more complex calculations in the region of strong spanwise nonuniformity in the vicinity of the holes.

The present experimental study should help to obtain more insight into the influence of important parameters affecting film cooling and thus help to optimize new design procedures.

The heat exchange between the hot gas and the film cooled wall depends upon numerous parameters, e.g. the blowing rate (defined as the ratio of velocity times density of the coolant to velocity times density of the mainstream gas), the ratio of momentum, the boundary layer thickness (relative to a characteristic length of the blowing geometry such as hole diameter), the relative hole spacing, the number and the spacing of the rows as well as the hole arrangement (staggered or in line), the injection angle (streamwise and lateral) and the shape of the holes. In addition to these typical film cooling parameters there are general heat transfer parameters like Reynolds number, temperature ratio, roughness, freestream turbulence, pressure gradient and wall curvature, which may change their influence due to film cooling.

The measurements reported here take into account the influence of blowing rate, relative hole spacing, inclination of the holes in the streamwise direction, pressure gradient, and wall curvature.

EXPERIMENTAL TECHNIQUE

The experiments and their results are based upon the adiabatic wall temperature concept. The heat flux is given by

$$\dot{q}_F = h_F \cdot (T_w - T_{wad})$$

T_{wad} is the adiabatic wall temperature downstream of the injection with the effect of the coolant film. T_{wad} is defined in terms of the film cooling effectiveness

$$\eta_F = \frac{T_o - T_{wad}}{T_o - T_c}$$

The heat exchange on a film cooled wall can be described by η_F and h_F , where $\frac{1}{\eta_F} = \frac{T_o - T_c}{T_o - T_w}$ ($h=0$) is the dimensionless temperature without heat transfer and h_F is the heat transfer coefficient for isothermal conditions

$$\frac{T_o - T_c}{T_o - T_w} = 0.$$

In the present test the adiabatic case is nearly realized and h_F is extrapolated assuming linearity between the measured heat transfer and

$$\frac{T_o - T_c}{T_o - T_w}.$$

This is valid because the governing energy equation is linear for constant-property, low-speed flow. In order to follow the mixing between the hot gas and the coolant jets, the distribution of the dimensionless temperature ratio

$$\theta = \frac{T_o - T}{T_o - T_c}$$

is given for some cases.

For measurements of three dimensional temperature distributions, models made from plastics with a poor thermal conductivity were used. Each heat transfer model has ten copper blocks, individually cooled by internal air flows, in the streamwise direction.

On the plastic models, the gas and adiabatic wall temperatures were measured by means of one very small thermocouple probe similar in appearance to a hot wire probe. The

temperature near the wall in nearly zero temperature gradient was assumed to be the adiabatic wall temperature. The coolant temperature was measured with the probe in the middle of a jet in the plane of the surface. The test section is shown in fig. 1.

RESULTS

The particular objective of this experimental study was to examine systematically the influence of hole spacing and inclination for different blowing rates, pressure gradients, and wall curvatures upon adiabatic effectiveness and heat transfer on a film cooled surface downstream of a single row of holes. To support efforts toward computational treatment of the complex three dimensional mixing processes, [10] the spreading of the coolant jets is described by temperature distributions in the region near the wall. For simpler design methods using empirical correlations or modified two dimensional boundary layer concepts it is thus known at what downstream distance the flow can be assumed to be two dimensional.

The literature is rich in reports of experiments which take into account different important film cooling parameters, but there is less information on the influence of hole spacing and important combined influences. All the test conditions of the present study are given in table I.

A comparison with results taken from the literature [9] is given in fig. 2. With nearly the same parameters the agreement for low blowing rate is good; looking at the differences for the higher blowing rate one must keep in mind a slightly different density ratio but the qualitative trend of the curves is the same.

The laterally averaged $\bar{\eta}_x$ -values are the area-weighted mean values of the local temperature measurements at constant x . The film cooling heat transfer coefficients are evaluated from effectiveness values based upon one thermocouple reading each in the middle of the ten copper bars of the heat transfer model, which can be assumed to be "streamwise" adiabatic without internal coolant flow. The lateral conductivity within the copper bars may influence the effectiveness such that for large hole spacing it is a little higher than on the plastic model and for small hole spacing vice versa. The differences are small.

The influence of hole spacing and inclination

For optimizing a film cooling design, the influence of film cooling effectiveness is more important than that of variations in heat transfer coefficient caused by film cooling.

Among the parameters affecting film cooling, the hole spacing is dominant. Fig. 3 demonstrates the general distinction of coolant mixing between the limiting case, the slot, and discrete hole blowing.

With slot injection, the mixing layer is completely two-dimensional. The injected coolant attaches to the wall, producing a high effectiveness which gradually decreases with increasing distance from the slot. In contrast, hole injection is a fully three-dimensional process. Even with almost tangential blowing through discrete holes ($\alpha = 10^\circ$, on the right of the figure), the temperature distribution along the extended centerline of a hole shows the typical mixing behaviour of hole injection. Near the hole, the jet lifts off and acts as a solid cylinder. The recirculating hot gas infiltrates the region downstream of the hole until the remainder of the jet reattaches. Farther downstream the jets combine and the flow field becomes more and more two-dimensional.

A single row of holes with hole spacing $s/d = 5$ behaves like multiple single jets (fig. 4): the mixing of an individual jet remains three-dimensional until far downstream, where the temperature differences finally disappear. With $\alpha = 45^\circ$ and high blowing rate ($\varphi = 2$) the jet mixes with the hot gas far away from the wall without reattaching; the lateral effectiveness is poor. While bending and mixing the jet assumes the typical kidney shape as a consequence of two counter-rotating vortices within the jet.

With the same inclination of the holes ($\alpha = 45^\circ$) and the same blowing rate, closer spacing of the holes leads to a different behaviour of the jets (fig. 5). Along the centerline close to the holes the typical liftoff occurs but the coolant very rapidly reattaches. The lateral temperature distribution shows an immediate spreading of the jets downstream of the injection and the jets grow together, while between the jets the coolant moves towards the wall. As a consequence of the rapid mixing of the jets the flowfield can be assumed to be two-dimensional at about 8-10 hole diameters downstream of the injection. The sketch in fig. 6 depicts the contrasting behaviors of a single jet ($s/d = 5$) and jets flowing close together. Although the blowing velocity is the same, the jets coming from a row of holes with small spacing don't penetrate as far. The secondary vortices of neighbouring jets form a counterrotating system of vortices with opposite orientation which may intensify the tendency to reattach to the wall.

The resulting influence of these different mixing processes with different hole spacing on the laterally averaged effectiveness is demonstrated in fig. 7. With $\alpha = 45^\circ$ as a representative inclination the streamwise development of the laterally averaged effectiveness $\bar{\eta}_x$ is shown for hole spacings $1.5 \leq s/d \leq 5$ and for slot injection for a high blowing rate. The greater the hole spacing, the farther downstream the reattachment after lifting off of the coolant occurs until no effect of reattachment is visible at $s/d = 5$. The diagram

on the right shows the influence of the blowing rate with different hole spacings at $x/d = 20$. With large hole spacing there is a significant maximum in lateral effectiveness for blowing rates of about 0.5. Even with slot injection a weak maximum is visible. Only with the small spacing of $s/d = 1.5$ does the effectiveness continue to increase with increasing blowing rate due to the above-mentioned marked tendency for mixing and reattachment. Similar results can be seen with 10° blowing (fig. 8) at higher levels of lateral effectiveness. With shallow injection the coolant film remains attached to the wall, which gives high effectiveness along the centerline of the jet and an enlarged region with high lateral temperature differences on the wall. (Fig. 9, lower). With 90° injection angle (Fig. 9, upper) the jets penetrate the slower parts of the flow and mix more rapidly away from the wall thus the lateral distribution of effectiveness is lower but becomes 2 dimensional closer to the injection site.

In addition to information on film-cooling effectiveness, the present study was concerned with determination of film-cooling heat transfer.

At small blowing rates, (below about 0.5) there is no or only small influence of hole spacing on heat transfer coefficient, but the heat transfer coefficient increases nearly linearly with higher blowing rates. Fig. 10 shows the ratio of the heat transfer coefficients with and without blowing at the position $x/d = 30$. This is approximately the middle of the region of interest. Farther downstream the ratio of heat transfer coefficients approaches unity.

With small hole spacing the highest heat transfer coefficients were measured immediately downstream of the holes, whereas large hole spacing causes lower laterally averaged heat transfer with blowing than without blowing at small blowing rates. This may be due to a "smoothing" effect of very small blowing rates.

The effect of hole inclination is shown on the right. Blowing at 90° does not affect the heat transfer very much because most of the injected coolant acts far away from the wall and does not affect the sublayer whereas with almost tangential blowing the turbulent mixing of the attached jets intensifies the heat transfer.

Summarizing the influence of hole spacing at the commonly-used 45° inclination, the heat transfer coefficients can be correlated. Using the product of the blowing rate and an equivalent slot ($\frac{b}{d} = \frac{\pi}{4(s/d)}$) as the abscissa the influence of the hole distance on heat

transfer is seen to be due only to the coolant mass flux (fig. 11 on the left), whereas the filmcooling effectiveness for different hole spacing cannot be related to the mass flux. The improvement in effectiveness with decreasing hole spacing is not only a consequence of higher mass flux, especially in the range from $s/d = 3$ to 1.5 (fig. 11 on the right) but also a consequence of intensified mixing due to interaction of the jets. An attempt was made to derive a rough empirical correlation for the laterally averaged effectiveness which takes into account the influence of hole spacing, the blowing rate and the streamwise distance, from a row of 45° -holes (fig. 12). For $x/d > 20$ all the results show a uniform tendency when plotted against the dimensionless parameter

$$X = \varphi^{-1.5} (s/d)^{1.5(1+\varphi)} x/d.$$

The effectiveness then is:

$$\bar{\eta}_F \approx 1.6 X^{-0.35}.$$

The influence of pressure gradient

The literature contains some contradictory results about the influence of pressure gradient on film cooling. The results presented here demonstrate that the influence of pressure gradient is very small and in most cases within the range of accuracy attainable by the tests described here. The different pressure gradients investigated are given in terms of velocity distributions along the test plate (fig. 13). The variation in pressure distribution starts upstream of the injection position, the opposite wall was adjusted so that the mainstream velocity at injection position was the same in all test cases, and the blowing rate given in the diagrams was related to that local velocity. On the right hand side of fig. 13 a small advantage in lateral film cooling effectiveness is shown for adverse compared to favourable pressure gradient. Adverse pressure gradient promotes the tendency to "lift off" in the vicinity of the holes but increases the effectiveness farther downstream. This behaviour is underlined by the temperature distribution along the centerline in fig. 14.

With favourable pressure gradient the jet does not penetrate as far. The region occupied by the coolant is flattened due to the contraction of the main flow and the coolant does not act as far in the streamwise direction as do the well-mixed jets in an adverse pressure gradient. There seems to be an optimum depending upon the blowing rate or the jet momentum respectively. With the same flow conditions and a higher blowing rate of $\varphi = 2$ the adverse pressure gradient only causes a thickening of the region affected by the coolant without having a measurable effect on the laterally averaged effectiveness (fig. 15). The described effect of pressure gradient seems not to be an effect of different boundary layer thickness. One would expect an increase in film cooling effectiveness as the boundary layer thickness decreases.

The present measurements suggest that the pressure gradient significantly affects the film cooling effectiveness only at low blowing rates and small hole spacing. Within

the range of variations of the present study the influence of pressure gradient on heat transfer was generally weak.

The influence of streamline curvature on filmcooling

There are many parameters involved in the mixing process of injected jets along a curved surface which act in one or another direction depending upon the quantity of special parameters and it is difficult to say what influence prevails.

Within an unblown boundary layer along a curved surface the parts with different velocities are affected differently by the centrifugal forces. In the presence of coolant jets the velocity distribution near the wall depends mainly upon the blowing rate and the blowing geometry, which may change the general influence of curvature. These influences may be overshadowed by buoyancy effects due to the centrifugal forces in the presence of density differences. In addition, the mixing of the jets is influenced by secondary motion in curved channels and by separation.

The results reported here are taken from models with the same boundary layer starting conditions as the flat plate. They are straight up to about 5 diameters downstream of the injection position. The pressure gradient in the streamwise direction for all curvatures was adjusted to be zero.

The results of heat transfer measurements typify the known trend of curvature effects far downstream of the injection (fig. 16): The stabilizing effect of convex curvature decreases the exchange of turbulence and thus the heat transfer, while concave curvature increases the heat exchange. For $x/d \geq 30$ there is no particular influence of curvature in the presence of blowing except for the higher level of heat transfer coefficients with high blowing rates. Immediately downstream from the holes the jets cause an effect opposite to that of curvature. The temperature distribution along the hole centerline on a convex surface (fig. 17) indicates an abrupt reattachment at about 5 hole diameters from the beginning of curvature. This produces disturbances near the wall which may give rise to increased heat exchange. A weak deflection of the flow at the beginning of a concave surface may cause the opposite effect until the destabilizing effect of concave curvature slightly increases the heat transfer rate.

The effect of curvature on film cooling effectiveness is small unless the coolant film separates on a convex surface with high blowing rates. With low blowing rates and on the upstream part of a wall, convex curvature is found to increase laterally averaged effectiveness whereas concave curvature is found to decrease effectiveness. In Fig. 18 this general behavior is demonstrated for a blowing configuration with small spacing ($s/d = 1.5$), $\alpha = 45^\circ$, and a curvature radius of ± 40 hole diameters. With low blowing (on the left of Fig. 18), a weak separation effect on the convex wall is indicated at a position 40 diameters downstream of the injection, whereas this separation starts at $x/d = 15$ with the higher blowing rate (on the right of Fig. 17). This can also be inferred from the temperature distribution in fig. 17.

The effect of different hole spacing on curved walls is shown in Fig. 19, where the laterally averaged effectiveness is plotted versus the curvature in terms of $1/R$ at the far-downstream position $x/d = 40$.

There is no difference between concave and flat walls for small spacing (on the left side of fig. 19). The effectiveness increases only with weak convex curvature and small blowing rate, whereas the flow begins to separate on the same wall with high blowing rate.

For the blowing configuration with large hole spacing, a slight increase in effectiveness was found for weak convex versus weak concave curvature, but in contrast to small spacing, the effectiveness slightly increases at strong concave curvature due to the poorer mixing and the tendency of the single jets with large spacing to reattach far downstream on the concave wall.

CONCLUSION

1. Filmcooling effectiveness and heat transfer coefficient following injection through a single row of holes are strongly affected by hole spacing. The measurements show a linear increase in filmcooling heat transfer coefficient with increasing coolant mass flux; the film cooling effectiveness significantly increases with s/d from 2.5 to 1.5 as a consequence of interaction of the jets. The lateral effectiveness with constant injection angle is correlated by a dimensionless parameter containing blowing rate, streamwise distance and hole spacing.

2. Small injection angles yield higher lateral effectiveness and heat transfer coefficient than large angle.

3. Favourable pressure gradient slightly decreases effectiveness while, adverse pressure gradient slightly increases effectiveness with small blowing rate. Except thickening of the boundary layer no influence on the wall was found with high blowing rates.

The effect of pressure gradient on filmcooling heat transfer coefficient is weak.

4. Film cooling effectiveness increases with increasing curvature ($-1/R$ to $+1/R$) especially for small blowing rates until the coolant film separates far downstream on a strongly convex wall.

ACKNOWLEDGMENTS

The author wish to thank Mr. Metzinger and Mr. Hoewel for their support during the test program as well as Dr. Mach for his assistance in correcting this paper.

REFERENCES

1. Brown, A. and Saluja, C.L. "Film Cooling From a Single Hole and a Row of Holes of Variable Pitch to Diameter Ratio", Int. J. Heat Mass Transf. Vol. 22 (1978).
2. Eriksen, V.L. and Goldstein, R.J. "Heat Transfer and Film Cooling Following Injection Through Inclined Circular Tubes", Journal Heat Transfer, May 1974.
3. Foster, N.W. and Lampard, D. "The Flow and Film Cooling Effectiveness Following Injection through a Row of Holes", Transaction ASME, Vol. 102, July 1980.
4. Hay, N., Lampard, D. and Saluja, C.L. "Effects of the Condition of the Approach Boundary Layer and of Mainstream Pressure Gradients on Heat Transfer Coefficient on Film-Cooled Surfaces", ASME Paper Nr. 84-GT-47 and: Effects of Cooling Films on the Heat Transfer Coefficient on a Flat Plate With Zero Mainstream Pressure Gradient, ASME Paper Nr. 84-GT-40.
5. Ito, S., Goldstein, R.J. and Eckert, E.R.G. "Film Cooling of a Gas Turbine Blade", Transaction ASME, Vol. 100, July '78.
6. Jubran, B. and Brown, A. "Film Cooling From Two Rows of Holes Inclined in the Streamwise and Spanwise Direction", ASME Paper Nr. 84-GT-286.
7. Liess, C. "Experimental Investigation of Film Cooling With Ejection From a Row of Holes: for the Application to Gas Turbine Blades", ASME Paper Nr. 74-GT-5.
8. Metzger, D.E., Biddle, J.R. and Warren, J.M. "Evaluation of Film cooling Performance on Gas Turbine Surface", AGARD-CP-73-71.
9. Pedersen, D.R., Eckert, E.R.G. and Goldstein, R.J. "Film Cooling With Large Density Differences Between the Mainstream and the Secondary Fluid Measured by the Heat-Mass Transfer Analogy", transaction ASME, Vol. 99, Nov. '77.
10. Rodi, W., Demuren, A.O. and Schönung, B. "Systematic Study of Film Cooling With a Three-Dimensional Calculation Procedure", Offered for presentation at ISABE 1985, Beijing International Gas Turbine Symposium and Exposition".
11. Smith, M.R. "A Study of Film Cooling Effectiveness With Discrete Holes and Slots", Report AT/2057/045/xR, NGTE, Pyestock, Oct. 1974.

Cross section	$A = 100 \times 100 \text{ mm}^2$	Blowing rate	$0,5 \leq \phi \leq 2,0$
Streamwise extension of measurements	$x_e \approx 120 \text{ mm}$	Relative hole spacing	$s/d = 5$
Freestream temperature	$T_o \approx 373 \text{ K}$		3
Density ratio	$\frac{\rho_c}{\rho_o} \approx 1,24$		2 (2,5)
			1,5
			slot
Freestream turbulence	$T_u \approx 2 \%$	Inclination of the holes	$\alpha = 10^\circ$
			45°
			90°
Thickness of the unblown turbulent boundary layer at blowing position	$\delta_o \approx 2 \text{ mm}$	Pressure gradient	$\frac{dp}{dx} = 0; u_o \approx 60 \frac{\text{m}}{\text{s}}$
Hole diameter	$d = 2 \text{ mm}$		$\frac{dp}{dx} < 0; 60 \frac{\text{m}}{\text{s}} \leq u_o \leq 90 \frac{\text{m}}{\text{s}}$
			$\frac{dp}{dx} > 0; 59 \frac{\text{m}}{\text{s}} \leq u_o \leq 51 \frac{\text{m}}{\text{s}}$
		Radius of surface curvature	$R = \infty$
			$R = \pm 80 \text{ mm}$
			$R = \pm 160 \text{ mm}$

Table I: Test conditions

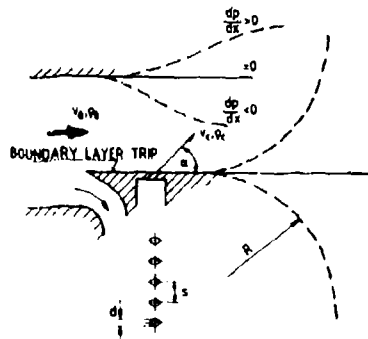


Fig. 1: Experimental configuration

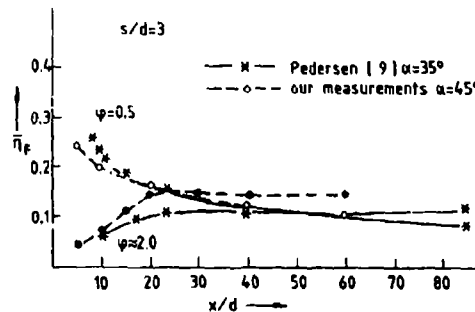
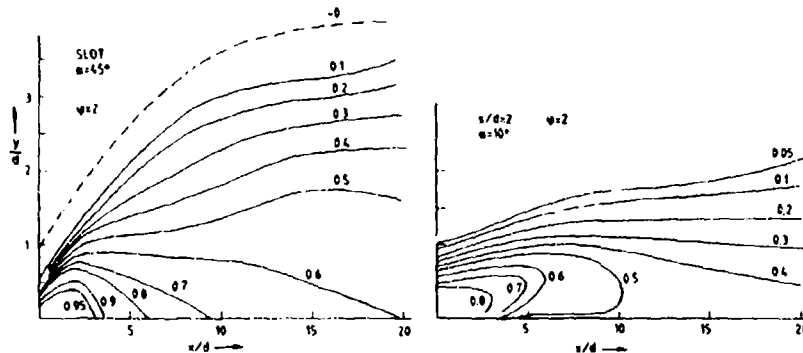


Fig. 2: Film-cooling effectiveness at a flat plate (Comparison with results from the literature)

Fig. 3: Constant temperature contours ($\theta = \frac{T_o - T}{T_o - T_c}$) downstream from slot and discrete hole injection (centerline)

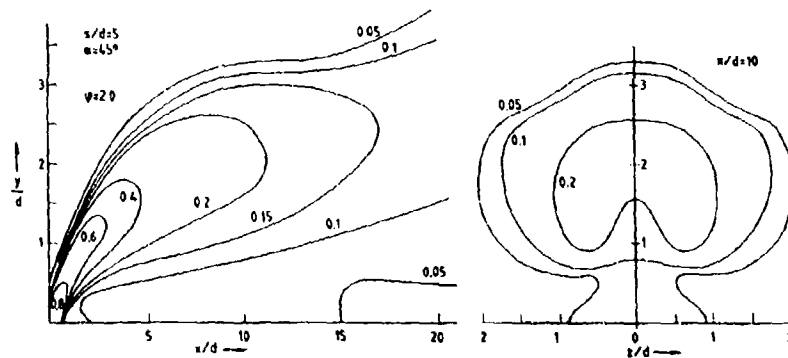


Fig. 4: Constant temperature contours along and perpendicular to the centerline for large hole spacing

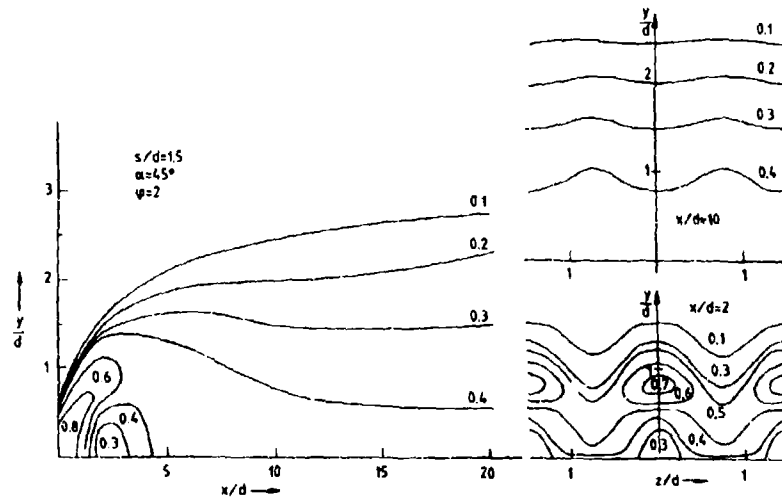


Fig. 5: Constant temperature contours along and perpendicular to the centerline for small hole spacing

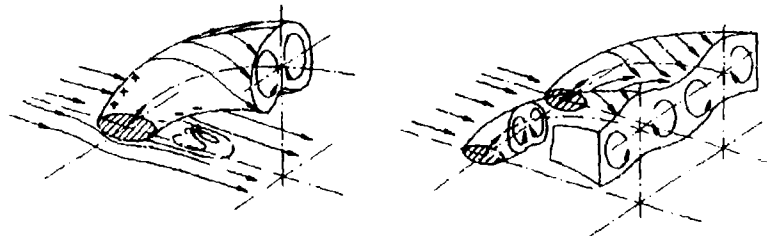


Fig. 6: Mixing of coolant jets from single holes and a row of holes

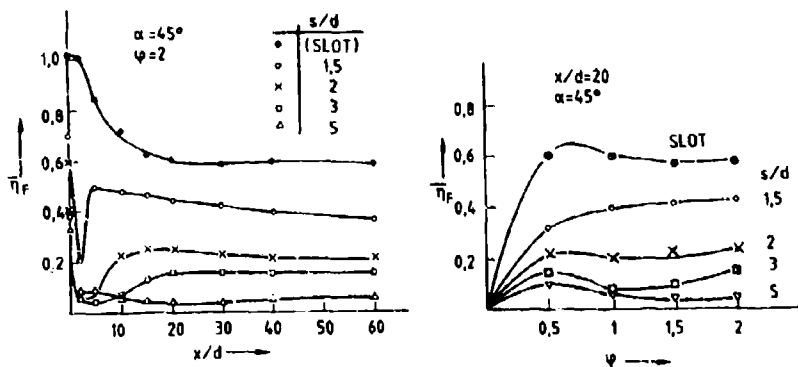


Fig. 7: Laterally averaged film cooling effectiveness for various hole spacings in streamwise direction and versus the blowing rate ($\alpha = 45^\circ$)

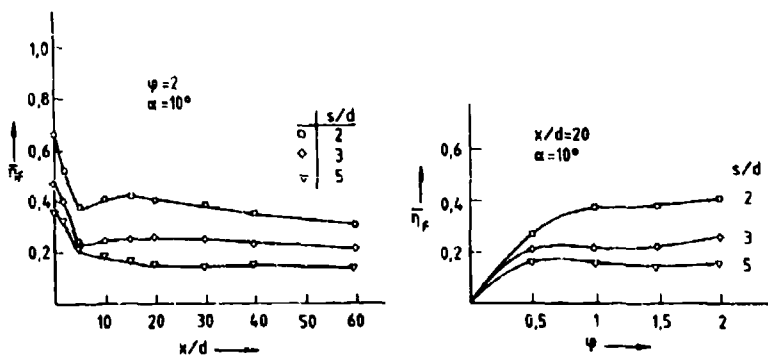


Fig. 8: Laterally averaged film cooling effectiveness for various hole spacing in streamwise direction and versus the blowing rate ($\alpha = 10^\circ$)

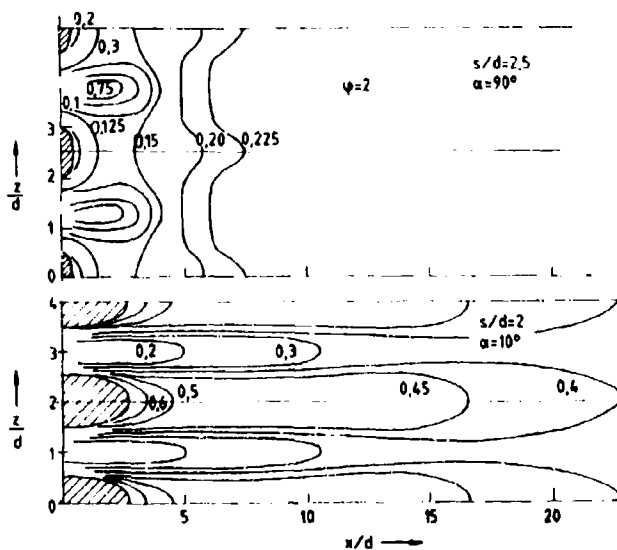


Fig. 9: Effectiveness footprint for shallow and normal injection

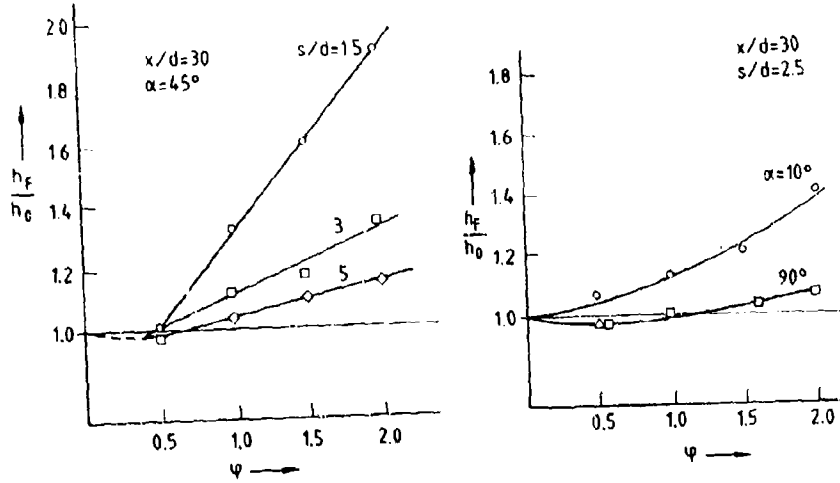


Fig. 10: Ratio of heat transfer coefficient with and without blowing for various configurations versus blowing rate

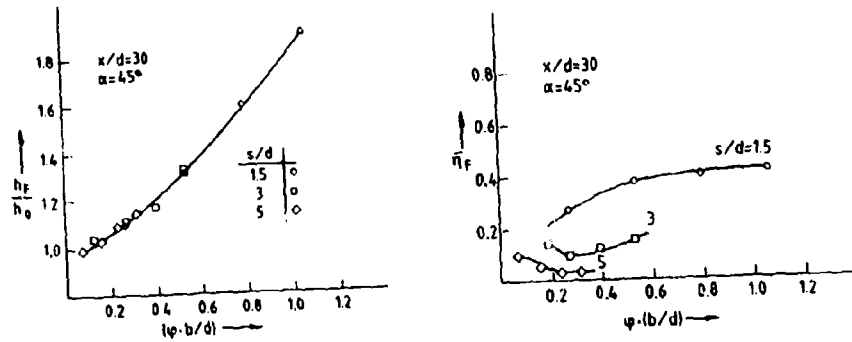


Fig. 11: Influence of coolant mass flux on heat transfer coefficient and effectiveness for various hole spacings

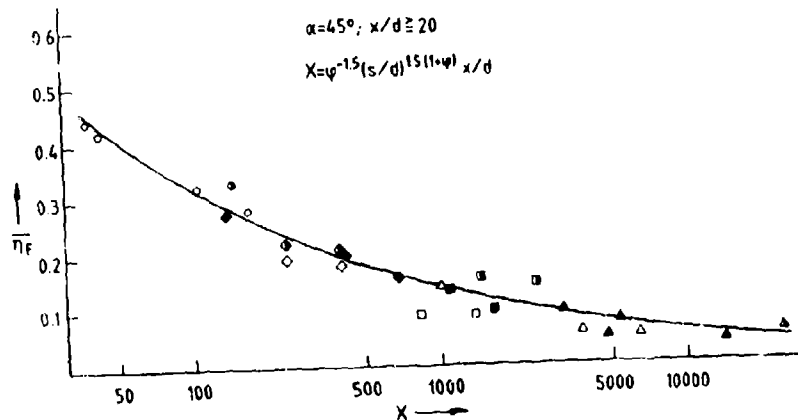


Fig. 12: Laterally averaged film-cooling effectiveness versus an empirical correlation factor embodying the blowing rate, hole spacing and streamwise distance

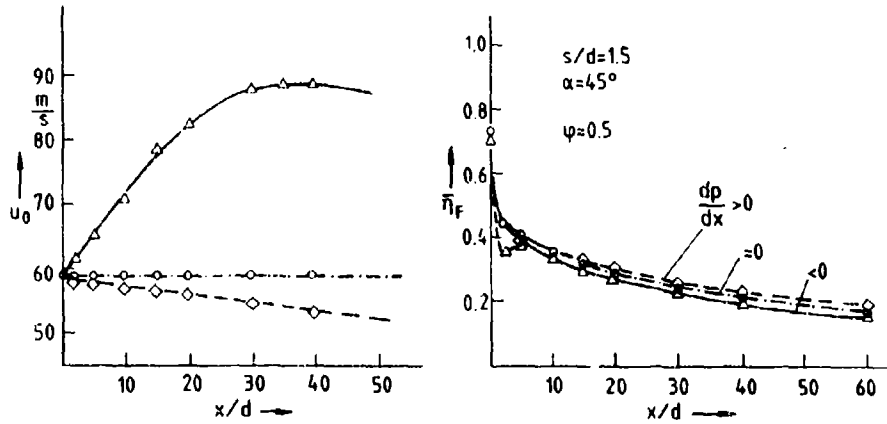


Fig. 13: Effect of streamwise pressure gradient on filmcooling effectiveness (streamwise velocity distribution on the left side)

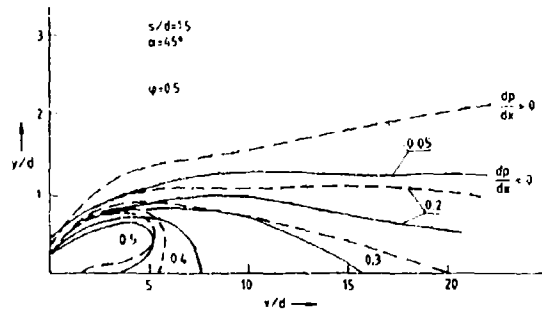


Fig. 14: Effect of streamwise pressure gradient on temperature contours along the jet centerline with small blowing rate

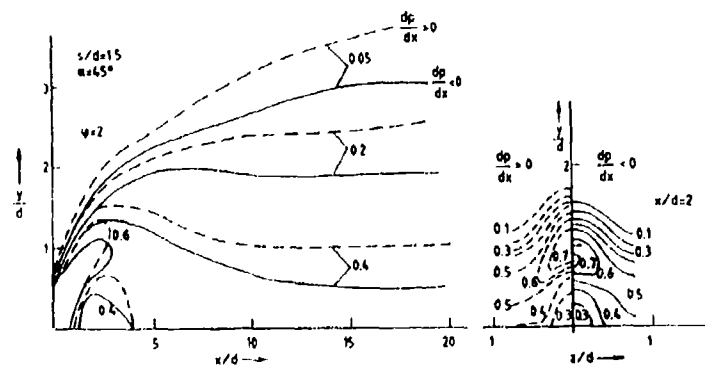


Fig. 15: Effect of streamwise pressure gradient on temperature contours with high blowing rate

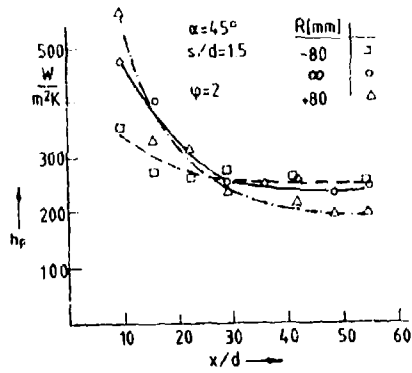


Fig. 16: Film cooling heat transfer coefficient at concave, flat and convex walls

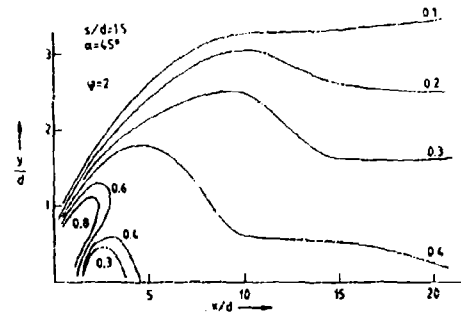


Fig. 17: Constant temperature contour along the centerline of a jet on a convex surface

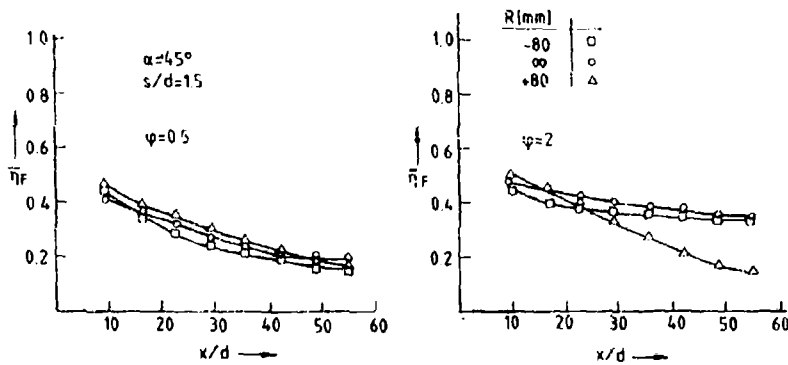


Fig. 18: Streamwise distribution of film-cooling effectiveness on concave, flat and convex walls

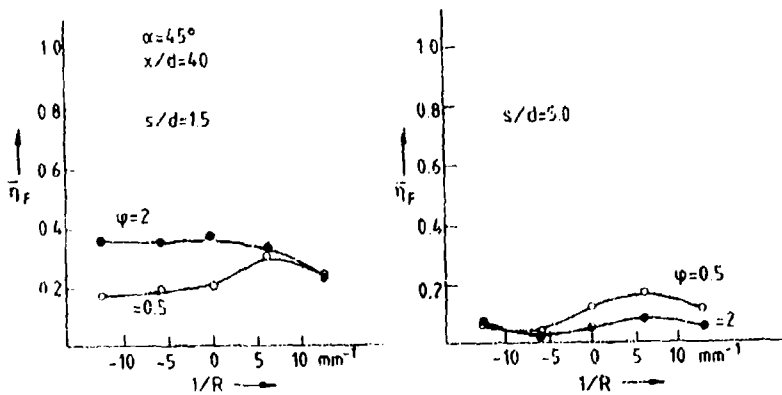


Fig. 19: Effect of curvature on laterally averaged effectiveness

DISCUSSION

G.E.Andrews, UK

There is little information available that allows the hole pitch and diameter to be optimised and your paper is a welcome contribution in this area. Your investigations have varied the pitch at a constant hole size, thus for the same hole blowing rate there must be a difference in total coolant flow as the pitch is increased due to the reduced number of holes. Thus the influence of s/d in Figs.7 and 8 is pessimistic and should have been carried out at constant total hole area i.e. a different value of d for each s/d .

In our work at Leeds on full coverage discrete hole film cooling systems we have varied s/d from 12 to 2 at constant pitch, by increasing the hole size. There was a very strong improvement in the overall cooling effectiveness with increased hole size due to the much lower blowing rates for a fixed coolant flow.

Author's Reply

It's right, we don't vary the hole diameter ($d = 2$ mm) and thus constant blowing rate yields decreasing total coolant flow with increasing pitch to diameter ratio s/d . In Fig.11 the results are related to the total coolant flow and we, too, found an improvement in film cooling effectiveness with decreasing s/d like in your tests, where the s/d is changed by varying the hole size.

D.Metzger, US

It would be helpful to know the value of acceleration parameter, K , for the test condition reported.

In this connection, it should be noted that the author's tests are conducted with a boundary layer trip. On an airfoil surface with naturally occurring transition delayed by the presence of strong favorable pressure gradient, film injection may have quite different effects on surface heat transfer than those observed in the present tests.

Author's Reply

From $x/d = 0$ (injection to $x/d \approx 20$ the acceleration parameter

$$K = \frac{v_n}{u_n^2} \cdot \frac{du_n}{dx}$$

changes from about 1×10^{-6} to 2×10^{-6} and from -0.5×10^{-6} to -0.6×10^{-6} respectively.

EFFECTS OF SURFACE ROUGHNESS ON HEAT TRANSFER
TO GAS TURBINE BLADES

A.B. Turner, F.H.A. Tarada and F.J. Bayley,
University of Sussex,
Falmer, Brighton, U.K.

SUMMARY

This paper presents a brief, preliminary sample of results of an investigation into the effect of surface roughness on heat transfer to gas turbine blades. Only the kind of roughness due to the accretion of dirt or dust is considered and this has been simulated in cascade flow by attaching various grades of abrasive powders to the blade surface with a water soluble adhesive.

A significant increase in heat transfer is reported particularly with high free stream turbulence levels. Roughness on the pressure surface alone is shown to increase the overall heat transfer without any corresponding increase in profile loss.

INTRODUCTION

It has been known for many years that, in general, surface roughness adversely affects the profile loss of gas turbine nozzle guide vanes and rotor blades (1), and although much work has been done on the consequent performance deterioration of turbomachines (2), very little has been reported on the associated effect on heat transfer. Commercial jet engines are estimated to lose a minimum of two per cent S.F.C. due to general service erosion and the operating life of vanes and blades in sandy areas is known to be as short as one third of the average, with some helicopter engines lasting only 50 - 250 hours (2). Industrial gas turbines operating in desert or coastal areas suffer from accretion due to very fine, 'face powder like' dusts which pass through the filters and fuse on the surfaces as a glassy deposit. Many failures of high temperature industrial engines have been attributed to such effects (2).

There are two types of roughness which are of importance to turbine blade designers and industrial engine operators. The first is machined, or intrinsic, roughness which arises from the nature of the manufacturing process or from the service erosion and pitting due to sand or carbon particles. Since it is known that significant improvements in S.F.C. are obtained if turbine vanes and blades are polished, manufacturers are interested in determining how much polishing is worthwhile. The second kind of roughness, and the kind which is the subject of this paper, is that which arises from the deposition of dirt, dust, sand, rust or carbon (accreted roughness). This can cause blockage of film cooling holes, severe disturbance of the external flow and the failure of components in service due to overheating.

Problems due to the accretion of dirt on blades are becoming more common especially since the introduction of industrial gas turbines operating with turbine inlet temperatures over 1300 K with cooled vanes and blades - the combination of the two exacerbates the problem. There is also increasing interest in the use of pulverized coal as a fuel in gas turbines and one of the major problems facing this development is the resulting erosion and the accretion due to fly ash. The two types of roughness can be similar in that severe erosion damage may result in surface roughness levels at the leading and trailing edges approaching the levels tested in the present investigation.

When profile loss alone is considered the pressure surface is of little importance since almost all the loss arises from the suction surface flow, but when heat transfer is considered it is the pressure surface which is most likely to suffer erosion damage and dirt and dust accretion (2).

The level of "admissible" roughness in engineering is generally taken to be that maximum height of individual roughness elements which causes no increase in drag, and for high pressure steam turbine blades this is reported (1) to be extremely small (<0.2 μ m or 8 μ inch). However, the value of admissible roughness for blades depends on whether the flow is laminar or turbulent. Increasing surface roughness would be expected to move the point of transition upstream and the effect of roughness on transition was studied by Feindt (1) although at nothing like the conditions experienced by modern turbine blades. The combined effect on transition of surface roughness, strong favourable flow acceleration and high mainstream turbulence is still very much unknown.

The most comprehensive experimental work on the effect of surface roughness on turbulent boundary layers is that by Stanford University, e.g. Coleman, Moffat and Kays (3). However, the maximum velocity gradient parameter ($(\nu/U^2) \cdot (du/dx)$, where ν is the kinematic viscosity and U is the freestream velocity) investigated was approximately two orders of magnitude below the relaminarization levels experienced on turbine blades.

For turbulent boundary layers the wall is usually considered to be hydraulically smooth if the roughness elements are contained within the laminar sublayer and for flat plates a simple roughness Reynolds number relationship based on the admissible roughness height, k_{adm} , has been shown to be valid by several cascade profile loss experiments (1,4). The limiting value of this roughness Reynolds number has been found to be 100 which gives $k_{adm} \leq 100 \nu/U$, where ν is the kinematic viscosity, and U is the free stream velocity. For 50 mm chord blades this predicts k_{adm} as 5 μ m for an exit Reynolds number of 10^6 (and 0.5 μ m for 10^7). These roughness heights apply only at the trailing edge and

the upstream values, because of the thinner boundary layers, would be much smaller. Although the flow over gas turbine blades is very different from flat plate flow, it should be remembered that the overall heat transfer in engines is not very different from the turbulent flat plate level (5,6).

Manufactured surface roughness of vanes and blades is generally of the order of $1.25 - 2.7 \mu\text{m}$, before any finishing process and any accretion of dirt and sand would produce values well in excess of this together with a very uneven distribution over the profile.

THE EXPERIMENTAL METHOD

The blade section used is a derivative of the Rolls Royce Olympus 593B HP turbine rotor blade and is the blade profile used by Bayley and Priddy (5). The profile and cascade arrangement is shown in figure 1. The turbulence grid of 3 mm bar size was mounted 90 mm upstream of the leading edge and the turbulence intensity is approximately 7% for that location.

The 'thin shell' method was used to determine the local heat flux. The centre instrumented blade was made from a steel/epoxy resin mix in the form of a thin shell 1.5 mm thick with fine thermocouples embedded in the inner and outer surfaces. Fourier's one dimensional heat conduction equation was used together with linear interpolation to determine the heat flux through the air cooled shell. The originally smooth outer surface was therefore perturbed by thermocouple grooves which created regular disturbances of approximately $5 \mu\text{m}$.

The blade was operated at an average temperature of approximately 600°C with the mainstream flow at 90°C . The maximum exit Mach number was 0.8 which, with blades of 64 mm chord, gave a maximum exit Reynolds number of 1.2×10^6 . The surface static pressure and Mach number distribution is shown in figure 2 for this maximum flow condition.

Our attention to date has been confined to accreted roughness, that which adheres to the surface during service, and to simulate this, abrasive powders of aluminium oxide and silicon carbide (7) were adhered to the surface in a uniformly distributed manner with a water soluble adhesive. The roughness grades referred to in the tests: 1, 3, 4 and 9, correspond to micron sized powders of 54, 76, 105 and 250 μm , respectively, with grade 4 being the only silicon carbide powder used. One of the tests, roughness 41, was conducted with powder 4 on the pressure surface only. It should be noted that the finest of these powders, No.1 at 54 μm is about two orders of magnitude larger than the roughness of a polished turbine blade.

The profile loss was determined by pitot tube exit traverse and the loss coefficient used is the ratio of the average total head loss to the average exit dynamic head.

DISCUSSION OF RESULTS

Although the effect of roughness on the aerodynamic efficiency was not the primary objective of this study, the profile loss was measured, figure 3, and in general was found to increase with increasing surface roughness. One unexpected result was that with roughness stuck only on the pressure surface, the aerodynamic loss was found to be slightly lower than the basic smooth profile (see also figure 11).

Figure 4 shows that accumulated roughness has a substantial effect on the overall, mean heat transfer coefficient, particularly at high free stream turbulence. With low turbulence levels, for the roughness levels used, a general overall increase of about 50% was produced but with 7% turbulence intensity the mean heat transfer was approximately doubled. This increase, however, is by no means uniformly distributed over the surface.

The basic heat transfer coefficient distribution for the smooth blade with low turbulence is illustrated in figure 5. The pressure surface shows a fairly uniform increase over the whole length with increasing exit velocity consistent with transitional flow. The suction surface shows a clear transition from the initial laminar state and this transition location moves downstream with increasing exit velocity. At the highest Mach number, 0.77, the transition coincides with the point at which the surface velocity falls below Mach 1 (see figure 2) and is thus probably induced by a shock wave, which, as the exit velocity is reduced, would move upstream due to the shift in the Mach number profile. This position of 80% on the suction surface is well downstream of the throat position at 55% chord.

Figure 6 illustrates, for the pressure surface, the now familiar effect of increasing turbulence intensity on heat transfer in a strong favourable pressure gradient (5,8,9). General transitional behaviour is evident since the velocity gradient parameter $((v/U^2) \cdot (dU/dx))$ is almost always above the critical value of 2×10^{-6} . The suction surface, however, still indicates a transition at about 30% chord with the resulting turbulent boundary layer now moving unaffected through the probable shock at about 75% chord.

Figures 7 and 8 show the effect on the local heat transfer coefficient of the four grades of roughness tested. Results are given for two exit Mach numbers, both with low levels of free stream turbulence ($< 0.5\%$). The general result is that the pressure surface heat transfer is approximately doubled and that there is now no clear transition on the suction surface. An interesting comparison between figures 7 and 8 is that the mean level on the suction surface again actually decreases with increasing Mach number,

probably due to the movement of the transition point within the first 20% of the surface.

With 7% free stream turbulence, figure 9, the rough blade heat transfer coefficients on the suction surface actually fall below the smooth blade levels at about 70% chord, again probably due to the upstream movement of transition. This strange "cross over" on the suction surface was also observed, figure 10, when the rough blade was tested with and without the turbulence grid. The leading edge heat transfer values are very much higher with the combination of a rough blade and appreciable mainstream turbulence, showing that the values of admissible surface roughness in this region appear to be very dependent upon the turbulence intensity.

In figure 11 a comparison is made between the smooth blade, the rough blade and the blade with roughness adhering to the pressure surface only (roughness 41). When this roughness was attached to the profile, care was taken to ensure a clean dividing line at the geometric leading edge. However, it is clear that the boundary layer development on the suction surface was also affected; probably due to the stagnation point being further round on the pressure surface from the geometric leading edge. The clear transition point was removed on the suction surface and the overall heat transfer much increased on this side. The profile loss coefficient for this condition (roughness 41 on figure 3), shows that the accretion of roughness on a blade may not adversely affect turbine efficiency, but could cause an appreciable increase in mean blade temperature and thus the likelihood of failure.

CONCLUSIONS

It has been shown that increasing surface roughness increases the overall mean level of heat transfer particularly in the presence of high free stream turbulence. The leading edge values have been shown to increase by as much as a factor of three and any laminar-turbulent transition on the suction surface moved very close to the leading edge.

The effect on the pressure surface was found to be akin to that of free stream turbulence in that a fairly uniform increase over the whole surface was produced. Roughness at the leading edge of the suction surface was found to promote early transition followed by a fairly uniform level of heat transfer over the remainder of the blade undisturbed by the existence of shock waves.

It is known that the suction surfaces of blades do not deteriorate significantly in service and the test simulating this, with roughness on the pressure surface only, produced an increased level of heat transfer on both surfaces with, if anything, a slight reduction in profile loss. This indicates that in service an increase in blade heat transfer can be produced by particulate flows without any reduction necessarily occurring in turbine efficiency. This anomalous behaviour, of increasing roughness producing a lower profile loss, has been observed in turbine practice but only for surface roughnesses an order of magnitude lower than those considered in the present work.

In their recent paper Elovic and Koffel (6) list a number of parameters which affect turbine airfoil heat transfer and point out that systematic investigations addressing their combined effects are grossly lacking. Although a recent work (10) has made a substantial contribution to this, there is much experimental work still to be done to provide a more realistic data base for turbine prediction procedures and in this respect these preliminary results indicate that the effects of free stream turbulence and surface roughness due to the accretion of dirt are additive and may be of the same relative importance.

REFERENCES

1. Schlichting, H. Boundary layer theory. McGraw Hill, 7th ed. 1979.
2. Tabakoff, W. Review - Turbomachinery performance deterioration exposed to solid particulates environment. J. of Fluid Engineering, Vol.106, June 1984.
3. Coleman, H.W., Moffatt, R.J. and Kays, W.M. Report HMT-24, Dept. of Mechanical Engineering, Stanford University, California. March 1976.
4. Bammert, K. and Sandstede, H. Measurements of the boundary layer development along a turbine blade with rough surfaces. ASME 80-GT-40, 1980.
5. Bayley, F.J. and Priddy, W.J. Effects of free-stream turbulence intensity and frequency on heat transfer to turbine blading. ASME 80-GT-79, 1980.
6. Elovic, E. and Koffel W.K. Some consideration in the thermal design of turbine airfoil cooling systems. Int.J. of Turbo and Jet-Engines. Vol.1, No.1, 1983/4.
7. Norton Materials UK, Blue Stem Road, Ransomes Industrial Estate, Ipswich IP3 9RR.
8. Turner, A.B. Local heat transfer measurements on a gas turbine blade. J.Mech.Eng. Sci., Vol.13, 1-12, 1971.
9. Kestin, J. The effect of free stream turbulence on heat transfer rates. Advances in Heat Transfer, 3. Academic Press, 1966.
10. Rued, K. and Wittig, S. Free-stream turbulence and pressure gradient effects on heat transfer and boundary layer development on highly cooled surfaces. Trans. ASME, J.Eng. Gas Turbines & Power, Vol.107, Jan.1985.

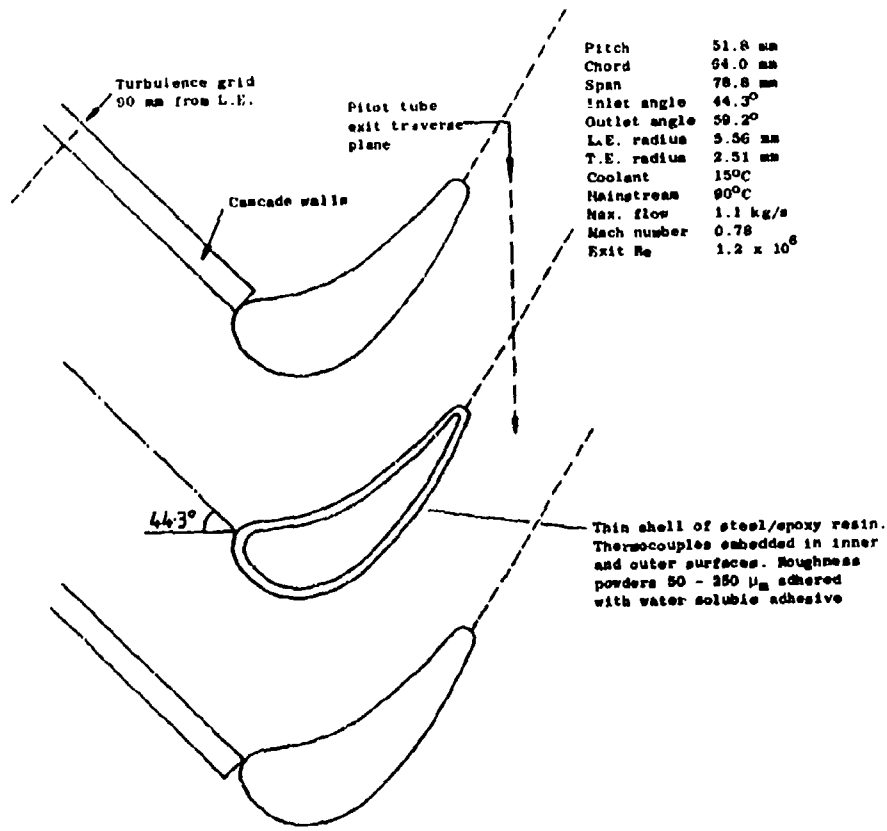


Fig.1 Cascade and blade details

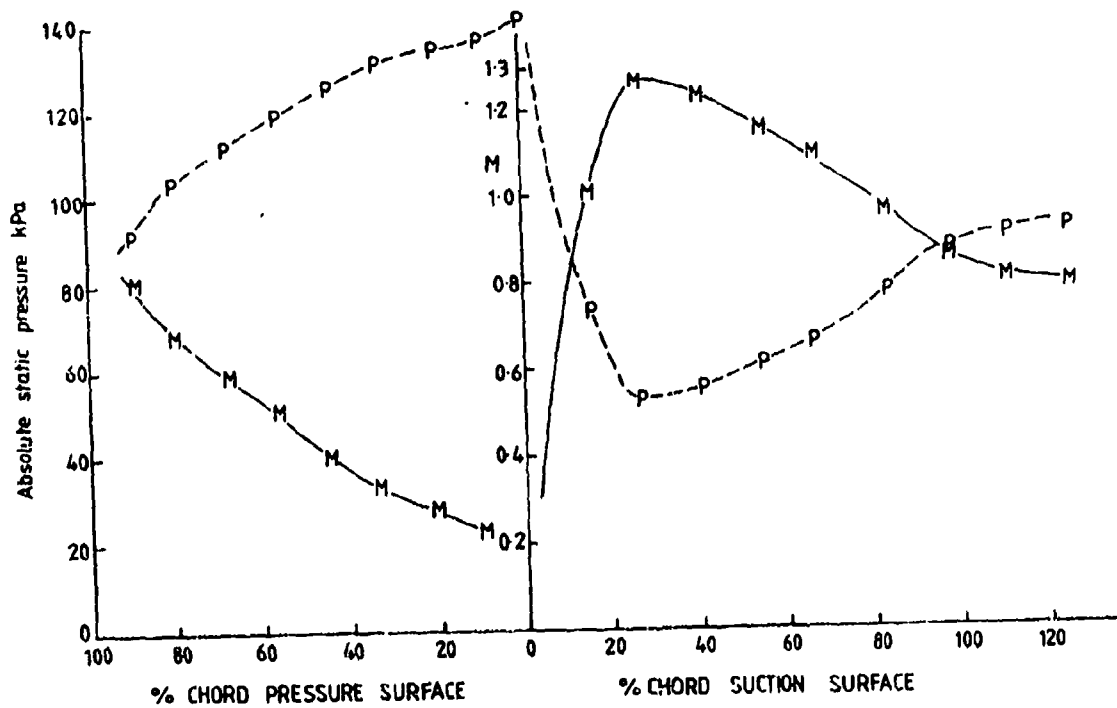


Fig. 2 Static pressure and Mach no. distribution. Exit Mach no 0.78

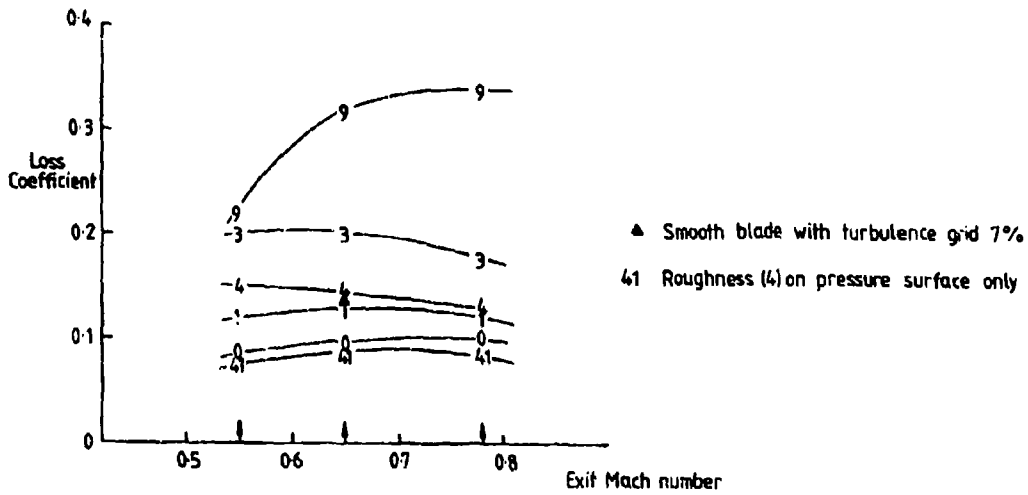


Fig. 3 Profile loss coefficients for smooth blade (0) and for various grades of roughness (1, 3, 4 and 9)

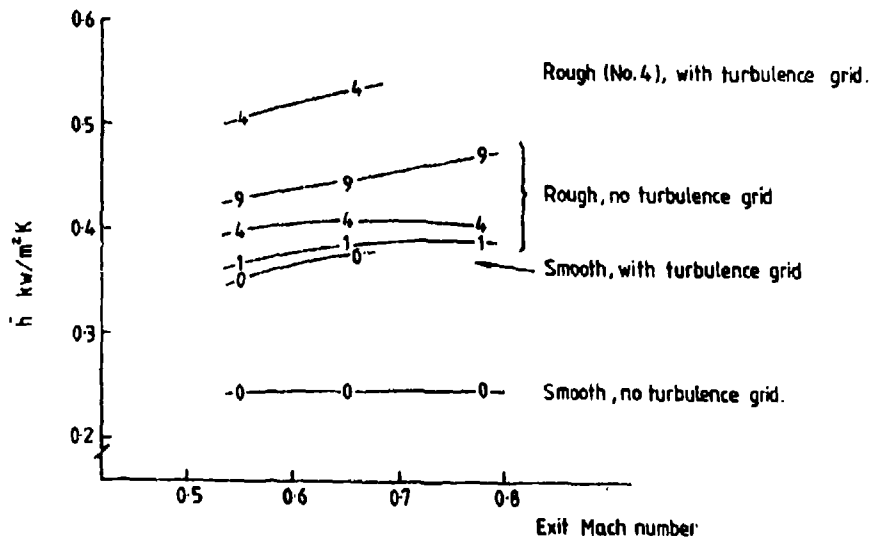


Fig. 4 Effect of roughness and free stream turbulence (7%) on overall, mean heat transfer coefficient.

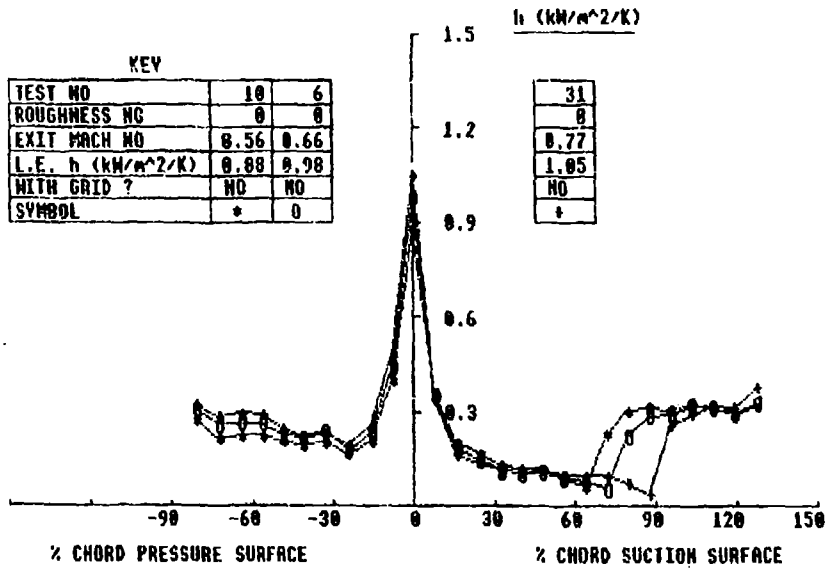


Fig. 5 Effect of increasing exit Mach number on local heat transfer coefficient. Smooth blade (O), no turbulence grid.

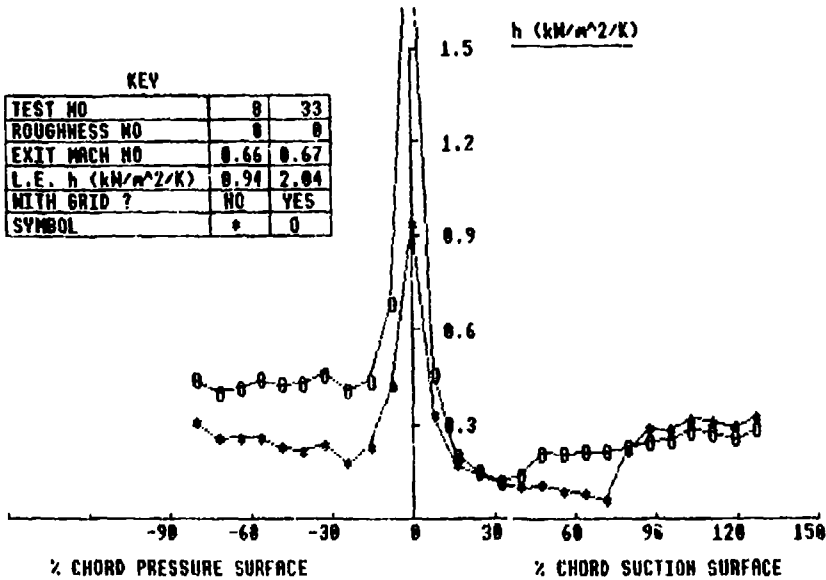


Fig. 6 Effect of turbulence grid (7%) on local heat transfer coefficient. Smooth blade (O)

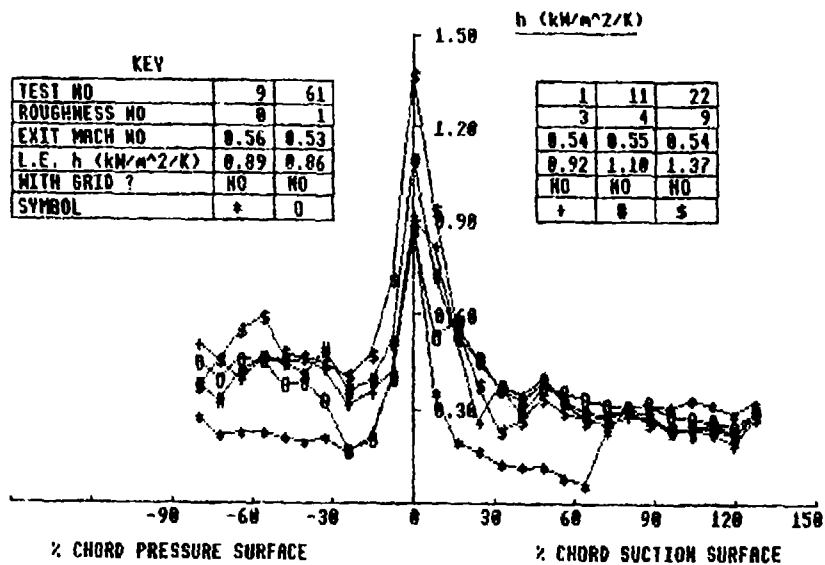


Fig. 7 Effect of different levels of roughness on heat transfer coefficient. No turbulence grid, $M = 0.55$.

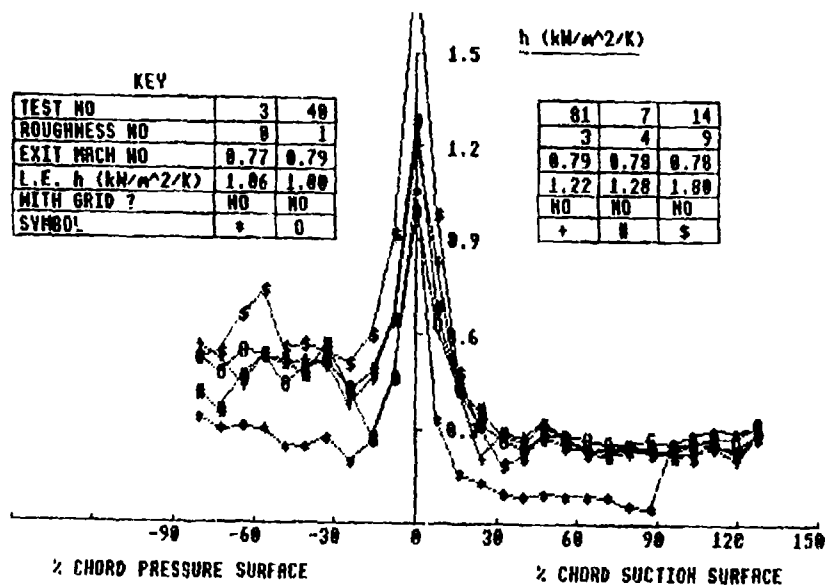


Fig. 8 Effect of different levels of roughness on heat transfer coefficient. No turbulence grid, $M = 0.78$.

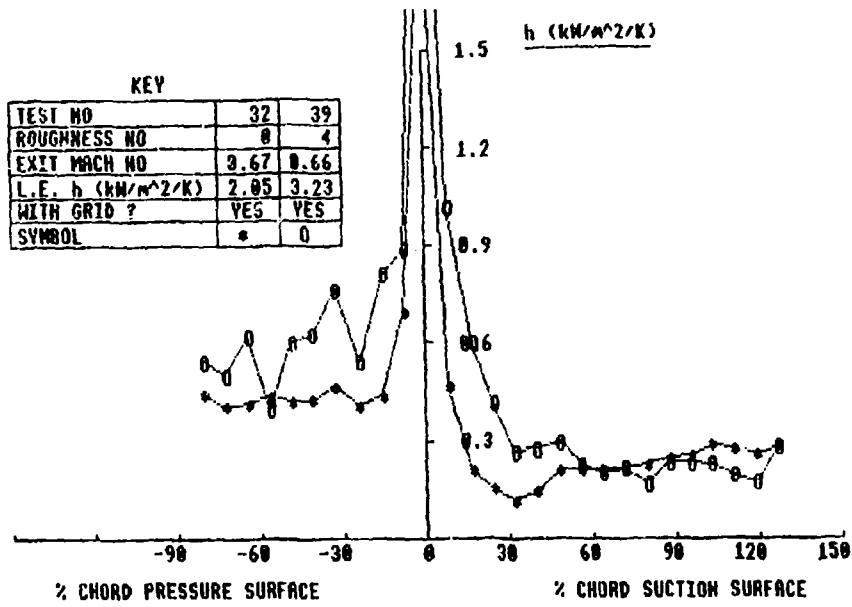


Fig. 9 Effect of turbulence grid (7%) on smooth and rough (No.4) blade heat transfer coefficients

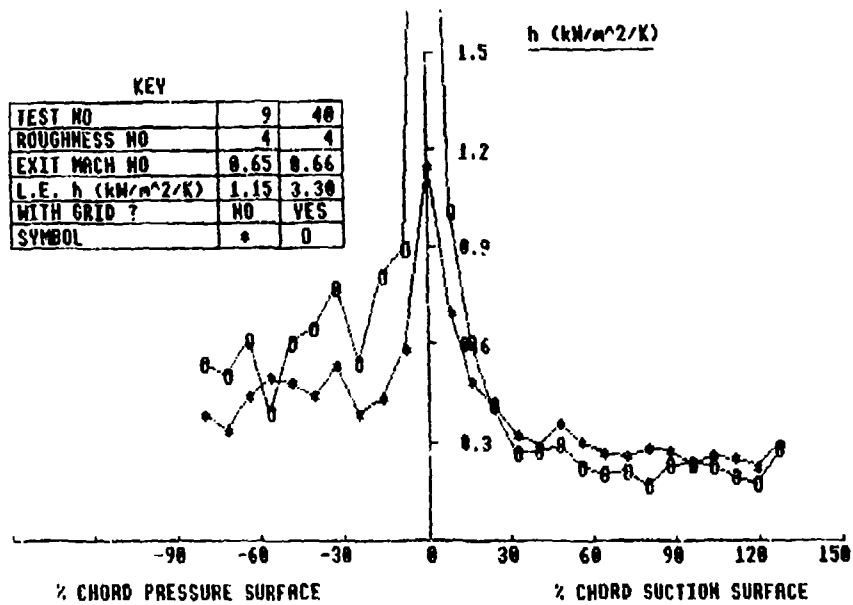


Fig. 10 Effect of turbulence grid (7%) on rough (No.4) blade

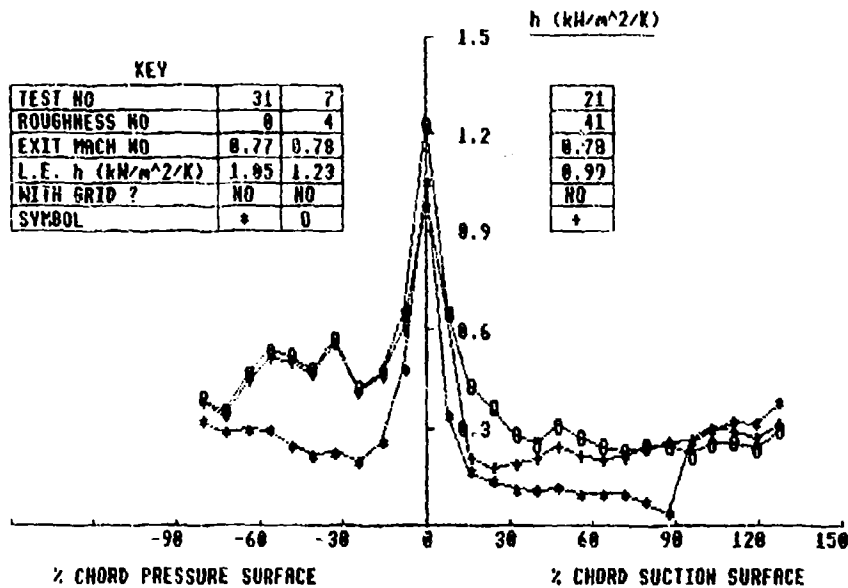


Fig.11 Effect of roughness (No.4) on pressure surface only.
No turbulence grid, $M = 0.78$.

DISCUSSION

H.I.H.Saravanamuttoo, Ca

In the oral presentation pictures were shown of both a new and a service expired blade from an Olympus 593; the paper would be enhanced by the inclusion of these pictures. It seems that this particular blade is an odd choice, as it operates in an environment which is very clean. This blade also operates continuously at very high temperature because of the Concorde flight regime. Were any other blades examined? It would seem likely that blades from marine engines such as the Tyne would be more exposed to conditions increasing the blade roughness significantly.

Author's Reply

The rough and pitted Olympus 593 blade was shown to indicate that erosion levels even in clean operation can reach the levels of accreted roughness tested. I include below two photographs of the surface of a "time served" aero engine blade, each about one inch square of surface. The leading edge of the suction surface at mid span has a roughness of 50–100 μ m and the trailing edge of the pressure surface 10–15 μ m.

Blades other than the Olympus 593 have been examined but we do not have enough data to form any firm conclusions as to how service operation in different areas on on different fuels affects erosion or the accretion of dirt. There seems to be little interaction between the maintenance departments and the blade cooling designers in most companies and we are finding it difficult to obtain sufficient data. We at Sussex would be grateful for samples of hardware, nozzle guide vanes or rotor blades, that have seen service to enable a picture to be built up of how roughness progresses in the different applications.

From our initial results it appears that a new engine with smooth, highly polished blades may have very different boundary layer flows to one which has served a thousand hours or so in a sandy or marine environment — even with filters. It would be to the advantage of all engine builders if the sparse and scattered data on service roughness were to be collected and its effects on heat transfer — and thus blade life — estimated.



THE EFFECT OF DENSITY RATIO ON THE FILM-COOLING OF A FLAT PLATE

C. J. P. Forth, P. J. Loftus and T. V. Jones

University of Oxford
Department of Engineering Science
Parks Road
Oxford
OX1 3PJ
U.K.

SUMMARY

The paper illustrates the effect of varying the ratio of coolant-to-freestream density on the film-cooling process. This effect is of great importance since most design data has been acquired at temperature ratios and hence density ratios far removed from those occurring in modern gas turbines. There is no consensus at present on how to scale this data to engine conditions. Experimental data is presented for heat transfer downstream from a single row of 30 degree-inclined film-cooling holes, obtained for air at a wide range of gas-to-coolant temperature ratios. These results exhibit a marked effect of density ratio. Scaling is discussed, and good collapse of data is achieved in the two regimes identified, characterised by weak and strong blowing. Conditions representative of the turbine environment are created using an Isentropic Light Piston Tunnel: the Mach Number $M = 0.55$, and the unit Reynolds Number $Re/m = 2.7 \times 10^7/m$. The experiments are unique in that they simulate the gas-to-coolant and gas-to-wall temperature ratios typical of those in gas turbines, producing density ratios hitherto only attained in experiments employing foreign gas injection.

NOMENCLATURE

a	Speed of sound, m/s
c_p	Specific heat at constant pressure, J/kgK
d	Hole diameter, m
h	Heat transfer coefficient, W/m^2K
k	Thermal conductivity, W/mK
p	Pressure, Pa
q	Heat transfer rate, W/m^2
T	Temperature, K
u	Velocity, m/s
x, y, z	Cartesian co-ordinates measured from hole centres, m
μ	Dynamic viscosity, kg/ms
ρ	Density, kg/m^3

Subscripts

cp	Incompressible, constant properties
i	Injection
o	Without injection
t	Total conditions
w	Wall
∞	Freestream

Non-dimensional Numbers

$G = \rho_i u_i / \rho_\infty u_\infty$	Blowing Rate
$J = \mu_i u_i^2 / \rho_\infty u_\infty^2$	Momentum Flux Ratio
$M = u_\infty / a_\infty$	Mach Number
$Nu = qx/k_{t\infty} (T_{t\infty} - T_w)$	Nusselt Number
$Re = \rho_\infty u_\infty X / \mu_\infty$	Reynolds Number

$$\theta = (T_{t\infty} - T_{ti}) / (T_{t\infty} - T_w)$$

INTRODUCTION

Film-cooling is one of the methods employed in gas turbines to ensure that the metal temperature is lower than that of the hot combusted mainstream gas. This is achieved by injecting a cooler secondary gas through discrete holes on the blade surface, so that downstream of the injection location, this fluid acts as an insulating layer and a heat sink. An increase in turbine entry temperature improves the thermodynamic efficiency, whilst lowering the surface temperature can dramatically increase component life.

The technique has been the subject of research for over thirty years and Goldstein's review[1] provides a summary of the main developments. Much of the early work, for example, Goldstein, Eckert and Ramsey[2] and Liess[3], used a slightly heated secondary fluid so that the injection-to-freestream density ratio was close to unity. The question remained as to how to utilise this data in a gas turbine environment where this density ratio is about 1.7. Goldstein, Eckert and Burggraf[4] simulate the effect of density ratio, which results from the injection-to-freestream temperature ratio, by using Freon vapour as an injection fluid. Other experimenters, for example Burns and Stollery[5], Pai and Whitelaw[6] and Pedersen et al.[7], also employ foreign gas injection but measure its mass fraction at an impermeable wall downstream. A mass transfer analogy is then invoked to infer heat transfer information. The results from these techniques indicate that there should be a significant effect of injection-to-freestream temperature ratio.

In addition to simulating representative injection-to-freestream density ratios, it is also important to ensure that the relevant surface temperature boundary condition is preserved. A film-cooled gas turbine blade is more closely approximated by an isothermal rather than an adiabatic surface. In the steady state experiments [2] to [7], adiabatic wall information was obtained; the present study, using a transient test facility, employs an isothermal surface.

In summary, the results presented reflect a desire to perform experiments which are directly applicable to the gas turbine environment. This is achieved in two ways:

(i) by ensuring that representative injection-to-freestream temperature ratios are used. This implies that not only will the density ratio be correct but also ensures that the temperature-induced property variations resulting from the difference in wall, injection and freestream temperatures will be present. In fact, two effects can be isolated: the injection-to-freestream temperature (or density) ratio effect, and the effect of transport property variations through the injection layer;

(ii) by preserving an isothermal surface boundary condition.

It should be noted that the present testing allows for the independent variation of injection-to-freestream velocity and density ratios. This is essential in order to determine the scaling parameters which govern film-cooling, a subject about which there is still considerable debate. It is of great interest since correct scaling should reveal information about the fundamental mechanisms of the process; in addition, it will allow data obtained at unrepresentative conditions to be used with accuracy in engine design. Injection and freestream pressures are also measured, since these quantities are known by the designer and any scaling which can be achieved using these will be independent of any assumption made about the manner in which the injected gas emerges.

DEFINITION OF HEAT TRANSFER COEFFICIENT - THE SUPERPOSITION MODEL

In this approach, following Metzger et al.[8], the wall temperature is referenced to the freestream temperature, so that the effect of injection can be contained wholly within a heat transfer coefficient:

$$q(x) = h(x)(T_w - T_{t\infty})$$

This description relies on the constant properties, incompressible flow form of the boundary layer energy equation, which is linear and homogeneous in temperature. Thus, superposition can be applied, and a sum of solutions with different sets of boundary conditions will also be a solution for the boundary condition which is the sum of those sets. As described by Loftus and Jones[9], a temperature field in the presence of film-cooling may therefore be represented as

$$T(x, y, z) = T_1(x, y, z) [T_w - T_{t\infty}] + T_2(x, y, z) [T_{ti} - T_w]$$

T_1 is the field for a unit temperature difference between wall and freestream, with the coolant at the wall temperature, and T_2 is the field for a unit temperature difference between coolant and wall, with the wall at the freestream temperature. Differentiating with respect to y , setting $y = 0$ and spanwise averaging gives

$$q(x) = h_1(x) [T_w - T_{t\infty}] + h_2(x) [T_{ti} - T_w]$$

where the suffices refer to the conditions above. Dividing this by the heat transfer rate without injection,

$$\frac{q}{q_0}(x) = \frac{h_1}{h_0}(x) + \frac{h_2}{h_0}(x) \frac{T_{t1} - T_w}{T_w - T_{t\infty}}$$

This may be rearranged in terms of the non-dimensional temperature parameter theta to give

$$\frac{q}{q_0}(x) = A(x) + B(x)\theta$$

At a given Reynolds Number, if there is no effect of gas-to-wall temperature ratio, this may be written in terms of the Nusselt Number as

$$\frac{Nu}{Nu_0}(x) = A(x) + B(x)\theta$$

$A(x)$ and $B(x)$ are dependent on the freestream and injection conditions, and will be constants for a given geometry and flowfield. Each has a concise physical interpretation: when the coolant is at the freestream temperature, theta is zero and A quantifies the change in heat transfer produced by the mixing of the two flows. B quantifies the change in heat transfer produced by the injection temperature being different from the mainstream temperature. The quotient $-B/A$ is the local adiabatic wall effectiveness occurring when the wall temperature is isothermal at the local adiabatic wall temperature.

Thus the superposition model predicts that for a given flowfield, the Nusselt Number is linearly dependent on theta. In order to keep the flowfield constant, the freestream and injection temperature must be held constant, so that the only satisfactory way in which to vary theta is to alter the wall temperature. The parameters A and B are the intercept and slope respectively of the Nusselt Number versus theta plots, non-dimensionalised by the unblown level of Nusselt Number at that position. It is the purpose of this investigation to show how these parameters A and B , (or linear combinations corresponding to given values of theta) scale with injection rate.

EXPERIMENTAL FACILITY

Results were obtained using an Isentropic Light Piston Tunnel, a comprehensive description of which can be found in [9] and [10]. It is a transient facility in which test gas is compressed in a tube by an air-driven piston before flowing through the working section at constant temperature and pressure. Schematics of the tunnel and working section are shown in Figs. 1 and 2.

The unit Reynolds Number was $2.7 \times 10^7/m$, and the Mach Number was 0.55, fixed by a downstream throat. Testing was carried out at four injection-to-freestream total temperature ratios, as shown in Table 1. It was possible to pre-cool either the test gas or the injection gas using a liquid nitrogen heat exchanger, and to heat the injection gas using electrical heaters. Similarly, the flat plate could be pre-heated or pre-cooled by forced convection over a range $280 < T_w < 365$ K. The upstream boundary layer was fully turbulent. The injection geometry was a single row of 30 degree-inclined holes, with a pitch-to-diameter ratio of 2.5. Data was collected at nine downstream locations over the range $2 < x/d < 98$.

Wall temperatures and spanwise-averaged heat transfer rates were measured using thin film gauges, the theory and use of which is described by Schultz and Jones[11]. Fast response micro-thermocouples were used to measure gas temperatures; the mainstream thermocouple was mounted in a stagnation probe. Absolute pressures were measured using Kistler transducers, and National Semiconductor transducers were employed for differential pressure measurements. The run time was about 0.5 s and data was acquired and processed on a PDP 11/10 mini-computer.

RESULTS AND DISCUSSION

1. Linearity of Nusselt Number with Theta

Figs. 3 and 4 are examples of results obtained for fixed injection and mainstream temperatures, varying theta by heating or cooling the wall prior to each run. These show that over the range of theta investigated, the heat transfer coefficient varies linearly with theta for a given mainstream and injection flow. This result is in agreement with Metzger et al.'s results for slot injection, and Loftus' results[12], and validates the superposition model.

Fig. 5 shows clearly that different lines, characterised by different values of A and B , result from changing the injection-to-freestream temperature ratio at the same blowing rate.

2. Effect of Property Variations Through the Injection Layer

It has been observed by Fitt et al. [13] that on an unblown flat plate, there is a dependence of the level of Nusselt Number on the gas-to-wall temperature ratio. This is due to temperature-induced property variations through the boundary layer, and can be represented as

$$Nu = Nu_{cp} \left(\frac{T_w}{T_{t\infty}} \right)^n$$

The experimentally derived value of n was used in order to non-dimensionalise the film-cooled levels of Nusselt Number by the unblown Nusselt Number at the corresponding gas-to-wall temperature ratio. It is possible that the choice of the isothermal adiabatic wall temperature would be preferred for use in this correction, but this does not affect the magnitude of the correction greatly. It should be noted that this effect is not large enough to noticeably affect the linear relationship of the Nusselt Number with theta over the relatively small variation in gas-to-wall temperature ratio produced by changing the wall temperature at constant mainstream temperature. However, when comparing the levels of Nusselt Number at different mainstream temperatures, the variation in gas-to-wall temperature ratio is large enough to become significant.

3. General Effects of Injection

The variation of A and B with distance and blowing rate at a given injection-to-freestream density ratio can be seen in Figs. 6 and 7. At low blowing rates, the value of A is very close to unity except close to the holes, where the mixing process enhances the heat transfer rate. As the blowing rate increases, the effect becomes more pronounced, particularly at small x/d , where there can be as much as 60% enhancement. At large blowing rates, the value of A tends to decrease again close to the holes, but continues to rise slowly at large values of x/d . The value of A at an injection-to-freestream density ratio of unity should be the same as the value of h/h_0 . A comparison between the present data and that of Liess and Hay et al. [14] is shown in Fig. 8.

Fig. 7 shows that at low blowing rates, the value of B is close to zero apart from at $x/d = 2$. This implies that the fact that the coolant is at a different temperature from the mainstream flow has considerable effect close to the holes, beyond which turbulent mixing causes the injection jets to become diluted by the mainstream. When the blowing rate is increased to $G = 0.39$ this injection temperature effect becomes larger at all x/d 's, but is most pronounced close to the hole where B reaches a value of -0.96 . Further increase in blowing rate causes a dramatic decrease in the magnitude of B close to the holes, whilst it continues to increase steadily far downstream. An interpretation of this is that if the injection jets lift off the surface, their effectiveness as a relatively cool insulating layer would be reduced. Further downstream, where these jets may have re-attached, the increased coolant mass flow will result in dilution by the mainstream being relatively less at a given position.

Fig. 9 shows that at $x/d = 2$, the combination of the mixing effect and the injection temperature effect results in a maximum in the effectiveness as the blowing rate is increased, for a given injection-to-freestream temperature ratio. This is qualitatively similar to results from adiabatic wall effectiveness investigations, such as [2]. It can also be seen that there is a significant effect of injection-to-freestream temperature or density ratio. As the injection-to-freestream temperature ratio decreases, the blowing rate corresponding to maximum effectiveness increases. Mass transfer results by Foster and Lampard [15] for the centreline effectiveness downstream from 90 degree holes, and by Pedersen et al. for 35 degree holes, also display this trend.

4. Scaling Parameters

It is concluded from the above results that the blowing rate is not a good scaling parameter of the injection process. For low injection rates, this may be because any lift off phenomenon associated with maximum cooling effectiveness may depend on the momentum flux of the injection flow relative to the freestream. Fig. 10 shows that this parameter, the momentum flux ratio, scales weak injection results (i.e. at injection rates below maximum effectiveness) very well. Following Pedersen et al., good collapse of the strong injection data was achieved using injection-to-freestream velocity ratio, Fig. 11.

Jones [16], using dimensional analysis, suggests a Weak Injection Parameter and a Strong Injection Parameter which can be defined purely in terms of stagnation conditions and a static pressure. This would be very convenient to the designer since no mass flow measurements are required. For weak injection, the flow within the injection hole is greatly affected by recovery of the freestream against the coolant and

$$\text{Weak Injection Parameter} = \frac{P_{t1} - P_{\infty}}{P_{t\infty} - P_{\infty}}$$

The Strong Injection Parameter is derived to be applicable for injection rates where the coolant emerges as a "solid" body against which the freestream recovers pressure. Then

$$\text{Strong Injection Parameter} = \frac{P_{ti} - P_{\infty}}{P_{t\infty} - P_w} \bigg/ \frac{P_{ti} T_{t\infty}}{P_{t\infty} T_{ti}}$$

Good correlation of data from Foster and Lampard, and Pedersen et al. was achieved using these two parameters [16]. Correlation with the Weak Injection Parameter is to be expected if data collapse is good with the momentum flux ratio. The present data at $x/d = 2$ is shown to scale well against the Strong Injection Parameter in Fig. 12. Fig. 13 shows that there is a similar dependence on the injection-to-freestream temperature ratio at $x/d = 8$. A value of $\theta = 1.3$ was chosen since the data was acquired in this region, and because it is a representative engine value. The minima of the curves for each injection-to-freestream temperature ratio are brought together when plotted against the Strong Injection Parameter, Fig. 14.

CONCLUSION

The effect of injection-to-freestream density ratio on the level of heat transfer to a film-cooled flat plate has been demonstrated close to the holes. As the density ratio increases, the blowing rate at which maximum cooling effectiveness occurs increases.

For this particular geometry, the results at low injection rates scale well with momentum flux ratio or the Weak Injection Parameter. At injection rates above that which gives a maximum in cooling effectiveness close to the holes, the results correlate with velocity ratio and with the Strong Injection Parameter. The two parameters proposed by Jones offer advantages as they do not require knowledge of the mass flow characteristics of the coolant holes.

REFERENCES

1. Goldstein, R. J., "Film Cooling", in *Advances in Heat Transfer*, Academic Press, 1971.
2. Goldstein, R. J., Eckert, E. R. G. and Ramsey, J. W., "Film Cooling with Injection Through Holes: Adiabatic Wall Temperatures Downstream of a Circular Hole", *Journal of Engineering for Power*, 80, 1968.
3. Liess, C., "Experimental Investigation of Film Cooling with Ejection from a Row of Holes for the Application to Gas Turbine Blades", *Journal of Engineering for Power*, 97, Pt. 1, 1975.
4. Goldstein, R. J., Eckert, E. R. G. and Burggraf, F., "Effects of Hole Geometry and Density on Three-Dimensional Film Cooling", *International Journal of Heat and Mass Transfer*, 17, 1974.
5. Burns, W. K. and Stollery, J. L., "The Influence of Foreign Gas Injection and Slot Geometry on Film Cooling Effectiveness", *International Journal of Heat and Mass Transfer*, 12, 1969.
6. Pai, B. R. and Whitelaw, J. H., "The Influence of Density Gradients on the Effectiveness of Film Cooling", *ARC CP 1013*, 1968.
7. Pedersen, D. R., Eckert, E. R. G. and Goldstein, R. J., "Film Cooling with Large Density Differences between the Mainstream and the Secondary Fluid Measured by the Heat-Mass Transfer Analogy", *Journal of Heat Transfer*, 99, 1977.
8. Metzger, D. E., Carper, H. J. and Swank, L. R., "Heat Transfer with Film Cooling Near Non-Tangential Injection Slots", *Journal of Engineering for Power*, 90, 1968.
9. Loftus, P. J. and Jones, T. V., "The Effect of Temperature Ratios on the Film Cooling Process", *ASME 82-GT-305*, 1982.
10. Jones, T. V., Schultz, D. L. and Hendley, A. D., "On the Flow in an Isentropic Light Piston Tunnel", *ARC 34217*, 1973.
11. Schultz, D. L. and Jones, T. V., "Heat Transfer Measurements in Short Duration Hypersonic Facilities", *AG 165*, 1973.
12. Loftus, P. J., "Determination of Heat Transfer Coefficients in the Presence of Film Cooling", *D.Phil. Thesis*, 1982.
13. Fitt, A. D., Forth, C. J. P., Robertson, B. A. and Jones, T. V., "Temperature Ratio Effects in Compressible Turbulent Boundary Layers", submitted for publication, *International Journal of Heat and Mass Transfer*.
14. Hay, N., Lampard, D. and Saluja, C. L., "Effects of Cooling Films on the Heat Transfer Coefficient on a Flat Plate with Zero Mainstream Pressure Gradient", *ASME 84-GT-40*, 1984.
15. Foster, N. W. and Lampard, D., "Effects of Density and Velocity Ratio on Discrete Hole Film Cooling", *AIAA Journal*, 13, No. 8, 1975.
16. Jones, T. V., "The Superposition Model of Film Cooling and Fluid Dynamic Scaling", *VKI Lecture Series*, 1982.

ACKNOWLEDGEMENTS

The authors are grateful to Rolls-Royce Ltd. and the SERC for their support.

Symbol	T_{E1} K	$T_{E\infty}$ K	$T_{E1} / T_{E\infty}$
□	270	540	0.50
x	300	500	0.60
o	300	365	0.82
+	345	280	1.23

Table 1
Key to Operating Temperature Ratios

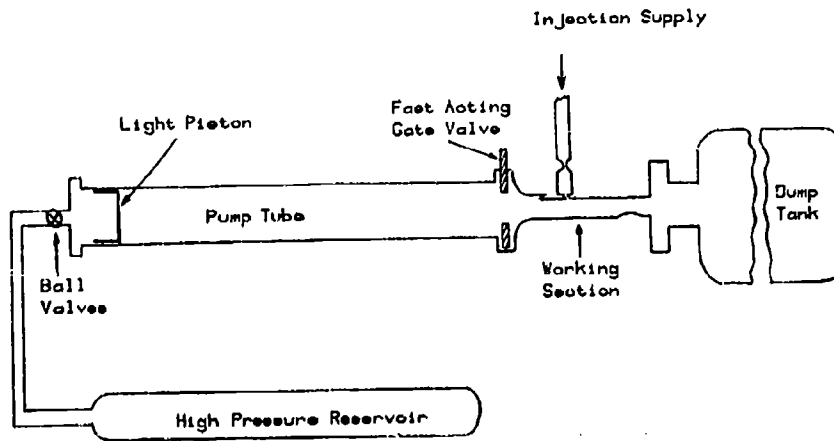


FIG 1 : Schematic of Tunnel.

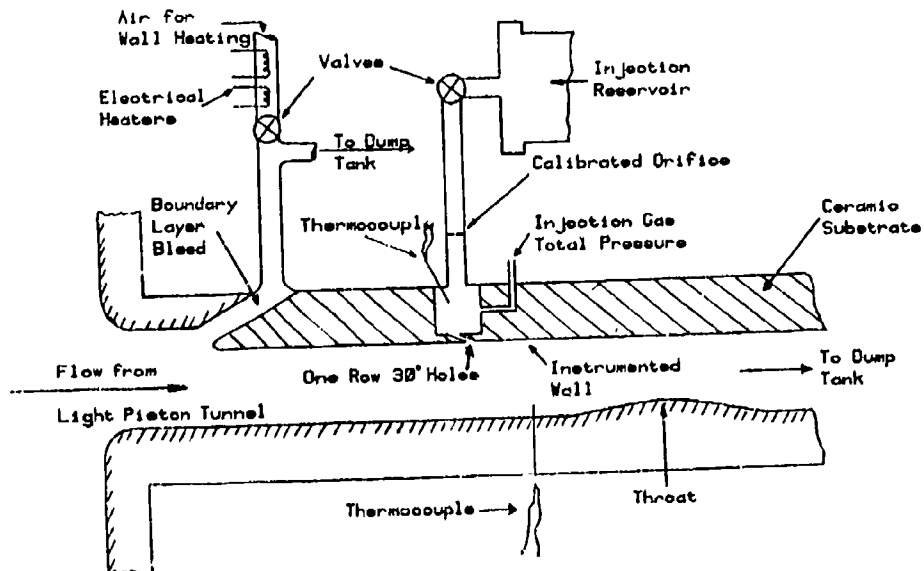


FIG 2 : Schematic of Working Section.

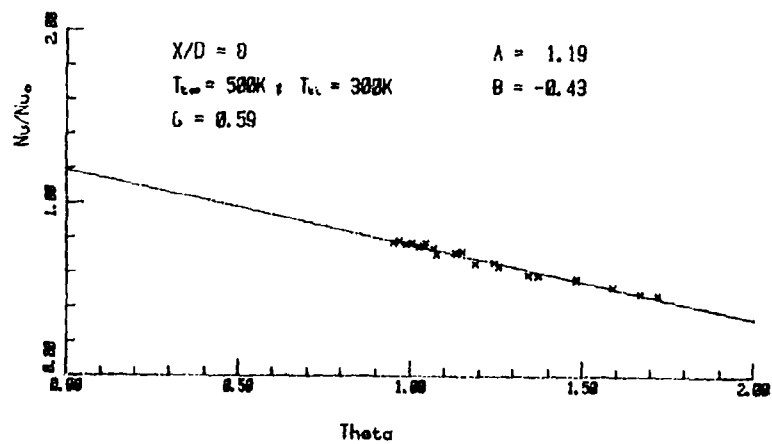


FIG 3

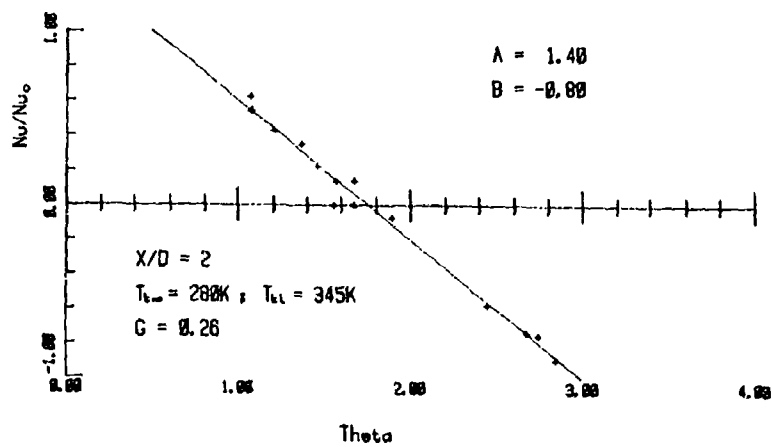


FIG 4

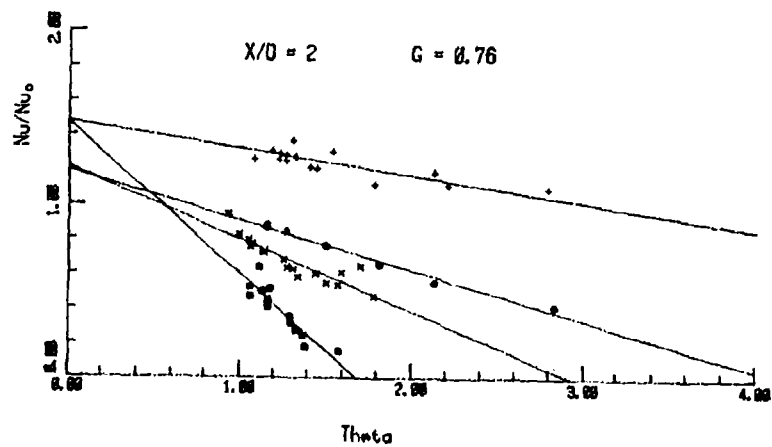


FIG 5

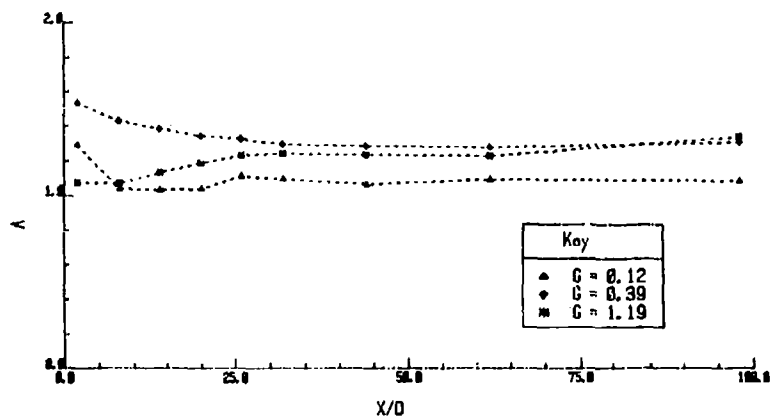


FIG 6 : Variation of λ with distance and Blowing Rate ;
Mainstream Temp. 500 K ; Injection Temp. 300 K.

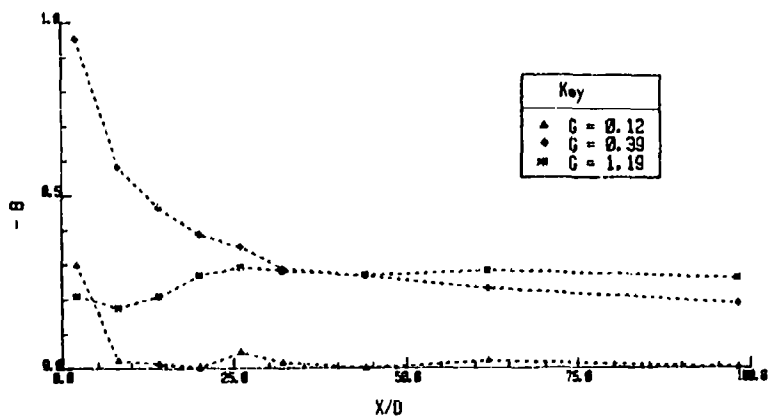


FIG 7 : Variation of B with distance and Blowing Rate ;
Mainstream Temp. 500 K ; Injection Temp. 300 K.

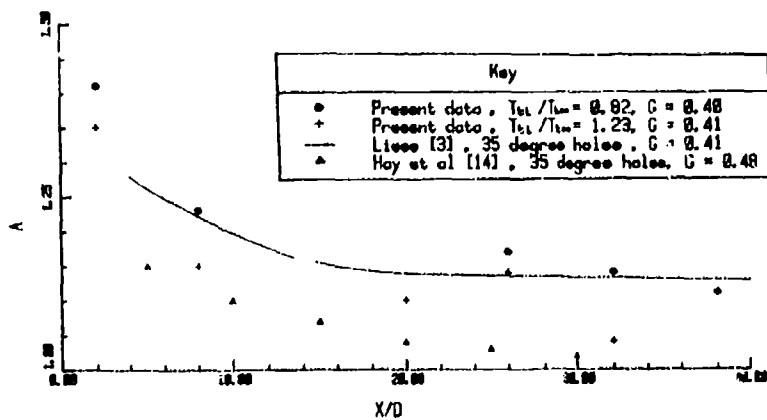


FIG 8 : Comparison of spanwise-averaged heat transfer
coefficient ratio h/h_0 with references [3] and [14].

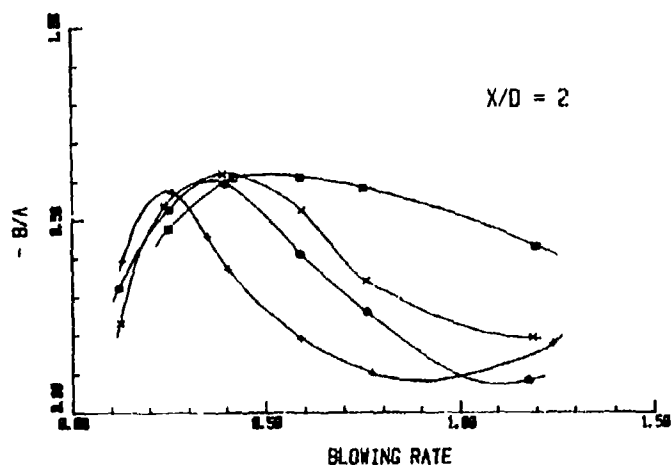


FIG 9 : Variation of Isothermal, Adiabatic Wall Effectiveness with Blowing Rate and Injection-to-freestream temperature ratio.

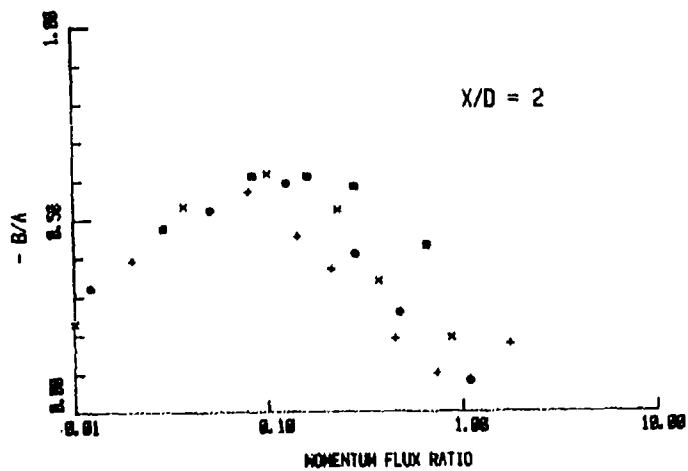


FIG 10 : Variation of Isothermal, Adiabatic Wall Effectiveness with Momentum Flux Ratio and Injection-to-freestream temperature ratio.

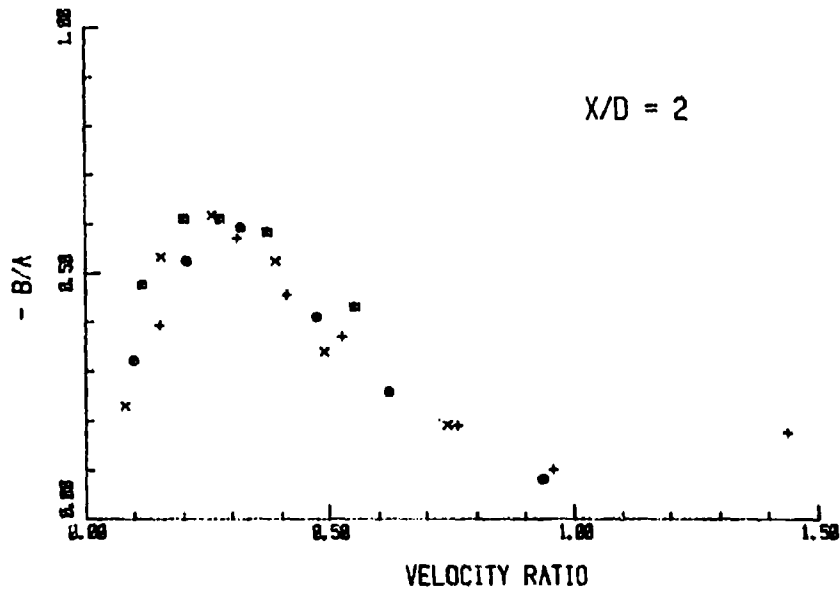


FIG 11 : Variation of Isothermal, Adiabatic Wall Effectiveness with Velocity Ratio and Injection-to-freestream temperature ratio.

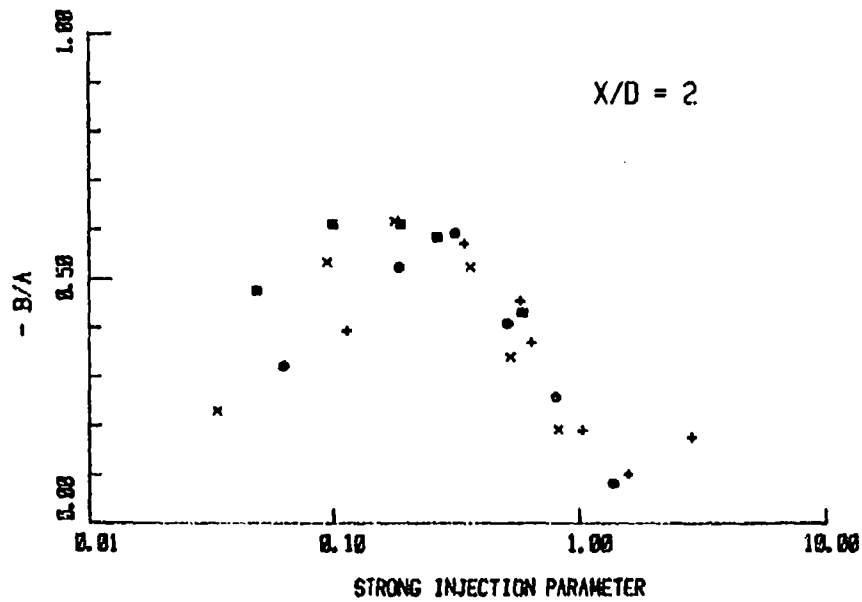


FIG 12 : Variation of Isothermal, Adiabatic Wall Effectiveness with Strong Injection Parameter and Injection-to-freestream temperature ratio.

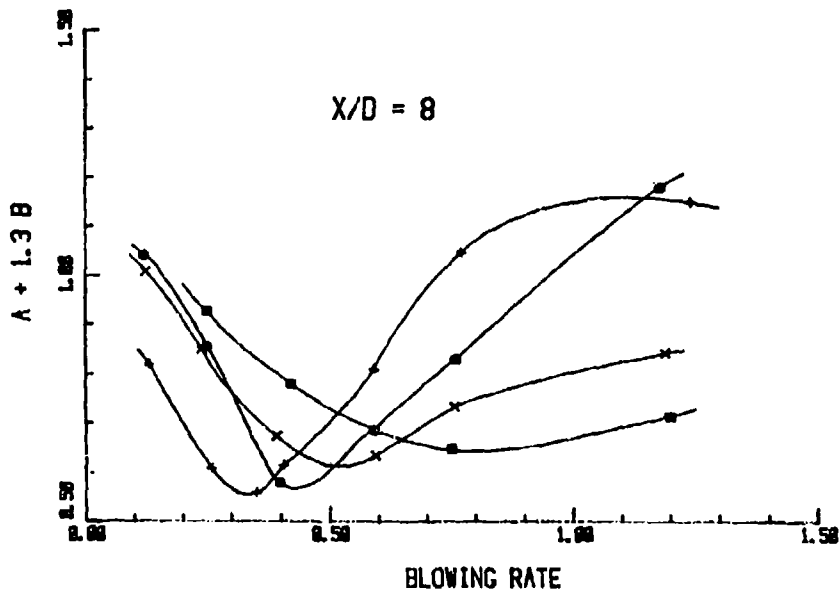


FIG 13 : Variation of Level of Heat Transfer with Blowing Rate and Injection-to-freestream Temperature ratio at Theta = 1.3 .

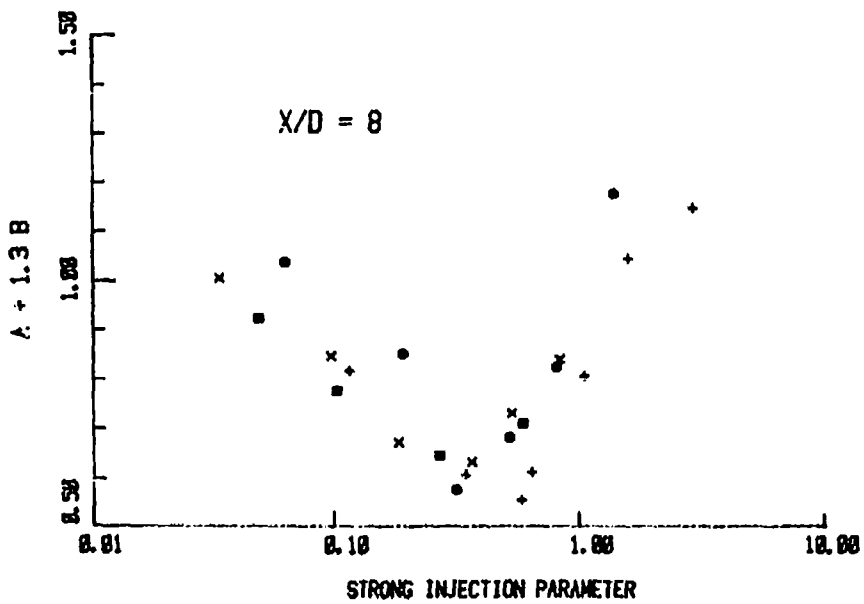


FIG 14 : Variation of Level of Heat Transfer with Strong Injection Parameter at Theta = 1.3 .

DISCUSSION

G.E.Andrews, UK

The simulation of correct density ratios by heating the mainstream gas has been a feature of film cooling research for combustion chamber applications for many years and our test rig at Leeds is typical of the types of test facility that has been used. However, as you have pointed out these types of investigations have been much less common in single row film cooling for turbine blade applications. Your results are most useful in distinguishing between the separate effects of mixing and density ratio. One aspect that may not be simulated in your work is the consequences of active heat transfer within the wall. The heating of the coolant air passing through the wall decreases the density ratio and θ but increases the coolant velocity. Was there any evidence in your results that this effect was significant for the heated wall situation where you used wall temperatures up to 365°K? In order that any potential effects can be calculated could you give more details on the hole geometry including the diameter and hole length? Was the coolant flow established at steady state prior to the actuation of the isentropic compression?

Author's Reply

We appreciate that experiments with large temperature ratios have been conducted in the field of combustion chamber film cooling. However, our results are unique in that they are a systematic study to characterize the effect of coolant to freestream temperature ratio on heat transfer. As you have observed, this throws light on the question of coolant-to-freestream density ratio. Heat transfer within the cooling holes obviously took place when the coolant was at a different temperature to the wall. However, as noted in the reply to the previous question, the coolant centre-line exit temperature was the same as the plenum temperature. The coolant flow was established at the same instant as the mainstream and this enabled the coolant conditions to be known accurately as well as preserving an essentially isothermal wall.

D.E.Metzger, US

You confirm that as long as you blow at low enough rate through the holes and you avoid separating the flow, the results correlate on the basis of momentum ratio, otherwise they correlate on velocity ratio. Is there an advantage that you see for correlating on the basis of what you call the "weak and strong injection parameter" versus what people have been correlating on momentum flux ratio or velocity ratio?

Author's Reply

The injection velocity is a rather fictitious value and so it appears to be slightly more concise to correlate in terms of measurable pressures, which are possibly known more accurately by the engine designer than will be these flow field measurements of density and velocity.

D.E.Metzger, US

Where must the designer measure the pressure associated with the injected flow?

Author's Reply

In the plenum itself.

M.Suo, US

The film cooling characteristics should depend upon the temperature of the gas as it is injected. The measured coolant temperature is in the plenum. Do you have an estimate of the coolant temperature as it enters the mainstream?

Author's Reply

The temperature of the gas leaving the injection holes has been measured using extremely fine thermocouples. It was found that the coolant exit centreline temperature was the same as the temperature in the plenum. This was to be expected, for the value of the length to diameter ratio of the holes was only five. The coolant therefore had a temperature profile at exit, being equal to the wall temperature at the wall and equal to the plenum temperature on the centreline. As shown in Loftus and Jones [9] the principle of superposition may still be applied if the coolant has a self similar temperature profile and the coolant temperature may be defined by the coolant exit centreline temperature. Thus the coolant temperature referred to in the paper may be considered as the coolant temperature in the plenum on the centreline exit temperature for the geometry examined.

ETUDES DES TRANSFERTS THERMIQUES
SUR LES PLATES-FORMES DE DISTRIBUTEUR DE TURBINE
AVEC ET SANS FILM DE REFROIDISSEMENT

par
Anne-Elisabeth BOURGUIGNON
Etudes Générales Aérothermiques
S.N.E.C.M.A.
Centre de Villaroche
77550 MOISSY-CRAMAYEL

RESUME

La sévérité de l'environnement aérothermique des distributeurs haute pression des moteurs modernes oblige à refroidir leurs plates-formes en utilisant les techniques jusqu'ici réservées aux aubages (convection, films...).

Des études expérimentales ont permis de mesurer les coefficients d'échange sur plusieurs plates-formes comportant différentes configurations de refroidissement par film, et de caractériser les écoulements au voisinage de la paroi.

Ce document présente l'analyse des résultats obtenus en les situant par rapport aux prédictions. Les corrélations déduites de cette analyse ont permis de mettre au point une méthode générale de détermination des coefficients de transfert thermique intégrant l'effet de l'injection d'air de refroidissement.

NOTATIONS

T : température des gaz chauds
T_p : température de paroi
h : coefficient de transfert thermique
x : abscisse curviligne
λ : conductivité thermique
μ : viscosité dynamique
A : constante adimensionnelle
Nu : nombre de Nusselt
Re : nombre de Reynolds
D : diamètre des orifices

1 - INTRODUCTION

L'augmentation des pressions et des températures qui règnent devant les turbines des moteurs modernes rend nécessaire le refroidissement de plus en plus efficace des plates-formes des distributeurs haute pression, pièces qui jusqu'ici n'étaient pas critiques. Afin d'optimiser celles-ci, une bonne connaissance des écoulements tridimensionnels qui régissent les échanges au niveau des parois de veine apparaît nécessaire, afin de mettre au point des méthodes de prédiction des coefficients de transfert thermique et des efficacités adiabatiques de film sur les plates-formes. Leur validation est assurée entre autre par la réalisation d'essais effectués sur des grilles d'aubes dans des conditions représentatives de celles rencontrées sur moteur.

Parallèlement au développement de ces méthodes de calcul dont la disponibilité n'est aujourd'hui prévue qu'à moyen terme, les essais effectués sont utilisés pour mettre au point des corrélations simplifiées permettant d'appréhender les coefficients d'échange et efficacités de film avec une bonne précision. Les résultats obtenus font l'objet de cette publication.

2 - ETAT DE L'ART

Peu d'études ont jusqu'ici été consacrées aux écoulements existants au niveau des plates-formes de distributeur HP. Une analyse bibliographique effectuée à ce sujet a permis de faire le point sur la connaissance des écoulements secondaires du point de vue aérodynamique et thermique.

2.1.- Description des écoulements secondaires

Les différentes études qui ont été entreprises et particulièrement les essais de visualisation ont permis de décrire les écoulements secondaires au niveau des plates-formes. La figure 1 illustre les phénomènes tridimensionnels rencontrés. Les lignes de courant se séparent au bord d'attaque de l'aubage et s'enroulent en deux bras qui dégènerent en zones tourbillonnaires: le tourbillon en fer à cheval. Le premier bras qui s'enroule au bord d'attaque et passe de l'intrados de l'aube à l'extrados de l'aube adjacente en traversant le canal est le tourbillon de passage; le second qui s'enroule en sens inverse et reste plaqué contre l'extrados de l'aube est le tourbillon de coin. La zone de séparation de ces tourbillons est considérée comme une zone de recirculation analogue à celle créée par une couche limite, qui se développant sur une plaque plane est perturbée par un obstacle cylindrique.

2.2.- Les transferts thermiques sur la plate-forme

L'analyse bibliographique effectuée à ce sujet a permis de recenser des expériences qui pour la plupart ne sont pas représentatives des phénomènes rencontrés sur moteur (maquettes grande échelle, vitesse et accélération trop faibles par rapport à ce qui existe sur un distributeur HP, grilles ne restituant pas la périodicité de l'écoulement...) et qui souvent ne sont pas exploitables du fait du manque d'informations relatives aux conditions d'essais.

A partir de l'étude des différents auteurs, il est impossible de conclure sur l'état de la couche limite qui est successivement considérée comme turbulente ou laminaire. L'hypothèse de la régénération d'une couche limite en aval du tourbillon en fer à cheval est souvent présentée. Des zones de relaminarisation en amont du col de la grille ont été décelées par certains auteurs. D'autre part, aucune méthode de calcul permettant d'appréhender les coefficients de transfert thermique avec une bonne précision n'apparaît : les méthodes de calcul bidimensionnelles de couche limite utilisant des modèles de turbulence montrent des écarts pouvant aller de 50 à 100% avec les résultats de mesure. Seule une corrélation $Nu = f(Re^{0,8})$, le Reynolds étant basé sur la ligne de courant moyenne de l'écoulement potentiel est proposée par un auteur, mais aucune validation de cette formule n'a pu être effectuée sur d'autres essais.

D'autre part, si certains résultats sont publiés sur les coefficients de transfert thermique qui règnent au niveau des plates-formes, aucune information n'apparaît sur la protection par film (influence sur les coefficients de transfert, efficacité, trajectoire...).

2.3. Nécessité de développer un programme d'études

Compte tenu des conditions de plus en plus sévères rencontrées sur les moteurs modernes, les plates-formes de distributeurs voient des températures de plus en plus élevées, qui pour une TET de 1850K peuvent atteindre localement 2070K. A ces valeurs intrinsèques, il faut ajouter les très fortes hétérogénéités des températures qui règnent dans ces régions d'écoulements secondaires et qui risquent d'engendrer sur la plate-forme, des gradients thermiques prohibitifs pour la tenue mécanique.

La recherche d'un refroidissement efficace est donc rendue nécessaire; afin de minimiser les débits de refroidissement utilisés, il est indispensable de connaître les conditions limites externes et en particulier les coefficients de transfert thermique qui pour des pressions supérieures à 25 bars ont des niveaux très élevés.

Aussi la SNECMA a-t-elle décidé de réaliser son propre programme d'essais permettant d'acquiescer dans des conditions de fonctionnement réalistes et sur du matériel représentatif des moteurs, les informations nécessaires à la mise au point des méthodes de calcul des échanges thermiques avec et sans film sur les plates-formes de distributeur.

3 - MONTAGE D'ESSAI

La campagne d'essais a eu lieu à l'Institut Von Karman sur une grille d'aubes représentative de ce qui est réalisé par la SNECMA sur les moteurs modernes.

3.1.-Veine d'essai

Le montage d'essai est composé d'une grille plane de huit aubes permettant de respecter la périodicité de l'écoulement dans le canal central qui est le canal d'étude. Les plates-formes inférieures et supérieures sont simulées par des plaques planes dans lesquelles viennent s'encastrent les aubages (figure 2). Les couches limites qui se développent à l'amont du modèle sont aspirées comme le montre la figure 3.

3.2.-Les perçages

Plusieurs types de perçage ont été réalisés sur les plates-formes. La maquette 1 (figure 4) présente trois rangées d'émissions dont les orifices sont percés parallèlement à l'axe moteur. La maquette 2 (figure 5) présente la même définition du perçage que la maquette 1, mais la ligne d'orifices a été déplacée de façon à ce que la rangée soit située sur une isomach. Quant à la maquette 3 (figure 5), elle ne diffère de la seconde maquette que par l'orientation des perçages par rapport à l'axe moteur, un drapage vers l'intrados ayant été introduit.

3.3.-Instrumentation

Chacune des plaques ainsi définies a été équipée d'une importante instrumentation :

- une cinquantaine de mesures de pression
- entre 90 et 100 mesures de flux suivant les capacités de chaque plaque.

Les deux types de prises de mesure étaient principalement implantés dans le canal central, quelques mesures de surveillance ayant été ajoutées dans les canaux latéraux. Une illustration de cette instrumentation est présentée sur la figure 6.

4 - CONDITIONS D'ESSAIS

L'instrumentation et les essais ont été réalisés à l'Institut Von Karman dans la soufflerie à rafales CT2 pour les essais thermiques et dans la soufflerie C3 pour les mesures aérodynamiques.

Les essais ont été réalisés de manière à respecter les conditions de similitude par rapport aux conditions qui sont rencontrées dans la réalité; les caractéristiques sont définies par :

- Nombre de Prandtl : 0,72
- Nombre de Mach aval : 1,30
- Nombre de Reynolds par mètre : $46 \cdot 10^6$
- Rapport des températures : $\frac{T}{T_p} : 1,32$

5 - MESURES AERODYNAMIQUES

5.1.-Répartition du nombre de Mach

Les répartitions de pression ont été mesurées sur les différentes plates-formes en présence ou non de chacune des trois zones d'émission. La répartition du nombre de Mach mesurée pour le fonctionnement sans film est présentée sur la figure 7. L'influence des émissions sur la répartition du nombre de Mach est faible, seule la présence des films situés au niveau du col (émission 3 pour les deux plates-formes 2 et 3) influe sur la répartition des lignes de Mach f et g situées en amont de la zone d'émission comme le montre la figure 8. La répartition aval reste quant à elle inchangée.

5.2.-Visualisation des lignes de courant à la paroi

Parallèlement aux mesures de pression qui ont été effectuées sur les plates-formes, les trajectoires des lignes de courant ont été visualisées à l'aide d'un dépôt d'huile mélangée avec un oxyde de titane et de la poudre de talc. Un exemple de visualisation est présenté sur la figure 9, pour un essai sans émission. La déviation des lignes de courant de l'intrados vers l'extrados apparaît nettement. De même, en présence de film, les trajectographies ont été réalisées comme le montre la figure 10, pour la plate-forme numéro 1, les trois zones d'émission étant alimentées.

La comparaison des lignes de courant visualisées avec et sans film est présentée sur la figure 11; si l'effet dû à la première rangée n'apparaît que très localement, les seconde et troisième rangées modifient les trajectoires des lignes de courant de façon importante, celles-ci se rapprochant de celles de l'écoulement potentiel. La même comparaison effectuée sur la plate-forme numéro 2 montre un résultat différent, les lignes de courant n'étant que très localement affectées par la présence des émissions, l'effet n'intervenant qu'à la sortie des émissions, comme le montre la figure 12. Il en est de même pour la troisième plate-forme où la modification des lignes de courant n'apparaît que sur quelques millimètres en aval des orifices d'émission. De ces résultats, il ressort que si l'angle de perçage affecte localement la trajectoire des lignes de courant, "l'effet de rangée" semble jouer un rôle primordial dans la déviation possible de celles-ci.

6 - MESURES DES COEFFICIENTS DE TRANSFERT THERMIQUE

6.1. Résultats sur les plates-formes sans film

Les mesures des flux thermiques au niveau de la paroi ont été dépeignées en utilisant les résultats aérodynamiques (répartition des lignes de Mach et des lignes de courant) obtenus lors de la première partie de la campagne d'essai.

Il a été recherché des corrélations donnant le transfert thermique sous la forme $Nu_x = f(Re_x)$, par analogie avec la plaque plane, avec :

$$Nu_x = \frac{h}{\lambda} x$$

$$Re_x = \frac{U \rho x}{\mu}$$

Ces relations ont été appliquées sur les lignes de courant telles de la plate-forme déterminées lors des visualisations. Deux régions distinctes apparaissent alors :

- une région dite "aval" où l'origine des lignes de courant se trouve à la paroi intrados de l'aube, les particules provenant d'un niveau supérieur et entraînées par l'écoulement transversal apparaissant sur la plate-forme à cet endroit.

- une région dite "amont" pour laquelle l'origine des lignes de courant est plus délicate à déterminer et qui a été fixée au niveau du film de chambre considéré comme point de départ de la couche limite après que celle issue du becquet ait décollé en cet endroit (cf figure 3).

Notons que la séparation des deux régions qui a été faite correspond physiquement à la position des points de la plate-forme par rapport au tourbillon en fer à cheval (tourbillon de passage).

L'analyse des mesures effectuées sur les trois plates-formes sans émission de film a permis de déterminer une corrélation pour la zone aval, de la forme (figure 1) :

$$Nu_x = A Re_x^{0,8}$$

Cette loi s'apparente fortement à celle obtenue pour une couche limite turbulente se développant sur une plaque plane, bien que le coefficient A qui a une valeur unique pour l'ensemble des lignes de courant soit différent; l'exposant affecté au nombre de Reynolds calculé en chaque point sur la ligne de courant tend à prouver, que dans la zone aval, l'écoulement est d'origine turbulente.

Une comparaison des résultats obtenus a été faite avec un programme de calcul de la couche limite le long de cette ligne de courant par différences finies, utilisant un modèle de comportement de la turbulence, et est présentée sur la figure 13 : une relaminarisation de la couche limite turbulente apparaît en amont du col, suivie d'une nouvelle transition, phénomène qui n'est pas confirmé par les mesures. Si ce type de méthode de calcul du développement de la couche limite apparaît tout à fait adapté à la prévision des échanges pour des écoulements bidimensionnels, son utilisation dans des zones d'écoulements secondaires n'apporte pas de résultats satisfaisants.

Pour la zone "amont", le même type de corrélation que pour la zone "aval" a été obtenue (Figure 14).

$$Nu_x = B Re_x^{0,8}$$

Toutefois, la grande dispersion des mesures observée dans cette région ne permet pas d'accorder à cette corrélation une grande valeur, l'importance des phénomènes tridimensionnels étant telle que seule la mise au point des méthodes de calcul sophistiquées permettra d'approcher de façon précise les échanges thermiques.

6.2. - Résultats sur les plates-formes en présence de film

En présence des films émis par chacune des zones d'émission des trois plates-formes, les mesures des échanges thermiques ont été effectuées. La comparaison de ces valeurs à celles mesurées sur les plates-formes non refroidies par film montre un comportement analogue à celui rencontré sur les plaques planes où seule la zone située immédiatement en aval des orifices d'émission présente une augmentation importante du coefficient d'échange, tandis qu'ailleurs sa valeur reste équivalente à ce qu'elle aurait été sans la présence du film comme l'illustre pour la seconde plate-forme la figure 15.

La méthode d'analyse des résultats est analogue à celle qui a été utilisée pour corréler les coefficients de transfert thermique sans film, les mesures ayant été dépouillées sur les lignes de courant visualisées. Toutefois, compte tenu de l'impossibilité actuelle de prévoir les lignes de courant en présence de film et afin de pouvoir aboutir à des corrélations utilisables pour le dimensionnement thermique des plates-formes, les différentes mesures ont été étudiées pour les trajectographies des plates-formes non refroidies par film.

Pour une valeur connue du taux de soufflage m , les rapports des coefficients d'échange avec film aux coefficients d'échange sans film ont été tracés sur la figure 16 en fonction du rapport x/D de la distance à l'injection au diamètre D des orifices d'émission. Bien que la dispersion des mesures soit assez grande, une corrélation, regroupant l'ensemble des résultats obtenus pour les trois plates-formes a pu être déterminée, donnant l'augmentation du coefficient de transfert thermique en fonction du rapport x/D . Conformément à l'analyse qualitative qui avait été faite précédemment, la corrélation obtenue montre qu'au delà de 10 diamètres, l'influence de la présence du film sur la valeur du coefficient de transfert thermique devient négligeable. L'incertitude qui apparaît est maximale dans la zone de forte modification du coefficient d'échange juste en aval du film ($x/D < 10$) : compte tenu de l'importance du phénomène de pompage thermique dû à la convection dans les orifices d'émission, et comme l'augmentation de coefficient d'échange reste relativement modérée, l'erreur qui sera faite sur l'estimation des coefficients de transfert thermique externes dans cette zone du fait de l'imprécision de la corrélation n'entraînera qu'une faible incertitude sur la prévision des températures métal.

6.3.-Efficacité de film

Bien que les résultats sur les efficacités de film ne fassent pas l'objet de cette présentation, il est intéressant de signaler que des mesures d'efficacité ont été réalisées pour chacun des films des trois plates-formes et ont permis de mettre en évidence certains résultats :

- un film émis en amont de la zone de séparation peut être entraîné dans le tourbillon de passage et réapparaître à la sortie de la grille avec une très forte efficacité;
- les caractéristiques géométriques qui influencent l'efficacité de film sont similaires à celles qui ont été déterminées pour la plaque plane;
- pour certains films, un comportement analogue à celui des films se développant sur une plaque plane a été constaté.

La mise au point des corrélations donnant les efficacités de film en fonction des paramètres géométriques des percages et des paramètres de l'écoulement a été entreprise à la SNECMA.

7 - APPORT DE L'ETUDE POUR LE DIMENSIONNEMENT DES PLATES-FORMES

7.1.-Etat de la couche limite

Les études entreprises à partir des essais que la SNECMA a fait réaliser à l'I.V.K ont permis de trouver, que pour des conditions de similitude par rapport à celles rencontrées sur moteur, la couche limite, dont le comportement est de type turbulent, se décompose en deux zones situées de part et d'autre du tourbillon de passage. La présence d'un film ne modifie globalement pas le comportement de cette couche limite.

7.2.-Application d'un modèle de calcul

Conformément aux résultats de l'analyse bibliographique, les méthodes de calcul bidimensionnelles de la couche limite se sont avérées inutilisables pour décrire les écoulements sur les plates-formes.

Des corrélations ont été mises au point permettant d'obtenir le coefficient de transfert thermique en chaque point de la plate-forme. Elles ont été appliquées aux expériences pour lesquelles nous disposions de suffisamment d'informations concernant les conditions d'essais : la séparation amont-aval de l'écoulement a été retrouvée et les formules appliquées sur les lignes de courant permettent de retrouver les résultats de mesure avec une précision correcte (20 %). Ces résultats permettent de valider notre démarche.

7.3.-Utilisation des corrélations

Les corrélations qui ont été mises au point sont appliquées au dimensionnement thermique des pièces moteur et permettent de prédire les coefficients d'échange sans film avec une bonne précision; une correction locale peut être appliquée à ces coefficients d'échange en présence d'un film représentatif de ceux qui ont été testés (nombre de rangées, taux de soufflage, position...).

L'amélioration des méthodes de prédiction des échanges au niveau des plates-formes des distributeurs HP permet d'envisager l'augmentation des conditions de température et de pression qui règnent devant les turbines avec confiance, le dimensionnement de leur système de refroidissement pouvant se faire avec un degré de confiance se rapprochant de celui qui existe aujourd'hui sur les aubages.

8 - CONCLUSION

Une série d'essais destinés à mettre au point des méthodes de calcul tridimensionnelles des transferts thermiques le long des parois baignées par les écoulements secondaires a été réalisée. Une analyse simplifiée des résultats obtenus a permis de définir des corrélations donnant les coefficients d'échange sur les plates-formes de distributeur en présence ou non de film; ces formules qui ont été validées sur d'autres essais réalisés par la SNECMA ou issus de recherches bibliographiques permettent de dimensionner le comportement thermique des plates-formes avec une bonne précision.

REFERENCES

- M.F. BLAIR "An Experimental study of heat transfer and film cooling on large-scale turbine endwalls".
ASME publication - J. of transfer, Nov 1974 - pp 524 - 529
- D.P. GEORGIU - M. GODARD - B.E. RICHARDS
"Experimental study of the iso-heat transfer rate lines on the endwall of a turbine cascade".
ASME paper 79 - GT - 20 - 1979

- L.S. LANGSTON - M.L. NICE - R.M. HOOPER
"Three - dimensional flow within a turbine cascade passage".
ASME paper - 76 - GT - 50
- R.A. GRAZIANI - M.F. BLAIR - J.R. TAYLOR - R.E. MAYLE
"An experimental study of endwall and airfoil surface heat transfer in a large scale turbine blade cascade".
ASME paper 79 - GT - 99 - 1979
- R.E. GAUGLER - L.M. RUSSEL
"Streakline flow visualization study of a horseshoe vortex in a large scale, two - dimensional turbine stator cascade".
ASME paper 80 - GT - 4 - 1980
- M.G. DUNN - F.J. STODDARD
"Measurement of heat transfer rate to a gas turbine stator"
Journal of engineering power - April 1970 - vol 101 - pp 275 - 280
"Studies of heat transfer to gas turbine components"
A.F. Aero propulsion laboratory TR 77 - 66 - october 1977
- D.K. WINSTANLEY - T.C. BOOTH - M.G. DUNN
"The predictability of turbine vane convection heat transfer"
AIAA/SAE/ASME 17th Joint Propulsion Conference July 27 - 29 - 1981
Colorado Spings
- YASUTOSHI SENOO "The boundary layer on the endwall of a turbine nozzle cascade"
ASME paper 57 - A - 172 - May 1957
- E.G. NAREZHNYI "Heat transfer of uncooled inter profil end surface of turbine stage"
Izvestiya VUZ - Aviatsionnaya Teknika Vol 20 - n°3 - pp83 - 80 - 1977
- Ph. MARCHAL - C.H. STEVERDING
"Secondary flows vithin turbomachinery bladings"
AGARD - CP - 214 - PARIS - 1977 - paper II
- MARI.C MATHIEU. J
"Méthode de prédiction de la transition de la couche limite"
AGARD Conference, Copenhagen (Mai 1977)

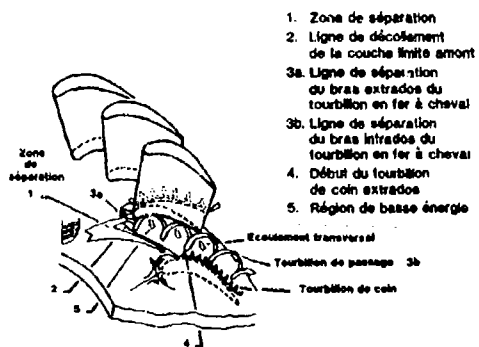


FIG. 1 ILLUSTRATION DE L'ÉCOULEMENT
TOURBILLONNAIRE AU NIVEAU DE
LA PLATE-FORME

1. Zone de séparation
2. Ligne de décollement de la couche limite amont
- 3a. Ligne de séparation du bras extrados du tourbillon en fer à cheval
- 3b. Ligne de séparation du bras intrados du tourbillon en fer à cheval
4. Début du tourbillon de coin extrados
5. Région de basse énergie



FIG. 2 MONTAGE D'ESSAIS

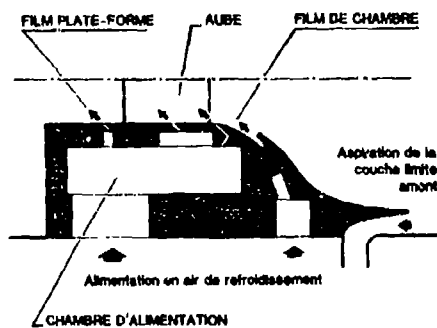


FIG. 3 COUPE TRANSVERSALE DANS
LE MONTAGE D'ESSAI

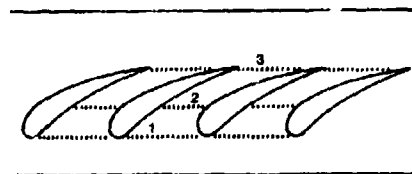


FIG. 4 POSITION DU PERCAGE - MAQUETTE N° 1

ORIENTATION PERCAGE { → maquette 2
→ maquette 3

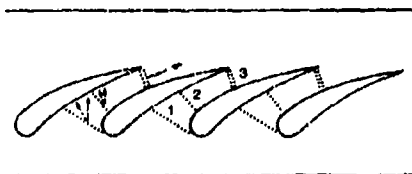


FIG. 5 POSITION DU PERCAGE -
MAQUETTE N° 2 ET N° 3

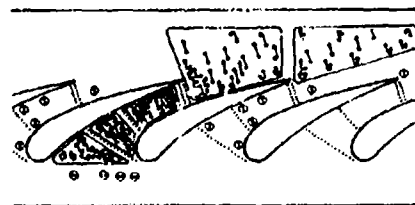


FIG. 6 INSTRUMENTATION EN FLUXMÈTRES DE
LA MAQUETTE 2

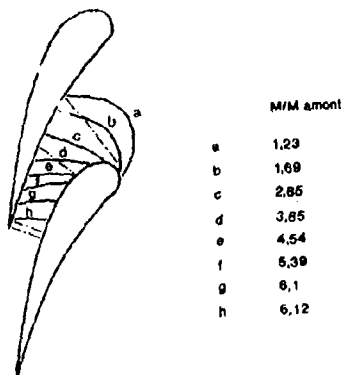


FIG. 7 REPARTITION DU NOMBRE DE MACH SUR LA PLATE-FORME SANS EMISSION

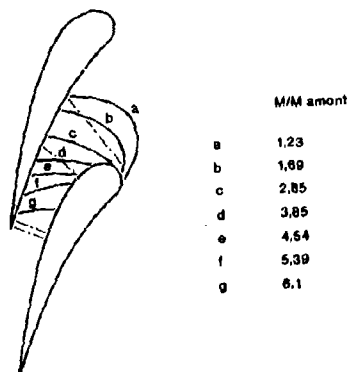


FIG. 8 INFLUENCE DES EMISSIONS SUR LA REPARTITION DU NOMBRE DE MACH



FIG. 9 VISUALISATION DES LIGNES DE COURANT SUR LES PLATES-FORMES NON PERCEES



FIG. 10 VISUALISATION DES LIGNES DE COURANT SUR LA PLATE-FORME N° 1 EN PRESENCE DES TROIS RANGÉES DE FILM

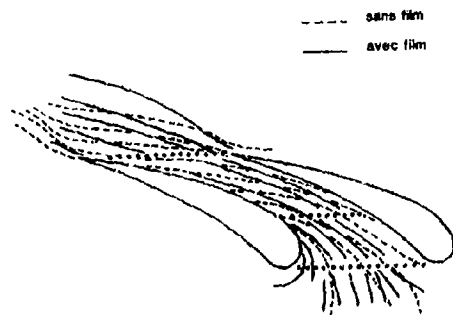


FIG. 11 COMPARAISON DES LIGNES DE COURANT SUR LA PLATE-FORME N°1 EN PRESENCE OU NON DES TROIS RANGÉES DE FILM

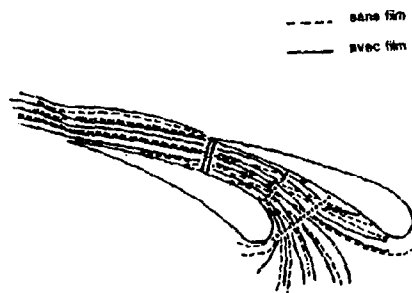


FIG. 12 COMPARAISON DES LIGNES DE COURANT SUR LA PLATE-FORME N°2 EN PRESENCE OU NON DES TROIS RANGÉES DE FILM

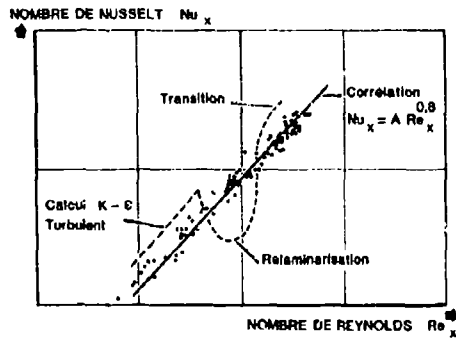


FIG. 13 EVOLUTION DES TRANSFERTS DE CHALEUR SUR UNE LIGNE DE COURANT REELLE DE LA PLATE-FORME COMPARAISON ESSAI-CALCUL

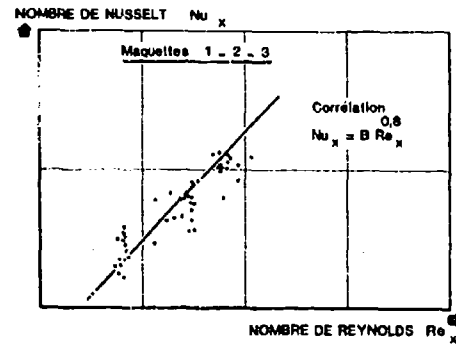


FIG. 14 CORRELATION $Nu_x = f(Re_x)$ -ZONE AMONT - MAQUETTES N° 1,2,3

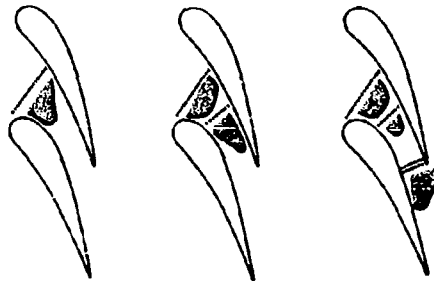


FIG. 15 PLATE-FORME N° 2 - ZONES OU LE COEFFICIENT D'ÉCHANGE EST FORTEMENT INFLUENCÉ PAR LA PRÉSENCE DU FILM

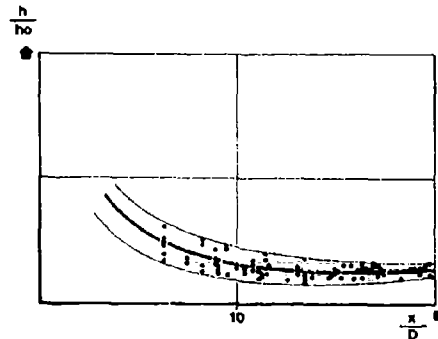


FIG. 16 INFLUENCE DU FILM SUR LE COEFFICIENT DE TRANSFERT THERMIQUE POUR LES PLATES-FORMES 1, 2, 3 ET POUR LES TROIS ÉMISSIONS

DISCUSSION

J.J.Witton, UK

Could you please give a value for the vertical axis of Fig.16?

Author's Reply

Je suis désolée, mais je ne peux pas.

SHROUD SEGMENTS FOR UNSHROUDED BLADE TURBINES

by
 Mr. R. S. Attwood C. Eng. M.I. Mech. E.,
 Mechanical Technology,
 Rolls Royce Limited,
 Moor Lane,
 P.O. Box 31,
 DERBY.
 DE2 8BJ
 U.K.

1. SUMMARY

For hot and high speed turbines it is desirable to use blades without tip shrouds, which are an embarrassment from the point of view of centrifugal weight and cooling. The static shroud segments are then exposed to very severe thermal conditions.

It is difficult to design shroud segments which will survive these conditions without demanding so much cooling air that the specific fuel consumption advantage of the shroudless blade is completely absorbed.

The problem involves two parameters:- cooling requirements and integrity.

Therefore, for a variety of possible segment section design concepts, the first part of this paper will examine fundamental relationships which control the cooling requirements.

The second part of the paper explains the decision to evaluate experimentally the integrity of section designs, and a description and technical justification of the chosen test technique, which overcomes the heat-transfer compromises involved in testing at atmospheric pressure.

2. NOMENCLATURE

		ASSUMED VALUE	
T _g	Gas temperature	1300	°C
h _g	Hot side heat transfer coefficient	17,400	w/m ² /°C
C _p	Specific heat of cooling air	1005	Joules/kg/°C
T _{c1}	Cooling air temperature	600	°C
T ₁	Temperature of hot surface of ceramic		°C
T ₂	Temperature of hot compliant metal surface		°C
T ₃	Temperature of hot metal surface		°C
T ₄	Temperature of cold metal surface		°C
T _{c2}	Cooling air outlet temperature		°C
η	Cooling efficiency		
q	Heat flux		w/m ²
K _m	Conductivity of metal substrate	20	w/m/°C
K _c	Conductivity of ceramic (YSZ)	.8	w/m/°C
K _i	Conductivity of Compliant Layer	1.1	w/m/°C
x _c	Thickness of ceramic		mm
x _i	Thickness of Compliant Layer		mm
x _m	Thickness of metal substrate	2.0	mm
M	Engine core gas mass flow	131.5	kg/sec
M	Cooling air flow		kg/sec
	Shroud area	.113	m ²

3. INTRODUCTION

The great majority of Rolls-Royce gas turbine aero-engines have used shrouded blade turbines, giving good tip sealing as well as good performance retention. The cooling of the static shroud segments against which the blade tip shrouds run is relatively easy and effective, since a film of cooling air, both from an annular release in front of the segments and from blade cooling air released from the blade tips, is easily established and maintained over the full axial length of the liner. This means that the cooling air requirements are quite low and relatively low temperature materials may be used.

Demands for increased gas turbine efficiencies in the longer term can be satisfied by running the turbine hotter and faster. In these circumstances the blade tip shroud is an embarrassment, from the point of view of its C.F. weight and the extra cooling air required, both for the shroud itself and for the aerofoil, so that it may carry the weight of the shroud. However, deletion of the tip shroud exposes the static shroud segments directly to the turbine gases. Also, in order to minimise over tip leakage, the tip clearance between the blades and the segments must be kept as low as possible, E.G. 0.2-0.3 mm. This gives a very high heat transfer coefficient, with little chance of maintaining a cooling film, so that the heat flux into the shroud segment is much greater than with shrouded blades.

Unless great sophistication is designed into the cooling system, together with the choice of the right materials, the efficiency gains from the use of the higher speed turbine will be sacrificed completely by the need for extra expensive cooling air. In addition to this there are a number of other criteria which need to be satisfied, abrasability, erosion and oxidation resistance, and mechanical integrity. Each of these aspects of performance merits a substantial programme of research. Therefore, in order to render the task manageable, this paper addresses only the problems of cooling and integrity in the conditions of extreme thermal cycling.

The first part of the paper examines the steady state thermal requirements, leading to estimates of required quantities of cooling air flow for different section constructions. The second part of the paper is concerned with the integrity of ceramic layers and examines the transient temperature behaviour in an idealised engine cycle, bearing in mind the need to define some simple rig tests which can be used to evaluate those designs featuring ceramic.

4. SHROUD COOLING ANALYSIS

Before specifying and developing a shroud design, it is important to understand the fundamental thermal constraints which apply to various types of section. The purpose of this exercise therefore, is to examine the requirements which must be satisfied by a shroud design. Various alternative design proposals are examined, starting with bare metal and progressing, via ceramic coated metal substrates, to ceramic coated substrates incorporating a compliant intermediate layer.

The thermal model chosen is simply a one dimensional heat transfer calculation through a slab or sandwich corresponding to the shroud segment design being investigated. The steady state conditions are calculated by solving a set of simultaneous equations, corresponding to the various layers of the section.

Many of the quantities used in the equations are themselves variable, but for this very basic assessment, representative constant values are used. This should not invalidate the broad and general conclusions produced by the analysis. In order to assess the cost of cooling air required, a hypothetical engine is considered. The dimensions, temperatures and air flows, together with the values of other constants used, are set out with the nomenclature.

The maximum local annulus gas temperature T_g , is assumed to be 1300°C (1573°K) this is approximately equal to the mean flame temperature at take off of an engine using shroudless blades, so it typically applies to a hot streak condition with some dilution due to combustion chamber wall cooling. The heat transfer coefficient, h_g , is assumed to be 17,100 watts/m²/°K. Information on heat transfer coefficients applying to the hot surface of a shroud segment is sparse. The chosen value is the best estimate available for a single value, to be applied for the whole of the segment.

The temperature of cooling air used to cool the shrouds is taken to be 600°C and corresponds to using HP compressor delivery air. As on the hot side, to do precise calculations, one should define a heat transfer coefficient for the cold side - h_c . This is, however, directly dependant on the mass of cooling air used and this needs to be minimised. Also, the choice of cooling system has yet to be resolved and this too affects h_c , so this method of procedure in this instance is not appropriate. Therefore the calculations in this paper avoid this difficulty by using the concept of cooling efficiency η . As a result the product ηM , which is a measure of the 'cooling demand', now appears as a parameter in the calculations. The virtue of this approach is that it allows the decisions on the type of cooling system and the quantity of cooling air used to be left to the end of the analysis.

$$\eta = \frac{\text{temperature gain of cooling air}}{\text{temperature differential, metal to cooling air}} = \frac{T_{c2} - T_{c1}}{T_4 - T_{c1}}$$

4.1 UNCOATED METAL SHROUDS (Impingement or convection cooled)

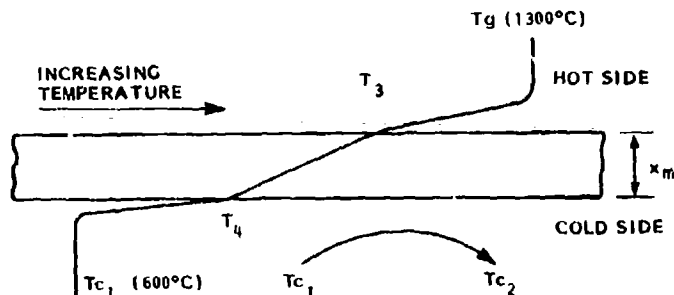


FIG 1 THERMAL GRADIENTS

The one-dimensional heat flux equations are set out below.

$$\text{HEAT FLUX } q \left\{ \begin{array}{l} = hg (T_g - T_3) \quad (1) \\ = \frac{K_m}{x_m} \times 10^{-3} (T_3 - T_4) \quad (2) \\ = M Cp (T_c2 - T_c1) = \eta M Cp (T_4 - T_c1) \quad (3) \end{array} \right.$$

$$\text{from (1)} \quad (T_g - T_3) = q/hg \quad (4)$$

$$\text{from (2) + (3)} \quad (T_3 - T_c1) = q \left(\frac{x_m \times 10^{-3}}{K_m} + \frac{1}{\eta M Cp} \right) \quad (5)$$

$$\text{divide (4) by (5)} \quad \frac{T_g - T_3}{T_3 - T_c1} = \frac{1000/hg}{\frac{x_m}{K_m} + \frac{1}{\eta M Cp}} \quad (6)$$

If T_3 is taken as 1050°C (maximum for an oxidation resistant coating or material like the 'MCrAlY' alloys).

$$\frac{T_g - T_3}{T_3 - T_c1} = \frac{1300 - 1050}{1050 - 600} = .555 \quad (7)$$

Transposing (6) and entering values for the constants, we get

$$\eta M = \frac{1}{1005} \cdot \frac{1000}{\frac{1000}{17400 \times .555} - \frac{x_m}{20}} \quad (8)$$

$$\eta M = \frac{19.9}{2.07 - x_m} \quad (9)$$

It is convenient to express the quantity ηM as a percentage, i.e. a decimal for η and a percentage of engine HP air used for cooling (M), i.e. $\frac{M}{131.5} \times 100$, for the area of the full shroud annulus (.113m²).

$$\text{Therefore } \eta M = .113 \times \frac{100}{131.5} \times \frac{19.9}{2.07 - x_m} = \frac{1.71}{2.07 - x_m} \% \quad (10)$$

This equation shows that the heat transfer coefficient on the hot side is so high that, even with an infinite heat sink on the cold side, the hot surface metal temperature cannot be brought down to 1050°C when the metal thickness exceeds 2 mm. The heat flux is so high that it needs a large temperature gradient to draw the heat through the metal and there is then left no temperature difference between the cool side metal and the cooling air.

4.2 METAL SHROUDS (Transpiration cooled)

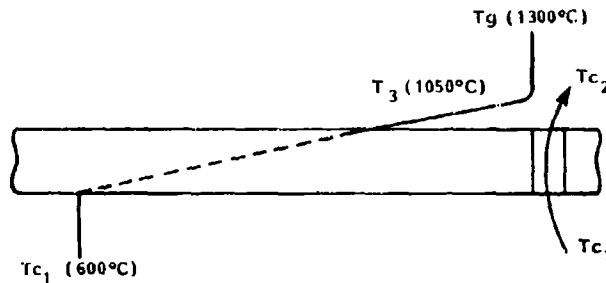


FIG 2 THERMAL GRADIENTS

For this configuration η must be redefined, substituting T_3 for T_4 for the cooled metal temperature, since the cooling air now has the potential for cooling the full metal thickness, including the metal at the highest temperature.

$$\eta = \frac{T_{C2} - T_{C1}}{T_3 - T_{C1}} \quad (11)$$

$$\text{HEAT FLUX } q \begin{cases} = h_g (T_g - T_3) \\ = \eta M C_p (T_3 - T_{C1}) \end{cases} \quad (12)$$

Processing these equations for the full shroud, in decimal-percentage terms as before yields:-

$$\eta M = .825 \% \quad (13)$$

This value is plotted as a single point on Fig 6, together with other curves generated later. Note that this is a constant value, not dependant on the thickness of the section. Note also that the cooling flow requirement may be halved, by halving the heat transfer coefficient (h_g), increasing the tolerable metal temperature (T_3) to 1150°C, decreasing the gas temperature (T_g) to 1175°C, or decreasing the cooling air temperature to 150°C.

If the insulating effect of the cooling air as a result of the formation of a film on the hot surface is ignored, the maximum value of η which might be assumed for this system is 0.3. This leaves a cooling air mass flow requirement of 2.75%, which is very high and demonstrates the desirability of effective film cooling with all - metal shrouds.

4.3 METAL SUBSTRATE WITH CERAMIC COATING

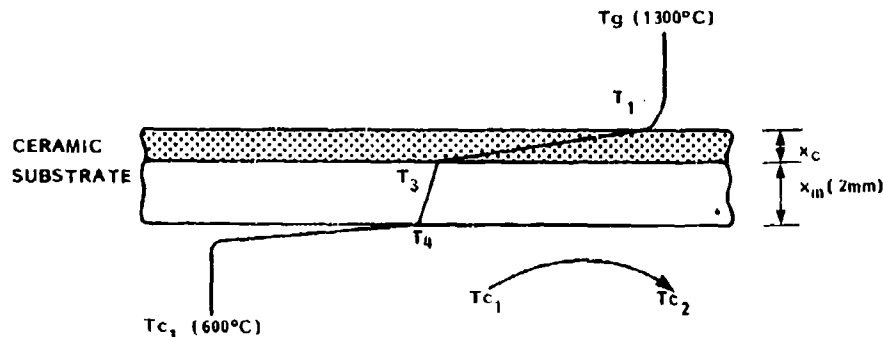


FIG 3 THERMAL GRADIENTS

Now η is defined as for 4.1, using T_4 in place of T_3 , giving the following equations:

$$\text{HEAT FLUX } q \left\{ \begin{array}{l} = hg (T_g - T_1) \quad (14) \\ = \frac{K_c}{x_c \times 10^{-3}} (T_1 - T_3) \quad (15) \\ = \frac{K_m}{x_m \times 10^{-3}} (T_3 - T_4) \quad (16) \\ = \eta M C_p (T_4 - T_{c1}) \quad (17) \end{array} \right.$$

Now by adding (14) and (15), then dividing by (16) + (17) we get:-

$$\frac{T_g - T_3}{T_3 - T_{c1}} = \frac{\frac{1000}{hg} + \frac{x_c}{K_c}}{\frac{1000}{\eta M C_p} + \frac{x_m}{K_m}} \quad (18)$$

It is now assumed that the maximum substrate temperature (T_3) is 950°C , to allow the use of a lower grade of metal for the substrate.

$$\text{Therefore } \frac{T_g - T_3}{T_3 - T_{c1}} = \frac{1300 - 950}{950 - 600} = 1 \quad (19)$$

Substitute this in equation (17) and re-arrange to get:-

$$\eta M = \frac{1000}{\left(\frac{1000}{hg} + \frac{x_c}{K_c} - \frac{x_m}{K_m} \right) C_p} \quad (20)$$

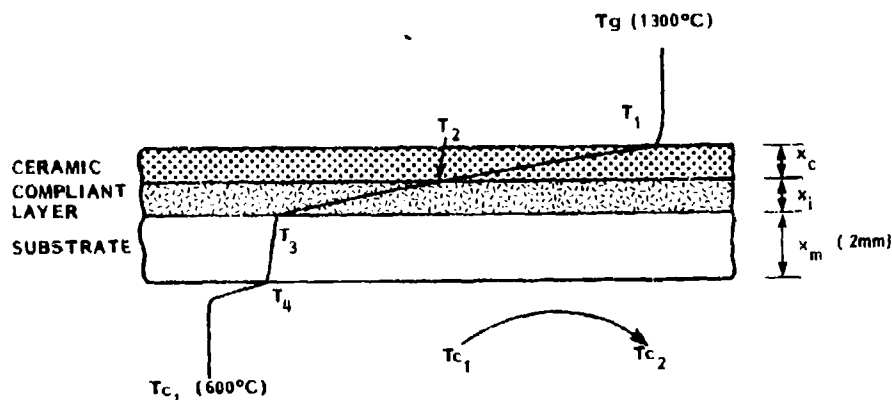
We may now substitute for the other constants and express the equation in decimal-percentage terms as before. Also a fixed value of x_m (2 mm) may be used to simplify the equation:-

$$\eta M = \frac{.0678}{x_c - .034} \quad (21)$$

The value of K_c taken is that of a low conductivity ceramic, in this case yttria stabilised zirconia (YSZ). The effect of the ceramic is to reduce the heat flux considerably, and so much less cooling air is required. The calculations show that about 1 mm of YSZ is needed to keep the product ηM down to about 0.1. This corresponds to about $\frac{1}{4}$ of cooling air with an impingement cooling system of 0.2 efficiency. The surface temperature of the ceramic is almost equal to the gas temperature and there is a large temperature drop across the ceramic. It should be noted that if ηM could be allowed to rise to 0.2 the ceramic could be made as thin as .35 mm, which is the sort of thickness used on other components with some success. Alternatively, if the maximum substrate temperature were set at 1050°C this thickness of ceramic (.35 mm) would only require a ηM value of 0.1.

4.4 METAL SUBSTRATE WITH A CERAMIC COATING ON AN INTERMEDIATE COMPLIANT LAYER

One possible method of alleviating the distress imposed on the ceramic by differential thermal expansion between the ceramic and the dominating substrate, is to interpose a relatively flexible, compliant layer, typically a sintered mat of oxidation resistant metallic wires. This section considers such a construction, which is cooled by passing air over the rear of the substrate.



The heat flux equations are as follows:

$$\text{HEAT FLUX } q \left\{ \begin{array}{l} = hg (Tg - T_1) \quad (22) \\ = \frac{K_c}{x_c \times 10^{-3}} (T_1 - T_2) \quad (23) \\ = \frac{K_i}{x_i \times 10^{-3}} (T_2 - T_3) \quad (24) \\ = \frac{K_m}{x_m \times 10^{-3}} (T_3 - T_4) \quad (25) \\ = \eta M C_p (T_4 - T_{c1}) \quad (26) \end{array} \right.$$

Add equations (22) + (23), then divide by the sum of (24) + (25) + (26)

$$\frac{Tg - T_2}{T_2 - T_{c1}} = \frac{\frac{1000}{hg} + \frac{x_c}{K_c}}{\frac{1000}{\eta M C_p} + \frac{x_m}{K_m} + \frac{x_i}{K_i}} \quad (27)$$

T_2 features in this equation, since the critical temperature in this construction is the highest temperature of the metallic compliant layer. If T_2 is set at 950°C , for long term oxidation resistance of the fine metallic wires.

$$\frac{Tg - T_2}{T_2 - T_{c1}} = \frac{1300 - 950}{950 - 600} = 1 \quad (28)$$

This may be substituted in equation (27), which when re-arranged becomes:-

$$\eta M = \frac{1000}{\left(\frac{1000}{hg} + \frac{x_c}{K_c} - \frac{x_m}{K_m} - \frac{x_i}{K_i} \right) C_p} \quad (29)$$

When values for the constants are substituted, x_m set at 2 mm and expressed in decimal - percentage terms for the hypothetical engine, the equation simplifies to:-

$$\eta M = \frac{.0678}{x_c \left(1 - .725 \frac{x_i}{x_c} \right) - .034} \quad (30)$$

The form of the graphs of this equation, for a range of values of $\frac{x_i}{x_c}$, is indicated in Fig 6. Note that if $\frac{x_i}{x_c}$ is greater than approximately 1.2 to 1.3 it becomes impossible to hold T_2 down to 950°C .

This calculation shows that the introduction of a compliant layer requires additional cooling air. This is because, as well as acting as an insulator ($K_i \approx K_c$), the temperature of the hot side of the layer now becomes the limiting factor, and it is on the wrong side of some of the insulation.

Ideally a very thin, highly conductive compliant layer is required, but this might militate against its compliance. On the other hand, the use of a thicker or less conductive compliant layer demands more cooling air.

The requirement for more cooling with thick compliant layers can be counteracted by increasing the thickness of the ceramic. Thus a typical design could be 2.5 mm of ceramic on 2.5 mm of compliant layer. The calculations predict that the product of ηM would be .1, and, as before, would correspond to using 1% of cooling air with an impingement cooling system of 0.2 efficiency. The calculated temperature distributions show that the ceramic surface is almost at gas temperature, there are large temperature drops of almost equal magnitude across the ceramic and the compliant layer, the temperature gradients are however much less steep than with ceramic alone.

4.5 METAL SUBSTRATE WITH A CERAMIC COATING ON A COMPLIANT LAYER WHICH IS COOLED BY THE TRANSPIRATION OF COOLING AIR

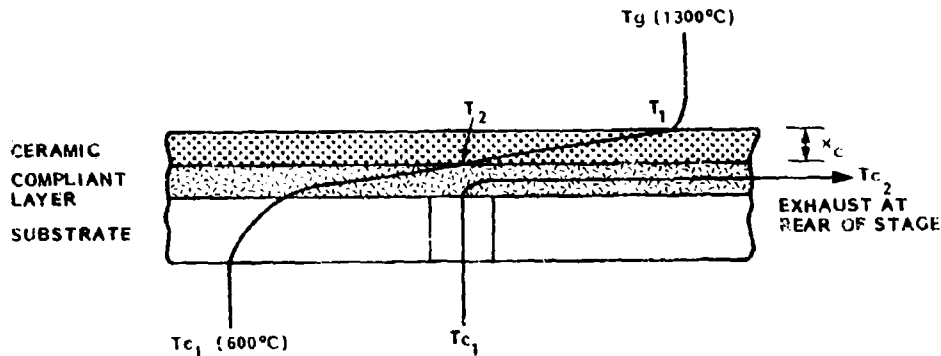


FIG 5 THERMAL GRADIENTS

The cooling air may now rise to temperature T_2 , therefore the cooling efficiency must be redefined as:

$$\frac{T_c2 - T_c1}{T_2 - T_c1}$$

$$\text{HEATFLUX } q \left\{ \begin{array}{l} = hg (T_g - T_1) \quad (31) \\ = \frac{Kc}{x_c \times 10^{-3}} (T_1 - T_2) \quad (32) \\ = \eta M C_p (T_2 - T_c1) \quad (33) \end{array} \right.$$

Equation (31) + (32) divided by (33) gives:-

$$\frac{T_g - T_2}{T_2 - T_c1} = \frac{\frac{1000}{hg} + \frac{x_c}{Kc}}{\frac{1000}{\eta M C_p}} \quad (34)$$

$$\text{then } \eta M = \left(\frac{1000}{hg} + \frac{x_c}{Kc} \right) C_p \quad (35)$$

Substitute for the variable and convert to decimal -% terms:

$$\eta M = \frac{.0678}{x_c + .046} \% \quad (36)$$

The ability to pass the cooling air through the compliant layer means that the low conductivity of the layer is no longer providing a restriction for heat flow. The compliant layer can be of any desired thickness. The cooling air can theoretically rise to the limiting temperature of the compliant layer, i.e. 950°C. This provides a very good system with a high cooling efficiency, due to the intimate contact of the cooling air with the compliant layer, which has a high surface area. Thus low thicknesses of ceramic can be considered. Most of the temperature drop is taken across the ceramic, whose surface is very close to the gas temperature.

4.6 CONCLUSIONS OF SHROUD COOLING ANALYSIS

The main numerical results of the above analysis are plotted on FIG. 6. Also FIG. 7 is a chart which indicates the cooling air costs, advantages and disadvantages of possible designs in the various configuration studied.

4.6.1 Uncoated Metal Shrouds (Impingement or convection cooled)

This is, of course not plotted on FIG. 6, since there is no ceramic involved. However the cooling demands are high and strongly dependant on metal thickness. In fact above a thickness of approximately 2 mm, it becomes impossible to keep the metal below 1050°C, no matter how efficient is the cooling.

4.6.2 Metal Shrouds (Transpiration Cooled)

Metal thickness is no longer a parameter and the shroud segments may be of any desired thickness. A single point is plotted on FIG. 6 (at $x_c = 0$) for reference. If some degree of film cooling is achieved with the exhausted cooling air, the cooling costs may be lower than quoted.

4.6.3 Metal Substrate with Ceramic Coating

Much depends on the thickness of the coating and the temperature to which the metal is to be cooled. The thicker coatings require the least cooling, but they are also the designs which suffer most from integrity problems.

4.6.4 Metal Substrate with Ceramic Coating on Compliant Layer (Impingement Cooled)

The compliant layer offers a solution to the integrity problem, but its presence increases the cooling costs and/or requires a thicker ceramic coating. In addition there is a relationship between the ratio of compliant layer to ceramic thickness and the cooling costs, with definite limits to the thickness ratio.

4.6.5 Metal Substrate with Ceramic Coating on Compliant Layer (Transpiration Cooled)

The constraints on compliant layer and ceramic thickness described above are removed. Also the direct cooling of the compliant layer is very efficient. The cooling costs are similar to those of the simple ceramic coating configuration, while the integrity advantage of the compliant layer is maintained.

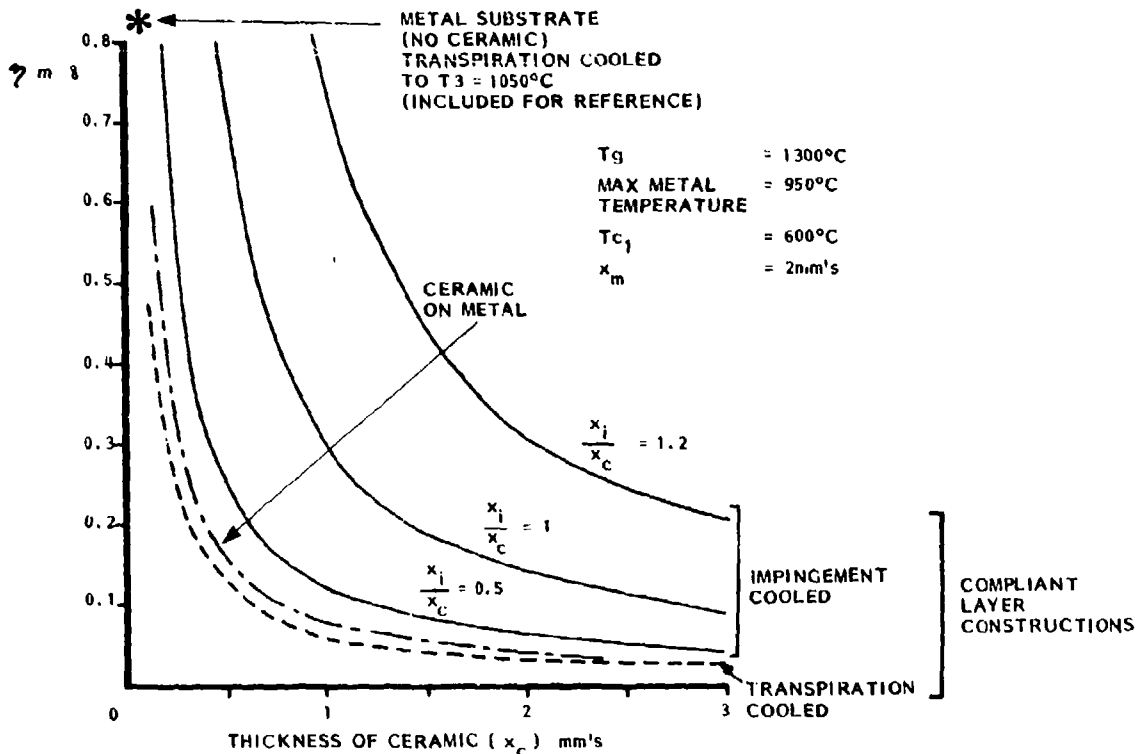


FIG 6 PREDICTED COOLING AIR REQUIREMENTS

SHROUD SECTION DESIGN	PREDICTED η_M	PROBABLE η M%	REMARKS
SIMPLE ALL-METAL - 2MM THICK IMPINGEMENT COOLED	INFINITE	.2 ∞	IMPOSSIBLE TO COOL TO 1050°C
SIMPLE ALL METAL (SAY 2MM THICK) TRANSPIRATION COOLED TO 1050°C	.02	.3 2.75	VERY EXPENSIVE ON COOLING AIR BUT MAY BE ACCEPTABLE ESPECIALLY IF HIGHER TEMPERATURE METALS ARE USED, OR EFFECTIVE FILM COOLING IS ACHIEVED.
TO 1150°C	.41	.3 1.4	
CERAMIC COATED SUBSTRATE (2 mm THICK) (SUBSTRATE IMPINGEMENT COOLED TO 950°C) WITH 1 mm OF YSZ	.07	.2 0.35	CHEAP COOLING, BUT HAS INTEGRITY PROBLEMS
WITH .35 mm OF YSZ	.20	.2 1.0	MORE EXPENSIVE COOLING, BUT BETTER INTEGRITY
CERAMIC COATED SUBSTRATE (2 mm THICK) (SUBSTRATE IMPINGEMENT COOLED TO 950°C) WITH 2.5 mm YSZ ON 2.5 MM COMPLIANT LAYER	.10	.2 0.5	CHEAP COOLING, BUT THICK COMPLIANT LAYER REQUIRES THICK CERAMIC COAT, WITH AT LEAST INTEGRITY PROBLEM.
WITH 1.5 MM YSZ ON 1.5 MM COMPLIANT LAYER	.18	.2 0.9	MORE EXPENSIVE COOLING, BUT BETTER INTEGRITY.
CERAMIC COATED SUBSTRATE (ANY THICKNESS) WITH TRANSPIRATION COOLED COMPLIANT LAYER (ANY THICKNESS) WITH 1 mm YSZ	.065	.5 0.13	VERY EFFICIENT COOLING, WITH ONLY CONSTRAINT ON COMPLIANT LAYER THICKNESS BEING THE ABILITY TO PASS THE REQUIRED AMOUNT OF AIR.
WITH 0.5 mm YSZ	.125	.5 0.25	

FIG 7 POSSIBLE SHROUD DESIGNS

5 CERAMIC COATING INTEGRITY

Having made an estimate of the cooling demands for a selection of shroud design concepts, it is also necessary to investigate the difficult problem of mechanical integrity of the designs, particularly with respect to the ceramic coating. The first requirement is that the shroud assembly should be capable of prolonged service at the elevated temperatures associated with engine service. However, the most difficult requirement is the need to survive the cyclic stresses, resulting from differential thermal expansions occurring during engine acceleration and deceleration.

Ideally, given a full understanding of the problem, a theoretical analysis of the designs should be performed. This would involve the calculation of transient thermal gradients in three dimensions, for the full engine cycle. The next step would be the application of the relevant mechanical and thermal properties of the various materials, which themselves are variable with temperature, in order to predict the three dimensional stress cycles. The final step would be the assessment of the stress data against a number of complex failure criteria. The first of these three steps might be feasible, though difficult to achieve with confidence. The second step involves material data which is at present poorly specified. Also, the final step requires the full knowledge of very complex and various failure criteria, which is not available at this time.

The performance of this theoretical analysis would therefore be a formidable task, with many possibilities for error, which would inevitably reduce confidence in the final conclusions.

The second part of this paper describes an alternative approach, for which only an element of the first of the three above steps is used, in order to specify a rig test experimental evaluation which will provide the required assessment of integrity.

The tests involve a test piece which, though lacking some of the details of an engine shroud segment, is representative in terms of size, shape and section design. To this test piece is applied a thermal cycle, which is chosen to give representative thermal gradients, while keeping the absolute temperatures at a reasonable level. The 'stress and failure analysis' is then performed by the rig test. The main compromise involved is the order difference in heat transfer coefficients, between the atmospheric pressure rig and the high pressure engine. This is corrected by two means. Firstly, the flame used in the rig is hotter than the annulus gas in the engine. The relevant quantity is the temperature difference between the flame and the hot surface of the test piece, not the absolute flame temperature, therefore this is quite a powerful factor. Secondly, in the engine, the annulus temperature will take several seconds to rise and fall, but on the rig the flame may be applied and removed from the specimen almost instantaneously. This factor can be used to steepen the transient gradients, to correct for the low heat transfer coefficient on the atmospheric rig.

The only analytical part of this method is the selection of the rig thermal cycle, which will give the correct thermal gradients. For this a computer program, giving transient one dimensional thermal gradients at a number of times through the cycle, is used for both rig and engine. FIG. 8 Illustrates the method used to select the cycle.

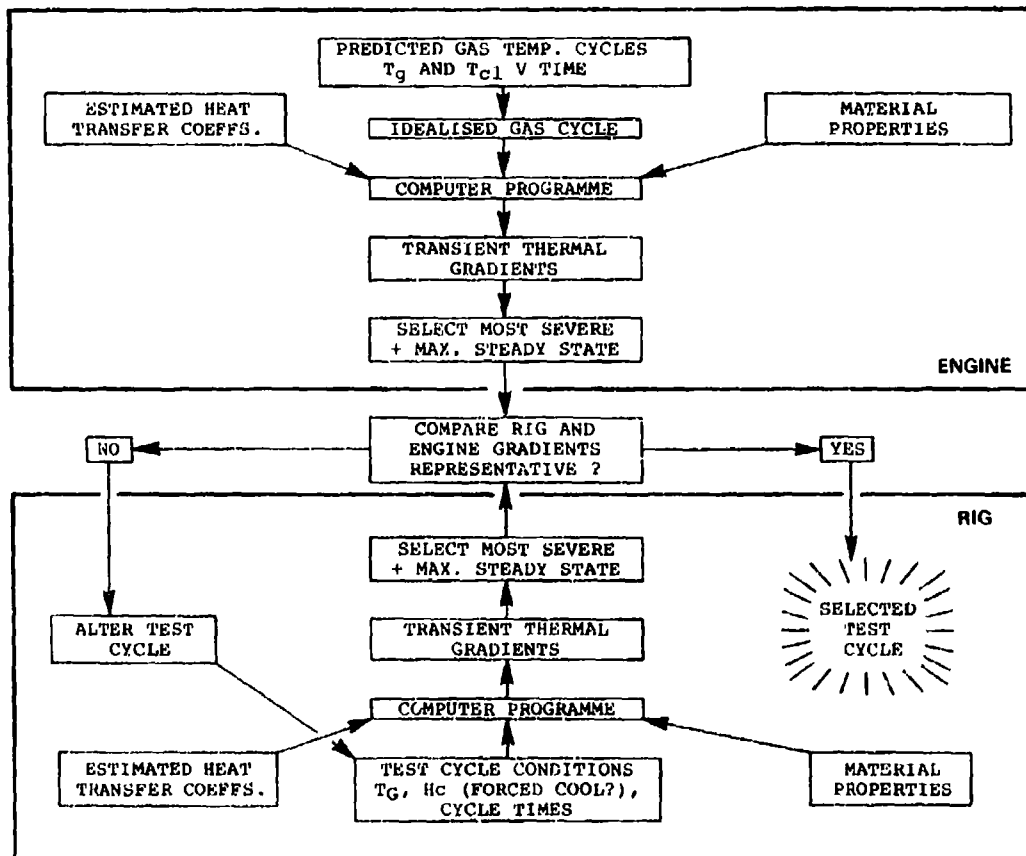


FIG 8 METHOD USED TO SELECT TEST THERMAL CYCLES

Note that the iterative alterations to the test cycle are chosen arbitrarily, but with increasing skill as the exercise proceeds. The final selected test cycle is specific to each design of section and it is then used as a guide for setting up the conditions. The predicted front and rear face temperatures are then used to monitor the cycle and for fine adjustments to the control parameters, e.g. flame power and cycle time.

The rig used is illustrated by FIG 9. The specimen, which is 50 mm square, is supported in a water cooled holder, which may be shuttled between heating and cooling positions by an automatically scheduled pneumatic ram. Heat is supplied by a large 180 kW oxy-propane burner, which not only has adequate power, but also is large enough to give even heating over the face of the specimen. For some cycles an active cooling jet is used, but not for all.

For most specimens only two pieces of instrumentation are used. A radiation pyrometer is used to record the front face temperature (T_1) and a thermocouple is attached to the rear face to record T_4 . During early tests more fully instrumented test pieces, with thermocouples embedded in the sections at each material discontinuity, were used to evaluate the test method. A typical output is shown in FIG. 10. The distribution of temperatures is as expected, showing that the values of thermal conductivity specified for the materials are approximately correct. These results then justified the use of only two temperature measurements on the main programme specimens.

The rig and test technique have been commissioned during a quite extensive programme, during which many of the basic conclusions which are widely published by other researchers have been confirmed. At this point the testing of sections involving ceramics was suspended, as the rig was diverted to another programme, which is not within the scope of this paper. It is now intended to return to a programme of research on the concepts described in this paper.

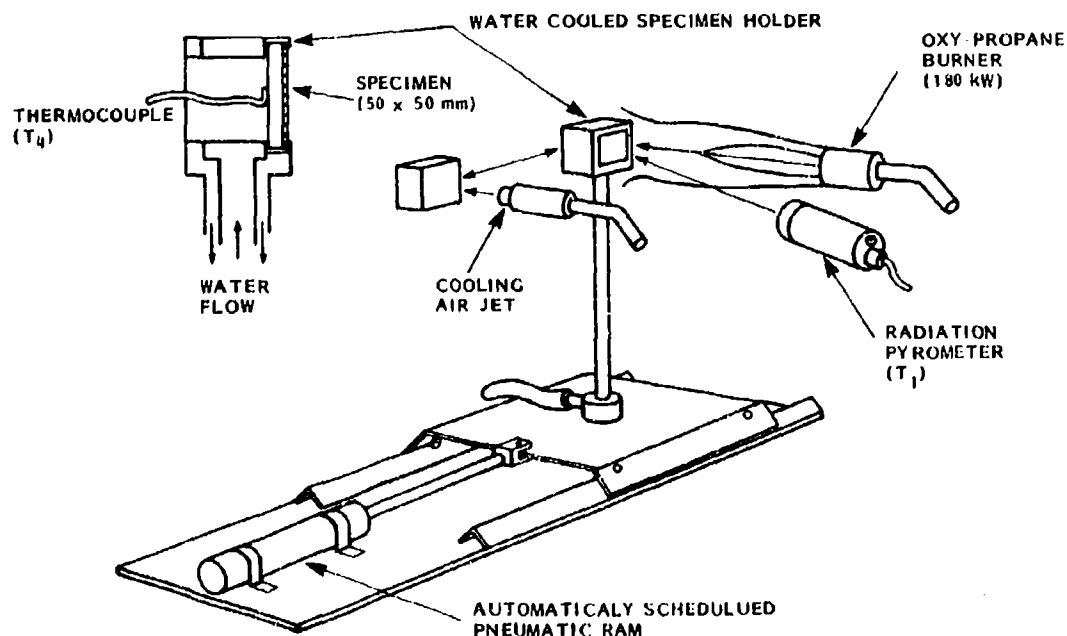


FIG 9 THERMAL CYCLING TEST RIG

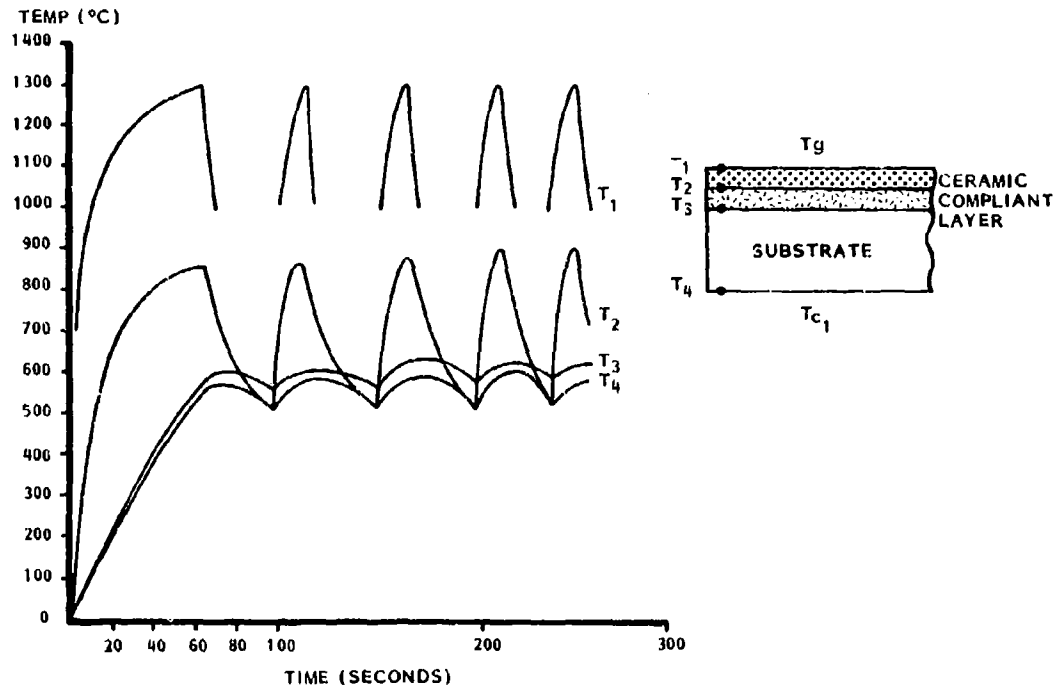


FIG 10 FULLY INSTRUMENTED TEST PIECE - RIG CYCLE RESULTS

6. CONCLUSIONS

This paper has explored two aspects of the design and development of shroud segments for turbines which use unshrouded blades. The first part of the paper is a general assessment of the thermal gradient through various types of section, to give a basic understanding of the thermal requirements. In particular, for sections involving ceramic coatings, it has defined the thickness of coating required and related this to the cost in terms of cooling air flow. In addition, a problem or limitation associated with the use of a compliant layer, as a result of its relatively low conductivity, has been high-lighted. A possible means of overcoming this problem, by means of the transpiration of cooling air through the porous compliant layer, has been described.

The second part of the paper described a method of comparative assessment of engine and rig thermal gradients and cycles. This has been used to define a set of test conditions, in which there will be some confidence that the test results will be meaningful and relevant.

Though no comprehensive programme of tests has yet been performed, the rig has been fully commissioned and it is intended to commence such a programme in the near future.

DISCUSSION

D.K.Hennecke, Ge

What ceramic material were you using?

Author's Reply

Though the type of analysis described may be used for a variety of materials, the properties used in this paper are for yttria stabilized zirconia. The experimental work done so far has confirmed that improved integrity is obtained with partial stabilization.

D.K.Hennecke, Ge

Was the ceramic coating also employed as abrasive or abradable coating?

Author's Reply

The lack of abradability is another of the difficult problems associated with the use of ceramics on static shrouds. It is very desirable that abrasion should remove material from the stator, rather than the rotor blade tips. The literature describes a number of conceptual solutions: porous, therefore abradable, top coats on the ceramic or abrasive caps on the blade tips. A more elegant solution would be the use of a reliable active tip clearance control system (possibly with mechanical activation). This should reduce the frequency of tip rubs, such that the consequent loss of performance, requiring a removal of the engine for refurbishment, would be acceptable.

D.K.Hennecke, Ge

In case of a rub-in of the blades into the coating wouldn't the compliant layer be squeezed so that the cooling flow would be reduced?

Author's Reply

The above remarks apply to this question but in any case I would anticipate that a severe rub, which might compress the compliant layer, would also remove the ceramic in a gross manner. If the flow characteristics of the compliant layer were designed to be self metering, such a design might be to a degree fail-safe.

D.A.Nealy, US

Just an observation. Our own work, primarily in the context of combustor cooling has shown that both normal (through thickness of layer) and axial temperature gradients through the transpiration cooled compliant layer may be very substantial. The strong axial material temperature gradients are in fact a consequence of the high intrinsic thermal efficiency of the transpiration cooled layer. I would simply like to point out that these thermal gradient details may have some important implications relative to ceramic layer thermal stresses.

Author's Reply

There is strong evidence to suggest that a coating which will be successful, from the point of view of avoidance of catastrophic failure, will necessarily suffer radial cracking at an early stage. This being the case, the coating will be effectively strain isolated in the axial direction. In any case I would expect that since the intermediate layer is to some extent compliant, its planar dimensions will be controlled by the solid substrate.

P.Ramette, Fr

Quelle est la nature du matériau utilisé pour la couche intermédiaire sous la céramique, et quel est son niveau de porosité pour permettre un refroidissement par film?

Author's Reply

The particular material which I have used for this exercise, is the commercial product 'Brumsbond'. This consists of a sintered mat of 0.125 mm (0.005 inch) diameter 'Hoskins 875' wires (randomly orientated). The density of the particular version considered is 35%. (i.e. 65% porosity).

J.M.Hannis, UK

The shroud segment gas temperature assumed was 1300°C — bearing in mind effects of combustor traverse, upstream vane platform cooling and discharge of cooling air from the rotor blade tip, what engine turbine inlet temperature does this represent?

Author's Reply

Given the qualitative and approximate nature of this analysis, I have assumed that the deltas you have listed may give a net variation of zero. I.e. the local gas temperature is equal to the turbine inlet temperature. I have assumed that the effect of film cooling will be minimal.

13-14

J.M.Hannis, UK

Can you say at what level of turbine inlet temperature it is necessary to introduce unshrouded rotor blading rather than shrouded blading?

Author's Reply

This is a decision which depends on many unconnected factors, as well as temperature levels.

ENGINE TESTS ON A COOLED GAS TURBINE STAGE

H.J. Graf

BBC Brown, Boveri & Company, Limited
CH-5401 Baden, Switzerland

SUMMARY

A new cooling system was designed for the 45 MW gas turbine type 8. Extensive tests were carried out in a new power station to verify the reliability of the cooled components. Wall temperatures were measured using thermocouples, thermal paints and pyrometers. Cooling air temperature, pressure and mass flow measurements allowed a detailed analysis of the first stage under operating conditions.

This paper presents the results and comparisons with design calculations. The applicability and accuracy of the three measuring techniques are discussed.

List of Symbols

Subscripts

D	diameter	ad	adiabatic
d	film hole diameter	c	cooling air
h	heat transfer coefficient	g	hot gas
l	blade height	h	hub
Ma	Mach number	ref	reference value
m	mass flow	t	tip
n	speed	w	wall
p	pressure	*	total
Re	Reynolds number	0	vane inlet
s	chord length	1	vane exit/blade inlet
T	temperature	2	blade exit
t	spacing		
w	velocity		
x	distance from stagnation point; axial distance		
α	injection angle		
η	= $(T_g - T_w)/(T_g - T_c)$ cooling effectiveness		
η_F	= $(T_g - T_{w_{ad}})/(T_g - T_c)$ film cooling effectiveness		

INTRODUCTION

The new gas turbine type 8 was developed for increased specific power output and improved efficiency. These goals were accomplished on the one hand by modifying the thermodynamic cycle parameters and on the other hand by optimizing the compressor and turbine efficiencies. By using more efficient cooling systems, it was possible to attain considerable progress on the turbine end. Even though the relative cooling air mass flow rate could be reduced, the service life of the parts subjected to the hot gas has not changed from that of the existing BBC gas turbine type 9, a 32 MW unit which has an identical design concept. Particular attention has been paid not only to mechanical stressing, but also to corrosion attack.

Modern theoretical tools were available for designing the cooling system. In addition, the most important functions were rechecked in model tests. A detailed report on these experiments was already presented in [1]. Nevertheless, various factors that have quite an important effect on the heat transfer within a turbine can neither be calculated exactly nor measured experimentally. These include, on the hot gas side, effects such as

- nonuniformities and fluctuations of the inlet flow
- the combined influence of free stream turbulence, pressure gradient, surface curvature and roughness on the boundary layer development

- the three-dimensional flow character including rotation and end wall secondary flow
- the injection of film cooling air

Additional problems arise in the prediction of the internal heat transfer: geometrical parameters and rotational effects have an important influence on the pressure loss and the local value of the heat transfer coefficient [2]. For that reason, it is absolutely necessary to check the design in the machine itself.

For the type 8 gas turbine, extensive measurements were taken in an installation set up for that purpose. With more than 100 measuring points for temperature and pressure, the operational reliability of the entire cooling system had to be demonstrated. At the same time, the design procedure used had to be verified on two specifically instrumented test vanes and blades. The third objective was to test new computer codes for the heat transfer prediction in boundary layers, provided that a sufficient measurement accuracy could be achieved. This paper discusses the results of these measurements on the first stage vanes and blades.

TEST ENGINE

A complete description of the type 8 gas turbine can be found in [3], [4] and [5]. In its design point, the machine operates with the cycle temperature and the pressure ratio shown in Fig. 1. These parameters are chosen based on economic and design considerations and provide a power output of 45 MW with a thermal efficiency of 32% at base load condition.

By increasing the circumferential speed, it was possible to limit the number of stages in the turbine to three despite the higher inlet pressure (compared to the four-stage type 9 turbine). For the same reason, the specific aerodynamic loading of the individual rows was small, so that high aerodynamic efficiencies were attained. Measurements in a model turbine [1] have confirmed this.

TABLE 1: GEOMETRIC AND AERODYNAMIC DATA AT MID-SECTION
BASE LOAD (IDLE)

			Vane	Blade
chord length	s	mm	91	56
aspect ratio	1/s	-	0.9	1.9
solidity	τ/s	-	0.87	0.84
diameter ratio	D_c/D_h	-	1.15	1.19
speed	n	min^{-1}	-	6300
inlet pressure	$P_{0,1}$	bar	14.3 (11.7)	9.0 (7.3)
exit pressure	$P_{1,2}$	bar	9.0 (7.3)	7.2 (5.6)
exit Mach number	Ma	-	0.84	0.65
exit Reynolds number based on chord length	Re	-	$2.6 \cdot 10^6 (3.4 \cdot 10^6)$	$1.1 \cdot 10^6 (1.4 \cdot 10^6)$

Table 1 lists the design conditions for the center cross-section of the first stage vane. The flow parameters taken from a streamline curvature through flow program were - where necessary - corrected using the results of three-dimensional calculations or experiments. Fig. 2 shows a comparison of the data measured with those computed for a geometrically similar single stage turbine. To calculate the pressure distribution along the profile, a time-marching procedure was used that was likewise checked against measurements (Fig. 3). The effect of film cooling injection on the pressure distribution, the exit flow angle and the losses was determined from cascade measurements [1]. The same computer programs were used for the test evaluation.

Another important factor for the heat transfer on blades is the approach flow at the turbine inlet. The conditions for this flow depend quite significantly on the type and on the arrangement of the combustion chamber. The turbine design and the test evaluation are supported by the long years of BBC experience with single combustors.

COOLING SYSTEM

The heat shields of the rotor and the vane carrier as well as four rows of the blading are cooled. Fig. 4 shows the individual flows of cooling air. The largest portion of the air, which is taken off mainly at the end of the compressor, cools the various rows of blades and vanes. The total consumption of cooling air is held as low as possible by means of an extensive system of seals in the area of the blade roots and the heat shield segments.

The precision cast test vane made of IN939 has a sheet metal insert (Fig. 5) and is impingement cooled in the leading edge zone. A portion of the cooling air exits on the suction side through three rows of film-cooling holes. The remaining air is used for convection cooling of the pressure and suction sides across longitudinal ribs. Heat transfer in the trailing edge section is increased by means of pins. The cooling air is then mixed with the mainstream through trailing edge slots.

For dimensioning the individual cooling air passages and guides, a computer program that is structured similar to TACT I [6] was used. Correlations for the determination of pressure losses, heat transfer coefficients (coolant side) and film cooling efficiencies, all derived from experimental investigations or literature data (see, for example, [7] and [8]), form the basis for the analysis of any cooling system. The discharge coefficients for the individual cooling air outlets were measured in the cascade test mentioned above. Using these data, the following mass flow distribution was calculated for the two test vanes:

Film holes row 1: 6%
 row 2: 10%
 row 3: 10%
 Trailing edge : 74%

Table 2 shows the corresponding film cooling parameters. The resulting distribution of temperatures and thermal stresses is calculated using a Finite Element program.

TABLE 2: FILM COOLING PARAMETERS (VANE)

			row 1	row 2	row 2
blowing rate	$\rho_c w_c / \rho_g w_g$	-	0.95	1.2	1.2
momentum flux ratio	$\rho_c w_c^2 / \rho_g w_g^2$	-	0.4	0.7	0.7
hole diameter	d	mm	0.6	0.6	0.6
hole spacing	t/d	-	3.3	3.3	3.3
injection angle	α	°	40	35	30
density ratio	ρ_c / ρ_g	-	2.0	2.0	2.0

A different cooling system was selected for the first stage test blade (Fig. 6), which is also precision cast (IN738). The leading edge is cooled by means of a radial hole with cross-ribs. The main radial channel in the mid-chord region of the airfoil has the same cross-ribs for heat transfer augmentation. Arrays of short cylindrical pins are placed in the trailing edge part which is fed with cooling air from the main channel via a deflection at the tip of the blade and a small opening in the hub area. The whole cooling air is discharged through trailing edge slots. The flow distribution at the outlet on the trailing edge was measured on a rotating water test stand [1]. With that it was possible to recheck the design, which was carried out in a manner analogous to the test vane.

INSTRUMENTATION

In order to obtain as great an accuracy as possible in the evaluation of the results, measurements were taken not only of a large number of wall temperatures, but also of boundary conditions, such as cooling air pressure, temperature and mass flow, wall pressures and hot gas temperatures. Fig. 7 shows the various measurement positions. Special measuring sensors made of Platinum-Rhodium were developed to determine the hot gas temperature at different radial and circumferential locations in the hot gas channel. They were fastened directly to the individual vanes. A layer of insulation between the measuring pin and the blade prevented any heat flow into the blade material, so that the difference between the measured temperature and the effective hot gas temperature became minimal (less than 2%). The error in measurement could be restricted to $\pm 1\%$ by means of a mathematical correction from a finite element analysis.

All wall temperatures were measured using sheathed chromel-alumel thermocouples. The thermocouple wires were laid in grooves machined into the blade surface (diameter 0.5 mm) and fastened mechanically by means of prick-punching which guaranteed a very exact positioning. The grooves were then filled with brazing material and ground over, in order to restore the original surface quality. The variation in depth of insertion was measured in a blade that was cut up, and found to be less than $\pm 2\%$ relative to the thickness of the walls. Errors in measurement of temperatures that correspond to this difference are negligible. Thus, the overall accuracy of measurement is given by the thermocouple itself, the wiring and by the measuring instruments. According to the laboratory specifications, values of $\pm 2\%$ for the vane and $\pm 3.5\%$ for the blade were attained.

The two adjacent test vanes were equipped with 13 thermocouples each on the circumference of the vane. One of these vanes had a separate cooling air feeding system which allowed precise measurement of the mass flow rate. In addition, it could be used for cyclic tests. Thermocouples were applied to various other vanes for purposes of control. Fig. 8 provides an overview. Also shown in that figure are vanes that were coated with thermal paints, and the point where the radiation pyrometer (which was used primarily for measurements on rotating blades) was checked. Uncertainties about the emissivity could be largely eliminated through laboratory calibration prior to the test.

The instrumentation for the rotating stage included significantly fewer thermocouples because a complex data transfer and acquisition system was necessary. The signals were transmitted by telemetry from different senders at the turbine end. A total of seven thermocouples were distributed on the test blade (Fig. 9). The use of the pyrometer yielded very valuable results; the wall temperature at a particular surface point can be obtained on every blade.

RESULTS AND DISCUSSION

First Stage Vane

Fig. 10 shows the wall temperatures as measured, compared with the design values. These values were computed using heat transfer coefficients on the hot gas side that were determined with the aid of an integral boundary layer calculation as described in [9]. The transition point from laminar to turbulent flow was artificially prescribed here at the leading edge to ensure that uncertainties due to free stream turbulence effects are reliably included. In addition, the heat transfer coefficient on the pressure side was raised using empirical values from previous experiments in order to take into account the influence of the concave curvature of the surface. The corresponding heat transfer coefficient distribution over the profile is shown in Fig. 11.

The agreement in the temperatures is remarkable on the pressure side. On the suction side, the values measured are slightly lower than those expected, which can be attributed mainly to an overestimation of the heat transfer coefficients, but also to the cautious evaluation of the film cooling effectiveness

$$\eta_F = (T_g - T_{w_{ad}}) / (T_g - T_c)$$

which varies from 0.24 behind the third row of holes to 0.03 near the trailing edge. No major differences can be observed in the comparisons between base load and idle conditions. Within the range of operation for a stationary gas turbine the influence of the Reynolds number seems to be negligible. Another point worthy of note is the outstanding correspondence of the measurements on the two test vanes. The differences in wall temperature at corresponding locations are within 15°C, thus confirming the estimated error from the preceding section of this paper. The pyrometer measurement also falls within the same range of variance. Table 3 shows in a non-dimensional form the hot gas and cooling flow conditions measured along with these results.

TABLE 3: MEASURED COOLING AIR AND HOT GAS DATA
FIRST STAGE VANE
BASE LOAD (IDLE)

temperature ratio	T_g/T_c	2.1 (1.5)
pressure ratio main stream	P_0/P_1	1.6
pressure ratio cooling air	P_c/P_1	1.72
mass flow ratio	\dot{m}_c/\dot{m}_g	0.045

In order to verify new design tools, test computations were run for the full load test case using a finite difference boundary layer code [8]. For degrees of free stream turbulence of 5% and 10%, calculations were run using various transition models (Seyb [11], Dunham [12], Abu Ghannam [13]). Fig. 11 shows the calculated distributions of the heat transfer coefficients. The corresponding wall temperatures are shown in Fig. 12 and compared with the measurements. Since the free stream turbulence, based on these computations, has only a small effect (indicated in Fig. 11 for the Abu Ghannam model) and the result of calculation according to Dunham and Abu Ghannam is practically identical, we will discuss below only the transition models according to Seyb 1 and Abu Ghannam 2. In the mid-section of the suction side, 1 produces expected values that are up to 20% too high. The results are somewhat better proceeding according to 2. For both models, the wall temperatures shortly after the leading edge are 15% lower than the measurement. The comparison on the pressure side is significantly better; only in the zone of strong concave curvature and laminar boundary layers, the values computed using both procedures are approximately 12% lower than measurement.

The fact that some of the deviations on the suction side are large suggests that the effect of the film cooling is not handled properly using correlations based on flat plate experiments. For that reason, the film cooling effectiveness has been corrected using the results from [14]. This takes into consideration both the effect of the convex curvature and the density ratio from cooling air to hot gas. Thus, the reference film cooling effectiveness behind the third row of holes is increased to 0.4. In addition, the local heat transfer coefficient is affected considerably by the injection of film cooling air into the laminar boundary layer [15]. An appropriate adjustment was made, indicated in Fig. 11 for model 1. With such corrections, the measured and computed values using the transition model according to Seyb lie within the margin of error for measurement, except for the first position on the suction side, where there is a deviation of over 15% (Fig. 12). This result is confirmed by comparable measurements made in a hot cascade facility at the NASA Lewis Research Center [16]. Similar computations using model 2 obviously give lower wall temperatures.

Measurements with thermal paint confirmed the above results (Fig. 13). However, without thermocouple measurements the accuracy is not adequate to draw any conclusions with regard to the various computer models. On the one hand, the main problems are the limited resolution and on the other hand the ambient effects which influence the color-changing behavior considerably.

Using the blade with the separate cooling air feeding system, the effect of a cooling air mass flow rate reduction on the average cooling effectiveness

$$\eta = (T_g - T_w) / (T_g - T_c)$$

was studied (Fig. 14). Agreement between measurements and calculations is good and confirms that the variation in the cooling air flow of $\pm 5\%$ (due to manufacturing tolerances) measured in a cold air test facility has no effect on the life time of the blade. In comparison to the cooling system of the gas turbine type 9 [17], we were able to increase the cooling effectiveness by more than 50%.

First Stage Blade

The comparison between measurement and design is shown in Fig. 15, analogous to that for the vane (flow conditions see Table 4). The agreement is better than for the vane on both the suction and the pressure side although unsteady effects due to wakes from the upstream blade row and the influence of rotation were not taken into consideration in the prediction of the blade heat transfer on the hot gas and coolant side. However, with the small number of points measured, a more exact analysis is impossible, although we were able to attain a very small margin of error in measurements of $\pm 3\%$. The average cooling effectiveness is approximately 0.4.

TABLE 4: MEASURED COOLING AIR AND HOT GAS DATA
FIRST STAGE BLADE
BASE LOAD (IDLE)

temperature ratio	T_g/T_c	2.0 (1.4)
pressure ratio main stream	P_1/P_2	1.27
pressure ratio cooling air	P_c/P_2	1.24
mass flow ratio	\dot{m}_c/\dot{m}_g	0.025

The temperature measured with the pyrometer is somewhat lower. Since the measurement had to be taken through the first vane, an influence of outside radiation from adjacent walls cannot be precluded. In this connection, it has to be mentioned that a precise adjustment of the pyrometer is essential to obtain reliable results. For these tests, an external focusing system allowed a continuous change of the pyrometer alignment. Nevertheless, this measuring procedure is better suited to demonstrating differences between individual rotating blades. Fig. 16 shows the results for all the blades in the first rotating row. The small temperature variation is caused by manufacturing tolerances and has no effect on the service life of the individual blades.

CONCLUSIONS

Extensive temperature measurements in the type 8 gas turbine have demonstrated the operational reliability of all cooled components. The procedure used for design, which is supported to a large extent by operating experience, proved to be dependable.

Due to the high level of measurement accuracy and the fact that most of the boundary conditions were measured during the tests or at least checked in model and cold air experiments, it was possible to show on two test vanes and blades that new computer codes can yield very good results in the area of turbulent boundary layers. In the specific case of the first stage vane, the transition model according to Seyb produced the closest agreement provided such parameters as wall curvature, momentum flux ratio, density ratio, etc. are taken into account in the correlation for the film cooling effectiveness. Greater deviations occur both on the suction and on the pressure side for laminar and for transitional boundary layers. For that reason, a further development of the present boundary layer code with regard to real turbo-machinery conditions is indispensable. In addition, further film cooling experiments are needed in order to obtain better documentation for an extended range of the influencing parameters. This confirms the comment made in the introduction: using the design tools available today, a time-consuming and expensive re-checking in the machine itself is still necessary to find the optimum regarding blade life time and cooling air consumption.

Among the methods used for the temperature measurements, thermocouples and pyrometers proved to be suitable for this type of investigation. Although the hot gas side heat transfer coefficient can be determined only within + 10% at best, the great differences between laminar and turbulent flow can still be identified. In contrast to these techniques, measurements with thermal paints can be used only to a limited extent. On the one hand, parameters such as fuel and surface quality, or the condition of the ambient air, have a great influence on the results since they can cause erosion or color changes of the thermal paint and transition or separation of the boundary layer. On the other hand, the resolution of the test results is not fine enough. However, used together with thermocouples, they make it possible to measure the temperature distribution over fairly large wall surfaces at a low cost.

ACKNOWLEDGEMENTS

Various departments at Brown Boveri & Cie. were involved in the realization of these extensive tests. My special thanks goes to our laboratory for the instrumentation and the construction of the testing equipment, to the commissioning department for carrying out the measurements, and to all my colleagues in the gas turbine research and development department who have collaborated actively in the preparation of this paper.

REFERENCES

- [1] Mukherjee, D.K., Wicki, A., "Development of the Gas Turbine Blading", Brown Boveri Review, Vol. 67, No.12, 1980.
- [2] Taylor, J.R., "Heat Transfer Phenomena in Gas Turbines", ASME 80-GT-172, 1980.
- [3] Endres, W., "The Medium Size Gas Turbine Type 8 from Brown Boveri, Development and Testing", ASME 83-Tokyo-IGTC-112, 1983.
- [4] Farkas, F., v.Rappard, A., "GT8 - A New BBC Gas Turbine", Brown Boveri Review, Vol. 70, No. 3/4, 1983.
- [5] Wicki, A., Farkas, F., "Design and Testing of a 45 MW Gas Turbine", ASME 84-GT-16, 1984.
- [6] Gaugler, R.E., "TACT 1, A Computer Program for the Transient Thermal Analysis of a Cooled Turbine Blade or Vane Equipped with a Coolant Insert", NASA TP-1271, 1978.
- [7] Yeh, F.C., Stepka, F.S., "Review and Status of Heat Transfer Technology for Internal Passages of Air-Cooled Turbine Blades", NASA TP-2232, 1984.
- [8] Kruse, H., "Measurements of Film Cooling Effectiveness and Heat Transfer on a Flat Plate", Proceedings of the 14th Symposium of the International Centre for Heat and Mass Transfer, Springer Verlag, 1982.
- [9] Walz, A., "Strömungs- und Temperaturgrenzschichten", G. Braun Verlag, Karlsruhe, 1966.
- [10] Patankar, S.V., Spalding, D.B., "Heat and Mass Transfer in Boundary Layers", Intertext, London, 1970.
- [11] Seyb, N.J., "The Role of Boundary Layers in Axial Flow Turbomachines and the Prediction of Their Effects", AGARD-AG-164, Paper I-14, 1972.
- [12] Dunham, J., "Predictions of Boundary Layer Transition on Turbomachinery Blades, AGARD-AG-164, Paper I-3, 1972.
- [13] Abu Ghannam, B.J., "Boundary Layer Transition in Relation to Turbomachinery Blades", Ph.D. Thesis, University of Liverpool, 1979.
- [14] Ito, S., Goldstein, R.J., Eckert, E.R.G., "Film Cooling of a Gas Turbine Blade", ASME Journal of Engineering for Power, Vol. 100, 1978.
- [15] Goldstein, R.J., Yoshida, T., "The Influence of a Laminar Boundary Layer and Laminar Injection on Film Cooling Performance", ASME 81-HT-38, 1981.
- [16] Liebert, C.H., Gaugier, R.E., Gladden, H.J., "Measured and Calculated Wall Temperatures on Air-Cooled Turbine Vanes with Boundary Layer Transition", ASME 83-GT-33, 1983.
- [17] Mukherjee, D.K., Frei, O., "Temperature Measurements on Cooled Gas Turbine Stator Blades", ASME 74-GT-31, 1974.

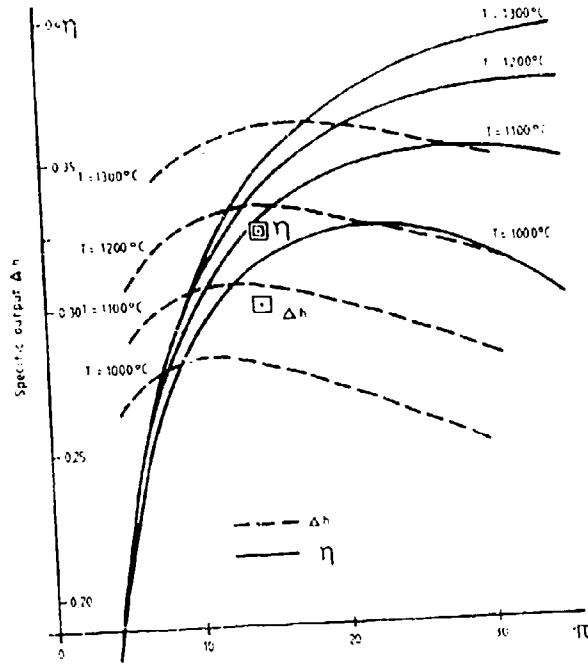


Fig. 1:
Specific output Δh and
efficiency η as a func-
tion of the compression
ratio π

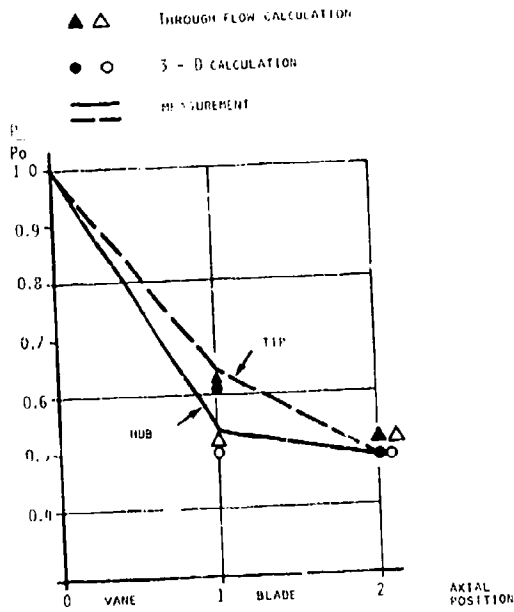


Fig. 2:
Wall pressure measure-
ments in a single stage
test turbine

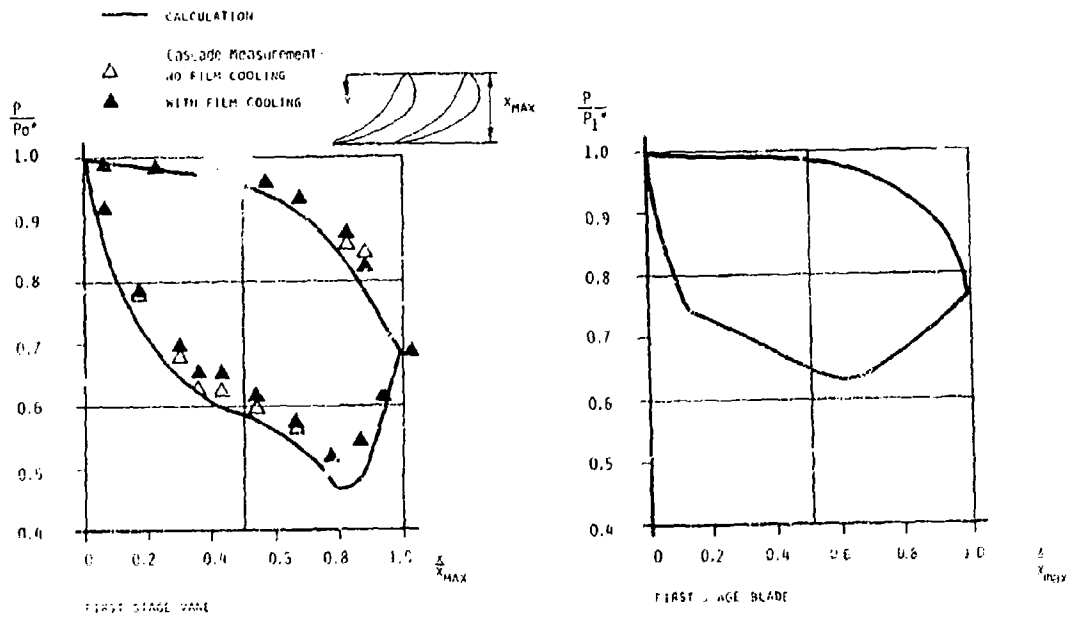


Fig. 3: Pressure distribution along the profile at mid section

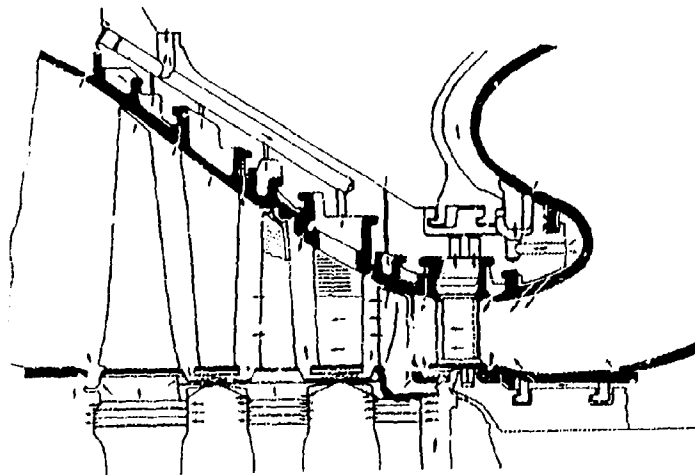


Fig. 4: Cooling system

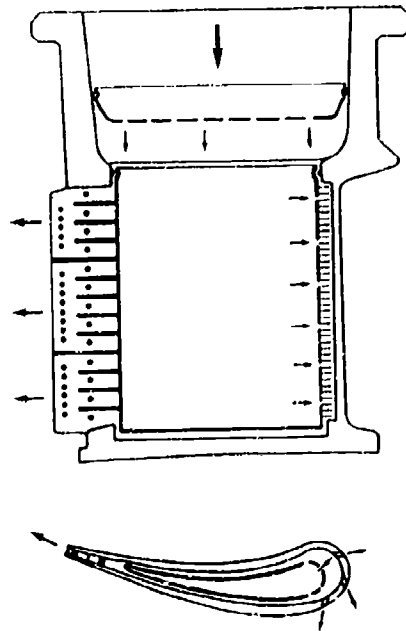


Fig. 5:
Schematic view of the
test vane

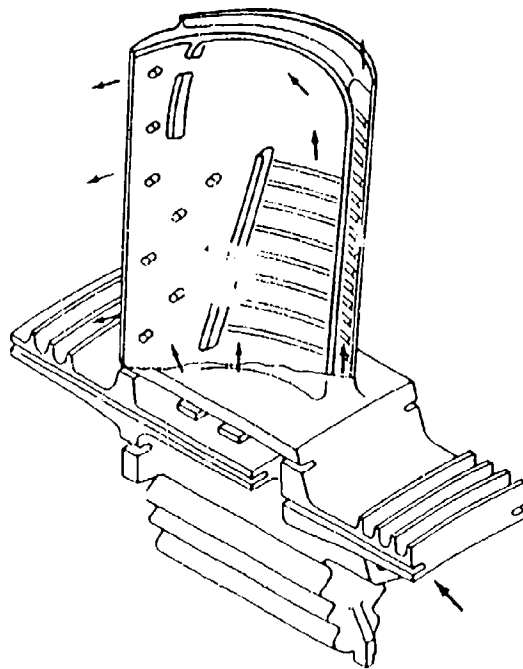


Fig. 6:
Schematic view of the
test blade

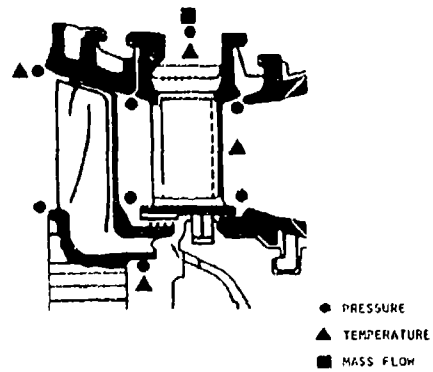


Fig. 7: Instrumentation in the hot gas and cooling system

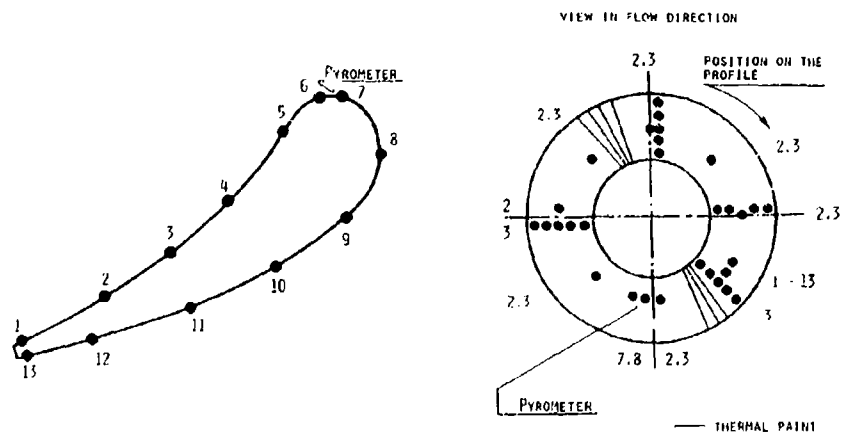


Fig. 8: Thermocouple locations on the first stage vane

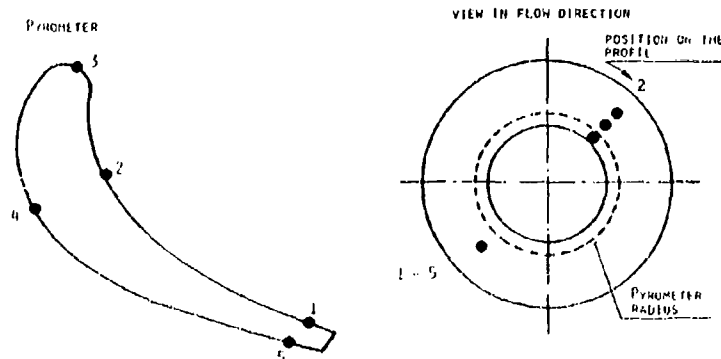


Fig. 9: Thermocouple locations on the first stage blade

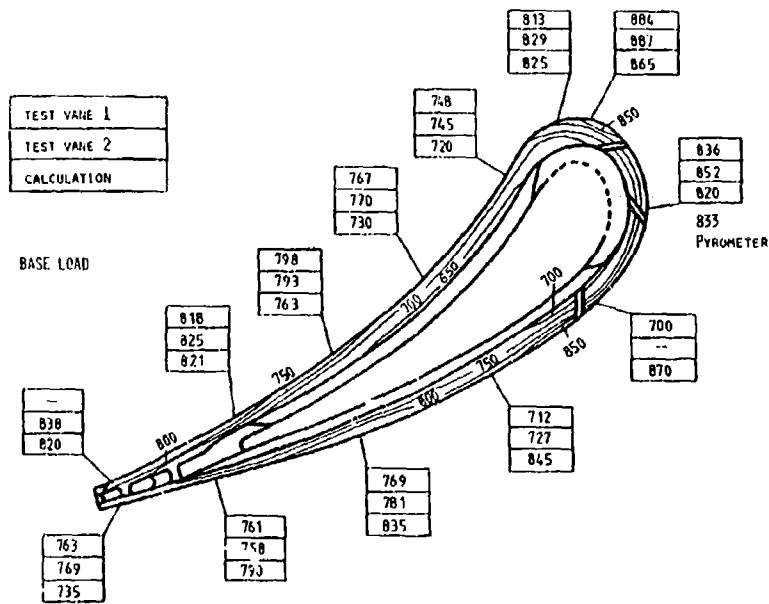
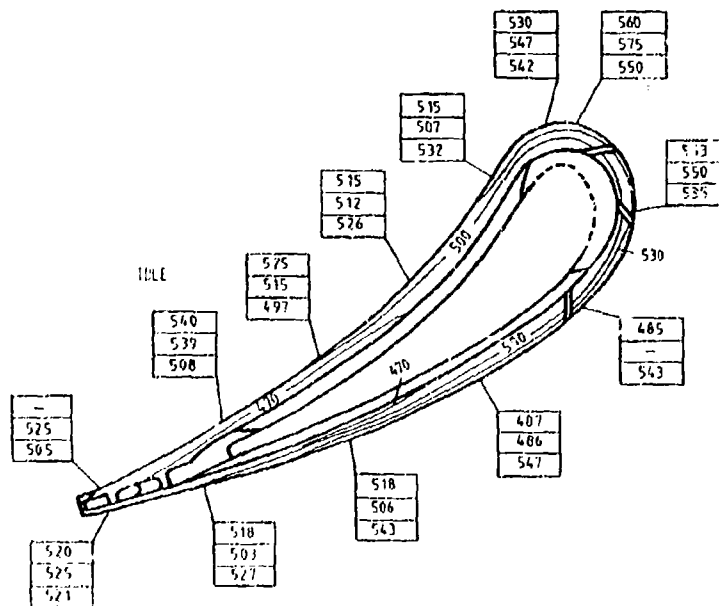


Fig. 10: Calculated and measured wall temperatures of the first stage vane



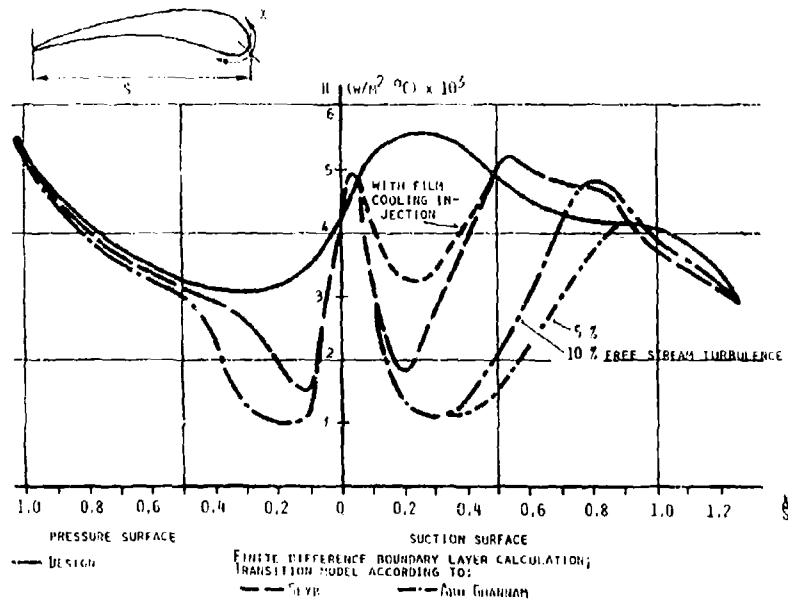


Fig. 11: Calculated gas-side heat transfer coefficients (vane)

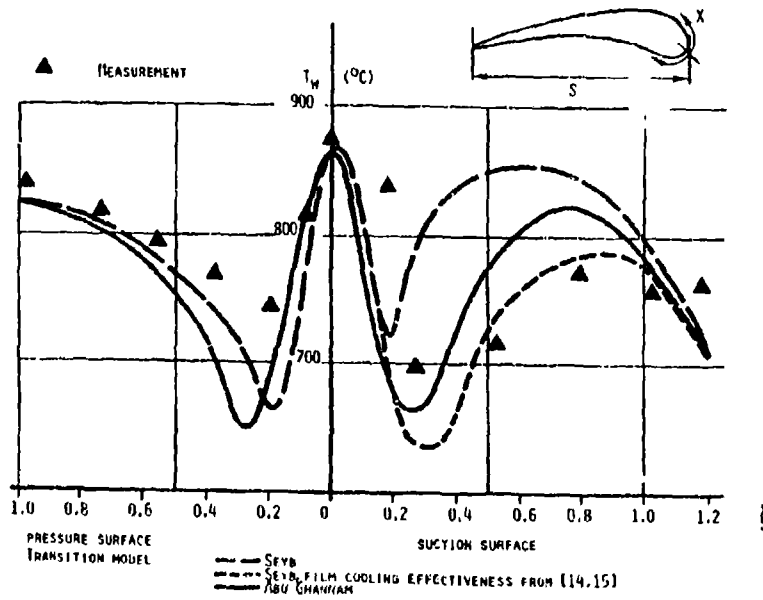


Fig. 12: Comparison of measured wall temperatures with analytical results

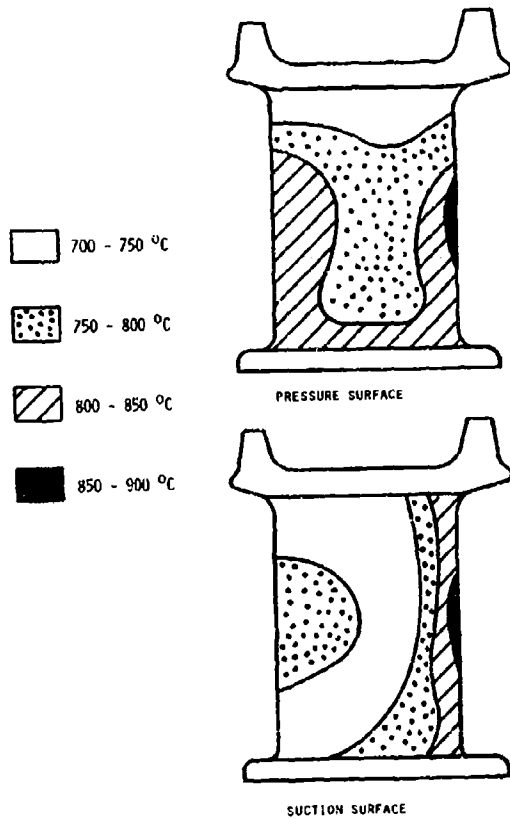


Fig. 13:
Thermal paint results (vane)

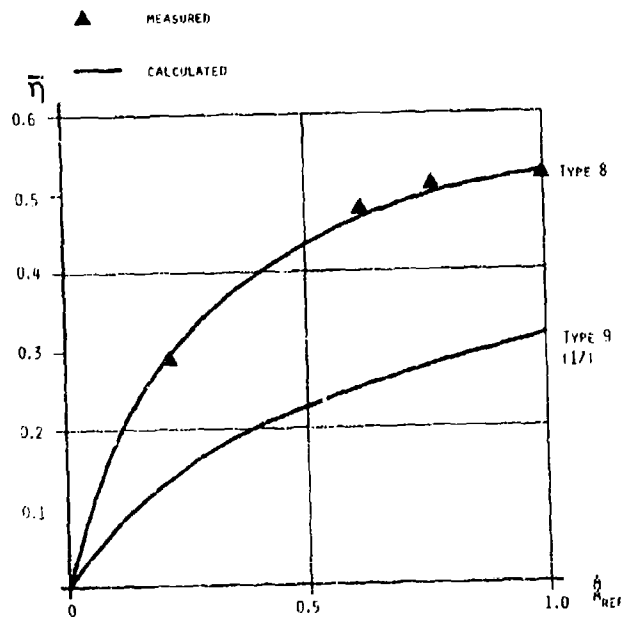


Fig. 14:
Average cooling effectiveness
as a function of the relative
cooling mass flow (vane)

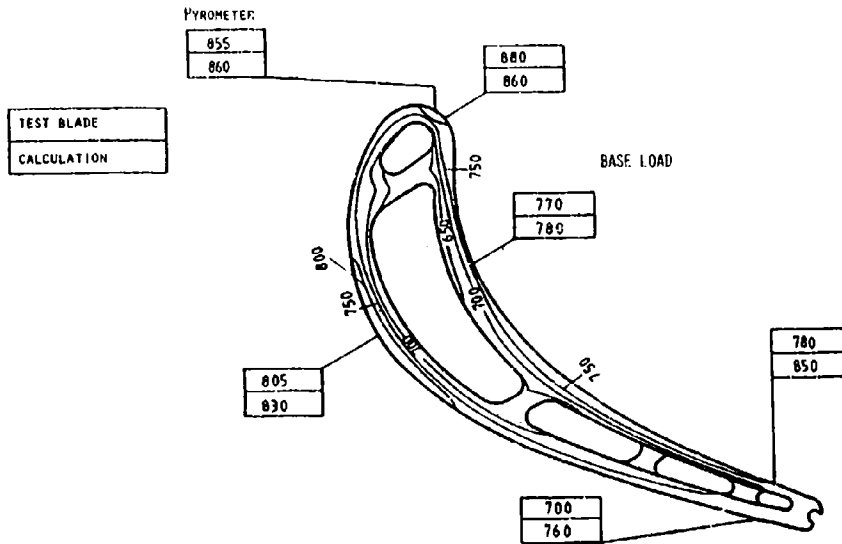


Fig. 15:
Calculated and measured
wall temperatures of
the first stage blade

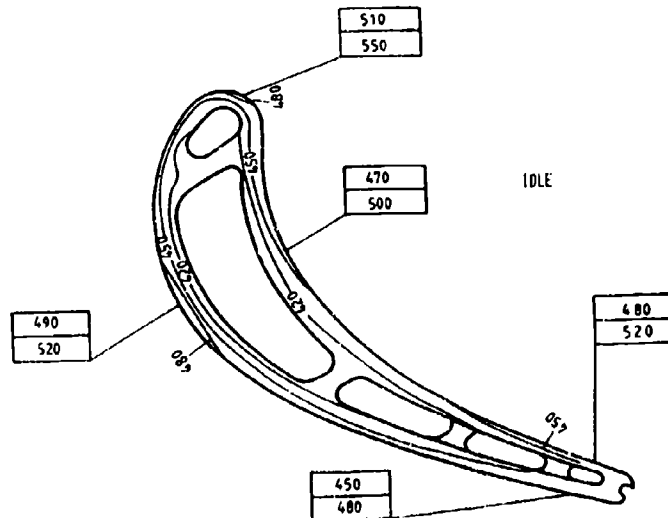
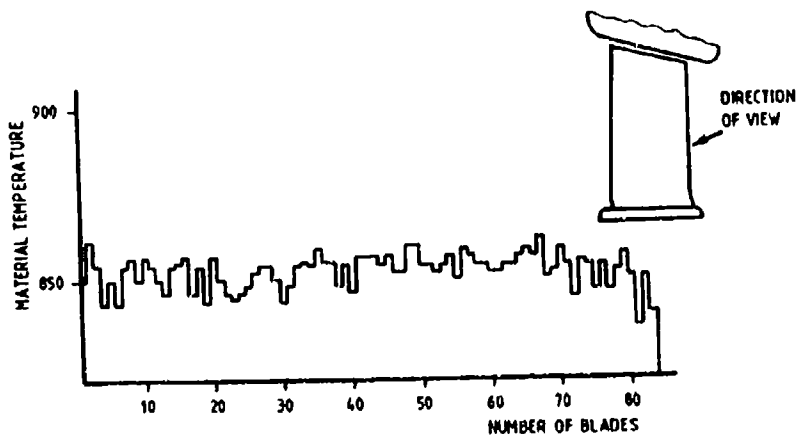


Fig. 16:
Temperatures of
metal surface of
first rotor blade
measured with
pyrometer



DISCUSSION

J.J.Witton, UK

Did your method of thermocouple attachment alter the blade surface roughness? Can you quote the roughness?

Author's Reply

Since all thermocouple grooves were first filled with brazing material and then ground over, there was little effect on the surface roughness. The equivalent sand grain roughness for case surface is in the order of 6–10 μ m.

G.M.Dibelius, Gc

You mentioned the pyrometric measurement of the metal temperature of the first stage moving blades. In that connection I would like to ask the following questions:

1. Have you experienced any fouling of the optical system considering the relatively long testing period of the turbine, or what has been done for avoiding fouling?
2. What was the effect of changes of the blade surface for instance by deposits?
3. Do you have any suggestions in case pyrometric temperature measurement will be used for control instead of the turbine exit thermocouples?

Author's Reply

The optical system was checked after each test. During normal operation, the lens surface was always clean because the probe was specially arranged to avoid hot gas contact. Nevertheless it cannot be ruled out that the problem may become more important burning a different type of fuel.

Atmospheric dust, fuel ash or additives can form deposits on the blade surface. Their influence on the pyrometer results is not only due to the change in emissivity but can also be due to the thermal barrier effect of the deposit. Special tests showed temperature variations of up to $\pm 30^{\circ}\text{C}$.

Before using a pyrometer for control purposes, the problems mentioned above have to be solved. Additional effects, such as hot gas temperature distribution, variations in the blade cooling system and reflections from the first stage vane, will have to be studied in detail.

HEAT TRANSFER TEST EVALUATION OF THE SHELL-SPAR BLADE COOLING CONCEPT APPLIED TO INDUSTRIAL GAS TURBINES

G.P. Butt * and W. Edward North **

* Senior Engineer, Westinghouse Canada Inc.,
P.O. Box 510, 30 Milton Avenue, Hamilton, Ontario, Canada L8N 3K2
** Fellow Engineer, Westinghouse Electric Corp.,
P.O. Box 251, Concordville, Pa. 19331, U.S.A.

SUMMARY

This paper describes a series of heat transfer experiments to verify the theoretical prediction techniques adopted for the design of shell-spar cooled turbine vanes and blades.

Tests were performed on flat plate specimens representing a wide range of channel geometries. Each specimen was installed in one wall of a test section downstream of a combustor which was run at various operating temperatures.

A recommended design approach was formulated from analysing the results.

The potential of shell-spar cooling applied to industrial gas turbines is discussed.

A = Area
C_p = Specific Heat at Constant Pressure
D = Duct Diameter
f = Friction Factor
h = Heat Transfer Coefficient
k = Thermal Conductivity
M = Mach Number
P = Pressure
Pr = Prandtl Number (= $C_p \mu / k$)
R = Universal Gas Constant
S = Perimeter
T = Temperature
V = Velocity
W = Mass Flow
W* = Cooling Flow Function [= $WC_p / \sqrt{h_o A_o}$]
X = Distance along Channel or Surface
 γ = Ratio of Specific Heats
 ρ = Density
 ϵ = Cooling Effectiveness [= $(\hat{T}_g - \bar{T}_{mo}) / (\hat{T}_g - T_{c,1})$]
 η_c = Cooling Efficiency [= $(T_{c,2} - T_{c,1}) / (T_{mo} - T_{c,1})$]
 μ = Viscosity
 ξ = Length of Unheated Starting Section

Subscripts

Pertaining to:—

c = Coolant
g = Gas
h = Mean hydraulic
i = Internal surface
m = Metal
o = Outer surface
t = Total Stagnation
w = Wall
1 = Inlet
2 = Exit
 ∞ = Free Stream

Superscripts

— = Average Value
 \wedge = Peak Value
 \ast = Non-dimensional

1.0 INTRODUCTION

The latest designs of industrial gas turbines have cooled vanes as complex as their in service aero-engine counterparts. Fig. 1 shows a typical first stage vane which includes, twin inserts, impingement and film cooling, and banks of pedestals in the trailing edge region. This vane uses compressor discharge air as coolant.

This paper is concerned with large industrial gas turbines of outputs exceeding 30 MW. Over 80% of these engines are run continuously at full load conditions and yet vane and blade lives are expected to exceed 30,000 hours. In addition the turbine aerofoils are at least double the size, see fig. 2, (and hence wall thickness) of the large aero-engines. These factors limit the effective burner outlet temperature (BOT) of these industrial engines to around 1500K, whereas aero-engines using this vane cooling technology have run successfully at BOT's far in excess of 1650K. Admittedly industrial engines free of weight restrictions can use coolants which would increase the BOT such as cooled compressor air, steam, water, etc; although air direct from the compressor is by far the most convenient.

As part of a joint Electrical Power Research Institute (EPRI), Allison Division of General Motors, (Allison) and Westinghouse, programme; a shell-spar cooled vane design was being developed which would enable BOT's in excess of 1500K to be realised using compressor discharge air. This design as shown on fig. 3 (extracted from ref. 1) enabled more efficient heat transfer by using a low effective wall thickness whilst maintaining the mechanical integrity of existing designs. This was achieved by means of a hollow investment cast structural spar with chordwise cooling channels cast in the outer surface, and a 0.5 mm thick formed sheet shell of corrosion resistant superalloy diffusion bonded to the spar. The spar was divided into three chambers, the leading and trailing regions supplying air to the channels via connecting holes, and the mid region acting as a discharge chamber. Air in the leading edge coolant channels was dumped into the discharge chamber from where it was ejected via film cooling holes into the gas stream just upstream of the vane suction surface throat. The cooling air in the trailing edge channels was vented at the vane trailing edge. The aerofoil section was bonded directly to inner and outer endwalls. The outer endwall was cooled using the shell concept.

The major technological difficulty was concerned with developing the manufacturing techniques and the majority of work had been involved with this activity. To determine the structural integrity a number of tests had been carried out to evaluate LCF behaviour. To validate the heat transfer and flow design methods a test was carried out in the wall of a test section downstream of a combustor running at BOT's between 1420 and 1530K.

This paper presents the heat transfer and flow tests carried out at Allison on a number of flat plate specimens representing a typical range of channel configurations.

2.0 DESCRIPTION OF TEST SPECIMENS

Four flat plate test specimens shown on fig. 4 and representing the full range of cooling configurations anticipated on the final aerofoil design were manufactured. The geometries included 3 and 5 plenum designs, different channel lengths, two varieties of channel flow areas and spacings, coolant flow parallel and counter to the mainstream flow, and variations in channel inlet geometry.

Each specimen was a box assembly 150 x 90 x 28 mm containing the plenum supply and discharge chambers simulating the spar. The cooling channels were etched into one surface with inlet and exit holes drilled through the channels to the appropriate plenum chambers as shown on fig. 5. The cooling channels were closed by means of a 0.5 mm thick plate, representing the shell, diffusion bonded to the simulated spar. Cooling air feed and discharge pipes connecting with the requisite plenum chambers were welded to the specimen rear surface.

Instrumentation was installed in each specimen to measure the following parameters.

- | | |
|---------------------|---|
| Gas Stream: | <ul style="list-style-type: none"> • Gas path total pressure • Gas Path total temperature • Surface static pressure |
| Coolant: | <ul style="list-style-type: none"> • Air Temperatures in each plenum • Plenum static pressure • Cavity static pressure |
| Metal Temperatures. | <ul style="list-style-type: none"> • Surface (15-20) • Plenum side of spar simulator • Plenum divider |

Figs. 6 and 7 show both sides of a typical completed specimen. The gas side on close examination reveals the surface thermocouples and static pressure taps whilst the reverse side shows the coolant tubes and instrumentation leads.

3.0 TEST FACILITY AND PROCEDURE

3.1 Facility

An existing Allison combustor rig used for the TF41 engine was modified to provide a downstream test section for the specimens. Test section and rig installation diagrams are shown on figs. 8 and 9.

Rig instrumentation upstream of the combustor consisted of 4 chromel/alumel thermocouples, 10 total pressure probes and 4 static pressure taps. Downstream of the test section were 3 static pressure taps, 16 skin thermocouples, and a three-element BOT rake.

3.2 Specimen flow calibration

This was carried out with cold air flows to obtain the flow characteristics of the various cooling circuits at supply plenum to ambient pressure ratios from 1.2 to 1.8. The cooling circuits are shown on fig. 4 and the combinations tested are given on table I, for each specimen.

3.3 Rig testing

Each specimen in turn was installed in the rig. The rig mainstream flow was brought to 3.2 Kg/s at 965 KN/m² and 700K. The specimen coolant flow was set to the maximum value and adjusted to a temperature of 480K. After reaching steady state conditions the combustor was ignited and the BOT was raised slowly to 1530K determined by the fuel to air ratio. The cooling flow was reduced to supply plenum to gas stream pressure ratios of 1.4, 1.2 and 1.1. A complete set of data was recorded at each condition.

A fourth point was recorded at the lowest pressure ratio and with a BOT of 1420K.

The experiment was terminated due to a test rig failure on the fourth data point of the last specimen.

4.0 TEST RESULTS

Each of the four specimens was tested at four conditions: three runs at constant gas path conditions but with decreasing cooling air flows, and one run at the lowest cooling air flow and 110 K lower gas temperature. An exception to this test procedure occurred with Specimen #1 (the last specimen tested) when a test rig malfunction terminated the test series.

All data collected represent the averages of twenty readings taken following the attainment of apparent steady-state conditions.

Gas path data included gas flow rates, temperatures and pressures. The main stream flow rate was maintained at a relatively constant level for all runs. A typical main stream Mach number value was 0.4.

4.1 Gas Path Data

Gas path temperature data was obtained from a fixed three-element probe immediately upstream of the test specimen and a single-element probe immediately downstream of the specimen. In the early stages of testing, the single-element probe was calibrated against the three-element probe. This enabled the subsequent removal of the three-element probe and its disrupting effect on gas flow over the specimen. The elements of the upstream probe were located at 2.5, 5, and 7.5 mm from the specimen wall. The element in the downstream probe was located at 5 mm from the wall. The probe data indicated a variation of only 6 K in the direction normal to the wall and 14 K axially along the specimen. Therefore, the data from the aft probe were used directly as the values of gas path temperature for data correlation.

Gas path total pressure distribution normal to the wall was measured using a three-element probe immediately downstream of the specimen. The elements were located at 2.5, 5, and 7.5 mm from the specimen wall. The variation from the middle element to the other two was approximately 50 mm Hg. This was considered small enough to ignore, thus the middle element pressure was taken as the gas path total for all test runs.

Gas path static pressure taps placed at four axial locations in the specimen wall showed a very small variation thus indicating that gas path axial velocity was essentially constant along the specimen.

4.2 Plenum Data

Cooling air temperatures and pressures were measured at all plenums along with cooling air flow rates at all supply plenums. Metal temperature data were obtained from thermocouples located on the plenum side of the spar. The plenums are designated "A" through "E" in the downstream direction for five-plenum specimens, and "A" through "C" for three-plenum specimens.

4.3 Surface Temperature Data

Most surface temperature thermocouples were located along a specimen center line over the center of a land between adjacent channels. At some locations, surface temperatures were also measured over the center of an adjacent channel. Each specimen also included one axial location where thermocouples were located at the centerline and also over lands, at approximately 1.5 cm on either side of the centerline.

Each thermocouple was applied to the shell by laying the individual leads in separate .25 mm grooves leading to a location at which the junction was created by laser beam welding the joined leads to a .17 mm deep spotface in the shell metal. High temperature ceramic cement was used to embed the leads in the grooves and to restore the gas side surface.

Figure 10 is a display of the data taken during a representative test run of Specimen #1. The figure contains a sketch of the specimen to aid in showing the axial locations of the thermocouples. The value for coolant pressure ratio displayed in the figure refers to the ratio of the pressure in Plenum "E" to the gas path static pressure downstream of the specimen. The other supply plenums were set at the same pressure as Plenum "E". Specimen #1 is considered to have the highest overall cooling effectiveness of the four specimens because of its five-plenum design and its relatively small channel pitch-to-size ratio. The data show that relatively high levels of cooling were attained. Spar temperatures were approximately 200°C cooler than the shell.

The data from Specimen #2, shown in Figure 11, had the same plenum configuration as Specimen #1; however, there were only four axial groupings of channels. Also, the channel pitch-to-size ratio of the second channel group was double that of the other channels. This model also was employed to study the conduction cooling in a channel dead space such as existed between Plenums "C" and "D". As expected, this configuration showed significantly lower cooling effectiveness and less temperature uniformity than did Specimen #1; however, the surface at the dead space was relatively well cooled.

The results of a representative test run of Specimen #3 are displayed in Figure 12. This model was characterized by its three-plenum, three-channel configuration. Also, channel cross-sectional dimensions were 1.0 mm wide by 0.8 mm deep as compared to the 1.0 mm square channels of Specimens #1 and #2.

Specimen #4 differed from Specimen #3 by having twice the channel pitch-to-size ratio in the second channel group. A typical set of data, shown in Figure 13, illustrates the relatively high degree of temperature nonuniformity of this configuration. No spar temperature data were obtained from this model.

5.0 DISCUSSION OF RESULTS

The purpose of the test series was to verify the cooling capability of the shell-spar technique and to demonstrate the ability to calculate temperature distribution in the structure. The approach was to compare test data to temperature distributions derived from two-dimensional finite element models of the specimens. A three-dimensional finite element model was constructed of one specimen to verify the accuracy of the two-dimensional modelling technique.

The two-dimensional finite element model on Figure 14 illustrates a five-plenum specimen. The sections modelled were taken in the longitudinal direction, normal to the shell surface, passing through the middle of a channel. The elements used were four-sided with single mid-side nodes. The computer code contained a discontinuous element feature which enabled the simulation of the correct convection heat transfer areas of the channels in the direction normal to the model even though conduction in that direction was neglected; however, conduction areas in the other two directions were correct. The resulting two-dimensional analyses produced average temperature in the transverse direction. It will be shown later that temperature differences in the transverse direction were small; thus, the two-dimensional modelling technique was valid.

5.1 Gas Temperatures

As described in the previous section, gas temperature values were taken to be those which were measured by the downstream single-element probe located 5 mm off the specimen surface. Errors in thermocouple readings could have resulted from conduction or radiation effects. The probe was uncooled and of considerable length so that conduction error was determined to be insignificant. Radiation error was estimated to be 0.5% and, therefore, was also considered to be insignificant. These considerations led to the conclusion that the aft probe produced true gas temperature values.

5.2 Cooling Air Temperature

Coolant temperatures were measured in the supply plenums. Local cooling air temperatures in the feed and exit holes and along the channels were determined by a heat balance calculation within the finite element program using the supply plenum temperatures as the initial values.

5.3 Gas Side Heat Transfer

The calculation of hot side convective heat transfer coefficients was based on the correlation for developing turbulent flow over a flat plate with constant free stream velocity².

$$h_g = 0.0295 \frac{k_g}{X} \left(\frac{\rho_g V_g X}{\mu_g} \right)^{0.8} Pr_g^{0.6} \quad (1)$$

Since the transition duct leading to the test specimen was not cooled to the same low level as the specimen, it was necessary to correct for this effect. Since the transition temperature distribution was not well defined, a modification to equation (1) was employed assuming an unheated starting length. The correlation for unheated starting length suggested by Kays² applied to equation (1) produces:

$$h_g = 0.0295 \frac{k_g}{X} \left(\frac{\rho_g V_g X}{\mu_g} \right)^{0.8} Pr_g^{0.6} \left(1 - \left(\frac{\xi}{X} \right)^{0.9} \right)^{-1/9} \quad (2)$$

Equation (2) applies to fluids with constant properties. In order to account for the variation of the transport properties with temperature through the boundary layer, a property ratio correction suggested by Kays² for flow being cooled produces the final form for the hot side heat transfer coefficient calculation:

$$h_g = 0.0295 \frac{k_g}{X} \left(\frac{\rho_g V_g X}{\mu_g} \right)^{0.8} Pr_g^{0.6} \left(1 - \left(\frac{\xi}{X} \right)^{0.9} \right)^{-1/9} \left(\frac{T_w}{T_\infty} \right)^{-0.25} \quad (3)$$

where X is measured from the upstream edge of the transition duct. Mass velocity was calculated from the isentropic flow relationship:

$$\rho_g V_g = \sqrt{\frac{\gamma}{RT_t}} P_t \frac{M}{\left(1 + \frac{\gamma-1}{2} M^2 \right)} \frac{\gamma+1}{2(\gamma-1)} \quad (4)$$

and Mach number was obtained from:

$$M = \sqrt{\frac{2}{\gamma-1} \left(\left(\frac{P_t}{P_s} \right)^{\frac{\gamma-1}{\gamma}} - 1 \right)} \quad (5)$$

The values for P_t and T_t were taken as those read from the total pressure and temperature probes located downstream of the specimen at 5 mm from the specimen surface. Static pressure was taken to be the average of the four static pressure taps located in the surface of the specimen.

5.4 Coolant Heat Transfer

The basic equation used for heat transfer inside a duct was:

$$h_c = 0.021 \frac{K_c}{D_h} \left(\frac{4 W_c}{S_t \mu_c} \right)^{0.8} Pr_c^{0.33} \quad (6)$$

which was employed directly to calculate heat transfer within the feed and exit holes, but was modified for the channels to include the effects of temperature dependent fluid properties, surface roughness and entrance effects.

The modification for temperature dependent fluid properties employed the temperature ratio method using the coefficient suggested by Kreith³ for flow being heated. The right side of equation (6) was thus multiplied by the factor:

$$\left(\frac{T_w}{T_c}\right)^{-0.575} \quad (7)$$

The surface roughness effect was accommodated by a factor suggested by Nunner⁴ applied to equation (6):

$$\sqrt{\frac{f_{\text{rough}}}{f_{\text{smooth}}}} \quad (8)$$

where the friction factors were obtained from a Moody diagram. The effects represented by equations (7) and (8) when applied to equation (6) produce:

$$h_c = 0.021 \frac{k_c}{D_h} \left(\frac{4W_c}{S_i \mu_c}\right)^{0.8} Pr_c^{-0.33} \left(\frac{T_w}{T_c}\right)^{-0.575} \sqrt{\frac{f_{\text{rough}}}{f_{\text{smooth}}}} \quad (9)$$

A correction for entrance effect was necessary to account for the fact that heat transfer is higher there than in the fully developed region further downstream. The entry to the channels was considered to be typified by a right angle turn formed by the entry hole and the channel. The entrance effect used here was obtained from Figure 9-14 of (2) which displays the effects due to many different entrance configurations. The factors thus obtained from the reference figure were applied to equation (9).

Heat transfer within the plenums was considered to be represented by the correlation for laminar flow over a flat plate:

$$h_p = \frac{k_c}{0.323 X} \left(\frac{W_p X}{A_{HP} \mu_c}\right)^{0.5} Pr_c^{-0.33} \quad (10)$$

The supply and discharge tubes were located off the specimen centerlines, therefore, the flow in the plenums was assumed to be transverse to mainstream flow. At the centerline of the model, the flow in the plenum was assumed to be one-half the total plenum flow. The value of "X" was taken to be one-half the plenum width in the transverse direction.

5.5 Cooling Flow Rate

An accurate knowledge of the cooling flow rate in each of the channel groups was necessary for the calculation of heat transfer coefficients. During each test run, the total cooling flow to each of the supply plenums was measured. However, since many of the plenums supplied more than one channel group, it was necessary to analytically model the cooling flow circuits so that individual flow rates could be determined for all test conditions. The modelling was based on the cold flow tests in which the individual channel groups were flowed separately (Table 1). The models accounted for channel inlet and exit effects and also allowed for the influences of temperature, pressure and Reynolds number variations. In general, good agreement was obtained with flow measurements during the test runs. Total calculated flows for the models were generally within four percent (4%) of the total measured flow with the worst test run calculation result being within ten percent (10%).

5.6 Comparison of Measured and Calculated Temperatures

Plots of the calculated temperature distributions of the two-dimensional models, along with the corresponding test data, are displayed in Figures 15 through 18.

The temperature plot for Specimen #1 is shown in Figure 15. The surface temperature distribution shows a relatively good agreement with the data except along the aft channel. This may be a result of the distortion of the test rig ducting which forced termination of testing shortly after this run. Another possible contributor to this discrepancy may have been the fact that the cold flow data showed the aft channels to be flowing at approximately one-half the rate expected. It is also noted that the calculated spar temperatures in this specimen, as well as the other specimens, were significantly higher than the test data. The method described previously for calculating plenum side heat transfer may be questioned since the flow patterns within the plenums was not well defined. Also, the instrumentation might have been inadequate to study the spar cooling condition. It is noted, however, that flow within the test plenums differed from that which would occur in an actual aerofoil; i.e., test flow entered or exited the plenums through the walls opposite from the shell surface, whereas plenum flow in an aerofoil would be supplied or exhausted in a direction transverse to the channels. Therefore, the heat transfer within an actual aerofoil plenum is likely to differ from that of the test specimens. It is also felt that the primary investigation effort of predicting shell surface temperatures is not affected to a large degree by plenum side heat transfer.

The comparative results for Specimen #2 are shown in Figure 16. Surface temperature correlation appears to be very good. One point of interest is the relative low level of cooling in the second channel group where the channel spacing was twice that of the other channels. Another point to note is the surface temperature prediction accuracy at the location of the dead space between plenums "C" and "D".

The results of the comparisons of the three-plenum configurations are displayed in Figures 17 and 18. As in the other specimens, the surface temperature agreement appears to be very good. It is noted that no spar temperature data was obtained from Specimen #4. The essential difference to be noted between the results of the two models is the relatively diminished cooling in the middle group of channels of Specimen #4 caused by the spacing being twice that of Specimen #3.

5.7 Comparison Of Two And Three-Dimensional Finite Element Models

As a check on the analytical accuracy of the two-dimensional finite element technique, a three-dimensional finite element model of Specimen #3 was constructed as shown in Figure 19. The model represented a section of the specimen covering one full channel width plus a half land width on either side of the channel. The comparative results for a particular section of the specimen are displayed in Figure 20. It is noted that the three-dimensional results show the transverse temperature variation on the shell surface to be very small. Furthermore, the agreement between the relative temperatures of shell surfaces of the two models is also very good.

Figure 21 illustrates an overall comparison among the data and the results of the two-dimensional and three-dimensional analyses for Specimen #3. The display supports the validity of the two-dimensional modelling techniques.

6.0 CONCLUSIONS

The shell-spar technique was conceived to deal with the problem of large conductivity losses in highly cooled turbine aerofoils. By transferring the load bearing structure away from the external aerofoil, the wall can be made thinner thus reducing temperature differences across the material. The small, closely spaced channels beneath the shell provide a large surface area advantage for the cooling medium. The results reported herein have demonstrated the viability of shell-spar cooling, namely:

- (1) A high level of cooling effectiveness has been verified.
- (2) The shell surface temperatures can be predicted using textbook heat transfer correlations for the cooling channels.
- (3) Temperature prediction for the specimen spars was not good; however, this is felt to be of minor concern because the plenum flows did not duplicate those which would occur in a turbine aerofoil. It should also be noted that measured spar temperatures were lower than calculated.

7.0 FUTURE POTENTIAL

The cooling performance chart for nozzle guide vanes (NGV's) shown on Figure 22 enables various cooling designs to be compared. The shaded region denotes where the majority of in-service aero-engine designs lie. Some experimental vanes have achieved cooling efficiencies greater than 120% with transpiration cooled versions at even higher levels of achievement.

The evolution of industrial cooled NGV's is typified by the W251 engine development from the early B2 to the latest B9/10 version (figure 1). Here a steady improvement in cooling performance may be seen with the B9/10 NGV design being within the shaded aero-engine region.

The shell-spar design (figure 3) shows a further improvement in performance which at the existing W251 B9/10 Vane Metal temperatures would allow an increase of over 100 K in firing temperature. The basic shell-spar concept is at an early stage of development. Even greater improvements in performance are possible with the introduction of standard heat transfer augmentation devices such as impingement and increased film cooling.

8.0 REFERENCES

- (1) Levari, G.N., Jeffries, R.E., Cohn, A., ASME, **Advanced Cooled First Stage Vane Design**, 1984, 84-GT-219,1.
- (2) Kays, W. M., **Convective Heat and Mass Transfer**, 2nd Edition, International Company, New York, 1966.
- (3) Kreith, F., **Principles of Heat Transfer**, 2nd Edition, International Textbook Company, Scranton, Pa, 1966.
- (4) Nunner, W., "Waermeuebergang and Drackabfall in Rauhen Rohren" (Heat Transfer and Pressure Drop in Rough Pipes), **VDI Forschungsheft 455, Series B, Volume 22, 1956**. English translation, AERE Lib./Trans. 786, 1958.

9.0 ACKNOWLEDGEMENTS

The authors wish to extend their appreciation to the Allison Division of General Motors, particularly to David Nealy and Wiley Davis.

TABLE I
COLD FLOW TEST COMBINATIONS

Specimen	Test No.	Plenum Condition*					Cooling Circuit(s) Tested
		A	B	C	D	E	
T827674 (Specimen No. 1)	1	X	X	X	X	S	5
	2	X	X	X	D	S	4
	3	X	X	S	D	X	3
	4	X	D	S	X	X	2
	5	S	D	X	X	X	1
	6	S	D	S	X	X	1 + 2
	7	X	X	S	D	S	3 + 4
	8	X	X	X	D	S	4 + 5
	9	S	D	S	D	S	1 + 2 + 3 + 4 + 5
	10	X	D	S	D	X	2 + 3
T827675 (Specimen No. 2)	1	X	X	X	X	S	4
	2	X	X	X	D	S	3
	3	X	X	X	D	S	3 + 4
	4	X	D	S	X	X	2
	5	S	D	X	X	X	1
	6	S	D	S	X	X	1 + 2
T827676 (Specimen No. 3)	1	X	X	S	—	—	3
	2	X	D	S	—	—	2
	3	S	D	X	—	—	1
	4	S	D	S	—	—	1 + 2
	5	X	D	S	—	—	2 + 3
	6	S	D	S	—	—	1 + 2 + 3
T827677 (Specimen No. 4)	1	X	X	S	—	—	3
	2	X	D	S	—	—	2
	3	S	D	X	—	—	1
	4	X	D	S	—	—	2 + 3
	5	S	D	S	—	—	1 + 2 + 3

* S = SUPPLY D = DISCHARGE X = CLOSED OFF

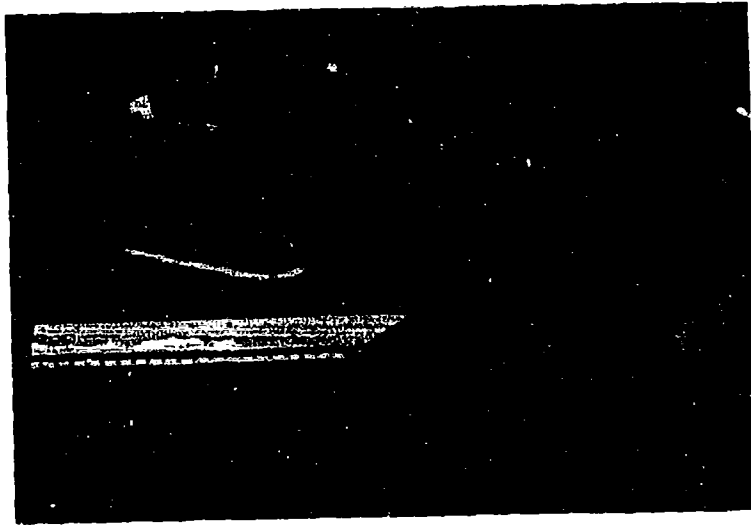


FIGURE 1 W251 B10 FIRST STAGE TURBINE VANE

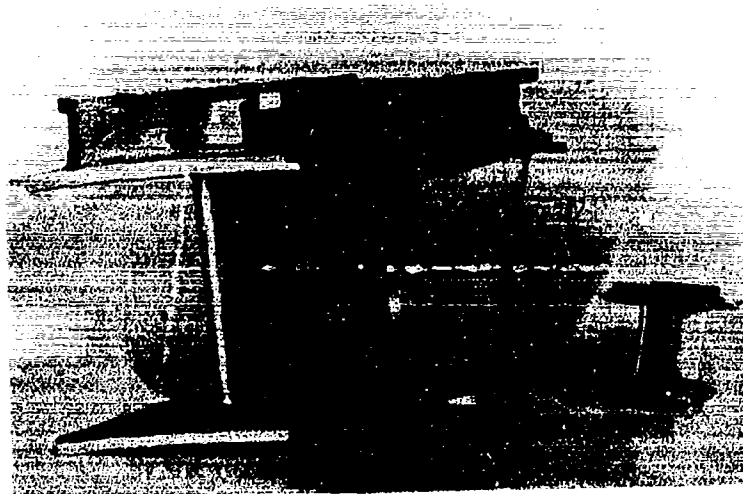


FIGURE 2 COMPARISON OF TYPICAL INDUSTRIAL TO AERO-ENGINE FIRST STAGE VANE SIZES- W251B2 (LEFT), TF(41) RIGHT

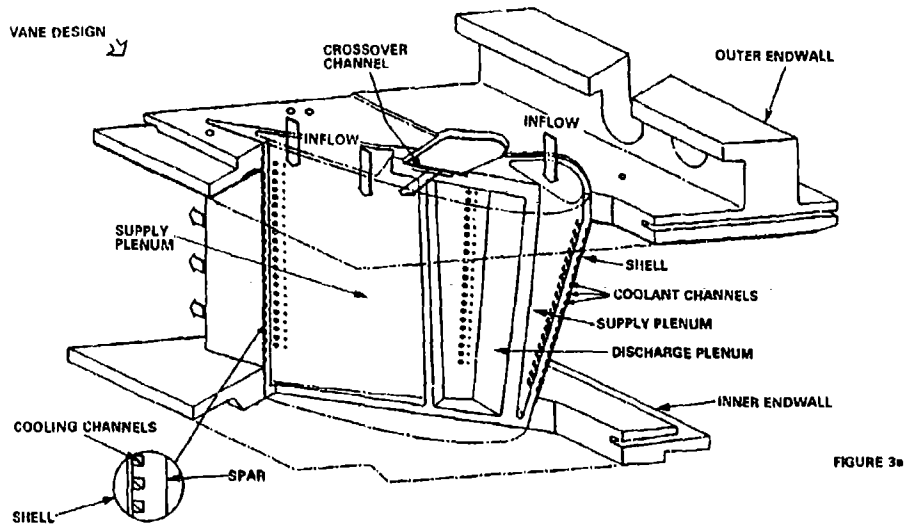


FIGURE 3a

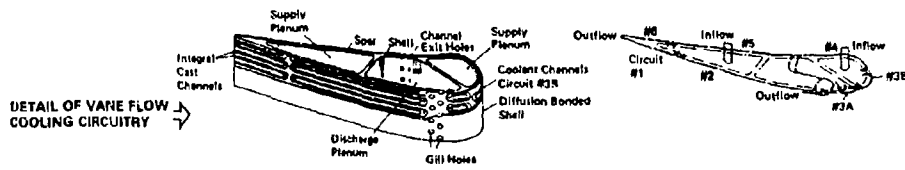


FIGURE 3b

CONCEPTUAL DESIGN OF THE SHELL-SPAR ADVANCED COOLED VANE

TEST SPECIMEN CONFIGURATIONS

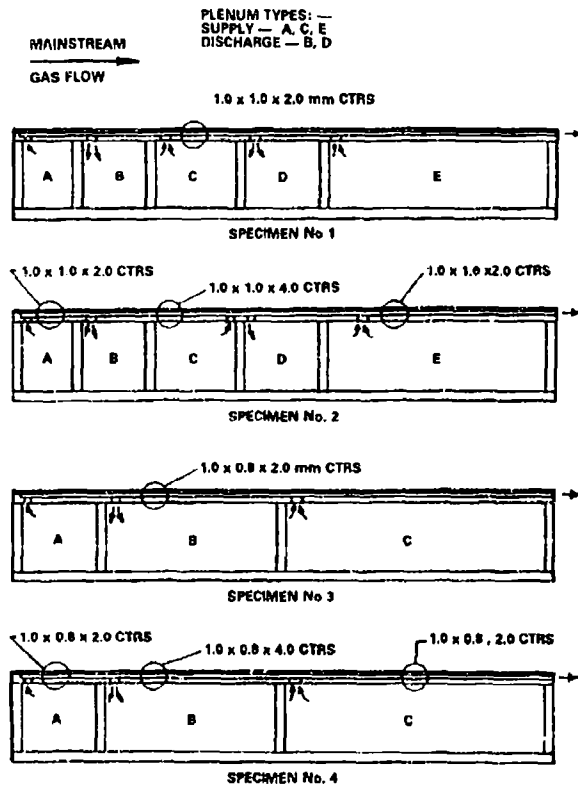


FIGURE 4

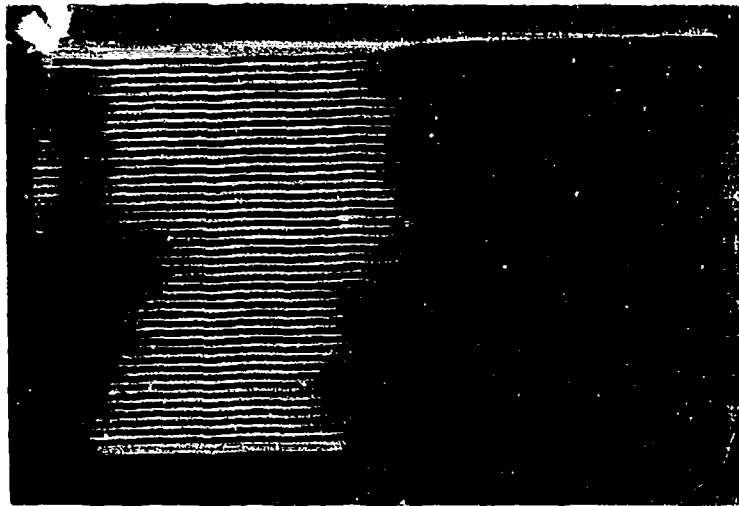


FIGURE 5 TEST SPECIMEN No. 1-COOLING CHANNELS PRIOR TO BONDING OF COVER SHEET



FIGURE 6 TEST SPECIMEN No. 1-GAS STREAM SURFACE OF COMPLETED SPECIMEN

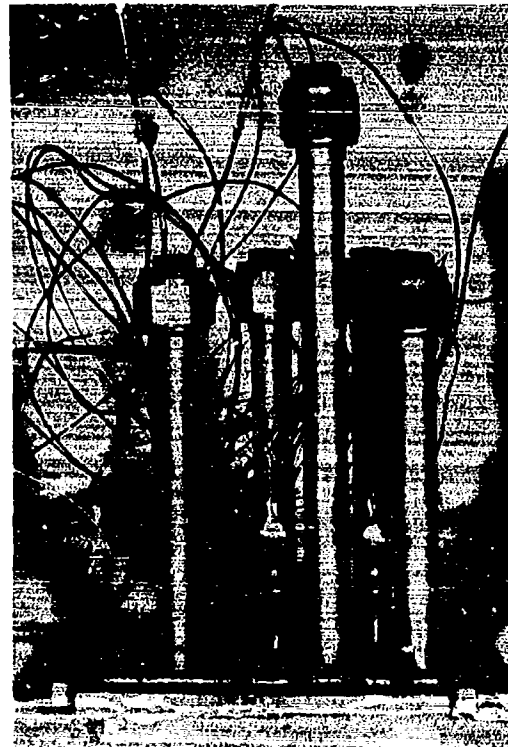


FIGURE 7 TEST SPECIMEN No. 1-BACK SURFACE OF COMPLETED SPECIMEN

TEST SPECIMEN INSTALLATION

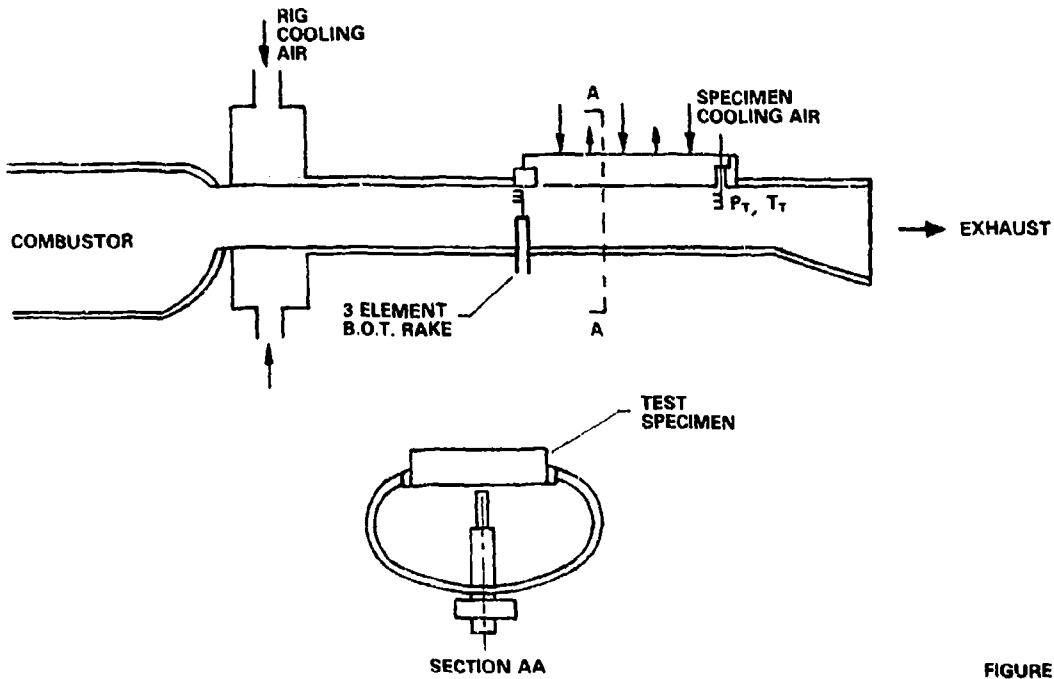


FIGURE 8

RIG INSTALLATION DIAGRAM

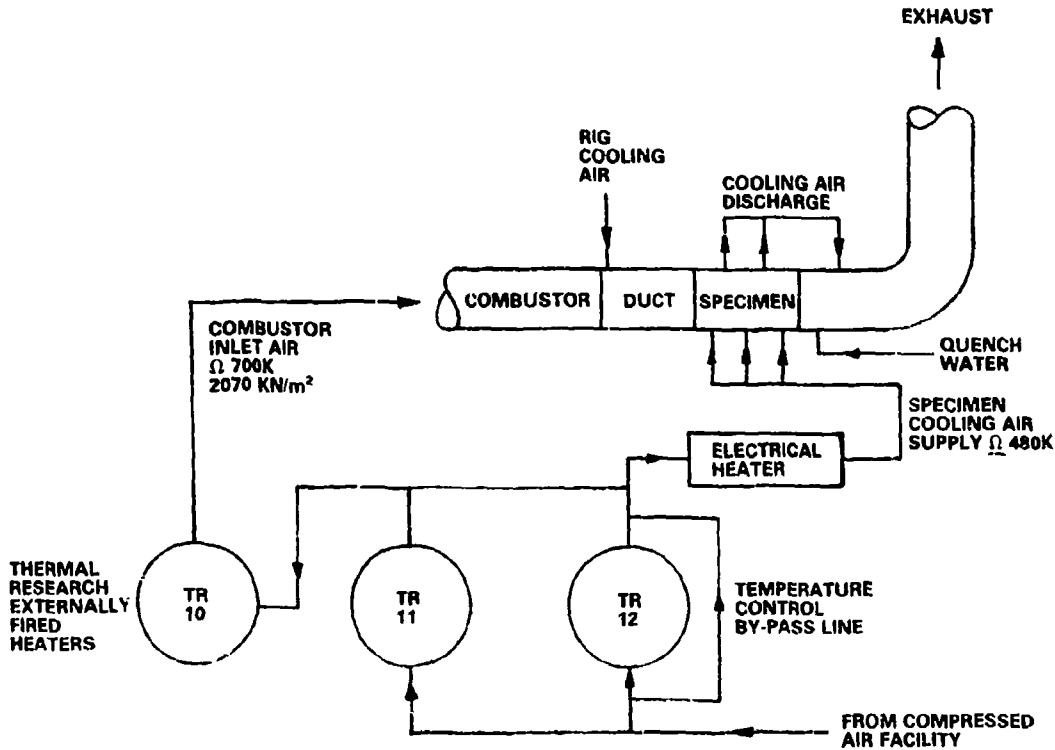


FIGURE 9

FIGURE 10: TEMPERATURE DATA - SPECIMEN No. 1

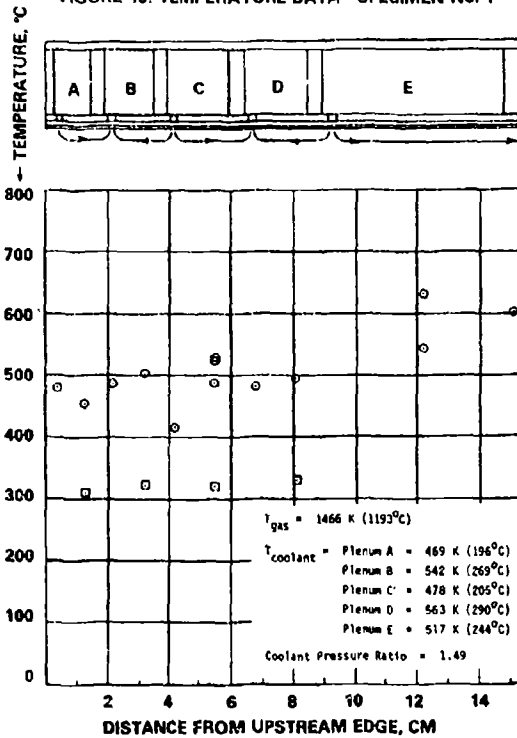


FIGURE 11: TEMPERATURE DATA - SPECIMEN No. 2

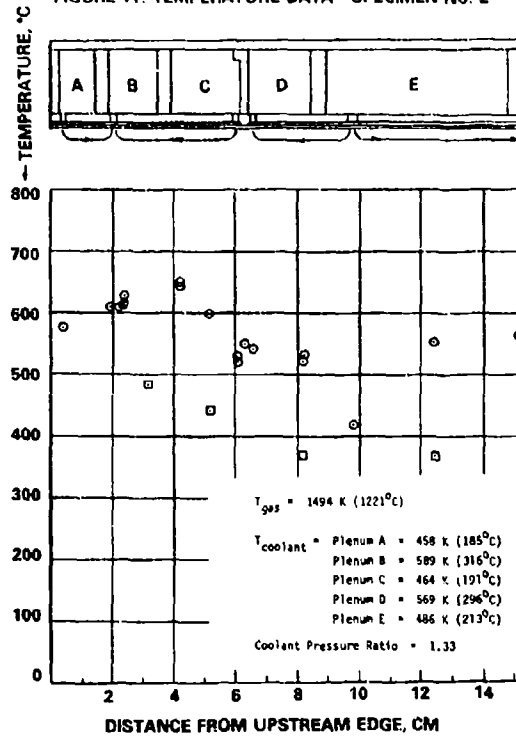


FIGURE 12: TEMPERATURE DATA - SPECIMEN No. 3

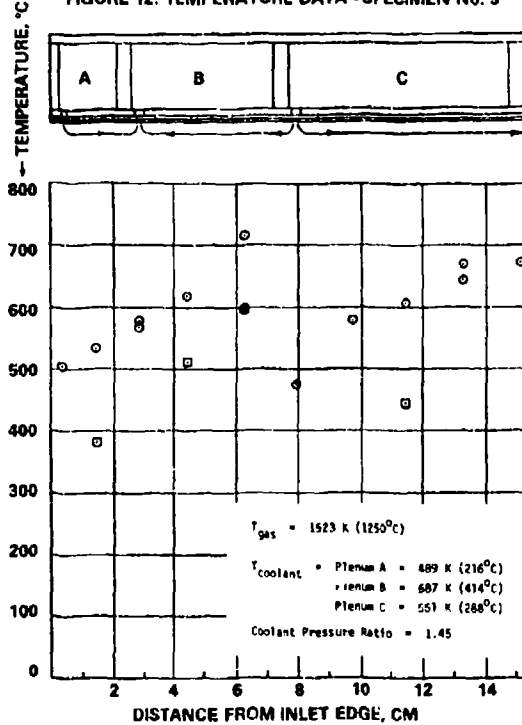
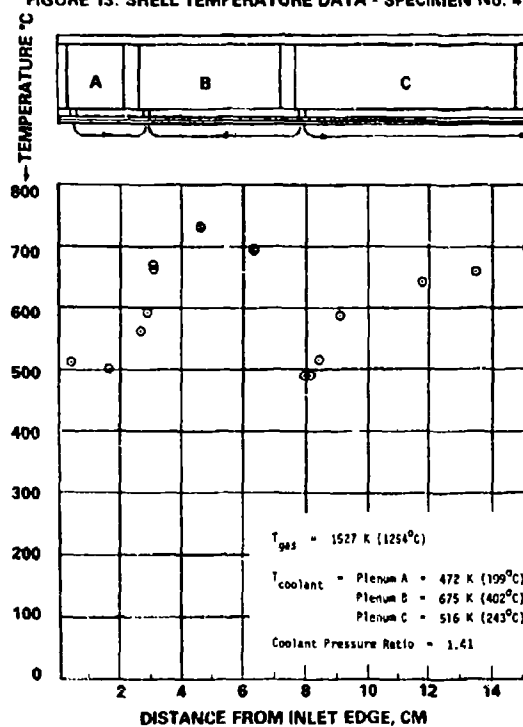
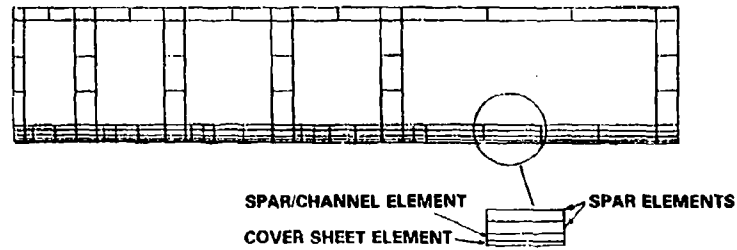
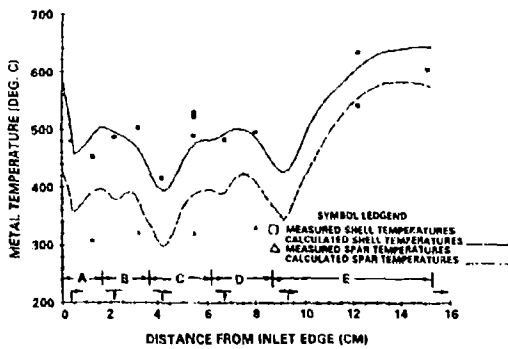
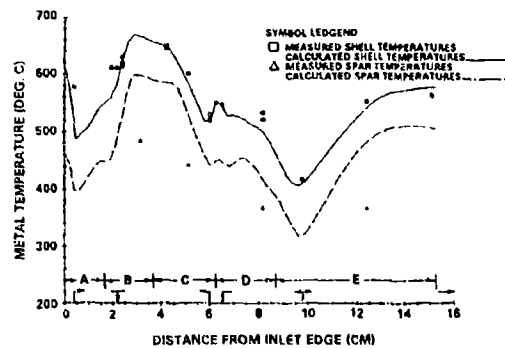
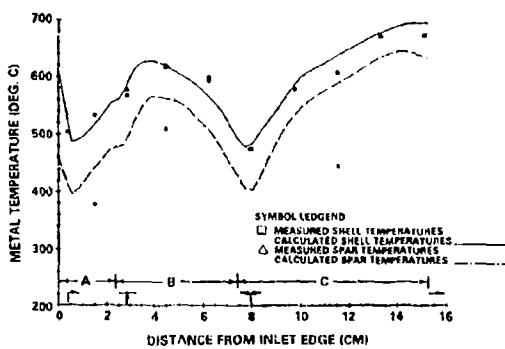
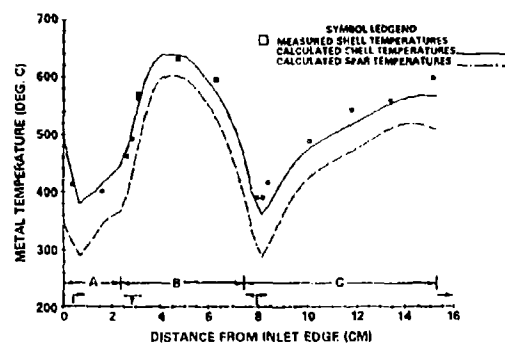


FIGURE 13: SHELL TEMPERATURE DATA - SPECIMEN No. 4



○ — SHELL SURFACE TEMPERATURES
 □ — TEMPERATURES OF PLENUM SIDE
 OF THE SPAR SIMULATOR

FIGURE 14: FINITE ELEMENT MODEL OF 5-PLENUM SPECIMEN

FIGURE 15: SHELL-SPAR TEST SPECIMEN No. 1
COMPARISON OF MEASURED AND CALCULATED TEMPERATURESFIGURE 16: SHELL-SPAR TEST SPECIMEN No. 2
COMPARISON OF MEASURED AND CALCULATED TEMPERATURESFIGURE 17: SHELL-SPAR TEST SPECIMEN No. 3
COMPARISON OF MEASURED AND CALCULATED TEMPERATURESFIGURE 18: SHELL-SPAR TEST SPECIMEN No. 4
COMPARISON OF MEASURED AND CALCULATED TEMPERATURES

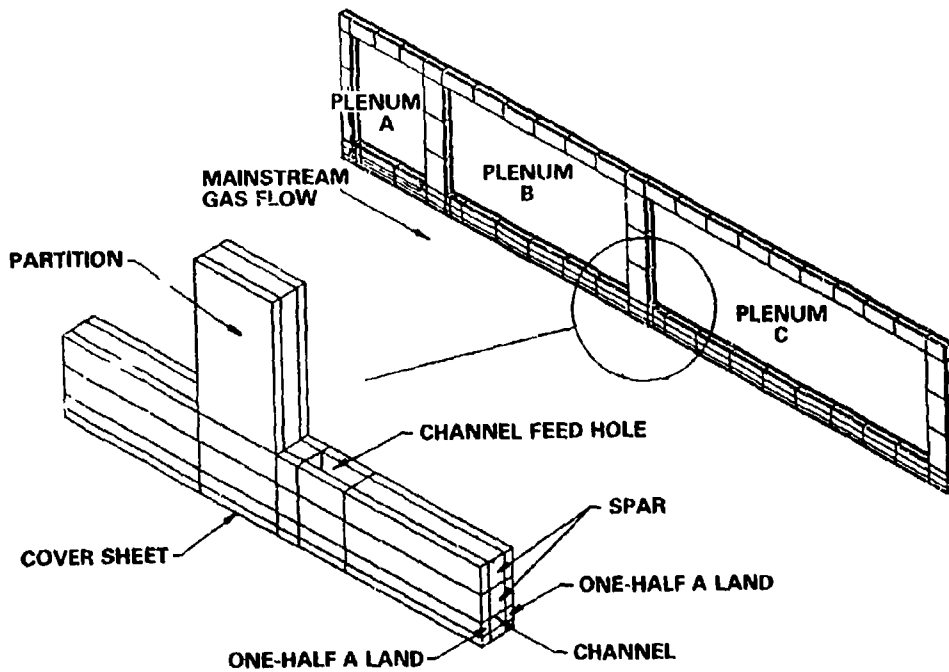


FIGURE 19: THREE-DIMENSIONAL FINITE ELEMENT MODEL OF SPECIMEN No. 3

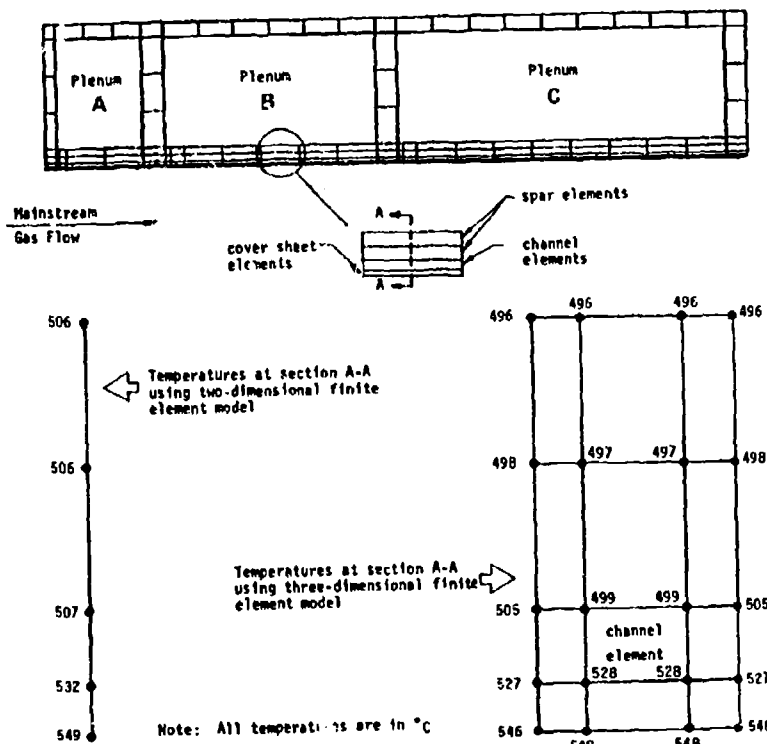
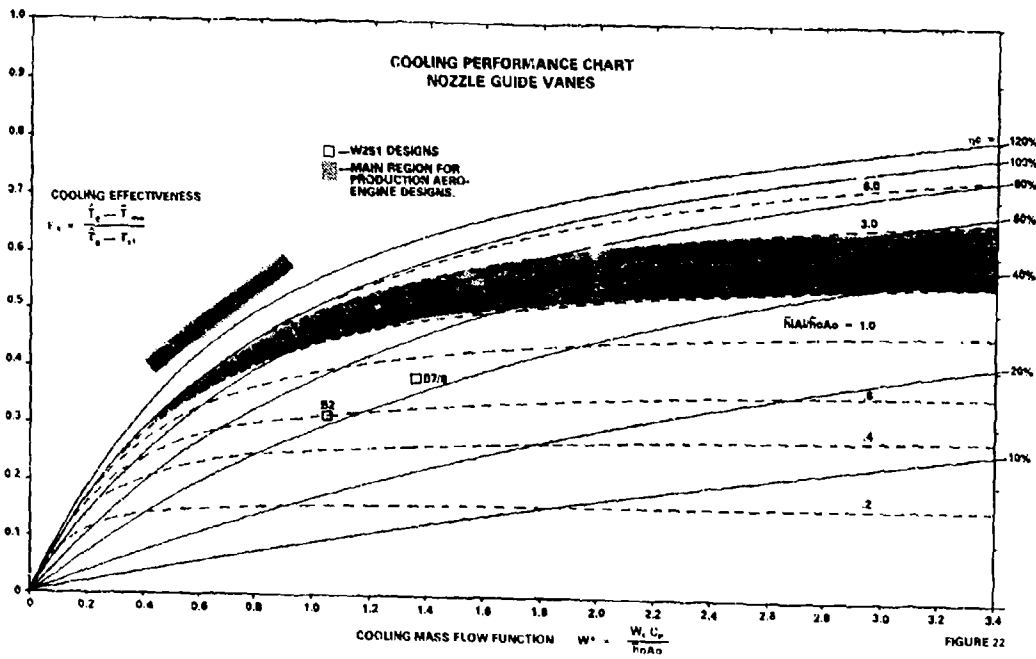
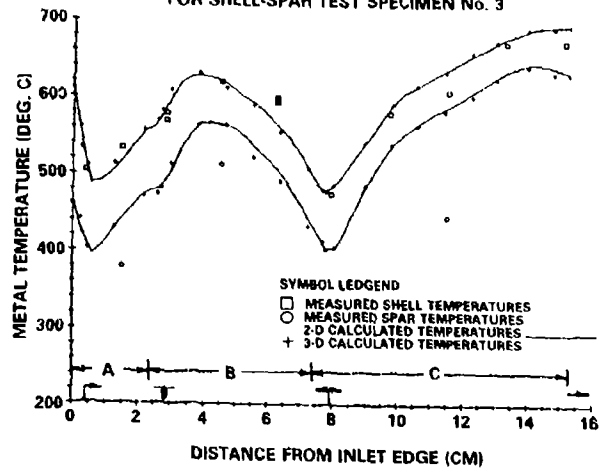


FIGURE 20: COMPARISON OF TWO- AND THREE-DIMENSIONAL CALCULATION RESULTS FOR A SECTION OF SPECIMEN NO. 3 AT A POINT 5.1 CM FROM THE UPSTREAM EDGE.

FIGURE 21: COMPARISON OF 2-D AND 3-D FINITE ELEMENT CALCULATIONS FOR SHELL-SPAR TEST SPECIMEN No. 3



DISCUSSION**G.E.Andrews, UK**

Your paper illustrates the potential that enhanced internal wall cooling techniques have in reducing metal temperatures. Your test-rig is similar to the one we have at Leeds. In our work at the temperatures that you operated with we have found that the temperature difference between the test-plate and the air-cooled duct can result in significant radiant cooling of the test-plate and hence test-temperatures that are too low. I would suggest that you should measure your duct temperature and correct for this effect. The correction procedure used at Leeds is detailed in Ref.11, paper No.26.

Author's Reply

The duct temperature was not measured. However since the duct cooling was less effective than the flat plate specimen cooling schemes, and that the coolant temperature in the duct was delivered at 700°K any radiation would have been from the duct to the specimen.

HEAT-FLUX MEASUREMENTS AND ANALYSIS FOR A ROTATING TURBINE STAGE

by
Michael G. Dunn
Physical Sciences Department
Arvin/Calspan Advanced Technology Center
Buffalo, New York 14225

SUMMARY

A measurement and analysis program is on-going at Calspan that utilizes: (1) a Garrett TFE 731-2 high-pressure turbine stage and (2) a Garrett low aspect ratio turbine (LART) stage. The major emphasis of this program has been placed on obtaining accurate measurements of heat-flux distributions in the full-scale rotating turbine stage. The experimental technique being used is the short-duration, shock-tunnel approach, in which fast-response, thin-film thermometers are used to measure the surface temperature histories at prescribed positions on the various component parts. Heat-flux values are then inferred from these temperature histories using standard data reduction procedures.

This paper provides a summary and discussion of the TFE 731-2 high pressure turbine results with particular emphasis on nozzle guide vane (NGV) tip endwall data not previously reported. A significantly more brief discussion of the LART stage instrumentation is also included. In addition, a summary discussion of the experimental technique and the associated instrumentation is included.

LIST OF SYMBOLS

<p>A = NGV inlet area</p> <p>Flow Function = $\frac{w_o \sqrt{\theta}}{\delta}$</p> <p>H₀ = total enthalpy</p> <p>H_w(T) = wall enthalpy</p> <p>N_{corr} = corrected rotor speed, $N_{phy} / \sqrt{\theta}$</p> <p>N_{phy} = physical rotor speed</p> <p>q(T) = heat flux corrected for variable thermal properties of the pyrex substrate</p> <p>S = distance on endwall measured along surface (see Figure 4)</p> <p>S_T = distance on endwall measured along surface from leading to trailing edge of vane.</p>	<p>T_w = initial wall temperature</p> <p>ΔT = measured surface temperature rise of pyrex substrate</p> <p>T₀ = total temperature</p> <p>T_c = coolant temperature</p> <p>W_c = coolant weight flow rate</p> <p>w_o = physical weight-flow rate</p> <p>x = local spanwise distance (see Figure 4)</p> <p>X_T = total local spanwise distance (see Figure 4)</p> <p>δ = Pt)/14,696 psia</p> <p>θ = T₀/518°R</p>
---	---

$$(\text{Stanton Number})_{\text{INLET}} = \frac{q(T)}{(w_o/A) [H_0 - H_w(T)]}$$

INTRODUCTION

The efficiency of gas turbine engines is influenced by the maximum turbine inlet temperature, and the performance improvements that can be realized by increases in this parameter are significant. Such increases are limited by hot section heat-transfer considerations. For this reason, many contemporary research efforts are aimed at achieving a better understanding of the flow and heat transfer in the combustor and turbine sections.

One such program is ongoing at Calspan, the major emphasis being placed on making accurate measurements of heat-flux distributions in a full-scale rotating turbine stage. However, to better understand these data, many other measurements are required in addition to heat flux. The experimental technique being used is the short-duration, shock-tunnel approach, for which a shock tube is used to create a reservoir of shock-processed test gas, a portion of which is subsequently passed through the turbine stage.

One major advantage of the short-duration technique is the ability to duplicate an operating point on the turbine performance map (N_{corr} and flow function) but the time for which the instrumentation is subjected to this environment is very short, i.e., on the order of 20 milliseconds. Because of this short exposure time, the metal portions of the stage remain essentially at room temperature thus making the structural problems associated with the experiment less severe than they might be otherwise. The experimental technique has the flexibility to also duplicate the engine environment values of T_w/T₀, T_c/T₀ and W_c/W_{engine}.

The short-duration technique is well suited to studying the interaction of rotor blades with stator vanes, which is becoming of importance to designers of gas turbine engines. In general, it is difficult to obtain full-stage measurements of this interaction for a particular point on the operating map. Within the past ten

years, high sampling frequency wave form recorders have made it possible to obtain instantaneous heat-flux data at prescribed positions on a rotor blade while this rotor blade is traversing the NGV exit passage. A measurement program investigating this interaction has been in progress at Calspan for several years.

Many results obtained at Calspan using the Garrett TFE 731-2 HP engine hardware and experimental techniques noted above have been reported in the literature. The first of these (1) described the flow-establishment process within the model containing the turbine hardware and the results of total temperature and pressure measurements, which confirmed that the gasdynamic behavior of the flow within the model was as designed. The second (2) reported detailed heat-flux results obtained at many locations within the nozzle guide vane. The geometry used in (2) was a 180 deg sector of inlet guide vanes (NGV's), but without a downstream rotor. Turning vanes were placed downstream of the nozzles to remove a substantial portion of the flow turning introduced by the nozzles. The third paper in this series (3) included heat-flux measurements for a full 360 deg section of NGV's and the associate downstream rotor in order to obtain full-stage data. The full-stage heat-flux results for the inlet nozzle were used to calculate a Stanton number and the results were compared with the previous (2) measurements obtained with an inlet nozzle in the absence of the rotor. The comparisons presented in (3) suggested that the rotor can have an upstream influence on the boundary-layer development on the NGV airfoil for a vane row with a subsonic exit Mach Number.

In (4), the initial 180 deg-sector data were compared with the predictions obtained using a flat-plate correlation, a two-dimensional parabolic boundary layer code (STAN5), and a three-dimensional viscous code (NANCY I). The measurements obtained for the rotor blade were later compared (5) with the predictions of (4). In addition, the comparisons earlier presented in (4) were updated to correct the heat-flux data for temperature variations in the thermal properties of the substrate.

The results of a measurement program intended to obtain Stanton number distributions for the vanes and endwall, the rotor blade, the blade tip, the blade platform, and the shroud for which: (a) the rotor speed and flow function were representative of typical engine values and (b) the ratio of wall temperature to gas total temperature, T_w/T_0 , was set at values of 0.21, 0.33, and 0.53 were reported in (6).

Heat-flux measurements in the presence of vane trailing edge cooling and with the rotor present versus being replaced with stationary flow straighteners for representative operating conditions were reported in (7). The full-stage versus NGV-only results were performed for essentially identical inlet conditions and were consistent with the results earlier reported in (3) for the same turbine hardware but at significantly different operating conditions.

A detailed description of the instrumentation and data recording techniques currently in use at Calspan in the performance of gas turbine related research in short-duration facilities is given in (8). By short-duration is meant total test times on the order of 20 milliseconds with the requirement of sampling rates in the range of 20 kHz to 2 MHz. Typical data records are included in (8) to illustrate the application of the techniques.

Predictions made by using two different analytical techniques have been compared (6) with the data presented here. The technique applied most extensively has been the Turbine Design System (TDS) (9) in use at the Air Force Aero Propulsion Laboratory. This system incorporates an axisymmetric throughflow solution, a blade-to-blade solution found by a streamline-curvature method, and a flat-plate prediction of the heat transfer rate based on the local pressure and velocity conditions. These conditions were also used as inputs to the Caugler modification of the STAN5 code (10), to generate heat-transfer rate predictions.

Many different facilities are currently being used to perform turbine related studies. These include the long run-time cascade facilities, such as those used by Blair (11), Graziani et al. (12), and Hylton et al. (13), and the low-speed rotating rig of Dring (14). Other groups have used short-duration facilities similar to that used in the present study. Louis (15,16) has used thin-film, heat-transfer gages to obtain heat-flux measurements on turbine components with a blow-down facility as the source of test gas. Jones, Schultz et al. at Oxford University (17-20) have also used thin-film heat-transfer gage techniques, with a light piston facility as the supply of test gas.

This paper will deal in the main with measurements obtained for the full-stage TFE 731-2 HP rotating turbine with particular emphasis on reporting much more extensive NGV tip endwall data than were previously available. For completeness, the previously reported vane and rotor measurements are also included. This paper also includes a brief discussion and several photographs of heat-transfer instrumentation used for the recently completed full-stage low aspect ratio turbine (LART) measurement program.

APPARATUS

A schematic of the experimental apparatus is shown in Figure 1 along with a typical x-t diagram. The shock tunnel consists of a driver tube, a double diaphragm section, a driven tube, a primary nozzle and a test-section device which houses the

turbine stage. In order to initiate an experiment, the test section is evacuated, the driver, the double diaphragm section, and the driven tube are pressurized to predetermined values. The rotor is brought up to the predetermined speed at which time the double diaphragm region is rapidly evacuated causing the upstream diaphragm to burst immediately followed by bursting of the downstream diaphragm. The incident shock wave forms in the driven tube and subsequently reflects from the shock tube endwall resulting in a supply of reflected-shock processed gas (condition ① in Figure 1). The specific heat ratio and speed of sound of the driver-tube gas are adjusted prior to running so that the impedance across the interface is nearly matched resulting in a tailored-interface condition (21), thereby increasing the duration of uniform conditions in the reflected-shock region. This reflected-shock processed gas is expanded in the primary nozzle, ①, so that the total pressure downstream of the standing shock wave can be tailored to the desired NGV inlet conditions. At the predetermined location in the expansion, a portion of the flow is intercepted by the test section device. A normal shock forms outside the model giving the desired conditions, ②, approaching the turbine stage inlet guide vanes (NGVs). The flow control nozzle is used to set the pressure ratio across the turbine stage. If the NGV operates at a subsonic exit condition, then the flow control nozzle also establishes the weight flow rate.

The shock-tunnel facility described above provides a clean, uniform, and well-known gas dynamic condition at the inlet to the NGVs. The experimental technique is not intended to duplicate every known parameter important to turbine heat-transfer studies, but the intent is to have the flow conditions sufficiently well known and enough parameters duplicated so that the measured heat-flux distributions can be used to validate and improve confidence in the accuracy of full-stage design data and predictive techniques under development. Several different types of measurements must be obtained in order to provide this information. The primary measurement is heat-flux which is obtained using platinum thin-film gages. These gages can be made in many sizes and shapes depending upon the particular portion of the turbine stage for which one is interested in obtaining data, i.e., the button gage, the leading edge gage, contoured strip gages, or stagnation-point gages. Pressure, total temperature, rotor speed history, and tip clearance are other parameters that are routinely measured in these experiments.

A photograph of a typical button-type heat-flux gages used in this work was taken through a Leitz microscope and is shown in Figure 2. The thin-film gages are made of platinum (~1000A thick) and are painted on a pyrex substrate 9.7×10^{-4} m (0.04 in.) in diameter in the form of a strip approximately 1.0×10^{-4} -m (0.004-in.) wide by about 5.1×10^{-4} -m (0.02-in.) long. In building these gages, the intent is to obtain a gage with a room temperature resistance on the order of 50 to 100Ω. The thickness of the pyrex substrate depends upon the gage location. Those gages located in the NGV trailing edge and near the rotor blade trailing edge are approximately 3.8×10^{-4} -m (0.015-in.) thick but gages at other locations are 7.1×10^{-4} -m (0.03-in.) thick. The response time of these heat-transfer elements can be shown to be on the order of 10^{-8} s. A coating of magnesium fluoride (~1200 Å thick) is vapor deposited over the gage to protect the platinum element against abrasion.

The button-type gages described above were installed in the TFE 731 turbine stage at the following locations: (a) on the NGV tip endwall, (b) on the NGV suction surface, (c) on the NGV pressure surface, (d) on the NGV airfoil leading edge, (e) on the rotor blade platform, (f) on the blade suction surface, (g) on the blade pressure surface, (h) in the blade tip and (i) in the shroud above the rotor. Figure 3 is a photograph of the NGV pressure surface and endwall instrumentation showing the leading edge gages and the airfoil gage coverage. Figure 4 is a sketch of the endwall gage locations. This sketch will be used later in the discussion of the endwall Stanton number data. As illustrated, s is the distance along the endwall surface in the flow direction and x is the spanwise direction measured along the solid lines shown on the sketch.

EXPERIMENTAL CONDITIONS

Table 1 gives the experimental conditions and measured parameters for the TFE 731-2 HP full-stage turbine results presented in this paper. This table includes the following quantities: (a) the stator inlet total temperature, T_0 , measured using a rake of thermocouple probes and also independently calculated from the shock-tube conditions; (b) the measured model wall temperature, T_w ; (c) the turbine weight flow, w_0 , calculated knowing the area of the exit channel, the orifice area, the turbine work extraction, the pressure in the exit channel, and the inlet total temperature; (d) the measured shock-tube, reflected-shock pressure; (e) the measured wall static pressure just ahead of the stator; (f) the average stagnation-point heat flux to a cylinder in cross flow obtained just ahead of the stator; and (g) the corrected rotor speed.

EXPERIMENTAL RESULTS

The Stanton number used here is based on conditions at the NGV inlet and was evaluated using the relationship

$$(\text{Stanton No.})_{\text{INLET}} = \frac{q(T)}{w_0/A (H_0 - H_w(T))}$$

The standard deviation was computed for the data set at the given test condition. The experimental reproducibility was generally within ± 5 percent for most locations. When these results are presented on the data plots, the symbol will indicate the mean value and the bar indicates the standard deviation. The absence of a bar means that the standard deviation was within the symbol.

TFE-731 NGV ENDWALL RESULTS

Figure 5 presents the Stanton number distribution at two locations on the NGV tip endwall for the TFE-731 HP turbine. Recall that the Stanton number discussed herein is based on inlet conditions and is computed in the manner described above. The numbers in the circles denote the heat-flux gage positions and their relative locations can be seen on Figure 4. The description "near pressure surface" or "near suction surface" means that the center of the gage is located on the endwall at approximately 2.8×10^{-3} m (0.110-in.) away from the intersection of the vane with the endwall. In the early portion of the flow passage, the inlet Stanton number is greater near the suction surface. At about 75% of the total flow distance along the wall, the measured values near the pressure surface become approximately equal to those near the suction surface and remain so until the exit plane with the exception of location (105) near the pressure surface which becomes the maximum value.

Figure 6 is a more detailed plot of the results obtained at the exit plane. Along a line from the suction surface towards the pressure surface (see Fig. 4), the Stanton number remains nearly constant over approximately 75% of the exit. However, near the pressure surface the Stanton number increases by approximately 25%.

Figure 7 presents similar spanwise results for three other locations (see Fig. 4) in the endwall passage. The line of gages represented by (79), (81), and 81 is along the inlet and resulting Stanton numbers are relatively uniform. The second line starts with position (83) which is 8.6×10^{-4} m (0.034-in.) away from the suction surface and ends with position (87) which is 2.05×10^{-3} m (0.081-in.) away from the pressure surface. The general trend along this line is for the Stanton number to decrease as the pressure surface is approached up to about 50% span where the trend is to level out. The third line starts with position (88) which is 2.2×10^{-3} m (0.087 in.) away from the suction surface and ends with position (92), which is 2.91×10^{-3} m (0.115-in.) away from the pressure surface. The Stanton number profile along this line is similar to that along the previous line, but the peaks and valleys occur at different spanwise locations. This endwall flow field is extremely complicated and at the present time we have not run a flow field computation to aid in analyzing these data. Techniques are available (22-24) and one of them may be applied to these data at a later date.

TFE-731 NGV AIRFOIL RESULTS

It was mentioned earlier that detailed Stanton number results had been presented in (6) for the full-stage rotating turbine of the Garrett TFE 731-2 engine. However, for the purposes of completeness, a few of the results presented in (6) that have been enhanced by more recent data at the $T_0 = 1000^\circ\text{R}$ operating condition (see Table 1) will be presented herein. In this portion of the paper, the experimental results are presented in detail and, where possible, the measurements are compared with the predictions obtained using the Wright-Patterson AFB Turbine Design System (TDS) computer code (9). In addition, predictions obtained using a modified STAN5 code (10) are also presented. It was shown in (6) that the predicted Stanton number distributions were relatively insensitive to the T_w/T_0 and thus only the $T_w/T_0 = 0.53$ predictions will be presented here. However, the experimental data obtained at $T_w/T_0 = 0.21, 0.33,$ and 0.53 will be presented. The measured and predicted distributions of Stanton number are compared on Figure 8 for the NGV airfoil midspan. On both the pressure and suction surface, data were obtained from the leading edge to approximately 94 percent chord. The solid and dashed lines on Figure 8 are the predicted distributions using TDS and STAN5, respectively. The TDS calculations assume that the boundary layer is either fully turbulent or fully laminar. However, the STAN5 predictions have been performed for a transition Reynolds number, Re_θ , of either 30 or 200. The important observation from Figure 8 is that on the suction surface, transition occurs much earlier than $Re_\theta = 200$. With a value of $Re_\theta = 200$, the STAN5 code significantly underpredicts the data at chord positions less than 30 percent and underpredicts the data by approximately 30 percent for chord positions beyond 50 percent. By contrast, the turbulent flat-plate prediction consistently overpredicts the data at all chord locations, the prediction being on the order of 20 percent above the data. Considering the degree of sophistication of the flat-plate prediction, the correlation is reasonably good. The suction-surface laminar flat-plate prediction is clearly far below the data and is only included for completeness. On the pressure surface, the turbulent flat-plate prediction overpredicts the data at less than 30 percent chord, is in reasonable agreement between 30 and 60 percent chord, and underpredicts towards the trailing edge. The STAN5 prediction significantly underpredicts the pressure surface data presumably because of the assumed laminar flow region from the leading edge up to $Re_\theta = 200$. This same trend continued with the STAN5 comparisons; thus, only a limited number of additional comparisons is shown.

A significant amount of rotor blade (pressure and suction surface, tip and platform locations) and shroud data were also obtained. The measured distribution of Stanton numbers on the blade pressure and suction surfaces are compared with the TDS and STAN5 predictions on Figure 9. This figure is plotted so that the tip is in the center and the platform is on each edge. The majority of the measurements were performed for chord positions in the range of 19 to 45 percent. One data point is presented for the 71 percent chord position near the tip. The respective predictions bounding the 19 and 45 percent chord positions are thus included on the plot. Note that the Stanton numbers deduced from the thin-film gages mounted in the tip are shown at the center of this figure and those obtained for the platform gages are shown on the left outer edge. On the pressure surface of the blade, the turbulent flat-plate prediction is a reasonably good representation of the measurements, but the STAN5 prediction is significantly low. Neither the flat plate nor the STAN5 predictions give a good comparison on the rotor blade suction surface. The laminar predictions are far below the data while the turbulent flat-plate prediction is above the data. At the 45 percent midchord position, the STAN5 prediction approaches the measured value as the platform is approached.

LOW ASPECT RATIO TURBINE (LART) MEASUREMENT PROGRAM

A very successful and detailed measurement program has recently been completed at Calspan that utilized the Garrett Turbine Engine Company low aspect ratio turbine. The specific measurements performed for this full-stage rotating turbine were local heat flux and surface pressure. The measurements were performed using the short-duration facility described above and the instrumentation techniques described in (8). Though the measurements have been completed at the time of this writing, the analysis of the data is still in progress. It is anticipated that this analysis will be completed in the near future, and at that time, portions of the data will be released. However, it is appropriate here to briefly describe the heat-flux instrumentation that was utilized because even though thin-film gages were still used, the configuration of the inserts holding the gages and the pattern density were significantly different from those used on the TFE-731 stage.

The LART instrumentation concentrated on the tip endwall and on the midspan portion of the vane and the blade. Figure 10 is a photograph of the heat-flux gage instrumentation on the LART NGV leading edge and on the pressure surface. In the leading edge region, the gages are painted on an insert that has been contoured to the airfoil geometry. The gages on this insert are spaced approximately 1.0×10^{-3} m (0.040 in.) apart starting at the geometric stagnation point and continuing around the pressure and suction sides of the insert. Also shown on Figure 10 is an adjoining airfoil that contains a contoured strip of pyrex onto which the thin-film gages have been painted at intervals of approximately 2.5×10^{-3} m (0.100-in.) from the termination of the leading edge insert to the trailing edge. If one looks to the left of the pressure surface insert on the tip endwall, then the button gages located on the endwall are also visible.

Figure 11 is a photograph of the suction surface heat-flux gage distribution for the LART NGV airfoil. Once again, a pyrex strip was contoured to the airfoil geometry and then the thin-film gages were painted on the surface at intervals of approximately 2.5×10^{-3} m (0.100 in.) starting near the termination of the leading edge insert and continuing to a location near the trailing edge as illustrated.

Figures 12 and 13 are photographs of the LART rotor leading edge insert and the button gage pattern on both the pressure and suction surfaces. The spacing used on the rotor installation was very similar to that used on the NGV airfoil. If one looks near the top of Figure 12, then the tip gages located on the blade above the one containing the leading edge insert are just visible.

For the LART measurement program, simultaneous measurement of surface pressures were obtained at selected locations on the NGV portion of the stage. In addition, the pressure upstream of the NGV and downstream of the rotor was also measured.

The high sampling frequency wave form recorders noted earlier in the text and described in (8) were used to obtain detailed information relative to rotor/stator interactions. These data are also currently being analyzed.

CONCLUSIONS

A review of an on-going measurement and analysis program at Calspan that utilizes full-stage rotating turbines has been described. Detailed Stanton number distributions throughout the stage of the Garrett TFE 731-2 HP turbine have been presented. In addition, a brief summary of a recently completed program that utilized a significantly different turbine stage has been given.

REFERENCES

1. Dunn, M.G., and Stoddard, F.J., "Application of Shock-Tube Technology to the Measurement of Heat Transfer Rate to Gas Turbine Components," 11th International Symposium on Shock Tubes and Waves, July 1977.

2. Dunn, M.G., and Stoddard, F.J., "Measurement of Heat Transfer Rate to a Gas Turbine Stator," ASME Paper No. 78-GT-119, ASME Journal of Engineering for Power, Vol. 101, No. 2, April 1979.
3. Dunn, M.G., and Hause, A., "Measurement of Heat Flux and Pressure in a Turbine Stage," ASME Paper No. 81-GT-88, ASME Journal of Engineering for Power, Vol. 104, No. 1, January 1982.
4. Winstanley, D.K., Booth, T.C., and Dunn, M.G., "The Predictability of Turbine Vane Convection Heat Transfer," Paper No. AIAA-81-1435, presented at the AIAA/SAE/ASME 17th Joint Propulsion Conference, July 27-30, 1981, Colorado Springs, Colorado.
5. Dunn, M.G., and Holt, J.L., "Turbine Stage Heat Flux Measurements," Paper No. 82-1289, AIAA/ASME 18th Joint Propulsion Conference, 21-23 June 1982, Cleveland, Ohio.
6. Dunn, M.G., Rae, W.J., and Holt, J.L., "Measurement and Analysis of Heat-Flux Data in a Turbine Stage: Part I: Description of Experimental Apparatus and Data Analysis; Part II: Discussion of Results and Comparison with Predictions," 28th International Gas Turbine Conf., Phoenix, Arizona, 27-31 March 1983, ASME papers No. 83-GT-121 and 122, ASME Journal of Engineering for Power, Vol. 106, January 1984, pp. 229-240.
7. Dunn, M.G., "Turbine Heat Flux Measurements: Influence of Slot Injection on Vane Trailing Edge Heat Transfer and Influence of Rotor on Vane Heat Transfer," 29th International Gas Turbine Conf., The Netherlands, June 1984, ASME paper No. 84-GT-175.
8. Dunn, M.G., Lukis, G., Urso, M., Heimenz, R.J., Orszulak, R., and Kay, N.J., "Instrumentation for Gas Turbine Research in Short-Duration Facilities," Aerospace Congress and Exposition, Long Beach, CA., 15-18 Oct. 1984, paper No. 841504.
9. Wyszog, R.R., et al., "Turbine Design System," AFAPL-TR-78-92, November 1978.
10. Gaugler, R.E., "Some Modifications to, and Operating Experiences with, the Two-Dimensional Finite-Difference, Boundary-Layer Code, STAN5," ASME Paper 81-GT-89 (March 1981).
11. Blair, M.F., "An Experimental Study of Heat Transfer and Film Cooling on Large-Scale Turbine Endwalls," ASME Journal of Heat Transfer, Vol. 96, November 1974, pp. 524-529.
12. Graziani, R.A., et al., "An Experimental Study of Endwall and Airfoil Surface Heat Transfer in a Large Scale Turbine Blade Cascade," ASME Journal of Engineering For Power, Vol. 102, April 1980, pp. 257-267.
13. Hylton, L.D., Mihelc, M.S., Turner, E.R., and York, R.E., "Experimental Investigation of Turbine Endwall Heat Transfer," Vols. I, II, and III, AFWAL-TR-81-2077, August 1981.
14. Dring, R.P., et al., "An Experimental Investigation of Film Cooling on a Turbine Rotor Blade," ASME Journal of Engineering for Power, Vol. 102, January 1980, pp. 81-87.
15. Louis, J.F., "Investigation of Factors Affecting Heat Transfer to Turbine End Walls," Air Force Aero-Propulsion Laboratory, TR-73-93, October 1973.
16. Louis, J.F., "Heat Transfer in Turbines," Air Force Aero-Propulsion Laboratory TR-75-107, September 1975.
17. Jones, T.V., and Schultz, D.L., "A Study of Film Cooling Related to Gas Turbines Using Transient Techniques," University of Oxford Report No. 1121/70, 1970.
18. Jones, T.V., et al., "Measurement of the Heat Transfer Rate to Turbine Blades and NGVs in the Transient Cascade," 6th International Heat Transfer Conference, Toronto, Canada, Paper EC-12, 1978.
19. Schultz, D.L., et al., "A New Transient Facility for the Measurement of Heat Transfer Rates," Conference Proceedings No. 229, High Temperature Problems in Gas Turbine Engines, September 1977, pp. 31-1 to 31-27.
20. Smith, M.R., "A Study of Film Cooling Effectiveness with Discrete Holes and Slots," University of Oxford Report No. 1100/74, 1974.
21. Wittliff, C.E., Wilson, M.R. and Hertzberg, A., "The Tailored Interface Hypersonic Shock Tunnel," J. Aerospace Sciences, Vol. 26, pp. 219-228, April 1959.
22. Boyle, R.J. and Haas, J.E., "Comparison of Experimental and Analytic Performance for Contoured Endwall Stators," NASA TM 82877, June 1982.

23. Hunter, I.H., "Endwall Boundary Layer Flows and Losses in an Axial Turbine Stage," 26th International Gas Turbine Conf., March 8-12, 1981, Houston, Texas, ASME Paper No. 81-GT-57.
24. Briley, W.R. and McDonald, H., "Computation of Three-Dimensional Horseshow Vortex Flow Using the Navier-Stokes Equations," 7th International Conference on Numerical Methods in Fluid Dynamics, Stanford University and NASA/Ames, June 23-27, 1980.

TABLE 1 - TEST CONDITIONS

Measured Reflected-Shock Pressure, psia	1,078
Calculated Reflected-Shock Temperature, °R	998
Measured NGV Inlet Total Temperature, °R	998
Measured NGV Inlet Total Pressure, psia	99.3
Cylinder in Cross Flow Stagnation Pt.	
Ht. Tr. Rate Ahead of NGV, BTU/ft ² sec	46.7
Calculated Average Weight-Flow Rate, lb/sec	22.0
Average Corrected Rotor Speed	Approx. 100%

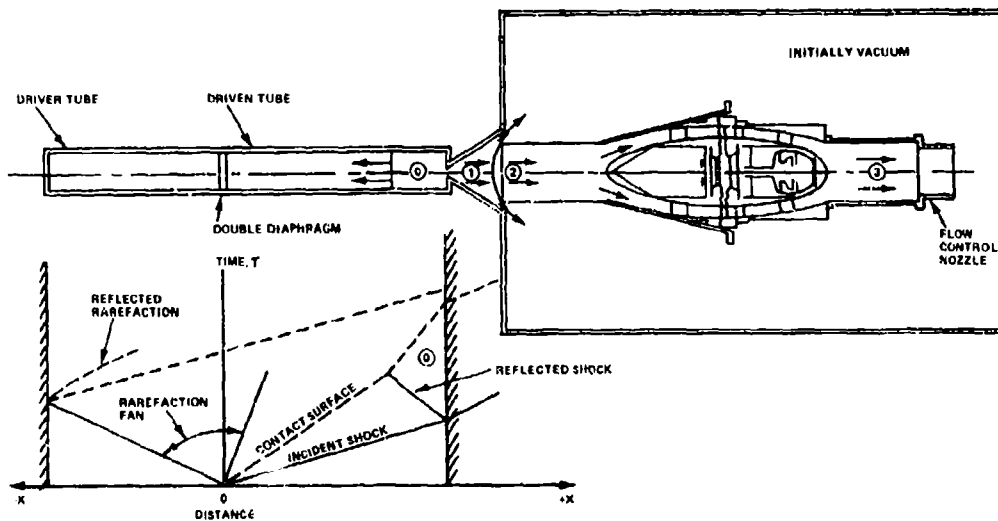


Figure 1 SCHEMATIC OF CALSPAN SHOCK-TUNNEL APPARATUS AND SKETCH OF WAVE DIAGRAM



Figure 2 PHOTOGRAPH OF HEAT-TRANSFER GAGE TAKEN THROUGH LEITZ MICROSCOPE



Figure 3 PHOTOGRAPH OF TFE 731 ENDWALL HEAT-FLUX GAGES

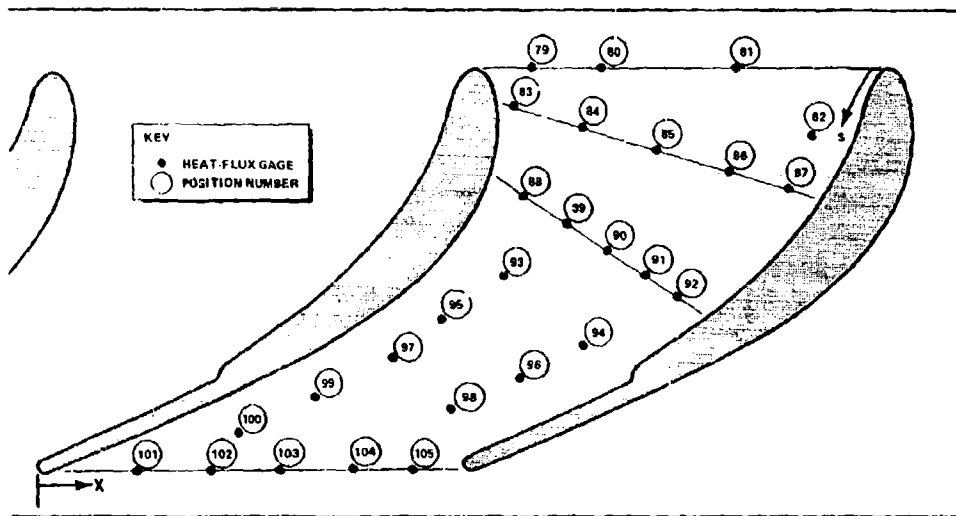


Figure 4 SKETCH OF TIP ENDWALL HEAT-FLUX GAGE LOCATIONS FOR TFE 731 NGV

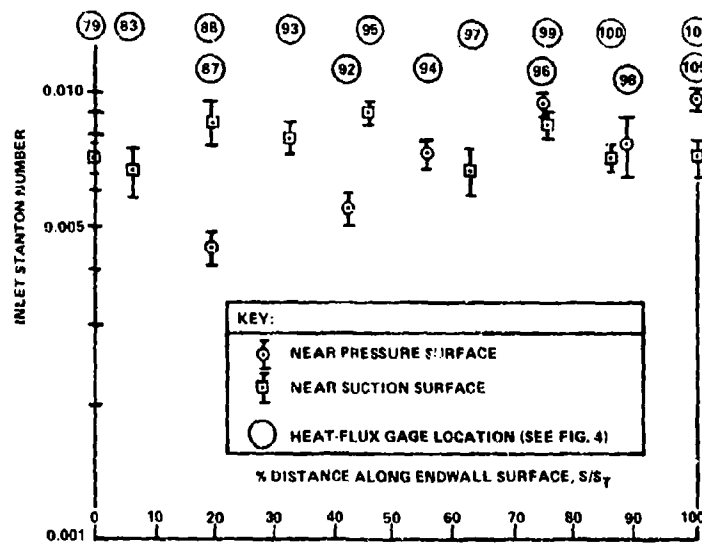


Figure 5 STANTON NUMBER DISTRIBUTION ON NGV TIP ENDWALL FOR THE TFE-731 TURBINE

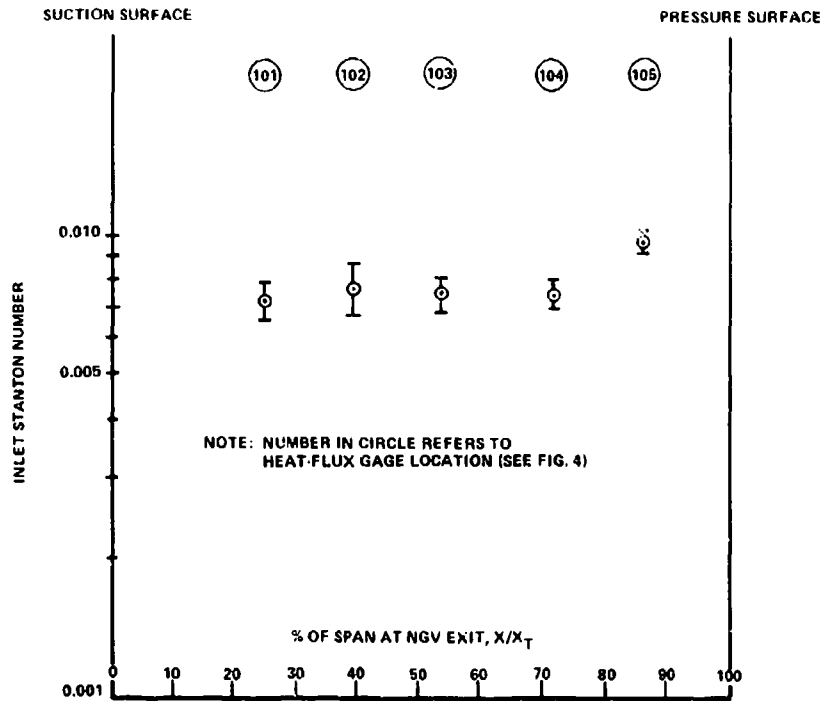


Figure 6 STANTON NUMBER DISTRIBUTION AT TIP ENDWALL EXIT FOR TFE-731 TURBINE

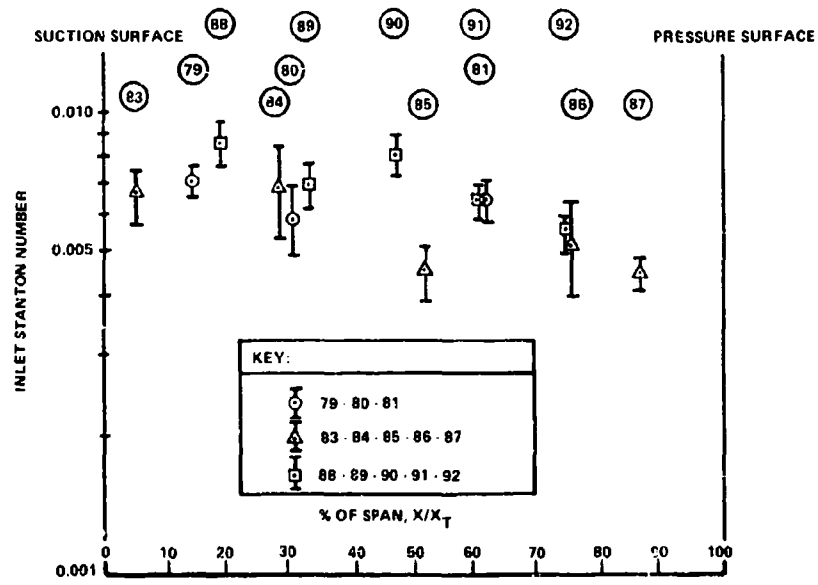


Figure 7 STANTON NUMBER DISTRIBUTIONS AT SELECTED SPANWISE LOCATIONS FOR ENDWALL OF NGV

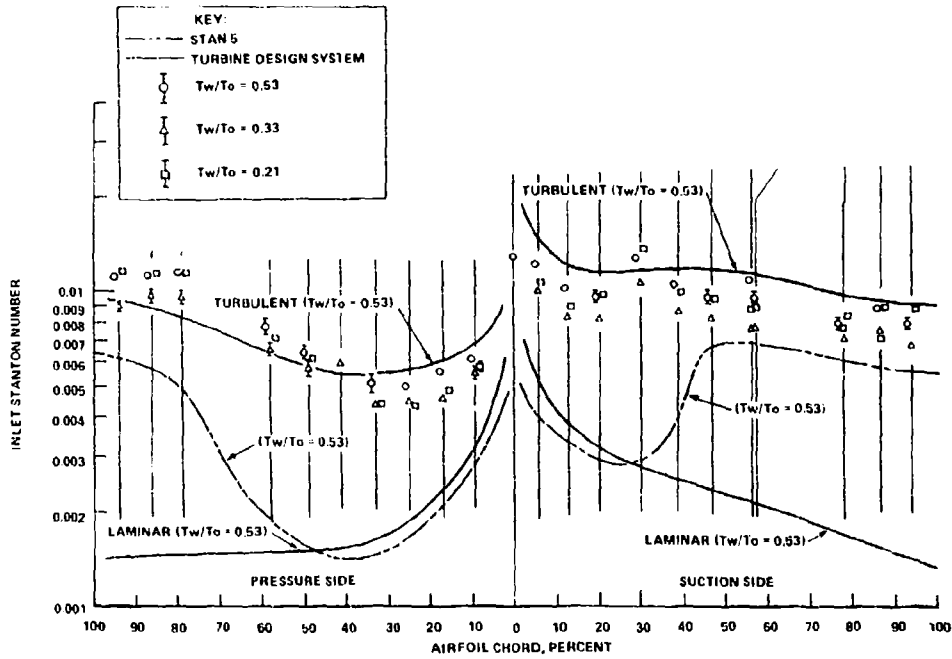


Figure 8 DISTRIBUTION OF STANTON NUMBER FOR NGV AIRFOIL MIDSPAN

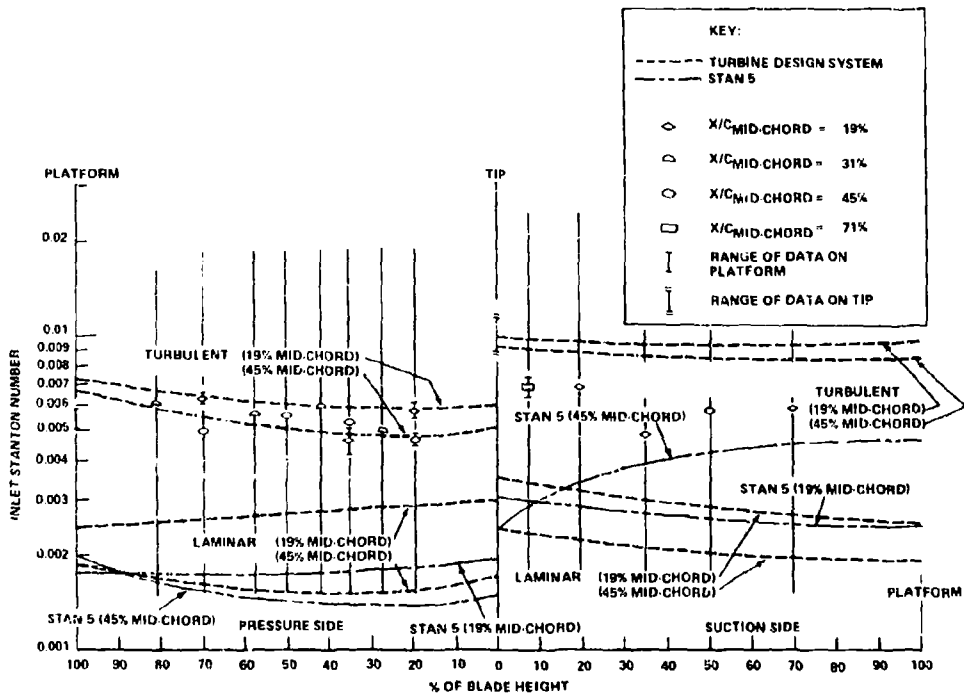


Figure 9 DISTRIBUTION OF STANTON NUMBER ON ROTOR BLADE FOR Tw/To = 0.53



Figure 10 LART LEADING EDGE AND PRESSURE SURFACE HEAT-FLUX GAGES

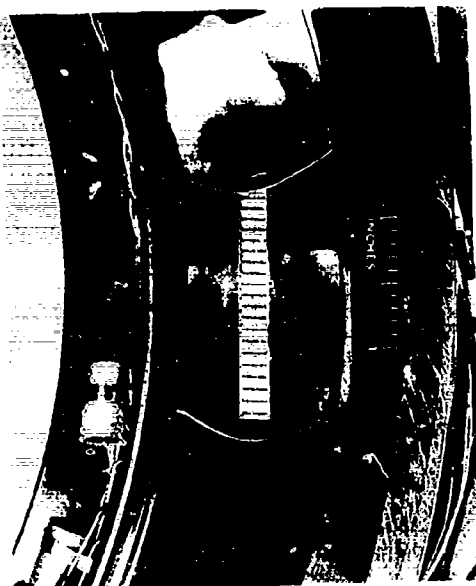


Figure 11 LART NGV SUCTION SURFACE HEAT-FLUX GAGES



Figure 12 LART ROTOR LEADING EDGE AND PRESSURE SURFACE GAGES

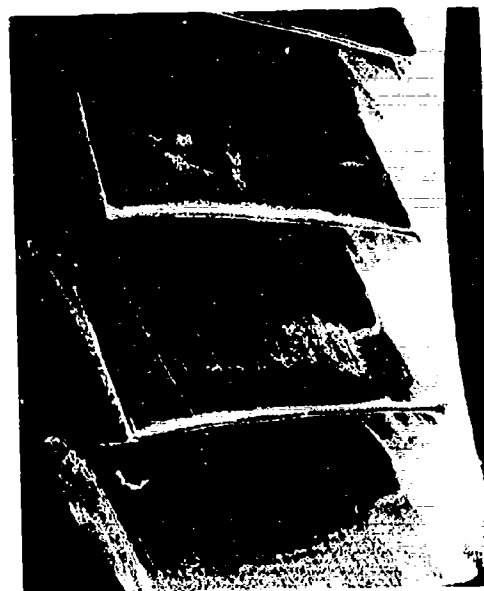


Figure 13 LART ROTOR SUCTION SURFACE HEAT-FLUX GAGES

DISCUSSION

R.Kiock, Gc

I have a question concerning the boundary layer state of the guide vane. Your measurements showed that transition occurs close to the leading edge on both suction and pressure side. Could you specify the degree of turbulence and the Reynolds number? Where do you see the reason for that early transition?

Author's Reply

1. We have measured the magnitude of free-stream turbulence to be on the order of 5% (see Ref.6). To the best of my memory, the vane inlet Reynolds number is on the order of 5×10^5 based on chord length. I could check this number for you when I return home if you like.
2. I believe at least one of the causes of this early transition is due to the relatively high free-stream turbulence. This turbulence could be the result of several things, two of which are:
 - a) The vane exit is subsonic and thus the rotor disturbance can be communicated forward. We have indeed seen this in the character of the pressure records, with and without the rotor (see Ref.7).
 - b) It is quite possible that the normal shock standing outside the model is in fact not completely stationary, even though it is always external to the model. In this way the shock can act as a turbulence generator.

D.J.Doorly, UK

1. I have found Dr Dunn's paper extremely interesting; my only regret is that there has not been sufficient space for a more detailed discussion of the time-resolved rotor heat transfer. The question of the rotor unsteady heat transfer is to my mind more interesting than the vane heat transfer since the rotor sees a far more unsteady flow and presents the designer with more severe headaches. To establish the rotor operating conditions, what was the rotor mean Reynolds number?
2. As regards the unsteady rotor flow, have the nozzle guide vanes wakes merged at the rotor inlet, or are they still discrete? On the time-resolved signals from the rotor, is it possible to observe discrete switching of the boundary layer from the laminar to the turbulent state as each nozzle guide vane wake impinges, or do the results suggest that the rotor boundary layer is continuously turbulent, and only secondary fluctuations are produced by the wake-impingement.
3. I have been somewhat concerned by Dr Dunn's use of insert-mounted thin films, since for the high Reynolds number rotor flow, even very slight surface discontinuities may trip the boundary layer. Has this in fact occurred?

Author's Reply

1. The inlet Reynolds number is about 2×10^6
2. Yes, wakes can be resolved. There are different effects whether there is a wake or a passage. The values of heat flux are bouncing between the turbulent level and the laminar level. The average value of the heat flux is above the laminar value and much closer to the turbulent one for this kind of turbine.
3. For that reason we went to use the inserts at the leading edge which are absolutely contoured smooth. You see that what looks like transition takes place on the leading edge very close to the stagnation point. The button gauges were put in under a microscope and they are very tiny.

C.T.J.Scrivener, UK

May I ask two questions. You described the instrumentation on the rotor tip and the rotor static outer shroud ring casing.

1. Can you describe how the distribution of static shroud ring heat transfer varies with rotor tip clearance?
2. How does the unshrouded rotor tip heat transfer compare to the measurements described earlier in the week by Prof. D.Metzger?

Author's Reply

1. The static shroud heat-flux distribution is not strongly influenced by the magnitude of the tip clearance. The shroud Stanton number distribution (based on inlet conditions) decreases by about 25 to 30% in going in an axial direction from directly above the blade leading edge towards the trailing edge. Once you exceed distances greater than the blade trailing edge, the Stanton number falls by approximately 50%. We have published the data you are asking for in Ref.6, I think.
2. During this conference, Prof. Metzger and I have discussed doing the comparison you ask about. As soon as he returns from Germany, we plan to do so.

S. Wittig, Ge

What is the thickness of your film gauges? In the light of what has been said earlier, would you be able to derive from the measurements the unsteady effects of the wakes on the material?

Author's Reply

1. The thickness of the thin-film gauge is approximately $0.1 \mu\text{m}$.
2. Yes, one could use the time-dependent heat-flux data as an input to the calculation of blade temperature history and in this manner, to predict the metal surface temperature fluctuation as a result of wake passage cutting. I caution you that the magnitude of the heat-flux fluctuation will depend upon the particular turbine, on the particular location on the blade, and on whether or not you have upstream cold gas injection.

CALCULATION OF LAMINAR-TURBULENT BOUNDARY
LAYER TRANSITION ON TURBINE BLADES

W. Rodi
Institut für Hydromechanik
Universität Karlsruhe
7500 Karlsruhe 1, F.R. Germany

G. Scheuerer
Lehrstuhl für Strömungsmechanik
Universität Erlangen-Nürnberg
8520 Erlangen, F.R. Germany

SUMMARY

Calculations are presented for the flow development and heat transfer in transitional two-dimensional boundary layers of relevance to turbine blades. They were obtained with the Patankar-Spalding finite difference program, using a low Reynolds number version of the $k-\epsilon$ turbulence model for simulating the turbulent transport. For the higher free-stream turbulence levels prevailing in gas turbines (say above 1%), the model is capable of simulating the physical transition mechanism which is governed by the transport of the turbulent fluctuations from the free stream into the laminar boundary layer. The calculation examples comprise a variety of flat-plate boundary layers with various favourable and adverse pressure gradients as well as various levels of free-stream turbulence, and a simulation of the boundary layer development of an experimentally investigated turbine blade. The calculations are compared with measurements in each case (mainly the distribution of heat transfer coefficients). The agreement is generally good, but the model has a tendency to predict a somewhat faster transition than was observed in the experiments.

1. Introduction

1.1 The Problem Considered

Knowledge of the external heat transfer rates is an important factor in the design of gas turbine blades as these rates determine the blade surface temperature which must be kept below a critical value in order to insure a reasonable life-time of the blades. Cascade experiments have shown that the heat transfer to turbine blades depends strongly on the occurrence of laminar-turbulent transition of the blade boundary layers. For instance, the heat transfer coefficients may be higher by a factor of five at the same location depending on whether the flow is laminar or turbulent. Hence, above all, a reliable method for calculating the heat transfer to turbine blades must be able to simulate transition realistically.

The present paper describes such a calculation procedure, which is based on a finite-domain solution of the boundary layer equations for two-dimensional, steady flow. The turbulent momentum and heat transfer is simulated by a low Reynolds number version of the $k-\epsilon$ turbulence model. For the high turbulence levels prevailing in gas turbines (say above 1%), this model is also used to mimic the transition mechanism which, in this case, is governed by the transport of the turbulent fluctuations from the free stream into the laminar boundary layer.

1.2 Previous Work

There have been several attempts to simulate laminar-turbulent transition with the aid of turbulence models in the past. These will now be discussed briefly. Turbulence models may be classified as zero-, one-, two-equation and Reynolds stress models, according to the number of transport equations they solve for turbulence variables, and the various models will be discussed in this order.

Zero-equation models. All these models make use of the eddy viscosity hypothesis, and either the eddy viscosity itself (Cebeci and Smith [1]) or the mixing-length distribution is specified algebraically. The calculation of the laminar-turbulent transition is performed on a purely empirical basis. Cebeci and Smith [1], Michel [2] and Forest [3] multiply the eddy viscosity with an intermittency function derived from experimental data. This function depends on the momentum-thickness Reynolds number, being zero in the laminar flow regime and increasing gradually to unity once the critical Reynolds number for instability is exceeded. This Reynolds number is usually calculated by means of the linear stability theory, which limits the applicability of these methods to low free stream turbulence intensities. Crawford and Kays [4] assign a large numerical value to the damping constant in their mixing-length model in order to suppress the Reynolds stresses in the laminar boundary layer. This damping constant is slowly decreased towards the typical value for fully turbulent flow, after an empirically specified transition Reynolds number has been reached in the calculations. In McDonald and Fish's [5] model, which has also been used by Mari and Mathieu [6] and, in a slightly modified form, by Hodge and Adams [7], the constant value of the mixing-length in the outer boundary layer region is determined from the solution of an integral form of the modelled turbulent kinetic energy equation. The free stream turbulence intensity

enters this equation implicitly via the integrated turbulent transport term. In the calculations, finite values of the free stream turbulence intensity cause a continuous energy flux into the boundary layer; this in turn leads to a gradual increase of the outer-layer mixing-length so that, after a certain distance, turbulent flow is predicted. In principle, this model is able to simulate the transition process typical for blade boundary layers, where disturbances intrude from the free stream into the laminar boundary layer.

Zero-equation models are liable to yield satisfactory results only for these flows which meet the empirical assumptions inherent in the mixing-length hypothesis and in the transition model. This is usually the case only for rather simple flows. Therefore, the results are often not very realistic for the more complicated flows prevailing in gas turbines.

One-equation models. Grundmann and Nehring [8] describe first attempts to simulate transition induced by free stream disturbance with a differential form of the turbulent kinetic energy equation in connection with an algebraic description of the length scale. They were able to calculate the transitional boundary layer on a turbine blade, but did not check their results against experimental data.

Two-equation models. Priddin [9] was the first to use the $k-\epsilon$ model for the calculation of transitional flows; his concern was mainly to show that the $k-\epsilon$ model can cope in principle with these flows and not to provide a detailed assessment of the model performance. Arnal et al. [10] applied the model of Jones and Launder [11] to transitional flows. They investigated the circumstances under which small perturbations in the k -profiles were amplified such that the flow became turbulent. They obtained very good agreement with their own experimental data even at very low free-stream turbulence intensities. However, their paper does not give the initial and boundary conditions specified in the calculations. In view of our results presented in Section 4, some of their predictions at low free-stream turbulence intensities appear doubtful. Dutoya and Michard [12] used their low-Reynolds-number version of the $k-\epsilon$ model to calculate transitional boundary layers. They also create the impression that their model simulates transition realistically even at very low free stream turbulence intensities without any additional empirical modifications. Their model has been found not to be very accurate for turbulent flows (see Patel et al. [13]).

Wilcox [14] has applied his model successfully to a large number of transitional boundary layers, e.g. flows with free stream turbulence, pressure gradients, surface roughnesses and compressibility. He achieved this success by calibrating one empirical function against experimental data. According to Wilcox [14], the model displays a distinct sensitivity to the initial and boundary conditions specified. In most of the test cases considered by Wilcox, these were not documented in sufficient detail. If one considers further the purely empirical way Wilcox specifies the wall boundary condition for his length scale variable, the predictive power of this model cannot be truly assessed. More recently, Wilcox [15] derived the empirical model function and the initial profiles for the turbulence variables from results obtained by applying the linear stability theory. This procedure has not yet been tested extensively. It is questionable whether it can be applied to the flow in gas turbines, where transition is triggered by free stream disturbances.

Arad et al. [16] used a low Reynolds number version of the $k-k_1$ model developed by Ng [17] to calculate transitional boundary layers. They obtained good agreement with empirical correlations for the transition Reynolds numbers. However, the results were not compared against specific experiments.

Reynolds stress models. One of the first attempts to simulate laminar-turbulent transition with the aid of turbulence models is due to Donaldson [18] who used transport equations for the Reynolds stress components and an algebraically prescribed length scale. Donaldson investigated the amplification (or damping) of small artificial perturbations in the model Reynolds stress equations. He observed either transition or complete stabilization of the disturbances depending upon the local Reynolds number. The paper gives more an impression of the qualitative model behaviour without recourse to experimental data.

Finson [19] has developed a low Reynolds number version of the Reynolds stress model involving a model equation for the dissipation rate. He employed his model to calculate transition as a function of free stream turbulence intensity but did not obtain good agreement with measured transition Reynolds numbers. Finson [19] also extended his model to calculate flows with surface roughnesses. In this case the agreement with existing data was satisfactory.

Summary. Especially the papers published on two-equation-model calculations create the impression that laminar-turbulent transition can be simulated simply by specifying the correct boundary conditions for the turbulence variables. This does not hold true in general as will be shown in the following sections. To obtain satisfactory results, empirical information has to be provided at least in form of the initial profiles for the turbulence quantities. Moreover, for the turbulence model described in this paper, transition triggered by transport of turbulence from the free stream into the boundary layer could not be obtained for free stream turbulence intensities less than 1%. This is physically plausible because, in these cases, transition is caused by Tollmien-Schlichting waves and this phenomenon cannot be simulated by models involving time-

averaged quantities. However, this problem is not addressed in any of the references given above. It is thus not clear how transition was attained in the model predictions of Arnal et al. [10] and Dutoya and Michard [12] without any transition-related modifications to these models.

1.3 Present Contribution

The purpose of this paper is to present calculations of transitional boundary layers relevant to the flow on gas turbine blades. Laminar-turbulent transition as well as the turbulent flow regime is simulated with the low-Reynolds-number version of the $k-\epsilon$ model of Lam and Bremhorst [20]. In all the calculations, transition ensued from the transport of free stream turbulence into the laminar boundary layer; this is the physical situation most likely to occur in blade boundary layers. The test cases considered comprise a variety of flat-plate boundary layers with various favourable and adverse pressure gradients as well as various levels of free-stream turbulence, and the boundary-layer development of an experimentally investigated blade. The calculations are compared with measurements in each case.

Two items have received insufficient attention in most previous articles on the calculation of laminar-turbulent transition with turbulence models: the description of the initial and boundary conditions used in the predictions and the selection of test cases against which the calculated results are to be compared. These topics are discussed in greater detail in the present paper.

2. Mathematical Model

2.1 Mean flow Equations

The mean flow is assumed to be steady and two-dimensional. Under these conditions the continuity, momentum and stagnation enthalpy equations read in a cartesian coordinate system:

Continuity equation:

$$\frac{\partial (\rho U)}{\partial x} + \frac{\partial (\rho \bar{V})}{\partial y} = 0 \quad (2.1-1)$$

Momentum equation:

$$\rho U \frac{\partial U}{\partial x} + \rho \bar{V} \frac{\partial U}{\partial y} = - \frac{dP}{dx} + \frac{\partial}{\partial y} \left(\mu \frac{\partial U}{\partial y} - \rho uv \right) \quad (2.1-2)$$

Stagnation enthalpy equation:

$$\rho U \frac{\partial H}{\partial x} + \rho \bar{V} \frac{\partial H}{\partial y} = \frac{\partial}{\partial y} \left\{ \frac{\mu}{Pr} \frac{\partial H}{\partial y} - \rho h'v \right\} + U \left\{ \left(1 - \frac{1}{Pr} \right) \mu \frac{\partial U}{\partial y} - \rho uv \right\} \quad (2.1-3)$$

In these equations U , V and u , v are respectively the mean and fluctuating velocity components in the x - and y -directions, and P is the static pressure. The stagnation enthalpy H

$$H = h + \frac{U^2}{2} + k \quad (2.1-4)$$

is composed of the static enthalpy h , the mean kinetic energy $U^2/2$ and the turbulent kinetic energy k . The symbol h' in equation (2.1-3) stands for the fluctuating enthalpy. The fluid is characterized by its density ρ , dynamic viscosity μ and molecular Prandtl number Pr . Time-averages are denoted by an overbar. The expression \bar{V} indicates mass-weighted averaging, (see Cebeci and Smith [1]) with

$$\rho \bar{V} = \rho V + \overline{\rho'v} \quad (2.1-5)$$

where ρ' represents the fluctuating density. The fluids considered in this paper were assumed to be ideal gases so that

$$\rho = \frac{P}{RT} \quad (2.1-6)$$

with R being the gas constant and T the static temperature.

Equations (2.1-2) and (2.1-3) contain the Reynolds stress $-\rho \overline{u'v'}$ and turbulent heat flux $-\rho h'v'$. A turbulence model for determining these quantities must be introduced in order to close the system of equations (2.1-1)-(2.1-6). This will be discussed in the next section.

2.2 Turbulence Model

In this study, the low Reynolds number version of the k - ϵ model developed by Lam and Bremhorst [20] has been used to simulate the turbulent momentum and heat transport. This model makes use of the eddy viscosity hypothesis, relating the Reynolds stress to the mean velocity gradient:

$$-\rho \overline{u'v'} = \mu_t \frac{\partial U}{\partial y} \quad (2.2-1)$$

The eddy viscosity μ_t depends on the turbulence structure; it is proportional to the turbulent kinetic energy k and to the energy dissipation rate ϵ . From dimensional analysis there follows:

$$\mu_t = \rho c_\mu f_\mu \frac{k^2}{\epsilon} \quad (2.2-2)$$

c_μ is an empirical constant and f_μ an empirical function accounting for the effects of molecular viscosity and wall proximity. In fully turbulent flow remote from walls $f_\mu = 1$ so that the Lam-Bremhorst model reduces to the standard k - ϵ model.

The local values of k and ϵ are calculated from the following semi-empirical transport equations:

$$\rho U \frac{\partial k}{\partial x} + \rho \tilde{v} \frac{\partial k}{\partial y} = \frac{\partial}{\partial y} \left[\left(\mu + \frac{\mu_t}{\sigma} \right) \frac{\partial k}{\partial y} \right] + P_k - \rho \epsilon \quad (2.2-3)$$

$$\rho U \frac{\partial \epsilon}{\partial x} + \rho \tilde{v} \frac{\partial \epsilon}{\partial y} = \frac{\partial}{\partial y} \left[\left(\mu + \frac{\mu_t}{\sigma} \right) \frac{\partial \epsilon}{\partial y} \right] + \frac{\epsilon}{k} (c_{\epsilon 1} f_1 P_k - \rho c_{\epsilon 2} f_2 \epsilon) \quad (2.2-4)$$

$$P_k = \mu_t \left(\frac{\partial U}{\partial y} \right)^2 \quad (2.2-5)$$

P_k is the production of turbulent kinetic energy. Four empirical constants appear in the model equations. For these, the following standard values [21] were adopted: $c_\mu = 0.09$, $c_{\epsilon 1} = 1.44$, $c_{\epsilon 2} = 1.92$, $\sigma_k = 1.0$, $\sigma_\epsilon = 1.3$. The functions f_μ and f_ϵ simulate viscous and near-wall influences and tend to unity for high turbulence Reynolds numbers. The low Reynolds number functions f_μ , f_1 and f_2 derived by Lam and Bremhorst [20] are

$$f_\mu = [1 - \exp(-0.0160 R_y)]^2 \left(1 + \frac{19.5}{R_T}\right) \quad (2.2-6)$$

$$f_1 = 1 + \left(\frac{0.06}{f_\mu}\right)^3 \quad (2.2-7)$$

$$f_2 = 1 - \exp(-R_T^2) \quad (2.2-8)$$

where the Reynolds numbers R_y and R_T are defined as

$$R_y = \frac{\rho \sqrt{k} y}{\mu}, \quad R_T = \frac{\rho k^2}{\mu \epsilon} \quad (2.2-9a, b)$$

An assessment of these functions is given in Patel et al. [13]. It should be noted that the numerical values in Equations (2.2-6) - (2.2-8) are slightly different from those of Lam and Bremhorst [20]; they have been chosen as they yield more accurate predictions for wall bounded shear flows (see Rodi et al. [22]).

The turbulent heat flux $-\rho h'v'$ is calculated from the following eddy diffusivity relation:

$$-\rho h'v' = \frac{\mu_t}{Pr_t} \frac{\partial h}{\partial y} \quad (2.2-10)$$

The eddy diffusivity is assumed proportional to the eddy viscosity μ_t (determined by the $k-\epsilon$ model), with the proportionality coefficient (turbulent Prandtl number) assumed to have the constant value $Pr_t = 0.86$.

2.3 Initial and Boundary Conditions

In this section the boundary and initial conditions used in the calculations are presented. Firstly, the boundary values at the wall and in the free stream are discussed and then the initial values employed to start the calculations.

Wall Boundary Conditions. Along the walls the no-slip condition was applied, which read for the mean velocities:

$$y = 0 : \quad U = \bar{V} = 0 \quad (2.2-11)$$

For the stagnation enthalpy at the wall, either the wall values (wall temperatures) or gradients at the wall (wall heat fluxes) were prescribed, i.e.

$$y = 0 : \quad H = H_w \quad \text{or} \quad \frac{\partial H}{\partial y} = -q_w \frac{Pr}{\mu_w} \quad (2.2-12)$$

According to the no-slip condition the turbulent kinetic energy at the wall was set to zero and so was the gradient of the dissipation rate :

$$y = 0 : \quad k = \frac{\partial \epsilon}{\partial y} = 0 \quad (2.2-13)$$

An evaluation of these boundary conditions can be found in Patel et al. [13].

Free Stream Boundary Conditions. In the free stream, the velocity was set equal to the potential velocity U which was taken from measurements in each case; the stagnation enthalpy in the free stream has a constant value which was also derived from experimental values:

$$y = y_e : \quad U = U_e ; \quad H = H_e = \text{const.} \quad (2.2-14)$$

Boundary values for k and ϵ were obtained by solving the transport equations (2.2-3) and (2.2-4) which reduce outside the boundary layer to

$$\rho U_e \frac{dk_e}{dx} = -\rho \epsilon_e \quad (2.2-15)$$

$$\rho U_e \frac{d\epsilon_e}{dx} = -\rho \epsilon_e 2 \frac{c_2}{k_e} \quad (2.2-16)$$

Appropriate initial values for k_e and ϵ_e necessary to solve these equations were taken from experimental data.

Initial values. The initial profile for the mean velocity in the laminar flow regime was prescribed with a Pohlhausen-profile, (see White [23]):

$$\frac{U}{U_e} = \left[2 \frac{y}{\delta} - 2 \left(\frac{y}{\delta} \right)^2 + \left(\frac{y}{\delta} \right)^3 \right] + \frac{\Lambda}{6} \frac{y}{\delta} \left(1 - \frac{y}{\delta} \right)^3 \quad (2.2-17)$$

where δ is the boundary layer thickness and $\Lambda = \delta^2 \rho / \mu \, dU/dx$ is the Pohlhausen parameter. The temperature was assumed to depend in a linear manner on the velocity:

$$\frac{T}{T_w} = 1 + \left(\frac{T_e}{T_w} - 1 \right) \frac{U}{U_e} \quad (2.2-18)$$

A starting profile for the stagnation enthalpy may be constructed from equation (2.2-17) and (2.2-18).

An important but also difficult task in the calculation of transitional flows is the specification of initial profiles for the turbulence variables. There are no experimental data available as basis for this specification. Also, results obtained with the linear stability theory cannot be used for the flow situations considered in this paper where transition is triggered by disturbances in the free stream. Therefore, the starting profiles for k and ϵ had to be derived on an ad hoc basis.

In the case of the turbulent kinetic energy there are some constraints which should be met by the initial profiles; these are: i) k has to vanish at the wall, ii) k should display a quadratic increase with wall distance and iii) k must asymptote to the free stream value k_e at the boundary layer edge. A relation meeting this requirements is

$$k = k_e \left(\frac{U}{U_e}\right)^2 \quad (2.2-19)$$

This equation was used in the computations.

There is much more liberty in setting up a starting profile for the dissipation rate ϵ . One necessary condition is that the experimental free stream value is recovered; in addition, it is plausible on physical grounds that the length scale within the boundary layer does not exceed that in the free stream. The starting profiles for ϵ used in the calculations were generated by the assumption that the dissipation rate should be proportional to the production rate of k , i.e.

$$\epsilon = a_1 k \frac{\partial U}{\partial y} \quad (2.2-20)$$

with $a_1 = -\overline{uv}/k$. The ϵ -values described by equation (2.2-20) tend to zero at the boundary layer edge, so that in addition the following condition was imposed:

$$\epsilon > \epsilon_e = \frac{k_e^{1/2}}{L_e} \quad (2.2-21)$$

In the course of testing the model it turned out that the coefficient a_1 in equation (2.2-20) could not be kept constant but had to be made a function of the free-stream turbulence intensity in order to obtain agreement with measured transition Reynolds numbers. For the test cases considered the best overall agreement was obtained with values of a_1 inside the shaded area in Figure 2.1. The full line in Figure 2.1 was used to determine a_1 for the calculations presented in Chapter 4. To provide some impression of the shape of the initial profiles for k and ϵ , Figure 2.2 shows an example for a turbulence intensity $Tu = \sqrt{u'^2}/U_e$ of 2.6%; the maximum value of the Reynolds stress inside the boundary layer implied by these k - and ϵ -values was $0.03 u_\tau^2$, with $u_\tau = \sqrt{\tau_w/\rho}$ being the friction velocity.

The calculations shown below were started at x -locations corresponding to a momentum thickness Reynolds number $Re_\delta = U_e \delta_e \rho_e / \mu_e$ of 100, where the flow was still stable and laminar and Equations (2.2-17) and (2.2-18) provided fair approximations to the physical situation.

3. Numerical Solution Procedure

The mean-flow and turbulence-model equations were solved with an adapted version of the GENMIX procedure described by Spalding [24]. The method is implicit and marching in the streamwise direction. The variables U , H , k and ϵ were solved successively at each cross stream line with no iteration. A non-equidistant grid with 100 nodes in the normal direction was employed; the first grid node was typically at $0.2 < y_1^+ < 1.0$ where $y_1^+ = y_1 u_\tau \rho_e / \mu_e$. The step size in the flow direction was set proportional to the momentum thickness δ_e with a proportionality factor of 0.25 for the calculations shown below. To enable a resolution of fast changes in the vicinity of the wall the step size was additionally restricted to five sublayer thicknesses, i.e.

$$\Delta x < 25 \frac{\delta_e}{\rho_e u_\tau} \quad (3-1)$$

4. Results and Discussion

4.1 Selection of Test Cases

The laminar-turbulent transition depends strongly on the turbulence field in the free stream, which may be characterized by a turbulence intensity Tu and a suitable length scale L_e . Preliminary calculations revealed that the choice of the free-stream length scale (or equivalently the dissipation rate) had a perceptible influence on the computed transition Reynolds numbers. Hence, the performance of a turbulence model should only be assessed by comparison with experiments for which both parameters, the intensity and the length scale, are available. In practice this means that data of k_e have been measured at least at two stations in the x -direction; Equations (2.2-15) and (2.2-16) then allow ϵ_e and therefore L_e to be determined.

Presently only two experimental studies meet these requirements, namely the ones of Blair and Werle [25], [26] and of Abu Ghannam [27]. Blair and Werle investigated the heat transfer behaviour along a flat plate. The free stream velocity was 30 m/s and the

temperature differences between the free stream and the wall were typically 10K. The free stream turbulence intensity was varied between 0.25 and 7.5%. All three components of the normal Reynolds stresses in the free stream were recorded and showed good isotropy. Two-dimensionality of the flow was checked with the aid of the 2D integral momentum and enthalpy equations and was found to be sufficient in all cases. Abu Ghannam conducted his measurements on a flat plate, but he did not investigate heat transfer. Different Reynolds numbers were achieved by altering the free stream velocities from 6 m/s to 30 m/s. Only the longitudinal fluctuating velocity was measured in this study and the free stream turbulence intensities ranged from 0.25 - 5%.

4.2 Boundary Layers with Zero Pressure Gradient

In this section results are presented for boundary layers without pressure gradient but various free-stream turbulence intensities. Figure 4.1 compares calculated Stanton numbers with the data of Blair and Werle [25]. The free stream turbulence intensities at the beginning of the calculations are indicated in the figure; they ranged from 1.3 to 7.5%. In the calculations transition is brought about by turbulent kinetic energy being continuously transported into the laminar boundary layer. After a certain development length, depending on the initial values of the dissipation rate, the entrained turbulent kinetic energy is amplified; this amplification takes place mainly in the near-wall zone where the velocity gradients and therefore also the production rates of turbulent kinetic energy are large. After a certain length, the predicted flow becomes fully turbulent.

Figure 4.1 shows very satisfactory agreement with the data for turbulence intensities of 2.5, 6.2 and 7.5%. The test plate of Blair and Werle had an unheated starting length in which no heat transfer data could be obtained. For the two higher turbulence intensities transition took place in this initial region so that, unfortunately, the transition behaviour cannot be compared for these cases. However, the computed transition Reynolds numbers are in agreement with the empirical correlation given by Abu Ghannam [27]; also the good simulation of the transitional zone ($x < 0.2$ m) is an indication that the point of transition is calculated correctly.

For the case with $Tu = 1.3\%$ the calculated transition point is somewhat too far downstream and transition occurs too rapidly. The latter is a characteristic feature of the turbulence model employed. The transition performance could be improved by modifying the low Reynolds number functions. The discrepancy between the calculated and measured transition locations is partly due to the experiments, where transition was hastened by sidewall effects in the test section. Generally, the agreement with the data is better for higher free stream turbulence intensities, because in these cases the transition length is decreased which complies with the model characteristics.

Figures 4.2 and 4.3 show comparisons with the data of Abu Ghannam for a turbulence intensity of 2.6%. The free stream velocity was 14 m/s in this case. The data for the momentum thickness Reynolds number are very well reproduced (Figure 4.3). The shape factor, (Figure 4.2), shows the transition process more clearly. It is evident that transition is somewhat faster in the calculations than in the experiments. However, for practical purposes the simulation is adequate.

4.3 Boundary Layers with Favourable Pressure Gradients

Favourable pressure gradients stabilize laminar boundary layers and delay transition. They counteract the effects of free stream turbulence. The test cases shown in this section were subject to both effects. Figure 4.4 shows an example with relatively mild acceleration, which was investigated by Blair and Werle [26]. The acceleration parameter

$$K = \frac{u_e}{\rho_e U_e^2} \frac{du_e}{dx} \quad (4.3-1)$$

was constant and equal to 2.0×10^{-6} . Compared to cases without pressure gradient, transition takes place further downstream and is more gradual. The calculated transition starts somewhat too late and occurs faster than in the experiments; however, the downstream displacement of the transition point caused by the acceleration is reproduced quite well. Overall, the agreement with the data is satisfactory.

At the same free stream turbulence intensity, but under a higher acceleration of $K = 0.75 \times 10^{-6}$, the flow becomes more stabilized and the onset of transition is indicated only by a gentle increase in the Stanton number data (Figure 4.5). For this case, the model yields a more distinct transition and larger differences to the data emerge. These can be reduced only by changes of the low Reynolds number functions in the turbulence model. The agreement with the data becomes better with increasing free stream turbulence intensities. For instance, Figure 4.6 shows a case with the same acceleration and a turbulence intensity of 5.3% which is in fairly good agreement with the data.

4.4 Boundary Layers with Adverse Pressure Gradients

Transition under adverse pressure gradient conditions is of less importance on gas turbine blades than the favourable pressure gradient case. As a consequence, fewer experimental data are available for this case. In fact only the work of Abu Ghannam [27] meets

the requirements set out in Section 4.1. In these experiments, the pressure rise was almost linear but weak enough to avoid premature separation. Abu Ghannam reports difficulties in keeping the flow two-dimensional in these experiments. Figure 4.7 shows an example of a calculation for the adverse pressure gradient case with an inlet velocity of 12 m/s and a free stream turbulence intensity of 1.8%. The shape factors are predicted very satisfactorily in this case.

4.5 Simulation of Blade Boundary Layers

Finally, in order to demonstrate the practical applicability of the calculation procedure, predictions are shown of heat transfer coefficients on a gas turbine blade. The blade profile is depicted in Figure 4.8. For this blade, heat transfer experiments were carried out by Daniels and Browne [28]. In the present paper calculations are presented for a chord Reynolds number Re_c of 6.7×10^6 with

$$Re_c = \frac{U_1 c \rho_1}{\mu_1} \quad (4.5-1)$$

The index "1" relates to values at the inlet, and c is the axial chord length of the blade. The exit Mach number was 0.94. The free stream turbulence intensity 12.7 cm upstream of the cascade was 4.2% and a value of 3% at the cascade entrance was used in the computations. The total temperature T_0 in the free stream was 432 K while the blade surface temperature was constant and equal to 288 K. Further details on the predictions and the test conditions are given by Rodi and Scheuerer [29].

Figure 4.9 shows a comparison of predicted and measured heat transfer coefficients for the suction side. The heat transfer coefficients α are defined as

$$\alpha = \frac{-q_w}{T_0 - T_w} \quad (4.5-2)$$

The various symbols in the figure label data obtained with differently instrumented blades. The calculations show a rapid decrease of α close to the leading edge which is in good agreement with the data. At $x/c = 0.3$ and a momentum thickness Reynolds number of 260, transition starts in the calculations. At this location the potential flow outside the boundary layer is slightly retarded and the onset of transition is physically plausible. On the other hand the experimental data indicate laminar flow up to $x/c = 0.45$. At this location the measurements show a discontinuity and it is not clear if this can be identified as transition. In view of the predictions presented in Section 4.3 it seems probable, however, that the transition process is predicted too rapidly.

The heat transfer coefficients on the pressure surface are shown in Figure 4.10. The outer flow is strongly accelerated along the whole pressure surface; the acceleration parameters K are about one order of magnitude higher than the criterion for relaminarization. Therefore, a fully turbulent flow does not develop. A transitional flow evolves along the whole pressure surface with a delicate balance between free stream turbulence and pressure gradient effects. With increasing distance x , the acceleration parameters K fall and the free stream turbulence penetrates deeper into the boundary layer; this leads to a rise in the heat transfer coefficients. The good agreement between the predictions and the data indicate that these interactions were modelled correctly.

5. Conclusions

The following conclusions may be drawn from the calculations presented above:

- o The calculation method presented in this paper is able to predict laminar-turbulent transition by simulating the transport of turbulence from the free stream into the laminar boundary layer. However, the turbulence intensities have to be sufficiently large (say $Tu > 1\%$) for this to happen. If, under this condition, suitable initial profiles for the turbulence variables are specified, a realistic prediction of the transition process emerges without further empirical changes to the turbulence model. In some cases, transition is predicted too rapidly when compared with experimental data. To improve the predictions in this regard, modifications of the low Reynolds number functions in the model are necessary.
- o There is a lack of well documented experimental data in transitional flows, so that an extensive testing of any model under various influences (e.g. pressure gradients, curvature, surface roughness, etc.) is rather difficult.
- o Realistic results can be obtained for heat transfer coefficients on gas turbine blades. This is especially true for the pressure surfaces where the model was able to cope with the opposing influences of free stream turbulence and relaminarization.

- o As with the boundary layer studies in transitional flows there is a shortage of well-defined test cases for simulating blade boundary layers. This hampers the development of prediction procedures; in particular more emphasis should be paid in future experimental studies to provide a more detailed description of the boundary conditions and the flow field.

6. Acknowledgement

Part of this work was sponsored by the Forschungsvereinigung Verbrennungskraftmaschinen. This support is gratefully acknowledged. The authors should also like to thank Miss M. Laternik for her expert typing of the manuscript.

7. References

- [1] Cebeci, T., Smith, A.M.O., Analysis of Turbulent Boundary Layers, New York, Academic Press Inc., 1974.
- [2] Michel, R., Prévion de L'Apparition et du Développement de la Transition de la Couche Limité, 1977, ONERA-TN 1977-6.
- [3] Forest, A.E., Engineering Predictions of Transitional Boundary Layers, 1977, AGARD CP-224, pp 22-1-22-19.
- [4] Crawford, M.E., Kays, W.M., STANS - A Program for Numerical Computation of Two-Dimensional Internal and External Boundary Layer Flow, 1976, NASA, CR-2742.
- [5] McDonald, H., Fish, R.W., Practical Calculations of Transitional Boundary Layers, Int. J. Heat Mass Transfer, Vol. 16, 1973, pp. 1729-1744.
- [6] Mari, C., Mathieu, J., Méthode de Prédiction de la Transition de la Couche Limité, 1977, AGARD CP-224, pp. 24-1-24-8.
- [7] Hodge, B.K., Adams, J.C., The Calculation of Compressible, Transitional, Turbulent and Relaminarizational Boundary Layers over Smooth and Rough Surfaces, 1974, Arnold Eng. Development Centre, AEDC-TR-77-96.
- [8] Grundmann, R., Nehring, U., Berechnung von zweidimensionalen, inkompressiblen, transitionellen Grenzschichten an gekrümmten Oberflächen, Z. Flugwiss. Weltraumforsch., Vol. 8, 1984, pp. 249-255.
- [9] Fridin, C.H., The Behaviour of the Turbulent Boundary Layer on Curved Porous Walls, 1975, Ph.D. Thesis, Imperial College, London.
- [10] Arnal, D., Habiballah, M., Delcourt, V., Synthèse sur les Methodes de Calcul de la Transition Developpées on DERAT, 1980, ONERA, Rapp. Techn., OA No. 11/5018 AYD.
- [11] Jones, W.P., Launder, B.E., The Prediction of Laminarization with a Two-Equation Model of Turbulence, Int. J. Heat Mass Transfer, Vol. 15, 1972, pp. 301-314.
- [12] Dutoya, D., Michard, P., A Program for Calculating Boundary Layers along Compressor and Turbine Blades, Numerical Methods in Heat Transfer ed. R.W. Lewis, K. Morgan, O.C. Zienkiewicz, J. Wiley & Sons Ltd., 1981, pp. 413-428.
- [13] Patel, V.C., Rodi, W., Scheuerer, G., A Review and Evaluation of Turbulence Models for Near Wall and Low-Reynolds-Number Flows, AIAA-J., accepted for publ., 1985.
- [14] Wilcox, D.C., A Model for Transitional Flows, AIAA-Paper 77-126, 1977.
- [15] Wilcox, D.C., Development of an Alternative to the e9-Procure for Predicting Boundary-Layer Transition, 1979, Office of Naval Research, Arlington, ONR-CR-29B-005-ZF.
- [16] Arad, E., Berger, M., Wolfshtein, M., Numerical Calculation of Transitional Boundary Layers, Int. J. for Num. Methods in Fluids, Vol 2, 1982, pp. 1-23.
- [17] Ng, K.-H., Predictions of Turbulent Boundary-Layer Developments Using a Two-Equation Model of Turbulence, 1971, Ph.D. Thesis, Imperial College, London.
- [18] Donaldson, C. duP., A Computer Study of an Analytical Model of Boundary-Layer Transition, AIAA-J., Vol. 7, 1969, pp. 271-278.

- [19] Finson, M.L., A Reynolds Stress Model for Boundary Layer Transition, 1975, Phys. Sc. Inc., Rep.-No. TR-34.
- [20] Lam, C.K.G., Bremhorst, K.A., Modified Form of the k - ϵ -Model for Predicting Wall Turbulence, J. Fluids Eng., Vol. 103, 1981, pp. 456-460.
- [21] Launder, B.E., Spalding, D.B., The Numerical Computation of Turbulent Flow, Comp. Math. in Appl. Mech. and Eng., Vol. 1, 1974, pp. 131-138.
- [22] Rodi, W., Celik, I., Demuren, A.O., Scheuerer, G., Shirani, I., Leschziner, M.A., Rastogi, A.K., Calculations for the 1980-81 AFOSR-HTTM-Stanford Conference on Complex Turbulent Flows, ed. S.J. Kline, B.J. Cantwell, G.M. Lilley, Vol. III, 1982, pp. 1495-1516.
- [23] White, F.M., Viscous Fluid Flow, New York, McGraw Hill, 1974.
- [24] Spalding, D.B., GENMIX - A General Computer Program for Two-Dimensional Parabolic Phenomena, Oxford, Pergamon Press, 1977.
- [25] Blair, M.F., Werle, M.J., The Influence of Free Stream Turbulence on the Zero Pressure Gradient Fully Turbulent Boundary Layer, 1980, UTRC, East Hartford, Rep.-No. R 80-914388-12.
- [26] Blair, M.F., Werle, M.J., Combined Influence of Free-Stream Turbulence and Favourable Pressure Gradients on Boundary Layer Transition and Heat Transfer, 1981, UTRC, East Hartford, Rep.-No. R 81-914388-17.
- [27] Abu Ghannam, B.J., Boundary-Layer Transition in Relation to Turbomachinery Blades, 1979, Ph.D. Thesis, Univ. of Liverpool, Liverpool.
- [28] Daniels, I.C., Browne, W.D., Short Duration Measurements of Heat Transfer to a Gas Turbine Rotor Blade, Int. J. Heat Mass Transfer, Vol. 24, 1981, pp. 871-879.
- [29] Rodi, W., Scheuerer, G., Calculation of Heat Transfer to Convection-Cooled Gas Turbine Blades, Proc., 1983 Tokyo, Intern. Gas Turbine Congress, 1983, pp. 13-21.

8. FIGURES

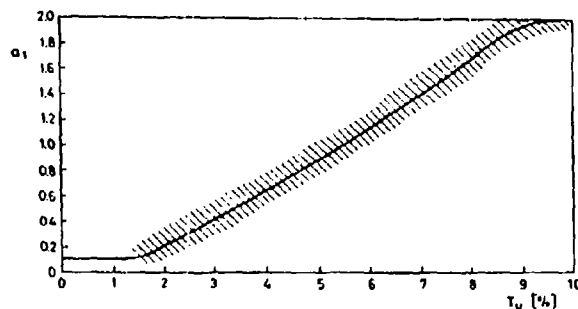


Fig. 2.1: Variation of the coefficient a_1 with turbulence intensity

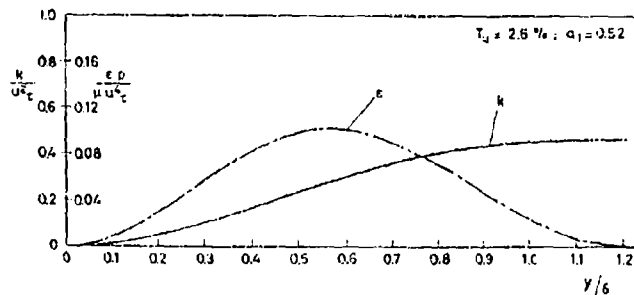


Fig. 2.2: Initial profiles for k and ϵ

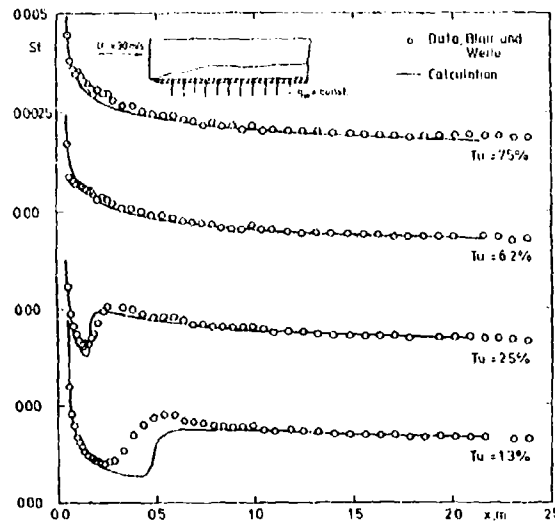


Fig. 4.1: Stanton numbers in transitional boundary layers with zero pressure gradient

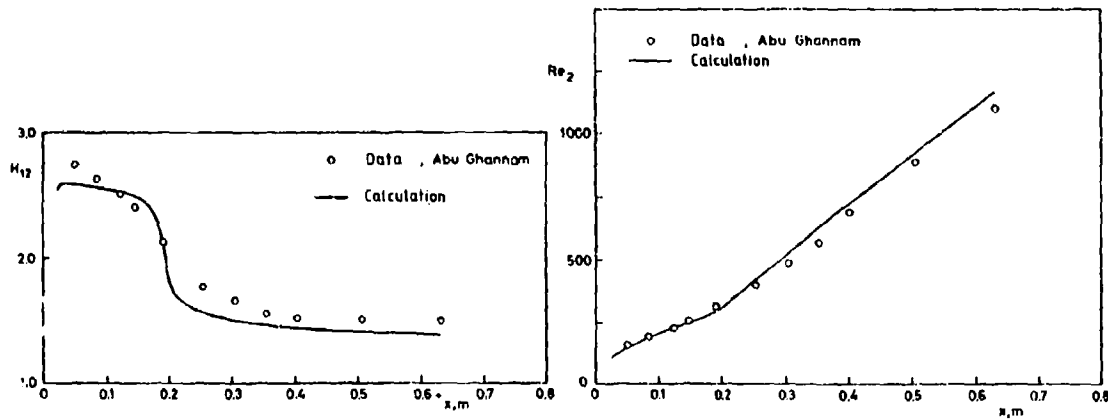


Fig. 4.2: Distribution of the shape factor H_{12} in a transitional flow

Fig. 4.3: Distribution of the momentum thickness Reynolds number in a transitional flow

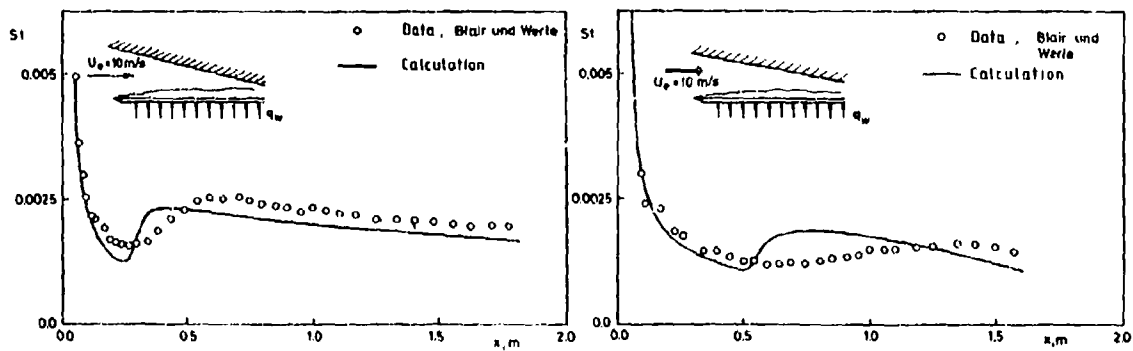


Fig. 4.4: Stanton numbers in a transitional accelerated boundary layer ($Tu = 2.1\%$, $K = 0.2 \times 10^{-6}$)

Fig. 4.5: Stanton numbers in a transitional accelerated boundary layer ($Tu = 2.1\%$, $K = 0.75 \times 10^{-6}$)

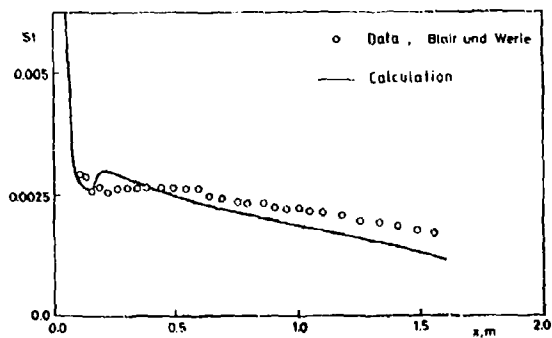


Fig. 4.6: Stanton numbers in a transitional accelerated boundary layer with high free stream turbulence ($Tu = 5.3\%$)

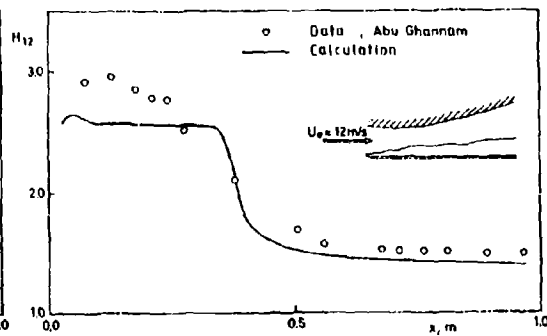


Fig. 4.7: Shape factors in a transitional flow with adverse pressure gradient ($Tu = 1.8\%$)

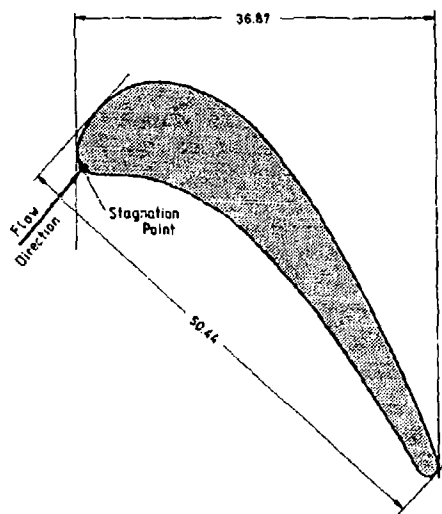


Fig. 4.8: Profile of the investigated turbine blade

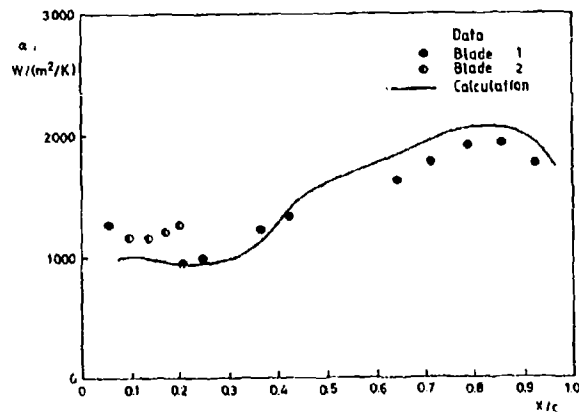


Fig. 4.10: Comparison of model predictions with experimental data on the pressure surface

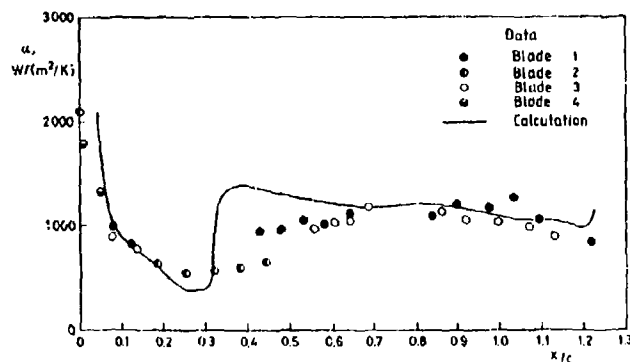


Fig. 4.9: Comparison of model predictions with experimental data on the suction surface

DISCUSSION

F.Tarada, UK

Your dissipation equation is questionable in the very-near-wall region. At the wall itself the equation would reduce to the statement 'viscous diffusion of anisotropic dissipation equals zero' which is a proposition of doubtful validity.

Author's Reply

It is true that the viscous diffusion of the dissipation rate is assumed to be zero in the model. However there is hardly any experimental evidence to defeat the validity of this assumption. For practical calculations this is not a major point. It is discussed in more detail in the paper by Patel (Ref.13).

S.C.Arora, Ca

In adverse pressure gradient flows, the turbulent pressure velocity correlation (\overline{pv}) of turbulent kinetic energy has been shown to be a significant term. It does not seem to have been included in your model. Why not?

Author's Reply

In the turbulent kinetic energy equation we do not neglect it but we lumped it together with the gradient diffusion model. We are not explicitly modelling it. There are other studies that show that the gradient diffusion model is appropriate. In any case for boundary layers the diffusion and convection terms are very small compared to the production.

A MODEL FOR CORRELATING FLAT PLATE
FILM COOLING EFFECTIVENESS FOR ROWS OF ROUND HOLES

M.R. L'Ecuyer
School of Mechanical Engineering
Purdue University
West Lafayette, IN 47906

F.O. Soechting
Pratt and Whitney Engineering Division
United Technologies Corporation
West Palm Beach, FL 33402

ABSTRACT

An effective method of cooling, that has found widespread application in aircraft gas turbines, is the injection of a film of cooling air through holes into the hot mainstream gas to provide a buffer layer between the hot gas and the airfoil surface. Film cooling has been extensively investigated and the results have been reported in the literature. However, there is no generalized method reported in the literature to predict the film cooling performance as influenced by the major variables. A generalized film cooling correlation has been developed, utilizing data reported in the literature, for constant velocity and flat plate boundary layer development. This work provides a basic understanding of the complex interaction of the major variables affecting film cooling performance.

NOMENCLATURE

a	= Thermal diffusivity decay parameter	β_p	= Peak effectiveness location (x/MS_e) _p
A_{hole}	= Cross-sectional metering area of cooling hole	β^*	= Critical effectiveness location at which diffusivity (ϵ_H) remains constant
D	= Hole diameter	δ^*	= Boundary layer displacement thickness
I	= Momentum ratio ($\rho_c V_c^2 / \rho_g V_g^2$)	ϵ_H	= Eddy diffusivity of heat
m	= Exponential constant	ϵ_M	= Eddy diffusivity of momentum
M	= Blowing ratio ($\rho_c V_c / \rho_g V_g$)	n	= Film effectiveness (local)
N_R	= Number of rows of holes	\bar{n}	= Spanwise average film effectiveness
P	= Pitch	η_p	= Spanwise average peak film effectiveness
Re_s	= Equivalent slot Reynolds number ($\rho_c V_c S_e / \mu_c$)	$\eta_p \sqrt{\beta_p}$	= Downstream effectiveness parameter
S	= Slot width	μ_c	= Coolant absolute viscosity
S_e	= Equivalent slot width	μ_g	= Freestream absolute viscosity
T_c	= Coolant temperature	ν_g	= Freestream kinematic viscosity
T_g	= Freestream temperature	ρ_c	= Coolant density
V_c	= Coolant velocity	ρ_g	= Freestream density
V_g	= Freestream velocity	ρ_c / ρ_g	= Coolant-to-freestream density ratio
V_c / V_g	= Coolant-to-freestream velocity ratio	$\rho_c V_c / \rho_g V_g$	= Blowing ratio (M)
x	= Distance downstream from injection hole		
α_c	= Hole injection angle		
β	= Local effectiveness location (x/MS_e)		

INTRODUCTION

State of the art gas turbine engines have demonstrated the need for turbine airfoil film cooling to supplement the thermal protection achieved through highly effective airfoil internal convective cooling schemes (impingement, trip strips, pedestal fins, etc). Film cooling is provided by one or more rows of discrete coolant holes. Consequently, the designer requires the capability to predict the distribution of the film cooling effectiveness as a function of the following major design variables (see Fig. 1):

- Freestream flow: $\rho_g V_g / \mu_g$, $V_g(x)$ turbulence, surface curvature.
- Coolant flow: $\rho_c V_c / \rho_g V_g$, ρ_c / ρ_g .
- Injection geometry: P/D , α_c , N_R , row spacing.

Extensive research reported in the literature, shows that one parameter of major importance is the coolant-to-freestream density ratio (ρ_c / ρ_g). The majority of film cooling experiments have been performed with low density ratio ($\rho_c / \rho_g \approx 1.0$) because of the experimental convenience of small temperature differences and/or heating of the injected flow. This results in a major uncertainty in the extrapolation of effectiveness data to turbine design conditions where $\rho_c / \rho_g \approx 2.0$. Some experiments have used air/freon mixtures for

the coolant flow to simulate density ratio in the range of interest. Despite the extensive film cooling research to date, there is no generalized method in the literature to predict the influence of density ratio on film cooling effectiveness.

The purpose of the work described herein was to use the film cooling effectiveness data in the literature to develop a generalized correlation model to predict the film cooling effectiveness distribution as a function of the blowing ratio (M), density ratio (ρ_c/ρ_g), and the injection geometry for rows of round holes. The study was restricted to a consideration of flat plate film cooling effectiveness data. Modeling of that case was considered essential. The influence of freestream acceleration and curvature may then be isolated through experiments utilizing more representative airfoil surfaces. Furthermore, attention in this study was focused on modeling the spanwise (i.e., hole-to-hole) average effectiveness ($\bar{\eta}$) since that is the initial requirement of a film cooling design system.

This paper summarizes the film cooling effectiveness data selected from the literature and identifies three flow regimes that characterize the effectiveness distribution. The development of an effectiveness correlation model is presented using the analytical results from a slot film cooling boundary layer model and a discrete hole moving energy sink model. The validity of the correlation is demonstrated by comparison of predicted effectiveness distributions with measured data from primary and secondary references.

FLAT PLATE EFFECTIVENESS DATA

An extensive literature search was performed to assemble a comprehensive bibliography of the film cooling literature (384 publications from 1964-1983) and to select the primary sources of data to be used in the development of the flat plate effectiveness correlation. Considering the many design variables that influence the effectiveness distribution (M , ρ_c/ρ_g , α_c , P/D , $V_g D/\nu_g$), the difficulty of quantitatively isolating the influence of each variable was compounded by the necessity to compare data from different sources where (a) simultaneous changes in more than one variable existed and (b) the influence of a given variable was the same magnitude as the uncertainty in the data between sources. As a consequence, the references included in the flat plate effectiveness data base were screened to satisfy the following criteria.

1. Data only from test plates closely approximating adiabatic surface conditions were required. (Experiments using the mass transfer technique of concentration measurements to determine the impermeable wall effectiveness give an exact simulation of the adiabatic surface condition. Experiments using the heat transfer technique ($T_c \leq T_g$) require a test plate of low thermal conductivity to minimize wall conduction errors.)
2. Data from large scale test plates were required to provide detail on the effectiveness distribution near the coolant holes ($x/D < 5$) and far downstream ($x/D > 100$).
3. Data only from single row or multiple rows of holes (not single holes) were required.
4. Data from flat test plates ($V_g = \text{constant}$) with low freestream turbulence intensity were required.
5. High quality, quantitative data were required in the form of a spanwise average effectiveness distribution, $\bar{\eta}(x)$.

The references selected as the data base for the flat plate correlation are listed in Table 1 which summarizes the range of parameters for which effectiveness data are reported. The data from the primary references were used as the basis for the correlation developed herein. The data from the secondary references were used to indicate the influence of select variables and to test the validity of the correlation developed. Some important features from key references are summarized below.

Pedersen (1), using the mass transfer technique, has provided a comprehensive study of the influence of coolant-to-freestream density ratio, ρ_c/ρ_g , for a single injection geometry. Foster, Lampard (9) also investigated the influence of ρ_c/ρ_g for a different injection angle.

Goldstein, Eckert, Eriksen, and Ramsey (2), one of the pioneer studies using the heat transfer technique, provide a sound comparison of heat transfer and mass transfer effectiveness data (low density ratio) with an injection geometry and wind tunnel identical to Pedersen's.

Blair, Lander (3) and Muska, Fish, Suo (4), using the heat transfer technique (low density ratio), have provided data for a double row of holes with a different value of P/D and α_c . The data of Afejuku (5) and Foster, Lampard (9,10) (high density ratio) provided additional information to assess the influence of injection angle.

Afejuku (5) used a reduced injection hole diameter (high density ratio) to duplicate Pedersen's (1) injection geometry and investigate the superposition of coolant films from two rows of holes spaced 10 to 40 diameters apart. Similar data for a 90° injection angle also were presented.

Kadotani (6) presented an extensive evaluation of the influence of the boundary layer displacement thickness (δ^*/D) through the variation of the freestream velocity. Liess (8) investigated δ^*/D effects by varying the injection hole diameter.

The Flat Plate Data were carefully examined to identify trends of the effectiveness distribution, $\bar{\eta}(x)$, that must be represented by a flat plate correlation model. Goldstein (20) presented a summary of several 2-D slot injection boundary layer models appearing in the literature. The key parameter characterizing the effectiveness distribution in all of these models is x/MS where:

*It should be noted that the method of spanwise averaging may have a significant influence on the value of $\bar{\eta}$ near the holes ($x/D < 10$). Previous studies (1,2,3,4,5,6,7) obtained local data $\eta(x,z)$ and used some approximation technique (straight line segments, curve fitting, etc.) to evaluate the integral $1/P \int \rho dz$. Liess (8) used spanwise copper strips to measure a conduction averaged $\bar{\eta}$. In the subject study, the values for $\bar{\eta}$ reported by each author were used directly. No attempt was made to modify the data to some standardized method of averaging.

x = distance downstream from the injection site
 M = coolant blowing ratio = $\rho_c V_c / \rho_g V_g$
 S = slot width

Previous studies (12) for film coolant injection through a row of holes have shown the applicability of the parameter x/MS_e for correlating the effectiveness for discrete hole injection by defining

$$S_e = \text{equivalent slot width} = A_{\text{hole}}/P$$

$$S_e/D = (\pi/4)/(P/D)$$

The initial step in developing the effectiveness correlation model described herein was an examination of the effectiveness distribution $\bar{\eta}$ vs x/MS_e . In general, the effectiveness distribution for injection from holes is governed by M , which indicates the relative thermal capacity of the injected coolant mass flow, and also by the individual values of ρ_c/ρ_g and V_c/V_g , which indicate the extent of the penetration and mixing of the coolant with the freestream.

Figure 2 presents some of Pedersen's (1) data showing the trends in the effectiveness distribution, $\bar{\eta}$ vs. (x/MS_e), as a function of M and ρ_c/ρ_g . Examination of the data revealed the following major trends characterizing the effectiveness distribution:

1. For low M and/or high ρ_c/ρ_g , the effectiveness distribution exhibits a typical decay trend indicating $\bar{\eta} \propto (x/MS_e)^m$, where the slope on log-log coordinates is approximated by $m = -0.5$ for x/MS_e up to 1000. Furthermore, the effectiveness level near the holes (low x/MS_e) may be noticeably greater than or less than the coverage, depending on the value of ρ_c/ρ_g .
2. For $M \leq 0.2$ the effectiveness distribution is independent of ρ_c/ρ_g .
3. As M increases above 0.2, the typical decay trend is observed but the effectiveness distribution depends on M and on ρ_c/ρ_g (i.e. V_c/V_g). For a given M , the effectiveness level decreases as ρ_c/ρ_g decreases and V_c/V_g increases. This effect is observed when $V_c/V_g > 0.25$.
4. When V_c/V_g increases above 0.69, the trend of effectiveness changes with x/MS_e (for $x/MS_e < 100$). The data show effectiveness increasing with x/MS_e for large velocity ratios, $1.0 < V_c/V_g < 2.0$.

Previous works have attempted to characterize the complex influence of ρ_c/ρ_g in terms of the momentum ratio, $I = \rho_c V_c^2 / \rho_g V_g^2$. The momentum ratio is recognized as a key physical parameter; however, it was concluded in the course of this study that the complex coolant penetration and coolant/freestream mixing processes cannot be adequately characterized by simply using I to account for the effect of ρ_c/ρ_g . This is illustrated in Figure 3 by comparing Pedersen's data (1) at constant momentum ratio. A similar conclusion regarding the importance of ρ_c/ρ_g was reached by Foster, Lampard (9). Consequently, in developing a prediction correlation, it was decided to characterize the "coolant injection condition" in terms of M (thermal capacity) and the individual values of ρ_c/ρ_g and V_c/V_g (penetration and mixing) and to define the relationship between density ratio and velocity ratio from the data.

Figure 4 presents some of the data of Blair, Lander (3) and Muska, Fish, and Suo (4) showing the effectiveness distribution as a function of M for a double row of holes ($\alpha_c = 30$, $P/D = 2$) where the density ratio was constant, $\rho_c/\rho_g = 1.1$. The downstream distance (x) was measured from the center of the downstream coolant hole. The equivalent slot width (S_e) was defined using the area of the coolant holes in both rows. Examination of the data from this large scale experiment reveals some important trends:

1. The typical decay rate determined from this set of data confirms the conclusion drawn from the Pedersen (1) data, i.e. slope = -0.5.
2. For $V_c/V_g = 0.62$, the effectiveness increases with x/MS_e near the holes, followed by a typical effectiveness decay.
3. For $V_c/V_g = 0.82$, the effectiveness increases gradually toward a peak level followed by a typical effectiveness decay.
4. A peak effectiveness level that does not exceed 0.77 occurs substantially downstream from the double row of holes that have 100% coverage.

The foregoing trends observed from the data of Pedersen (1) suggested the definition of the following regimes characterizing the effectiveness distribution:

1. Mass Addition Regime (mas) -
Effectiveness level increases with M due to increased thermal capacity of the coolant, but the effectiveness distribution is independent of the individual values of ρ_c/ρ_g and V_c/V_g .
2. Mixing Regime (mix) -
Effectiveness distribution depends on M and ρ_c/ρ_g (or V_c/V_g) due to the opposing influence of (a) increased coolant thermal capacity ($\eta \uparrow$ as $M \uparrow$), and (b) increased coolant/freestream mixing and penetration ($\eta \uparrow$ as $V_c/V_g \uparrow$, $\rho_c/\rho_g \uparrow$).
3. Penetration Regime (pen) -
Effectiveness distribution is dominated by a complex interaction of (a) excessive coolant penetration and augmented turbulent diffusivity due to a high velocity ratio, and (b) turbulent diffusion of the coolant's thermal effect toward the surface.

These three regimes were found to be useful in characterizing the flat plate effectiveness data from all references. The values of V_c/V_g defining the regime boundaries for one injection geometry determined from the data of Pedersen (1) were:

1. Mass Addition Regime $V_c/V_g \leq 0.25$	}	$\alpha_c = 35^\circ$
2. Mixing Regime $0.25 \leq V_c/V_g \leq 0.8$		
3. Penetration Regime $V_c/V_g > 0.8$		
		$P/J = 3$
		$N_R = 1$

Examination of the data of Blair, Lander (3) and Muska, et al (4) showed that the value of V_c/V_g defining the mixing/penetration regime boundary varied with geometry.

The consistency of the large scale effectiveness data of Pedersen (1) and Blair, Lander (3), Muska, et al (4) revealed features of the effectiveness distribution that could be described by the definition of the following parameters:

Peak Effectiveness Level (η_p)

Peak level of effectiveness is observed at some point downstream from the coolant injection. The effectiveness increases with (x/MS_e) up to η_p , apparently due to diffusion of the coolant's thermal effect hole-to-hole and toward the surface. For the mass addition regime, η_p would occur very near the coolant hole giving the appearance of maximum effectiveness at the hole. For the mixing regime, η_p is clearly observed on large scale experiments, in the range $10 < x/D < 25$. η_p may occur as far downstream as $x/D = 80$ for the penetration regime, depending on V_c/V_g .

Peak Effectiveness Location (β_p)

$\beta_p = (x/MS_e)_p$ defines the surface location to the peak level of effectiveness. The data show that the peak level of effectiveness generally does not occur at the injection holes except in the mass addition regime. There is apparently some transport time, i.e. downstream distance, for the thermal effect of the coolant to diffuse hole-to-hole and toward the surface in the mixing and penetration regimes.

The concept of a peak effectiveness level (η_p) and the corresponding surface location of the peak (β_p) is a fundamental feature of the effectiveness correlation model described herein.

CORRELATION OF FLAT PLATE EFFECTIVENESS DATA

One major goal in the present study was to develop an effectiveness equation that was:

1. capable of representing the varied effectiveness distributions identified from data for the mass addition, mixing, and penetration regimes, and
2. compatible with accepted boundary layer description of the flow downstream from the coolant injection site.

Near the injection site, with injection from a row (or rows) of holes, a flat or rising effectiveness distribution can be exhibited over long surface distances, depending on the value of velocity ratio. The effectiveness distribution should be governed by boundary layer characteristics exhibiting a typical $\bar{\eta}$ vs. (x/MS_e) decay for distances far downstream from injection.

The moving energy sink solution given by Burggraf (13) and Kadotani, Goldstein (14) (assuming constant turbulent thermal diffusivity) yields an effectiveness equation that incorporates those trends and is of the form:

$$\bar{\eta} = \eta_p (\beta/\beta_p)^{-1/2} e^{1/2[1-(\beta/\beta_p)^{-1}]} \quad (1)$$

where $\beta = x/MS_e$. The moving energy sink model approximates the temperature field due to coolant injection through a single hole as a point energy sink over the cooling hole. The strength of the sink results in a three-dimensional temperature distribution in the infinite medium (mainstream flow) moving in steady uniform flow past the sink. Spatially, an effectiveness distribution along the wall can be obtained and, for multiple holes, a spanwise average film effectiveness distribution can be obtained by integrating over the pitch.

This moving energy sink solution requires two unique constants, η_p and β_p , which are the values of the peak film effectiveness and the location of the peak film effectiveness. The film effectiveness far downstream is proportional to η_p/β_p , with an effectiveness decay slope (-0.5) that agrees with the trends exhibited by the data. This is shown schematically in Figure 5.

Initially, eq. (1) was used to curve fit the effectiveness data, using downstream data to evaluate η_p/β_p , and obtaining η_p by inspection. The value of β_p was calculated. It was found that any individual data set in the mass addition and mixing regimes could be accurately represented by appropriate choice of constants (η_p , η_p/β_p).

For the effectiveness data in the penetration regime, it was found that eq. (1) was not adequate to represent the rising/flat trend of the data over large distances ($0 < x/D < 100$). The exponential term dependent on one constant (β_p) was not capable of offsetting the $\beta^{-1/2}$ decay term to yield the rising/flat trend. It was concluded that eq. (1) was not suitable as a general effectiveness equation for all three regimes (mas, mix, pen).

To obtain an effectiveness equation suitable for all three regimes, an empirical modification of eq. (1) was introduced to allow for a thermal diffusivity that decays with distance from the injection site. The resulting effectiveness equation is:

$$\bar{\eta} = \eta_p (\beta/\beta_p)^{(a-1)/2} e^{1/2[1-(\beta/\beta_p)^{a-1}]} \quad (2)$$

The additional empirical constant, "a", represents the exponent corresponding to a power law decay of the thermal diffusivity, $\epsilon_H(x)$.

The concept of a decaying thermal diffusivity was prompted by previous film cooling studies that used the moving energy sink model to curvefit effectiveness data. Ramsey (15,16), Eriksen, et al (17) and Kadotani (6) found a decaying trend for $\epsilon_H(x)$ implied by the effectiveness data. The value of $\epsilon_H(x)$ required for the moving energy sink equation to fit the data was largest at the coolant holes and decayed to some asymptotic limit as x/D increased. This trend is consistent with experimental boundary layer measurements on a film cooled surface. Yavuzkurt, et al (18) used hot wire measurements and the mixing length model to determine the eddy diffusivity, $\epsilon_M(x)$, showing a peak level near injection and a decay of $\epsilon_M(x)$ downstream. Crawford, et al (19) modeled the diffusivity distribution as an exponential decay and showed good agreement between predicted and measured heat transfer distributions for a turbulent film cooled flat plate.

The choice of a power law decay for the thermal diffusivity in eq. (2) (rather than an exponential decay) required the specification of some location along the surface, $\beta^* = (x/MS_0)^*$, where the decay of the diffusivity terminates. It would be unrealistic to allow the diffusivity to decay below the level typical of the turbulent boundary layer. Film effectiveness data in the penetration regime did not extend sufficiently far downstream to accurately determine the location, β^* , where the decaying diffusivity remained a constant. Therefore, it was assumed that the diffusivity remained a constant beginning at the peak effectiveness location, β_p .

Using eq. (2), with decaying diffusivity ($a > 0$) for $\beta < \beta_p$, and constant diffusivity ($a = 0$) for $\beta \geq \beta_p$, the generalized effectiveness equation utilized in the present study was (see Figure G):

$$\begin{aligned} \beta < \beta_p \\ \bar{\eta} = \eta_p (\beta/\beta_p)^{(a-1)/2} e^{1/2[1-(\beta/\beta_p)^a-1]} \end{aligned} \quad (2)$$

$$\begin{aligned} \beta > \beta_p \\ \bar{\eta} = \eta_p (\beta/\beta_p)^{-1/2} e^{1/2[1-(\beta/\beta_p)^{-1}]} \end{aligned} \quad (2a)$$

$$\begin{aligned} \beta \gg \beta_p \\ \bar{\eta} = \eta_p \sqrt{\beta_p} e^{1/2} \beta^{-1/2} \end{aligned} \quad (2b)$$

Three empirical constants (η_p , η_p/β_p , a) were required to curve fit measured effectiveness data. The procedure was modified by selecting values for "a", to obtain the best fit of the data.

The effectiveness data for each experimental test condition (M, ρ_c/ρ_g , injection geometry) from the Primary References (1), (2), (3), (4) (Table 1) were curve fit to determine the empirical constants. The three constants were determined by iteration to obtain the smallest difference in effectiveness between prediction and data, over the range (x/D) of each data set. During this process, each constant was required to exhibit a smooth variation with respect to M, ρ_c/ρ_g , V_c/V_g , P/D and α_c to facilitate correlation of the empirical constants*.

Curve fitting of the data of Pedersen (1), Goldstein, et al (2), and Blair, Lander (3), Muska, et al (4) resulted in the constants listed in Table 2. The injection conditions listed in Table 2 are classified according to the flow regimes (mas, mix, pen) identified from the data. In general, the curve fits represent the data within an effectiveness band width of ± 0.02 for the worst case and ± 0.01 (or better) for most cases for the entire range of M, ρ_c/ρ_g and x/D .

Examination of the curve fit constants in Table 2 revealed several important trends.

1. The peak effectiveness (η_p) for a given M decreases as the velocity ratio (V_c/V_g) increases in the mixing regime.
2. The peak effectiveness (η_p) for a given M tends to decrease and then increase as the velocity ratio (V_c/V_g) increases in the penetration regime.
3. The downstream parameter (η_p/β_p) increases with M and approaches an asymptotic limit for large M with a given value of ρ_c/ρ_g .
4. The peak effectiveness (η_p) increases as the hole-to-hole spacing (P/D) decreases for given values of ρ_c/ρ_g and M.
5. The downstream constant (η_p/β_p) increases as (P/D) decreases for given values of ρ_c/ρ_g and M.

It should be noted that no data in the literature are sufficient to conclusively verify trend 3 above.

Correlation of Peak Effectiveness Parameter

In general, the peak effectiveness (η_p) was found to vary with M, ρ_c/ρ_g (or V_c/V_g), P/D and α_c . The data of Pedersen (1), for constant ρ_c/ρ_g , showed that η_p decreased as V_c/V_g increased in the mixing regime. Select points for $V_c/V_g = \text{constant}$ (Table 2, $V_c/V_g = 0.53, 0.69$) showed that η_p increased as ρ_c/ρ_g increased. A parameter of the form $\eta_p/(\rho_c/\rho_g)^b$ was found to correlate the influence of density ratio, with the data of Pedersen (1) and Foster, Lampard (9) indicating a value of $b = 1/3$.

The peak effectiveness was found to level out and increase gradually as V_c/V_g increased in the penetration regime. The limited data (1,2) available shows $\eta_p/(\rho_c/\rho_g)^{1/3}$ to be a unique function of velocity ratio for both the mixing and penetration regimes.

*It should be noted that when η_p is low (e.g. ≈ 0.10), small uncertainties in η_p (e.g. ≈ 0.02) can result in a significant change in the effectiveness distribution due to the squaring of the uncertainty, $\beta_p = (\eta_p/\beta_p/\eta_p)^2$.

The moving energy sink model was utilized to develop a parameter to correlate the influence of P/D . The expression for the peak effectiveness indicates a direct dependence of η_p on S_e/D and M , and an indirect dependence of η_p on ρ_c/ρ_g and V_c/V_g . The best correlation was obtained with $\eta_p/(\rho_c/\rho_g)^{1/3}(S_e/D)$ as a function of V_c/V_g . Figure 7 presents the correlation of all data of Pedersen (1) and Goldstein, et al (2).

An analytic function was defined to represent the correlation of the data for $\eta_p/(\rho_c/\rho_g)^{1/3}(S_e/D)$ shown in Figure 7. The following physical constraints were postulated to ensure correlation function trends that are consistent with physical reasoning:

1. $\eta_p = 0$ when $M = 0$, i.e., $V_c/V_g = 0$;
2. η_p increases as M increases in the mass addition regime;
3. η_p decreases as (V_c/V_g) increases in the mixing regime;
4. The onset of the penetration regime occurs when the velocity ratio exceeds a critical value, $(V_c/V_g)_{pen}$.
5. η_p approaches an asymptotic limit as V_c/V_g increases in the penetration regime.

Correlation of Downstream Effectiveness Parameter

The moving energy sink model was also examined to determine the parameters that influence the downstream effectiveness constant, η_p/β_p . The model suggested the form, $\eta_p/\beta_p/(S_e/D)^{1/2}$, as a useful quantity for correlating the influence of geometry.

Figure 8 illustrates the data of Pedersen (1) showing the influence of blowing ratio and density ratio on $\eta_p/\beta_p/(S_e/D)^{1/2}$. One major trend inferred from the data was that η_p/β_p increases with M and reached an asymptotic limit for $M = .5$. Figure 8 shows that the asymptotic limit for η_p/β_p decreases as ρ_c/ρ_g decreases.

A mathematical function was defined to obtain a correlation of the data shown in Figure 8. The following constraints were imposed to ensure correlation function trends that are consistent with physical reasoning:

1. $\eta_p/\beta_p = 0$ when $M = 0$.
2. At low M , the parameter η_p/β_p increases with M due to a mass addition effect.
3. The beneficial effect of mass addition deteriorates due to enhanced coolant penetration and mixing as M and/or V_c/V_g increase.
4. An asymptotic limit for η_p/β_p as M increases results when the enhanced penetration and mixing cancels the beneficial effects of mass addition.

Postulates 1 and 4 are required for physically realistic limits as the coolant blowing ratio is reduced toward zero or increased to extreme values. Justification for 2 and 3 is based on observations from the data of Pedersen (1).

Correlation of Thermal Diffusivity Decay Parameter

The moving energy sink solution for a constant thermal diffusivity (eq. (1)) was found suitable for representing the effectiveness distribution for the mass addition and mixing regimes. However, for high blowing ratio (M) and/or low density ratio (ρ_c/ρ_g), the rising/flat effectiveness distribution characteristic of the penetration regime was not represented by eq. (1). In view of the importance of valid effectiveness predictions for high M ($V_c/V_g > 0.8$) characteristic of the turbine airfoil pressure (concave) surface, it was considered essential that the effectiveness correlation equation be capable of representing the effectiveness distribution for all three regimes. Therefore, the moving energy sink solution was modified to incorporate the decay of the thermal diffusivity away from the injection site.

The values of the diffusivity decay parameter required to fit the penetration regime data of Pedersen (1) and Goldstein, et al (2) are illustrated in Figure 9. It was observed that "a" decreased as V_c/V_g increased for a given injection geometry. The data of Pedersen and Goldstein, et al provided a smooth variation of "a" for $0.89 \leq V_c/V_g < 2.37$. For simplicity, it was desired to correlate "a" with parameters already defined. Therefore, a simple correlation was found using "a" vs. $(V_c/V_g)/(V_c/V_g)_{pen}$. The solid line in Figure 9 is a mathematical correlation of the data for "a". It was reasoned that "a" approaches zero as V_c/V_g approaches zero, i.e., no diffusivity decay for low blowing ratio. In view of the limited data, the complexity of the penetration regime phenomena and the empirical parameter "a" introduced to provide a simple model, the correlation for "a" should receive further scrutiny to determine its generality.

Correlation Development

The data of Pedersen (1), the primary reference used in developing the film effectiveness correlation, are shown by the symbols in Figures 10. The solid lines represent the prediction from the effectiveness correlation using the mathematically derived fit of the constants $(\eta_p/(\rho_c/\rho_g)^{1/3}(S_e/D)$, $\eta_p/\beta_p/(S_e/D)^{1/2}$ and "a").

In general, the agreement between the predicted effectiveness and the data of Pedersen (1) is excellent, with a typical error of 0.01 in effectiveness.

When the correlation developed from Pedersen's data was applied to other primary and secondary references, it was observed that several modifications were required to predict the film effectiveness for other values of Reynolds number, $V_g D/\nu_g$ and hole angle, α_c .

The correlation developed from data in the literature based on the moving energy sink model has an effectiveness decay of β^{-5} far downstream from the injection holes. As demonstrated, this trend is in good agreement with all flat plate effectiveness data. Analysis of a film cooled turbulent boundary layer (21)

suggests that the effectiveness level far downstream from the injection site should vary as $(x/MS)^{-0.8}$ and $(Re_s \mu_c/\eta_c)^{0.2}$ if a typical 1/7 power law turbulent profile is assumed. However, analysis and data for 2D slot injection indicate that the slope of effectiveness with x/MS approaches -0.8 at values of $x/MS > 1000$. This could not be verified by the data for discrete hole coolant injection because of the limited range of x/MS . It is expected that the downstream effectiveness decay rate will increase to that typical of turbulent boundary layer development. The level of film effectiveness far downstream should be directly dependent on the Reynolds number to the 0.2 power. Therefore, the downstream effectiveness constant (η_p/β_p) defined by the moving energy sink model should be dependent on the equivalent slot Reynolds number to the 0.2 power.

This effect was verified by several sources of data. Afejuku (5) and Foster, Lampard (10) used Pedersen's geometry. However, their hole diameter and free-stream velocity conditions resulted in a Reynolds number that was approximately one-third of the Reynolds number Pedersen tested. Afejuku's effectiveness levels, for the mixing regime ($V_c/V_g < 0.8$), were lower than Pedersen's as expected by the turbulent boundary layer analysis.

Comparison of Afejuku and Pedersen's data in the penetration regime shows a trend opposite that expected from the turbulent boundary layer analysis. This could imply that the peak effectiveness correlation from Pedersen's data requires a Reynolds number correction for the penetration regime.

Leiss (8) conducted experiments investigating equivalent slot Reynolds number effects with Pedersen's geometry by varying hole size and freestream velocity. His tests were conducted in the mixing regime, and the trends of the effectiveness data could also be explained by the aforementioned change in equivalent slot Reynolds number. The trends of the mixing regime data obtained by other investigations (6,7), also utilizing Pedersen's geometry, with different equivalent slot Reynolds number, also could be predicted with a Reynolds number correction on the downstream effectiveness constant (η_p/β_p) . Consequently, there appears to be an ordered trend of downstream effectiveness with slot Reynolds number in the mixing regime. However, there were insufficient data to conclude that this trend applies in the penetration regime.

The effect of the injection angle on film cooling for a fixed hole spacing was reported for 35° , 55° , and 90° by several investigators (5,9,10). In examining the data, it was concluded that the downstream effectiveness constant (η_p/β_p) is unaffected by the injection angle. The critical velocity ratio defining the onset of the penetration regime and the peak effectiveness (η_p) was found to be directly affected by changes in the injection angle. Figure 11 shows the adjustments required in correlating peak effectiveness as a function of velocity ratio for the injection angles reported in the literature. A decrease in peak effectiveness is observed at low coolant-to-freestream velocity ratios as the injection angle is increased. At high velocity ratios, indicative of the penetration regime, the peak effectiveness is insensitive to injection angle.

The critical velocity ratio defining the onset of the penetration regime was found to be inversely proportional to the sine of the injection angle. The critical velocity ratio is infinite, for shallow injection ($\alpha_c = 0$), since the coolant flow does not penetrate the boundary layer. However, as the angle of the coolant hole is increased the critical velocity ratio defining the onset of penetration decreases.

Comparison with Reference Data

The generalized correlation developed was evaluated against all the data from the primary and secondary reference sources in Table 1. In general, good predictive agreement was found with the reported data. It should be noted that the experimental data obtained from the several references have inherently different sources and magnitude of experimental error. This is due to the use of different wind tunnels, instrumentation and methods of measuring and defining average film effectiveness. However, examples of the predictive capability of the correlation are shown by comparing the trends predicted by the correlation with measured data to illustrate the effect of: 1) Reynolds number, 2) hole angle and 3) hole spacing-to-diameter ratio (P/D).

The data reported in the literature were obtained from both mass transfer and heat transfer measurements. The primary correlation developed from Pedersen's data (mass transfer) can be directly applied to the heat transfer data of Goldstein, et al (2) as demonstrated in Figure 12. The comparison to measured data is made for the same coolant hole geometry and wind tunnel utilized by Pedersen but with a Reynolds number that is 2x larger. The prediction compares favorably to the results, where the maximum deviation in effectiveness is 0.02 and typically deviates only 0.01.

The effect of Reynolds number ($V_g D/V_g$) was examined further by comparing the prediction to the data of Pedersen (1), Afejuku (5), and Foster, Lampard (10) for the same coolant hole geometry. Afejuku and Foster, Lampard utilized a Reynolds number that was approximately one-third that of Pedersen. Figure 13 shows a comparison of the predictions to the data. The dashed line represents the prediction for Pedersen's Reynolds number, which is in good agreement with the data. The solid line represents the prediction for the Afejuku and Foster, Lampard case which also is in good agreement with the data for most of the test surface ($25 \leq x/D \leq 125$). Near the coolant holes ($5 \leq x/D \leq 25$) there is a significant variation between the two data sources and the prediction. Experiments by Goldstein, Yoshida (7) suggest that such discrepancies may be due to variations in the coolant velocity profile at injection.

The correlation was further tested by evaluating the effect of the injection angle. Foster and Lampard (10) obtained data for 35° , 55° and 90° injection geometries. Figure 14 shows favorable agreement of the prediction to the measured data. There are insufficient data in the literature to completely test the model for a large range of conditions for different injection angles.

A comparison for a coolant hole geometry different from Pedersen's is shown in Figure 15. These data were reported by Blair, Lander (3) and Muska, Fish, Suo (4) for a two-row geometry with a pitch-to-diameter ratio of 2.0 and injection angle of 30 degrees (Pedersen's values were one-row, 3.0 and 35° , respectively). The primary effect on the effectiveness prediction was caused by a reduction in P/D and not hole angle. Figure 15 shows excellent agreement between the prediction and data indicating that the geometry parameter (P/D) is adequately represented in the correlation.

CONCLUSIONS

1. A film effectiveness prediction model has been developed for a row or multiple rows of round holes from flat plate data that accurately predicts the effect of ρ_c/ρ_g , V_c/V_g , geometry and equivalent slot Reynolds number.
2. Three flow regimes, mass addition, mixing and penetration identified from film effectiveness data aided development of the correlation. The regimes are dependent on the coolant-to-freestream velocity ratio. Steeper coolant injection angles cause the penetration regime to occur at lower velocity ratios.
3. A model resulting from a constant thermal diffusivity assumption was acceptable for predicting data in the mass addition and mixing regimes. The model required a decaying thermal diffusivity assumption to accurately predict data in the penetration regime. Three correlative constants were required: Peak effectiveness (τ_p), downstream effectiveness parameter (η_p/β_p) and the turbulent diffusivity decay parameter (α).
4. The effect of equivalent slot Reynolds number on film effectiveness in the penetration regime is the largest uncertainty in the model due to the limited data in the literature.

REFERENCES

1. Pedersen, D.R., "Effect of Density Ratio on Film Cooling Effectiveness for Injection Through a Row of Holes and a Slot," Ph.D. Thesis, University of Minnesota, 1972.
2. Goldstein, R.J., Eckert, E.R.G., Eriksen, V.L., Ramsey, J.W., "Summary Report: Film Cooling Following Injection Through Inclined Circular Tubes," NASA CR-72612, November 1969.
3. Blair, M.F., Lander, R.D., "New Techniques for Measuring Film Cooling Effectiveness and Heat Transfer," AIAA Paper No. 74-674, ASME Paper No. 74-HT-8, July 1974.
4. Muska, J.F., Fish, R.W., Suo, M., "The Additive Nature of Film Cooling from Rows of Holes," ASME Paper No. 75-WA/GT-17, December 1975.
5. Afejuku, W.O., "Superposition of Cooling Films," Ph.D. Thesis, University of Nottingham, 1977.
6. Kadotani, K., "Effect of Main Stream Variables on Heated and Unheated Jets Issuing from a Row of Inclined Round Holes," Ph.D. Thesis, University of Minnesota, 1975.
7. Goldstein, R.J., Yoshida, T., "The Influence of a Laminar Boundary Layer and Laminar Injection on Film Cooling Performance," ASME Journal of Heat Transfer, Vol. 104, 1982, pp. 355-361.
8. Liess, C., "Experimental Investigation of Film Cooling with Ejection from a Row of Holes for the Application to Gas Turbine Blades," ASME Journal of Engineering for Power, Vol. 97, 1975, pp. 21-27.
9. Foster, N.W., Lampard, D., "Effects of Density Ratio and Velocity Ratio on Discrete Hole Film Cooling," AIAA Journal, Vol. 13, No. 8, pp. 1112-1114.
10. Foster, N.W., Lampard, D., "The Flow and Film Cooling Effectiveness Following Injection Through a Row of Holes," ASME Journal of Engineering for Power, Vol. 102, 1980, pp. 584-588.
11. Sasaki, M., Takahara, K., Kumagai, T., Hamano, M., "Film Cooling Effectiveness for Injection from Multi-row Holes," ASME Paper No. 78-GT-32, April 1978.
12. Goldstein, R.M., Eckert, E.R.G., Burggraf, F., "Effects of Hole Geometry and Density on Three-Dimensional Film Cooling," International Journal of Heat and Mass Transfer, Vol. 17, 1974, pp. 595-606.
13. Burggraf, F., "Local Film Effectiveness with a Point Source Analytical Model for 90° and 35° Injection from a Single Hole," G.E. Report No. R72AEG172, 1972.
14. Kadotani, K., Goldstein, R.J., "Effect of Mainstream Variables on Jets Issuing from a Row of Inclined Round Holes," ASME Paper No. 78-GT-138, April 1978.
15. Ramsey, J.W., "The Interaction of a Heated Air Jet with a Deflecting Flow," Ph.D. Thesis, University of Minnesota, 1969.
16. Ramsey, J.W., Goldstein, R.J., "Interaction of a Heated Jet with a Deflecting Stream," ASME Journal of Heat Transfer, Vol. 93, 1971, pp. 365-372.
17. Eriksen, V.L., Eckert, E.R.G., Goldstein, R.J., "A Model for Analysis of Temperature Field Downstream of a Heated Jet Injected into an Isothermal Crossflow," NASA CR-72990, July 1971.
18. Yavuzkurt, S., Moffat, R.J., Kays, W.M., "Full-Coverage Film Cooling: 3-Dimensional Measurements of Turbulence Structure and Prediction of Recovery Region Hydrodynamics," NASA CR-3104, March 1979.
19. Crawford, M.E., Kays, W.M., Moffat, R.J., "Full-Coverage Film Cooling on Flat, Isothermal Surfaces: A Summary Report on Data and Predictions," NASA CR-3219, January 1980.
20. Goldstein, R.J., "Film Cooling," Advances in Heat Transfer, Vol. 7, Academic Press, 1971.
21. Mayle, R.E., Kopper, F.C., "Adiabatic Wall Effectiveness of a Turbulent Boundary Layer with Slot Injection," ASME Journal of Heat Transfer, Vol. 98, 1976, pp. 240-244.

Table 1
Flat Plate Effectiveness Data Base

Reference	Technique	Coastal Hole Geometry	ρ_c/ρ_g	M	V_c/V_g	V_c/D_g	x^2/D
PRIMARY REFERENCES							
Pedersen (1)	Mass Transfer	$\alpha_c = 35^\circ$ D = 11.7 mm P/D = 3, $R_g = 1$	0.75-4.17	0.2	27.7	0.18x10 ³	0.15x
Goldstein, Eckert, Ersson, Ramberg (2)	Heat Transfer	$\alpha_c = 35^\circ$ D = 11.8 mm P/D = 3, $R_g = 1$	0.31	0.5-2.0	30.5	0.22 x 10 ³	0.12x
Blair, Lander (3)	Heat Transfer	$\alpha_c = 30^\circ$ D = 12.7 mm P/D = 2, $R_g = 2$ Multiple Rows	1.1	0.1-1.3	21.2	0.172x10 ³	
Afeyahu (5)	Mass Transfer	$\alpha_c = 35^\circ, 50^\circ$ D = 2.27 mm P/D = 3, $R_g = 1$ Multiple Rows	2.0	0.5-3.0	24.7	0.034x10 ³	0.1x
SECONDARY REFERENCES							
Redantoni (6)	Heat Transfer	$\alpha_c = 35^\circ$ D = 11.8 mm P/D = 3, $R_g = 1$	0.85	0.35-1.5	15.5	0.11 x 10 ³	0.2x
Goldstein, Yoshida (7)	Heat Transfer	$\alpha_c = 35^\circ$ D = 11.8 mm P/D = 3, $R_g = 1$	0.85	0.5, 1.0	4.5	0.014x10 ³	0.1x
Liess (8)	Heat Transfer	$\alpha_c = 35^\circ$ D = 2 mm P/D = 3, $R_g = 1$	0.77	0.15-2.0	32.8	0.14x10 ³	0.04-0.42
Foster, Lampard (9)	Mass Transfer	$\alpha_c = 50^\circ$ D = 2.27 mm P/D = 3, $R_g = 1$	1.5-6.1x	0.5-3.75	30.5	0.042x10 ³	0.42
Foster, Lampard (10)	Mass Transfer	$\alpha_c = 35^\circ, 55^\circ, 90^\circ$ D = 2.27 mm P/D = 3, $R_g = 1$	2.0	0.5, 1.0, 1.8	24.7	0.038x10 ³	0.18-0.63
Sasaki (11)	Heat Transfer	$\alpha_c = 45^\circ$ D = 12 mm P/D = 3, $R_g = 1$ Multiple Rows	0.91	0.11-0.54	20.1	0.15 x 10 ³	0.10x

Table 2
Curvefit Constants for Equations (2a), (2b)

Ref.	M	ρ_c/ρ_g	V_c/V_g	I	Heat Transfer	α_c	x^2/D	ρ_c	α
Single Row of Holes									
(1)	0.1018	4.17	0.9503	0.0105	mass	0.560*	1.2147	5.1x	**
(1)	0.2534	2.065	0.1304	0.0210	mass	0.445*	1.2147	8.21	**
(1)	0.2130	1.447	0.1453	0.0330	mass	0.179*	1.2147	10.21	**
(1)	0.7088	1.193	0.1350	0.0385	mass	0.385*	1.2147	11.93	**
(1)	0.2112	0.554	0.2210	0.0466	mass	0.191*	1.2147	13.81	**
(1)	0.5470	4.17	0.3718	0.0818	mass	0.560*	1.2147	14.78	**
(1)	0.5121	1.998	0.2563	0.1313	mass	0.419*	1.4579	11.55	**
(1)	0.5078	1.434	0.3399	0.1226	air	0.361*	1.8994	13.90	**
(1)	0.5474	1.183	0.4407	0.2298	air	0.286*	1.2018	21.82	**
(1)	0.5126	0.360	0.5339	0.2737	air	0.235	1.2062	31.37	**
(1)	0.5236	0.753	0.6961	0.3649	air	0.181	1.0910	59.87	**
(1)	1.021	4.17x	0.2559	0.2374	air	0.549	1.4963	7.37	**
(1)	1.050	1.968	0.5334	0.5339	air	0.270	1.4579	29.16	**
(1)	1.033	1.497	0.4901	0.7129	air	0.177	1.4296	64.15	**
(1)	1.019	1.181	0.8886	0.9325	air	0.110	1.3018	141.36	0.75
(1)	1.045	0.957	1.102	1.1822	air	0.096	1.2542	200.11	0.67
(1)	1.936	4.17x	0.4636	0.8800	air	0.405	1.4967	73.55	**
(1)	1.247	1.996	0.9725	1.0992	air	0.115	1.4579	162.72	0.71
(1)	0.936	1.498	2.224	2.6021	air	0.100	1.4296	207.74	0.60
(1)	0.994	0.967	2.0136	4.1390	air	0.116	1.2062	109.65	0.35
(2)	0.5	0.85	0.5937	0.2958	air	0.184	1.1643	28.68	**
(3)	1.5	0.85	1.7152	2.6429	air	0.093	1.1643	145.09	0.425
(3)	2.0	0.85	2.3608	4.7315	air	0.120	1.1643	90.93	0.275
Double Row of Holes									
(1)(1)	0.039	1.103	0.0995	0.0095	mass	0.761	1.4213	4.41	**
(1)(4)	0.303	1.124	0.2496	0.0617	mass	0.750	2.1354	7.18	**
(1)(6)	0.498	1.127	0.4419	0.2201	air	0.730	2.4132	10.93	**
(1)(8)	0.733	1.126	0.6143	0.4389	air	0.640	2.6130	15.84	**
(1)(10)	0.897	1.126	0.7196	0.7145	air	0.420	2.7895	22.74	0.75
(1)(14)	1.302	1.107	1.1762	1.5315	air	0.440	2.7895	19.00	0.44

* - not available
** - not required for $\alpha > \beta$

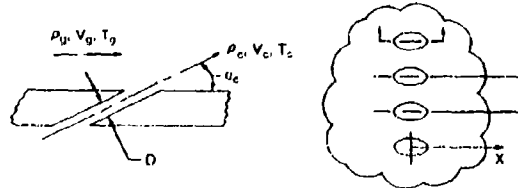


Figure 1 Film Cooling Parameters

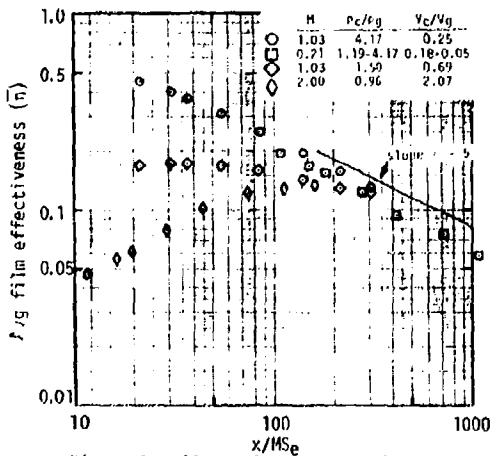


Figure 2 Effect of Density Ratio on Film Effectiveness from Pedersen (1)

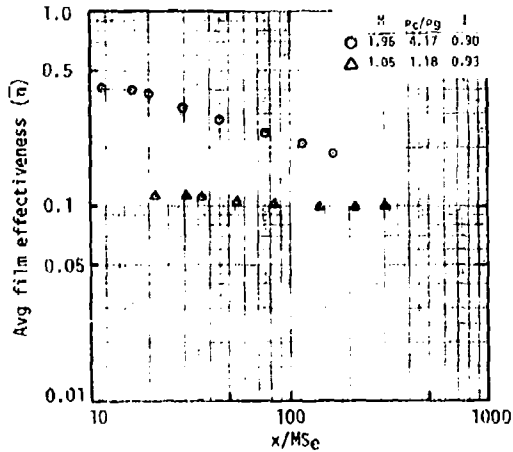


Figure 3 Film Effectiveness Data from Pedersen (1) for Constant Momentum Ratio

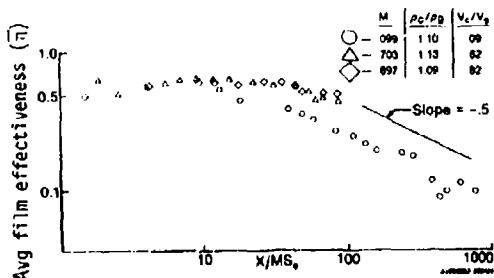


Figure 4 Film Effectiveness Data of Blair, Lander (3) and Muska, Fish, Suo (4)

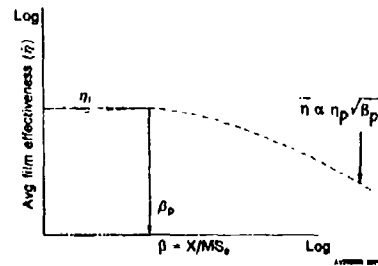


Figure 5 Effectiveness Distribution from Moving Energy Sink Model (Constant Diffusivity)

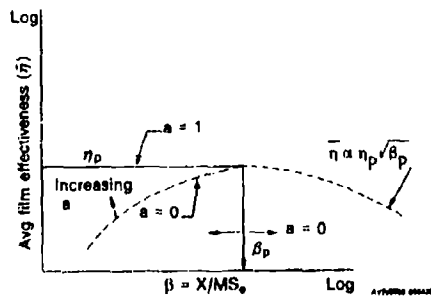


Figure 6 Effectiveness Distribution from Moving Energy Sink Model (Variable Diffusivity)

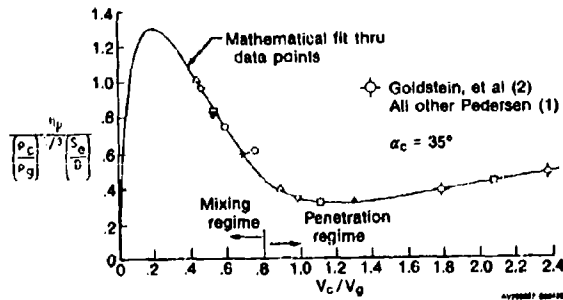


Figure 7 Correlation of Peak Effectiveness Parameter

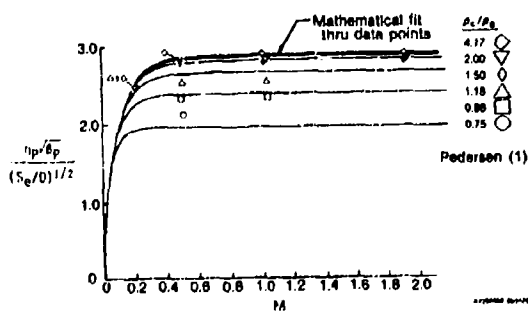


Figure 8 Correlation of Downstream Effectiveness Parameter

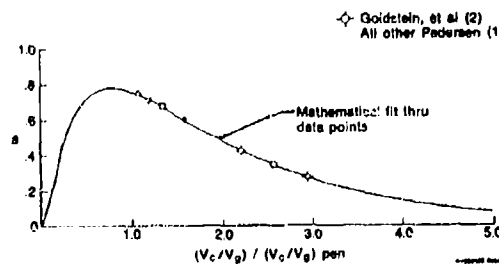


Figure 9 Correlation of Thermal Diffusivity Decay Parameter

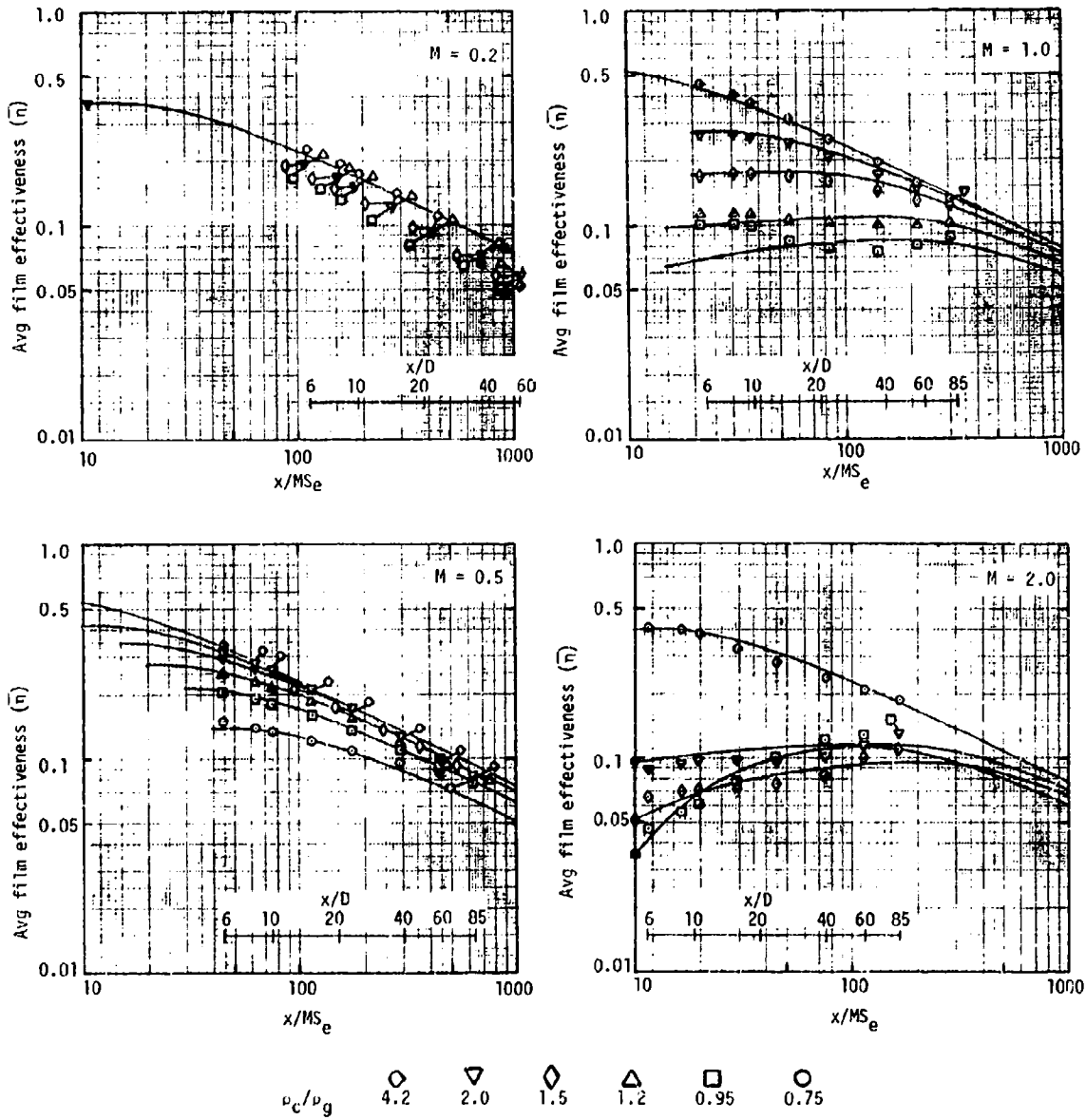


Figure 10 Comparison of Correlation Prediction with Data from Pedersen (1)

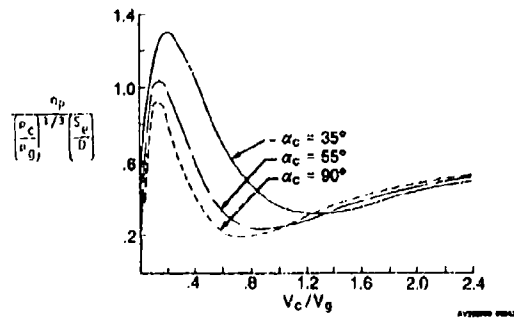


Figure 11 Effect of Injection Angle on Peak Effectiveness Correlation

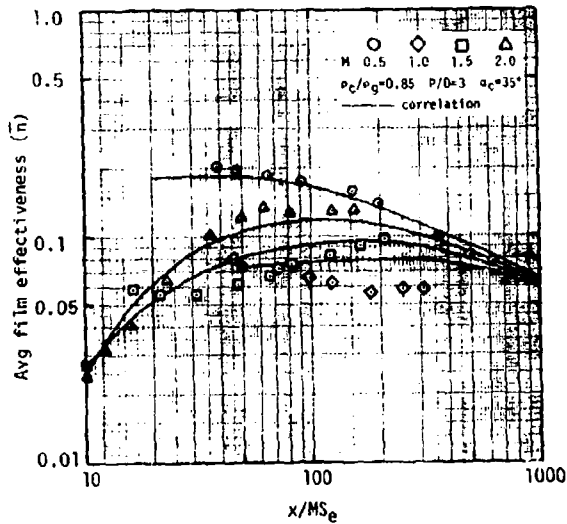


Figure 12 Comparison of Correlation Prediction with Data from Goldstein, Eckert, Eriksen, Ramsey (2)

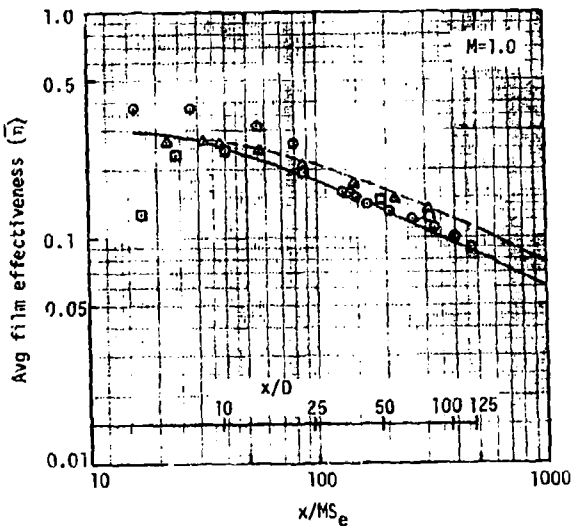
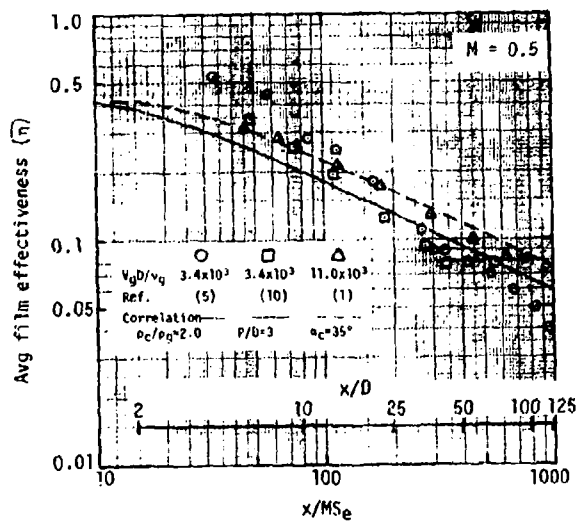


Figure 13 Effect of Reynolds Number on Film Effectiveness in Mixing Regime

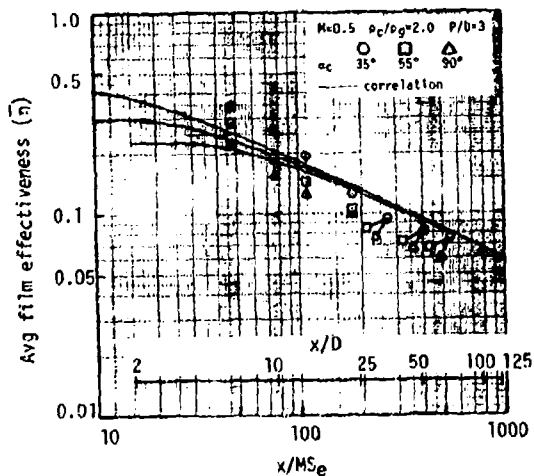


Figure 14 Effect of Injection Angle on Film Effectiveness from Foster, Lampard (10)

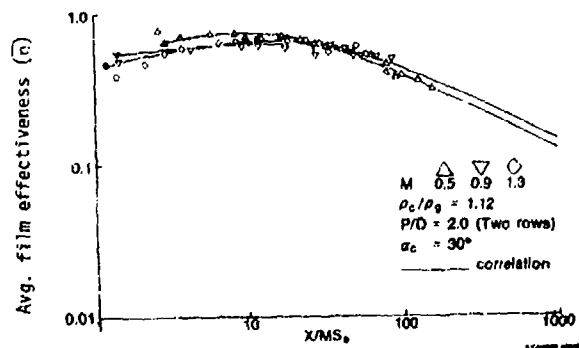


Figure 15 Effect of Hole Spacing on Film Effectiveness from Blair, Lander (3) and Muska, Fish, Suo (4)

COMPUTATION OF THERMAL RADIATION FOR GAS TURBINE CONDITIONS

by

M.C. Trivalho, D.F.C. Durão and F.C. Lockwood*
 Instituto Superior Técnico
 Mechanical Engineering Department
 1096 Lisbon, Portugal

*Imperial College of Science and Technology
 Mechanical Engineering Department
 London SW7 2BX, England

ABSTRACT

The present paper is concerned with the prediction of the fluid flow, combustion and heat release processes in a "can" combustion chamber of a gas turbine. A three-dimensional numerical solution technique is used to solve the governing time-averaged partial differential equations and the physical modelling for the turbulence, combustion and thermal radiation.

The thermal radiation modelling is emphasised in this paper. The implications of neglecting radiative heat transfer in gas turbine combustion chamber calculations are explored and discussed.

NOMENCLATURE

a	- weighting coefficient in the gas emittance equation
A	- area normal to Ω
C_{μ}, C_1, C_2, C_D	- constants in turbulence model
E_b	- black body emissive power (σT^4)
f	- mixture fraction
h	- specific enthalpy
I	- radiation intensity in the direction of Ω
k	- turbulent kinetic energy
k_g	- gas absorption coefficient
k_s	- soot absorption coefficient
L	- path length
p_w	- partial pressure of water vapour
p_c	- partial pressure of carbon dioxide
$p(f)$	- probability density function of f
$q_{+,p}$	- radiation energy leaving a wall
$q_{-,p}$	- radiation energy incident on a wall
q_p	- net radiation wall heat flux
r	- cylindrical co-ordinate
s	- distance in the direction of I
S_ϕ	- source term in the ϕ -equation
T	- temperature
u	- time averaged velocity component in the x-direction
\bar{u}_j, u_j'	- mean and fluctuating velocity in direction j
v	- time-averaged velocity component in the r-direction
w	- time-averaged velocity component in the θ -direction
x	- cylindrical co-ordinate
x_j	- co-ordinate direction j
δ_{ij}	- Kronecker delta
ϵ	- dissipation rate of turbulence energy
ϵ_w	- wall emissivity
θ	- cylindrical co-ordinate
μ_T	- turbulent viscosity
Ω	- solid angle
ρ	- fluid density
σ	- Stefan Boltzmann constant
$\sigma_k, \sigma_\epsilon$	- turbulent Prandtl/Schmidt numbers
ϕ	- surrogate variable for U, V, W, K, ϵ , h and f
$\bar{\cdot}$	- unweighted time-average
$\rho \bar{\cdot}$	- density-weighted time-average
"	- fluctuation about the density-weighted mean.

1. INTRODUCTION

Gas turbine combustion chambers have recently been the subject of extensive investigations in consequence of the tighter pollution-control regulations and requirements, see e.g. [1,2]. Although, little attention was paid to the heat transfer by thermal radiation. It was thought to be rather small and in any case there was no means by which it could be reliably calculated. Gas turbines, have however, grown continually in size, and the pressure ratios at which they operate have also persistently increased. Both of the factors have augmented the combustor thermal radiation. One of the first investigations of the radiation heat transfer in combustor "can", at 25 bar, was performed by Lockwood et al [3].

The present paper describes the application of a prediction procedure resulting from the combination of a three-dimensional computational procedure for the flow and the chemical reaction [4] and a technique for the computation of the radiation heat transfer [5] capable of economically handling any degree of

geometrical complexity, to a "can" combustion chamber of a gas turbine. Predictions are presented and discussed of the heat transfer distributions. The influence of the pressure ratio is analysed comparing the solutions obtained for the same geometrical configuration for two different working pressures: 6 and 25 bar.

2. FLOW CONFIGURATION

The geometry of the combustion chamber studied is sketched in Figure 1. The combustor has 18 separated burners. As the geometry of the combustor repeats itself every 20° , and the flow pattern also, only a single 20° sector of the chamber is studied. Gaseous fuel (propane) enters the combustor through the inner of the two annular rings with a velocity of 80 m/s. The combustion air is introduced through a concentric annular ring with a velocity of 60 r/s. Secondary and dilution air are introduced through four round holes in the inner and outer annulus walls as shown in Figure 1. The air has been specified as entering only with a radial velocity component through these holes, the actual values of the velocity varying between 40 and 60 m/s. The overall air-fuel ratio is of approximately 30 and the mass flow rate of the combustion air represents 15% of the total air mass flow rate. The air enters the combustor at 500 K and the mean static pressure of the combustor is 6 bar. A second set of predictions were performed for a mean static pressure of 25 bar.

3. GOVERNING EQUATIONS

A mathematical model has been used to calculate the internal flame-tube flow and temperature field which is believed sufficiently accurate to allow the prediction of many of the major features of gaseous-fuelled combustors. It is based, as far as the treatment of the combustion chemistry is concerned, on the assumption that all reactions are sufficiently fast for instantaneous chemical equilibrium to be taken as being a reasonable approximation. If the heat loss from the flame is negligible then the instantaneous thermodynamic state of the gas is describable in terms of a single strictly conserved scalar quantity. Any conserved scalar may be chosen and a convenient choice is the mixture fraction f defined as the mass fraction of fuel present both burnt and unburnt.

Time-averaged balance equations were solved for: the momenta in the r, θ, x co-ordinate directions, the mixture fraction, f , and the specific enthalpy, h . The balance equations appropriate to the high Reynolds number flows all have the form:

$$\frac{\partial}{\partial x_j} (\rho \bar{u}_j \phi) = - \frac{\partial}{\partial x_j} \bar{\rho} u_j'' \phi'' + S_\phi \quad (1)$$

where ϕ is a dependent variable: U, V, W, f and h in this case, S_ϕ is a source term. An overbar represents an unweighted time-average and a tilde a density-weighted average; lower case letters are used to signify fluctuations about the mean values. Note that for brevity the equations above and below are written in cartesian tensor form; for the geometry shown in Figure 1 it is of course most convenient to cast the equations in a cylindrical polar co-ordinate system, and this form has been used in obtaining the results presented below.

A turbulence model is required to calculate the turbulent fluxes on the right-hand side of the above equation. The "standard" $k-\epsilon$ turbulence model was employed [6,7]. In the absence of a turbulence modelling breakthrough, the $k-\epsilon$ formulation still constitutes the best combination of economy and accuracy for engineering purposes. In density weighted form the turbulence fluxes are:

$$\bar{\rho} u_i'' u_j'' = \frac{2}{3} \bar{\rho} \delta_{ij} k - \mu_T \left[\frac{\partial \bar{u}_i}{\partial x_j} + \frac{\partial \bar{u}_j}{\partial x_i} - \frac{2}{3} \delta_{ij} \frac{\partial \bar{u}_k}{\partial x_k} \right] \quad (2)$$

$$\bar{\rho} u_j'' \phi'' = - \frac{\mu_T}{\sigma_T} \frac{\partial \phi}{\partial x_j} \quad (3)$$

where: $\mu_T = C_\mu \bar{\rho} k^2 / \epsilon$ and k and ϵ are obtained from solution of the transport equations:

$$\frac{\partial}{\partial x_j} (\bar{\rho} \bar{u}_j k) = \frac{\partial}{\partial x_j} \left(\frac{\mu_T}{\sigma_k} \frac{\partial k}{\partial x_j} \right) - \bar{\rho} u_i'' u_j'' \frac{\partial \bar{u}_i}{\partial x_j} - \frac{\mu_T}{\rho^2} \frac{\partial \bar{\rho}}{\partial x_i} \frac{\partial \bar{P}}{\partial x_i} \dots \bar{\rho} \epsilon \quad (4)$$

$$\frac{\partial}{\partial x_j} (\bar{\rho} \bar{u}_j \epsilon) = \frac{\partial}{\partial x_j} \left(\frac{\mu_T}{\sigma_\epsilon} \frac{\partial \epsilon}{\partial x_j} \right) - C_1 \frac{\epsilon}{k} \left[\bar{\rho} u_i'' u_j'' \frac{\partial \bar{u}_i}{\partial x_j} \dots \frac{\mu_T}{\rho^2} \frac{\partial \bar{\rho}}{\partial x_i} \frac{\partial \bar{P}}{\partial x_i} \right] - C_2 \bar{\rho} \frac{\epsilon^2}{k} \quad (5)$$

The model constants appearing in the above equations were assigned the following values, taken unchanged from Launder and Spalding [8]: $C_\mu = 0.09$, $C_1 = 1.44$, $C_2 = 1.92$, $\sigma_k = 1.0$, $\sigma_\epsilon = 1.3$ and $\sigma_T = 0.9$.

The instantaneous gas composition, temperature and density can be determined as function (albeit non-linear ones) of the instantaneous mixture fraction f [9,10]. Since however f will fluctuate as any other variable in a turbulent flow, knowledge of the probability density function (pdf) of f is required if mean values of the functions of f are to be calculated. An assumed-shape pdf approach is adopted here with the pdf of f described in terms of its first two moments, namely the mean value f and the variance

f''^2 . The modelled transport equation for the latter is:

$$\frac{\partial}{\partial x_j} (\bar{\rho} \bar{u}_j f''^2) = \frac{\partial}{\partial x_j} \left(\frac{u_T}{\sigma_T} \frac{\partial f''^2}{\partial x_j} \right) + 2 \frac{u_T}{\sigma_T} \left(\frac{\partial f''}{\partial x_j} \right)^2 - C_D \bar{\rho} \frac{\epsilon}{k} f''^2 \quad (6)$$

The additional constant C_D in this equation was assigned the value 2.0.

A density-weighted pdf is used whose definition allows the determination of the density-weighted mean value of any quantity which is a function of f alone, thus:

$$\bar{\phi} = \frac{1}{\int_0^1 \phi(f) p(f) df} \quad (7)$$

A β -function pdf has been utilized in the present calculations.

The "discrete transfer" radiation prediction procedure of Lockwood and Shah [5] has been utilized in this study. This method combines ease of use, economy and flexibility of application. This last feature is of particular importance in the real world of geometrically intricate combustion chambers. The claimed advantages of the method have now survived the rigours of several industrial applications, see [9] and [4] for example.

The "discrete transfer" method is founded on a direct solution of the radiation transfer equation for a direction $\hat{\Omega}$ which runs:

$$\frac{dI}{ds} = (k_g + k_s) \left(\frac{E}{\pi} - I \right) \quad (8)$$

where I is the radiation intensity in a $\hat{\Omega}$ direction, s is distance in that direction, $E = \sigma T_g^4$ is the black body emissive power, and k_g and k_s are respectively the gas and soot absorption coefficients. The scattering terms do not appear, although they are easily accommodated, since the only particulate matter present in the present application is the soot particles which are much too small to scatter significantly. Many radiation methods are based on the solution of the much more complex integro-differential equation which results when equation (8) is rewritten for the whole solid angle Ω . In our opinion this is unsatisfactory since the numerical solution treatment of such an equation is necessarily very elaborate.

We prefer to solve the much simpler equation (8) within discretisations $d\hat{\Omega}_i$ of the whole solid angle Ω about selected directions $\hat{\Omega}$. Assuming that E , k_g and k_s are constant over a finite distance increment δs , equation (8) may be integrated to yield the simple recurrence relation:

$$I_{n+1} = \frac{E}{\pi} \left(1 - e^{-(k_g + k_s)\delta s} \right) + I_n e^{-(k_g + k_s)\delta s} \quad (9)$$

where n and $n+1$ are successive locations along $\hat{\Omega}$ separated by the increment δs . The relation is applied along the chosen $\hat{\Omega}$ from known conditions at point Q, say, (either guessed or pertaining to those of the previous iteration) on one wall to the point of impingement, P say, of the direction $\hat{\Omega}$ on an opposite wall.

If the hemisphere above P is discretized into subangles $\delta\hat{\Omega}_r$, within which the intensity is considered to be uniform, the energy flux arriving at P is:

$$q_{+,P} = \int_{\hat{\Omega}} I_P \delta\hat{\Omega} = \sum_{\text{all } r} I_{P,r} \hat{\Omega}_r \quad (10)$$

The wall boundary condition is:

$$q_{-,P} = (1 - \epsilon_w) q_{+,P} + \epsilon_w E_w \quad (11)$$

where $q_{-,P}$ is the energy leaving the wall at P, ϵ_w is the wall emissivity, and $E_w = \sigma T_w^4$ is the wall emissive power. The value of $I_{O,r}$ at point Q, the initial value required for the application of the recurrence relation (9), is $q_{-,P}/\pi$. The net radiation heat flux is of course:

$$q_p = q_{+,P} - q_{-,P} \quad (12)$$

The net heat gain or loss within a control volume of the flow procedure is:

$$S_R = (I_{n+1} - I_n) \delta A \quad (13)$$

where the locations n and $n+1$ correspond to the "entry" and "exit" of a direction $\hat{\Omega}$ into and from a control volume, and δA is the cell wall area projected normal to $\hat{\Omega}$. The energy sources S_R are appended to the energy balance equation solved for by the flow code.

The gas absorption coefficient k_g is calculated from the "two grey plus a clear gas" fit of Truelove [11]. Water vapour and carbon dioxide are the prime contributors to the gaseous radiation. The total gas emittance is expressed by:

$$\epsilon_g = \sum_n a_{g,n}(T) \left[1 - \exp(-k_{g,n}(p_w + p_c)L) \right] \quad (14)$$

where the summation n is over the three gases of the assumed mixture, the $k_{g,n}$ are presumed constant with the temperature dependence of the emittance being accommodated in the weighting coefficients $a_{g,n}$, p_w and p_c are the partial pressures of the water vapour and carbon dioxide and L is the path length. The values of the $k_{g,n}$ and $a_{g,n}$ are tabulated in [11]. The value of k_g required for our calculations is obtained from the pseudo grey gas approximation:

$$\epsilon_g = 1 - e^{-\frac{k_g L}{p}} \quad (15)$$

which has worked well in many furnace heat transfer computations (see, e.g. [4]). Since the Truelove correlation was formulated for furnace applications, the predicted mol fractions must be multiplied by the current pressure to obtain the correct partial pressures.

4. COMPUTATIONAL DETAILS

The equations presented above, together with appropriate boundary conditions as described in the previous section have been applied to the geometry shown in Figure 1. The set of differential equations has been solved using finite-difference techniques. A grid of $13 \times 13 \times 13$ nodes (r, θ, x -directions) was used with cyclic boundary conditions being applied on the two extreme circumferential planes and a zero gradient condition specified at the downstream end. Computational time was approximately 13 seconds CPU time per iteration. The number of iterations required for a convergent solution was 220. An VAX 11/780 computer was used to perform the calculations.

5. DISCUSSION OF RESULTS

The total air/fuel mass ratio employed in the present calculations is taken as 30 although this ratio experienced in real combustors is of the order of 100. The used value gave rise to relatively high temperatures in the combustor. The maximum temperature detected is 50 K below the adiabatic flame temperature. The air/fuel ratio of the inlet stream is accordingly lower than that of the stoichiometric value. Hence the combustion is not complete in the initial region and for the completion of the combustion some secondary and dilution air is used. This results in low temperatures in the inlet region and the flame front consequently moves further down. This effect is enhanced by the absence of swirl.

The main input from the flow calculations part of the numerical procedure into the radiation model is the local gas temperature, although as explained in section 3, species concentrations and the working pressure are also required for the specification of absorption coefficients. The working pressure is selected to investigate their influence on the radiative heat transfer. The radiation heat transfer contours to the backplate, inner annulus wall and outer annulus wall are displayed in Figure 2. They were obtained for the geometry of Figure 1 and for the conditions described in section 2 for a working pressure of 6 bar. The heat flux to the backplate is rather uniform, wavering about a value of approximately 35 kW/m^2 although there are a potential heat spot where the flux is greater than 50 kW/m^2 , that corresponds to the entrance of fuel. The heat transfer to the cylindrical walls reflects the distribution of the cooling holes; where the net heat flux through the holes is more than to the walls but since the holes cover less than 5% of the total wall area this fact is not significant. Away from the hole locations and in the first half of the combustion, the heat flux distribution is again rather uniform. The total radiation heat transfer to the walls (all 18 sectors) is 80 kW. This is less than 3% of the energy supplied to the combustor justifying the adiabatic assumption on which the flow reaction calculations are based.

Figure 3 shows the radiation heat transfer contours to the inner annulus wall and outer annular wall for a working fluid pressure of 25 bar. The radiative wall heat fluxes contours is very similar to the ones showed in Figure 2 but the radiative wall heat fluxes increased. For a working pressure of 25 bar the total radiation heat transfer to the walls (all 18 sectors) is 216 kW. The flow geometry was kept unchanged as well as the air/fuel ratio. However as the inlet pressure of the oxidant and fuel are higher (25 bar) their densities also increased, leading to a higher energy supplied to the combustor. The total radiation heat transfer to the walls is 4% of the total energy supplied.

6. CONCLUDING REMARKS

The computational procedure on which this paper is based constitutes a comprehensive design tool for the flow, reaction and heat transfer in a gas turbine combustor "can". The incorporation into the computational scheme of a technique for calculating the distribution of the radiation transfer represents the principal contribution of this paper. The working pressure of the combustor showed to have influence on the radiative heat transfer. The immediate task is one of consolidating our observations about the behaviour of the radiation heat transfer in gas turbine combustors with higher air/fuel ratios and different flow configurations.

The authors want to acknowledge the support of Instituto Nacional de Investigação Científica, Lisbon, through CIAM/FUTL.

REFERENCES

- [1] - JONES, W.P., PRIDDIN, C.H., Predictions of the flow-field and local gas composition in gas turbine combustors. Proceedings of 17th Symposium (Int) on Combustion (1978).
- [2] - Combustion Problems in Turbine Engines, Agard Conference Proceedings nº 353, Turkey, 3-5 October 1983.

- [3]- LOCKWOOD, F.C., MCGUIRK, J.J. AND SHAH, N.G., Radiation transfer in gas turbine combustors. Presented at AIAA 18th Thermophysics Conference, Paper n° AIAA-83-1506, June, 1983.
- [4]- CARVALHO, M.D.M.D.S., Computer simulation of a glass furnace. Ph.D. Thesis, London University, 1983.
- [5]- LOCKWOOD, F.C. AND SHAH, N.G., A new radiation solution method for incorporation in general combustion prediction procedures. Proceedings of 18th Symposium (Int) on Combustion, 1981.
- [6]- LAUNDER, B.E., MORSE, A.P., RODI, W. AND SPALDING, D.B., The prediction of free shear flows - a comparison of the performance of six turbulence models. Proc. Nasa Conf. on Free Shear Flows, Langley, 1972.
- [7]- JONES, W.P. AND LAUNDER, B.E., Predictions of low Reynolds number phenomena with a two-equation model of turbulence. Int. J. Heat and Mass Transfer, Vol. 16, p.119, 1973.
- [8]- LAUNDER, B.E. AND SPALDING, D.B., The numerical computation of turbulent flows. Computer Methods in Applied Mechanics and Engineering, Vol. 3, 1973.
- [9]- GOSMAN, A.D., LOCKWOOD, F.C., MEGAHED, I.E.A. AND SHAH, N.G., The prediction of the flow, reaction and heat transfer in the combustion chamber of a glass furnace. AIAA 18th Aerospace Sciences Meeting, California, 1980.
- [10]- ABOU ELLAIL, M.M.M., GOSMAN, A.D., LOCKWOOD, F.C. AND MEGAHED, I.E.A., Description and validation of a three-dimensional procedure for combustion chamber flows. J. Energy, AIAA, April 1978. Also Progress in Astronautics and Aeronautics, Turbulent Combustion, Vol. 58, Editor: Lawrence A. Kennedy, Published by AIAA, 1977.
- [11]- TRUHLER, J.S., A mixed grey gas model for flame radiation. AERE Harwell Report n° HL76/3448/KE.

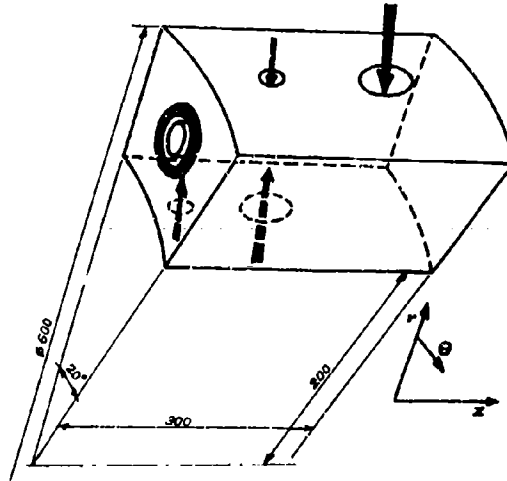
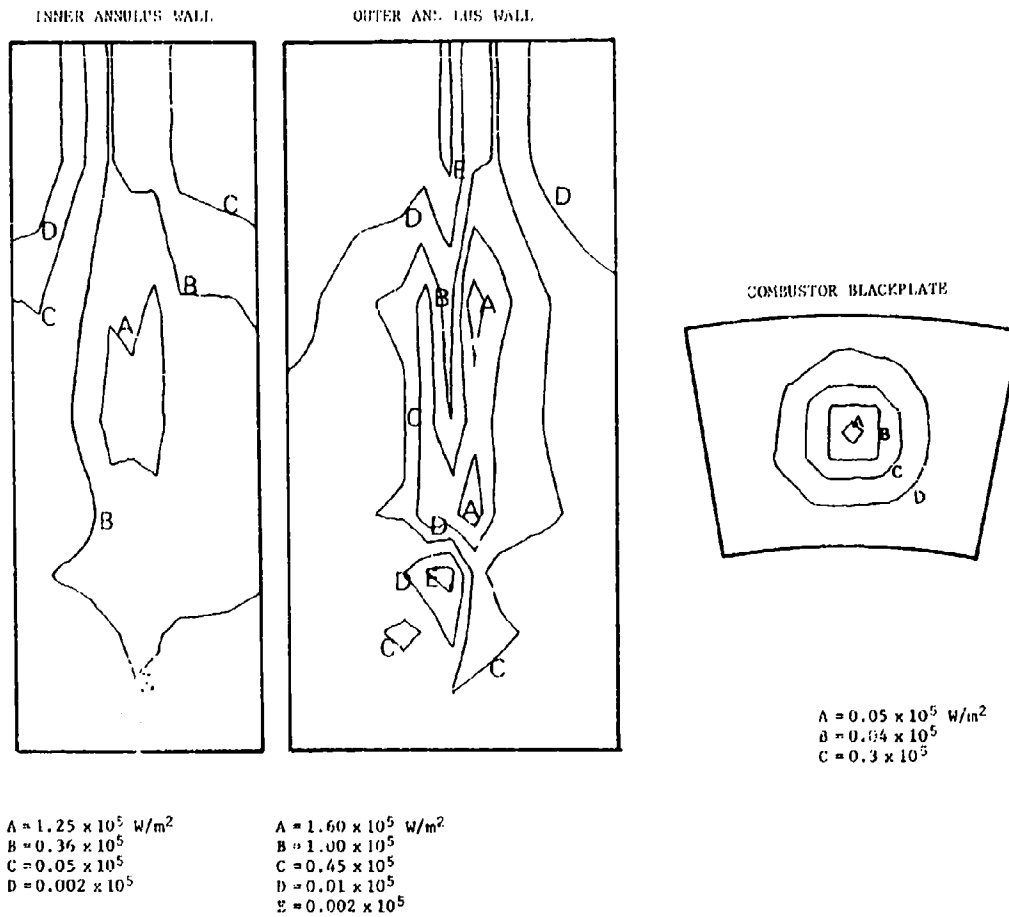


Figure 1 - Annular combustor geometry

Figure 2 - Radiative wall heat fluxes $p = 6 \text{ bar}$.

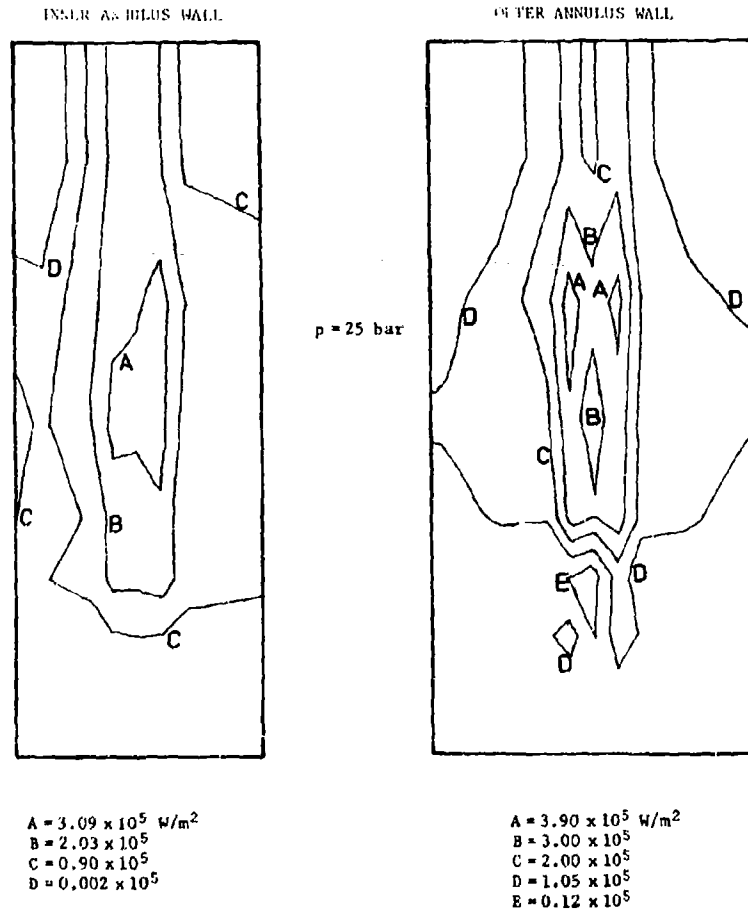


Figure 3 - Radiative wall heat fluxes $p = 25 \text{ bar}$.

DISCUSSION

G.E. Andrews, UK

Your temperatures are calculated without taking dissociation into effect. For temperatures above 2000°K dissociation is significant and your temperature in this region will be too high. The T^4 dependence of radiation magnifies greatly any error in the temperature prediction and would result in an overprediction of the radiative heat flux. Have you any data that indicates that your predicted radiative fluxes are of the correct order of magnitude? Is your predictive technique capable of being extended into the luminous flame region, where the problems of predicting soot concentrations occur?

Author's Reply

The present work did not account for dissociation. For the flow conditions analyzed in the present paper (relatively low ratio m_{air}/m_{fuel}) dissociation may be relevant. Nevertheless for values of m_{air}/m_{fuel} that are commonly used in gas turbines, dissociation is not important.

In some computations we calculated the influence of soot concentration. Some guidance on how this was done is offered by [4]. For the case of $p = 25 \text{ bar}$, the total heat transfer was raised only marginally to 265 KW. So we concluded that, because the non-luminous gas absorptivity is increased so much by the high combustor pressure, the increase of radiation due to the presence of soot is much less than at atmospheric conditions.

PREDICTION OF TRANSIENT TEMPERATURES FOR AN AIR-COOLED ROTATING DISC

C.A. Long and J.M. Owen
Thermo-Fluid Mechanics Research Centre
School of Engineering and Applied Sciences
University of Sussex
Falmer, Brighton, BN1 9QT, England.

SUMMARY

The numerical solution of Fourier's conduction equation has been used to compute the transient temperature distribution in a rotating disc. The convective boundary conditions for the disc surfaces are based on simple formulae obtained from the solutions of the boundary-layer equations, and the computed surface temperatures are compared with measurements made on a rotating-disc rig. Free-disc tests, at rotational Reynolds numbers up to $Re_\phi = 2.5 \times 10^6$, are used to provide a datum from which to judge the numerical method. Although the numerical solution tends to overestimate the cooling rate of the heated free disc at high Reynolds numbers, the agreement between computed and measured temperatures is considered reasonable. Rotating-cavity tests, in which a heated disc is cooled by a radial outflow of air, are used to examine the suitability of the simple convective boundary conditions. As the computed temperatures show reasonable agreement with the measured values, it is suggested that the proposed formulae for convection in a rotating cavity might be useful for design purposes.

LIST OF SYMBOLS

a	inner radius of cavity
b	outer radius of disc or cavity
C	constant
C_p	specific heat at constant pressure
$C_w \equiv Q/vb$	dimensionless volumetric flow rate
$G \equiv s/b$	gap ratio of the cavity
h	heat transfer coefficient
k	thermal conductivity
i	disc half-thickness
n	exponent of power-law surface temperature profile
N	number of time-steps
$Nu \equiv q_s r / k(T_s - T_f)$	local Nusselt number
$Nu_{av} \equiv q_{s,av} b / k(T_s - T_f)_{av}$	average Nusselt number
$Pr \equiv \nu/\alpha$	Prandtl number
q	heat flux
Q	volumetric flow rate
r	radial coordinate
r_i	inner radius of finite difference model
R	recovery factor
$Re_r \equiv Q/2\pi vr$	radial Reynolds number
$Re_\phi \equiv \Omega b^2/\nu$	rotational Reynolds number
$Re_\phi^* \equiv \Omega r^2/\nu$	local rotational Reynolds number
s	axial spacing between discs
t	time
T	temperature
V_ϕ	tangential velocity in the core, relative to stationary axis
$x \equiv r/b$	dimensionless radial coordinate
z	axial coordinate
$\alpha = k/\rho C_p$	thermal diffusivity
Δr	radial step-length
Δt	time step-length
Δz	axial step-length
$\theta \equiv (T_s - T_a) / (T_{s,i} - T_a)$	dimensionless temperature ratio
$\lambda = 0.665 C_w^{-5/8} Re_\phi^{1/2}$	parameter for Ekman-layer flow
ν	kinematic viscosity
ρ	density
Ω	rotational speed

Subscripts

a	pertaining to ambient
av	radially-weighted average
b	pertaining to the back face
d	pertaining to disc
e	pertaining to edge of source region
f	pertaining to the front face
I	pertaining to inlet to cavity
l	laminar flow
max	maximum value
ref	reference value
s	pertaining to disc surface
ss	steady state value
t	turbulent flow

1 INTRODUCTION

A typical arrangement for the internal flow of cooling air in a gas turbine aero-engine is illustrated in Fig.1. The cooling air, which is extracted from the compressor, is used to cool the bearings, turbine discs and blades, and some of it is also used to prevent or reduce the ingress of hot mainstream gas into the 'wheel space' between the rotating discs and adjacent stationary casings. The flow over these discs can be classified into two systems: (i) the rotor-stator system, where the flow occurs in the space between a rotating disc and a stationary casing; (ii) the rotating cavity, where the flow occurs in the annular space between two corotating discs, which are usually joined together by circular shrouds. A review of the flow and heat transfer in such systems is given by Owen [1].

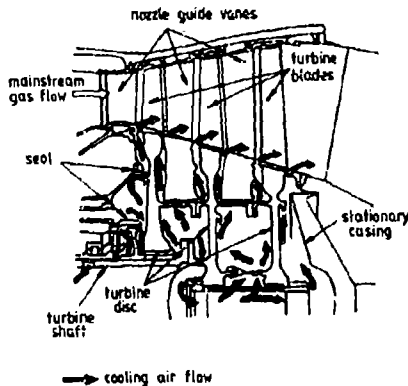


Fig.1 Air-cooled gas-turbine discs

The aero-engine designer needs to calculate the temperature distribution in these highly-stressed rotating discs under transient (during 'take-off' and 'land') conditions as well as under steady-state ('cruise') conditions. Accurate solutions of the thermal conduction equations require a knowledge of the convective (and often the radiative) boundary conditions on the surfaces of the discs. In turn, a knowledge of the convection is usually obtained by empirical methods (for example, tests on experimental rigs) or by theoretical techniques (for example, from the numerical solution of the boundary-layer equations). In this paper, theoretical and empirical equations are used to provide the convective boundary conditions for rotating discs, and the predicted transient temperatures are compared with measurements made on a rotating-disc rig.

The rig and associated instrumentation is described in Section 2, and a brief review of convection in the relevant rotating disc systems is presented in Section 3. The numerical solution of the conduction equation is outlined in Section 4, and a comparison between the predicted and measured temperatures for the cases of flow over a free disc (a disc rotating in a quiescent, infinite environment) and flow in a rotating cavity is presented in Section 5.

2 THE EXPERIMENTAL APPARATUS

Only the salient features of the apparatus are presented here; further details are given by Long [2].

The rig used for the rotating-cavity tests is shown in Fig.2. The rotating cavity was formed from two steel discs, of 762 mm diameter and with an axial spacing of 102 mm, together with a peripheral outer shroud made from paxolin (a fibre-reinforced plastic material). Cooling air was fed into the cavity through a central hole of 76 mm diameter in one of the discs (referred to as the 'upstream disc'), and the air left via holes in the shroud (30 holes of 28.6 mm diameter were arranged at 12-degree angular intervals in the mid-axial position of the shroud). A variety of centrifugal blowers was used, and the maximum flow rate was approximately one kg/s; the air was cooled to about 20°C before it entered the cavity. The flow rate was measured, to an accuracy of approximately 3%, by orifice plates or by other differential-pressure measuring devices. The cavity could be rotated up to 2000 rev/min by a variable-speed electric motor, and the speed was controlled and measured to a precision of ± 1 rev/min.

The 'downstream disc' of the cavity was heated by an equispaced array of thirty, 750-Watt, radiant 'firebar' elements. Each element was arranged in a radial line extending from a radius of $r = 230$ mm to $r = 380$ mm, approximately equal to the outer radius of the cavity. The axial distance between the 'back face' of the downstream disc and the outer surface of the elements was approximately 30 mm. Reflectors were used behind the elements to increase the useful radiative flux, and the back face of the disc was covered with 'solar foil' to increase the absorptivity and to reduce the emissivity of the surface. The electrical input power, which was thyristor-controlled, was

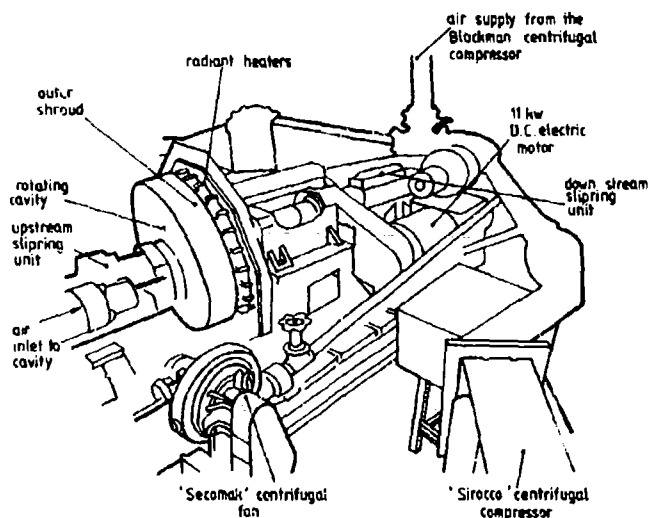


Fig.2 The rotating-cavity rig

Twelve chromel-constantan thermocouples, of 0.13 mm diameter, were embedded on each face of the heated downstream disc, and ten on each face of the unheated upstream disc. The surfaces of each disc were 'divided' into a number of rings of approximately equal area, and a thermocouple was placed at the edge of each ring. The signals from the thermocouples were brought out via two silver slip-ring assemblies (one for each disc). For each assembly, the temperature of the junctions between the silver and the thermocouple wires was measured using a semi-conductor temperature sensor, which was calibrated to an accuracy of 0.1°C. These temperatures were used as the cold-junction reference temperatures for the upstream and downstream discs. The temperature of the cooling air at inlet to the cavity was measured using a stationary chromel-constantan thermocouple probe.

Signals from the thermocouples and temperature sensors, which were measured using a Solartron data-logger controlled by a PDP11/34 minicomputer, could be scanned at a rate of 33 channels/s with a resolution of 1 μ V (which corresponds to 0.015°C for chromel-constantan thermocouples), and the data were stored on magnetic discs and tapes for subsequent analysis. The overall accuracy of the measurement of the surface temperatures of the rotating disc depends on a number of factors, not least of which is the thermal-disturbance error of an embedded thermocouple (see [2]). However, for the tests reported in this paper, the temperatures are believed to be accurate to within $\pm 0.5^\circ\text{C}$.

For the free-disc tests, only the heated downstream disc was used: the upstream disc and shroud were removed. The ambient air temperature was measured using a stationary semi-conductor temperature sensor located in the air on the unheated ('front face') side of the disc. To reduce the heat loss from the disc, its outer radius was surrounded with thermal insulation (with thermal conductivity $k = 0.03 \text{ W/mK}$ and a radial thickness of 15 mm). In all other respects, the apparatus was the same as that used for the rotating-cavity tests. For both the free disc and rotating cavity tests the central hole in the downstream disc was fitted with a perspex plug.

3 CONVECTIVE HEAT TRANSFER IN ROTATING-DISC SYSTEMS

3.1 Dimensionless Groups

A schematic diagram of the flow structure in a rotating cavity with a radial outflow of fluid is shown in Fig.3. The salient dimensionless groups relevant to the flow and heat transfer in the cavity are defined below.

Dimensionless radial coordinate:

$$x = r/b \quad (1)$$

where r is the radial coordinate, measured from the centre of the cavity, and b is the outer radius of the cavity.

Gap ratio:

$$G = s/b \quad (2)$$

where s is the axial spacing between the discs in the cavity.

Rotational Reynolds number:

$$Re_{\phi} \equiv \Omega b^2/\nu \quad (3)$$

where Ω is the rotational speed of the cavity, and ν is the kinematic viscosity of the fluid.

Local rotational Reynolds number:

$$Re_{\phi}^* \equiv \Omega r^2/\nu = x^2 Re_{\phi} \quad (4)$$

Dimensionless flow rate:

$$C_w \equiv Q/\nu b \quad (5)$$

where Q is the volumetric flow rate of the fluid in the cavity.

Radial Reynolds number:

$$Re_r \equiv Q/2\pi r\nu = C_w/2\pi x \quad (6)$$

Prandtl number:

$$Pr \equiv \nu/\alpha \quad (7)$$

where α is the thermal diffusivity of the fluid.

Average Nusselt number:

$$Nu_{av} \equiv q_{s,av} b/k(T_s - T_I)_{av} \quad (8)$$

where q_s is the heat flux from the disc to the fluid, T_s is the surface temperature of the disc, T_I is the fluid temperature at inlet to the cavity, k is the thermal conductivity of the fluid, and the subscript 'av' refers to the radially-weighted average.

Local Nusselt number:

$$Nu \equiv q_s z/k(T_s - T_I) \quad (9)$$

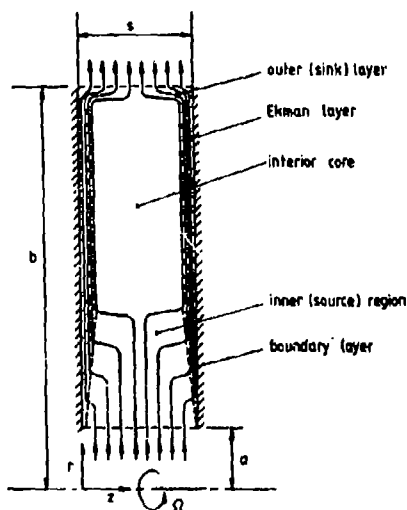


Fig.3 Simplified representation of a rotating cylindrical cavity with a radial outflow from a uniform source to a uniform sink

3.2 The free disc

The heat flux, q , from the disc to the fluid is given by

$$q = h(T_s - T_{ref}) \quad (10)$$

where T_s is the local surface temperature of the disc and T_{ref} is the reference temperature. Owen [3] used the Reynolds analogy to show that

$$T_{ref} = T_a + \frac{1}{2} R \Omega^2 r^2 / C_p \quad (11)$$

where T_a is the ambient temperature of the surrounding fluid, C_p its specific heat at constant pressure, and R is the recovery factor. By comparison with the flow over a flat plate, it is suggested that $R = Pr^{1/3}$ for fluids with moderate Prandtl numbers ($Pr = O(1)$).

Dorfman [4] obtained theoretical expressions for the Nusselt numbers for a free disc with a 'power-law temperature profile' (that is, $(T_s - T_{ref}) = x^n$, n being a constant). For laminar flow ($Re_\phi^* < 2 \times 10^5$)

$$Nu = 0.308 (n + 2)^{0.5} Pr^{0.5} Re_\phi^{*0.5} \quad (12)$$

For turbulent flow ($Re_\phi^* > 2 \times 10^5$)

$$Nu = 0.0197 (n + 2.6)^{0.2} Pr^{0.6} Re_\phi^{*0.8} \quad (13)$$

These expressions are consistent with the results of many experiments (for example, Cobb and Saunders [5], Owen, Haynes and Bayley [6], Long [2]), and are used, where appropriate, in Section 4 below.

3.3 The rotating cavity with a radial outflow of fluid

Using apparatus similar to that described in Section 2 above, heat transfer measurements in a rotating cavity were made by Owen and Bilimoria [7] and by Owen and Onur [8]. The average Nusselt numbers for the heated disc were correlated for three forced-convection regimes:

$$\text{Regime I: } Nu_{av} = 1.94 C_w^{2/3} G^{1/6} \quad (14)$$

$$\text{Regime II: } Nu_{av} = 0.07 C_w^{1/3} Re_\phi^{1/2} \quad (15)$$

$$\text{Regime III: } Nu_{av} = 4.11 C_w^{1/2} Re_\phi^{1/9} G^{1/9} \quad (16)$$

The results were obtained for $0.13 < G < 0.4$, $2800 < C_w < 28000$, $2.3 \times 10^4 < Re_\phi < 2.5 \times 10^6$, and the boundaries between the regimes can be found by the intercepts of the three equations. In particular, regime I occurs at relatively high flow rates or low rotational Reynolds numbers where the flow (which, in the experiments, entered the cavity axially through the centre of the upstream disc and impinged on the heated downstream disc) forms a wall jet on the downstream disc. Under these conditions, rotation has no significant effect, and the results are similar to those for a single round jet impinging on a stationary plate (see Martin [9]).

The heat transfer in a rotating cavity with a radial outflow is best understood by first considering the fluid dynamics. Referring to Fig.3, it can be seen that the flow structure consists of four regions: (i) a source region; (ii) a sink layer; (iii) Ekman layers; and (iv) an interior core. In the source region, the flow (which is shown originating from a uniform radial source in Fig.3) is distributed into the two Ekman layers; in the sink layer, the flow from the Ekman layers is fed into the sink (which is shown in Fig.3 as a central slot in the shroud). The Ekman layers are boundary layers in which linear Coriolis forces dominate over nonlinear inertial and centrifugal forces; in the interior core, the radial and axial components of velocity either are zero (for isothermal flow) or are weak (for nonisothermal flow). In a rotating coordinate system, if the nonlinear inertial and centrifugal terms are neglected the resulting Ekman-layer equations are linear.

Isothermal source-sink flow in a rotating cavity has been studied by Chew, Owen and Pincombe [10] and by Owen, Pincombe and Rogers [11]. From solutions of the (linear and nonlinear) integral momentum equations for the Ekman layers on the rotating discs, the latter authors were able to predict the radial variation of the tangential component of velocity, V_ϕ , in the central core and the radial extent of the source region for both laminar and turbulent flow. They suggested that transition from laminar to turbulent flow in the Ekman layers occurred at $Re_\phi = 180$, and the theoretical predictions of V_ϕ were in good agreement with measured values for $G = 0.133$ and 0.267 , $a/b = 0.1$, $170 < C_w < 1800$ and $2.9 \times 10^4 < Re_\phi < 8 \times 10^5$.

Inside the source region, the boundary layer on each rotating disc behaves like that on a free disc. In particular the entrainment rate is similar to that of a free disc. Hence, the radial extent of the source region can be estimated by determining the radius at which all the flow entering at the source is entrained into the boundary layers on the rotating discs. It therefore follows that

$$x_{l,e} = C_L C_w^{1/2} Re_\phi^{-1/4} \quad (17)$$

and

$$x_{t,e} = C_t C_w^{5/13} Re_\phi^{-4/13} \quad (18)$$

where $x_{l,e}$ and $x_{t,e}$ are the values of x at the edge of the source region for laminar and turbulent flow, respectively. The constants C_L and C_t depend on whether the flow enters the cavity radially as a uniform source or axially as a wall jet on the downstream disc. For both discs with a radial inlet, and for the upstream disc with an axial inlet, $C_L = 0.424$ and $C_t = 1.37$; for the downstream disc with an axial inlet, $C_L = 0.559$ and $C_t = 1.79$.

Northrop and Owen [12] obtained solutions of the integral energy equation for turbulent Ekman-layer flow in a rotating cavity. They assumed that (linear) Ekman layers extended over the entire surface of the discs (that is, the sizes of the source region and sink regions were negligible); they also neglected buoyancy effects and assumed that both discs in the cavity were heated to the same temperature. For the case of $(T_s - T_f) = x^{13/8}$ (which is appropriate for the results discussed below), their solution is

$$\text{Nu} = 1.625 \frac{C_w \text{Pr}}{4\pi x} (1 - \exp(-\lambda x^{13/8})) \quad (19)$$

where

$$\lambda = 0.665 C_w^{-5/8} \text{Re}_\phi^{1/2} \quad (20)$$

Long [2] used transient-analysis techniques, which are outlined in Section 4, to determine average and local Nusselt numbers for both the free disc and the rotating cavity. For the case of a rotating cavity with a radial outflow and axial inlet of coolant, flow visualization confirmed that eqns (17) and (18) were valid for estimating $x_{t,e}$ and $x_{t,a}$. It is clear, from eqn (18) with $C_t = 1.79$, that turbulent Ekman-layer flow can only occur on the downstream disc if

$$\text{Re}_\phi > 6.63 C_w^{5/4} \quad (21)$$

and, for smaller Reynolds numbers, Long noted that the local Nusselt numbers were virtually independent of rotational speed. For this so-called 'wall-jet regime', he proposed the empirical correlation (based on eqn (14))

$$\text{Nu} = 1.46 C_w^{2/3} c^{1/6} \quad (22)$$

For larger Reynolds numbers, Ekman layers occur on the outer part of the disc, and eqn (19) was found to provide a reasonable approximation of the Nusselt numbers for $x > x_{t,e}$. For $x < x_{t,e}$ in the source region, the flow in the boundary layer on the discs can, as stated above, behave like that on a free disc; Long observed that the local Nusselt number in this region could be approximated by eqn (13) (or by eqn (12) for $\text{Re}_\phi^* < 2 \times 10^5$).

In Section 4, the Nusselt numbers given by eqns (12), (13), (19) and (22) are used to provide the appropriate boundary conditions for the heated disc in the rotating cavity. It should be pointed out, however, that work on the solution of the nonlinear momentum integral equations and the energy integral equation is well advanced (see Rogers [13]). These 'nonlinear solutions' provide more accurate predictions of the Nusselt numbers than those given by the 'linear solutions', and they are likely to provide better predictions of disc temperature than those presented in Section 5.

4 THE NUMERICAL METHOD

A schematic diagram of the heated disc is shown in Fig.4. The front face forms either the inner face of the cavity (for the rotating-cavity tests) or the unheated face of the free disc (for the free-disc tests). An outline of the solution of Fourier's equation, for transient conduction in the disc, and the boundary conditions used, are presented below; further details are given by Long [2].

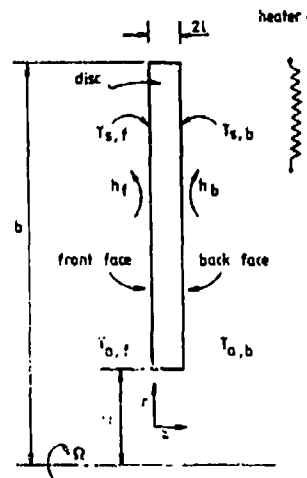


Fig.4 Schematic diagram of the heated disc

4.1 Transient conduction inside the disc

Fourier's equation for the transient, axisymmetric conduction of heat can be expressed in cylindrical-polar coordinates as

$$\frac{1}{r} \frac{\partial}{\partial r} \left(r \frac{\partial T}{\partial r} \right) + \frac{\partial^2 T}{\partial z^2} = \frac{1}{\alpha_d} \frac{\partial T}{\partial t} \quad (23)$$

where T is the temperature at time t at a radial distance r from the centre and an axial distance z from the front face. The thermal diffusivity, α_d (the subscript 'd' is used throughout to distinguish the properties of the disc from those of the air, which are not given a subscript), is defined as

$$\alpha_d = k_d / \rho_d C_{pd} \quad (24)$$

where the density, ρ_d , specific heat, C_{pd} , and thermal conductivity, k_d , are assumed to be constant. For the steel disc used in the tests, $\rho_d = 7880 \text{ kg/m}^3$, $C_{pd} = 502 \text{ J/kgK}$ and $k_d = 16.8 \text{ W/mK}$.

The finite-difference equations were formed using the Crank-Nicolson method. The disc was divided into 21 radial grids, with a step-length of $\Delta r = 15 \text{ mm}$, and 7 axial grids, with a step-length of $\Delta z = 2.12 \text{ mm}$, and the time step-length, Δt , was typically $2s < \Delta t < 8s$. The resulting finite-difference equations were solved using Gaussian elimination, and 'numerical experiments' with finer meshes showed that truncation errors were acceptably small (and insignificant compared with the uncertainty in the experimental data).

If the precise variation of temperature with time is known for all surfaces of the disc, then the heat transfer coefficients on the front and back faces can be determined from the numerical solution of eqn (23); h being calculated from eqn (10), where the surface heat flux q is evaluated from the numerical differentiation of the computed temperature distribution inside the disc. This so-called 'inverse solution' of Fourier's equation is error-prone: Owen [14] has shown that small uncertainties in the measured surface temperature can result in large errors in the computed values of h . Long [2], who used the inverse solution to determine the heat transfer coefficients for both free disc and rotating cavity tests, has shown that the resulting errors can be significantly reduced by determining h during cooling tests (where the heaters are turned off, and the disc temperature reduces with time). He used smoothing techniques, in both space and time, to minimize errors in measured temperatures, and was able to obtain good agreement between the heat transfer coefficients obtained from his free-disc measurements and those given by available theory.

In this paper, solution of the 'direct problem' is discussed: assumed values of h (based on the expressions given in Section 3) are used as boundary conditions on the front and back faces of the disc. The temperature distribution on the front face is computed, from the numerical solution of eqn (23), and is compared with measured temperatures. The boundary conditions that were used are discussed below.

4.2 Boundary conditions on the disc

4.2.1 The back face ($z = 2t$)

In this paper, only cooling tests are considered, and so the radiant flux from the heaters (shown in Fig.4) to the back face of the disc is not modelled. However, Long [2] has also considered quasi-steady-state tests, where the heater flux is modelled, and the reader is referred to this work for further details.

The convective heat transfer coefficient for the back face was calculated from eqns (12) and (13); for air, $Pr = 0.72$, and for the temperature profile on the disc it was assumed that $n = 2$ (a value that was shown, from earlier experiments, to be a reasonable approximation). It was found that the air temperature, T_a , between the heater and the back face could be between 5°C and 25°C above the ambient air temperature in the laboratory. The precise value of T_a was difficult to determine, but, for the computations carried out in this paper, it was assumed to be 15°C above the measured ambient temperature. This value was used in eqn (11) to calculate the reference temperature for eqn (10).

4.2.2 The front face ($z = 0$)

For the free-disc tests, the convective heat transfer coefficient for the front face was calculated from eqns (12) and (13) with $Pr = 0.72$ and $n = 2$. The air temperature, T_a , used in eqn (11), was taken as the measured ambient air temperature in the laboratory.

For the rotating-cavity tests, turbulent Ekman-layer flow occurs when $Re_\tau > 180$ and $Re_\tau > 6.63 C_w^{5/4}$. Under these conditions, the heat transfer coefficients in the source region ($x < x_{t,e}$) are obtained from eqns (12) and (13), with $Pr = 0.72$ and $n = 2$, for $Re_\tau^* < 2 \times 10^5$ and $Re_\tau^* > 2 \times 10^5$, respectively. In the Ekman layers ($x > x_{t,e}$), the heat transfer coefficients are obtained from eqn (19). When $Re_\tau < 6.63 C_w^{5/4}$, Ekman-layer flow does not occur, and eqn (22) is used to specify the heat transfer coefficients for the entire front face. For all these tests, the reference temperature was taken as the cooling air temperature measured at inlet to the cavity. The convective flux was at least an order of magnitude greater than the radiant flux from the disc, so the effect of radiation has been ignored in this paper.

4.2.3 The outer edge ($r = b$)

For the free-disc tests, the outer edge of the disc was thermally insulated. For this

case, the boundary condition was taken to be

$$\left(\frac{\partial T}{\partial r}\right)_{r=b} = 0 \quad (25)$$

For the rotating-cavity tests, it was not practicable to insulate the outer edge. The boundary condition used for these tests was the 'quasi-one-dimensional assumption' that

$$\frac{\partial}{\partial r} \left(r \frac{\partial T}{\partial r} \right)_{r=b} = 0 \quad (26)$$

or, from eqn (23),

$$\left(\frac{\partial^2 T}{\partial z^2}\right)_{r=b} = \frac{1}{\alpha_d} \left(\frac{\partial T}{\partial t}\right)_{r=b} \quad (27)$$

Long [2] used eqn (27) as the boundary condition for the 'inverse solution' of Fourier's equation (from which the 'measured' Nusselt numbers in the rotating cavity were determined). He also experimented with other boundary conditions, and showed that their influence on the solution of Fourier's equation was only significant for $0.85 < r < 1$. In the absence of any other evidence, it seems reasonable to use eqn (27) as the boundary condition for the 'direct solution' of Fourier's equation.

4.2.4 The inner edge ($r = r_i$)

Again, in the absence of other evidence, the 'quasi-one-dimensional assumption' was used such that

$$\left(\frac{\partial^2 T}{\partial z^2}\right)_{r=r_i} = \frac{1}{\alpha_d} \left(\frac{\partial T}{\partial t}\right)_{r=r_i} \quad (28)$$

If this boundary condition is incorrect, the resulting errors in the predicted temperatures should only be significant at small radii.

4.2.5 The initial condition ($t = 0$)

As discussed by Long [2], numerical tests were conducted where the initial temperature distribution was obtained from either the solution of Laplace's equation (that is, eqn (23) with $\partial T/\partial t = 0$), or from linear axial interpolation of the measured surface temperatures. The two techniques show very little difference (less than 0.1%) in the calculated Nusselt numbers or temperatures after the fifth time-step, and so for simplicity, and to reduce program size, the axial interpolation method was used.

5 COMPARISON BETWEEN THE COMPUTED AND MEASURED TEMPERATURES

At this stage, it is convenient to recapitulate. The temperature distribution on the front face of the heated disc is computed from the 'direct solution' of Fourier's equation. The boundary conditions on all four faces of the disc are assumed; they are not measured. In particular, the boundary conditions for the front and back faces of the disc involve assumptions about the convective heat transfer coefficients; the boundary conditions for the inner and outer radii involve quasi-one-dimensional assumptions.

As the flow structure in the rotating cavity is more complicated than the flow over the free disc, it is more convenient to use the latter as a datum from which to judge the numerical method: this is discussed in Section 5.1. If the numerical method is found to be satisfactory for the free disc, a comparison between the computed and measured temperatures for the rotating cavity should produce evidence from which to draw conclusions about the suitability of the simple convective formulae presented in Section 3: this is discussed in Section 5.2.

5.1 The free disc

Figs 5, 6 and 7 show the comparison between the predicted and measured temperatures on the front (unheated) face of the free disc for $Re_d/10^6 = 0.16, 0.40, \text{ and } 2.5$, respectively. In each of these (and subsequent) figures, graphs (a) and (b) show the respective radial variations of the local Nusselt number and the dimensionless temperature. The latter is defined by

$$\theta = (T_B - T_A)/(T_{SS} - T_A) \quad (29)$$

where T_B is the local temperature on the front face at time t , T_{SS} is the maximum 'steady state' temperature on the front face, which was measured before switching off the heaters, and T_A is the ambient air temperature. For the tests discussed below, $T_{SS} = 100^\circ\text{C}$ and $T_A = 20^\circ\text{C}$.

The experiments were conducted by heating the disc until it reached an approximately steady temperature, and then (at time $t = 0$) the heaters were turned off and the disc was allowed to cool. The measured values for Nu and θ are shown in the figures for $N = 1, 10, 30, 50, 70$ and 90 , where N is the number of finite-difference time steps in the solution of Fourier's equation. The actual time can be calculated from

$$t = N\Delta t \quad (30)$$

where Δt is the numerical time-step specified on the figure legend.

For the Nusselt numbers, the dashed line represents the variation of Nu (calculated as described in Section 4.2) used as the boundary condition for the front face of the disc, and that for the back face is shown by the dotted line. The symbols represent the front face values measured by Long [2]; these values, which were not used in the computation procedure, provide a comparison between the 'experimental' and 'theoretical' values of Nu .

For the temperature variation, the solid lines represent the computed radial variation of θ at each time step. The symbols represent the measured temperatures on the front face at each time step; their radial locations correspond to the positions of the thermocouples on the disc.

Referring to Fig. 5a, for $Re_d = 1.6 \times 10^5$ the flow should be laminar over the entire surface of the disc; the approximate agreement between the theoretical laminar Nusselt number (eqn (12)) and the measured values supports this contention. It can also be seen from Fig. 5b that the agreement between the measured and computed values of θ is good even for $N = 90$ ($t = 711s$).

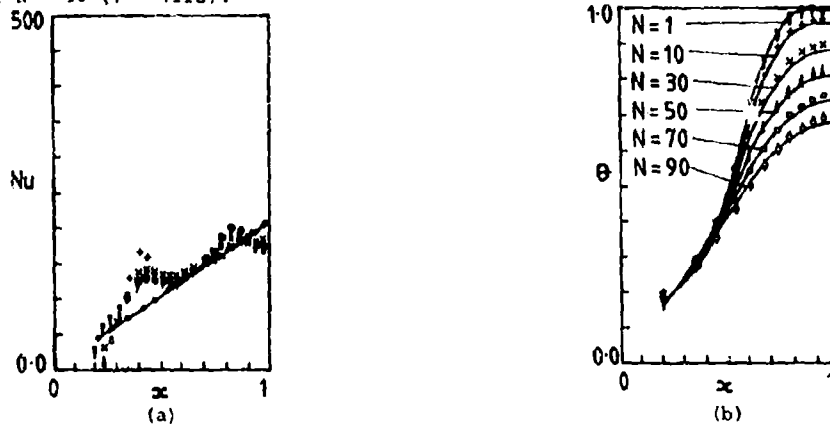


Fig.5 Results for the free disc: $Re_d = 1.6 \times 10^5$, $\Delta t = 7.9s$

(a) local Nusselt numbers; (b) predicted and measured temperatures

----- correlated Nusselt numbers for the front face
 -----•----- correlated Nusselt numbers for the back face
 ----- predicted temperatures for the front face

Measured values for the front face

	∇	+	x	Δ	\square	\diamond
N (eqn (30))	1	10	30	50	70	90

For Fig. 6, with $Re_d = 4 \times 10^5$, transition from laminar to turbulent flow is assumed to occur at $x = 0.707$ (where $Re_d^* = 2 \times 10^5$). The theoretical Nusselt number, which is used for the boundary conditions, assumes a step-change from the laminar value, given by eqn (12), to the turbulent value, given by eqn (13). Not surprisingly, the measured values do not exhibit such a discontinuity, and there is experimental evidence of a more gradual transition for $0.7 < x < 0.8$.

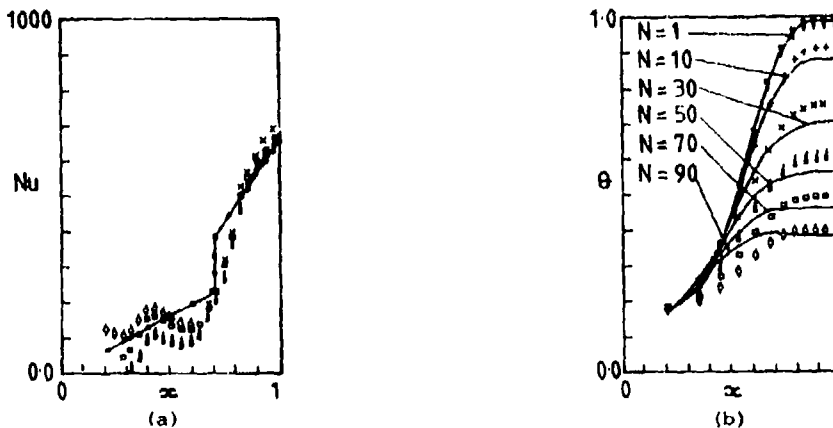


Fig.6 Results for the free disc: $Re_d = 4 \times 10^5$, $\Delta t = 7.7s$
 Symbols as for Fig.5.

Considering the difference in Nusselt numbers, the agreement between the measured and computed values of θ appears to be reasonable. Additional computations of θ were made, using the measured values of Nu as boundary condition, and these results (which are not shown in Fig. 6b) were not significantly better than those obtained using the theoretical values of Nu. The errors in the computed values of θ cannot, therefore, be attributed to the differences between the measured and theoretical Nusselt numbers. One possible explanation for the errors is that the reference temperature used for the back face was incorrect (see Section 4.2.1). Another reason is that the electric heaters still radiated heat as they cooled down; this 'residual radiation', which is unaccounted for in the numerical model, would reduce the cooling rate of the outer part of the disc.

Fig. 7 shows the results for $Re_d = 2.5 \times 10^6$, where transition from laminar to turbulent flow is assumed to occur at $x = 0.283$. The good agreement, except near the outer part of the disc, between the measured and theoretical Nusselt number (calculated from eqn (13)) suggests that the flow is indeed turbulent over most of the disc surface.

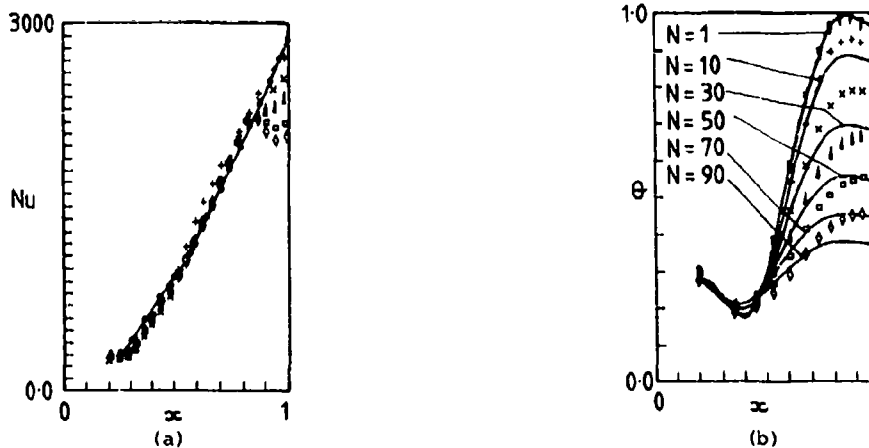


Fig.7 Results for the free disc: $Re_d = 2.5 \times 10^6$, $\Delta t = 2.1s$
Symbols as for Fig.5.

Referring to Fig.7b, the agreement between the measured and computed values of θ at this comparatively high value of Re_d is not as good as that for the lower Reynolds numbers. As Nu increases with increasing Re_d , the disc cools off faster at the higher speeds, whereas the decay of 'residual radiation' from the heaters is unlikely to be significantly affected by Re_d . Consequently, the 'residual radiation' effect should be significant for a larger proportion of the test time at high Re_d . This could explain why, for the larger values of x in Fig.7, the measured cooling rates are smaller than the computed values.

Another point to note in Fig.7b is that a minimum value of θ occurs at $x = 0.4$; for $x < 0.4$, the measured and computed values of θ vary little with time. This effect is attributed to heat transfer from the shaft bearing, adjacent to the back face of the disc, into the disc itself; the heat transfer is likely to be more significant at high speeds than at low speeds. The fact that the predicted values of θ are in good agreement with the measured values at these small radii gives ground for confidence in the use of eqn (28) for the boundary condition at the inner radius.

Having used the free disc as a datum from which to judge the numerical method, it is convenient to turn to the rotating cavity.

5.2 The rotating cavity

Figs 8 to 11 show the comparison between the computed and measured temperatures on the front face of the heated disc for a number of rotational speeds and coolant flow rates; all tests were conducted with a gap ratio of $G = 0.267$. The experiments were carried out in a similar way to that described for the free disc, and the symbols are defined in Section 5.1. The boundary conditions used for the computations presented below were the same as those used for the free disc with the exception that (for Figs 8, 9 and 10) Nusselt numbers appropriate for the rotating cavity (see Section 4.2.2) were used for the front face; these Nusselt numbers (together with values measured for the front face of the heated disc in the rotating cavity by Long [2]) are shown in the figures. To demonstrate the sensitivity of the computation of θ to the boundary conditions assumed for the front face, free-disc boundary conditions were used for both faces of the disc in the computations shown in Fig.11.

Referring to Fig.8, (where $Re_d = 1.6 \times 10^5$ and $C_w = 14000$), $Re_d < 6.63 C_w^{5/4}$ and so, according to the criterion given in Section 3.3, Ekman-layer flow does not occur in the rotating cavity. For this 'wall-jet regime', eqn (22) is used to provide the assumed boundary condition for the front face of the heated disc. Despite the fact that, as Fig. 8a shows, there are significant differences between the measured and assumed values of Nu for the front face, Fig. 8b illustrates that there is reasonable agreement between the

measured and computed values of θ . Other computations (not presented here) have also shown that eqn (22) produces reasonable predictions of θ in the 'wall-jet regime'.

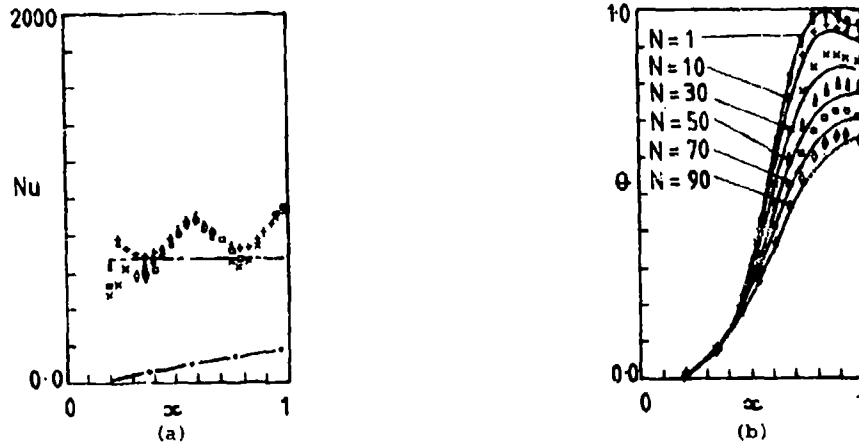


Fig.8. Results for the rotating cavity with radial outflow: $Re_d = 1.6 \times 10^5$, $C_w = 14000$, $\Delta t = 3.9s$

(a) local Nusselt numbers; (b) predicted and measured temperatures

— correlated Nusselt numbers for the front face
 —•— correlated Nusselt numbers for the back face
 — predicted temperatures for the front face

Measured values for the front face	▽	+	x	△	□	◇
N (eqn (30))	1	10	30	50	70	90

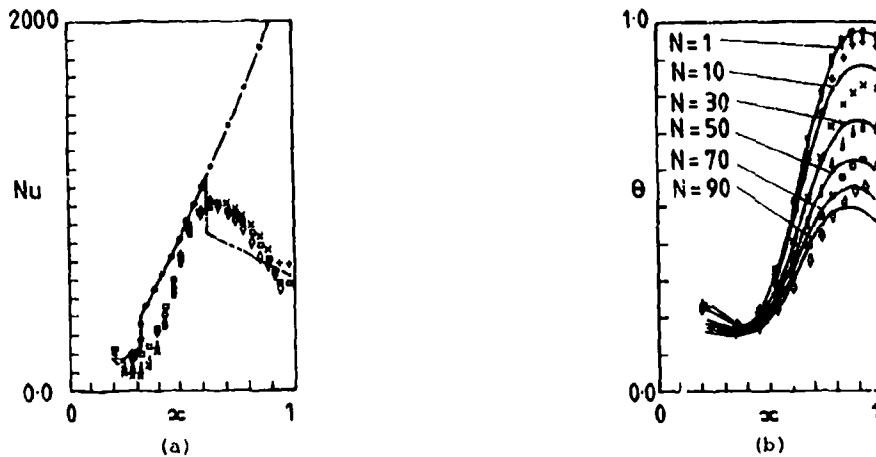


Fig.9 Results for the rotating cavity with radial outflow: $Re_d = 2 \times 10^6$, $C_w = 7000$, $\Delta t = 3.9s$
 Symbols as for Fig.8

In Fig.9, (where $Re_d = 2 \times 10^6$ and $C_w = 7000$), eqn (18) (with $C_t = 1.79$) implies that Ekman-layer flow should occur for $x > 0.65$, and eqn (19) is used to calculate Nu for the front face of the heated disc in this region. In the source region, laminar and turbulent free-disc flow is assumed to occur for $x < 0.32$ and $0.32 < x < 0.65$, respectively; eqns (12) and (13), respectively, are used to calculate the laminar and turbulent Nusselt numbers. It can be seen from Fig.9a that these three equations provide only a rough approximation to the measured values: the latter do not exhibit discontinuities. However, although Fig.9b shows that the computed values of θ tend to overestimate the measured cooling rate, the errors are not significantly worse than those shown in Fig.7 for the free disc at $Re_d = 2.5 \times 10^6$. As explained in Section 5.1, the overestimate in the cooling rate is attributed largely to residual radiation from the heaters to the back face of the disc and uncertainty in the back-face air temperature; even if the assumed front-face Nusselt numbers were correct, the computed values of θ would still be in error.

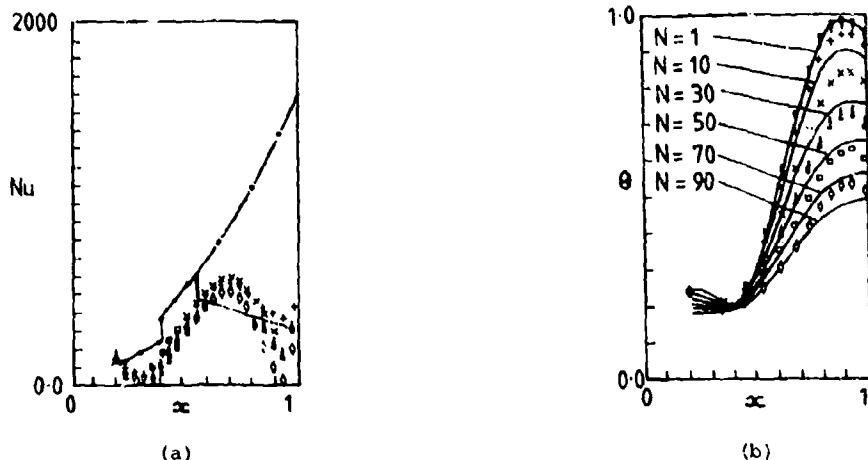


Fig.10 Results for the rotating cavity with radial outflow: $Re_\phi = 1.2 \times 10^6$,
 $C_w = 3500$, $\Delta t = 3.9s$
 Symbols as for Fig.8

In Fig. 10, (where $Re_\phi = 1.2 \times 10^6$ and $C_w = 3500$), Ekman-layer flow is assumed to occur in the rotating cavity for $x > 0.56$; laminar and turbulent free-disc flow is assumed to take place in the source region for $x < 0.41$ and $0.41 < x < 0.56$, respectively. Again, as shown in Fig.10a, these three equations provide only a rough approximation to the measured Nusselt numbers; but the computed values of θ presented in Fig.10b are in reasonable agreement with the measurements.

The preceding three figures could create the impression that large errors in the front-face boundary condition have little effect on the accuracy of the computed temperature: Fig.11 is intended to disabuse the sceptic. The values of Re_ϕ and C_w in this figure are the same as those in Fig.10; the difference is that, in Fig.11, free disc boundary conditions (eqns (12) and (13)) are used for the front face as well as for the back face of the disc. Fig. 11a shows that these boundary conditions produce Nusselt numbers significantly greater than the measured values for the rotating cavity. As a consequence, the errors between the measured and computed values of θ are much larger in Fig. 11b than they are in Fig.10b. For example, referring to eqn (29), with $T_{ss} = 100^\circ C$ and $T_a = 20^\circ C$, the maximum difference between the measured and computed values of T_s at $N = 90$ ($t = 351s$) is less than $5^\circ C$ in Fig.10b and approximately $20^\circ C$ in Fig.11b.

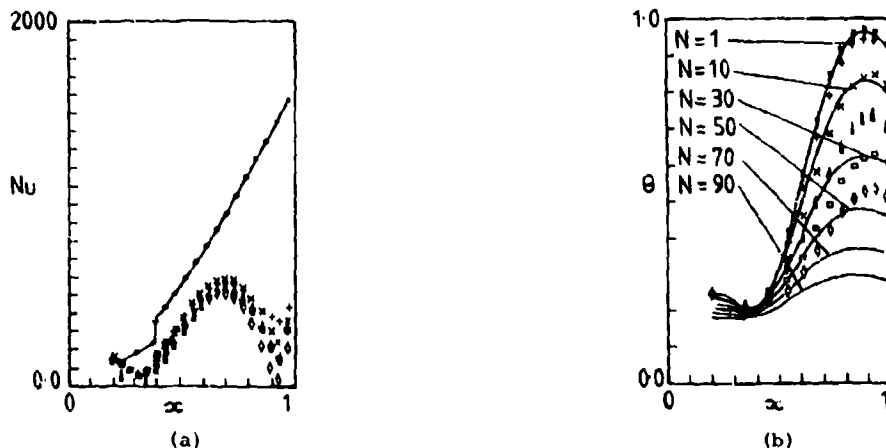


Fig.11 Results for the rotating cavity with radial outflow, using the free disc correlation for both faces: $Re_\phi = 1.2 \times 10^6$, $C_w = 3500$, $\Delta t = 3.9s$
 Symbols as for Fig.8

Despite experimental uncertainties and differences between the measured and the assumed Nusselt numbers, it would appear that the simple convective formulae presented in Section 3 could be used for design purposes to predict the transient temperature distribution in the heated disc in a rotating cavity. No claims are made that these formulae would produce acceptable results if used to predict the temperature distribution of a geometrically-complicated gas turbine disc operating at higher rotational Reynolds numbers, and under more extreme conditions, than those discussed in this paper. However, as stated in Section 3, work on the nonlinear boundary-layer equations is well advanced: solutions of these equations are expected to produce better predictions and have greater generality than those obtained from the linear equations on which the simple formulae were based.

In addition, heat transfer results have also been obtained from instrumented compressor discs at engine conditions (see Chew [15] and Long and Owen [16]). At these conditions, the measured temperatures are often 'noisy', and the computed heat fluxes are subject to large errors. It is therefore not always possible to compare the heat transfer results obtained from engines with those obtained in the laboratory. However, the validity of future experimental and theoretical correlations could be tested, under engine conditions, by extending the model discussed in this paper to predict the temperatures in an instrumented turbine disc.

6 CONCLUSIONS

Temperatures computed from the numerical solution of Fourier's equation have been compared with transient measurements made in a rotating-disc rig. The experiments were conducted for a heated free disc and for a heated disc in a rotating cavity with a radial outflow of cooling air. In both cases, the disc was heated to approximately 100°C, and then the heaters were turned off and the surface temperature of the disc was measured as it cooled down. For the computations, convective boundary conditions were assumed for the back (heated) face and for the front (cooled) face of the disc.

For the free-disc tests, the Nusselt numbers for both faces were based on accepted theoretically-derived formulae for laminar and turbulent flow over a free disc. For the lowest rotational speed ($Re_\delta = 1.6 \times 10^5$), the computed temperatures were in good agreement with the measured values. For the higher speeds ($Re_\delta = 4 \times 10^5$ and 2.5×10^6), the computations overestimated the cooling rate. This overestimate was attributed mainly to uncertainties in the air temperature adjacent to the back face and to 'residual radiation' from the heaters after they were turned off.

For the rotating-cavity tests, the assumed Nusselt numbers for the front face of the heated disc depended on the coolant flow rate and the rotational speed. At relatively high flow rates, where Ekman-layer flow was not expected to occur, an empirical 'wall-jet' correlation was used. At relatively high rotational speeds, where Ekman-layer flow should occur, a theoretically-derived formula was used to calculate the Nusselt numbers for the Ekman-layers in the outer part of the cavity, and the free-disc Nusselt numbers were used for the source region in the inner part of the cavity. In all the tests, the free-disc Nusselt numbers were used for the back face of the disc. Computed temperatures, obtained using these Nusselt numbers to provide boundary conditions, were in reasonable agreement with measured values for a range of rotational speeds and flow rates. It was concluded that the simple formulae, from which the Nusselt numbers had been determined, could be used for design purposes to predict the transient temperature distribution in the heated disc of a rotating cavity. However, care would be necessary if the formulae were used for gas-turbine applications.

7 REFERENCES

- [1] Owen, J.M. Fluid flow and heat transfer in rotating disc systems. XIV ICHMT Symposium on Heat and Mass Transfer in Rotating Machinery, Dubrovnik, 1982.
- [2] Long, C.A. Transient heat transfer in a rotating cylindrical cavity. 1984. D.Phil thesis, University of Sussex, England.
- [3] Owen, J.M. The Reynolds analogy applied to flow between a rotating and a stationary disc. *Int. J. Heat Mass Transfer*, 14, 1971, p.451.
- [4] Dorfman, L.A. Hydrodynamic resistance and the heat loss of rotating solids. Oliver and Boyd, Edinburgh, 1963.
- [5] Cobb, E.C. and Saunders, O.A. Heat transfer from a rotating disk. *Proc. R.Soc. Lond. A*, 236, 1956, p.343.
- [6] Owen, J.M., Haynes, C.M. and Bayley, F.J. Heat transfer from an air-cooled rotating disk. *Proc. R. Soc. Lond. A*, 336, 1974, p.453.
- [7] Owen, J.M. and Bilimoria, E.D. Heat transfer in rotating cylindrical cavities. *J. Mech. Eng.Sci.* 19, 1977, p.175.
- [8] Owen, J.M. and Onur, H.S. Convective heat transfer in a rotating cylindrical cavity. *J. Eng. Power*, 105, 1983, p.265.
- [9] Martin, H. Heat and mass transfer between impinging gas jets and solid surfaces. *Adv. in Heat Tran.*, 13, 1977, p.1.
- [10] Chew, J.W., Owen, J.M. and Pincombe, J.R. Numerical predictions for laminar source-sink flow in a rotating cylindrical cavity. *J. Fluid Mech.* 143, 1984, p.451.
- [11] Owen, J.M., Pincombe, J.R. and Rogers, R.H. Source-sink flows inside a rotating cylindrical cavity. *J. Fluid Mech.* To be published in 1985.
- [12] Northrop, A. and Owen, J.M. Heat transfer measurements in the modified Mark II rotating cavity rig. Part II: Rotating cavity tests. 1983. Report No. 83/TMRC/59, School of Engineering and Applied Sciences, University of Sussex, England.

- [13] Rogers, R.H. Computation of heat transfer in a rotating cavity with a radial outflow of coolant. Part I: The symmetrically-heated cavity. 1985. Report No. 85/TFMRC/71, School of Engineering and Applied Sciences, University of Sussex, England.
- [14] Owen, J.M. On the computation of heat transfer coefficients from imperfect temperature measurements. *J. Mech. Eng. Sci.*, 21, 1979, p.323.
- [15] Chew, J.W. Heat transfer calculations from temperature measurements on a gas turbine compressor disc. 1982. Report. No. 82/TFMRC/49, School of Engineering and Applied Sciences, University of Sussex, England.
- [16] Long, C.A. and Owen, J.M. Transient analysis of temperature measurements on compressor discs of the RB199 engine. 1984. Report No. 84/TFMRC/66, School of Engineering and Applied Sciences, University of Sussex, England.

ACKNOWLEDGEMENTS

The authors wish to thank Motoren-und Turbinen-Union, Rolls Royce Limited, and the Science and Engineering Research Council for supporting the research reported in this paper.

DISCUSSION

D.E. Metzger, US

In some of the Nusselt number distributions presented in the paper, NU goes to zero and perhaps even negative at the outer radius. Can you give some explanation for this behaviour?

Author's Reply

The reference temperature used in the definition of the Nusselt number is T_c , the temperature of the air entering the cavity. As the Ekman layers on the discs do not entrain fluid (although there may be some mass exchange between the Ekman layer on the hot disc and that on the cold disc), there may be a point on the disc where the temperature of the fluid reaches that of the disc itself. If, as happens in our experiments, the disc temperature decreases with increasing radius at the outer part of the disc, then the heat will flow from the 'cooling' fluid to the hot disc: under these conditions, the Nusselt numbers become negative. Such negative Nusselt numbers have been measured, and predicted, at the University of Sussex.

J. Fabri, Fr

Did you try out your correlation on less simple geometries?

Author's Reply

We have plans to investigate the effect of non-axisymmetric geometry on the flow and heat transfer in rotating cavities. However, paper No.36 by Reile, Radons and Hennecke provides evidence that correlations obtained on simple rotating cavities can be used to predict the temperatures in compressor rotors. More investigations are necessary before we can be confident that cross-axisymmetric geometry does not produce significant changes to the flow structure. The advice for the designer is to proceed with caution: caveat emptor!

S.C. Arora, Ca

Did you make any turbulence measurements? If not, then why not?

Author's Reply

We have made velocity measurements using LDA inside rotating cavities, and these are reported in Reference 11. However, turbulence measurements are difficult to make, and they are likely to be of less importance for the understanding of Ekman-layer flow than is the case for the boundary layer flow that occurs on turbine blades.

HEAT TRANSFER IN GAS TURBINE COMBUSTORS

A DISCUSSION OF MATHEMATICAL MODELING OF COMBUSTION, HEAT AND MASS TRANSFER WITH EMPHASIS ON HEAT TRANSFER IN GAS TURBINE COMBUSTORS

BY

Ojorn F. Magnussen
Professor, Engineering Thermodynamics
The Norwegian Institute of Technology
N-7034 Trondheim, Norway

ABSTRACT

The paper deals with heat transfer problems in gas turbine combustors. The basis for the discussion is the treatment of the heat generation in the combustor.

The heat is generated through chemical reactions that take place when reactants are mixed at molecular scale at sufficient high temperature. It is known that the microscale processes which are decisive for the molecular mixing as well as the dissipation of turbulence energy into heat are severely intermittent, i.e. concentrated into isolated regions whose entire volume is only a small fraction of the volume of the fluid.

The paper reviews the Eddy Dissipation Concept (EDC) for chemical reactions in turbulent flow developed by Magnussen. The EDC is a reactor concept which is unique in that it takes into account the intermittent behaviour of the smallscale structures on the chemical reactions. Both fast and slow chemical reactions can be treated simultaneously. Flame stabilization, extinction and ignition characteristics, as well as blow-off, turbulent flame propagation velocities and reaction rates will be discussed in relation to the EDC.

Computations of heat transfer rates to the walls taking into account the cooling effect of the secondary air will be demonstrated. The physical implications of the various sub-models will be discussed.

NOMENCLATURE

a	constant
b^0	constant
c_i	concentration (kg/m^3)
c_i	local time mean concentration
c_i^p	concentration of products
c_p^p	specific heat
D^p	nozzle diameter
F	flatness factor
F	characteristic fine structure flatness factor
G	turbulence energy production term
g	linear termination coefficient or gravitation constant
g_0	coefficient of linear termination on soot particle
ΔH_R	reaction enthalpy difference
i	internal energy
k	turbulence kinetic energy
L^A	characteristic length scale of fine structures
L^A	conditional characteristic length scale of time structures
L^*	characteristic turbulence length scale, mixing length
L^*, L''	characteristic turbulence length scale at different structure level
m	mass concentration (kg/kg)
\dot{m}	exchange rate of mass with fine structures
\dot{m}_A	exchange rate of mass with fine structures within fine structure region
m	mass of soot particle (kg/part)
n^p	concentration of soot particles (part/m^3)
n	nucleus concentration (part/m^3)
n_u	rate of spontaneous formation of nucleus ($\text{part}/\text{m}^3/\text{s}$)
p	pressure
R	Reynolds number
R_{fu}^p	rate of fuel combustion ($\text{kg}/\text{m}^3/\text{s}$)
R_{nu}^p	rate of nucleus combustion ($\text{part}/\text{m}^3/\text{s}$)
R_{nf}^p	rate of nucleus formation
R_{sf}^p	rate of soot combustion
R_{sf}^p	rate of soot formation
Re_A^p	turbulence Reynolds number
r_{fu}	stoichiometric oxygen requirement to burn 1 kg fuel
S	source term
T	temperature (K)
ΔT	excess temperature of reacting fine structures
U_D	turbulent flame velocity
U_L	laminar flame velocity
U, u_j	mean flow velocity
u^*	characteristic velocity of fine structures

u^*	conditional characteristic velocity of fine structures
u'	turbulence velocity
u'', u^n	characteristic turbulence velocity at different structure level
x	axial coordinate
Y	fractional conversion parameter
Y_k	mass fraction of specie k
y	lateral coordinate
ρ	density
ϵ	rate of dissipation of turbulence kinetic energy
ϵ^*	conditional dissipation rate for fine structures
μ_{eff}	effective viscosity
μ_t	effective turbulent viscosity
σ	turbulent Prandtl/Schmidt number
σ_{ij}	stress tensor
ν	kinematic viscosity
γ^*	intermittency factor, mass fraction occupied by fine structures
γ_λ	mass fraction occupied by fine structures regions
γ_λ^*	mass fraction of fine structure regions occupied by fine structures
τ^*	time scale for the fine structure
τ_{ch}	chemical time scale
τ_λ	time scale for the fine structure regions
τ_M	bulk mixing timescale

INTRODUCTION

The heat transfer in a gas turbine combustor is strongly dependent on the evolution of the combustion. Characteristics of the combustion is dependent on chemical and physical properties of the fuel as well as on flow and turbulence characteristics.

In this respect the fine structures of turbulence are believed to play an important part. The characteristics of these structures are in developed turbulence structure, dependent on turbulence quantities like the turbulence kinetic energy, its rate of dissipation and consequently on length scales.

These quantities are strongly dependent on the flow evolution from the intake to the completion of the combustion and consequently on the interaction between the flow and the surrounding walls.

The various physical processes going on in the combustor are strongly linked, and therefore make the discussion of the influence of a certain parameter difficult. However, the processes are of general physical nature and may be encountered in many different flow and combustion situations.

Today there exist models of many of the important physical processes going on in the combustion chamber. The preceding discussion is therefore based on general theoretical considerations, mathematical models and numerical simulations. Of special interest in this respect, is the Eddy Dissipation Concept for chemical reactions in turbulent flow, (EDC), developed by the author. This concept has been widely used for calculation of diffusion flames, premixed flames, explosion development, soot formation and combustion, and internal combustion engines, as well as for the study of extinction processes in turbulent combustion.

TURBULENT STRUCTURE AND CHEMICAL REACTIONS

Chemical reactions take place when reactants are mixed at molecular scale at sufficiently high temperature. In turbulent flow the reactant consumption is strongly dependent on the molecular mixing. It is known that the microscale processes which are decisive for the molecular mixing as well as dissipation of turbulence energy into heat are, severely intermittent i.e. concentrated in isolated regions whose entire volume is a small fraction of the volume of the fluid.

These regions are occupied by fine structures whose dimensions are small in one or two directions, however not in the third. These fine structures are believed to be vortex tubes, sheets or slabs whose characteristic dimensions are of the same magnitude as the Kolmogorov microscale.

The fine structures are responsible for the dissipation of turbulence into heat. Within these structures one can therefore assume that reactants will be mixed at molecular scale. These structures thus create the reaction space for non-uniformly distributed reactants.

In a modelling context one can assume that the reactants are homogeneously mixed within the fine structures. Thus, in order to be able to treat the reaction within this space, it is necessary to know the reaction volume and the mass transfer rate between the structures and the surrounding fluid.

The following describes a concept for treating chemical reactions in turbulent flow which include basic features of the preceding.

Turbulence energy dissipation

In turbulent flow energy from the mean flow is transferred through the bigger eddies to the fine structures where mechanical energy is dissipated into heat. This process is schematically described in Fig.1.

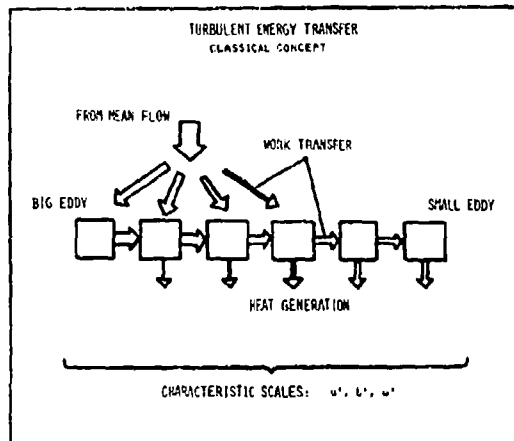


Fig. 1. Turbulent energy transfer

In general, high Reynolds number turbulent flow will consist of a spectrum of eddies of different sizes. Mechanical energy is mainly transferred between neighbouring eddy structures as indicated in Fig. 1. For the same reason the main production of turbulence kinetic energy will be performed by the interactions between bigger eddies and the mean flow.

The dissipation of kinetic energy into heat, which is due to work done by molecular forces on the turbulence eddies, on the other hand mainly takes place in the smallest eddies.

Important turbulent flow characteristics can for nearly isotropic turbulence be related to a turbulence velocity, u' , and a turbulent length, L' . These quantities are linked to each other through the turbulent eddy velocity:

$$v_t = u' \cdot L' \quad (1)$$

Modelling interstructural energy transfer

Figure 2 schematically illustrates a model for the transfer of mechanical energy from bigger to smaller turbulent structures.

The first structure level represents the whole spectrum of turbulence which in an ordinary way is characterized by a turbulence velocity, u' , a length scale, L' , and vorticity, or characteristic strain rate

$$\omega' = u'/L' \quad (2)$$

The rate of dissipation can for this level be expressed by

$$\epsilon' = \zeta^2 \left(12 \frac{u'}{L'} \cdot u'^2 + 15 \cdot v \left(\frac{u'}{L'} \right)^2 \right) \quad (3)$$

where ζ is a numerical constant.

The next structures level represent part of the turbulence spectrum characterized by a vorticity

$$\omega'' = 2\omega' \quad (4)$$

velocity, u'' , and length scale, L'' . The transfer of energy from the first level to the second level is expressed by

$$\epsilon'' = \zeta^2 \cdot 12 \frac{u'}{L'} \cdot u'^2 \quad (5)$$

Similarly the transfer of energy from the second to the third level where

$$\omega''' = 2\omega'' \quad (6)$$

is expressed

$$\epsilon''' = \zeta^2 \cdot 12 \frac{u''}{L''} \cdot u''^2 \quad (7)$$

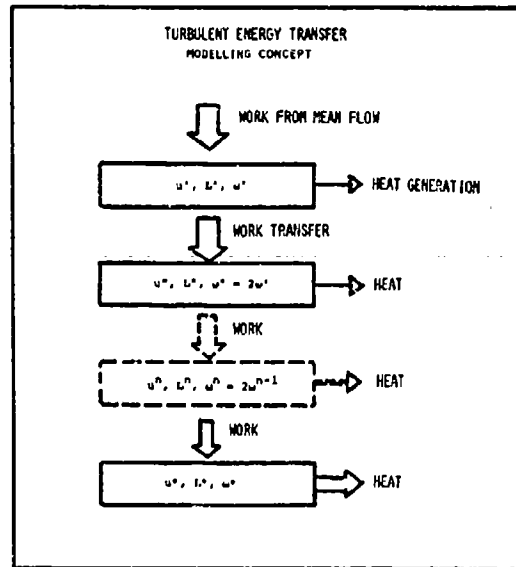


Fig. 2. A modelling concept for transfer of energy from bigger to smaller turbulent structures

The part which is directly dissipated into heat is expressed

$$q'' = \zeta^2 \cdot 15\nu \left(\frac{u''}{L''}\right)^2 \quad (8)$$

The turbulence energy balance for the second structure level is consequently given by

$$\zeta^2 \cdot 12 \frac{u''}{L''} \cdot u''^2 = \zeta^2 \left(12 \frac{u''}{L''} \cdot u''^2 + 15 \cdot \nu \left(\frac{u''}{L''}\right)^2 \right) \quad (9)$$

This sequence of turbulence structure levels can be continued down to a level where all the produced turbulence kinetic energy is dissipated into heat. This is the fine structure level characterised by, u'' , L'' , and ω'' .

The turbulence energy transferred to the fine structure is expressed by

$$w'' = \zeta^2 \cdot 6 \frac{u''}{L''} \cdot u''^2 \quad (10)$$

and the dissipation by

$$q'' = \zeta^2 \cdot 15\nu \left(\frac{u''}{L''}\right)^2 \quad (11)$$

According to this model nearly no dissipation of energy into heat takes place at the highest structure level. Similarly it can be shown that 3/4 of the dissipation takes place at the fine structure level.

Taking this into account and by introducing $\zeta = 0.18$ the following three equations are obtained for the dissipation of turbulence kinetic energy for nearly isotropic turbulence:

$$c = 0.2 \frac{u''^3}{L''} \quad (12)$$

$$c = 0.267 \frac{u''^3}{L''} \quad (13)$$

$$c = 0.67 \nu \left(\frac{u''}{L''}\right)^2 \quad (14)$$

Introducing the Taylor microscale a fourth equation is obtained

$$c = 15 \nu \left(\frac{u''}{\lambda}\right)^2 \quad (15)$$

By combination of equations (13) and (14) the following characteristics (scales) for the fine structures are obtained

$$u^* = 1.74 (\epsilon \cdot \nu)^{1/4} \quad (16)$$

and

$$L^* = 1.43 \nu^{3/4} / \epsilon^{1/4} \quad (17)$$

where u^* is the mass average fine structure velocity. The scales are closely related to the Kolmogorov scales.

The fine structures

The tendency towards strong dissipation intermittency in high Reynolds number turbulence was discovered by Batchelor and Townsend¹, and then studied from two points of view: different statistical models for the cascade of energy starting from a hypothesis of local invariance or selfsimilarities between motions of different scales, and then by consideration of hydrodynamic vorticity production due to stretching of vortex lines.

It can be concluded that the smallscale structures who are responsible for the main part of the dissipation are generated in a very localized fashion. It is assumed that these structures consist typically of large thin vortex sheets, ribbons of vorticity or vortex tubes of random extension folded or tangled throughout the flow. (Figs. 3 and 4.)

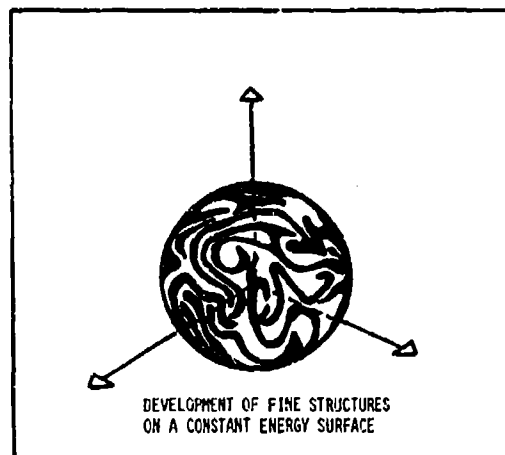


Fig. 3. Schematic illustration of fine structures developed on a constant energy surface

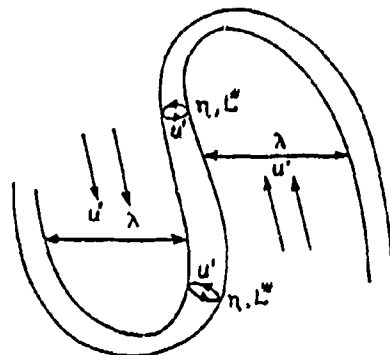


Fig. 4. Schematic illustration of fine structure vortex^R

6

The fine structures are localized in certain fine structure regions whose linear dimensions are considerably larger than the fine structures therein. These regions appear in the highly strained regions between the bigger eddies.

Modelling characteristics of the fine structures

It is assumed that the mass fraction occupied by the fine structures, on the basis of consideration of the energy transfer to these structures (eqs. 12 and 13) can be expressed by

$$\gamma^* = \left(\frac{u^*}{u}\right)^3 \quad (18)$$

If it is assumed that the fine structures are localized in nearly constant energy regions, then the mass fraction occupied by the fine structure regions can be expressed by

$$\gamma^* = \gamma_\lambda \cdot \left(\frac{u^*}{u}\right)^2 \quad (19)$$

giving the following expression

$$\gamma_\lambda = \frac{u^*}{u} \quad (20)$$

Assuming nearly isotropic turbulence and introducing the turbulence kinetic energy and its rate of dissipation the following expressions are obtained:

$$\gamma^* = 9.7 \cdot \left(\frac{v \cdot \epsilon}{k^2}\right)^{3/4} \quad (21)$$

and

$$\gamma_\lambda = 2.13 \cdot \left(\frac{v \cdot \epsilon}{k^2}\right)^{1/4} \quad (22)$$

Similarly by introducing the turbulence Reynolds number

$$\gamma^* = 40.2 \cdot Re_\lambda^{-3/2} \quad (23)$$

and

$$\gamma_\lambda = 3.42 \cdot Re_\lambda^{-1/2} \quad (24)$$

Kuo and Corrsin⁸ have given some results for the flatness factor of $\partial u/\partial t$ as a function of Re_λ (Fig. 6). In order to compare the above results with these results an empirical expression has been developed for the relationship between the flatness factor and the intermittency factor:

$$F_M = 1.5 \cdot (1 + 1/\gamma) \quad (25)$$

Figure 5 shows a comparison between some experimental results¹⁰ and the given empirical expression.

When eq. (25) is applied the following expression for the flatness factor for the fine structures is obtained.

$$F_\lambda = 1.5 + 0.44 \cdot Re_\lambda^{0.5} \quad (26)$$

Equation (26) is compared with the experimental results of Kuo and Corrsin⁸ in Fig. 6.

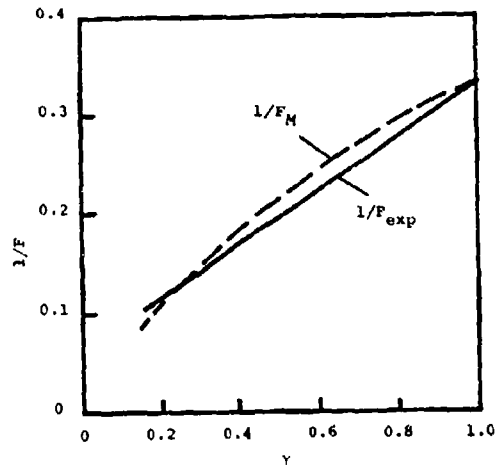


Fig. 5. Comparison between experimental results and empirical expression for the flatness factor as a function of the intermittency factor

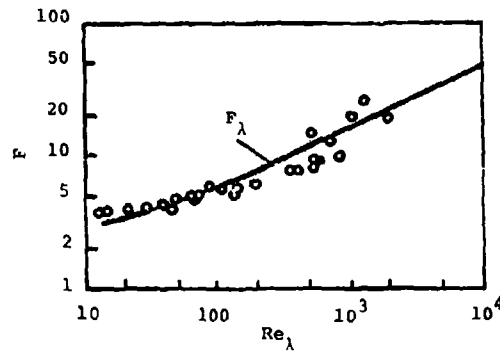


Fig. 6. Flatness factor of $\partial u/\partial t$ as a function of Re_λ compared with theoretical flatness factor for the fine structures.

From this comparison it can be concluded that the overall features of the physics seem to have been taken care of by the suggested expressions.

On the basis of simple geometrical considerations the transfer of mass per unit of fluid and unit of time between the fine structures and the surrounding can be expressed as follows

$$\dot{m} = 2 \cdot \frac{u^*}{L^*} \cdot \gamma^* \quad (1/s) \quad (27)$$

Expressed by k and ϵ for nearly isotropic turbulence eq. (27) turns into

$$\dot{m} = 23.6 \cdot \left(\frac{\nu \cdot \epsilon}{k^2} \right)^{1/4} \cdot \frac{\epsilon}{k} \quad (1/s) \quad (28)$$

The dissipative fine structures are localized within the fine structure regions. The localized mass transfer rate between the fine structures and the surrounding fluid may consequently be expressed

$$\dot{m}_\lambda = \frac{\dot{m}}{\gamma_\lambda} \quad (1/s) \quad (29)$$

which combined with Eqs. (20) and (27) leads to

$$\dot{m}_\lambda = 2 \cdot \frac{u^*}{L^*} \cdot \gamma^* \quad (1/s) \quad (30)$$

23-8

and consequently

$$\dot{m}_\lambda = 11.08 \cdot \frac{\epsilon}{\kappa} \quad (1/s) \quad (31)$$

The conditional dissipation rate for the fine structures may be expressed

$$\bar{\epsilon}^* = \frac{\epsilon}{\gamma^*} \quad (32)$$

which combined with Eqs. (13) and (18) transformed into

$$\bar{\epsilon}^* = 0.267 \cdot \frac{u'^3}{L^*} \quad (33)$$

Consequently the individual structures may be characterized by

$$\bar{u}^* = u' \quad (34)$$

and

$$\bar{L}^* = L^* \quad (35)$$

The characteristic time for the fine structures may be expressed as follows

$$\tau^* = \frac{\gamma^*}{\dot{m}} \quad (36)$$

or

$$\tau^* = \frac{\gamma_\lambda^*}{m_\lambda} \quad (37)$$

where γ_λ^* , the mass fraction of the fine structure region occupied by the fine structures is

$$\gamma_\lambda^* = \frac{\gamma^*}{\gamma_\lambda} \quad (38)$$

Molecular mixing and reaction processes

The rate of molecular mixing is determined by the rate of mixing between a certain fraction, χ , of the fine structures and the rest of the fluid, R_i , can for a certain specie, i , be expressed as follows:

$$R_i = \dot{m} \cdot \chi \cdot \left(\frac{c_i^*}{\rho^*} - \frac{c_i}{\rho} \right) \quad (39)$$

where ρ^* and ρ refer to conditions in the fine structures and the surrounding.

The mass transfer rate can also be expressed per unit volume in the fine structure fraction, χ , as

$$R_i^* = \frac{\dot{m} \cdot \rho^*}{\gamma^*} \cdot \left(\frac{c_i^*}{\rho^*} - \frac{c_i}{\rho} \right) \quad (40)$$

Finally, the concentration of a specie, i , in the fraction, χ , of the fine structures and in the surrounding is related to the mean concentration by:

$$\frac{\bar{c}_i}{\rho} = \frac{c_i^*}{\rho^*} \cdot \gamma^* \cdot \chi + \frac{c_i}{\rho} \cdot (1 - \gamma^* \cdot \chi) \quad (41)$$

It is now possible to put up balance equations for reacting fine structures and the surrounding fluid including chemical kinetic rate expressions.

Combustion rates

If the rate of reaction between fuel and oxygen is considered infinitely fast, the rate of reaction will be limited by the mass transfer between the bulk and the fine structures. If the reaction took place in all the fine structures, the rate of combustion would be expressed by:

$$R_{fu} = \dot{m} \cdot \frac{\bar{c}_{min}}{1 - \gamma^2} \quad (42)$$

where \bar{c}_{min} is the smallest of \bar{c}_{fu} and \bar{c}_{O_2}/r_{fu} , where \bar{c}_{fu} and \bar{c}_{O_2} are the local mean concentrations of fuel and oxygen, and r_{fu} the stoichiometric oxygen requirement.

Not all the fine structures will be sufficiently heated to react. This is obviously the case in combustion of premixed gases where both fuel and oxygen are present in the fine structures.

The fraction of the fine structures which reacts can be assumed proportional to the ratio between the local concentration of reacted fuel and the total quantity of fuel that could react:

$$\chi = \frac{1}{\gamma_\lambda} \frac{\bar{c}_{pr}/(1 + r_{fu})}{\bar{c}_{pr}/(1 + r_{fu}) + \bar{c}_{min}} \quad (43)$$

where \bar{c}_{pr} is the local mean concentration of reaction products. Equation (43) implies the assumption that the reaction will take place within the fine structure regions where the concentration of reactive species and temperature are high, for the rate determining species, significantly higher than the time mean values.

In cases where the concentration of reaction products are very small, γ_λ in the denominator implies that the products are kept within the fine structure regions.

By combination of equations (42) and (43) the following general equation is obtained for the rate of combustion at infinite reaction rate between fuel and oxygen:

$$R_{fu} = \dot{m} \cdot \frac{\chi}{1 - \gamma^2 \chi} \cdot \bar{c}_{min} \quad (44)$$

The reacting fine structures under these conditions will have a temperature, ΔT , in excess of the local mean temperature:

$$\Delta T = \frac{\Delta H_R \cdot \bar{c}_{min}}{\dot{e} \cdot c_p} \quad (45)$$

where ΔH_R is the heat of reaction and c_p the local specific heat capacity. The temperature, T^* , of the reacting fine structures is consequently:

$$T^* = \bar{T} + \Delta T \quad (46)$$

and the surrounding temperature:

$$T^0 = \bar{T} - \Delta T \cdot \frac{\gamma^* \cdot \chi}{1 - \gamma^* \cdot \chi} \quad (47)$$

where \bar{T} is the local time mean temperature.

Chemical controlled reaction rate

On the basis of the previous there can be defined characteristic mixing time scales:

The bulk mixing time scale

$$\tau_H = 1/\dot{m} \quad (48)$$

The fine structure time scales

$$\tau^* = \gamma^*/\dot{m} \quad (49)$$

$$\tau_\lambda = \gamma_\lambda/\dot{m} \quad (50)$$

These time scales can be compared with chemical kinetic time scales in order to establish whether the reaction is mixing or chemical controlled, and even established criteria for extinction of flames.

Extinction

According to the previous concept heat and mass balance including chemical kinetics can easily be set up for the fine structures and the surrounding fluid. Consequently, knowing the chemical kinetics, a criterium for the extinction of the fine structures can be obtained. When a typical timescale for the combustion reaction is small compared to τ^* the fuel consumption is independent of chemical kinetics and is purely a hydrodynamic problem. However, when the residence time becomes smaller than a typical chemical time scale, the reaction will not be completed in the fine structure and the fuel consumption is strongly influenced by chemical kinetics. As the residence time decreases extinction will finally occur.

The chemical time scale, however, is not a uniquely defined quantity. Many different expressions can be found in the literature describing the various steps in the reaction process. In addition it is very difficult to find relevant data for different fuels.

In a typical turbulent combustion situation it is believed that radicals are already present in the regions where the fine structures are located. When it is further assumed that the internal mixing inside the fine structures are fast, then the fine structures can be considered as a well stirred reactor

On the basis of the previous the fractional conversion parameter for the reactor is defined as (cfr. Fig. 7) ref. 5.

$$Y = \frac{c_{fu}^0 - c_{fu}^k}{c_{fu}^0} \frac{Q^0}{Q^k} \quad (51)$$

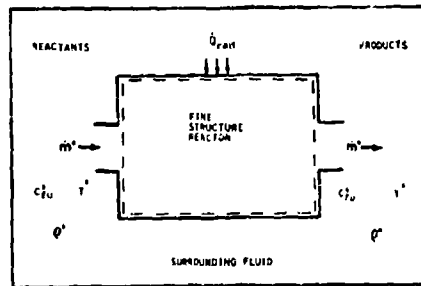


Fig. 7. Schematic illustration of a reacting fine structure

For a one step irreversible reaction the mass and heat balance for the fine structure can be expressed as

$$Y = \frac{R_{fu}^k \cdot \tau^k}{c_{fu}^0} \cdot \frac{Q^0}{Q^k} \quad (52)$$

and

$$Y = \frac{c_p (T^k - T^0) Q^0}{\Delta H_R c_{fu}^0} \quad (53)$$

where the fine structure is considered to be adiabatic and the specific heat of the fluid is assumed to be constant. The extinction time scale can then be found from eq. (52) and (53) according to Fig. 8, where the extinction time scale τ_{ext}^* is indicated.

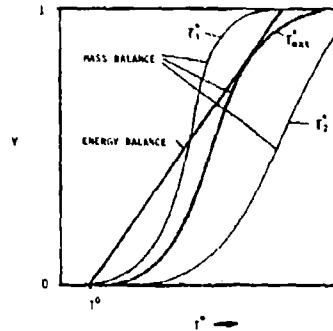


Fig. 8. Schematic illustration of Extinction in the fine structure
 $r_1^* > r_{ext}^* > r_2^*$

Turbulent flame propagation

The propagation of a plane flame in turbulent flow can be expressed by

$$U_B \frac{\partial c_{fu}}{\partial x} = \frac{\nu_T}{\sigma} \frac{\partial^2 c_{fu}}{\partial x^2} + R_{fu} \quad (54)$$

where U_B is the turbulent flame propagation velocity, ν_T is the turbulent viscosity and σ is the turbulent Schmidt number. With R_{fu} expressed according to eq. (44) the only physically meaningful solution to eq. (54) reads

$$U_B = 2 \left(\frac{\nu_T}{\sigma} \right)^{1/2} \quad (55)$$

By introducing the turbulent viscosity from the k- ϵ -model this transform into

$$U_B = 2 \left(\frac{k}{\sigma} \right)^{1/2} \quad (56)$$

In a typical shear flow situation $k \approx u'^2$ and $\sigma \approx 1$. This gives a turbulent flame propagation velocity

$$U_B \approx 2u' \quad (57)$$

This is generally in relatively close agreement with the experimental data collected by Bradley et al. (1981), fig. 9 and data from Andrews et al. (1981), fig. 10.

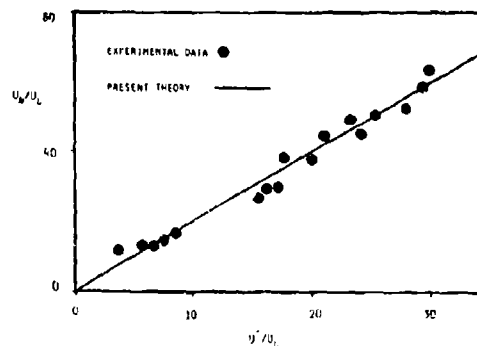


Fig. 9. Comparison of predicted flame velocity experimental data by Abdel-Gayed and Bradley¹⁴

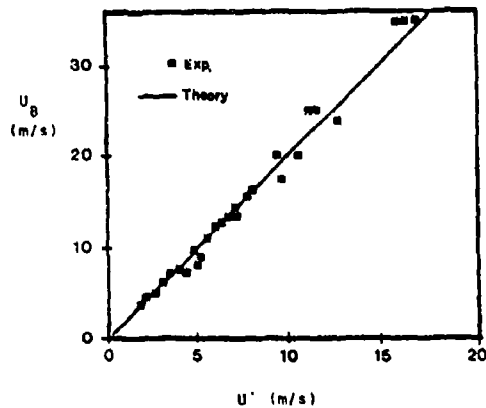


Fig. 10. Comparison of predicted flame velocity experimental data by Al Dabbagh and Andrews¹⁸

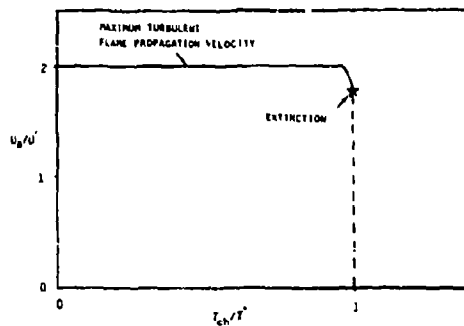


Fig. 11. Schematic illustration of the turbulent flame propagation velocity variation.

The abrupt extinction has been shown experimentally by Chou-lak et. al. (1982)². In these experiments extinction for a methane mixture occurred at a fine structure time scale of approximately $\tau^* \sim 10^{-4}$ s. This is in close agreement with the chemical time scale deduced from the global reaction rate used by Bradley et. al. (1976) (1976)^{15,16} and is also in reasonable agreement with the multistep kinetic calculations for methane-air mixture reported by Martenay (1970)¹.

Modeling of soot formation and combustion in turbulent flames.

The modeling of soot formation has been based on the two equations as used previously by Magnussen et al. (23, 24, 25). An equation for the rate of formation of radical nuclei is expressed by

$$R_{n,f} = n_0 + (f-g)n - g_0 n N \quad (\text{part/m}^3/\text{s}) \quad (58)$$

where n is the concentration of radical nuclei, N is the concentration of soot particles and n_0 is the rate of spontaneous formation of radical nuclei,

$$n_0 = a_0 \bar{c}_{fu} \exp(-E/RT) \quad (\text{part/m}^3/\text{s}) \quad (59)$$

where \bar{c}_{fu} is the mean concentration of fuel (kg/m^3), f , g , g_0 , and a_0 are certain constants. The rate of soot particle formation is expressed by

$$R_{s,f} = m_p (a - bN)n \quad (\text{kg/m}^3/\text{s}) \quad (60)$$

where m_p is the mass of a soot particle (kg/part), and a and b are constants.

Soot was allowed to be formed both in the heated fine structures and in the surrounding fluid, and it was assumed that the mass fraction of the fuel contained in the heated fine structures was proportional to $\gamma^2 X$. Local equilibrium with the surrounding fluid was assumed for the fine structures leading to the following equations:

$$R_{n^A, f} - \frac{\dot{m}_0}{\gamma^2} \left(\frac{n^A}{\rho^A} - \frac{n^A_0}{\rho^0} \right) = 0 \quad (61)$$

and

$$R_{s^A, f} - \frac{\dot{m}_0}{\gamma^2} \left(\frac{c_{s^A}}{\rho^A} - \frac{c_{s^A}^0}{\rho^0} \right) = 0 \quad (62)$$

The mean rates of reaction could then be expressed by

$$R_{n, f} = n_{O, f} \gamma^2 X \bar{\rho} + n_{O, f} (1 - \gamma^2 X) \bar{\rho}^0 + ((f-g)\bar{n} - g_0 n^A N^A \gamma^2 X \bar{\rho} / \rho^A - g_0 n^O N^O (1 - \gamma^2 X) \bar{\rho} / \rho^0) \quad (63)$$

and

$$R_{s, f} = m_p (a - bN^A) n^A \gamma^2 X \bar{\rho} / \rho^A + m_p (a - bN^O) n^O (1 - \gamma^2 X) \bar{\rho} / \rho^0 \quad (64)$$

The mean rates of nucleus and soot particle combustion are expressed by Eq.(64) as follows:

$$R_{n, c} = R_{fu} \bar{n} / \bar{c}_{fu} \quad (\text{part}/\text{m}^3/\text{s}) \quad (65)$$

and

$$R_{s, c} = R_{fu} \bar{c}_s / \bar{c}_{fu} \quad (\text{kg}/\text{m}^3/\text{s}) \quad (66)$$

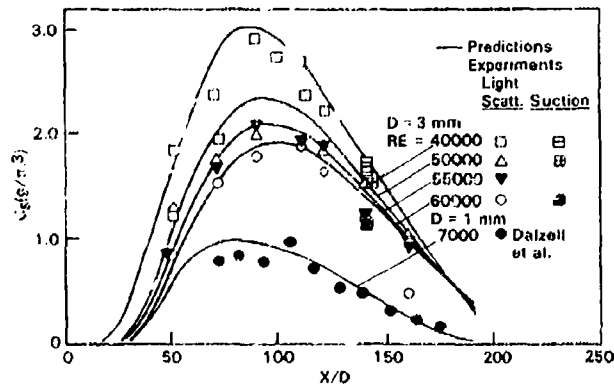


Fig. 12 Variation of mean value of soot concentration along the axis of acetylene diffusion flame. Comparison between prediction and experimental results.

HEAT TRANSFER TO THE INTERNAL WALLS OF A COMBUSTOR

Simplified calculations of the surface temperature of the internal wall of a combustor by application of film cooling have been performed, Fig. 13.

The calculation domain was divided into two regions, the central region and the film boundary region, Fig. 14.

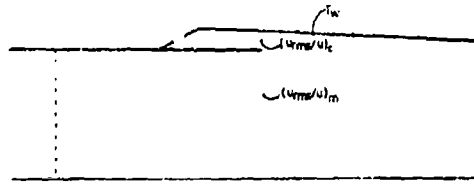


Fig. 13. Film cooling of combustor wall.

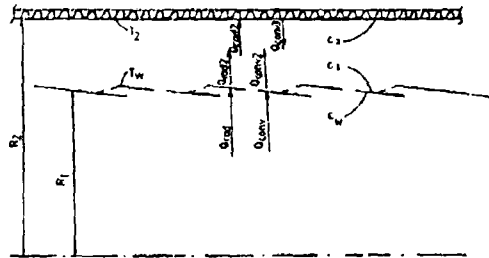


Fig. 14. Film cooling of combustor wall, Heat transfer.

Combustion, heat and mass transfer in the central region was calculated on the basis of the methods described above. A boundary layer calculations was performed for the film boundary region. The calculations were compared with experimental data from Ref. 26. A comparison between experimental and calculated film cooling efficiency is shown in Fig. 15. (For the case where the radiation heat transfer is negligible). The main problem in this case, was the establishment

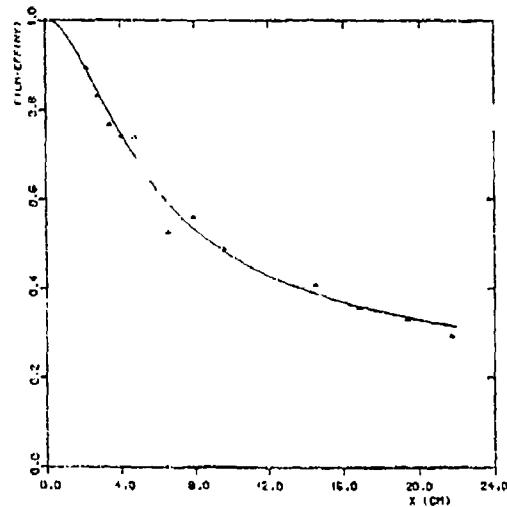


Fig. 15. Film cooling efficiency as a function of distance downstream from inlet slot.

of the flow conditions at the inlet of the slot for the turbulence kinetic energy k , and its rate of change dk/dx .

Figure 16 gives a comparison between experimental data and calculations for a combustion case and two slot heights.

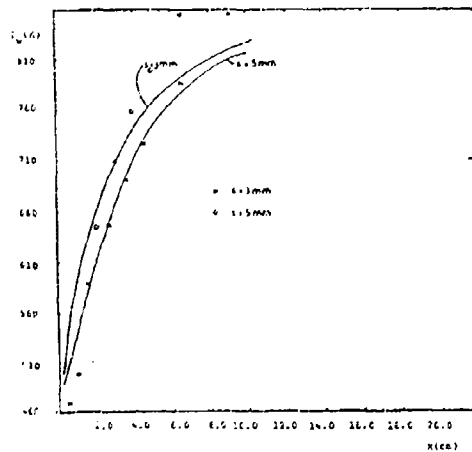


Fig. 16. Wall surface temperature for two different slot heights, s , as a function of the distance downstream from inlet slot.

CONCLUSION

This paper has reviewed in detail a method for calculation of combustion characteristics of gas turbine combustors. The method which is extensively used may treat stationary as well as non-stationary combustion problems. Some simplified calculations of internal surface temperature of a combustor by film cooling is shown. This problem is both a computational problem as well as a mathematical modeling problem, where especially the boundary problems are considerable.

It may, however, be concluded that calculations of practical relevance may be performed even for rather complex geometries.

APPENDIX.

Conservation equations.

Mass;

$$\frac{\partial \rho}{\partial t} + \frac{\partial (\rho u_j)}{\partial x_j} = 0 \quad (67)$$

Momentum;

$$\frac{\partial (\rho u_i)}{\partial t} + \frac{\partial (\rho u_i u_j - \sigma_{ij})}{\partial x_j} = 0 \quad (68)$$

Internal energy; i

$$\frac{\partial (\rho i)}{\partial t} + \frac{\partial (\rho i u_j - \sigma_{ij} u_i - \frac{\nu_{eff}}{i} \frac{\partial i}{\partial x_j})}{\partial x_j} = S_i \quad (69)$$

where

$$\sigma_{ij} = p \delta_{ij} + \sigma'_{ij}$$

$$\sigma'_{ij} = \sigma'_{ij,1} + \sigma'_{ij,t} = \mu_{eff} \left(\left(\frac{\partial u_i}{\partial x_j} + \frac{\partial u_j}{\partial x_i} \right) - \frac{2}{3} \frac{\partial u_k}{\partial x_k} \delta_{ij} \right) - \frac{2}{3} \rho k \delta_{ij} \quad (70)$$

$$(71)$$

$$\mu_{eff} = \mu_1 + \mu_t \quad (72)$$

and

$$\mu_t = C_\mu \rho \frac{k^{1/2}}{\epsilon} \quad (73)$$

Turbulence kinetic energy; k

$$\frac{\partial (\rho k)}{\partial t} + \frac{\partial (\rho k u_j - \frac{\nu_{eff}}{k} \frac{\partial k}{\partial x_j})}{\partial x_j} = S_k \quad (74)$$

Dissipation of turbulence kinetic energy; ϵ

$$\frac{\partial}{\partial t} (\rho \epsilon) + \frac{\partial}{\partial x_j} (\rho u_j \epsilon - \frac{\nu_{eff}}{\sigma_\epsilon} \cdot \frac{\partial \epsilon}{\partial x_j}) = S_\epsilon \quad (75)$$

Mass fraction of specie k; Y_k

$$\frac{\partial}{\partial t} (\rho Y_k) + \frac{\partial}{\partial x_j} (\rho Y_k u_j - \frac{\nu_{eff}}{\sigma_{Y_k}} \cdot \frac{\partial Y_k}{\partial x_j}) = S_{Y_k} \quad (76)$$

Source terms

$$S_i = R_{fu} \cdot \Delta H_R \quad (77)$$

$$S_k = G - \rho \epsilon \quad (78)$$

$$S_\epsilon = C_1 \frac{\epsilon}{k} \cdot G - C_2 \rho \frac{\epsilon^2}{k} + C_3 \cdot \rho \cdot \epsilon \cdot \frac{\partial u_k}{\partial x_j} \quad (79)$$

$$S_{Y_k} = R_{Y_k} \quad (80)$$

$$R_{fu} = \dot{m} \frac{X}{1 - Y^{H_2O}} \cdot \rho Y_{min} \quad (81)$$

where

$$\rho Y_{min} = \bar{c}_{min} \quad (82)$$

$$G = \nu_t C_{ij} \frac{\partial u_k}{\partial x_j} \left(\nu_t \frac{\partial u_k}{\partial x_k} + \rho k \right) \quad (83)$$

$$G_{ij} = \frac{\partial u_i}{\partial x_j} \left(\frac{\partial u_i}{\partial x_j} + \frac{\partial u_j}{\partial x_i} \right) \quad (84)$$

Constants

$$C_\mu = 0.09, \quad C_1 = 1.44, \quad C_2 = 1.92, \quad C_3 = -0.373$$

$$\sigma_k = 1.0, \quad \sigma_\epsilon = 1.3, \quad \sigma_i, \sigma_{Y_k} = 0.7$$

REFERENCES

- Magnussen, B.F., "On the Structure of Turbulence and a Generalized Eddy Dissipation Concept for Chemical Reactions in Turbulent Flow", 19th AIAA Sc. meeting, St. Louis, USA, 1981
- Chomiak, J., and Jarosinski, J., "Flame Quenching by Turbulence", Comb. and Flame, 1982, 48, 241
- Ahnadi-Befruel, O., and Gosman, A.U., Lockwood, F.C., and Watkins, A.P., "Multidimensional Calculation of Combustion in an Idealized Homogeneous Charge Engine: a Progress Report", Soc. of Automotive Eng., Detroit, Michigan, 1981.
- Grasso, F. and Bracco, F.V., "Evaluation of a Mixing-Controlled Model for Engine Combustion", Comb. Sci. Tech., 1982, 4, 105.
- Byggsteyl, S. and Magnussen, B.F., "A Model for Flame Extinction in Turbulent Flow", Proc., Turbulent Shear Flow Symp., Karlsruhe, 1983, 10, 32.
- Kolmogorov, A.N., "A Refinement of previous Hypotheses concerning the Local Structure of Turbulence in a viscous incompressible Fluid at high Reynolds number", J. Fluid Mech., 1962, 13, 82.
- Corrsin, S., "Turbulent Dissipation Correlations", Phys. Fluids, 1962, 13, 32
- Tennekes, H., "Simple Model for Small-Scale Structure of Turbulence", Phys. Fluids, 1968, 11, 3.
- Kuo, A.Y., and Corrsin, S., "Experiments on Internal Intermittancy and Fine Structure Distribution Function in Fully Turbulent Fluid", J. Fluid Mech., 1971, 50, 285.
- Kuo, A.Y., and Corrsin, S., "Experiments on the Geometry of the Fine Structure Regions in fully Turbulent Fluid", J. Fluid Mech., 1972, 56, 477.

- 11 Magnussen, B.F., "Some Features of the Structure of Mathematical Model of Turbulence, Report, NTH, 1975
- 12 Batchelor, G.K., and Townsend, A.A., "The Nature of Turbulent Motion at large Wave-Numbers", Proc. Roy. Soc., 1949, A 199, 238.
- 13 Wagnanski, I. and Fiedler, H.J., "Some Measurements in the Self-Preserving Jet", J. Fluid Mech., 1969, 38, 577.
- 14 Bradley, D., and Abdel-Gayed, R.G., "A two Eddy Theory of Premixed Turbulent Flame Propagation", Proc. Roy. Soc., 1981, A 1457, 1.
- 15 Bradley, D., Chin, S.B., Draper, H.S., and Hankinson, G., 16 Int. Symp. on Comb., 1976, 1571.
- 16 Byggstøyl, S., and Magnussen, B.F., "Flame Extinction in Turbulent Structure", Task Leaders Conf., IEA, Italy, 1982.
- 17 Martenay, P., "Analytical Study of the formation of Nitrogen Oxides in hydrogen air combustion", Comb. Sci. Tech., 1970, 1, 461.
- 18 Dabbagh, A.I., and Andrews, G.E., "Weak extinction and Turbulent Burning Velocity for Grid Plate Stabilized Premixed Flames", Comb. and Flame, 1984, 55, 31.
- 19 Byggstøyl, S., "Mathematical Modeling of Turbulence Structure Effects in Reacting and Non Reacting Flows", Dr. Thesis, NTH, 1984.
- 20 Grimsø, B., and Magnussen, B.F., "Numerical Simulation of Turbulent Flow in a Homogenous Charge Spark Ignition Engine. Simulation of a complete four Stroke Cycle", Task Leaders Conf., IEA, USA, 1984.
- 21 Magnussen, B.F., "Effects of Turbulence on Combustion Relating to Internal Combustion Engines", FVV-Werkshop, Turbulence in Internal Combustion Engines", Frankfurt, Germany, January 1985.
- 22 Magnussen, B.F., "Modeling of Reaction Processes in Turbulent flames with Special Emphasis on soot formation and combustion", Particulate Carbon Formation During Combustion, Plenum Publishing Corporation, 1981.
- 23 Magnussen, B.F., Hjertager, B.H., Olsen, J.G., and Bhaduri, D., Seventeenth Symposium (International) on Combustion, The Combustion Institute, Pittsburgh, (1979), p. 1383.
- 24 Magnussen, B.F. and Hjertager, B.H., Deuxieme Symposium Europeen sur la Combustion, Section Francaise du "Combustion Institute", (1975), p.385.
- 25 Magnussen, B.F. and Hjertager, B.H., Sixteenth Symposium (International) on Combustion, The Combustion Institute, Pittsburgh, (1976), p.719.
- 26 Sturgess, G.J., "Account of Film Turbulence for Predicting Film Cooling Effectiveness in Gas Turbine Combustors", ASME 79-GT-200.
- 27 Launder, B.E., and Spalding, D.B., "Mathematical Models of Turbulence", Academic Press, 1972.

DISCUSSION

A.M.Mellor, US

Do you plan to measure or predict (1) liquid spray flames or (2) flames with much higher turbulence intensity so that your results are more representative of gas turbine conditions?

Do the output parameters of your soot formation/oxidation model meet all requirements for a four or six flux radiation model calculation?

Author's Reply

We have been working with the experimental study and modeling of soot formation and combustion of various gaseous fuels. We are now starting a study dedicated towards combinations of gaseous and liquid fuels.

Due to the industry structure of our country we have not been especially directed towards gas turbine problems. However, we have been much occupied by combustion in highly strained turbulent flow, including flame quenching in the turbulent structure.

The output of the soot models readily goes into flux radiation models. We are generally using four or six flux models, like the model of Lockwood and Shaq.

EFFECTIVENESS MEASUREMENTS FOR A COOLING FILM DISRUPTED BY A SINGLE JET WITH WALL PLUNGING

B.L. Button

Department of Mechanical Engineering
Trent Polytechnic
Nottingham, NG1 4BU
United Kingdom

SUMMARY

Experimental measurements of the effectiveness downstream of a slot airflow with the jet airflow normal to the wall have been performed in a wind tunnel. The separate and combined effects of the slot and jet airflows with and without wall plunging on the effectiveness and flow characteristics are presented over a range of slot and jet airflow conditions relevant to gas turbine combustors.

The slot consisted of three rows of holes inclined at 10 degrees to the main airflow. The jet centre line was positioned one, two and three diameters downstream from the slot exit. The jet diameter corresponded to five slot heights. Three wall plunge heights were used and corresponded to 0.2, 0.4 and twelve jet diameters. The main airflow was constant at a Mach number of 0.05 and various combinations of the slot mass velocity ratio (0.5, 1.0 and 1.5) with the jet mass velocity ratio (0.5, 1.0 and 2.0) were tested. The effectiveness measurements covered an area eight jet diameters downstream of the slot exit by four jet diameters laterally.

The results show that the major interactions between the three airflows occur downstream of the jet centre line in a small region about three diameters long and two diameters wide. In general, such interactions reduce the effectiveness by up to forty percent when compared to the values with no jet injection. The combined and the separate effectiveness of the slot airflow and of the jet airflow are presented.

NOMENCLATURE

c_{cj} = helium concentration in jet airflow at exit	x_{sj} = distance between slot exit and jet centre line
c_{cs} = helium concentration in slot airflow at exit	y = lateral distance from the jet centre line
c_{ij} = helium concentration at wall for jet airflow	z = distance measured vertically from wall
c_{is} = helium concentration at wall for slot airflow	β = angle of wool tuft or cotton thread to direction of main airflow
D = jet diameter	δ^* = displacement boundary layer thickness
Ma = main airflow Mach number	η_j = impermeable-wall jet effectiveness
M_j = mass velocity ratio for jet ($\rho_j U_j / \rho_m U_m$)	η_s = impermeable-wall slot effectiveness
M_s = mass velocity ratio for slot ($\rho_s U_s / \rho_m U_m$)	$\eta_{sj} = \eta_s + \eta_j$
U_j = mean jet airflow velocity	ρ_j = jet airflow density
U_m = mean main airflow velocity	ρ_s = main airflow density
U_s = mean slot airflow velocity	ρ_m = slot airflow density
x = distance downstream from slot exit	

INTRODUCTION

The walls of gas turbine combustors are usually maintained at acceptable temperatures by cooling films of an injected parallel to the wall through slots. However, air needs to be added to the primary, secondary and tertiary zones of the combustor. This is achieved by injecting jets of air normal to the wall, which inevitably disrupt the cooling film and give rise to high temperature areas and hot spots downstream of the jets.

In order to obtain a detailed understanding of some of the phenomena involved a program of research has been undertaken (1). This covers flow visualisation, effectiveness and heat transfer coefficient measurements downstream of a slot exit, for various combinations of slot and jet geometries and airflow conditions. For a range of jet and slot airflow conditions, some of the flow visualisation and effectiveness results are presented here for a single jet disrupting a cooling film from a slot. The paper aims to describe how the wall plunge heights for the jet and the distance of the jet centre line downstream of the jet slot exit affect the effectiveness.

A brief description of the airflow rig, the working section base plate and some of the measurement techniques used, are included. Further information can be found in (2), and a comprehensive description of the design and construction of the airflow rig, its instrumentation and verification can be found in (1).

AIRFLOW RIG AND MEASUREMENT TECHNIQUES

The airflow rig consists of three separate systems each supplying an airflow to the working section. For the main system, or wind tunnel, ambient air is drawn in through filters by a centrifugal fan with a variable speed drive. The air then passes through a diffuser, a settling chamber containing a honeycomb and five screens and a contraction used to meter the flow. Although different in size the slot and jet systems prepare the airflows in a similar way.

The working section is 200 mm square and 710 mm long. It has fixed walls, an adjustable roof and the base, shown in figure 1, contains: the slot for the boundary layer bleed; the test specimen for the effectiveness measurements and exits for the slot and jet airflows; different plunge heights were obtained by fitting jet inserts into the end of the jet pipe. Also shown in figure 1 are details of the slot geometry, which is based on the pulse drilled designs that are now in use in some combustors. The outlet velocity and turbulence intensity profiles at the jet exit are similar to those for fully developed turbulent pipe flows and to a first approximation resemble those found in combustors.

The flow visualisation studies were made using tufts and DISA hot-wire anemometry with miniature probes. Initially 25 mm long nylon wool tufts were used, but subsequently it was found cotton thread 15 mm long was more sensitive. The results were photographed or sketched.

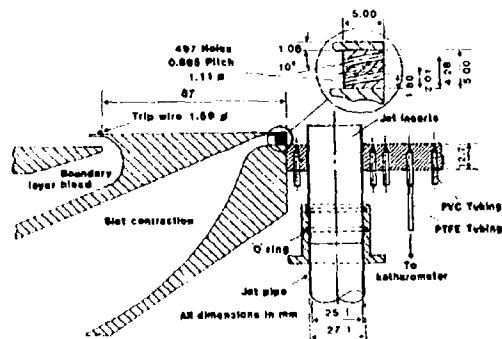


Figure 1 Slot, jet and wall plunging geometries

The impermeable-wall effectiveness was determined from helium concentrations at the wall and at the point of injection for the slot and jet separately, i.e. $\eta_j = c_{ij}/c_{cj}$ and $\eta_s = c_{is}/c_{cs}$. About one percent of helium in air by volume was used. For each test forty-eight samples were measured with a katharometer. They were selected automatically every 20 s by a multi-port valve at a sampling flow of 2.5 cm³/s. The samples were drawn from the test specimen through the valve, katharometer and rotameter by a vacuum pump.

EXPERIMENTAL MEASUREMENTS

The results of the preliminary calibration and verification experiments are summarised briefly in (2). Table 1 summarises the airflow conditions, tests and geometries. The measurement positions and the estimated 95 percent confidence intervals for the velocity and turbulence intensity profiles, and the tuft and effectiveness measurements are given below.

TABLE 1 Airflow conditions, tests and geometries

$U_m/(m/s)$	16 (Ma = 0.05)								x_{sj}/mm	x_{jp}/mm	
$U_g/(m/s)$	0		16		24						
M_s	0.5		1.0		1.5						
$U_j/(m/s)$	0	16	32	4	16	32	0	16	32		
M_j	0.5		1.0	2.0	0.5	1.0	2.0	0.5	1.0	2.0	
(a)	+				+					25.0	0
(a)	§*			§*	§*	§*		§*	§*	25.0	0 5.0 10.0
(a)	§										2.5
(b)	§	§	§	§	§	§	§	§	§	25.0	0 5.0 10.0
(b)						*		+		25.0	0* 10.0*
(c)	§*	§*	§*	§*	§*	§*	§*	§*	§*	25.0	0 5.0 10.0
(c)		§		§	§*	§*		§*		50.0	75.0 0
(c)		§		§	§	§		§		25.0	2.5 7.5
(c)					§*					50.0	75.0 5.0 10.0
(d)		§*			§*			§*		25.0	300

§ Reported in (1)

§* Test

(a) Velocity and turbulence measurements

(c) η_g and η_j measurements

* Reported here

+ Reported in (2)

(b) Tuft measurements

(d) η_s measurements, $U_j = 0$

The pressure gradient is zero in the working section with no slot or jet airflow present.

Measurement Positions (all dimensions in mm)

(a) $x = 43.3, 75.0, 100.0$ and 187.5 ; $y = 0$, and $0 < z < 100$. (b) As (a) but $y = 0$ and every 25 up to 100, and wool tufts every 10 with z and immediately upstream, downstream and on either side of the jet exit. For a few tests a cotton thread was used at more positions. (c) and (d) A selection of 45 coordinates from an intersecting grid of x every 6.25 up to 75, every 12.5 up to 125 and then every 25.0 up to 187.5; and $y = 0$ and every ± 12.5 up to ± 50 .

Estimates of 95 Percent Uncertainty Intervals

$U_m < 0.1$ percent; U_s and $M_s < 2$ percent; U_j and $M_j < 3$ percent; $\beta < 5^\circ$; η_j and $\eta_s < 1$ percent; $\eta_{sj} < 2$ percent; x , y and $z < 0.1$ mm and low turbulence intensity < 12 percent. For turbulence intensities of 10, 25 and 50 percent based on (3) the uncertainties are 10.4, 12.5 and 20.0 percent respectively.

DISCUSSION OF RESULTS

Tufts

Like the results in (2) for $z_{jp}/D = 0$, these results for $z_{jp}/D = 0.2$ and 0.4 provide some indication of the direction and extent of the separate and combined airflows at the different test conditions. They show that increasing z_{jp}/D increases the jet penetration for a given combination of M_j and M_s , and show which airflow enters underneath the trajectory of the jet airflow. It is mainly slot airflow when $z_{jp}/D = 0.2$ and when $z_{jp}/D = 0.4$ it is main airflow as well. The most significant contribution by the wool tuft results, and confirmed for some cases by using a cotton thread, is the position and size of the zone where reverse flows occur downstream of the jet, e.g. see figure 2. Some of the other detailed results are included in the subsequent sections where they assist in understanding the interacting airflows.

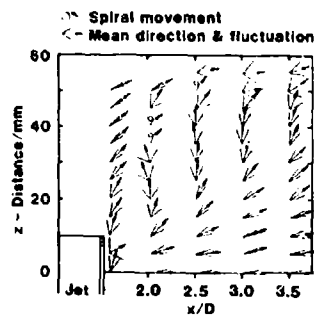


Figure 2 Sketch of cotton threads for $z_{sj}/D = 1.0$, $y/D = 0$ and $z_{jp}/D = 0.4$ for $M_s = 1.0$ and $M_j = 2.0$

Velocity and Turbulence Intensity Profiles

Velocity and Turbulence Intensity Profiles for Slot Geometry. Figure 3 shows the type of velocity and turbulence profiles that can be expected to approach the jet airflows as they issue from the wall ($z_{jp}/D = 0$), or the wall plunging ($z_{jp}/D = 0.2$ and 0.4). These profiles can only be an indication, because at the three downstream positions ($x/D = 1, 2$ and 3) they are measured without the jet being present; similarly for $x/D = 0$ for the boundary layer above the slot, the slot was not present. On figure 3, the height of the wall plunging is shown in relation to the superimposed cross-sectional drawing of the slot.

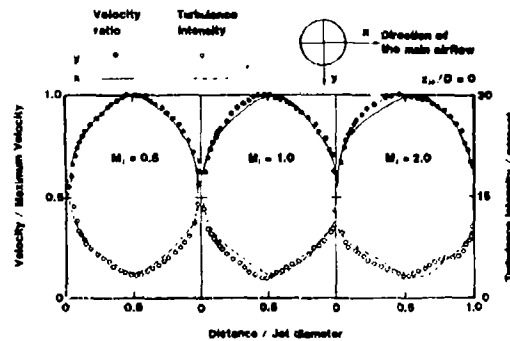
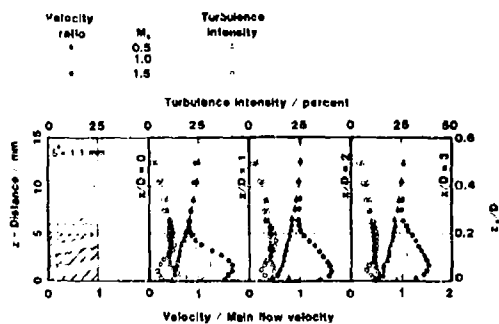


Figure 3 Velocity and turbulent intensity profiles with x/D and z for $y/D = 0$ and variations in M_s Figure 4 Velocity and turbulent intensity profiles with x/D and y/D for variations in M_j

At $x/D = 0$ the profiles are for the turbulent boundary layer generated by the trip wire upstream of the slot exit. As this boundary layer airflow moves downstream, it mixes and so contributes to the development of the slot airflow. For $z_{jp}/D = 0$, the approaching airflow is always boundary layerlike when $M_s = 0.5$ and wall jetlike when $M_s = 1.0$ and 1.5 . For $z_{jp}/D = 0.2$, the jet exit plane is almost level with the top of the slot, so except for small changes due to increases in M_s , the approaching airflow is predominantly the main airflow slightly modified by the turbulence boundary layer from above the slot exit. For $z_{jp}/D = 0.4$ the jet exit plane is almost in the uniform velocity and turbulent region of the main airflow.

Velocity and Turbulence Intensity Profiles for Jet Geometry. These are shown in figure 4 at two mutually perpendicular diameters in the jet exit plane for jet mass velocity ratios of 0.5, 1.0 and 2.0. The velocity and turbulence profiles are similar to fully developed turbulent pipe flow. In the y direction the profiles are symmetrical about the jet centreline, but in the x direction they are not because of a right-angled bend upstream of the jet exit.

Velocity and Turbulence Intensity Profiles for Combined Slot and Jet Geometries. For a limited number of flow conditions, these profiles quantify and show clearly and in more details than with wool tufts, many features of the jet airflows.

Figure 5 shows how the resultant airflow from the jet at $M_j = 1.0$ and the slot at $M_s = 1.0$ changes as the wall plunging increases from $z_{jp}/D = 0$ to 0.2 and 0.4. At $x/D = 1.72$ there is a region of low velocity and high turbulence intensity which is characteristic of wake flow and increases in depth from the wall as z_{jp}/D increases. Above this region, the velocity profiles are similar to the fully developed pipe flow of the entering jet airflow; but distorted downwards and accelerated. The turbulence intensity "peaks" above and below these profiles at the mixing region between the top of the jet airflow and the main airflow, and between the bottom of the jet airflow and the slot and/or main airflows. The velocity of the airflow in the wakes for $z_{jp} = 0.2$ and 0.4 are higher than for $z_{jp} = 0$ and the turbulence intensities lower, probably because the slot airflow can pass more easily round the wall plunging than the interacting jet airflow. There is little difference between the velocities in the wakes for the wall plungings because they are deeper than the slot airflow (figure 3). However the turbulence intensity is lower for $z_{jp}/D = 0.2$ probably because the interaction is between the slot and jet airflows, whereas for $z_{jp}/D = 0.4$ it is between the jet, slot and main airflows.

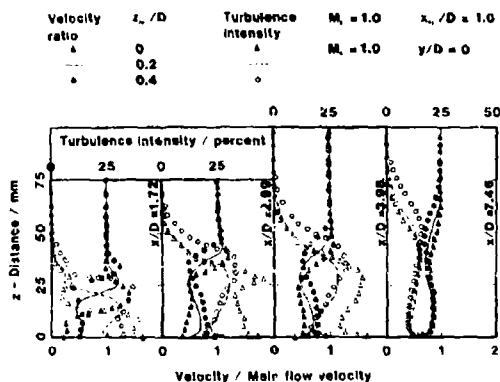


Figure 5 Velocity and turbulence intensity profile with x/D and z for $M_s = M_j = 1.0$, $y/D = 0$, and variations in z_{jp}/D

At $x/D = 2.99$ for $z_{jp}/D = 0$ the wake is deeper and has a slightly higher velocity but the airflow above it has decelerated considerably. For $z_{jp}/D = 0.2$ and 0.4 the velocity profiles close to the wall are no longer wakelike but are wall jetlike with an associated reduction in turbulence intensity, indicating that the slot airflow coming around the wakes has reestablished at the centre line. As might be expected, the velocity for $z_{jp}/D = 0.4$ is larger than for $z_{jp}/D = 0.2$ because it is easier for the slot airflow to enter underneath a jet airflow which is further above the wall. With the jet penetration and spread increasing into the same main airflow conditions, the difference between the maximum velocities is reduced. From the tuft results for $z_{jp} = 0$ at $z = 10, 20$ and 30 mm, $\beta = 30, 10$ and 5°, these correspond to $\beta = 30, 20, 15$ ° for $z_{jp} = 0.2$ and to $\beta = 40, 40$ and 20° for $z_{jp}/D = 0.4$.

From $x/D = 2.99$ to 7.46, the development of the resultant airflows can be divided into two regions, one above and the other below the locus of the maximum turbulence intensity away from the wall. Above the locus, the mixing of the main and the jet airflows continues to move outwards, moving in this direction, the local airflow velocities first increase and then decrease. Below the locus, as z_{jp}/D decreases, the amount of the airflow reaching the centre line increases. Close to the wall the wakelike airflow for $z_{jp}/D = 0$ becomes wall jetlike as the velocity increases and the turbulence decreases. For $z_{jp}/D = 0.2$ and 0.4 the form of the profiles is wall jetlike and does not change with increasing x/D . Further downstream at $x/D = 3.98$ wool tufts show that the airflow is still moving away from the wall. For $z_{jp}/D = 0$ at $z = 10, 20, 30, 40$ and 50 mm, $\beta = 20, 20, 10, 5$ and 5°, these correspond to $\beta = 20, 30, 20, 10$ and 5° for $z_{jp}/D = 0.2$ and to $\beta = 20, 30, 30, 15$ and 5° for $z_{jp}/D = 0.4$. Between $x/D = 3.98$ and 7.46 and below $z = 30$ mm, the velocity and turbulence intensity profiles undergo a significant development towards those for a turbulent boundary layerlike flow. Above this height, the mixing region continues to spread upwards into the main airflow and has reached $z = 70$ mm at $x/D = 7.46$. At this position, $\beta = 10$ ° for all z .

Figure 6a shows that the penetration of the jet airflow is not altered significantly by increasing M_s from 0.5 to 1.5 for $z_{jp}/D = 0.2$ at $M_j = 1.0$. This is because the jet exit is above the slot airflow and the predominantly main airflow is not altered by increases in M_s , see figure 3. However, at any x/D the amount of airflow below the mixing region increases with M_s . This probably arises because as the jet airflow moves away from the wall, the slot airflow moves into and behind the wake downstream of the wall plunging. For $z_{jp}/D = 0.4$, see figure 6b, the distance from the wall to the mixing region is by comparison everywhere longer than for the corresponding x/D for $z_{jp}/D = 0.2$. The penetration of the jet airflow is again not altered significantly with M_s because the jet airflow issues into the uniform main airflow, but a trend with M_s is discernable between $x/D = 1.72$ and 3.98. At $x/D = 1.72$ it is likely that the turning distorted jet

airflow is drawn towards the wall as M_s decreases because less air is available to fill the wake. This lack of air is noticeable particularly at the wall for $M_s = 0.5$ at $x/D = 2.99$.

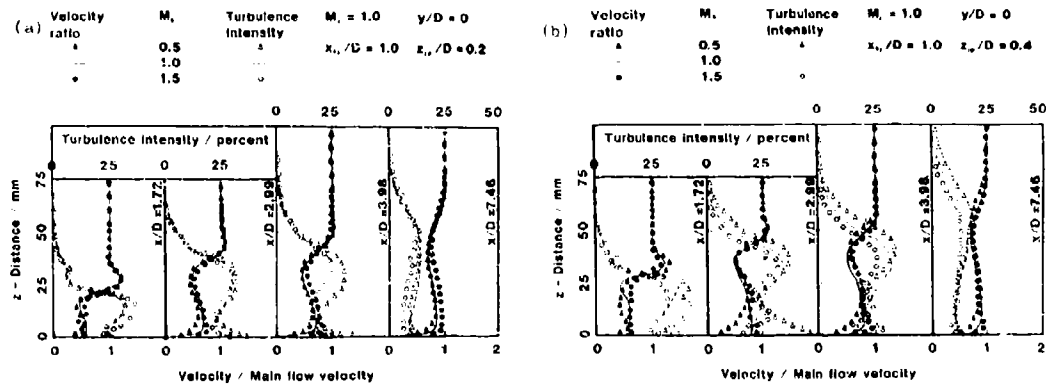


Figure 6 Velocity and turbulence intensity profiles with x/D and z for $x_{sj}/D = 1.0$, $y/D = 0$, $M_j = 1.0$, variations in M_s and (a) $z_{jp}/D = 0.2$ and (b) $z_{jp}/D = 0.4$

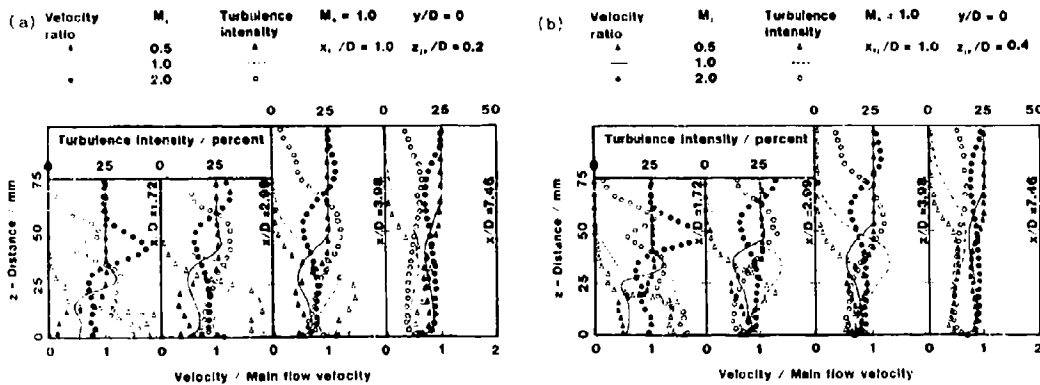


Figure 7 Velocity and turbulence intensity profiles with x/D and z for $x_{sj}/D = 1.0$, $y/D = 0$, $M_s = 1.0$, variations in M_j and (a) $z_{jp}/D = 0.2$ and (b) $z_{jp}/D = 0.4$

Figures 7a and b show that the resultant airflow changes are considerable as M_j increases. Figure 7a shows at $x/D = 1.72$ the velocity of the airflow in the wake increases as M_j increases, indicating it is easier for the slot and main airflows to enter underneath the jet airflows. By $x/D = 2.99$ the velocity and turbulence intensity profiles are similar for $M_j = 1.0$ and 2.0 and close to the wall they are boundary layerlike, but for $M_j = 0.5$ wakelike flow exists at least to $x/D = 3.98$. The development of the airflows close to the wall for $z_{jp}/D = 0.4$ shown by figure 7b is more rapid because the jet exit is further from the wall. Also the higher wall plunging guides the slot and main airflows into the wake as shown at $x/D = 1.72$. This is particularly noticeable for $M_j = 2.0$ where the velocity profile retains its wall jetlike profile at a velocity ratio of nearly one. Between $x/D = 1.72$ and 2.99 the developments of the airflows close to the wall are nearly complete; the airflow for $M_j = 0.5$ needing a further distance to achieve the same development as the other two.

Effectiveness

Included in figures 8 to 10 are the effectiveness results for the slot without the jet, and the jet without the slot, i.e. a flat surface from the trip wire to the jet. These are respectively referred to as the "slot alone" or the "jet alone". It is relevant to note that by presenting η_j , η_s and in effect $1 - \eta_{sj}$, the composition of the resultant airflow at the wall can be apportioned to the jet, slot and main airflows respectively.

Variations with Wall Plunge Height. The main features of figures 8, 9 and 10 are discussed first. These provide an overview of how increasing z_{jp} from 0 to 0.2 and 0.4 alter η_j , η_s and η_{sj} with x/D , M_s and M_j for $x_{sj}/D = 1$ and $y/D = 0$.

In general, increasing z_{jp}/D decreases η_j (figure 8) because the jet exit is lifted above the wall, increases η_s (figure 9) because the slot airflow can enter between the wall and the underside of the jet airflow, and decreases η_{sj} (figure 10) for $M_j = 0.5$ and 1.0 but increases η_{sj} for $M_j = 2.0$. The wakes formed downstream of the wall plunging seem to extend to about $x/D = 4$, e.g. see the η_j and η_s for $z_{jp} = 0.2$ and 0.4 when $M_s = 1.0$ and $M_j = 0.5$ on figures 8 and 9 respectively. Downstream of the wake, all the results for η_j and η_s with x/D decrease slightly or are constant. With a few exceptions, all the large changes for

η_j and η_s with x/D occur in the wake region downstream of the wall plunging. Only when $M_j = 0.5$ and $z_{jp}/D = 0$ or 0.2 are the η_{sj} results similar to those for the slot alone, otherwise they are lower by more than 0.2.

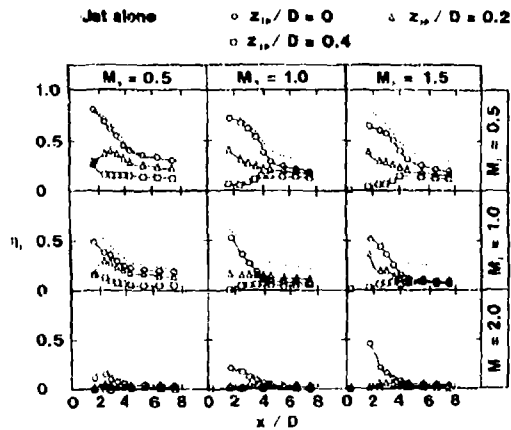


Figure 8 η_j with x/D for $x_{sj}/D = 1.0$, $y/D = 0$ and variations in z_{jp}/D , M_s and M_j

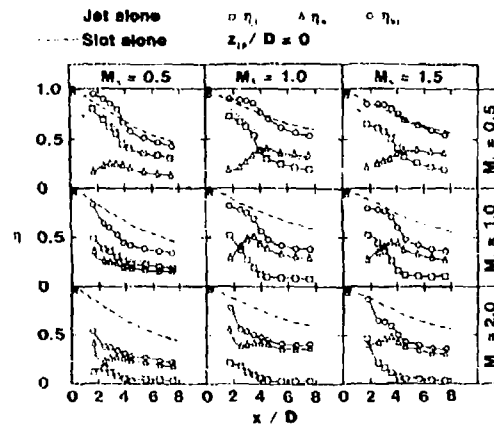


Figure 11 η_j , η_s and η_{sj} with x/D for $x_{sj}/D = 1.0$, $y/D = 0$, $z_{jp}/D = 0$ and variations in M_s and M_j

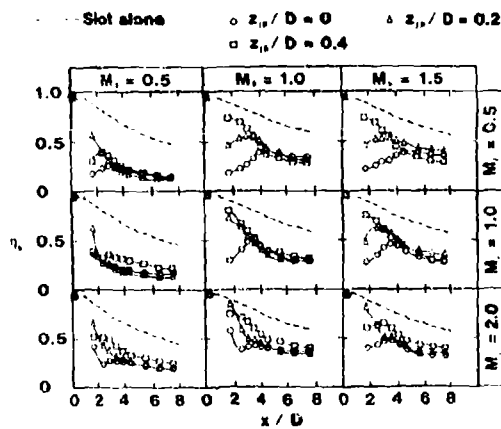


Figure 9 η_s with x/D for $x_{sj}/D = 1.0$, $y/D = 0$ and variations in z_{jp}/D , M_s and M_j

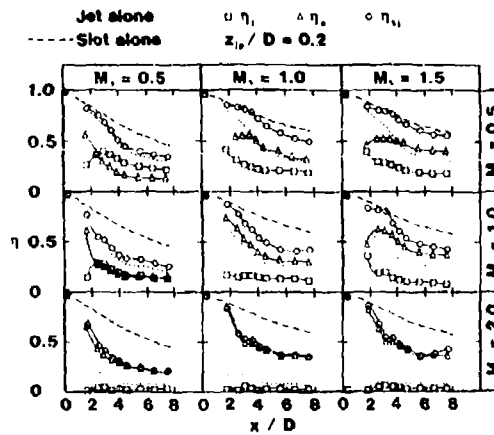


Figure 12 η_j , η_s and η_{sj} with x/D for $x_{sj}/D = 1.0$, $y/D = 0$, $z_{jp}/D = 0.2$ and variations in M_s and M_j

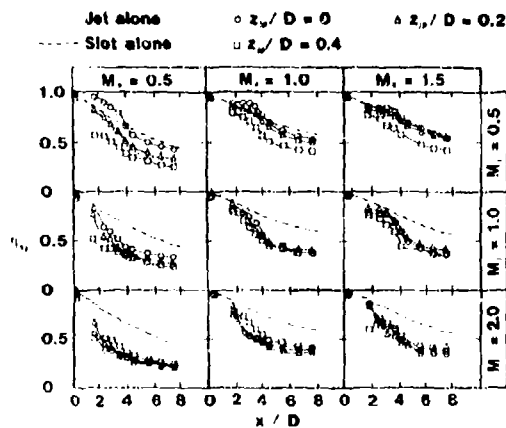


Figure 10 η_{sj} with x/D for $x_{sj}/D = 1.0$, $y/D = 0$ and variations in z_{jp}/D , M_s and M_j

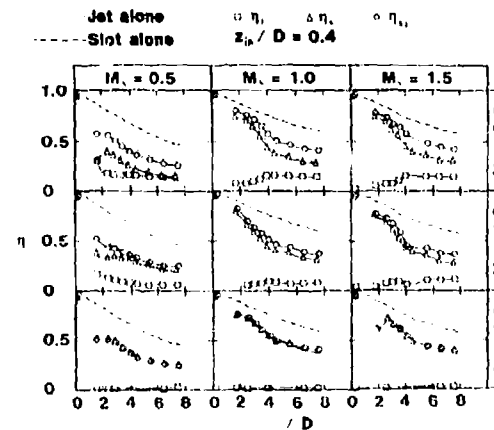


Figure 13 η_j , η_s and η_{sj} with x/D for $x_{sj}/D = 1.0$, $y/D = 0$, $z_{jp}/D = 0.4$ and variations in M_s and M_j

Figures 11, 12 and 13 are included to provide an overview of the contribution of η_j and η_s to η_{sj} , with x/D , M_s and M_j for $x_{sj}/D = 1$ and $y/D = 0$, when $z_{jp}/D = 0, 0.2$ and 0.4 respectively. After a general description of these results, during which a number of trends will be identified, a detailed discussion of the results for $z_{jp}/D = 0.2$ with x/D and y/D will follow.

For $z_{jp}/D = 0$, figure 11 shows that except for the wake zone for $M_j = 0.5$, the η_{sj} results are lower than the corresponding results for the slot alone. If the results at $x/D = 1.72$ and $M_j = 2.0$ are excluded with those for $M_s = 0.5$ and $M_j = 1.0$, then the trend of η_j with x/D always decreases and the trend for η_s always has a maximum at the end of the wake zone where x/D is between 3 and 4. The contribution of η_s to η_{sj} is generally lower when the slot airflow is boundary layerlike ($M_s = 0.5$) than when it is wall jetlike ($M_s = 1.0$ and 1.5).

For $z_{jp}/D = 0.2$, figure 12 shows that close to the jet exit the η_{sj} results are the same or slightly lower than those for the slot alone. Further downstream, the differences increase with x/D and M_j , by about 0.3 at $M_j = 2.0$. The trends for η_j and η_s with x/D , when $M_s = 1.0$ and 1.5 with $M_j = 0.5$ and $M_s = 1.5$ with $M_j = 1.0$, are the same as those for $z_{jp}/D = 0$. For all the other results, the trend is for η_s to decrease with x/D . When $M_s = M_j = 1.0$, the trend is for η_j to decrease with x/D . The trend for the remaining η_j results with x/D show η_j is a maximum at about $x/D = 3$; when $M_j = 2.0$ this is just discernible. The contribution of η_j to η_{sj} decreases as M_j increases.

For $z_{jp}/D = 0.4$, figure 13 shows that the results for η_{sj} with x/D are similar when the slot airflow is wall jetlike ($M_s = 1.0$ and 1.5), and similar but lower when the slot airflow is boundary layerlike ($M_s = 0.5$). When $M_s = 0.5$ with $M_j = 0.5$ and 1.0 the trends in η_j and η_s are the same as those described for $z_{jp}/D = 0$; excluding the results at $x/D = 1.72$ for $M_j = 1.0$. All the other results for η_s decrease with x/D . The results for η_s , when they are not zero ($M_j = 2.0$) first increase and then become constant.

Wall Plunge Height of 0.2. Figure 14 shows that the results for η_j with x/D and y/D resemble a "long sloping mound". The slot airflow has caused all the results to be lower than those for the jet alone. Large differences occur in the wake region, e.g. see figure 5, which extends downstream of the jet exit to about $x/D = 4$. Downstream of this the developments of the jet airflows are similar. For all the results some of the jet airflow remains in contact with the wall, even though it is only just discernible when $M_j = 2.0$ and $x/D > 4$.

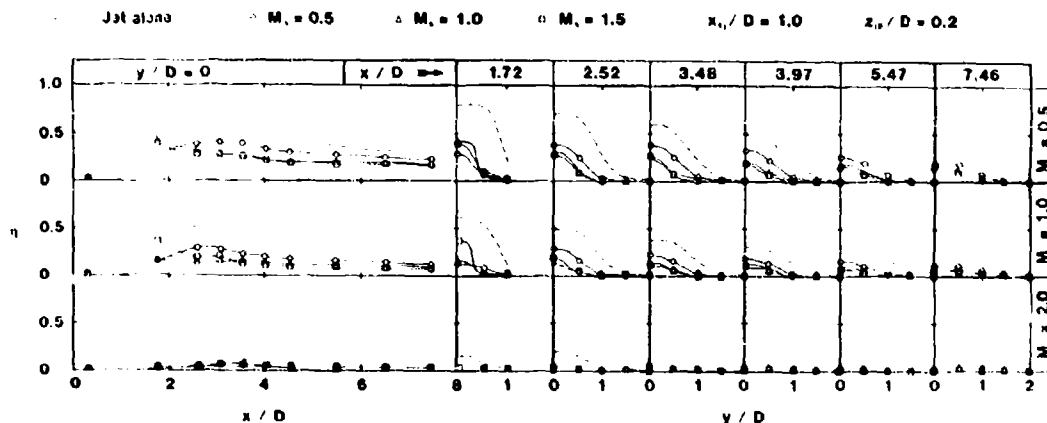


Figure 14 η_j with x/D and y/D for $x_{sj}/D = 1.0$, $z_{jp}/D = 0.2$ and variations in M_s and M_j

The results for η_j with x/D and y/D for $M_j = 0.5$ and $M_s = 1.0$ and 1.5 are almost identical and similar to those for $M_s = 1.5$ and $M_j = 1.0$. The decrease in η_j with x/D indicates the jet airflow is spreading as it moves downstream and away from the wall. For $M_s = M_j = 0.5$, η_j has a maximum at $x/D = 3$. This is consistent with the jet airflow being drawn down to the wall as it spreads and moves downstream. For $M_s = M_j = 0$, η_j with x/D is almost constant. This is because the mean velocity of the jet, slot and mean airflows are the same.

Figure 15 shows that η_s with x/D and y/D resembles a "valley" when compared to η_s for the slot alone. For $M_j = 0.5$ and $M_s = 1.0$ at $y/D = 0$ and $x/D = 3$, η_s is a maximum. This position is about coincident with the end of the wake. It is suggested that the increases in η_s which occur up to $x/D = 3.48$ and extend to about $y/D = 0.5$ are caused by the slot airflow as it moves downstream entering progressively the sides of the wake. After which the slot airflow moves in behind the wake and underneath the developing airflow. The same trends occur for η_s when $M_s = 1.5$ and $M_j = 0.5$ and 1.0 .

For all the other results η_s decreases more rapidly with x/D at $y/D = 0$ than for the slot alone. This is probably because the slot airflow not only mixes with the main airflow but it moves underneath and mixes with the jet airflow as well. Downstream of the wake for $M_j = 1.0$ and $M_s = 0.5$ air is drawn up underneath the jet airflow as it moves away from the wall, and this extends beyond $y/D = 2.0$ for $x/D = 5.47$ to 7.46 . The trend is more pronounced for $M_j = 2.0$. For $M_j = 1.0$ and 2.0 for $M_s = 1.0$ it is less pronounced because the horizontal momentum of the slot airflow is greater, and so less likely to be drawn up underneath the jet airflow, e.g. see η_s with y/D at $x/D = 7.46$ compared to the corresponding conditions for $M_s = 0.5$.

Another trend present in nearly all the results is for $y/D > 1$ when η_s with y/D is higher than η_s for the slot alone, e.g. when $M_s = M_j = 0.5$ at $x/D = 2.52$ to 7.46. This is an indication that the slot airflow is forced to move out at the wall and go around the obstruction caused by the wall plunging and the jet airflow.

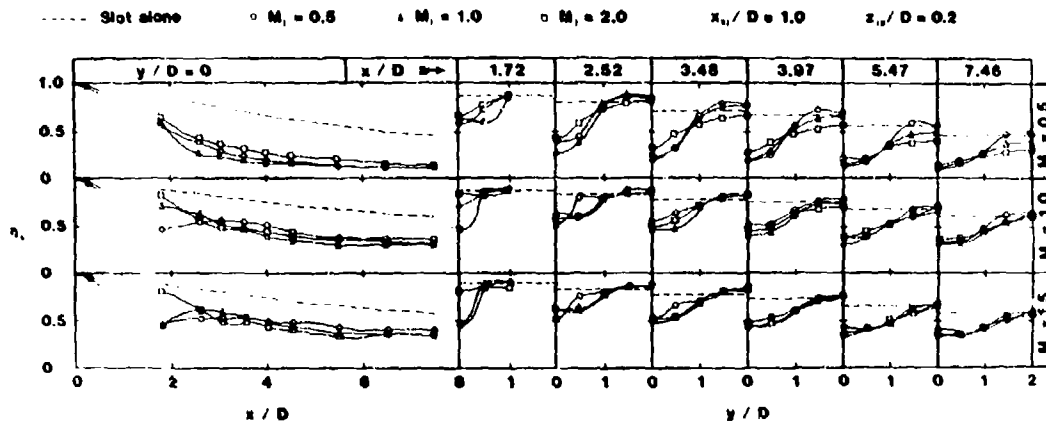


Figure 15 η_s with x/D and y/D for $x_{sj}/D = 1.0$, $z_{jp}/D = 0.2$ and variations in M_s and M_j

At $x/D = 1.72$ for $M_j = 2.0$ and $M_s = 1.0$ and 1.5 η_s is constant with y/D , whereas at $x/D = 2.52$ there is evidence of a wake. This is consistent with the slot airflow being drawn up behind the jet airflow, see figure 2.

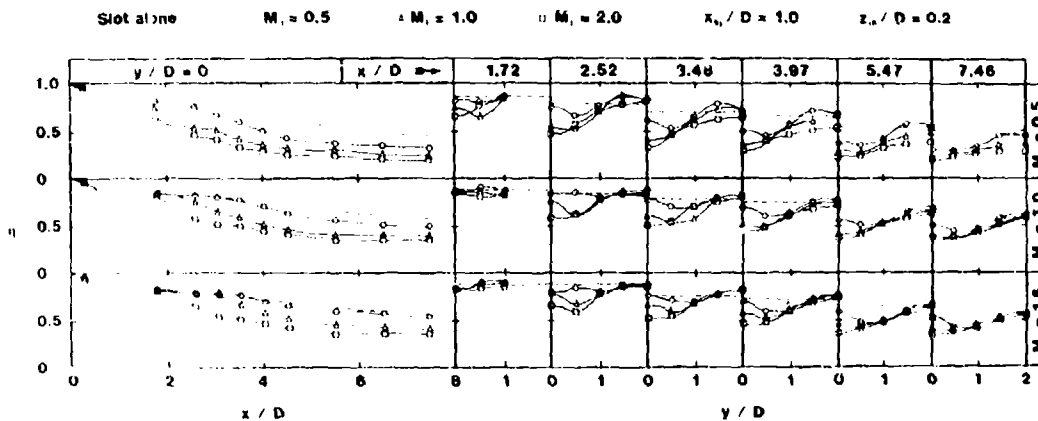


Figure 16 η_{sj} with x/D and y/D for $x_{sj}/D = 1.0$, $z_{jp}/D = 0.2$ and variations in M_s and M_j

All the η_{sj} results with x/D at $y/D = 0$ shown by figure 16 have the same trend and are lower than the corresponding results for the slot alone. Increasing M_j always decreases η_{sj} . At other y/D s there are some instances where η_{sj} is lower and higher than for η_s for the slot alone, e.g. when $M_j = M_s = 0.5$ at $x/D = 2.48$. Only for the results for $M_s = 0.5$ and $M_j = 1.0$ and 2.0 does the jet airflow disrupt the slot airflow beyond $y/D = 2$.

Wall Plunge Heights of 0.4 and 1.2. To examine the effect of increasing z_{jp}/D above 0.4 a limited number of tests were undertaken with the wall plunging extended to become a cylinder from the base to the roof of the working section, i.e. $z_{jp}/D = 1.2$ and $M_j = 0$. These results for η_s are shown in figure 17 with x/D and y/D for $M_s = 0.5, 1.0$ and 1.5. These results are compared to the corresponding η_s results for $z_{jp}/D = 0.4$ and $M_j = 2.0$, where the jet airflow does not provide any of the airflow adjacent to the wall, i.e. $\eta_j = 0$ and so $\eta_{sj} = \eta_s$ (see figure 13). Nevertheless the airflow adjacent to the wall is affected by the jet airflow. This is very evident for $M_s = 0.5$ at $y/D = 0$ and $x/D = 1.72$ and 2.52. The differences are due to the wake downstream of the cylinder extending along its whole length, whereas the wake for the wall plunging only extends below the jet airflow as it moves away from the wall; see figure 7a at $x/D = 1.72$ for $M_j = 2.0$ and although for $M_s = 1.0$ and not $M_s = 0.5$ it will represent the type of airflow adjacent to the wall. Thus the wake downstream of the wall plunging can be filled from above by the main airflow entering underneath the jet airflow, but the wake for the cylinder can only enter from the sides. The jet airflow also draws up air as

It moves away from the wall causing η_s for the cylinder to become larger off the centre line than for $z_{jp}/D = 0.4$ as x/D increases, see figure 17 at $x/D = 3.48$ to 7.46 . At $x/D = 5.47$ and 7.46 the η_s results for $M_s = 0.5$ when compared to those for the slot alone show that the disturbance caused by the cylinder and the wall plunging extend beyond $y/D = 2$.

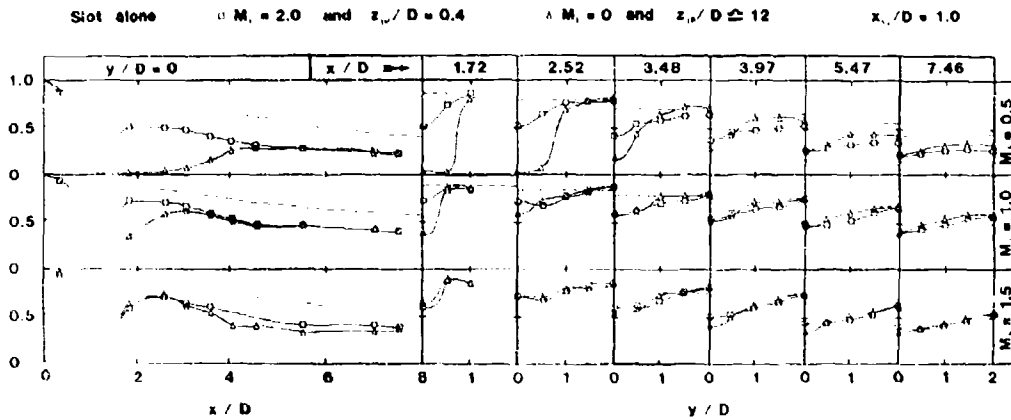


Figure 17 η_s with x/D and y/D for $z_{jp}/D = 0.4$ and $M_j = 2.0$ and $z_{jp}/D = 12$ and $M_j = 0$

The effect of the jet, compared with the cylinder is to increase η_s immediately downstream of the jet, the effect being greater for $M_s = 0.5$ and 1.0 . At $x/D = 1.72$ the results with y/D show that as η_s increases, the wake size downstream decreases. At positions off the centre line the entrainment of air by the jet acts to reduce η_s for x/D from 3.48 to 7.46 ; the effect being greater for lower M_s .

Variations with Downstream Distances of Jet Centre Line from Slot Exit and Wall Plunge Height. The effect of moving the jet further downstream of the slot exit from $x_{sj}/D = 1$ to 2 and 3 on η_{sj} , with x/D at $y/D = 0$ and for $z_{jp}/D = 0$ and 0.2 at $M_s = M_j = 1.0$ is shown by figure 18. The η_{sj} results for $z_{jp}/D = 0.4$ are not included because they are very similar to those for $z_{jp}/D = 0.2$.

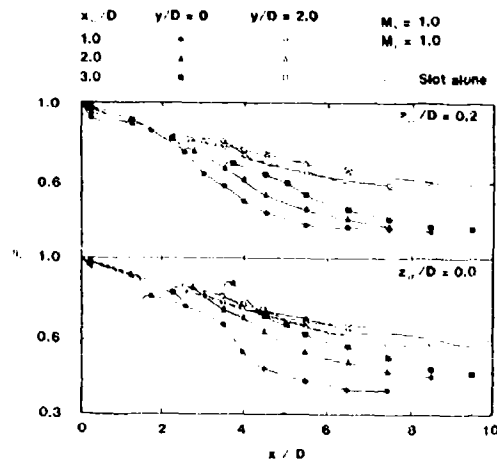


Figure 18 η_{sj} with x/D and $y/D = 0$ and $y/D = 2.0$, $M_s = M_j = 1.0$ and variations in x_{sj}/D for $z_{jp}/D = 0$ and 0.2

For $z_{jp}/D = 0$ and 0.2 at $y/D = 0$ the η_{sj} results for increases in x_{sj}/D move closer to (or exceed $z_{jp}/D = 0$ for $x_{sj}/D = 2$ and 3 just downstream of the jet exit) those for the slot alone. In general, this is because adjacent to the wall more of the slot airflow upstream of the jet is undisturbed and there is less slot airflow downstream to be disturbed. For $z_{jp}/D = 0$ η_{sj} is greater than η_s for the slot alone because the contribution of η_j increases with increases in x_{sj}/D jet downstream of the jet exit. Figure 3 gives some indication of how the slot airflow at the wall is reduced and develops as it approaches the jet exit for $x_{sj}/D = 1$ to 3 . For $x_{sj}/D \geq 2$ at $y/D = 2$ the η_{sj} results are greater than those for the slot alone for $z_{jp}/D = 0$ and 0.2 . This indicates that obstruction to the slot airflow caused by the jet airflow with or without plunging is wider.

CONCLUSIONS

1. Experimental data showing the interaction of the jet and slot airflows, with and without plunging, and at three slot exit to jet centre line distances (x_{sj}) have been presented and some significant features discussed. In addition the separate contributions of the slot and jet airflows to the effectiveness are shown.

2. As is well known, the penetration of the jet into the mainstream increases with the jet mass velocity ratio (M_j) and as expected also with wall plunging height (z_{jp}/D).

3. The results show that the major interactions between the three airflows occur in a small region just downstream of the jet centre line (3 D long by ± 1 D wide).

4. The effect of wall plunging is to increase the combined slot and jet effectiveness (η_{sj}) for large jet mass velocity ratios (i.e. $M_j = 2.0$) but to reduce it for $M_j = 1.0$ and 1.5.

5. For most practical combustors, where $M_j \gg 2$ and the slot mass velocity ratio ($M_s > 1$), η_{sj} is lower than the undisturbed slot effectiveness (η_s) by about 0.3. Under these conditions increasing the wall plunging height (z_{jp}/D) appears to give a small increase in η_{sj} . Although increasing z_{jp}/D beyond 0.4 is not likely to be beneficial.

Based on results for $M_s = M_j = 1$ the effect of the jet upon η_{sj} can be reduced by increasing the slot exit to jet centre line distance (x_{sj}/D).

ACKNOWLEDGMENTS

The research reported here was carried out in the Department of Mechanical Engineering at Coventry (Lanchester) Polytechnic with a grant from the Science and Engineering Research Council. The use of the facilities and the financial support are gratefully acknowledged. The help given by Mr. B.M. Robbins, Mr. J. Grimes and Mr. S. Kapasi in preparing this paper was invaluable.

REFERENCES

1. Button, B.L., **Jet Penetration of a Cooling Film**. PhD thesis, CHAA - Coventry (Lanchester) Polytechnic, 1980.
2. Button, B.L., Effectiveness Measurements for a Cooling Film Disrupted by a Single Jet. **Journal of Engineering for Gas Turbine and Power**, 106, 1984, 606-611.
3. Ramsey, J.W., **The Interaction of a Heated Air Jet with a Deflecting Flow**. PhD thesis, University of Minnesota, 1969.

DISCUSSION

R. Eggebrecht, Gc

- (1) Can you please quote absolute values of concentration rates for injection?
- (2) Did you measure local concentrations and what percentage of fluid flow was sucked for measurements?
- (3) Finally, can you please quote the typical range of measurement errors?

Author's Reply

- (1) One percent by volume for helium.
- (2) There were 48 tappings three of which we used for reference (cyclic every 20 seconds). The suction rate was 2.5 cm³/s although I did explore a range of a factor of 10 on that - 2 up to 2.5 cm³/s to see whether taking it away from the wall had any bearing on it - and it did not. So I am satisfied.
- (3) On all the work we do we estimate the uncertainty on all the measured quantities and we calculate it on all those coming out. The results are all given in the paper.

S. Wittig, Gc

In correlating your data you use the mass velocity ratio. It seems, however, that the impulse ratio is the proper parameter as has been used in the work by Cox et al. as well as in our own work. Which approach is to be preferred?

Author's Reply

No attempt has been made to regress the experimental data, only to describe the phenomena. The mass velocity ratios have been used to identify the experimental levels for the slot and jet airflow. The choice of mass velocity or momentum would not affect the presentation of the data. If regression of data is to be attempted it should be based on a model which could include four features of the interacting flows. These would include: boundary layerlike and wall jetlike features and when the jet airflow does and does not lift off from the wall. For the slot airflow the mass velocity ratio would be appropriate. However for the jet airflow, its distance from the wall influences its contribution to the cooling at the wall. Therefore the momentum ratio would be appropriate.

ALTERNATE COOLING CONFIGURATIONS FOR GAS TURBINE COMBUSTION SYSTEMS

D. A. Nealy, S. B. Reidor, and H. C. Mongia
Allison Gas Turbine Division
General Motors Corporation
Indianapolis, Indiana

SUMMARY

The purpose of this paper is to briefly review some of the work at Allison that has been aimed at the synthesis, characterization, and evaluation of several alternate types of advanced wall cooling schemes — specifically, film-convection cooling, laminated porous wall cooling, and angled, multihole (effusion) cooling. The concept definition, heat transfer performance characterization, and design problems associated with each basic concept will be reviewed, and relevant rig and engine experience will be cited. A brief assessment of the structural limitations of the several cooling schemes will also be made, together with a review of the key materials and fabrication considerations.

I. INTRODUCTION

Over the past 15 years, the problem of combustor liner cooling has received increasing attention. This trend reflects the continuing emphasis on turbine engine component performance improvement, as well as the concern regarding durability and service life depreciation as operating temperatures are increased. Although attention to cooling problems has traditionally been focused on the high pressure (HP) turbine for obvious reasons, combustor liner cooling should be viewed as a technical problem of at least equal importance, and one which must be systematically addressed if projected performance gains and durability improvements (in both combustor and turbine components) are to be achieved.

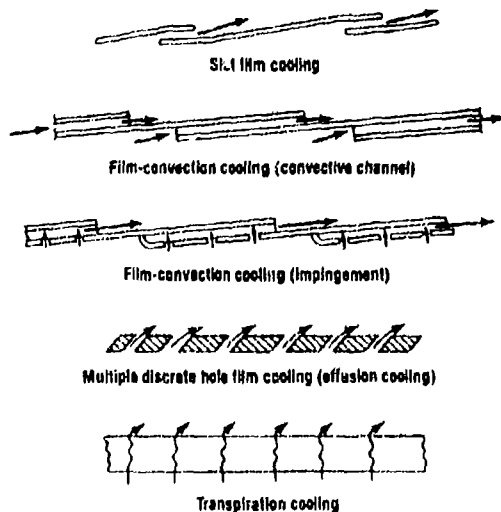
At the comparatively modest burner outlet temperature (BOT) levels typical of all but the most recent production turbine engines (BOT $\leq 1510\text{K}$), experience has shown that liner wall cooling could be effectively achieved with simple film cooling from slots and louvers. In this situation, relatively massive tangential slot flows provide sufficient gas side cooling air film protection so that gas to wall heat flux levels can be reduced to manageable levels. The system has the inherent advantage of simplicity, and fabrication techniques are well in hand. Furthermore, the large tangential slot flows tend to produce a more nearly two-dimensional (2-D) flow situation in the near wall region, masking to some extent the troublesome three-dimensional (3-D) flow field effects always present in combustors.

The principal disadvantage of the pure film cooling approach is that the heat sink potential of the cooling air (in terms of active wall cooling) is not effectively utilized, and cooling air flows represent a significant portion of the total flow entering the combustor — often as much as 50 or 60% of the total. This situation becomes aggravated as burner outlet temperatures are progressively increased because the percentage of total airflow required to support combustion (and effectively control burner pattern) soon exceeds that which is available. Consequently, attention must be focused on wall cooling schemes that make more efficient use of cooling air, allowing the designer more latitude in overall secondary airflow management.

The purpose of this paper is to briefly review some of the work at Allison that has been aimed at the synthesis, characterization, and evaluation of three alternate types of advanced wall cooling schemes: film-convection cooling, transpiration cooling, and effusion cooling. In the material to follow, the concept definition, heat transfer performance characterization, and design problems associated with each basic concept will be reviewed, and relevant engine experience will be cited.

II. GENERAL LINER COOLING CONSIDERATIONS

The principal schemes, which, reflecting practical considerations, represent candidate approaches to combustor liner wall cooling, are shown conceptually in Figure 1. As stated in the Introduction, simple slot film cooling has traditionally received the most attention both in terms of application and fundamental studies. Because the integrity of the slot air film is the key to cooling performance in these systems, most fundamental work has been focused on characterization of slot jet interaction with the wall and the mainstream, and the extent to which mixing destroys the insulating effect of the air film. These studies range from characterization of asymptotic (far downstream) behavior in low turbulence situations (Ref 1-4) to more detailed studies of flow/heat transfer behavior in the near slot region, including the effects of slot geometry and mainstream turbulence (Ref 5-11). More recently, studies of film cooling through arrays of holes (as opposed to continuous slots) have also been made, although most of these studies are relevant to systems involving more active (internal wall) cooling than is present in pure film cooled liners (Ref 12-15). Detailed studies of circular jet/mainstream flow interactions have also been performed to enhance fundamental understanding of these inherently 3-D mixing processes (Ref 16-22).



TE85-2080

Figure 1. Combustor cooling approaches.

Although the work cited has greatly enhanced the understanding of film flow behavior, significant reduction of cooling flows in pure slot film cooled combustors has not been forthcoming. This is due in part to the difficulty in maintaining film integrity in a highly turbulent environment characterized by significant recirculating flows. Another factor limiting the effectiveness of pure film cooling is that the insulating film primarily affects the convective component of heat transfer, and has little effect on the significant radiative heat transfer from the highly luminous gas.* Recognizing this basic limitation, significant reductions in cooling flow requirements will be achieved only if the heat sink capability inherent to the coolant is more fully utilized in the active mode prior to injection as a film. This has been clearly pointed out by Colladay (Ref 23), and confirmed by our own studies, Figure 2. The results shown in Figure 2 should not be interpreted as universal trends, but they do show the large gains to be made if the coolant is used to cool the liner wall actively prior to injection onto the surface as a film.

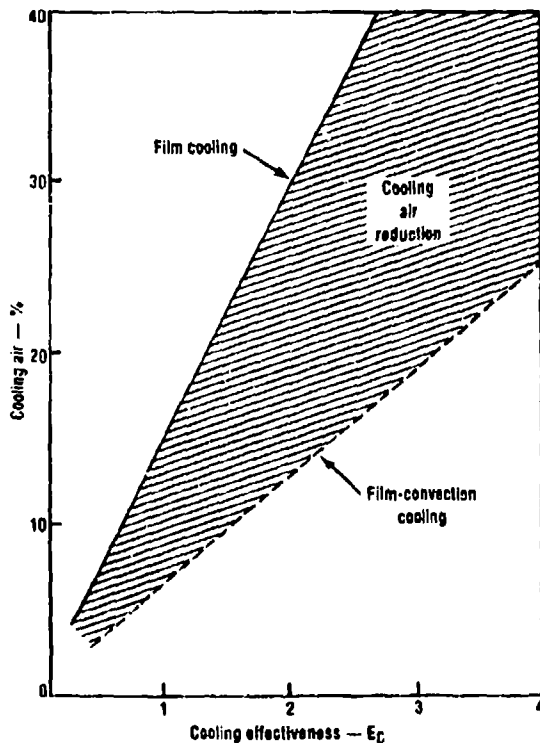
The foregoing considerations have led to the development of several alternate liner cooling concepts that now show considerable promise from the cooling effectiveness standpoint. In the sections that follow, three of the more promising approaches are discussed in more detail.

III. ADVANCED LINER COOLING CONCEPTS

FILM-CONVECTION SYSTEMS

General Description

Reflecting the considerations discussed previously, use of the coolant to cool the liner wall convectively prior to ejection as a film should offer some advantage in terms of better use of coolant heat sink potential. Two schemes that show considerable promise in combustor cooling applications are illustrated conceptually in Figure 3. Both schemes provide active convection cooling of the wall, ultimately discharging the coolant through tangential slots to provide additional film insulation. The multijet impingement cooling approach, borrowed from turbine blade cooling technology, produces reasonably intense coolant side heat transfer coefficients by means of subsonic, highly turbulent jets. The principal design variables in the impingement system, include hole diameter, hole pitch (spacing to diameter ratio), gap height, axial extent of each impingement array, and (to a limited extent) pressure ratio across impingement holes. The heat transfer performance of multijet impingement cooling systems has been reasonably well characterized by the experimental study of Kercher (Ref 24). The axial extent of the impingement array is important because the axial cross-flow of air collected from upstream jets degrades local heat transfer to downstream jets. The designer can control this to some extent by hole spacing to diameter ratio, and by limiting the axial extent of each impingement segment, the latter at the expense of more segments and increased fabrication complexity.



TE5035

Figure 2. Cooling effectiveness trends.

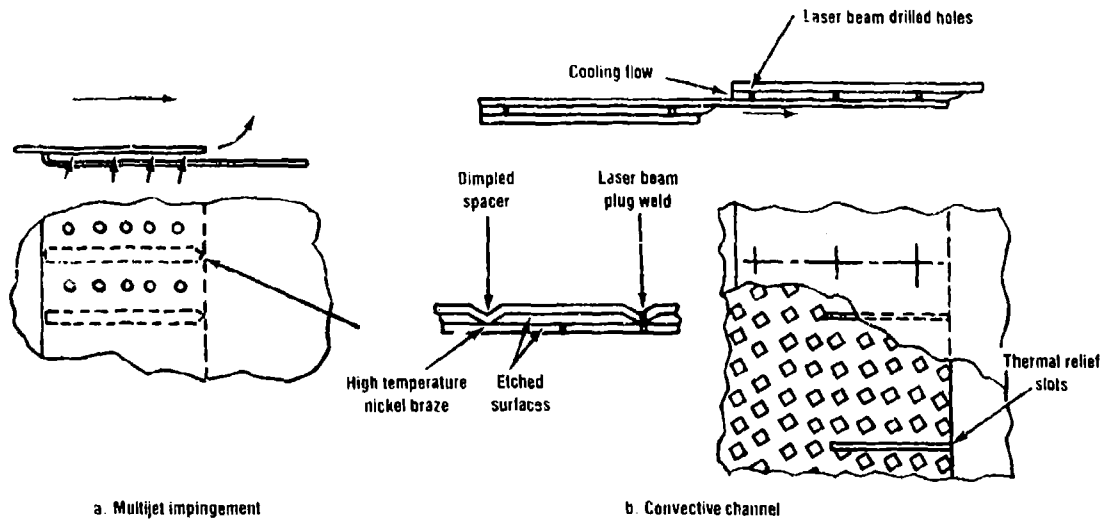
*An exception is the near slot region where the gas side wall surface may actually be convectively cooled by the slot film (i.e., recovery temperature < wall temperature).

The convective channel cooling arrangement shown in Figure 3b relies largely on the axial velocity of the coolant through the double wall channel region to achieve active cooling of the liner inner surface prior to tangential injection of the air film. In general, the convective heat transfer rates can be enhanced by artificially roughening one or both of the coolant side channel surfaces. The work at Allison has involved development of a number of geometrically different roughness element patterns, all of which are produced by electrochemical etching techniques. Figure 4 illustrates several of the geometric arrangements considered in this work. The principal design variables in systems of this type include roughness element pattern geometry, extent to which roughness elements are used, channel gap height, channel segment length (and degree of wall overlap), and transverse spacing of separator stakes. Pressure drop across the convective channels might be considered another variable, but in general it is established by combustor aerodynamic considerations and cycle performance constraints.

For reasons to be discussed later, most of our attention has been focused on the roughened convective channel designs rather than the multijet systems. Consequently, the material to follow is concerned primarily with the former type of cooling system.

Heat Transfer Characteristics of Convective Channel Systems

The importance of effective heat transfer in convectively cooled channels needs no amplification. A strong relationship exists between coolant pressure drop and heat transfer in narrow coolant channels with augmented heat transfer surfaces (roughened walls, finned walls, etc). To evaluate the critical pressure drop/heat transfer relationships in convective passages properly, comprehensive bench test programs were warranted.

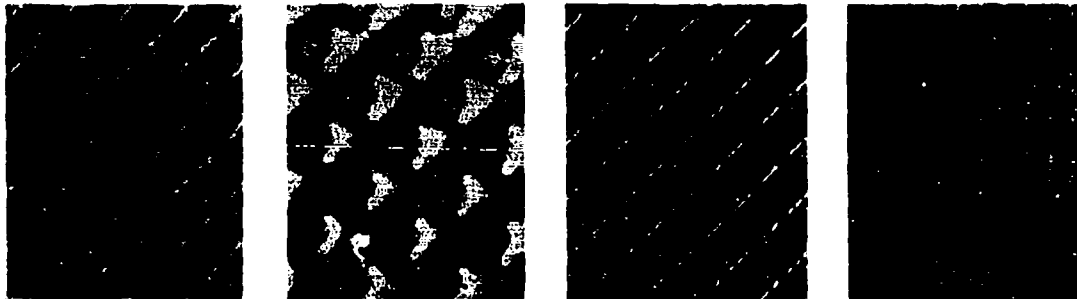


a. Multijet impingement

b. Convective channel

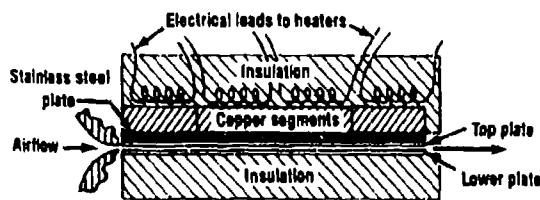
TE85-2081

Figure 3. Film-convection cooling schemes.



TE85-2085

Figure 4. Typical roughened surface configurations (magnified).



TE85-2082

Figure 5. Convection channel heat transfer test rig.

Appropriate submodels of actual convective passage geometries (including converging channels with pin fins) have been experimentally evaluated using electrically heated test sections similar to that shown in Figure 5. By enclosing the entire test section in a pressure vessel, it is possible to produce channel pressure ratios (Mach numbers) as well as channel pressure levels (Reynolds numbers), which are consistent with reference engine levels. Measurements of flow rate, upstream pressure, downstream pressure, and local channel static pressures provide sufficient data to evaluate overall pressure loss and effective channel friction factors. Measurements of electrical energy dissipation, test surface temperature distribution, and air temperature distribution through the test section provide sufficient information to evaluate local passage heat transfer coefficients.

Testing has been accomplished for a number of different convective channel geometries of interest. Each test covered a wide range of Mach number and Reynolds number conditions.

Data are represented in the form shown in Figure 6, providing considerable insight into the trade-off between heat transfer improvements (surface area and/or turbulence augmentation) and increases in coolant pressure drop (friction factor increase). The region of data shown in Figure 6 is considered representative of the performance improvements that can be achieved by artificial roughening of the surfaces. Obviously, those configurations that exhibit performance characteristics in the upper left-hand region of Figure 6 are preferred from an overall effectiveness standpoint. The data showed the best configurations (highest Stanton number ratio, lowest friction factor ratio) to be those with the higher ratios of roughness element height to channel gap height. Also those channels with only one roughened surface exhibited about half the pressure drop (at a given flow rate) of a comparable channel with both surfaces roughened. However, the configurations with only one roughened surface exhibited almost the same heat transfer coefficient levels as the channel with both surfaces roughened. Apparently the induced turbulence and extended surface area of the heated wall alone control the overall heat transfer rates to a significant extent. (A more detailed report on this work may be found in Ref 25.)

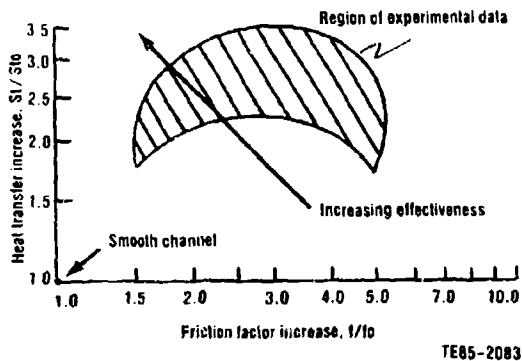


Figure 6. Heat transfer performance characteristics of artificially roughened channels.

At this point some comments are needed to put the two types of film-convection systems in proper perspective. As stated previously, most attention has been focused on the convective channel systems. This was based in large measure on the comparative assessment of the two types of systems shown in Figure 7. These results are based on performance data of the type shown in Figure 6 and (for the multijet system) the data of Kercher (Ref 24). When both systems are compared on a common basis, namely effective heat transfer coefficient at a given coolant flow rate and pressure drop, the roughened convective channel system is clearly superior. Note, however, that these comparisons have been made at cooling system pressure drops representative of turbine engine combustors. The performance of multijet impingement systems is enhanced considerably at higher impingement system pressure ratios (Ref 24) and would compare much more favorably with the roughened convective channel schemes at pressure ratios more typical of cooled turbine blade designs, for example. However, at the relatively low ΔP (%) levels typical of combustors, the roughened convective channel designs appear superior from a cooling air usage standpoint. The multijet impingement system does offer some advantage in flow control (machined holes versus hard-to-maintain channels gaps), and in the ability to better distribute cooling flow for surface temperature uniformity.

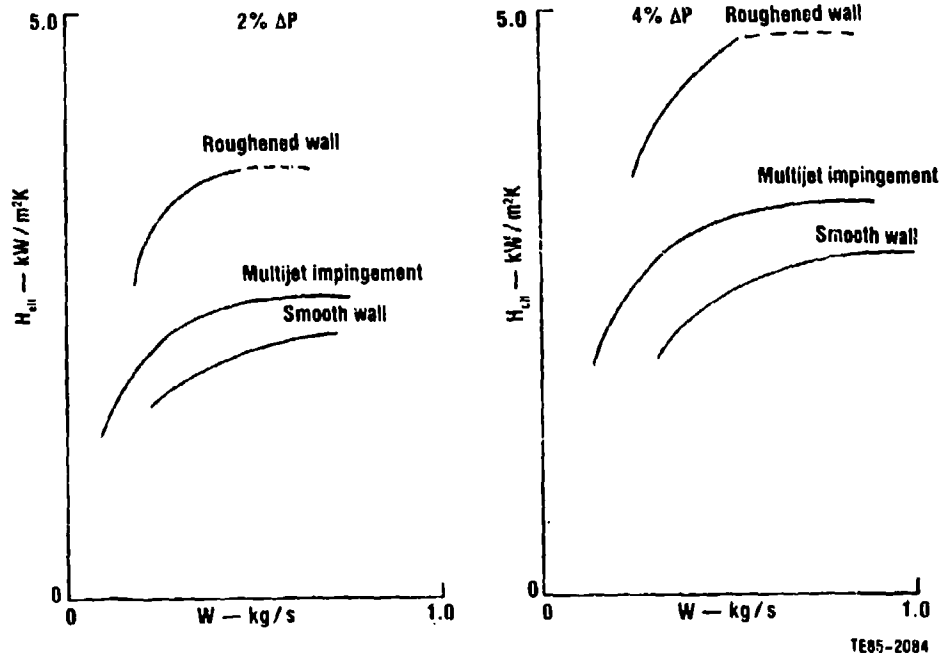


Figure 7. Comparison of convective channel and multijet impingement cooling effectiveness.

Mechanical Design/Manufacturing Considerations

The mechanical configuration of a typical convective-film slot cooling geometry is shown in Figure 3b. A series of overlapping cylinders or cones are formed corresponding to the geometry of the combustor. These are then dimpled to form spacers for precise gap control. The gap size or height of these spacers is generally in the range of 0.54 to 1.02 mm, depending on the local heat flux in the combustor. A critical consideration in this method is the required roughness in the channel to obtain the increased frictional effect. Mechanical methods of achieving the required "roughness" were unacceptable. Therefore, depending on the material, either photochemical etching is used (for nickel based materials such as Hastelloy X) or photoelectromechanical etching is used for cobalt based materials such as Haynes 188. Typically the roughness is applied in a 0.18 mm deep diamond pattern. Figure 8 shows the sequence of joining steps used for the inner and outer walls. Laser beam drilled holes are first drilled through the outer sheet. The unit is then assembled by laser tacking the assembly together. Final assembly is accomplished by applying nickel braze material in the valley of each dimple. Braze flows through the laser drilled holes bonding the dimple to the etched surface. The bond quality is inspected by high resolution ultrasonics.

Engine Experience—Convective Channel Designs

Convective film cooling is now employed in the Allison 570-K engine, originally designed for the heavy lift helicopter, and subsequently modified for industrial use. It is rated at 5,347 kW operating at a burner outlet temperature of 1478K with a pressure of 1220 kPa. The combustor shown in Figure 9 is uncoated, has a pitch diameter of 389 mm, is 216 mm long with a 72.4 mm

combustor height and uses 12 airblast nozzles. Only 24.5% of the combustor air is used for cooling resulting in a cooling flux of 7.03 kg/s/m². Over 110,000 hr has been accumulated with this system, operating on a range of fuels from natural gas to DF-2. The high time combustors have 12,000 hr on gas and 1800 hr on DF-2. Both are still in service.

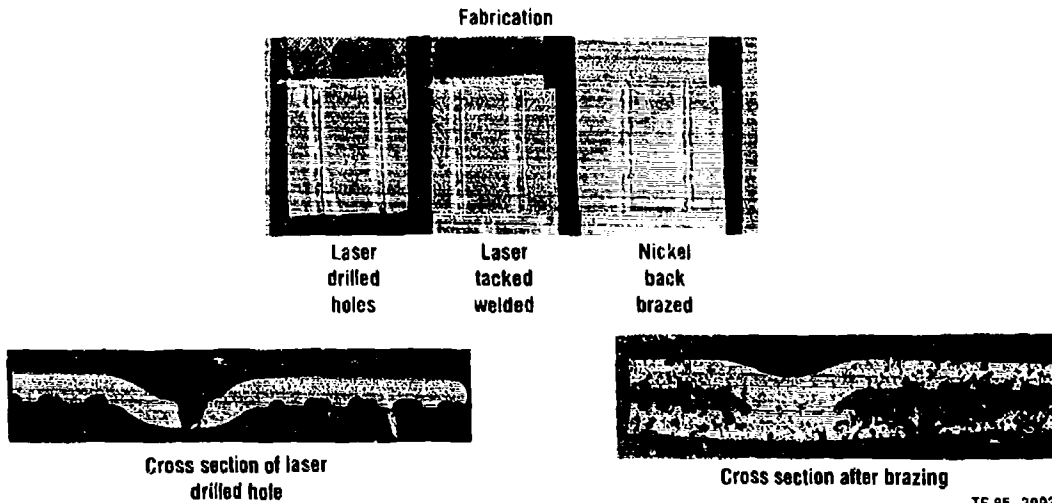


Figure 8. Fabrication sequence of convection film-cooled panels.

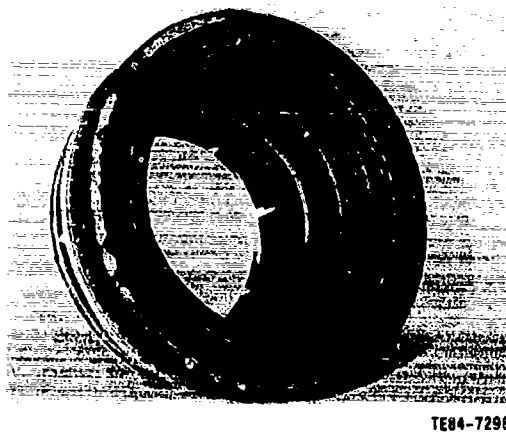


Figure 9. Model 57C-K convection film-cooled combustor.

Beyond the convective channel cooling technology discussed, further improvements in cooling air usage will require a departure to more effective mass transfer cooling approaches such as transpiration or effusion cooling. The development work leading to incorporation of such systems into combustors will be reviewed in the following sections.

LAMINATED POROUS WALL SYSTEMS

General Description

While transpiration cooling potentially represents the most thermodynamically efficient approach to combustor cooling, practical implementation of the method has been hampered by the limitations of porous materials. In general, conventional porous-wall structures have not compared favorably with solid-wall (cast) structures in terms of strength or oxidation resistance. Considerable difficulty in predicting or controlling local permeability (flow resistance) has also been encountered, and susceptibility to foreign particle clogging continues to be a problem.

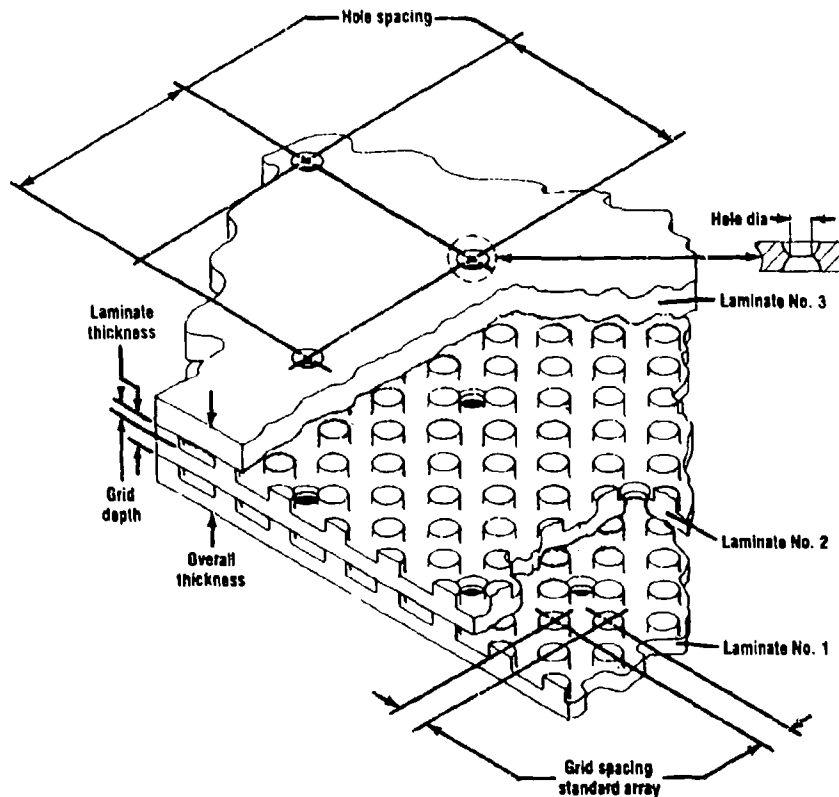
Advances in metal joining techniques over the past several years have led to the development of a multiple-laminate porous structure fabricated from several diffusion-bonded, photoetched metal sheets (Figure 10). This porous material (Lamilloy)* shows considerable promise relative to application in the high-temperature combustor environment.

The approach described provides extraordinary design flexibility relative to flow resistance control and optimization of heat transfer performance. Design variables include hole size and spacing (in general different from one laminate to another), laminate thickness, number of laminates, grid depth, grid diameter, and grid spacing. In general, internal surface area densities (internal heat transfer surface area to volume ratio) far in excess of more conventional cooling arrangements can be achieved. Larger internal surface area densities, and hence improved thermal effectiveness** levels, can be achieved by reducing all dimensions so that the internal structure approaches that of a fine capillary mesh. In general, however, practical minimum dimensions are dictated by clogging considerations and (to a lesser extent) by fabrication limitations. Improved cooling effectiveness can also be achieved by simply increasing the number of laminates. In this instance, internal cooled surface area increases directly with no increase in heated (face) area. The principal drawback to this approach is the attendant increase in normal temperature gradient across the structure. Based on experience to date, the structure can be fabricated from virtually any of the high temperature wrought alloys currently available commercially.

The development of a thermal design approach involving a structure as complex as Lamilloy has necessarily involved a semiempirical approach to the problem. An overview of the basic experimental work required to characterize heat transfer and fluid flow behavior is presented in the following subsection.

*Lamilloy is a registered trademark of the General Motors Corporation.

**Defined as actual coolant temperature rise divided by ideal rise, $\frac{\Delta T_c}{T_s - T_{ci}}$



TE-270

Figure 10. Typical geometric arrangement of laminated porous wall structure.

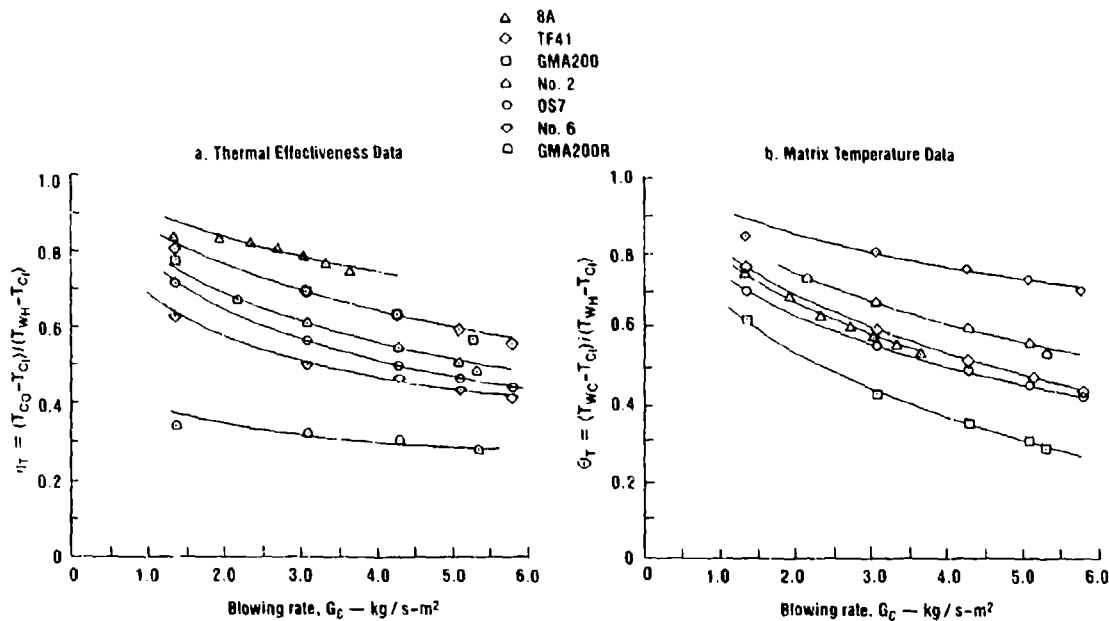
Heat Transfer Characteristics

Knowledge of the internal (matrix) heat transfer characteristics of Laminloy is an essential empirical input to the design system. The principal results of direct usefulness are the coolant temperature rise through the matrix (thermal effectiveness) and the metal temperature gradient across the structure in the direction of coolant flow. A good heat transfer data base is now available for the Laminloy configurations of interest to the various Allison high temperature, combustor/afterburner liner applications. The data were obtained by testing simple disk specimens, mounted in a fixture and heated by a high intensity radiant energy source. During these active cooling tests, measurements were made of coolant flow rate, upstream and downstream pressures, upstream and downstream matrix face temperatures, and coolant inlet and exit temperatures over a range of flow rates at essentially constant heat flux. Coolant flux rates (internal Reynolds number level) were held at levels consistent with turbine applications by control of the upstream pressure level.

Typical dimensionless fluid and metal temperature trends for several selected configurations relevant to combustor liner applications are shown in Figure 11. The intrinsic internal "heat exchanger" effectiveness parameter, η_i , is particularly important since in general, liner cooling requirements will be inversely proportional to this parameter. While specimen to specimen differences in cooling performance (η_i) are obvious, the results shown in Figure 11 serve to illustrate that it is possible to develop geometric configurations that approach ideal transpiration cooling effectiveness ($\eta_i = 1.0$). The rather pronounced specimen to specimen variances in effectiveness (η_i) and matrix thermal gradient (θ_s) reflect internal heat transfer performance trends attributable to sheet to sheet differences in such key geometric design variables as

- o sheet hole diameter
- o sheet hole spacing
- o etch depth (pedestal height)
- o pedestal diameter
- o pedestal spacing

Empirical data, such as that shown in Figure 11 are analyzed using a one-dimensional porous wall thermal exchange model to evaluate mean matrix to coolant heat transfer coefficient and effective matrix thermal conductivity. Finally, working correlations are established that relate mean matrix to coolant heat transfer coefficient to coolant flux (G_c) and the several geometric parameters cited previously. Such generalized correlations, established via multiple linear regression analysis techniques, allow the designer to explore effects of alternate geometric configurations on thermal (cooling) performance, and to predict thermal effectiveness and matrix temperature gradient trends at any actual engine operating condition of interest. The ability to analytically assess the influence of geometric configuration on heat transfer performance represents an important design capability because geometric configuration influences many other key design requirements/considerations including LCF life, flow resistance, weight, cost and manufacturability.



TE85-2086

Figure 11. Lamilloy heat transfer evaluation.

Mechanical Design/Manufacturing Considerations

Lamilloy consists of thin metallic sheets contoured to contain many discrete holes and connecting grooves as shown in Figure 10. The hole and groove pattern, which is generated by the photoetching process, can be varied within a single sheet. When these precision photoetched sheets are accurately registered, assembled, and solid-state diffusion bonded, a precision-designed porous structure results.

Allison has aggressively pursued the fabrication of Lamilloy structures from nickel- and cobalt-based superalloys, and has further demonstrated adaptation of a full spectrum of other materials for a range of applications, including:

- low-alloy steel
- 300 and 400 series stainless steels
- Hastelloy X and Haynes 188 (solid solution-strengthening alloys)
- René 41 and Udiment 700 (nickel-based precipitation-strengthening alloys)
- TD Ni, TD NiCr, and TD Co (dispersion-strengthening alloys)
- aluminum alloys
- titanium alloys
- tungsten sheet

The Lamilloy porous structure requires very thin sheet stock ranging in thickness from 0.254 mm to 0.635 mm. Conventional, mill-reduced stock in 300 and 400 series stainless steels, Haynes 188, and Hastelloy X alloy in thin strip stock are commercially available as starting stock for initial Lamilloy processing.

Surface cleaning of the strip is perhaps the most important of these process refinements. Mill finishes, in terms of roughness, are sometimes adequate, but additional abrasive polishing is necessary to remove the very stable compounds of metallic oxides found on the surface of these mill products.

The Lamilloy manufacturing sequence is shown in Figure 12. The tooling for the processing of sheet is essentially the photographic transparency. Oversize detailed drawings are prepared including the necessary grooves and holes for each sheet of the laminate. Additional data covering the location of laminate alignment holes, forming or machining reference holes, pattern extensions for uniform photoetching, trim stock, lateral etch factors, and photoreduction comprise the principal features of the detailed process. Next, this information is translated into input data for a special computer program that allows direct reduction of design configurations into artwork for photoetch configurations without manual layout.

After preparing the surfaces to be bonded by finishing to a low surface roughness, a uniform layer of nickel is applied by electroplating to promote diffusion bonding and the plated surface is coated with a photosensitive acid resist.

The Lamilloy pattern for either holes or grooves is then printed on the photoresist by exposing it through a photographic negative of the proper pattern. The photoresist mask is further processed by washing off the unexposed areas and curing the mask in a hot air oven. The Lamilloy pattern is then produced on the metal plate by either chemically or electrochemically removing metal from the unprotected surface.

Interlayer diffusion bonding is accomplished by placing the entire assembly in a vacuum furnace and maintaining this assembly under vacuum at high temperatures (1367K) for sufficient time (4 hr) to effect a bond. This demonstrated bonding method will produce Lamilloy sheets of high quality. The diffusion-bonded sheets are inspected for airflow, bond integrity, and microstructure. Bond integrity is evaluated via high resolution ultrasonics. The technique is capable of resolving each of the 0.76 mm dia pedestals in the Lamilloy structure.

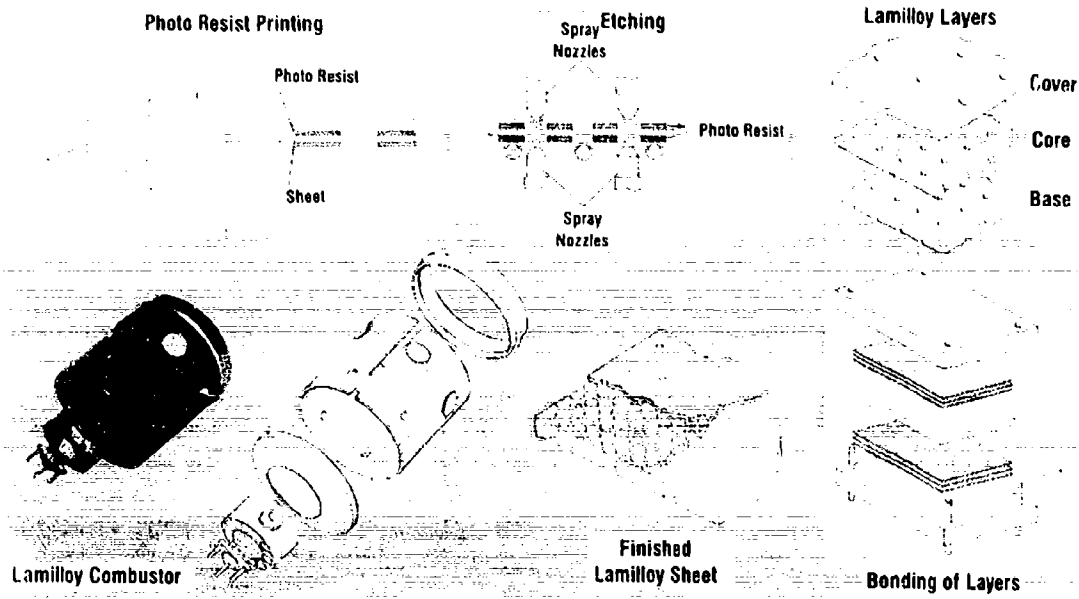


Figure 12. Lamilly processing.

TEB5-2087

Engine Experience

The applications of Lamilly to difficult cooling situations have been numerous, the most recent being a Lamilly annular combustor for the T800/ATE109, a 1200 hp turboprop engine. Other Allison Lamilly combustor applications include the following:

- o IGT 404 (Patriot)
- o Model 250-C30
- o Model 250-C20
- o NASA-HPF
- o ATDE/GMA300
- o AGT 5
- o TF41
- o NASA—reverse-flow

In some of these applications, a direct substitution of Lamilly for film cooling was used to provide substantial reductions in wall temperature. For example, the dome wall temperature of the Industrial Gas Turbine (IGT 404) combustor was reduced from 1010 °C to 727 °C, only 78 °C above the cooling air temperature of 649 °C. The IGT 404 (Patriot) combustor (Figure 13) is currently in production. Over 30,000 hr have been accumulated with the high time combustor having 6600 hr and still being serviceable.

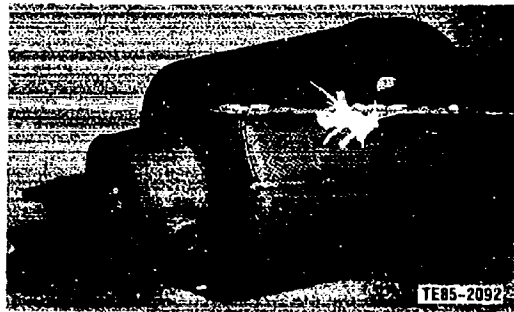


Figure 13. IGT 404/Patriot Lamilly combustor.

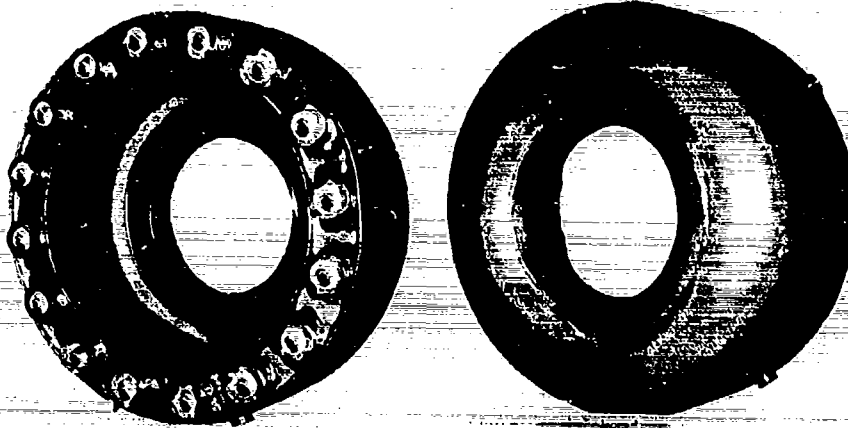
Other applications more representative of aircraft annular experience include the ATDE/GMA500 reverse-flow combustor, Figure 14. This application illustrates the fabricability of Lamilly structure; the contour was readily controlled using a hydro-forming process. It used 38% of combustor airflow resulting in an overall cooling flux of 5.8 kg/s/m². The combustor shown in Figure 15 was designed and fabricated for NASA for ultimate operation at 4045 kPa and 2478K burner outlet temperatures. The liner uses 40% less air than a conventional film-cooled liner. Testing to date has been carried out to temperature levels of 2430K at 12 atm pressure with no cooling or durability problems.

EFFUSION COOLING SYSTEMS

General Description

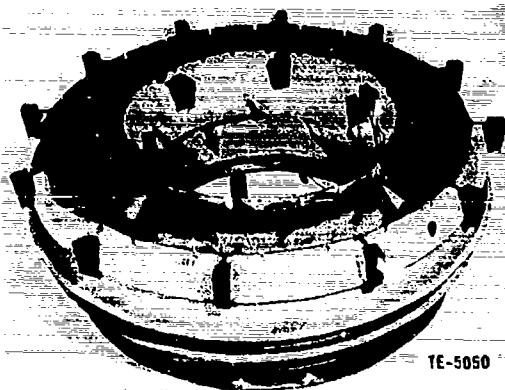
As used herein, effusion cooling refers to the multiple, drilled, angled hole cooling configuration shown schematically in Figure 1. This cooling configuration has an intrinsic advantage of simplicity in that the more complex fabricated, rolled, overlapping ring structures characterizing traditional film or film convection liners are replaced by a single layer sheet in which flow characteristics and cooling performance are controlled by a relatively few geometric parameters including the following:

- o sheet thickness
- o hole size
- o hole spacing
- o hole plunge angle



TE-5049

Figure 14. ATDE/GMA500 reverse-flow Lamilloy combustor.



TE-5050

Figure 15. NASA HPF Lamilloy combustor.

Recent advances in electron-beam and laser drilling techniques have brought the concept of closely tolerated, shallow angle, variable pitch, small diameter holes to a position of "technology readiness." In theory, the effusion cooling concept can approach transpiration cooling performance in the limit as hole diameters and spacing/diameter ratios are reduced to miniscule (capillary pore) dimensions. However, our studies have shown that when "practical minimum" hole sizes, hole spacings, and plunge angles are considered, effusion cooling performance most probably lies between the two systems previously described in this paper. Again, a principal motivation for this approach lies in its inherent simplicity in structural and manufacturing terms.

Heat Transfer Characteristics

As stated previously, first order considerations would argue that effusion cooling effectiveness would depend principally on a relatively few geometric parameters including wall thickness, hole diameter, hole spacing, and hole plunge angle. As in the case of the two systems previously described, the modeling of heat transfer in effusion cooling systems is

largely empirically based. The basic working relationships between cooling flow rate, effusion hole array geometry, and cooling performance were established via a series of heat transfer tunnel tests in which effusion hole arrays were machined into the leading edges of cylinders in cross-flow (Figure 16). These tests, which were originally carried out to establish a design model for airfoil leading edge showerhead film cooling, are described in more detail in a recent ASME publication (Ref 23). Although the work described in (Ref 26) is focused on the air foil leading edge cooling problem, the modeling of internal (wall) heat transfer processes in that work is equally applicable to the combustor liner problem. Leaving the details to reference (Ref 26), the development of the effusion wall cooling model can be summarized by noting that measured overall cylinder cooling effectiveness trends such as those shown in Figure 17 were effectively synthesized (reproduced) by the wall cooling model using an independent experimental study (Ref 27) to establish the external (gas to wall) heat transfer rates. The internal wall heat transfer model evolved from this work framed the wall heat transfer problem in terms of the key geometric variables cited previously, and included consideration of heat transfer processes within the wall as well as the very significant upstream (coolant inlet face) heat transfer component (Ref 28, 29).

The cooling performance trends for an effusion-cooled wall are perhaps best illustrated by the comparative study shown in Table I where cooling flow requirements for several alternate effusion cooling configurations are compared with that for a Lamilloy wall.* While this comparative study was made for a specific (TF41) combustion liner and cannot be considered universally applicable, the results are considered at least representative and serve to illustrate the influence of the principal geometric variables on effusion cooling performance. Note the following key observations:

- o The "best" effusion geometry (represented by $\alpha = 20$ deg, $d = 0.38$ mm) requires about 2/3 more cooling flow than does a representative Lamilloy wall (Configuration A versus Configuration L).
- o Effusion cooling requirements are increased by about 1/3 when wall thickness is halved (Configurations A versus E, B versus F, etc).
- o The effect of hole angle is significant. Decreasing hole angle from 45 deg to 20 deg will reduce cooling requirements by about 35% (Configurations A versus B, C versus D, etc).

*Liner wall surface temperature and gas to wall heat flux were considered identical for both systems.

- o Reducing hole diameter by a factor of two has an effect comparable to the influence of hole angle cited previously (Configurations A versus C, B versus D, etc)
- o The significant cooling performance advantage of small holes is partially offset by a requirement to drill significantly more holes (approximately 2 1/2 times more holes for the case cited)
- o Wall normal temperature gradients in effusion cooling systems appear to be considerably lower than in Laminoly walls of the same overall thickness (Configurations A, B, C, D versus L).

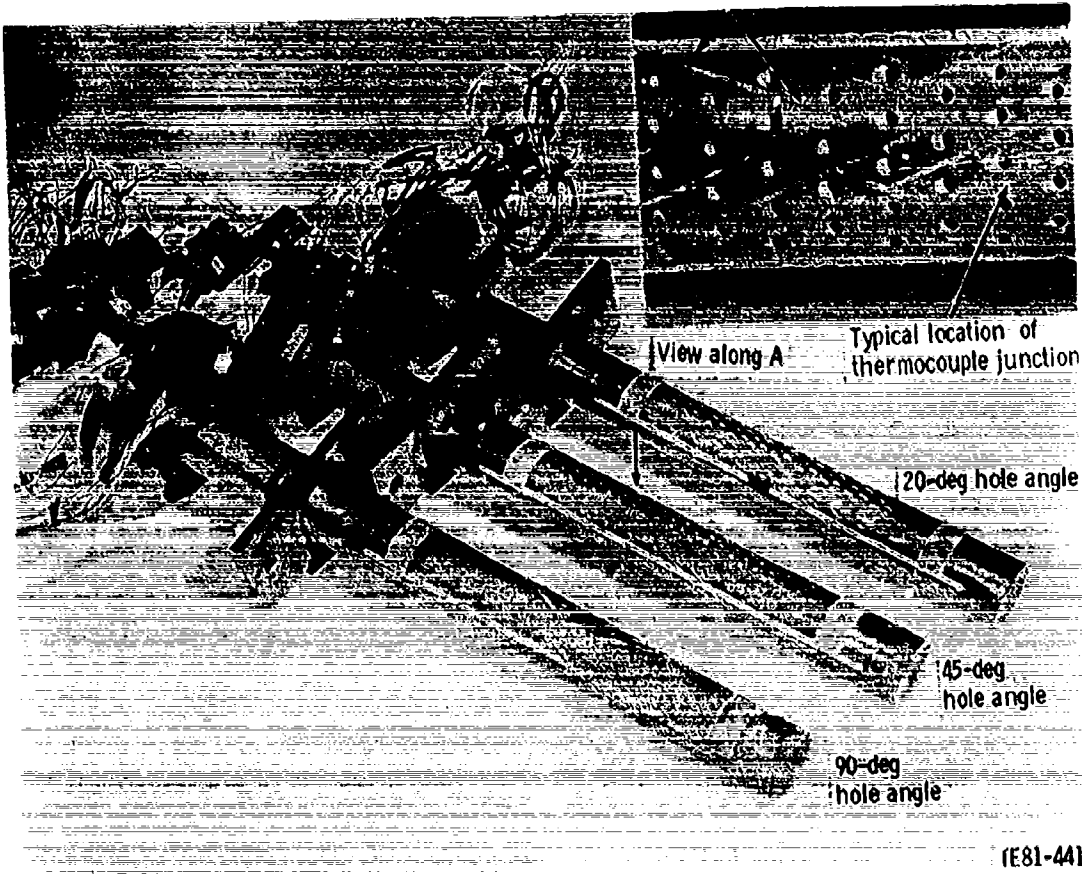


Figure 16. Typical effusion-cooled cylinder specimen.

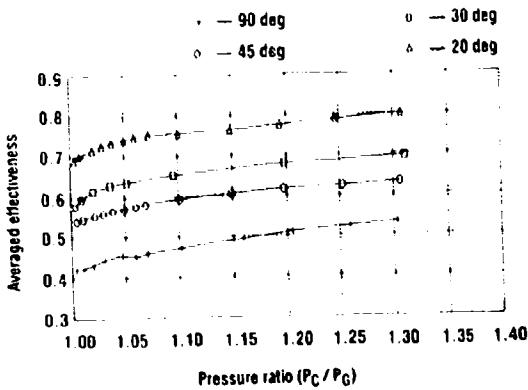


Figure 17. The effect of coolant-to-gas-stream pressure ratio on average cooling effectiveness (leading edge Reynolds number = 44,000; free-stream Mach No. = 0.178).

Mechanical Design/Manufacturing Considerations

Perhaps the simplest cooling configuration to implement with current advanced laser and electron beam technology in conjunction with computer controlled manufacturing is the effusion-cooled combustion liner. Messer Griesheim of Germany manufactures a numerically controlled electron beam drilling machine capable of drilling twenty holes (0.52 mm dia by 4.45 mm long) per second through both nickel and cobalt steels at angles up to 20 deg from the surface. It is currently producing parts for reverse flow combustion liners with material thickness of 1.1 mm, drilling 3748 holes of 0.9 ± 0.05 mm dia in 60 minutes. Allison has manufactured several combustion liners using a low divergence Nd:YAG laser. By pulsing these lasers, very high peak powers may be achieved, allowing cutting, drilling, and welding on both nickel and cobalt base materials. At the same time, the thermal duty cycle is very low causing little or no thermal distortion. Figure 18 shows a typical 0.51 mm dia hole cut through 1.52 mm thick Haynes 188 cobalt material at an angle of 20 deg from the liner surface. It is also feasible to drill the holes as low as 15 deg from the surface and thereby increase the internal heat transfer effectiveness by implementing a larger length to diameter for the same

TE81-441

TE84-8160

size hole. The process for the manufacture of combustion liners is very simple, since only a single thickness material need be rolled or formed to the final shape of the combustor. All the holes, including both cooling and combustion air holes, can then be drilled at the same time. The combustor, shown in Figure 19 for an experimental version of the T56 turboshaft engine, has 14,500 cooling holes and was fully machined (including air holes) in less than 7 hr.

Table I. Effusion Cooling — Performance Trends.

Configuration	Description	Cooling flux requirement — kg/s-m ²	Hole spacing to diameter ratio	Number of holes (per liner)	Wall normal temperature gradient — °C
L	Lamilloy (baseline)	7.03	4.0	6,812	168
A	$\alpha = 20$ deg $d = 0.038$ $r = 0.152$	11.25	7.12	11,052	81
B	$\alpha = 45$ deg $d = 0.038$ $r = 0.152$	17.37	5.90	16,117	81
C	$\alpha = 20$ deg $d = 0.076$ $r = 0.152$	17.58	5.78	4,199	83
D	$\alpha = 45$ deg $d = 0.076$ $r = 0.152$	27.36	4.73	6,255	85
E	$\alpha = 20$ deg $d = 0.038$ $r = 0.076$	15.05	6.24	14,390	42
F	$\alpha = 45$ deg $d = 0.038$ $r = 0.076$	23.35	5.13	21,306	42
G	$\alpha = 20$ deg $d = 0.076$ $r = 0.076$	23.35	5.05	5,488	43
H	$\alpha = 45$ deg $d = 0.076$ $r = 0.076$	36.08	4.14	8,172	43

α — effusion hole plunge angle (measured from horizontal)
 d — effusion hole diameter (cm)
 r — liner wall thickness (cm)

Table I. Effusion-cooling — performance trends.

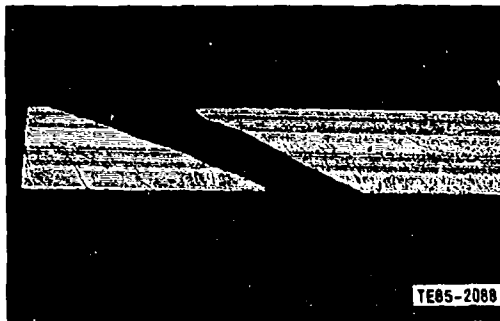


Figure 18. Microsection of 0.050 cm diameter hole in 0.152 cm thick Haynes 188 at 20 deg to surface.

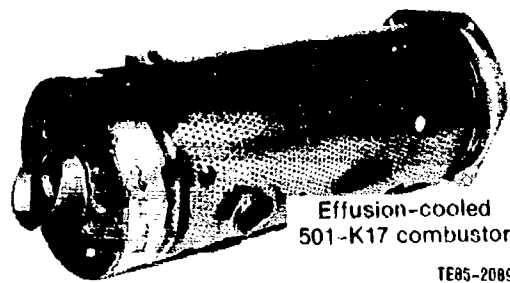


Figure 19. Effusion-cooled Model 501-K17 combustor.

Rig/Engine Experience

Several studies have been conducted to apply this effusion-cooled concept to Allison's product line. For example, a 135 deg segment of effusion material was fabricated and then assembled into the primary zone outer wall region of a ATDE/GMA500 combustor, a reverse flow configuration currently manufactured from Lamilloy, and used in an 800 shaft horsepower helicopter engine. Three hole densities were included in equal areas of the segment yielding a coolant flux equal to 1.25 and 1.75 of the surrounding Lamilloy. Burner rig tests conducted to 1688K burner outlet temperature indicate that metal temperatures in the primary zone were 871 °C for the effusion-cooled sample (compared with 760 °C for the Lamilloy.) The influence of cooling flow rate for effusion cooling is shown in Figure 20. The estimated thermal gradient across the effusion-cooled sample is only 22 °C compared with 111 °C through the Lamilloy. Engine tests of fully effusion-cooled liners will be conducted in the near future.

IV. SUMMARY AND GENERAL OBSERVATIONS

A basic assessment of several alternate combustor wall cooling approaches has been made, reflecting the specific considerations of cooling effectiveness, design flexibility, fabrication complexity, and special operational and durability problems.

Our studies have shown that artificially roughened convective channel, effusion, and transpiration-cooled liner approaches offer the potential of substantial reductions in liner cooling flow requirements with little sacrifice in durability. Furthermore, the advanced cooling approaches cited have demonstrated the capability of successful operation at burner outlet temperatures approaching the near stoichiometric regime. The payoff of the advanced cooling schemes in terms of outlet pattern improvement and achievable BOT level has been demonstrated in both engine and rig tests.

While the results to date are encouraging, application of the more effective cooling approaches discussed herein has been largely confined to development engines, and many problems still remain. Specifically, further research and development activity is indicated in the following areas:

- o Further improvements in fabrication technology will be required to reduce cost, extend cooling design flexibility, and achieve better process tolerance control. For example, recent advances in electromechanical machining (ECM) and laser milling technology may offer cost, flexibility, and accuracy advantages compared with current electrochemical etching techniques.

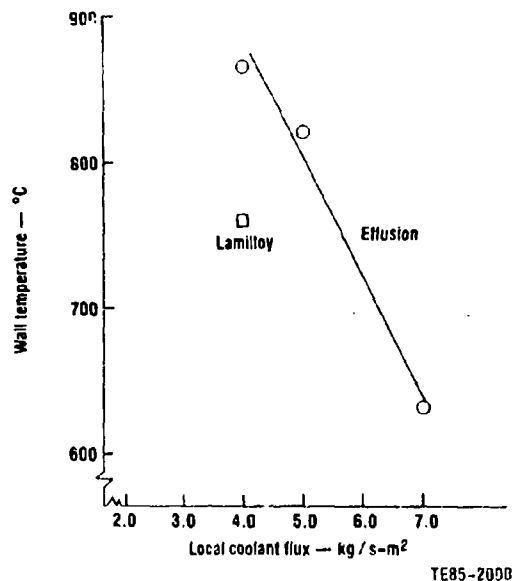


Figure 20. Effusion-cooling trends — GMA500 combustor.

- o As alternative processes offer additional flexibility in design, better characterization of wall cooling concepts in terms of fluid flow, heat transfer, and mechanical behavior will be required. Relative to the latter, special attention must be given to interactive behavior (creep/fatigue), notch effects, cumulative damage rules, and (perhaps to a lesser extent) fracture mechanics.
- o More sophisticated and detailed thermal/structural modeling techniques are required to better represent local temperature and stress distributions throughout the complex cooled wall structure. The eventual achievement of realistic life prediction capability will necessarily require the extension of current finite element methodology to include plastic behavior and creep-fatigue interaction.
- o Recent advances in the more sophisticated numerical modeling approaches capable of addressing the three-dimensional turbulent flow field must be fully verified, and exploited by the combustor designer. The physics of turbulent shear transport, reflecting the combined effects of 3-D wall jets, discrete site coolant injection, inlet swirl, and chemical reaction are clearly beyond adequate description by present first order analytical techniques.
- o The reduction of liner wall cooling flows to minimum acceptable levels will demand that much more careful attention be given to peripheral details such as welds, mechanical attachments, scoops, and other flow-path protuberances. Most of the gains (in coolant flow usage) achieved by use of advanced cooling techniques can be easily lost through wasteful local cooling "fixes" of poorly conceived mechanical design features.

REFERENCES

1. J. Stollery and A. A. M. El Ehwany, "A Note on the Use of a Boundary Layer Model for Correlation Film Cooling Data," *International Journal of Heat & Mass Transfer*, Vol 8, pp 55-66, January 1965.
2. J. P. Hartnett, R. C. Birkebak, and E. R. G. Eckert, "Velocity Distributions, Temperature Distributions, Effectiveness and Heat Transfer for Air Injection through a Tangential Slot into a Turbulent Boundary Layer," *Trans ASME, Journal of Heat Transfer*, Vol 83, pp 293-306, August 1961.
3. J. Librizzi and R. J. Cresci, "Transpiration Cooling of a Turbulent Boundary Layer in an Axisymmetric Nozzle," *AIAA Journal*, Vol 2, pp 617-624, 1964.
4. P. T. Ross, "An Experimental Investigation of Adiabatic and Non-Adiabatic Wall Film Cooling with Injection from a Continuous Slot," Allison RN 71-14, May 1971.
5. S. Sivasegaram and J. H. Whitelaw, "Film Cooling Slots: The Importance of Lip Thickness and Injection Angle," *Journal of Mechanical Engineering Science*, Vol II, No. 1, pp 22-27, 1969.
6. S. C. Kacker and J. H. Whitelaw, "The Effect of Slot Height and Slot Turbulence Intensity on the Effectiveness of the Uniform Density, Two-Dimensional Wall Jet," *Trans ASME, Journal of Heat Transfer*, Vol 90, pp 469-475, November 1968.
7. S. C. Kacker and J. H. Whitelaw, "An Experimental Investigation of the Influence of Slot-Lip Thickness on the Impervious-Wall Effectiveness of the Uniform Density, Two-Dimensional Wall Jet," *International Journal of Heat & Mass Transfer*, Vol 12, pp 1196-1201, 1969.

8. D. R. Ballal and A. H. Lefebvre, "A Proposed Method for Calculating Film-Cooled Wall Temperatures in Gas Turbine Combustion Chambers," ASME Paper No. 72WA/HT-24, November 1972.
9. F. Burgraff and R. W. Huffmeier, "Film Effectiveness and Heat Transfer Coefficient Downstream of a Metered Injection Slot," ASME Paper No. 73-HT-31, August 1973.
10. A. J. Juhasz and C. J. Marek, "Combustor Liner Film Cooling in the Presence of High Free-Stream Turbulence," NASA TN D-6360, July 1971.
11. R. A. Seban, "Heat Transfer and Effectiveness for a Turbulent Boundary Layer with Tangential Fluid Injection," Trans ASME, *Journal of Heat Transfer*, Vol 82, pp 303-312, 1960.
12. R. E. Mayle and F. J. Camarata, "Multi-Hole Cooling Film Effectiveness and Heat Transfer," presented at the AIAA/ASME Thermophysics and Heat Transfer Conference, Boston, July 1974 (AIAA Paper No. 74-675, ASME Paper No. 74-HT-9).
13. M. E. Crawford, W. M. Kays, and R. J. Moffat, "Heat Transfer to a Full-Coverage, Film-Cooled Surface with 30-Deg Slant Hole Injection," Report No. HMT-25, Thermosciences Div, Dept of Mechanical Engineering, Stanford University, May 1976.
14. D. E. Metzger, D. I. Takeuchi, and P. A. Kuensler, "Effectiveness and Heat Transfer with Full-Coverage Film Cooling," ASME Paper No. 73-GT-18, April 1973.
15. R. D. Anderson and D. A. Nealy, "Influence of Surface Injection on Turbulent Heat Transfer and Laminated Porous Materials," Allison EDR 6112, February 1969 (also in AFAPL TR-69-41).
16. G. Bergeles, A. D. Gosman, and B. E. Launder, "Near Field Character of a Jet-Discharged through a Wall at 30 Deg to a Mainstream," *AIAA Journal*, Vol 15, p 449, 1977.
17. G. Bergeles, A. D. Gosman, and B. E. Launder, "The Near Field Character of a Jet Discharged through a Wall at 90 Deg to the Mainstream," ASME Paper No. 75 WA/HT-108, December 1975.
18. S. V. Patankar and D. B. Spalding, "A Calculation Procedure for Heat, Mass, and Momentum Transfer in Three Dimensional Parabolic Flows," *International Journal of Heat & Mass Transfer*, Vol 15, pp 1787-1806, 1972.
19. B. E. Launder and D. B. Spalding, "The Numerical Computation of Turbulent Flows," *Computer Methods in Applied Mechanics and Engineering*, Vol 3, pp 269-289, 1974.
20. V. L. Ericksen and R. J. Goldstein, "Heat Transfer and Film Cooling Following Injection through Inclined Circular Tubes," Trans. ASME, *Journal of Heat Transfer*, Vol 96, pp 239-245, 1974.
21. D. J. Wilson, V. L. Ericksen, and R. J. Goldstein, "Predicting Heat Transfer Coefficients with Film Cooling from a Row of Holes," Trans ASME, Vol 96, pp 258-260, 1974.
22. M. Y. Jabbari and R. J. Goldstein, "Adiabatic Wall Temperature and Heat Transfer Downstream of Injection through Two Rows of Holes," ASME Paper No. 77-GT-50, March 1977.
23. R. S. Colladay, "Importance of Combining Convection with Film Cooling," AIAA Paper No. 72-8, January 1972.
24. D. M. Kercher and W. Tabakoff, "Heat Transfer by a Square Array of Round Air Jets Impinging Perpendicular to a Flat Surface Including the Effects of Spent Air," Trans ASME, *Journal of Engineering for Power*, pp 73-82, January 1970.
25. V. D. Baker, R. E. Chupp, and J. M. Forry, "VISTOL Deflector Nozzle Model Test Report," Allison EDR 7940, September 1973.
26. A. R. Wadia and D. A. Nealy, "Development of a Design Model for Airfoil Leading Edge Film Cooling," ASME Paper No. 85-GT-120, March 1985.
27. D. W. Luckey and M. R. L'Ecuyer, "Stagnation Region Gas Film Cooling -- Spanwise Angled Injection from Multiple Rows of Holes," NASA CR 165330, April 1981.
28. G. E. Andrews, M. L. Gupta, and M. C. Mkpadi, "Full Coverage Discrete Hole Wall Cooling: Cooling Effectiveness," ASME Paper No. 84-GT-212, June 1984.
29. E. M. Sparrow and M. Carranco Ortiz, "Heat Transfer Characteristics for the Upstream Face of a Perforated Plate Positioned Normal to an Oncoming Flow," *International Journal of Heat & Mass Transfer*, Vol 25, No. 1, pp 127-135, 1982.

DISCUSSION

G.M. Dibellus, Ge

Fig. 11 of your paper is still a puzzle to me: First, the intrinsic internal heat exchanger effectiveness and the dimensionless temperature gradient do not allow a comparison of the Lamilloy-Cooling-System with other cooling configurations. Secondly, the audience doesn't know the meaning of the various geometric parameters such as 8 A through GMA 200 R. Therefore, nobody knows why one geometry has for instance a low effectiveness but a high temperature gradient. Is there any other reason for showing these figures beside indicating that Allison is good?

Author's Reply

In answer to the first question, Fig. 11a simply shows representative trends of coolant temperature rise ($T_{co} - T_{ci}$) normalized by the difference between the average hot surface (gas side) metal temperature (T_{WH}) and coolant supply temperature (T_{ci}). These trends are plotted against coolant mass flux (G_c) which is a measure of the total coolant flow per unit heated (gas side) surface area of the cooled wall. The foregoing parameters could be computed for any alternate cooling system of interest, at least on a zonally averaged basis, and compared to Fig. 11a. Similarly, Fig. 11b simply allows one to determine the overall hot surface to coolant entry surface structural (metal wall) temperature difference, ($T_{WH} - T_{wc}$), in terms of G_c and T_{ci} . Again these parameters can be established for alternate cooling configurations and compared to Fig. 11b to provide some perspective.

In response to the second question, we are still ourselves attempting to fully sort out a geometric explanation for certain of the observed trends shown in Fig. 11. Each geometry has a unique, simultaneous influence on internal surface area density, effective layer to layer thermal conductance, impingement array heat transfer coefficient (layer to layer) and pedestal array convective heat transfer coefficient (layer to layer). The two parameters ηT and θT are clearly coupled since both not only depend on geometry and heat transfer coefficient, but ηT also depends on mean level of wall temperature which depends on both T_{WH} and T_{wc} . While we are not in a position to fully explain these trends, the results do provide some perspective relative to the ideal transpiration cooling case where $\eta T = 1.0$ and

$$\theta_1 = e^{-\frac{G_c C_{pc} \tau}{k_m}}$$

where C_{pc} = mean coolant specific heat
 τ = overall wall thickness
 k_m = effective porous thermal conductivity
 G_c = coolant flux as defined previously

Internal heat transfer coefficients in Lamilloy appear to be sufficiently large that the above equation for θ_1 is approximately valid for Lamilloy in a first order sense. Therefore, the results in Fig. 11b may at least be composed to an ideal porous wall of given Kn/τ .

When we are in a position to more fully reconcile our measured heat transfer trends with specific geometric details we intend to more fully report on the work.

D.K. Hennecke, Ge

You correctly point out that the multi-layered structures have the intrinsic problem of the temperature gradient induced stresses. Therefore, some people now attach the gas side layer to the outer structure like roof shingles such that they can expand freely. What is your opinion about these systems and are you planning to go in that direction?

Author's Reply

The so-called 'floating wall' systems clearly have merit in terms of addressing the thermally induced low cycle fatigue problem. The inherent cooling efficiency of such systems does, however, tend to be lower than our multi-layered approach which relies on the layer to layer bonding (thermal coupling) to provide the "thermal path" to the highly effective internal active cooling elements of the laminated structure. Any mechanical (and thermal) uncoupling of the laminated porous wall (layer to layer) would relieve thermal stresses but at the expense of rendering inner layers of the wall useless in terms of active cooling. Our approach to the thermal LCF problem therefore remains one of retaining the bonded structure and attempting to minimize thermally induced strains by

1. Geometric designs which maximize layer to layer effective thermal conductance while maintaining high internal surface area density.
2. Selection of different materials (layer to layer) with sufficiently different coefficients of thermal expansion to offset layer to layer temperature differences.

S. Wittig, Ge

In comparing Lamilloy with effusion cooling in your last figure, which hole plunge angle was applied?

Furthermore, what is your experience with clogging of the holes in effusion cooling?

Author's Reply

The plunge angle for the configuration in question was 20° nominal. In answer to the second question, operational experience with effusion cooling has been too limited to draw any conclusion. However, it might be mentioned that minimum passage (hole) dimensions in practical effusion cooled systems will almost certainly be larger than the minimum passage dimensions in Lamilloy, which has shown no tendency to clog in field service to date (30,000 hours cumulative time). Furthermore in a carefully monitored accelerated dust ingestion test in another engine, a Lamilloy combustor exhibited insignificant degradation in cooling flow capability at the point where the engine test was terminated due to erosion-induced compressor performance deterioration. Thus while clogging concerns certainly cannot be dismissed out of hand, we have reason to believe that it will not be a major problem.

G.E. Andrews, UK

One of the major advantages of effusion cooling, apart from its simplicity, is the much lower thermal gradients compared with Lamilloy. Our result at Leeds with a pitch to diameter ratio of approximately 10/1 and hence potentially worse thermal gradients than in your work, showed that at a wall temperature of 900°C the maximum temperature difference between the holes was 13°C and 26°C through the wall thickness (ASME paper 84-GT-212).

These figures compare well with your 22°C temperature difference at an 871°C metal temperature for the GMA 500 combustor.

Have these effusion cooling designs been applied to turbine blades or any estimations of potential blade cooling air reductions made?

Author's Reply

We have applied effusion cooling designs of the type described here to turbine blading, but only in the leading edge region in the form of "shower head" film cooling. In fact, the design data base for the effusion cooling approach originated as an attempt to establish a leading edge cooling configuration model (Ref.26 in the present paper). The approach would appear to have some promise for cooling other regions of the blade, particularly when combined with backside impingement cooling as you have suggested. In very high temperature applications, such a system (applied in the sense of "full coverage film cooling") could very well look attractive assuming potential aerodynamic and structural penalties can be identified and resolved.

FULL COVERAGE IMPINGEMENT HEAT TRANSFER:
THE VARIATION IN PITCH TO DIAMETER RATIO AT A CONSTANT GAP

by
G.E. Andrews, A.A. Asere, C.I. Hussain and M.C. Mkpadi
Department of Fuel and Energy,
University of Leeds,
Leeds LS2.9JT,
U.K.

Summary

Impingement heat transfer is widely used in turbine blade cooling and is becoming more common in combustion chamber wall cooling. For the latter application, geometries that give impingement cooling of large surface areas are required. The geometrical requirement of full coverage heat transfer for combustion chamber cooling are outlined. A series of hole sizes, D , are investigated at a constant pitch, X , and constant impingement gap Z . The usual practice of keeping Z/D constant as X/D has been varied and has been rejected as unrealistic. Design considerations limit practical values of Z to a fairly narrow range of 2-12 mm and it is shown that over this range, Z , has no influence on the impingement heat transfer. The application of the present type of heat transfer correlation to the prediction of impingement cooling chambers is considered. Measured wall temperature data is presented for an impingement/effusion wall cooling geometry. The heating of the impingement plate by the impingement jets being deflected backwards is identified as an area where no heat transfer correlations exist. At low coolant flow rates the temperature rise of the impingement air as it passes through the impingement plate is significant and unless it is taken into account the impingement cooling effectiveness will be overpredicted.

Introduction

Future high temperature gas turbines require better methods of cooling turbine blades and combustor walls (1,2). To achieve better cooling, improved cooling effectiveness and lower coolant mass flows are required. One method of achieving this is transpiration cooling (3,4). However, this technique has mechanical problems such as structural strength and the oxidation and blockage of the small flow passages. Materials such as Lamilloy (5) and Transply (6) have been developed to overcome some of these problems. These materials are examples of full coverage discrete hole wall cooling but with the hole inlet and outlet staggered and connected by internal flow passages. These materials are not generally available and involve a complex manufacturing process which limits the range of hole geometries. This makes it difficult to utilise the optimum geometry in terms of cooling effectiveness, wall pressure loss and coolant mass flow for a given wall cooling application.

Transpiration cooling involves two modes of heat transfer: firstly, there is the internal porous wall heat transfer as the coolant passes through the wall and secondly there is the film cooling by the coolant air adjacent to the wall. Andrews and Asere (7,8) have shown that by measuring the temperature adjacent to a porous (Rigid Mesh RMSOA) wall an adiabatic film cooling effectiveness as well as an overall cooling effectiveness could be measured. Fig. 1 summarises these results which show that at high coolant flow rates, film cooling is the dominant process where at low G values internal wall cooling is of equal importance. Fig. 1 also shows for comparison Transply (6) and Lamilloy (7) data which show a best performance close to that of transpiration but with a very large dependence on the scientific geometry.

The authors (9-12) have been investigating full coverage discrete hole film cooling as a simple means of achieving the film cooling performance of transpiration systems with some internal wall cooling due to the finite hole length within the wall. The overall cooling effectiveness for three geometries are shown in Fig. 1 and demonstrate values within the data range for Lamilloy and Transply at the low coolant flow rates for which they were designed. Measurements of the adiabatic film cooling effectiveness (8) for these full coverage discrete hole film cooling geometries are shown in Fig. 2. This shows at low coolant flow rates that the full coverage discrete hole designs achieve a comparable film cooling performance to the transpiration situation.

The overall cooling effectiveness values in Fig. 1 for the full coverage discrete hole (effusion cooling) designs can only be increased by increasing the internal wall heat transfer. Considerations of the internal wall heat transfer (10-12) have shown that this cannot be done merely by increasing the wall thickness, even if this were possible. The addition of impingement cooling has been investigated as the best method of drastically increasing the internal wall cooling. It was the objective of the investigations to optimise the full coverage discrete hole film cooling and impingement cooling geometries separately in order that the best combined geometry could be achieved.

Combined impingement/effusion cooling results in all the impingement air passing through the effusion plate and there is no net cross flow in the impingement gap. An alternative use of impingement heat transfer is to use all the combustion air for impingement heat transfer prior to passing as preheated air to the main combustion system. These two applications require different impingement geometries. Existing data on impingement cooling (13-35) gives little direct information on impingement geometry effects. The objective of the authors work on impingement heat transfer is to establish design correlations that enable optimum impingement geometries to be specified for a given coolant flow rate, pressure loss and surface area to be cooled. In the present work the influence of the hole size, D , is investigated over a range of fixed values of the impingement gap, Z . A knowledge of the influence of D is crucial for the design of an impingement system to achieve a desired pressure loss at a specified coolant flow rate.

Impingement geometry considerations

The two applications of impingement cooling result in different design conditions. The first requires much larger hole sizes than the second. The hole pitch (X) to diameter (D) ratio (X/D) achieved by varying the hole size at a constant pitch is a major geometrical parameter, together with the impingement gap size (Z). Many previous workers on impingement cooling using arrays of jets have varied X/D by

varying X (16-35) and this results in very high jet velocities and associated plate pressure losses for large X/D . The method of varying X/D may have an important influence on the impingement aerodynamics. By increasing D at a constant X the jet edges become closer together. For the same Z varying X/D by increasing D decreases Z/D and increases Z/X as compared with increasing X/D by increasing X with D constant. Thus the dependence of heat transfer on Z may be different for the two situations.

In the present work the X/D effect on impingement heat transfer has been investigated by varying D at a constant X for a range of fixed Z values. Previous work by the authors has investigated the X/D effect at a constant Z/D of 4.5 (14). The values of Z that resulted from some of the geometries were much larger than were practical for gas turbine applications. Consequently, it was considered more practical to investigate whether there was a range of Z over which there was little influence of Z on the impingement heat transfer. Previous work on the influence of Z/D at constant X/D (13) showed that the influence of Z/D was relatively small particularly for $1 < Z/D < 10$ as shown in Fig. 3. Comparison with other published data (13) also show a similar lack of influence of Z/D in the range $1 < Z/D < 6$ as shown in Fig. 4. This range of Z/D covers the practical range and also implies a range of Z values over which a change in D will have little influence on the impingement heat transfer. It was the objective of the present work to determine this range of Z .

Impingement Test Plate Designs

Coolant mass flow per square meter of wall area, G , is related to the total coolant flow area per square metre of wall area, A , and the combustor wall pressure loss, ΔP , by Equation (1):

$$G = C_D A (2\rho\Delta P)^{0.5} \quad (\text{kg s}^{-1}\text{m}^{-2}) \quad (1)$$

where C_D is the discharge coefficient of the impingement holes. The dimensionless area parameter A is equivalent to the percentage open area referred to by Chance (16). The determination of the discharge coefficient is not straightforward as the hole sizes are small and the metal thickness significant; this results in the hole length to diameter ratios (t/D) being greater than unity for many impingement geometries. Also the back pressure caused by the impingement plate may influence the discharge coefficient. Andrews and Mkpadi (9) have investigated these problems and show that C_D is not influenced by the impingement plate unless the Z/D ratio is less than unity. C_D was found to be mainly influenced by the hole t/D and method of manufacture (9). The reason for the lack of significant influence of the impingement plate on C_D is that the unity dynamic head exit pressure loss is replaced by an equivalent bend pressure loss (9).

Equation (1) may also be expressed as:

$$G = C_D A P \left(\frac{2}{RT} \frac{\Delta P}{P} \right)^{0.5} \quad (2)$$

An impingement flow parameter, G_p , results from Equation (2) which is independent of the combustor operating pressure, P :

$$G_p = \frac{G}{P} = \frac{uA}{RT} = C_D A \left(\frac{2}{RT} \frac{\Delta P}{P} \right)^{0.5} \quad (3)$$

For a fixed geometry and impingement flow pressure loss, G_p is dependent only on the operating temperature. G_p determines the impingement jet velocity, u , as shown in Equation (4). The present results are:

$$u = \frac{G}{\rho A} = \frac{G_p RT}{\rho A} = C_D \left(2RT \frac{\Delta P}{P} \right)^{0.5} \quad (4)$$

obtained at 10^5 Pa nominal operating pressure; equivalent engine impingement mass flow rates can be obtained from Equation (3).

For a fixed value of G , the impingement hole geometry used to achieve the desired value of A depends on the number of holes per square metre of impingement surface, n . The impingement hole diameter, D , is given by Equation (5) and the impingement hole pitch, X , for a square array of holes by Equation (6). Combining Equations (5) and (6) gives Equation (7) for the pitch to diameter ratio X/D , which is independent of the number of holes:

$$D = \left(\frac{4}{\pi} \frac{A}{n} \right)^{0.5} \quad (5)$$

$$X = n^{-0.5} \quad (6)$$

$$\frac{X}{D} = \left(\frac{\pi}{4A} \right)^{0.5} \quad (7)$$

It may be shown that the impingement hole Reynolds number, Re , which is used in the correlation of the impingement heat transfer data, is given by Equation (8):

$$Re = \left(\frac{4}{\pi An} \right)^{0.5} \frac{G}{\mu} \quad (8)$$

where μ is the coolant viscosity.

To select the hole geometries applicable to the full coverage combustion chamber wall cooling situation, it is necessary to know the required coolant mass flow per unit surface area. To enable realistic geometries to be selected, a survey of coolant flows per unit surface areas for a range of aero and industrial gas turbines was carried out. The results are shown in Table 1; the data were obtained by dividing the engine mass flow by the operating pressure and the flame tube surface area. The latter parameter was only evaluated approximately by taking combustion chambers as simple cylinders or annular rings; however, the resultant G values are reasonably reliable (+ 10 percent) for the purposes of design evaluation. A typical proportion, C, of the mass flow used for cooling in a conventional engine is approximately 40 percent. Table 1 indicates that a range of G values from 0.9 to 1.5 kg/sm² bar is representative of current techniques. If the proportion of air used for wall cooling is to be reduced, then G values in the range 0.2-0.4 are required. This represents coolant flow in the range 10-20 percent of the total flow rate, which is a substantial reduction on conventional techniques.

Table 1: Coolant air flow at 1 bar per unit surface area, G-kg/sm², for a range of gas turbines A-H.

C%	A	B	C	D	E	F	G	H
10	0.22	0.14	0.24	0.20	0.23	0.33	0.10	0.30
20	0.45	0.28	0.47	0.41	0.47	0.67	0.20	0.60
30	0.67	0.43	0.71	0.61	0.70	0.99	0.30	0.90
40	0.90	0.57	0.95	0.82	0.93	1.32	0.40	1.20
50	1.12	0.71	1.18	1.02	1.16	1.65	0.50	1.50

Table 2: Impingement geometries of combustor wall cooling

$\frac{\Delta P}{P}$ %	T (°C)	X/D									
		(kg s ⁻¹ m ⁻¹ at 10 ⁵ Pa)									
		G									
		0.2	0.3	0.4	0.5	0.6	0.8	1.0	1.5	2.0	3.0
3	27	16.6	13.2	11.5	10.2	9.3	8.1	7.2	5.9	5.1	4.2
	427	13.1	10.7	9.3	8.3	7.6	6.6	5.9	4.8	4.1	3.4
5	27	18.4	15.0	13.0	11.6	10.6	9.2	8.2	6.7	5.8	4.8
	427	14.9	12.2	10.5	9.4	8.6	7.4	6.7	5.4	4.7	3.8

For impingement cooling of combustion chamber walls the maximum available pressure loss is the combustor pressure loss. The effusion cooling studies have shown that for optimum film cooling performance a large effusion hole size is preferable with consequently a low pressure loss (12). For impingement/effusion applications it is therefore valid to assume that all the pressure loss would occur at the impingement plate. The design of the impingement plate is mainly specified by the desired pressure loss $\Delta P/P$ and the required coolant flow per unit surface area, G. Combining Equations (2) and (7) it may be shown that the impingement hole pitch to diameter ratio is specified by Equation (9).

$$\frac{X}{D} = \left[\frac{\pi}{4} C_D P \right]^{0.5} \left[\frac{2}{RT} \right]^{0.25} \frac{(\Delta P/P)^{0.25}}{G^{0.5}} \quad (9)$$

For a C_D of 0.8 (9) and a pressure P of 1 bar Equation (9) may be reduced to Equation (10)

$$\frac{X}{D} = 72.4 \left(\frac{\Delta P/P}{T} \right)^{0.25} \frac{1}{G^{0.5}} \quad (10)$$

Table 2 presents the values of X/D for two practical values of $\Delta P/P$, at two coolant temperatures and a range of G from 10% to 100% of the combustion air flow as summarised in Table 1. Table 2 shows that for combustion chamber wall cooling applications impingement heat transfer correlations for a range of X/D from 3 to 18 are required. There have been no systematic investigations of the X/D effect at constant X and variable D and the present work and that of Ref. 14 covers the X/D range 2-21.

Equation (6) shows that the hole pitch X is purely a function of the number of holes per unit surface area, n. The influence of n on impingement heat transfer is being investigated in an associated research programme. The present work has been carried out for a fixed number of holes, n, of 4306 per square metre. An impingement plate size of 152 mm square has been used with a 10 by 10 square array of holes with a pitch, X, of 15.2 mm. Table 3 lists the range of plates used to achieve the 2 to 22 variation in X/D. All the plates were 6.3 mm thick Nimonic 75.

Experimental Apparatus

The experimental apparatus has been described previously (13-15) and is shown in Fig. 5. It consists of a filtered and metered air supply from a compressor to an insulated 152 mm square plenum chamber with two flow distribution grid plates. The 152 mm square Nimonic 75 impingement test plate was

bolted to the plenum chamber and then bolted at the four corners through 10 mm diameter PTFE spacing rods to the impingement target plate. The four corner spacing rods were interchangeable so that the impingement gap, Z, could be varied. A single insulated (150 mm thick) silicone rubber mat heater was used to heat the 152 mm square Nimonic 75 impingement target plate. The target plate was instrumented with fourteen uniformly spaced mineral insulated grounded junction Type K thermocouples.

Table 3: Test Plate Design Details (Constant X = 15.24 mm)

at G=0.4kg/sm ²					
D mm	$\frac{\Delta P}{P}$	u m/s	M	$\frac{X}{D}$	$\frac{A}{Z}$
8.18	.002	1.4	0.004	1.86	22.63
3.27	.055	8.5	0.026	4.66	3.62
2.33	.28	17.8	0.054	6.83	1.68
1.38	2.17	46	0.140	11.03	0.65
1.18	3.80	63	0.190	12.92	0.47
0.71	18.30	127	0.384	21.46	0.17

Heat Transfer Correlation Procedure

It was shown in Ref. 15 that the target plate temperature variations were less than 2% for a Z/D of 4.5. Consequently, the mean target plate temperatures could be used to determine the mean impingement heat transfer coefficient. For each flow rate the system was allowed half an hour to come into thermal equilibrium before all the temperatures were noted. The temperature difference between the target plate and the impingement plenum chamber air temperature was kept at approximately 120°C, measured with a resolution of 0.1°C. An average heat transfer coefficient, h, was determined, by Equation (11) for the entire target surface area

$$h = \frac{Q}{A_s(T - T_m)} \quad (11)$$

where Q is the electrical heat supply (watts) less a 3% allowance for heat losses (16,22,35), A_s is the target surface area (m^2), T is the target mean temperature and T_m is the log-mean temperature of the impingement grid plate and the air temperature inside the plenum. The log-mean temperature has been used as a closer temperature to the impingement jet outlet than the upstream temperature (15). This has also been used by other workers (21,23,26,33).

The impingement heat transfer results are generally correlated by a dimensionless equation of the form of Equation (12) (16,17,21-23,27).

$$Nu = \frac{hD}{k} = C \left(\frac{X}{D}\right)^a \left(\frac{Z}{D}\right)^b Re^y Pr^{1/3} \quad (12)$$

where Reynolds number is defined by Equation (8). For air the Prandtl number term may be regarded as a constant (C_{Pr}/k). Many previous workers have not evaluated the exponents a and b but left the results in a graphical form. The evaluation of the exponent y has been extensively studied. In the present investigations the exponents a and y will be determined over a range of impingement gaps, Z. Also the dependence of the exponent y on X/D will be investigated for a range of Z.

In the present work the variables investigated are G, D and Z. It may be shown from Equation (12) and (2-8) that h is related to these parameters by Equation (13).

$$h = \text{const. } Z^b D^{-(1+a+b+y)} G^y \quad (13)$$

It is the objective of the present work to show that for a limited range of Z, there is no influence of Z on h and it can be included in the constant so that Equation (13) simplifies to Equation (14)

$$h = \text{const. } D^{-(1+a+y)} G^y \quad (14)$$

The exponent for the hole diameter will be termed j, as defined by Equation (15).

$$j = 1+a+y \quad (15)$$

Influence of Impingement Hole Reynolds Number

The Re has been varied by changing G for each value of X/D in Table 3. Fig. 6 shows the results for a constant Z of approximately 6 mm plotted on the basis of Equation (12) and Fig. 7 on the basis of Equation (13). A least squares fit to the data on these graphs has been used to evaluate the exponent y in Equations (12) and (13). The variation of y with X/D for a range of Z from 3-12 mm is shown in Fig. 8. This also shows equivalent data for a constant Z/D of 4.5 (14). Fig. 8 shows that there is some indication of a weak dependence of y on both X/D and Z. However, to include these relationships in Equations (12) and (13) would create a cumbersome correlation. A constant value of y of 0.72 has been used in previous work (13,14) and represents a reasonable mean value of the results in Fig. 8.

Influence of Impingement Gap, Z

Figs. 9 and 10 show the similar results to Figs. 6 and 7 for Z = 3, 6 and 12 mm and two values of X/D. These show that for this range of Z there is little influence of Z on the heat transfer relationships.

This supports the result in Figs. 3 and 4 (13) which show that there is a range of Z/D over which the impingement heat transfer shows little dependence on Z/D. Fig. 11 shows that the exponent y is not dependent on Z, except at very small values of Z. The influence of X/D on y shown in Fig. 8 is also apparent in Fig. 11.

The variation of h with Z for a range of X/D is shown in Figs. 12 and 13 which differ only in the G value. All the test results, except for an X/D of 1.9, show that for $2 < Z < 12$ mm, there is little influence of Z on h. For values of Z larger than 12 mm, h gradually decreases as Z is increased. The anomalous results for a X/D of 1.9 were due to the low values of Re (< 2000). The results in Figs. 9-13 clearly support the conclusion that for $2 < Z < 12$ mm there is no influence of Z on the impingement heat transfer. The range of Z is the practical range for gas turbine combustion chamber and turbine blade impingement cooling.

Influence of X/D

Fig. 14 shows the influence X/D on $Nu/PR^{1/3}$ for a range of Re and a constant Z of 6 mm. Fig. 15 shows the equivalent data for the dependence of h on X/D for a range of G at a constant Z of 6 mm. Fig. 16 shows similar results to Fig. 15 for a Z of 1.5 mm. These results show a uniform relationship with X/D in contrast with the previous results (14) at a constant Z/D of 4.5. These showed a uniform dependence on X/D only at high values of X/D. The reason for this was that at low X/D and a Z/D of 4.5, the impingement gap was considerably greater than the 10 mm maximum value found in this work for the heat transfer to be independent of Z.

A least square fit to the data in Figs. 15 and 16 has been made to evaluate the exponent j in Equation (15). This shows some dependence on G as shown in Fig. 17. Excluding the data for Z = 1.5 mm, the results may be correlated by Equation (16) for $3 < Z < 19$

$$j = 0.54 + 0.05 G/\bar{G} \quad (16)$$

However, in spite of the dependence of j on the flow rate G, the inclusion of Equation (16) in Equations (12) and (13) produces a cumbersome correlation. In the present work a mean value for j of 0.64 has been taken. This value of j taken with the 0.72 value for y gives from Equation (15) a value of -1.08 for a. This is shown in Fig. 14 to be in good agreement with the results correlated in terms of Equation (12).

General Correlations

Using Equation (13) the present results may be correlated by Equation (17).

$$h = 75 \left(\frac{X}{D}\right)^{0.64} G^{0.72} \quad (17)$$

$$\text{for } 2 < Z < 12 \text{ mm}$$

The equivalent correlation for a constant Z/D of 4.5 in Ref. 14 was

$$h = 63 \left(\frac{X}{D}\right)^{0.72} G^{0.72} \quad (18)$$

The agreement of the experimental data with Equation (17) is shown in Figs. 18-20 to be good and comparison of these figures indicates a minimal influence of Z over the range 3-12 mm. This data scatter is greatest at low G values where the flow is often of low Re. However, the level of agreement justifies the use of simple fixed values for the exponents j and y rather than more complex forms such as Equation (16).

The equivalent dimensionless correlation of the results in Equation (17) may be arranged in the form of Equation (12), but without any Z/D influence, as in Equation (19).

$$Nu = 27 D^{1.08} Re^{0.72} \quad (19)$$

In the present work X was constant at 15.2 mm and Equation (19) may only apply to this value of X or this value of n. Further work is in progress to investigate the influence of X or n. The present value of X may be incorporated into Equation (19) to introduce X/D as a parameter as in Equation (20).

$$Nu = 0.29 \left(\frac{X}{D}\right)^{-1.08} Re^{0.72} \quad (20)$$

The present results are shown for Z = 6 mm in Fig. 21. The data scatter in Fig. 21 and Figs. 18-20 is random and shows no systematic dependence on X/D.

Combined Impingement/Effusion Cooling

The test rig has been described previously (7-12) for work on single full coverage discrete hole film cooling systems (effusion cooling). It consists of the same coolant air supply system as in Fig. 1. The impingement gap was formed using a 6 mm flange with gaskets on each side bolted through to seal for any leaks between the impingement and effusion plates. This 152 mm square impingement/effusion cooling system was flush mounted in the wall of a 152 mm by 76 mm air cooled duct. The air flow in this duct was heated by a propane fired preheater to approximately 750K. The coolant air was not preheated and this gave a coolant to hot gas density ratio of approximately 2.5, which is typical of combustor primary zone conditions. The test rig could also achieve actual combustor conditions using a JetMix (36,37) rapid fuel and air mixing lean burning kerosene fired combustion system. At the 750K low temperature of the present

work this Jet Mix system was not fuelled and it acted as a grid plate to generate realistic turbulence levels in the crossflow. The geometry of the system involved radiative heat transfer between the test plate and the duct walls (11). Correction techniques have been developed for this for a single effusion plate (11), but for impingement/effusion cooling a knowledge of the impingement heat transfer is required. The present work gives correlations which may be used for a correction procedure. In the present work with a 750K mainstream temperature the correction term was small, except at very low G values. Hence, the uncorrected test results may be used to illustrate the additional influence of impingement cooling to effusion cooling.

Each test plate was instrumented with five grounded junction type K mineral insulated thermocouples, vacuum brazed to the test plate with the thermocouple junction flush with the metal surface adjacent to the hot gas cross flow. The thermocouples were positioned 25 mm apart on the centreline of the test plate and between rows of holes as detailed in Ref. 10. The temperature gradients between the holes were small and at the maximum were only 3% of the plate temperature (10). The five thermocouples were used to determine the axial development of the overall cooling effectiveness defined in Equation (21).

$$\eta = \frac{T_g - T_w}{T_g - T_c} \quad (21)$$

The crossflow hot gas temperature, T_g , was measured using a traversing mineral insulated thermocouple positioned 50 mm normal to the centre of the test plate. This temperature was corrected for radiative heat losses using the mean duct velocity and the measured duct wall temperature. The coolant temperature T_c was that at the flow metering station.

The cooling effectiveness values 127 mm downstream of the leading edge, for one of the present impingement plates, $X/D = 11.03$ and $Z = 7$ mm, in combination with an effusion plate with a total hole area 2.85 times greater are shown in Fig. 22. Equation (2) shows that this will give a pressure loss difference by a factor of 8.1, thus the pressure loss will be mainly at the impingement plate. The impingement holes were equal in number to the effusion holes ($D=2.33$ mm) and were offset half a hole pitch from the effusion holes. Thus the impingement jet was directed in the centre of the square array of effusion holes. The effusion cooling alone has been investigated separately (12) and the cooling effectiveness values are shown for comparison in Fig. 22. There is clearly a significant improvement in the cooling effectiveness with impingement cooling. Comparison with Fig. 1 shows that the results are comparable with some of the best results for more complex materials such as Transply and Lamilly.

Impingement Plate Heating

A problem that has been found in the present work is that not only is the target plate cooled by the impingement cooling, but the impingement plate is heated. This has been found both on the impingement heat transfer test rig and in the combined impingement/effusion tests. Calculations have shown that only a small proportion of this heating can be accounted for by radiation from the hotter target plate. Fig. 23 shows the magnitude of the effect for the impingement tests (15). This heating of the impingement plate was the reason for using the log-mean temperature in the determination of the heat transfer coefficient in Equation (11). No other investigators have reported measurements of the impingement plate temperature and generally have used the impingement air supply temperature in the impingement correlations. It is the coolant temperature at the impingement plate exit holes that is required in the impingement correlations and the use of the log-mean temperature is an attempt to use a coolant temperature close to this in Equation (11).

For the impingement/effusion cooling situation the temperature rise of the impingement plate is much greater than for the very low temperature impingement heat transfer test rig. Fig. 24 shows the magnitude of this effect. To use the present impingement correlations it is clearly necessary to predict the coolant outlet temperature from the impingement plate. Techniques for this have been developed for effusion cooling (10,11,12) and may be applied to the impingement plate. Such predictions are shown in Fig. 24 to be in agreement with experimental measurements of the gap temperature. However, if a general prediction procedure is to be developed for impingement/effusion wall cooling it is necessary to be able to predict the impingement plate temperature.

The heating of the impingement plate is considered to be due to both radiative and convective heat transfer. The former can be easily predicted but no information exists for the convective heating of the impingement plate as the phenomena has not previously been recognised. It is considered that the convective heating is caused by the deflection of the impinging jets back from the target plate onto the impingement plate. It is likely that this effect may be a strong function of Z and some evidence for this is given in Fig. 23. It is the intention of the authors to provide data for the convective heat transfer to the impingement plate as an essential prerequisite of a full impingement/effusion wall cooling prediction programme.

Conclusions

1. The influence of X/D on impingement heat transfer, with D as the variable at constant X , is an important parameter for gas turbine applications. For combustor wall cooling the relevant range is $3 < X/D < 18$.
2. The impingement gap, Z , has little influence on the impingement heat transfer for $2 < Z < 12$ mm. It is preferable to investigate the X/D effect at constant Z rather than constant Z/D , as the variation in Z is much greater than the 2-12 mm range.
3. The influence of X/D on impingement heat transfer may be correlated by Equations (17) and (20).

$$h = 75 (X/D)^{0.64} G^{0.72} \quad (17)$$

$$Nu = 0.29 (X/D)^{-1.08} Re^{0.72} \quad (20)$$

4. Impingement combined with effusion cooling gives a significant increase in cooling effectiveness. The relatively simple wall cooling geometries have a cooling performance as good as the much more complex Transply and Larmilloy wall materials.
5. Impingement cooling results in coolant jet deflection of the impinging jets back onto the impingement plate causing convective heating. This phenomena has not been previously recognised and no convective heat transfer data exists.

Acknowledgements

We would like to thank the U.K. Science and Engineering Research Council for Research Grants GR/B/67827, GR/R/00336 and GR/C/59192 in support of this work. A.A. Asere was supported by a grant from G.E.C. Ruston Gas Turbines and we would like to thank M.F. Cannon of G.E.C.-Ruston Gas Turbines, Lincoln for the manufacture of some of the test plates and for technical discussions.

References

1. Jackson, S.R. and Odgers, J., 'Factors influencing heat release in combustion chambers'. Combustion in Advanced Gas Turbine Systems, Cranfield, 1968, Pergamon Press.
2. Nealy, D.A., 'Combustor cooling - old problems and new approaches', In: Gas Turbine Combustor Design Problems, Ed. Lefebvre, A.H., Hemisphere, New York, 1978, pp.151-185.
3. Bayley, F.J., Carnforth, J.W. and Turner, A.B., 'Experiments on a transpiration cooled combustion chamber', Proc. I. Mech. E., Vol. 187, 1973, p.158.
4. Wolf, J.C., Moskowitz, S. and Manning, G.R., 'Development of a high temperature turbine for operation on coal-derived fuel', ASME Paper No.80-GT-188, 1980.
5. Nealy, D.A. and Reider, S.R., 'Evaluation of laminated porous wall materials for combustor linear cooling', ASME Paper No. 79-GT-100, 1979.
6. Wassell, A.B. and Bhangu, K., 'The development and application of improved combustor wall cooling techniques', ASME Paper No. 80-GT-66, 1980.
7. Andrews, G.E. and Asere, A.A., 'Transpiration cooling of gas turbine combustion chamber walls', 1st U.K. National Heat Transfer Conference, Leeds, I.Chem.E. Symposium Series No.86, Vol.2, p.1047-1056.
8. Andrews, G.E., Asere, A.A. and Mkpadi, M.C., 'Transpiration and full coverage discrete hole film cooling', I.Chem.E. 11th Annual Research Meeting Proceedings, p.92-96, 1984.
9. Andrews, G.E. and Mkpadi, M.C., 'Full coverage discrete hole wall cooling - discharge coefficients', ASME Paper 83-GT-79 and also Trans. ASME, J. Eng. Power, Vol. 106, p.183-192, 1984.
10. Andrews, G.E., Gupta, M.L. and Mkpadi, M.C., 'Full coverage discrete hole wall cooling: Cooling effectiveness', ASME Paper 84-GT-212. Presented at the 1984 ASME International Gas Turbine Conference, Amsterdam. Also to be published in The International Journal of Turbo and Jet Engines, 1985.
11. Andrews, G.E., Gupta, M.L. and Mkpadi, M.C., 'Combined radiative and convective heat transfer in an enclosure', 1st U.K. National Heat Transfer Conference, Leeds, I.Chem.E. Symposium Series, No. 86, Vol.2, p.929-988, 1984.
12. Andrews, G.E., Asere, A.A., Gupta, M.L. and Mkpadi, M.C., 'Full coverage discrete hole film cooling: The influence of hole size', Accepted for publication at the 1985 ASME International Gas Turbine Conference, Houston, March 1985. Also accepted for publication in the International Journal of Turbo and Jet Engines, 1985.
13. Andrews, G.E. and Hussain, C.I., 'Impingement cooling of gas turbine components', 1983, Tokyo International Gas Turbine Conference, p.67-74, JSME, ASME, I.Mech. E., 1983, High Temperature Technology, Vol.2, p.99-106, 1984.
14. Andrews, G.E. and Hussain, C.I., 'Full coverage impingement heat transfer: The influence of impingement jet size', 1st U.K. National Heat Transfer Conference, Leeds, I.Chem.E. Symposium Series No.86, Vol.2, p.1115-1124, 1984.
15. Andrews, G.E. and Hussain, C.I., 'Impingement cooling using large arrays of holes', I.Chem.E. 11th Annual Research Meeting Proceedings, p.86-91, 1984.
16. Chance, J.L. 'Experimental investigation of air impingement heat transfer under an array of round jets', Tappi 57, No.6 (June 1974) pp.108-112.
17. Tabakoff, W. and Clevenger, W., 'Gas turbine blade heat transfer augmentation by impingement of air jets having various configurations', ASME, J. of Engng. for Power (January, 1972) pp.51-60.
18. Metzger, D.E. et al, 'Heat transfer characteristics for inline and staggered arrays of circular jets with crossflow of spent air', ASME, J. of Heat Transfer 101, No.3 (August 1979) pp.526-531.
19. Friedman, S.J. and Mueller, A.C., 'Heat transfer to flat surfaces', Proc. of General Discussion on Heat Transfer (The Inst. of Mech.Engrs., London, 1951), pp.138-142.

20. Gauntner, J.W. et al, 'Crossflow effects on impingement cooling of a turbine vane', NASA, TM.X-3029 (Lewis Research Centre, Cleveland, OH, March 1974).
21. Huang, G.C., 'Investigations of heat transfer coefficients for air flow through round jets impinging normal to a heat transfer surface', ASME, J. of Heat Transfer (August 1963) pp.237-245.
22. Hollworth, B.R. and Berry, R.D., 'Heat transfer for arrays of impinging jets with large jet-to-jet spacing', ASME, paper no. 78-GT-117.
23. Kercher, D.M. and Tabakoff, W., 'Heat transfer by a square array of round air jets impinging perpendicular to a flat surface including the effect of spent air', ASME J. of Engng for Power (January 1970) pp.73-82.
24. Livingood, J.N.B. and Gauntner, J.W., 'Local heat transfer characteristics of a row of circular air jets impinging on a concave semicylindrical surface', NASA TN.D-7127 (January 1973).
25. Dyban, E.P., et al, 'Heat transfer and hydrodynamics of an array of round impinging jets with one sided exhaust of spent air', Int. J. of Heat Mass Transfer 23 (1980) pp.667-676.
26. Hilgeroth, E., 'Wärmeübergang bei Düsenströmung senkrecht zur Austauschfläche' (Translation: 'Heat transfer from a jet stream at right angles to the exchange surface') Chemie Ing Techn 37 No.12 (1965) pp.1264-1272.
27. Behbahani, A.I. and Goldstein, R.J. 'Local heat transfer to staggered arrays of impinging circular air jets', ASME paper no. 82-GT-211.
28. Ott, H.H., 'Wärmenbergang an einer durch Luftstrahlen gekühlten platte', (Translation: Heat transfer to a plate cooled by air flow') Schweiz Bauzeitung 79 No.46 (16 November 1981) pp.834-840.
29. Chupp, R.E. et al, 'Evaluation of internal heat transfer coefficients for impingement cooled turbine airfoils', AIAA, paper no. 68-564.
30. Florschuetz, L.W. et al, 'Streamwise flow and heat transfer distributions for jet array impingement with crossflow', ASME, paper no.81-GT-77.
31. Florschuetz, L.W. and Isoda, Y., 'Flow distribution and discharge coefficient effects for jet array impingement with initial crossflow', ASME, paper no. 82-GT-156.
32. Hrycak, P., 'Heat transfer from a row of impinging jets to concave cylindrical surfaces', Int. J. Heat Mass Transfer 24 (1981) pp.407-419.
33. Metzger, D.E. and Korstad, R.J., 'Effects of crossflow on impingement heat transfer', ASME, J. of Engng. for Power 94 (January, 1972) pp.35-41.
34. Metzger, D.E. et al, 'Impingement cooling of concave surfaces with lines of circular air jets', Trans. ASME, Series A, 91, No.3 (July 1979) pp.149-158.
35. Saad, N.R. et al, 'Local heat transfer characteristics for staggered arrays of circular impinging jets with crossflow of spent air', ASME, paper no. 80-HT-23.
36. Andrews, G.E., Al-Dabbagh, N.A. and Abdul Aziz, M.M., 'Mixing and fuel atomisation effects on premixed combustor performance', ASME Paper 83-GT-55, 1983. Also to be published in Int. J. Turbo and Jet Engines, 1985.
37. Abdul-Aziz, M.M. and Andrews, G.E., 'Smoke emissions from lean well mixed gas turbine primary zones', 1985, ASME, Beijing International Gas Turbine Conference.

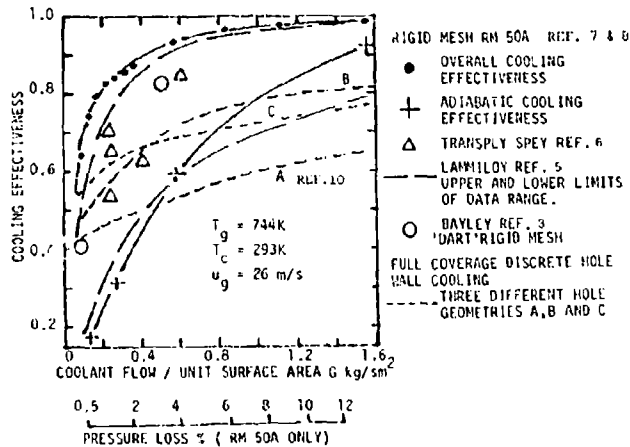


FIG. 1 COOLING EFFECTIVENESS AS A FUNCTION OF COOLANT FLOW RATE G

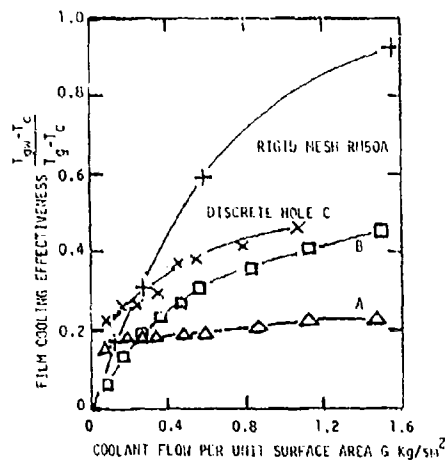


FIG. 2 FILM COOLING EFFECTIVENESS AS A FUNCTION OF G

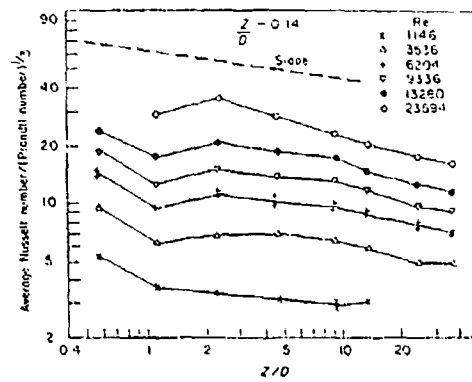
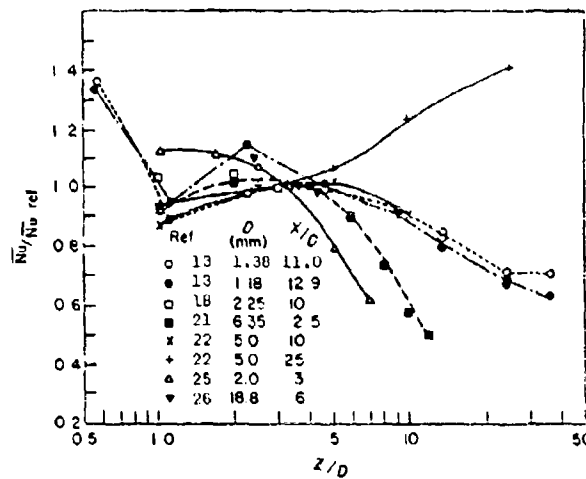
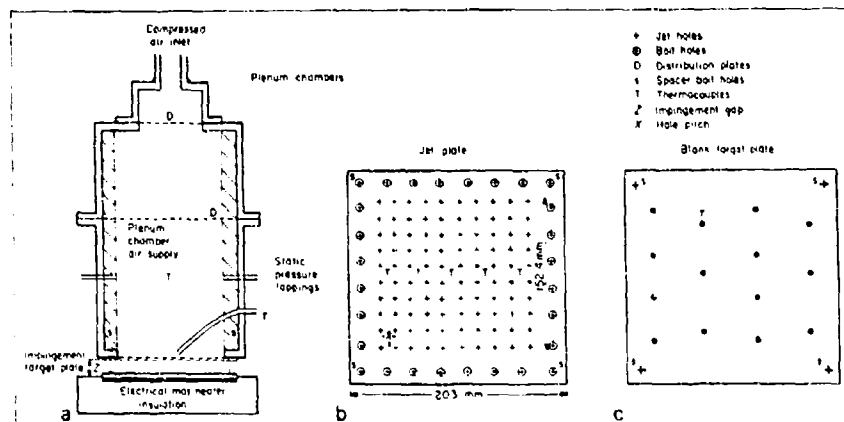
Figure 3 Influence of Z/D on heat transfer: $X/D = 12.9$ Figure 4 Comparison of the influence of Z/D on heat transfer with previous data: \bar{Nu}_{ref} at $Z/D \sim 3$ 

FIG. 5 IMPINGEMENT HEAT TRANSFER TEST RIG

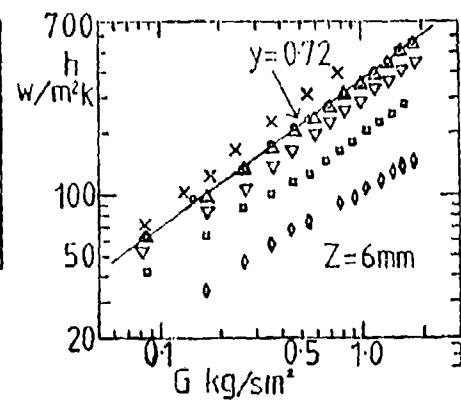
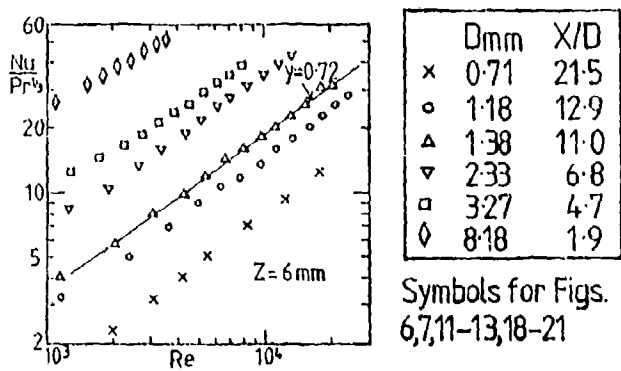


Fig. 6 Nu. v Re at Z=6mm for various X/D

Fig. 7 Variation of h with G at Z=6mm

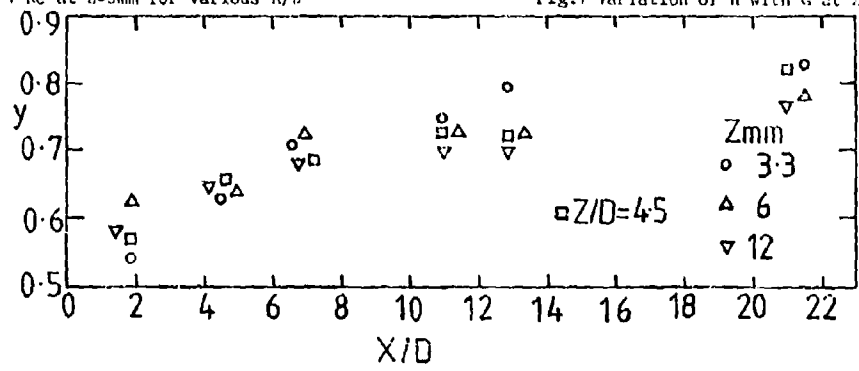


Fig. 8 Variation of the Re exponent y with X/D for a range of Z.

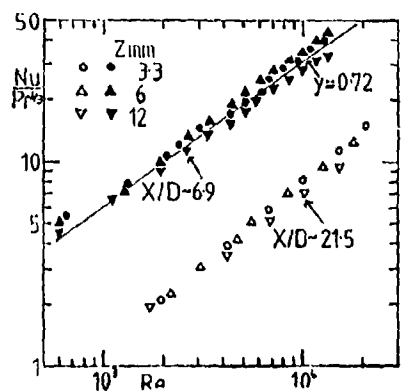


Fig. 9 Nu v Re for a range of Z

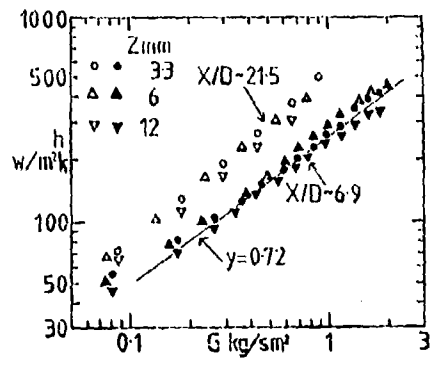


Fig. 10 h v G for a range of Z

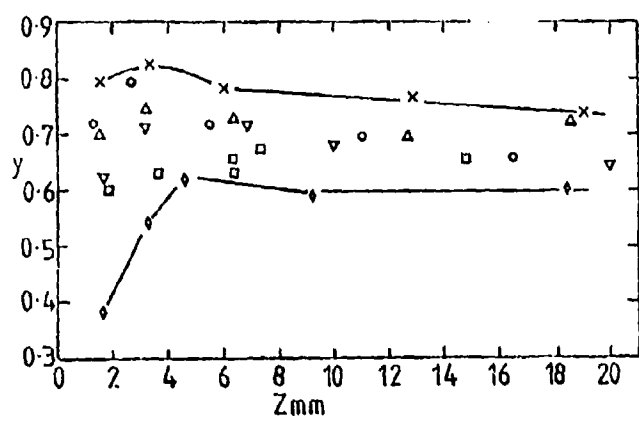
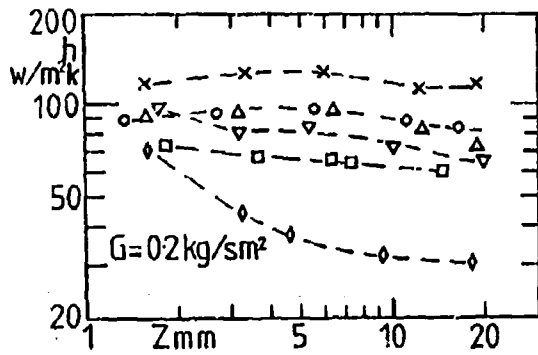
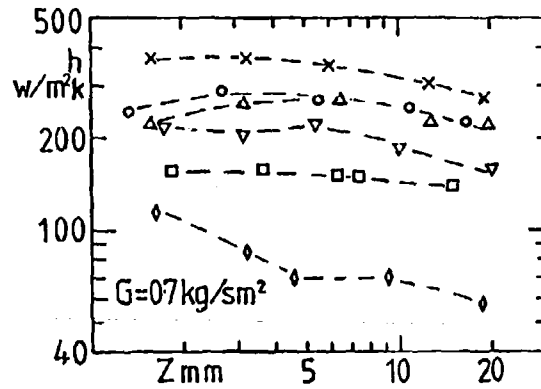
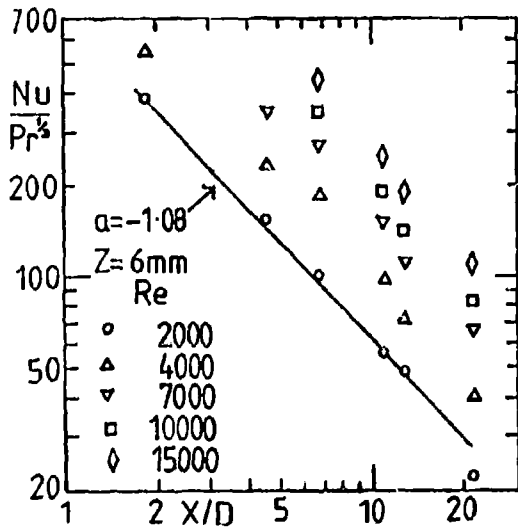
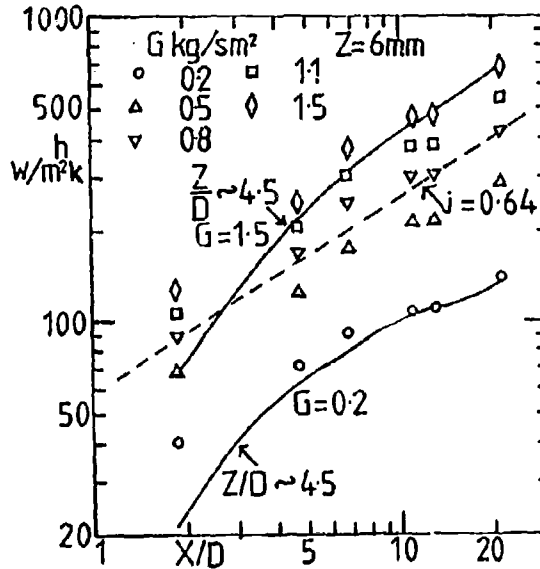
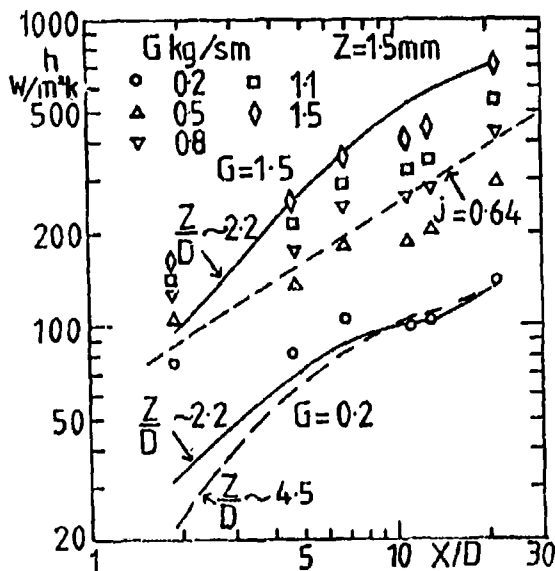
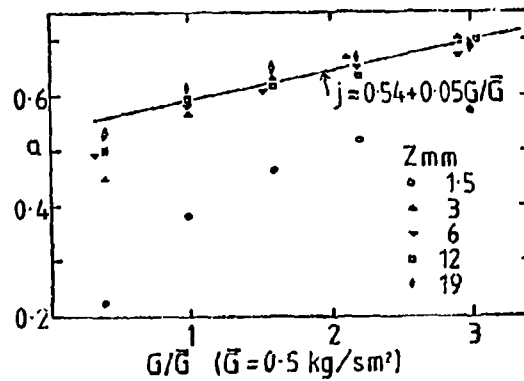


Fig. 11 Variation of the Re exponent y with Z for a range of X/D

Fig. 12 h v Z for a range of X/D at $G=0.2 \text{ kg/sm}^2$ Fig. 13 h v Z for a range of X/D at $G=0.7 \text{ kg/sm}^2$ Fig. 14 Nu v X/D for various Re at $Z=6 \text{ mm}$ Fig. 15 h v X/D for various G at $Z=6 \text{ mm}$ Fig. 16 h v X/D for various G at $Z=1.5 \text{ mm}$ Fig. 17 X/D exponent ' a ' as a function of coolant flowrate for various Z

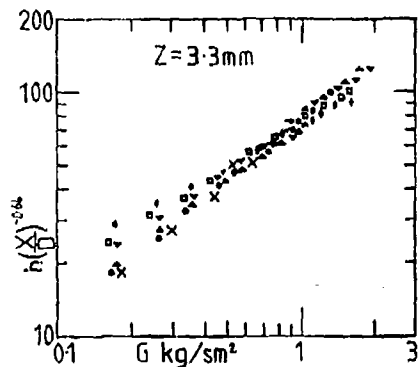
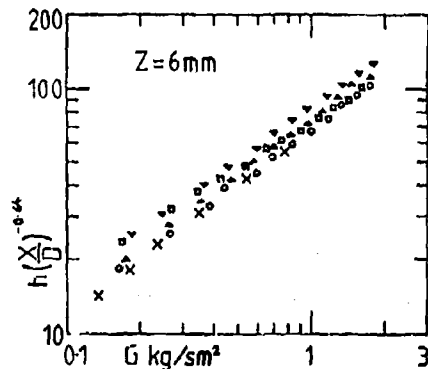
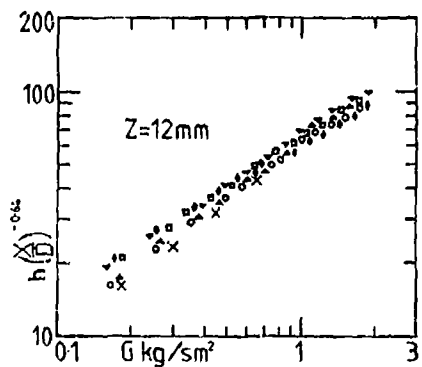
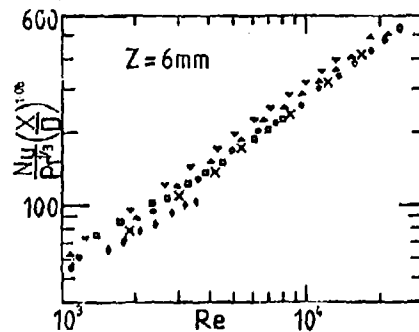
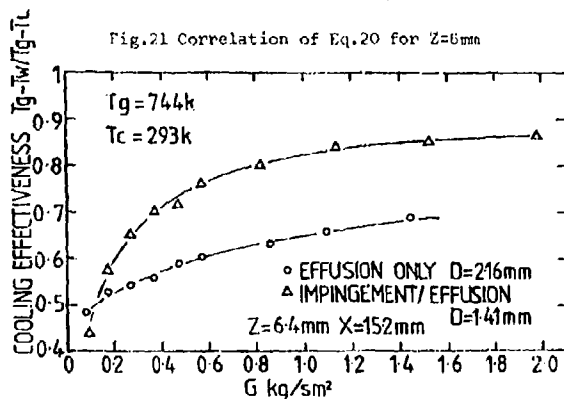
Fig. 18 Correlation of Eq. 17 for $Z=3.3\text{mm}$ Fig. 19 Correlation of Eq. 17 for $Z=6\text{mm}$ Fig. 20 Correlation of Eq. 17 for $Z=12\text{mm}$ Fig. 21 Correlation of Eq. 20 for $Z=6\text{mm}$

Fig. 22 Cooling Effectiveness as a function of G for Impingement/Effusion and Effusion alone with $X/D = 11$ for the Impingement plate and 7 for the Effusion plate with $Z = 6.4\text{mm}$



T_I = Impingement plate mean temperature
 T_m = Target plate mean temperature
 T_c = Plenum chamber coolant temperature

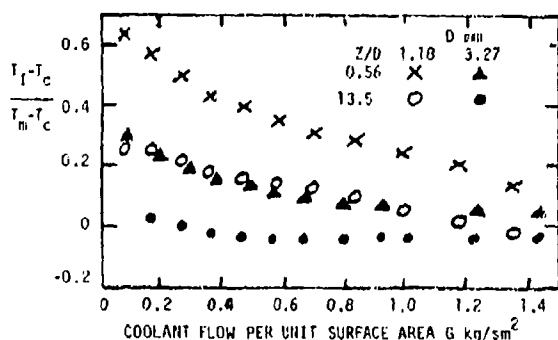


FIG. 23 IMPINGEMENT PLATE HEATING AS A FUNCTION OF FLOW RATE

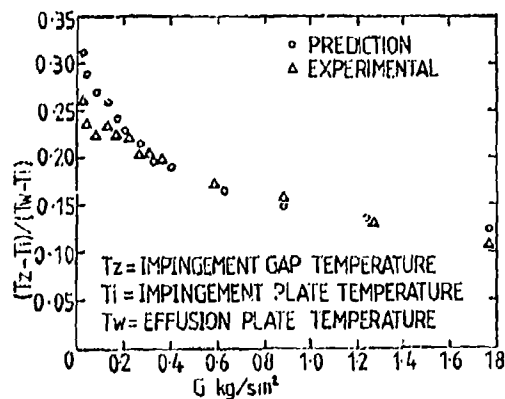


Fig. 24 Heating of the Impingement plate by the hot Impingement air for the Impingement/Effusion high temperature tests.

DISCUSSION

S.C.Arora, Ca

I am a bit confused about your geometric variables. Is it X/D and Z/D or X, Z and D ? If it is X/D and Z/D then it should not matter whether a specific value of the variable is obtained by varying X and Z or only D .

Author's Reply

In the work mostly D is the variable whereas X and Z are constant.

D.E.Metzger, US

The results in the paper are all derived from measurements of average heat transfer over the test plate. It appears that these results are given for Z/D values as low as 0.3. These low values of Z/D also occur, since D was varied at constant X , at low values of X/D . For this situation, significant variation of jet velocity between the center and edges of the jet array are expected, accompanied by corresponding variation in local heat transfer coefficients. How then can these results be used to predict the combined impingement/film cooling application where jet crossflow in the array will not be present?

Author's Reply

The use of the average surface temperature in the heat transfer coefficient, h , in Eq.11 is one of the main reasons for data scatter in the results. The reason for this is that the temperature does vary over the target plate with an associated variation in h . However, these variations are generally low and only use as high as $\pm 10\%$ of the mean for extreme conditions and the case that you quote of small Z/D at a small X/D is one of these. Some details of these heat transfer coefficient variations for this situation have been published in Ref.15 and at the 7th ISABE meeting (Sept. 1985).

The main contributing factor to these variations in h is the crossflow of the impingement air experienced by the outer jets of the array. As you have pointed out for the 8-18 mm holes situation the static pressure gradient in the impingement gap can cause a maldistribution of the airflow between the holes. However, in the smaller hole tested the hole dynamic pressure loss is greater than any impingement gap pressure gradient and this flow maldistribution effect will be much smaller. The main effect then is that of the impingement gap mass flow velocity which can contribute to the convection cooling of the target plate. For most of the geometries we have investigated crossflow enhances the heat transfer slightly. This effect is greatest at small values of Z and is the major factor contributing to the lower limit of Z in the correlation.

The aim of the very large hole impingement systems was to determine whether low pressure loss high mass flow impingement systems were feasible. The intended application for the low X/d data was not combined impingement/effusion cooling. Our design estimates indicate that hole sizes in the 3-8 mm range, for $X = 15.2$ mm, may be required for this application with coolant mass flows, G , 2-3 kg/(sm²) at 1 bar. The proposed impingement correlation indicates values of h in the range 200-400 W/(m²K) will be possible, this is also demonstrated in Fig.7. For a 3% type pressure loss at the impingement plate and a low coolant mass flow for a combined impingement/effusion application, the equivalent value of h for the necessarily larger X/D systems is approximately 150 W/(m²K). Consequently, the intended application may be feasible although further work on the crossflow effect for these small X/D systems will be required, although Fig.13 indicates that this may be beneficial.

TECHNIQUES DE REFROIDISSEMENT DES CANAUX DE RECHAUFFE DES TURBOREACTEURS

M. DESAULTY - P. TROUILLOT - S. COUTOR

S.N.E.C.M.A
Centre de Villaroche
77550 NOISSY-CRAMAYEL - FRANCERESUME

L'augmentation des performances des turboréacteurs avec rechauffe exige, de la part des constructeurs, un effort de recherche technologique dans le domaine de la protection des parois des canaux de rechauffe.

Les procédés utilisés pour refroidir les chemises de protection thermique ont connu une évolution importante qui, associée à des méthodes de calcul permettant une optimisation plus poussée, a permis de réaliser des gains substantiels tant sur le plan de la masse que sur le plan de l'efficacité du refroidissement.

NOMENCLATURE

A	Section de passage de l'écoulement entre chemise et carter
Ac	Section de passage de l'écoulement principal
B	Périmètre de frottement entre chemise et carter
Bc	Périmètre de frottement de l'écoulement principal
CF	Coefficient de frottement entre chemise et carter
CFc	Coefficient de frottement dans l'écoulement principal
dx	Longueur d'une tranche élémentaire de calcul
M	Nombre de Mach entre chemise et carter
Mc	Nombre de Mach dans le flux principal
P	Pression totale entre chemise et carter
PC	Pression totale dans l'écoulement principal
T	Température totale entre chemise et carter
TC	Température totale dans l'écoulement principal
Y	Rapport des chaleurs spécifiques dans l'écoulement entre chemise et carter
Yc	Rapport des chaleurs spécifiques dans l'écoulement principal
η	Efficacité adiabatique
η_{PC}	Rendement de rechauffe

INTRODUCTION

L'augmentation des performances des turboréacteurs avec rechauffe passe par des conditions de fonctionnement de plus en plus sévères en températures (augmentation de la température du flux primaire) et par une réduction des débits d'air consacrés au refroidissement du canal.

Cette recherche de performances toujours améliorées a conduit les motoristes à faire évoluer la technologie vers des procédés de refroidissement des parois plus élaborés.

Cette évolution technologique est ici présentée par la comparaison des chemises de protection thermique de plusieurs moteurs SNECMA.

Les principales étapes du développement d'une chemise sont ensuite présentées depuis la conception, les essais partiels jusqu'aux essais sur moteur.

1 - EVOLUTION DE LA TECHNOLOGIE SUR LES MOTEURS SNECMA

Depuis une trentaine d'années, des progrès importants ont été accomplis dans la conception des chemises de protection thermique des canaux de rechauffe et notamment en ce qui concerne l'efficacité du refroidissement et la masse.

a) - Moteurs monoflux

Sur le moteur ATAR (figure 1), le refroidissement de la chemise est assuré par convection forcée au moyen d'air provenant de la turbine et qui est donc à une température de l'ordre de 1000 K.

Ceci conduit à une température moyenne de chemise relativement élevée de l'ordre de 1220 K à 1350 K et nécessite d'avoir recours à un canal en acier et à une chemise segmentée et ondulée circonférentiellement.

Sur le moteur OLYMPUS, le taux de PC est très réduit (10 % sur OLYMPUS 593) et la chemise se réduit à une zone anti-scratch destinée à amortir les phénomènes vibratoires.

Néanmoins, un canal en acier doit être employé.

b) - Moteurs double flux

Sur les moteurs double flux (figure 1), une partie du flux secondaire est utilisée pour refroidir la chemise et protéger thermiquement le canal, ce qui permet d'utiliser pour la fabrication de ce dernier du titane, nettement plus léger que l'acier.

Les technologies de refroidissement de chemise ont connu une évolution comparable à celles qui sont utilisées sur chambre (figure 2) :

- * Sur M53-4, le refroidissement a tout d'abord été assuré par 7 films à alvéoles. Ce type de refroidissement présente une grande hétérogénéité circumférentielle due à la présence de pontets destinés à maintenir l'écartement entre parois et un niveau d'efficacité moyen très inférieur à celui d'une fente pure.

Ce mode de refroidissement a rapidement été remplacé par un dispositif de 11 films chaudronnés possédant une meilleure efficacité et une meilleure homogénéité circumférentielle.

- * Sur M53-5, le dispositif à 11 films a été amélioré par l'adjonction d'une zone multiperforée située en fin de virole, de perméabilité 0,8 % et destinée à diminuer les gradients de température longitudinaux.

Cependant, ces films chaudronnés possèdent un certain nombre d'inconvénients :

- ils nécessitent l'emboîtement de nombreux éléments coniques assemblés par rivetage,
- les languettes de films se déforment quand elles sont soumises à une surchauffe (sillage) ce qui a tendance à amplifier les points chauds et à propager la déformation à d'autres viroles situées en aval.

D'autre part, le recours à des films mécaniques taillés dans la masse n'était pas envisageable sur le plan du coût et du poids, ce qui a conduit à la conception de chemises entièrement multiperforées.

- * Sur M53-P2 et M88, la chemise est une virole de faible épaisseur ondulée et multiperforée (planche 2), ce qui s'est traduit par une réduction de la masse (environ 20 %) et du prix de revient associée à une amélioration des performances de tenue thermique :

- diminution du niveau moyen de température
- réduction des gradients longitudinaux et transversaux
- effacement des sillages provenant de l'amont.

Le tableau ci-dessous traduit en température de chemise l'évolution de la technologie.

Moteurs	ATAR 9K50	M53-2	M53-5	M53-P2
Poussée 0/0 plein gaz PC (daN)	7040	7600	8810	9495
Taux de rechauffe	0,43	0,51	0,62	0,48
Température de refroidissement (K)	993	400	412	421
Température flux chaud amont réchauffe (K)	993	1090	1155	1155
Température de chemise (K)	> 1123	900	870	800

Pour le futur, l'utilisation de chemises en composite est envisagée, ce qui laisse espérer un gain de masse et de débit de refroidissement permettant d'améliorer le taux de rechauffe et le rendement de profil.

2 - LES ETAPES DU DEVELOPPEMENT2.1 - Généralités

Le refroidissement de la chemise est déterminé de manière à garantir une température de canal compatible avec sa tenue thermique et les spécifications de l'avionneur. Sur un moteur double flux moderne, l'utilisation d'un canal en titane nécessite de maintenir la température de ce dernier à une valeur inférieure à 300° C.

On est donc conduit à dimensionner le refroidissement de la chemise à une valeur suffisante pour combattre les importantes hétérogénéités circumférentielles de température génératrices de sillages chauds.

Cependant, l'utilisation d'air pour le refroidissement a des conséquences négatives sur les performances du moteur : d'une part, cet air n'est pas utilisé pour la combustion, ce qui limite le taux de rechauffe et d'autre part, son introduction progressive dans le foyer tend à accentuer le profil de température en sortie de tuyère ce qui se répercute sur la poussée.

Il convient donc d'utiliser au mieux la perte de charge pour obtenir un refroidissement efficace. Sur les moteurs récents, le débit alloué au refroidissement représente approximativement 10 % du débit d'air total et est mélangé au flux principal soit par l'intermédiaire des dispositifs de refroidissement ($\sim 60\%$), soit au niveau des volets de tuyère en extrémité de la chemise afin d'assurer la ventilation de ces derniers.

2.2 - Position du problème

Les écoulements à l'intérieur des foyers de rechauffe se caractérisent par des niveaux de pression modérés ($P \leq 4$ bar) mais des vitesses d'écoulement élevées. Les fronts de flamme qui prennent naissance au niveau des anneaux brûleurs s'élargissent progressivement vers l'aval jusqu'à rencontrer les parois où ils peuvent engendrer d'importantes hétérogénéités circumferentielles en température. L'une des qualités essentielles d'un refroidissement de chemise est de pouvoir combattre efficacement ce type d'hétérogénéités et en particulier d'en empêcher la propagation longitudinale.

D'autre part, l'élévation progressive de la température moyenne de l'écoulement à l'intérieur du foyer (figure 4) a deux conséquences :

- la chute continue de la pression statique du flux primaire longitudinalement (figure 3),
- une charge thermique sur les parois de chemise qui va croissant de l'amont vers l'aval.

Etant donné qu'un surdimensionnement mécanique de la chemise serait pénalisant sur le plan du bilan de masse, il faut, pour satisfaire aux critères de tenue à l'implosion, maintenir un écart de pression relativement constant longitudinalement entre l'air circulant entre canal et chemise et le flux principal. Des diaphragmes, chargés de créer des pertes de charge singulières sont donc disposés dans l'espace annulaire entre chemise et canal et contribuent à maintenir une différence de pression statique acceptable entre les deux écoulements.

Enfin, bien que dans un souci de simplicité de fabrication et de coût, le mode de refroidissement soit généralement constitué d'un motif unique répété le long de la chemise (voir figure 2), l'augmentation longitudinale de la charge thermique des parois est limitée par un effet de cumul des films de refroidissement de virole à virole.

Cet effet de cumul est naturellement d'autant mieux réalisé que l'efficacité unitaire de chaque film est importante. La figure 5 présente par exemple, sur une longueur de chemise correspondant à 2 ondulations, la contribution de chacune des zones multiperforées à l'efficacité globale. Cette dernière est calculée par la formule suivante :

$$1 - \eta = \prod (1 - \eta_i)$$

η_i désignant l'efficacité de la zone i à l'abscisse x

2.3 - Le dimensionnement

Les caractéristiques mécaniques et géométriques de la chemise sont déterminées à partir de calculs aérodynamiques et thermiques qui permettent de s'assurer que dans l'ensemble du domaine de vol :

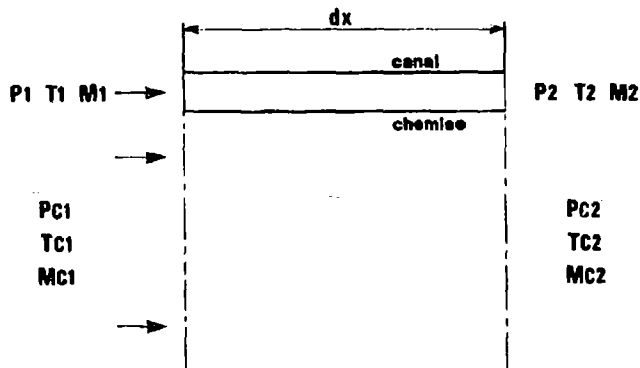
- le dimensionnement des diaphragmes situés entre chemise et carter est tel que les écarts de pression de part et d'autre de la chemise, et de part et d'autre du canal restent inférieurs à la valeur fixée en objectif (de l'ordre de 300 mbar pour la chemise) ;
- la température maximale de la chemise reste inférieure à une valeur compatible avec son objectif de durée de vie. A régime donné, cette température dépend essentiellement de la température du flux secondaire et de la perte de charge disponible au niveau de la chemise ;
- la température maximale du canal reste inférieure à la limite fixée. Cette température qui dépend du débit et de la température du flux secondaire ainsi que de l'air de ventilation de la nacelle, augmente avec l'altitude (réduction de la convection externe, augmentation de la température de chemise) et avec la vitesse de l'avion (augmentation de la température secondaire).

2.3.1 - Le calcul aérodynamique

Au stade de l'avant-projet, la répartition du débit de refroidissement dans les différents orifices peut être déterminée au moyen d'un code de calcul utilisant une formulation monodimensionnelle compressible du théorème de la quantité de mouvement (1) et pouvant prendre en compte :

- les pertes de charge par frottement et apport de chaleur entre canal et chemise, et dans le flux principal.

On obtient par exemple pour une tranche de longueur dx les formules suivantes :



$$\frac{P_2}{P_1} = 1 - \gamma M_1^2 \left[\frac{T_2 - T_1}{T_1} \times \frac{1}{2 + (\gamma - 1) M_1^2} + C_F \frac{B dx}{8A} \right]$$

$$\frac{PC_2}{PC_1} = 1 - \gamma_c MC_1^2 \left[\frac{TC_2 - TC_1}{TC_1} \times \frac{1}{2 + (\gamma_c - 1) MC_1^2} + C_{FC} \frac{BC dx}{8AC} \right]$$

- le calcul de l'évolution de la pression au passage d'un diaphragme ;
- le calcul du débit d'orifices de film ou de multiperforation.

Pour ne pas alourdir la méthode de résolution, les calculs aérodynamiques et de tenue thermique de la chemise ont été découplés et sont réalisés successivement. Cependant, compte-tenu de la nécessité de connaître la température des gaz dans chaque section de calcul, un traitement schématique des problèmes thermiques et de combustion, est néanmoins réalisé à ce niveau :

- utilisation d'une loi de rendement universelle rentrée point par point ;
- formulation moyennée des équations de transfert de chaleur permettant d'estimer l'échauffement du débit d'air entre canal et chemise.

Enfin, d'autres outils de calcul bi ou tridimensionnels sont également à la disposition de l'ingénieur pour traiter les problèmes locaux pouvant surgir en cours de développement (8).

2.3.2 - Le calcul thermique

La description du comportement thermique d'une part de la chemise et d'autre part du canal nécessite la mise en oeuvre d'un logiciel de calcul simulant de manière réaliste les transferts conductifs, convectifs et radiatifs.

Les transferts conductifs :

La description des transferts conductifs est réalisée au moyen d'une méthode aux volumes fins instationnaires. Une méthode bidimensionnelle (description de la conduction dans les sens radial et longitudinal) et une méthode tridimensionnelle (description de la conduction dans les sens radial, longitudinal et tangentiel) sont disponibles. La difficulté essentielle dans le dernier cas étant la détermination des profils circonferentiels de températures de gaz et surtout de coefficients convectifs (simulation des sillages).

Les transferts radiatifs :

Plusieurs modèles de transferts radiatifs sont utilisables suivant l'état d'avancement du projet :

- une formulation monodimensionnelle (2) considérant les échanges entre deux corps gris semi-infinis séparés par un gaz semi-transparent et isotherme ;
- la méthode par zones permettant de tenir compte de l'évolution longitudinale de la température du gaz à l'intérieur du canal (3) ;

- la méthode à G flux qui nécessite l'utilisation préalable d'un code 2D ou 3D de description de l'écoulement à l'intérieur du canal de manière à connaître le champ de températures et de concentrations à l'intérieur de celui-ci (4).

Ces modèles nécessitent la connaissance des propriétés radiatives du gaz de combustion qui sont calculées :

- soit au moyen de la formule empirique de Reeves (2) supposant le gaz gris ;
- soit au moyen d'un modèle de type larges bandes (modèle d'Edwarda) (5) ;
- soit au moyen d'un modèle de type bandes étroites (6 , (7).

Les transferts convectifs :

Le calcul des transferts convectifs à la paroi, sur la face interne de la chemise de protection thermique nécessite l'utilisation :

- de la température des gaz au voisinage de la paroi, déduite de la loi d'efficacité adiabatique ;
- des coefficients d'échange.

Malgré les progrès importants réalisés ces dernières années dans la description des écoulements réactifs tridimensionnels, ces lois de comportement demeurent essentiellement expérimentales et sont issues des essais sur un banc partiel de refroidissement décrit dans la suite de cet article.

Un exemple de calcul de température de paroi d'un canal ondulé multiperforé est présenté sur la figure 9. Ce calcul montre la relative homogénéité longitudinale des parois et cela malgré l'élévation de température du flux principal qui passe d'une valeur de l'ordre de 1200 K au niveau du plan des accroche-flammes, à une valeur supérieure à 2000 K en sortie de chemise.

2.3.3 - Les essais au banc partiel

2.3.3.1 - But des essais

Des recherches technologiques doivent être mises en oeuvre afin de maîtriser les techniques nouvelles avant de les appliquer sur des moteurs de développement.

Pour mener à bien ces recherches, on est conduit à réaliser des essais au banc partiel, d'une part pour mettre au point et optimiser les concepts technologiques nouveaux et d'autre part pour acquérir des informations expérimentales qui serviront à ajuster les lois utilisées dans les méthodes de modélisation.

La SNECMA dispose d'un banc partiel de refroidissement présenté sur la figure 6 et sur lequel sont essayés dans des conditions représentatives de température et de vitesse des secteurs de chemise.

La veine d'essai est de section rectangulaire mais le dispositif à étudier est implanté sur une tôle ayant une courbure pour améliorer le comportement mécanique compte-tenu des gradients de température élevés.

Deux alimentations en air réglables séparément permettent de simuler respectivement le débit principal et le débit entre canal et chemise.

Dans le flux principal, deux types de montages sont possibles correspondant à des objectifs d'essais différents :

- dans le premier cas, l'obstacle et l'anneau brûleur ne sont pas montés. La préchambre amont assure alors une alimentation homogène dans la section du flux principal. Par conséquent, l'aérodynamique au niveau du système de refroidissement est bidimensionnelle ce qui permet de se ramener dans les conditions d'application des formules semi-empiriques classiques (2) et d'en ajuster les coefficients ;
- dans le second cas, la présence de l'obstacle et de l'anneau brûleur en aval de la chambre de préchauffe engendre d'importantes hétérogénéités de température de flux chaud. L'étude du comportement du dispositif de refroidissement en présence d'un sillage peut alors être réalisée et des comparaisons entre différentes variantes effectuées.

2.3.3.2 - Les possibilités de mesure

Les possibilités de mesure qui sont offertes par le banc de refroidissement sont les suivantes :

- Mesures d'efficacité adiabatique

Celles-ci peuvent être réalisées par prélèvement et analyse de gaz, soit en utilisant le CO₂ issu de la combustion comme traceur quantifiant le mélange entre le flux principal et l'air de refroidissement, soit en procédant à l'injection dans le circuit d'air de refroidissement d'un gaz inerte tel que l'Hélium. Un exemple de courbe expérimentale d'efficacité obtenue sur une plaque simulant plusieurs ondulations d'une chemise de type M53-P2 est présenté sur la figure 8. Cette courbe expérimentale met clairement en évidence l'effet de cumul des efficacités entre les viroles successives, ce qui peut être restitué par le calcul par une formulation analytique telle que celle qui est présentée en 2.2.

- Mesures de température de paroi

Plusieurs techniques peuvent être employées :

- * les thermocouples qui fournissent une valeur précise mais ponctuelle de température. Ils sont surtout employés pour réaliser des recoupements quantitatifs entre calcul et expérience ;
- * la peinture thermosensible qui fournit une image de la répartition de température sur toute la plaque et qui permet donc d'estimer qualitativement l'homogénéité des températures obtenues au moyen d'un dispositif de refroidissement. La figure 7 présente par exemple une comparaison des dispositifs de refroidissement envisageables, met clairement en évidence l'intérêt des chemises ondulées multiperforées ;
- * la thermographie infrarouge : le schéma du montage est présenté sur la figure 6. La thermographie fournit également une image de la répartition de température sur toute la plaque mais permet aussi, d'une part de réaliser plusieurs conditions de fonctionnement durant le même essai, ce qui n'est pas le cas de la peinture thermosensible, et d'autre part d'étudier le comportement du refroidissement lors d'un régime transitoire. En revanche, elle ne fournit des résultats quantitatifs qu'à condition que les caractéristiques d'émissivité du matériau soient bien connues et n'évoluent pas durant l'essai. Une illustration des possibilités de visualisation offertes par la thermographie infrarouge est présentée sur la figure 10.

2.3.4 - Les essais sur moteur

Les essais de validation au banc partiel sont toujours suivis par des essais sur des moteurs de développement qui ont pour objectifs :

- de vérifier les calculs aérodynamiques et thermiques sur l'ensemble du canal ;
- de compléter l'expérience acquise au banc partiel concernant l'aptitude du refroidissement à atténuer les éventuels sillages ;
- de s'assurer du comportement de la chemise mise dans des conditions réelles de fonctionnement (sensibilité aux vibrations de combustion, évolution de l'efficacité du refroidissement dans le temps : risques d'encrassement) ;
- de simuler un fonctionnement accidentel de la chemise (obturation d'orifices de refroidissement).

Sur la figure 11 est présentée par exemple, une chemise de type ondulée et multiperforée qui a fait l'objet d'essais de tenue thermique dans les conditions plein gaz PC 0/0.

3 - CONCLUSION

Les recherches technologiques menées dans le domaine des techniques de refroidissement des foyers de rechauffe ont permis :

- d'améliorer l'efficacité globale du refroidissement ainsi que d'homogénéiser les températures de paroi, ce qui s'est traduit par la possibilité d'utiliser des températures d'entrée et de sortie de rechauffe plus élevées ;
- de réaliser un gain en masse à la fois sur la chemise et sur le canal qui peut maintenant être réalisé en titane.

Enfin, ces recherches se sont accompagnées de la mise au point de méthodes de calcul améliorant la précision des dimensionnements et réduisant de ce fait les temps et les coûts de développement.

BIBLIOGRAPHIE

- 1 - ASCHER H. SHAPIRO
The dynamics and thermodynamics of compressible fluid flow (1953)
- 2 - M. BUISSON - J.P. GAILLAC - B. DEROIDE
Revue des techniques de protection thermique des parois des foyers principaux et de rechauffe des
turboréacteurs
AGARD CONFERENCE PROCEEDINGS N° 229 (1977)
- 3 - HOTTEL, H.C. - SAROFIM, A.F.
Radiative Transfer, pp 365, 247, 279
Mac Graw-Hill 1967
- 4 - W. SELÇUK
"Evaluation of multi-dimensionnal flux models for radiative Transfer in combustion chambers :
A Review"
AGARD CONFERENCE PROCEEDINGS N° 353 (1983)
- 5 - EDWARDS, D.K.
Radiation Interchange in a Nongray enclosure containing an isothermal Carbon - Dioxide -
Nitrogen gas mixture
Journal of Heat Transfer - February 1962
- 6 - J. TAINE
A line by line calculation of low-resolution radiative properties of CO₂ - CO - transparent
nonisothermal gases mixtures up to 3000 K
JQSRT vol. 30 p. 371 (1983)
- 7 - J.M. HARTMANN - R. LEVI DI LEON - J. TAINE
"Line by line and narrow-band model calculations for H₂O"
à paraître dans JQSRT
- 8 - F. DUPOIRIEUX
"Prédiction d'Écoulements Turbulents Réactifs"
AGARD CONFERENCE PROCEEDINGS N° 353 (1983)

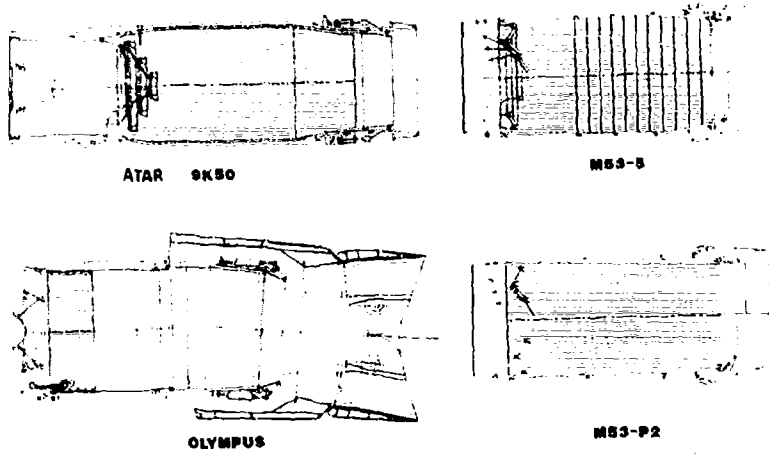


FIGURE 1 : CANAUX DE RECHAUFFE

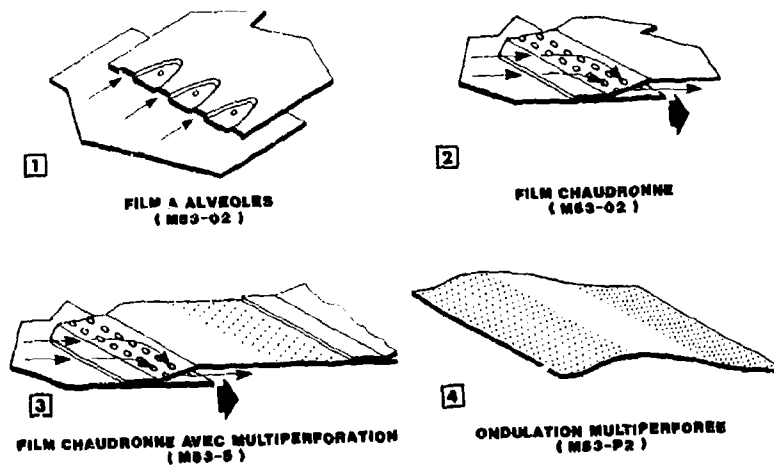


FIGURE 2 : LES DISPOSITIFS DE REFROIDISSEMENT

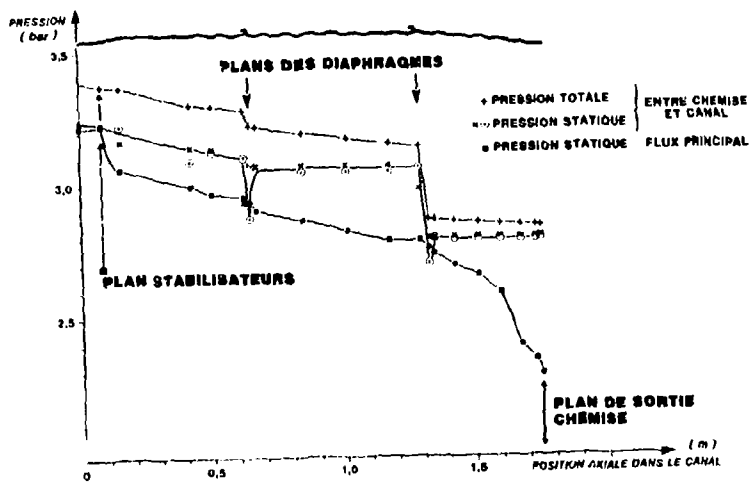


FIGURE 3 : EVOLUTION LONGITUDINALE DES PRESSIONS

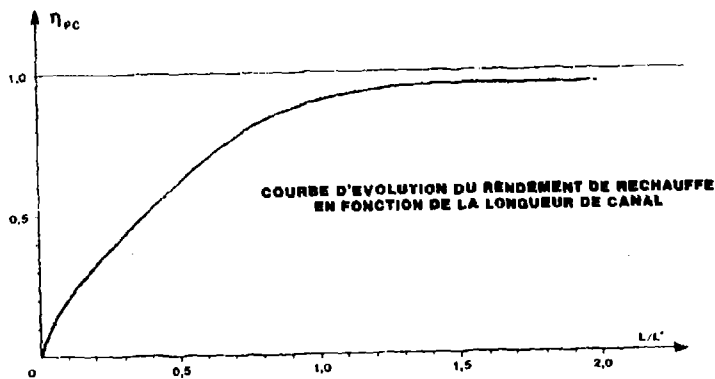


FIGURE 4 : EVOLUTION DU RENDEMENT DE COMBUSTION LE LONG DU CANAL

FIGURE 5 : EVOLUTION DES EFFICACITES
ELEMENTAIRES D'UNE PLAQUE
ONDULEE MULTIPERFOREE

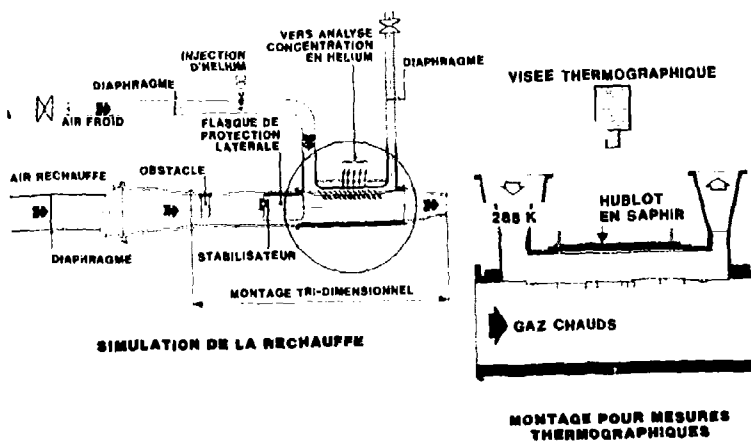
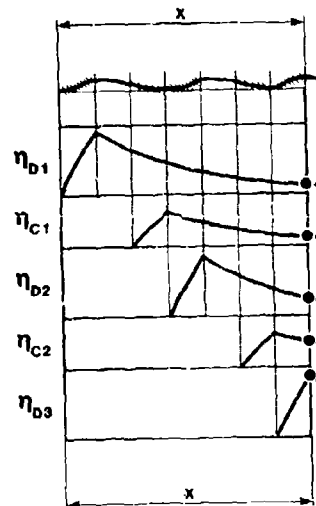


FIGURE 6 : SCHEMA D'UN BANC D'ETUDE DU REFROIDISSEMENT PARIETAL

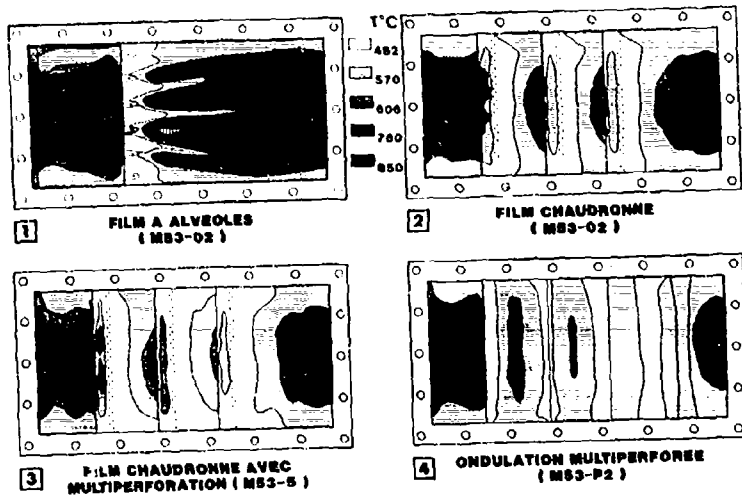


FIGURE 7 : COMPARAISON DU COMPORTEMENT THERMIQUE DES 4 TECHNOLOGIES

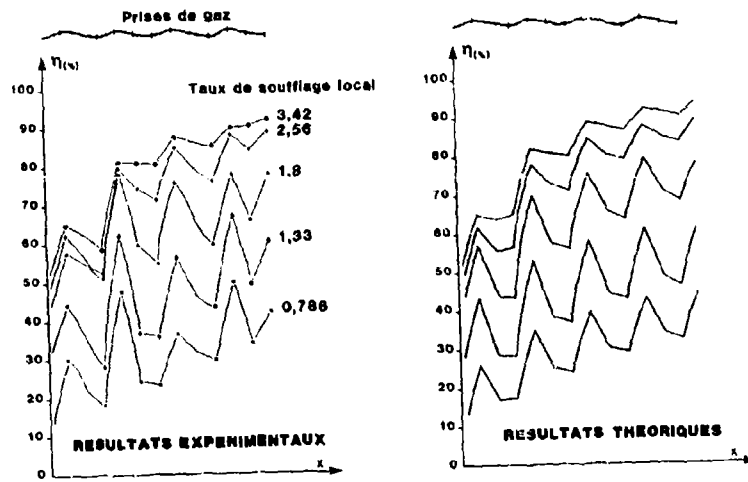


FIGURE 8 : EFFICACITE ADIABATIQUE CALCUL - MESURE POUR CONFIGURATION ONDULEE MULTIPERFOREE

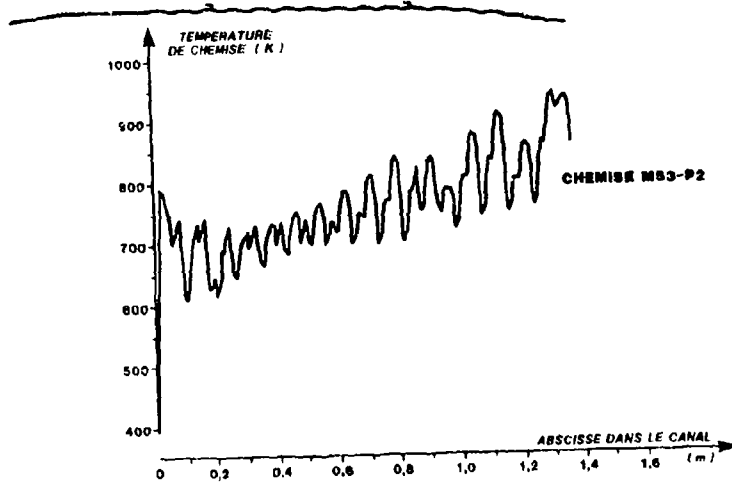


FIGURE 9 : EVOLUTION LONGITUDINALE DE LA TEMPERATURE D'UNE CHEMISE ONDULEE (CALCUL)

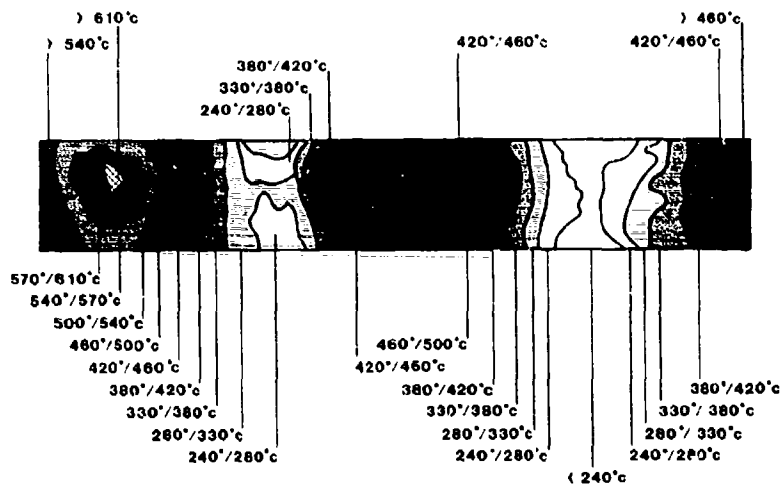


FIGURE 10 : PLAQUE MULTIPERFOREE ONDULEE MESURE DE THERMOGRAPHIE

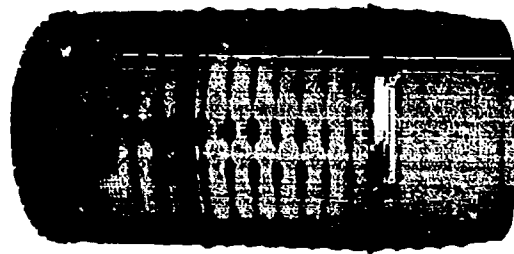


FIGURE 11 : CHEMISE DE PROTECTION THERMIQUE MULTIPERFOREE M53-P2

DISCUSSION

J.Fabri, Fr

Quelle est le temps d'acquisition avec votre système infrarouge?

Author's Reply

Ce doit être de l'ordre de six images par seconde, je crois.

THE MEASUREMENT OF LOCAL HEAT TRANSFER
COEFFICIENTS IN BLADE COOLING GEOMETRIES

P. T. Ireland and T. V. Jones

University of Oxford
Department of Engineering Science
Parks Road
Oxford
OX1 3PJ
U.K.

SUMMARY

An account is given of the experimental technique employed in measuring heat transfer coefficients in blade cooling passages. A hot air flow is suddenly started through a perspex model of the blade cooling passage. The surface temperature of the model is monitored during this time and the internal heat transfer coefficient deduced from this temperature history. Thin and thick walled models are employed and the surface temperature measured using liquid crystal thermochromic indicators. The analysis for the interpretation of the experimental results is given together with the experimental precautions required for the measurement. The use of liquid crystals in this form of transient experiment is discussed. A study of the detailed heat transfer distribution around pedestals and other heat transfer enhancement devices is also described. These devices are tested at approximately x 100 scale in order to obtain the required detail and full scale Reynolds number is simulated.

INTRODUCTION

The convective heat transfer within blade cooling passages is studied at Oxford using a transient hot flow facility. Large scale models of internal cooling geometries are constructed from a thermal insulator, such as perspex, and overall maps of heat transfer coefficient are obtained by employing a liquid crystal surface temperature indicator. In the past, phase change paints were used successfully by Clifford, Jones and Dunne[1] for this measurement in complex engine cooling ducts and the technique has been refined by the present authors. The following report outlines the transient technique and the analysis used and then gives two examples of heat transfer results obtained. The first case is for the complicated flow in a representative blade trailing edge passage where the effect of rib heat transfer promoters is studied. The second, more fundamental study deals with an isolated heat transfer enhancer in the form of a pedestal in two-dimensional channel flow.

THE TRANSIENT TECHNIQUE

Transient heat transfer techniques, for internal flow, depend on the temperature rise of the passage wall when subjected to a step change in convective heating. If an insulator is used then the local surface temperature rise can be used to calculate heat transfer coefficients. Models with thick walls may be employed where the internal surface temperature is monitored or thin walled models where it is possible to use either the internal or external surface temperature. A thick walled model is defined by Schultz and Jones[2] as a test piece of wall thickness greater than the diffusion length $4\sqrt{at}$, where a is the model thermal diffusivity and t the experimental time. For this form of duct with a small surface curvature, the insulator can be treated as a semi-infinite substrate and provided that the thermal properties do not change with temperature the heat transfer coefficient is related to the non-dimensional surface temperature rise by:

$$\frac{T_{\text{wall}} - T_{\text{initial}}}{T_{\text{gas}} - T_{\text{initial}}} = 1 - e^{-\gamma^2} \operatorname{erfc}(\gamma)$$

where T_{wall} , T_{initial} and T_{gas} are the surface wall temperature at time t , the initial wall temperature and the constant gas temperature respectively and

$$\gamma = \frac{h\sqrt{t}}{\sqrt{\rho ck}}$$

where h is the heat transfer coefficient and ρ , c and k are the density, specific heat and thermal conductivity of the wall.

In practice, for the two examples reported, a numerical solution to the one-dimensional transient conduction equation which permits variable thermal properties and changing gas temperature is employed. The analysis required for thin walled models with the thermal indicator applied to the external surface is more complicated, here allowance is made for heat lost from the external surface to the surroundings.

Errors in heat transfer coefficient distribution due to lateral conduction will be unimportant provided that the second derivative of heat transfer coefficient with respect to distance along the surface is small compared to the value of the heat transfer coefficient divided by the square of the thermal diffusion depth. For heat transfer distributions which change rapidly with distance the experimental test time must be short to

minimise the thermal diffusion length. In such cases, thick walled models are more suitable since the thermal indicator is applied to the region of the wall at the highest temperature. Run times chosen for thin walled models, on the other hand, must be sufficiently long to allow the rear wall to reach a measureable change in temperature, and at the same time short enough to render lateral conduction along the wall unimportant.

Thermochromic liquid crystals are used to monitor the surface temperature and each heat transfer test recorded on video tape. Thus the time taken for any point on the surface to reach the temperature corresponding to a particular liquid crystal colour can be found. This time, together with the initial wall, local gas and liquid crystal indication temperatures, permits an overall map of heat transfer coefficient to be calculated.

Liquid crystal which is applied to the external face of the thin walled models is supplied dispersed in a polymer matrix in the form of a thin grease. A very thin backing sheet of mylar protects the indicator from chemical contamination and also enhances visibility. Thick walled models require that the liquid crystal is exposed to the internal flow. The same sort of liquid crystal (a chiral nematic) is used but this is encapsulated in gum arabic spheres of about 10 μm diameter. These micro-capsules are screen printed onto the surface resulting in a layer one capsule thick. The response of such a layer to variations in surface temperature is extremely rapid and the authors have confirmed experimentally that the response time is more than adequate for the tests of approximately ten seconds duration reported here. In addition the accuracy of the liquid crystal indicator was monitored over a series of tests with a fast response thermocouple embedded within the coating.

APPLICATIONS OF THE TECHNIQUE

(a) Rib Roughness in a Trailing Edge Passage

The first example deals with the highly complicated flow in a seven times scale model of a trailing edge blade cooling passage using rib roughness of square cross section, shown schematically in Fig. 1. A thin walled perspex model was used with liquid crystal applied to the outer surface for experiments with a rib spacing of 10 rib heights. The duct was instrumented with fast response thermocouples sensing the gas temperature on the duct centre-line.

The velocity and temperature profiles of the flow entering the model section closely approximated fully developed conditions. Flow within the model duct was complicated due to the mass flow leaving from bleed holes along the entire length. Thus the streamlines crossed the ribs at different angles as the ribs were perpendicular to the centre-line of the duct.

The heat transfer coefficient variation is shown in Fig. 2 for three positions in the duct. In this figure it can be seen that there is a periodic variation of heat transfer between the ribs at the stations shown. Such a variation has previously been observed by Sparrow and Tao[3] who measured mass transfer in a rectangular duct with rod-like rib roughness. It should be emphasised, however, that the geometry of the duct tested is unique so that the relevance to previous work must be limited. The complex nature of the flow due to the progressive bleed which results in flow at an angle to the ribs was examined using surface flow visualisation. The flow field revealed is shown in Fig. 3 where it can be seen that the flow separates behind the ribs and reattaches approximately half way between the ribs. Due to the cross flow, however, the secondary flows spiral downwards in the direction of the flow. It is of interest to note that the peak in heat transfer coefficient was found to be situated ahead of the reattachment point.

(b) Isolated Pedestal Heat Transfer

The second example concerns a detailed heat transfer study of an isolated pedestal situated in channel flow. A thick walled idealised model at one hundred times full engine size was constructed from perspex and encapsulated liquid crystal applied both to the internal passage wall and over the cylinder itself. The progression of the liquid crystal colour change line with time from the start of the experiment is shown in Fig. 4 where the clarity with which this may be observed is evident. Velocity and temperature profiles immediately upstream of the cylinder are shown in Fig. 5. Heat transfer coefficients based on the duct centre-line temperature immediately upstream of the cylinder and obtained using the analysis previously described are given in Figs. 6 and 7. Fig. 6 clearly shows the effect of the intense enhancement of heat transfer caused by the horseshoe vortex on the side wall. The maximum heat transfer coefficient due to the vortex is seen to be over ten times that of the rectangular duct in the absence of the cylinder. In addition, two regions of high heat transfer occur behind the cylinder at approximately one diameter from the centre. Fig. 7 shows clearly the decrease in heat transfer on the cylinder away from the duct centre-line. This effect was observed by Sparrow, Stahl and Traub [4] (for a cylinder on a flat plate) using the mass diffusion analogy for a naphthalene coated cylinder.

Flow visualisation using smoke showed the essential features of the horseshoe vortex and the flow field is sketched in Fig. 8. The extent of the vortex found is indicated in the heat transfer result in Fig. 7.

CONCLUSIONS

The transient technique using liquid crystals as a surface temperature indicator has proved to be very successful. In particular the degree of spatial resolution over large

areas confirms the importance of the method for internal heat transfer measurements.

REFERENCES

1. Clifford, R. J., Jones, T. V. and Dunne, S. T., Techniques for Obtaining Detailed Heat Transfer Coefficient Measurements within Gas Turbine Blade and Vane Cooling Passages, ASME Paper 83-GT-58, 1983.
2. Schultz, D. L. and Jones, T. V., Heat Transfer Measurements in Short Duration Hypersonic Facilities, AGARDOGRAPH No. 165, 1973.
3. Sparrow, E. M. and Tao, W. Q., Enhanced Heat Transfer in a Flat Rectangular Duct with Streamwise-Periodic Disturbances at One Principal Wall, ASME, J. of Heat Transfer, Vol. 105, November, 1983, pp. 851 - 861.
4. Sparrow, E. M., Stahl, T. J. and Traub, P., Heat Transfer Adjacent to the Attached End of a Cylinder in Crossflow, Int. J. Mass Transfer, Vol. 27, No. 2, 1984, pp. 223 - 242.

ACKNOWLEDGEMENT

The internal heat transfer work at Oxford has been supported by Rolls-Royce Ltd. and the Ministry of Defence.

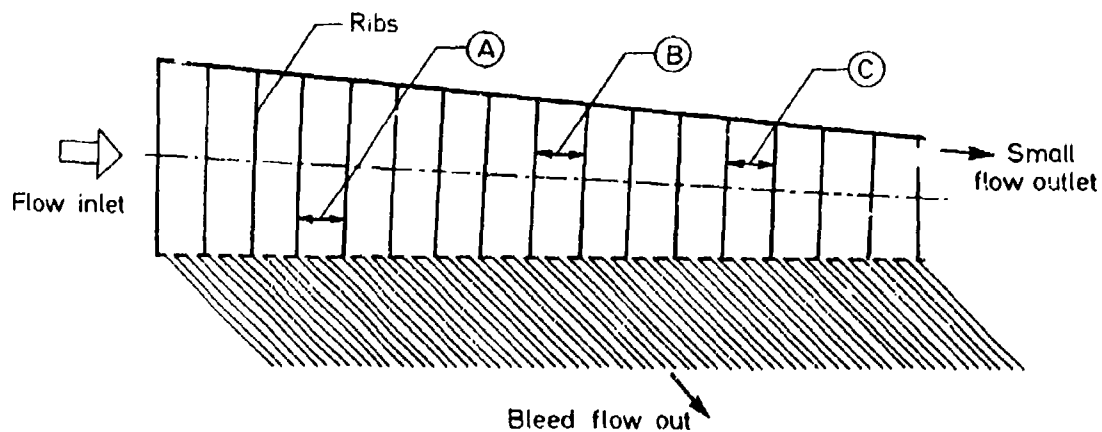


Fig. 1 Schematic of the Blade Cooling Passage Model
(A, B and C indicate positions where
Measurements in Fig. 2 are Obtained)

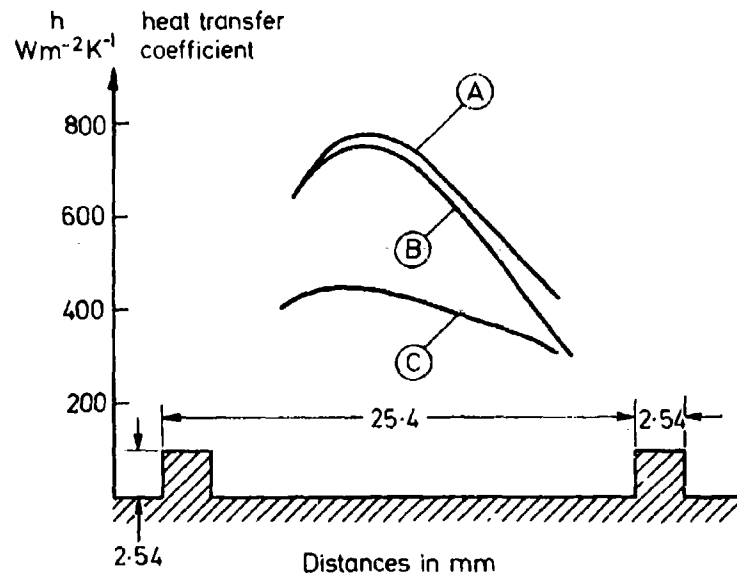


Fig. 2 The Variation of Heat Transfer Coefficient between the Ribs at the Three Stations shown in Fig. 1

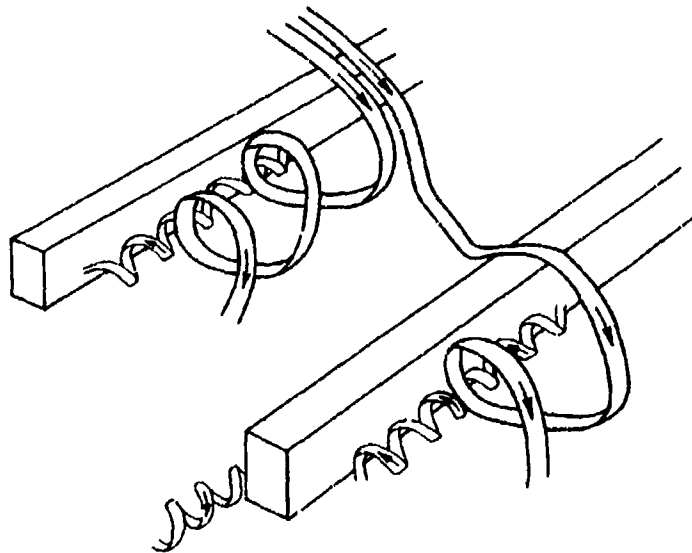


Fig. 3 The Flow Over the Ribs Determined from Surface Visualisation

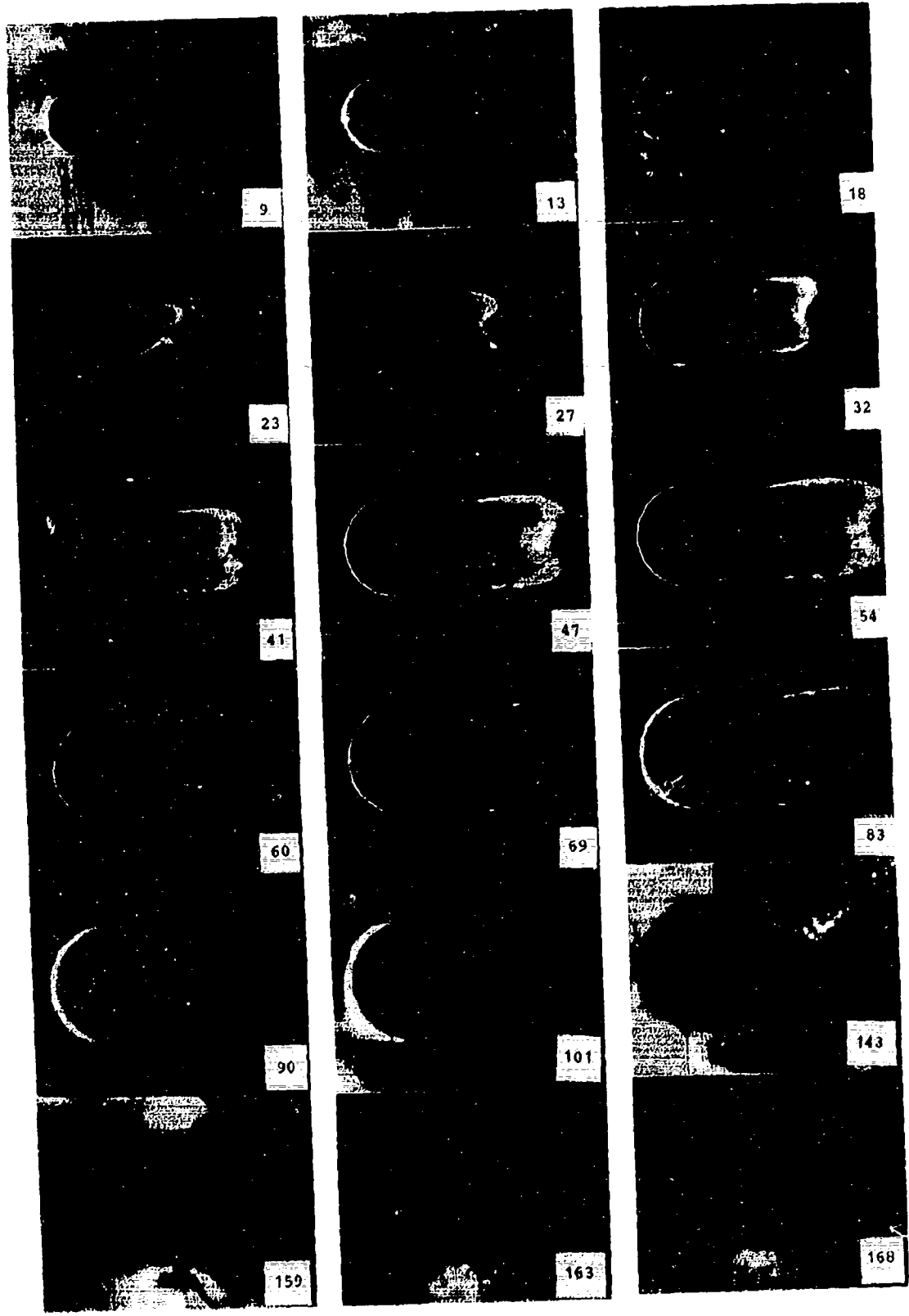


Fig. 4 Photographs of the Colour Change at
Increasing Times Given in Seconds

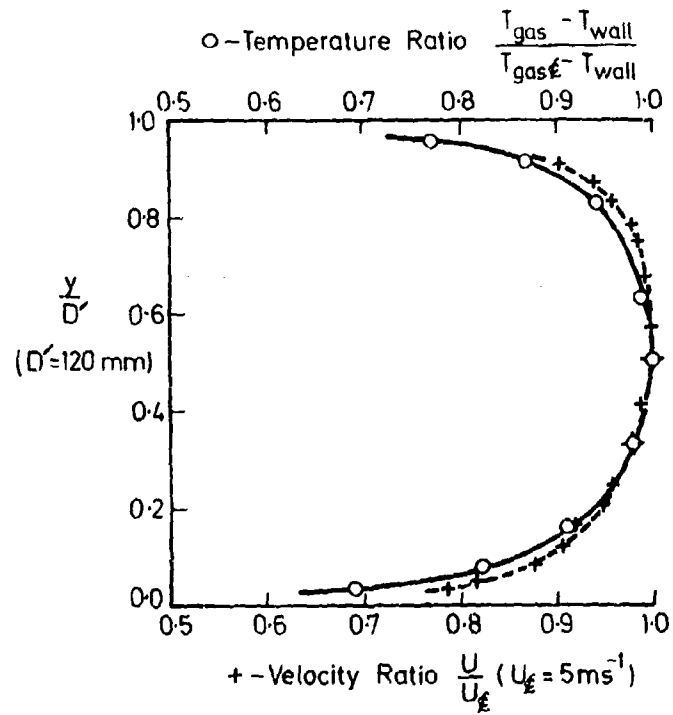


Fig. 5 Temperature and Velocity Profiles Immediately Upstream of the Pedestal

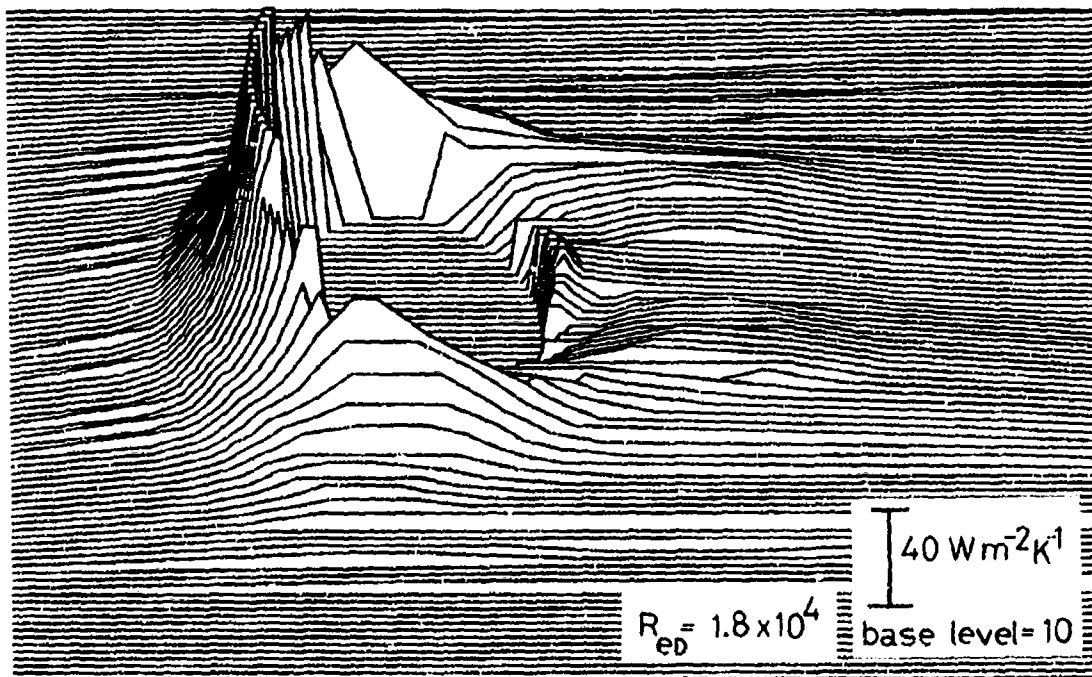


Fig. 6a Heat Transfer on the Duct Side Wall Presented as a Surface Plot Where the Height of the Surface is Proportional to Heat Transfer Coefficient

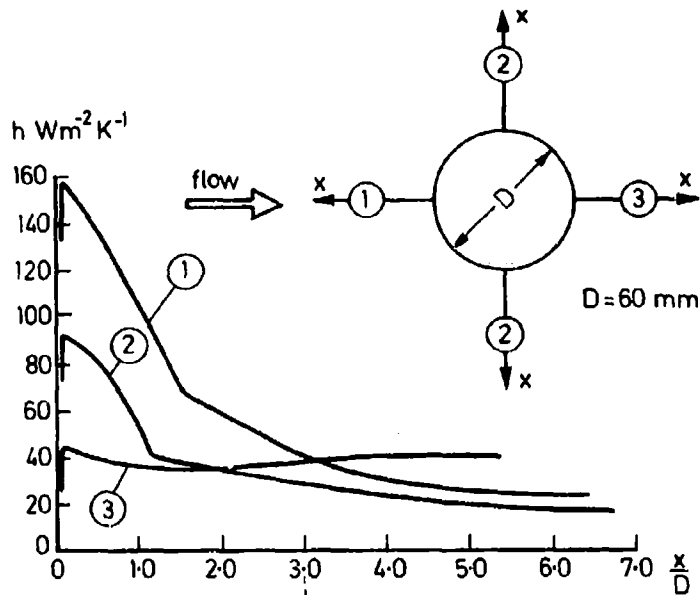
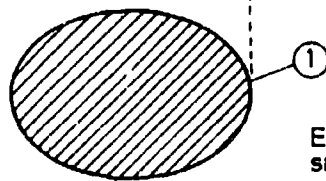
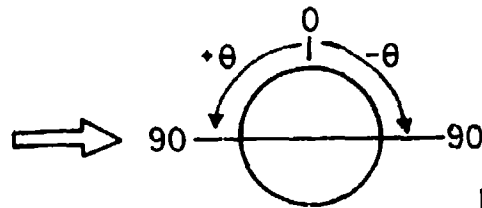


Fig. 6b The Heat Transfer Variation on the Duct Side Wall Upstream, Downstream and at Right Angles to the Flow Direction



Extent of vortex from smoke visualisation



h contours
 $\text{Wm}^{-2} \text{K}^{-1}$

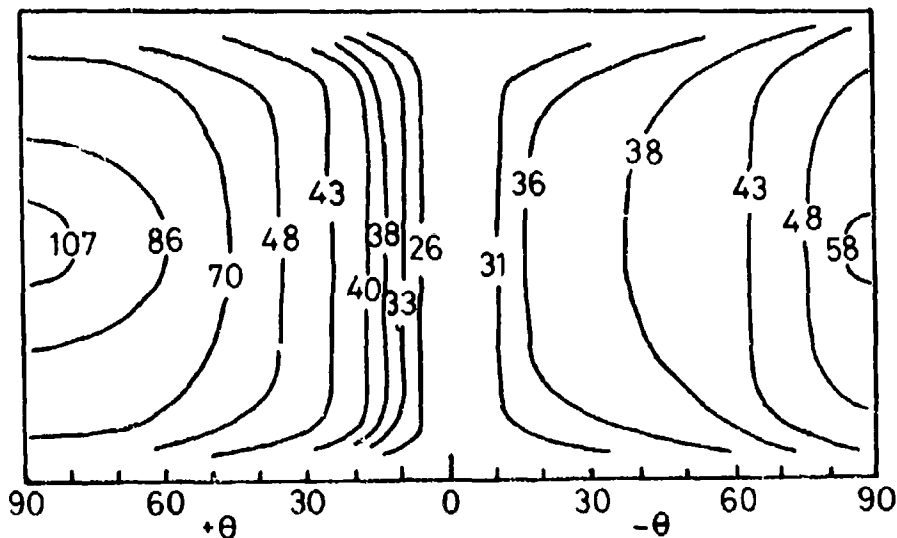


Fig. 7 Heat Transfer Contours on the Cylinder Wall

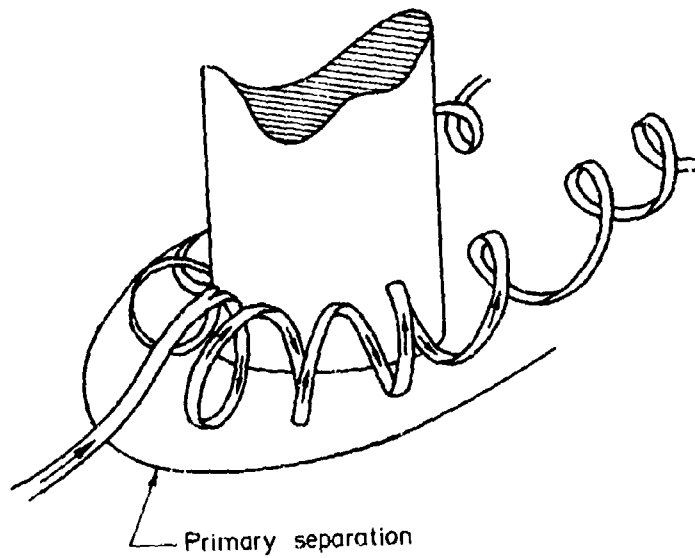


Fig. 8 The Flowfield Observed Around the Pedestal
using Smoke Visualisation

**PYROMETRE OPTIQUE INFRAROUGE
POUR LA MESURE DES TEMPERATURES D'AUBES DE TURBINE**

par

Marc Charpenel and Jean Wilhem
ONERA
29 Avenue de la Division Leclerc
92320 Châtillon sous Bagneux
France

RESUME

L'établissement par des techniques pyrométriques de la cartographie des températures de surface des aubes mobiles d'une turbine refroidie, a nécessité la mise au point d'un pyromètre infrarouge à grande résolution spatiale et temporelle. Typiquement, le temps de réponse de cet appareil doit être inférieur à la micro-seconde. L'utilisation d'un détecteur à l'arséniure d'indium refroidi à -40° permet d'obtenir cette caractéristique et, compte tenu de sa très bonne détectivité, le seuil de température détectable est d'environ 450°C pour un pouvoir de résolution à la surface de l'aube de $2\text{ mm}^2/$.

Les visées pyrométriques sont effectuées par endoscopie, suivant une optique de renvoi montée dans un tube refroidi, la sonde étant placée entre la roue fixe et la roue mobile, ou derrière celle-ci. Elle a été étudiée de manière à supporter les conditions de température et pression régnant dans la veine et à subi sans dommage 20 bars et 2100 K.

L'utilisation de ce pyromètre sur la turbine expérimentale étudiée spécialement pour qualifier les nouvelles techniques de refroidissement des aubes, a montré que la pyrométrie présente quelques difficultés liées,

- d'une part au coefficient de réflexion non nul des aubes (émissivité inférieure à 1),
- d'autre part au rayonnement propre des gaz.

Ces difficultés ont été analysées et des solutions ont été proposées ; notamment un programme de correction des températures tenant compte des réflexions mutuelles entre aubes a été mis au point.

AN OPTICAL PYROMETER TO MEASURE TURBINE BLADE SURFACE TEMPERATURE

The development of a cooled infrared pyrometric probe, with a high spatial and temporal resolving power, made it possible to establish by pyrometric methods surface temperature charts of the mobile blades of a turbine. The use of a sensor with a 1 sec time constant yields a resulting power on the blade surface of the order of 2 mm^2 . This sensor is cooled at -40°C , which ensures a good detectivity and temperature measurements above 450°C .

A water cooled metallic tube, ending by a right angle deflecting prism, makes up the light guide of the pyrometer and can be inserted between the various turbine stages. The probe has been designed to withstand the pressure and temperature conditions prevailing in the turbine blade test section, and was subjected without damage to 20 bar and 2100 K.

The use of this pyrometer with the experimental turbine specially designed for qualifying new blade cooling methods has shown that pyrometry involves difficulties connected to :

- the non-zero blade reflection coefficient (emissivity lower than 1),
- the gas radiation due to the gases.

The above difficulties have been analyzed and solutions have been proposed ; in particular a correcting program for the temperatures has been perfected which takes into account the blade to blade mutual reflections.

1. INTRODUCTION

Un effort de recherche important est actuellement consenti pour porter le fonctionnement des turbines de turboacteurs à des températures et des pressions de plus en plus élevées. Il en résulte un accroissement des flux de chaleur qui rend les aubes plus sensibles aux problèmes de fatigue et leur tenue est davantage fonction des températures locales que des températures moyennes. Cela a entraîné une diversification des techniques de refroidissement, en améliorant la convection d'abord, en ayant recours à la protection par film gazeux ensuite. Le rôle de l'environnement moteur devient alors important, les hétérogénéités de pressions et de températures, le niveau de turbulence, les sillages et la centrifugation pouvant modifier les coefficients d'échange et les efficacités de film. C'est ce qui a conduit l'ONERA à développer une instrumentation de mesure, et particulièrement la mesure des températures de surface des aubes mobiles par pyrométrie infrarouge, adaptée aux essais sur machines industrielles, principalement sur la turbine MINOS (Montage Inter Onera Snecma installé au CEPR à Saclay) étudiée spécialement pour qualifier les nouvelles techniques de refroidissement des aubes (1-2-3).

La mesure, à l'aide de thermocouples, des températures locales d'aubes mobiles est souvent utilisée sur bancs industriels. Pour obtenir des renseignements précis sur le comportement d'une aube, il convient de disposer d'un grand nombre de thermocouples et la transmission des signaux fournis par les thermocouples est un problème complexe et délicat.

Sur le banc MINOS, la possibilité d'effectuer de telles mesures a été prévue.

Cependant cette technique apparaît insuffisante pour établir la carte détaillée des températures de surface d'aubes qui est souhaitable pour toute vérification expérimentale des méthodes de calcul.

L'utilisation d'un pyromètre optique, télécommandé, à très court temps de réponse et à pouvoir de résolution spatiale à la surface de l'aube de l'ordre du mm^2 constitue une solution à ce problème.

Une représentation détaillée du pyromètre, développé par l'ONERA dans le cadre du projet MINOS a été faite dans (4). Nous allons ici rappeler ses principales caractéristiques et discuter des problèmes que soulève ce type de mesure.

2. PRINCIPE DE LA MESURE PYROMETRIQUE ET DESCRIPTION DU PYROMETRE

Un tube métallique, terminé à son extrémité par une prisme de renvoi à 90° placé devant une ouverture circulaire, constitue le tube de visée du pyromètre et se comporte à la manière d'une sonde que l'on plonge dans les gaz chauds et qui capte le rayonnement infrarouge émis par un petit élément de surface des aubes qui défilent devant elle (figure 1). La température est déduite, après étalonnage préalable, de la mesure de l'intensité du rayonnement prélevé.

Le dispositif est refroidi par circulation d'eau, et un courant d'air frais ou d'azote circule dans le tube pour éviter les effets d'absorption des gaz, et protège l'optique d'entrée de toute salissure.

La sonde a été étudiée de manière à supporter les conditions de température et pression régnant dans la veine d'essai d'aubes de turbine, et a subi sans dommage 20 bars et 2100 K. D'un diamètre de 16 mm, elle peut être placée entre les différents étages de la turbine.

Sur MINOS on a placé 2 pyromètres, l'un en amont et l'autre en aval de la roue mobile, de manière à effectuer une cartographie la plus complète possible de la température sur les aubes. Pour cela 2 déplacements de mise en position des sondes peuvent être exécutés et commandés à distance :

- un mouvement axial par vérin pneumatique permettant le déplacement du point visé le long d'une génératrice d'une aube, et le retrait de la sonde hors du courant de gaz chauds ; ce retrait peut s'effectuer très rapidement en cas d'échauffement anormal de la sonde détecté par un thermocouple placé à son extrémité ;
- un mouvement de rotation autour de l'axe de la sonde, assuré par un moteur pas à pas et permettant l'orientation de la sonde de manière à obtenir un angle d'incidence sur l'aube compris entre 45° et 90° . Ce mouvement peut également assurer une fonction de balayage cyclique dans le cas de mesures sur une aube ou une maquette fixe.

Un tube supportant l'optique (figure 2) coulisse dans la sonde refroidie, ce qui permet la mise au point à ouverture constante. Cette optique en verre fait à la fois usage de filtre (elle ne laisse passer que le rayonnement inférieur à $2,5\mu\text{m}$) et permet la focalisation de l'énergie sur la surface sensible du détecteur. On coupe le rayonnement au-delà de $2,5\mu\text{m}$ pour éviter l'émission et l'absorption des gaz, notamment de la vapeur d'eau et du gaz carbonique, importante pour ces longueurs d'onde.

La surface sensible du détecteur est de 2 mm^2 environ et la focalisation se fait avec un grandissement de 1 de telle sorte que la résolution spatiale est, elle aussi, de 2 mm^2 .

Compte tenu de la vitesse de rotation de la turbine (150 à 200 tours par seconde) pour que cette résolution ne soit pas affectée par l'effet de défilement, la constante de temps du détecteur doit être de l'ordre de 1 μs . On utilise un détecteur à l'arséniure d'indium qui a cette caractéristique. L'électronique associée doit présenter la même bande passante.

Ce détecteur est refroidi à -40°C ce qui lui assure une très bonne détectivité ; le minimum de température détectable est inférieur à 450°C . Le pyromètre n'étant pas accessible durant le fonctionnement de la machine, on a adopté un refroidissement thermoélectrique du détecteur (effet Peltier) qui supprime la recharge fréquente en fluide de refroidissement.

L'ensemble du détecteur-préamplificateur ne passe pas le continu et il est nécessaire de recalibrer périodiquement le zéro en coupant le flux infrarouge incident par un écran tournant. Cette modulation s'effectue à basse fréquence et nous verrons que le principe du dépouillement nécessite son synchronisme avec la vitesse de rotation de la turbine. On choisit de couper la mesure 1 sur 2 soit à 70 Hz environ.

Tout cet ensemble est monté dans un boîtier parallélépipédique de dimensions (140 x 170 x 450) qui peut se fixer sur un bossage de la machine. L'aspect du pyromètre, placé sur un montage simulant les roues fixe et mobile d'une turbine, est présenté sur la figure 3.

3. RESTITUTION DES TEMPERATURES DE LUMINANCE A LA SURFACE DES AUBES

Le dépouillement s'effectue en différé après acquisition des signaux pyrométriques. Ces signaux présentent une double périodicité :

- périodicité haute fréquence due au passage des aubes,
- périodicité basse fréquence due à l'interruption des mesures un tour sur deux.

Deux techniques d'acquisition ont successivement été utilisées. Pour la première, un enregistreur magnétique à large bande passante (500 kHz) a été utilisé. La restitution des signaux pour le traitement numérique sur mini ordinateur HP1000 s'effectue à une vitesse de lecture 16 fois plus lente.

L'inconvénient de l'enregistrement sur magnétique est de détériorer beaucoup le rapport signal sur bruit. Pour le restituer un traitement numérique dit "moyennage" est nécessaire.

Il consiste à effectuer un grand nombre de fois les mêmes mesures correspondant aux mêmes points visés sur l'aube. Ce nombre nécessaire est environ 200. Le bruit est alors atténué dans le rapport 200. Ce traitement suppose :

- que le champ des température est stationnaire pendant 400 tours,
- et qu'il est possible de numériser à chaque fois les mesures correspondant aux mêmes points à la surface des aubes.

Cette dernière condition peut être remplie grâce à l'enregistrement sur le magnétique d'un top par tour délivré par un capteur magnétique dont l'un des ergots est sur le rotor et l'autre sur le stator. Ce top par tour permet en outre la synchronisation de la modulation à la vitesse de la turbine et aussi le repérage des aubes et des points visés sur l'aube.

La figure 4 donne un oscillogramme représentant le champ des luminances au bord de fuite de quelques aubes successives de la turbine MINOS, et dans la partie supérieure le top de synchronisation délivré à chaque tour de roue.

La seconde chaîne d'acquisition est constituée par l'association d'un oscilloscope numérique NICOLET "Explorer III" et d'un ordinateur de bureau HP9845. Les deux convertisseurs analogique-numérique rapides du NICOLET (un pour chaque pyromètre) permettent de numériser les signaux à une cadence inférieure ou égale à 2.10^6 par seconde. Ce sont des convertisseurs de 12 bits dont la précision de conversion est donc de $2,5.10^{-4}$ à pleine échelle. Les mesures ainsi numérisées (4096 points au maximum) sont ensuite stockées sur une mémoire tampon et peuvent, soit être visualisées sur l'écran cathodique de l'oscilloscope, soit transférées sur le miniordinateur grâce à une liaison rapide (16 bits parallèles) et stockées sur cassettes. L'avantage de cette dernière technique d'acquisition est de ne pas détériorer le rapport signal sur bruit. Dans la plupart des cas il n'est plus nécessaire d'effectuer le traitement de "moyennage". Il est cependant toujours possible d'effectuer un tel traitement grâce à une acquisition en séquence pilotée par le top par tour, dans le cas de températures particulièrement basses par exemple.

A la suite de l'acquisition, l'utilisation du mini-ordinateur dans lequel ont été introduites d'une part les courbes d'étalonnage des pyromètres, et d'autre part les caractéristiques géométriques de la roue et des visées pyrométriques (notamment les angles de visée dont le repérage doit être assez précis) permet de tracer la cartographie des températures à la surface des aubes.

Cette restitution du champ des températures de luminance est le plus couramment effectuée à un rayon donné. Pour la roue de turbine MINOS, elle nécessite quatre séries de mesures correspondant à :

- 3 angles de visée différents ($+4^{\circ}$, $+52^{\circ}$, -44°) pour le pyromètre amont,
- 1 angle de visée ($+30^{\circ}$) pour le pyromètre aval.

Dans ces conditions, seule une étroite zone située au milieu de l'extrados échappe à l'analyse pyrométrique, mais il est souvent possible de compléter le profil de température par interpolation entre les mesures voisines.

Ces mesures, préalablement numérisées, sont stockées sur une bande magnétique numérique et le programme permet la recherche automatique de chacune de ces séries de mesures pour des aubes parfaitement définies sur la roue.

4. CORRECTION DES EFFETS D'ÉMISSIVITÉ

Pour remonter à la température vraie à partir d'une mesure pyrométrique, il faut connaître l'émissivité de la surface visée. Sur le montage MINOS l'émissivité des aubes a été déterminée à la fois par des mesures en laboratoire avant et après essai et "in situ" par la comparaison des mesures pyrométriques et des mesures effectuées à l'aide de thermocouples.

Deux cas ont été examinés. Pour le premier, le traitement de surface des aubes dit de chromer-aluminisation a été supprimé ; les aubes sont alors très noires et l'émissivité très élevée. L'accord entre les mesures pyrométriques et thermocouples est excellent comme le montre la figure 5.

Lorsque le traitement de surface est effectué, des mesures d'émissivité en laboratoire donnent 0,65 à 0,75. La comparaison des mesures pyromètre et thermocouples sur une aube au bord de fuite extradados présentée sur la figure 6, montre un assez bon accord de l'émissivité ainsi déterminée avec la mesure en laboratoire, au voisinage immédiat du bord de fuite, mais s'en écarte sensiblement lorsque l'on pénètre plus profondément à l'intérieur de la cavité constituée par deux aubes successives.

Ceci peut s'expliquer par le rayonnement mutuel entre aubes adjacentes. En effet, le pyromètre prélève non seulement le rayonnement émis par un petit élément de surface de l'aube visée, mais aussi le rayonnement provenant de l'aube voisine qui, si l'émissivité est différente de 1, se réfléchit sur l'aube visée et pénètre dans le pyromètre (figure 7).

Pour tenir compte de cet effet de rayonnement mutuel un programme de calcul a été établi afin de corriger les températures mesurées. On effectue le calcul dans le cadre de l'approximation bidimensionnelle. Cela suppose, non seulement que la géométrie de la cavité est bidimensionnelle, c'est-à-dire que chaque élément de surface a une génératrice parallèle à une direction fixe, chaque élément de surface ayant une longueur infinie, mais aussi que chaque élément de surface est isotherme. Les indications des pyromètres pour le rayon considéré sont donc étendues à tous les rayons.

On admet que la réflexion est purement diffuse c'est-à-dire que la réémission s'effectue selon la loi de Lambert. Cela permet d'effectuer le calcul par la méthode simple de Poljack (5). Si l'on découpe la cavité inter-aubes en K_e éléments, la luminance relevée par le pyromètre visant l'élément K (on parle alors de radiosité) est donnée par :

$$R(K) = \epsilon_K \cdot L(T_K) + \rho_K \sum_{I=1}^{K_e} R(I) F_{I,K}$$

avec $\rho_K = 1 - \epsilon_K$ le coefficient de réflexion.

ϵ_K est l'émissivité et $L(T_K)$ la luminance à la température T_K de l'élément K. On voit que cette formule permet de calculer $L(T_K)$ à partir de l'ensemble des mesures $R(k)$ à condition de déterminer au préalable les coefficients d'influence entre les éléments de surface $F_{I,K}$ en tenant compte que les réflexions se font de façon isotrope dans les trois dimensions. On tient compte schématiquement du rayonnement ne provenant pas des aubes mobiles (rayonnement du fond de chambre, distributeur, etc...) en supposant que les surfaces fictives reliant d'une part les deux bords d'attaque et d'autre part les deux bords de fuite rayonnent comme des corps noirs à des températures qui peuvent être déterminées en visant entre deux aubes successives. Ces températures sont généralement assez faibles.

Afin de vérifier que la réflexion est bien diffuse et non spéculaire ou mixte on a comparé les résultats de mesures à un rayon donné effectués par le pyromètre amont et par le pyromètre aval pour différents angles de visée (figure 8). On voit que les différents profils se superposent assez bien mais on note la difficulté qu'il y a à raccorder les profils obtenus par les deux pyromètres. L'indépendance de la mesure vis-à-vis de l'angle de visée démontre que la réflexion sur les aubes est isotrope et donc totalement diffuse.

La figure 9 présente un résultat de calcul de correction tenant compte du rayonnement mutuel entre aubes et la comparaison du profil des températures ainsi obtenu avec celui donné par la simple correction d'émissivité. La correction la plus complète a pour effet de creuser davantage le profil de température au milieu des intrados et extradados et de permettre de raccorder les mesures pyrométriques amont et aval.

L'importance de ces corrections dépend bien entendu des écarts de température entre les intrados et extradados des deux aubes définissant le canal interaubes considéré et aussi du niveau de l'émissivité de la surface des aubes.

Dans les conditions d'essais MINOS les corrections à apporter en certains points des aubes peuvent atteindre jusqu'à 40 K, ce qui est appréciable, et elles deviennent alors nécessaires pour permettre une étude quantitative de l'équilibre thermique des aubes expérimentées.

5. INFLUENCE DE LA RAÏONNEMENT DES GAZ

La correction de réflexions mutuelles entre aubes donne satisfaction tant que la température des gaz n'est pas trop élevée (900°C pour les premières campagnes MINOS), le rayonnement propre des gaz à l'intérieur de la cavité pouvant alors être négligé. Les difficultés rencontrées lors de la campagne MINOS 1500 (température des gaz égale à 1500°C) ont conduit à mettre en oeuvre une expérience pour quantifier cette perturbation, l'évaluation par le calcul se révélant trop imprécise.

Une maquette grossièrement profilée est plongée dans un écoulement de gaz chauds. Cette maquette est creuse et peut être refroidie par une circulation d'air frais. Sur l'axe de symétrie de l'une des faces latérales on a placé une série de 4 thermocouples. L'expérience consiste à viser successivement, au cours d'un même essai caractérisé par une température des gaz T_g , cette maquette, puis une maquette identique mais violemment refroidie par une circulation d'eau et placée derrière la première (figure 10). On prend soin de placer le pyromètre à égale distance des deux maquettes de telle sorte que l'épaisseur de gaz traversée soit identique et on admet l'homogénéité en température des gaz. Sur la maquette chaude le pyromètre vise au niveau d'un thermocouple dont la température est relevée (signal pyrométrique équivalent S_1). On admet que la maquette froide est suffisamment refroidie pour que son rayonnement soit négligeable. Dès ces conditions le signal pyrométrique (S_2) donne la température de luminance de la couche des gaz. La figure 11 permet de comparer, en fonction de la température des gaz T_g , la température pyrométrique compte tenu de la correction d'émissivité (signal S_2/ϵ) et la température thermocouple. Pour les températures de gaz élevées, l'écart entre ces deux températures peut dépasser 200°. Cet écart est par contre inférieur à 30° pour les températures de gaz en dessous de 900°C. Pour corriger les températures pyrométriques il suffit de remplacer le signal S_2/ϵ par $(S_2 - S_1)/\epsilon$. Dans ces conditions l'accord entre mesures pyrométriques et thermocouple est très bon quelque soit la température des gaz (écart maximum 12°). Cependant le principe de cette correction, qui nécessite de pouvoir viser une surface violemment refroidie, n'est pas toujours possible. Il est alors nécessaire de limiter au maximum la perturbation apportée par les gaz, d'une part en se rapprochant au plus près de la surface dont on veut relever la température, d'autre part en filtrant le rayonnement dont on sait que pour les gaz il est constitué de bandes, essentiellement celles de la vapeur d'eau et du gaz carbonique. La figure 12 montre un spectre obtenu sur une flamme de foyer dit "homogène" à la température d'environ 2100 K.

L'optique en verre du pyromètre permet déjà de couper le rayonnement au-dessus de 2,5 μm et ne subsistent donc que les bandes les plus faibles. On vient de voir qu'à haute température cela n'est pas suffisant. Aussi on a pensé utiliser un filtre interférentiel pour limiter l'intervalle spectral au trou situé entre les bandes à 1,85 et 2,7 μm . Cette technique a évidemment pour inconvénient de réduire la détectivité du pyromètre et ne peut donc être utilisée que pour la mesure des hautes températures (supérieure à 700°C), ce qui est généralement le cas lorsque la température des gaz est élevée. Elle a été utilisée pour assurer les essais du moteur M88 au CÉPR et a donné de bons résultats.

6. APPLICATION A DES MESURES EN TRANSITOIRE

Une application intéressante des visées pyrométriques est la détermination des coefficients d'échange locaux sur les aubes mobiles. La méthode consiste à analyser la montée en température des aubes après arrêt de leur refroidissement. En reconstituant à partir des mesures locales de température l'évolution en fonction du temps du champ thermique dans cette paroi, on déduit les coefficients d'échange extérieur le long des aubes (6). L'analyse est principalement effectuée dans la zone médiane de la hauteur de l'aube et pour cette application, la solution pyrométrique offre les avantages de la précision et de la simplicité de mise en oeuvre. Les coefficients d'échange peuvent être mesurés en présence ou non de film gazeux.

Le traitement numérique de "moyennage" n'est possible que parce que la constante de temps d'évolution des températures locales est grande, de l'ordre de la seconde. Il est cependant nécessaire de diminuer le nombre de moyennes et de le ramener de 200 à 20 ce qui impose de tolérer un rapport signal sur bruit trois fois plus faible. L'utilisation du convertisseur analogique-numérique rapide permet maintenant d'éviter cet inconvénient. Un exemple d'évolution des profils de température correspondants à la remise du débit d'air de refroidissement interne est présenté sur la figure 13.

7. CONCLUSIONS

L'établissement par des techniques pyrométriques de la cartographie des températures de surface des aubes mobiles d'une turbine refroidie, a nécessité la mise au point d'un pyromètre infrarouge à grand pouvoir de résolution spatial et temporel. Typiquement le temps de réponse de cet appareil doit être inférieur à la micro-seconde. L'utilisation d'un détecteur à l'arséniure d'indium refroidi à -40°C permet d'obtenir cette caractéristique et, compte tenu de sa très bonne détectivité, le seuil de température détectable est d'environ 450°C pour un pouvoir de résolution à la surface de l'aube de 2 mm^2 .

Les visées pyrométriques sont effectuées par endoscopie, suivant une optique de renvoi montée dans un tube refroidi, la sonde étant placée entre la roue fixe et la roue mobile, ou derrière celle-ci. Elle a été étudiée de manière à supporter les conditions de température et pression régnant dans la veine et a subi sans dommage 20 bars et 2100 K.

Aucun opérateur ne devant s'approcher du banc en fonctionnement, la sonde est commandée à distance, et permet d'explorer la plus grande surface possible des aubes. Pour cette même raison, on a opté pour un refroidissement thermo-électrique du détecteur qui, s'il réduit la détectivité, supprime la recherche fréquente en fluide de refroidissement.

L'utilisation de ce pyromètre sur la turbine expérimentale étudiée spécialement pour qualifier les nouvelles techniques de refroidissement des aubes, a montré que la pyrométrie présente quelques difficultés liées,

- d'une part au coefficient de réflexion non nul des aubes (émissivité inférieure à 1),
- d'autre part au rayonnement propre des gaz.

Ces difficultés ont été analysées et des solutions ont été proposées ; notamment un programme de correction des températures tenant compte des réflexions mutuelles entre aubes a été mis au point pour améliorer la méthode qui permet des mesures très complètes et qui est plus simple d'emploi que les techniques utilisant de, thermocouples.

REFERENCES

- (1) - FRANCOIS (J), LE BOT (Y), MICHARD (P.J.) et DEGUEST (P) - Adaptation d'un banc de turbine aux recherches pour les hautes températures. In "High temperature problems in gas turbine engines", AGARD CPP 229, 1977.
- (2) - LE BOT (Y), CHARPENEL (M) et MICHARD (P.J.) - Techniques de mesures dans les turbines à haute température. In "High temperature problems in gas turbine engines", AGARD CPP 229, 1977.
- (3) - COURNUT (A.E.), LAROCHE (M), LE BOT (Y) et MICHARD (P.J.) - Qualification of cooling systems for high temperature on a turbine facility. Congrès ASME - New Orleans - Mars 1980.
- (4) - CHARPENEL (M) et WILHELM (J)) Pyromètre infrarouge destiné à la mesure des températures d'ailettes de turbine. Mesures, Régulation, Automatisation, vol. 41, April 1976, pp. 41-50.
- (5) - POLJAK - Analysis of heat interchange by radiation between diffuse surfaces. Tech. Phys. URSS, vol. 1, n° 5-6, pp. 555-590, 1935.
- (6) - MICHARD (P.J.) - Mesures de flux de chaleur sur aubes fixes de turbines. In "High temperature turbines", AGARD CP 73, 1971.

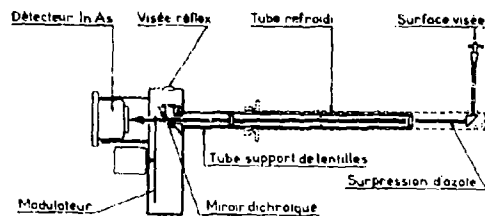


Fig. 1 - Principe de la mesure pyrométrique.

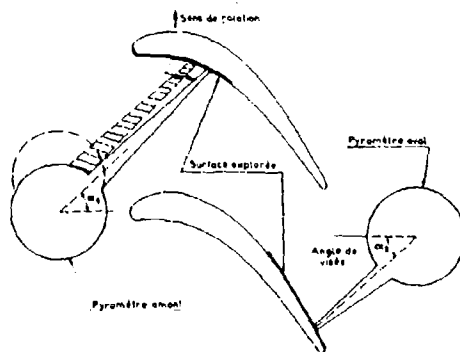


Fig. 2 - Schéma de la sonde pyrométrique à très court temps de réponse.

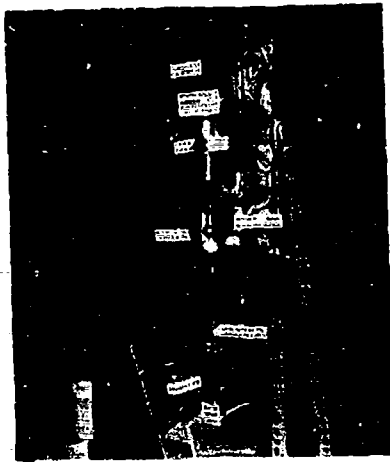


Fig. 3 - Pyromètre optique pour la mesure des températures de surface sur aubes.

Fig. 4 - Relevé des luminances au bord de fuite de deux aubes successives et top par tour.

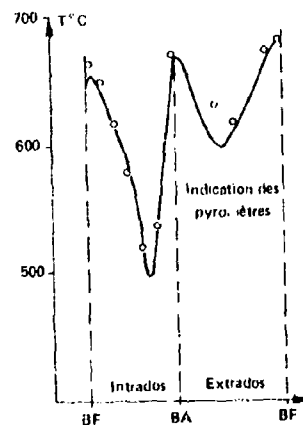
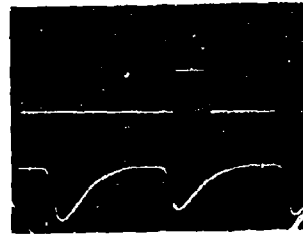


Fig. 5 - Comparaison des mesures par pyrométrie et par thermocouples : aube de très forte émissivité.

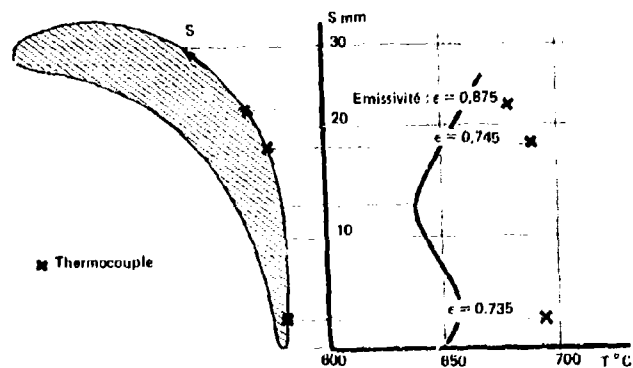


Fig. 6 - Comparaison des mesures par pyrométrie et par thermocouples : détermination de l'émissivité.

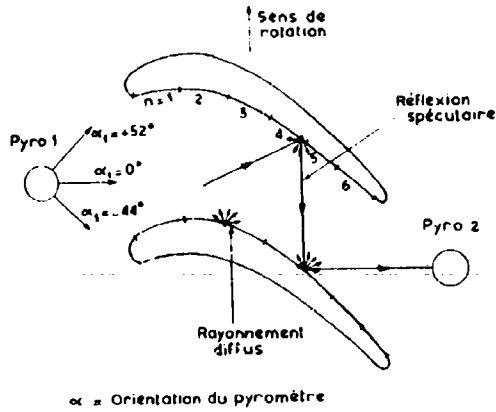


Fig. 7 - Calcul correctif du rayonnement mutuel entre aubes.

Fig. 8 - Influence de l'angle de visée sur la mesure pyrométrique.

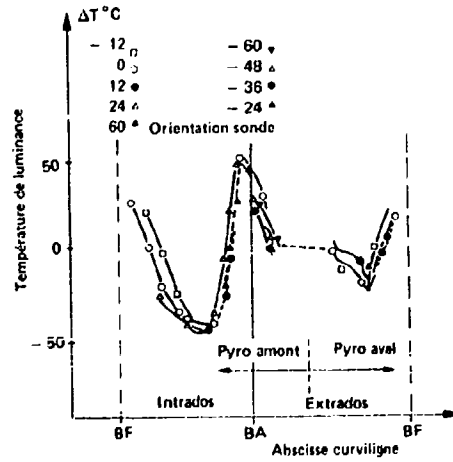


Fig. 9 - Evolution des températures brutes ($\epsilon = 1, \rho = 0$) et corrigées :
- de l'émissivité ($\epsilon = 0,7, \rho = 0$), - de l'émissivité et des réflexions mutuelles ($\epsilon = 0,7, \rho = 0,3$).

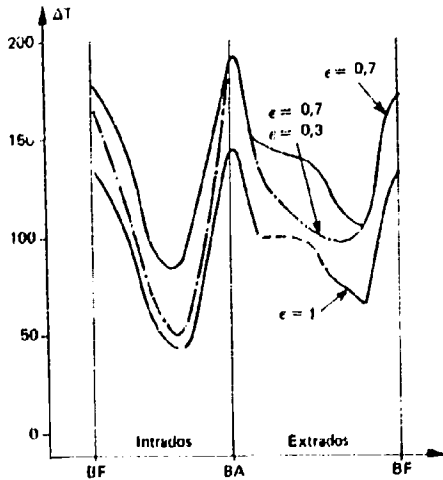
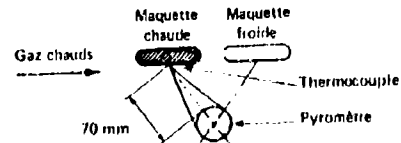


Fig. 10 - Expérience pour quantifier l'effet des gaz.



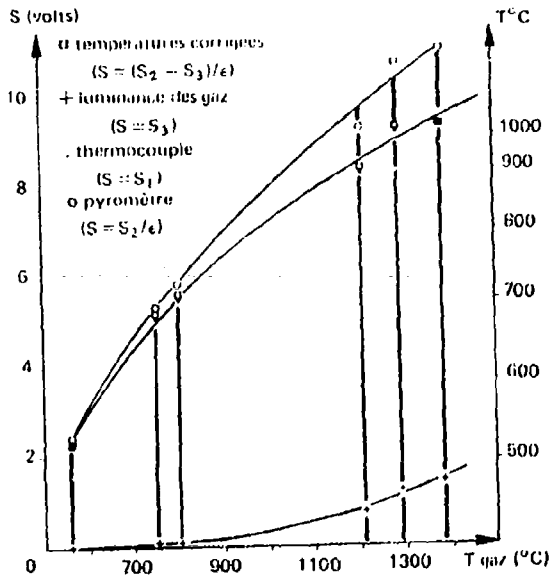


Fig. 11 - Influence de l'émission des gaz en fonction de leur température.

Fig. 12 - Utilisation d'un filtre interférentiel pour limiter l'émission des gaz.

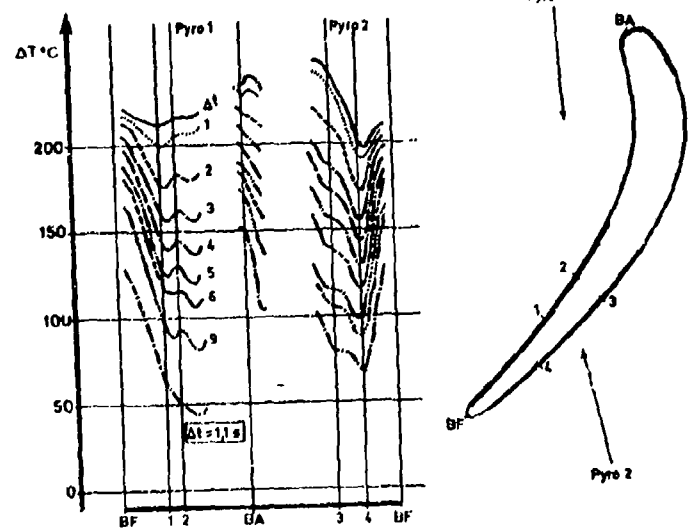
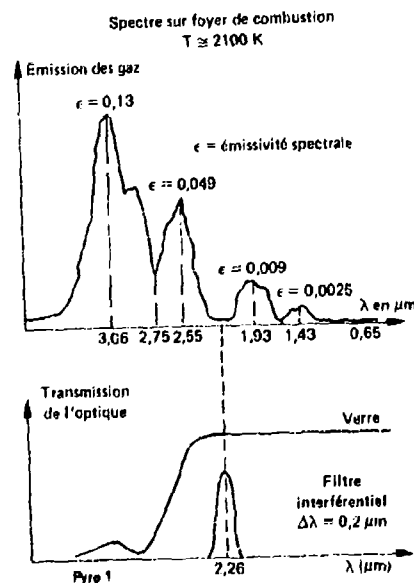


Fig. 13 - Transitoire : remise du débit de refroidissement.

DISCUSSION

W.Koschel, Gc

Which is the upper limit of the time response of your measuring system including amplifiers etc.?

Réponse d'Auteur

La constante de temps du détecteur et de son préamplificateur est d'environ 1 micro-seconde. Le système d'acquisition (un convertisseur analogique-numérique rapide NICOLET) permet de numériser les mesures avec un intervalle entre points pouvant être aussi faible que 0.5 μ s. Habituellement on se contente d'un pas de 2 μ s.

C.T.J.Scrivener, UK

Rolls-Royce has successfully developed a similar pyrometry system. This has run successfully in demonstrator engines at temperatures above 1700 K. Our experience is that particular techniques have to be employed to allow radiation originating from the combustion flame and particles in the gas stream.

Have you observed these effects, and if so, what correction do you make for them?

Réponse d'Auteur

J'ai exposé dans l'article l'influence de l'émission propre des gaz provenant essentiellement des molécules H₂O et CO₂ et comment on la minimisait. Si la combustion n'est pas suffisamment propre et l'émissivité des suies non négligeable la méthode proposée n'est plus applicable. Par ailleurs, le signal pyrométrique est bien reproductible et on ne voit pas, comme on a pu le voir avec un pyromètre 'hand' fonctionnant dans le très proche infra-rouge, des pics de température que l'on interprète comme le passage de très grosses particules.

HIGH FREQUENCY RESPONSE HEAT FLUX GAUGE FOR METAL BLADING

A.H. Epstein, G.R. Guenette - Massachusetts Institute of Technology, USA
 R.J.G. Norton - Rolls Royce, Inc, USA
 Cao Yuzhang - Beijing Institute of Aeronautics & Astronautics, PRC

Summary

Double-sided, high frequency response heat flux gauge technology developed specifically for use on metal turbine blading in short duration turbine test facilities is described in detail. The gauges consist of a metal film (1500A) resistance thermometer sputtered on both sides of a thin (25 μm) polyamide sheet. This sheet, containing 25 gauges, is then adhesively bonded (and completely covers) the airfoil surface. The temperature difference across the polyamide is a direct measure of the heat flux at low frequencies, while a quasi-1D analysis is used to infer the high frequency heat flux from the upper surface temperature history. The design criteria, construction and application techniques, and calibration procedures are discussed in detail. Sample measurements in a high pressure turbine are presented.

1.0 Introduction

Accurate measurement of the heat transfer rate to turbine blading has long been recognized as a key to the improvement of high pressure turbine stages. The development of heat flux instrumentation for hot, warm, and cold machines has therefore been an active research area. In hot turbines, the harsh, oxidizing environment is a severely limiting constraint. Here, thermal gradient devices such as Gardon gauges are becoming increasingly practical for measurement of the time average heat flux level [Ref. 1].

The development of short duration turbine test facilities (30 to 700 ms test times) over the past decade has stimulated the development of heat flux instrumentation specifically optimized for the relatively benign environment (500-800°K gas temperatures) typical of these facilities [Refs. 2,3,4,5]. Calorimeter and thin film semi-infinite instruments have been extensively used in these applications [Ref. 6].

The goal of the work described herein was the development of a heat transfer gauge technology which would permit simultaneous measurement of both the steady state and time resolved heat flux distribution about the rotor blades in the MIT Blowdown Turbine facility [Ref. 5]. The specific requirements for this instrumentation are: that it be compatible with the rig environment (500°K gas temperature, 290°K metal temperature, 200 KW/m² leading edge heat flux levels); that it be capable of withstanding the high centrifugal stresses inherent to the rotor environment; that it have frequency response extending from DC to 5 to 10 times blade passing frequency; that it be usable in relatively large numbers per airfoil (10-20 per spanwise station); that it require minimal modification to the blading; and that it introduce the minimum disruption to, or interference with, the flow field and heat transfer.

Four candidate techniques were considered in some detail: calorimeter, blade temperature conduction models, thin film semi-infinite, and multilayer thin film gauges. All four techniques have been demonstrated, at least in stationary measurements, and are probably realizable in the rotating frame.

The calorimeter type gauges consist of insulated slugs of known thermal mass inset into the blade surface, the heat flux rate being deduced from the time rate of change of the slug temperature [Ref. 7]. A severe disadvantage to this type of instrument is the disruption of the thermal boundary layer due to the thermal discontinuities introduced by the sensor material [Ref. 8]. The blade temperature-conduction model technique can be considered an extension of the calorimeter approach into three dimensions with the entire blade acting as a calorimeter. Here, the temperature history is measured at a large number of points about the airfoil and the spatial distribution of heat transfer rate is inferred with the aid of time accurate, 3-D heat conduction calculation. This technique has the advantage of requiring a minimal modification to the blading and little flow disruption, but empirically requires a very large number of sensors (100 about the chord) and is very dependent upon the robustness of the 3-D calculational procedure [Ref. 9], thus reducing its attractiveness for rotor applications.

The thin film semi-infinite gauge consists of a thin film resistance thermometer mounted on an insulating substrate. Assuming that the substrate appears infinitely thick to thermal waves propagating from the surface, the time dependent heat flux can be inferred using a one-dimensional heat conduction model. In practice, this technique has been brought to a high degree of perfection in stationary cascades by fabricating entire airfoils from ceramic material, thus eliminating flow disruption problems [Ref. 6]. Direct application of this technique would require fabrication of ceramic or plastic rotor airfoils, a formidable task. Alternatively, a metal airfoil might be coated with a suitable insulator, but this too is not simple in the rotor environment.

The technique selected was that of the multilayer heat flux gauge consisting of two temperature sensors on either side of a thin insulating substrate which is applied to the blade surface (Fig. 1). This is a thermal shunt. The temperature difference across the insulator is a direct measure of the heat flux to the surface. This direct proportionality between temperature difference and heat flux is valid only below a certain frequency.

This frequency, however, increases as the insulator thickness is reduced. Conversely, above another frequency, the substrate appears semi-infinite to the upper sensor and a quasi-one-dimensional assumption can be used to infer the heat flux as with the semi-infinite gauges described above. In addition, the multilayer gauge could be considered an elaboration of the semi-infinite gauge in which a second sensor is placed within the substrate to eliminate the gauge performance dependence on the blade material properties. Alternatively, the gauges can be viewed as developments of the commercially available thermopile sensor, low frequency response gauges [Ref. 10] with the low response sensors replaced by high response resistance thermometers. For the 25 μm thick polyamide insulator chosen, the direct response (shunt) mode frequency response is DC to 20 Hz, while the semi-infinite assumption is good above 1.5 kHz. In the MIT Blowdown Turbine tunnel for which these gauges were designed, rotor blade passing frequency is 6 kHz. Furthermore, as we shall see, the response in the intermediate 20-1500 Hz region can be reconstructed through proper numerical signal processing.

The multilayer gauges are fabricated many to a sheet of insulating material, tested, and then glued to the blade or test article surface using standard strain gauge adhesive bonding techniques. The blade is completely covered by the polyamide. The specific advantages of this heat flux gauge technology include: frequency response from DC to tens of kilohertz, conventional metal blading may be used, no thermal or geometric discontinuities are introduced, and the gauges are fabricated and tested independently of the airfoil.

This paper details the theory, fabrication, testing, and data reduction of these high frequency response multilayer heat flux gauges.

2.0 Gauge Model

We will now construct a generic multilayer, time dependent, conduction model of the double sided heat flux gauge to use in the gauge design and calibration, and as a guide to its proper application. A cross-section of a mounted gauge is illustrated in Fig. 1. When mounted on a blade profile or test item, the gauge becomes part of a five-layered structure consisting of the top thin film thermometer temperature sensor, the gauge insulating substrate, a second film thermometer, an adhesive layer, and finally the test article itself. In general, the thermal properties of each layer will differ and thus, to be fully rigorous, a five-layer model might be employed. In practice, however, the film thermometer sensors are sufficiently thin to appear thermally transparent to the applied heat flux, thereby permitting use of a three-layer model. Also, the sensors will be excited at power dissipation levels sufficiently low that their influence as sheet sources of heat can be neglected. The quantitative conditions required to meet these criteria will be derived later.

The model can be further simplified to two layers if we assume that the sensor substrate and adhesive have similar thermal properties and that the sensors are embedded in the upper layer. In detail, this adhesive thickness will represent not the exact physical thickness but an equivalent thickness including effects of unevenness and property variations. A similar assumption will be made about any surface coating (protective or dirt) which may be on top of the upper gauge surface. The gauge adhesive, substrate and surface coating will therefore form Layer 1 of the model and the test article or blade will form Layer 2 (Fig. 2). The top sensor will lie under a surface layer of thickness $h = f_h d$ and the bottom sensor will lie a distance $g = f_g d$, representing the glue layer, above the interface, where d represents the sensor separation and f_g , f_h the glue and surface coating fractions respectively. Thus $x_u = f_h d$ and $x_b = (1 + f_h)d$, and if l is the thickness of Layer 1, then $(1 + f_h + f_g)d = l$.

The heat conduction equations will be solved for the temperature distribution in a two layered semi-infinite medium of unlimited lateral extent subject to a spatially uniform surface heat flux, $q(t)$. The flow of heat may therefore be considered to be one-dimensional. We further assume that the thermal properties within each layer are uniform and that the layers make perfect thermal contact. Thus, the temperature in each layer is governed by,

$$\text{Layer 1: } \frac{\partial T_1}{\partial t} = \kappa_1 \frac{\partial^2 T_1}{\partial x^2} \quad 0 \leq x \leq L \quad (1)$$

$$\text{Layer 2: } \frac{\partial T_2}{\partial t} = \kappa_2 \frac{\partial^2 T_2}{\partial x^2} \quad l \leq x \leq \infty \quad (2)$$

(where $\kappa = k/\rho c$ is the thermal diffusivity), subject to the interface conditions,

$$T_1(L, t) = T_2(L, t) \quad (3)$$

$$k_1 \frac{\partial T_1}{\partial x} \Big|_{x=L} = k_2 \frac{\partial T_2}{\partial x} \Big|_{x=L} \quad -\infty < t < +\infty \quad (4)$$

and the semi-infinite condition,

$$T_2(\infty, t) = 0 \quad (5)$$

To fully specify the problem, upper surface boundary conditions and initial conditions must be provided and these will depend upon the form of the driving surface heat flux to be investigated. We will consider two cases: 1) a steady sinusoid, and 2) a step in

surface heat flux. The solution to these problems employs the standard techniques described in Ref. [11]. The results will be given in a form useful to the subsequent analysis and only the solution for the temperature in the layer containing the sensor, $T_1(x,t)$, will be reported.

2.1 Response to a Steady Harmonic Variation in Surface Heat Flux

Initial conditions cannot be specified since the steady solution valid for all time is being sought. For the surface heat flux,

$$\dot{q}_s(t) = -k_1 \frac{\partial T_1}{\partial x} \Big|_{x=0} = Q_0 \exp(j\omega t) \quad -\infty < t < +\infty \quad (6)$$

the temperature distribution in Layer 1 is,

$$T_1(x,t) = (Q_0 d/k_1) M \exp(j(\omega t - \phi)) \quad 0 \leq x \leq L \quad (7)$$

where,

$$M = \sqrt{2} \left(\frac{\omega}{\omega_c} \right)^{-1/2} \exp \left\{ -\frac{1}{2} \left(\frac{\omega}{\omega_c} \right)^{1/2} \frac{x}{d} \right\} \left\{ \frac{A^2 + B^2}{C^2 + D^2} \right\}^{1/2} \quad (8)$$

$$\phi = \frac{1}{2} \left(\frac{\omega}{\omega_c} \right)^{1/2} \frac{x}{d} + \frac{\pi}{4} - \tan^{-1} \left\{ \frac{BC - AD}{AC + BD} \right\} \quad (9)$$

A sensor characteristic frequency ω_c has been introduced based upon the sensor spacing d .

$$\omega_c = \frac{k_1}{2d^2} \quad (10)$$

The other quantities are defined as follows:

$$A = 1 - R \exp \left\{ -\left[\frac{\omega}{\omega_c} \right]^{1/2} \left[\frac{L-x}{d} \right] \right\} \cos \left\{ \left[\frac{\omega}{\omega_c} \right]^{1/2} \left[\frac{L-x}{d} \right] \right\} \quad (11a)$$

$$B = R \exp \left\{ -\left[\frac{\omega}{\omega_c} \right]^{1/2} \left[\frac{L-x}{d} \right] \right\} \sin \left\{ \left[\frac{\omega}{\omega_c} \right]^{1/2} \left[\frac{L-x}{d} \right] \right\} \quad (11b)$$

$$C = 1 + R \exp \left\{ -\left[\frac{\omega}{\omega_c} \right]^{1/2} \left[\frac{L}{d} \right] \right\} \cos \left\{ \left[\frac{\omega}{\omega_c} \right]^{1/2} \left[\frac{L}{d} \right] \right\} \quad (11c)$$

$$D = -R \exp \left\{ -\left[\frac{\omega}{\omega_c} \right]^{1/2} \left[\frac{L}{d} \right] \right\} \sin \left\{ \left[\frac{\omega}{\omega_c} \right]^{1/2} \left[\frac{L}{d} \right] \right\} \quad (11d)$$

$$R = \frac{r-1}{r+1} \quad (12)$$

$$r = \frac{\sqrt{(pCk)_2}}{\sqrt{(pCk)_1}} \quad (13)$$

2.2 Response to a Step in Surface Heat Flux

Here, both the transient and steady solutions to the problem are of interest. The initial conditions are,

$$-\infty < t < 0 \quad \begin{cases} T_1(x,t) = 0 & 0 \leq x \leq L \\ T_2(x,t) = 0 & L \leq x < \infty \end{cases} \quad (14)$$

For the surface heat flux,

$$\dot{q}_s(t) = -k_1 \frac{\partial T_1}{\partial x} \Big|_{x=0} = \begin{cases} 0 & -\infty < t < 0 \\ Q_0 & 0 \leq t < +\infty \end{cases} \quad (15)$$

the temperature distribution in Layer 1 is given by,

$$T_1(x,t) = (Q_0 d/k_1) \sqrt{\frac{t}{\tau}} \sum_{n=0}^{\infty} (-R)^n (\text{ierfc } P_n - R \text{ierfc } Q_n) \quad (16)$$

where

$$P_n = \frac{(x/d)}{\sqrt{t/\tau}} + 2n \frac{(L/d)}{\sqrt{t/\tau}} \quad (17a)$$

$$Q_n = -\frac{(x/d)}{\sqrt{t/\tau}} + 2(n+1) \frac{(L/d)}{\sqrt{t/\tau}} \quad (17b)$$

and $\text{ierfc}()$ is the first integral of the complementary error function. A gauge time constant τ has been introduced, again based upon gauge thermal diffusivity and sensor spacing,

$$\tau = \frac{d^2}{4\kappa} \quad (18)$$

The temperature is referenced to the quantity $(Q_0 d/k_1)$ which represents the steady state temperature drop required to "drive" a heat flux Q_0 across the distance d .

The characteristic frequency ω_C and the time constant τ are defined with respect to the gauge film spacing d and not the layer thickness L . Thus, the expressions for the solution may appear a little more cumbersome than necessary to describe the temperature distribution but they are in the proper form for the subsequent analyses of the gauge response characteristics.

2.3 Gauge Model Discussion

The solutions for the temperature distribution in Layer 1, $T_1(x,t)$, depend intrinsically upon the properties of the gauge through $\sqrt{\rho c \kappa}$ and k/d . These parameters form the basis for the normalization of the independent variables through the definitions of τ and ω_C . We will adopt these as the fundamental parameters which characterize the gauge and which, therefore, must be known to interpret its output. Additional influence comes from the thickness fractions of the surface coating and adhesive (f_h and f_g respectively) and the $\sqrt{\rho c \kappa}$ of Layer 2 which enters through the parameter R .

We will now use the gauge model to show that only the film thermometer scale factor, $\sqrt{\rho c \kappa}$ and k/d need calibration. Variations in adhesive thickness and test article properties (f_h , f_g , R), although they influence the temperature levels, do not significantly affect the heat flux level inferred.

2.4 Gauge Model Response

We will use the limiting case solutions of the low frequency direct mode and the high frequency semi-infinite mode to provide a framework for gauge design and calibration.

In the direct or shunt mode, the surface heat flux is assumed to be proportional to the measured temperature drop across the gauge. While this is valid for static measurements, a uniform temperature gradient will not exist across the gauge if there are frequency components for which the thermal penetration depth is comparable to, or smaller than, the gauge thickness. The gauge is considered to be in the semi-infinite mode for those frequency components which are effectively damped by the gauge substrate. In this case, the heat flux may be obtained entirely from the upper film thermometer. It should be understood that 'direct' and 'semi-infinite' are terms used to describe limiting processes within the gauge substrate and are in no way exclusive of each other in actual operation of the gauge.

For steady harmonic excitation in the direct measurement mode, the upper and lower film temperatures are provided by Eq. (7),

$$T_u = T_1(x_u, t) = (Q_0 d/k_1) M_u e^{j(\omega t - \phi_u)} \quad (19a)$$

$$T_l = T_1(x_l, t) = (Q_0 d/k_1) M_l e^{j(\omega t - \phi_l)} \quad (19b)$$

where $M_u = M(x_u)$, etc.; $x_u = f_h d$ and $x_l = (1+f_h)d$ are the positions of the upper and lower thermometers; and $L = (1+f_h+f_g)d$ is the total thickness of Layer 1. The direct mode heat flux \dot{q}_D indicated by an 'ideal' gauge, (i.e., error-free measurements of T_u and T_l , and perfect knowledge of k_1/d), is

$$\dot{q}_D(t) = (k_1/d)(T_u - T_l) \quad (20)$$

Substituting for the temperatures using Eqs. (19), the ratio of the measured to actual heat flux is,

$$\frac{\dot{q}_D(t)}{\dot{q}_S(t)} = M_u e^{-j\phi_u} - M_l e^{-j\phi_l} \quad (21)$$

This may be put into the more useful magnitude-phase form,

$$\frac{\dot{q}_D(t)}{\dot{q}_S(t)} = M_D e^{-j\phi_D} \quad (22)$$

where

$$M_D = (M_u^2 + M_l^2 - 2M_u M_l \cos(\phi_u - \phi_l))^{1/2} \quad (23)$$

$$\phi_D = \tan^{-1} \left(\frac{M_u \sin \phi_u - M_l \sin \phi_l}{M_u \cos \phi_u - M_l \cos \phi_l} \right) \quad (24)$$

represent the magnitude M_D and phase ϕ_D response for direct mode.

These are plotted in Fig. 3 as a function of the normalized frequency ω/ω_C , for several values of glue fraction, f_g . The case shown is for a polyamide substrate mounted upon an aluminum test body, $R=0.96$. The results show that the direct temperature

difference mode is valid, in this example, for frequencies up to the cutoff frequency ω_c , and that in this region the adhesive layer has negligible influence upon the performance of the gauge. Parametric studies show similar conclusions for the influence of R and f_h .

The results thus far show that, in the direct mode, the temperature rise per unit of surface heat flux can be approximated by,

$$\frac{\Delta T}{Q} = \frac{d}{k} \quad (25)$$

up to the cutoff frequency,

$$\omega_c = \frac{k}{2d^2} = \frac{1}{2} \left(\frac{k/d}{\sqrt{\rho ck}} \right)^2 \quad (26)$$

If k/d is eliminated from these expressions, a constraint between gauge sensitivity $\Delta T/Q$ and the response bandwidth f_c (in Hz) is obtained,

$$\frac{\Delta T}{Q} f_c^{1/2} = \frac{1}{2\sqrt{\pi}} \frac{1}{\sqrt{\rho ck}} \quad (27)$$

i.e., the overall trade between signal strength and cutoff frequency depends only on the thermal property $\sqrt{\rho ck}$ of the gauge substrate. Thus, both low thermal inertia ρc (more precisely high diffusivity), good for high f_c , and low thermal conductivity, good for high $\Delta T/Q$, are desirable.

The solution for steady harmonic excitation, Eq. (19b), shows that the response of the lower sensor is fully damped for frequencies above approximately $100 \omega_c$. In the case of the semi-infinite mode, the expression for the surface temperature, Eq. (19a), (for $x=0$) reduces to

$$T_u(t) = \frac{Q_0}{\sqrt{\rho ck}} \omega^{-1/2} e^{j(\omega t - \frac{\pi}{4})} \quad (28)$$

Thus, the condition for maximum high frequency temperature sensitivity is the same as for the direct measurement mode, low $\sqrt{\rho ck}$, except now it is seen that sensitivity also diminishes with frequency, as $\omega^{-1/2}$. This means that, for a fixed temperature measurement capability, low values of $\sqrt{\rho ck}$ will help to improve the upper frequency response limit of the semi-infinite mode.

In summary, this steady sinusoidal theory provides the basis for the gauge design, i.e., substrate and thickness selection. Low $\sqrt{\rho ck}$ is desirable for a high sensitivity-bandwidth product in the direct measurement mode and for high sensitivity and frequency response in the semi-infinite mode. For a given $\sqrt{\rho ck}$, the trade between f_c and $\Delta T/Q$ is then set by the choice of substrate thickness, d .

Now we will look at the semi-infinite mode step response, which is shown for the upper and lower thermometers in Fig. 4. The region in which the response of the upper thermometer is linearly proportional to \sqrt{t} is that for which the semi-infinite assumption is valid. Here, the solution for $x=0$ is,

$$T_u(t) = \frac{2Q_0}{\sqrt{\pi} \sqrt{\rho ck}} t^{1/2} \quad (29)$$

We will use this equation for the $\sqrt{\rho ck}$ calibration procedures discussed later. Note that, although increasing the adhesive fraction tends to extend the duration of the semi-infinite regime, it does not influence the performance of the gauge while in that regime. Similar conclusions follow for R and f_h .

The step response for the direct difference mode is obtained from Eqs. (16) and (20) (Fig. 5). The effect of the glue layer is more evident from its influence upon the rise time of the measured response than it was from its effect upon the frequency response. Also shown is a discriminant $(T_u - T_1)/T_u$, which can be used to estimate the effective thickness of the adhesive from test data.

These results clearly show the behavior of the semi-infinite ($t < \tau$) and steady state ($t > 20\tau$) limits. The actual data is reduced with a numerical technique which reconstructs the entire frequency domain, as will be described later.

2.5 Design of the Thin Film Temperature Sensors

This section discusses the design of the thin film resistance thermometers used as temperature sensors in the multilayer heat flux gauge. These sensors are nothing more than metal film resistors whose resistance changes with temperature. For a change δT about a temperature T , the increment in film resistance may be expressed by a Taylor series expansion in powers of δT ,

$$\delta R = R(T + \delta T) - R(T) = R(T) \alpha(T) \delta T + \text{higher order terms in } \delta T. \quad (30)$$

The temperature coefficient of resistivity $\alpha(T)$, a fundamental material property, represents the fractional change in resistance about a given temperature,

$$\alpha(T) = d(\ln R)/dT. \quad (31)$$

For the metals commonly employed in resistance thermometers, $\alpha(T)$ is usually a very weak function of temperature over ranges of practical interest. Thus, in many applications, a convenient form of Eq. (30) may be obtained by assuming constant α and neglecting the higher order terms,

$$\Delta R = R_0 \Delta T. \quad (32)$$

(For the sensor here, this results in errors of order 0.1C over a 60C range.)

For a sensor excited at constant current, the change in voltage across the sensor, ΔV , is

$$\Delta V = (V_0) \Delta T, \quad (33)$$

where V represents the total voltage drop across the film. Thus, the sensitivity of the sensor is directly proportional to both its temperature coefficient and the excitation voltage. The excitation voltage is constrained, however, by the V^2/R heat dissipation in the film sensor,

$$Q_E = V^2/(Rlw), \quad (34)$$

(where l and w are the active length and width of the film). This heat dissipation must be kept small compared to the heat flux being measured.

To quantify this constraint, film resistance will be expressed in terms of film geometry and volume resistivity, ρ ,

$$R = (\rho l)/(wt), \quad (35)$$

where t is the film thickness. Substituting into Eq. (34) yields

$$V = (\rho/t)^{1/2} l Q_E^{1/2}. \quad (36)$$

This expression sets the excitation voltage. Note that this result is independent of the width of the film. The level of Q_E can be adjusted for each measurement application. The film parameters (ρ/t , l , w , t), however, must be selected beforehand by the design process. Substitution of Eq. (36) into Eq. (33) yields a form of the sensitivity equation useful for design,

$$\Delta V/\Delta T = (\rho/t)^{1/2} \alpha l Q_E^{1/2}. \quad (37)$$

This expression implies that long, thin films with high volume resistivity and temperature coefficient are best for high temperature measurement sensitivity. There are, however, many other conditions which must be considered to arrive at an overall optimum design of film resistance sensors for heat transfer gauges, some of which are discussed below.

The first two factors in Eq. (37), $(\rho/t)^{1/2} \alpha$, show the influence of film thickness and electrical properties on film sensitivity. Table I presents a ranking of some candidate film materials based upon the sensitivity parameter $\alpha/\sqrt{\rho}$, derived using the bulk properties of the materials. Note, however, that these properties are a function of film thickness in the region below $1 \mu m$ (where data is available for only a few substances [Ref. 12]). This table does provide some general guidance for maximizing temperature sensitivity, the final choice being also influenced by:

- a) surface temperature changes resulting from the thermal resistance and capacity of the film,
- b) abrasion resistance and substrate adhesion of the film,
- c) residual stresses induced by the deposition process, and
- d) changes in ρ and α from their known bulk property values.

The third factor in Eq. (37) shows the influence of sensor surface geometry. The maximum length of the sensor, hence its sensitivity, will be determined by the spatial resolution requirements of the heat flux measurement. If this is characterized by a single length scale λ , for example, the film will be constrained to lie in a roughly square region, λ on a side. Since the sensitivity has been shown to be independent of film width, a serpentine pattern may be employed to significantly increase the film sensitivity, if the minimum width that can be reliably deposited is much smaller than λ . For the film geometry chosen, $l = 14\lambda$. There are, however, several potential disadvantages to these thin, long and narrow film sensors. First, they will be more vulnerable to small scale nicks and scratches. Second, they may prove unsuitable for calibration of substrate physical properties by the electrical self-heating method, which requires that the film width be much larger than the thermal penetration depth over the required calibration time. Third, the sensitivity advantage of a long, thin, narrow film can be reduced by the reduction in its inherent signal to noise ratio which arises due to its increased resistance.

We will now estimate the signal to noise ratio of this thin film resistance thermometer. All resistors produce electrical noise as a result of the thermal motion of their electrons. The mean squared value of this thermal noise voltage is $\overline{V_n^2} = 4kTB R$; where k is the Boltzmann constant, T the resistor absolute temperature, B the bandwidth over which this (white) noise voltage is measured, and R the resistance. A second contributor to resistor noise arises when the resistor 'feels' the flow of an externally applied current. All electrical currents have inherent fluctuations, arising from the fact that

charge comes in discrete lumps (electrons). For a current of (average) magnitude I , the mean squared value of these fluctuations is $I_e^2 = 2eIB$, where e is the electron charge. Passing through a resistor, these fluctuations appear as a voltage noise $V_e^2 = I_e^2 R^2 = 2eVRB$, shot noise. Since these sources are uncorrelated, the total resistor noise may be expressed as,

$$\bar{V}_n^2 = \bar{V}_t^2 + \bar{V}_s^2 = (4kT + 2eV)RB \quad (38)$$

Note that \bar{V}_n^2 , a measure of the noise power, is proportional to the product of the observation bandwidth with the resistance (and implicitly with the gain of the film sensor).

The mean squared signal power (obtained from Eq. (37)) is,

$$\delta \bar{V}^2 = (\rho/t) a^2 l^2 Q_E \delta T^2 \quad (39)$$

Forming the ratio of mean squared signal to noise powers yields the signal to noise ratio,

$$S/N = \frac{a^2 Q_E (lw) (\delta T)^2}{(4kT + 2e \sqrt{Q_E} (\rho/t) l) B} \quad (40)$$

where Eqs. (35) and (36) have been used for R and V in Eq. (38).

The film noise will result in an indicated RMS temperature fluctuation, δT_n , which may be found from Eq. (40) by setting $S/N=1$,

$$\delta T_n = \delta T \Big|_{S/N=1} = \left\{ \frac{4kTB}{Q_E l w a^2} \left[1 + \frac{e \sqrt{Q_E} (\rho/t)}{2kT} \right] \right\}^{1/2} \quad (41)$$

For the nominal operating conditions of the sensors designed here, this temperature is equal to 0.002°K , quite negligible. A more rigorous optimization of film design would include all the tradeoffs between the film, amplifier, and data acquisition system. This was not done in this case since this gauge noise level is less than the 0.08°K peak to peak equivalent noise of the amplification system used.

3.0 Fabrication and Mounting

Given the guidelines implicit in the gauge theory, the gauge design consisted of selection of the substrate material, the film resistor material, and the sensor geometry. All three must be compatible with the fabrication technique selected. Vapor deposition and photolithography were chosen as being compatible with both large scale, low cost fabrication of these gauges and the fine sensor structure implied by the relatively high film sensor resistance desired.

Over fifty materials were studied as candidates for the gauge substrate. Polyamide (Kapton) was by far the most attractive material. It has the lowest $\sqrt{\rho CK}$ of any material studied (and thus the highest sensitivity bandwidth product), has excellent thermal and mechanical properties up to 600°K , has a well-developed adhesive technology (due to its wide use in strain gauges), is widely available, and is used in vapor deposition applications (for spacecraft). The substrate thickness, d , was selected as $25 \mu\text{m}$ to yield a direct mode response upper limit of 20 Hz and a semi-infinite mode lower limit of 1500 Hz .

The resistance thermometers are fabricated from $0.13 \mu\text{m}$ thick pure nickel. Nickel was chosen because of its relatively high net sensitivity (Table I) and because of its very good adhesion characteristics in thin film applications. The sensor geometry selected (Fig. 6) was a square serpentine pattern to maximize the sensor length in an area compatible with the expected disturbance length in the flow field and thus maximize the signal to noise ratio as discussed earlier. The sensor resistance is approximately 500Ω . Low resistance gold leads or 'tags' $1 \mu\text{m}$ thick are deposited from the sensor to the edge of the polyamide sheet. Signals from the bottom sensor come through 0.5 mm diameter 'plated through' holes, laser drilled in the substrate before the deposition process. Twenty-six gauges are fabricated on a single polyamide sheet whose dimensions are compatible with a turbine airfoil surface area.

The vapor deposition is done by d.c. sputtering at a pressure of 5×10^{-4} torr of argon. The deposition rate of the nickel is 0.2 nm per second. The geometrical delineation is done using a liftoff process, the two gauge sides being done separately. The manufacturing yield and material properties are very strongly process variable dependent. The principal problem with the gauges is a high batch to batch variation in manufacturing yield which is not yet understood. The problem appears as a high level of intrinsic stress in the nickel, resulting in cracking of the sensors. Work is underway to solve this problem.

Originally, a silicon dioxide overcoat was applied to the bottom sensor surface to serve as an electrical insulator. This was discontinued in favor of anodizing the surface of the aluminum blading, a practice which has proven completely satisfactory.

The gauge sheets are simply cut to conform to the blade surface outline and then bonded to the surface using conventional strain gauge cement and mounting techniques. Thermal time response testing has indicated that the glue layer is $5 \mu\text{m}$ thick. Seventy-five micron diameter wires are soldered to the far ends of the gold tags to bring out the signals in a region far removed from the measurement area.

4.0 Calibration of the Heat Flux Gauges

As in most experimental techniques used to determine heat flux, temperature is the physical quantity measured, from which surface heat flux is inferred by one of several techniques: direct processing of the temperature signal by a physical RC analog network, numerical integration of the measurement with a kernel function, or processing of the measurement by a numerical analog of the gauge heat flow. These techniques are based upon a model of the heat conduction process within both the gauge and, in most cases, the test article. The model not only provides the physical and mathematical framework for each approach but also the form of the fundamental parameters which govern the behavior of the gauge.

The multilayer gauge provides two temperature measurements: at the surface, and at a depth d below the surface. From the model derived earlier, it can be seen that two constants must be determined - $\sqrt{\rho c k}$ (the conventional parameter used with surface thermometry based upon the semi-infinite assumption), and k/d (representing the steady state heat flux per unit temperature drop across the gauge).

Careful calibration of these parameters is particularly important for this gauge since there is far less experience with Kapton as a substrate than with the more conventional quartz, Pyrex, or machinable ceramic materials. Significant deviations from the 'nominal' or advertised thermal and physical properties might occur within the manufacturing tolerances of the Kapton sheet. Furthermore, it is not yet known what influence, if any, the film thermometer deposition process might have upon these properties. Thus, given that the upper and lower film sensors have been calibrated as thermometers and that all the assumptions pertaining to the sensor model are satisfied, knowledge of $\sqrt{\rho c k}$ and k/d will fully characterize the operation of the heat flux sensor.

The temperature coefficient of resistivity of the thin film thermometers is conventionally calibrated by placing the gauges in a heated immersion bath and varying the bath temperature. All sensors on a test specimen are tested together. The accuracy of the calibration is limited by that of the reference thermometer to approximately 0.05°C .

Many calibration schemes for $\sqrt{\rho c k}$ and k/d place boundary conditions on the gauge for which exact solutions of the heat conduction equation can be found. The calibration coefficients may then be inferred from a simple comparison of the experimental data with the theoretical solution. The overall accuracy of the result will be dependent upon both the quality of the various physical measurements required and the accuracy to which the assumed boundary conditions are realized. This latter condition is especially crucial since its validity may not necessarily be apparent from the test data alone. Thus, there is a practical virtue in making these boundary conditions as simple as possible, i.e., that the flow of heat be one-dimensional and that the gauge appear thermally semi-infinite. Given these conditions, simple analytical solutions can be found for the surface temperature response to a wide variety of surface heat flux time histories. For example, the top surface response to a step in surface heat flux, Q , is given by,

$$T(t) = \frac{2Q}{\sqrt{\pi} \sqrt{\rho c k}} t^{1/2} \quad (42)$$

Commonly, the step in surface heat flux is applied by pulsing current through the film, i.e., resistive dissipation in the sensor itself [Ref. 6]. This technique cannot be used with this gauge geometry, however, since the sensor width is on the order of the insulator thickness, violating the uniform heating assumption and introducing errors on the order of 100%. Instead, a calibration technique is used in which the gauge is radiantly heated by a laser pulse, simultaneously yielding $\sqrt{\rho c k}$ and k/d .

Conceptually, step radiant heating can be used as a direct calibration, i.e., a known heat rate is applied to the top gauge surface with $\sqrt{\rho c k}$ being inferred from the top sensor rise time and k/d simply computed from the top and bottom sensor temperatures. In practice, this can be difficult to achieve since the measurement accuracy is directly proportional to the absolute accuracy to which the pulse power is known, dependent upon absorption characteristics of the surface, and is sensitive to the energy distribution in the laser beam. Rather than attempt to perform an accurate absolute measurement, a relative calibration technique was developed which depends upon ratios, not absolute values.

In the relative calibration, the step response is measured with the sensor both covered and uncovered by a reference fluid of known $\sqrt{\rho c k}$. The method is based upon the principle that the applied surface coating acts as a sheet source of heat at the interface of two semi-infinite substances. Theory shows that the ratio of heat entering each substance equals the ratio of their respective values of $\sqrt{\rho c k}$ (since both materials see the same interface temperature), and this fact may be exploited to measure this ratio [Ref. 6]. Since the method involves the comparison of measurements, absolute knowledge of the incident heat flux and film thermometer scale factor are not needed, being replaced instead only with the requirement that these quantities remain stable over the duration of the tests. However, any change in the total heat flux absorbed by the surface coating as a result of the application of the reference fluid (by mechanisms such as meniscus focusing, absorption by the fluid or by reflections from its surface) must either be negligible or quantifiable.

For the first set of tests, the sensor is placed in vacuum or still air. If Q_f represents the surface heating, the resulting temperature rise according to the theory is,

$$T_I(t) = \frac{2Q_I}{\sqrt{\pi}\sqrt{(\rho ck)_S}} t^{1/2} \quad (43)$$

For the second set of tests, the sensor is placed in good thermal contact with a material of known $\sqrt{\rho ck}$ by covering it with a fluid of high electrical resistivity. If Q_S represents the heat flux entering the sensor, and Q_F that entering the fluid, than at their common boundary the temperature rise is given by,

$$T_{II}(t) = \begin{cases} \frac{2Q_S}{\sqrt{\pi}\sqrt{(\rho ck)_S}} t^{1/2} \\ \frac{2Q_F}{\sqrt{\pi}\sqrt{(\rho ck)_F}} t^{1/2} \end{cases} \quad (44)$$

from which it can be concluded that,

$$\frac{Q_S}{Q_F} = \frac{\sqrt{(\rho ck)_S}}{\sqrt{(\rho ck)_F}} \quad (45)$$

If the total heat flux absorbed by the coating for this second series of tests is Q_{II} , where $Q_{II} = Q_S + Q_F$, the flux into the sensor is found to be,

$$Q_S = \left[1 + \frac{\sqrt{(\rho ck)_F}}{\sqrt{(\rho ck)_S}} \right]^{-1} Q_{II} \quad (46)$$

and the temperature rise at the surface is therefore,

$$T_{II}(t) = \left[1 + \frac{\sqrt{(\rho ck)_F}}{\sqrt{(\rho ck)_S}} \right]^{-1} \frac{2Q_{II}}{\sqrt{\pi}\sqrt{(\rho ck)_S}} t^{1/2} \quad (47)$$

If m_I and m_{II} are the slopes of the linear region of sensor temperature, T , versus the square root of time (i.e., from Eqs. (43) and (47)) for the two conditions, then

$$m_I = \frac{2Q_I}{\sqrt{\pi}\sqrt{(\rho ck)_S}} \quad (48)$$

$$m_{II} = \left[1 + \frac{\sqrt{(\rho ck)_F}}{\sqrt{(\rho ck)_S}} \right]^{-1} \frac{2Q_{II}}{\sqrt{\pi}\sqrt{(\rho ck)_S}} \quad (49)$$

and by forming their ratio,

$$\sqrt{(\rho ck)_S} = \left[\left(\frac{Q_{II}}{Q_I} \right) \left(\frac{m_I}{m_{II}} \right) - 1 \right]^{-1} \sqrt{(\rho ck)_F} \quad (50)$$

If the total heat absorbed by the coating is the same in both tests (as has been verified in this case), this relation becomes,

$$\sqrt{(\rho ck)_S} = \left[\left(\frac{m_I}{m_{II}} \right) - 1 \right]^{-1} \sqrt{(\rho ck)_F} \quad (51)$$

and serves as the basic relative calibration formula. Note that only ratios of the quantities appear.

A simultaneous calibration of k/d may be obtained by extending the heating time to values very much larger than the characteristic time of the sensor, $\tau = d^2/4\kappa$. The lower sensor begins to respond to the surface heating at approximately time τ ($\tau = 1.6$ ms for these gauges), with steady state conditions being achieved by $t = 20\tau$. For $t > 20\tau$, the steady state temperature difference, $(T_u - T_t)_{SS}$, between the upper and lower surfaces of the sensor becomes proportional to the applied heat flux, thus k/d may be found from,

$$\frac{k}{d} = \frac{Q}{(T_u - T_t)_{SS}} \quad (52)$$

given that Q is known.

The magnitude of Q could be obtained from an independent measurement of beam intensity and surface absorptivity (as would be required for an absolute calibration). However, when the k/d calibration is merged with the relative procedure, Q may be calculated directly by combining the initial step response data from the first set of tests, Eq. (48), with the value of $\sqrt{(\rho ck)_S}$ determined from the reference fluid tests, Eq. (51). Substituting this result into Eq. (52) then yields the desired expression for k/d ,

$$\frac{k}{d} = \left(\frac{\sqrt{\pi}}{2} \right) \left(\frac{m_I m_{II}}{m_I - m_{II}} \right) \frac{\sqrt{(\rho ck)_F}}{(T_u - T_t)_{SS}} \quad (53)$$

It should be pointed out that, unlike the $\sqrt{\rho c k}$ testing, this expression requires that the film thermometer temperature coefficients of resistivity be calibrated or, more precisely, that their scale factors, if unknown, at least be equal.

4.1 Calibration Results

An argon ion laser was used as the radiant heat source, providing an incident flux of approximately 30 kW/m² over an area slightly larger than the 1 mm square of the film thermometer. The laser output was modulated by an electro-optic modulator producing a light step with a 25 ns rise time. The surface of the sensor was blackened with a Staedtler Lumograph Model-316 non-permanent marking pen, commonly used for view-graph presentations. The coating has good opacity and low thermal inertia, as verified by comparing the measured temperature responses with the parametric theory presented earlier, and its selection was the result of a large number of empirical tests. This coating has the advantage, unlike many of the other coating materials evaluated, of possessing both high electrical resistivity and poor solubility in the reference fluids.

The reference fluid chosen was dibutylphthalate, a commonly used heating bath medium with electrical equipment, because of its inert properties and high electrical resistivity. Its thermal properties were obtained from the manufacturer and checked against the properties of the more commonly employed glycerol using the electrical heating technique on a platinum-quartz film sensor. Its value of $\sqrt{\rho c k}$ is estimated to be 495 ± 5%. Since it is much less viscous than glycerol, it does not produce measureable beam focusing effects, as did the latter fluid.

A sample calibration is shown in Fig. 7, from which it can be seen that the top sensor output is linear with the square root of time. The slopes m are then calculated from the least square fits to the data as illustrated by the lines. From these measurements, we conclude that $\sqrt{\rho c k}$ for this gauge is 575 (W/m²) (√sec)/°K and k/d is 8086 W/(M²°K). This represents a 20% variation from nominal published data.

Since the gauges are intended for a highly stressed rotor environment, gauge sensitivity to strain must be considered. This was evaluated by pulling an aluminum specimen bearing a gauge in a tensile test machine. Strain sensitivity proved to be negligible, equivalent to 0.003°C at 2% strain.

5.0 Data Reduction - Numerical Analysis Technique

The heat flux gauges have been shown to be suitable for evaluation of the surface heat flux to turbine blading at low and high frequencies when the gauge characteristics can be simply defined. At low frequencies, the heat flux can be evaluated directly from the measured temperature difference across the insulator, and at high frequencies through the use of semi-infinite procedures. The numerical technique described here of reducing the two temperature histories to heat flux expands the frequency range of the gauges to include the regime between DC and semiinfinite response.

As with most numerical techniques, discretization of the governing equations is required, including distribution of calculational stations or nodes through the insulator. In order to provide accurate prediction of the surface heat transfer rate, the distribution of the calculation nodes must be such as to accurately capture the varying temperature field in the insulator.

The governing heat conduction equation is:

$$\frac{\partial^2 T}{\partial x^2} = (\rho c/k) \frac{\partial T}{\partial t} \quad (54)$$

For low frequency heat transfer rate variations, the time derivative in the above equation approaches zero, and thus a constant temperature gradient is expected across the insulator. Since this is a linear solution, the exact placement of nodes in the substrate is not crucial.

As the excitation frequency increases, however, the upper surface temperature signal is attenuated through the insulator until, at very high frequencies, the insulator appears semi-infinite. The expected temperature solution will be:

$$T = Ae^{-Kx} \cos(\omega t - Kx) \quad \text{where: } K = \sqrt{(0.5\rho c \omega/k)} \quad (55)$$

or

$$|T| = Ae^{-Kx} \quad (56)$$

Thus, the magnitude of T decays exponentially through the insulator and a logarithmic spacing can be used to capture the temperature profile efficiently in the numerical scheme. The numerical technique utilizes a lumped network of discrete elements of logarithmically varying thermal conductivity and thermal capacity to calculate the surface heat transfer rates. The increasing thermal impedance of each element of the network corresponds to placing the temperature nodes at logarithmically increasing distance into the substrate.

The heat conduction equation is discretized in finite-difference form (for non-uniform node spacing) as:

$$\frac{1}{k} \frac{dT_i}{dt} = \frac{T_{i-1} - T_i}{\Delta x_i} - \frac{T_i}{\Delta x_i} \left(\frac{1}{\Delta x_i} + \frac{1}{\Delta x_{i+1}} \right) + \frac{T_{i+1}}{\Delta x_i \Delta x_{i+1}} \quad (57)$$

where the node number i ranges from 1 to the number of sections N .

The solution of this lumped network equation is an extension of the work published by Oldfield et al. [Ref. 14] for the design of high frequency lumped R.C. networks for the analogue evaluation of heat transfer rates to semi-infinite substrates. Oldfield's work was concerned with the simulation of the semi-infinite heat conduction process, thus is not directly applicable to the finite thickness heat flux gauges described in this paper. The finite thickness heat flux gauge was accounted for by adding an extra thermal resistance at the end of the lumped network, thereby transforming it from a semi-infinite to a finite length line.

Equation (57) can be written in matrix form (simulating a finite length line) as:

$$\frac{1}{k} \frac{dT}{dt} = AT + \frac{T_u(t)}{\Delta x_1 \Delta x_1} + \frac{T_l(t)}{\Delta x_N \Delta x_{N+1}} \quad (58)$$

The finite length line now requires two inputs, the temperature of the upper surface, T_u , of the insulator and the temperature of the lower surface, T_l . The resulting set of coupled equations is solved by a fourth order Runge-Kutta method to generate the upper surface heat flux rate from the calculated temperature drop across the first element of the network.

The selection of the thermal impedance of each of the elements is set to satisfy the following conditions:

- 1) the finite thickness of the insulator must be mirrored in the total thermal impedance of the network;
- 2) $\rho c k$ for each element must equal the physical value;
- 3) the thermal impedance of the first element is set by the required network bandwidth; and
- 4) the number of nodes required in the insulator sets the logarithmic spacing of all but the first element.

The accuracy of such a lumped network simulation can be established by back-calculating the incident heat transfer rate for exact analytical upper and lower temperature solutions in specific cases. Two cases were studied: a step change in heat flux, and a sinusoidal heat flux variation.

Figure 8 shows the normalized heat transfer rate variation calculated using exact upper and lower surface temperature solutions for a step change in heat transfer rate applied to a gauge glued to an aluminium substrate. The calculated response is shown for five network upper frequency limits, all with nine stages used to discretize the temperature field.

Figure 9 shows the frequency response of a 100 kHz bandwidth network with nine stages. The input temperatures were exact solutions to the heat conduction equation for a sinusoidal heat flux variation on a gauge glued to an aluminium substrate. The magnitude and phase data presented in this figure is therefore relative to the driving heat flux rate variation. The agreement between the exact and numerical methods is within 0.3% over the 5 to 2000 Hz band which is difficult to recover otherwise.

The effect of changing the number of elements used in the network on the error in reconstructing a sinusoidal heat transfer rate for a nominal 100 kHz bandwidth is shown in Fig. 10. It can be seen that the errors are relatively insensitive to the number of stages chosen for the network, and are more closely tied in with the specification of the thermal impedance of the first element in the network.

6.0 Heat Flux Measurements

As an initial test of the gauge technology, the heat flux gauges were mounted on the stationary outer tip casing above the rotor of a transonic turbine in the MIT Blowdown Turbine Facility. A time history of the top and bottom temperature sensors of a gauge is shown in Fig. 11. At time equal to zero, the tunnel is in vacuum and the sensors are the same temperature. After the starting transient, the tunnel operation is then quasi-steady (from 250 ms). The metal substrate temperature remains constant while the inlet temperature slowly drops, reflecting the isentropic expansion from the supply tank. This is seen in the decrease in the top-bottom temperature difference and thus in heat flux over the test time. The thick line of the top sensor output is the envelope of the high frequency heat flux components.

The heat flux, as calculated by the numerical data reduction technique from these two signals starting at 300 ms, is shown in Fig. 12. The blade passing frequency is approximately 6 kHz and the sampling frequency is 200 kHz. Note that the relatively small amplitude of the high frequency temperature fluctuation on the top sensor in Fig. 11 actually represents an ac heat flux modulation of 80%. The small ac temperature signal relative to the dc reflects the $\omega^{1/2}$ rolloff in sensitivity discussed in the gauge theory.

The heat flux time variation on the tip casing was quite periodic with blade passing. This facilitated construction of a contour plot of the casing heat flux distribution from a line of gauges arranged over the blade chord. This is shown in Fig. 13 along with a simultaneous wall static pressure measurement. The blade outlines are indicated, as are the transducer locations. Overall, a very high level of both mean and time varying heat flux is seen with the peak levels on the order of that at nozzle guide vane leading edge.

7.0 Conclusions

A multilayer heat flux gauge has been developed which successfully meets all of its design criteria. It is directly applicable to metal blading in large numbers, has frequency response extending from DC to 100 kHz, does not introduce flow disturbance, and is well suited to rotating frame applications. These gauges are now being extensively used in the turbine research program at MIT.

8.0 References

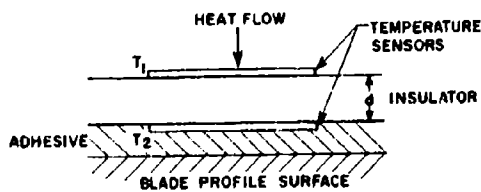
1. Atkinson, W.H., and Strange, R.R., "Development of Advanced High Temperature Heat Flux Sensors," NASA CR 165618, Sept. 1982.
2. Richards, B.E., "A Review of Heat Transfer Work in the VKI Hot Cascade Tunnel," AGARD Specialists Meeting on "Testing and Measurement Techniques in Heat Transfer and Combustion," Brussels, AGARD CP-281, May 1980.
3. Baines, N.C., Oldfield, M.L.G., Jones, T.V., Schultz, D.L., King, P.I., Daniels, L.C., "A Short-Duration Blowdown Tunnel for Aerodynamic Studies of Gas Turbine Blading," ASME 82-GT-312, 1982.
4. Dunn, M.G., Hause, A., "Measurement of Heat Flux and Pressure in a Turbine Stage, J. of Eng. for Power, 104, 1, January 1982.
5. Epstein, A.H., Guenette, G.R., Norton, R.J.G., "The Design of the MIT Blowdown Turbine Facility," ASME Paper 84-GT-116, 1984.
6. Schultz, D.C., and Jones, T.V., "Heat Transfer Measurements in Short Duration Hypersonic Facilities," AGARD AG-165, Feb. 1973.
7. Bachmann, R.C., Chambers, J.T., Giet, W.H., "Investigation of Surface Heat Flux Measurements with Calorimeters," ISA Trans, 4, 2, 1965.
8. Sprinks, T., "Influence of Calorimeter Heat Transfer Gauges on Aerodynamic Heating," AIAA J., 1, 2, 1963, p. 497.
9. Hylton, L.D., Mikelc, M.S., Turner, E.R., Nealy, D.A., York, R.E., "Analytical and Experimental Evaluation of Heat Transfer Distribution Over the Surfaces of Turbine Vanes," NASA CR 168015, 1983.
10. RFD Corp., Hudson, NH.
11. Carslaw, H.S., and Jaeger, J.C., Conduction of Heat In Solids, 2nd Ed., Oxford University Press, Oxford, 1959.
12. Schwartz, N., and Berry, R.W., "Thin Film Components and Circuits," in Physics of Thin Films, Vol. 2, Hass and Thun, Eds., Academic Press, New York, 1967.
13. Weast, R., and Selby, S., Eds., Handbook of Chemistry and Physics, 63rd Ed., Chemical Rubber Co., Cleveland OH, p. F-133.
14. Oldfield, M.L.G., Burd, H.J. and Doe, N.G., "Design of Wide-Bandwidth Analogue Circuits for Heat Transfer Instrumentation in Transient Tunnels," Heat and Mass Transfer in Rotating Machinery, papers from the 16th Symposium of the International Center for Heat and Mass Transfer, held in Dubrovnik, September 1982, Hemisphere Publ. Corp., NY.

9.0 Acknowledgements

The authors were ably assisted in the gauge calibrations by W. Cook. They would like to acknowledge many useful discussions with Professors M.L.G. Oldfield and E. Covert. This work was supported by the Office of Naval Research, Mr. M. Keith Ellingsworth technical monitor, and Rolls-Royce Inc.

TABLE I
SENSITIVITY FACTORS FOR VARIOUS FILM THERMOMETER MATERIALS
(FOR EXCITATION AT CONSTANT HEAT FLUX) [Ref. 13]

Metal	T(°C)	Resistivity ρ ($\mu\Omega\text{cm}$)	Temp. Coeff. $\alpha \times 10^3$ ($1/^\circ\text{C}$)	Sensitivity α/ρ	Rank
Zirconium	20	40.0	4.4	27.8	1
Iron	20	9.71	6.51	20.2	2
Nickel	20	6.84	6.9	18.0	3
Tin	0	11.0	4.7	15.5	4
Tantalum	25	12.45	3.83	13.5	5
Platinum	20	10.6	3.927	12.7	6
Gold	20	2.24	8.3	12.4	7
Palladium	20	10.54	3.74	12.1	8
Cadmium	0	6.83	4.2	10.9	9
Chromium	0	12.9	3.0	10.7	10
Zinc	20	5.916	4.19	10.1	11
Copper	20	1.678	6.8	8.8	12
Aluminum	20	2.6548	4.29	6.9	13



(Not To Scale)

Fig. 1 Schematic cross-section of multi-layer heat flux gauge

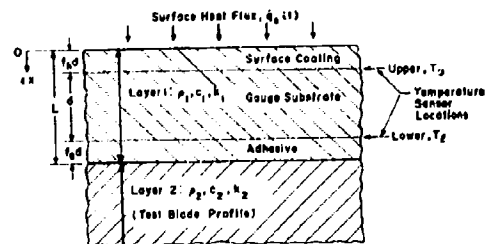


Fig. 2 Geometry of gauge in analytical model

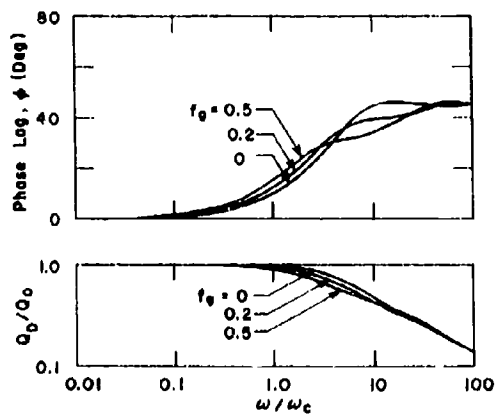
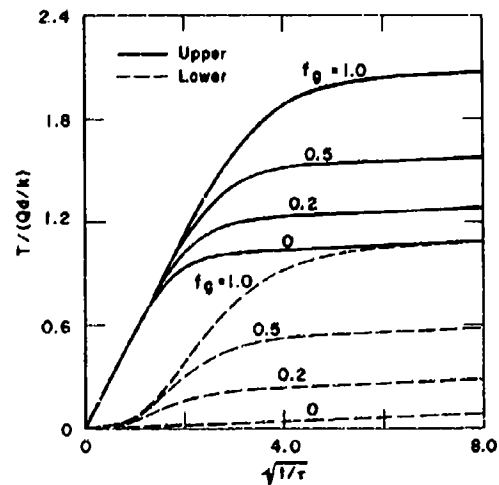
Fig. 3 Harmonic frequency response of gauge normalized to the direct or shunt mode frequency, ω_c , as a function of cutoff fractional glue thickness

Fig. 4 Semi-infinite mode normalized time response of upper and lower sensors to a step in heat flux as a function of fractional glue thickness.

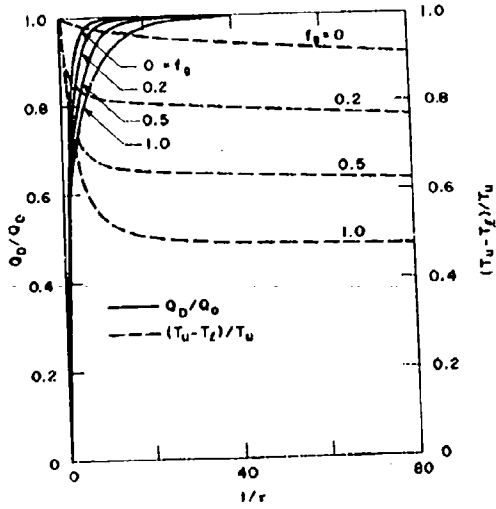


Fig. 5 Direct mode normalized response to a step input of heat flux as a function of fractional glue thickness

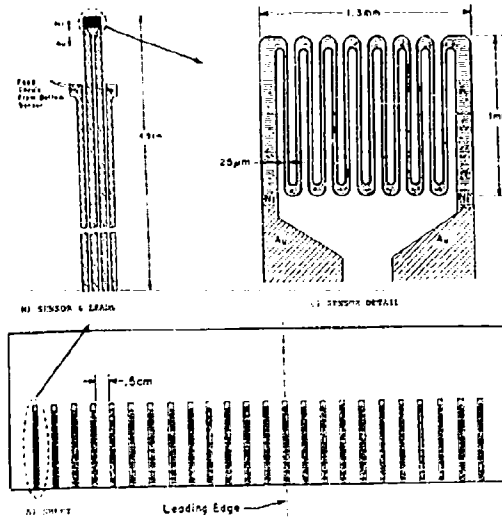


Fig. 6 Gauge geometry showing sensor detail, sensor and leads, and gauges on manufacturing sheet

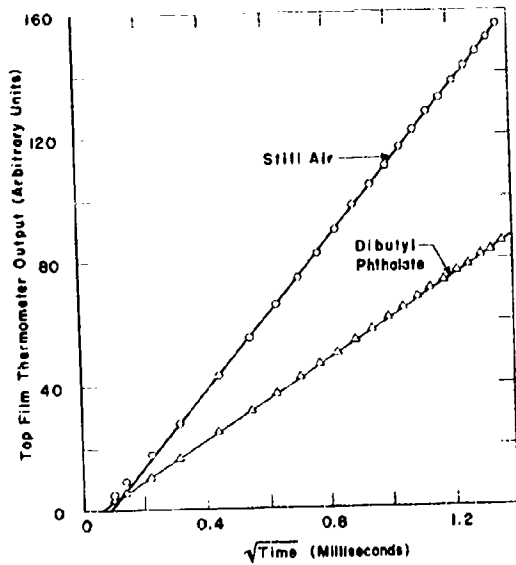


Fig. 7 Gauge thermal calibration data, $\sqrt{\text{lock}}$, is proportional to the difference in slope of the curves

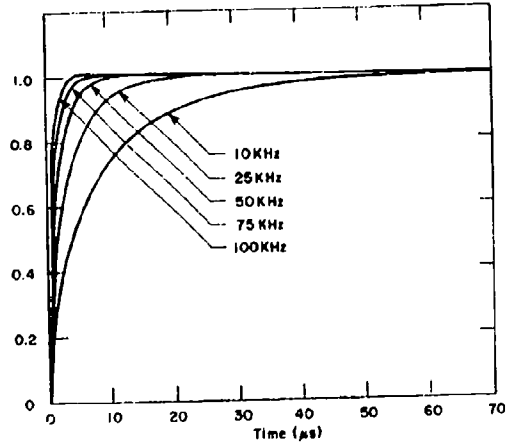


Fig. 8 Rise time of the numerical data reduction model as a function of model bandwidth

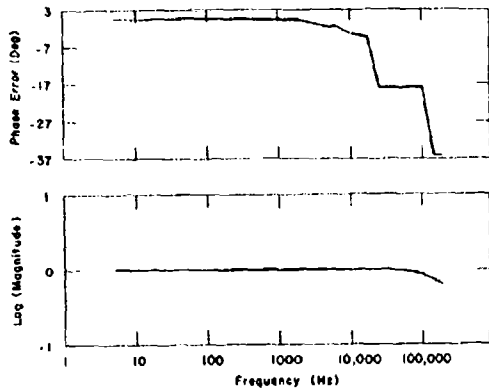


Fig. 9 Frequency response of 100 kHz bandwidth data reduction numerical scheme

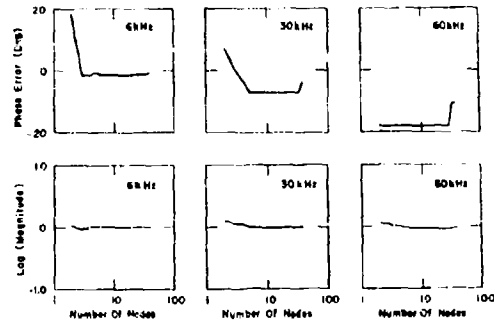


Fig. 10 Data reduction scheme response as a function of the number of calculational nodes

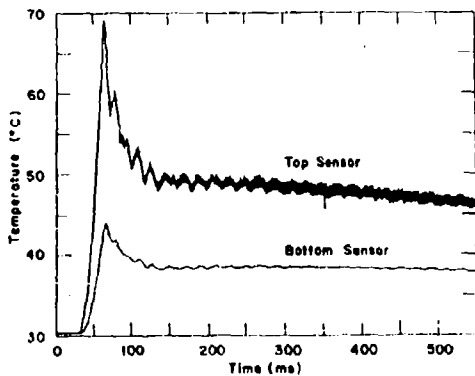


Fig. 11 Time history of gauge sensors mounted on the stationary casing above a transonic turbine rotor tip

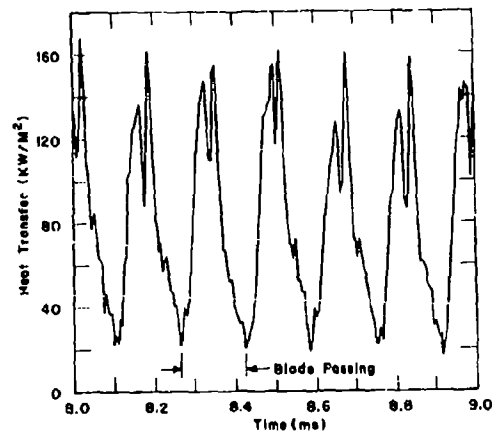


Fig. 12 Heat flux calculated from the data in Fig. 11 starting at 300 ms



Fig. 13 Heat flux static pressure distribution calculated from sensor distribution as indicated

DISCUSSION

P.Ramette, Fr

What is the temperature limitation for the heat flux gauges that you presented?

Do you try to develop heat flux gauges for higher temperature ranges?

Author's Reply

The 600°K upper temperature limit is a very real one for both this material and the technique of using a flexible film in general. Kapton is the highest temperature flexible material which we have identified which is comparable with bonding techniques required for on blade use.

For hot engine environments, work is proceeding at several establishments using refractory materials (zirconia, etc.) deposited directly on the blade surface. Obviously, this is a much more difficult environment, and is not being addressed at MIT at this time.

R.Eggebrecht, Ge

I would like to comment on a foregoing question concerning the maximal operating temperatures. At MTU, we also work very successfully with Kapton and Ni-layers. As the author mentioned Kapton is limited to about 600°C max. In order to increase temperature capabilities, we are looking at ceramic layers as for instance zirconia oxide.

My question to the author:

Did you experience problems with stable, reproducible electrical resistance as we did at MTU? These properties seem to depend on smallest deviations in fabrication processes. Furthermore, the mode of heating during calibration or test may affect the results. What is your experience?

Author's Reply

Yes! We have traced problems with changing resistance to cracking of the metal films caused by intrinsic stress induced in the metal during deposition. Often these cracks are a) multiple and b) not visible even under high magnification. The stress level is very sensitive to the processing details (deposition rate and process pressure in particular). Only gauges which are crack free give usable results and these have proven to be extremely stable (>0.2% on TCR).

Originally, we used an oven for TCR calibration and did not get very good results. We now use a liquid circulation bath of a fluorocarbon liquid (Dow Flouinest FC-77) and find the results to be extremely reproducible. The dynamic calibration was initially attempted using the capacitive discharge technique used by Oldfield and his colleagues at Oxford. This did not give satisfactory results because the films are not wide compared to the insulation thickness, thus the heat addition cannot be considered one-dimensional. Also, we found the Kapton to be quite hygroscopic. Washing the surface with water would introduce superior results of large magnitude.

A.E.Bourguignon, Fr

Nous utilisons actuellement des fluxmètres pelliculaires du même type. Nous avons rencontré un certain nombre de problèmes: tenu du Kapton sur les aubes, température limitée acceptable par les fluxmètres, durée de vie de ceux-ci. Pourriez-vous nous dire si vous avez rencontré les mêmes problèmes?

Author's Reply

We find no problem with using Kapton at 550°K. The gauges have been aged at temperature for 72 hours with no appreciable change in calibration. We also thermally cycle the gauges by thermally shocking them (sudden immersion in a heated liquid) and see only minor calibration shifts. Note that we anneal the Kapton at 400°C for 1 hour before gauge manufacture in order to reduce the stresses introduced during the film production. In general, gauges manufactured with minimal intrinsic stresses in the metal have proven to be extremely stable over a period of weeks and months. Of course, the actual time during which our gauges are exposed to the gas flow field in the turbine sums to only a few seconds since we use them only in a short duration test facility, thus mechanical durability has not been a problem.

**THE ISENTROPIC LIGHT PISTON ANNULAR CASCADE FACILITY
AT RAE PYESTOCK**

A.J. Brooks, D.E. Colbourne, E.T. Wedlake,
Royal Aircraft Establishment
Propulsion Dept
Pyestock, Farnborough
Hants GU14 0LS UK

T.V. Jones, H.L.G. Oldfield, D.L. Schultz,
University of Oxford
Dept of Engineering Science
Parks Road
Oxford OX1 3PJ UK

P.J. Loftus,
University of Maryland
Dept of Mech Eng
College Park
Maryland 20742 USA
(formerly Oxford University and RAE)

SUMMARY

An accurate assessment of heat transfer rates to turbine vanes and blades is an important aspect of efficient cooling system design and component life prediction in gas turbines.

Techniques have been developed at Oxford University which permit such measurements to be obtained in test rigs which provide short duration steady flow through a turbine cascade. The temperature ratio between the gas stream and the turbine correctly models that found in an engine environment. Reynolds number and Mach number can be varied over a wide range to match engine conditions. The design, construction and operation of a new facility at RAE Pyestock, incorporating these techniques, is described.

Heat transfer and aerodynamic measurements have been made on aerofoil surfaces and endwalls of a fully annular cascade of nozzle guide vanes. These results are discussed, and compared with those obtained from the same profile in 2-D cascade tests, and with computed 3-D flow predictions.

RÉSUMÉ

Une évaluation précise des flux de chaleur aux aubes et ailettes de turbines constitue un facteur important pour une bonne conception des systèmes de refroidissement et pour la prédiction de la durée de vie des composantes, dans les turbines à gaz.

Des techniques ont été mises au point à l'Université d'Oxford, qui permettent d'obtenir ces mesures dans des bâtis qui assurent un écoulement constant de courte durée à travers d'une grille de turbine. Le rapport entre la température du jet de gaz et celle de la turbine reproduit fidèlement celui observé dans un milieu moteur. On peut varier le nombre de Reynolds et le nombre de Mach sur une gamme étendue pour correspondre aux conditions de fonctionnement des moteurs. L'exposé donne donc des précisions au sujet de la conception, construction et mise en oeuvre d'une nouvelle installation réalisée au RAE Pyestock où ces techniques sont appliquées.

Des mesures de transfert thermique et aérodynamiques ont été prises sur les surfaces de profil et les parois d'extrémité d'une grille d'aubes directrices complètement annulaire. Ces résultats sont, dans l'exposé, discutés et comparés avec ceux obtenus avec le même profil lors d'essais de grilles à deux dimensions ainsi qu'avec les calculs de l'écoulement à trois dimensions.

NOMENCLATURE

A_b^*	test section choked throat area	V_r	reservoir volume
A_r^*	reservoir exit choked throat area	W	pump tube volume
M	Mach number	a_0	speed of sound in air under initial pump tube conditions
P	pressure	c	specific heat
\bar{P}	matching pressure in tube during run	k	thermal conductivity
Re	Reynolds number	l	blade chord or other characteristic length
T	temperature	γ	ratio of specific heats
\bar{T}	test gas total temperature under matching conditions	ρ	density
T_r	reservoir gas total temperature		

$$\beta \left(\frac{2}{\gamma+1} \right)^{\frac{\gamma+1}{2(\gamma-1)}} \text{ equal to } 0.578 \text{ for } \gamma = 1.4$$

SUBSCRIPTS

a	conditions on inlet side of piston	Des	design conditions
b	conditions on exit side of piston	init	initial conditions in pump tube

1. INTRODUCTION

For many years it has been recognised within the gas turbine industry, and by its customers, that the design of an efficient high pressure turbine with adequate component life is crucial to the success of any gas turbine engine project, military or civil. The interactions between the demands of the aerodynamicist, the blade cooling specialist, the metallurgist, the stress engineer and the production engineer are unique and make the evolution of efficient, reliable, designs one of the most challenging tasks in the industry. Inherent in the design process is the need to predict accurately the aerodynamic flow and external heat transfer distributions around the aerofoils and on the endwall surfaces.

The increasingly complex three-dimensional geometry of HP turbine components compounds the problems of accurate prediction. Whilst theoretical techniques have improved, there are still deficiencies in the industry's knowledge which must be remedied in order to reduce the need for a protracted development phase for new projects. The need for high quality experimental data is still paramount, both to understand the performance of current and proposed designs and as a basis for the development and validation of theoretical prediction methods.

Some major advances in the techniques for measuring heat transfer to turbine blading originated from research at the Department of Engineering Science of Oxford University. Studies of blade cooling using shock tunnels and specialised instrumentation techniques for measurement of heat transfer began in the late 1960's, leading to the development of a novel form of intermittent wind tunnel specifically for this work.

The Isentropic Light Piston Tunnel (ILPT) in the Osney Laboratory at Oxford¹ has been producing high quality heat transfer and aerodynamic data for over a decade. The results of this work have been used to improve prediction methods. However, detailed knowledge is still lacking in two areas, endwall heat transfer and rotational effects. Correct simulation of endwall heat transfer requires an annular cascade where secondary flows develop in a realistic environment. This paper describes the design and acquisition of such a facility at RAE Pyestock, known as the Isentropic Light Piston Cascade (ILPC). The design of the new tunnel was such that it could be developed at a later date to address the second problem area mentioned above, that of rotational effects.

2. THE PRINCIPLES

The techniques and facilities developed at Oxford have been widely reported^{1,2,3,4}, but for completeness a brief summary of the principles is included.

For measurement of heat transfer from the gas to turbine components it has been shown⁵ that it is acceptable to model the gas to metal temperature ratio rather than actual temperatures. Thus, although the gases entering a turbine may be at around 1500K and the blades at 1000K, tests with blades at ambient temperature (288K) only require a test gas temperature of 432K. By using thin film resistance thermometers on an insulating substrate of known thermal properties to record local surface temperatures on the blades, and by considering the flow of heat into the body of the blade to be one-dimensional over short time periods, local heat transfer rates may be deduced.

Heat transfer measurements may therefore be made by passing moderately heated gas over test blades for a period just long enough to record the response of surface temperatures to the passage of the hot gas. The ILPT and its associated instrumentation techniques were developed to do this.

A gas total temperature of 432K can be obtained by an isentropic compression of modest pressure ratio from an initial temperature of 288K. The test gas is contained within a tube and is compressed isentropically by a piston which is driven along the tube by a flow of air from a high pressure reservoir. When the gas has been compressed, and hence heated to the required temperature, a fast acting valve is opened, which allows the compressed gas to flow through a cascade of aerofoils in the working section (Fig 1).

Initial pressures in the pump tube and downstream of the working section can be pre-set to control the Reynolds number and Mach number of the flow through the working section. The area of the throat admitting high pressure air behind the piston is matched to the throat area of the test cascade so that volumetric flow rates into and out of the tube are equal and thus conditions in the working section are constant over the test period. An idealised pressure-time relationship during a run is shown in Fig 2.

Signals from instrumentation in the test cascade are recorded during the run. Even in the short times available (typically 0.5 seconds) it is practical to record aerodynamic as well as heat transfer data provided that care is taken to minimise transducer tubing lengths and volumes.

The derivation of heat transfer rates from surface temperatures may be done numerically. However it can be done much more simply and directly by the use of an electrical analogue circuit.

The one-dimensional heat conduction equation

$$\partial^2 T / \partial x^2 = (\rho c / k) (\partial T / \partial t)$$

for a body with density ρ and thermal properties c and k is analogous to the equation

$$\partial^2 V / \partial x^2 = RC (\partial V / \partial t)$$

for the variation of voltage with distance and time along an RC transmission line. Thus if the voltage outputs from thin film resistance thermometers are fed into suitable analogue circuits, the current outputs from these circuits will be proportional to heat transfer rate.

The advantages of using such analogues, and details of the circuits, are covered fully in Ref 4, and the design of more recent analogues with improved frequency response is given in Ref 6.

Testing at reduced temperature offers two further benefits. Firstly, as may be seen from Fig 3, at the lower temperatures a design Reynolds number simulation can be achieved at only 20-25% of the pressure levels required at typical engine temperatures. This significantly reduces rig stressing problems. Secondly, easily machineable materials can be used for the construction of test blades and other parts.

The use of short duration test facilities is also advantageous from the point of view of power requirements. To test a full scale set of nozzle guide vanes for a typical civil engine at maximum operating conditions in a continuous flow rig would require approximately 20 MW. The high pressure compressor for the ILPC is rated at 45 kW.

3. THE REQUIREMENTS

The specification for the new tunnel required it to be capable of testing a full size annular cascade of nozzle guide vanes from a large civil engine at correct Reynolds number and Mach number. This demanded a pump tube with a large volume. The bore of the tube must be within close tolerances and have a fine finish to permit smooth travel of the free piston. Experience with the Oxford University tunnels had shown that a surface finish of $0.4 \mu\text{m}$ was a realistic target. The pump tube for the cascade facility at Oxford has an internal diameter of 0.6 m, and the manufacturers of that tube estimated that a maximum bore of 1.2 m was possible with a length of 9 m. These dimensions were therefore adopted as the basis of the design of the new facility.

The tunnel was to be provided with a comprehensive instrumentation system, including 64 channels of heat transfer data and 96 channels of pressure data.

A prime requirement was that the operation of the tunnel should not be labour intensive and should as far as practical be independent of site air supplies.

4. THE DESIGN

4.1 REYNOLDS NUMBER AND MACH NUMBER CAPABILITY

The Reynolds numbers relevant to the HP nozzle guide vanes of large civil bypass engines are in a range up to approximately 4.75×10^6 (based on inlet total conditions, exit Mach No. and true chord). For military applications the sea level dash conditions may increase this to around 7×10^6 with only minor changes in nozzle exit Mach number. The advantages to be gained from testing at lower gas temperatures have been outlined earlier. Taking as an example an engine turbine entry temperature of 1750K (consistent with the Reynolds number of 4.75×10^6) and nozzle exit Mach number $M=1$, it can be seen from Fig 3 that the cascade operating pressure would be reduced by a factor of approximately 3.67 relative to engine conditions by operating the test rig at a temperature of 432K. Thus a test rig pressure of only 0.68 MPa would be needed to correctly simulate an engine pressure of 2.5 MPa. Accordingly the cascade design maximum pressure was set at 1.2 MPa, which allows a significant increase in Reynolds number above design values. Similar conclusions apply to military engine applications where, for a gas to wall temperature ratio of 1.5, a Reynolds number of 7×10^6 can be obtained with a total pressure of approximately 0.825 MPa. Once again, a maximum design pressure of 1.2 MPa is more than adequate.

The free piston cascade has considerable flexibility in its operating regime. The total temperature may be varied over a range from ambient to approximately twice ambient simply by increasing the compression ratio. For purely aerodynamic studies such as Mach number distribution and loss measurements it is not necessary to operate the cascade with an elevated total temperature. The maximum flow duration is obtained by driving the air in the pump tube through the working section without any compression.

The initial pressure required in the pump tube before compression may be obtained from the required temperature ratio by the isentropic relationship

$$\frac{P}{P_{\text{init}}} = \left(\frac{T}{T_{\text{init}}} \right)^{\frac{\gamma}{\gamma-1}}$$

As an example, a gas-to-wall temperature ratio of 1.5 gives a ratio of P/P_{init} of 4.13, so that for a cascade operating pressure of 0.8 MPa an initial pressure of 0.19 MPa would be required. For operation at reduced Reynolds numbers the initial pump tube pressure may be below atmospheric so that modest vacuum sealing is required.

Exit Mach numbers from the nozzles of modern engines are in the range 0.7 to 1.3, corresponding to pressure ratios across the cascade of approximately 1.4 to 2.8. This defines the working pressure range for the dump tanks. The examples quoted previously would require dump tank initial pressures of 0.383 MPa and 0.436 MPa. A maximum design pressure of 0.5 MPa and a minimum pressure of 10 kPa were used for the tank design. Should higher nozzle exit pressures be required in the future, a second throat could be fitted between the cascade and the dump tanks.

4.2 FLOW DURATION

The 'tube time', ie the time taken to expel all the gas initially in the pump tube through the vane throats, is defined² by

$$\tau_{\text{tube}} = \frac{W}{\beta a_0 \Lambda_b^*}$$

Where W = Pump tube volume
 Λ_b^* = Cascade throat area
 a_0 = speed of sound at initial pump tube conditions
 and $\beta = f(\gamma)$

The actual flow duration is less than this because of the compression required to heat the gas, thus

$$\tau_{\text{run}} = \frac{W}{\beta a_0 \Lambda_b^* \left(\frac{\bar{T}}{T_{\text{init}}} \right)^{\frac{\gamma+1}{2(\gamma-1)}}$$

The flow duration is seen to be strongly dependent upon the temperature ratio \bar{T}/T_{init} . A plot of τ_{run} against Λ_b^* for a range of values of \bar{T} from an initial temperature of 288K is shown in Fig 4 for $W = 9.5 \text{ m}^3$, the design target. It may be seen that for vane throat areas in the range 0.02 to 0.04 m^2 the flow duration varies from 0.6 secs to 0.3 secs with $\bar{T} = 432\text{K}$. This was considered to be more than adequate for heat transfer rate measurements. For purely aerodynamic measurements, running the tunnel "cold" is acceptable and it can be seen from Fig 4 that for a value of \bar{T} of 288K the corresponding flow durations are increased to 2.6 and 1.3 seconds respectively.

4.3 MATCHING

Constancy of total pressure during the run time of the cascade requires that the volumetric flow rate from the high pressure cylinders into the region behind the piston is equal to that leaving through the NGV throat area.

If it is assumed that the reservoir gas is brought to rest in the tube, thereby recovering the reservoir temperature T_r , the volumetric flow rate entering the pump tube from the reservoir is given by

$$\dot{V}_a = \frac{\dot{m}_r RT_r}{P_a}$$

The volumetric flow rate through the NGV throats is given by

$$\dot{V}_b = \beta a_b \Lambda_b^*$$

"Matching" of these two volumetric flow rates occurs when $\dot{V}_b = \dot{V}_a$ at a pressure in the pump tube $\bar{P} = \bar{P}_a = \bar{P}_b$, so that the matching mass flow from the reservoirs \dot{m}_r is given by

$$\dot{m}_r = \frac{\beta a_b \Lambda_b^* \bar{P}}{RT_r}$$

In practice the necessary adjustments in \dot{m}_r may be achieved either by changing the reservoir throat area or, more readily, by changing the reservoir pressure.

5. THE FACILITY

Installation was completed at Pyestock in the Spring of 1984.

The main features of the cascade and its associated plant can be seen on Fig 5. The driver system comprising high pressure reservoirs, inlet valves and pipework, is mounted above the pump tube. Air from these reservoirs is admitted to the tube through the collector ring. The annular working section containing the test vanes exhausts into three interconnected dump tanks.

The pump tube and dump tanks may be pressurised by a medium pressure compressor or evacuated by vacuum pumps prior to a run.

A bursting disc is fitted at the dished end of the pump tube to vent the system should the pressure in the pump tube exceed 1.2 MPa. A bursting disc is also provided on the dump tanks to prevent inadvertent over-pressurisation beyond their 0.5 MPa design pressure. Two large hydraulically operated clamp rings are used to hold the dished end onto the collector ring and the bolster plate onto the pump tube (see Fig 6). These specially designed clamp rings permit rapid removal of the dished end, for inspection of the piston and pump tube bore, and of the working section. A large reinforced rubber bellows between the intermediate exhaust tank and the dump tanks allows for expansion between the pump tube and working section assembly and the dump tanks. The pump tube and working section are rigidly mounted on bedplates in the test cell.

The Pyestock facility differs from the Oxford tunnel in two major areas. Firstly, because of the annular cascade, a plug valve is used to isolate the working section rather than the gate valve on the Oxford tunnel which has a linear cascade. Secondly, it was decided that by using an ultra-lightweight piston constructed from carbon fibre reinforced composite materials, it would be possible to dispense with the compensating system (which provides additional inlet flow during the compression phase¹) and thus simplify the facility.

The control room containing the data acquisition computer with its associated electronic equipment and the plant and rig control panels is situated above the cascade. The facility is equipped with its own high pressure (21 MPa) and intermediate pressure (2 MPa) compressors and vacuum pumps and is thus independent of the site air supplies.

To simplify the preparation of the facility before each test run, a programmable logic controller is used to interlock all valve operation. This controller is linked to the main rig computer so that different logic sequences can be fed to the controller for different rig operating requirements.

5.1 PLUG VALVE

The tunnel is designed to accommodate full 360° cascades of vanes so that a concentric inlet flow is required. This is achieved by using a central fast-acting plug valve, which can be seen in schematic form in Fig 6.

In its forward or closed position the valve seals the working section from the pump tube. In its fully retracted position the nose of the plug forms a smooth inlet to the diffuser. The valve has two internal chambers which are pneumatically isolated by a fast-acting shuttle valve. The forward chamber is pressurised to a level sufficient to keep the valve closed against the maximum pump tube pressure for the particular operating condition. The rear chamber is maintained at a lower pressure. The valve motion is initiated from the rise in pressure in front of the piston as it travels down the tube. At a pre-set level this pressure rise triggers the shuttle valve and the two chambers are interconnected. Gas from the front chamber vents into the rear, lowering the pressure in the front chamber. The valve body accelerates rearwards under the influence of the differential pressure on its front face. The concentric piston on the central shaft acts as a damper as it passes through the central orifice which carries the shuttle.

The valve opening time is in very close agreement with predictions and is typically of the order of 30 ns.

5.2 LIGHTWEIGHT PISTON

In the 0.6 m dia tunnel at Oxford the pressure fluctuations during the run, due to finite piston mass, are eliminated by use of a fast-acting compensation system to increase the driver mass flow by a factor of about 2.7 (for a temperature ratio of 1.5) during the compression phase.

Initially the Pyestock tunnel was conceived with a similar compensating system. However, it was then realised that by using modern carbon fibre composite technology it would be possible to construct an ultra-lightweight piston which, as well as minimising pressure fluctuations due to piston mass, would offer the following benefits:

- (a) simpler operation of the tunnel because of the elimination of compensator mass flow and timing adjustments as operating conditions are changed;
- (b) a simpler and smaller driver system using fewer storage cylinders - the reduced cost outweighed the extra cost of the high technology piston;
- (c) the simpler system would be more reliable, and should thus improve the productivity of the tunnel.

The first carbon fibre piston used is shown in Fig 7. It was designed for use up to tunnel pressures of 0.834 MPa and has a mass of 14.25 Kg. The front face is cut from a 40 mm thick aluminium honeycomb panel with 4-ply carbon fibre reinforced skins. The front face is designed to resist the differential pressure across the piston when it covers the plug valve opening at the end of the run. Hydraulic testing of a sample of the front face panel confirmed the design assumptions.

A 10 mm square PTFE piston ring around the periphery of this panel provides a gas tight seal and supports the piston in the pump tube. To save weight, only one piston ring is fitted, and the piston is stabilised in the tube by six small PTFE pads mounted on the rear corners of a hexagonal skirt bonded to the back of the piston front face. This skirt was fabricated by folding and bonding lightweight carbon fibre skinned aluminium honeycomb panels.

During structural tests of the piston materials a number of unexpected failure modes were encountered. For example, it was found that leakage through the skin could pressurise a single honeycomb cell which would burst, pressurise the next cell and lead to a progressive failure of the honeycomb material along a line, without any visible surface damage. The material is then less able to withstand the working stresses, so that it is important to ensure that the outer skins are completely sealed. Some details of the construction can be seen on Fig 7.

This piston is now in regular use and has given no problems.

A second piston for use at higher pressures has been designed and fabricated jointly with Materials and Structures Department of RAE. By using more sophisticated fabrication techniques and a moulded circular section skirt, the mass has been kept to 21 Kg (a 45% increase over the first piston) even though the design pressure has been doubled to 1.6 MPa.

5.3 RESERVOIR AND DRIVER SYSTEM

The principles governing the required driver reservoir volume V_r and driver throat area A_r^* are given in Ref 1.

For simplicity, a modular driver system was chosen, with identical driver modules each consisting of a high pressure air cylinder and associated valves. The safety isolating valves are opened a few seconds before the run, which is controlled by the simultaneous opening and, later, closing of the main inlet valves.

The design conditions for the driver system were:

Test section throat area	$A_b^* = 0.035 \text{ m}^2$
Maximum working section pressure	$\bar{P} = 1.2 \text{ MPa}$
Maximum driver pressure	$P_r = 21 \text{ MPa}$
Temperature ratio	$\bar{T}/T_r = 1.5$

The flow area A_r^* is controlled by the gate valve settings, and as the valves are choked this area may be calculated² from the expression

$$\frac{A_r^*}{A_b^*} = \left(\frac{\bar{P}}{P_r}\right)^{\frac{1}{\gamma}} \frac{P_r}{P_r}$$

$$\text{Thus } A_r^* = 0.00245 \text{ m}^2$$

For the chosen valves, this total area is achieved with four modules in parallel. Fig 5 shows how these are mounted above the pump tube and feed into a collector ring at the end of the tube. Additional modules could be added if a greater mass flow rate were required. If the driving throat area is set to give the correct mass flow at the start of the test run, then the drop in total pressure as the reservoirs empty will produce a slight fall in \bar{P} during the run, Fig 8(a).

This fall in reservoir pressure ΔP due to the finite reservoir volume may be shown² to be

$$\frac{\Delta P}{\bar{P}} = \frac{\gamma(3\gamma-1)}{4} \frac{W \bar{P}}{V_r P_r} \left(\frac{P_r}{\bar{P}}\right)^{2/\gamma}$$

$$= 3.6\% \text{ at the design conditions given above.}$$

By increasing the throat area slightly above the "matching" value, \bar{P} can be made to rise slightly over the first part of the run as shown in Fig 8(b). Using this technique the value of ΔP can be reduced by a factor of 4, to 0.9%, which is acceptable.

5.4 INSTRUMENTATION, DATA ACQUISITION AND PROCESSING

A block diagram of the instrumentation system is shown in Fig 9. It includes:-

- 96 pressure measuring channels
- 64 heat transfer rate channels
- 16 tunnel monitoring channels
- 128 computer A/D channels (~20,000 samples/sec)
- BEC PDP 11/24 computer employing the RT11 operating system
- 8 channel, 2 MHz, fast transient recorder
- 12 channel UV recorder

For the large number of pressure channels required the Scanivalve ZOC (Zero, Operate, Calibrate) system was adopted. This system uses multiple silicon pressure sensors which have been partially temperature compensated, and which have their zero, range drift and linearity corrected immediately prior to making a measurement. The system has its own microprocessor which, by controlling pneumatic valves built into the transducer modules, zeroes and calibrates each transducer before the tunnel is run. The system stores the pressure data taken during the run, scales them according to the calibrations and later downloads them to the main PDP 11/24 computer.

Tunnel operating conditions are monitored by a further 16 discrete pressure transducers.

The heat transfer instrumentation uses platinum thin film thermometers on the surface of blades as can be seen in Fig 10(a). The blades are manufactured from Corning MACOR machinable glass-ceramic as described in Refs 3 and 4. The heat transfer rates to the blades are derived from the surface temperature signals by the 100 kHz bandwidth analogue circuits described in Ref 6.

Figure 10(b) shows a typical instrumented endwall "tile" with an array of static pressure tappings.

The 8 channel transient recorder is also available for high speed data acquisition. This enables studies to be made of transient phenomena such as boundary layer transition and shock induced fluctuations in heat transfer rate. The 12 channel UV recorder is available for tunnel diagnostic purposes.

The complete instrumentation system is run and monitored by a tunnel operating system software package which was developed at Oxford (Ref 7) and is currently used on four transient wind tunnels. It is a user-friendly, modular, menu-driven system which is used to set up the instrumentation before a run, acquire data during the run, and subsequently process, print and plot the results.

6. THE COMMISSIONING TESTS

For commissioning the facility, a set of constant section nozzle guide vanes was manufactured. These corresponded to the mid-height section of the vanes from a single-stage transonic turbine previously tested in a cold-flow rig at Pyestock⁸. The profile had also been tested in the two-dimensional cascade at Oxford⁹.

Tests of the complete facility commenced in March 1984, and regular running has been maintained with no major system faults. Run times have been as predicted. Turn-round times of 20-25 minutes between runs can be achieved, although 45 minutes is probably more typical allowing time for processing the data, output of results and on-line assessment of the displays.

At the time of writing, the commissioning tests are nearing completion. A brief selection of the results is presented to illustrate the range and quality of the data which have been acquired.

6.1 INLET FLOW QUALITY

To assess the flow distribution entering the working section, total pressure rakes and surface static pressure tappings were fitted at two planes 180° apart in the section upstream of the annulus of test blades. In Fig 11, results for two runs are given which demonstrate excellent run-to-run repeatability. Differences between top and bottom of the annulus are insignificant, and the total pressure variation across the annulus is well within acceptable limits, demonstrating good control of the flow through the transition from circular to annular cross-section.

6.2 PROFILE AERODYNAMIC MEASUREMENTS

The Mach number distribution around the mid-height section of the aerofoil, calculated from measured surface static pressures, is shown in Fig 12. Results from two runs at similar conditions are plotted, again showing excellent repeatability. Considerable importance is attached to obtaining good repeatability with a test rig of this type. Since only a limited number of instrumentation channels are available for measurements at several stations along the blades, as well as on inner and outer endwalls, it becomes necessary to repeat test conditions with different combinations of instrumentation.

Typical results from pressure tappings at the root, mid and tip sections of the vanes are shown in Fig 13. The three-dimensional effect of the cascade is immediately apparent, with pressure surface velocity increasing and the shock wave intensifying towards the root where the blade pitch is less.

Variations in the flow distribution as exit Mach number is varied are shown in Fig 14. Since the flow through the vanes is choked, the effects of Mach number change only become apparent on the suction surface downstream of the shock. Results for the pressure surface and the forward part of the suction surface serve to demonstrate again the extremely good repeatability of the results.

Two other sources of data are available for comparison to give confidence in the results being acquired from the ILPC. Data from 2-D tests in the Oxford tunnel are plotted against the ILPC results for the mid-height section in Fig 15, showing good agreement. In the ILPC the shock wave appears to occur slightly earlier, probably a three-dimensional effect. Whilst the ILPC has the capacity to acquire more data points per run than the Oxford tunnel, for this build the pressure tappings were spread over the three sections (root, mid and tip) and thus the distribution at any one section is less well defined than in the 2-D cascade tests. The flow through this geometry has also been computed, using a Denton 3-D time-marching program. Except for a small region on the suction surface, and also around the trailing edge, favourable agreement can be seen in Fig 16. Increased flow blockage due to viscous effects in the experiment (not modelled by the inviscid calculation) explains the increased velocities near the trailing edge.

6.3 PROFILE HEAT TRANSFER MEASUREMENTS

Two typical sets of heat transfer data from two different runs of the tunnel are shown in Fig 17. The degree of repeatability is well within acceptable limits for this type of measurement.

In Fig 18 the distribution (here plotted as Nusselt number) is compared with that obtained from tests in the Oxford tunnel at the same Reynolds number and Mach number. Reasonable agreement can be seen, the divergence towards the suction surface trailing edge is consistent with the slightly earlier shock wave seen in Fig 15. The higher levels measured in the pressure surface trailing edge region appear to indicate earlier onset of transition in the Pyestock cascade.

6.4 ENDWALL HEAT TRANSFER MEASUREMENTS

Initial results for the heat transfer (Nusselt number) distribution on the outer endwall are shown on Fig 19 for two values of exit Mach number. High heat transfer rates clearly follow the line of the vortex moving across the passage from the leading edge.

7. CONCLUSIONS

A new facility has been installed at the Royal Aircraft Establishment, Pyestock, for testing annular cascades.

The design and procurement of the rig involved close co-operation between the RAE and the Department of Engineering Science at Oxford University. This co-operative effort proved very effective.

The ILPC exploits modern computer technology to provide a relatively low cost method of obtaining accurate heat transfer and aerodynamic measurements on turbine nozzle guide vanes, at conditions which correctly model those in a gas turbine.

Results from commissioning tests have demonstrated that good quality heat transfer and aerodynamic data can be acquired from this facility, with excellent repeatability.

REFERENCES

1. Schultz, D.L., Jones, T.V., Oldfield, M.L.G. and Daniels, L.C., A New Transient Facility for the Measurement of Heat Transfer Rates, AGARD, CP229, 1977.
2. Jones, T.V., Schultz, D.L. and Hendley, A.D., On the Flow in an Isentropic Light Piston Tunnel, ARC, R&M 3731, 1973.
3. Oldfield, M.L.G., Jones, T.V. and Schultz, D.L., On-Line Computer for Transient Turbine Cascade Instrumentation, IEEE Trans on Aerospace and Electronic Systems, Vol AES-14, Sept 1978, p738.
4. Schultz, D.L. and Jones, T.V., Heat Transfer Measurements in Short Duration Hypersonic Facilities, AGARD, AG-165, 1973.
5. Sucec, J., Application of Differential Similarity to finding Non-dimensional Groups important to tests of Cooled Engine Components, NASA TM X-3484, 1977.
6. Oldfield, M.L.G., Burd, H.J. and Doe, N.C., Design of Wide-Bandwidth Analogue Circuits for Heat Transfer Instrumentation in Transient Wind Tunnels, Paper in [proceedings of] the 16th Symposium of the International Centre for Heat and Mass Transfer (Heat and Mass Transfer in Rotating Machinery) Dubrovnik, August 1982, ed Daryl E Metzger, Hemisphere Publ. Corp., NY, 1984.
7. Baines, N.C., Laboratory Data Acquisition, Processing and Display System. Users and Programmers Guide, Oxford University Engineering Laboratory Report 1462/83.
8. Bryce, J.D., Litchfield, M.R. and Leversuch N.P., The Design, Performance and Analysis of a High Work Capacity Transonic Turbine, Paper for presentation at the 30th ASME International Gas Turbine Conference, Houston, Texas, March 1985.
9. Litchfield, M.R. and Norton, R.J.G., Heat Transfer Measurements on a Transonic Nozzle Guide Vane, ASME Paper No. 82-GT-247, March 1982.

ACKNOWLEDGEMENTS

The authors wish to acknowledge the considerable assistance given by Mr. K.J. Walton of Oxford University Engineering Laboratories, particularly during the development and bench testing of the plug valve system.

Thanks are also due to Mr. G.C. Horton of RAE Pyestock for computing the 3-D flow predictions.

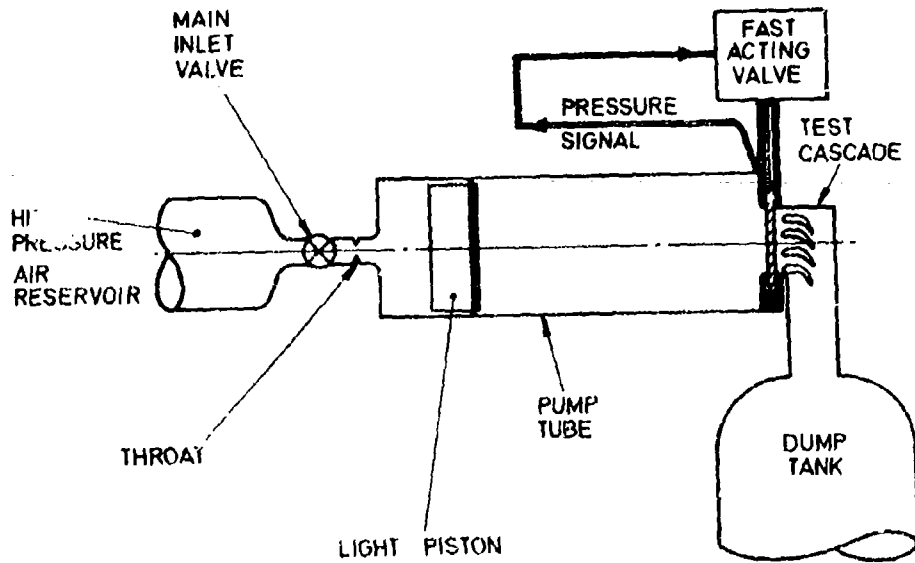


FIG 1 PRINCIPLES OF THE ISENTROPIC LIGHT PISTON TUNNEL

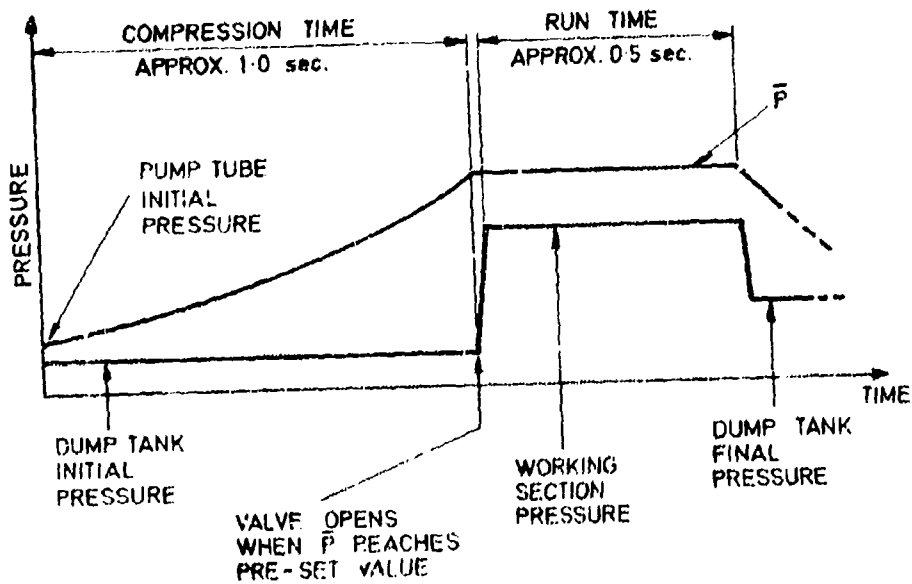


FIG 2 IDEALISED PRESSURE-TIME HISTORY

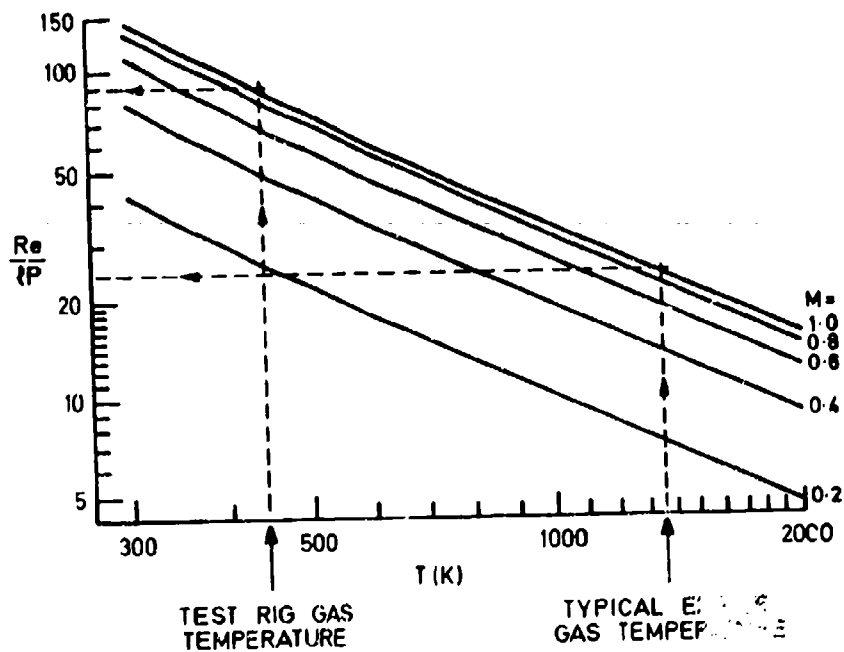


FIG 3 VARIATION OF UNIT REYNOLDS NUMBER WITH TEMPERATURE AND MACH NUMBER

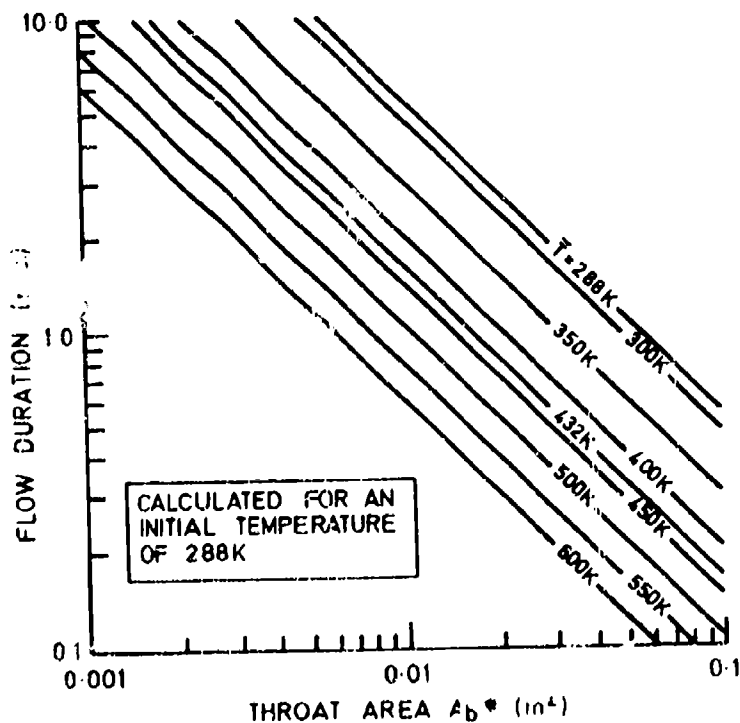


FIG 4 VARIATION OF FLOW DURATION WITH THROAT AREA AND OPERATING TEMPERATURE

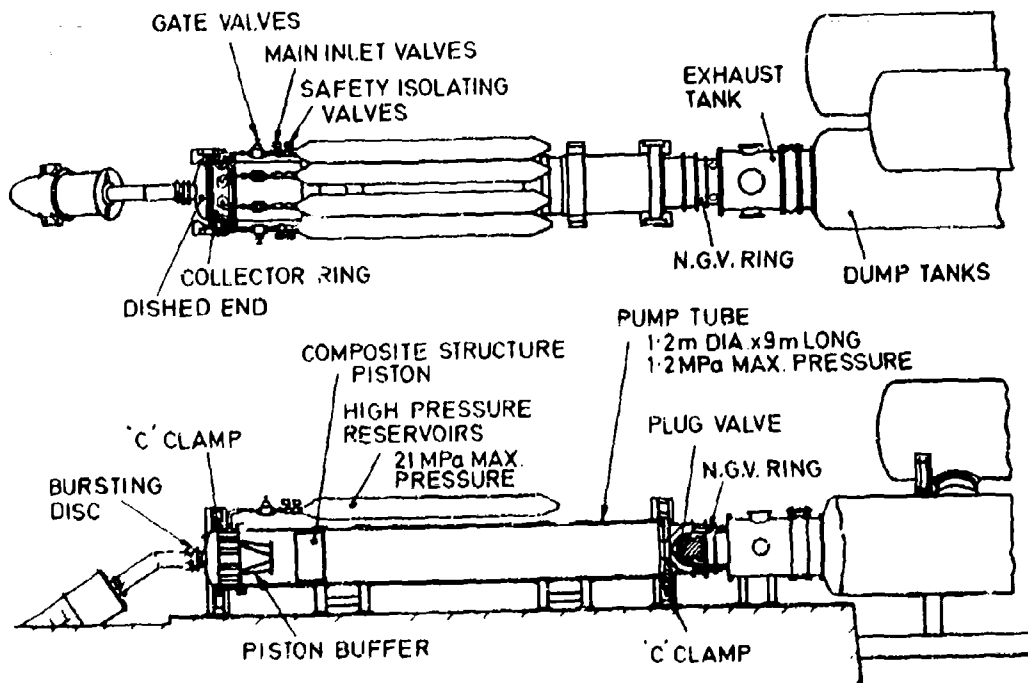


FIG 5 GENERAL ARRANGEMENT OF THE PYESTOCK ILPC FACILITY

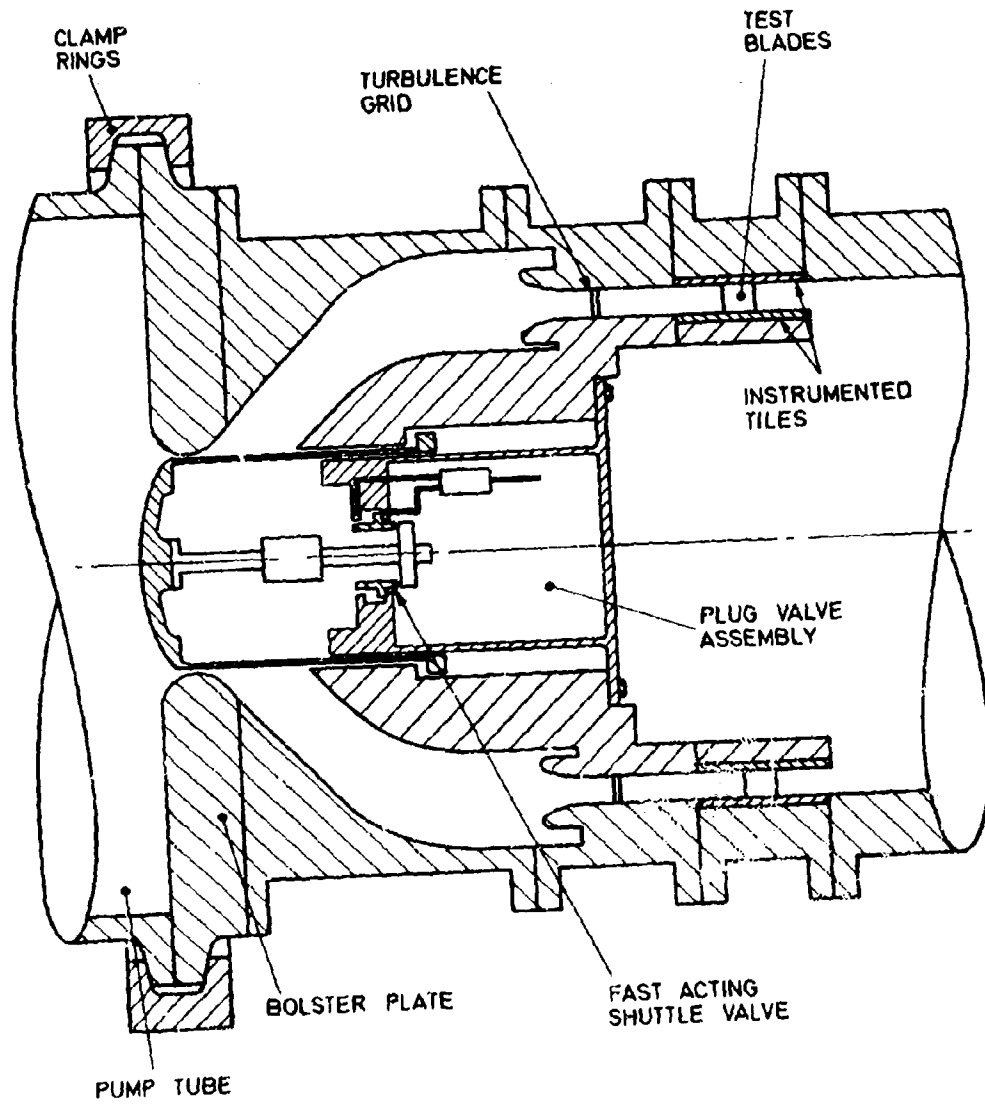


FIG 6 WORKING SECTION AND PLUG VALVE

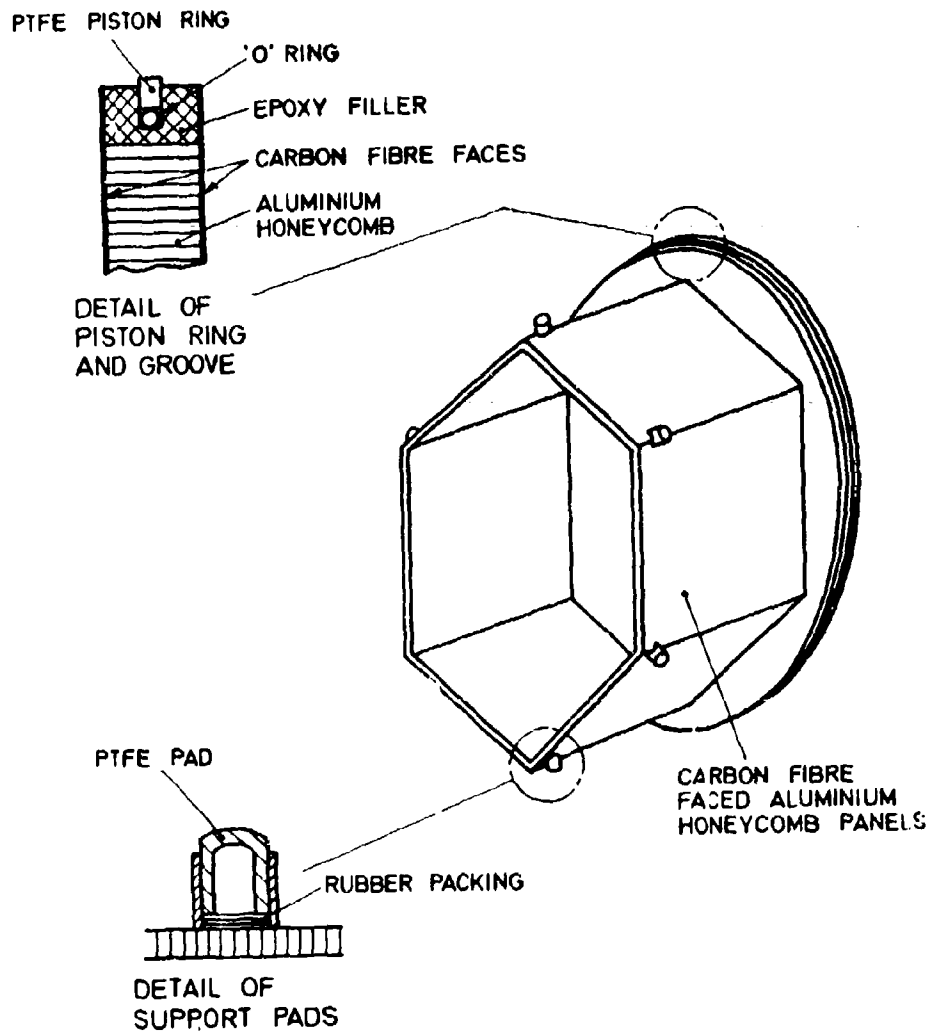


FIG 7 COMPOSITE PISTON

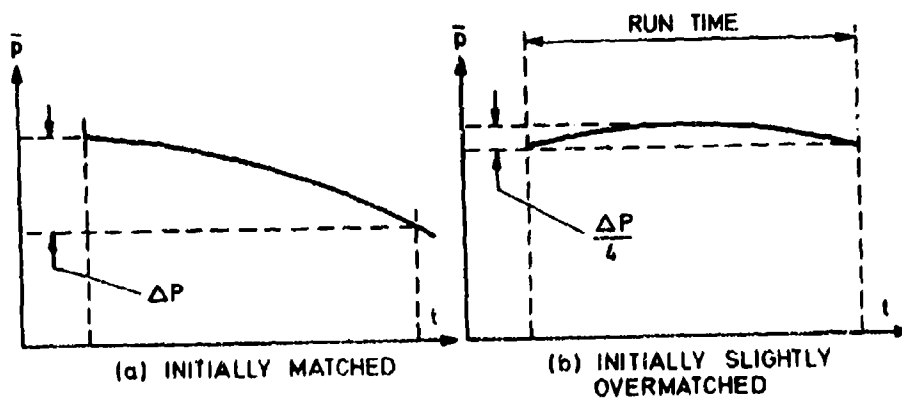


FIG 8 EFFECT OF MATCHING ON PRESSURE DROP DURING RUN

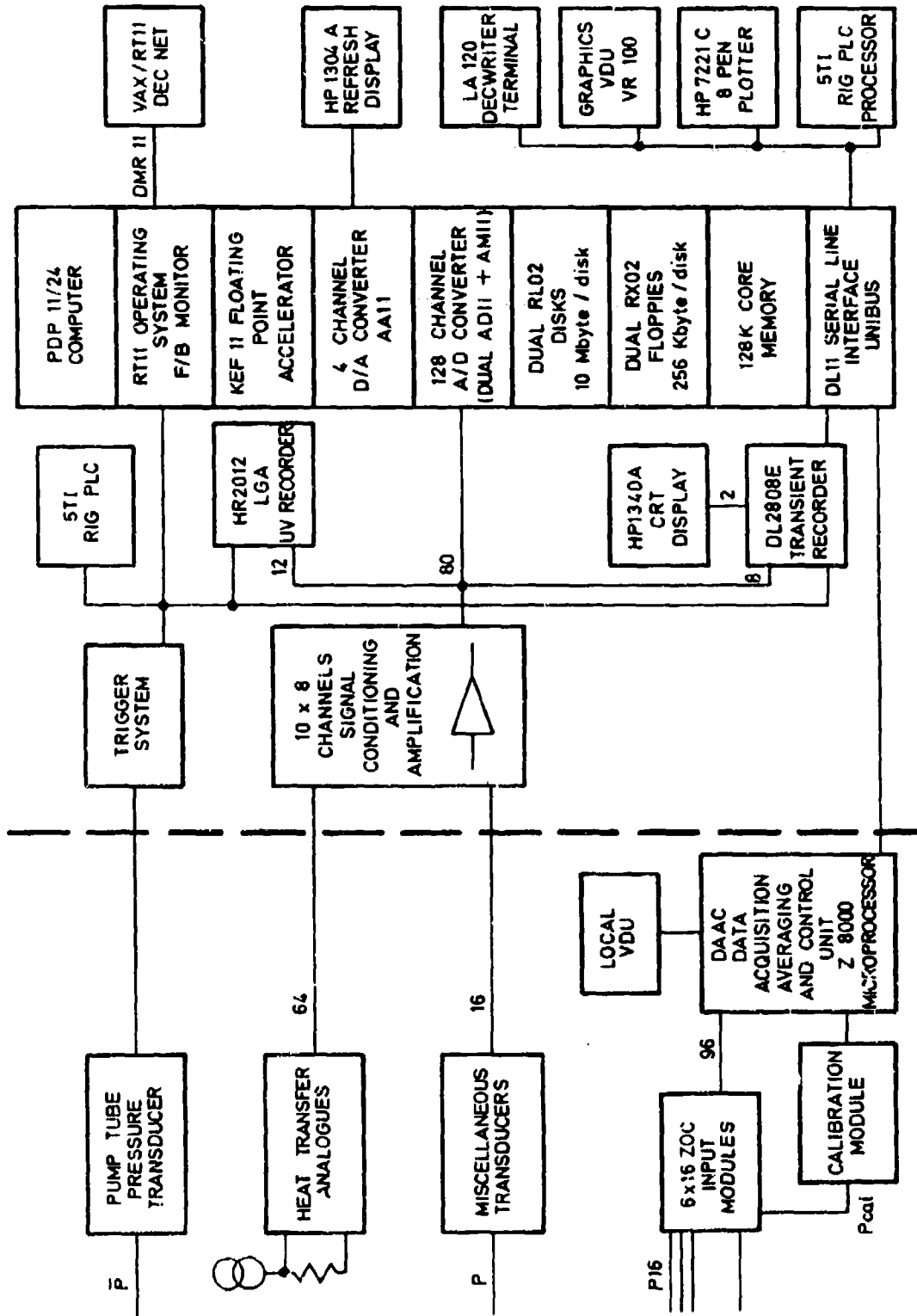


FIG 9 ILFC DATA ACQUISITION AND PROCESSING SYSTEM



FIG 10(b) A TYPICAL "TILE" SHOWING
ENDWALL STATIC PRESSURE
TAPPINGS

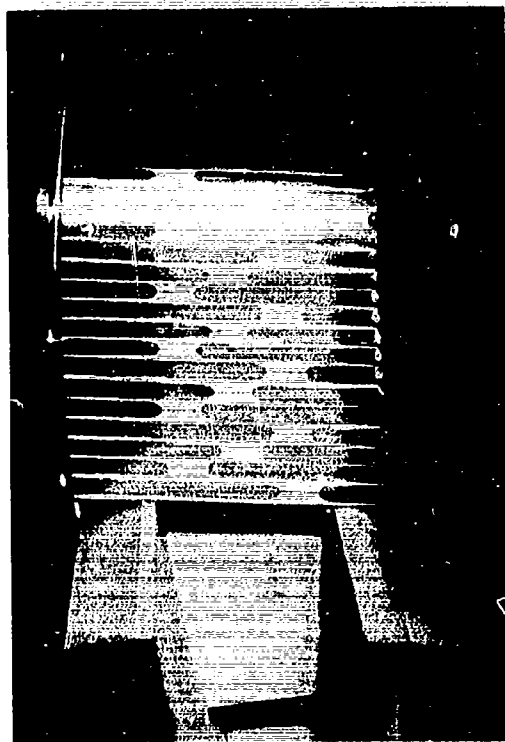


FIG 10(a) AN INSTALLED BLADE SHOWING
THIN-FILM HEAT TRANSFER
GAUGES

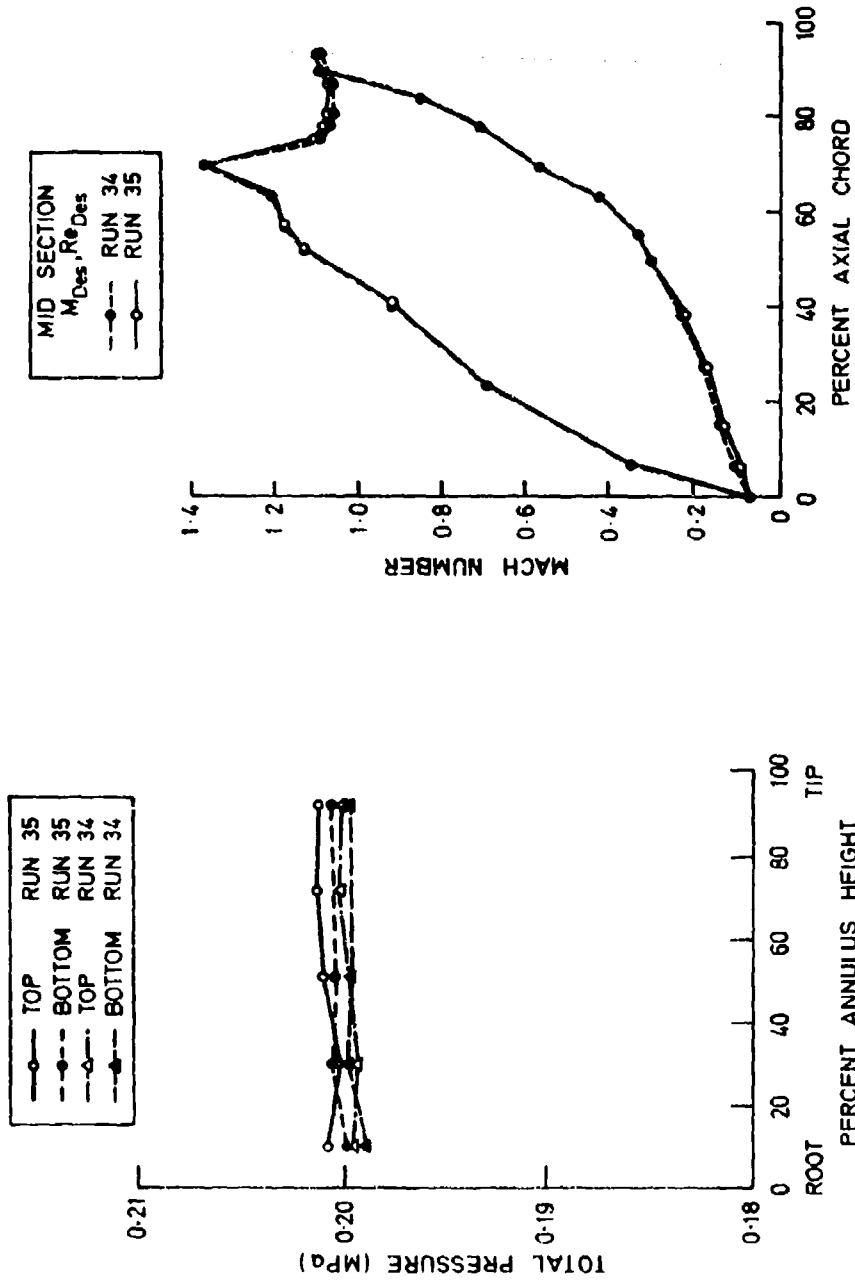


FIG 11 FLOW DISTRIBUTION AT INLET TO THE CASCADE

FIG 12 TYPICAL MACH NUMBER DISTRIBUTION AROUND A BLADE

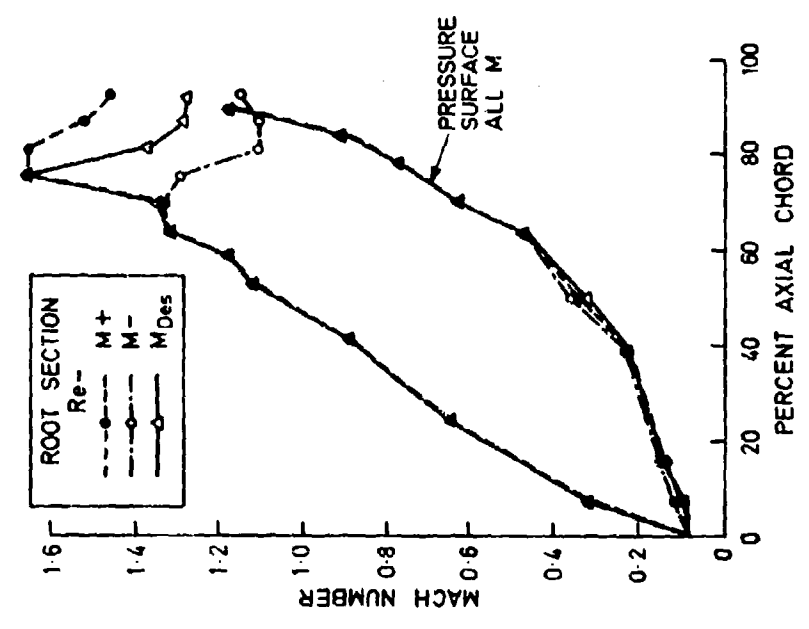


FIG 14 VARIATION OF MACH NUMBER DISTRIBUTION WITH EXIT MACH NUMBER

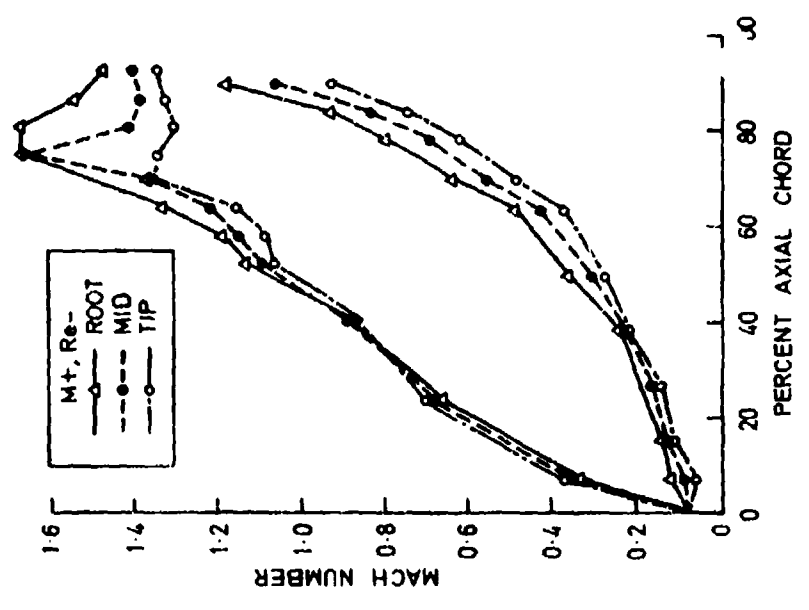


FIG 13 VARIATION OF MACH NUMBER DISTRIBUTION WITH POSITION ON BLADE

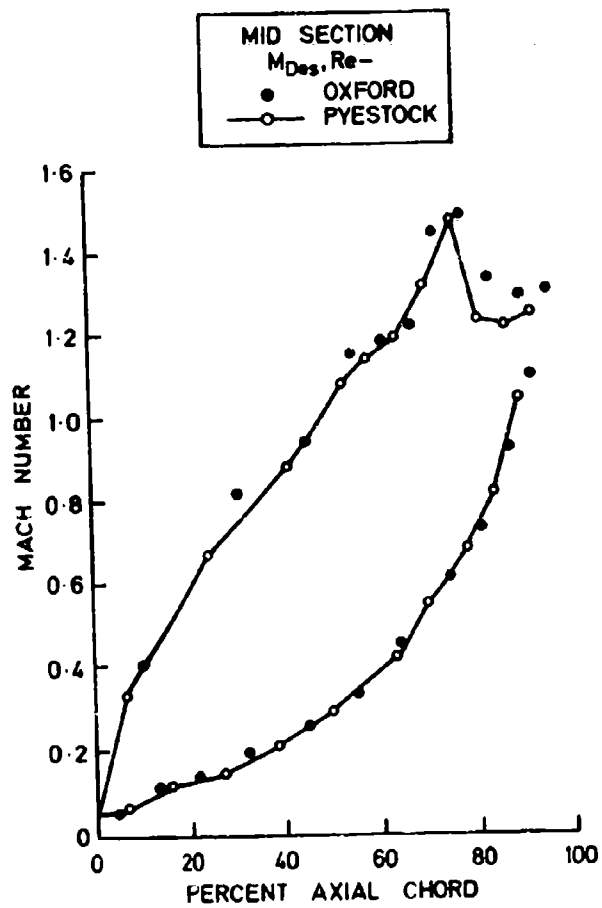


FIG 15 COMPARISON OF MACH NUMBER
DISTRIBUTION MEASURED AT
PYESTOCK AND OXFORD

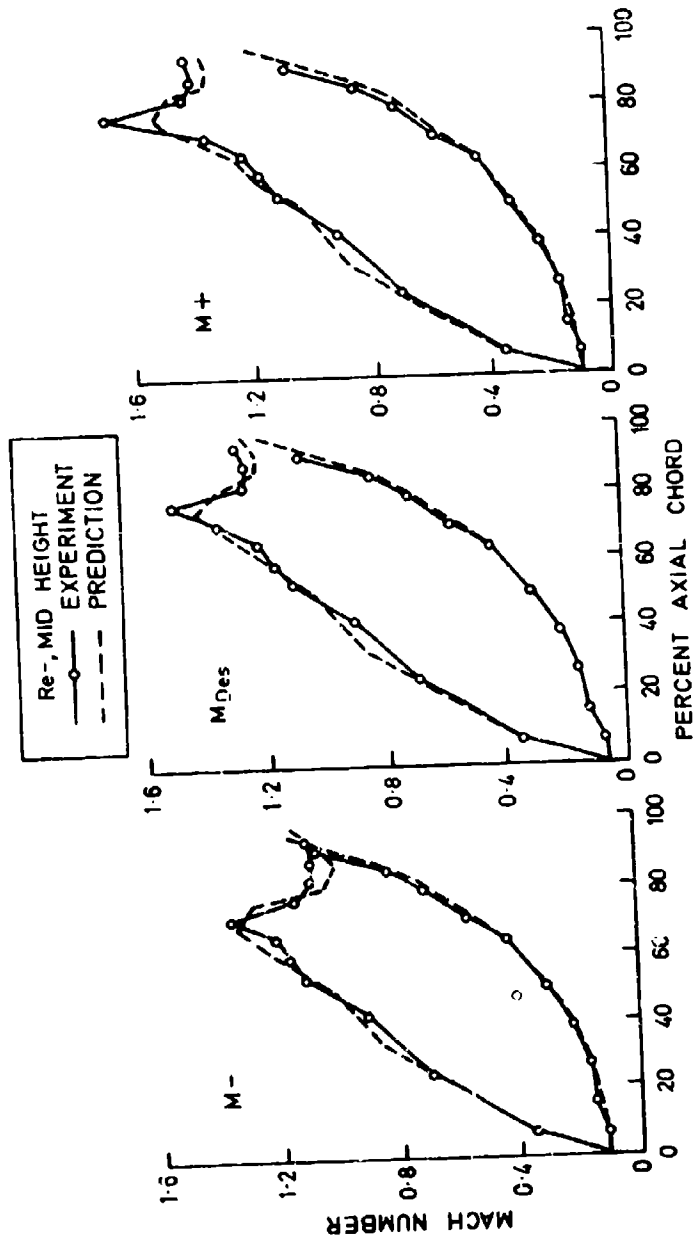


FIG 16 COMPARISON OF MEASURED AND PREDICTED MACH NUMBER DISTRIBUTION

M Des, Re -
 TIP SECTION
 ---●--- RUN 34
 ---○--- RUN 35

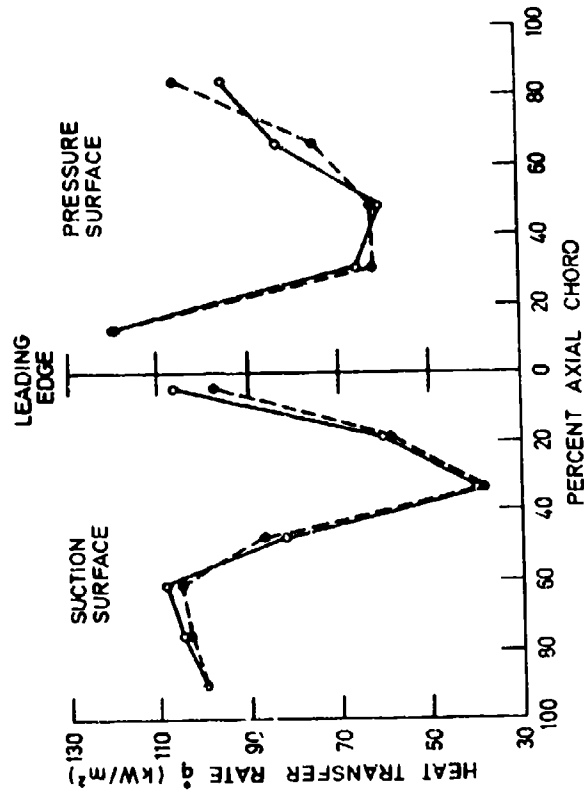


FIG 17 TYPICAL HEAT TRANSFER DISTRIBUTION AROUND A BLADE

M Des, Re -
 MID SECTION
 ● OXFORD
 ○ PYESTOCK

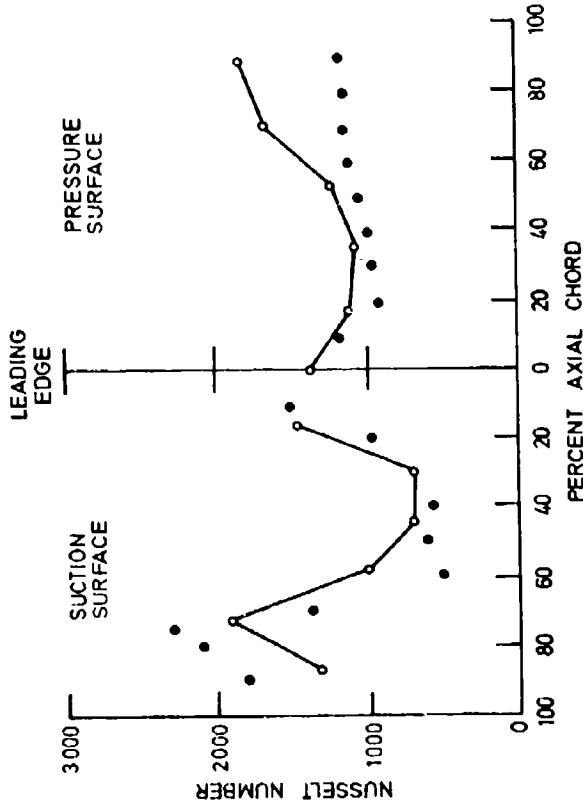


FIG 18 COMPARISON OF HEAT TRANSFER MEASURED AT PYESTOCK AND OXFORD

NUSSELT NUMBER CONTOURS

CONTOUR INTERVAL = 250

3 — 3 = 3 000 CONTOUR etc.

● = MEASUREMENT LOCATIONS

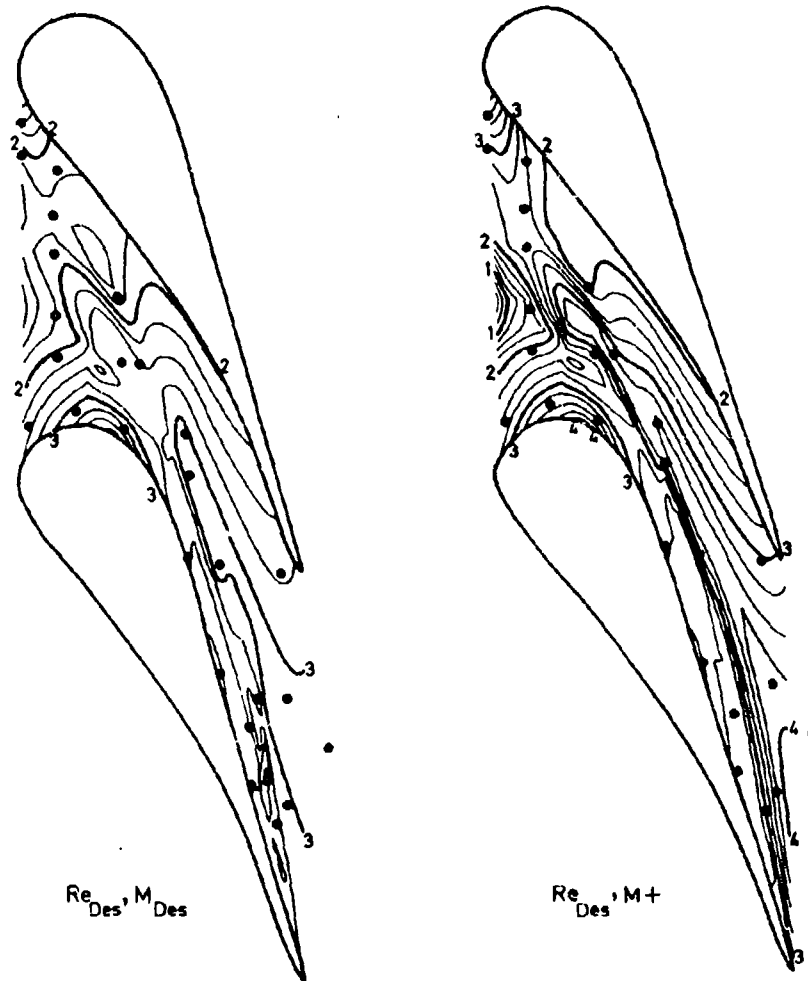


FIG 19 ENDWALL HEAT TRANSFER DISTRIBUTION

DISCUSSION

J.Fabri, Fr

How large were your investment costs?

Author's Reply

The external expenditures were about £750,000 and our internal costs were approximately of the same order.

T.Arts, Be

1. What are the relative dimensions and weight of the piston? Did you observe any piston oscillations after shutter opening?
2. What are the dimensions of the platinum thin films? What is the technique to deposit them?

Author's Reply

1. The free piston is 1.2 m diameter, and the hexagonal skirt about 600 mm long. The total weight is 14.25 kg.

Yes, piston oscillations have been observed. Indeed, one of the main reasons for attempting to achieve a lightweight design is to minimize these inherent oscillations. The design predicted pressure fluctuations of around $\pm 2\%$ at design conditions. Results during the commissioning tests appear to show that fluctuations are larger than this, due to two differences between the ILPC and the smaller Oxford tunnels. As we have an annular cascade there is a much larger volume to be filled between the (plug) valve and the working section, and the mass of the slug working fluid is greatly increased. These aspects have been studied by Dr T.V.Jones, and a solution involving modulation of the plug valve opening sequence has been proposed.

2. The platinum thin films are approximately 10 mm \times 1 mm. As is done with all such gauges at Oxford University, they are painted on — which I gather is the technique you have adopted at VKI.

A.B.Turner, UK

You are still not going to be able to simulate the high frequency of turbulence associated with a combustion chamber upstream of the blade. In this respect how valid do you think the results are going to be with regard to real engine conditions.

Author's Reply

As was shown on the slide (Fig.6), there is a turbulence generating grid upstream of the vanes. We believe this will give about 4% Tu (hot-wire anemometry measurements just upstream of the vane leading edge are at this moment being undertaken). Whilst combustor generated fluctuations are likely to be much greater than this, the shape of the exit duct from a combustion chamber will tend to accelerate and significantly modify the flow into the turbine, and hence reduce the local turbulence levels.

H.J.H.Saravanamuttoo, Ca

Could you expand on the choice of an annular cascade rather than rectangular? For full scale turbine investigations major changes to the working section must be necessary to accommodate changes in blade span, diameter, hub-tip ratio etc.

Author's Reply

Our original research proposals identified endwall heat transfer as one of the topics about which very little data were available. If the secondary flows which strongly influence the endwall heat transfer are to be correctly generated, a sector cascade, at least, had to be used. As the design study for the ILPC proceeded, the use of at least a 180° sector was considered, and it was eventually decided that a fully annular cascade was required if any remaining doubts about cascade end effects were to be dispelled. In fact, compared with a sector, the annular cascade was also easier to engineer.

The design of the facility is essentially modular downstream of the pump tube, so that even major changes to the working section, including upstream geometry, can be relatively easily incorporated. A second, smaller, plug valve is being manufactured to ensure that all foreseeable hub-tip ratios can be accommodated.

Finally, the other topic which I have suggested that is important for further study is rotational effects, i.e. not only the heat transfer to the rotating components but also the effects of a rotor on upstream (and downstream) stators. The ILPC was designed so that a rotor could be added at a later stage. A feasibility study for this enhancement has now been completed, and further design studies on particular aspects have been initiated.

M.Suo, US

1. On Fig.6 there appears to be a rounded inlet just upstream of the turbulence grid. Is there boundary layer bleed at that point?

2. Is there no flow control device downstream of the cascade? It would then appear that the downstream Mach number is not controlled.

Author's Reply

1. Fig.6 is an accurate representation of the geometry for the commissioning build. The rounded inlet protrudes into the main annular channel for a significant distance, which will prevent ingestion of boundary layer air during the main part of a test run.

For a future build, for which the inner and outer walls upstream of the cascade will be profiled to model combustor exit geometry, the facilities for positively bleeding off boundary layer air through the walls has been included.

2. The cascade Mach number is set by adjusting the dump tank starting pressure downstream of the cascade, relative to the upstream pressure which will be generated in the pump tube at the test temperature ratio and Reynolds number. The dump tanks have been made so large (80 m³) that the increase in downstream pressure during a test is minimal. At the design conditions for the current test, the pressure rise during a test will cause less than 1% change in cascade exit Mach number.

MEASUREMENTS OF FLUCTUATING GAS TEMPERATURES
USING COMPENSATED FINE WIRE THERMOCOUPLES

by

M.N.R.Nina and G.P.Pita
Department of Mechanical Engineering
Instituto Superior Técnico
1096 Lisboa Codex
Portugal

SUMMARY

Thermocouples with three different wire diameters (15 μ m, 40 μ m and 50 μ m) were used in association with an analog compensation circuit connected to a data acquisition system.

Measurements of the time constant were performed using two different heating techniques: Joule effect and external heating by laser beam.

The thermocouples were used to quantify the fluctuating temperature field in a hot air jet and in a premixed propane flame. In the reacting case the catalytic effect was evaluated by comparing coated and uncoated wires.

Conclusions were also obtained regarding frequency spectra, temperature pdf and time constant.

NOMENCLATURE

E - thermocouple e.m.f.
C_p - specific heat
Gr - Grashof number
h - convection coefficient
i - intensity of electric current
k - thermal conductivity
L - Wire length
Nu - Nusselt number
Pe - Peltier coefficient
 \dot{q}_{cat} - rate of catalytic heating per unit area
r - Jet radial coordinate
R - thermocouple wire radius
 ρ - electrical resistivity
t - time
T - temperature of wire
T₀ - initial temperature of wire
T_g - temperature of gas
T_{gc} - effective radiation temperature of surroundings
x - Jet axial coordinate
 σ - Stefan-Boltzman constant
 ϵ - surface emissivity
 ρ - specific mass
 τ - thermocouple time constant

INTRODUCTION

The accurate measurement of unsteady local gas temperature has occupied the attention of a growing number of investigators during the past thirty years as this effort is essential to our knowledge of combustion processes.

Associated with a measurement technique are errors that result from its principle of operation, design and construction limitations and from the disturbance imposed on the reacting flow by the presence of a probe.

A spectroscopic temperature method is favorable in the sense that utilizes no solid probe but on the other hand needs the knowledge of the thermodynamic nonequilibrium state existing at the flame front where different degrees of freedom of the particles show different temperatures. This means that, at the present state of the art, the new optical techniques, in addition to requiring expensive and complex hardware do not give reliable and straightforward readings of temperature; some do interfere with the reacting flow field due to the high energy beams associated with their techniques.

On the other hand some of the uncertainties associated with probe measurements are difficult to evaluate; fine wire thermocouples are in this category but compare very favorably from the principle of operation, cost and hardware complexity aspects with the new optical methods; therefore thermocouples will continue to be used in reacting flow studies.

This paper describes the application of small diameter thermocouples of platinum versus platinum-13% rhodium alloy for local unsteady gas temperature measurements in a premixed propane air flame. It attempts to list and quantify the most important phenomena associated with thermocouple error sources.

Three wire diameters (15 μ m, 40 μ m and 50 μ m) were used and their performance compared. Two different methods of evaluating thermocouple time constant were applied and compared; one uses a laser beam to heat

the junction, the second is based on Joule effect DC heating.

The thermocouple signal, amplified one hundred times is compensated in frequency by means of an analog circuit. Errors from method of evaluation of time constant, Peltier effect, catalytic effect, differences in thermal properties between platinum and Pt-Rd alloy were considered.

GENERAL CONSIDERATIONS

The nature of the function that connects the local turbulent reacting gas temperature to the e.m.f. of a thermocouple immersed in the flow is a complex one; the temperature of the metal junction depends on the balance of different modes of energy transfer described in principle by the following equation

$$\pi R^2 dx \rho C_p \frac{dT}{dt} = 2\pi R dx h(T - T_g) - \pi R^2 k \frac{d^2 T}{dx^2} dx + 2\pi R dx \epsilon \sigma (T^4 - T_{ge}^4) + 2\pi R dx q_{cat} \quad (1)$$

assuming uniform radial temperature in the wire and in the surrounding gas close to its surface. The geometry of the junction was a cylinder with approximately the same diameter as that of the wire as shown in figure 1, not a sphere as commonly assumed; the thermal inertia of the wire, represented by the l.h.s. of the equation was limitative when performing fluctuating temperature measurements; conduction along the wire was low due to the very small wire diameter ($L/R=200$ to 500) but was important during the cooling phase of time constant evaluation.

The flames under study were non luminous and therefore T_{ge} was approximately the temperature of the nearby metal surfaces. For measurements in the hot air jet the equation could be simplified due to the fact that T_{ge} was ambient temperature and there was no catalytic effect, the gas temperature being:

$$T_g = T + \frac{\epsilon \sigma T^4}{h} - \frac{R \rho C_p}{2h} \frac{dT}{dt} \quad (2)$$

the radiation term was small for air temperature around 500°C .

During the heating phase by Joule effect, the difference in magnitude of the electrical resistivity of Pt and Pt-Rd alloy (see table A) induced a strong longitudinal temperature gradient in the junction zone. To represent the transient cooling used to evaluate the time constant, the following form of the equation was used:

$$\frac{R \rho C_p}{2h} \frac{dT}{dt} = T - T_g - \frac{Rk}{2h} \frac{d^2 T}{dx^2} + \frac{\epsilon \sigma}{h} T^4 \quad (3)$$

the coefficient of the temperature gradient in the l.h.s. of the equation is the thermocouple time constant, τ :

$$\tau = \frac{R \rho C_p}{2h} \quad (4)$$

In a situation where there is no longitudinal conduction and radiation loss, the response of a heated thermocouple initially at T_0 , immersed in a cooler gas of temperature T_g is:

$$(T - T_g) / (T_0 - T_g) = e^{-t/\tau} \quad (5)$$

But τ is not constant during the cooling period due to the variation of the convection coefficient with temperature and wire Reynolds number, as shown by the many correlations that have been proposed for Nu (Andrews et al. 1972)

EVALUATION OF THE TIME CONSTANT

To estimate the value of τ experimental methods have been used by several authors, Kunugi and Jinno (1959), Odidi (1974), Yule et al (1978), Lenz and Gunther (1980), Lockwood and Moneib (1980 and 1982), Petit et al (1982). All the experiments are based on the analysis of the thermocouple response during a cooling period.

The different methods proposed to evaluate the thermocouple time constant are only able to evaluate a mean time constant.

It has been one of the purposes of the present work to study the variation of the thermocouple time constant during the cooling period after it has been heated either by Joule effect due to passage of a D.C. current or by using a laser beam focused on the thermocouple junction.

a) Joule heating

Figure 2 shows two curves corresponding to the cooling history of a $15 \mu\text{m}$ Pt, Pt-13%Rh thermocouple heated up to 300°C and 1006°C due to the passage of a D.C. current through the thermocouple wires, when placed in a stagnant atmosphere at room temperature. The two curves are not coincident due to the influence of temperature on the heat transfer coefficient and to the heat conduction along the wires. The temperature gradient along the wire, in the junction zone, is due to the different resistivity of platinum and platinum, 13% rhodium as shown in tab. A.

In figure 2 the predicted curves are also plotted. Predictions are based on equation 3 where the heat transfer coefficient was calculated with the constants adjusted to the specific configuration of the thermocouple, neglecting radiation loss and using the following Collis and Williams (1959) correlation:

$$Nu^{-1} = 0.83 - 0.8 \log_{10} Gr \quad (6)$$

The Grashof number was evaluated at ambient temperature and the Nusselt number at film temperature.

The initial temperature profile of the wires, has also been predicted, based on equation 3A (with two terms added to the heat balance equation to take into account the Peltier effect in the junction and the Joule effect along the wires); Thompson effect was a second order effect that has not been included in this evaluation.

$$0 = -2\pi R h dx (T - T_g) + \pi R^2 dx k \frac{d^2 T}{dx^2} + \frac{\pi i^2 dx}{\pi R^2} \pm Pe i \quad (3a)$$

As the wire diameter is very small the Peltier effect, acting as a source or as a sink of energy, influences the temperature profile along the wire during the heating period, as shown by Petit et All (1982).

This influence is evident in figure 3 where the predicted temperature profiles along the wires are plotted when a D.C. current flows from the Pt-13%Rh to the Pt wire (negative Peltier effect) of a 15um thermocouple placed in a stagnant atmosphere at room temperature. A positive Peltier effect, obtained by inverting the current, is also shown.

Figure 4 shows the instantaneous values of τ evaluated along the predicted curves of figure 2. The time constant has been calculated according to three different expressions.

Curves 1 and 4

$$\tau = \frac{R\rho C}{2h} \quad (7)$$

Plus a correlation for the Nusselt number.

Curves 2 and 5

$$\tau = \frac{T - T_g}{dT/dt} \quad (8)$$

Curves 3 and 6

$$\tau = -t/2n [(T - T_g)/(T_o - T_g)] \quad (9)$$

The value of τ from curves 3 and 6 has a value 40% lower than the value obtained with the other two curves. This is because the cooling curve is not a true exponential one due to the influence of the temperature in the heat transfer coefficient and to the heat conduction along the wires. The difference between the values of τ calculated with the three different expressions are much lower when the thermocouple is placed in an air stream ($v=10m/s$) at room temperature, due to the increased importance of the convection term.

b) Laser heating

Figure 5 shows the predicted wire temperature profiles during the cooling period evaluated from equation 2. The initial temperature profile was obtained from thermocouple temperature readings when the laser beam is moved along the wires.

Figure 6 compares the experimental value of τ evaluated using the two experimental techniques, when the thermocouple is placed in a stagnant atmosphere at room temperature. A difference of 50% in the value of τ is observed due to the different initial temperature profiles of the wires as shown in figures 3 and 5.

Figure 7 shows the thermocouple temperature curve when a laser beam focused on the junction is chopped by a rotating disc. The thermocouple is placed in an air jet ($u = 10 m/s$) at room temperature. The temperature decay is faster than with the D.C. heating method, also shown in figure for the same condition. In both cases the thermocouple was initially heated up to 250°C.

The experimental time constants based on the cooling curves of figure 7 and evaluated by expression (9) are plotted in figure 8. The thermocouple time constant based in the cooling curve (laser heating) has a value 30% lower. This difference is due to the different initial temperature distribution along the wire.

In turbulent flows the gas temperature fluctuates and the measured decay curve is distorted by the local temperature fluctuations. The evaluation of the mean local time constant of the thermocouple is made with expression 9 based on the ensemble average curve of several recorded decaying curves.

TEMPERATURE FLUCTUATIONS IN HOT AIR JET

a) Experimental setup

Temperature fluctuations have been measured in a 30mm diameter hot air jet, exit temperature 470°C and velocity 13m/s, using a 15µm Pt,Pt-13%Rh thermocouple.

The output voltage from the thermocouple goes through a processing circuit whose principal components are: (I) a preamplifier that amplifies 100 times the thermocouple output, (II) the compensation circuit that performs the operation figure 9,

$$(1 + \tau \frac{d}{dt})E \quad (10)$$

The circuit permits the continuous adjustment of τ between 0 and 30 ms, (III) a low pass filter cut-off frequency normally set at 1.5 KHz which guarantees a good signal to noise ratio, (IV) an analog to digital converter and (V) a data acquisition system controlled by the Apple II microcomputer with a maximum sampling rate of 12KHz.

An auxiliary circuit heats the thermocouple by passing a D.C. current. During the heating period the preamplifier is switched from the main thermocouple to an auxiliary thermocouple maintained at an adjusted temperature equal to the main thermocouple mean temperature in order to avoid transients.

The performance of the compensation circuit is shown in figure 10 where the trace of compensated temperature with time, heating the thermocouple with a chopped laser beam, is a quasi-square wave. The wave is not perfectly square because the thermocouple time constant varies during the cooling period as previously shown in figure 7, and the compensation circuit only allows the adjustment of mean values of time constant.

Figure 11 shows the mean time constant variation with jet radius for two different wire diameters 15µm and 50µm. The values of τ were measured using the joule heating pulse technique.

An average cooling curve was obtained from 20 to 100 recorded curves depending on the local turbulence level; the value of τ is the time taken to reach 63% of the final value of the average decay temperature.

At a given station in the mixing region of the jet, one jet diameter downstream, the mean time constant of the 50µm thermocouple is 32ms and of the 15µm thermocouple is 5ms. Setting the compensation at 30ms it is possible to go up to 200Hz with the 50µm thermocouple with an acceptable signal to noise ratio. Frequencies up to 400 Hz were detected in this region and as the mean life time of the 15µm thermocouples in this flow was of the order of 30 min (even more if care was taken not to overheat them during the heating periods) they were used to perform the measurements.

b) Measurements

Temperature fluctuations measured at one diameter downstream of the jet exit and at 15mm from the axis, are shown in figure 12 for six different levels of compensation. For this location, τ was evaluated at 5.3ms using the D.C. heating technique. Comparing the two curves, for 5.3ms and 7.2ms, only the second clearly exhibits the bimodal shape that would be expected in such a flow location.

Due to the variation of τ with temperature, a mean time constant will always introduce an error, either undercompensating the lower temperature fluctuations or overcompensating the higher ones.

The variation of the RMS temperature fluctuations with the compensation level is plotted in figure 13: the "correctly" compensated signal has an increase of 30% in the temperature rms to the uncompensated signal. An overcompensation of 50% of the τ value gives an increase of 50% in the measured temperature rms.

In figure 14 the influence of the compensation level in the temperature spectra is plotted. Frequencies up to 400 Hz are detected even without a compensation of the thermocouple output signal due to the low time constant of the 15µm thermocouple, however the energy contained in the higher frequencies is a function of the compensation level as expected.

MEASUREMENTS IN A PREMIXED FLAME

A disc and tube premixed flame burner was used and a 40µm thermocouple located near the edge of the stabilizer, 5mm downstream, in the flame front region. Radial temperature profiles were obtained with coated and uncoated thermocouples. The silica coating technique used was that described in (Fristrom and Westenberg). The principal cause of catalytic effect is surface recombination of flame front radicals, and therefore the number of free radicals available for reaction is important. We have clearly detected the effect of local fuel air ratio on the uncoated thermocouple reading. Figure 15 shows two different mixing situations for propane and air: the one referred as "with inner tube" gives a higher fuel air ratio at the thermocouple location.

As expected the coated thermocouple (curve 5) shows the lowest temperature but its higher diameter and different emissivity will contribute to alter the radiation exchange (equation 1). With uncoated wire, "going into" the flame front does not give the same temperature profile as "going out" and this is due to sustained reaction on the wire by catalytic effect on "going out". Temperature differences can be as high as 250°C at 1300°C.

Curve 3 and 4 are almost coincident indicating that the catalytic effect is not present in this situation of lower fuel air ratio.

In addition to the local fuel air ratio, the catalytic effect is strongly influenced by wire temperature and conduction along the wires in steep gradient flame zones can be important. The effect of higher thermal conductivity of platinum as compared to Pt-Rd alloy was clearly observed when only half of the thermocouple wire was glowing red. Heating up one support in the flame front, with the noncoated junction immersed in the cold flow of reagents, would produce a visible advance in the catalytic reaction (red glowing) along the wire after a short time.

Errors induced by catalytic effect are difficult to quantify but limit the accuracy of measurements of mean and fluctuating gas temperatures in the radical rich flame zones.

Radial measurements performed further downstream from the stabilizer showed a decrease in the catalytic effect, although temperature was kept high.

The use of coated wires reduces the frequency response and our analog compensator and Joule pulsed heating system could not perform adequately in this case.

CONCLUSIONS

Time constants evaluated by two different heating methods vary from 20% to 30% due to the different initial temperature distribution along the wire associated with each technique.

The initial wire temperature selected for the heating will affect the value of τ .

Peltier effect is not significant compared with the differences in electrical resistivity of the two metals.

Temperature rms and pdf are very sensitive to the value of τ ; an overcompensation of 50% of τ results in a 50% increase in rms.

When the pdf is bimodal the use of a mean value of the time constant, required by the analog compensator, will result in substantial errors either on the lower or on higher temperature readings.

In reacting flows, the catalytic effect can induce large errors depending on the flame zone, temperature gradients and probe orientation, local excess air and type of fuel. Temperature fluctuations are almost not detected when the catalytic effect is present.

Coated thermocouples will not be affected by catalytic reactions but have a larger thermal inertia.

ACKNOWLEDGEMENTS

The construction of the premixed flame rig was partially funded by AFOSR Grant 82-319.

AGARD project P-3 supported visits to Imperial College, London by one of the authors (M. Nina).

REFERENCES

1. Andrews, C.E., Bradley, D. and Hundy, G.F. (1972)
Hot wire anemometer calibration for measurements of small gas velocities
Int. J.H.M.T., vol 15, pp 1765-1786
2. Ballantyne, A., Boon, D.J. and Moss, J.B. (1976)
Measurements of Fluctuating Temperature in Open Diffusion Flames Employing Fine Wire Thermocouples
AASU Memo. N 76/3
3. Ballantyne, A., Moss, J.B. (1977)
Fine Wire Thermocouple Measurements of Fluctuating Temperature
Combustion Science and Technology vol 17, pp 63-72
4. Bradley, D. and Entwistle, A.G. (1966)
The total hemispherical emittance of coated wires
Brit. J. Appl. Phys., vol. 7, pp 1155-1164
5. Collis, D.C. and Williams, M.J. (1959)
Two-dimensional convection from heated wires at low Reynolds numbers
J. Fluid Mech. 6, pp 357-384
6. Fristrom, R.M. and Westbrook, A.A. (1965)
Flame Structure, McGraw-Hill
7. Hayhurst, A.N. and Kittelson, D.B. (1977)
Heat and Mass Transfer Considerations in the Use of Electrically Heated Thermocouples of Iridium versus an Iridium/Rhodium Alloy in Atmospheric Pressure Flames
Combustion and Flame 28, pp 301-317
8. Kunugi, M. and Jinno, H. (1959)

- Measurements of Fluctuating Temperature.
Seventh Symposium (Internacional) on Combustion p.942
9. Lenz, W. and Gunther, R. (1980)
Measurements of fluctuating Temperature in a free-jet Difusion Flame.
Combustion and Flame 37, p. 63
 10. Lockwood, F.C. and Moneib, H.A. (1980)
Fluctuating Temperature Measurements in a Heated Round Free Jet
Combustion Science and Technology vol 22, pp 63-81
 11. Lockwood, F.C., And Moneib, H.A. (1982)
Fluctuating Temperature Measurements in Turbulent Jet Diffusion Flame
Combustion and Flame vol 47, pp 291-314
 12. Odidi, A.,O. (1974)
The influence of turbulence on the time-mean rate of chemical reactions
Thesis, Doctor of Philosophy, Faculty of Engineering, University of London
 13. Petit, C., Gajan, P., Lecordier, J.C. and Paranthoen, P. (1982)
Frequency response of fine wire thermocouple
J. Phys. E: Sci. Instrum., vol 15, pp 760-764
 14. Yule, A.J., Taylor, D.S., and Chigler, N.A. (1978)
On-line digital Compensation and processing of thermocouple signals for Temperature measurements in turbulent flames
AIAA 16th Aerospace Sciences Meeting Huntsville, Alabama
(New York:AIAA) paper 78-30

TABLE A

Thermal properties of Pt and Pt-13Zr

	Pt	Pt-13Zr
k ($\text{W m}^{-1}\text{K}^{-1}$)	69	26
R ($\Omega \text{ m}$)	11×10^{-8}	19.6×10^{-8}
C_p ($\text{J Kg}^{-1}\text{K}^{-1}$)	136	--
ρ (Kg m^{-3})	21450	19610


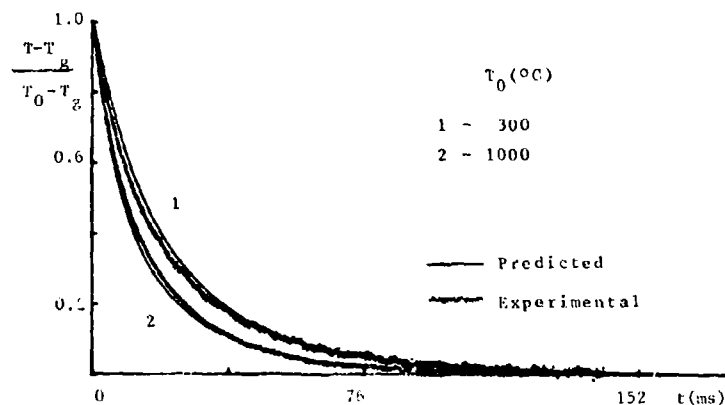


Fig.1 Thermocouple junction
15 μm diameter (x400)

Fig.2 Cooling curves of a 15 μm thermocouple

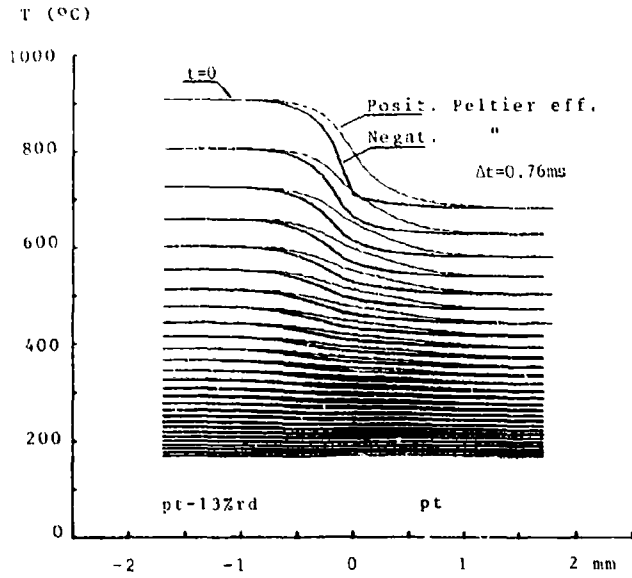


Fig.3 Temperature profiles along the wires during the cooling period (Joule heating)

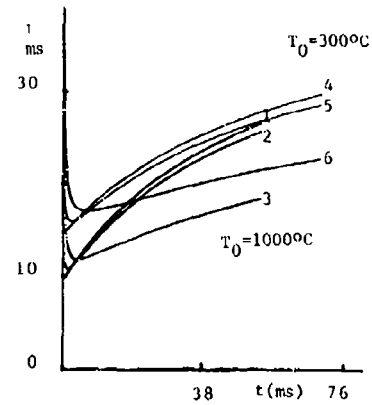


Fig.4 Predicted time constant as a function of time

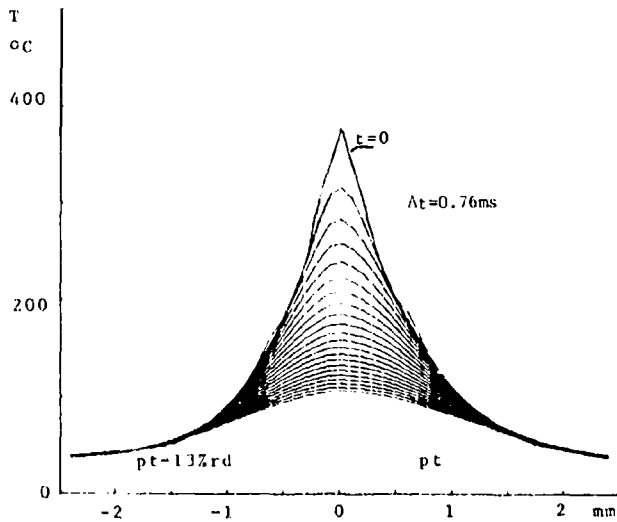


Fig.5 Temperature profiles along the wires during the cooling period (laser heating)

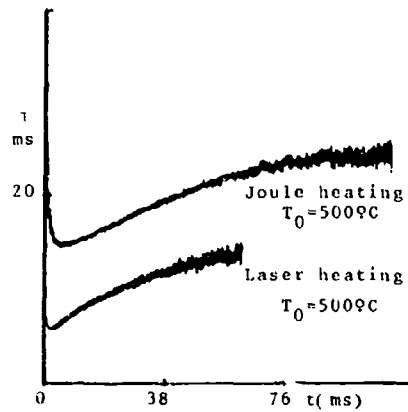


Fig.6 Comparison of experimental values of τ (in a stagnant atmosphere)

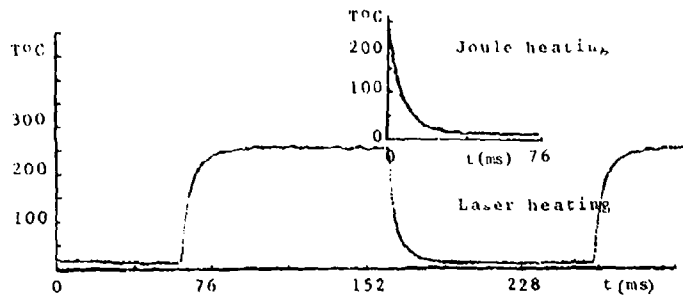


Fig. 7 Junction temperature histories

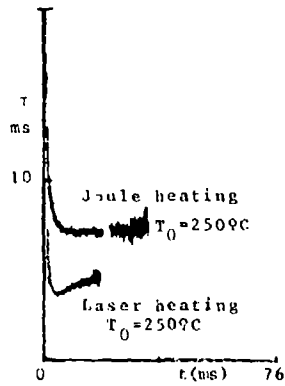
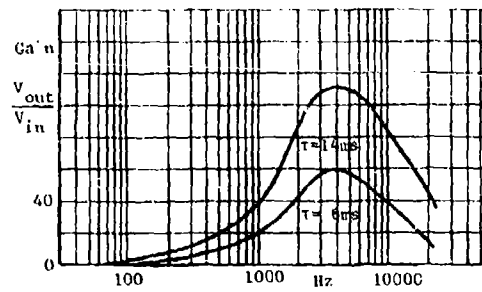
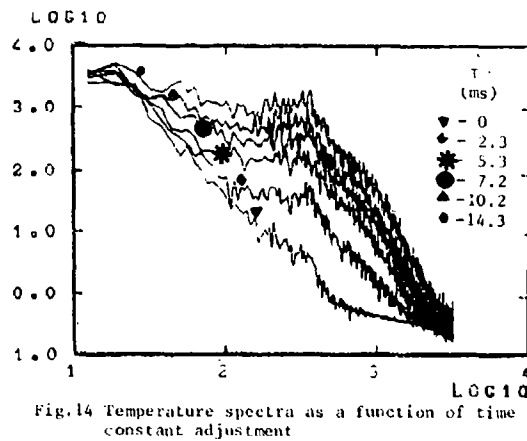
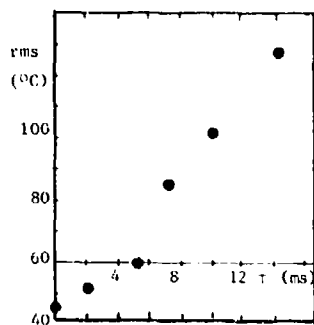
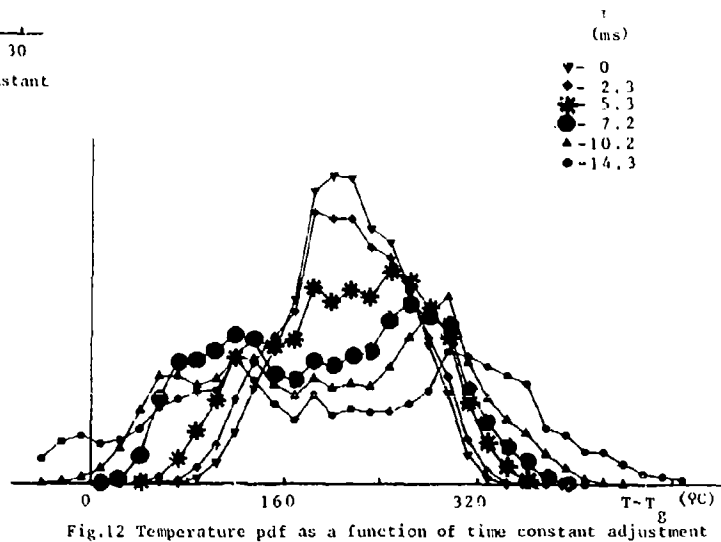
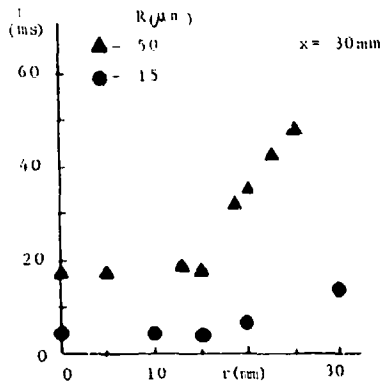
Fig. 8 Experimental time constant ($\tau = 10\text{ms}$)

Fig. 9 Compensation circuit transfer function



Fig. 10 Compensated junction temperature history (laser heating)



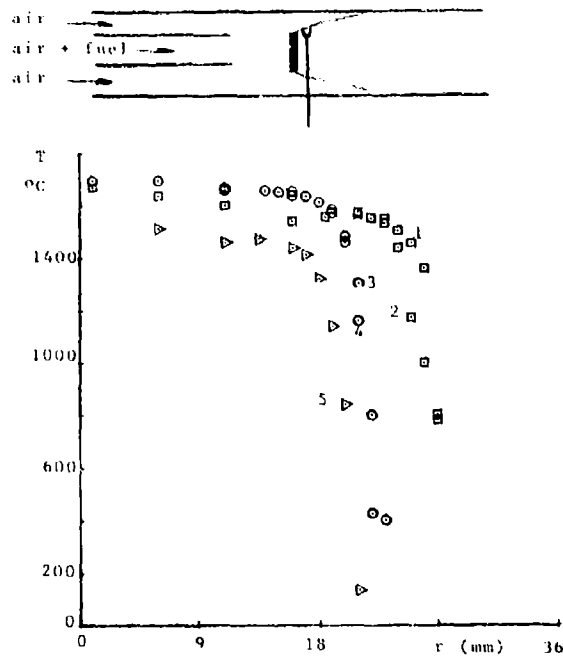


Fig.15 Temperature profiles in a premixed flame

	with inner tube	without inner tube
coated	5	-
uncoated	1 (going out)	3 (going out)
	2 (going in)	4 (going in)

DISCUSSION

G.Winterfield, Ge

What type of coating did you use and how long did this coating persist in the hot gas environment?

Author's Reply

A silica coating was used as described in Fristrom and Westenberg (1965). The coated wire diameter was about 80 μm . The coating life time was at least one hour, depending on the temperature and the temperature gradients it has been submitted to.

F.Tarada, UK

In Figure 2 reference is made to a 'predicted' curve of the decay of nondimensional temperature with respect to time. How was this predicted curve obtained?

Author's Reply

Two predicted cooling curves are shown in Figure 2 corresponding to heating by Joule effect but with two different initial temperatures (300°C and 1000°C). Equation (3) was used and the convection coefficient obtained from equation (6). Figure 3 represents the temperature distribution along the wires; the initial conditions are for $\Delta t = 0$.

111

TWO SPOT LASER VELOCIMETER
MEASUREMENTS OF VELOCITY AND TURBULENCE INTENSITY
IN SHOCK TUBE DRIVEN TURBINE FLOWS

by

Richard B. Rivir
Aero Propulsion Laboratory
Air Force Wright Aeronautical Laboratories
Wright-Patterson Air Force Base OH 45433-6563, U.S.A.

William C. Elrod
Air Force Institute of Technology
Wright-Patterson Air Force Base OH 45433-6583, U.S.A.

Michael G. Dunn
Calspan Advanced Technology Center
Buffalo NY 14225, U.S.A.

Summary

Full-scale rotating turbine heat transfer tests have been under way at Calspan for a number of years. The turbine is driven by a shock tube of short duration. Heat transfer distributions are measured during the test by thin film surface gages on the various component parts. Direct measurement of the velocity and turbulence intensity is needed to accurately compute the heat transfer for comparison with the measured values. An investigation to determine if measurements of velocity and turbulence intensity could be obtained with a two-spot laser velocimeter in the turbine for these short duration shock driven flows was undertaken. Two seed materials were investigated with satisfactory results: propylene glycol and Dow 200. The velocimeter was initially set up on a low-pressure-ratio shock tube which could be cycled quickly to determine the seeding requirements. The velocimeter was transferred to the high-pressure, full-scale turbine after successful measurements in the low-pressure shock tube.

1.0 Introduction

A measurement and analysis program has been underway at Calspan for several years that utilizes a full scale high pressure rotating turbine stage (1-7). The experimental technique being used is the short-duration, shock-tunnel approach, in which fast-response, thin-film thermometers are used to measure the surface temperature histories at prescribed positions on the various component parts. Heat-transfer rates are then inferred from the temperature histories, using standard data reduction procedures. The shock-tunnel facility provides a clean, uniform, and well-known gasdynamic condition at the inlet to the stationary nozzles. The shock tube driven flow is not intended to duplicate every parameter important to turbine heat-transfer studies. The intent is to have the flow conditions sufficiently defined and adequate parameters duplicated such as the flow function, the corrected speed, and the wall to total temperature ratio. The measured heat-flux distributions are used to validate and improve the accuracy of full-stage design and prediction techniques.

The turbulence intensity is a parameter which is a significant variable when the various predictive codes are used for the correlation of heat transfer data. A measurement of the free stream turbulence intensity which is associated with the particular heat transfer data set is required to calculate the theoretical heat transfer. An equally important quantity is the turbulence scale; however, at the present time no attempt is being made in these measurements to ascertain the scale. A heat-flux measurement technique that was used to estimate the turbulence intensity associated with the Calspan experimental data has been described in reference 6. An array of thin-film gages located on a cylinder in cross flow was used to infer the relative magnitude of the turbulence intensity in the annulus flow just upstream of the nozzle guide vanes (NGV). Because of the importance of the turbulence intensity in the development of hot-section predictive techniques, Dunn, Rae and Holt (6) suggested that a method should be investigated that has the potential for a more accurate determination of the turbulence intensity than does the cylinder in cross-flow approach. Calspan and Wright-Patterson Air Force Base (WPAFB) undertook a joint effort to use the WPAFB two-spot laser system in the Calspan experiments. Prior to the measurements at Calspan, initial feasibility measurements were undertaken at the Air Force Institute of Technology (AFIT) which utilized a low-pressure-ratio shock-tube driven flow. From the outset, one of the major concerns with this measurement technique was whether or not satisfactory velocimeter measurements could be performed within the 15 to 25 millisecond time period available in the short duration sampling times associated with both the AFIT and the Calspan experiments.

Laser Transit Anemometer (LTA) measurements rely upon the correlation of a number of scattering events. The time for an individual event is given by one to two times the spot-to-spot transit time. Figure 1 is a transducer record illustrating a typical pressure history measured at a location immediately upstream of the NGV of the full scale shock driven turbine in the immediate vicinity of the laser measurement site.

This record illustrates that the order of 20 milliseconds is the total time available within which to perform the laser measurements. A typical axial flow velocity at this location in the Calspan facility is 75 meters/sec (250 ft/sec). For a spot separation of 432 micrometers one has a nominal 6 microseconds as an event time. There are on the order of 10^4 events (or number of times the correlation can be attempted) in the available test time. By contrast, a continuous experiment might typically run for 10⁷ to 10⁹ events, so the short-duration application represents a significant reduction in the statistical sampling level. It was, therefore, important to determine if, and to what accuracy, it is feasible to measure the velocity and turbulence intensity in a short-duration facility using the two-spot system.

2.0 Experimental Apparatus

2.1 Low Pressure Shock Tube Configuration

The AFIT 0.102 x 0.204-m (4 x 8 in) shock tube was used for the initial feasibility measurements. Schlieren windows and adequate extensions of the test section necessary to provide increased test time already existed for the test section portion of this tube. The ideal incident shock test time, defined as the time elapsed between arrival of the incident shock and the interface, was on the order of 0.68 to 0.29 milliseconds/ft of driven tube length for the range of incident shock Mach numbers used here ($1.4 < M_s < 1.5$). Thus for a tube length of 3.51-m (11.5 ft) the ideal incident shock test time was on the order of 7.8 to 3.3 milliseconds. Even though the ideal test time for this tube was significantly less than the desired 20 milliseconds, we obtained a 20-millisecond-duration flow, of reasonably uniform conditions which was sufficient for the feasibility study. Note that the turbulence intensity and velocity measured in this environment may be somewhat different than the intensity one would associate with the test-time region of a uniformly shock-processed flow.

This shock tube is a low-pressure tube and thus the desired flow velocity, pressure and temperature could not be matched simultaneously. The shock-tube arrangement is shown schematically in Figure 2 and in the photograph of Figure 3. The test section of this facility was reduced to 0.0254-m (1-in) square by 2.44-m (8-ft) long. The LTA was built by Spectron and is shown schematically in Figure 4. The LTA produces two measurement volumes which are polarized at right angles to one another. The two measurement volumes were separated by 432 micrometers, each 25 micrometers in diameter and 1.25 millimeter in length for the lens combinations used in these measurements. The outer third of the projecting lens system collects the backscattered light from the measurement volumes. This reflected signal is separated into its two polarized components and imaged on two optical fibers to carry the signals to the photomultiplier tubes. The photomultiplier signals are filtered and amplified before being cross-correlated by the Malvern correlator. Velocity is then given by the time of flight of the cross-correlated photomultiplier signals and the turbulence intensity is related to the width of the cross-correlated signal. The hardware is controlled and the data reduced, and then stored by an Apple II. The measurement volumes are aligned with the flow by rotating a Wollaston prism within the optical head. One must set up the LTA on continuous flow to select the flow angle. The two spots for the lens combination necessary for the Calspan experiment require spot alignment with the flow to better than 1-1/2 degrees.

Continuous flow was brought into the top of the shock tube as shown in Figure 2. As anticipated, seeding was required to achieve short-duration measurements. The seed was introduced into the center of the tube with a 0.0159-m (5/8-in) diameter tube on a 0.051-m (2-in) radius. A TSI, Inc. Model 9306 Six Jet Atomizer was used to introduce propylene glycol into the tube. Two axial locations and three configurations were investigated in selecting the configuration utilized. Sharp corners and contractions were avoided because both tended to cause condensation. Locating the seed injection point within the continuous-flow entrance mixing zone was also more effective than injection in the flowing stream. One to six jets were tried, with one jet giving the best results.

The test-section back wall was originally polished aluminum. The resulting flare was so intense that the photomultipliers were shut down by the over current protective circuitry at less than half of their normal operating voltage. A number of wall treatments were investigated to reduce this flare: black paint, glass bead blast, anodization, and the three wall cavities shown in figure 5. All three of the cavities were successful in reducing flare so that nearly the full operating voltage of the photomultiplier could be used. The simplest cavity, the single cone, was used for most of this investigation. The conical surface was blasted with glass beads, redrilled and anodized, but the maximum obtainable photomultiplier voltage fell off by 26% for both the bead blast and the anodized surface. Although the anodized surface would have been usable, it was removed for the remainder of the measurements.

The window for this test section was a 0.0254-m (1-in)-thick Schlieren window. The window transmitted 94% at half angles of 1-1/2, 3, 6, 9, and 11° incidence. Continuous measurements were made at 3° to 11° incidence with only small differences in the resulting measurements. The beam reflected from the front window surface just missed the collecting aperture at 3°. The 6° incidence beam was used as the standard or reference condition for the resulting measurements since it showed a lower background noise level on initial setup.

2.2 The Shock Driven Tunnel Configuration for the Full Scale Turbine

The Calspan shock-tunnel apparatus, shown schematically in Figure 6, consists of an 0.20-m (8-in) i.d. helium-driven shock tube with a 12.2-m (40-ft)-long driver tube and a 15.2-m (50-ft)-long driven tube, as a short-duration source of heated air, driving the test-section device mounted near the exit of the primary shock-tunnel nozzle. The receiver tank is initially evacuated to a pressure of approximately 1 torr to minimize the starting air load on the turbine wheel and to improve the flow-establishment characteristics of the model. The test-section device, shown schematically in Figure 7, consists of a forward transition section with a circular opening facing the supersonic primary nozzle flow. The circular opening is followed by a complete 360 degree annular passage containing the NGV. The LTA was focused on mid annulus at a location approximately 0.046-m (1.8-in) upstream of the NGV. Figures 8 and 9 are photographs of the LTA set up and optical locations, respectively.

A cylinder of 0.00878-m (0.375-in) diameter with eight thin-film gages located on a stagnation line was placed across the flow channel at 0.046-m (1.8-in) upstream of the NGV, primarily to measure the uniformity of the flow across the channel for each experiment. A secondary use of these rake data was to infer the freestream turbulence intensity in the flow entering the NGV for comparison with the LTA data obtained here. It was recognized (6) that turbulence intensity data obtained in this manner are only approximate, but to date are the only values available for comparison. Hot wire measurements can be obtained in the future in these tests for comparison with both the LTA and the film gage measurements. The hot wire measurements cannot be used later in combustion driven flows whereas the LTA measurements can be used for comparison of the shock tube driven flows with combustion driven flows. A photograph of this rake is shown in Figure 10. Figure 9 shows the location of the rake relative to the LTA.

Figures 8 and 9 illustrate that access to the turbine stage is via two separate windows. The outer window is 0.18-m by 0.41-m by 0.0063-m thick (7-in by 16-in by 0.25-in thick) and the inner two windows are 0.051-m diameter by 0.0063-m thick (2-in diameter by 0.25-in thick). The material is float glass, flat and parallel to one wavelength at 5145 Å over 0.0031 to 0.0127-m diameter (0.125 to 0.50-in diameter). The transmission of the window material for normal incidence was in excess of 90%. The volume between the outer window and the inner windows is protected from the by-pass tunnel flow by a shroud. To reduce the flare coming from the model wall, a tiny cone cavity similar to that described in Section 2.1 was machined in the wall and the surroundings were painted flat black (see Figure 9). The LTA optics used in the Calspan experiments were essentially the same as those used at AFIT.

2.2.1 Introduction of Seedant Material into Test Gas

Several runs were made at Calspan to obtain LTA data without introducing seed material into the test gas. These runs resulted in inadequate signal to noise ratios to the photomultiplier tubes. The introduction of either propylene glycol or Dow 200 as additional particle sources was pursued. Dow 200 was used in several of these measurements since its vaporization temperature is significantly higher than that of propylene glycol. Dow 200 has a flash point of 1029°R and a very low vapor pressure. A sample of Dow 200 was heated in a furnace to 928°R, soaked for 5 minutes, and then allowed to cool for 5 minutes. The sample lost 9.1% of its weight and exhibited no change in color. The introduction of seed material for the experimental conditions of interest required modifications to the atomizer system. The maximum total temperature of the shock-driven flow was 1000°R at a pressure of approximately 100 psia at the NGV inlet or at a pressure of 1100 psi (also a temperature of 1000°R) in the reflected-shock reservoir.

The Dow 200 particle size distribution was measured by TSI, Inc. The measurement employed two analyzers; an electrostatic analyzer to measure particles with diameters less than one micron and an aerodynamic analyzer to measure particles with diameters greater than 0.5 micron. A TSI, Inc. aerosol generator model 9036 atomized the Dow 200 using a single jet with a nominal 5 to 10 second on time, a dilution flow setting of 15 on the flow meter, and a dilution pressure of 60 psi. The aerosol generator and the flow settings for the particle distribution measurements were similar to those used in the Calspan tests. The seed and dilution flow filled a plastic reservoir with a volume of approximately 2.5 cubic feet. Two sample tubes, one for each analyzer of 1/4-inch diameter polyflow tubing, also penetrated the sample volume as shown in Figure 11.

The sample volume was filled and 6 samples were taken at one minute twenty second intervals with a measurement sample time of 10 seconds for the aerodynamic analyzer measurements. Three of the interval measurements for the aerodynamic samples are shown in Figure 12. The distribution remained constant in both magnitude and shape with a peak at 0.626 microns. For the shock tube measurements, the driven tube was filled and the atomized seed was introduced into the driven tube just prior to the shot. The shot normally occurred within one to three minutes after the seed material injection. The seed material can, therefore, be expected to maintain its particle size distribution for the shock driven flow for at least the pre-shock arrival time period.

The electrostatic analyzer results are shown in Figure 13. The electrostatic measurements indicated a peak for numbers of particles at 0.467 micron, a peak by concentration at 0.563 micron, and a peak by volume concentration at 0.603 micron. There was a slight indication of a secondary peak at 0.058 micron in the number distribution. The electrostatic analyzer measurements were made with full dilution flow on during the

measurement and the seed flow off after an initial burst of a few seconds. The dilution flow was necessary to maintain the reservoir conditions since the electrostatic analyzer is considerably slower in collecting the individual channel data.

The aerodynamic analyzer as well as the electrostatic analyzer have indicated that the Dow 200 has a very stable submicron particle distribution with a peak at an effective nominal value of .5 to .6 microns. It was concluded that Dow 200 was a good choice as a seed material for the 1000°R maximum total temperature associated with the experimental conditions.

The same TSI, Inc. Model 9306 Six Jet Atomizer that was used at AFIT was used at Calspan to introduce the seed material. In a normal configuration, the atomizer is at room temperature and pressure conditions and is injected into an environment that is on the order of one atmosphere pressure. However, because of the much higher pressure conditions existing in the Calspan shock driven flow, it was necessary to construct a vessel capable of being pressurized to house the entire atomizer. In this way, a differential pressure on the order of 10 to 20 psi could be maintained on the atomizer thus permitting introduction of the seed material into the driven-tube gas just prior to running the experiment (initial driven-tube pressure was 150 psia) or it could be injected tangentially into the model flow just upstream of the NGV using a configuration illustrated by the schematic of Figure 14. Both of these injection techniques were found to be acceptable with either propylene glycol or Dow 200, provided that the injection pressure was maintained at a value of approximately 5 psi in excess of that of the local flow field into which the seed material was being injected. If the atomizer were not pressurized, then the flow of seed material would stop when the test gas arrived.

2.2.2 Initial Adjustments of Laser Transit Anemometer

As mentioned in Section 2.1, it was necessary to set up the LTA using a continuous flow in order to select the proper flow angle. One of the stringent requirements of LTA measured flows is that the spot alignment with the flow must be within 1-1/2 degrees for the lens combination used. The continuous flow atmospheric alignment and base line settings were established using a flow tube inserted into turbine inlet. Full annulus flow was not available for alignment during the LTA test period. The continuous-flow calibration technique was one of the weakest links of the procedure. A large blower capable of supplying 8500 cfm at a few inches of water-head has recently become available for use in this calibration. This device would supply continuous air flow to the entire turbine annulus at the proper flow velocity. Neither the total pressure nor the total temperature environments would be duplicated but, for the purposes of spot alignment, having continuous uniform flow through the entire annulus at the proper velocity would be adequate.

2.2.3 Pre-Run Calibrations in AFIT Shock Tube

A continuous-flow measurement is shown in Figure 15 using the single-cone wall termination and an event time of 10^8 events. The measured velocity is 222.8 meters per second and the turbulence intensity is 6.6% for the measurement in Figure 15. Normalized velocity and the turbulence intensity measurements for continuous flow are shown in Figures 16 and 17 as the event time is reduced from 10^9 to 10^4 . The resulting velocity showed a spread of 2% to 4% as the event time was reduced. Some of this spread could be attributed to the non-steady reservoir conditions. Turbulence intensity showed a spread of approximately 1% across the range, with up to 1/2% attributable to the mean velocity variations. Lower turbulence levels were observed with constant LTA sensitivities and seed flow at a constant velocity, but these cases were clearly deficient in data and not an inherent problem.

2.2.4 Pre-Run Calibration in Calspan Turbine Model

As discussed above, a continuous-flow calibration was also necessary prior to running a LTA experiment in the turbine model. Figure 18 is a typical result of such a calibration for an event time of 10^4 . For this figure, the measured velocity was 88.41 meters/sec, the turbulence intensity was 3.35%, and the data/background ratio was 20.16.

3.0 Discussion of the Results

3.1 LTA Measurements in the AFIT Shock Tube

The general procedure was to load the driver tube to its operating pressure (the range of pressures used here was 45 to 65 psia), start the correlator manually with one photomultiplier input channel gated off, inject the seed material manually into the driven tube at atmospheric pressure for a predetermined length of time, from 5 to 15 seconds. The diaphragm was then broken, initiating the shock wave in the tube. An Endevco pressure transducer located in the test section detected passage of the shock wave and generated a trigger pulse from a Berkley model CT-2 gate generator. This trigger pulse was used to start the LTA's gate circuit with a programmable delay and gate width. A delay of 1 millisecond and a gate width of 15 milliseconds was used for the AFIT measurements, just allowing the slowest shock to pass the LTA test section. The location of the LTA generated gate relative to the sidewall pressure in the test section is illustrated in Figure 19.

As noted earlier in Section 2.1, and demonstrated by the pressure record shown in Figure 19, the gate duration exceeded the ideal shock-tube test time. For this particular test condition, the elapsed time (at a fixed shock-tube location) between the shock wave and the interface was on the order of 4 milliseconds. Recall that the static pressure does not change at the interface for the driver technique used here. Wave diagram calculations suggest that the rather abrupt decrease in pressure illustrated in Figure 19 is the result of a rarefaction wave originating at the open end of the tube at the dump tank location. For the feasibility study, the non-uniformity in pressure could be removed by adding length to the test section. It is mentioned here only because we believe that the rarefaction wave could contribute to the magnitude of the turbulence intensity measured in these experiments, giving a value somewhat larger than would be associated with this actual test-time portion of the shock-tube flow. The pressure transducers used for calculation of shock speed are spaced 0.058-m (2-in) apart in the test section of the tube and 0.0508-m (2-in) behind the trigger transducer.

A measurement of flow velocity and turbulence intensity with test gas is shown in Figure 20. This run used a seed fill time of 10 seconds and a 15-millisecond gate. The measured velocity for this run was 192.6 meter/sec and the turbulence intensity was 10.2%. There were 6760 good data samples in this measurement and a background noise level of 130 samples for a signal to noise ratio of 51.8. Continuous-flow measurements in similar long-duration (10^7 to 10^8 event times) experiments give a signal-to-noise ratio of 562 to 1944. In general, 3000 to 6000 valid samples are needed to make a good measurement in the shock-tube driven flows. This means that we need to have a higher data rate, by approximately 16 times, than would normally be used in setting up a continuous measurement. The individual continuous photomultiplier data rates are a factor of nearly 10 greater than the valid data rate for the shock-tube measurements shown in Figure 20. The desirable percentage of seed-to-test-gas for the shock-driven measurement is on the order of 10^{-12} %. The photomultiplier settings and the background noise suppression level (threshold) settings for the shock-driven flows were initially taken as the values obtained in the continuous-flow setup with a 15-millisecond gated pulse. We tended to get better results in setting up for continuous flow by maximizing the correlation growth rate on the 10^5 to 10^6 event scales and then making small adjustments in threshold and photomultiplier levels for the 10^3 to 10^4 scales. This procedure generally would result in a higher signal rate on the downstream spot by a factor greater than 2. Additional small adjustments to both the threshold and the photomultiplier settings were necessary to obtain the shock-flow measurements because the density of the shock flow was 1.8 times that of the continuous-flow.

The flow velocity data obtained at AFIT with the LTA in the shock-driven flows are in good agreement with the predicted flow velocities. Shock tube theory was employed to determine the Mach number in the 0.10 x 0.20-m drive-tube section and (8) was used to calculate the Mach number in the 0.0254-m square test section. Constant specific heats for the test gas was assumed for this analysis. A comparison between the measured and calculated flow velocities is given in Figure 21. The measured velocities are a little less than predicted at the lower diaphragm pressure ratios but become higher than the predicted values at the higher pressure ratios. Expansion of the flow as shown in Figure 19 after approximately 4 milliseconds would result in measured velocities higher than predicted by theory. This effect would be more pronounced at the higher Mach numbers associated with the higher diaphragm pressure ratios.

3.2 LTA Results Obtained Using Calspan Turbine Model

LTA measurements performed to date for this configuration were obtained at a location approximately 0.0457-m (1.8 in) upstream of the NGV inlet. Data were obtained for the cases of: (1) no seed material added to the flow, (2) seed material injected at a single location in the model annulus just upstream of the NGV, and (3) seed material added to the driven-tube test gas just prior to diaphragm rupture. Either propylene glycol or Dow 200, injected under pressure, was used as a seed material and both were found to be satisfactory. LTA measurements performed for non-pressurized injection of seedant revealed that the seed material could not penetrate the test gas. Useful signal to noise ratios were achieved for the pressurized injection techniques, for items (2) and (3) above, and will be described.

3.2.1 Pressurized Injection of Seedant Just Ahead of NGV

The injection technique illustrated in Figure 14 was used to introduce seed material into the flow at a location just ahead of the NGV. On the basis of previous work with this model, the flow velocity at this location is known to be approximately 75.5 m/sec (247.5 ft/sec) and the turbulence intensity determined from the stagnation point heat-flux rate was approximately 5.7%. Figure 22 presents the time history of the following measured quantities, from top to bottom: (1) the gate duration, (2) the monitor signal for photomultiplier B, (3) the monitor signal for photomultiplier A, (4) EP4, the static pressure on the bullet nose just ahead of the NGV, (5) the LTA discriminator signal B, and (6) the LTA discriminator signal A. Dow 260 was used as the seedant for the run shown in Figure 22. The recorded time histories for the continuous flow calibration which was illustrated in Figure 18 is shown in Figure 23 for comparison with the shock-driven-flow time histories.

The seed flow was initiated approximately 1 second prior to the arrival of the test gas, was continued for the duration of the experiment, and the vessel containing the

atomizer was pressurized to approximately 120 psia. The pressure field within the model, as indicated by the EP4 trace, was uniform during the time that the gate was active. The LTA channel A and B monitors both indicate that the seedant was being actively injected into the flow and that useful signals were being obtained. For this particular run, the indicated flow velocity was 77.5 m/sec and the turbulence intensity was 9.65. Although this result was felt to be encouraging, it was not considered to be accurate because very few samples were counted. The value of the data rate/backscatter rate was 19.5, which is low but not unacceptable. Figure 14 shows that injection in this manner is not a particularly good technique because the seed material must mix through the boundary layer which usually results in a higher concentration of seedant in the boundary layer. Continuous flow to set up the seedant flow rate would be required since the actual distribution of seedant is uncertain. Therefore, an alternate technique of injecting the seedant into the driven-tube test gas just prior to diaphragm rupture was investigated and will be described in the next section.

3.2.2 Pressurized Injection of Seedant into Driven-Tube Test Gas Just Before Running

To obtain a more uniform dispersion of the seedant material into the test gas and thus relax some of the injection requirements, we elected to inject into the driven-tube gas just prior to breaking the diaphragm. The initial driven-tube pressure was approximately 150 psia, requiring that the atomizer be pressurized. Figures 24 and 25 represent a comparison of the LTA output signals on the same time-base as the pressure history, EP4, obtained just ahead of the NGV. For this run, the seed material, Dow 200, was loaded for a period of 22 seconds prior to the run. The 22 seconds was the scaled time required to obtain the same mass of seedant loading as was used in the AFIT shock tube. Figure 24 illustrates that the pressure field was uniform during the laser-gate period. The same data shown in Figure 24 are displayed using a variable time base in Figure 25 with the gate-on time at an expanded time-base. The initial portion of the record is displayed at 4 ms/div; then the time-base is stretched to 0.08 ms/div instead of the 2 ms/div used on Figure 24. Figure 26 is the correlator print-out for this particular run. The LTA result indicates a velocity of 82.2 m/sec and a turbulence intensity of 4.62%, compared to the target values of 75.5 m/sec and 5.7%. The ratio of data rate/backscatter rate was not particularly good at a value of 7.3. To obtain acceptable data, this value would have to be increased significantly but we believe that with improved calibration and laser alignment techniques, this increase can be achieved.

4.0 Conclusions

The feasibility of using the LTA to obtain useful velocity and turbulence intensity data in a short-duration flow environment has been demonstrated. The velocity measurement appeared unaltered by shortening of the measurement time; whereas the indicated turbulence intensity showed an approximate increase of 10% for continuous-flow measurement.

The data obtained in the shock-tunnel model demonstrate that seedant can be injected and dispersed uniformly into these relatively high-pressure environments. Seedants useful in the 1000°R environment were demonstrated and a sufficient data rate can be achieved to allow flow velocity and turbulence intensity measurements to be made in these short-duration environments. The initial indications of velocity and turbulence intensity, without prealignment with the flow direction, are in agreement with computed values.

REFERENCES

1. Dunn, M. G. and Stoddard, F. J., "Application of Shock-Tube Technology to the Measurement of Heat-Transfer Rate to Gas Turbine Components," 11th International Symposium on Shock Tubes and Waves, July, 1977.
2. Dunn, M. G. and Stoddard, F. J., "Measurement of Heat Transfer Rate to a Gas Turbine Stator," J. Engineering for Power, Vol. 101, No. 2, April, 1979 (also see ASME Paper No. 78-GT-119).
3. Dunn, M. G. and Hause, A., "Measurement of Heat Flux and Pressure in a Turbine Stage," J. Engineering for Power, Vol. 104, No. 1, January, 1982 (see also ASME Paper No. 81-GT-88).
4. Winstanley, D. K., Booth, T. C., and Dunn, M. G., "The Predictability of Turbine Vane Convection Heat Transfer," Paper No. AIAA-81-1435, presented at the AIAA/SAE/ASME 17th Joint Propulsion Conference, July 27-30, 1981, Colorado Springs, CO.
5. Dunn, M. G. and Holt, J. L., "Turbine Stage Heat Flux Measurements," Paper No. 82-1289, AIAA/ASME 18th Joint Propulsion Conference, June 21-23, 1982, Cleveland, OH.
6. Dunn, M. G., Rae, W. J., and Holt, J. L., "Measurement and Analysis of Heat-Flux Data in a Turbine Stage: Part I: Description of Experimental Apparatus and Data Analysis and Part II: Discussion of Results and Comparison with Predictions," J. of Engineering for Power, Vol. 106, No. 1, January, 1984, pp. 229-240.

7. Dunn, M. G., "Turbine Heat-Flux Measurements: I. Influence of Slot Injection on Vane Trailing Edge Heat Transfer and II. Influence of Rotor on Vane Heat Transfer," 29th Inter. Gas Turbine Conference, paper No. 84-GT-175, June 3-7, 1984, Amsterdam, The Netherlands (also accepted for publication in J. of Engineering for Power).
8. Witham, G. B., "On the Propagation of Shock Waves Through Regions of Non-Uniform Area of Flow," J. Fluid Mechanics, Vol. 4, pp. 337, 1958.

ACKNOWLEDGEMENTS

Dow 200 particle size distributions were not available in the literature. We would like to express our appreciation to TSI, Inc. for providing these measurements.

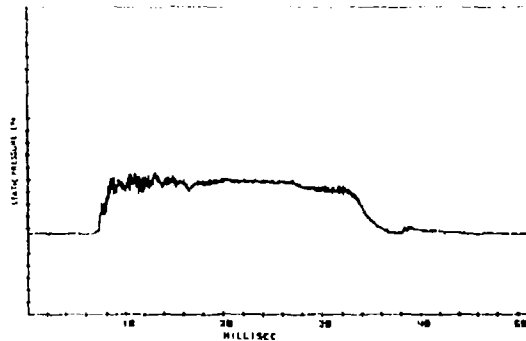


Figure 1. Typical Pressure Record Obtained Just Upstream of Nozzle Guide Vane

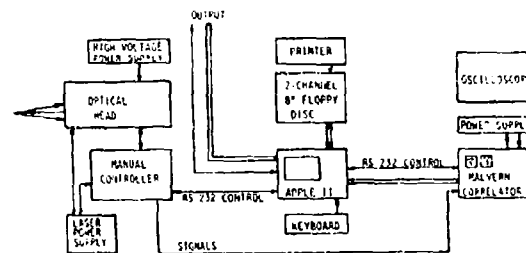


Figure 4. Schematic of Spectron Laser Transit Anemometer



A. ALTERNATE LASER BEAM TERMINATION DESIGNS

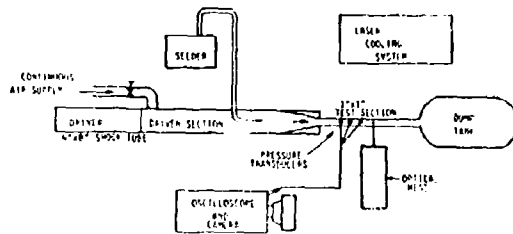


Figure 2. Schematic of AFIT Shock-Tube-Flow System

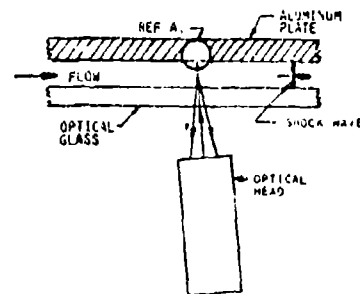


Figure 5. Laser Beam Terminations Investigated for AFIT Shock-Tube Measurements

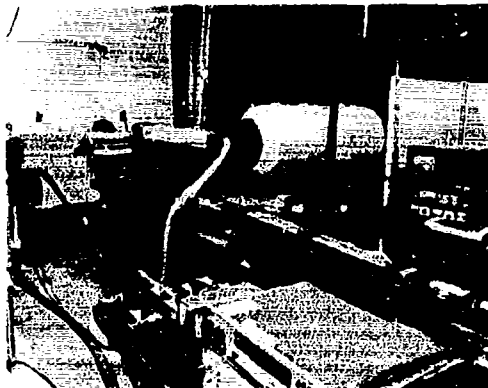


Figure 3. Photograph of AFIT Shock-Tube Test

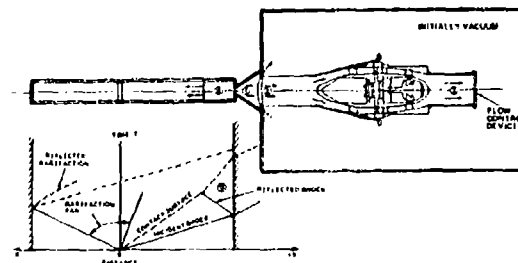


Figure 6. Schematic of Calspan Shock-Tunnel Apparatus

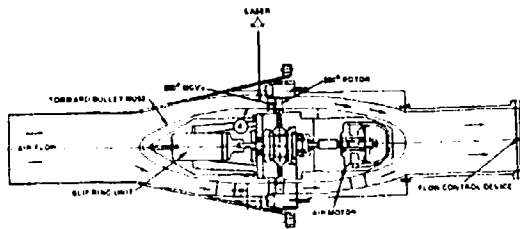


Figure 7. Schematic of Test-Section Apparatus for Full-Stage Turbine Experiments

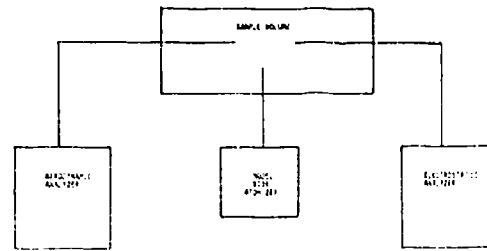


Figure 11. Schematic of the Measurement of Dow 200 Particle Size from Model 9036 Atomizer



Figure 8. Photograph of Laser Set Up from Outside of Vacuum Tank



Figure 9. Photograph of LTA Access Windows at Model

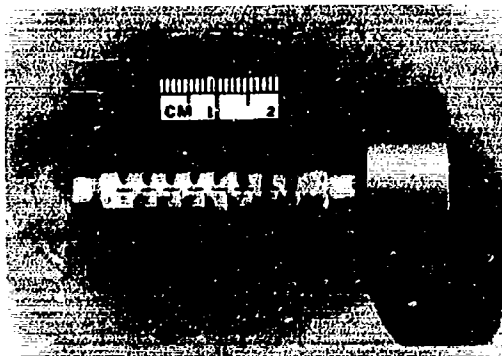


Figure 10. Photograph of Stagnation Point Heat Flux Rake

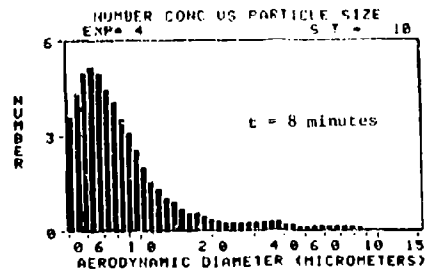
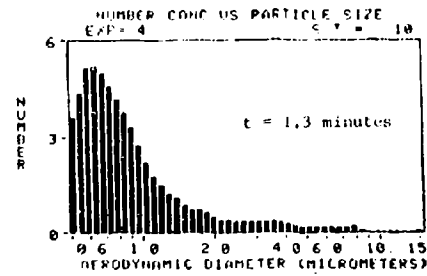
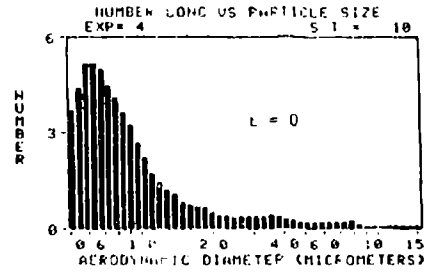


Figure 12. Aerodynamic Analyzer Interval Measurements

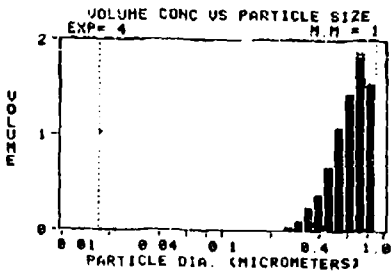
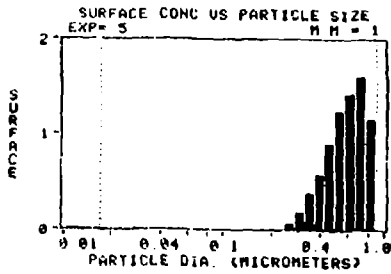
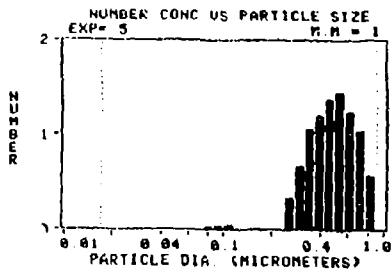


Figure 13. Electrostatic Analyzer Measurement

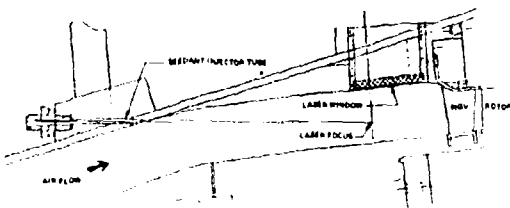


Figure 14. Sketch of Seedant Injection Technique at Location Just Ahead of NGV

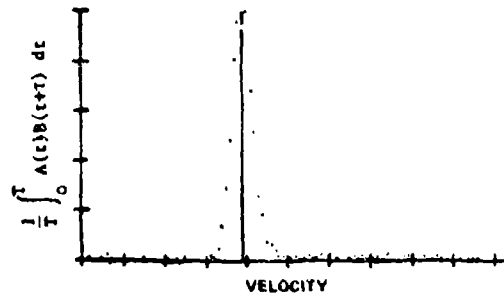


Figure 15. Results of a Continuous Flow Measurement in the AFIT 0.254 x 0.0264-m Test Section

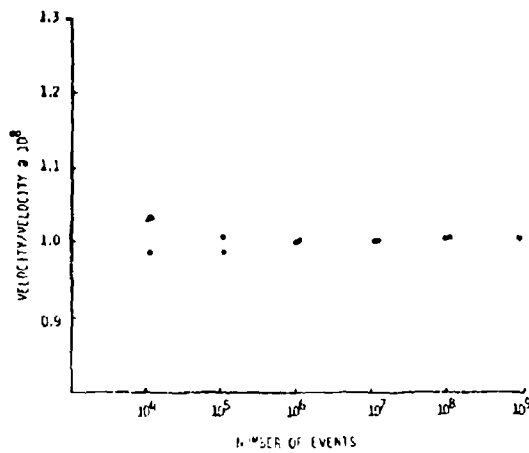


Figure 16. Velocity Dependence on Event Time

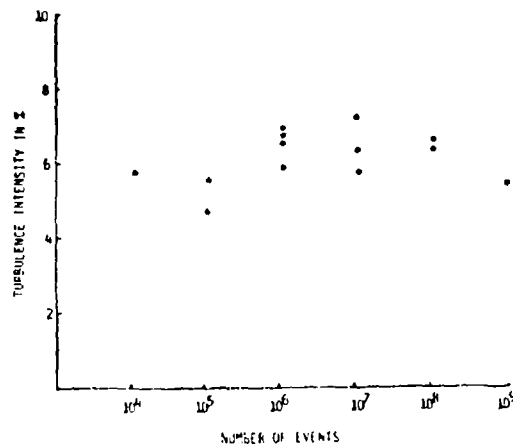


Figure 17. Turbulence Intensity Dependence on Event Time

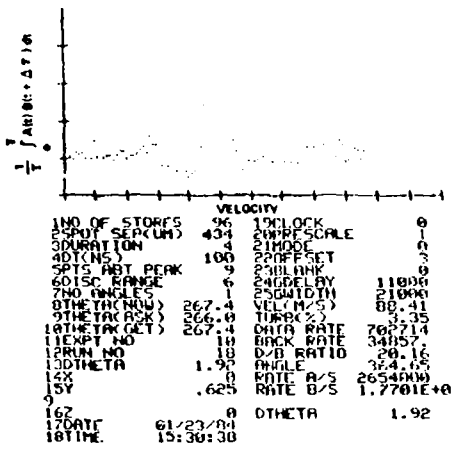


Figure 18. LTA Record for Continuous Flow Calibration in Calspan Set Up

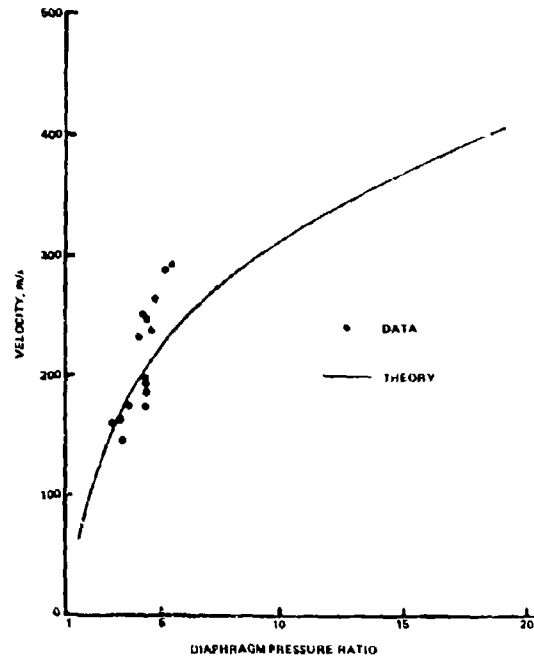


Figure 21. Comparison Between LTA Measured and Predicted Flow Velocities for AFIT Shock-Tube Measurements

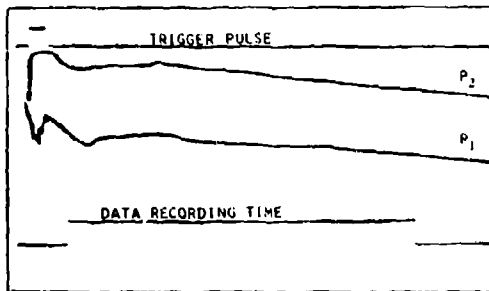


Figure 19. AFIT Shock-Tube Pressure History and Gating Pulse

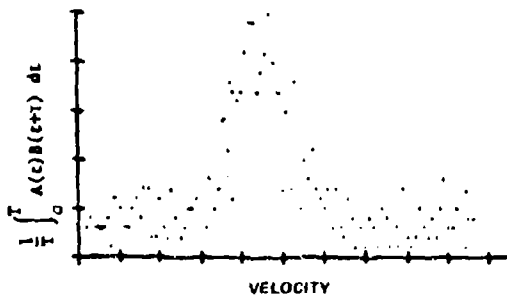


Figure 20. LTA Measurement for Shock-Driven Flow in AFIT 0.0254 x 0.0254-m Test Section

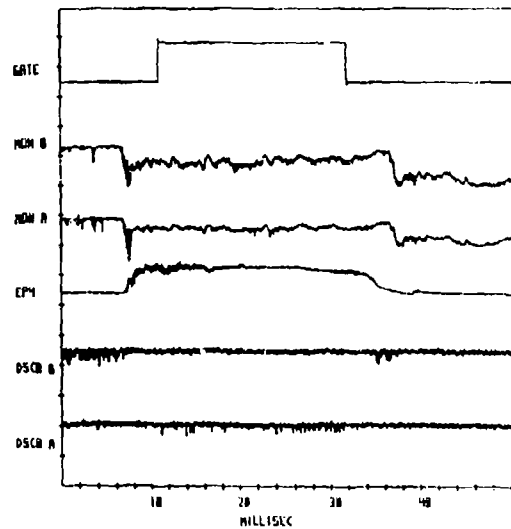


Figure 22. LTA Measurement in Full Stage Turbine Model at a Location Just Head of NGV

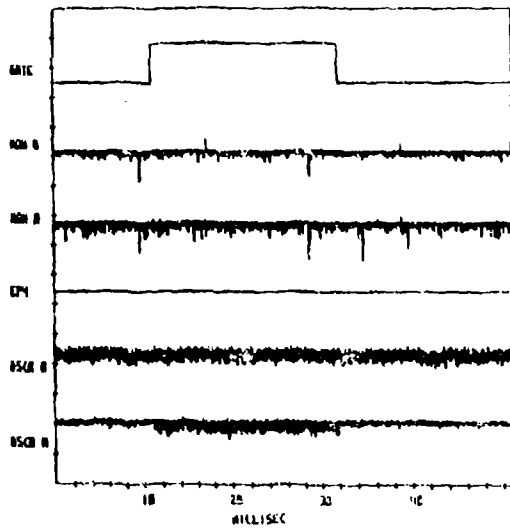


Figure 23. Results of a Continuous Flow Calibration in Calspan Turbine Model

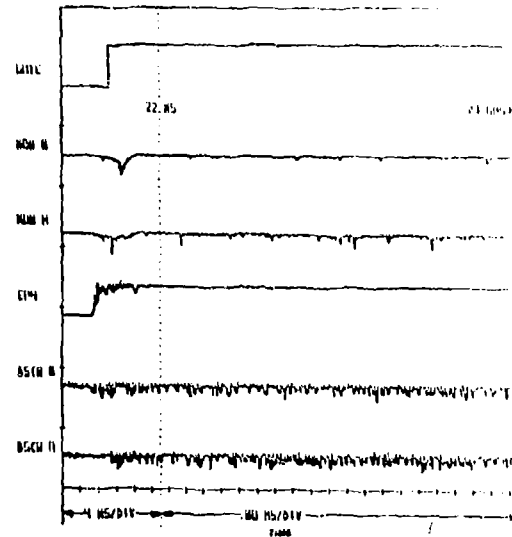


Figure 25. LTA Measurement in Full Stage Turbine Displayed on Dual Time Base

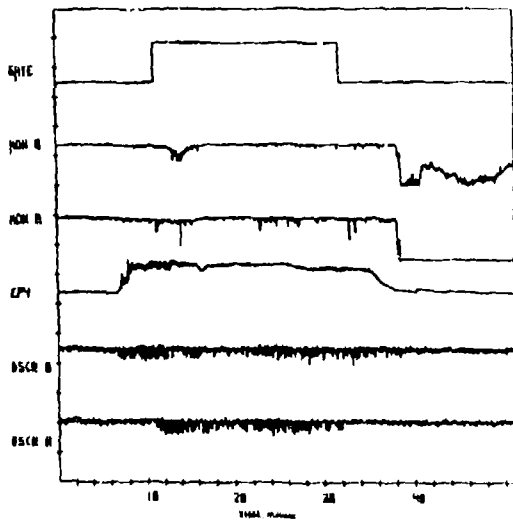


Figure 24. LTA Measurement in Full Stage Turbine Model at a Location Just Ahead of NGV

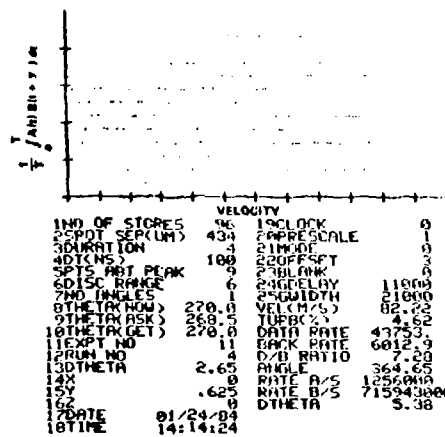


Figure 26. LTA Data Record for Shock-Tunnel Measurement

DISCUSSION

P. Ramette, Fr

Have you already done laser velocimetry measurements inside the rotor blade channels?

Author's Reply

No, we have not yet attempted measurements in the rotor for the shock driven turbines. The program of course is the prealignment of the two measurement volumes with the flow prior to the shot; we will make these measurements in the shock driven turbine in the future.

S. Wittig, Ge

A major advantage of the L2F technique in comparison to the LDA is its capability to make measurements close to the wall. Do you feel that there is a chance to determine boundary layer properties — i.e. turbulence intensities etc. — in your facility using the L2F instrument?

Author's reply

We would only make turbulence measurements in the freestream in the shock driven turbine flows. I think it is not possible to make boundary layer measurements in the shock driven turbine flows. The time required to make these measurements are made much better in continuous large scale facilities.

INFLUENCE ET MESURE DU JEU EN BOUT D'AUBES DANS LES TURBOMACHINES

par Jacques PAULON

Office National d'Etudes et de Recherches Aéronautiques
29, avenue de la Division Leclerc
92320 CHATILLON (France)

Résumé

L'évolution du jeu entre l'extrémité des aubes et le carter d'une turbomachine est un paramètre important pour les performances d'un moteur. Quelques exemples permettent d'illustrer et de chiffrer les effets de ce jeu.

Il serait donc souhaitable de pouvoir le contrôler de façon permanente et d'asservir thermiquement les carters pour fonctionner dans les conditions optimales.

A cet effet un capteur capacitif est en cours de développement à l'ONERA et les résultats obtenus, comparés à un appareil de conception différente, se sont révélés encourageants.

INFLUENCE AND TIP CLEARANCE MEASUREMENT IN TURBOMACHINES

Abstract

The clearance between the tip of the blades and the casing of a turbomachine is an important parameter. The performances of an engine are strongly subject to tip clearance. These gap effects are illustrated and numbered through some examples.

Then, it would be desirable to control it permanently and to adjust the temperature of the casing in order to operate in optimum conditions.

To this effect, a capacitive transducer is in development at ONERA and good results have been obtained in comparison with a various device.

NOTATIONS

d = débattement m

f = fréquence de passage des aubes Hz

G = débit kg/s

h = partie de hauteur d'aube par rapport au moyeu m

H = hauteur d'une aube m

j = jeu m

N = vitesse de rotation t/mn

P = pénétration m

R = rayon m

T = température génératrice K

U = vitesse périphérique m/s

 η = rendement Π = taux de compression

1 - INTRODUCTION

Des progrès considérables ont été obtenus au cours de ces dernières années dans la définition et la mise au point de turbomachines à hautes performances et à rendements élevés. Ces améliorations ont pu être atteintes grâce au développement rapide des méthodes d'analyse mais aussi grâce à la mise en service de moyens de mesures sophistiqués qui permettent aujourd'hui d'acquérir de précieux renseignements, hier inaccessibles.

Il devient donc de plus en plus difficile d'accroître le rendement de telles machines de façon notable, sauf en se penchant avec beaucoup de soin sur des points particuliers, encore peu étudiés mais susceptibles de conduire à des gains non négligeables. Parmi ces points particuliers, le jeu en bout d'aubes des compresseurs et turbines est un paramètre important que l'on tente de maîtriser de différentes façons [1].

Après avoir posé le problème et indiqué quels sont les effets du jeu en bout d'aubes sur le fonctionnement des turbomachines nous passerons en revue les moyens en cours de développement pour limiter le jeu que ce soit "passivement" ou "activement" et donnerons des indications sur la méthode capacitive de mesure du jeu en bout d'aubes en cours de développement à l'ONERA.

2 - INFLUENCE DU JEU EN BOUT D'AUBES SUR LES PERFORMANCES D'UN TURBOREACTEUR

Dans un moteur aéronautique classique, les principaux points sensibles aux effets de jeu sont :

- a) le compresseur BP, généralement axial et à performances élevées ; d'où des accroissements importants de température et des effets thermiques sensibles ;
- b) le compresseur HP, qui peut être de type centrifuge et où les jeux sont alors axiaux et surtout tributaires des déformations de la roue ;
- c) et d) les turbines HP et BP où les problèmes sont analogues à ceux rencontrés sur le compresseur BP.

Si maintenant, nous considérons figure 1, le champ de caractéristiques, débit-pression-rendement d'un compresseur axial multistages expérimenté dans deux configurations géométriques différentes, on note que l'augmentation du jeu relatif, se traduit par une perte simultanée de taux de compression, de rendement et de débit.

Les jeux périphériques importants se traduisent par une détérioration de l'écoulement et un travail insuffisant des coupes de tête comme l'illustre la figure 2 qui représente l'angle de sortie de l'écoulement issu d'une turbine HP en fonction de la hauteur relative et du jeu relatif.

La giration résiduelle de l'écoulement, pratiquement nulle sur toute la hauteur de voine, lorsque le jeu relatif est faible, peut prendre des valeurs importantes conduisant jusqu'à des angles de 40° par rapport à la direction axiale lorsque le jeu est plus que doublé. Cet effet se fait d'ailleurs sentir sur environ 30 % de la hauteur des aubes.

Il en est de même pour les compresseurs centrifuges comme le montre la figure 5 qui représente la perte de rendement en fonction du débatement.

Un autre aspect de l'effet du jeu en bout d'aubes concerne la consommation spécifique d'un moteur [2]. A titre indicatif, une perte, dû au jeu en bout d'aubes, de 1 % sur le rendement de chaque étape BP et HP des compresseurs et turbines d'un moteur se traduit par une augmentation de la consommation de 2 à 3,5 % selon le type de moteur. Ce qui a bien sûr un effet notable sur les dépenses d'exploitation [3] [4] [5].

Pour toutes les raisons indiquées ci-dessus, le contrôle du jeu présente donc un intérêt certain, mais le problème est délicat et difficile étant donné que les moteurs sont soumis, à certains moments, à des conditions de fonctionnement sévères caractérisées par des accélérations rapides suivies généralement de décélérations également rapides. Lors de ces périodes transitoires, les différentes parties du moteur ne travaillent pas de la même façon, les problèmes ne sont pas les mêmes au niveau compresseur et au niveau turbine, mais ils ne sont pas non plus les mêmes s'il s'agit d'un compresseur axial ou d'un compresseur centrifuge.

Si nous considérons une accélération rapide depuis le ralenti jusqu'au décollage d'un avion, le diamètre du rotor grossit très rapidement du fait des forces centrifuges et des phénomènes thermiques qui affectent rapidement les aubes.

Ce premier "gonflement" du rotor prend environ le temps nécessaire pour que le moteur atteigne son régime maximum, c'est-à-dire de l'ordre de 5 secondes. Puis le rotor continue à se dilater mais plus lentement. Cette dilatation correspond à la lente expansion thermique des disques qui ont une masse relativement importante et qui se trouvent en dehors de l'écoulement principal. Cet effet thermique lent dure de 5 à 10 minutes.

Contrairement au rotor, le carter, qui n'est pas soumis aux forces centrifuges, se gonfle lentement par effet thermique mais finit par atteindre une augmentation diamétrale plus importante que celle du rotor.

Le résultat de ces dilatations différentes et déphasées est qu'il y a risque de contact entre le rotor et le carter si le jeu à froid ou au départ est trop faible mais également il y aura, en régime de croisière, un jeu plus grand que le jeu de départ, ce qui n'est pas favorable.

Pour illustrer ce qui précède, la figure 3 représente l'évolution des rayons turbine et carter lors de l'accélération d'un moteur ne comportant aucun système de refroidissement ou de contrôle du jeu en bout d'aubes. Dans le cas présenté, le carter est revêtu d'abradable pour protéger le rotor lors de la phase contact avec le carter et pour réduire partiellement le jeu en régime asymptotique.

Il est évident que des phénomènes voisins seraient observés après décélération d'un moteur au régime nominal suivie d'une réaccélération lorsque le carter se serait refroidi tandis que le disque serait encore chaud.

Même si l'emploi de matériaux abradables permet de réduire les jeux en bout d'aubes, une évolution de ceux-ci, telle que le montre la figure 3 laisse à désirer et doit être améliorée. Des méthodes pratiques et efficaces doivent donc être élaborées.

3 - METHODES DE CONTROLE DES JEUX EN BOUT D'AUBES

Un moyen d'influer sur le jeu en bout d'aubes consiste à modifier le comportement thermique des roues et des carters. On peut par exemple envisager une ventilation de la cavité entre les disques par de l'air prélevé en amont. Cette méthode n'est toutefois pas très souple ni très efficace ; c'est pourquoi les efforts ont portés sur les parties fixes ou carters.

Les moyens actuellement en cours de développement sur moteur reposent sur des méthodes de calcul sophistiquées [6] [7] [8] qui sortent du cadre de cet exposé. Nous indiquerons que deux types de contrôle sont développés : contrôle passif et contrôle actif.

3.1 - Contrôle des jeux en bout d'aubes par méthode passive

Les méthodes passives peuvent être envisagées lorsque la zone d'étude est difficile d'accès et d'encombrement réduit. Dans ce cas, le circuit d'air secondaire et le carter externe sont dessinés avec soin et calculés avec précision au point de vue thermique car il n'y a aucune possibilité d'intervention au cours des différents cycles du moteur.

La figure 4 montre un exemple d'application au niveau de la turbine BP d'un moteur MTU de type hélicoptère [9].

Sans entrer dans le détail, nous indiquerons que le dispositif comporte deux anneaux concentriques suspendus élastiquement et séparément. L'anneau interne, de faible masse, est refroidi par de l'air projeté à travers les trous situés dans l'anneau externe. Signalons également que l'anneau interne est recouvert de nid d'abeilles, en guise d'abradable, sur sa face en regard des aubes.

3.2 - Contrôle des jeux en bout d'aubes par méthode active

Les méthodes actives sont envisageables lorsque la place le permet mais elles sont généralement préférables car par principe plus souples et adaptables à des conditions de fonctionnement diverses. Elles consistent à régler la température du carter à une valeur optimale liée au régime du moteur, à l'aide d'un dispositif de refroidissement utilisant de l'air prélevé le plus en amont possible et en liaison avec des méthodes complexes de calculs d'effets thermiques en transitoire prenant également en compte le rotor.

La figure 5 montre un exemple d'application à un étage de turbine BP d'un moteur double flux PW. Le carter turbine est entouré de tubes à travers lesquels l'air de refroidissement est projeté pour amener le carter à la température voulue. Grâce à une régulation par vannes du débit d'air, il est donc possible de contrôler activement la température du carter en fonction du point de fonctionnement.

A titre d'exemple, la figure 6 montre, au niveau d'une turbine dont le carter est refroidi, l'évolution du jeu en fonction du temps lors d'une accélération.

Le carter étant revêtu d'abradable, il y a légère pénétration lorsque l'on atteint le régime de croisière, ce qui permet de fonctionner à jeu pratiquement nul.

Si de telles méthodes actives sont efficaces et utilisables, par contre elles nécessitent des méthodes de prévision sophistiquées pour les calculs thermiques en transitoire et une architecture spécifique des roues comme des carters, qui est obligatoirement source de difficultés.

Une autre façon de contrôler activement le jeu consiste à mesurer en permanence ce jeu et à réguler en conséquence la température carter.

A cet effet, l'ONERA a entrepris la mise au point d'un capteur pour la mesure des jeux en bout d'aubes ; la méthode développée est une méthode capacitive.

4 - CAPTEUR CAPACITIF POUR LA MESURE DU JEU EN BOUT D'AUBES

Diverses tentatives ont été décrites dans la littérature technique pour mesurer les jeux de façon continue [10] [11] [12].

Les capteurs utilisant les courants de Foucault sont rapidement limités à une fréquence de passage des aubes de l'ordre de 4 kHz et à une température de fonctionnement ne dépassant guère 100 C.

A notre connaissance, seule la technique "à électrode" utilisée par ROTADATA [13] a atteint le stade opérationnel et la commercialisation. Toutefois, cette sonde qui nécessite une durée d'échantillonnage de l'ordre de 20 s n'indique que le jeu minimum et ne permet pas d'effectuer des mesures en transitoire.

Quant aux capteurs capacitifs décrits, il ne semble pas qu'ils aient atteint le stade de l'emploi systématique sur machine.

Cette technique capacitive est celle que nous avons également choisie à l'ONERA, car à notre avis, la mieux adaptée aux fréquences élevées de passage des aubes (20 à 30 klz) et aux températures élevées (1000 à 1200 C).

Le principe en est fort simple, puisqu'il consiste à mesurer la variation de capacité existant entre l'extrémité d'une aube et l'âme centrale du capteur lorsque l'une et l'autre sont en regard et que la distance varie entre l'aube et le capteur.

La figure 7 montre un tel capteur dont l'architecture repose sur une technique triaxiale indispensable à l'élimination des effets des capacités parasites liées aux variations de température. D'autre part, une technique particulière de réalisation évite que l'élément sensible du capteur puisse, en fonction de la température, se déplacer par rapport à la gaine externe elle-même, alignée au montage avec la paroi interne du carter.

Une électronique de mesure, associée au capteur, permet de visualiser sur oscilloscope le passage de toutes les aubes et de mesurer chaque 10 tours de roue, le jeu entre le carter et l'aube la plus longue, c'est-à-dire le jeu minimal. L'électronique permet également d'effectuer un étalonnage sur site ou en laboratoire avec un morceau d'aubes identique à celles de la roue considérée.

Comme exemple de résultats obtenus avec un tel capteur, la figure 8 visualise le passage des aubes d'une roue comportant 90 aubes mais également deux secteurs diamétralement opposés, chacun de ces secteurs se composant de 9 aubes de hauteur dégressive par 0,05 mm puis 0,10 mm. L'écart entre l'aube la plus courte et une aube dite longue est de 0,6 mm.

La figure 9 montre l'évolution du jeu minimum mesuré au droit de cette même roue en fonction de la vitesse de rotation ou de la fréquence de passage des aubes. La réduction du jeu, due essentiellement aux effets centrifuges dans ce cas, est bien mise en évidence. Un tel capteur répond jusqu'à une fréquence de passage des aubes de l'ordre de 20 klz et fonctionne actuellement jusqu'à des températures de l'ordre de 600 C. Quant à sa précision, elle est d'autant plus grande que le jeu est petit : de l'ordre de 5 % pour un jeu voisin de 0,2 mm et de l'ordre de 15 % pour un jeu voisin de 0,8 mm.

Pour juger de la validité des résultats obtenus avec ce capteur, des mesures comparatives ont été effectuées, sur la roue précédente, avec une sonde ROTADATA.

Pour des raisons techniques, les mesures n'ont pu être effectuées en même temps avec les deux capteurs mais des précautions ont été prises pour que les conditions de fonctionnement soient les plus voisines possibles. Les résultats obtenus sont représentés sur la figure 10 et l'on observe un recouvrement d'ensemble satisfaisant si l'on ne perd pas de vue que la sonde ROTADATA mesure le jeu minimum tandis que le capteur capacitif numérise le signal maximum qui peut provenir d'une aube un peu plus épaisse mais un peu plus courte que l'aube effectivement la plus longue ; les mesures ne sont donc pas forcément effectuées sur la même aube.

5 - CONCLUSION

Il est clair que les performances aérodynamiques des compresseurs et des turbines des moteurs modernes et particulièrement des machines de petite taille, sont influencées par les jeux en bout d'aubes. Viser à optimiser ce paramètre quelque soit le régime de fonctionnement est donc un objectif important, source possible de gains non négligeables.

Des méthodes passives ou actives de contrôle du jeu en bout d'aubes sont en développement et même en application et conduisent à des résultats positifs. Il semble toutefois qu'un système permanent de mesure du jeu, associé à une technique de contrôle actif permettrait une meilleure optimisation.

Des résultats encourageants et intéressants ont été obtenus sur le capteur capacitif en cours de développement à l'ONERA.

Des améliorations peuvent certes être apportées tant au point de vue précision que domaine d'utilisation vers les hautes températures rencontrées dans les turbines.

REFERENCES

- [1] - HENNECKE, D.K., TRAPPMANN, R.
Turbine tip clearance control in gas turbine engines, AGARD-PEP 60th Symposium on "Engine Handling", Marathon, Greece, 11-14 oct. 1982.
- [2] - HELLMANN, W.
Advanced shaft power engines, IIA-Colloquium on Fuel saving aero-engines for air transportation in the nineties, 24 may 1982.
- [3] - JONES, E.J.
Design to life-cycle costs, integration of engine and aircraft, AGARD Lectures Series n° 107 on The application of design to cost and life cycle cost to aircraft engines, may 1980.
- [4] - APEL, J.R., and WILTSE, D.E.
Applying design-to-life cycle cost methods during engine advanced development, SAE Paper 78 1030, (1978).
- [5] - TIMSON, F.S.
Turbine engine technology and fighter aircraft life cycle cost, AGARD Lectures Series n° 107 on The application of design to cost and life cycle cost to aircraft engines, may 1980.
- [6] - HENNECKE, D.K.
Heat transfer problems in aero-engines, XIV ICHHT Symp. on Heat and mass transfer in rotating machinery, Dubrovnik, Yugoslavia, (1982).
- [7] - ZIENKIEWICZ, O.C., and PARAKH, C.H.
Transient field problems : two-dimensional and three-dimensional analysis by isoparametric finite elements, Int. J. Num. Meth. Engng. 2, pp. 67-71, (1970).
- [8] - KOHLER, W., and PITTR, J.
Calculation of transient temperature fields with finite elements in space and time dimensions, Int. J. Num. Meth. Engng. 8, pp. 625-631, (1974).
- [9] - HOURMOUZIADIS, J., and KREINER, H.B.
Advanced component design basis for next generation medium power helicopter engines, ACARD-CP-302, (1981).
- [10] - SCOTTO, M.J., and EISMEIER, M.E.
High-speed noncontacting instrumentation for jet engine testing, ASME-Gas Turbine Conference, New Orleans, march 10-13, 1980.
- [11] - DOEBELIN, E.O.
Measurement systems : application and design, Mc Graw Hill Book Company, 1966.
- [12] - KNOELL, H., SCHEDL, K., and KAPPLER, G.
Two advanced measuring techniques for the determination of rotor tip clearance during transient operation, 5th ISABE, Bangalore, India, feb. 1981.
- [13] - DAVIDSON, D.P., De ROSE, R.D., and WENNERSTROM, A.J.
The measurement of turbomachinery stator to drum running clearances, ASME Paper n° 83-GT-204.

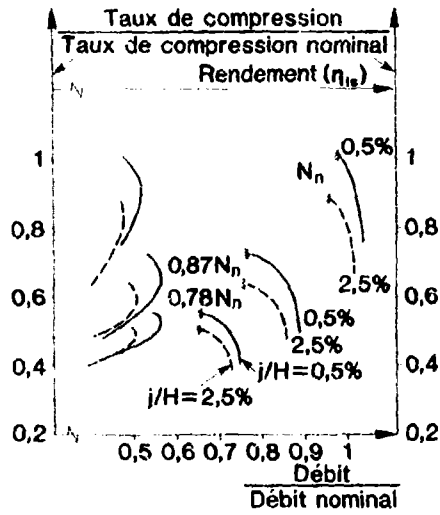


Fig. 1 - Compresseur axial multiétages
Influence du jeu radial en tête des aubes sur le rendement et le taux de compression (les jeux sont indiqués en pour cent de hauteur d'aube)

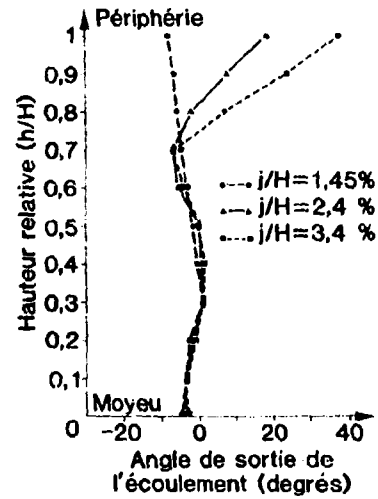


Fig. 2 - Turbine : évolution de l'angle de sortie roue en fonction du jeu relatif en tête d'aube

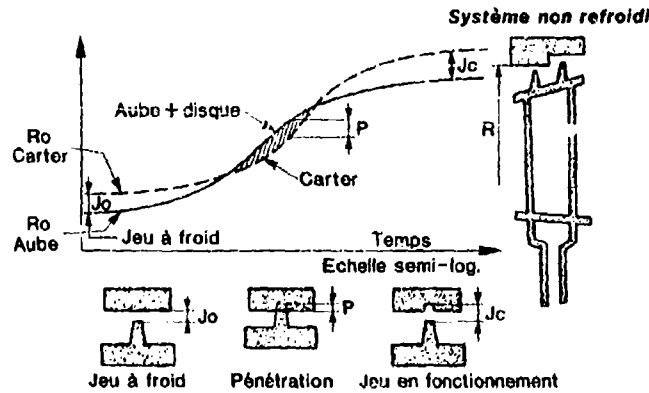


Fig. 3 - Evolution des jeux radiaux turbine lors d'une accélération

Fig. 5 - Exemple d'application d'un système actif de contrôle du jeu en bout d'aubes (turbine PN)

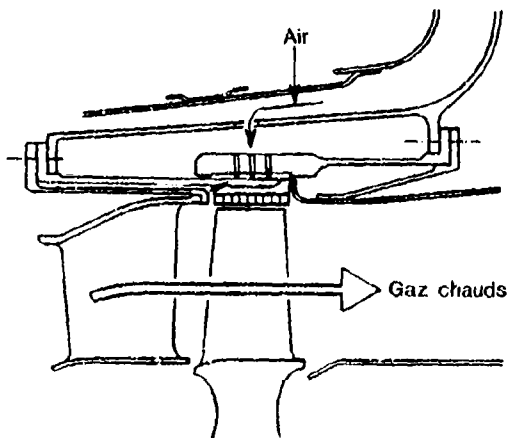
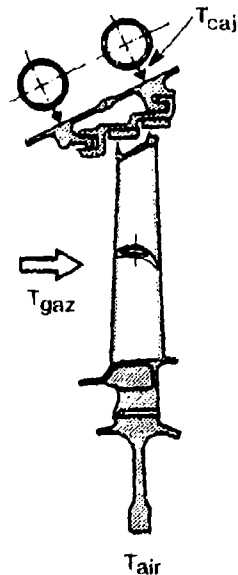


Fig. 4 - Exemple d'application d'un système passif de contrôle du jeu en bout d'aubes (turbine MTU)



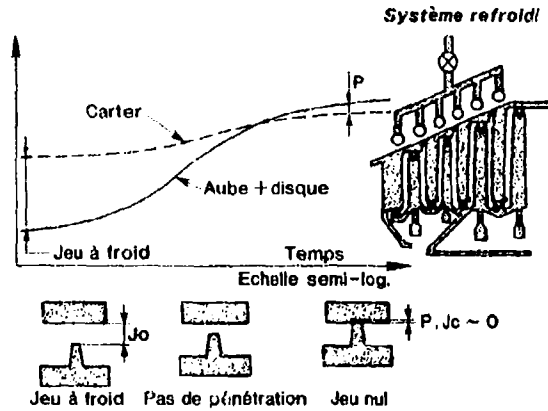


Fig. 6 - Evolution des jeux radiaux turbine lors d'une accélération

Fig. 7 - Vue d'un capteur capacitif pour la mesure du jeu en bout d'aubes

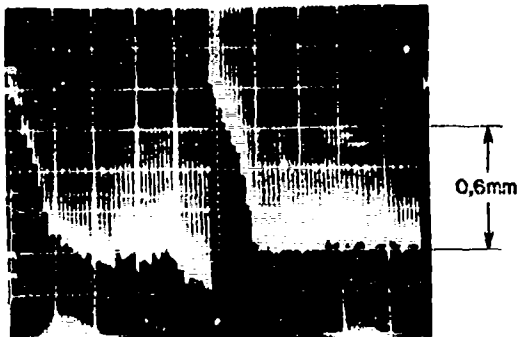
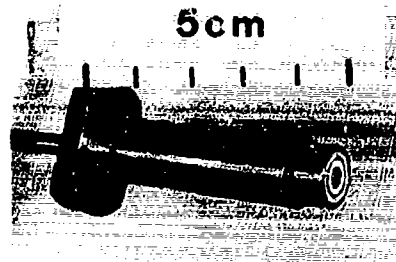


Fig. 8 - Visualisation du passage des aubes d'une roue comportant 90 aubages

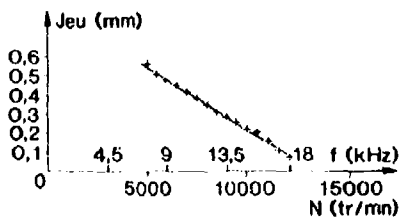


Fig. 9 - Evolution du jeu mesuré entre l'extrémité d'une aube et le carter

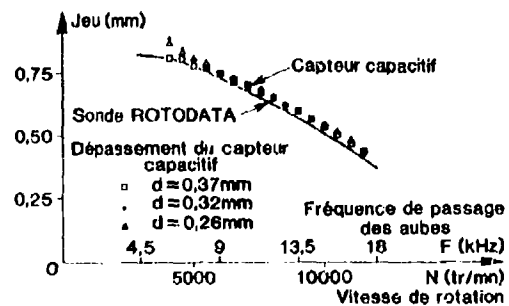


Fig. 10 - Comparaison des résultats bruts de dépouillement des essais par capteur capacitif aux résultats obtenus par sonde rotodata

DISCUSSION

D.K.Hennecke, Ge

At what maximum temperature can you operate the tip clearance probe? Is it already suited for actual use in an engine as part of the control system?

Réponse d'Auteur

La limite d'utilisation est compatible avec des mesures sur turbine mais il faut s'assurer, qu'en fonction de la température, la partie sensible du capteur ne se déplace pas dans un sens ou dans l'autre par rapport à la face de référence constituée par la gaine externe du capteur. C'est uniquement un problème technologique.

L'intérêt final d'un tel capteur est de piloter un système de contrôle actif du jeu.

G.M.Dibelius, Ge

L'étalonnage du capteur capacitif est-il effectué pour les conditions dans la machine ou du laboratoire? Est-ce qu'il y a un effet de température ou de composition du gaz?

Réponse d'Auteur

L'étalonnage est fait sur la machine à l'arrêt ou éventuellement en laboratoire. Nous n'avons pas actuellement d'information sur l'influence de la température du gaz et sur l'influence de la composition. C'est un contrôle qu'il faudrait effectivement faire.

F.Tarada, UK

Have you attempted to predict the variation of tip clearance with rotational speed and thermal conditions using a finite element package or any other predictive device?

Réponse d'Auteur

La variation du jeu avec la vitesse de rotation n'a pas été étudiée théoriquement.

R.Eggebrecht, Ge

One of your examples of power turbines uses a rotating shrouded ring of turbine blades. Do you see possibilities to apply the capacity method to rotating shrouds where you do not have discrete signals, and have you actually done measurements?

Réponse d'Auteur

La technique capacitive peut être appliquée à des mesures de jeu dans le cas de roues à jointe. La mesure est même plus facile car le problème de réponse en fréquence ne se pose plus.

Nous n'avons pas effectué des mesures systématiques dans une telle configuration.

**SIMULATION NUMERIQUE D'ÉCOULEMENTS TURBULENTS
DANS DES CAVITÉS ANNULAIRES ENTRE DISQUES FIXES ET MOBILES**

par

Denis Dutoya
ONERA
29 Avenue de la Division Leclerc
92320 Châtillon sous Bagneux
France

RESUME

Cet article présente les premiers développements d'un code de simulation numérique des écoulements et des transferts thermiques à l'intérieur des cavités annulaires entre disques fixes ou mobiles des turbomachines.

Il comporte une description succincte de la méthode de calcul et du modèle de turbulence utilisé, puis montre quelques exemples de simulations numériques effectuées dans des configurations géométriques simples : calculs d'acoustique dans des cavités, puis de divers écoulements turbulents avec pertes de charges singulières, et enfin simulation d'écoulements dans des cavités annulaires interdisques, alimentées ou non par un débit centrifuge. La confrontation avec des résultats de mesures publiés dans la littérature permet d'apprécier les qualités et les limites de la modélisation choisie pour représenter les phénomènes turbulents.

**SIMULATION OF FLOW AND HEAT TRANSFER IN ANNULAR CAVITIES
BETWEEN DISKS IN TURBOMACHINERY**

This paper presents the first developments of a numerical code for prediction of flow and heat transfer within the annular cavities extending between the rotating and stationary disks of turbomachines.

It presents a short description of the numerical method and of the turbulence model used, and shows a few examples of calculations performed in simple flow configurations : acoustics within cavities, some turbulent flows with singular head losses, and flow calculations in shrouded disk systems with or without radial outflow. Comparison with published experimental data allows to measure the qualities and limits of the chosen turbulent model.

NOTATIONS

a	rayon extérieur du disque rotor (m)
A_0, A_1	sections d'entrée et de sortie
b	rayon du moyeu (m)
c_p, c_v	chaleurs spécifiques à pression et à volume constants (J/K/kg)
C_m	coefficient de couple $2 C / \frac{1}{2} \rho \Omega^2 a^5$
C_p	$= (p_0 - p_1) / \frac{1}{2} \rho U_{max}^2$ avec $U_{max} = \text{Max}(U_0, U_1)$
$C_{p_{is}}$	C_p isentropique (conditions génératrices p_0, T_0 à l'entrée et pression statique p_2 à la sortie)
C_w	$= \dot{m} / \mu a$, débit réduit
c_0	vitesse du son (m/s)
D_0, D_1	diamètres des canaux d'entrée et de sortie (m)
D	tenseur de déformation
E	énergie totale (J/kg)
G	$= \lambda / a$
G_c	$= b_c / a$
H	enthalpie d'arrêt (J/kg)
T	tenseur unité (δ_{ij})
K	énergie cinétique de turbulence
l	longueur de mélange
L	longueur du canal

\dot{m}	débit masse	(kg/s)
\dot{m}_{75}	débit masse isentropique (conditions génératrices p_a, T_a à l'entrée et pression statique p_s à la sortie)	
p	pression statique	
p_s	pression statique de sortie	
p_a	pression d'arrêt d'entrée	
Re, Re_t	nombre de Prandtl (laminaire et turbulent)	
Q^t, Q^c	flux d'énergie totale et de chaleur	
r	rayon	
Re_c	$= \rho U_c D / \mu$	nombre de Reynolds de l'écoulement dans un canal $\phi = D_c$
Re_n	$= \rho \Omega a^2 / \mu$	nombre de Reynolds de rotation
δ	épaisseur de la cavité entre rotor et stator	(m)
δ_c	épaisseur du jeu à la périphérie	(m)
t	temps	
T	température statique	(°K)
T_a	température d'arrêt d'entrée	
\underline{u}	vecteur vitesse	
U_c, U_s	vitesse moyenne à l'entrée et à la sortie du canal	(m/s)
U	composant radiale de la vitesse	(r)
V	" tangentielle	(θ)
W	" axiale de la vitesse	(z)
z	coordonnée axiale	
γ	$= L_r / L_s$	
∇	gradient	
θ	coordonnée azimutale	
μ, μ_t	viscosités laminaire et turbulente	(S.I.)
Ω	vitesse angulaire du disque rotor	(rad./sec)
ρ	masse volumique	(kg/m ³)
τ	pas en temps du calcul	
$\underline{\sigma}$	tenseur des contraintes	
ξ	coefficient de décentrement de l'intégration temporelle	
	<u>Indices</u>	
a	conditions génératrices d'entrée	
s	statique	
o	entrée canal	
i	sortie canal	

1. INTRODUCTION

Les phénomènes de transfert de masse et de chaleur dans les cavités annulaires interdiques des turbomachines ont un effet important sur les performances globales et sur la durée de vie des moteurs : les écoulements qui les traversent participent à la poussée axiale, à la puissance dissipée et aux fuites. Ils conditionnent le refroidissement des disques de turbine, prennent part à l'échauffement du voile du compresseur, et peuvent dégrader l'écoulement principal par soufflage ou par aspiration de fluide au niveau des jeux. C'est aussi à travers ces cavités que la chaleur s'écoule des parties chaudes vers les parties froides, ce qui détermine l'état thermique (contraintes et dilatations) des pièces métalliques, aussi bien en régime permanent qu'au démarrage.

Ces problèmes sont généralement traités de façon globale, à l'aide de corrélations expérimentales et de calculs fondés sur des méthodes intégrales [3] à [11], car la géométrie des cavités, dessinée plus en fonction de contraintes pratiques d'encombrement ou de résistance des matériaux que suivant des critères d'aérodynamique, se prête difficilement aux analyses détaillées. Les écoulements qui en résultent sont en général complexes : tridimensionnels, ils sont le siège de décollements importants,

de mélanges de jets à forte vitesse, d'accéléérations brutales à travers les jeux, et de phénomènes de centrifugation près des parois tournantes. C'est pourquoi les phénomènes irréversibles-mélanges turbulents, dissipation, instabilités diverses jouent un rôle déterminant, aussi bien sur les transferts de chaleur que sur l'écoulement lui-même.

L'étude engagée à l'ONERA, en collaboration avec les sociétés SNECMA et TURBOMECA, comporte un volet expérimental, en cours de réalisation, et une partie numérique, dont on présente ci-dessous les premiers développements.

La simulation numérique a pour objectif de faire la part des divers phénomènes entrant en jeu, de comprendre leurs mécanismes et leurs interactions. Elle repose d'une part sur une technique d'intégration des équations de l'écoulement (Navier Stokes turbulent), et d'autre part sur la modélisation des transferts turbulents. La principale différence avec d'autres études du même type, par exemple [12], [13], et [14], réside dans la tentative de traiter des géométries plus complexes.

Cet article présente les grandes lignes de la méthode de calcul et du code qui en résulte, et montre quelques exemples de simulations numériques effectuées sur des configurations géométriques simples dans le but d'apprécier les qualités et les défauts du code et, éventuellement d'améliorer les hypothèses.

2. LA METHODE NUMERIQUE ET LE CODE DE CALCUL

2.1. Les équations de l'écoulement

L'écoulement tridimensionnel est supposé axisymétrique ($\partial/\partial\theta = 0$) : la masse volumique ρ , l'énergie totale ρE , et les trois composantes de la vitesse \underline{u} , soient U (radiale), W (axiale) et V (tangentielle), ne dépendent que de la position r, z dans le plan méridien, et du temps t . Cette hypothèse allège considérablement les calculs, mais exclut évidemment les injections par orifices discrets, les instabilités tangentielles et les décollements tournants.

Le fluide est un gaz parfait, compressible, visqueux et conducteur de chaleur, avec transferts moléculaires et, éventuellement, turbulents.

Sous forme différentielle conservative, les équations de bilan de l'écoulement peuvent s'écrire :

$$(1) \quad \begin{cases} \frac{\partial}{\partial t}(\rho r) + \frac{\partial}{\partial r}(\rho U r) + \frac{\partial}{\partial z}(\rho W r) = 0 \\ \frac{\partial}{\partial t}(\rho U r) + \frac{\partial}{\partial r}(\rho U^2 r) + \frac{\partial}{\partial z}(\rho W U r) = -r \frac{\partial p}{\partial r} + \rho U^2 + \frac{\partial}{\partial r}(r \tau_{rr}) + \frac{\partial}{\partial z}(r \tau_{rz}) - \tau_{\theta\theta} \\ \frac{\partial}{\partial t}(\rho W r) + \frac{\partial}{\partial r}(\rho U W r) + \frac{\partial}{\partial z}(\rho W^2 r) = -r \frac{\partial p}{\partial z} + \frac{\partial}{\partial r}(r \tau_{rz}) + \frac{\partial}{\partial z}(r \tau_{zz}) \\ \frac{\partial}{\partial t}(\rho V r) + \frac{\partial}{\partial r}(\rho U V r) + \frac{\partial}{\partial z}(\rho W V r) = -\rho U V + \frac{\partial}{\partial r}(r \tau_{r\theta}) + \frac{\partial}{\partial z}(r \tau_{z\theta}) + \tau_{\theta\theta} \\ \frac{\partial}{\partial t}(\rho E r) + \frac{\partial}{\partial r}(\rho U H r) + \frac{\partial}{\partial z}(\rho W H r) = \frac{\partial}{\partial r}(-r q_r^c) + \frac{\partial}{\partial z}(-r q_z^c) \end{cases}$$

$$\begin{aligned} \text{avec} \quad H &= E + p/\rho \\ E &= C_p T/\gamma + (U^2 + V^2 + W^2)/2 \\ p &= (\gamma-1)/\gamma \rho C_p T \\ \text{et} \quad \underline{q}^{bt} &= \underline{q}^c - \underline{\tau} \cdot \underline{u} \end{aligned}$$

Le tenseur des contraintes $\underline{\tau}$ et le vecteur densité de flux de chaleur \underline{q}^c sont la somme des parties laminaires et turbulentes. On définit, par analogie avec la viscosité moléculaire μ , un coefficient de viscosité turbulente μ_t , ce qui permet de relier $\underline{\tau}$ au tenseur des déformations \underline{D} :

$$(2) \quad \underline{\tau} = (\mu + \mu_t) \underline{D} - \frac{2}{3} [k + (\mu + \mu_t) \nabla \cdot \underline{u}] \underline{I}$$

\underline{I} étant le tenseur unité et k l'énergie cinétique de turbulence. De même :

$$(3) \quad \underline{q}^c = - \left(\frac{k}{\rho} + \frac{\mu_t}{\rho} \right) \nabla T$$

La viscosité turbulente μ_t , ainsi que k , sont exprimées en fonction des conditions locales suivant une hypothèse de type longueur de mélange ℓ .

$$(4) \quad \mu_t = \rho \ell^2 (\underline{D} : \underline{D})^{1/2}$$

Enfin, la longueur de mélange est reliée soit à la géométrie de la cavité au voisinage du point considéré avec les constantes classiques, soit à la taille de la maille (volume/surface) suivant la technique de la "turbulence de sous-grille".

Il faut souligner que les hypothèses (2) et (3) de turbulence isotrope sont, au moins autant que la relation (4) exprimant un équilibre statistique local, sujettes à caution dans les zones de décollement.

2.2. La méthode d'intégration

On construit sur le domaine de calcul un réseau qui définit un ensemble de volumes élémentaires, dont la trace sur un plan méridien est rectangulaire (voir figure 1). Un code attaché à chaque cellule définit sa structure :

- cellule fluide de calcul, caractérisée par la masse, l'énergie et la quantité de mouvement tangentielle qu'elle contient,
- cellule fluide d'entrée ou de sortie, permettant l'injection ou l'aspiration de fluide suivant des conditions données (état générateur p_a , T_a , ρ_a ou pression statique p_a par exemple),
- cellule solide (paroi), dont les caractéristiques définissent la vitesse angulaire Ω_p et les conditions thermiques locales désirées.

Le mouvement du fluide dans le plan méridien est défini par les flux de masse ρU et ρW à travers les interfaces x et z entre les cellules.

Le système (1) est discrétisé sur les mailles du réseau suivant une technique de volumes finis [1], qui garantit la conservativité. Afin de limiter la dissipation numérique, les hypothèses permettant d'exprimer les flux d'interfaces sont symétriques (centrées). Entre paroi et fluide, les échanges sont exprimés à l'aide de "lois de paroi", qui pré-intègrent les portions de couche limite correspondantes.

Le système d'équations différentielles ordinaires ainsi obtenu est alors intégré au cours du temps grâce à une méthode implicite linéarisée [1], plus ou moins centrée grâce à un paramètre ξ que l'on peut ajuster de $\xi = 1/2$ (Crank-Nicholson) à $\xi = 1$ (totalement implicite).

Cette méthode permet, en principe, de s'affranchir du critère CFL de stabilité linéaire, et donc de choisir un pas en temps τ en fonction du temps de relaxation le plus grand et non en fonction de l'acoustique locale. Une méthode de factorisation [1] est cependant nécessaire pour remplacer l'inversion de la matrice globale ainsi obtenue par une succession d'inversions de matrices tridiagonales par bloc.

Le code de calcul, nommé ICARE, ainsi obtenu permet d'obtenir, pour une simulation d'écoulement turbulent de nombre de Reynolds égal à un million, une solution stationnaire à partir du repos en 1200 à 1600 itérations, à condition de choisir convenablement le pas en temps τ . Le temps de calcul est de $4.5 \cdot 10^{-4}$ seconde par maille fluide et par itération sur un ordinateur CYBER 170/750. Le nombre de variables à stocker est de l'ordre de 20 fois le nombre de cellules fluides. La géométrie et différents types de conditions aux limites (4 types de parois fixes ou tournantes et 4 types d'entrées-sorties) sont introduits facilement au niveau des données. Le programme permet d'effectuer des calculs 2D plan ou 3D axisymétriques.

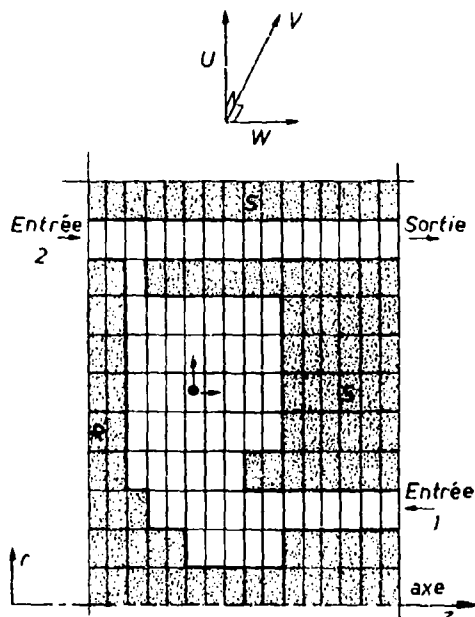


Fig. 1 - Géométrie et réseau de calcul. Exemple : 1 rotor
R - 2 stators S, 3 entrées/sorties

3. PRESENTATION DE QUELQUES RESULTATS DE CALCULS-TEST

Avant d'étudier les configurations de cavités complexes, et en attendant les premières campagnes de mesures sur le banc d'essai, il est nécessaire d'analyser les propriétés de la simulation numérique, et de confronter les résultats du calcul aux données expérimentales disponibles dans la littérature. Plutôt que de nous concentrer sur une configuration unique, nous avons préféré, dans un premier temps, simuler des écoulements de formes les plus diverses possibles, sans entrer dans le détail de chacun des cas considérés. C'est ainsi que sont présentés ci-dessous quelques calculs de principe d'acoustique, puis diverses configurations d'écoulements simples avec pertes de charges "singulières", et enfin des confrontations avec les mesures effectuées dans des cavités annulaires au MIT [6] et à l'Université de Sussex [9], [10], [11].

3.1. Propriétés acoustiques du code ICARE

Un programme d'écoulement prétendant à calculer l'instationnaire doit évidemment être capable de simuler dans ses grandes lignes le phénomène le plus simple : l'acoustique linéaire. Divers calculs ont montré que de ce point de vue, et si on se cantonne au qualitatif, la méthode utilisée n'induit pas de dissipation numérique notable sur les ondes, et restitue les systèmes d'ondes stationnaires bien connus dans les cavités -fermées ou ouvertes à l'atmosphère- autant que le permet la discrétisation spatiale.

La figure 2 montre trois configurations, la première unidimensionnelle, avec un côté fermé et un côté ouvert à l'atmosphère, les deux autres bidimensionnelles. L'excitation des modes est réalisée dans les deux premiers cas par la montée progressive (en 50 itérations) de la pression ambiante, et dans le troisième cas 2C par obturation brutale de l'ouverture de la cavité 2b en cours d'évolution.

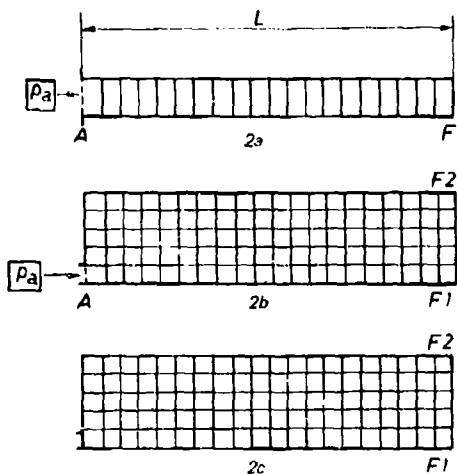


Fig. 2 - Configurations de calculs pour les phénomènes acoustiques.

Les figures 3, 4 et 5 montrent l'évolution périodique de la pression au fond F des cavités, sans dissipation notable au bout de plusieurs dizaines de périodes. Les différents modes apparemment calculés sont à rapprocher des valeurs théoriques, figurées sous forme d'échelles, soient $T_0 = 4L/c$, $T_0/3$, $T_0/5$, ... pour la cavité 2a et $T_0 = 2L/c$, $T_0/2$, $T_0/3$, ... pour 2C. Ces calculs sont effectués pour une valeur du paramètre ξ égale à 1/2. La figure 6 montre qu'un moyen commode d'étouffer artificiellement ces ondes, "mémoires" du processus de démarrage, est de choisir $\xi = 1$.

Enfin, on a pu vérifier que, dans le cas d'un écoulement dans un canal de longueur L, dont l'état générateur p_a, T_a est fixé à l'entrée, et dont la pression statique $p_0 < p_a$ est donnée à la sortie, la solution stationnaire se stabilise au bout d'un temps égal à cinq ou six fois le temps de séjour L/U , résultat qui peut être démontré théoriquement à partir des équations d'Euler. Ce temps peut cependant augmenter considérablement si les phénomènes visqueux ont un effet notable sur la pression à l'équilibre.

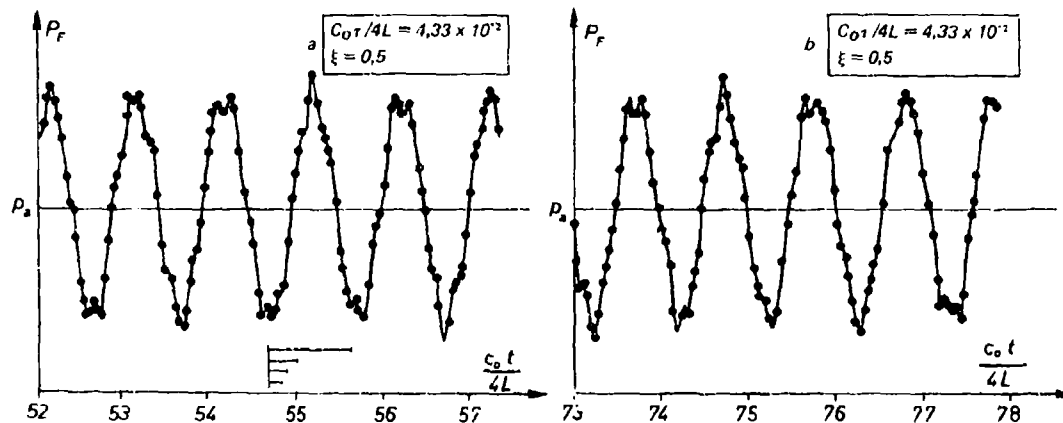


Fig. 3 - Oscillations de pression - Configuration 2a.

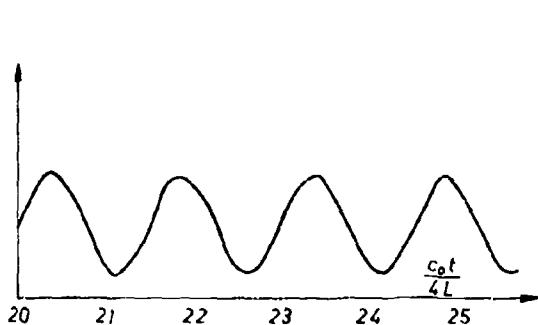


Fig. 4 - Oscillations de pression - Configuration 2b.

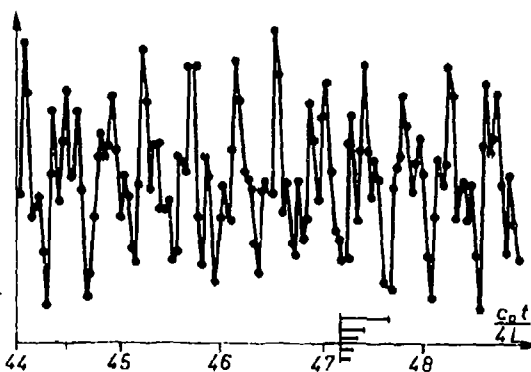
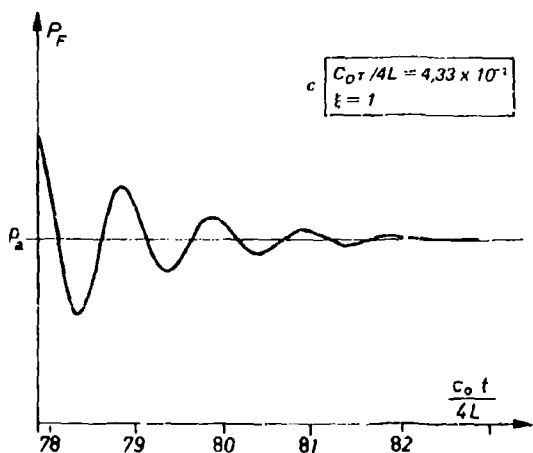


Fig. 5 - Oscillations de pression - Configuration 2c.

Fig. 6 - Oscillations de pression, avec dissipation artificielle $\xi = 1$ - Configuration 2a.

3.2. Calculs de pertes de charge dans des configurations simples

Les débits injectés dans certaines cavités entre les disques de turbines peuvent être assez élevés. Dans ce cas, les pertes de charge induites par les décollements, les changements de direction du fluide et les interactions de jets déterminent, au moins autant que la centrifugation, les profils radiaux de pression. Il s'avère donc capital d'apprécier, sur des configurations simples, la façon dont la simulation numérique peut représenter de tels phénomènes, eu égard au modèle de turbulence rudimentaire et à une éventuelle diffusion numérique. Des calculs ont donc été effectués dans diverses configurations de principe, telles que celles représentées sur les figures 7 à 10, soient :

- un canal cylindrique dont la section est augmentée brusquement de A_0 à A_1 ($A_1/A_0 = 2.25$) : configuration I.A,
- un canal cylindrique associé à un diffuseur tronconique, de longueur L_d et de rapport de sections $A_1/A_0 = 2.25$, soit un demi-angle d'ouverture de 11° environ : I.B,
- un canal cylindrique avec rétrécissement brusque ($A_0/A_1 = 2.25$) : I.C,
- un écoulement plan avec virage brusque ($A_1/A_0 = 1$) : I.D,
- un écoulement plan avec deux coudes consécutifs ($A_0/A_0 = 1$), la distance entre les deux coudes étant choisie de façon que, d'après les mesures [2], le deuxième coude n'induisse que peu de pertes supplémentaires : I.E.

Dans tous les cas, l'état générateur (p_0, T_0) est donné à l'entrée, et la pression statique (p_s) est fixée à la sortie. Le nombre de Mach est inférieur à 0.3. Le calcul fournit, en plus des profils de vitesse montrés sur les figures 7 à 10, les profils de pression (figures 11, 12, 13 et 14) sur les parois et sur l'axe (pour I.A, I.B et I.C), et sur la paroi concave (I.D et I.E).

Bien que, dans les trois derniers cas, les longueurs des canalisations aval ne semblent pas suffisantes, les variations de pression C_p entre l'entrée et la sortie et les débits \dot{m} ainsi calculés ont été comparés aux quantités correspondantes C_p et \dot{m} obtenues à partir des données expérimentales (pertes de charges singulières et par frottement pariétal) tirées de [2]. C'est ce que montre le tableau 1, dans lequel on a ajouté les valeurs isentropiques pour apprécier l'effet de la perte de charge.

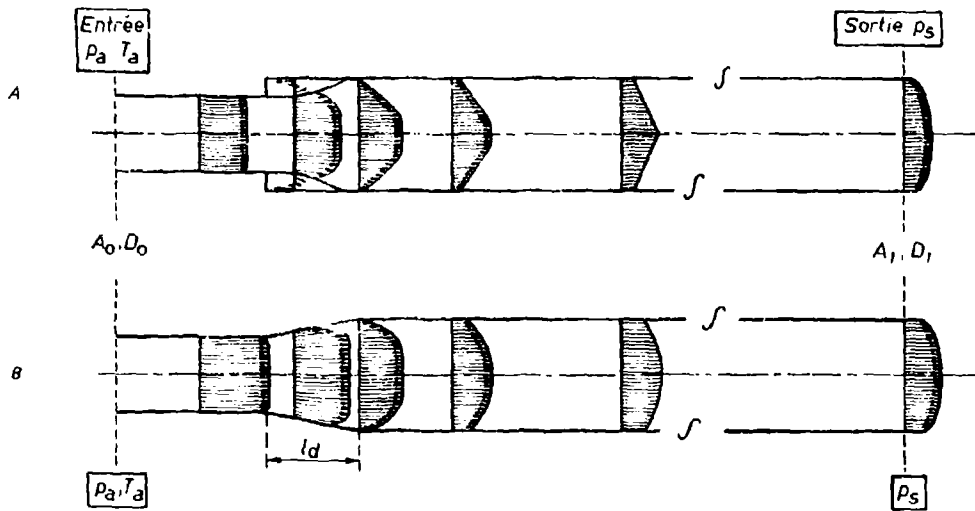


Fig. 7 — Ecoulements calculés dans un canal axisymétrique avec élargissement brusque (A) et avec diffuseur tronconique (B). $D_1/D_0 = 1,5$; $L_d/D_0 = 0$ ou $1,25$.

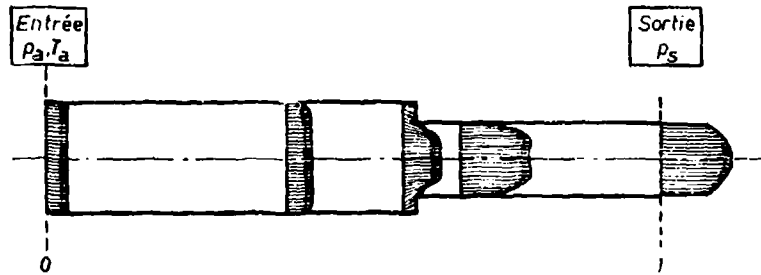


Fig. 8 — Calcul d'écoulement dans un canal axisymétrique avec rétrécissement brusque - configuration C. $D_0/D_1 = 1,5$.

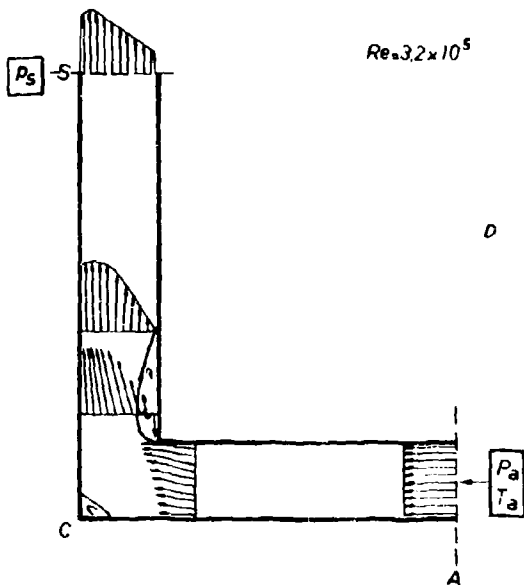


Fig. 9 — Calcul d'écoulement dans un canal plan avec virage brusque (configuration D).

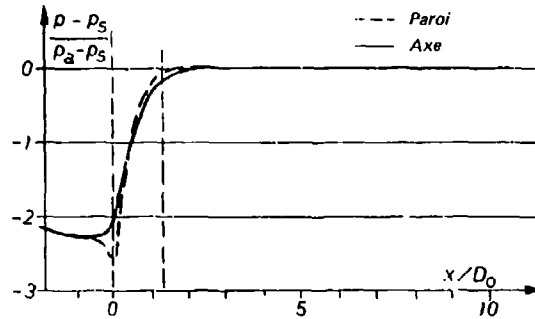
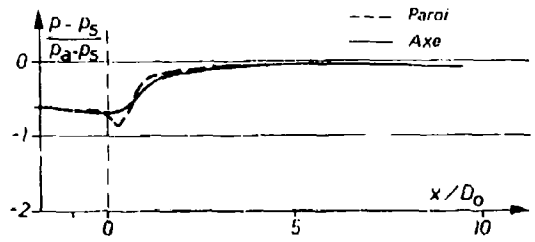
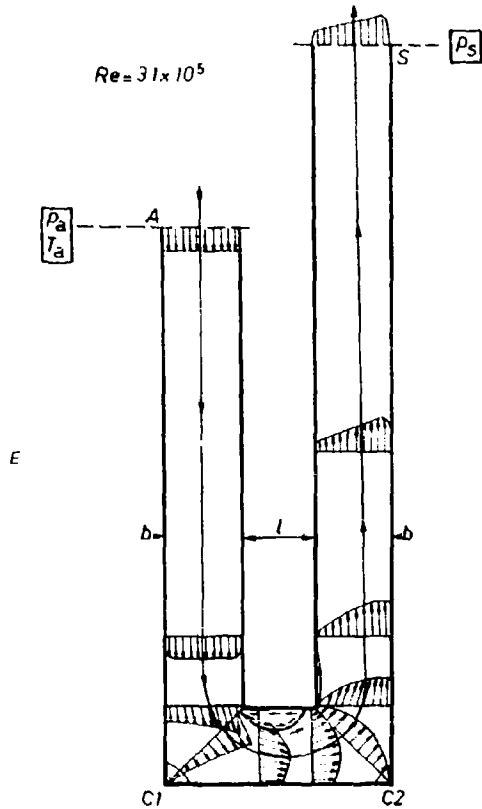


Fig. 11 - A - Elargissement brusque $\alpha = 90^\circ$;
B - Diffuseur tronconique $\alpha = 11^\circ \cdot l/D_0 = 1,25$.

Fig. 10 - Calcul d'écoulement dans un canal plan avec 2 virages consécutifs $l/b = 1$ (config. E).

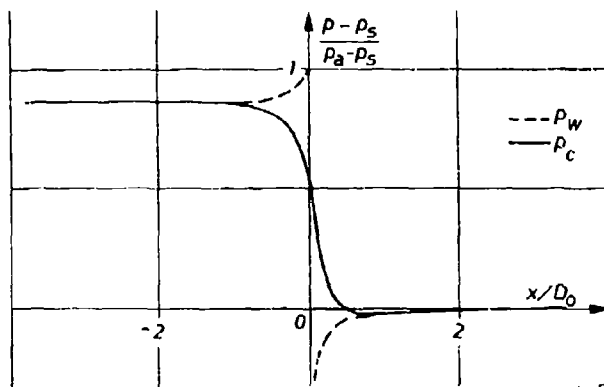
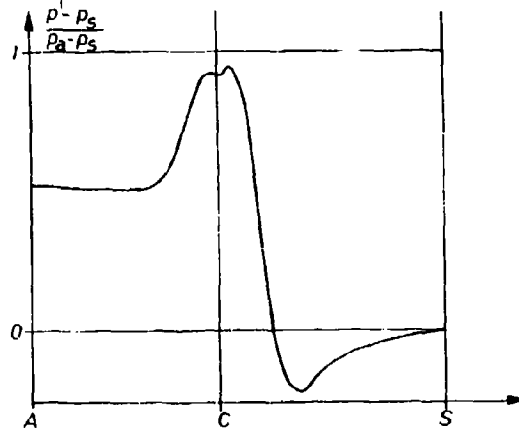


Fig. 12 - Profils de pression sur l'axe et sur la paroi - configuration C.

Fig. 13 - Distribution de pression calculée le long de la paroi externe de la configuration D.



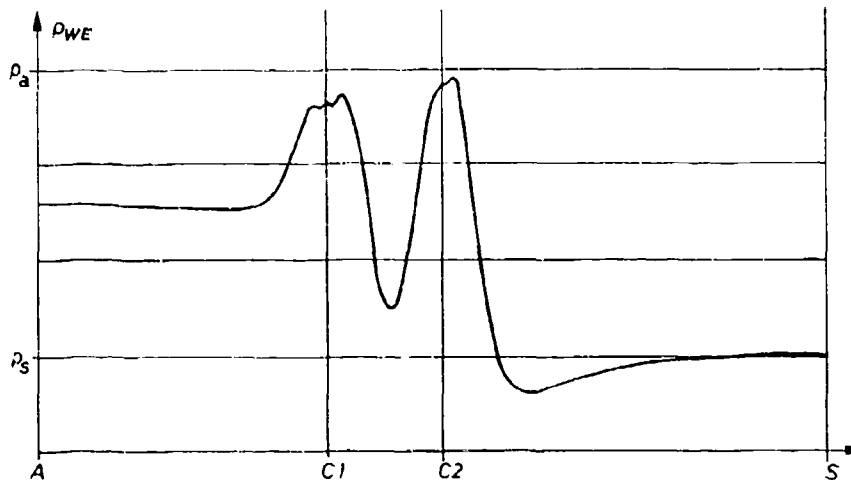


Fig. 14 - Distribution de pression calculée le long de la paroi externe A-C1-C2-S de la configuration E.

Configur.	Calcul		Calcul		
	C_{D1S}	\bar{C}_p	C_p	\tilde{m}/\dot{m}_{1S}	\dot{m}/\dot{m}_{1S}
A	-0,80	-0,45	-0,43	0,60	0,59
B	-0,80	-0,67	-0,69	0,78	0,80
C	0,80	1,13	1,28	0,87	0,82
D	0	0,86	1,08	0,73	0,69
E	0	1	1,14	0,71	0,68

↑ Mesures ↑ Mesures

Tableau I

La confrontation s'avère bonne, mais ne permet pas de conclure sur l'extension des décollements et sur la longueur d'homogénéisation, qui fixent le gradient de pression $\frac{dp}{dx}$. D'autres calculs effectués avec une longueur de mélange plus faible ($l/\lambda = 0.05$ au lieu de 0.09) ont montré que \tilde{m} et C_p ne sont pas notablement modifiés (sauf dans le cas I.E.), mais que l'extension longitudinale des décollements et des zones de variation de pression est plus que doublée.

3.3. Calculs d'écoulement dans les cavités entre disques fixe et mobile

3.3.1. Cavités fermées

Ce problème a été étudié, entre autres, par F. SCHULTZ-GRUNOW [3], puis plus récemment par S.L. SOO [4], F. KREITH [5] et par J.W. DAILY et R.E. NECE [6] au MIT.

La figure 15 montre, dans un plan méridien, l'écoulement secondaire calculé dans une cavité identique à celle de [6], pour un nombre de Reynolds de rotation $Re_A = \rho \Omega R^2 / \mu = 4.4 \cdot 10^6$, pour une épaisseur réduite $\lambda/a = 0.115$ et pour un nombre de Mach $\lambda a/c_0$ très faible (0.02). Sur la figure 16, qui présente quelques profils de vitesse radiale U , on peut voir le noyau central, la couche limite de centrifugation le long du rotor, et la "couche limite" induite par continuité sur le stator. Les calculs ont montré que, conformément aux analyses de S.L. SOO [4] et du MIT [6], un régime sans noyau central peut exister si on réduit l'épaisseur ($\lambda/a = 0.0255$) à Re_A constant ($Re_A = 11 \cdot 10^6$ par exemple). L'effet de l'épaisseur λ sur le gradient de pression calculé (figure 18) et sur le coefficient de couple C_m (figure 17) est voisin de celui obtenu expérimentalement [6]. Il en est de même pour les profils axiaux de vitesses tangentielles V et radiales U , comme on peut le voir sur les figures 19 ($\lambda/a = 0.0637$) et 20 ($\lambda/a = 0.0255$).

La surestimation observée des épaisseurs de couche limite peut être réduite si on choisit un niveau de longueur de mélange inférieur à la valeur classique (soit $l/\lambda = \text{Min}(0.09, 0.4 \frac{1}{\lambda/a}, 0.4 (1 - \frac{1}{\lambda/a}))$).

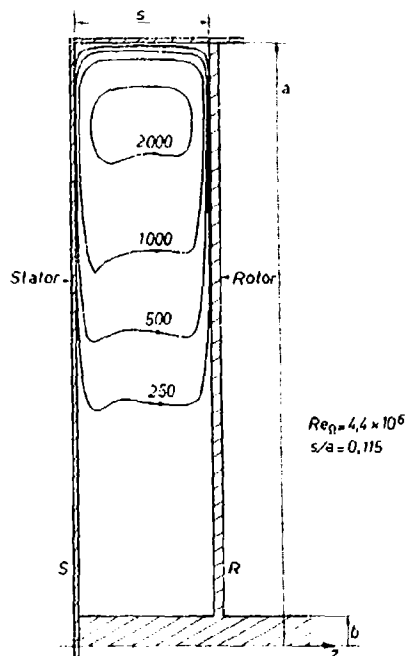


Fig. 15 - Cavity fermé - Lignes de courant dans le plan méridien.

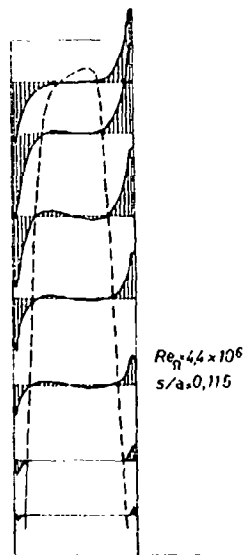


Fig. 16.

Fig. 17 - Effet de l'épaisseur de la cavité sur le couple (exercé sur le fluide par le rotor) : $C = \int_b^a 2\pi r p^r dr$
 Comparaison calcul - mesures MIT ; $C_M = 2C/1/2 \rho \Omega^2 a^3$.

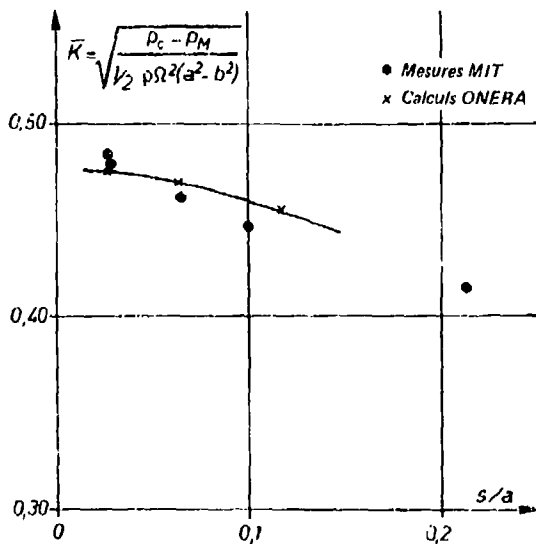
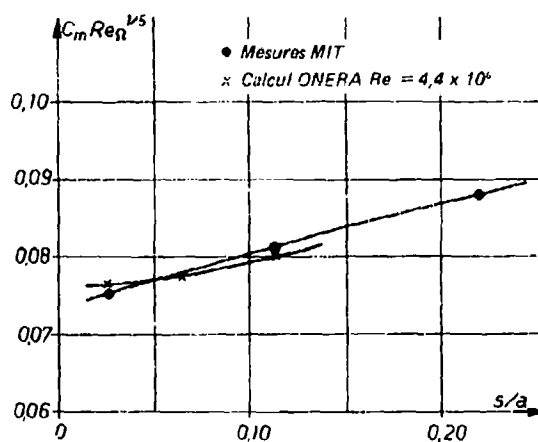


Fig. 18 - Effet de l'épaisseur de la cavité sur la différence de pression $P_C - P_M$ entre carter et moyeu. Comparaison (?) calcul - mesures MIT.

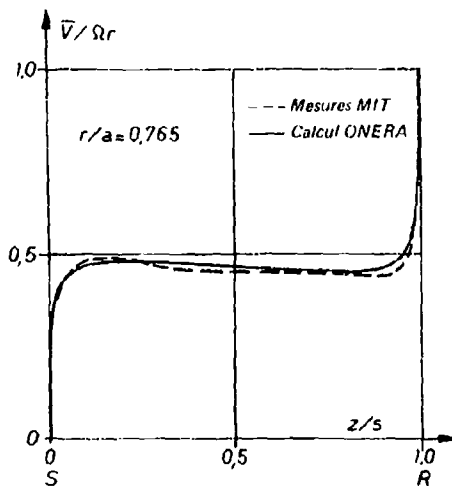


Fig. 19a - Cavité fermée $Re_{\Omega} = 4,4 \times 10^6$; $s/a = 0,0637$
Comparaison calcul-mesures. Vitesse azimutale.

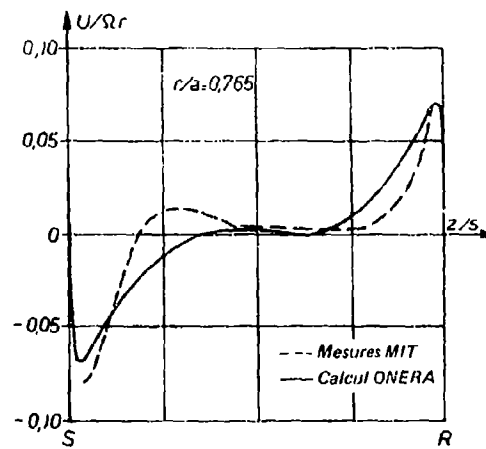


Fig. 19b - Cavité fermée $Re_{\Omega} = 4,4 \times 10^6$; $s/a = 0,0637$
Comparaison calcul-mesures. Vitesse radiale.

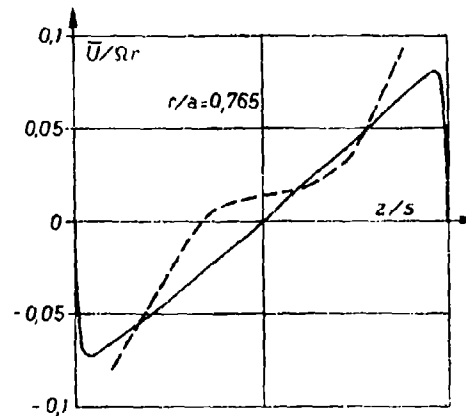
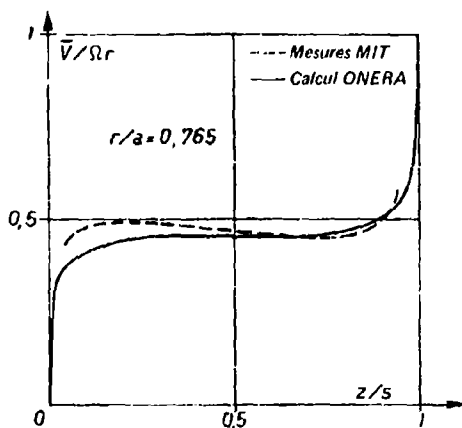


Fig. 20 - Cavité fermée $Re_{\Omega} = 4,4 \times 10^6$; $s/a = 0,0255$
a - Vitesse azimutale - Calcul et mesures ; b - Vitesse radiale -
Calcul et mesures.

3.3.2. Cavités interdiaques avec débit centrifuge

L'effet d'un écoulement forcé de débit \dot{m} , injecté axialement au voisinage de l'axe et évacué par un jeu axial d'épaisseur δ_e à la périphérie, a été analysé théoriquement et expérimentalement par F. KREITH [7], V.M. KAPINOS [8], et par J.M. OWEN et ses collègues [9], [10] et [11].

De nombreuses simulations numériques ont été effectuées pour différentes épaisseurs de la cavité ($G = \delta_e/a$), du jeu ($G_c = \delta_c/a$) pour différentes vitesses de rotation ($Pe_A = \rho \Omega a^2 / \mu$) et divers débits ($C_w = \dot{m} / \mu a$). La figure 21 en montre un exemple. Il apparaît que pour les débits élevés, la rotation du rotor a peu d'effet. Ce n'est pas le cas pour des débits plus faibles, au voisinage de l'écoulement de centrifugation naturelle ($p_A = p_S$). Le jeu δ_e a évidemment une influence prépondérante sur les niveaux de pression dans la cavité, ce qui requiert un réseau de calcul serré à la périphérie, et un soin particulier pour les conditions de sortie. La géométrie de l'injection a aussi un rôle important : au voisinage de l'axe, les vitesses débitantes sont élevées, et l'écrasement du jet incident sur le disque conditionne l'extension du décollement. Le paramètre G n'a au contraire qu'un effet secondaire (entre cinq et vingt pour cent).

La figure 22 montre l'effet du débit C_w sur les profils radiaux de pression le long du stator, pour $Re_A = 8 \times 10^5$, $G = 0,10$ et $G_c = 0,01$, et la comparaison avec les mesures de Owen et Phadke. On remarque qu'aux petits débits, la concordance est bonne, mais que pour des débits plus élevés, la confrontation est moins satisfaisante. La même tendance est indiquée sur la figure 23 pour $Pe_A = 0$, $G = 0,10$ et $G_c = 0,04$: les calculs semblent surestimer l'ampleur du décollement, et la modification de la longueur de mélange ne permet pas, dans ce cas, d'améliorer sensiblement les résultats. Une cartographie des vitesses mesurées dans la cavité serait souhaitable pour poursuivre et orienter la discussion.

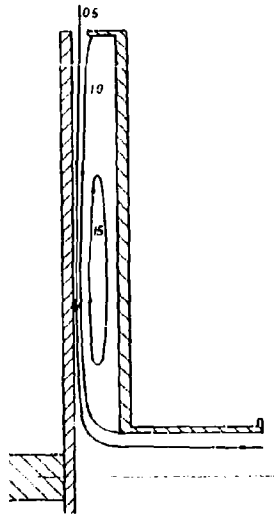


Fig. 21 - Lignes de courant calculées; $G = 0,10$; $G_c = 0,04$
 $Re_{11} = 0$; $C_w = 21500$.

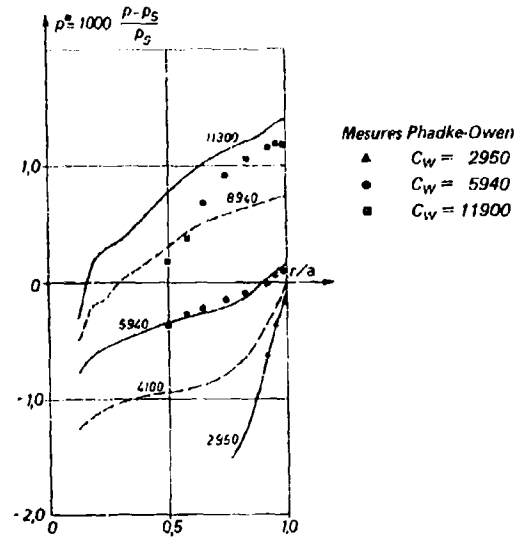


Fig. 22 - Effet du débit (C_w) sur la distribution radiale de pression. Calculs et mesures. $Re_{11} = 0,8 \times 10^6$; $G = 0,10$; $G_{ca} = 0,01$.

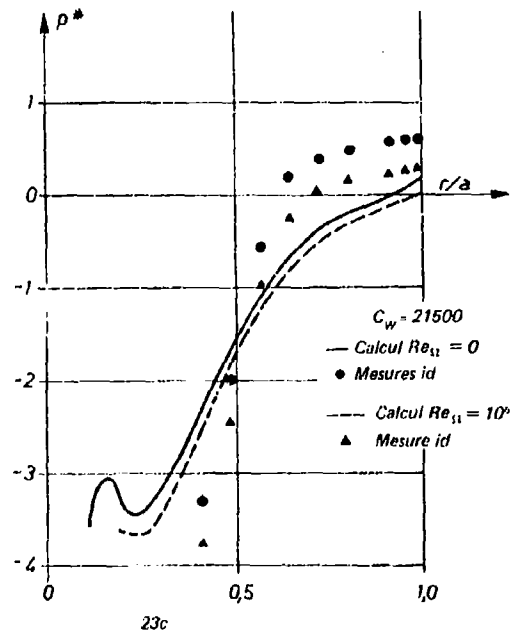
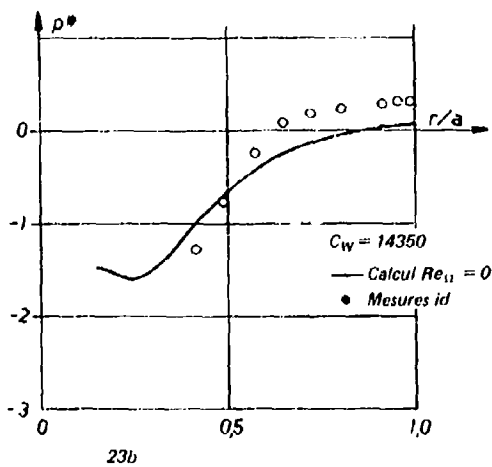
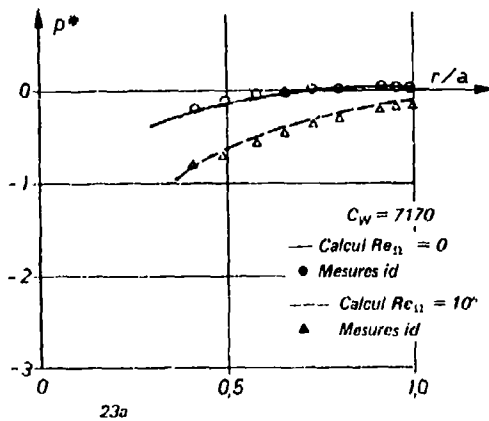


Fig. 23 - Effet du débit (C_w) sur la distribution radiale de pression. $Re_{11} = 0$ et 10^6 ; $G = 0,10$; $G_c = 0,04$.

4. CONCLUSION

Un code de calcul d'écoulement tridimensionnel axisymétrique a été développé pour étudier les écoulements dans les cavités annulaires interdisques des turbomachines. Sa souplesse d'utilisation a permis d'évaluer les propriétés de la simulation numérique dans des configurations géométriques simples, de formes très diverses. Les confrontations avec les données expérimentales issues de différentes publications ont permis d'apprécier les qualités et les limites de la modélisation utilisée. Une analyse plus approfondie pourra être réalisée grâce aux mesures tirées d'un banc d'essai en cours de réalisation. En attendant, de nouvelles confrontations avec les mesures effectuées à l'Université de Sussex ainsi qu'au MIT sont prévues.

REFERENCES

- [1] D. DUTOYA, P.J. MICHARD "Une méthode de volumes finis de type implicite pour le calcul des écoulements elliptiques".
La Recherche Aérospatiale n° 1980-2
- [2] I.E. IDELICK "Hemento des Pertes de Charge". Collection de la Direction des Etudes et Recherches d'Electricité de France. Ed. Eyrolles. Paris (1969)
- [3] F. SCHULTZ-GRUNOW "Der Reibungswiderstand Rotierender Scheiben im Gehäusen" ZAMM 15, 191-204 (1935)
- [4] S.L. SOO "Laminar Flow over Enclosed Rotating Disk"
Trans ASME. vol 80 (1958)
- [5] F. KREITH "Influence of Centrifugal Forces on Heat Transfer and Flow"
Final Report of NSE Research Program. G.3067 (nov 1958)
- [6] J.W. DAILY, R.E. NECE "Chamber Dimension Effect on Induced Flow and Frictional Resistance of Enclosed Rotating Disks"
Journal of Basic Engineering (mars 1960)
- [7] F. KREITH, E. DOUGHMAN, H. KOZLOWSKI "Mass and Heat Transfer from an Enclosed Rotating Disk with and without Source Flow"
Journal of Heat Transfer. Trans ASME series C vol.85 n° 2 (mai 1963)
- [8] V.M. KAPINOS "Heat Transfer from a Disk Rotating in Housing with a Radial flow of Coolant"
Journal of Engineering Physics vol 8 (1965)
- [9] F.J. BAYLEY, J.H. OWEN "The Fluid Dynamics of a Shrouded Disk System with a Radial Outflow of Coolant"
Journal of Engineering for Power (Juillet 1970)
- [10] J.M. OWEN, U.P. PHADKE "An Investigation of Ingress for a Simple Shrouded Rotating Disk System with Radial Outflow of Coolant"
ASME 80 GT.49.
- [11] U.P. PHADKE, J.H. OWEN "An Investigation of Ingress for an Air Cooled Shrouded Rotating Disk System with Radial Clearance Seals" ASME 82. GT.145.
- [12] F.J. BAYLEY, J.H. OWEN "Flow between a Rotating and a Stationary Disk". The aeronautical Quarterly n° 20 (1969).
- [13] COSMAN A.D. et al "Transfer of Heat in Rotating Systems"
ASME 76.GT.25.
- [14] E.I. SHARMA "Prediction of Local Heat Transfer Disk by a Two Equations Model of Turbulence"
Journal of Heat Transfer (Février 1977).

DISCUSSION

J.M.Owen, UK

The author is to be congratulated on presenting a useful paper on the prediction of flow in rotor-stator systems. Have you experienced difficulty in obtaining convergence of your solutions at large rotational Reynolds numbers, and what is the maximum value of Re_θ for which reliable results have been obtained? Also, in the experimental rig that you are building, what is the maximum Reynolds number that you will be able to achieve?

Réponse d'Auteur

Les principaux problèmes posés par les calculs à plus grand nombre de Reynolds et par les calculs dans des cavités épaisses sont du même type: il s'agit moins, pour cette méthode numérique implicite, d'un problème de stabilité que d'un problème de précision: le réseau de calcul doit être très fortement resserré, près des disques d'autant plus que Re et G sont grands, si on veut calculer correctement les échanges fluide-paroi. C'est donc une question de capacité, de stockage et de coût de calcul.

Une solution pourrait être d'améliorer les "modèles de paroi" reliant les flux pariétaux aux quantités locales calculées en y incorporant l'effet des forces d'inertie.

Sur le montage expérimental prévu, le disque rotor, de 60 cm de diamètre, doit en principe tourner de 3000 à 12000 tours par minute, à pression atmosphérique.

J.Fabri, Fr

I would like to ask Dr Owen if in his computations he also finds recirculation zones similar to those shown by the author.

Dr Owen's Reply

The two flows — the flow between a rotor and a stator, that you are considering, and the flow inside a rotating cavity — have certain similarities but they have a large number of differences. And in the source region of the flow in the rotating cavity inertial effects are significant and the flow is broadly similar to that which occurs in a rotor-stator system. But in the Ekman layer region where the rotational speed of the fluid is large (or of the same order) compared with the speed of the disc itself Coriolis effects make for the flow structure that you get there. So that peculiar characteristic of the rotating cavity with the non-entraining Ekman layer does not appear in a rotor-stator system. The flow is a different one in that respect.

B.Johnson

1. Does your procedure account for the buoyancy terms in conservation equations?
2. Have you calculated the flow and heat transfer from confined disks with both disks rotating and the flow driven by free convection?

Réponse d'Auteur

1. Les forces d'Archimède dues aux différences de température sont incluses dans les équations de conservation telles qu'elles sont modélisées. Mais il n'y a pas pour l'instant de correction au niveau du modèle de turbulence.
2. Non, pas en détail.

D.K.Hennecke, Ge

Did I understand you correctly that you are using Reynolds' analogy to compute the heat transfer coefficient? Since you solve the energy equation there would be no need for it. Besides it is likely not to be valid for the present case.

Réponse d'Auteurs

Je voulais dire que j'utilise l'analogie de Reynolds au niveau local, c'est à dire que je définis, pour exprimer la corrélation vitesse/température $u^+ T^+$ en fonction de gradient moyen ∇T , un coefficient de diffusion thermique turbulent proportionnel à la viscosité turbulente. Il en est de même pour les fonctions de paroi, qui relient les frottements et flux thermiques aux conditions moyennes locales.

TRANSIENT THERMAL BEHAVIOUR OF A COMPRESSOR ROTOR WITH VENTILATION -
TEST RESULTS UNDER SIMULATED ENGINE CONDITIONS

by
E. Reile, U. Radons, D.K. Hennecke *)
MTU Motoren- und Turbinen-Union München GmbH
Postfach 50 06 40, 8000 München 50, West Germany

SUMMARY

The development of advanced compressors for modern aero-engines requires detailed knowledge of the transient thermal behaviour of the rotor disks to enable accurate prediction of rotor life and, additionally, of the thermal growth of the rotor for the evaluation of tip clearances. In his quest for longer life and higher reliability of the parts as well as reduced clearances even at transient conditions, the designer has to be able to influence the thermal behaviour of the rotor. A very effective way is to vent small amounts of air through the rotor cavities.

This paper presents the design of such a vented rotor. The main emphasis is placed on a detailed description of a test rig specially built for this purpose. The testing was carried out under simulated engine conditions for a wide range of parameters. The results are compared with those obtained with a theoretical model derived from fundamental tests at the University of Sussex, where heat transfer in rotating cavities is investigated. Good agreement is observed.

Some final tests were done in an engine. The results also exhibit good agreement with the rig results under simulated conditions, when the proper dimensionless parameters are considered, proving the validity of the simulation.

LIST OF SYMBOLS

C1...C5	Simulated idle condition
H1...H5	Simulated full-load condition
m_{vent}	Ventilation mass flow [%]
p_{vent}	Pressure [bar]
r	Radial coordinates [m]
t	Time [s]
T_{vent}	Ventilation air temperature [K]
$T2...T5$	Temperature at disk 2 - 5
τ	Time constant for temperature relaxation
t_{ref}	Time constant for temperature relaxation at hub of disk 5 for simulated acceleration C5 - H5
α	Heat-transfer coefficient

Indices

bolt	in bolt area of the disk
hub	at the hub of the disk
in	at the rotor entry
out	at the rotor exit
rim	at the rim of the disk
vent	for the ventilation air

1. INTRODUCTION

One of the most important factors limiting the life of compressor and turbine disks in modern aero-engines is the rapid sequence of stress cycles occurring in service. During rapid accelerations and decelerations, the temperature at the rim of the disk responds appreciably more quickly to the temperature of the main flow than does the temperature at the hub. The consequent radial temperature gradients result in high stresses and reduced disk life. Another aspect that must be considered is the thermal response of the rotor. Because thermal growth of the casing structure normally occurs more quickly than that of the rotor, during an acceleration phase the radial clearance at the blade tips will be the greater, the slower is the thermal growth of the rotor disks. This has disadvantageous effects on the surge limit and power output.

The thermal-response characteristics of the disk hubs can be speeded up by purposeful ventilation of the hub area. Because a loss in performance always occurs if air is bled from the main flow, the amount of air used for ventilation must be kept small and it must be conducted in such manner as to permit it to be used further in the secondary air system.

Below is a description of rotor ventilation using a multistage compressor of a modern jet engine as an example. The effects of ventilation on the thermal behaviour

*) present address: Technische Hochschule Darmstadt, Fachgebiet Flugantriebe,
Petersenstr. 30, 6100 Darmstadt

are investigated on the component test rig. The test results are then compared with the findings of the computer model used for calculating the thermal behaviour of the rotor under realistic operating conditions.

2. RIG TESTS

The rotor used on the component test rig is represented in Fig. 1. It is made up of the last three stages of an HP compressor rotor (disks 2 - 4) plus two seal disks (1,5). The disks and spacers are bolted together in such manner that the spaces between the disks form outer and inner cavities. The rotor is machined to a uniform diameter. The rims of disks 2 - 4 can be heated to desired temperatures by impingement heat transfer. The ventilation air m_{vent} is supplied through 10 vents arranged in the vicinity of the bolt, is distributed through the three inner rotor cavities and is discharged through holes in the right-hand flange. For tests without ventilation the inlet and outlet openings are closed off, leaving just a single inlet open, to enable the pressure in the rotor assembly to be set.

The rotor assembly is provided with 38 temperature-measuring points. All important measuring-points are shown in Fig. 1. The measurements are transmitted from the rotating system via slip-rings.

The purpose of the tests was to measure the temperatures under simulated full-load and idle points as well as the transient temperature behaviour for a simulated acceleration and deceleration. The test conditions selected were such that the Reynolds number, Rossby number, Grashof number and Nusselt number, which are the determinative parameters for the flow and heat transfer, agreed with the values occurring in the engine at full load and idle. For the simulated full-load and idle conditions, a maximum temperature of 500 K and 350 K respectively was chosen. The accompanying pressure and speed values were then derived according to the similarity principle. Tests were conducted using three ventilation mass flows as well as one test without ventilation at two pressure levels. The steady-state conditions for the simulated full load (H1 - H5) and simulated idle (C1 - C5) are listed in Tab. 1.

The arrangement of the rotor in the rig is shown in Fig. 2. The air for heating and cooling the rim of disks 2 - 4 and rotor ventilation is taken from two main lines carrying high- and low-temperature air. Mixing valves with programmed settings are provided for adjusting the desired air temperature for lines 2 - 5 for each test-point. In the transient-state tests all valves were thus switched simultaneously from cold to hot condition or vice-versa. The time-response characteristics of the main operating parameters according to Tab. 1 (speed, ventilation mass flow, pressure and temperature) are represented in Fig. 3 by way of example of a load cycle C1 - H1 (simulated acceleration).

The speed N attains its final value approx. 10 s after the start of acceleration after slight overshooting. The ventilation air m_{vent} requires roughly the same time as the speed to reach its full value. Following an initial rapid increase, the pressure takes about 20 s to reach a virtually stable value. Because of the relatively massive rig casing, the temperature of the rotor-ventilation air T_{vent} increases appreciably more slowly. In the simulated acceleration C1 - H1 the time constant of the temperature increase τ_{vent} is about 24 s. Similar time-response characteristics are shown by the material temperatures at the rims $T_{2,rim}$, $T_{3,rim}$ and $T_{4,rim}$ of disks 2 - 4.

3. ANALYSIS OF RIG-TEST RESULTS

As part of the analysis of the test results, temperature calculations were made using a two-dimensional finite element method. The isoparametric finite element network is illustrated in Fig. 4. The computer program solves the transient heat conduction equation using temperature-related material data, and simultaneously calculates the local fluid temperature by means of the thermal balance between the component and surrounding flow. The computation method, which is described in greater detail in Ref. 1, generates axisymmetric temperature distributions. Components that are not axisymmetric are smeared in the circumferential direction in substitute system and are treated in such manner that the heat flux and thermal capacity are reproduced faithfully.

In the present case of a compressor rotor, the component temperatures are very largely determined by the following parameters, controlled from the outside.

- Temperature at the rim of disks 2, 3 and 4
- Mass flow through the rotor
- Temperature of the air at the entry to the rotor
- Pressure in the rotor

The computer model is thus designed so that the component temperatures are calculated with the air temperatures with the rotor in relation to the input variables for these parameters.

For the vented rotor, the computer model is based on the air system according to Fig. 1. The air entering the rotor is distributed to the three inner rotating cavities. It flows in Ekman layers across the disk surface radially inwards, collecting again in the hub area, and exits via holes in the right-hand flange. In contrast, the air entering the outer cavities of the rotor forms a recirculating flow, driven by buoyancy resulting from the difference in temperature between the disks.

Because flow-fields are not calculated in the computer model, the recirculation is acquired from the thermal balance between the walls and a purely mathematical mass flow. Although these flow rates are much smaller than the rotor ventilation flow, they still affect the heat transfer between the rim and bolt area to a considerable extent.

For the tests without ventilation, a somewhat altered model is used; whereas the outer cavities are treated in the same way as the ventilated version, a recirculating flow that is unaffected by the neighbouring cavities is assumed for the inner cavities.

For the computer model, heat transfer coefficients for a system with rotating disk and stationary wall was assumed for the front of disk 1 and rear of disk 5. At the surfaces of the inner and outer cavities, relations for corotating disks with and without radial flow were used. These calculations were based on flow and heat-transfer investigations by Owen et al. (Ref. 2, 3) using idealised geometries, where the flow pattern and heat transfer for a large range of rotary Reynolds, Grashof and flow numbers were acquired.

Other boundary conditions were to be defined for the flow in the bolt area and at the disk hubs (ducted flow), as well as at the seal between disks 1 and 5 and the casing. At the rims of disks 2, 3 and 4 the temperatures measured on the rig were applied. Similarly, measured values were used for the boundary temperature at the exposed sides of disks 1 and 5. All boundary temperatures within the rotor system were determined simultaneously with the component temperatures.

The result of the steady-state calculation for case H1 with maximum ventilation mass flow and for the unvented case H5 is represented in Fig. 5 in the form of isotherm plots. It can be clearly seen that the temperatures at the disk rim remain unchanged, whereas ventilation produces nearly the same temperatures at the hub of disks 3 - 5. The influence of the rotor flow on the calculated steady-state hub temperatures is illustrated in Fig. 6. It becomes apparent that even relatively small ventilation flow rates suffice to bring about a clear increase in the temperatures at the rear disks and that a further increase in the rotor flow has hardly any more influence on the steady-state temperature.

Taking disk 3 as an example, Fig. 7 shows a comparison of the measured component temperatures and the calculated values for simulated full-load condition; showing the calculated temperature distribution at the disk midplane for three rotor flows, in addition to the measured values. For the unventilated case H5 there is good correspondence between measurement and calculation; only three out of seven test-points exhibit somewhat lower temperatures than calculated. For the ventilated cases there is very good correspondence between the measurements and calculations for the outer area; but greater discrepancies occur in some cases for the inner area.

The steady-state calculations are not adequate for checking the computer model, because the radial temperature gradients are too small and the heat transfer coefficients are of lesser significance than in the transient case. The transient calculations were made on the basis of the measured behaviour of all the parameters used in the calculation (see Tab. 1). The good correspondence between measurement and calculation of the air temperature at the rotor exit during an acceleration, as shown in Fig. 8, proves that the heat balance between the air and rotor is treated correctly in the calculation. In the ventilated cases, during most of the acceleration, maximum temperature deviations of approx. 5 K occur. In the unventilated case, the calculated behaviour depends on the inadequately known mass flow of recirculating air. Hence, it is not surprising that there is a greater discrepancy between measurement and calculation here. The time-response characteristics of the component temperatures, plotted in Fig. 9 for all test-points as an example, exhibit very good agreement between measurement and calculation. That this correspondence was attained for all tests (acceleration, deceleration with different degrees of ventilation) confirm the assumptions made in the computer model. Furthermore, the heat transfer correlations for corotating disks, worked out using greatly simplified models, can also be used with success with more complex systems.

4. THERMAL BEHAVIOUR OF VENTILATED ROTOR

The calculated time-response characteristics of the temperature difference in disk 4 between the rim and middle of the outer cavity, as per Fig. 10, upper, makes it clear that ventilation of the rotor has little effect on the temperature gradients in the outer part of the disk. Irrespective of the ventilation, the maximum value sets in shortly after commencement of the acceleration and varies by only approx. 15 K. In contrast, the desired effect of rotor ventilation is shown in the temperature difference between the bolt area and hub of disk 4, plotted in Fig. 10, lower. At maximum ventilation it is reduced by more than half and, furthermore, applies for a much briefer period. The behaviour is similar with the other disks. The reason for this lies in the behaviour of the disk hubs, which speeds up with increasing ventilation mass flow, and which can thus be used for measuring the effectiveness of the rotor ventilation. The time constant for the temperature relaxation at the hub of disk 3 is plotted in Fig. 11 over the rotor flow as per final condition for all the acceleration and deceleration events investigated on the rig. There is very good agreement between the measurements and calculations throughout the flow range. The values of the time constants are slightly less during an acceleration than a deceleration with the same flow rate, because the heat transfer coefficients are smaller at the lower load-point than at the end of the acceleration. It also becomes apparent that small ventilation flow rates are sufficient for bringing about an appreciable improvement in the time-response characteristics.

Consequently, it is possible that it suffices to divert air from the secondary system through the rotor without having to bleed additional air from the main stream, thereby avoiding detrimental effects on the engine performance.

Further to the rig tests described above, tests have now been carried out in the engine, in which the air and component temperatures in the rotor were likewise measured and the signals transmitted via telemetry for remote evaluation. The results of the engine measurements are shown in Fig. 12 and 13, taking disk 4 as an example. Because the boundary conditions in the rig tests were such that the main dimensionless flow and heat transfer parameters were the same as in the engine, dimensionless comparison of the radial temperature profile in the disk can be made. Fig. 12 shows the steady-state radial temperature distribution for the full-load point. The figure shows the difference between the local material temperature and the point of lowest temperature at the disk rim, related to the maximum possible difference between the temperature of the air at the rotor entry and the temperature at the disk rim. There is good correspondence over most of the disk. The temperature profile with maximum temperature difference between the disk rim and hub, occurring during an acceleration, as per Fig. 13, similarly exhibits very good correspondence between the rig test and engine measurement. The values are plotted in dimensionless form in relation to the ventilation temperature at idle, divided by the temperature rise of the ventilation air from idle to full-load. The transient measurements on the rig and in the engine can be compared directly, since the increase in speed and in the ventilation temperature exhibit the same time-response characteristics.

If the time constants of the rig and engine measurements are plotted against the heat transfer coefficients applied in the inner rotating cavities, as in Fig. 14, all results will be brought to lie along a common curve.

As the corresponding results of the engine test and rig test C1 - H1 as per Fig. 14 show, the temperatures at the disk hubs react more quickly in the engine than on the rig. The reason is that for the same Nusselt numbers the heat transfer coefficients are clearly higher in the engine, because of the higher temperature level.

Even with relatively small amounts of air, purposeful ventilation of the rotor cavities can contribute towards a considerable speeding-up of the thermal-response characteristics. As shown by the stress and life calculations, it is thus possible to attain an improvement in the life of more than 50 % for a typical mission. An improvement of this order signifies a considerable gain in maintenance costs and, thus, reduced life-cycle costs. Yet another advantage of the more rapid thermal behaviour of the rotor lies in the fact that the thermal growth of the rotor is more in harmony with the transient thermal growth characteristics of the casing. This means that smaller clearances between the blade tips and casing can be achieved, resulting in improved compressor efficiency and greater surge margin.

5. CONCLUDING REMARKS

The investigations under discussion demonstrate that clear advantages are to be had from the purposeful ventilation of the compressor rotor. The computer model, which to a great extent works with heat transfer coefficients for corotating disks, obtained with models of simple geometry, gives a good reproduction of the steady-state and transient measurements.

In other words, with the HP compressor under review or similar configurations, the computer model is capable of faithfully describing the temperature development for a simple load cycle, and thus also for a complete mission.

REFERENCES

- 1 Hennecke, D.K., Trappmann, K.: Turbine tip clearance control in gas turbine engines, AGARD-CP-324 on engine handling, Paper 16 (1983)
- 2 Owen, J.M.: Rotating disks and enclosures. Proceedings of the Int. Centre for Heat and Mass Transfer 16; XIV. Symp. on Heat Transfer Problems in Rotating Machinery, held Sept. 1982 in Dubrovnik, Yugoslavia, Metzger, D.E. and Afgan, N.H., Eds., Hemisphere Publ. Corp., Washington (1984)
- 3 Long, C.A. and Owen, J.M.: Prediction of transient temperatures for an air-cooled rotating disc. Paper to be presented at AGARD 65th PEP Symposium on Heat Transfer and Cooling in Gas Turbines, Bergen, Norway, May 1985

Table 1: - STEADY-STATE CONDITIONS FOR SIMULATED FULL-LOAD AND IDLE TESTS

		m_{vent} %	P_{out} bar	N %	$T_{2_{rim}}$ K	$T_{3_{rim}}$ K	$T_{4_{rim}}$ K	T_{vent} K
simulated full-load	H1	100	4.5	100	423	446	469	500
	H2	65	4.5	100	423	446	469	500
	H3	20	4.5	100	423	446	469	500
	H4	0	4.5	100	423	446 <td 469	500	
	H5	0	2.9	100	423	446	469	500
simulated idle	C1	40	1.4	75	318	329	342	350
	C2	27	1.4	75	318	329	342	350
	C3	6	1.4	75	318	329	342	350
	C4	0	1.4	75	318	329	342	350
	C5	0	1.1	75	318	329	342	350

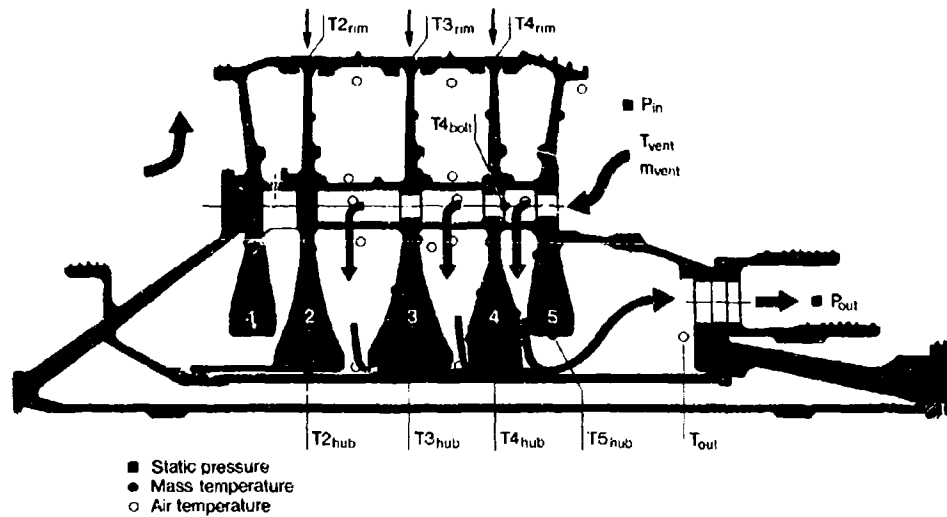


Fig. 1: Rotor of the disk-ventilation rig; Air System and location of rotating measuring-points

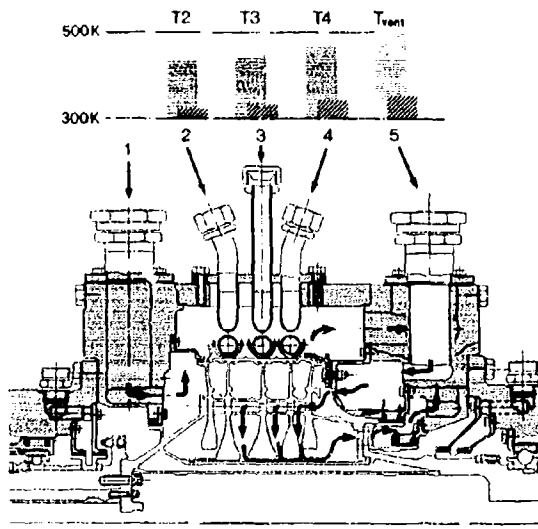


Fig. 2: Disk-ventilation rig

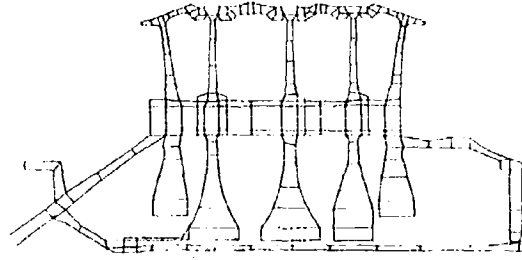
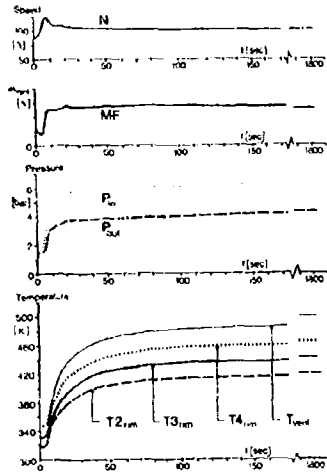


Fig. 4: Finite element grid of the rotor

Fig. 3: Transient behaviour of the most important operating parameters in a simulated acceleration

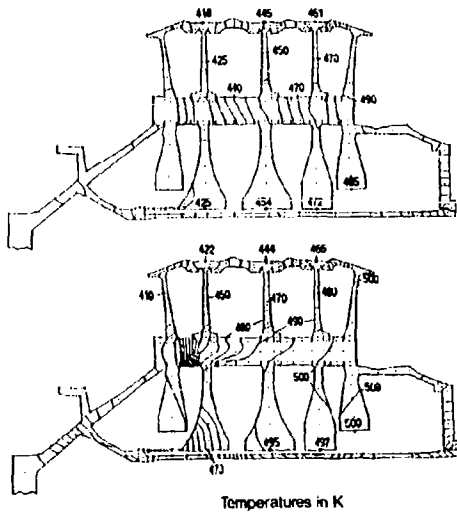


Fig. 5: Calculated temperature distribution for simulated full-load; top: unventilated, $m_{vent} = 0\%$ (H5) bottom: ventilated $m_{vent} = 100\%$ (H1)

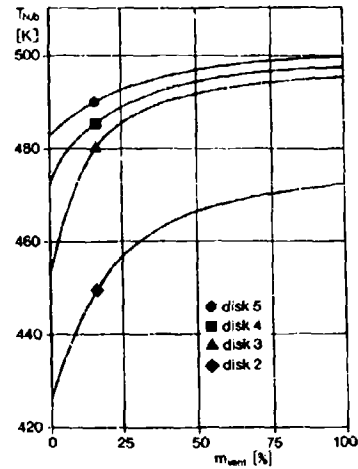
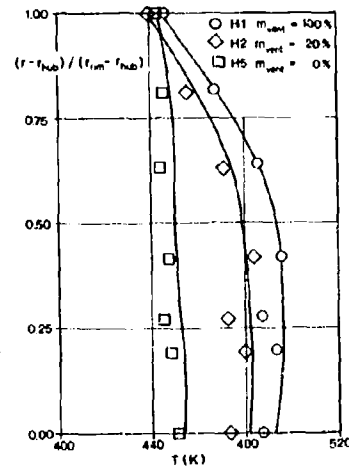


Fig. 6: Calculated temperatures at disk hub against ventilation flow for simulated full-load

Fig. 7: Radial temperature distribution in disk 3 for simulated full-load. Comparison between measurement and calculation



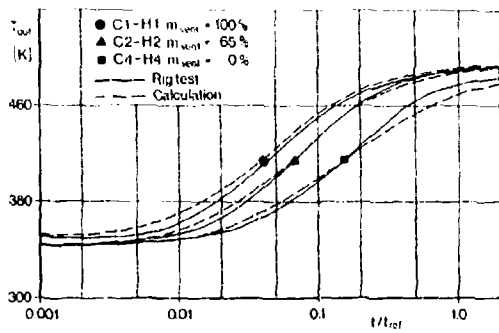


Fig. 8: Air temperature of ventilation flow at the rotor exit during a simulated acceleration. Comparison between measurement and calculation

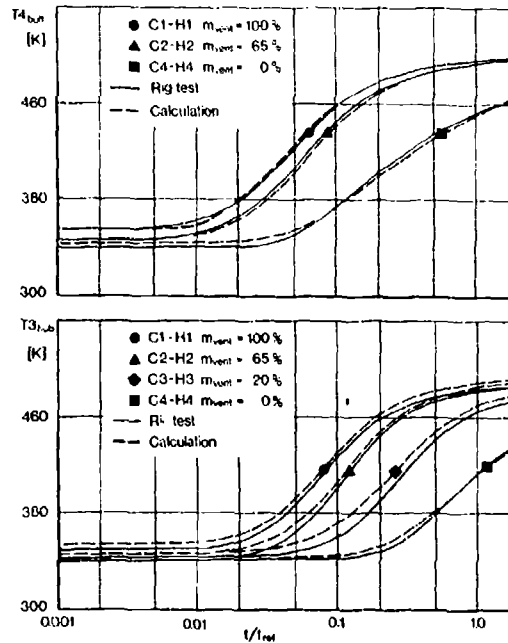


Fig. 9:

Comparison of measured and calculated component temperatures in a simulated acceleration.

Top: temperature T_{4bolt} in bolt area of disk 4;
Bottom: temperature T_{3hub} at hub of disk 3

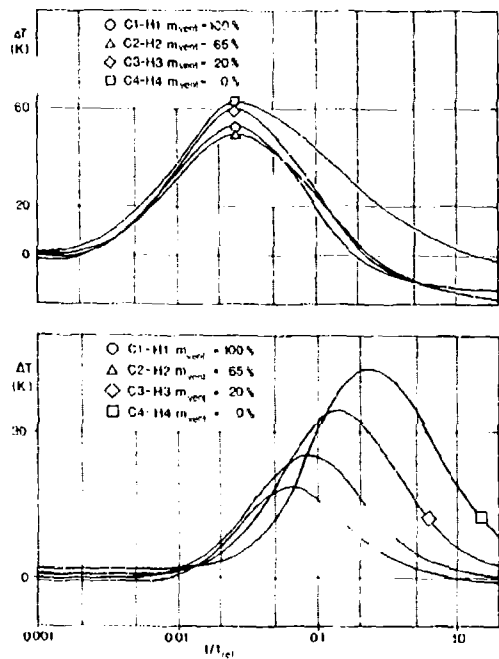


Fig. 10:
Temperature difference in disk 4 during a simulated acceleration. Top: temperature difference between the rim and middle of the outer cavity; Bottom: temperature difference between the bolt and hub

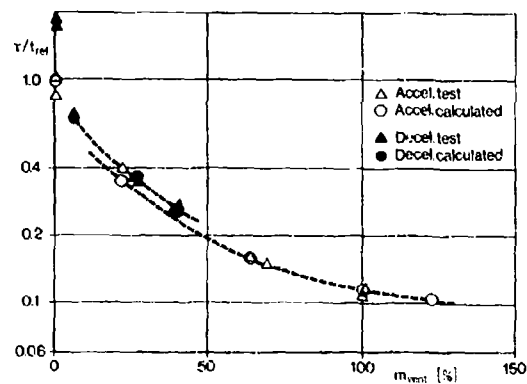


Fig. 11:

Time constant for temperature relaxation at the hub of disk 3 in relation to the ventilation mass flow, referred to the time constant in the unventilated case C5-H5

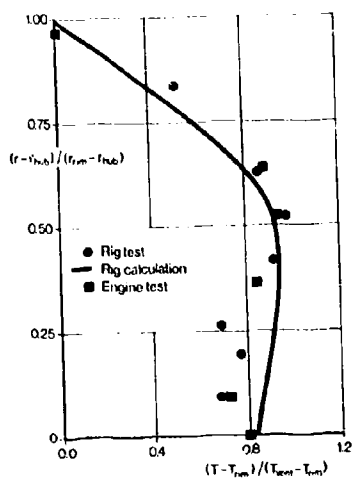


Fig. 12:
Radial temperature distribution
in disk 4 for steady-state
full-load. Comparison between
rig test and engine measurement

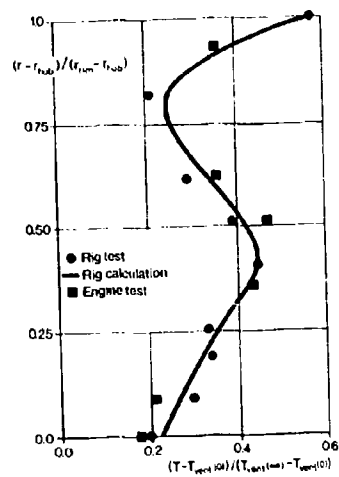


Fig. 13:
Radial temperature distribution
at instant $t = \tau_{vent}$ during
acceleration. Comparison between
rig test and engine measurement

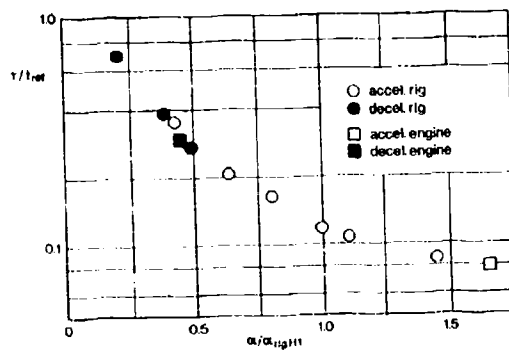


Fig. 14:
Time constant for temperature
relaxation at the hub of disk 3
in relation to the effective
heat-transfer coefficients.
Comparison between calculated
rig tests and engine measurement

DISCUSSION

J.M.Owen, UK

The authors are to be congratulated for obtaining good agreement between their predicted and measured temperatures in both the compressor rig and the engine itself. This work is complementary to that presented in paper No. 21 by Dr Long and myself, in which the temperature distributions on the discs in a geometrically simple rotating cavity were predicted from simple correlations, and it suggests that the results derived for simple geometries may be applicable to engine geometries. However large errors in the convective boundary conditions may have only a small effect on the calculated disc temperatures. Did the authors examine the effect of the variation of the correlated Nusselt numbers on the calculation of the temperatures?

Author's Reply

As you said, this is a well conditioned problem. We did calculations with different heat transfer coefficients compared to those which you used for your correlations (the factor was about 0.8 up to 1.2). This variation had only a very small effect.

J.M.Hannis, UK

You mentioned the importance of re-using the compressor ventilating air for cooling purposes elsewhere in the engine to avoid excessive performance penalty. Is the pressure loss in the ventilation air circuit imposed by the radial inflow between the compressor discs likely to be a problem in achieving this?

Author's Reply

The pressure loss will be no problem in this case, as the ratio of inner to outer diameter of the cavity is about 0.6. The investigations of Owen show that high pressure losses occur at high radial mass flow rates, when the source region for radial inflow fills the entire cavity. This maximum pressure loss is the higher, the smaller is the ratio of inner to outer radius of the cavity.

C.T.J.Scrivener, UK

You have described the performance and life improvements with this disc cooling system. There is an additional factor which may cause a performance loss — this is the additional power consumed on the disc in pumping the air. Have you any estimates for this power either from measurements or calculations?

Author's Reply

We did not look at this point in detail, but we think, that the effect will not be significant.

H.H.Saravanamuttou, Ca

The prediction of tip clearances is very difficult, especially in dynamic situations; these may be slowly varying (e.g. climb in a civil aircraft) or rapidly varying (e.g. combat manoeuvring). In the case of a compressor the temperature effects may not be too critical, but accurate knowledge of the disc temperatures would appear essential for turbine clearance predictions.

- (1) Could the author indicate the expected radial clearance at full load both for the compressor and the turbine.
- (2) Could the author indicate the expected thermal and centrifugal growths of the disc-blade combination for the compressor and the turbine.

Author's Reply

The thermal and centrifugal growths of the discs depend on a number of parameters. For lower disc temperatures, the thermal growth may be of the order of 30% of the total growth.

At very high temperature levels, the thermal growth can reach 90% of the total growth.

The corresponding tip clearances depend on the thermal behaviour of both the rotor and the casing structure. As there are different design features for the casing (active or passive clearance control) the tip clearances depend on the individual configuration.

HEAT EXCHANGERS IN REGENERATIVE GAS TURBINE CYCLES

by
M.N.R. NINA and M.P.N. AGUAS
Department of Mechanical Engineering
Instituto Superior Técnico
1096 Lisboa Codex
Portugal

SUMMARY

Advances in compact heat exchanger design and fabrication together with fuel cost rises continuously improve the attractiveness of regenerative gas turbine helicopter engines. In this study cycle parameters aiming at reduced specific fuel consumption and increased payload or mission range, have been optimized together with heat exchanger type and size.

The discussion was based on a typical mission for an attack helicopter in the 900 kw power class. A range of heat exchangers was studied to define the most favourable geometry in terms of lower fuel consumption and minimum engine plus fuel weight. Heat exchanger volume, frontal area ratio and pressure drop effect on cycle efficiency were considered.

NOMENCLATURE

P	- Pressure, Pa
ΔP	- gain in total weight, kg
R	- compressor pressure ratio
SFC	- specific fuel consumption, g/kwh
ASFC	- gain in SFC, g/kwh
T	- temperature, K
V	- exchanger matrix volume, m ³
β	- heat transfer surface area density, m ² /m ³
ϵ	- heat exchanger effectiveness
η_{cy}	- thermal efficiency of cycle
η_c	- isentropic compressor efficiency
η_t	- isentropic turbine efficiency

GENERAL CONSIDERATIONS

Helicopters operate at low engine loads for most of the duration of their missions resulting in high specific fuel consumptions. The standard gas turbine engines with high pressure ratio have a high thermodynamic efficiency at design point but its value decreases very drastically with load. In contrast, the regenerative engine can be designed to have its lowest specific fuel consumption (S.F.C.) at part load resulting also in a low weight heat exchanger.

For this type of application the compact heat exchangers are well suited but the design must be carefully optimized in order to achieve favourable operational characteristics.

Two typical approaches can be adopted in this respect:

- (1) The total helicopter weight at take-off to be the same as the reference (non-regenerative) helicopter, thus achieving a low SFC: no gain in total weight means that the difference saved in fuel weight for a given mission is used up by a regenerator with a high effectiveness.
- (2) The heat exchanger is chosen so that a minimum weight at take-off is obtained. This leads to a higher SFC than in the previous case because the heat exchanger is smaller with a lower effectiveness, but has the advantage of increased payload or maneuverability.

The flow diagram for a regenerative cycle is shown in fig. 1. Its thermal efficiency (with $\epsilon=1$) is (Haywood):

$$\eta_{cy} = 1 - (R/\alpha)$$

where $\alpha = P_2/P_1$ and $\alpha = \eta_c \eta_t T_4/T_1$, showing that η_{cy} falls linearly with pressure ratio increase. There is a maximum value of R for a given α , because the heat exchanger can only be useful when the turbine outlet temperature is larger than the compressor outlet temperature. Practical heat exchangers will have effectivenesses of less than 0.8 and as shown in fig.2, this will affect the value of η_{cy} as a function of R.

An additional irreversibility that must be taken into account when analysing practical cycles is the pressure drop in combustion chambers, heat exchanger passages, ducts, etc. because these losses will have a significant effect on cycle efficiency and on optimum parameter values.

The present work was based on the following fixed assumptions:

Inlet temperature, T_0 : 290 K
Inlet pressure, P_0 : 101330 Pa
Specific humidity = 6.0083 Kg H₂O/Kg dry air
Inlet filter pressure drop = 0,05 of P_0

Combustion chamber pressure drop = 0,03 of P_3
 Turbine inlet temperature, $T_4 = 1400$ K
 Compressor isentropic efficiency, $\eta_c = 0,8$
 Turbine isentropic efficiency, $\eta_t = 0,9$
 Combustion efficiency = 0,95
 Fuel lower heating value = 46 000 KJ/Kg

The engine was designed for 900 KW at full power and the optimization performed at 46% part load (414 KW) for a typical mission duration of 2h30min (plus 20 min reserve).

SELECTION OF HEAT EXCHANGER TYPE

All heat exchangers were assumed to have a square frontal area on the gas passage; the length of the air passage resulted always much larger than that of gas due to the approximately equal pressure drop distribution and the differences in pressure and temperature; Copper was the material used to evaluate matrix weight.

Different types of heat exchangers were tested: four tubular and thirteen plate type. The geometries used are defined in (Kays and London).

Those with finned tubes were:

- 1 - circular tubes and fins
- 2 - circular tubes, continuous fins
- 3 - flat tubes, staggered, continuous fins
- 4 - flat tubes, in line, continuous fins

Tests were made for ϵ between 40% and 60% and pressure ratios of 5 and 8. The results confirmed that this type of exchangers are not well adapted to aeronautical use. Although they exhibit very low pressure drops, their weight is high. On trying to design a lighter one ($\epsilon=45\%$) the gain in SFC was moderate (21g/KWh). They were excluded from further study.

Tests on plate heat exchangers were run with:

- 1 - plain fins (5)
- 2 - louvered fins (3)
- 3 - strip fins (3)
- 4 - wavy fins (2)

Pressure ratios between 5 and 8 and ϵ between 40% and 70% were used. Three exchangers were selected from those thirteen, based on minimum total weight (fuel at take-off + exchanger matrix):

- 1 - Plate wavy fins 17.8-3/8 W
- 2 - Plate wavy fins 11.44-3/8 W
- 3 - Plate strip fins 3/32-12.22

CYCLE OPTIMIZATION

The three selected exchangers, tested in the range of pressure ratios between 5 and 16, showed an optimal R of about 8.

Figure 3 shows the difference in weight and SFC compared to the reference helicopter for the 17.8-3/8 W wavy fin. The influence of the value of ϵ is significant in both accounts and the effect of pressure ratio is mixed.

If the first criterion is used, that is an helicopter with the same weight and payload at take-off, the optimum pressure ratio is 8, ϵ will be around 70%, with a gain in SFC of 44g/KWh.

On the other hand, if the criterion for minimum weight is used, a pressure ratio of 10 would be selected, $\epsilon=60\%$ saving 14Kg in weight and 32g/KWh in SFC.

Similar study is presented on figures 4 and 5 for heat exchangers 11.44-3/8W and 3/32-12.22, but the results are somewhat different.

Maximum gains in SFC are obtained for pressure ratio around 8 but are somewhat lower than for type 17.8-3/8W. Maximum weight savings are also obtained with R of 10. Table 1 compares the performance of the three types of exchangers showing that 17.8-3/8 W is the best choice for both criteria and also presents the lowest matrix volume.

Figure 6 (A, B, C) shows heat exchanger type 17.8-3/8 W volume, passage length and weight reduction as a function of ϵ and pressure ratio: a decrease in effectiveness from 70% to 60% will reduce the matrix volume to less than half.

0: Table 2 the main cycle temperatures and typical mission fuel consumptions are compared.

FULL POWER RATING

It is necessary to analyse full power performance in order to compare the effect of increased mass

flow on cycle parameters. The study was made for the two cases ($\Delta P=0$ and Δi max) with one heat exchanger (type 17.8-3/8 W) varying shaft output between 46% (optimization) and 100% (900 KW).

Figure 7 (A, B, C, D) shows that for case 1 ($\Delta P=0$) the larger heat exchanger ($\epsilon=70\%$) the decrease in due to full load higher mass flow is moderate (7%) and the increase in pressure drop (air and gas sides) noticeable, rising from total of 5% to 15%, the SFC reaches 240g/KWh but is still less than the reference SFC (255 g/kwh).

The analysis of case 2 (ΔP max) with the smaller heat exchanger ($\epsilon=60\%$) shows that a by-pass system is required, except for the R=12.5 engine. The pressure drops rise very steeply with high load mass flows.

CONCLUSIONS

The regenerative helicopter gas turbine engines exhibit a number of characteristics that make them competitive using present day technology.

The requirement of moderate pressure ratios saves on compressor complexity and weight.

Optimization procedure selected a plate wavy fin exchanger type 17.8-3/8 W as the most favourable on both criteria, enabling fuel savings of up to 20%.

It was possible to have an exchanger that could cope with high mass flow at full load without the need for a by-pass system.

The IR suppressor, if required, will be lighter due to lower gas temperature T_6 .

New arrangements for the matrix and the ducts will be needed to improve the regenerative engine layout. Fin materials lighter than copper can be used.

The regenerative helicopter in the 900 kW class will be able to pay for its additional procurement cost with the cost of fuel saved during its service life, depending on the number of hours of flight per year and years in service. Lighter exchangers and rising fuel costs will also contribute toward this goal. With fuel cost at US\$ 0,30/Kg, a service life of 20 years at 500 hours of flight per year, the fuel saved will amount to US\$110,000.00 that would pay for the additional procurement cost resulting from the implementation of two regenerators.

To take full advantage of the regenerative cycle characteristics, all components need to be adapted and in particular the flame tubes that are exposed to higher air inlet temperatures. The use of distinct geometries in air and gas passages was not included in this study and will probably result in added advantages on weight and pressure drop.

REFERENCES

1. Haywood, R.W. "Analysis of Engineering Cycles", Pergamon Press (1980)
2. Kays, W.M. and London, A.L. "Compact Heat Exchangers", McGraw-Hill (1964)
3. Kakaç, S., Bergles, A.E. and Mayinger, F. "Heat Exchangers", Hemisphere Publ. Co (1981)
4. Helicopter Propulsion Systems - AGARD CP-302 (1981)

TABLE 1 - HEAT EXCHANGER PERFORMANCE COMPARISON

ϵ (%)	Δ SFC (g/KWh)			Δ P (Kg)			V ($\times 10^{-3}$ m)					
	1	2	3	1	2	3	1	2	3			
	R=8	55	60	65	70	55	60	65	70	55	60	65
	17	28	37	44	5	11	10	0	14	20	30	45
	25	33	39	46	10	12	5	-12	22	32	47	78
	25	32	40	43	10	9	2	-15	24	34	53	88
	28	28	28	28	13	14	13	14	22	24	24	24
R=10	55	60	65	70	55	60	65	70	55	60	65	70
	24	31	37	42	13	14	13	-2	14	19	30	45
	28	33	38	42	14	11	10	3	22	34	47	76
	28	33	38	43	10	3	1	-17	24	34	53	81
	28	28	28	28	-2	-17	-18	-18	24	24	24	24

TABLE 2 - CYCLE TEMPERATURES (K)

Point	Reference R=12.5	Case 1 E=70% R=8	Case 2 E=60% R=10
0	290	290	290
1	286	286	286
2	696	590	636
3	-	821	782
4	1400	1400	1400
5	-	920	879
6	828	702	741
Typical Mission (one engine)			
SPC (g/KWh)	255	211	224
Fuel (Kg)	299	247	262
Matrix (Kg)	-	52	23
Total (Kg)	299	299	285

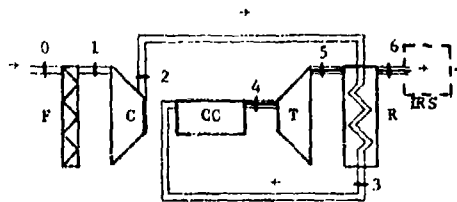
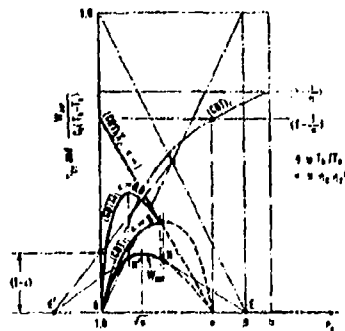


Fig.1 - Regenerative Cycle Flow Diagram

Fig.2 - Variation of n_{cy} with R (Haywood)

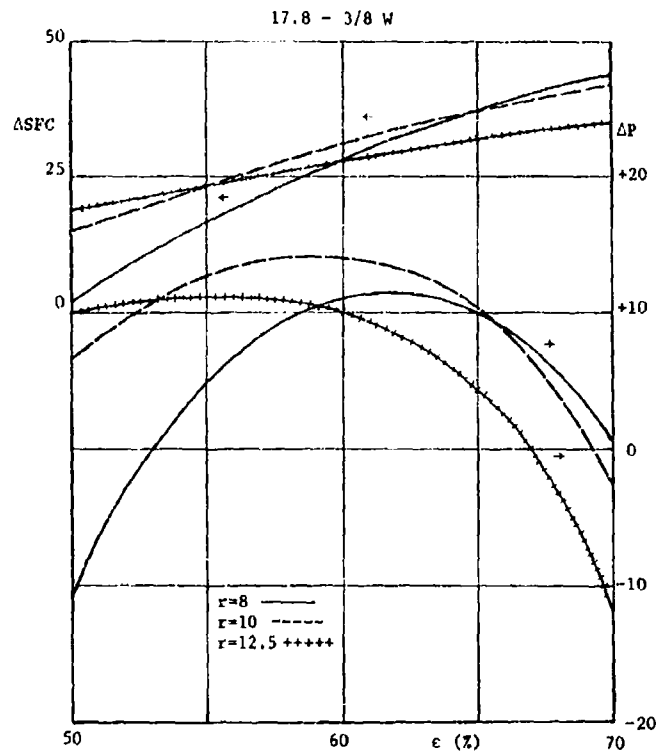


Fig.3 - Variation of SFC and weight with effectiveness

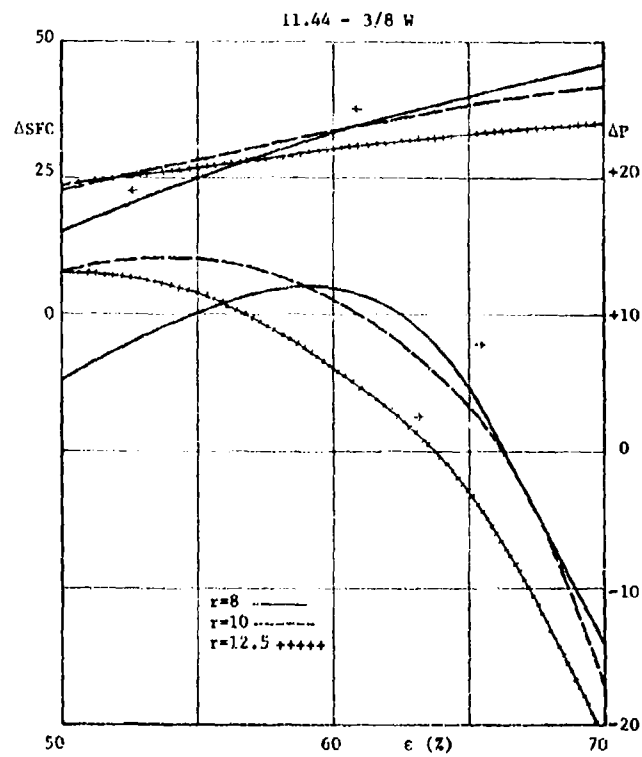


Fig.4 - Variation of SFC and weight with effectiveness

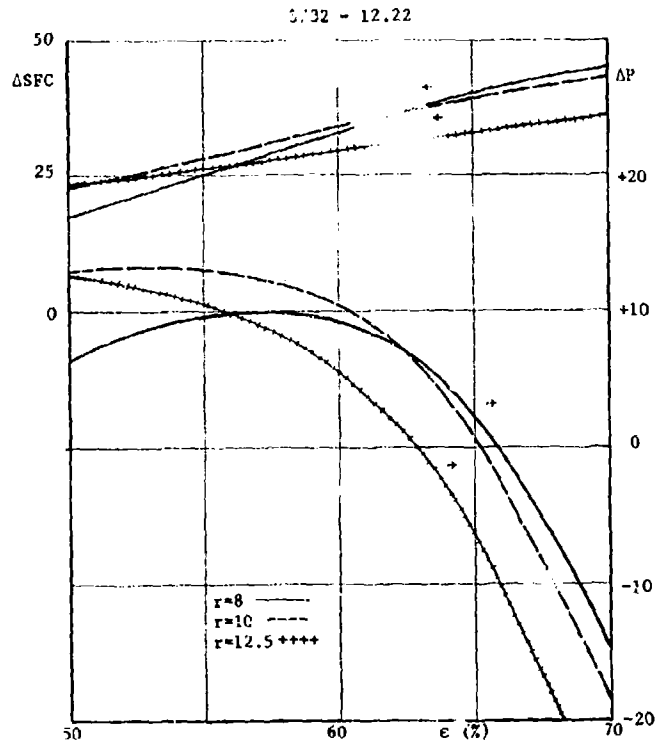


Fig. 5 - Variation of SFC and weight with effectiveness

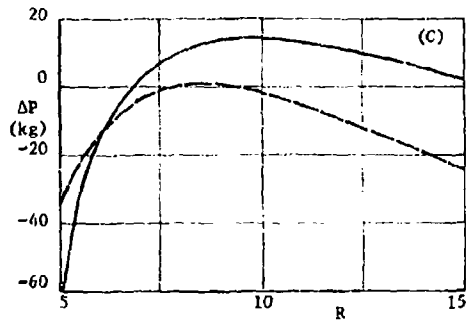
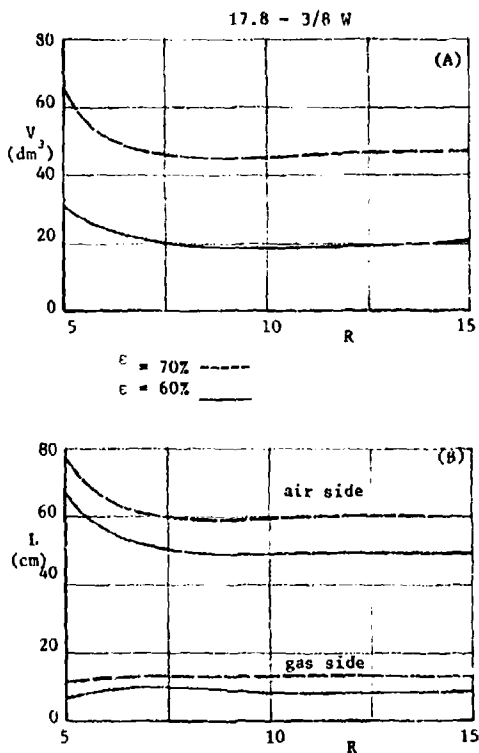


Fig. 6 - Variation of volume, passage length and weight for type 17.8-3/8 W

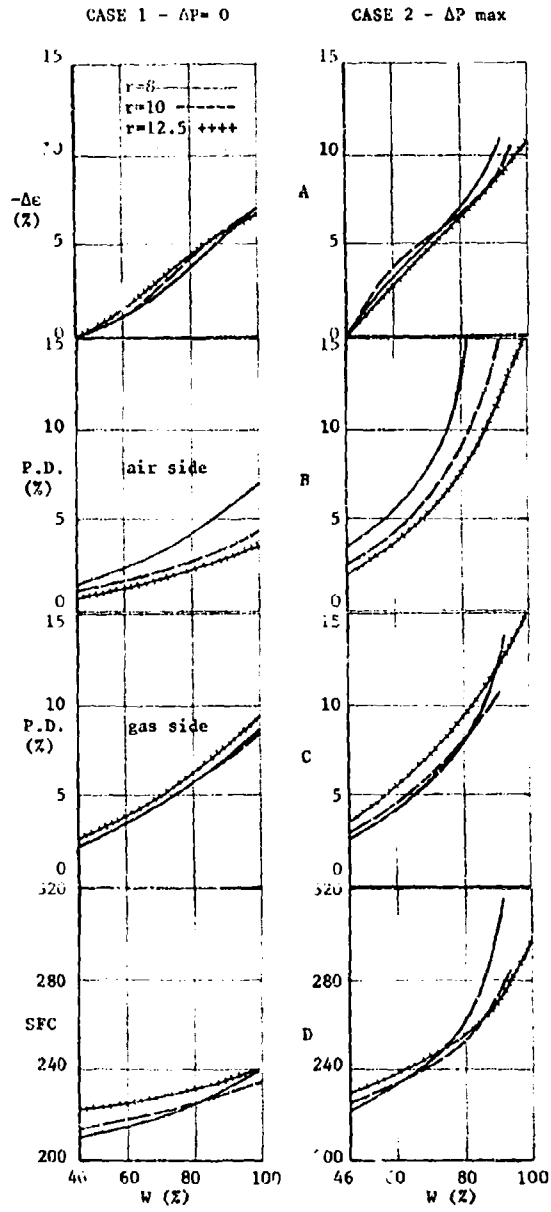


Fig. 7 - Variation of c , pressure drops, and SFC as a function of engine power (W) for cases 1 and 2

DISCUSSION

H.G. Bree, Ge

1. From modern helicopter engines we will require an emergency rating i.e. 2.5 minutes at higher temperature. What are you considering to protect the heat exchanger from overheating?
2. Flying rates of 500 hrs/year do not appear to be applicable to military use. Our army helicopters have a rate of about 200 hrs/year.

Author's Reply

1. Higher temperatures resulting from the emergency rating requirement would have to be taken up both by the heat exchanger system and the turbine itself. The solution would be either to use appropriate materials (perhaps too expensive) or to design a dilution system with a by-pass from a compressor intermediate stage to the turbine outlet.
2. Perhaps the additional procurement costs for implementation of two regenerators will not exceed US \$44,000 (for two regenerators) depending on the number of engines manufactured.

R. Eggebrecht, Ge

I fully agree with your main conclusion that the regenerative helicopter gas turbine exhibits attractive advantages. However, you have chosen heat exchanger matrix data available from standard literature for quite a long time. I want to point out that a thorough matrix optimization for a given performance cycle and mission profile is necessary in order to find out the best suited heat exchanger configuration (aspects of fabrication and mechanical integrity). You jumped to the conclusion that configurations of tubular matrices exhibit disadvantages. Do you plan to look at further heat exchanger matrix optimization and do you expect to arrive at different conclusions at this end?

Author's Reply

This first phase of our study was directed towards cycle optimization based on exchanger selection from existing data (Kays and London) and using the same configuration for air and gas passages on plate type.

We are presently starting the optimization of the matrix itself, based on the experience gained during the first phase, especially on parameter sensitivity.

The manufacturing and integrity aspects will not be included until we obtain relevant data.

A.B. Turner, UK

Have you considered the integrity, i.e. life of the heat exchanger from the operational point of view as materials such as Inconel are very expensive.

Author's Reply

We have not studied either the aspects related to integrity or to manufacture.

P. Ramette, Fr

Avez-vous étudié le cas des échangeurs en céramique?

Que-pensez vous de l'augmentation de trainée d'un hélicoptère liée au volume de l'échangeur (en particulier le diamètre)?

Author's Reply

1. Les caractéristiques thermohydrauliques des échangeurs en céramique étant très peu traitées dans la littérature ouverte, on n'a pas pu les inclure dans nos études, notamment en ce qui concerne les valeurs possibles pour β et les pertes de charge.
2. Pour le cas des hélicoptères, nos études montrent que des échangeurs métalliques, ayant un plein de β élevé, sont acceptables du point de vue poids-volume: la figure 6B indique pour l'échangeur 17.83/8W une aire frontale de 48 cm x 48 cm avec 60% d'efficacité, donc la trainée de l'hélicoptère ne sera pas augmentée.

INTERET DES ECHANGEURS EN CERAMIQUE
POUR TURBINE A GAZ OU TURBOREACTEURS

par Serge BOUDIGUES et Jean FABRI

Office National d'Etudes et de Recherches Aérospatiales
29, avenue de la Division Leclerc
92320 CHATILLON (France)

Résumé

Les échangeurs en acier placés en aval de la dernière turbine des turboréacteurs et des turbomoteurs sont trop lourds et trop encombrants.

Avec un échangeur en carbure de silicium, on peut au contraire arriver à des bilans de masse, de performance, d'encombrement et de coûts capables de séduire certains usagers civils ou militaires.

En effet, la bonne tenue à chaud du carbure de silicium permet de placer l'échangeur en cours de détente. On peut montrer qu'on gagne sur les pressions du flux chaud et du flux froid, ce qui favorise considérablement les échanges, diminuant ainsi la longueur et le diamètre de l'échangeur. La densité de 3,2 conduit alors à des gains de masse spectaculaires.

On envisage la possibilité de permettre à une partie du flux froid de court-circuiter l'échangeur moyennant un paramètre d'adaptation. Ceci permet un genre de rechauffe en n'utilisant qu'un seul foyer et avec un processus thermodynamique de rendement très supérieur.

CERAMIC HEAT EXCHANGERS
FOR GAS TURBINES OR TURBOJET ENGINES

Abstract

Heat exchangers made of steel and placed downstream of the last turbine of a turbojet engine or any gas turbine are too heavy and too cumbersome.

With a heat exchanger made of silicon carbide mass, performance, volume and cost balances much interesting for civilian or military use can be obtained.

Silicon carbide has good thermal performance and makes it possible to situate the heat exchanger between turbine stages. Both the pressure of cold and hot gases are thus increased, the heat exchange processes are amplified, the length and the diameter of the exchanger are reduced. The density of this material being only 3.2, the overall mass of the exchanger is considerably reduced.

It is also possible to shortcut part of the cold air, and obtain thus a controlling parameter. A kind of after burner effect is obtained, although a single combustor is used, and the corresponding thermodynamic process has a higher efficiency than the after burning process.

1 - INTRODUCTION

L'intérêt des échangeurs de chaleur dans les moteurs thermiques est bien connu. Leur rôle consiste, en général, à réintégrer dans le cycle des calories qui, sans échangeur, seraient perdues dans l'atmosphère. Cette réintégration est réalisée au niveau de pression maximum.

Les critiques formulées à l'égard des échangeurs sont multiples :

- pertes de charge,
- masse,
- encombrement (longueur, diamètre),
- encrassement,
- fuites,
- prix.

Le conflit entre pertes de charge d'une part et masse et encombrement d'autre part, conduit pour les installations terrestres de turbines à gaz à des dimensions de l'échangeur qui écrasent la turbine à gaz proprement dite.

Pourtant la firme Bristol a fait voler le Thésée turbopropulseur avec échangeur vers les années 1954. Mais il n'a pas dépassé le stade des prototypes. Notons qu'un brevet pris au Canada protégeait dès 1948 l'utilisation des échangeurs sur les turboréacteurs.

Des calculs exécutés vers 1950 nous persuadaient de l'intérêt thermopropulsif de cette formule en même temps que de l'impossibilité de la mettre en oeuvre en raison de sa masse et son encombrement.

L'apparition de pièces en carbure de silicium a permis de reprendre le problème avec un matériau très conducteur, très léger et résistant à très haute température. L'intérêt thermopropulsif est valorisé par les températures plus élevées. La masse n'est plus un multiple mais une fraction de la masse du moteur. Enfin l'encombrement n'aggrave pas sensiblement celui qu'imposent les doubles flux.

En effet en thermopropulsion le rôle de l'échangeur est double :

- a) en réintégrant dans le cycle des calories au niveau de la pression maximum, il économise le carburant qu'il aurait fallu pour ce faire. Il améliore donc le rendement thermique ou bien permet, à rendement thermique donné de diminuer le rapport de pression ;
- b) en diminuant la température (et la pression) des gaz chauds il diminue la vitesse d'éjection de ces gaz et améliore ainsi le rendement propulsif, ou permet, à rendement propulsif donné, de diminuer le taux de dilution.

L'échangeur sur turboréacteur mono ou double flux apparaît ainsi comme une complication qui simplifie d'autres problèmes :

- forts rapport de pression,
- forts taux de dilution.

Sans jeu de mots on peut dire que l'échangeur échange non seulement des calories mais des masses, des encombrements, des prix.

Aujourd'hui l'échangeur en céramique paraît s'imposer pour les petits propulseurs civils (avions d'affaires, ou d'aéroclubs, missiles de croisière...) dans la mesure où l'on saura résoudre les problèmes que pose le carbure de silicium et son mariage avec le reste métallique du propulseur.

Pour les moteurs de moyenne et de forte poussée, l'échangeur en carbure de silicium apparaît comme une possibilité qui mérite d'être examinée avec une attention d'autant plus forte que les températures maximum des cycles iront en augmentant.

L'ONERA* s'est attaché, avec le soutien de la DRET**, à conduire des études théoriques sur les avantages (et les inconvénients) thermopropulsifs de cette formule. En parallèle, des études théoriques sur les échangeurs ont été développées avec des modélisations simplifiées prenant en compte les propriétés du carbure de silicium et les avantages d'une technologie originale que la firme CERAVER*** a su mettre en oeuvre. L'analyse du comportement d'un échangeur de 120 g/s de débit a pu être menée sur un banc d'essai spécialement aménagé par l'ONERA. Ces essais ont montré une bonne confirmation de la modélisation et quelques difficultés dans la liaison céramique métal.

2 - LES BASES THERMODYNAMIQUES

Sur la planche 1 nous avons fait figurer les divers cycles théoriques dérivés du cycle simple (CS) de la turbine à gaz avec en référence le cycle de Carnot et le cycle d'Erickson moins connu mais qui possède le même rendement théorique grâce à une compression et une détente isotherme avec un échangeur qui récupère les calories en fin de détente pour chauffer à pression constante l'air en fin de compression. Le cycle d'Erickson est, à la turbine à gaz, ce que le cycle de Stirling est aux moteurs volumétriques, c'est-à-dire une asymptote technologique très intéressante mais difficile à réaliser.

C'est bien la technologie qui limite les performances des cycles théoriques. C'est pour ça sur la planche 2 nous avons fait figurer sur le même graphique les rendements en fluide parfait et les rendements en fluide réel de 7 cycles qui ont reçu ou pourraient recevoir des réalisations aéronautiques. Nous n'avons pas mis le cycle de Carnot ni le cycle d'Erickson en fluide réel car ils semblent conduire à trop de complications, trop de volume et trop de poids. Il est possible cependant qu'un cycle d'Erickson soit mis en oeuvre en turbine terrestre ou navale en remplaçant, bien sûr, les compressions et détente isothermes par des microstructures en dents de scie.

Sur la planche 2 les rendements en fluide réel sont très dépendants des qualités des composants (compresseur et turbine) et des pertes de charge dans les conduits ou les foyers. On notera en abscisse la variable $\frac{T_{4i} - T_{2i}}{T_{2i}}$ qui représente l'enthalpie apportée par le compresseur rapportée à l'enthalpie à l'entrée.

Ce paramètre nous semble préférable au rapport de pression qui mélange l'apport d'enthalpie et la qualité de cet apport. Nous utiliserons donc par la suite ce paramètre.

On notera sur la planche 2 que la compression refroidie (C.R.) donne le meilleur rendement. Notons cependant que la courbe ne prend pas en compte l'énergie nécessaire au refroidissement ce qui est réalisé pour une turbine navale ou pour une turbine terrestre au bord d'une rivière, mais ce pourrait être valable pour un double flux qui, servant à refroidir la compression primaire, utiliserait, sous l'angle propulsif, les calories prélevées. Mais ce bon rendement est obtenu avec une très forte enthalpie de compression. Ainsi à la difficulté de l'échangeur s'ajoute la complication d'un très grand nombre d'étages de compression et de détente.

A l'opposé on trouve l'échangeur aval (EA) qui atteint un rendement du même ordre mais avec une très faible enthalpie de compression. Certes cet échangeur pose plus de problème que celui qui refroidit la compression mais le nombre d'étages de compression et de détente est considérablement diminué.

Très près on trouve l'échangeur intermédiaire (EI). Nous l'appelons intermédiaire car il se place en cours de détente entre les turbines. Deux formules sont possibles :

- EI₁ entre la turbine du générateur et la turbine de puissance,
- EI₂ entre deux roues de turbine du générateur.

Dans ce dernier cas la position doit être optimisée en fonction de la température maximum et de la qualité des composants (ce qui est le cas de la planche 2).

On notera que EI₂ est plus mauvais que EI₁ et qu'il réclame une plus forte enthalpie de compression (pourtant, en fluide parfait EI₂ est supérieur à EI₁).

L'enthalpie de compression est plus élevée que celle de EA mais reste très inférieure à celle du cycle simple. L'avantage de EI₁ vient de ce que les valeurs de sa longueur, de son diamètre et de sa masse sont très inférieures aux valeurs de EA (dans un rapport de 1 à 3). En effet le cycle est plus comprimé donc l'air en sortie de compression tient moins de place et fournit un meilleur coefficient d'échange. De même les gaz sont à une pression qui vaut 4 ou 5 fois la pression atmosphérique qui est celle de l'échangeur aval. On a donc les deux mêmes effets que pour l'air.

De plus soulignons l'apparition récente, comme matériau d'échangeur, du carbure de silicium SiC. Avec une masse volumique de 3200 kg/m³, une contrainte de traction admissible supérieure à 400 MPa jusqu'à 1400°C, une conductibilité supérieure de 100 % à 0°C et de 30 % à 800°C à celle de l'acier ce matériau convient parfaitement pour les échangeurs EI ou EA. Il est clair que pour EI il est le seul possible avec les températures T_3 aujourd'hui utilisées. Sa mise en oeuvre en tube nervurés ne pose pas de problème. La difficulté vient essentiellement de son faible coefficient de dilatation (4.10⁻⁶ au lieu de 16.10⁻⁶ pour les aciers). La liaison avec les pièces métalliques pose donc des problèmes d'étanchéité ou de bridage mais qui paraissent pouvoir être surmontés.

Au passif de l'échangeur intermédiaire il faut mettre le fait qu'il diminue très sensiblement la puissance par unité de débit. Mais pour les petits propulseurs ça peut devenir un avantage. Par ailleurs l'échangeur intermédiaire peut être court-circuité, partiellement ou totalement, lorsqu'on veut la pleine puissance ce qui est une façon de valoriser les régimes réduits. (Un paramètre d'adaptation de la turbine ou de la tuyère en aval de l'échangeur est nécessaire si l'on veut donner au processus sa pleine efficacité).

La rechauffe en cours de détente R₁ ou R₂ est plus mauvaise que le cycle simple en fluide parfait, ça se confirme en fluide réel. La rechauffe augmente la puissance par unité de débit mais détériore le rendement. Le procédé est utilisé (sous la forme R₁) dans les turbofacteurs militaires. L'effet est le même que le court circuit de EI₁ mais thermodynamiquement il vaut mieux court-circuiter un échangeur qu'allumer une rechauffe (ce qui réclame aussi un paramètre d'adaptation de la tuyère).

3 - L'ASPECT PROPULSIF

Sur un monoflux la vitesse d'éjection est considérablement diminuée. On retrouve les vertus (et les vices) du double flux, c'est-à-dire un bon rendement propulsif mais un encombrement et un poids plus élevés. Toutefois l'échangeur peut être court-circuité (en particulier au décollage ou en fin de mission pour un missile) alors que la dilution ne peut pas être escamotée. La tuyère à section variable nécessaire est plus simple qu'avec une rechauffe traditionnelle puisque la température est celle qu'auraient les gaz s'il n'y avait pas d'échangeur. En dosant le débit court-circuité on a un véritable moteur à cycle variable avec le choix entre forte poussée et bonne consommation spécifique.

Sur double flux, la présence de l'échangeur diminue la vitesse d'éjection du flux primaire et, de ce fait, diminue la mauvaise influence que ce flux exerce sur le rendement propulsif global. Par ailleurs le taux de dilution optimum pour une température donnée se trouve abaissé puisque le flux primaire fournit moins de puissance par unité de débit, comme par ailleurs l'enthalpie de compression et de détente du flux primaire sont plus faibles il en résulte une grande simplification technologique (absence de réducteur, facilité pour un inverseur, faible nombre d'étages de compresseur et de turbine). Le maître couple est sensiblement identique. On peut donc dire qu'on a un moteur un peu plus gros en primaire, un peu moins gros en secondaire de diamètre, de longueur et de masse sensiblement équivalents.

C'est une autre façon de résoudre le problème que pose l'augmentation des températures T_{5i} , qui, en formule classique entraîne de trop forts $T_{4i} - T_{2i}$ (donc beaucoup d'étages de compression et de turbine), de trop forts taux de dilution imposant la présence d'un réducteur, ou bien un nombre très élevé d'étages de turbine.

En gros, comme nous l'avons dit dans l'introduction, l'échangeur échange non seulement des calories, mais des difficultés technologiques. L'apparition du carbure de silicium vient renforcer considérablement l'intérêt des échangeurs et tout particulièrement de l'échangeur intermédiaire.

Après ces généralités thermopropulsives nous décrivons ci-dessous quelques cas d'applications de l'échangeur en cours de détente.

4 - ECHANGEUR SUR MONOFLUX

4.1 - Propulseurs pour avions d'aéroclubs

Pour ce type d'avions l'hélice entraînée par un moteur alternatif possède aujourd'hui le monopole. Pour les conditions $Z = 2000$ m, $M = 0,2$ (240 km/h) nous avons établi les courbes des planches 3 et 4. Nous avons pris des rendements de compression $\eta_c = \eta_D = 0,85$ conformes à ce que donnent des compresseurs centrifuges et des turbines centripètes dans cette gamme de débit (deux à trois kg/s).

Pour le refroidissement des aubes nous avons admis une loi que nous conserverons pour les autres calculs : Q étant le débit propulsif, l'air de refroidissement est $p_i Q$ tel que :

$$p_i = 0,02 + \frac{T_{5i} - 1200}{10000}$$

Pour la perte de charge de chacun des échangeurs (en % de leurs pressions amont respectives) :

$$\epsilon_{ef} = \epsilon_{ec} = (0,03 - 0,025 E) \frac{E}{1-E}$$

F comme froid,

C comme chaud.

Cette loi est conforme à nos premiers résultats d'essais. Elle sera conservée dans la suite. De même nous avons pris pour tous les cas :

pertes de pression : - à l'admission $\epsilon_a = 0,01$
 - dans le foyer $\epsilon_f = 0,05$
 - à l'éjection $\epsilon_e = 0,03$

Sur les planches 3 et 4 on voit que l'optimum optimum (point A) pour ce cas de vol et dans le cadre de nos hypothèses réalistes est obtenu pour une température de 1000°K et une variation de température de 180° dans le compresseur. Cette valeur est très facile à réaliser par un compresseur centrifuge en aluminium. La charge aérodynamique et thermique de la turbine centripète est, elle aussi, très acceptable. On a pour le point A :

$$\left\{ \begin{array}{l} C_s = 0,675 \text{ kg/h.daN} \\ \frac{F}{Q} = 340 \text{ m/h} \end{array} \right.$$

Par court-circuit de l'échangeur on obtiendrait au décollage le point B ($e = 0$, $T_{5i} = 1300$ K) pour lequel $\frac{F}{Q} = 690$. Avec un débit de 3 kg/s on aurait une poussée au décollage de 200 daN c'est ce que donne approximativement un moteur de 160 CV entraînant une hélice.

En croisière la consommation horaire serait de :

$$340 \times \frac{1}{10} \times 0,675 \cdot 3 = 69 \text{ kg/h de kérosène au lieu de 35 kg/h d'essence avion.}$$

La consommation est doublée mais avec un carburant deux fois moins cher. Pour une autonomie de 2 h 1/2 de vol on perdrait $34 \times 2,5 = 85$ kg de carburant mais le réacteur avec échangeur pèserait environ 70 kg au lieu des 200 kg de l'accouplement moteur alternatif et hélice. Au bilan on gagne 45 kg.

Il est clair que ces chiffres approximatifs devraient être précisés par un constructeur de moteur et par un constructeur d'avion. Mais en gros le bilan financier est approximativement nul, le bilan de masse semble à l'avantage du turboréacteur avec en prime beaucoup moins de bruit et une meilleure facilité d'installation.

4.2 - Propulseurs pour missiles subsoniques

Les planches 5 et 6 reprennent, avec les mêmes hypothèses sur les rendements et les pertes de pression, les courbes $C_s (T_{4i} - T_{2i}) \frac{F}{Q} (T_{4i} - T_{2i})$

Pour ce cas de vol $Z = 0$, $M = 0,7$ l'optimum optimum est obtenu pour une température de 1300 K mais nous proposons de choisir plutôt le point A à 1200 K qui perd à peine 2 % en C_s et qui évite tout

refroidissement des aubes. La C_3 est alors de 0,925 kg/h.daN c'est-à-dire celle que donnerait un double flux ayant $T_{4i} - T_{2i} = 450^\circ$ et un taux de dilution de 3. Au point A $T_{4i} - T_{2i} = 250^\circ$ beaucoup plus facile à réaliser avec un seul compresseur centrifuge et une turbine centripète alors que la formule classique réclame deux étages axiaux de soufflante qui gavent un centrifuge chargé de réaliser encore 300° , un étage de turbine HP et deux étages de turbine BP.

Une étude grossière montre que l'encombrement des deux moteurs est du même ordre et que le débit propulsif est sensiblement le même.

Notons enfin que par court-circuit de l'échangeur on obtient le point B ($\epsilon = 0$) avec $\frac{F}{Q} = 550$ soit un supplément de poussée de $\frac{550 - 340}{340} = > 62\%$

Pour ce cas encore, ces chiffres demandent à être avalisés par un motoriste mais les ordres de grandeurs paraissent attractifs en particulier au niveau du prix du moteur.

Sur la planche 7 nous avons regardé ce que coûterait de doubler les pertes de charges ϵ_{ef} , ϵ_{ac} que nous avons portées à 8% pour chacun du flux. La perte de C_3 est alors de 7% mais on gagnerait en diamètre de l'échangeur. A l'opposé on a cherché ce que donneraient 3 points de mieux sur les rendements de compresseur et de turbine (formule axiale) le gain est alors de 6% en C_3 .

5 - ECHANGEUR INTERMEDIAIRE SUR DOUBLE FLUX

Le thème retenu est la propulsion d'un avion à $M = 0,8$ pour une altitude $Z > 11000$ m.

Pour cette partie les planches 8, 9, 10 et 11 portent en abscisse le rapport de pression compte tenu que nous gardons pour ces planches le même rendement polytropique de compression $\eta_c = 0,87$. Cette valeur est aussi celle du rendement polytropique de détente $\eta_p = 0,87$.

Les double flux sont à flux séparés avec un seul étage de soufflante comprimant à 1,6. Le taux de dilution est obtenu pour chaque cycle en écrivant que le taux de détente dans la tuyère primaire est de 1,8.

Sur la planche 8, pour la gamme de température aujourd'hui utilisée on a tracé en fonction du rapport de pression $\frac{P_{4i}}{P_{2i}}$ les courbes de consommations spécifiques C_3 pour les doubles flux classiques et pour les doubles flux avec échangeur intermédiaire.

Sur la partie basse on a figuré l'évolution des taux de dilution λ .

On note :

- le gain de C_3 est de : 5,8% sur les optimums à 1200 K,
3,3% " " " 1600 K ;
- avec échangeur les optimums sont obtenus à rapport de pression beaucoup plus faibles :
13 au lieu de 28 à 1200 K,
31 au lieu de 57 à 1600 K ;
- les taux de dilution avec échangeurs sont très inférieurs à ceux du moteur classique. Sur la C_3 min
 $\lambda = 2,5$ au lieu de 3 à 1200 K,
 $\lambda = 5$ au lieu de 6,5 à 1600 K.
Notons que si l'on se place à gauche de l'optimum (ce qui se fait toujours) l'écart va en croissant.

Sur la planche 9 on envisage pour l'avenir des températures plus élevées. Le gain de C_3 s'amenuise mais il reste que ce gain est obtenu avec des rapports de pression beaucoup plus faibles et des taux de dilution très inférieurs.

Sur la planche 10 on envisage de ne pas chercher un gain de C_3 mais de réaliser la même C_3 .

Le rapport de pression est alors de : 6 au lieu de 28 à 1200 K,
18 " " 57 à 1600 K.

Il sera de 40 au lieu de 85 pour 1900 K,

$\lambda = 1,5$ au lieu de 3 à 1200 K
 $\lambda = 6$ au lieu de 6,5 à 1600 K

On aura $\lambda = 6,5$ au lieu de 9,5 à 1900 K.

La planche 11 donne la poussée F par unité de débit total $(1 + \lambda)Q$ pour $\epsilon = 0 - 0,6 - 0,7 - 0,8$. On remarque sur les courbes du bas de la planche que pour les C_3 minimums les poussées par unité de débit total ne dépendent pratiquement pas de l'efficacité de l'échangeur, y compris sans échangeur ($\epsilon = 0$).

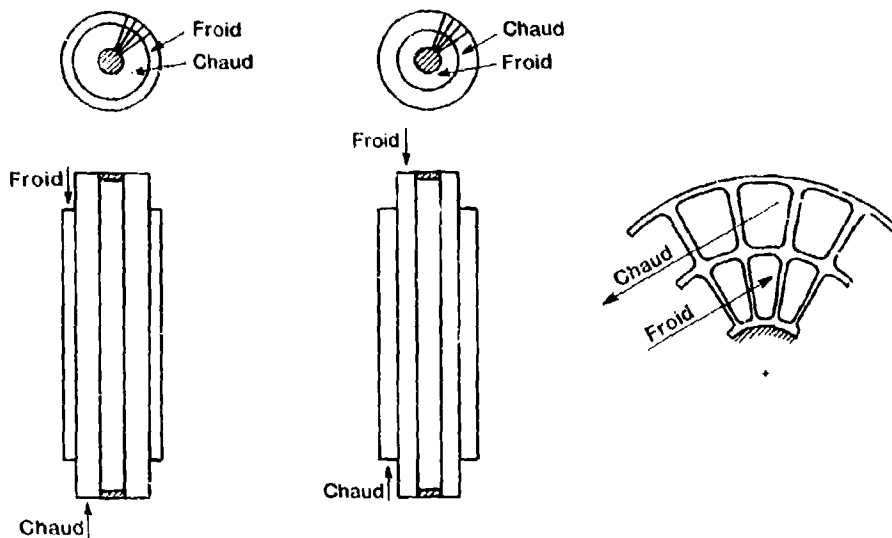
On notera sur les planches 8, 9, 10, 11 le faible écart de performances entre les efficacités 0,8 - 0,7 - 0,6. La complication de l'échangeur (grande efficacité) conduit avant tout à une simplification des phases de compression et de détente et à une diminution du taux de dilution. Dans le cas du double flux encore, l'échangeur est une alternative pour obtenir, par des moyens différents des formules

classiques, une performance donnée. Nous pensons qu'il est utile d'avoir à l'esprit cette alternative.

6 - L'ECHANGEUR EN CERAMIQUE TUBULAIRE NERVURE

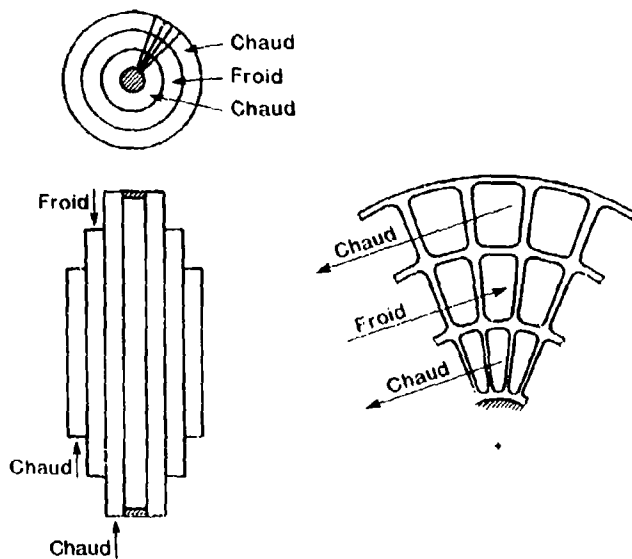
Après de nombreux échanges de vue avec le fabricant CERAVER*** sous l'égide de la DRET** nous sommes aujourd'hui arrivés à la définition suivante :

Tubes à trois cylindres



L'air froid et les gaz chauds circulent à contre courant dans des tubes. L'essentiel de l'échange est réalisé par des nervures radiales à section constante ou évolutive, une partie de l'échange (15 à 20 %) est réalisé par le tube médian entre les nervures.

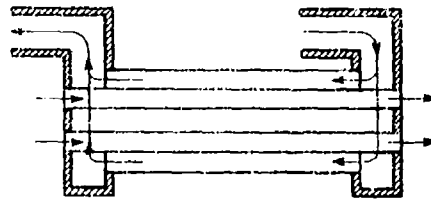
Tubes à quatre cylindres



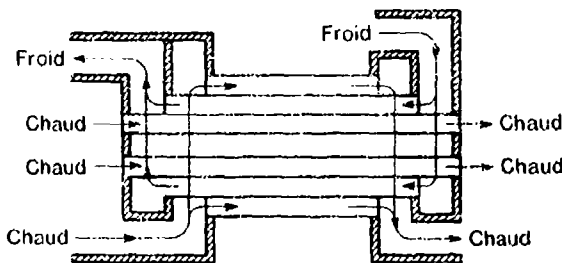
Le flux froid est encadré par deux flux chauds qui circulent dans le même sens et en sens inverse du flux chaud. L'essentiel de l'échange passe par les nervures radiales à section constante ou évolutive. Une partie de l'échange (15 à 20 %) passe par les deux cylindres médians entre les nervures. Un calcul détermine le pourcentage du flux chaud qui passe à l'intérieur ou à l'extérieur.

Les sections de passage du flux froid étant très inférieures à celles du flux chaud il semble logique de fractionner le flux chaud et non le froid.

Alimentation des tubes



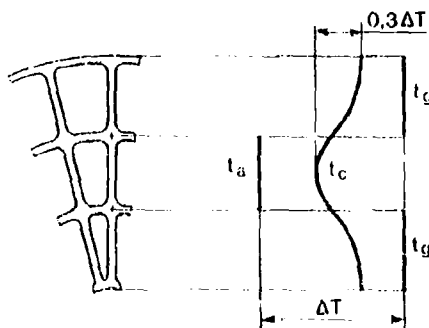
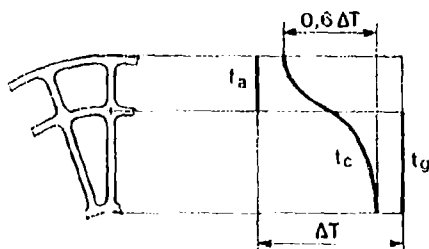
Tubes à trois cylindres



Tubes à quatre cylindres

L'alimentation des tubes à 4 cylindres est plus complexe mais cette formule possède de grands avantages :

- gain en longueur,
- gain en encombrement radial,
- d'où gain en volume et en masse,
- contraintes thermiques plus faibles dans les nervures et dans les tubes.



t_a : température air
 t_g : température gaz
 t_c : température céramique

$\Delta T = t_g - t_a$

Si les tubes à 4 cylindres confirment expérimentalement ces avantages il est clair que l'on pourra étudier une généralisation à des tubes plus compliqués.

Problèmes rencontrés

La fabrication des tubes nervurés est bien au point jusqu'à des longueurs de 600 mm qui semblent suffisantes pour des efficacités d'échangeurs inférieures ou égales à 0,8.

Pour des raisons de légèreté et de rapidité d'exécution les premiers tubes avaient des épaisseurs de nervures de 0,2 mm et il n'y avait pas de rayon de raccordement entre les nervures et les cylindres. Il en est résulté une certaine fragilité des tubes. Les prochaines fournitures auront 0,4 mm et de bons rayons.

Les problèmes les plus sérieux viennent de la liaison entre tubes et flasques. La brasure de verre assurant la liaison doit avoir un coefficient de dilatation voisin de celui du carbure de silicium. Par ailleurs le dépôt manuel de cette brasure est encore artisanal.

Enfin il faut souligner la difficulté de liaison de l'échangeur avec les structures métalliques qui le supportent. Les coefficients de dilatation sont très différents ce qui impose d'interposer des dispositifs très déformables surtout lors des régimes réduits.

7 - CONCLUSION

L'augmentation croissante des températures T_3 , impose des augmentations d'enthalpie également croissantes. En gros si l'on suit augmenter T_3 de 100° il faut augmenter η_3 de la moitié. Les fuites en bout de pale, l'épaississement des couches limites risquent alors d'annuler le bénéfice que l'on attend d'un accroissement de T_3 . Ce point de vue est déjà applicable aux petits moteurs mais risque de s'appliquer bientôt aux propulseurs de moyenne ou de forte poussée.

De même l'augmentation de T_3 , conduit à des augmentations du taux de dilution et déjà on est amené à envisager un réducteur.

La présence d'un échangeur apporte certes une complication, mais peut être une porte de sortie qui contourne les deux difficultés liées aux pressions élevées et aux forts taux de dilution.

L'apparition sur le marché du carbure de silicium permettant la mise en oeuvre d'un échangeur en cours de détente a considérablement atténué les critiques que l'on pouvait faire sur l'encombrement, la masse et le prix des échangeurs.

* ONERA - Office National d'Etudes et de Recherches Aérospatiales
 ** DRET - Direction des Recherches, Etudes et Techniques
 *** CERAVIER - Usine de fabrication de céramiques

CS : Cycle simple
 CR : Compression refroidie
 R : Rechauffe
 EA : Echangeur aval
 EI : Echangeur intermédiaire

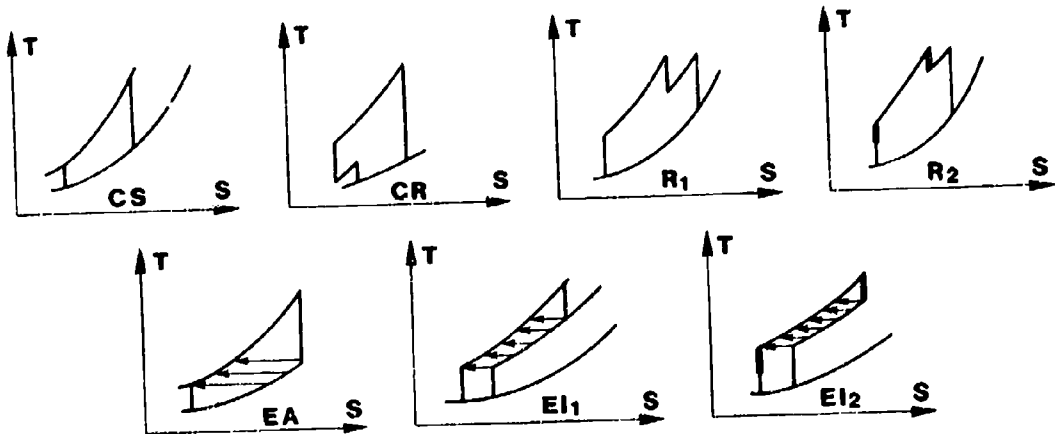
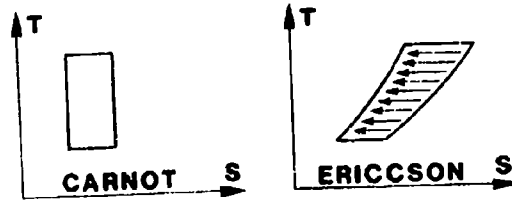
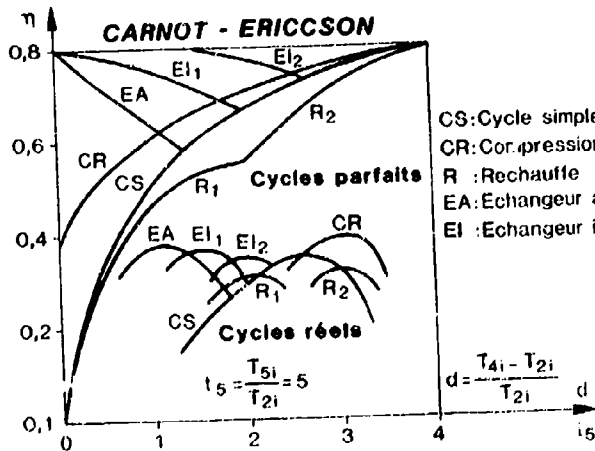
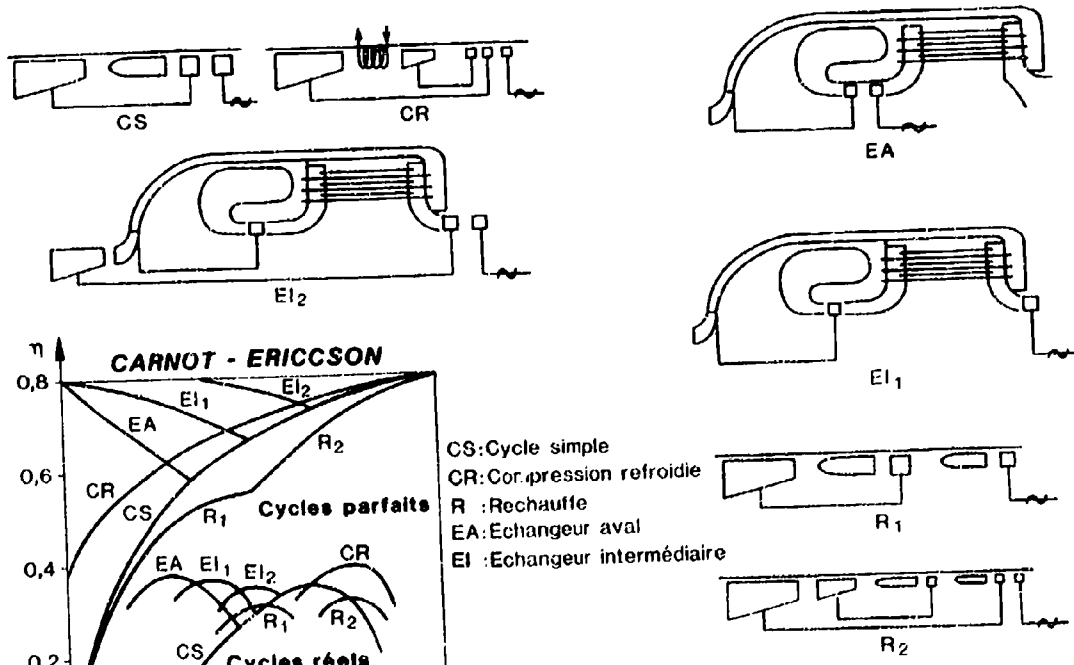


Planche 1



CS: Cycle simple
 CR: Compression refroidie
 R : Rechauffe
 EA: Echangeur aval
 EI : Echangeur intermédiaire

Planche 2

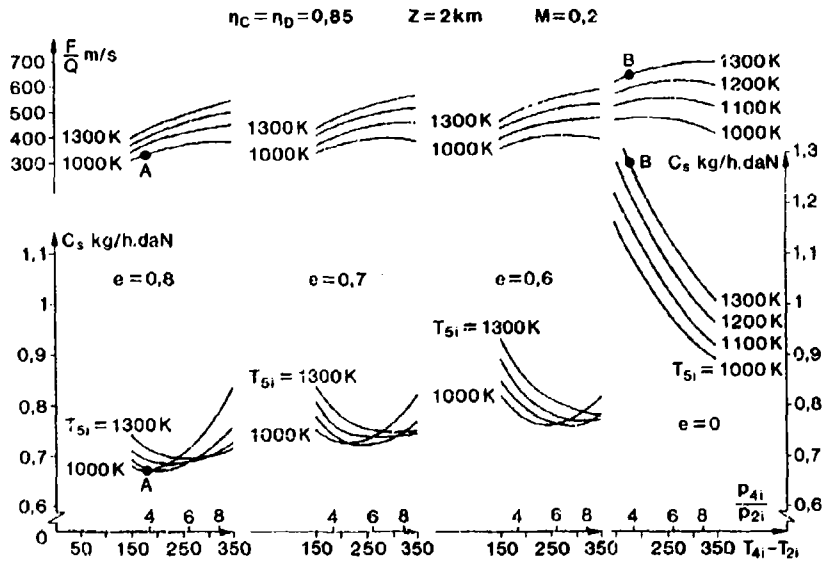


Planche 3

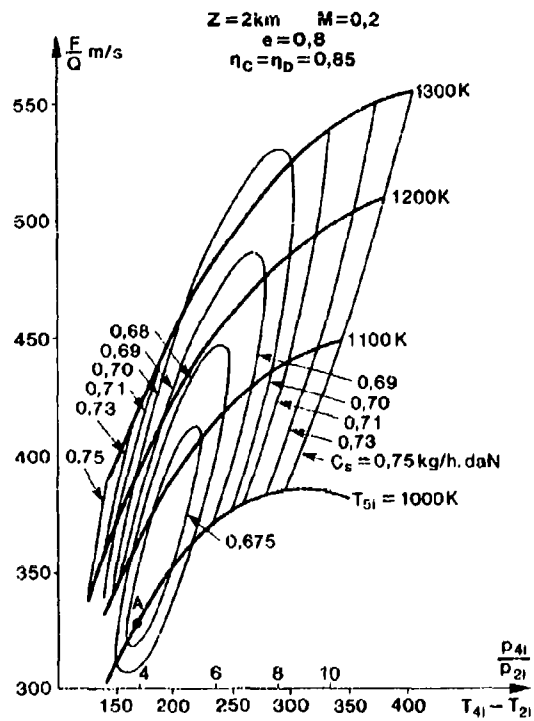


Planche 4

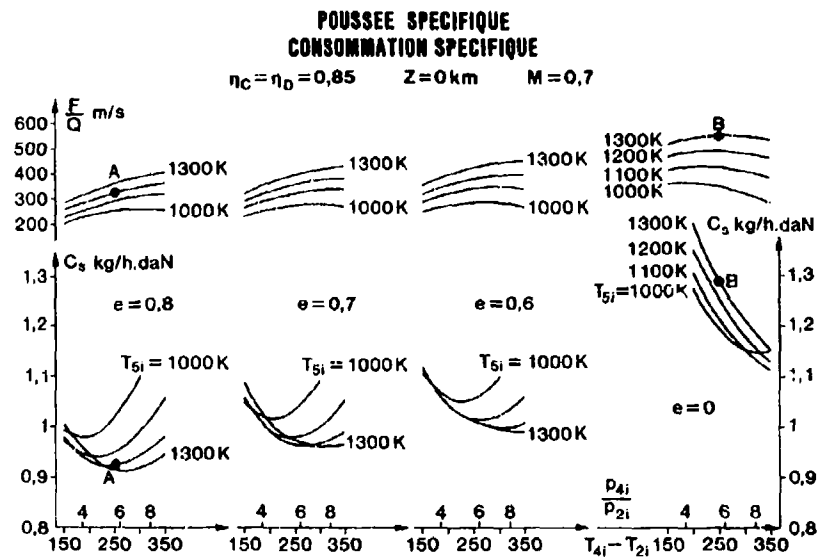


Planche 5

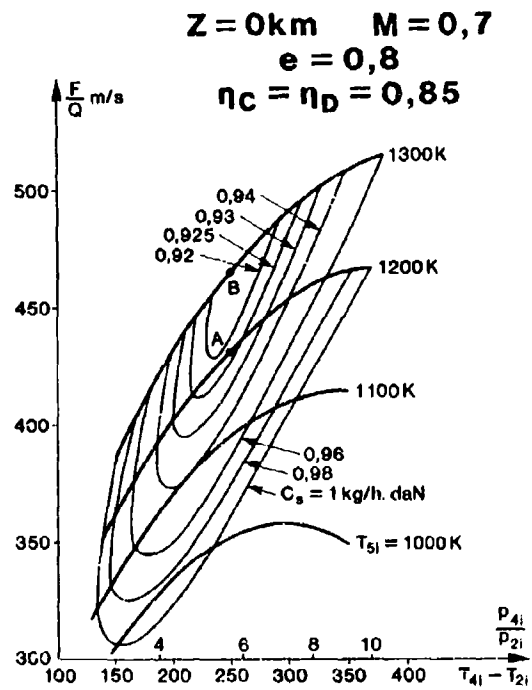


Planche 6

INFLUENCE DES PERTES DE CHARGES DE L'ECHANGEUR
INFLUENCE DES RENDEMENTS $\eta_c \cdot \eta_0 = \eta$

$Z=0\text{km}$ $M=0,7$
 $T_{s1}=1200\text{K}$ ———
 $T_{s1}=1300\text{K}$ - - - -

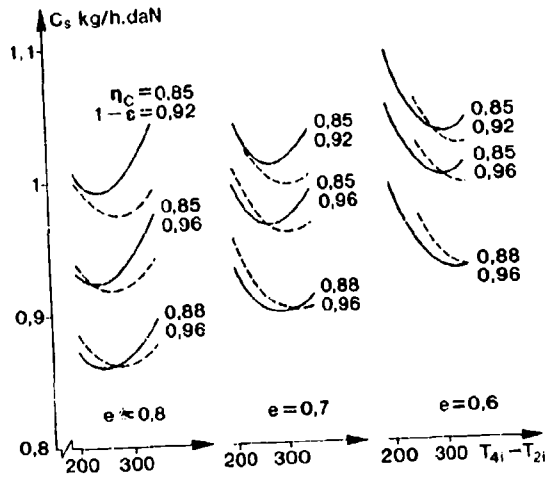


Planche 7

INFLUENCE DE LA TEMPERATURE MAXIMUM

$Z \geq 11\text{km}$ $M = 0,8$
 $\eta = 0,87$

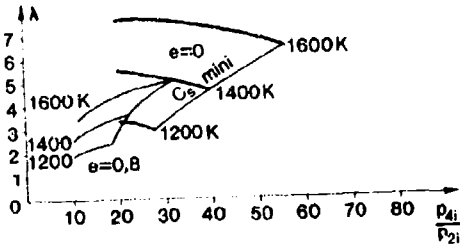
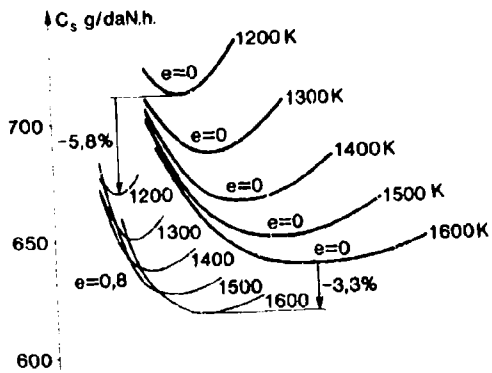


Planche 8

INFLUENCE DE LA TEMPERATURE MAXIMUM

$Z \geq 11\text{km}$ $M = 0,8$
 $\eta = 0,87$

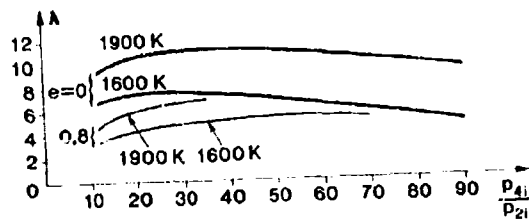
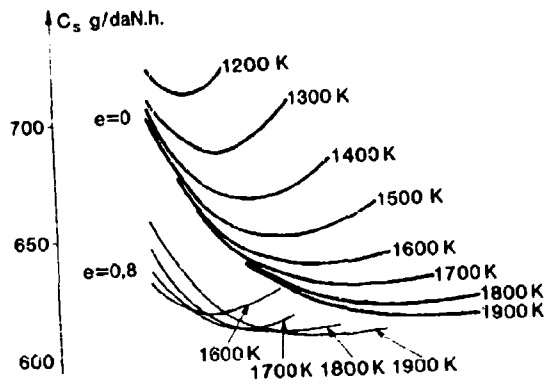


Planche 9

INFLUENCE DE L'EFFICACITE DE L'ECHANGEUR

$Z = 11 \text{ km}$ $M = 0,8$

$\eta = 0,87$

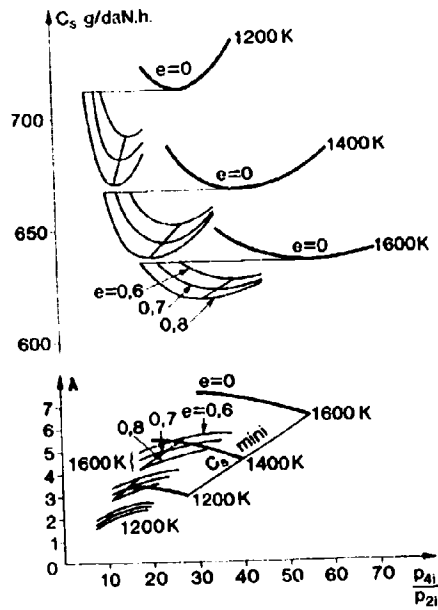


Planche 10

POUSSEE PAR UNITE DE DEBIT TOTAL

$Z = 11 \text{ km}$ $M = 0,8$

$\eta = 0,87$

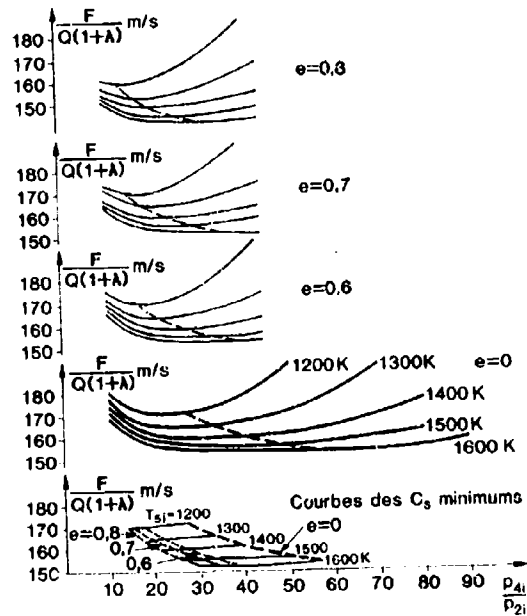


Planche 11

DISCUSSION

V.Mihail, Fr

Vous avez parlé de deux applications très intéressantes: moteurs à piston et double flux. L'application de ce type de propulseur nécessite la performance mais aussi l'endurance. Quel est l'état exact de vos recherches en ce dernier paramètre?

Réponse d'Auteur

L'O.N.E.R.A. ne saurait se substituer aux constructeurs de turbomachines pour les problèmes d'endurance. Notre ambition est de mettre en lumière, sur banc d'essai spécialisé, les difficultés de mise en oeuvre d'un matériau beaucoup moins bien connu que les alliages métalliques.

A.E.Bourguignon, Fr

Où en êtes-vous au niveau des études technologiques concernant les problèmes de compatibilité métal-céramique et en particulier les problèmes d'étanchéité?

Réponse d'Auteur

Le plus grand problème vient de la liaison tubes-flasques-métal. Jusqu'à présent on est arrivé à des durées de fonctionnement de 10 heures avec cycles thermique.

EFFECT OF FILM COOLING ON THE AERODYNAMIC PERFORMANCE OF A TURBINE CASCADE

by

O. Köllen and W. Koschel
 Institute for Jet Propulsion and Turbomachinery
 Technical University of Aachen
 Templergraben 55, D-5100 Aachen

SUMMARY

The aerodynamic performance of a film cooled turbine cascade for a typical design with multiple rows of cooling holes has been investigated in an annular cascade rig with air at room temperature. The work was concentrated on the individual effect of the injection row position on the aerodynamic cascade losses and on the downstream flow field. For 6 different single row configurations the tests were conducted in a wide range of varying coolant mass flow rates and main stream Mach numbers. Typical results of these measurements are presented and discussed. Three models for the aerodynamic loss prediction based on different theoretical approaches, which are known from literature, have been examined and improved. The presented two mixing layer models take into account the penetration of the injected cooling air into the main stream, whereas the third model predicts flow losses by a boundary layer calculation with film cooling air injection. Some tests with flow visualization by Schlieren photography have been carried out showing the mixing effects of the injected coolant flow. Finally results of the predicted performance are compared with the experimental data.

NOMENCLATURE

A	area	ρ	density
c	velocity	ψ	circumferential coordinate
c _p	specific heat	ψ_t	pitch angle at mean diameter
d ^D	trailing edge thickness	Subscripts	
m	mass flow	a	axial direction
M	Mach number	D	pressure side
N	number of cooling holes	K	coolant flow
p	static pressure	m	mixed
p _A	ambient pressure	ML	mixing layer
p _B	base pressure	M	aftermixed state
r	radius	s	isentropic
s ₁	cooling hole diameter	S	suction side
T ₁	temperature	t	stagnation condition
Y _K	coolant mass flow ratio	te	trailing edge
α	flow angle	u	circumferential direction
δ^*	boundary layer displacement thickness	Superscripts	
δ^{\dagger}	boundary layer momentum thickness	-	averaged value
δ^{\ddagger}	boundary layer enthalpy thickness	*	critical state
ζ^H	energy loss coefficient		
κ	specific heat ratio		

1. INTRODUCTION

The film cooling technique has become common for both stator and rotor blades in high-temperature turbines in the last years. Due to the high stress levels in these components rows of discrete holes arranged along the blade surface are used rather than slots to eject the cooling air. A lot of work has been spent on the investigation of film cooling effectiveness concerning single and multiple row configurations [1, 2, 3, 4]. Some papers have been published dealing with the effect of cooling flow injection on the aerodynamic performance of turbine cascades with film cooling [5, 6, 7, 8]. The present work extends the study to the individual effects of the injection row position along the blade surface and of the coolant mass flow rate on the cascade aerodynamic performance. The film cooling row arrangement on the turbine blade is based on a typical industrial design. The loss characteristics of 6 different single row configurations derived from the full film-cooled blade have been investigated for a wide range of main stream Mach numbers in an annular turbine cascade. Measurements of the flow angle and the pressures were taken at the cascade exit in order to analyze the influence of the local film cooling air injection on the downstream flow field. Additionally some visualization tests using Schlieren photography have been carried out with the purpose to get a better understanding of the mixing process between the injected cooling air and the main flow. The observed flow phenomena support the idea of Hartsel [5], who introduced a mixing layer model for aerodynamic loss prediction. Since his model is limited to the case of an incompressible and inviscid flow, an improved theoretical approach has been developed considering the compressibility of the flow and the boundary layer effects. Further on a comparison is made with the theory of Crawford, Kays and Moffat [9], which has been mo-

dified for the present study in such a manner that partial penetration of the injected coolant flow into the main stream is admitted. The results for the cascade losses predicted according to the different theories are finally compared with the experimental results for some single row configurations.

2. APPARATUS

2.1 FILM COOLING CONFIGURATIONS

The experimental investigation has been carried out for a given design of a typical film cooled guide vane. The arrangement of the cooling row positions along the blade surface is shown in Fig. 1. Number, diameter and inclination angles of the cooling holes can be drawn from this figure. Rows A and B are staggered. The front and the rear coolant mass flows are separately controlled. The design cooling mass flow ratio is fixed to 3% at a cascade exit Mach number of $\bar{M}_{c1s} = 0.8$.

The 6 different single row configurations which have been manufactured and tested separately are shown in Fig. 2. Size and arrangement of the cooling holes are derived from the full-film-cooled vane.

2.2 TEST RIG

The tests were conducted in an annular turbine cascade rig shown in Fig. 3. Details of the coolant air supply and the probe positions can be seen in the sectional view of the experimental set-up. Flow measurements are taken at fixed probe positions by shifting the guide vane support in the circumferential direction. The test rig is supplied by compressed air at room temperature level.

The main dimensions of the turbine cascade, the characteristic data of the blade geometry and the axial positions of the measuring planes are shown in Fig. 4.

The exit Mach number of the main flow has been varied between $\bar{M}_{c1s} = 0.4$ and $\bar{M}_{c1s} = 1.0$. For the full-film-cooled configuration the overall coolant mass flow rate was kept constant for all tests. Variations for this case were only made by partitioning the front and the rear coolant flows. During the tests with the 6 different single row configurations the coolant mass flow ratio has been changed between $\dot{m}_k/\dot{m} = 0\%$ and about 1.5%.

The visualization tests have been performed in a plane cascade rig instrumented with a Schlieren optical apparatus. Carbondioxide was injected through the film cooling holes in order to provide a mass flux ratio of the coolant flow to the main stream similar to that in a high-temperature turbine.

3. EXPERIMENTAL RESULTS

The aerodynamic performance reported herein is calculated from the measured values of the total pressure, the total temperature, the static pressures and the flow angle taken in the exit plane and from the measured coolant temperature and flow rate. The calculation of the blade energy loss coefficient is based on the determination of a hypothetical state where the flow has mixed to a circumferential uniform condition. The conservation equations have been applied to an annular sector control volume to obtain this so-called aftermixed state. The use of the aftermixed blade energy loss coefficient is preferred herein because it is theoretically independent of the axial measuring location and therefore well suited for comparison reasons. It should be noted that the aftermixed energy loss coefficient comprises the blade profile viscous loss and the mixing losses. The energy loss coefficient is defined as the ratio of the actual aftermixed kinetic energy to the sum of the ideal aftermixed kinetic energies of both the primary and the coolant flows.

$$\epsilon_M = 1 - \frac{\rho_M \cdot c_M^3 \cdot \sin \alpha_M \cdot t}{\int_0^N \rho_1 \cdot c_1 \sin \alpha_1 \cdot c_{1s}^2 \cdot r \cdot d\psi + \sum_{i=1}^N \dot{m}_{K,i} \cdot c_{K,i,s,M}^2} \quad (1)$$

Additionally an aftermixed total pressure loss coefficient is used according to the definition given by Goldman [8].

$$\eta_M = \frac{P_{t0} - P_{tM}}{P_{t0} - P_M} \quad (2)$$

The great amount of experimental data obtained during the tests makes it necessary to select only some typical results, which will be discussed in the present paper. In Fig. 5 the circumferential distributions of the measured flow angle and the total pressure coefficient in the exit plane are shown for the two single row configurations B and C. The results indicate that the local value of the flow angle is slightly influenced by raising the coolant mass flow ratio at a constant Mach number, whereas the averaged cascade exit flow angle will be nearly unaffected. The pattern of the total pressure coefficient shows a strong dependency of the coolant mass flow variations for both configurations. Similar results have been obtained for the other tested single row configurations.

In Fig. 6 the total loss coefficient, defined by equation (2) is plotted versus the coolant mass flow ratio at two different Mach numbers for the configurations B and E. The adverse tendencies observed by comparison of these two curves cannot only be explained by the different location of the cooling flow injection. Probably there may be a further effect due to the differences of the inclination angles of the corresponding cooling holes. Results of the experiments show the general behaviour that the film cooling air injection at the leading edge region leads to higher total pressure loss coefficients for increased coolant flow rates. For the other cases of cooling row positions as well on the suction side as on the pressure side it was found that after reaching a maximum value at low blowing rates the total pressure loss coefficient decreases at higher coolant mass flow rates.

The full-film-cooled guide vane has been investigated for different portions of the front and the rear coolant mass flow rates. Herein the overall cooling air flow ratio was kept constant at 3%. The effect of these variations on the total pressure loss coefficient and on the energy loss coefficient are shown in Fig. 7. From these result it can be deduced that a correct partitioning of the coolant flow may contribute to a good aerodynamic cascade performance. For this evaluation the energy loss coefficient should be used as the criterion rather than the total pressure loss coefficient because it balances the kinetic energies of both the main flow and the injected coolant flow.

4. PREDICTION METHODS AND RESULTS

Only a few theoretical studies on the effect of coolant injection on the aerodynamic losses of film cooled turbine cascades have been published in the literature. Tabakoff and Hamed [6] considered the effect of coolant injections on the boundary layer growth assuming that the coolant flow is completely immersed into a two-dimensional boundary layer. Crawford, Kays and Moffat [9] presented a computer code which enables to solve the two-dimensional boundary layer equations including coolant ejection into the boundary layer. Herein the assumption is also made that the coolant flow mixes completely with the boundary layer flow.

From measurements and calculations it becomes evident that the profile boundary layer of the high-turning guide vanes is very thin as compared to the size of the cooling holes which are realized in the industrial design. Therefore it is supposed that only a small portion of the injected cooling air flow remains within the boundary layer. Results of the visualization tests performed with the 6 different single row configurations support this presumption. In Fig. 8 a Schlieren photograph is shown for a test run with configuration B at an exit Mach number $M_{e1s} = 0.8$ and a mass flux ratio of about 1.0. The penetration of the coolant jet into the main stream can be seen very clearly. Similar results have been obtained for the other configurations tested at varying mass flux ratios and exit Mach numbers.

Based on these observations it seems to be more adequate to introduce a mixing layer model for the loss prediction of turbine guide vanes with film coolant flow injection as proposed by Hartsel [5] and modified by Ito, Eckert and Goldstein [6].

Following Hartsel's idea a so-called mixing layer can be introduced in which the injected coolant flow mixes with a part of the main stream at the location of the injection row, as shown in Fig. 9. Downstream the cascade at the aftermixed-state "M" a total mixing of the mixing layer with the remainder of the main flow will be assumed by definition. The control volume for the constant pressure mixing of the injected coolant flow with the main stream used in the mixing layer model is depicted in Fig. 10. In extension to the above mentioned theories the mixing layer model used during the present work accounts for compressibility effects.

For the prediction of the overall two-dimensional cascade loss the boundary layer and trailing edge effects must be included. A generalized analysis for the calculation of two-dimensional aerodynamic losses using integral boundary layer parameters was presented by Goldman and Gaugler [8]. This method has been refined considering the losses caused by the base pressure in the trailing edge region. The governing equations with regard to the control volume in Fig. 10 are presented in Appendix A. The resulting aerodynamic loss coefficient including the viscous losses, the trailing edge blockage, the trailing edge coolant injection and the base pressure effect is defined by the equation as follows.

$$\xi_P = 1 - \frac{(1 + Y_K) c_M^2}{c_{1s}^2 + Y_K c_K^2}, \text{ te, M} \quad (3)$$

with the abbreviation $Y_K = \frac{\dot{m}_K}{\dot{m}}$

Herein c_n is a function of the integral boundary layer parameters and of the base pressure. A brief derivation of equation (3) is given in Appendix A. The integral boundary layer parameters used to determine the energy loss coefficient have been calculated with the STAN5 computer program [10].

The new concept for the overall loss prediction developed during this investigation is based upon the assumption that the foregoing described losses can be superimposed to the losses produced in the mixing layer. From the detailed loss analysis of the mixing layer the following expression for the loss coefficient at the aftermixed state can be obtained:

$$\xi_I = 1 - \frac{(1 + Y_K) \cdot c_M^2}{c_{1s}^2 + Y_K \cdot c_{K,M}^2} \quad (4)$$

The ideal coolant velocity is derived by assuming an isentropic expansion of the coolant flow from the location of the injection to the aftermixed station "M".

$$c_{K,M} = \sqrt{\frac{2\kappa}{\kappa-1} \cdot R \cdot T_{tK} \cdot \left[1 - \left(\frac{p_M}{p_{tK}} \right)^{\frac{\kappa-1}{\kappa}} \right]} \quad (5)$$

The mixing layer modeling is presented in detail in Appendix B.

Thus the overall energy loss coefficient can be determined by summing up ξ_P and ξ_I .

$$\xi_M = \xi_P + \xi_I \quad (6)$$

By evaluating the boundary layer parameter the question arises how the boundary layer is affected by the coolant flow injection. Two opposite views of this problem are found in the literature. Ito, Eckert and Goldstein [7] neglected the influence of the coolant injection on the boundary layer development whereas other investigators assumed a total merging of the coolant flow into the boundary layer. In the latter case the boundary layer will be thickened which results in higher frictional losses. In the present paper two different approaches have been applied to the calculation of the integral boundary layer parameters for the suction side. For the first one, which is called "Theory I", the assumption is made that the boundary layer becomes turbulent at the location of the coolant injection. In the second case ("Theory II") the influence of the injected airflow on the boundary layer development has been neglected and the transition point has been determined using conventional criteria.

The third loss prediction model, which is denoted as "Theory III", is based on the STANCOOL computer program [9]. The injection model used in this program has been modified in order to take account for a partial penetration of the coolant flow into the main stream.

The overall energy loss coefficients have been calculated for the 6 tested single row configurations following the 3 different loss prediction methods. The results are shown in Fig. 12, Fig. 13 and Fig. 14 for the configurations A, B and E respectively. The cooling injection rows are located for these configurations along the profile suction side. The predicted losses are compared with the corresponding experimental data. It can be seen from the plots of the overall energy loss coefficient versus the coolant mass flow rate that the losses at high blowing rates will be overestimated if "Theory III" is applied. This result implies that despite the modification of the injection model the portion of the coolant flow forced to remain within the boundary layer is too high. This fact leads to a blowing-up of the boundary layer and consequently to increased losses. Especially for the configuration E with coolant injection near the stagnation point, where the boundary is usually very thin, this effect becomes more evident.

The best agreement with experiment is obtained if the overall energy loss coefficient is predicted by using "Theory I". This statement is valid for all investigated test cases. Since "Theory II" does not account for the influence of the cooling air injection on the boundary layer development, the viscous losses and thus the overall loss coefficient will be underestimated.

5. CONCLUSIONS

Results of detailed flow measurements carried out on turbine cascades with different film cooling hole arrangements at varying coolant mass flow rates and main stream Mach numbers are presented and discussed. It turned out that the averaged cascade exit flow angle is not affected by the film cooling air injection. Different tendencies in the total pressure loss coefficient versus the coolant mass flow rates were observed for front and rear film cooling row locations. As shown by the results obtained for the guide vane with full film cooling the partitioning of the coolant mass flow can be optimized as regard to the overall aerodynamic cascade performance.

From the theoretical analyses it can be concluded that the best approach for the overall energy loss prediction in comparison to the experimental results will be achieved by superimposing the mixing layer model and the integral boundary layer calculation method.

ACKNOWLEDGEMENT

Financial support for this study by the Ministry of Science and Research of North-Rhine-Westphalia, Düsseldorf, is gratefully acknowledged.

REFERENCES

- [1] Sasaki, K., Takahara, K., Kumagai, T. and J. Hamano: Film Cooling Effectiveness for Injection from Multirows of Holes
ASME Journal of Engineering for Power, Jan. 1979, Vol. 101

- [2] Kruse, H.: Film Cooling Measurements.
DFVLR-Report No. 352-74/1, 1974
- [3] Goldstein, R.J., Kornblum, V. and E.R. Eckert: Film Cooling Effectiveness on a Turbine Blade
ISRAEL JOURNAL OF TECHNOLOGY, Vol. 20, 1982
- [4] Jubran, B. and A. Brown: Film Cooling from Two Rows of Holes Inclined in the Streamwise and Spanwise Directions
ASME-Paper 84-GT-286, 1984
- [5] Hartsel, J.E.: Prediction of Effects of Mass-Transfer Cooling on the Blade Row Efficiency of Turbine Airfoils.
AIAA-Paper No. 72-11, 1972
- [6] Tabakoff, W. and A. Hamed: Theoretical and Experimental Study of Flow through Turbine Cascades with Coolant Flow Injection
AIAA 8th Fluid and Plasma Dynamics Conference, Hartford, Connecticut, June 16-18, 1975
- [7] Ito, S., Eckert, E.R. and R.J. Goldstein: Aerodynamic Loss in a Gas Turbine Stage with Film Cooling
ASME Journal of Power, Oct. 1980, Vol. 102
- [8] Goldman, L.J. and R.E. Gaugler: Prediction Method for Two-Dimensional Aerodynamic Losses of Cooled Vanes Using Integral Boundary-Layer Parameters
NASA TP-1623, Cleveland, Ohio, 1980
- [9] Crawford, M.E., Kays, W.M. and R.J. Moffat: Full-Coverage Film Cooling on Flat Isothermal Surfaces: A Summary Report on Data and Predictions
NASA CR-3219, Stanford University, California, Jan. 1980
- [10] Crawford, M.E. and W.M. Kays: STAN5 - A Program for Numerical Computation of Two-dimensional Internal and External Boundary Layer Flows
NASA-CR-2742, Stanford University, California, Nov. 1976

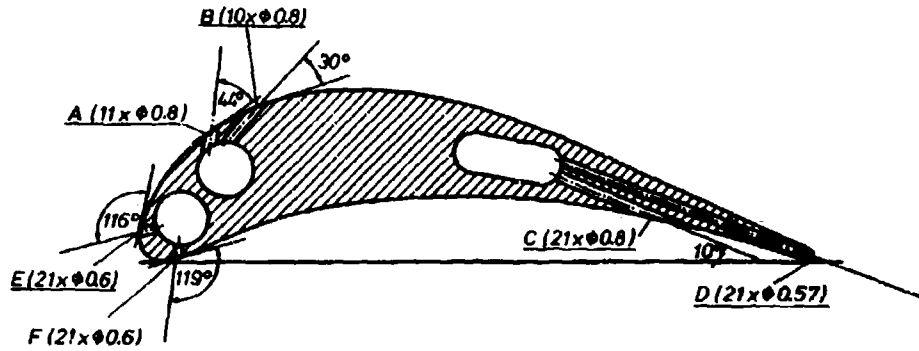


Fig. 1: Fully film cooled turbine guide vane

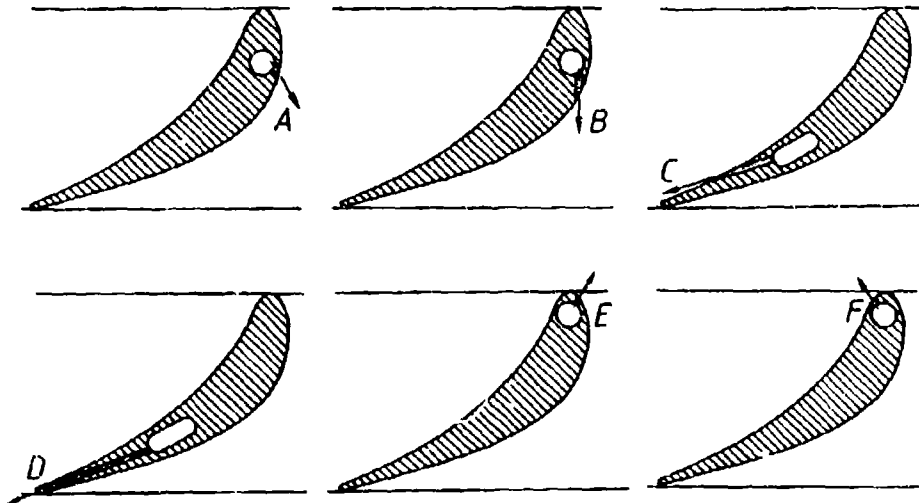


Fig. 2: Single row configurations

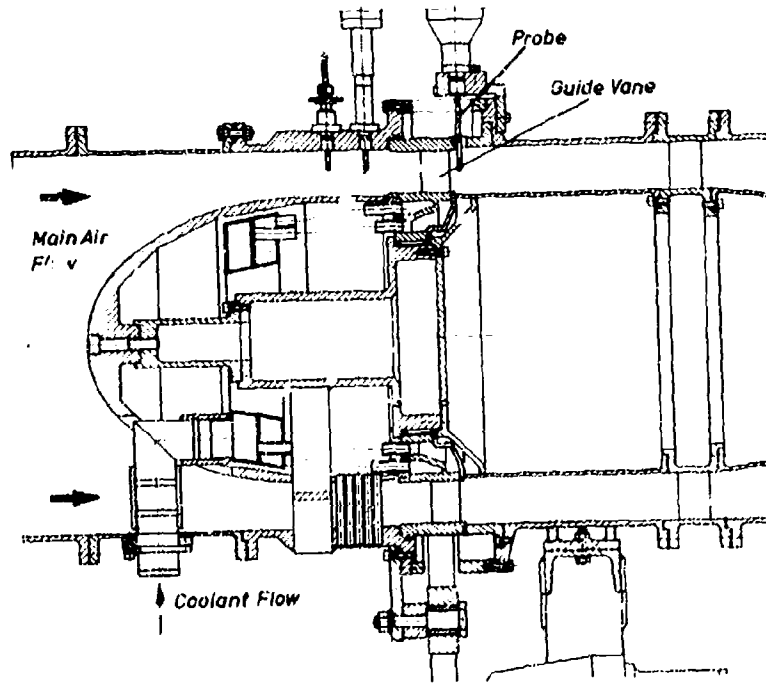


FIG. 3: Cross sectional view of the cascade test rig

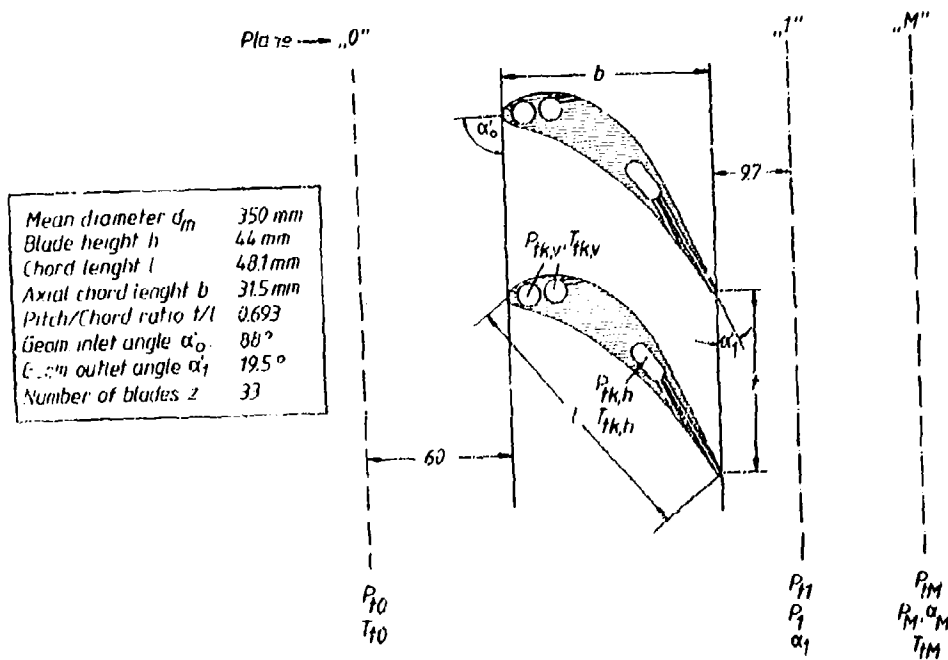


FIG. 4: Blade profile

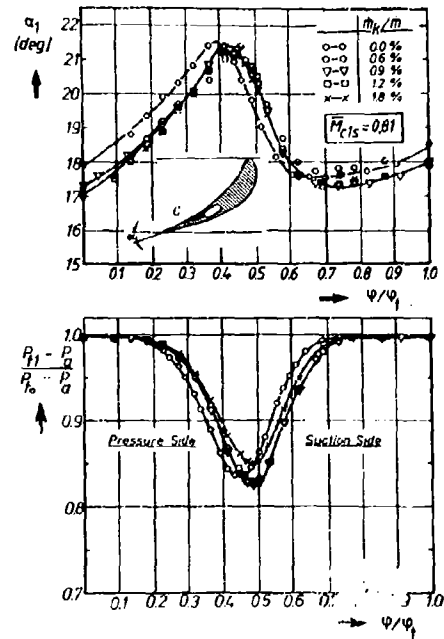
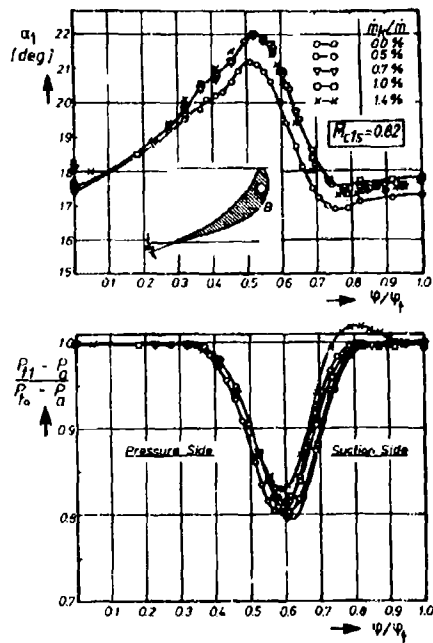


Fig. 5: Circumferential distribution of the flow angle and the total pressure coefficient in the cascade exit plane

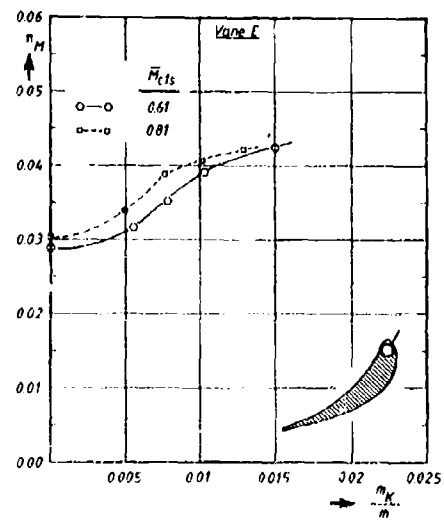
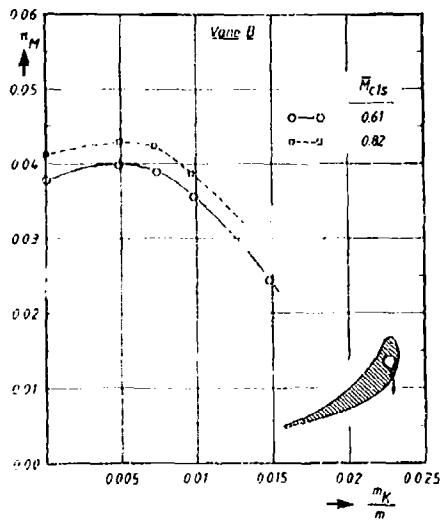


Fig. 6: Influence of the cooling mass flow rate on the total pressure loss coefficient

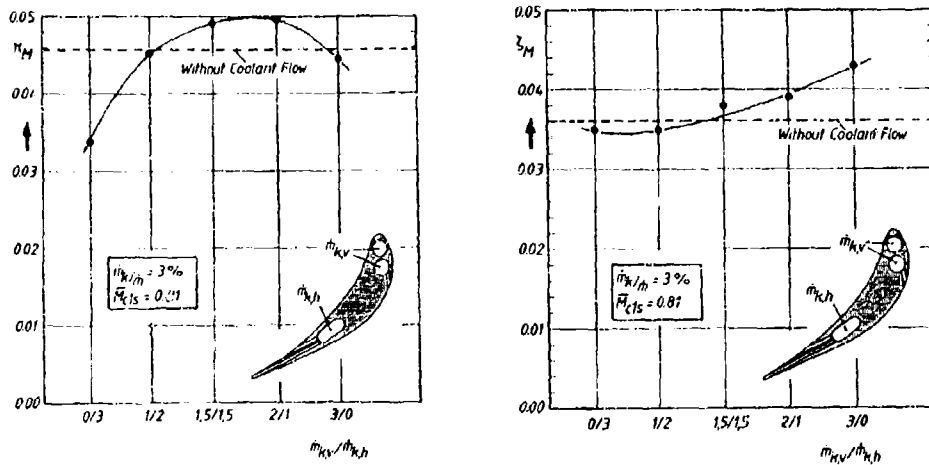


Fig. 7: Comparison of the total pressure loss coefficient and the energy loss coefficient for different partitioning of the cooling mass flow

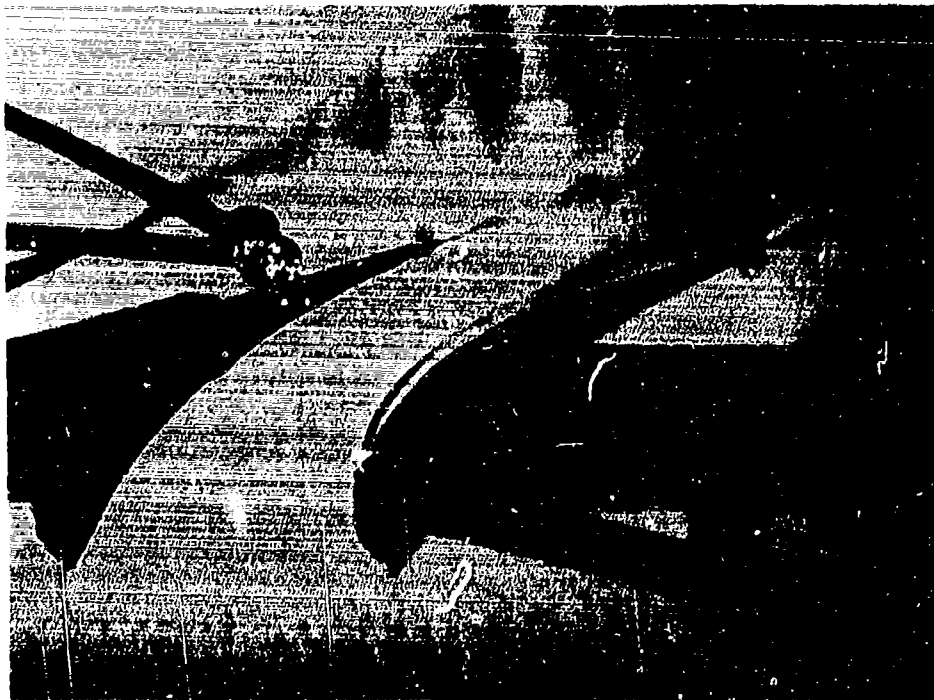


Fig. 8: Visualization of the injected carbon dioxide jet for the single row configuration B

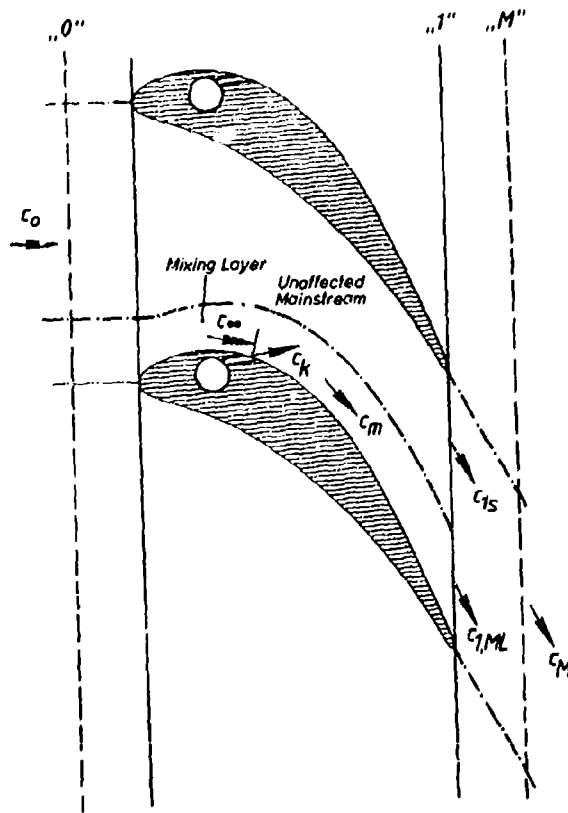


Fig. 9: Film cooling loss model with a mixing layer

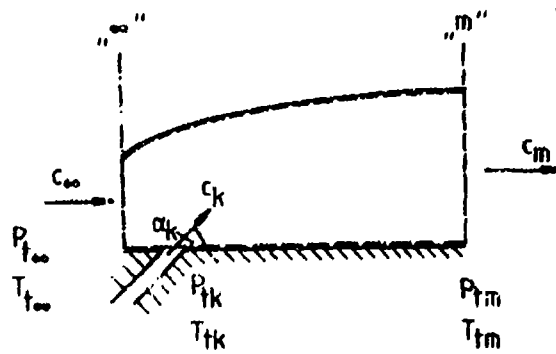


Fig. 10: Flow channel for constant pressure mixing

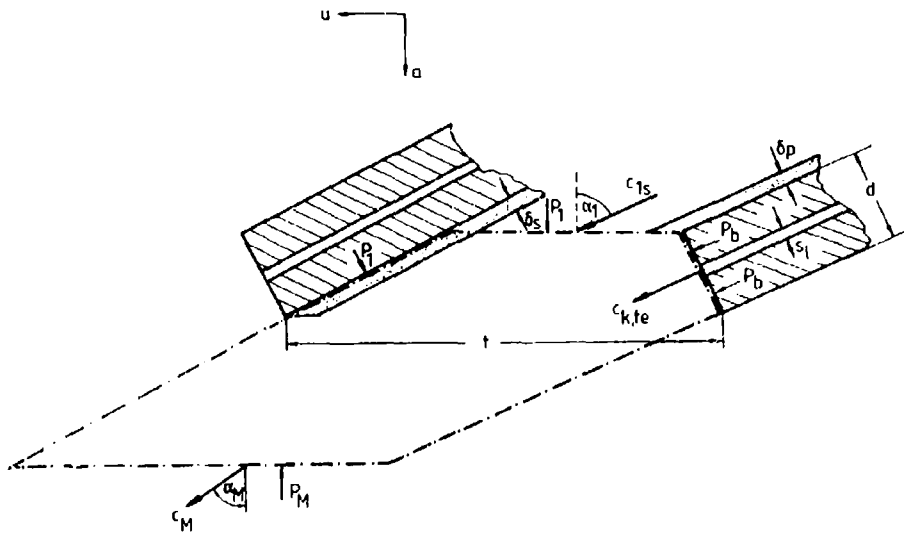


Fig. 11: Mixing model for the exit region

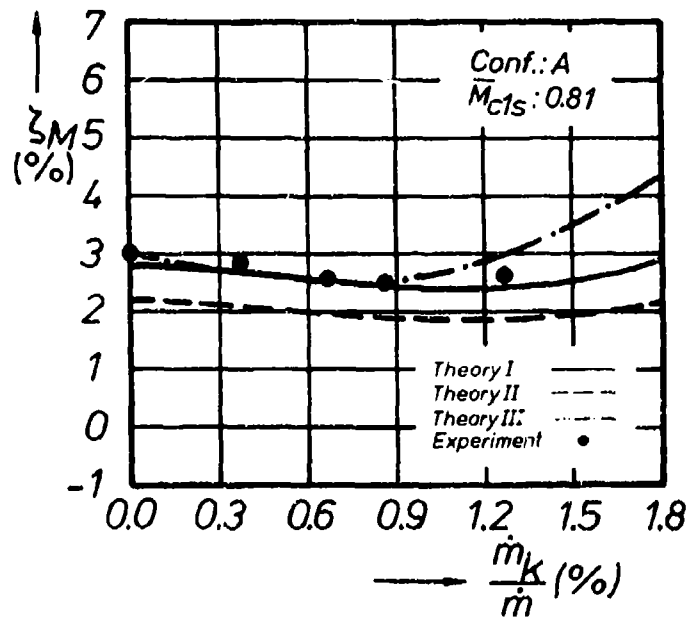


Fig. 12: Comparison of the predicted and the experimental overall energy loss coefficients for the single row configuration A

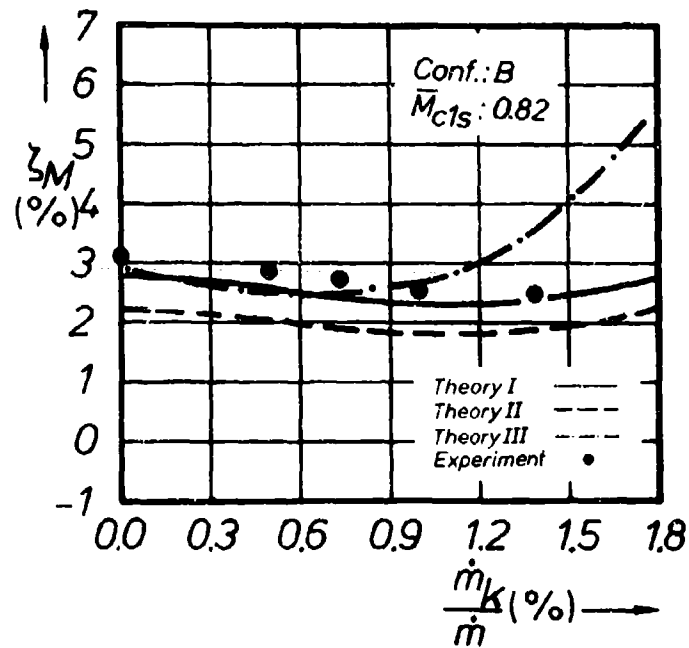


Fig. 13: Comparison of the predicted and the experimental overall energy loss coefficients for the single row configuration B

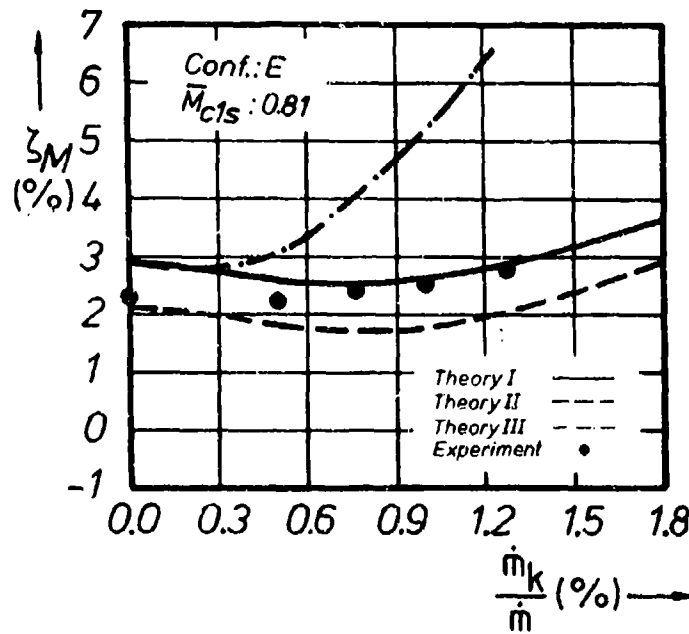


Fig. 14: Comparison of the predicted and the experimental overall energy loss coefficients for the single row configuration E

APPENDIX A

AERODYNAMIC LOSS COEFFICIENTS IN TERMS OF BOUNDARY-LAYER PARAMETERS

In order to obtain the aerodynamic loss coefficient at station "M" the aftermixed conditions have first to be determined in terms of the boundary-layer parameters at station "1" (see Fig. 11). The conservation of mass, axial and tangential momentum and energy between stations "1" and "M" results in the following equations if the static pressure p_1 and the exit angle α_1 are considered to be constant in the circumferential direction:

Mass conservation

$$\rho_1 \cdot c_{1s} \cdot \cos \alpha_1 \cdot F + \int_0^{z_1} \rho \cdot c \cdot \cos \alpha_1 \cdot du + \int_0^{z_2} \rho \cdot c \cdot \cos \alpha_1 \cdot du + \rho_{K,te} \cdot c_{K,te} \cdot n \cdot \frac{\pi \cdot s^2}{4 \cdot h} = \rho_M \cdot c_M \cdot \cos \alpha_M \cdot t \quad (A1)$$

Axial momentum

$$\rho_1 \cdot c_{1s}^2 \cdot \cos^2 \alpha_1 \cdot F + \int_0^{z_1} \rho \cdot c^2 \cdot \cos^2 \alpha_1 \cdot du + \int_0^{z_2} \rho \cdot c^2 \cdot \cos^2 \alpha_1 \cdot du + \rho_{K,te} \cdot c_{K,te}^2 \cdot \cos \alpha_1 \cdot n \cdot \frac{\pi \cdot s^2}{4 \cdot h} + \rho_1 \cdot (t - d \cdot \cos \alpha_1) + p_B \cdot d \cdot \cos \alpha_1 = (\rho_M \cdot c_M^2 \cdot \cos^2 \alpha_M + p_M) \cdot t \quad (A2)$$

Tangential momentum

$$\rho_1 \cdot c_{1s}^2 \cdot \sin \alpha_1 \cdot \cos \alpha_1 \cdot F + \int_0^{z_1} \rho \cdot c^2 \cdot \sin \alpha_1 \cdot \cos \alpha_1 \cdot du + \int_0^{z_2} \rho \cdot c^2 \cdot \sin \alpha_1 \cdot \cos \alpha_1 \cdot du + \rho_{K,te} \cdot c_{K,te}^2 \cdot \sin \alpha_1 \cdot \cos \alpha_1 \cdot n \cdot \frac{\pi \cdot s^2}{4 \cdot h} + (p_B - p_1) \cdot d \cdot \sin \alpha_1 = \rho_M \cdot c_M^2 \cdot \cos \alpha_M \cdot \sin \alpha_M \cdot t \quad (A3)$$

Energy equation

$$\rho_1 \cdot c_{1s} \cdot T_{t0} \cdot \cos \alpha_1 \cdot F + \int_0^{z_1} \rho \cdot c \cdot T_t \cdot \cos \alpha_1 \cdot du + \int_0^{z_2} \rho \cdot c \cdot T_t \cdot \cos \alpha_1 \cdot du + \rho_{K,te} \cdot c_{K,te} \cdot T_{tK,te} \cdot n \cdot \frac{\pi \cdot s^2}{4 \cdot h} = \rho_M \cdot c_M \cdot \cos \alpha_M \cdot T_{tM} \cdot t \quad (A4)$$

with

$$F = t - d \left(\frac{\sin^2 \alpha_1}{\cos \alpha_1} + \cos \alpha_1 \right) - \frac{\delta_S + \delta_D}{\cos \alpha_1}$$

$$z_1 = \frac{\delta_S}{\cos \alpha_1}$$

$$z_2 = \frac{\delta_D}{\cos \alpha_1}$$

Introducing the dimensionless boundary-layer parameters:

$$\bar{\delta}_1^* = \frac{\delta_{1S}^* + \delta_{1D}^*}{t \cdot \cos \alpha_1} \quad (A5a)$$

$$\bar{\delta}_2^* = \frac{\delta_{2S}^* + \delta_{2D}^*}{t \cdot \cos \alpha_1} \quad (A5b)$$

$$\bar{\delta}_H = \frac{\delta_{HS} + \delta_{HD}}{t \cdot \cos \alpha_1} \quad (A5c)$$

and using

$$\bar{\delta}_{te} = \frac{d}{t \cdot \cos \alpha_1} \quad (A6a)$$

$$\bar{t}_{s1} = \frac{n \cdot \pi \cdot s^2}{t \cdot \cos \alpha_1 \cdot 4 \cdot h} \quad (A6b)$$

$$\bar{\delta}_{te} = \frac{d}{t} \cdot \cos \alpha_1 \quad (A6c)$$

$$\overline{B}_{te} = \frac{\rho_{K,te} \cdot c_{K,te}}{\rho_1 \cdot c_{1s}} \quad (A7a)$$

$$\overline{J}_{te} = \frac{\rho_{K,te} \cdot c_{K,te}^2}{\rho_1 \cdot c_{1s}^2} \quad (A7b)$$

$$\overline{E}_{te} = \frac{\rho_{K,te} \cdot c_{K,te} \cdot T_{tK,te}}{\rho_1 \cdot c_{1s} \cdot T_{t0}} \quad (A7c)$$

the simplified conservation equations can be obtained as follows:

$$\rho_1 \cdot c_{1s} \cdot \cos \alpha_1 \cdot T_1 = \rho_M \cdot c_M \cdot \cos \alpha_M \quad (A8)$$

$$\rho_1 \cdot c_{1s}^2 \cdot \cos^2 \alpha_1 \cdot T_2 + p_1 \cdot (1 - \overline{\delta}_{fe}) + p_H \cdot \overline{\delta}_{fe} = \rho_M \cdot c_M^2 \cdot \cos^2 \alpha_M + p_M \quad (A9)$$

$$\rho_1 \cdot c_{1s}^2 \cdot \cos \alpha_1 \cdot \sin \alpha_1 \cdot T_2 + (p_B - p_1) \cdot \tan \alpha_1 \cdot \overline{\delta}_{fe} = \rho_M \cdot c_M^2 \cdot \cos \alpha_M \cdot \sin \alpha_M \quad (A10)$$

$$\rho_1 \cdot c_{1s} \cdot T_{t0} \cdot \cos \alpha_1 \cdot T_3 = \rho_M \cdot c_M \cdot T_{tM} \quad (A11)$$

with

$$T_1 = 1 - \overline{\delta}_1^* - \overline{\delta}_{te} + \overline{B}_{te} \cdot \overline{\delta}_{s1}$$

$$T_2 = 1 - \overline{\delta}_1^* - \overline{\delta}_2^* - \overline{\delta}_{te} + \overline{J}_{te} \cdot \overline{\delta}_{s1}$$

$$T_3 = 1 - \overline{\delta}_1^* - \overline{\delta}_H - \overline{\delta}_{te} + \overline{E}_{te} \cdot \overline{\delta}_{s1}$$

From the definition for the critical Mach number and the expression for the critical velocity in a perfect gas

$$M^* = \frac{c}{c^*}$$

$$c^* = \sqrt{\frac{2 \cdot \kappa}{\kappa + 1} \cdot R \cdot T_t}$$

we get the axial and tangential components of the critical exit Mach number at station "M" from the equations A8 to A11:

$$M_{M,u}^* = D \quad (A12)$$

$$M_{M,a}^* = \frac{\kappa}{\kappa + 1} \cdot C - \sqrt{\left(\frac{\kappa}{\kappa + 1}\right)^2 \cdot C^2 - 1 + \frac{\kappa - 1}{\kappa + 1} D^2} \quad (A13)$$

where is

$$C = \sqrt{\frac{T_{t0}}{T_{tM}}} \cdot \frac{T_2 \cdot \cos^2 \alpha_1 \cdot M^*{}^2 c_{1s} + \frac{\kappa + 1}{2\kappa} \left(1 - \frac{\kappa - 1}{\kappa + 1} M^*{}^2 c_{1s}\right)^{\frac{1}{\kappa - 1}} \cdot \frac{p_B}{p_{t0}} + \frac{\kappa + 1}{2\kappa} (1 - \overline{\delta}_{fe}) \cdot \left(1 - \frac{\kappa - 1}{\kappa + 1} M^*{}^2 c_{1s}\right)}{T_1 \cdot \cos \alpha_1 \cdot M^* c_{1s}}$$

$$D = \sqrt{\frac{T_{t0}}{T_{tM}}} \cdot \frac{T_2 \cdot \sin \alpha_1 \cdot \cos \alpha_1 \cdot M^*{}^2 c_{1s} + \left(1 - \frac{\kappa - 1}{\kappa + 1} M^*{}^2 c_{1s}\right)^{\frac{1}{\kappa - 1}} \cdot \frac{(p_B - p_1)}{p_{t0}} \cdot \left(\frac{\kappa + 1}{2\kappa} \tan \alpha_1 \cdot \overline{\delta}_{fe}\right)}{T_1 \cdot \cos \alpha_1 \cdot M^* c_{1s}}$$

Then the critical Mach number at station "M" can be calculated by

$$M_M^* = \sqrt{M_{M,a}^*{}^2 + M_{M,u}^*{}^2} \quad (A14)$$

The temperature ratio T_{tM}/T_{t0} used in the expressions C and D can be determined by the combination of equations A8 and A11.

$$\frac{T_{tM}}{T_{t0}} = \frac{T_3}{T_1} \quad (A15)$$

The conservation equations have been solved in a similar method as given by L.J. Goldman and R.E. Gaugler. The present theory take into account the fact that at thick trailing edges the pressure downstream the trailing edge may differ considerably from that in the free stream. Thus the base pressure terms in the axial and tangential direction are added to the momentum equations.

The energy loss coefficient can be calculated from the following equation

$$\xi_M = 1 - \frac{(1 + Y_K) \cdot c_M^2}{c_{1s}^2 + Y_K \cdot c_{K,te,M}^2} \quad (A16)$$

where

$$c_M^* = \sqrt{\frac{2\kappa}{\kappa+1} \cdot R \cdot T_{tM}} \quad (A17)$$

$$c_{K,te,M} = \sqrt{\frac{2\kappa}{\kappa-1} R \cdot T_{tK,te} \cdot \left[1 - \left(\frac{p_M}{p_{tK,te}} \right)^{\frac{\kappa-1}{\kappa}} \right]} \quad (A18)$$

$$c_M = M_M^* \cdot c_M^* \quad (A19)$$

APPENDIX B

The calculation method for the mixing process between the coolant flow injected into the mainstream at various locations at the blade profile with the main fluid is briefly described.

The following assumptions are made

- Friction is neglected,
- Coolant and mainstream fluid are perfect gases,
- Coolant and mainstream fluid have the same specific heats independent of temperature,
- The inlet total pressure p_{t0} and the static pressure p_1 at station 1 are not influenced by the coolant injection,
- The mainstream velocity at the location of injection before mixing takes place is not influenced by coolant injection.

The mixing process in the mixing layer is considered to be a constant pressure mixing process. Fig. 10 sketches this mixing process at constant pressure in a one-dimensional channel. The conservation equations can be written as

$$\rho_\infty \cdot c_\infty \cdot A_\infty + \rho_K \cdot c_K \cdot A_K = \rho_m \cdot c_m \cdot A_m \quad (B1)$$

$$\rho_\infty \cdot c_\infty^2 \cdot A_\infty + \rho_K \cdot c_K^2 \cdot A_K \cdot \cos \alpha_K = \rho_m \cdot c_m^2 \cdot A_m \quad (B2)$$

$$\rho_\infty \cdot c_\infty \cdot A_\infty \cdot c_p \cdot T_{t\infty} + \rho_K \cdot c_K \cdot A_K \cdot c_p \cdot T_{tK} = \rho_m \cdot c_m \cdot A_m \cdot c_p \cdot T_{tm} \quad (B3)$$

Introducing

$$Y_K = \frac{\dot{m}_K}{\dot{m}_\infty} \quad (B4)$$

$$\text{with } \dot{m}_K = \rho_K \cdot A_K \cdot c_K \quad (B5)$$

$$\dot{m}_\infty = \rho_\infty \cdot A_\infty \cdot c_\infty \quad (B6)$$

and solving the equations B1 to B3 gives the aftermixed exit Mach number M_m as follows

$$M_m^2 = \frac{1}{\frac{(1+Y_K)(T_{t\infty} + Y_K \cdot T_{tK})(1 + \frac{\kappa-1}{2} M_\infty^2)}{(Y_K \cdot \frac{c_K}{c_\infty} \cdot \cos \alpha_K + 1)^2 \cdot M_\infty^2 \cdot T_{t\infty}} - \frac{\kappa-1}{2}} \quad (B7)$$

The total pressure loss $p_{tm}/p_{t\infty}$ than can be determined by

$$\frac{p_{tm}}{p_{t\infty}} = \frac{\left(1 + \frac{\kappa-1}{2} M_m^2\right)^{\frac{\kappa}{\kappa-1}}}{\left(1 + \frac{\kappa-1}{2} M_\infty^2\right)^{\frac{\kappa}{\kappa-1}}} \quad (B8)$$

assuming that $p_\infty = p_m$.

The mixing process downstream the blade row between the mixing layer and the unaffected mainstream is sketched in Fig. 9. The equations of conservation can be written

$$\dot{m}_O(1-\sigma) + \sigma \cdot \dot{m}_O + \dot{m}_K = \dot{m}_M = \rho_M \cdot c_M \cdot A_M \quad (B9)$$

$$(\dot{m}_O + \dot{m}_K) \cdot c_M - \dot{m}_O(1-\sigma) \cdot c_{1s} - (\dot{m} \cdot \sigma + \dot{m}_K) \cdot c_{ML} = (P_1 - P_M) \cdot A_M \quad (B10)$$

$$(\sigma \cdot \dot{m}_O + \dot{m}_K) \cdot T_{tML} + \dot{m}_O(1-\sigma) \cdot T_{tO} = (\dot{m}_O + \dot{m}_K) \cdot T_{tM} \quad (B11)$$

where

$$c_{pO} = c_{p1} = c_{pM}; \quad A_1 = A_M$$

and σ is the ratio of the mass flow of the fluid in the mixing layer approaching the blade row to the total mass flow in the mainstream.

Rearranging and solving the equations B9 to B11 gives the aftermixed velocity c_M to

$$c_M = \frac{A}{2} - \sqrt{\frac{A^2}{4} - \frac{2\kappa}{\kappa+1} \cdot R \cdot T_{tM}} \quad (B12)$$

where

$$A = \frac{2\kappa}{\kappa+1} \left[\frac{1-\sigma}{1+Y_K} \cdot c_{1s} + \frac{\sigma+Y_K}{1+Y_K} \cdot c_{ML} + \frac{P_1 \cdot A_M}{\dot{m}_O(1+Y_K)} \right] \quad (B12a)$$

The aftermixed total temperature T_{tM} can be determined by

$$T_{tM} = \frac{1-\sigma}{1+Y_K} \cdot T_{tO} + \frac{\sigma+Y_K}{1+Y_K} \cdot T_{tML} \quad (B13)$$

The quantities T_{tML} and c_{ML} in the equations B12 to B13 can be calculated using the procedure for constant pressure mixing developed above. The static pressure in the aftermixed station "M" can be obtained by

$$P_M = \left[T_{tM} - \frac{c_M^2(\kappa-1)}{2\kappa \cdot R} \right] \cdot \frac{R \cdot (1+Y_K) \cdot \dot{m}_O}{A_M \cdot c_M} \quad (B14)$$

Thus the energy loss coefficient ξ_I due to mixing of the coolant flow with the mainstream can be calculated from

$$\xi_I = 1 - \frac{(1+Y_K) \cdot c_M^2}{c_{1s}^2 + Y_K \cdot c_{K,M}^2} \quad (B15)$$

where $c_{K,M}$ is determined by

$$c_{K,M} = \sqrt{\frac{2\kappa}{\kappa-1} \cdot R \cdot T_{tK} \left[1 - \left(\frac{P_M}{P_{tK}} \right)^{\frac{\kappa-1}{\kappa}} \right]} \quad (B15a)$$

ETUDE EXPERIMENTALE ET THEORIQUE
D'UN JET TRIDIMENSIONNEL INTRODUIT DANS L'ÉCOULEMENT
SECONDAIRE D'UNE GRILLE DISTRIBUTRICE DE TURBINE**

A. Onvani ; Doct. de 3^{em} cycle
C. Ollivier ; Ingénieur Société Métra.lu
F. Bario ; Doct. de 3^{em} cycle - Ingénieur CNRS
F. Leboeuf ; Doct. ès Sciences - Maître-Assistant
Laboratoire de Mécanique des Fluides, Associé au CNRS-UA 263
ÉCOLE CENTRALE DE LYON
36 Avenue Guy de Collongue - BP 163
69131 ECULLY CEDEX - FRANCE.

Résumé

Cette étude est abordée uniquement du point de vue aérodynamique et a pour objet de définir les effets d'un écoulement tridimensionnel sur un jet placé en incidence et en dérapage. La trajectoire, la vitesse, les dimensions du jet sont déterminées.

Sur le plan expérimental, des mesures de pression et de vitesse sont réalisées. La mesure d'un coefficient d'intermittence du jet au moyen d'un système de détection par fil chaud permet de caractériser la trajectoire et la forme de celui-ci.

Les résultats expérimentaux montrent que la trajectoire du jet est peu influencée par l'angle de dérapage pour les rapports de quantités de mouvement utilisés.

Sur le plan théorique, une méthode intégrale de calcul, basée sur l'utilisation des équations de continuité et de Navier-Stokes moyennées sur la section transversale du jet est employée. D'autre part, la vorticit  longitudinale g n r e dans le jet, d termin e par une  quation de transport et l'introduction d'un effet "puits" permettent de calculer les vitesses transversales induites.

La confrontation entre les r sultats du calcul et de l'exp rience indique un accord satisfaisant.

Summary

The objective of this paper is to define, the interaction effects between a jet introduced from the side wall and the 3-D secondary flow of a turbine inlet guide vane.

Only aerodynamical effects are studied. The trajectory, velocity and characteristic lengths of the jet are determined.

The experimental work gives the measurements of pressure and velocity. The measurement of an intermittence coefficient with a hot wire allows also the definition of the trajectory and the shape of the jet.

Experimental results show that the jet trajectory is weakly influenced by yaw angle of the hole for the ratio of momentum quantities used.

Theoretical prediction is done with the help of an integral calculation method based on the use of continuity and Navier-Stokes equations averaged on the transverse section of the jet. The streamwise vorticity generated in the jet and predicted with a transport equation, and the introduction of a sink effect allow the computation of the induced transverse velocities. Experimental results and calculated quantities are in a good agreement.

Liste des Symboles

a	Demi grand axe de l'ellipse
C_{ax}	Corde axiale
C_D	Coefficient de tra�n�e
C_p	Coefficient de pression $C_p = (p - p_r) / \frac{1}{2} \rho V^2$ (1 r�f�rence amont)
h_s, h_b, h_m	m�triques associ�es au syst�me (s, b, n) (figure 1)
\mathbb{I}	Matrice identit�

K_{sm}, K_{sb}	Courbures de la trajectoire respectivement selon n et b.
N, B	Rep�re (\vec{N}, \vec{B}) (figure 1) ou coordonn�es dans ce rep�re
P	Pression statique
P_r	Pression d'arr�t
P_{rref}	Pression d'arr�t de r�f�rence � l'amont de la grille.
R_o	Rayon de l'orifice d'injection

** Travaux financ s par la DRET.

$(\vec{s}, \vec{b}, \vec{n})$ Repère curviligne orthogonal où \vec{s} est tangent à la trajectoire du jet.
 s, b, n Coordonnées associées au repère $(\vec{s}, \vec{b}, \vec{n})$
 $(\vec{s}, \vec{N}, \vec{B})$ Repère de Fresnet
 \vec{V} Vitesse de l'écoulement.
 \vec{V}_0 Vitesse de l'écoulement de référence (en absence de jet)
 V' Excès de vitesse ($V - \vec{V}_0$)
 V_j Maximum de vitesse V' dans la section transversale du jet.
 V_0 Vitesse initiale du jet à l'orifice
 V_{ex} Vitesse extérieure au point d'injection
 X, Y, Z ; x, y, z Système d'axes (Figure 1) ou grandeurs originaires : X au bord d'attaque, Y à la paroi, Z à l'extrados.

α_b, α_m Angle d'incidence et de dérapage
 β Angle entre \vec{V} et la direction X
 Γ Coefficient d'intermittence

Γ_1, Γ_2 Circulation à l'infini des tourbillons
 $\vec{\Omega}_1, \vec{\Omega}_2$
 λ, μ Inclinaison de (\vec{N}, \vec{B}) par rapport à (\vec{s}, \vec{n})
 ρ Masse volumique
 S_0 Surface transversale du jet
 \vec{h}_1, \vec{h}_2 Vecteur tourbillon.
 λ Indice de référence à l'écoulement de base sans injection
 \circ Indice de référence du point d'injection.

I. INTRODUCTION

L'augmentation des performances aérodynamiques d'une turbomachine nécessite de disposer d'un certain nombre de méthodes de calcul capables de prendre en considération l'ensemble des phénomènes physiques rencontrés. Dans cette optique la compréhension des phénomènes associés aux écoulements secondaires, provoqués par le développement dans une roue mobile ou fixe des couches limites sur le moyeu et sur le carter de la machine, est un des points clef du problème. Cette étude aborde les interactions des écoulements secondaires avec des écoulements de refroidissement. En effet, pour le cas des turbines à gaz, l'accroissement des performances peut être obtenu en utilisant des températures en entrée de la turbine élevées. Un dispositif de refroidissement des aubes et des parois de la machine s'avère alors obligatoire. Ce refroidissement des parois de la machine, constituées par le moyeu et le carter (ou plateformes), s'effectue dans la zone d'influence des écoulements secondaires. Il est en général réalisé par injection discrète de fluide à basse température. La présence de ces injections par orifices peut entraîner des pertes aérodynamiques dans les premiers étages de turbine refroidis. Il est alors primordial de connaître d'une part la physique du développement des jets dans un passage interaube de turbine et d'autre part de mettre en évidence la modification du comportement des écoulements secondaires en présence de ces injections. Deux aspects de ce problème sont à étudier, l'aspect thermique et l'aspect aérodynamique, seul le dernier sera considéré dans cette étude.

La première partie de ce travail est de nature expérimentale. Une grille plane d'aubes distributrices de turbine a été utilisée. Le développement des écoulements secondaires en absence et en présence d'injections à la paroi a été étudié. Dans ce papier, nous présenterons particulièrement les trajectoires de jets isolés introduits selon différentes configurations (débit, angle de dérapage, localisation dans la grille). L'ensemble des résultats relatifs à l'étude expérimentale des écoulements secondaires en absence d'injection est présenté dans la référence [1]. La seconde partie de ce papier est de nature théorique. La méthode de calcul d'un jet unique, introduit dans un écoulement tridimensionnel, est présentée. Ceci constitue une première étape dans la réalisation d'un calcul complet de l'écoulement dans une grille distributrice de turbine à gaz en présence d'injections partielles discrètes. La méthode utilise une décomposition du champ de vitesse \vec{V} de l'écoulement en une partie \vec{V}_0 , donnée par la grille d'aubes en absence de jet et une autre \vec{V}' qui caractérise le jet.

La décomposition précédente est introduite dans les équations de conservation générales qui sont ensuite traitées en appliquant une série d'hypothèses de type couche limite liées à la direction privilégiée d'évolution du jet. Les équations obtenues sont intégrées dans la section transversale du jet pour aboutir à une formulation intégrale.

Avant d'aborder ces divers points, nous allons donner une description qualitative des phénomènes observés dans un jet introduit en incidence et dérapage dans un écoulement extérieur tridimensionnel.

II. PHYSIQUE DU DEVELOPPEMENT D'UN JET INJECTE DANS UN ECOULEMENT TRIDIMENSIONNEL

Un jet injecté à partir d'une paroi dans un écoulement bi ou tridimensionnel peut être décomposé en trois zones :

. Une première zone dite "à potentiel" à proximité immédiate de l'orifice (de 1 à quelques

diamètres). Elle est caractérisée par un noyau au sein duquel la pression d'arrêt reste constante et où il se crée une vorticit   importante sur la p  riph  rie sous forme de tourbillons organis  s.

. Une zone interm  diaire, zone de m  lange et d'interaction forte avec l'  coulement ext  rieur. Les structures tourbillonnaires form  es vont s'adapter    l'  coulement ext  rieur puis   voluer vers leur destruction. Le jet va s'aligner avec l'  coulement externe.

. Une zone   loign  e du jet (10    30 diam  tres) o   la vitesse moyenne dans le jet est pratiquement   gale    celle de l'  coulement ext  rieur.

Trois effets importants r  gissent la dynamique du jet (Figure 1).

Les effets de tra  n  e

La zone proche de l'orifice du jet a   t     tudi  e en d  tail par Moussa et al. [2]. Au niveau de l'orifice, le jet se comporte comme un corps solide souple. Moussa et al. ont montr   ainsi, que l'  coulement transversal ext  rieur    un jet rond subissait une d  c  l  ration tr  s similaire    celle ressentie autour d'un cercle ou d'une ellipse pour le cas d'un jet rond en incidence. En aval du jet se d  veloppe un sillage. Celui-ci est sous certains aspects tr  s semblable    celui   mis en aval d'un cylindre solide, en particulier les fr  quences d'  mission des tourbillons de Karman sont identiques dans les deux cas pour un m  me   coulement externe. La pr  sence du sillage en aval du jet introduit au niveau du jet une diff  rence de pression statique entre les faces amont et aval du jet, que l'on peut associer globalement    une force de tra  n  e. Sous l'action de cette tra  n  e, le jet va alors se courber. La nature particuli  re du jet, par rapport    un corps solide souple   quivalent, va alors se manifester, d  s l'apparition de cette courbure, par la mise en mouvement de zones tourbillonnaires dans le jet lui-m  me [1].

Effet des tourbillons contrarotatifs

Une des caract  ristiques fondamentales de l'interaction de l'  coulement ext  rieur et du jet est l'apparition de deux tourbillons contrarotatifs dans le jet. Ceux-ci ont une trajectoire situ  e sous le vent du jet et pr  sentent une structure organis  e. Le processus de production tourbillonnaire est li      l'existence de gradients de vitesse transversaux du type $\frac{\partial v}{\partial x}$, $\frac{\partial w}{\partial x}$ et d'une certaine d  flexion du jet sous l'influence de l'  coulement ext  rieur traduites par les courbures K_{sb} , et K_{sm} . Le m  canisme de production tourbillonnaire est par ailleurs tout    fait similaire    celui qui pr  siede    l'apparition des tourbillons de passage dans une grille d'aubes (Leboeuf, Navier [3], Ollivier [4]). Par leurs moments cin  tiques respectifs, les tourbillons auront tendance    rigidifier le jet, s'opposant ainsi    la d  flexion qui les a cr  s.

Effets d'entra  nements

Le d  bit mesur   au travers de diff  rentes sections du jet augmente de l'amont vers l'aval. Cette augmentation para  t   tre due    deux ph  nom  nes, l'un li      la diffusion turbulente transversale du jet que l'on peut rapprocher de l'effet d'entra  nement dans un jet monodimensionnel, l'autre li      un effet potentiel caract  risant la captation des lignes de courant de l'  coulement situ      l'ext  rieur du jet. Cette captation peut se comprendre de la fa  on suivante : Le fluide observ   dans un plan transversal est convect   vers le centre du jet puis, entra  n   le long de la trajectoire S par la vitesse longitudinale. Dans ce plan transversal, cet effet tridimensionnel peut alors   tre mod  lis   par un puits localis   vers le centre du jet (r  f. [4],[6], Figure 1).

III. ETUDE EXPERIMENTALE

III.1. Les moyens d'essais

Dispositif exp  rimental

L'  tude a   t   r  alis  e sur une soufflerie de grille d'aubes plane. La grille d'aubes est une grille directrice de turbine    gaz. Les aubages non vrill  s pr  sentent une envergure $c = 0.274$ m et une corde $c = 0.163$ m (allongement $e/c = 1.68$). Le pas interaube est $g = 0.141$ m (solidit   $c/g = 1.16$). Le calage λ compt   par rapport    la direction axiale est $\lambda = 41^\circ 30'$. La grille est constitu  e de 9 aubages.

Un syst  me command   par une centrale d'acquisition permet de d  placer une sonde dans la veine d'essais. La sonde est introduite    l'int  rieur de la veine au travers de fentes r  alis  es dans la paroi en plexiglace oppos  e    celle sur laquelle se d  veloppe la zone visqueuse      tudier. Ces fentes sont parall  les au front de grille (Figure 2). Elles d  terminent les stations de mesure.

Le dispositif d'injection utilis  

Trois positionnements diff  rents du jet dans le passage interaube ont   t     tudi  s (Figure 2). Le premier (0) est situ   au bord d'attaque et au milieu du passage, les deux autres au niveau du col entre les fentes 8 et 9 l'une    0.025 m de l'extrados (A), l'autre    0.020 m de l'intrados (B). Le diam  tre de l'orifice est 0.022 m. L'angle α_b form   par la direction du jet en sortie avec le plan (X, Z) est $\alpha_b = 60^\circ$. L'orifice est fix   sur une pi  ce cylindrique qui peut tourner autour de son axe Y pour d  finir diff  rents angles α_m dans le plan X - Z. Les diff  rents param  tres utilis  s pour chaque positionnement de jet sont pr  sent  s Table 1.

Deux rapports de vitesse ont été étudiés : $V_0/V_{ex} = 0.65$ et $V_0/V_{ex} = 2.58$ (où V_{ex} représente la vitesse locale de l'écoulement externe à la zone visqueuse et où V_0 représente la vitesse débitante en sortie d'orifice).

Un système de chauffage du jet permet d'augmenter de 50°C la température de l'air injecté par rapport à la température de l'écoulement dans la grille.

Moyens de mesure

Mesures de pression dans l'écoulement

Les mesures de pression sont réalisées à l'aide d'une sonde "5 trous" de type "cobra", le diamètre de la tête de sonde est de .0015 m. Un étalonnage de la sonde associé à une utilisation d'une méthode de zéro (alignement de la sonde avec l'écoulement) permet d'obtenir les angles du vecteur vitesse par rapport à la grille, la pression d'arrêt, la pression statique et le module de la vitesse de l'écoulement. Le champ aérodynamique est alors complètement défini.

Mesures de pression sur l'aube

Un aubage muni de prises de pression statique (dont le nombre avoisine 1 200) permet de connaître le champ de pression statique sur l'aube.

Détection thermique du jet

Nous verrons qu'il est difficile de détecter au moyen de la sonde de pression le jet en particulier dans le cas du petit rapport de vitesse. Un système de détection thermique a été mis au point. Son principe est simple. Le jet est chauffé à une température d'environ 50° au dessus de la température de l'écoulement dans la grille. Un fil chaud à faible coefficient de surchauffe est utilisé comme thermomètre. Le traitement du signal pris aux bornes du fil chaud est effectué électroniquement. La localisation du jet se réduit alors à une mesure du coefficient d'intermittence I .

Le signal aux bornes du fil chaud, amplifié 50 000 à 100 000 fois et dont l'allure est présentée Figure 3, est introduit dans un système "contrôleur de seuil" qui permet de ramener le niveau "froid" du signal à un seuil de référence. On évite ainsi les problèmes de dérive de la température de l'air de la soufflerie. Le second étage électronique est utilisé en détection des bouffées chaudes issues du jet. On compare à un seuil réglable. En sortie, un signal logique est obtenu, de niveau 0 Volt pour le fluide froid et 5 Volts pour le fluide chaud que l'on utilise en commande d'un générateur 1 MHz. Le comptage des impulsions donne la mesure du coefficient d'intermittence I , I étant alors le rapport entre la somme des durées des signaux à 5 Volts (correspondant aux bouffées chaudes du jet) et la durée totale de la mesure.

III.2. Présentation et interprétation des résultats expérimentaux

Conditions aérodynamiques en amont de la grille

Le nombre de Reynolds calculé sur la corde du profil et la vitesse amont est $Re = V_{ex}c/\nu = 165\ 000$. L'épaisseur de la couche limite sur les plateformes est voisine de $\delta = 0.050$ m, l'épaisseur de déplacement est $\delta_x = .0043$ m pour un facteur de forme $H_{12} = 1.34$. Le coefficient de frottement calculé à l'aide de la méthode de Clauser a pour valeur $C_f = 3.5 \cdot 10^{-3}$. L'angle β fait par l'écoulement avec la direction axiale est voisin de $\beta = 0$ en dehors de la couche limite. Il existe cependant un très léger vrillage de celle-ci (Figure 4) à proximité de la paroi.

Répartition de pression statique sur l'aubage

Les répartitions de pression statique en absence d'injection à la paroi, sont présentées Figure 5 sous la forme d'un coefficient de pression $C_p = (p - p_1) / \frac{1}{2} \rho V_{ax}^2$. À l'extrados une accélération importante jusqu'à $x/c_{ax} = 0.50$ existe, puis une décélération faible est présente jusqu'au bord de fuite. L'écart maximum des coefficients entre l'intrados et l'extrados existe à $x/c_{ax} = 0.50$. Sur cette même figure sont comparées les répartitions de pression en fonction de la position en envergure des prises de pression. La pression à l'intrados n'est pas modifiée en fonction de la position en envergure, par contre, à l'extrados une différence très importante est observée. La pression statique augmentant lorsque l'on se rapproche de la paroi. Cette variation de pression essentiellement due à la présence du tourbillon de passage est responsable de déficits de force d'aubages [7].

Ces répartitions de pression statique ne sont pas modifiées en présence des injections utilisées.

Injection au point 0 avec un rapport de vitesse $V_0/V_{ex} = 2.58$ et sans dérapage $\alpha_m = 0^\circ$

Les courbes isopression d'arrêt montrent que le jet est parfaitement détecté au moyen de la sonde de pression pour les stations 6, 7, 8. Un accroissement de la pression d'arrêt est observé au centre du jet, il existe également une modification de la forme des courbes isopression d'arrêt près de la paroi, le sillage de la partie potentielle du jet étant visiblement détecté pour la station 6 (Figure 6a). Le champ de pression statique n'est que localement perturbé, le minimum de pression statique dans le jet correspond au maximum de la vitesse locale V_s (Figures 6b, 6c). La présence du jet est nettement distinguée par

observation des vecteurs-vitesses ($\vec{V}_m + \vec{V}_n$) (Figure 7). On note la tendance globale du jet à tourner dans le même sens que l'écoulement secondaire. Les courbes iso-intermittence présentées Figures 8a à 8e montrent que le développement du jet se fait avec une diffusion pratiquement équivalente dans les directions Y et Z. Il existe deux centres à fort coefficient d'intermittence \bar{I} . Ces centres correspondent à des noyaux de fluide chaud issu du jet. Notons que le centre situé près de l'intrados a tendance à rester très marqué vis à vis de l'autre. Également la rotation de l'axe reliant ces deux centres est assez prononcée lors de l'évolution dans le passage tout en conservant une structure en "haricot". Près de la paroi existe une zone non influencée par le jet dont l'épaisseur est voisine de 0.005 m, ce qui peut s'expliquer par la valeur initiale assez importante de l'angle d'incidence α_b . Le développement de l'écoulement secondaire n'est pas sensiblement influencé par la présence du jet, ce dernier peut être considéré comme une perturbation locale qui se superpose à un écoulement principal obtenu dans la grille en absence d'injection.

Injection au point 0 avec un rapport de vitesse $V_0 / V_{cx} = 0.65$ et sans dérapage $\alpha_m = 0^\circ$

Le jet ne modifie pas sensiblement la répartition de pression d'arrêt sauf très près de la paroi (Figure 9). Le champ de pression statique n'est pas modifié. Il n'est plus possible de distinguer le jet autrement que par détection thermique. Les courbes iso-intermittences présentent encore une structure de type "haricot" (Figures 10a, 10b, 10c, 10d). La diffusion du jet se fait de façon privilégiée dans le sens extrados-intrados (direction Z). Le rapport des largeurs de jet étant environ égal à 2.

Injection au point 0 avec un rapport de vitesse $V_0 / V_{cx} = 0.65$ et un dérapage $\alpha_m = -45^\circ$ et $\alpha_n = +45^\circ$ (Figures 11a, 11b, 11c et 12a, 12b, 12c)

Dès qu'un dérapage du jet par rapport à l'écoulement de grille existe, la structure en "haricot" présentée par les courbes iso-intermittence disparaît ; il semblerait qu'il n'existe plus alors qu'un seul centre organisé. Il n'est malheureusement pas possible, dans ce cas d'injection, de tirer des conclusions précises sur les structures tourbillonnaires issues de la déflexion du jet. Les niveaux maximum du coefficient d'intermittence diminuant rapidement vers l'aval dans le passage. Les courbes iso-intermittence ont alors une allure similaire à celles rencontrées dans un jet rond non défléchi, bien que la diffusion dans le sens Z soit encore nettement prépondérante par rapport à celle existant dans le sens Y.

Injection au point A et au point B

L'angle de dérapage a été choisi égal à $\alpha_m = 45^\circ$ ce qui correspond sensiblement à un alignement de l'axe du jet avec l'écoulement moyen dans la section d'injection. Le rapport de vitesse est également de $V_0 / V_{cxm} = 0.65$ où V_{cxm} est la vitesse absolue moyennée dans la section sur le canal interaube. Une diffusion importante peut être identifiée du côté de l'extrados de l'aubage pour chacune des injections (Figures 13, 14).

Description des trajectoires des jets

Le lieu des maxima du coefficient d'intermittence est tracé Figures 2 et 15. Dans le cas de l'injection au point 0 pour un débit fort ($V_0 / V_{cx} = 2.58$), le jet a tendance à s'éloigner de la plateforme en se rapprochant de l'intrados par rapport au cas similaire à faible débit ($V_0 / V_{cx} = 0.65$). Ceci s'explique aisément par la différence entre l'énergie cinétique du jet et celle du fluide de l'écoulement de grille. Cependant pour les cas d'injection au point 0 à différents angles de dérapage, la trajectoire du jet est peu influencée par les conditions initiales imposées par cet angle. La comparaison de la position de la trajectoire du jet avec celle des lignes de courant obtenues à l'aide d'un calcul aube à aube de l'écoulement sain est fournie Figure 2. On note une surdéflexion de ces trajectoires par rapport aux lignes de courant, surdéflexion engendrée par la présence de l'écoulement secondaire créé par la grille elle-même, et associé au développement de la couche visqueuse pariétale.

Dilution des jets dans l'écoulement de grille

Deux grandeurs peuvent décrire la dilution du jet dans l'écoulement de grille. En premier lieu la valeur du maximum du coefficient d'intermittence caractérise la façon dont le noyau du jet se mélange à l'écoulement principal. La décroissance de ce maximum est pratiquement identique pour tous les jets issus d'un même orifice (Figure 16). En second lieu, l'évolution de la section du jet dans le plan X-Z donne une idée de la diffusion transversale du jet (Figures 8, 10, 11, 12).

IV. LA METHODE DE CALCUL

Nous avons porté notre choix sur une méthode intégrale, ceci pour des raisons de rapidité de calcul et de facilité de mise en oeuvre, mais aussi afin de permettre un traitement ultérieur de plusieurs rangées de jets simultanément immergés dans l'écoulement tridimensionnel existant dans la grille.

Nous décrirons dans la suite toutes les étapes qui nous ont amenés à un système de six équations (continuité, 3 équations de quantité de mouvement et 2 équations de production tourbillonnaire) à six inconnues qui sont les suivantes :

- V_s : excès de vitesse maximum dans la section du jet pour la zone établie.
- S : surface transversale.

α_b, α_n : angles définissant la trajectoire (Figure 1).

Γ_1, Γ_2 : circulations respectives des deux tourbillons contrarotatifs

Dans la zone potentielle, à proximité immédiate de l'orifice du jet, nous utiliserons, à la place de V_i , une variable k . Celle-ci détermine la fraction de la surface σ totale occupée par la zone potentielle elle-même.

IV.1. Equations générales

Si \vec{V} a une forme conservative, les équations du mouvement s'écrivent dans un repère fixe :

$$\begin{aligned} \nabla \cdot (\rho \vec{V}) &= 0 \\ \nabla \cdot (\rho \vec{V} \otimes \vec{V} - \overline{\overline{\sigma}}) &= \vec{f}_k \end{aligned}$$

Si nous négligeons les forces de volume \vec{f}_k le système devient :

$$\begin{aligned} \nabla \cdot (\rho \vec{V}) &= 0 \\ \nabla \cdot (\rho \vec{V} \otimes \vec{V} - \overline{\overline{\sigma}}) &= 0 \end{aligned} \quad (1)$$

où $\overline{\overline{\sigma}}$ est le tenseur des contraintes : $\overline{\overline{\sigma}} = -p \overline{\overline{I}} + \overline{\overline{C}}$

$\overline{\overline{C}}$ comprend les tensions de Reynolds.

Les équations sont écrites pour un problème stationnaire dans un repère curviligne orthogonal (s, n, b) : s est associée à la direction de la trajectoire du jet (Figure 1). Quelques hypothèses apportent des simplifications notables aux équations, nous supposons ainsi que la surface (b, n) est plane ($h_b = h_n = 1$) ; également, les phénomènes de diffusion selon la direction s seront négligés ($\partial \overline{\overline{C}}_{ij} / \partial s \sim 0$). Les équations résultantes sont exprimées en détail dans la référence [4]. Dans ce qui suit, nous considérons, tout d'abord, le système de base formé de l'équation de continuité et des trois composantes de l'équation de quantité de mouvement.

IV.2. Moyenne des équations

La décomposition du champ de vitesse :

$$\vec{V} = \vec{V} + \vec{V}' \quad (2)$$

est introduite dans le système de base. Puis les équations obtenues sont simplifiées par l'utilisation d'une série de 6 hypothèses.

H1 : Les rayons de courbures des lignes s selon b et n sont grands devant une dimension caractéristique du plan transversal du jet. Les conséquences de cette hypothèse sont les suivantes [4] :

$$\begin{aligned} \frac{\partial V_i}{\partial i} &\gg \frac{V_i}{h_s} \frac{\partial h_s}{\partial i} \\ \frac{1}{h_s} \frac{\partial (h_s \overline{\overline{C}})}{\partial i} &\approx \frac{\partial \overline{\overline{C}}}{\partial i} \quad \text{avec } i = n \text{ ou } b \end{aligned} \quad (3)$$

H2 : Le terme $\partial p / \partial s$ est imposé par l'écoulement extérieur associé à \vec{V}' .

H3 : Les tensions de résistance à l'avancement sont nulles sur le bord du jet. Cette hypothèse est assez grossière (Moussa [2]), cependant les termes correspondants seront négligés dans les équations du mouvement.

H4 : Le champ extérieur de vitesse \vec{V}' varie peu sur l'étendue de la surface transversale du jet.

H5 : Hors du jet, la composante V_s , s'identifie à la composante \hat{V}'_s donnée par l'écoulement extérieur.

H6 : De plus et parce que seuls les phénomènes aérodynamiques nous occupent ici, nous supposons que la masse volumique ρ est imposée par l'écoulement extérieur et est constante dans la section du jet.

Le système d'équations après utilisation de (2) et de ces hypothèses est intégré sur l'étendue de la surface transversale du jet. Nous obtenons le système suivant [4] :

$$\frac{d}{ds} (\hat{e} \hat{V}'_s \sigma) + \frac{d}{ds} \iint_{\sigma} \hat{e} V'_s d\sigma = E \quad (4a)$$

$$\begin{aligned}
& \cdot \frac{d}{ds} \left[\hat{p} \left[2 \hat{V}_s \iint_{\sigma} V'_s d\sigma + \iint_{\sigma} V_s'^2 d\sigma \right] + \hat{p} \hat{V}_s^2 \frac{d\sigma}{ds} - \hat{V}_s E + 2 \hat{p} \iint_{\sigma} V'_s d\sigma \left[K_{sb} \hat{V}_b + K_{sm} \hat{V}_m \right] \right. \\
& \quad \left. + 2 \hat{p} K_{sb} \left[\hat{V}_s \iint_{\sigma} V'_b d\sigma + \iint_{\sigma} V'_s V'_b d\sigma \right] + 2 \hat{p} K_{sm} \left[\hat{V}_s \iint_{\sigma} V'_m d\sigma + \iint_{\sigma} V'_s V'_m d\sigma \right] \right] = 0 \quad (4b) \\
& \cdot \frac{d}{ds} \left[\hat{p} \hat{V}_b \iint_{\sigma} V'_s d\sigma \right] - E \hat{V}_b + \hat{p} \hat{V}_s \hat{V}_b \frac{d\sigma}{ds} - \hat{p} K_{sb} \left[2 \hat{V}_s \iint_{\sigma} V'_s d\sigma + \iint_{\sigma} V_s'^2 d\sigma \right] \\
& \quad + \frac{d}{ds} \hat{p} \left[\hat{V}_s \iint_{\sigma} V'_b d\sigma + \iint_{\sigma} V'_s V'_b d\sigma \right] - \hat{p} \hat{V}_s V'_b \frac{d\sigma}{ds} + \hat{p} \hat{V}_b \iint_{\sigma} \frac{\partial V'_b}{\partial b} d\sigma \\
& \quad + 2 \hat{p} \iint_{\sigma} V'_b \frac{\partial V'_b}{\partial b} d\sigma + \hat{p} \hat{V}_m \iint_{\sigma} \frac{\partial V'_b}{\partial m} d\sigma + \hat{p} \iint_{\sigma} V'_m \frac{\partial V'_b}{\partial b} d\sigma + \hat{p} \iint_{\sigma} V'_b \frac{\partial V'_m}{\partial b} d\sigma \\
& \quad + \hat{p} K_{sb} \left[2 \hat{V}_s \iint_{\sigma} V'_b d\sigma + \iint_{\sigma} V_b'^2 d\sigma \right] + \hat{p} K_{sm} \left[\hat{V}_b \iint_{\sigma} V'_m d\sigma + \hat{V}_m \iint_{\sigma} V'_b d\sigma + \iint_{\sigma} V'_m V'_b d\sigma \right] \\
& = \iint_{\sigma} \left[\frac{\partial \hat{p}}{\partial b} - \frac{\partial \hat{p}}{\partial b} \right] - \frac{1}{R_e} \left[\frac{\partial \hat{c}_{bb}}{\partial b} - \frac{\partial \hat{c}_{bm}}{\partial m} \right] d\sigma \quad (4c)
\end{aligned}$$

L'équation de quantité de mouvement selon n est obtenue en intervertissant dans (4c) les indices n et b, cette équation sera 4d.

Les courbures K_{sb} et K_{sm} peuvent s'écrire directement en fonction des angles α_b et α_m [4] (inconnues du problème) :

$$\begin{aligned}
K_{sb} &= -\frac{d\alpha_b}{ds} \\
K_{sm} &= -\cos \alpha_b \frac{d\alpha_m}{ds}
\end{aligned} \quad (5)$$

Le terme E (4a, 4b) traduit l'entraînement de masse du fluide extérieur dans le jet. Notons la présence du terme de fluctuation $\iint_{\sigma} V'_s d\sigma$ qui modifie sensiblement l'influence de E sur l'évolution de σ . L'équation de quantité de mouvement selon s (4b), admet plusieurs termes sources associés aux fluctuations de vitesse V'_b , V'_m , aux courbures K_{sb} , K_{sm} de la ligne S et à l'entraînement de quantité de mouvement du fluide extérieur ($\hat{V}_s E$). Notons l'absence des forces de traînée (hypothèse H3). Les équations de quantité de mouvement selon n et b comportent en plus une traînée qui est isolée dans le second membre de 4c, 4d. Ajouté aux termes précédents de fluctuation et d'entraînement ($E \hat{V}_b$), ce terme permet l'introduction dans le calcul du phénomène de courbure du jet.

IV.3. Les relations de fermetures

a.- Forme de la surface transversale σ et profils de vitesse V'_j

Dans la zone établie, la forme de la surface transversale est modélisée par une ellipse dont le rapport du grand axe sur le petit axe est donné par $a/b = 4$. Le profil de vitesse V'_j est choisi par une relation affine sur l'ellipse, selon la loi suivante [8] :

$$V'_j = V_j \left(1 - \frac{B^2}{a^2} - \frac{N^2}{b^2} \right)^{5/2} \quad (6)$$

le petit axe est aligné avec la normale principale à la trajectoire \vec{N} , le grand axe avec le vecteur de torsion \vec{T} .

Dans la zone potentielle le rapport a/b sera variable de façon à obtenir une adaptation continue de la forme du jet à l'orifice (cercle) vers l'ellipse d'excentricité 4. Le profil de vitesse aura une forme similaire mais tronquée dans sa partie supérieure [4] pour tenir compte de l'étendue de la zone à pression d'arrêt constante.

De ces différents modèles nous déduisons l'expression des intégrales suivantes [4] :

$$\iint_{\sigma} V'_s d\sigma = V_j \frac{\sigma}{S_{00}} \quad (7a)$$

$$\iint_{\sigma} v_s'^2 d\sigma = V_j^2 \sigma \frac{S_{10}}{S_{00}} \quad (7b)$$

avec dans la zone établie :

$$S_{00} = 3.5 \quad (8)$$

$$S_{10} = .5833$$

et dans la zone potentielle

$$S_{00} = 7/(2 + 5k^2) \quad (9)$$

$$S_{10} = 7(1 + 5k^2)/6(2 + 5k^2)$$

k est une variable substituée à la variable principale V_j dans la zone potentielle. Cette variable vaut 1 initialement et s'annule à l'extrémité avale de la zone potentielle.

b.- La traînée

Les termes de tension et de gradient de pression normaux à la trajectoire du jet (second membre des équations 4c, 4d) seront inclus dans une force de traînée supposée dirigée selon la projection de \vec{v} dans le plan orthogonal au jet [4] soit :

$$\iint_{\sigma} \left\{ \left[\frac{\partial P}{\partial b} - \frac{\partial P}{\partial m} \right] - \frac{1}{R_c} \left[\frac{\partial \bar{G}_{bb}}{\partial b} - \frac{\partial \bar{G}_{bm}}{\partial m} \right] \right\} d\sigma \vec{b}$$

$$+ \iint_{\sigma} \left\{ \left[\frac{\partial P}{\partial m} - \frac{\partial P}{\partial b} \right] - \frac{1}{R_c} \left[\frac{\partial \bar{G}_{mm}}{\partial m} - \frac{\partial \bar{G}_{mb}}{\partial b} \right] \right\} d\sigma \vec{m} = a \frac{C_0}{2} \sqrt{V_m^2 + V_b^2} (\vec{V}_m \vec{m} + \vec{V}_b \vec{b}) \quad (10)$$

avec $C_0 \approx 1.8$ [9].

c.- L'entraînement

L'entraînement de fluide extérieur dans le jet a deux origines principales :

- La première est liée à la diffusion turbulente. L'entraînement est alors proportionnel au périmètre du jet et à l'excès de vitesse axiale au sein du jet [9] :

$$E_1 = \rho K_1 V_j \sqrt{\sigma}$$

$$K_1 = 0.137$$

- La seconde est liée à l'effet de traînée, en considérant la présence d'un puits potentiel situé sous la partie avale du jet (Figure 1). L'entraînement s'exprime alors par (Le Grives [10]) :

$$E_2 = \rho \frac{C_0}{2} a \sqrt{V_m^2 + V_b^2} \quad (11b)$$

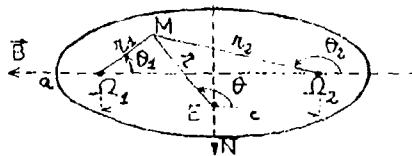
L'expression finale du coefficient d'entraînement est alors :

$$E = E_1 + E_2 \quad (12)$$

d.- Modélisation des vitesses transversales

Le champ de vitesse transversale est induit par les deux tourbillons contrarotatifs d'intensité Γ_1 , Γ_2 et le puits d'intensité E_2 (11b). A partir d'une modélisation déjà utilisée par Fern et Weston [11] nous avons choisi une répartition surfacique de ces trois randeurs. La localisation de ces singularités est schématisée sur la Figure ci-après.

Les tourbillons sont localisés aux points focaux de l'ellipse, tandis que le puits est situé dans le quart inférieur de l'ellipse (\vec{N} est dirigé vers le centre de courbure).



Les répartitions surfaciques sont les suivantes :

$$\Omega_i = \frac{\Gamma_i}{2\pi a^2} e^{-\frac{v_i^2}{2}} \quad \text{avec } v_i = \frac{r_i}{a} \text{ pour } \begin{cases} i=1 \\ i=2 \end{cases} \quad (13a)$$

$$E = \frac{1536}{\pi a^2} E_2 \left(\frac{1}{8} - v \right) \quad \text{si } v < \frac{1}{8} \quad \text{avec } v = \frac{r}{a} \quad (13c)$$

$$E = 0 \quad \text{si } v > \frac{1}{8}$$

Les vitesses induites se déduisent de ces répartitions par l'application des théorèmes de circulation et des principes de conservation du débit :

$$V'_B = -\frac{\Gamma_1}{2\pi a} f(v_1) \sin \theta_1 - \frac{\Gamma_2}{2\pi a} f(v_2) \sin \theta_2 - \frac{E_2}{2\pi a} F(v) \cos \theta \quad (14a)$$

$$V'_N = \frac{\Gamma_1}{2\pi a} f(v_1) \cos \theta_1 + \frac{\Gamma_2}{2\pi a} f(v_2) \cos \theta_2 - \frac{E_2}{2\pi a} F(v) \sin \theta \quad (14b)$$

avec les définitions :

$$f(v) = \frac{1 - e^{-\frac{v^2}{2}}}{v}$$

$$F(v) = \frac{1}{a} \quad \text{si } v > \frac{1}{8}$$

$$F(v) = 3072 \left(\frac{v}{16} - \frac{v^3}{3} \right) \quad \text{si } v < \frac{1}{8}$$

Enfin Γ_1 et Γ_2 sont déterminés par l'écriture de l'équation de transport des tourbillons Ω_i et Ω_2 écrite dans un repère (S,b,n) [4] :

$$\frac{d}{ds} \left(\frac{\Omega_i}{\rho V_s} \right) = \frac{2}{\rho V_s} \left(K_{sb} \frac{\partial V'_i}{\partial m} - K_{sm} \frac{\partial V'_i}{\partial b} \right) \quad (15)$$

Cette équation est également moyennée sur σ en utilisant 13a et 13b, on obtient :

$$\left[\iint_{\sigma_i^u} e^{-\frac{v_i^2}{2}} d\sigma \right] \frac{d}{ds} \left(\frac{\Gamma_1}{V_s} \right) + \left[\iint_{\sigma_i^u} e^{-\frac{v_i^2}{2}} d\sigma \right] \frac{d}{ds} \left(\frac{\Gamma_2}{V_s} \right) - \frac{1}{2\pi a ds} \left[\int_{\sigma_i^u} \frac{e^{-\frac{v_i^2}{2}}}{V_s} d\sigma + \Gamma_2 \int_{\sigma_i^u} \frac{e^{-\frac{v_i^2}{2}}}{V_s} d\sigma \right] + (-1)^{i+1} \frac{5\pi^2 a}{16} \frac{V_{s_i}}{V_s} (\nu K_{sm} + \lambda K_{sb}) = 0 \quad (16)$$

où σ^u est une ellipse de référence de grand-axe 1 et de petit axe 1/4.

$\int_{\sigma_i^u} \frac{e^{-\frac{v_i^2}{2}}}{V_s} d\sigma$ correspond à chaque demi surface contenant le tourbillon Ω_i ($i = 1, 2$), correspond au contour de σ_i^u , et V_s est une vitesse longitudinale moyenne périmètre de l'ellipse :

$$\overline{V_s} = \hat{V}_s + \frac{2}{7} V_{s_i} \quad (17)$$

Le champ de vitesses \vec{V} déterminé par les équations (14) est alors projeté dans le repère (\vec{b}, \vec{n}) :

$$\begin{aligned} V'_b &= \mu V'_b + \lambda V'_n \\ V'_n &= \lambda V'_b - \mu V'_n \end{aligned} \quad (18)$$

avec

$$\begin{aligned} \lambda &= \vec{b} \cdot \vec{N} \\ \mu &= \vec{b} \cdot \vec{B} \end{aligned} \quad (19)$$

Les relations (13) à (19) nous permettent alors de calculer les différentes intégrales contenues dans les équations (4).

Notons que cette étude présentée ignore les effets de parois ou des autres jets adjacents mais que ceux-ci peuvent être introduits dans la modélisation.

IV.4. Comparaison du calcul et de l'expérience

Les résultats du calcul sont présentés Figures 17 à 22. Ils correspondent aux cas d'expériences présentés précédemment. Les évolutions des trajectoires, des vitesses et de la vorticité sont présentées. Les données du calcul sont : les conditions d'injection à l'orifice ($V_{j0}, \sigma_0, \alpha_{b0}, \alpha_{n0}$) et l'écoulement extérieur \hat{V} . Ce dernier est moyenné selon z. Ainsi nous avons :

$$\begin{aligned} \hat{V}_x &= \hat{V}_x(x, y) \\ \hat{V}_y &= 0 \\ \hat{V}_z &= \hat{V}_z(x, y) \end{aligned} \quad (20)$$

Les trajectoires

Les trajectoires issues du calcul sont comparées aux résultats expérimentaux Figures 17, 18, 19. Les trajectoires dans le plan (x, z) (Figures 17, 18) se rapprochent moins de l'extrados que ne l'indique l'expérience. La déflexion des jets par rapport aux lignes de courant de l'écoulement sain étant due à l'écoulement secondaire (tourbillon de passage), il est vraisemblable que la moyenne selon z appliquée sur \hat{V} ait détruit l'effet local de \hat{V} .

Dans le plan (x, y) les trajectoires correspondent assez précisément à celles déterminées expérimentalement (Figure 19). Cependant le calcul n'inclut ni les effets de parois ni la présence de vitesses \hat{V}_y non nulles (imposées par l'écoulement secondaire en particulier près de l'extrados où $\hat{V}_y > 0$) ; ainsi la tendance du jet injecté en λ à s'éloigner de la paroi est incorrectement prédite.

Evolution de la vitesse maximale dans le jet

Elle est décrite Figure 20. Les résultats expérimentaux et théoriques, malgré le peu de points de comparaison, paraissent en accord. Il existe une légère augmentation de V_j dans la zone accélérée de la grille d'aube, qui semble trouver son origine dans le terme ($\hat{V}_z \cdot \vec{e}_z$) de l'équation de quantité de mouvement selon z. Nous présentons également Figure 21 un calcul effectué avec les mêmes conditions d'injection, mais avec un profil de vitesse \hat{V} bidimensionnel non accéléré, de type couche limite. Dans ce dernier calcul V_j tend régulièrement vers 0, ce qui correspond bien à une évolution espérée.

Evolution de la vorticité (Figure 21)

Nous remarquons une forte production près de l'orifice d'injection, puis, après avoir atteint un maximum, la circulation se met à décroître régulièrement.

La production importante est due à une forte déflexion associée aux gradients de vitesse $\partial V_j / \partial x, \partial V_j / \partial b$ importants dans la première zone du jet (Cf. équation (15)). Quant à la diminution, elle est due à la rotation de la surface transversale du jet. Cette rotation a pour effet d'inverser les signes de λ et μ (égalité (19)) entraînant ainsi un changement de signe du terme de production dans les équations 16-1, 16-2.

Sur la Figure 23 est présentée l'évolution de la vorticité dans un écoulement \hat{V} bidimensionnel avec des conditions d'injections identiques à celles utilisées précédemment (Figure 22). La rotation de la surface est alors absente et les courbures s'annulant, la circulation tend vers une valeur constante. Rappelons en effet que la dissipation n'agit pas directement sur l'évolution de la vorticité d'après (16-1).

V. CONCLUSIONS

Du point de vue expérimental, nous avons pu, par l'utilisation d'un système de détection par fil chaud, décrire les trajectoires et formes de jets uniques injectés sous différentes conditions dans la grille d'aubes. Il apparaît que le champ aérodynamique créé par le jet ne modifie que localement celui créé par la grille d'aubes. L'un des tourbillons générés par la déflexion du jet reste marqué alors que l'autre est détruit par l'écoulement secondaire. L'influence de l'angle de dérapage sur l'évolution du jet est faible. La diffusion latérale est dans chaque cas plus importante que la diffusion normale à la paroi. Du point de vue prédiction théorique, la méthode de calcul semble bien adaptée à la situation aérodynamique complexe rencontrée. Les effets de parois pourraient être pris en compte assez simplement en superposant au champ de vitesse transversale calculé, le champ de vitesse induit par un jet image par rapport à la paroi. Les fermetures peuvent sans doute être améliorées notamment au niveau de l'entraînement de type potentiel.

Ce travail présente des perspectives intéressantes en ce qui concerne l'étude expérimentale et théorique de jets multiples. Le formalisme de la méthode de calcul restant le même, l'influence des jets entre eux pouvant être introduite facilement au travers des vitesses transversales induites.

REFERENCES

- [1] A. Onvani, "Etude expérimentale des écoulements secondaires en grille d'aubes de turbine en absence et en présence d'injections discrètes à la paroi", Thèse de 3ème Cycle Université LYON I, Septembre 1983.
- [2] Z.W. Moussa, J.W. Trischka, S. Eskinazi, "The near field in the mixing of a round jet with a cross-stream", J. Fluid Mech. 80(1), pp. 49-80, 1977.
- [3] F. Leboeuf, H. Navière, "Etude expérimentale et théorique des couches visqueuses pariétales dans un compresseur mono-étage transsonique", AGARD, CP. 351, 1983.
- [4] C. Ollivier, "Calcul d'un jet introduit en incidence et dérapage avec prise en compte de la vorticit  induite dans le jet", Rapport DEA, ECL-LYON I, 1974.
- [5] F. Leboeuf, "Etude expérimentale et théorique de l'écoulement dans une turbomachine axiale transsonique", Thèse Docteur-Ingénieur, LYON I, 1978.
- [6] H. Werle, "Le tunnel hydrodynamique au service de la recherche aérospatiale", Publication ONERA n° 165, pp. 48-49, 1974.
- [7] F. Bario, F. Leboeuf, K.D. Papailiou, "Study of secondary flows in blade cascade of turbomachines", ASME Paper n° 81 GR GT4, Patras, Greece. J. of Eng. for Power, 104, pp. 491-509, April 1982.
- [8] P. Haim, "Etude théorique de l'influence d'une injection pariétale sur une couche limite bidimensionnelle", Rapport DEA, ECL-LYON I, 1981.
- [9] Ph. Ramette and J.F. Louis, "Analytical study of the thermal and fluid mechanical evolution of a cooling film injected from a single line of inclined round holes", Int. J. of Turbo. and Jet-Engines, 1(1), 1984.
- [10] E. Le Grives, "Mixing process inducted by the vorticity associated with the penetration of a jet into a cross-flow", NRL TR 7107U, 1977.
- [11] R.L. Fern, R.P. Weston, "Vorticity associated with a jet in a cross-flow", AIAA Journal 12, pp. 1666-1671, December 1974.

	★	□	•	△	■	▲
ORIGINE DU JET	○	○	○	○	A	B
V_0 / V_{ex}	2.58	0.65	0.65	0.65	0.65	0.65
α_n (deg)	0	0	45	-45	45	45
α_b (deg)	60					

Table 1

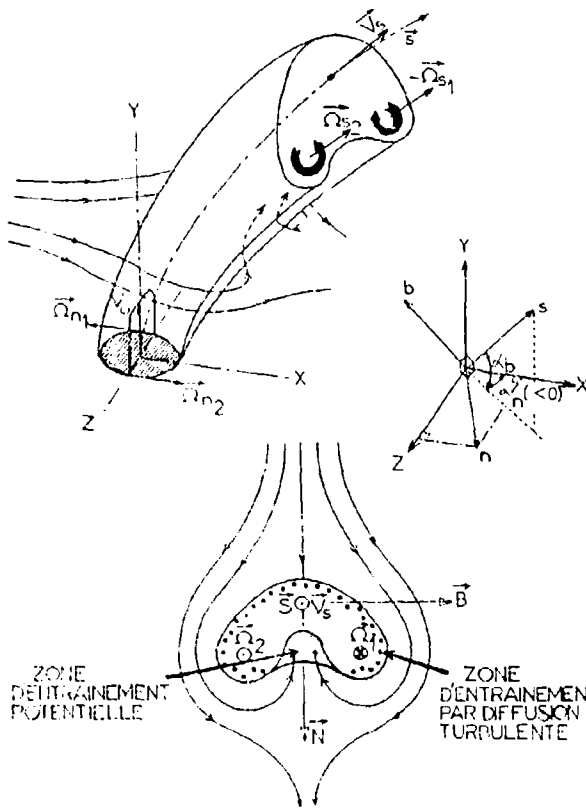


Fig. 1. Représentation et coupe transversale du jet, systèmes d'axes.

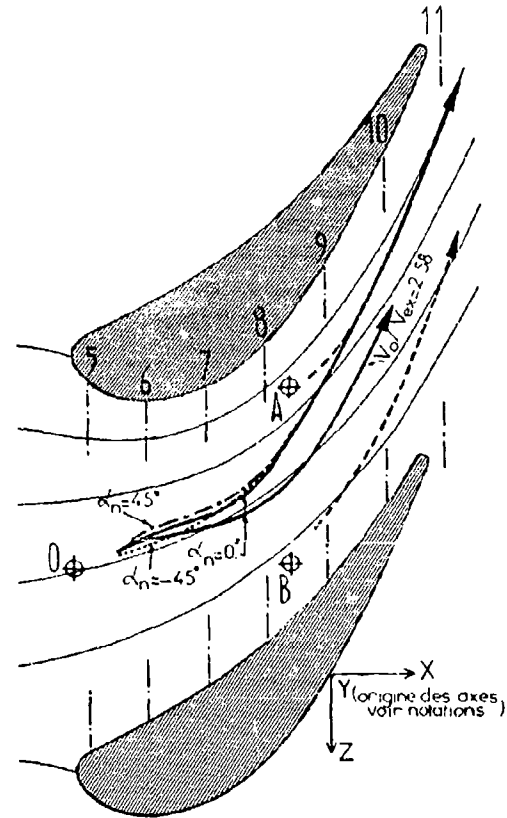


Fig. 2. La grille d'aubes, stations de mesure, trajectoires des jets et lignes de courant extérieures

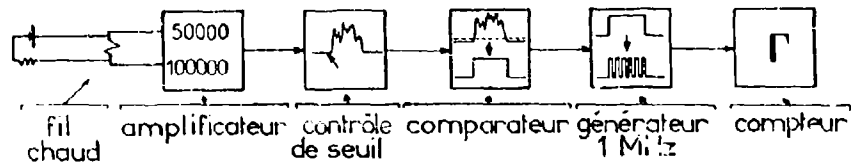


Fig. 3. Système électronique de détection et de mesure du coefficient d'intermittence.

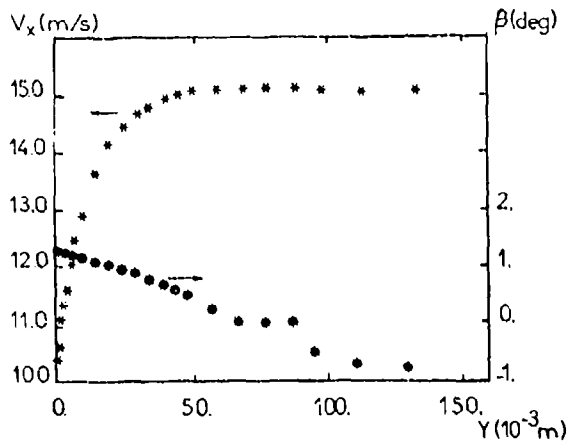


Fig. 4. Conditions aérodynamiques en amont de la grille.

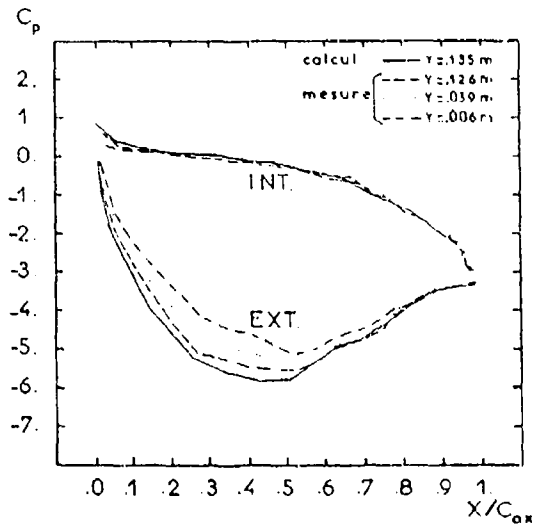


Fig. 5. Répartition de la pression statique sur l'aube.

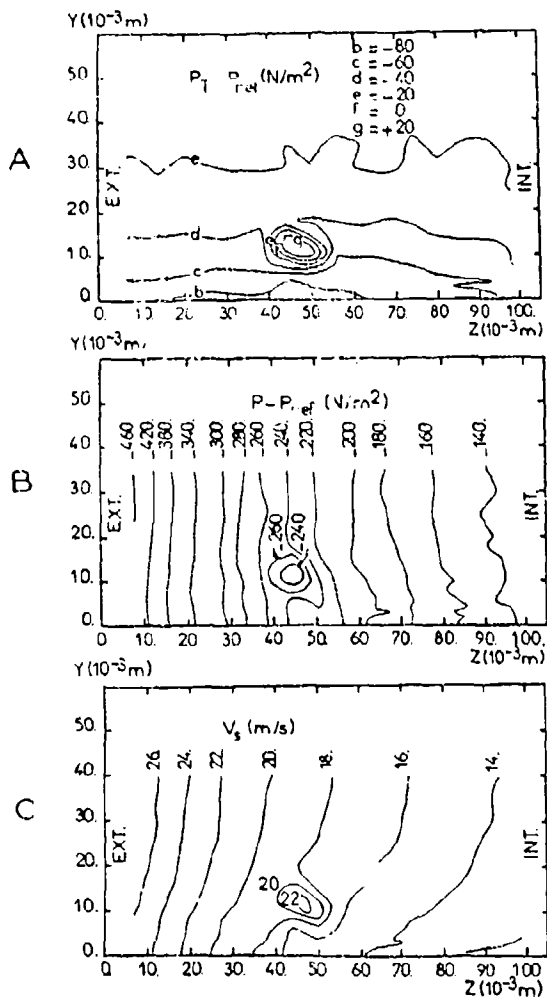


Fig. 7. Vecteurs vitesse $\vec{V}_N + \vec{V}_R$ station 7 jet (0)
 $v_0/v_{ex} = 2.58$.

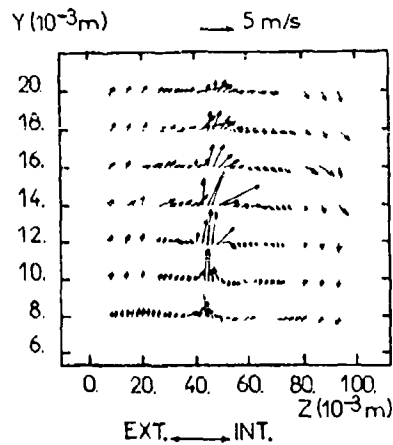


Fig. 6. Curves iso-valeurs station 6 jet (0),
 $v_0/v_{ex} = 2.58$

A pression d'arrêt
 B pression statique
 C vitesse V_s

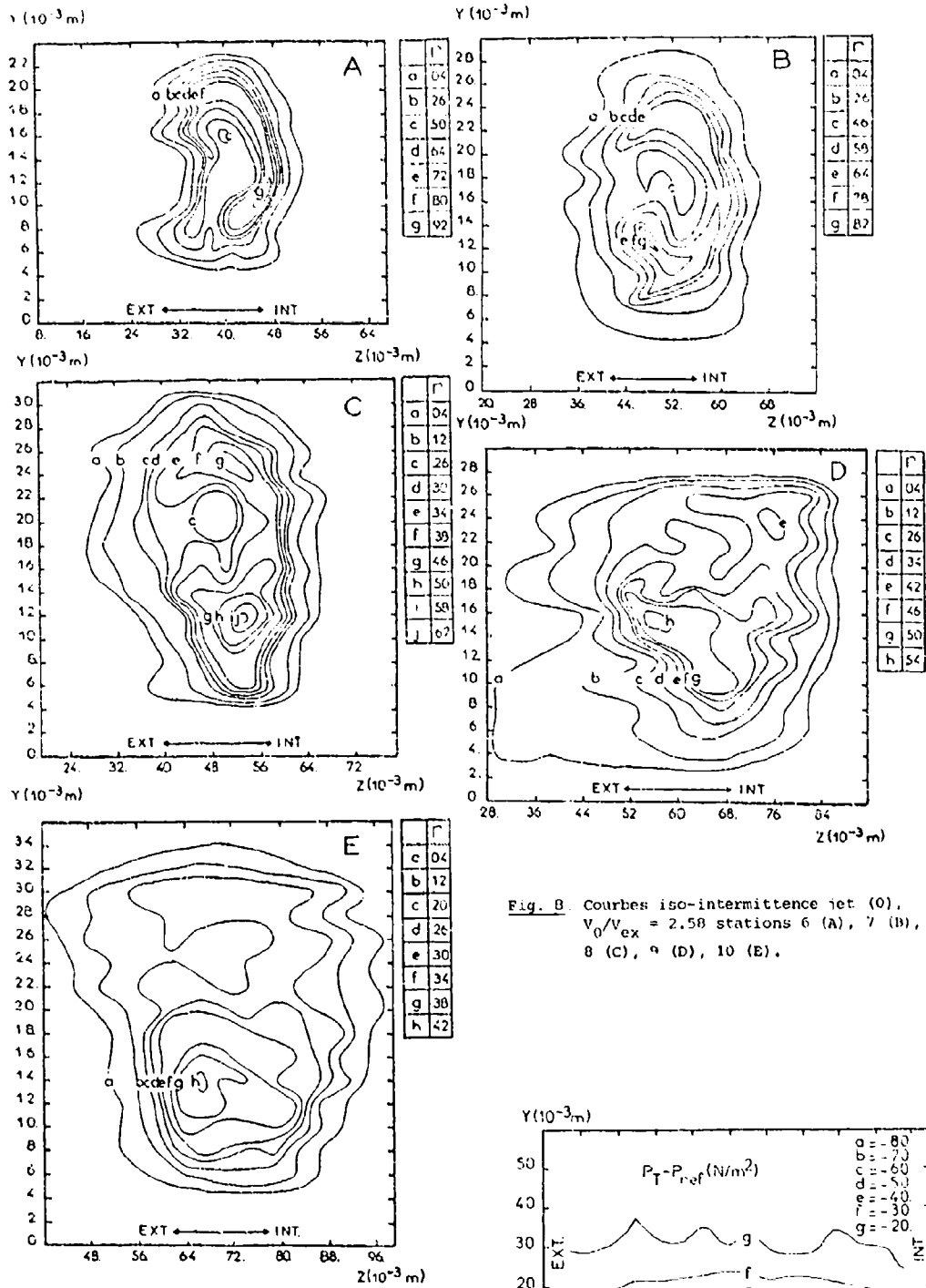


Fig. 8 Courbes iso-intermittence jet (0), $V_0/V_{ex} = 2.58$ stations 6 (A), 7 (B), 8 (C), 9 (D), 10 (E).

Fig. 9. Courbes iso-pression d'arrêt jet (0), $V_0/V_{ex} = 0.65$ station 6.

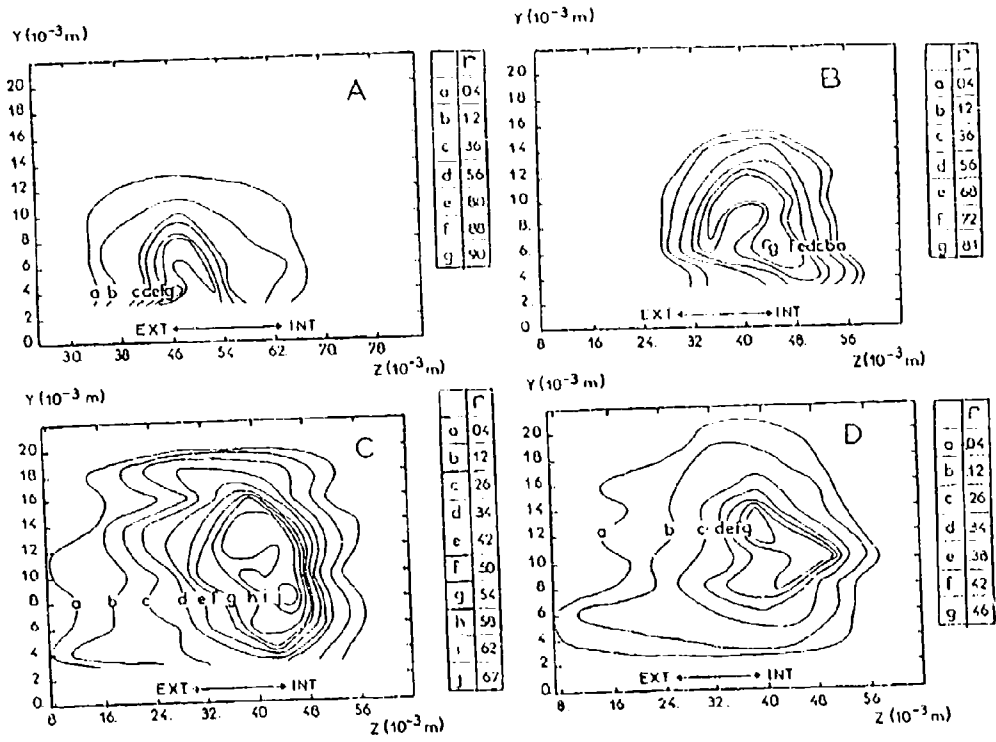


Fig. 10. Courbes iso-intermittence jet (0), $V_0/V_{ex} = 0.65$, $\alpha_n = 0^\circ$ stations 6(A), 7(B), 8(C), 9(D).

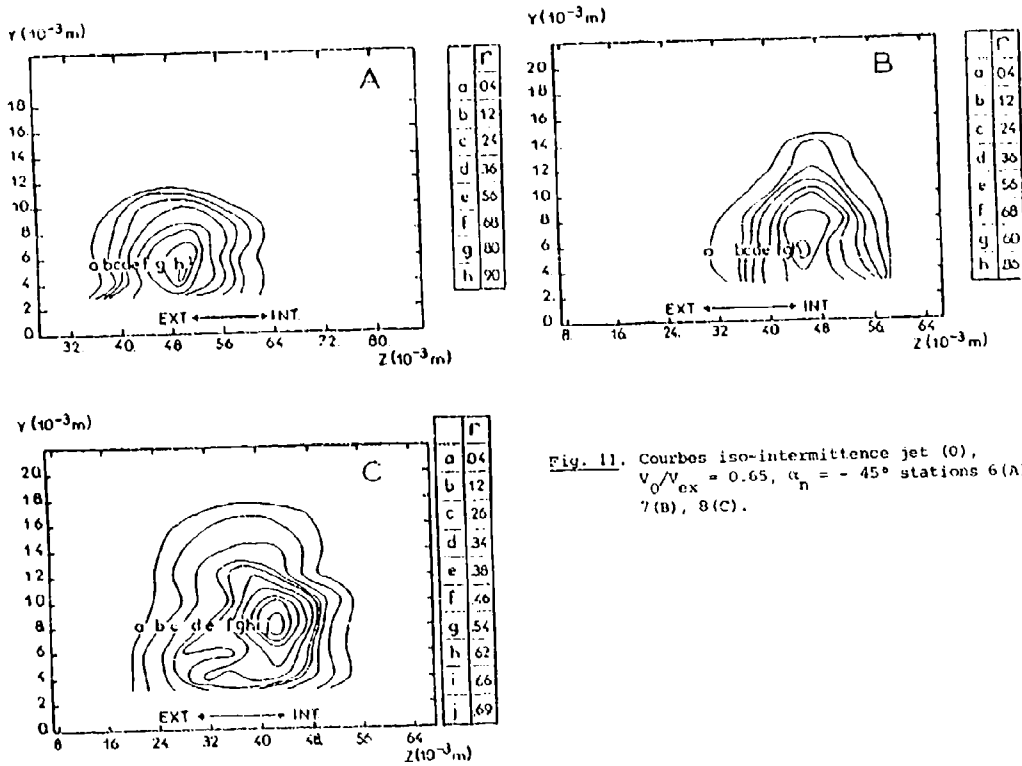


Fig. 11. Courbes iso-intermittence jet (0), $V_0/V_{ex} = 0.65$, $\alpha_n = -45^\circ$ stations 6(A), 7(B), 8(C).

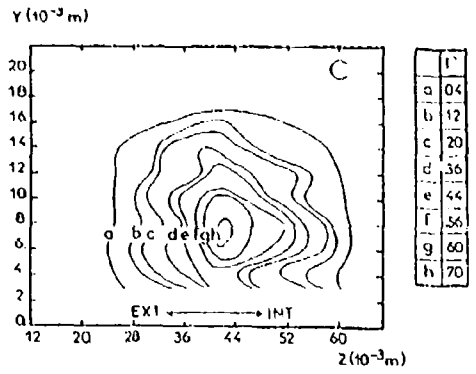
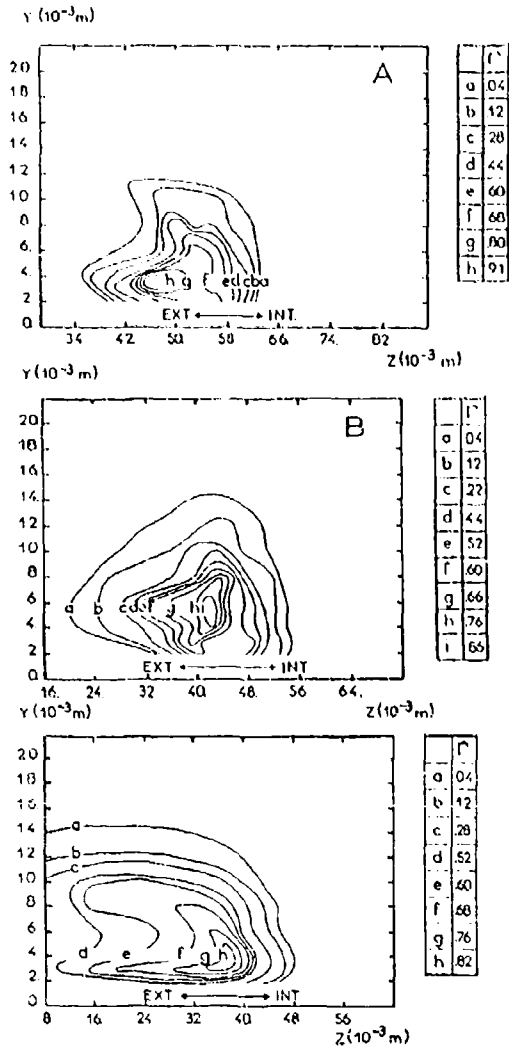


Fig. 12. Courbes iso-intermittence jet (0), $V_0/V_{ex} = 0.65$, $\alpha_n = 45^\circ$ stations 6(A), 7(B), 8(C).

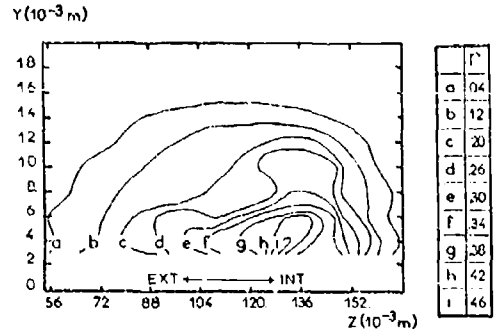
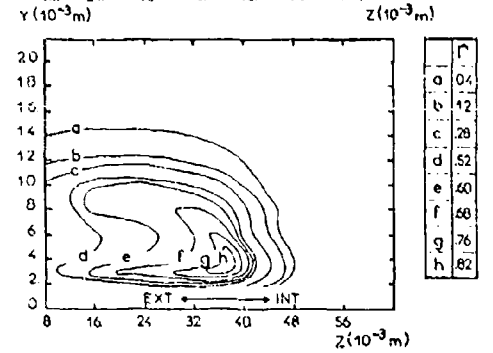


Fig. 14. Courbe iso-intermittence jet B station 11.

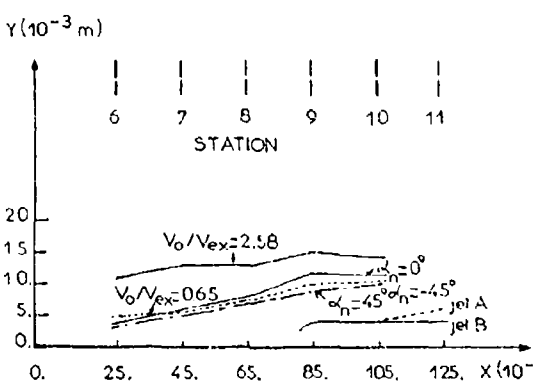


Fig. 15. Trajectoires des jets, plan (X,Y).

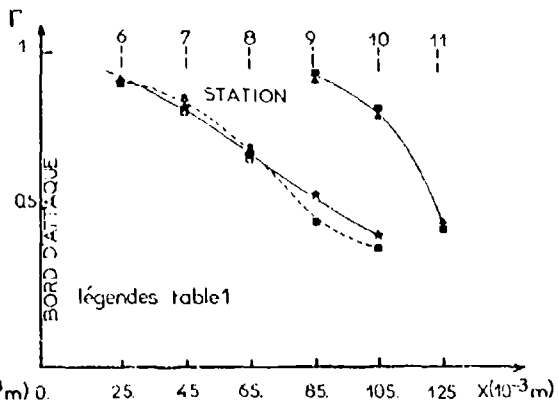


Fig. 16. Coefficient d'intermittence maximum des jets.

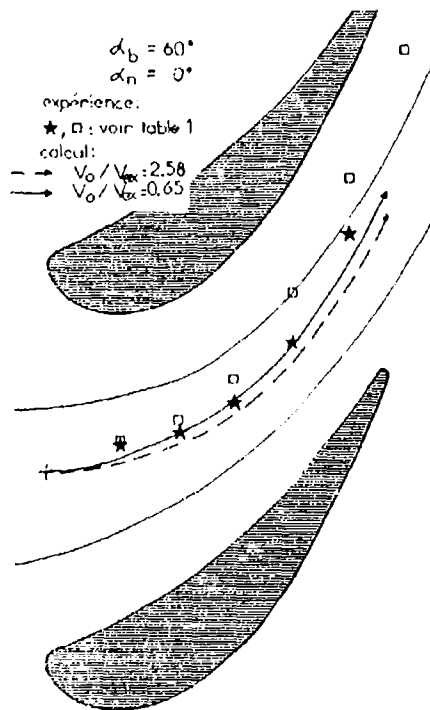


Fig. 17. Trajectoires, comparaison calcul-expérience.

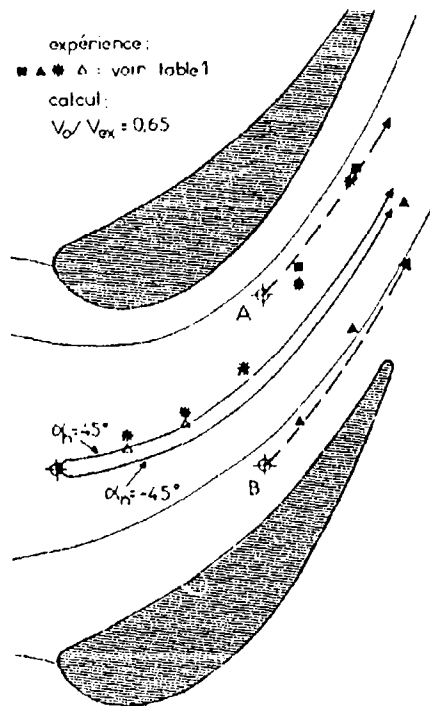


Fig. 18. Trajectoires, comparaison calcul-expérience.

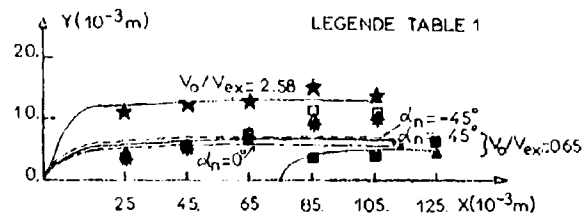


Fig. 19. Trajectoires, comparaison calcul-expériences.

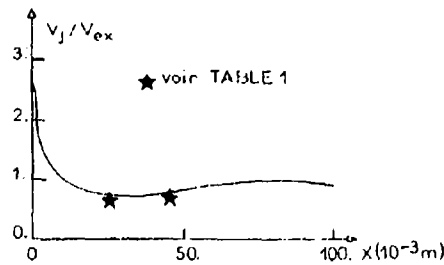


Fig. 20. Calcul de la vitesse : jet (0) $V_0/V_{ex} = 2.58$.

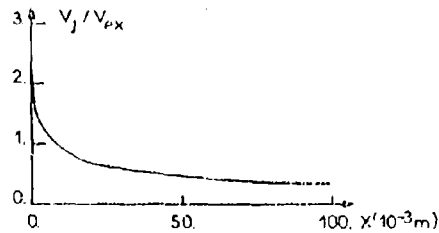


Fig. 21. Calcul de la vitesse dans un écoulement bidimensionnel à gradient de pression nul.

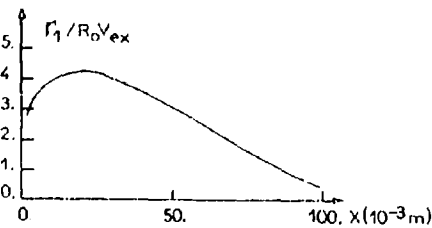


Fig. 22. Calcul de la vorticité : jet (0) $V_0/V_{ex} = 2.58$.

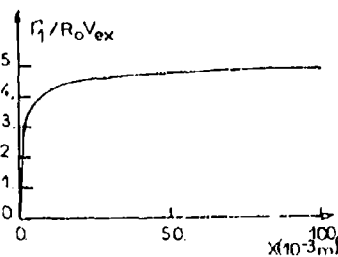


Fig. 23. Calcul de la vorticité pour un écoulement bidimensionnel à gradient de pression nul.

DISCUSSION

G.M.Dibelius, Gc

Your subject has been a most rewarding one from the point of view of the study. Could you please comment on the practical background of the subject; who would like to introduce jets from the side wall for cooling purposes in such a fashion?

Author's Reply

Madame Bourguignon (from the SNECMA) shows us in the presentation of a previous paper that it is necessary, due to high temperature in IIP turbine, to cool the blades and also the sidewalls of the stage. We think that on the blade, the aerodynamical interaction can be calculated by 2-D boundary layer and jet calculations. In the region of the sidewall, where the flow is 3-D, the problem is more difficult. We decided to study this situation.

F.Tarada, UK

You mentioned in your oral presentation the dearth of experimental data regarding jets injected into a three-dimensional free-stream. Could you please elaborate on your sources for the empirical correlations required for the closure of the conservation equations? Have you any plans to improve the empirical correlations, and in particular the physical justifications behind them?

Author's Reply

We use empirical correlations available in the literature about the evolution of jets injected in 2-D flows (see references). For example, the drag force correlation is that presented in a work of Ramette and most other authors. In our case, where very few literature references exist, we can look at the effect of the variation of our empirical correlations on the results of the computation. We want also to develop other experiments on single and multijet evolutions in 3-D secondary flows.

AERODYNAMIC EFFECT OF COOLANT EJECTION IN THE REAR PART
OF TRANSONIC ROTOR BLADES

by

F.H. Kost
DFVLR/AVA
Institut für Experimentelle Strömungsmechanik
3400 Göttingen, W.-Germany

A.T. Holmes
ROLLS-ROYCE LTD.
Turbine Aerodynamics Department
Bristol, U.K.

SUMMARY

DFVLR/Göttingen made an investigation on transonic turbine blades designed by Rolls-Royce/Bristol concerning the aerodynamic penalties of coolant flow for two alternative cooling configurations. Rolls-Royce designed a blade with a thick trailing edge where the coolant is ejected through slots in the trailing edge and a second blade with a thin trailing edge where coolant is ejected through a row of holes on the pressure side and a row of holes on the suction side. Tests were performed in the plane cascade wind tunnel at DFVLR. The results indicate the sensitivity of the blade performance to cooling configuration and coolant flow rate. By combining measured data from blade surface and wake traverses it was possible to separate the various loss mechanisms. So the separate losses due to the momentum of the coolant, change of base pressure, change of blade friction could be determined quantitatively as a function of coolant flow rate.

NOMENCLATURE

c chord length
 $c_B = (p_B - p_2) / (p_{02} - p_2)$ (base pressure coefficient)
 c_m ratio of coolant mass flow to main stream mass flow
I kinetic energy deficit of coolant (see chapter 'Aerodynamic effect of Film Cooling')
Ma Mach number
 $Ma_{T,1}$ surface Mach number derived from local static pressure and inlet total pressure
o throat width
p static pressure
 p_0 total pressure
 s/s_0 non-dimensional surface length
t pitch
 t_e trailing edge thickness
 T_0 total temperature
w velocity
x bitangential coordinate
 α angle
 β_{st} stagger angle
 κ ratio of specific heats
 ρ gas density

$$\xi = 1 - \frac{w_2^2}{w_{2B}^2} = \frac{1 - \left(\frac{p_{02}}{p_{01}}\right)^{\frac{\kappa-1}{\kappa}}}{1 - \left(\frac{p_{02}}{p_{01}}\right)^{\frac{\kappa-1}{\kappa}} + \frac{\kappa-1}{2} Ma_2^2} \quad (\text{energy loss coefficient})$$

$$\xi^* = 1 - \frac{(1+c_m) w_2^2}{w_{2s}^2 + c_m w_{cs}^2} \quad (\text{thermodynamic efficiency loss})$$

ξ' profile loss (see chapter 'Evaluation of Results')
 d_c equivalent slot width = coolant holes area/span

Subscripts

1	inlet	B	Base (trailing edge)
2	uniform outlet flow	s	isentropic
c	coolant	D	pressure side
L	local main flow	S	suction side

INTRODUCTION

With the continuing trend to increase the working gas temperature in high pressure turbines, air cooling of the blades is an indispensable feature. One of the most difficult parts of the blade to cool is the trailing edge region, because of the need to maintain as fine a trailing edge as possible, in order to minimize the aerodynamic loss. If convection cooling is employed, the trailing edge is necessarily thick in order to accommodate the internal holes or slots. However, it may be that the ejected coolant energizes the wake and mitigates the aerodynamic losses. Alternatively a thin trailing edge with film cooling can be considered. In this case it is possible to have films on one or both surfaces of the rear part of the blade. Here the interaction between the coolant and the main stream gas is a potential source of aerodynamic loss.

EXPERIMENTAL ARRANGEMENT

The experiments were performed in the rectilinear cascade tunnel at DFVLR-AVA. This facility is a suction type tunnel and a detailed description is given in reference₅[1]. The Reynolds number based on chord length and design exit conditions was 8.8×10^5 . During the basic measurements, there were 10 - 12 solid blades in the flow. During the measurements with simulated coolant ejection, three of them were replaced by hollow blades equipped with cooling slots or holes. The blade chord was 60 mm and the blade span 125 mm. Thus the span/chord aspect ratio was slightly above two to ensure two-dimensional flow at the mid span.

The cooling slots or holes of the hollow blades extended over only two-thirds of the blade span, but as the experimental values were only taken in the mid span of the blade this should not influence the results. The bleed air was supplied to the hollow blades from both sides to ensure constant conditions over the blade span. Furthermore more than 30 pressure tapings were distributed on the mid span of the profile contour to measure the pressure distribution. The design conditions of the two blades can be seen from Table 1.

Fig. 1 shows the hollow blade RE with the position of the pressure tapings and the position and geometry of the cooling holes. Blade RE has a thin trailing edge, the ratio of trailing edge thickness to throat width being 8.6%. The row of cooling holes on the pressure side is at $x/c = 0.875$ and on the suction side it is at $x/c = 0.842$. The holes are inclined at an angle of 22° to the pressure surface and at an angle of 29° to the suction surface. Fig. 2 shows the blade RF. This blade's ratio of trailing edge thickness to throat width is 22.6%, which is relatively thick in order to accommodate a slot in the trailing edge, especially in a small sized turbine.

Table 1 - design conditions

	RE	RF
Ma_1	0.452	0.452
Ma_2	1.15	1.15
α_1	150°	150°
α_2	20.6°	20.6°
β_{st}	57.2°	59.6°
t/c	0.76	0.90
o/t	0.343	0.334
te/c	0.086	0.226

EVALUATION OF RESULTS

In order to determine the performance of the cascade, wake flow measurements are made by traversing a wedge-type probe behind the cascade (fig. 3). From the data on the inhomogeneous flow in the traverse plane, the properties of the equivalent uniform outlet flow are obtained by applying the equations of conservation of mass, momentum, and energy [2,3]. One of the results is the total pressure loss or the equivalent energy loss ξ of the cascade. The total pressure loss or the energy loss ξ do not give a true impression of the aerodynamic effect of ejection because they are affected by the coolant flow but exclude its energy input. The energy loss derived from thermodynamic efficiency, denoted ξ^* here does include it, but in order to compute ξ^* one needs the properties of the coolant flow at the exit of the cooling holes or slots. Of the properties of the coolant (see fig. 3) the total temperature T_0 and the total pressure p_0 were measured. But p_0 was measured only inside the hollow blades. If one assumes that the static pressure at the exit of the cooling holes is equal to the measured surface static pressure (measured with cooling flow) this pressure p_c is also known. In the case of choked conditions inside the cooling holes or slots one sets the cooling flow Mach number to 1 and gets from this condition also the static pressure of the coolant. From the known mass flow of the coolant and the known static pressure p_c it is possible to compute the total pressure p_0 of the coolant at

the exit of the cooling holes or slots by using the continuity equation. These values can then be used to compute the thermodynamic efficiency loss ξ^* .

In order to know the aerodynamic effect of the coolant flow, it is desirable to separate the effects of coolant energy and of mixing on the measured total loss from the effect of the coolant flow on the real profile loss which comes from boundary layers, base pressure etc. Referring to fig. 3, the main flow mixes with the coolant flow near the exit of the cascade. If the local properties of the main flow where it mixes with the coolant flow are known, then one can compute the homogeneous downstream flow by integrating and using the same equations of continuity, momentum and energy as were used for computing the homogeneous flow values from the inhomogeneous flow measured by the probe. As only the local surface static pressure and the values of the downstream homogeneous flow are known, one has to perform the reverse procedure. To put it simply, one uses the measured downstream values of the mixed homogeneous flow and the known properties of the coolant flow to compute iteratively a homogeneous 'main flow' at the exit of the cascade, where the main flow begins to mix with the coolant and with the wake. The wake just at the trailing edge is assumed to have a thickness equal to the trailing edge thickness, and a static and total pressure equal to the measured base pressure. The computed loss of this 'main flow', including the base loss, will be denoted here as profile loss ξ' .

The procedure described above is similar to the analytic method of Prust [4]. But whereas Prust analytically predicts the total loss from the coolant flow properties and assumes the basic profile loss to be the same as without coolant, we have computed the effect of the coolant on the profile loss itself and so had to 'subtract' the mixing loss and the coolant energy from the measured total energy loss to get the real profile loss. A second difference to Prust is that he uses a separate formula for each effect as for example the effect of a finite trailing edge thickness or the effect of the expansion work done by the coolant, whereas our procedure includes all relevant equations (continuity, momentum, energy) and so handles these effects automatically. The concept of a layer where the coolant flow mixes with the main flow near the cooling holes as it is described in ref. [5,6] is not necessary here as the cooling holes are already near the blade exit where the mixing is assumed to begin.

A result of the evaluation procedure can be seen in fig. 4 for an exit Mach number below design where the profile loss ξ' is indicated by the dashed line. The difference between the profile loss ξ' and the total loss ξ (solid line) is due to the mixing of coolant flow and main flow. This difference includes the coolant kinetic energy or momentum, the expansion work done by the coolant or the compression work done by the main flow to compress the coolant to the downstream static pressure, and the loss which comes from the different velocities of main flow and coolant (often only the latter is called mixing loss). The coolant momentum may have a positive or negative effect on total efficiency depending on the discharge angle. In fig. 4 it is shown that for coolant flow rates larger than 2.5 to 3% the difference is positive which is due to the effect of coolant momentum. If we use the procedure as an analytical tool it is possible to predict the effect of changing coolant flow properties. In fig. 4 two other curves are shown which give the computed total energy loss ξ by assuming that the profile loss ξ' remains unchanged but the coolant has either a lower total temperature or a different discharge angle.

RESULTS FOR THE AERODYNAMIC EFFECT OF FILM COOLING

The experimental work on blade RE can be separated into three parts: basic tests on solid blading, tests with simulated coolant ejection through a row of holes in the rear part of the pressure side and coolant ejection through holes on the pressure side and the suction side simultaneously. In this paper only the tests with simulated coolant ejection are reported.

During the tests with coolant ejection on the pressure side only, the holes on the suction side were filled in and the surface was smooth. Figs. 4 and 5 show results for a subsonic and a supersonic exit Mach number respectively. The minimum profile loss ξ' is at a coolant flow rate of 2% in the subsonic case and 1% for the supersonic Mach number.

Figs. 6 and 7 give selected results for the loss coefficients when simultaneously blowing air through holes on suction and pressure sides. The total loss maximum near 2% coolant flow rate is clearly related to a maximum in mixing loss. For both the subsonic and the supersonic exit Mach number the difference between total loss and profile loss coefficients is zero near a coolant flow rate of 4.5% which means that the useful kinetic energy of the coolant exceeds the mixing loss for higher flow rates. The profile loss coefficient ξ' itself has its minimum at a coolant flow rate of 2% for the supersonic Mach number but for the subsonic exit Mach number the minimum profile loss extends from a flow rate of 1% to 4.5%. The decrease of profile loss is effected by the useful coolant momentum having a positive effect on the boundary layers.

In figs. 8 and 9 the variation of profile loss ξ' with coolant flow rate μ for pressure side ejection is compared with the profile loss for suction and pressure side ejection. For the subsonic exit Mach number the additional suction side ejection lowers the profile loss up to a suction side coolant flow rate of $\mu_{sg} = 2.1\%$, but the largest decrease of profile loss is achieved by a flow rate of only $\mu_{sg} = 0.5\%$. A loss decrease can also be observed for the supersonic exit Mach number and pressure side ejection (see dashed

line in fig. 9). So we may conclude that a decrease of profile loss can be achieved when injecting coolant flow into a locally subsonic main flow.

If ρw^2 is interpreted as 'kinetic energy density' then

$$I = (1 - (\rho w_c^2) / (\rho w_L^2)) \cdot cm$$

may be called 'kinetic energy deficit' of the coolant compared to local main flow. This kinetic energy deficit can be correlated with the mixing loss minus coolant kinetic energy, as is evident when comparing fig. 10 with figs. 4-7. But there also seems to be a negative correlation with profile loss, because for subsonic local conditions minimum profile loss seems to coincide with a maximum of the value of 'I'. If the coolant flow is not choked then I is equal to a 'Mach number deficit'

$$I = (1 - Ma_c^2 / Ma_L^2) \cdot cm, \text{ because } \rho w^2 = \rho p Ma^2.$$

If the coolant Mach number reaches 1.0 inside the holes (see arrows in fig. 10) there seems to be a negative effect on profile loss. Then the coolant flow has to expand to the lower surface pressure outside of the hole. This seems to push the main flow away from the surface and on simultaneously taken schlieren photos the flow appears to be separated. When injecting coolant on the rear part of the suction side into a locally supersonic main flow a loss increase was always observed (see fig. 9). Fig. 11 shows the effect of coolant ejection on the surface velocity distribution at exit Mach number 1.14. The pressure side ejection influences also the suction side because it decreases the main mass flow. The influence of suction side ejection is more or less confined to the location of the holes. But contrary to pressure side ejection it can already be seen from the velocity distribution that suction side ejection is unfavourable for supersonic flow, as the first shock on the suction side, which comes from the trailing edge of the neighbouring blade, is more intense and a second smaller shock is induced just in front of the row of holes. Already without delivering coolant air there is a throughflow from pressure to suction side driven by the pressure difference. This leads to a loss increase at $cm = 0$. (see figs. 9 and 11).

RESULTS FOR THE BLADE RF WITHOUT COOLANT EJECTION

The experiments on blade RF were already partly published in [7]. Some of the results will be reviewed here and some further added.

A first rather unusual result is plotted in fig. 12. For subsonic exit Mach numbers there is a big difference between the losses of the solid and the slotted blade. Of course some further measurements had to be taken to validate these unexpected results: First the coolant air supply at the side of the slotted, hollow blades was removed and the supply tubes closed. By closing the slot in the trailing edge with cello-tape the loss returned to its high value. A small disturbance in the solid trailing-edge like a short splitter-plate gave again low losses. The mechanism giving rise to such a remarkable loss difference is not understood, but it is probably connected with the unsteady separation at the trailing edge and also with three dimensional flow at the trailing edge. A similar effect which he named "cavity effect" was reported by Nash [8]. The base pressure coefficient for the solid blade was much lower than for the slotted at exit Mach number 0.76 (see fig. 15). This base pressure was not correctly given in ref. [7].

With the above mentioned evaluation method to compute the profile loss, the profile loss in front of the trailing edge can also be computed. First the measured base pressure and the measured total loss of the slotted blade were used to compute the profile loss of the slotted blade in front of the trailing edge. Then this profile loss was assumed to be constant and the base pressure changed to the value measured for the solid blade. The result is indicated in fig. 13 and it is seen that a large part of the loss increase from the slotted to the solid blade is in fact due to the increased base loss.

RESULTS FOR COOLANT EJECTION FROM A SLOT IN THE TRAILING EDGE

Tests were carried out using air at flow rates up to 6.5% of the main stream mass flow. For two exit Mach numbers figs. 13 and 14 show the different evaluated loss coefficients. The difference between solid and dashed lines is again the mixing loss due to injection of coolant air into the main flow. This difference is strongly correlated to the kinetic energy deficit 'I' plotted in fig. 16. The profile loss itself has its minimum at a coolant flow rate of 4 - 6% for subsonic flow and at 3% for supersonic flow.

The development of base pressure coefficient with coolant flow rate is shown in fig. 15. The base pressure seems to be correlated with the kinetic energy deficit I, too. If low momentum coolant flows into the wake the base pressure rises, but if the momentum (or kinetic energy) of the coolant is comparable to the main flow momentum, that is when the energy deficit goes to small positive or to negative values, then the base pressure decreases again.

The dashed-dotted line in fig. 13 and 14 gives the profile loss in front of the trailing edge, that is the profile loss ξ' minus the base loss. It is nearly constant with coolant flow rate as expected. When the profile loss ξ' (dashed line) is lower than the profile loss in front of the trailing edge a negative base loss is implied. This appears to

be unusual but it should be borne in mind that it occurs only when coolant is ejected and the base pressure rises above downstream static pressure. So the air in the base region is able to do work by expanding to the downstream pressure. Thus the minima in profile loss ξ' are only due to the maxima in base pressure. But as the maxima in base pressure seem to be correlated with the inflow of low momentum coolant both effects partly cancel each other, so the total loss ξ may have a flat minimum as here for the supersonic Mach number (fig. 14) or a flat maximum as in fig. 13 for subsonic flow.

COMPARISON BETWEEN BLADE RE AND RF

In fig. 17 a comparison of blades RE and RF is made at design exit Mach number $Ma_2 = 1.15$. The two blades, which have the same gas deflection, display a thermodynamic efficiency difference of 3.7% with zero coolant. This is mainly due to the thick trailing edge of blade RF. Above a coolant flow rate of 3.5% the efficiency difference shrinks to only 0.6%. Now you see from geometry that the higher pitch/chord ratio of RF allows to design a rotor with RF-profiles which has less weight than a rotor with RE-profiles. Furthermore RF needs less coolant total pressure than RE to eject the same amount of coolant. So we may conclude that blade RF is comparable or even superior to blade RE if coolant flow rates above 3.5% are necessary.

CONCLUSIONS

From the results of this investigation the following conclusions can be drawn:

- By ejecting a moderate amount of coolant from a row of holes into subsonic local flow a decrease of profile loss will be achieved if the coolant momentum has a component in the main flow direction.
- Injecting coolant with a Mach number higher or equal to 1.0 into subsonic main flow or injecting coolant into a locally supersonic main flow will lead to an increase of profile loss.
- A blade with a thick trailing edge and coolant ejection into the base region may be similar in performance to a blade with much thinner trailing edge and film cooling just in front of the trailing edge, if the blades are compared at higher coolant flow rates.

ACKNOWLEDGEMENT

The authors wish to thank Rolls-Royce Ltd., and DFVLR for permission to publish this paper. The work has been carried out with the support of the Procurement Executive, Ministry of Defence.

REFERENCES

- [1] Heinemann, H.-J. The test facility for rectilinear cascades (EGG) of the DFVLR DFVLR-AVA IB 222 - 83 A 14, (1983)
- [2] Amecke, J. Anwendung der transsonischen Kühlichkeitsregel auf die Strömung durch ebene Schaufelgitter VDI-Forschungsheft, 540, S. 16 - 28, (1970)
- [3] Oldfield, M.L.G. Loss measurements using a fast traverse in an ILPT transient cascade
Schultz, D.L. Proceedings of the Symposium 'Measurement Techniques in Transonic and Supersonic Flows in Cascades and Turbomachines', Lyon, Oct. 15-16, (1981)
Nicholson, J.H.
- [4] Prust, H.W. An analytical study of the effect of coolant flow variables on the kinetic energy output of a cooled turbine blade row
AIAA Paper No. 72-12, (1972)
- [5] Hartsel, J.E. Prediction of effects of mass transfer cooling on the blade row efficiency of turbine airfoils
ASME Paper No. 72-11, (1972)
- [6] Ito, S. Aerodynamic loss in a gas turbine stage with film cooling
Eckert, E.R.G. ASME Paper No. 80-GT-38, (1980)
Goldstein, R.J.
- [7] Michel, G.W. The effect of coolant flow on the efficiency of a transonic HP turbine profile suitable for a small engine
Kost, F.H. ASME Paper No. 82-GT-63, (1982)
- [8] Nash, J.F. Experiments on two-dimensional base flow at subsonic and transonic speeds
Quincey, V.G. A.R.C. R & M No.2427, January, 1963
Callinan, J.

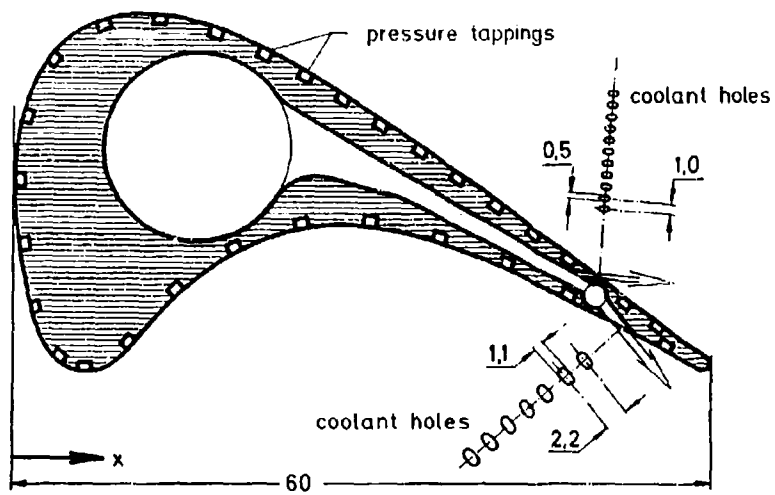


Fig. 1 Blade RF equipped with two rows of holes

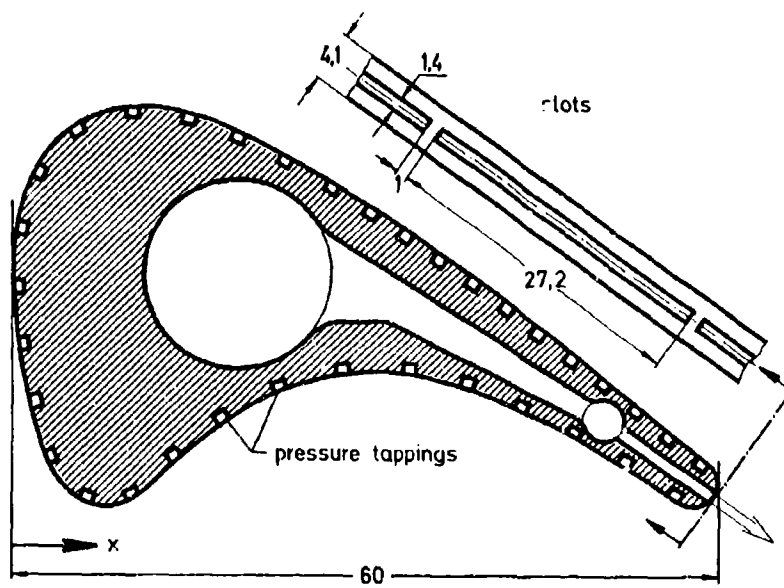


Fig. 2 Blade RF equipped with a slot in the trailing-edge

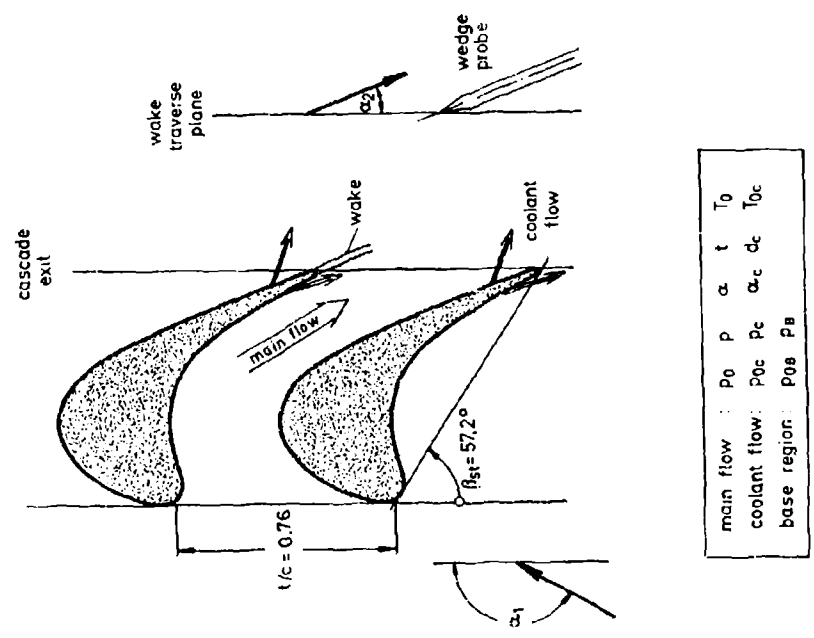
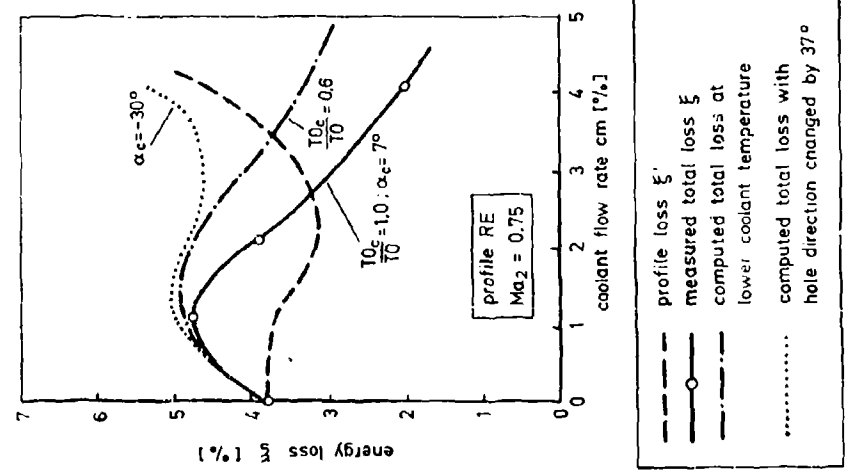
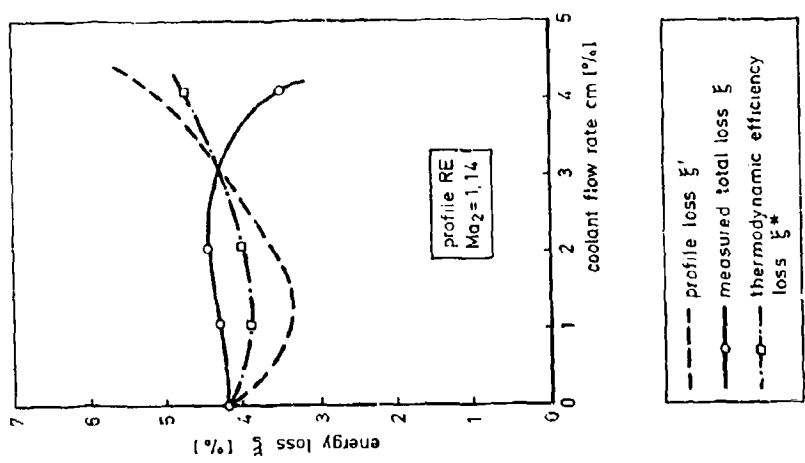


Fig. 3 Sketch of blade geometry with profile RE

Fig. 4 Pressure side coolant ejection (subsonic exit Mach number)

Fig. 5 Pressure side coolant ejection (near design)

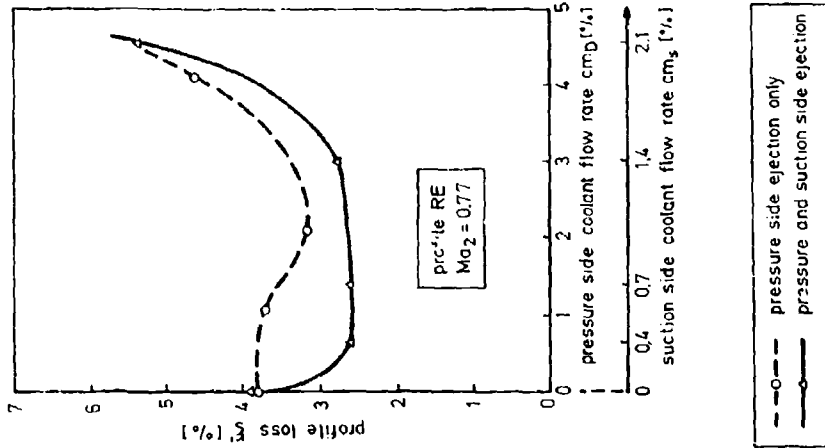


Fig. 6
(subsonic exit Mach number)

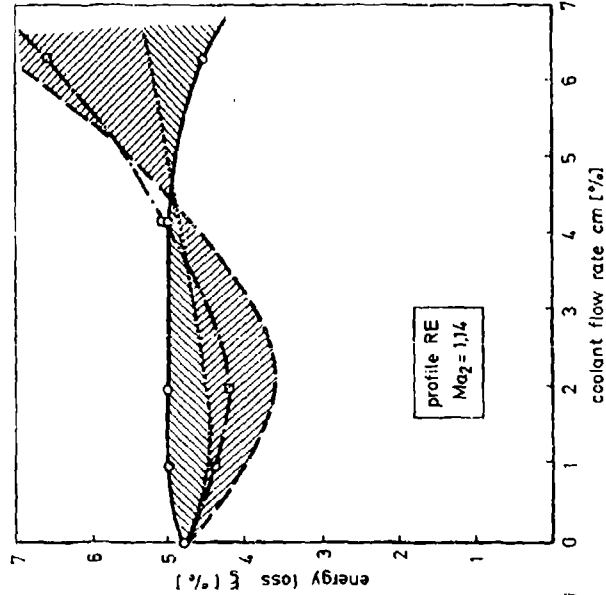


Fig. 7
(near design)

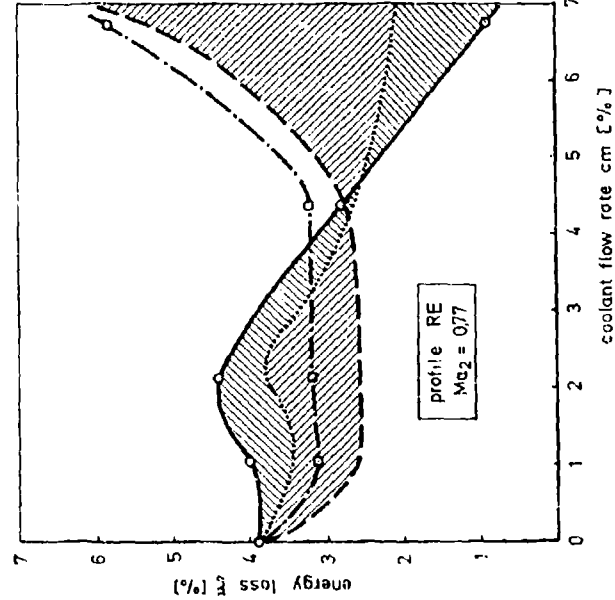
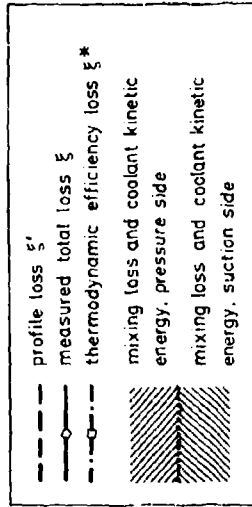
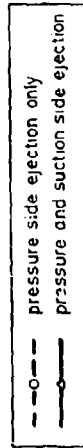


Fig. 8
(subsonic exit Mach number)



Pressure and suction side coolant ejection

Fig. 8 Comparison of profile losses
(subsonic exit Mach number)



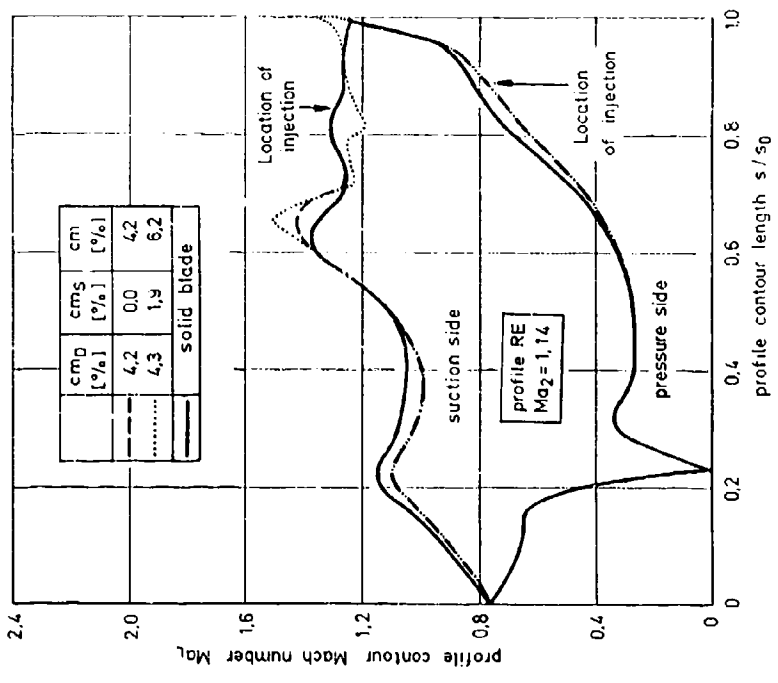


Fig. 11 Surface Mach number distribution of profile RE (near design)

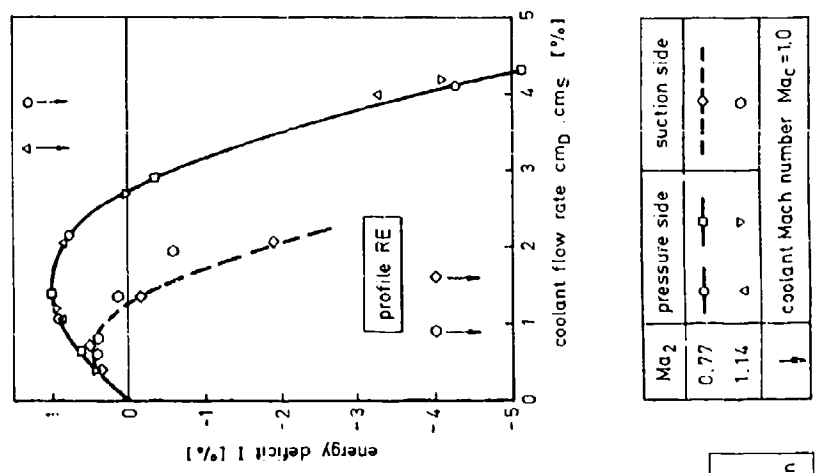


Fig. 10 Kinetic energy deficit (excess) of coolant

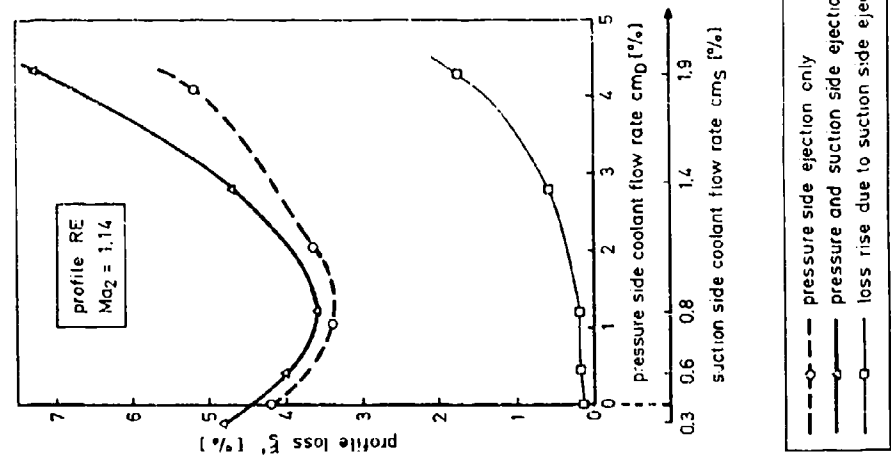


Fig. 9 Comparison of profile losses (near design)

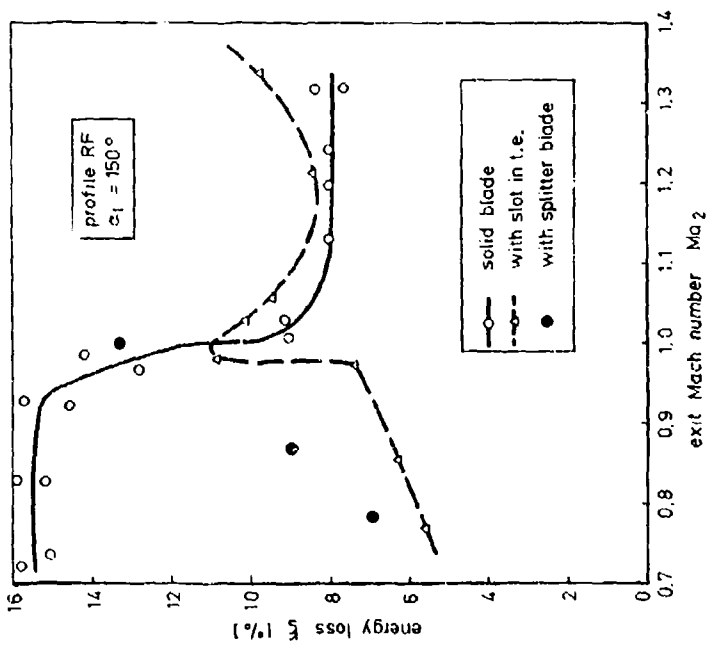


Fig. 12 Comparison of different trailing edge configurations without coolant ejection

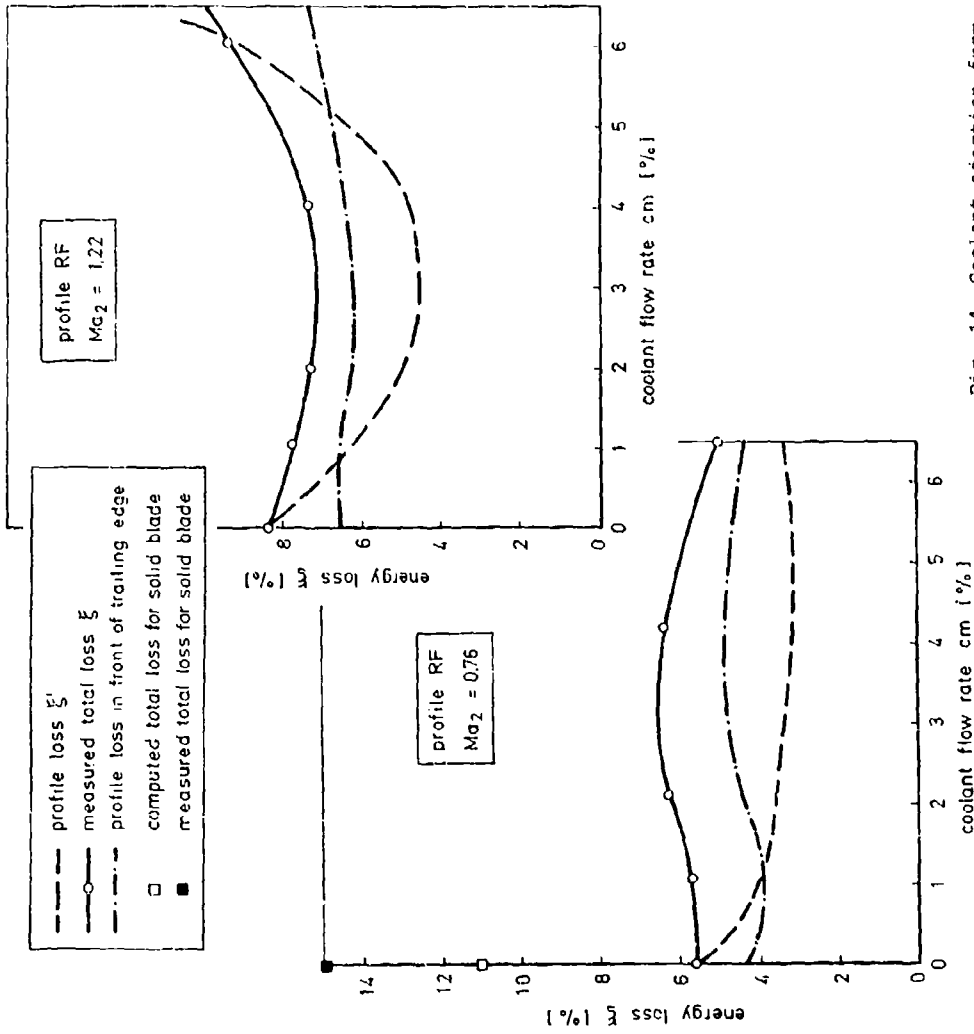


Fig. 13 Coolant ejection from slot in the trailing edge (subsonic exit Mach number)

Fig. 14 Coolant ejection from slot in the trailing edge (supersonic exit Mach number)

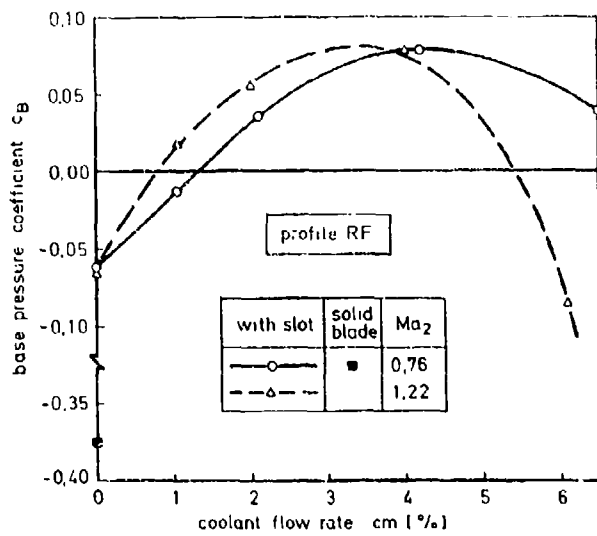


Fig. 15 Base pressure coefficient with trailing edge ejection

Fig. 16 Kinetic energy deficit of coolant

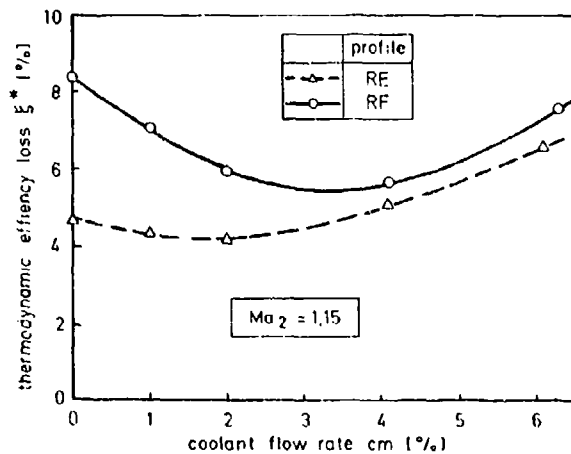
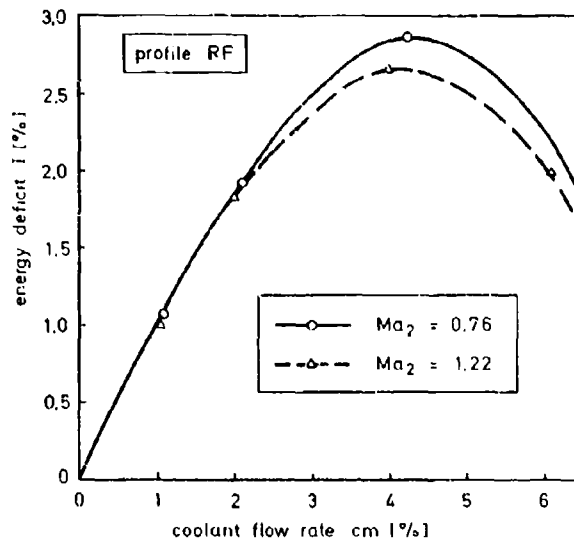


Fig. 17 Comparison between blade RE and RF

DISCUSSION

G.P. Butt, Ca

1. With reference to the effect of trailing edge ejection, I have observed that when the loss is at a minimum the ratio of ejection velocity to mainstream flow exit velocity = 0.5. Did you calculate this ratio (perhaps you could elucidate later)?
2. Could the explanation of reducing thermodynamic loss with film blowing at low cooling mass flow ratios be due to the closeness of the traverse plane to the trailing edge. That is, would you measure more wake loss shear at say one chord downstream.

Author's Reply

1. At exit Mach number 0.76 the ratio of coolant slot exit velocity to downstream aftermixed velocity is 0.59 with $c_m = 4.3\%$ and at exit Mach number 1.22 this ratio is 0.49 with $c_m = 3\%$.
2. The properties of the homogeneous downstream (aftermixed) flow are independent of the axial distance of the probe from the cascade exit. This was also checked but it results already from the evaluation procedure.

T.V. Jones, UK

Loss measurements are presented as a function of coolant mass flow and the effect of the coolant separating from the surface is considered to be important. The latter is not governed by the coolant mass flux and therefore coolant mass flow might not be the correct scaling parameter when extending these results to engine conditions. Do you have information on this question of scaling?

Author's Reply

It has been tried to correlate profile loss to a quantity derived from coolant momentum. This quantity, called 'energy deficit or excess' of coolant is in the paper.

F. Tarada, UK

I have two questions:

1. Did you take into consideration the reduction in stagnation pressure due to the passage through shocks on the suction side when computing the surface Mach number distribution (Fig. 11)?
2. Why does the Mach number go to zero on the pressure side (Fig. 11)? You mentioned that you took Schlieren photographs of the shocks on the suction side of the blade; your paper would in my opinion be much enhanced by the inclusion of such photographs.

Author's Reply

1. The surface Mach number plotted in Fig. 11 is computed from surface static pressure and inlet total pressure so it does not take into account any reduction in total pressure.
2. This is the position of the stagnation point, please compare the definition of zero x-coordinate in Fig. 1.

S.C. Arora, Ca

Your loss coefficients are shown as a function of coolant mass flow rate. Turbine has to expend some energy to pump this coolant to the blade. This pumping energy will depend on the amount of coolant being pumped. Will this expended energy affect your loss coefficient and how can this be taken into consideration to interpret and modify your loss coefficients?

Author's Reply

The pumping energy does not affect my loss coefficients as the energy of the coolant used in computing the loss was the energy at the exit of the holes or slots. The pumping energy could be included in the loss definition by taking it into account in the coolant energy.

THE BOUNDARY LAYER BEHAVIOUR OF AN ADVANCED GAS TURBINE ROTOR BLADE
UNDER THE INFLUENCE OF SIMULATED FILM COOLING

R. Kiock and H. Hoheisel
Institute for Design Aerodynamics, DFVLR
Postfach 3267, D-3300 Braunschweig, W.-Germany

H.J. Dietrichs
Motoren- und Turbinen-Union
Postfach 500640, D-8000 München 50, W.-Germany

A.T. Holmes
Rolls-Royce Ltd.
P.O. Box 3, Filton Bristol BS12 7QE, England

SUMMARY

The aerodynamic properties of highly loaded turbine blades are strongly influenced by local supersonic flow fields and cooling air ejection. The boundary layer interaction with shock waves and simulated cooling flows was examined in a cascade wind tunnel by means of boundary layer and wake traverses and pressure distribution measurements as well as by the application of Schlieren observation. Air was ejected through holes and slots at different locations of the blade contour. Special emphasis was put on magnitude and direction of the local jet velocity in case of multiple cooling operation. The characteristics of the blade without and with different cooling configurations were determined. The results show the effects of air ejection on boundary layer transition and shock configurations.

SYMBOLS

c	chord	x, y	profile coordinates, bitangential
c_Q	mass flow coefficient, ratio of coolant flow rate \dot{m}_c of one blade to mainstream flow rate \dot{m} between two adjacent blades for the same width in blade height direction	β, β_S	flow angle and blade angle rela- tive to cascade axis, see fig. 1
		δ_1, δ_2	displacement and momentum thick- ness
h	blade height = span	η	coordinate normal to blade surface
H_{12}	shape factor, $H_{12} = \delta_1/\delta_2$	κ	ratio of specific heats
i	enthalpy	μ	dynamic viscosity
M	blade surface Mach number, $M = f(p/p_{01})$	$\epsilon_S, \epsilon_S^*, \epsilon_S^{**}$	loss coefficients, see appendix
$M_{2,th}$	isentropic exit Mach number, $M_{2,th} = f(p/k/p_{01})$	ρ	density
\dot{m}	mass flow rate	Subscripts	
o	throat between two blades	1	measurement plane upstream of cascade
p	static pressure	2	transferred to homogeneous exit flow from cascade
p_0	total pressure	c	coolant
q	dynamic head, $q \approx p_0 - p$	i	individual location of ejection, $i = 1$ to 7
R	gas constant	K	tank
Re	Reynolds number, $Re = w_p c / \mu$	nom	design
s	blade spacing, surface coordinate	P	pressure side
s/s_0	dimensionless surface coordi- nate, s_0 means surface length from $x/c = 0$ to 1	S	suction side
T_0	total temperature	th	isentropic flow
Tu	degree of turbulence $Tu = 100 \sqrt{w'^2/w}$	tot	sum of individual values of one blade
w	flow velocity		

1. INTRODUCTION

The required increase in the performance of advanced jet engines leads to a rise in total pressure ratio (TPR) and turbine entry temperature (TET). The RB 199 was designed 15 years ago for a combat aircraft with a TPR of 23 : 1 and a TET around 1600 K. The corresponding goals for a jet engine of the next generation are TPR = 25 : 1 and TET = 1750 K with cooled single crystal turbine blades. For comparison, the PW 2037 designed 5 years ago for a civil aircraft reaches TPR = 30 : 1 and TET = 1669 K with cooled single crystal turbine blades.

These high turbine entry temperatures can be obtained only by careful cooling of the turbine blades. Cooling techniques such as convection, impingement, film, transpiration or thermal barrier are applicable. However, the designer of the cooling configuration has also to consider its effect on the aerodynamic performance of the turbine because cooling often reduces the efficiency of the blading.

This aspect was discussed on the basis of cold air cascade testing by several authors: C.H. Hauser et al. [1] summarized the comprehensive test series at NASA Lewis on stator-vane film cooling simulation with the result that the additional losses due to single row ejection can be added in order to obtain the loss for multi-row ejection. S. Ito et al. [2] investigated single-row ejection near the leading edge on both suction and pressure side. Pure trailing edge ejection was studied by O. Lawaczeck [3], C.H. Sieverding [4] and G.W. Michel and F.H. Kost [5] who found a maximum gain in efficiency for a mass flow coefficient of $c_{Q,bl} = 3$ to 4%. W.G. Hess [6] and B. Barry [7] reported on both suction/pressure side and trailing edge ejection. A turbine stage was investigated by J. McDonel and J.E. Eiswerth [8] with TET = 783 K. A cooled vane/cooled blade configuration gave a turbine thermodynamic efficiency of $\eta_{th} = 0.83$ compared with $\eta_{th} = 0.865$ for the solid vane/solid blade configuration ("discrete" film cooling, $c_{Q,vane} = 5.0\%$, $c_{Q,blade} = 8.15\%$).

The paper presented here summarizes the influence of simulated cooling on the aerodynamic performance of an advanced turbine blade. This is the rotor midspan section of an alternative design of the RB 199 HP turbine with unshrouded blades. In total, the influence of Mach number, Reynolds number, degree of turbulence and inlet flow angle was investigated for five configurations of simulated cooling. Here, the design case and three configurations only are considered. In particular, the effect of ejection holes and coolant jets at different locations around the blade surface on the blade boundary layer is discussed.

2. TEST MODEL

The cascade was designed for two-dimensional turning of $\Delta\alpha = 100^\circ$ for an isentropic exit Mach number of $M_{2,th} = 0.985$, see fig. 1. The profile coordinates are given in table 1. Seven blades with a chord length of $c = 100$ mm were installed in the test section. The centre blade was used for wake traverse and boundary layer measurements, whereas the adjacent blades were equipped with tappings staggered in four rows along 18 mm width in the midspan region of the blade. After the implementation of these measurements, glass windows were installed in both side walls for Schlieren observations.

The first set of blades consisted of solid blades. For the simulation of cooling, the three blades in the centre were exchanged for hollow blades. This restriction to three blades is permissible because the variation of the aerodynamic parameters is marginal.

A second set of three blades was fitted with two rows of holes at the leading edge and with slots in the trailing edge, configuration A, see fig. 2 and table 2. Later two additional rows of holes were drilled on the suction side immediately downstream of the throat and on the rear pressure side, configuration B.

Finally, a third set of three blades was provided with three rows of holes in the leading edge region but no slot in the trailing edge, configuration E.

All holes in the leading edge region were inclined at 45° with respect to the turbine axis. This arrangement reduces the danger of ingestion of mainstream air into the blade cavity near the stagnation point. Further, experiments in [1] showed considerably better cooling effectiveness in the case of such compound angle arrangements.

By these configurations the following cooling techniques could be simulated:

- A Film cooling of front part, convection cooling of rear part of blade
- B Film cooling of large parts of blade surface, convection cooling of rear part
- E Film cooling of front part of blade only.

The metal blades were manufactured by MTU München from aluminium alloy. A check of the blade contour on a ZEISS profile measuring machine -see R. Lindemann [9]- showed values for average and standard deviation of -0.15 and ± 0.08 mm normal to the surface, i.e. the metal blade is thinner than it should be. Therefore, the true throat is bigger than the nominal one, see table 3. The variation of the average throat from one configuration to another lies within 0.1 mm.

3. APPARATUS AND TEST PROGRAMME

The experiments were carried out in the High Speed Cascade Wind Tunnel of Braunschweig (10). This facility operates continuously and allows the independent variation of Mach number and Reynolds number by changing the pressure level p_k of the tank. Upstream of the cascade a turbulence grid is installed in order to produce a turbulence level Tu_1 of 4 % (11). The test section has a span of $h = 300$ mm and an adjustable height of $H_1 = 250$ to 500 mm. Fig. 3 shows a view of the blade supports arranged for cooling simulation and Schlieren observation. The mainstream air has a total temperature of 313 K. The coolant, which is air at 303 K, is delivered from a separate screw-compressor power plant station (12) and fed through both side walls into the three hollow blades. The mass flow rate was measured by a Venturi nozzle or by an orifice of DIN with standard installation. The distribution of coolant in the spanwise direction as well as over the three hollow blades was checked immediately downstream of the slots. The local mass flow deviates only by 3 % from the average value.

For the wake traverse measurements, a wedge probe (10) was used 40 % of chord axially downstream of the blade trailing edge plane. The average values were evaluated applying the laws of conservation, see J. Amecke (13). The inclusion of the coolant into the loss coefficient is explained in the appendix.

The boundary layer was measured by flattened Pitot probes: A probe of 0.15×1.30 [mm] head size was applied at $(s/s_0)_c = 0.98$ in order to obtain velocity profile and integral quantity. A correction was applied on the basis of a comparison with flat plate experiments and the law of the wall (14). Another probe of 0.30×0.80 [mm] was moved from $(s/s_0)_c = 0.45$ to 1.0 in order to detect boundary layer transition (15). All boundary layer data were calculated under the assumption of constant static pressure across the boundary layer.

From the surface pressure distribution, the surface Mach number distribution was evaluated with the assumption of constant total pressure. Schlieren observations were made using a Comb! Spark flash with 200 ns half-intensity period and two concave mirrors (Z arrangement).

4. COOLANT CONDITIONS

According to the individual mass flow coefficients in table 2 the total values at design should be as follows:

Configuration A	$c_{Q,tot,nom} = 3.2 \%$
B	5.2 %
E	1.2 %

Tests were carried out at $c_{Q,tot} = 0, 0.5, 1.0$ and 1.25 times the above mentioned design values. In order to check the individual mass flow coefficients of each row of ejection, the following procedure was applied: First the slots 1.6 were kept open only and all the other ejection holes were blocked. The total pressure p_{0c} of the coolant which was measured in the hollow centre of the blade at cascade design flow conditions was plotted versus the measured total mass flow coefficient. In a second step the holes of one row i were opened and the results were plotted again. Now the difference of the two $c_{Q,tot}$ values at $p_{0c} = const.$ yields the individual mass flow coefficient c_{Qi} .

This procedure was continued for the other cases. It was also found that the total pressures measured in the cavities of one blade were equal, and that the pressures in all three blades were the same.

Fig. 4 shows how the coolant total pressure p_{0c} rises with the total mass flow coefficient. When the location of the stagnation point coincides with that of an ejection row, mainstream air is blown into the blade for $c_{Q,tot} < 0.4 \%$ at configuration E, 4.2% at A and 6.2% at B. For $p_{0c} = const.$ different mass flow rates can be obtained depending on surface pressure, cross sectional area and coolant loss of the individual ejection row.

This figure shows also that considerable mass flow rates can be ejected with a coolant total pressure p_{0c} which is lower than the mainstream total pressure p_{01} , although a small amount of the ejected coolant consists of air ingested at the leading edge, see fig. 5.

The results of the calibration for the individual mass flow coefficients are plotted in fig. 5. Mainstream air is blown into the blade at the ejection rows 1.1 and 1.2 for configuration A, at 1.1, 1.2 and 1.7 for B and 11.1 and 11.2 for E as shown by the shaded areas ("SUCTION"). As an example: In the case of B, $c_{Q,tot} = 0$, there is suction (negative) or ejection (positive) of the following mass flow rates:

$$c_{Q,tot} = c_{Q1} + c_{Q2} + c_{Q3} + c_{Q6} + c_{Q7}$$

$$= - 0.30 - 0.55 + 0.25 + 1.10 - 0.50 = 0$$

A comparison with the individual nominal values shows that the design flow rates could

not be obtained in some cases. There is too much coolant through the slots I.6 and too little through the leading edge rows, I.1 and I.2 (A and B), i.e. the important leading edge cooling could not be achieved. The other rows deliver sufficient coolant, such as I.3 and I.7 for B and II.1, II.2 and II.3 for E. That means that E would provide the designed leading edge cooling.

The situation could be improved in the following way:

- a) Change of row location - change of surface pressure $p(s/s_0)$
- b) Change of geometry of the holes connecting the two cavities within the hollow blades, see fig. 2 - change of individual coolant total pressure $P_{oc,i}$
- c) Change of cross sectional area of individual row - change of individual mass flow rate c_{Qi}
- d) Change of ratio area/length of individual row - change of individual coolant flow loss

5. RESULTS

The results reported herein concern only the design conditions, $\beta_1 = 37.9^\circ$, $M_{2,th} = 0.985$, $Re_2 = 8.4 \cdot 10^5$. The aerodynamic behaviour of the cascade with simulated cooling is discussed on the basis of surface Mach number distributions, Schlieren pictures, boundary layer and wake traverse data.

5.1 Surface Mach number distributions

The surface Mach number distribution was predicted for the solid blade by a time-marching method after H.-W. Happel [16], see fig. 6. There it can be compared with experiments on the solid blade and on cooling configuration A. The result of the inviscid calculation based on the true profile coordinates agrees quite well with the Mach number distribution of the solid blade. The calculated shock position is in good agreement with the test results. The measured lower peak-Mach number is caused by the shock-boundary layer interaction which triggers a laminar separation bubble. Better agreement is found by comparison with configurations B and E. In these cases the separation is suppressed due to the different structure of the boundary layer as will be shown later. In any case the flow is supersonic along the rear three quarters of the suction side. Unfortunately, $c_{Q,tot} = 0\%$ has not been measured. The results for $c_{Q,tot} = 1.6\%$ and 3.2% look very similar to 4.0% . They are omitted here for clarity.

The measured values of M show a step in the deceleration following the peak value of M . This is characteristic of a laminar boundary layer undergoing a separation, followed by transition and reattachment. Taken together with evidence discussed in sections 5.3 and 5.5, it is possible to deduce that the boundary layer is laminar up to $s/s_0 \approx 0.63$, and that the roughness of the ejection holes at I.2 does not provoke transition. The trailing edge ejection clearly influences the M distribution on the rear suction surface, displacing the local shock.

The experimental M distributions of configuration B (rows I.3 and I.7 in addition to A) are shown in fig. 7. The pressure side varies very little, i.e. the coolant is mixed quickly with the mainstream air due to the strong favourable pressure gradient. However, the effect of coolant around the location I.3 on the suction side is quite clear: the flow is retarded upstream and accelerated downstream relative to the condition of the solid blade. Secondly, a higher peak Mach number is obtained for all flow rates of B including $c_{Q,tot} = 0\%$. Downstream of that point, the M distribution does not show a step like the solid blade. The local mass flow coefficient amounts to $c_{Q3} = 0.3$ to 0.9% , see fig. 5 and causes transition before the location of M_{max} is reached.

The corresponding surface Mach number distributions of configuration E (ejection only in the leading edge region) are plotted in fig. 8. Local acceleration is visible downstream of the locations II.1 and II.3. In the range of $c_{Q,tot} = 0$ to 1.5% , the local mass flow coefficient amounts to $c_{Q3} = 0.3$ to 0.5% , see fig. 5, and gives rise also to transition of the suction side boundary layer because the M distribution in the rear half looks similar to that of B. There is no separation associated with the shock.

5.2 Base pressure

The relative base pressure p_b was plotted versus the total mass flow coefficient in fig. 9. The base pressure lies close to the back pressure p_k for the solid blade and for configuration E. However, when coolant is ejected through the trailing edge as for A and B, the base pressure is considerably higher: the mainstream air is displaced by the jet and the streamline curvature becomes concave. The maximum Mach number of the trailing edge jet was evaluated to be 0.88 and therewith lower than the base Mach number of 0.92 in that case. The outer flow entrains a part of the bleed. The same tendency of $p_b = f(c_Q)$ was shown by G.W. Michel and F.H. Kost [5], fig. 11, and by C.H. Sieverding [4], fig. 12 and 14. The latter obtained a maximum increase in base pressure coefficient of $(p_b - p_b^*)/0.5 \rho_2 w_{2,th}^2 = 0.15$ with p_b^* for no bleed. This value agrees well with 0.16 in our case (B , $c_{Q,tot} = 2.6\%$, p_b^* from solid blade because $c_{Q6} = 0\%$, not measured).

5.3 Schlieren pictures

Fig. 10 to 12 show Schlieren photographs of the configurations A, B and E for the minimum and maximum total mass flow coefficient. The two centre passages are formed by blades with simulated film cooling and show nearly identical flow behaviour. However, the middle of the suction side of the upper blade is characterized by a stronger shock configuration originated by the trailing edge of the adjacent solid blade which cannot be seen in these photographs. This stronger shock agrees with the higher Mach number gradient of the solid blade at $(s/s_0)_s = 0.65$ to 0.75 compared with that of the blades with simulated cooling, see fig. 6 to 8. The laminar bubble due to shock boundary layer interaction at this location, also seen in the Mach number distribution on fig. 6, is visible best on the lower blade in fig. 10. The trailing edge jet is hard to see at $c_{Q,tot} = 0\%$ (left-hand photographs in fig. 10 and 11) because of the low local mass flow coefficients of $c_{Q6} = 1\%$. It can be observed clearly at $c_{Q,tot,max}$ (right-hand photographs in fig. 10 and 11) because of $c_{Q6} = 4\%$. The strength of the trailing edge shock on the suction side is reduced with increasing values of c_{Q6} (left to right in fig. 10 and 11) due to the change of streamline curvature and Mach number gradient, compare fig. 7.

In the lower passage of fig. 10, light lines are visible at $(s/s_0)_s = 0.48, 0.53, 0.87, 0.90$ and 0.93 which can be identified as Mach lines. Their inclinations with respect to the suction surface yield Mach numbers which agree with those derived from the surface pressure distribution and p_{01} . These Mach lines were caused by the pressure tappings which act as small local disturbances.

Fig. 11 shows the different local flow behaviour around the location I.7 on the pressure side: Left black and white because of $c_{Q7} = -0.5\%$ (suction), right black because of $c_{Q7} = +1\%$ (ejection), but the jet itself cannot be seen.

The solid t.e. of configuration E in fig. 12 produces another shock configuration: A clear line starts from the wake "throat" and meets the suction side of the adjacent blade with no bubble generation. The boundary layer is clearly thicker at the trailing edge on the suction side for both B and E in comparison with A which agrees with the Mach number distributions.

Although the shock behaviour is unsteady in transonic cascade flow, repeated Schlieren photographs showed consistency of the shock configurations. The calculated shock position, see fig. 13, corresponds quite well with the Schlieren picture in figs. 11 and 12.

5.4 Boundary layer of blade suction side near trailing edge

The velocity profiles at $(s/s_0)_s = 0.98$ were plotted in fig. 14. The boundary layer thickness δ with $w/w_\infty = 0.99$ is as follows ($c_{Q,tot} = 0$):

Configuration A	$\delta = 1.7$ mm
B	2.5 mm
E	2.4 mm

This tendency agrees with the observation in the Schlieren pictures. The influence of $c_{Q,tot}$ on δ is small for each configuration, but it affects the shape of the velocity profile in the inner part of the boundary layer. The fuller shape indicates a turbulent boundary layer with no separation.

The momentum thickness δ_2 in fig. 15 behaves similar to δ : little variation with $c_{Q,tot}$ and B and E are roughly 50% higher than A. This verifies again the similar suction side boundary layer behaviour due to ejection on the front part of this surface for the configurations B and E.

The shape factor in the lower diagram of fig. 15 indicates a turbulent boundary layer. The high level of H_{12} for A at high $c_{Q,tot}$ shows that the boundary layer is not far from separation due to the displacement of the main streamlines by the trailing edge jet. Suction side ejection (configuration B) promotes stability, see the lower H_{12} values. Configuration E possesses the most stable boundary layer because H_{12} is lowest.

5.5 Transition measured by a traversing probe

The typical change of the shape of the velocity profile was used in order to detect boundary layer transition, see [15]. Care has to be taken when compression shocks interact with the boundary layer. Results from two other experiments are discussed first, in order to illustrate the principle of the method clearly.

5.5.1 Examples of flat plate and airfoil

Data from laminar and turbulent shock boundary layer transition on a flat plate of $l = 550$ mm with pressure gradient are taken from the "classic" work of J. Ackeret et al. [17], test I and III, and shown here in fig. 16. The second example concerns an investigation of H. Sobieczky and E. Stanewsky [18] on the airfoil CAST 10-2 of $c = 200$ mm,

see fig. 17.

In the upper diagrams, the boundary layer is laminar at the suction peak ($x = 150$ mm in fig. 16, $x/c = 0.42$ in fig. 17) for the following reasons:

- The surface pressure distributions p/p_0 and c_p show a step downstream of this location due to bubble separation. The location of the kink at the end of the step coincides with the location of the minimum in the near wall velocity or Mach number.
- The near wall velocity $w_{0.3}/w_\infty$ and the near wall Mach number $Mo_{0.1}$ might be negative or close to zero in the bubble region. The difference between the local minimum and maximum Mach number is large, e.g. $\Delta Mo_{0.1} = 0.53$ in fig. 17.
- Around the location of the critical pressure ratio, both surface pressure and near wall Mach number rise.
- The shape factor H_{12} of the velocity profiles reaches very high values in the bubble region, see fig. 16.
- Typical laminar velocity profiles are shown in [17], [18]. λ -shocks are indicated in [17].

Transition onset is defined by the end of the pressure plateau which agrees with the location of $Mo_{0.1, \min}$ in fig. 17. Transition ends at the location of $Mo_{0.1, \max}$ because the near wall Mach number and the velocity profile as well change steadily further downstream. In fig. 16, transition ends approximately at $x = 260$ mm as deduced from the velocity profiles given in [17].

Very high values of the shape factor H_{12} are also shown in [19] around the transition point in the case of bubble transition. There is very good agreement in the results of probe measurements and of laser-Doppler application was obtained.

In the lower diagram of fig. 16, the case for increased Reynolds number is shown and the boundary layer is now turbulent at the location of the suction peak, $x = 200$ mm. In fig. 17 the lower diagram shows the case where transition is forced by Carborundum grit at $x/c = 0.15$. The turbulent boundary layer is verified by the following items:

- There is no pressure step indicating separation as in the case of the laminar boundary layer.
- The minimum of the near wall velocity and Mach number lies clearly above zero. It occurs at the location of the critical pressure ratio or somewhat downstream. The difference between the local minimum and maximum Mach number is less than in the laminar case, e.g. $\Delta Mo_{0.1} = 0.20$ in fig. 17.
- Around the location of the critical pressure ratio, the surface pressure rises but the near wall Mach number falls.
- The shape factor changes to a smaller extent in the region of the critical pressure ratio.
- Typical turbulent velocity profiles are shown in [17], [18]. The Schlieren pictures in [17] indicate no λ -shock.

The above criteria were used to assist the investigations on the cascade in order to detect boundary layer transition.

5.5.2 Transition of the blade boundary layer

The traversing probe results along the blade suction side are shown in fig. 18 to 20. For convenience, the ratio of dynamic heads

$$\frac{q(\eta = 0.15)}{q_\infty} = \frac{P_0(\eta = 0.15) - p}{P_{0m} - p}$$

was plotted rather than w/w_∞ . The left-hand diagram of fig. 18 shows the typical transition behaviour: Minimum of q/q_∞ close to zero and close to the location of the incident shock in the Schlieren photograph (fig. 10, $(s/s_0)_s = 0.65$), followed by a rise to a maximum. Therefore the transition is defined to take place between $(s/s_0)_s = 0.61$ and 0.82 . At higher ejection flow rate, the behaviour is less clear, see right-hand diagram in fig. 18: The minimum is wider so that the definition of the location of transition onset becomes more difficult. The q/q_∞ minimum lies on a higher level and the difference maximum-minimum is smaller. The rise in q/q_∞ from $(s/s_0)_s = 0.80$ to 0.87 occurs in parallel to an increase in surface Mach number which does not correspond to the behaviour of laminar shock-boundary layer interaction in fig. 17. As the Mach number distribution shows a step with a kink at $(s/s_0)_s = 0.65$ and the Schlieren picture a bubble, the right-hand curve in fig. 18 is explained with transition approximately at $(s/s_0)_s = 0.65$ as in the case of $c_{Q, \text{tot}} = 0\%$ but with reduced length of the transition range.

The shape of the left-hand curve for configuration B in fig. 19 looks similar. The minimum is close to the location where nearly sonic conditions are reached (fig. 7, $(s/s_0)_S = 0.77$). Immediately upstream, q/q_∞ drops down while the surface pressure rises. In agreement with the discussion about the Mach number distributions and the Schlieren pictures, it is indicated that transition has already occurred upstream of the point $(s/s_0)_S = 0.45$. There the traversing probe could not be applied because of the high curvature of the blade suction surface. The increase in q/q_∞ between $(s/s_0)_S = 0.75$ and 0.87 is caused by thinning of the turbulent boundary layer due to the local acceleration, compare fig. 7 as well as K. Bamert and H. Sandstede [20]. In the right-hand diagram of fig. 19, the plateau of q/q_∞ between $(s/s_0)_S = 0.78$ and 0.88 corresponds to the plateau of the surface pressure in fig. 7. The shock strength decreases slightly with increasing ejection flow rate as can be seen from the Schlieren pictures.

The minima in fig. 20 for configuration E lie on a low level, and the difference between the local minimum and maximum is considerable. However, the minimum lies clearly downstream of the suction peak in fig. 8. The steep decrease between $(s/s_0)_S = 0.58$ and 0.68 agrees with the fall in surface Mach number and with the distinct shock in fig. 12. The following rise in near wall dynamic head up to $(s/s_0)_S = 0.93$ indicates a thinning of the boundary layer due to the acceleration shown by the surface M distribution. The final drop in q/q_∞ agrees again with the steep M fall and with the trailing edge shock in the Schlieren photograph. This behaviour indicates that transition occurs again upstream of the range considered in fig. 20, i.e. probably already by the jets at the location II.3.

All boundary layer measurements were found to be in the subsonic range, i.e. the local Mach number lies below unity except the velocity profiles in case E, see fig. 14. Here $M(n) = 1$ is obtained at $n/c = 0.026$ for $c_{Q,tot} = 0\%$ and at $n/c = 0.029$ for $c_{Q,tot} = 1.5\%$.

5.6 Wake traverse results

The loss coefficients defined in the appendix are plotted on fig. 21. The loss coefficient ξ_S does not take into account the coolant energy in the inlet plane. ξ_S falls with increasing total mass flow coefficient for all configurations. At E, the coolant total pressure is mostly higher than the mainstream total pressure, compare fig. 4, so that the average downstream total pressure may increase a little for this reason with $c_{Q,tot}$. At A and B, p_{0c} is mostly lower than p_{01} , but the wake is filled more and more by the trailing edge jets resulting in a relative increase of exit total pressure as well. G.W. Michel and F.H. Kost [5] observed that strong vortices are generated by a thick solid trailing edge in combination with low base pressure, and the action of trailing edge jets results in a relative increase in exit energy.

The results of ξ_S show that the available exit energy exceeds the primary inlet energy for $c_{Q,tot} > 3.2\%$ at A and 4.2% at B. In any case, the average exit total pressure is lower than the inlet total pressure. The loss of B is higher than that of A by $\Delta\xi_S = 0.012$ due to the additional suction and pressure side ejection. The losses of B and E at $c_{Q,tot} = 0\%$ are higher than those of the solid blade because coolant is ejected on the suction side ($c_{Q3} = 0.3\%$ at B, $c_{Q3} = 0.3\%$ at E).

The loss coefficient ξ_S^* takes into account the energy of the coolant after leaving the coolant channels. Hence, this coefficient describes best the aerodynamic loss due to cooling simulation. The loss coefficient can be reduced at A and B with $c_{Q,tot,nom}$ by $1/3$ relative to the solid blade due to the filling of the wake by the trailing edge jets. E is worst because the loss increase due to leading edge ejection cannot be compensated by any favourable trailing edge jets as in the cases A and B.

Finally, the loss coefficient ξ_{SS} includes the losses in the narrow coolant channels inside the blade. Therefore, ξ_{SS} exceeds ξ_S^* , in particular at the configuration A and B because of the high jet Mach number and the length of the slots. A has the same value as the solid blade, while B and E produce higher losses in this definition.

It was stated by C.H. Hauser et al. [1] that additional losses occur by ejection on suction and pressure surface. Though it depends on the surface pressure distribution and on the local flow rate, the order of magnitude found in [1] agrees with the results presented here: For nominal conditions, there is an increase in ξ_{SS} from A to B by $\Delta\xi_{SS} = 0.008$ due to ejection at I.3 and I.7. There is also an increase from the solid blade to E by $\Delta\xi_{SS} = 0.007$ due to ejection at II.1, II.2 and II.3. The loss minimum for single trailing edge ejection found by O. Lwaczek [3] and by G.W. Michel and F.H. Kost [5] with $c_Q = 3$ to 4% agrees with the minimum observed here, $c_{Q6} = 3\%$ ($c_{Q,tot} = 2\%$ at A and 3% at B).

The measured exit flow angle of the solid blade agrees with the nominal one, see fig. 22. With cooling simulation, β_2 is lower because of

- trailing edge ejection at an even lower angle (A and B)
- the thicker suction side boundary layer (ejection by I.3 at B and II.3 at E).

Trailing edge ejection causes also the decrease of β_2 with increasing total mass flow coefficient (A and B). The maximum deviation with respect to the solid blade is obtained with $\Delta\beta_2 = 1.3^\circ$ for B at maximum $c_{Q,tot}$.

6. CONCLUSIONS

The aerodynamic behaviour of an advanced gas turbine rotor cascade was investigated under the influence of simulated cooling. The tests were carried out in the High Speed Cascade Wind Tunnel of DFVLR Braunschweig at $\beta_1 = 37.9^\circ$, $M_{2th} = 0.985$, $Re_2 = 8.4 \cdot 10^5$, $Tu_1 = 4\%$. Cold air was used as "coolant" and ejected at several locations on the suction and pressure sides and through the trailing edge as well. The following three configurations were investigated:

- A Two locations in the leading edge region, slots in the trailing edge
- B One additional location on both suction and pressure side
- E Three locations in the leading edge region only

At B, a maximum total mass flow rate of $c_{0,tot} = 6.6\%$ was ejected. From surface Mach number distributions, boundary layer and wake traverse measurements as well as from Schlieren observations it is concluded:

1. The nominal ejection flow rate of A and B requires a coolant cavity pressure of 92 or 95 % of the mainstream total pressure. However, the leading edge cannot be served by a coolant film because mainstream air is sucked into the cavity. Leading edge film cooling is obtained at E but a higher pressure of $p_{0c}/p_{01} = 1.08$ has to be provided.
 2. The roughness due to the ejection holes near the leading edge does not influence the blade boundary layer behaviour. Case A is characterized by laminar shock boundary layer interaction and by a thin suction side boundary layer near the trailing edge.
 3. Ejection at the throat location on the suction side, $(s/s_0)_S = 0.29$, causes boundary layer transition (case B). Individual ejection flow rates of $c_{03} = 0.3$ to 0.9% double the momentum thickness measured on the suction side near the trailing edge.
 4. Ejection at the suction side in the leading edge region, $(s/s_0)_P = 0.018$, causes transition as well (case E). The momentum thickness is of the same order of magnitude as at B.
 5. The trailing edge jets give rise to a certain displacement of the rear blade boundary layer which is verified by the increased base pressure relative to the solid blade. However, a part of the wake is filled by the trailing edge jets so that the energy content in the exit plane increases with increasing ejection flow rate and can exceed the mainstream energy level in the inlet plane (cases A and B). Hence trailing edge ejection of $c_{06} = 0$ to 4% is favourable.
 6. The energy balance is also influenced by the level of the coolant total pressure. The inlet energy level of E is higher than that of the solid blade because p_{0c} is mostly bigger than p_{01} , but it is lower at A and B because p_{0c} is mostly smaller than p_{01} .
 7. The energy losses are defined by the coefficients ξ_S , ξ_S^* and ξ_{SS}^* which consider the coolant energy in different ways:
 - Coolant energy not taken into account (ξ_S)
 - Energy at the end of the coolant channels entering the blade passage (ξ_S^*)
 - Energy in the cavity inside the blade (ξ_{SS}^*).
- ξ_{SS}^* can be 50 % higher (B and E) than for the solid blade.
8. The exit flow angle is up to 1.3° lower than that of the solid blade due to trailing edge ejection at an even lower angle with respect to the cascade axis (A and B), and due to the thicker suction side boundary layer by ejection at $(s/s_0)_S = 0.29$ (B) and $(s/s_0)_P = 0.018$ (E).

ACKNOWLEDGEMENT

The authors wish to express their appreciation to Motoren- und Turbinen-Union München GmbH and to Rolls-Royce Limited for their permission to publish this material.

REFERENCES

- [1] Hauser, C.H.
Haas, J.E.
Reid, L.
Stepka, F.S. Turbomachinery technology.
In: Aeropropulsion 1979. NASA Conf. Publ. 2092 (1979), pp. 231-272.
- [2] Ito, S.
Eckert, E.R.G.
Goldstein, R.J. Aerodynamic loss in a gas turbine stage with film cooling.
ASME paper no. 80-GT-38 (1980).
- [3] Lawaczeck, O. The influence of jets of cooling air exhausted from the trailing edges of a supercritical turbine cascade on the aerodynamic data.
AGARD-CP-229 (1978), pp. 30-1 to 30-12.
- [4] Sieverding, C.H. The influence of trailing edge ejection on the base pressure in transonic turbine cascades.
ASME paper no. 82-GT-50 (1982).
- [5] Michel, G.W.
Kost, F.H. The effect of coolant flow on the efficiency of a transonic HP turbine profile suitable for a small engine.
ASME paper no. 82-GT-63 (1982).
- [6] Hess, W.G. Advanced cooled turbine airfoil aerodynamic investigation.
AIAA paper no. 77-950 (1977).
- [7] Barry, B. The aerodynamic penalties associated with turbine blade cooling.
In: Turbine blade cooling. LS 83, von Karman Institute, Rhode-St.-Genèse, Belgium (1976).
- [8] McDonel, J.D.
Eiswerth, J.E. Effects of film injection on performance of a cooled turbine.
AGARD-CP-229 (1978), pp. 29-1 to 29-11.
- [9] Lindemann, R. Messen von aerodynamischen Profilen auf einer Drei-Koordinaten-Meßmaschine.
Fachtagung "Erfahrungsaustausch Drei-Koordinaten-Meßgeräte'77", Institut für Produktionstechnik und Automatisierung, Stuttgart (1977).
- [10] Hoheisel, H.
Kiock, R. Zwanzig Jahre Hochgeschwindigkeits-Gitterwindkanal des Instituts für Aerodynamik der DFVLR in Braunschweig.
Zeitschrift für Flugwissenschaften und Weltraumforschung, Vol. 1, No. 1 (1977), pp. 17-29.
- [11] Kiock, R.
Laskowski, G.
Hoheisel, H. Die Erzeugung höherer Turbulenzgrade in der Meßstrecke des Hochgeschwindigkeits-Gitterwindkanals Braunschweig, zur Simulation turbomaschinenähnlicher Bedingungen.
DFVLR-FB 82-25 (1982).
Translation: The generation of higher levels of turbulence in the test section of the High Speed Cascade Wind Tunnel Braunschweig for simulation of turbomachinery conditions.
ESA TT 815 (1983).
- [12] Hoheisel, H. Beschreibung der Sekundär-Luftversorgungsanlage des Niedergeschwindigkeitswindkanals der DFVLR Braunschweig.
DLR-Mitt. 73-14 (1973). See also DFVLR IR 151-77/17 (1977).
- [13] Amecke, J. Anwendung der transsonischen Ähnlichkeitsregel auf die Strömung durch ebene Schaufelgitter.
VDI-Forschungsheft 540 (1970), pp. 16-28.
- [14] Hoeger, M.
Hoheisel, H. On the accuracy of boundary layer measurements in cascades at high subsonic speeds.
7th Symposium on Measuring Techniques for Transonic and Supersonic Flow in Cascades and Turbomachines, Aachen (1983). Mitteilung 1/64 des Instituts für Strahltriebwerke der RWTH Aachen (1984).
- [15] Oldfield, M.L.G.
Kiock, R.
Holmes, A.T.
Graham, C.G. Boundary layer studies on highly loaded cascades using heated thin films and a traversing probe.
Trans. ASME, J. of Eng. for Power, Vol. 103 (1981), No. 1, pp. 237-246.

- [16] Happel, H.-W. Anwendung neuer Entwurfskonzepte für axiale Turbomaschinen. Teil I: Erweiterung eines zweidimensionalen zeitabhängigen Elementenverfahrens für die Nachrechnungsaufgabe im rotierenden Relativsystem.
Endbericht ZTL-Programm 1978 Aufgabe 4.14-2
MTU-München, Techn. Bericht 78/054 A (1978).
- [17] Ackeret, J.
Feldmann, F.
Rott, N. Untersuchungen an Verdichtungsstößen und Grenzschichten in schnell bewegten Gasen.
Mitt. Inst. f. Aerodynamik ETH Zürich Nr. 10 (1946).
Translation: Investigations of compression shocks and boundary layers in gases moving at high speed.
NACA TM 1113 (1947).
- [18] Sobieczky, H.
Stanewsky, E. The design of transonic airfoils under consideration of shock wave boundary layer interaction.
ICAS paper no. 76-14 (1976).
- [19] Hoheisel, H.
Hoeger, M.
Meyer, P.
Korber, G. A comparison of laser-Doppler anemometry and probe measurements within the boundary layer of an airfoil at subsonic flow.
Second Int. Symp. on Applications of Laser Anemometry to Fluid Mechanics, Lisbon, Portugal, 2-4 July, 1984.
- [20] Bannert, K.
Sandstedt, H. Measurements of the boundary layer development along a turbine blade with rough surfaces.
ASME Paper No. 80-GT-40 (1980).
- [21] Brown, D.B.
Helon, R.M. Cold air aerodynamic study in a two-dimensional cascade of a turbine stator blade with suction-surface film cooling.
NASA TM X-2685 (1973).

APPENDIX

DEFINITION OF THE LOSS COEFFICIENTS

The aerodynamic loss of the flow through the cascade is expressed by the ratio of energies. The energy of the coolant is not included at the inlet plane in the parameter ξ_S :

$$(A-1) \xi_S = 1 - \frac{0.5 w_2^2 (\dot{m}_1 + \dot{m}_c)}{(0.5 w_1^2 + \Delta i_{th}) \dot{m}_1} = 1 - \frac{1 - \left(\frac{p_2}{p_{02}}\right)^{\frac{\kappa-1}{\kappa}}}{1 - \left(\frac{p_2}{p_{01}}\right)^{\frac{\kappa-1}{\kappa}}} (1 + c_{Q,tot})$$

When the coolant energy is also included in the inlet plane, another parameter ξ_S^* is defined:

$$(A-2) \xi_S^* = 1 - \frac{0.5 w_2^2 (\dot{m}_1 + \dot{m}_c)}{(0.5 w_1^2 + \Delta i_{th}) \dot{m}_1 + \sum_i (0.5 w_{ci}^2 + \Delta i_{c,th,i}) \dot{m}_{ci}} =$$

$$= 1 - \frac{\left[1 - \left(\frac{p_2}{p_{02}}\right)^{\frac{\kappa-1}{\kappa}}\right] (1 + c_{Q,tot})}{\left[1 - \left(\frac{p_2}{p_{01}}\right)^{\frac{\kappa-1}{\kappa}}\right] + \sum_i \left[1 - \left(\frac{p_2}{p_{0,jet,i}}\right)^{\frac{\kappa-1}{\kappa}}\right] c_{Qi}}$$

Here it is assumed that the total temperatures of mainstream, coolant and mixed out flow are approximately equal, $T_{01} = T_{0c} = T_{02}$. $p_{0,jet,i}$ means the individual jet total pressure and is evaluated by the surface pressure p_i . \dot{m}_B means the total ejection mass flow rate \dot{m}_B measured at the orifice, the jet total temperature T_{0c} and the sum of the cross sectional areas F_{ci} of all ejection holes and slots of one location i :

$$(A-3) p_{0,jet,i} = \left\{ 0.5 p_i^{\frac{\kappa-1}{\kappa}} + \left[\frac{(e_i \dot{m}_B)^2}{\left(\frac{\kappa-1}{\kappa}\right)^5} \frac{T_{0c} R(\kappa-1)}{2\kappa F_{ci}^2} + \left(0.5 p_i^{\frac{\kappa-1}{\kappa}}\right)^2 \right]^{\frac{1}{2}} \right\}^{\frac{\kappa}{\kappa-1}}$$

e_i is known from the calibration, see fig. 5:

$$(A-4) \quad e_i = c_{Qi}/c_{Q,tot}$$

Hence ξ_S^* does not take into account the pressure loss in the coolant channels. This is considered in $\xi_{c,c}^*$ which agrees with the definition given in eqn. (A-2) except that $P_{o,jet,i}$ is exchanged for the cavity pressure P_{oc} .

This parameter ξ_{SS}^* is directly related to the "thermodynamic efficiency" η_T and η_{th} of B. Barry [7] and of NASA Lewis [21] and it agrees with the definition of ξ of O. Lawaczeck [3]. In similar way, ξ_S of eqn. (A-1) is connected with the "performance efficiency" η_P of B. Barry and with the "primary-air-efficiency" of NASA. It holds:

$$(A-5) \quad \xi_{SS}^* = 1 - \eta_T = 1 - \eta_{th} = \xi$$

$$(A-6) \quad \xi_S = 1 - \eta_P$$

x [mm]	y _S [mm]	x [mm]	y _P [mm]
0.10000E 03	0.22400E 01	0.20000E 00	0.48300E 01
0.99650E 02	0.31700E 01	0.53000E 00	0.38300E 01
0.98950E 02	0.39000E 01	0.10000E 01	0.30000E 01
0.98000E 02	0.43800E 01	0.17000E 01	0.20800E 01
0.97000E 02	0.48900E 01	0.24000E 01	0.14400E 01
0.96000E 02	0.53800E 01	0.31600E 01	0.94000E 00
0.94910E 02	0.59000E 01	0.47400E 01	0.25000E 00
0.93600E 02	0.65800E 01	0.65000E 01	0.0
0.91000E 02	0.78300E 01	0.77200E 01	0.14000E 00
0.88530E 02	0.90200E 01	0.94000E 01	0.76000E 00
0.84000E 02	0.11160E 02	0.10700E 02	0.15800E 01
0.80810E 02	0.12600E 02	0.11580E 02	0.21900E 01
0.78000E 02	0.13880E 02	0.14000E 02	0.37000E 01
0.74460E 02	0.15470E 02	0.16310E 02	0.51000E 01
0.72000E 02	0.16530E 02	0.18000E 02	0.60400E 01
0.69020E 02	0.17890E 02	0.20140E 02	0.70000E 01
0.66000E 02	0.19180E 02	0.23160E 02	0.81700E 01
0.63160E 02	0.20350E 02	0.26100E 02	0.90900E 01
0.60000E 02	0.21630E 02	0.29020E 02	0.97900E 01
0.57330E 02	0.22670E 02	0.32280E 02	0.10310E 02
0.54000E 02	0.23850E 02	0.35090E 02	0.10610E 02
0.51230E 02	0.24740E 02	0.37000E 02	0.10780E 02
0.49000E 02	0.25460E 02	0.38950E 02	0.10810E 02
0.46950E 02	0.26070E 02	0.41750E 02	0.10810E 02
0.43820E 02	0.26910E 02	0.43600E 02	0.10700E 02
0.41050E 02	0.27610E 02	0.45610E 02	0.10580E 02
0.37230E 02	0.28350E 02	0.48740E 02	0.10300E 02
0.34100E 02	0.28810E 02	0.52000E 02	0.99100E 01
0.32600E 02	0.29000E 02	0.53960E 02	0.96300E 01
0.30530E 02	0.29240E 02	0.57000E 02	0.91800E 01
0.29000E 02	0.29320E 02	0.59790E 02	0.86700E 01
0.27370E 02	0.29400E 02	0.63000E 02	0.81000E 01
0.26000E 02	0.29420E 02	0.65860E 02	0.75200E 01
0.23580E 02	0.29350E 02	0.69000E 02	0.68800E 01
0.22000E 02	0.29200E 02	0.71660E 02	0.62800E 01
0.20280E 02	0.29000E 02	0.76000E 02	0.53000E 01
0.18000E 02	0.28600E 02	0.78530E 02	0.47500E 01
0.16170E 02	0.28140E 02	0.83000E 02	0.36800E 01
0.14000E 02	0.27410E 02	0.86310E 02	0.28800E 01
0.11930E 02	0.26520E 02	0.90000E 02	0.19600E 01
0.10000E 02	0.25560E 02	0.92000E 02	0.14700E 01
0.79600E 01	0.24220E 02	0.93260E 02	0.11600E 01
0.64000E 01	0.22920E 02	0.95000E 02	0.71000E 00
0.47000E 01	0.21230E 02	0.96000E 02	0.45000E 00
0.38000E 01	0.20080E 02	0.97000E 02	0.22000E 00
0.28100E 01	0.18550E 02	0.97890E 02	0.0
0.20000E 01	0.17070E 02	0.98950E 02	0.25000E 00
0.11600E 01	0.15230E 02	0.99400E 02	0.62000E 00
0.80000E 00	0.14200E 02	0.99820E 02	0.13500E 01
0.35000E 00	0.12020E 02		
0.10000E 00	0.97500E 01		
0.50000E 01	0.87700E 01		
0.0	0.64600E 01		

$$d/l = 0.216$$

$$r_N/l = 0.065$$

$$r_H/l = 0.0224$$

Table 1: Profile coordinates (nominal)

Location	Surface coordinate	Bitangential coordinate	Diameter, width	Pitch	Inclination with respect to chord	Individual mass flow coefficient, nominal	Blade set no.
i	$(s/s_o)_P$	x/c	d_B [mm]	t_B/d_B	α	c_{Qi} [%]	
I.1 ¹⁾	0.102	0.073	1.0	3	80.0°	0.6	I
I.2 ¹⁾	0.056	0.030	1.0	3	52.5°	0.6	
1.3	0.290 ²⁾	0.214	1.0	2	47.5°	1.0	
I.6 Slot	1.000	1.000	1.7	-	160.0°	2.0	
1.7	0.790	0.792	1.4	2	143.0°	1.0	
II.1 ¹⁾	0.155	0.128	1.0	3	157.0°	0.4	II
II.2 ¹⁾	0.088	0.060	1.0	3	90.0°	0.4	
II.3 ¹⁾	0.018	0.006	1.0	3	24.0°	0.4	

1) 45° inclined with respect to turbine axis

2) Suction side, $(s/s_o)_S$

Table 2: Geometry of holes and slots for simulated cooling

Configuration	ϕ [mm]	$\arccos\left(\frac{\phi}{s}\right)$
Nominal	33.66	63.37°
Solid blade	33.93 ± 0.08	63.14° ± 0.07°
A	33.91 ± 0.17	63.16° ± 0.15°
B	33.89 ± 0.16	63.17° ± 0.14°
E	33.84 ± 0.13	63.22° ± 0.12°

Table 3: Average and standard deviation of throat and gauging angle over four central pitches ($s = 75.1$ mm)

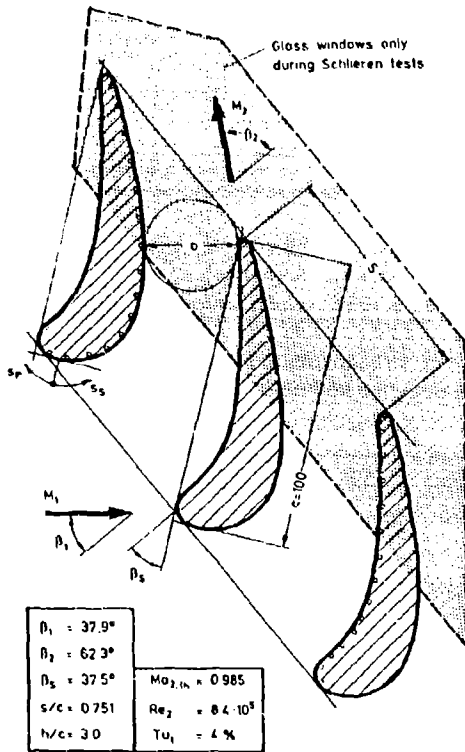


Fig. 1. Geometry of cascade

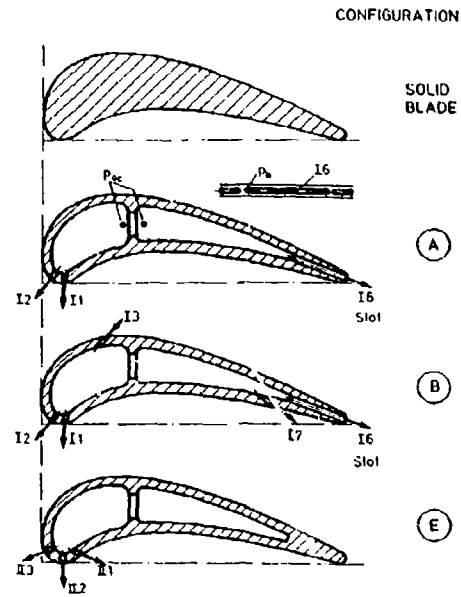


Fig. 2. Investigated configurations in view of cooling simulation

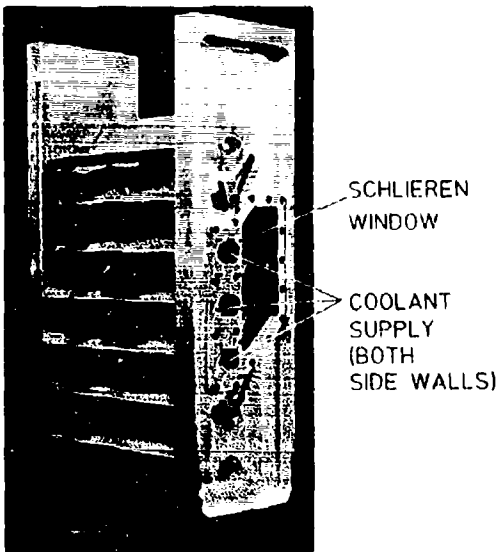


Fig. 3. View of investigated cascade

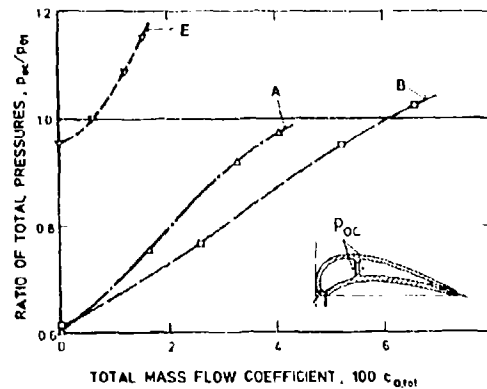


Fig. 4. Cavity pressure

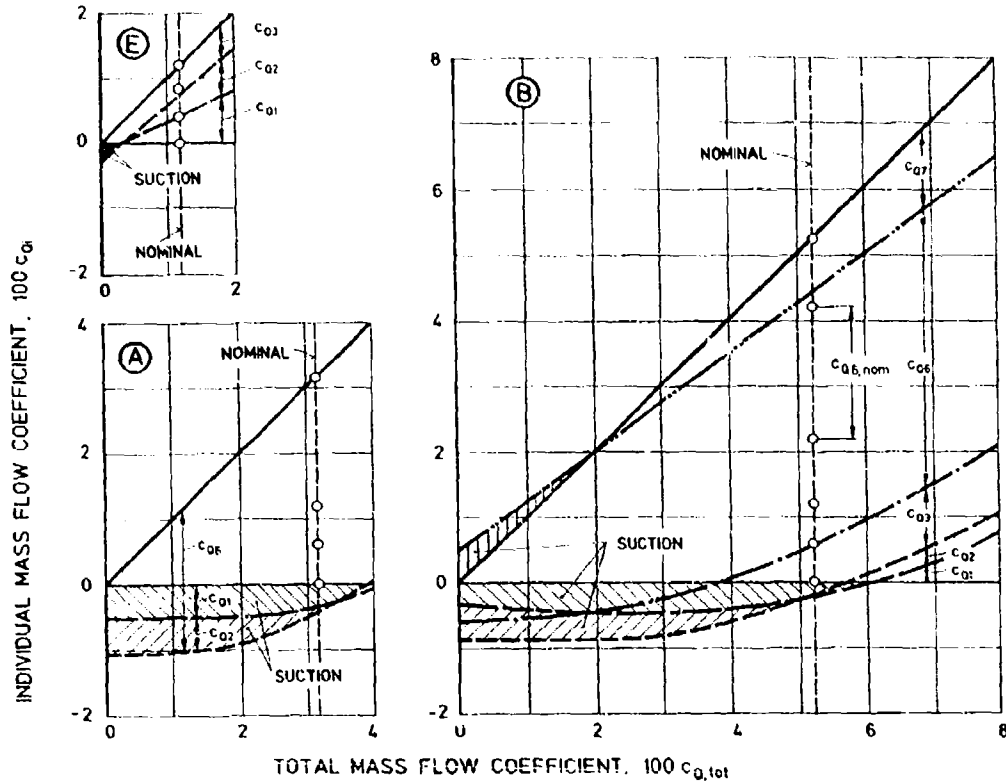


Fig. 5. Individual mass flow coefficients

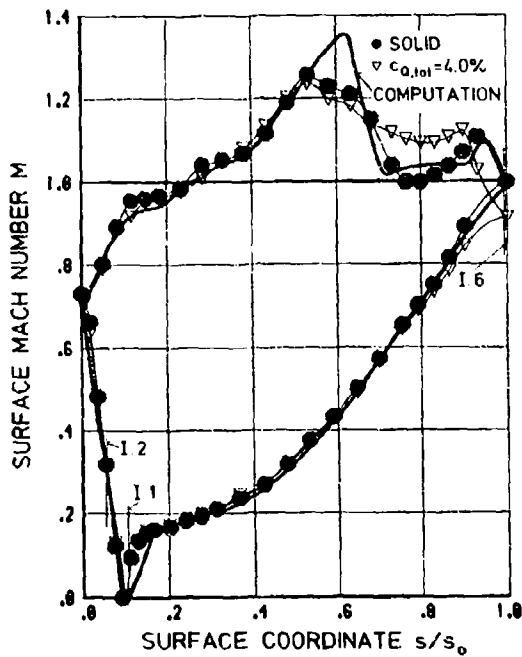


Fig. 6. Surface Mach number distributions as computed for the solid blade and measured for the solid blade as well as for configuration A

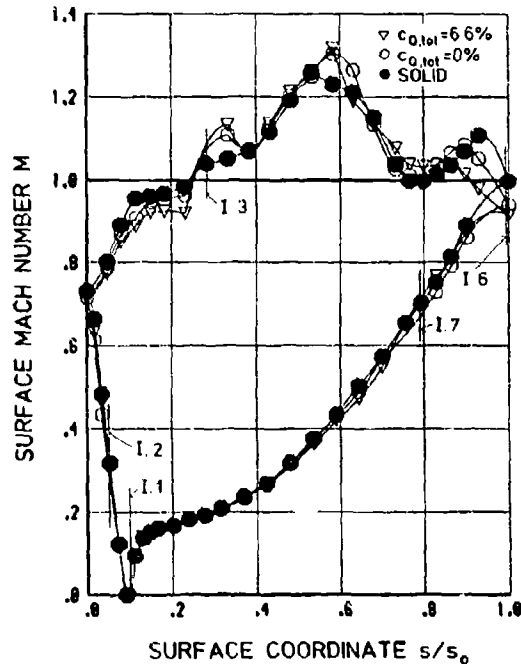


Fig. 7. Measured surface Mach number distribution for configuration B

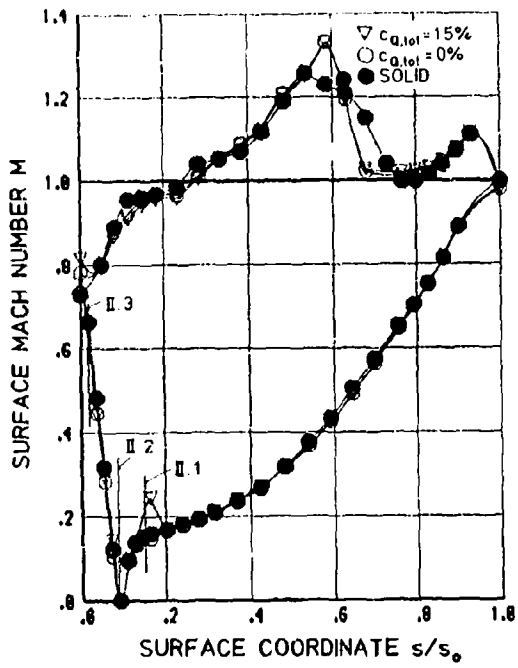


Fig. 8 Measured surface Mach number distribution for configuration E

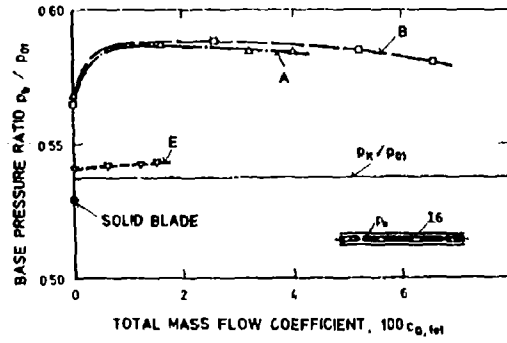


Fig. 9. Base pressure



Fig. 10. Schlieren pictures configuration A



Fig. 11. Schlieren pictures configuration B



Fig. 12. Schlieren pictures configuration E

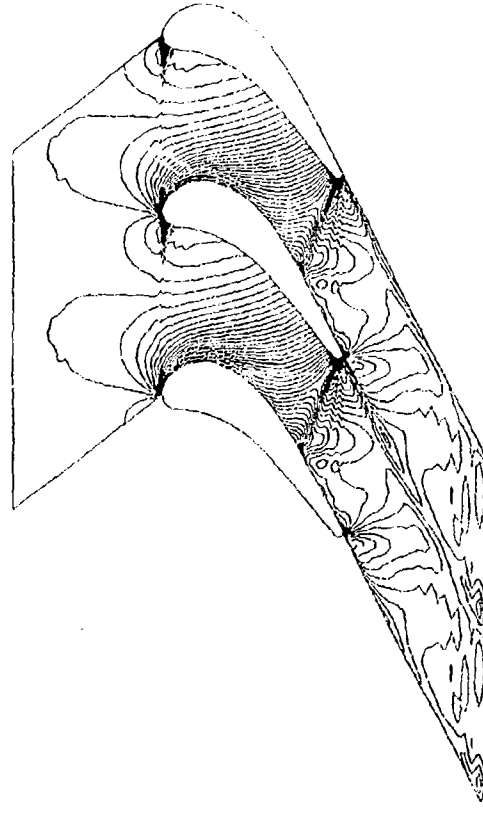


Fig. 13. Inviscid calculation isodensity contours, solid blade

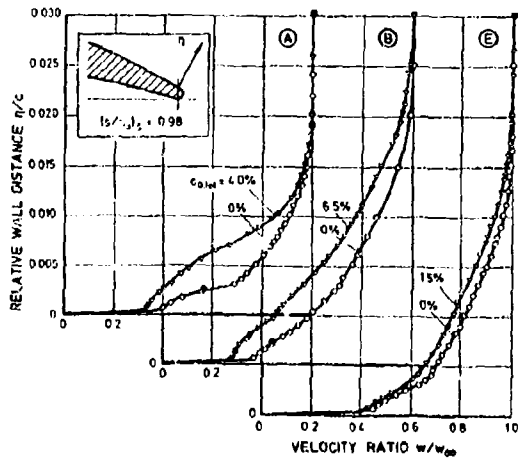


Fig. 14. Velocity profiles of the blade boundary layer near the trailing edge

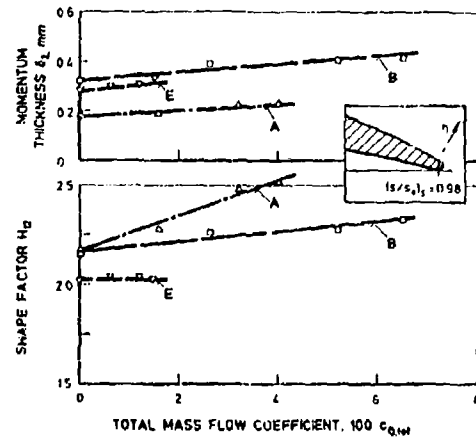


Fig. 15. Momentum thickness and shape factor

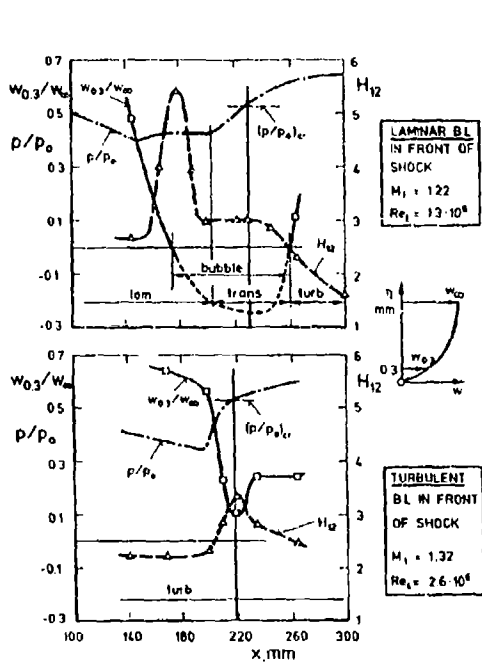


Fig. 16. Laminar and turbulent shock-boundary layer interaction on a flat plate with pressure gradient, after Ackeret et al. [17]

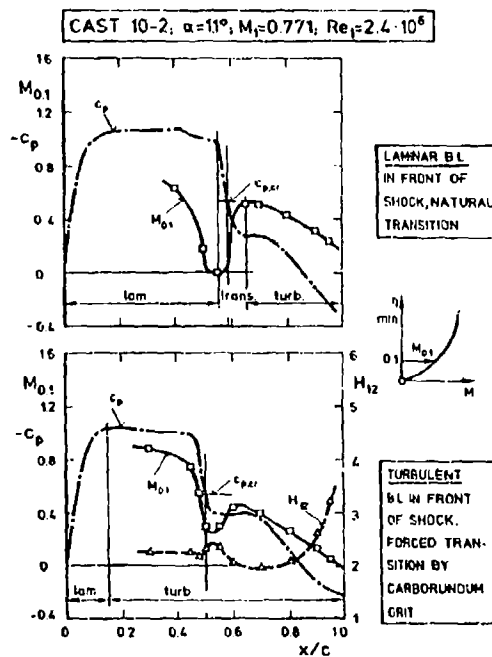


Fig. 17. Laminar and turbulent shock-boundary layer interaction on a CAST-profile, after Sobieczky and Stanewski [18]

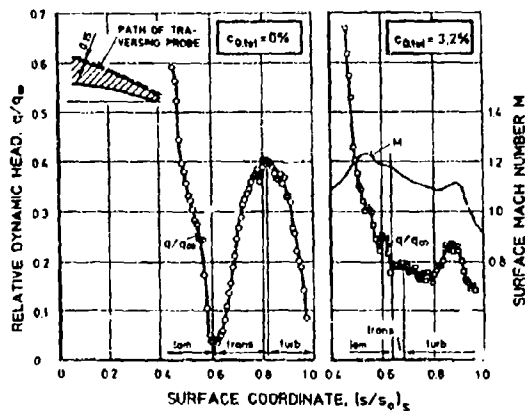


Fig. 18. Pitot surface probe results configuration A

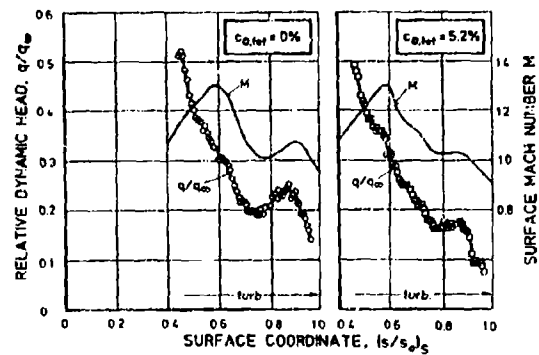


Fig. 19. Pitot surface probe results configuration B

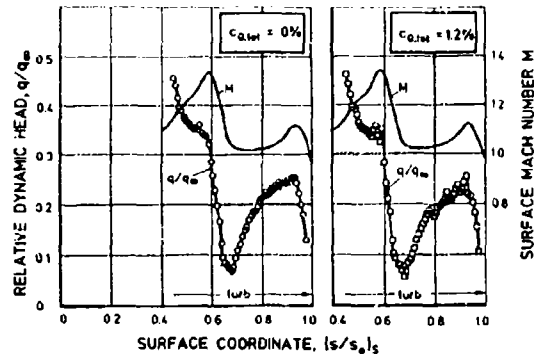


Fig. 20. Pitot surface probe results, configuration E

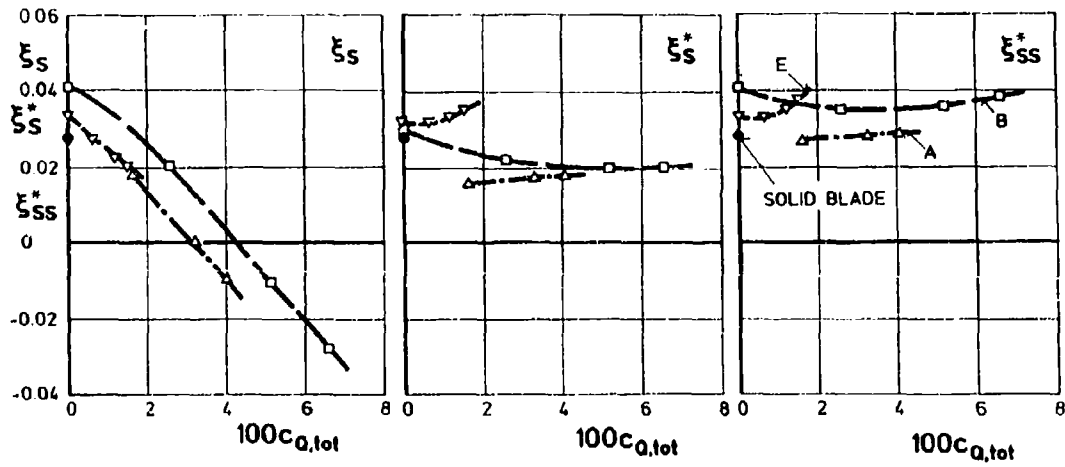


Fig. 21. Loss coefficients versus total mass flow coefficient

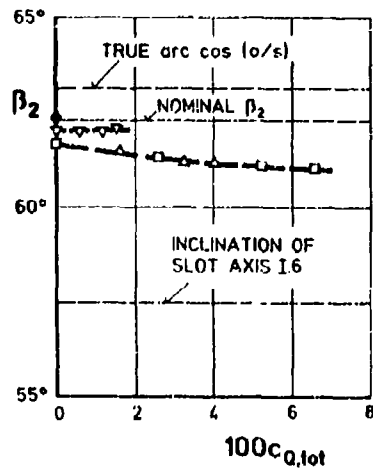


Fig. 22. Exit flow angle versus mass flow coefficient

DISCUSSION

R.Eggebrecht, Ge

Can I conclude from one of your last figures, that configuration A with a properly designed LE coolant ejection and convection cooled TE has no adverse thermodynamic effect at all?

Author's Reply

Due to the particular design of configuration A and due to the investigated range of $C_{D, tot} = 0$ to 4%, no coolant was ejected through the leading edge holes as shown in Figure 5. Trailing edge ejection is favourable in the case of moderate mass flow coefficients.

S.C.Arora, Ca

It is interesting to see that the trailing edge ejection has favourable effect and reduces the overall loss. This confirms the finding of other workers and one of them is by Anderson but not referred to in your work. This work appeared probably in early 70s in ASME or AIAA. You may be interested in looking into this work.

Author's Reply

Thank you for your advice. In fact, trailing edge ejection has a favourable effect on the cascade performance as has been shown in Reference [3] to [59].

REPORT DOCUMENTATION PAGE

1. Recipient's Reference	2. Originator's Reference	3. Further Reference	4. Security Classification of Document								
	AGARD-CP-390	ISBN 92-835-0378-3	UNCLASSIFIED								
5. Originator	Advisory Group for Aerospace Research and Development North Atlantic Treaty Organization 7 rue Ancelle, 92200 Neuilly sur Seine, France										
6. Title	HEAT TRANSFER AND COOLING IN GAS TURBINES										
7. Presented at	the Propulsion and Energetics Panel 65th Symposium, held in Bergen, Norway, 6-10 May 1985.										
8. Author(s)/Editor(s)	Various	9. Date	September 1985								
10. Author's/Editor's Address	Various	11. Pages	542								
12. Distribution Statement	This document is distributed in accordance with AGARD policies and regulations, which are outlined on the Outside Back Covers of all AGARD publications.										
13. Keywords/Descriptors	<table> <tr> <td>Heat transfer</td> <td>Blade cooling</td> </tr> <tr> <td>Cooling in gas turbines</td> <td>Combustion system</td> </tr> <tr> <td>Heat exchanger</td> <td>Rotating heat transfer</td> </tr> <tr> <td>Turbine cooling</td> <td>Film cooling</td> </tr> </table>			Heat transfer	Blade cooling	Cooling in gas turbines	Combustion system	Heat exchanger	Rotating heat transfer	Turbine cooling	Film cooling
Heat transfer	Blade cooling										
Cooling in gas turbines	Combustion system										
Heat exchanger	Rotating heat transfer										
Turbine cooling	Film cooling										
14. Abstract	<p>The Conference Proceedings contain 39 papers presented at the Propulsion and Energetics 65th Symposium on Heat Transfer and Cooling in Gas Turbines, which was held 6-10 May 1985 in Bergen, Norway.</p> <p>The Technical Evaluation Report is included at the beginning of the Proceedings. Questions and answers of the discussions follow each paper. The Symposium was arranged in the following sessions: Turbine Blade Internal and External Heat Transfer (9); Turbine Cooling (5); Modelling (5); Combustion Systems (5); Experimental Techniques (7); Compressors/Heat Exchangers (4); and Interaction (4).</p> <p>The purpose of the Symposium was to bring together experts from industry, research establishments and universities to discuss fundamental and applied heat transfer problems relevant to gas turbines, and to exchange practical experience gained in component and engine development and testing. The achievements were listed in the Technical Evaluation Report which includes also some recommendations for future applications and investigation efforts.</p>										

<p>AGARD Conference Proceedings No. 390 Advisory Group for Aerospace Research and Development, NATO HEAT TRANSFER AND COOLING IN GAS TURBINES Published September 1985 542 pages</p>	<p>AGARD-CP-390</p> <p>Heat transfer Cooling in gas turbines Heat exchanger Turbine cooling Blade cooling</p>	<p>AGARD Conference Proceedings No. 390 Advisory Group for Aerospace Research and Development, NATO HEAT TRANSFER AND COOLING IN GAS TURBINES Published September 1985 542 pages</p>	<p>AGARD-CP-390</p> <p>Heat transfer Cooling in gas turbines Heat exchanger Turbine cooling Blade cooling</p>
<p>The Conference Proceedings contain 39 papers presented at the Propulsion and Energetics 6.5th Symposium on Heat Transfer and Cooling in Gas Turbines, which was held 6-10 May 1985 in Bergen, Norway.</p> <p>The Technical Evaluation Report is included at the beginning of the Proceedings. Questions and answers of the discussions follow each paper. The Symposium was</p> <p>P.T.O.</p>	<p>AGARD-CP-390</p> <p>Heat transfer Cooling in gas turbines Heat exchanger Turbine cooling Blade cooling Combustion system Rotating heat transfer Film cooling</p>	<p>The Conference Proceedings contain 39 papers presented at the Propulsion and Energetics 6.5th Symposium on Heat Transfer and Cooling in Gas Turbines, which was held 6-10 May 1985 in Bergen, Norway.</p> <p>The Technical Evaluation Report is included at the beginning of the Proceedings. Questions and answers of the discussions follow each paper. The Symposium was</p> <p>P.T.O.</p>	<p>AGARD-CP-390</p> <p>Heat transfer Cooling in gas turbines Heat exchanger Turbine cooling Blade cooling Combustion system Rotating heat transfer Film cooling</p>
<p>AGARD Conference Proceedings No. 390 Advisory Group for Aerospace Research and Development, NATO HEAT TRANSFER AND COOLING IN GAS TURBINES Published September 1985 542 pages</p> <p>The Conference Proceedings contain 39 papers presented at the Propulsion and Energetics 6.5th Symposium on Heat Transfer and Cooling in Gas Turbines, which was held 6-10 May 1985 in Bergen, Norway.</p> <p>The Technical Evaluation Report is included at the beginning of the Proceedings. Questions and answers of the discussions follow each paper. The Symposium was</p> <p>P.T.O.</p>	<p>AGARD-CP-390</p> <p>Heat transfer Cooling in gas turbines Heat exchanger Turbine cooling Blade cooling Combustion system Rotating heat transfer Film cooling</p>	<p>AGARD Conference Proceedings No. 390 Advisory Group for Aerospace Research and Development, NATO HEAT TRANSFER AND COOLING IN GAS TURBINES Published September 1985 542 pages</p> <p>The Conference Proceedings contain 39 papers presented at the Propulsion and Energetics 6.5th Symposium on Heat Transfer and Cooling in Gas Turbines, which was held 6-10 May 1985 in Bergen, Norway.</p> <p>The Technical Evaluation Report is included at the beginning of the Proceedings. Questions and answers of the discussions follow each paper. The Symposium was</p> <p>P.T.O.</p>	<p>AGARD-CP-390</p> <p>Heat transfer Cooling in gas turbines Heat exchanger Turbine cooling Blade cooling Combustion system Rotating heat transfer Film cooling</p>

<p>arranged in the following sessions: Turbine Blade Internal and External Heat Transfer (9); Turbine Cooling (5); Modelling (5); Combustion Systems (5); Experimental Techniques (7); Compressors/Heat Exchangers (4); and Interaction (4).</p> <p>The purpose of the Symposium was to bring together experts from industry, research establishments and universities to discuss fundamental and applied heat transfer problems relevant to gas turbines, and to exchange practical experience gained in component and engine development and testing. The achievements were listed in the Technical Evaluation Report which includes also some recommendations for future applications and investigation efforts.</p> <p>ISBN 92-835-0378-3</p>	<p>arranged in the following sessions: Turbine Blade Internal and External Heat Transfer (9); Turbine Cooling (5); Modelling (5); Combustion Systems (5); Experimental Techniques (7); Compressors/Heat Exchangers (4); and Interaction (4).</p> <p>The purpose of the Symposium was to bring together experts from industry, research establishments and universities to discuss fundamental and applied heat transfer problems relevant to gas turbines, and to exchange practical experience gained in component and engine development and testing. The achievements were listed in the Technical Evaluation Report which includes also some recommendations for future applications and investigation efforts.</p> <p>ISBN 92-835-0378-3</p>
<p>arranged in the following sessions: Turbine Blade Internal and External Heat Transfer (9); Turbine Cooling (5); Modelling (5); Combustion Systems (5); Experimental Techniques (7); Compressors/Heat Exchangers (4); and Interaction (4).</p> <p>The purpose of the Symposium was to bring together experts from industry, research establishments and universities to discuss fundamental and applied heat transfer problems relevant to gas turbines, and to exchange practical experience gained in component and engine development and testing. The achievements were listed in the Technical Evaluation Report which includes also some recommendations for future applications and investigation efforts.</p> <p>ISBN 92-835-0378-3</p>	<p>arranged in the following sessions: Turbine Blade Internal and External Heat Transfer (9); Turbine Cooling (5); Modelling (5); Combustion Systems (5); Experimental Techniques (7); Compressors/Heat Exchangers (4); and Interaction (4).</p> <p>The purpose of the Symposium was to bring together experts from industry, research establishments and universities to discuss fundamental and applied heat transfer problems relevant to gas turbines, and to exchange practical experience gained in component and engine development and testing. The achievements were listed in the Technical Evaluation Report which includes also some recommendations for future applications and investigation efforts.</p> <p>ISBN 92-835-0378-3</p>

AGARD

NATO  OTAN

7 RUE ANCELLE · 92200 NEUILLY-SUR-SEINE
FRANCE

Telephone 745.08.10 · Telex 610176

DISTRIBUTION OF UNCLASSIFIED
AGARD PUBLICATIONS

AGARD does NOT hold stocks of AGARD publications at the above address for general distribution. Initial distribution of AGARD publications is made to AGARD Member Nations through the following National Distribution Centres. Further copies are sometimes available from these Centres, but if not may be purchased in Microfiche or Photocopy form from the Purchase Agencies listed below.

NATIONAL DISTRIBUTION CENTRES

BELGIUM

Coordonnateur AGARD — VSL
Etat-Major de la Force Aérienne
Quartier Reine Elisabeth
Rue d'Evere, 1140 Bruxelles

CANADA

Defence Scientific Information Services
Dept of National Defence
Ottawa, Ontario K1A 0K2

DENMARK

Danish Defence Research Board
Ved Idraetsparken 4
2100 Copenhagen Ø

FRANCE

O.N.E.R.A. (Direction)
29 Avenue de la Division Leclerc
92320 Châtillon

GERMANY

Fachinformationszentrum Energie,
Physik, Mathematik GmbH
Kernforschungszentrum
D-7514 Eggenstein-Leopoldshafen

GREECE

Hellenic Air Force General Staff
Research and Development Directorate
Holargos, Athens

ICELAND

Director of Aviation
c/o Flugrad
Reykjavik

UNITED STATES

National Aeronautics and Space Administration (NASA)
Langley Research Center
M/S 180
Hampton, Virginia 23665

ITALY

Aeronautica Militare
Ufficio del Delegato Nazionale all'AGARD
3 Piazzale Adenauer
00144 Roma/EUR

LUXEMBOURG

See Belgium

NETHERLANDS

Netherlands Delegation to AGARD
National Aerospace Laboratory, NLR
P.O. Box 126
2600 AC Delft

NORWAY

Norwegian Defence Research Establishment
Attn: Biblioteket
P.O. Box 25
N-2007 Kjeller

PORTUGAL

Portuguese National Coordinator to AGARD
Gabinete de Estudos e Programas

CLAFIA
Base de Alfragide
Alfragide
2700 Amadora

TURKEY

Department of Research and Development (ARGE)
Ministry of National Defence, Ankara

UNITED KINGDOM

Defence Research Information Centre
Station Square House
St Mary Cray
Orpington, Kent BR5 3RE

THE UNITED STATES NATIONAL DISTRIBUTION CENTRE (NASA) DOES NOT HOLD STOCKS OF AGARD PUBLICATIONS, AND APPLICATIONS FOR COPIES SHOULD BE MADE DIRECT TO THE NATIONAL TECHNICAL INFORMATION SERVICE (NTIS) AT THE ADDRESS BELOW.

PURCHASE AGENCIES

Microfiche or Photocopy

National Technical
Information Service (NTIS)
5285 Port Royal Road
Springfield
Virginia 22161, USA

Microfiche

ESA/Information Retrieval Service
European Space Agency
10, rue Mario Nikis
75015 Paris, France

Microfiche or Photocopy

British Library Lending
Division
Boston Spa, Wetherby
West Yorkshire LS23 7BQ
England

Requests for microfiche or photocopies of AGARD documents should include the AGARD serial number, title, author or editor, and publication date. Requests to NTIS should include the NASA accession report number. Full bibliographical references and abstracts of AGARD publications are given in the following journals:

Scientific and Technical Aerospace Reports (STAR)
published by NASA Scientific and Technical
Information Branch
NASA Headquarters (NIT-40)
Washington D.C. 20546, USA

Government Reports Announcements (GRA)
published by the National Technical
Information Services, Springfield
Virginia 22161, USA



Printed by Specialised Printing Services Limited
40 Chigwell Lane, Loughton, Essex IG10 3TZ

ISBN 92-835-0378-3